ARMS 2021

12th National Conference and Exhibition on Aerospace & Defence Related Mechanisms

02 - 04 DECEMBER 2021

PROCEEDINGS

Organised at
Armament Research & Development Establishment
Pashan, Pune - 411 021

Proceedings
of
12th National Conference and Exhibition on Aerospace & Defence Related Mechanisms

ARMS 2021

02-04 December 2021

Organized at

Armament Research & Development Establishment

Pashan, Pune - 411 021

CONTENTS

Test and Evaluation of Mechanisms (TEM)

Warhead Mechanisms (WHM)

Armament Mechanisms

Design Optimization of Extractor Force Transfer Mechanism

Ashutosh Kumar
Aerial Delivery R & D Establishment
Defence Research & Development Organization
Agra
ashutosh_kumar@adrde.drdo.in

R Shriniwasan
Hinode Technologies Pvt Ltd
Chennai
r.sriniwasan@hinode.in

***Abstract*—To paradrop any palletized cargo from military transport aircrafts through its aft ramp, extractor parachute, connected to EFRL (extraction fastening and release lock) of cargo pallet with parachute riser line, is deployed. Once the Platform front end clears the cargo floor ramp, extraction force is transferred from EFRL to main parachute bags for deploying the recovery parachutes & subsequently retarding the pallet speed for safe touchdown. Extraction Force Transfer is a key event in the paradrop operation and it is achieved with help of EFRL mechanism. Any malfunction of EFRL, may inadvertently open the recovery parachute while the platform is still inside the cargo compartment. The excessive drag produced by the large parachutes, may stall the aircraft. This emergency situation could be a catastrophic. While designing the EFRL, in advertent opening of EFRL was noticed. For design optimization and incorporation of a reliable locking feature, a Multi Body Dynamics (MBD) Analysis of the EFRL- Platform system, locked on a guide rail system akin to aircraft cargo floor of C130J aircraft, was carried out using MSC ADAMS. In this paper, effect of geometrical features of mechanism links on EFRL unlocking force has been studied. Study results in identification of critical areas requiring special attention during fabrication and inspection. After the minor modification in the shape of interfering surfaces significant increase in unlocking forces was observed.**

Keywords- Extraction Force Transfer; Multi Body Dynamics; paradrop.

1. Introduction

EFRL plays pivotal role in paradrop operation. Use of MBD software enables the optimization, failure mode identification & failure investigation of these mechanisms. Limited literatures are available on failure modes of these mechanisms. Role of geometric parameters in locking mechanism was analysis for delayed platform separation from aircraft locks [2]. The EFRL unlocking and subsequent force transfer to main parachute bags is caused by the rotation of spring loaded Tripler attached at the front end of the Platform. The rotation of spring loaded Tripler results in the pulling of a cable attached with Catch. Displacement of Catch results in loss of contact with Lock. After that Lock is free to rotate and Lug & Shackle becomes free from the mechanism. This process happens only when Tripler has crossed the ramp edge. Before that, rotation of Tripler is prevented by the contact force due to Cargo Floor. A general arrangement of EFRL, Tripler, Platform and Cargo Floor is shown in Fig. 1. The basic EFRL mechanism and various links are shown in Fig. 2. The Tripler is shown in Fig. 3. After initial observations, study was focused on the profile and contours of the two links i.e Catch & Lock. Further iterations were carried out with increment of catch angle in steps of 1 degree and simulated to find the maximum extraction load the EFRL can withstand before disconnection.

A. Analysis Procedure

CAD models of all the participative components were generated in the SOLIDWORKS and assembly was imported in MSC ADAMS in parasolid format.3D. Contacts between the interacting components were defined in ADAMS. One spring & actuating cable were defined mathematically in the simulation. Extraction parachute force was also defined as a function of canopy inflation time. Extractor Parachute drag was estimated analytically. The force-time curve of this force is shown in Fig 5. Initial run was done at base design. Orthogonal surface of Catch was modified. Contact angle as shown in fig 4 was increased from 0˚ to 5˚. Also the fillet radius was also increased on Lock. The maximum force that could be applied at Lug & Shackle was compared with that of base model.

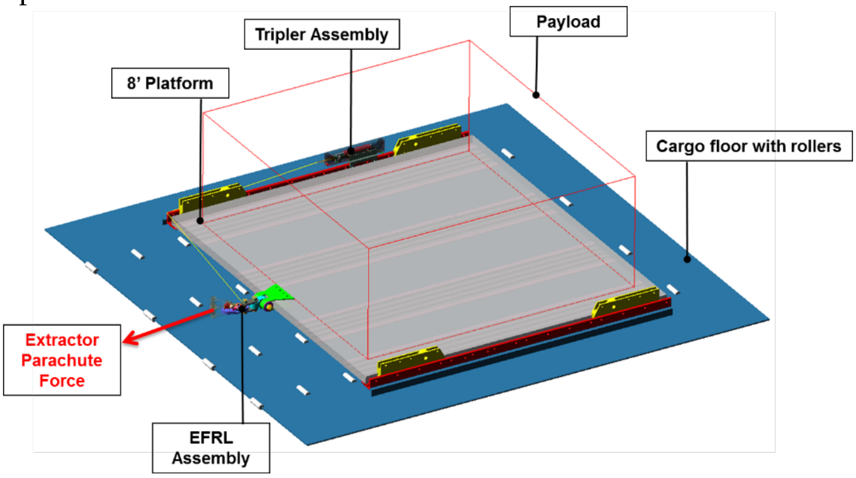

Fig 1: Platform with PFRL & Locking Beam

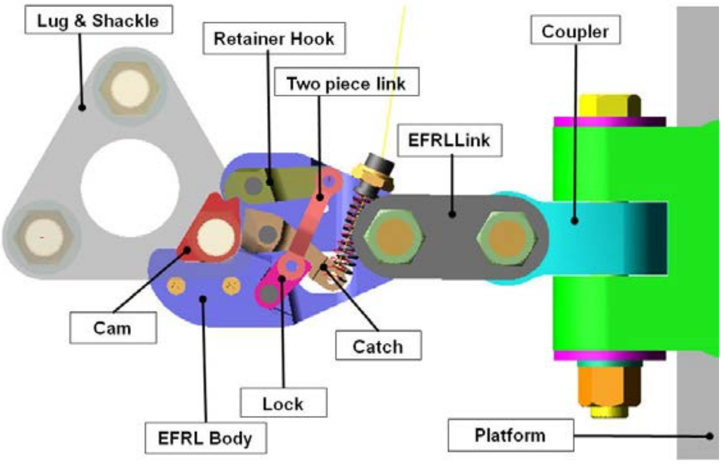

Fig 2: EFRL Assembly and its various links

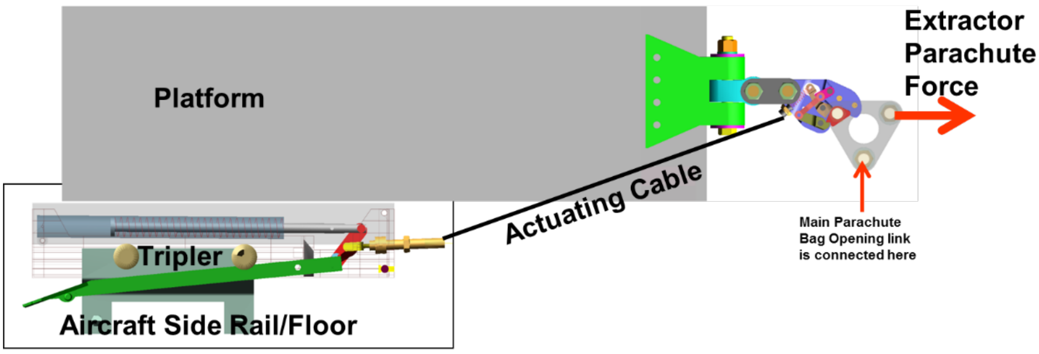

Fig 3: EFRL, Platform and Tripler connection

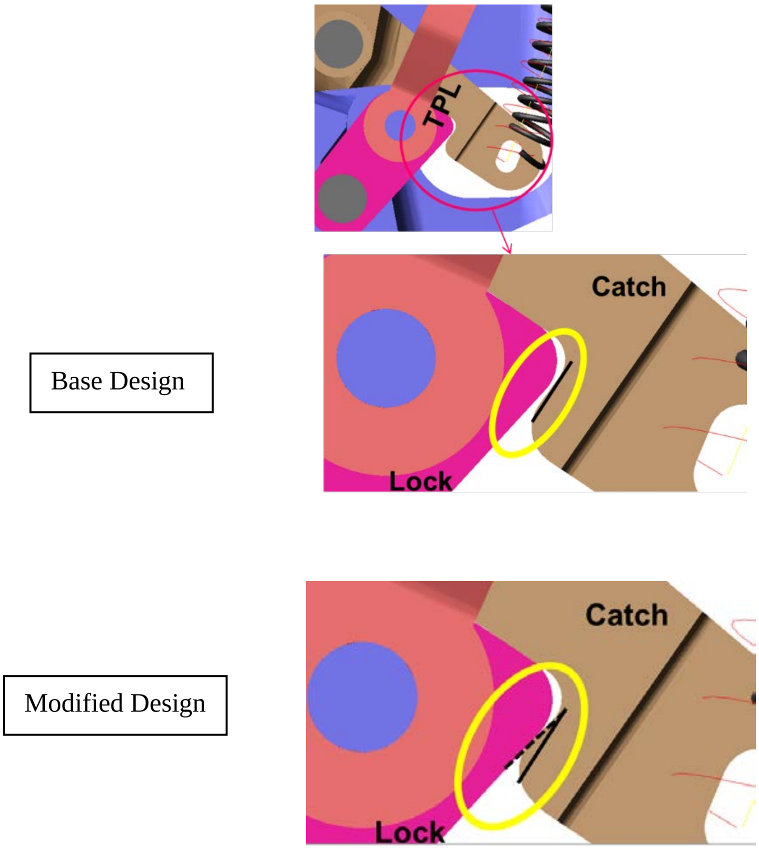

Fig 4: The Base design & Modified profile of Catch and Lock under study.

The modifications were carried out in two parts, namely Catch & Lock. The geometrical changes are depicted in Fig. 4.1 & 4.2.

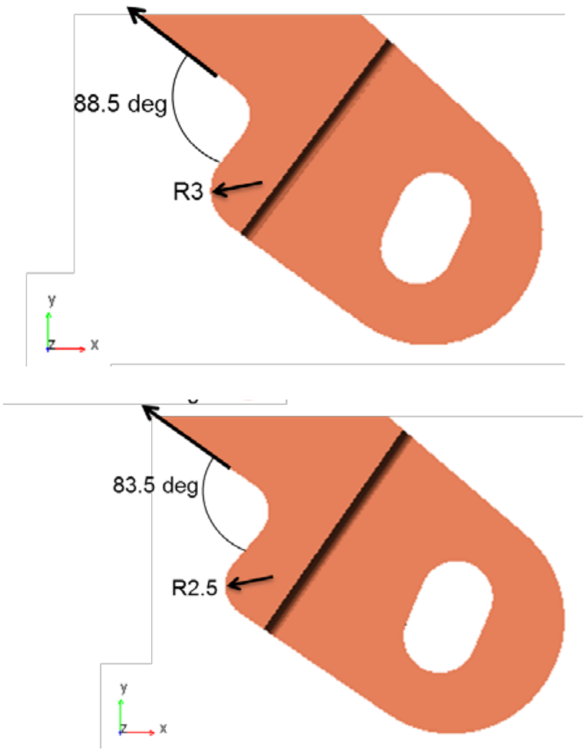

Fig 4.1: The Base design & Modified profile of Catch under study.

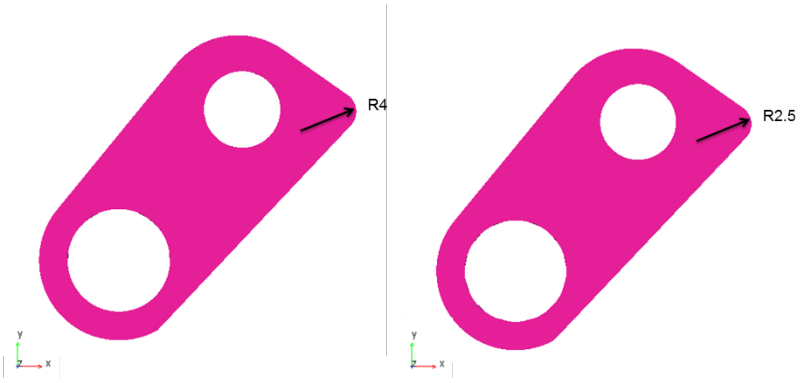

Fig 4.2: The Base design & Modified profile of Lock under study.

B. Simulation Condition
   (i) Extractor Chute Force is applied on Lug & Shackle.
   (ii) Extractor Force is ramped up from 0 to 37000 N from 0.5 sec to 1.0 sec and continued till simulation end.
   (iii) Simulation is carried out for 3.0 sec, with 1000 steps per second.

A base model was prepared and several iterations were done to check its consistency and forces obtained as output were compared with practical values. Sensitivity of the mating plane inclination was checked.

2. Results and Discussion

Before force transfer, Lug & Shackle/Cam link is retained by EFRL Body and Retainer hook. The presence of contact force between Cam and Retainer hook indicates the attachment of Cam/Lug & Shackle with EFRL Body. At the Force transfer point, the contact force diminishes to Nil as lock gets opened. Extraction force was increased and contact force was plotted against extraction force. Iterations were carried out with increment of catch angle in steps of 1 degree and simulated to find the maximum extraction load the EFRL can withstand before disconnection. After that, 5 different geometries having 1˚, 2˚, 3˚, 4˚ and 5˚ angle with original profile were subjected to the analysis. Contact Force and extraction Force are plotted in Fig 6. It can be seen that with original profile the contact force was lost when extraction force reached 73 kN.

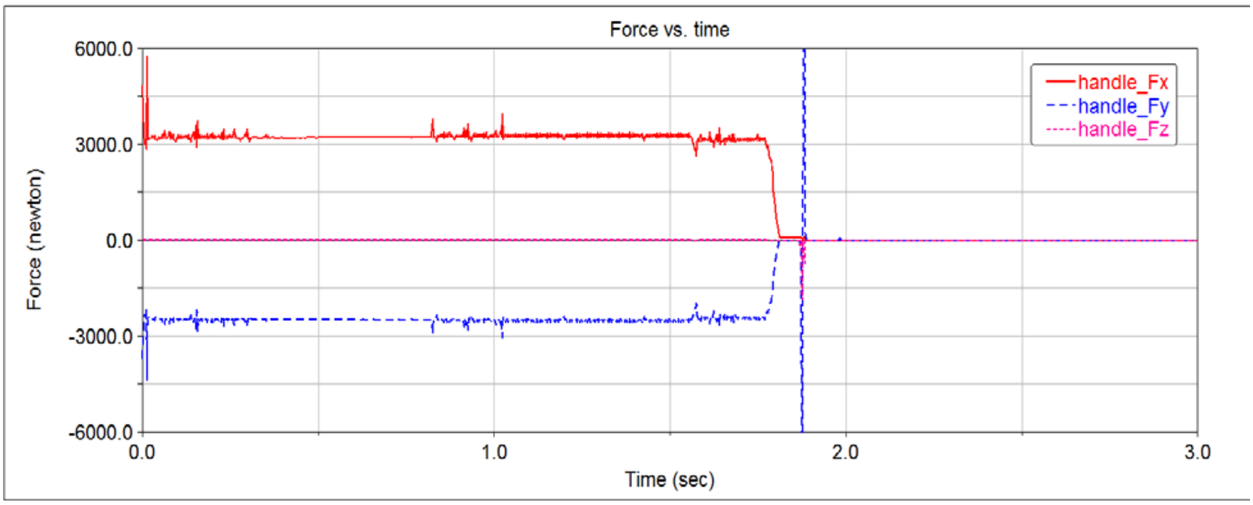

Fig 5: Tripler Handle Force Vs Time

Tripler handle force is plotted in Fig 5. The Tripler handle force depicts the extraction process. Sudden drop in Tripler Handle Force is observed 1.8 seconds after the force application.

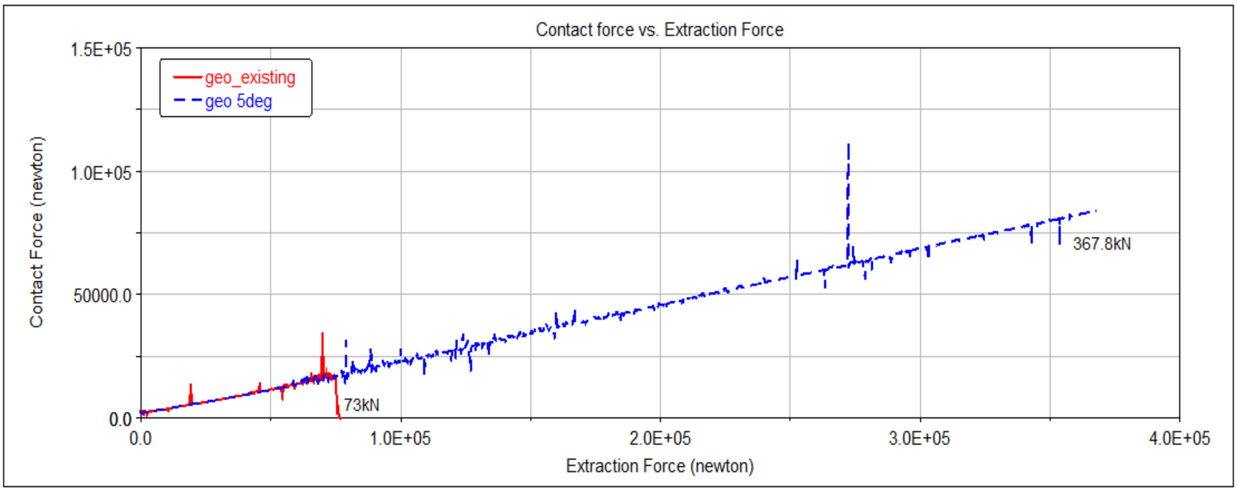

Fig 5.1: Retainer hook - Cam Contact force vs. Extraction force

As it is clear from Fig. 5.1 that retainer hook- Cam contact force diminishes at 73 kN, it indicates the EFRL disconnection.

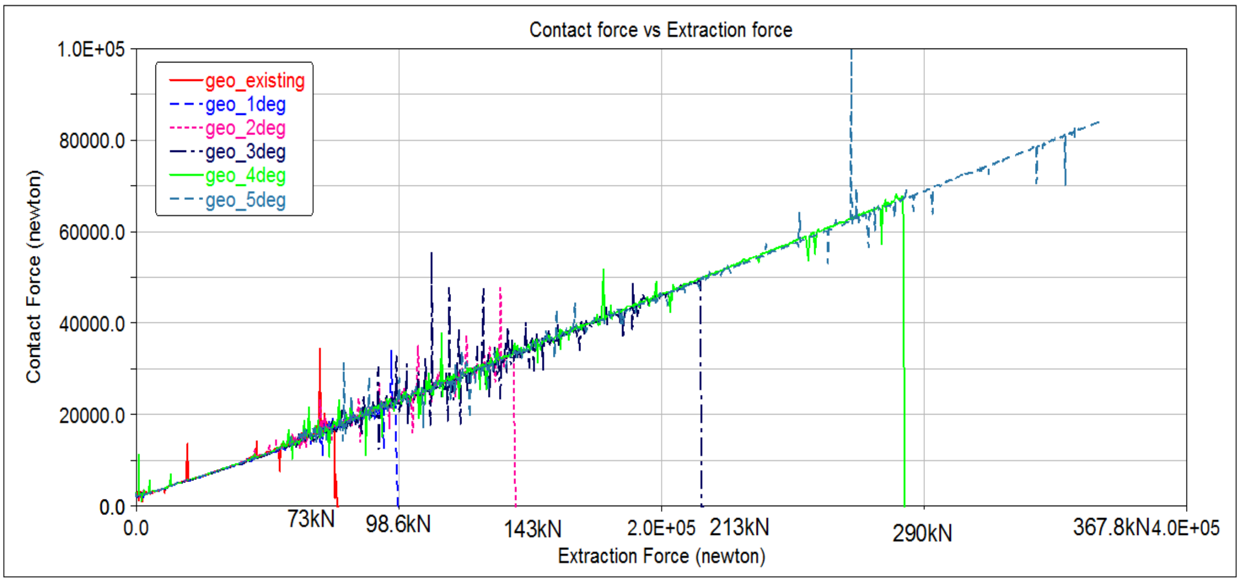

Fig 6: Retainer Hook - Cam Contact force vs. Extraction force

Variation of lock and Catch force has been plotted in Fig. 7. The sudden drop in force can be noticed at the force transfer point.

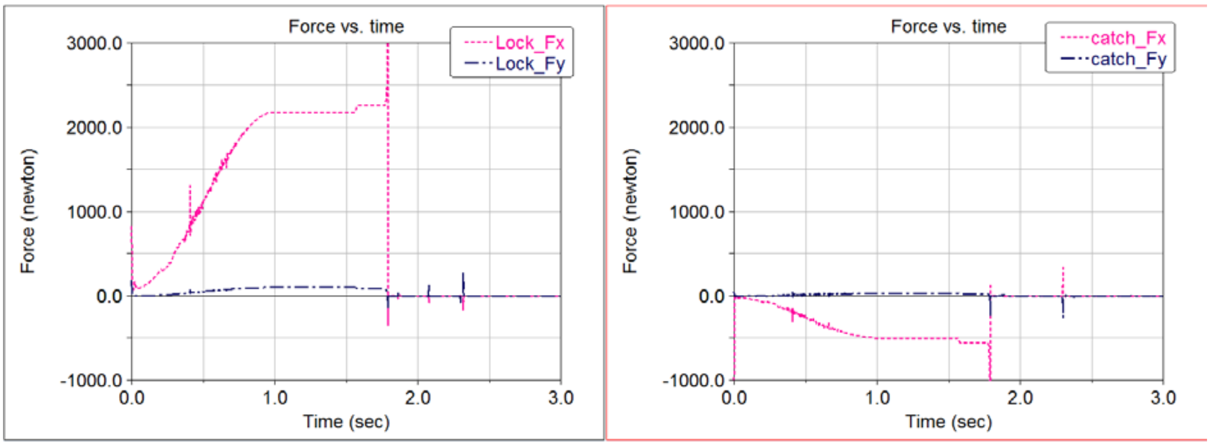

Fig 7: Variation of Retainer Hook force vs. Time

To check the structural strength of the contacting links, an FEA analysis in ANSYS was carried out at full extraction load i.e 370 kN. The boundary conditions are plotted in Fig 8.

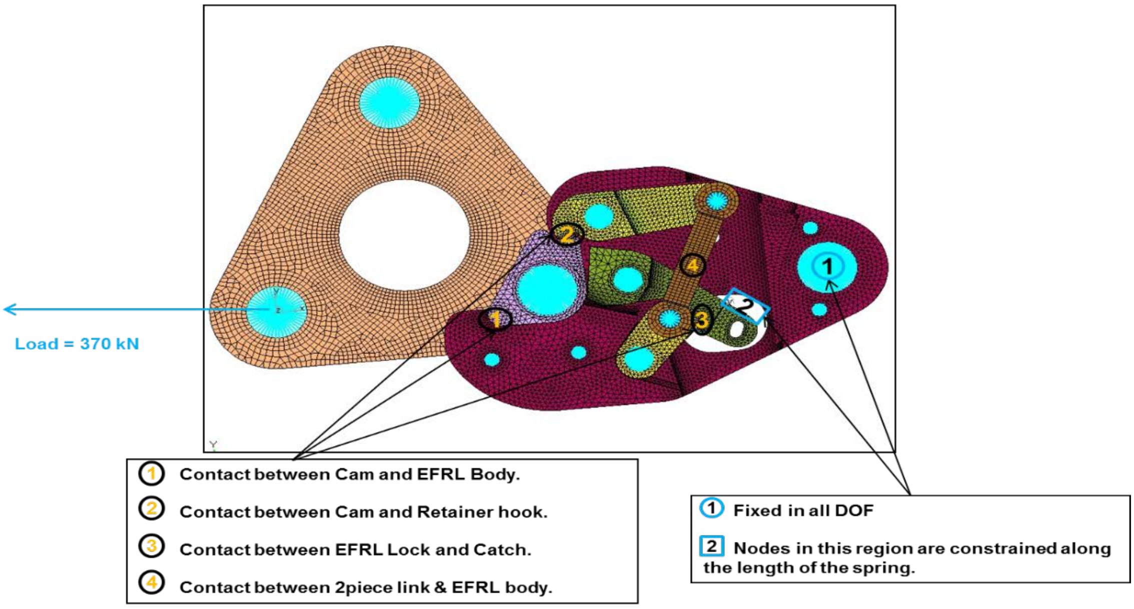

Fig 8: Boundary conditions for FEA of EFRL

Stress plots are shown in Figures 9, 10 & 11 respectively. It can be seen that maximum stress induced in catch is 1118 MPa and Lock is 1093 MPa.

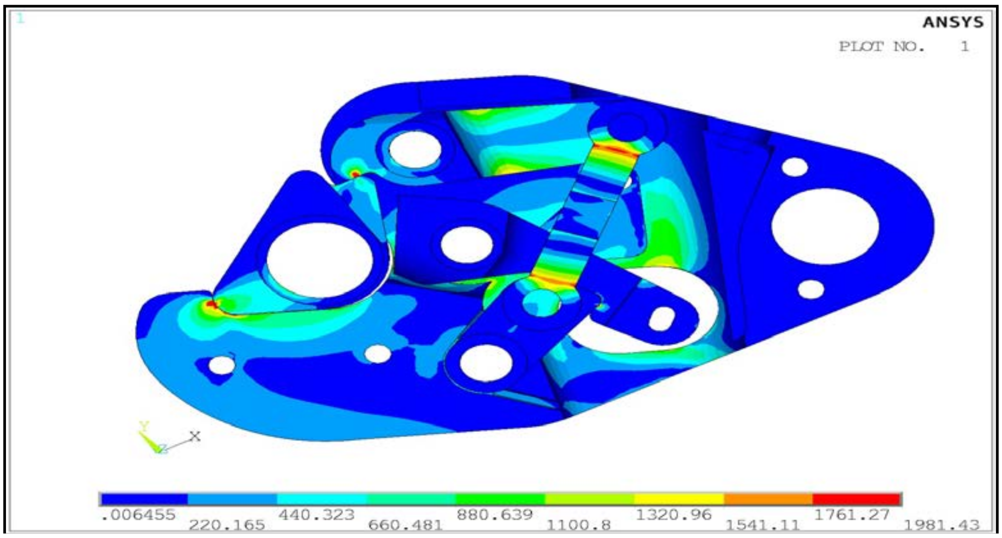

Fig 9: Stress results of complete EFRL

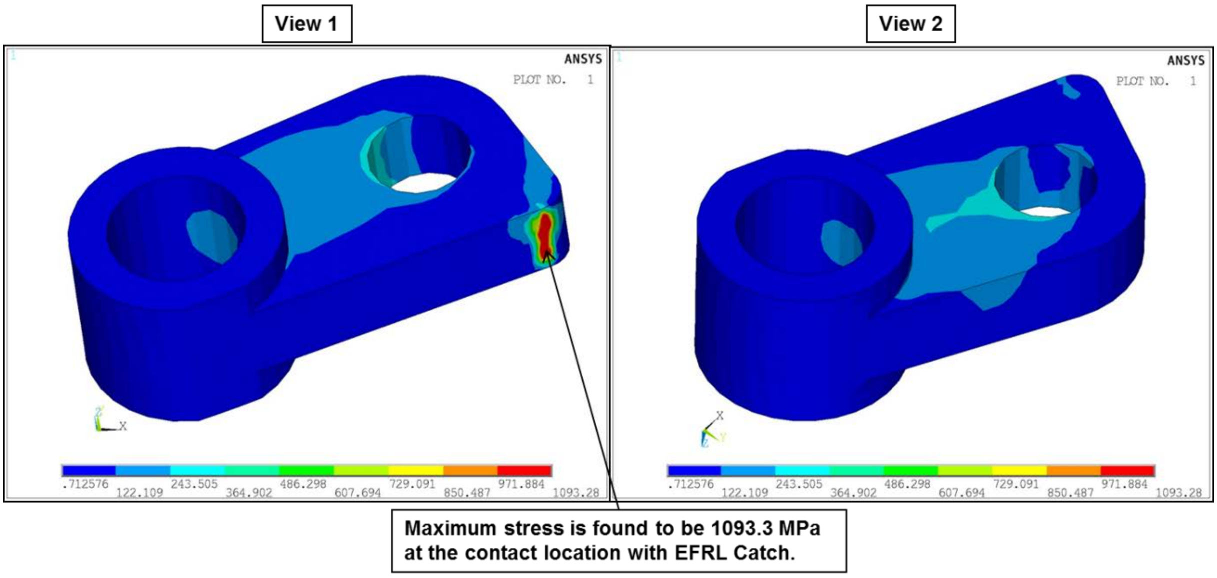

Fig 10: Stress results of complete EFRL Lock

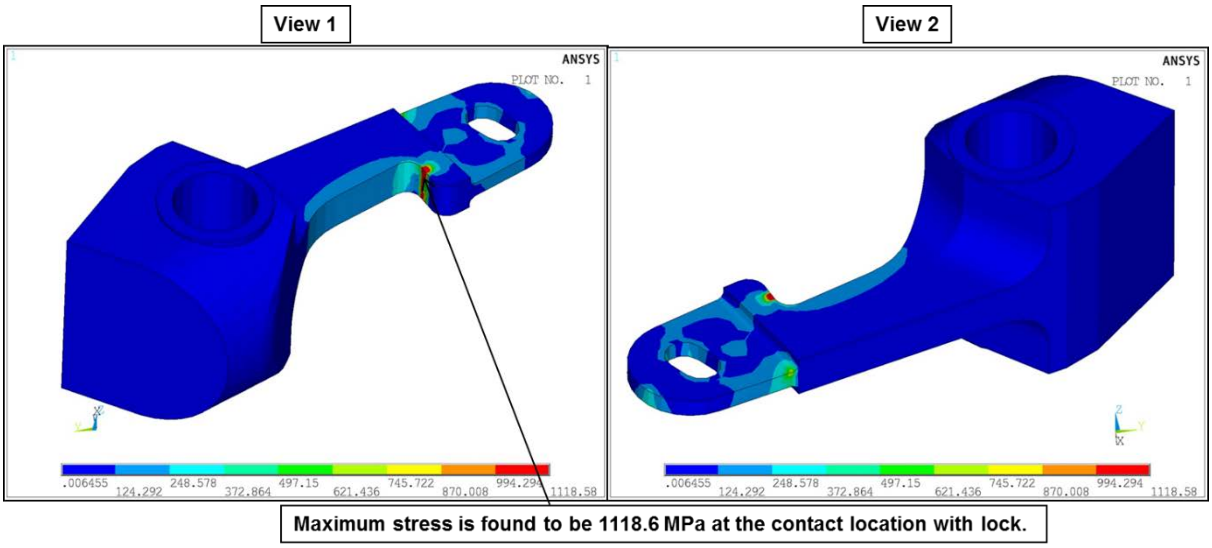

Fig 11: Stress results of complete EFRL Catch

Based on the MBD analysis and FEA, one prototype EFRL mechanism has been fabricated (fig 12). The EFRL has been subjected to functional tests and same has been found satisfactory. After due Airworthiness certifications, the EFRL would be used in flight trials.

Fig 12: Realized hardware of EFRL Mechanism

3. Conclusion

A MBD model was prepared for the simulation of Platform System separation mechanism. In the simulation, it was found that modification and shape optimization has increased the lock's retention force from 73 kN to 367 kN. The structural strength of the related link were also checked and found safe for an extraction load up to 370 kN. FEA is carried out for the redesigned catch & lock with EFRL assembly and deflections & stress contours are plotted. MBD analysis has resulted in identification of critical area for focused attention during fabrication and inspection. This modification can eliminate the need of additional devices required for inadvertent disconnection of the EFRL mechanism.

4. References

[1] MSC ADAMS Software manual/help document.

[2] Ashutosh Kumar, "Study of Role of Geometrical Features of Platform Locking Mechanism", 10th National Symposium and Exhibition on Aerospace and Related Mechanism (ARMS 2016). Thiruvananthpuram, India, November 24-25, 2016

Effect of Inbore Balloting of Artillery Shell at Muzzle Exit

R B Sarsar
Armament Research and Development Establishment
DRDO
Pune
rahulbsarsar@arde.drdo.in

L K Gite
Armament Research and Development Establishment
DRDO
Pune

M Aleem
Armament Research and Development Establishment
DRDO
Pune

***Abstract* — Inbore motion of the projectile, wobbling or balloting inside the barrel damages gun barrel as well as projectile due to lateral impact of the projectile on the gun barrel. The lateral impacts of the projectile on the barrel during in-bore motion also affect the sensitive components of projectile such as fuze, driving band or nubs. Damage to any of such components may results into projectile failure or accidents. Wobbling motion of the projectile develops muzzle jump affecting accuracy of the gun at target end. In this paper, analysis has been carried out to see the effect of balloting on projectile motion. Simulation study has been done for cases where projectile component failure of driving band or nubs has been considered. Effects of these failures on projectile cross acceleration, initial yaw and angular velocity during in-bore motion has been analysed.**

Keywords — In-Bore Motion, Balloting, Cross Acceleration, Driving Band, Artillery Projectile, Nubs

1. Introduction

Balloting analysis can help designer and developers to better understand the interaction between projectile and gun barrel. Balloting is the lateral motion of a projectile perpendicular to its longitudinal axis during in-bore motion. This motion can arise due to various reasons, among these are clearance between projectile and barrel wall, lack of barrel straightness and asymmetry in projectile due to manufacturing tolerances. Balloting motion generates lateral loads which, if grows to significant level will cause excessive dispersion and structural damage to the projectile during in-bore motion. When CG of the projectile and principle axis are offset from the bore axis then the applied force due to base pressure forms an overturning moment with the barrel resistance force. This moment produces the balloting motion of projectile inside the gun barrel. The stiffness and mass distribution of the projectile determines the response to this overturning moment and lateral impact forces. A more flexible structure allows greater CG displacement and subsequent balloting motion. Projectile in-bore motion analysis will help the designer to quantify the dispersion at target end.

In recent past, various researcher and scholars have conducted experiments and numerical analyses on inbore processes. Transverse motion of a traveling projectile through a deformed smooth gun barrel was investigated by Chen who found that balloting is expected to be magnified because of imperfect straightness of gun tube [1]. An analytical model for balloting of FSAPDS shot has been studied where impact of various disturbance source parameters and design parameters for balloting analysis is analysed by R Bhandari et al [2]. A numerical model for in-bore motion of a typical artillery shell has been developed to study the maximum stress & strain developments [3]. A nonlinear dynamic analysis of a balloting-projectile with six-degree-of-freedom coupled model of the projectile and gun tube system is presented by Ansari et al [4]. There are many perturbing factors which may possibly contribute to balloting motion of a projectile inside the gun barrel. In this work, in bore balloting motion analysis has been carried out for cases where artillery projectile component failure like driving band or nub has been considered. Effects of these failures on projectile cross acceleration, initial yaw and angular velocity during in-bore motion has been analysed.

2. Mathematical Model of Projectile Balloting Motion

Artillery gun and projectile are subjected to relatively high dynamic forces. The barrel of a gun moves transversely while the projectile is still in the bore. This has contributed to gun jump as well as aerodynamic jump and to the initial yawing rate of the projectile which are the main cause of dispersion. There are many perturbing factors which leads to the transverse motion of a gun barrel such as projectile load and loads related to recoil acceleration. It all depends upon the propellant gas pressure and projectile's displacement and velocity inside the gun barrel.

The mathematical model developed in this study is a six-degree-of-freedom coupled model of the gun tube and projectile. The gun tube and projectile will have axial, lateral and rotational motion due to recoil and vibration. As the projectile moves down the gun bore, the bourrelet and the obturator will impact with the bore wall and then rebound from it. This effect has been included by using simple restoring springs to represent the interaction between the bore and the projectile. The Lagrange's equations of motion are given below [4].

$$\frac{d}{dt}\left(\frac{dL}{d\dot{r}_i}\right) - \frac{dL}{dr_i} = F_i, \quad i = 1, 2, \cdots 6 \qquad \cdots(1)$$

Where, L Lagrangian function, which is the difference between the system kinetic energies and potential energies, F_i is the non – conservative force acting in each coordinate direction r_i and $\dot{r}_i$ is velocity associated with the coordinate r_i . The six coordinates considered here are three each for gun and projectile; in axial, lateral and rotational motion. The expression for Lagrangian function L is given by equation (2).

$$L = \left\{\frac{1}{2}m_g\left(\dot{X}_g^2 + \dot{Y}_g^2\right) + \frac{1}{2}I_g\dot{\theta}^2 + \frac{1}{2}m_g\left(\dot{X}_p^2 + \dot{Y}_p^2\right) + \frac{1}{2}I_p\dot{\alpha}^2\right\}$$
$$- \left\{m_g g Y_g + m_p g Y_p + \frac{1}{2}S_b d_b^2 + \frac{1}{2}S_o d_o^2 + \frac{1}{2}S_{o1}\left(d_0 - RC_o\right)^2\right\} \qquad \cdots(2)$$

Where, m_g and m_p are gun and projectile mass respectively. X_g and Y_g are displacement of gun in X and Y axes. X_p and Y_p are displacement of projectile in X and Y axes. I_g and I_p are moment of inertia of gun and projectile respectively. θ and α are angular displacement of gun and projectile in the direction of positive Z axis. g is acceleration due to gravity. S_b is spring constant for bourrelet and gun-bore contact spring deflection model. S_o is stiffness of obturator plastic band in obturator transverse spring model. d_b is displacement of projectile into the gun bore at contact between bourrelet and gun bore. d_o is projectile displacement at obturator. S_{o1} is stiffness of metallic part in obturator transverse spring model. RC_o is radial clearance between obturator and gun bore. The equation (1) can be written in matrix form as follows.

$$[A_1]\{\ddot{r}_i\} + [A_2]\{\dot{r}_i\} + [A_3]\{r_i\} = \{F_i\} \qquad \cdots(3)$$

Where, $[A_j]$ are 6 x 6 matrices, $\{F_i\}$ is force column matrix and r_i is a vector of generalized coordinates. To carry out the simulation study, simulation model of projectile and gun barrel needs to be developed. The projectile and gun barrel model are developed in PRODAS software.

3. BALANS Model for In-bore Motion

ERFB-BT projectile and 155mm Barrel are modelled and inbore motion of projectile is simulated in PRODAS (Projectile Rocket Ordnance Design and Analysis Software). The barrel and projectiles are divided into sections called nodes. Projectile is divided into 29 nodes as shown in Figure 1 and barrel into 23 nodes as shown in Figure 2. The main objectives of the study is to simulate the conditions of in-bore balloting of the projectile and effect of stress on projectile. To see the effect on point of contact of projectile surface to gun bore and gun bore to the structure, springs are placed at required nodes in both model of projectile and barrel. ERFB – BT 155mm projectile is modelled with springs are located at obturator forward Bourrelet, linear spring is taken at obturator end, since gap is not allowed at obturator whereas non-linear spring is taken at forward Bourrelet as shown in Fig. 1. A 155mm barrel is modelled with three springs on gun tube placed at breech end, for recoil and for forward support as shown in Fig. 2.

The mass properties of the projectile and gun barrel are calculated using PRODAS. The axial location wise mass of each node of projectile and gun barrel is given in Table 1.

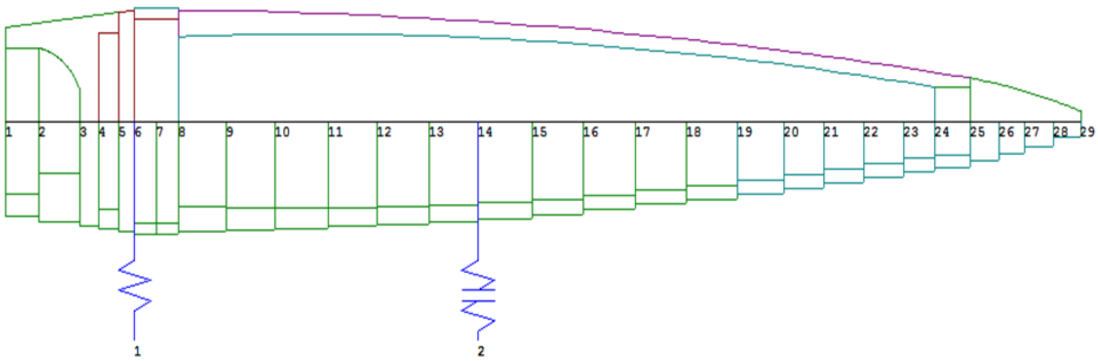

Figure 1: ERFB Projectile Model and Its Nodes

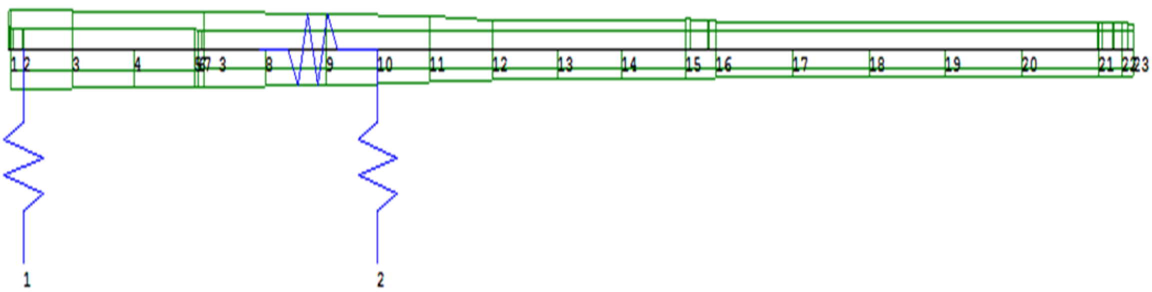

Figure 2: Barrel and Its Nodes

4. Simulation and Results

In-bore motion of the projectile and balloting simulation reduces development and production risk by enabling the program manager to understand the effect of uncontrollable variables on system performance prior to committing the design to production. Simulation study has been carried using 155mm ERFB BT shell with 45kg of weight and 155mm x 52 cal barrel. Simulation is carried out for following cases, i) Nominal case, ii) Driving band failure, iii) Nubs failure.

Table 1: Projectile and Gun Barrel Nodes Location and their Masses

Projectile						Gun Barrel					
Node	**Axial Location**	**Mass**	**Node**	**Axial Location**	**Mass**	**Node**	**Axial Location**	**Mass**	**Node**	**Axial Location**	**Mass**
	mm	**kg**		**mm**	**kg**		**mm**	**kg**		**mm**	**kg**
1	0	0.23	16	525	1.70	1	15	27	16	5071	59
2	30	0.66	17	565	1.56	2	103	112	17	5619	78
3	65	0.96	18	605	1.41	3	455	155	18	6168	75
4	80	1.31	19	645	1.20	4	895	171	19	6717	73
5	100	1.93	20	680	1.01	5	1335	85	20	7266	70
6	115	2.46	21	715	0.91	6	1360	14	21	7815	44
7	135	2.93	22	750	0.80	7	1400	105	22	7983	15
8	152	3.25	23	785	0.62	8	1838	168	23	8063	5
9	200	3.63	24	810	0.57	9	2276	141			
10	250	3.38	25	845	0.43	10	2646	119			
11	300	3.59	26	870	0.22	11	3016	115			
12	350	3.31	27	890	0.14	12	3470	94			
13	395	2.24	28	915	0.07	13	3932	85			
14	440	2.23	29	940	0.02	14	4394	81			
15	485	1.95				15	4856	58			

A. Nominal Case:

The developed projectile and gun barrel model are simulated using PRODAS. Muzzle velocity and peak pressure are obtained using internal ballistics model of PRODAS and validated with experimental results. The simulated muzzle velocity is 883 m/s with 321 MPa peak chamber pressure as shown in Fig. 3 whereas experimental result show 879 m/s muzzle velocity with 320 MPa peak chamber pressure. This validate the model developed for projectile and gun barrel in PRODAS. The remaining study will be carried out with this model for three different failure conditions stated above.

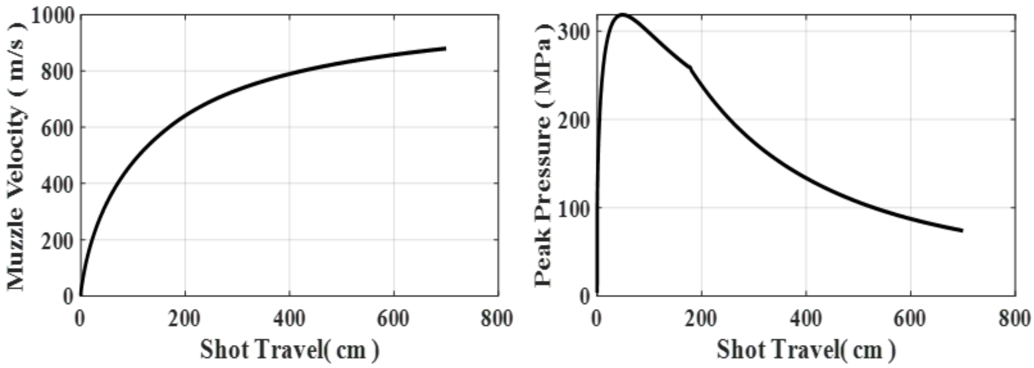

Figure 3: Pressure and Muzzle Velocity Profile

B. Driving Band Failure Case:

The driving band failure is simulated with the assumption that all contacts are intact and only diameter of driving band is reduced to barrel diameter. Driving band failure and nominal case are found to give similar results Since the support at rear and front end is intact throughout the motion of the projectile inside the barrel, drive band failure does not affects cross acceleration and yaw rate (Fig. 4). It is observed that driving band failure doesn't affect the yaw angle and also the cross velocity as compared with nominal case.

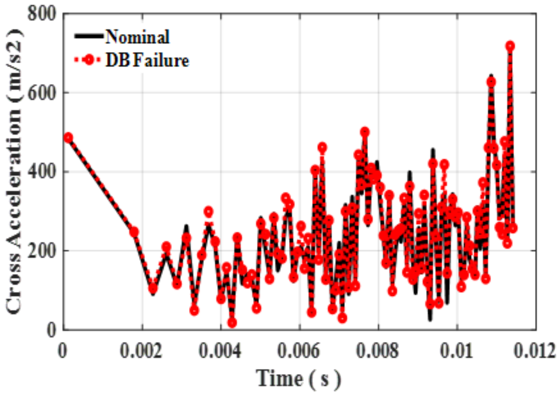

Figure 4: Driving Band Failure effect on Cross Acceleration and Yaw Rate

C. Nubs Failure Case:

It is observed that if all nubs failure occur during projectile motion inside the barrel then large cross velocity and cross acceleration are generated, which indicates in-bore balloting of projectile. The yaw angle which is 0.21 deg and maximum yaw rate is 3 rad/s at muzzle end in nominal case, increase to 2.37 deg and to 54 rad/s respectively in all nubs failure case as shown in Fig. 5. The yaw rate is increased due to which large yaw angle fluctuations are observed during all nubs failure. The effect of all nubs failure increases the cross acceleration which is as high as 14475 m/s^2 during in bore motion, increasing the cross velocity upto 22.90 m/s at muzzle end compared with 1.32 m/s in nominal case.

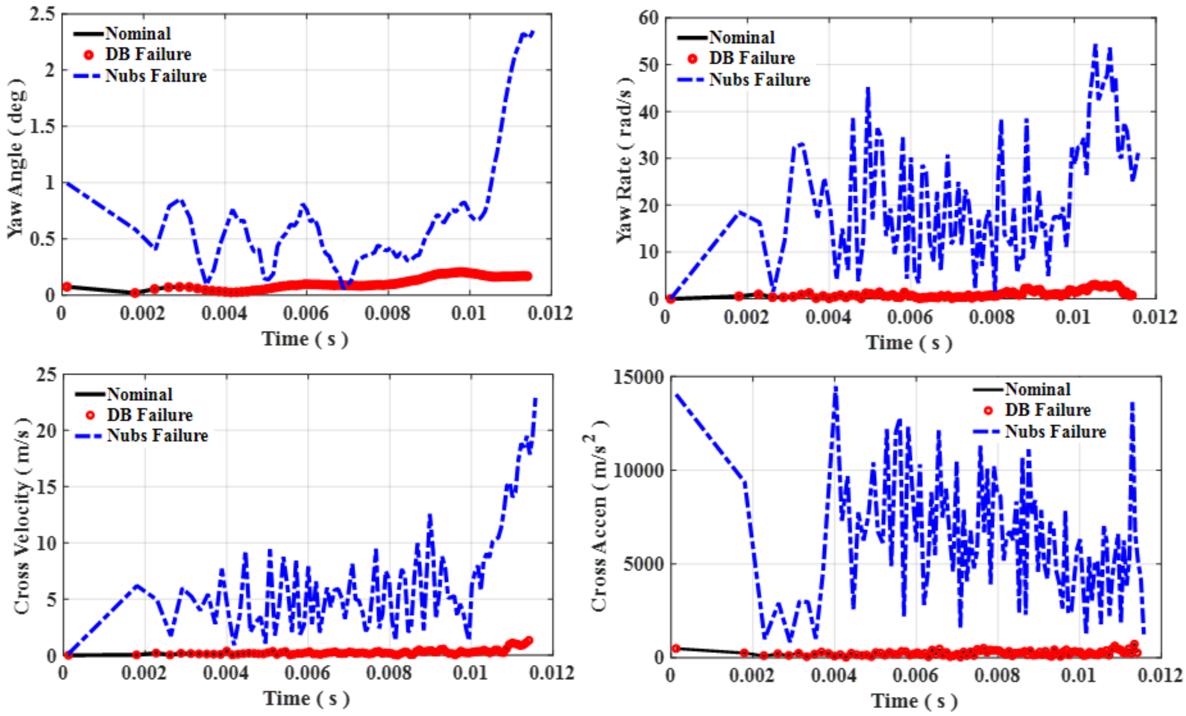

Figure 5: All Nubs Failure effect on Inbore Motion

The displacement of each node of projectile is computed at every instance of time. The maximum displacement, shear force, centripetal force and bending moments experienced by each node during travel by the projectile are converted to equivalent stress. In case of two and all nubs failure, simulation indicate that projectile undergoes high stress where, maximum equivalent stress increases by 580 MPa in all nubs failure case as shown in Fig. 6.

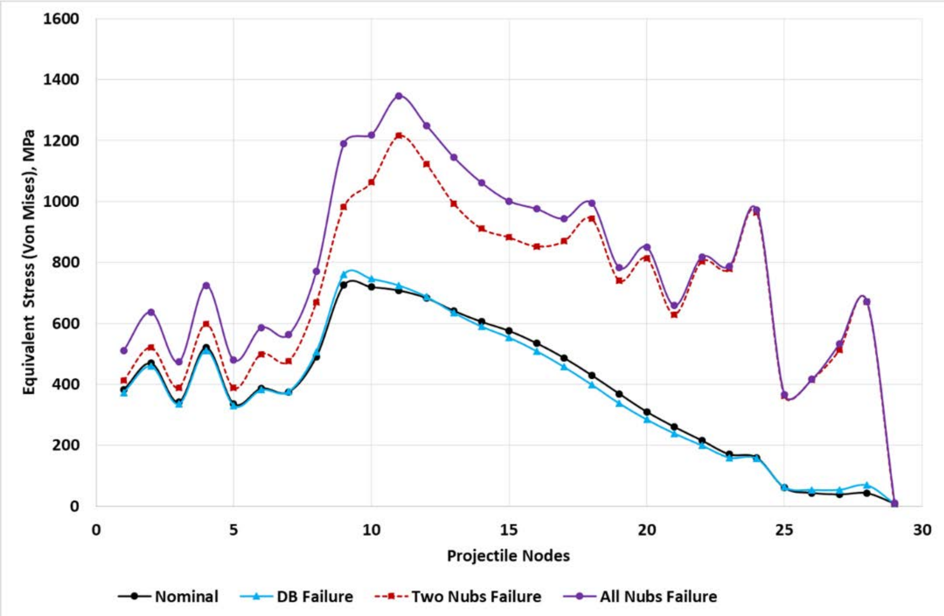

Figure 6: Equivalent Stress on Projectile during In-Bore Motion

5. Conclusion

The ERFB-BT projectile and Barrel model has been developed in PRODAS and in-bore motion of the projectile is simulated using PRODAS. The projectile failure cases has been analysed and compared with nominal case. It is observed that cross acceleration and equivalent stress are high in nubs failure case. This results into large yaw rate and yaw angle at muzzle exit which is not desirable in terms of accuracy at target end.

6. References

[1] M. M. Chen, “Projectile Balloting Attributable to Gun Tube Curvature”, Vol. 17, Shock and Vibration, pp. 39 – 53, 2010.

[2] R. Bhandari, R. L. Saini, and R. D. Misal, “An Analytical Model for In-bore Balloting of FSAPDS Projectile”, 2nd National Conference on Advances in Armament Technology, pp. 581 – 586, 2018.

[3] T. R. Panda, A. Banerjee, “Numerical Simulation of The In-Bore Motion of A Typical Artillery Shell and Investigation of Balloting”, 31st International Symposium On Ballistics Hyderabad, India, pp. 1149 – 1160, 2019.

[4] K. A. Ansari and J. W. Baugh, “Dynamics of A Balloting Projectile In A Moving Gun Tube”, Battelle Pacific Northwest Labs Richland Wa, 1988.

[5] D. E. Carlucci and S. S. Jacobson, “Ballistics: Theory and Design of Gun and Ammunition”, CRC Press, London, 2008.

[6] J. Corner, “Theory of the Interior Ballistics of Gun”, Wiley, New York, 1950.

[7] “Text Book of Ballistics and Gunnery”, Volume 1, 1987.

155 mm Ramjet Projectile Design for Artillery Guns

Navaneeth P
Anna University
Chennai
nadnavap@gmail.com

Mythily D
Anna University
Chennai
apjigniters@gmail.com

Abstract – Works are being made to improve the range of ballistic properties since centuries by people at every level of academic achievement, some of the world's greatest mathematician and physicist such as Newton, Lagrange Bernoulli and others solved problem in mathematics and mechanics that either directly or indirectly were applied to various ballistic discipline. The stochastic behaviour that dominates all of the ballistic disciplines stems from the tremendous number of parameters that affects muzzle velocity, initial yaw, flight behaviour etc. The development of a ramjet-based artillery with effective PGK system overcomes all these parameters which coordinates an advancement in gun projectile charge combination, a detailed work of developing and testing a ramjet-based artillery projectile design which is of 155mm base shot from latest ATGS system with same internal calibre made indigenously. The study consists of two design variants with analysis and complete graphical design overview. This class of ramjet artillery system comes under extreme range category producing high performing artillery ammunition, this is a hybridization of ramjet system and an artillery shell, thus we are talking about a range that is five to eight times greater than conventional artillery ammunition with the guidance system, we can consistently hit an area as small as the centre of football field and even though the payload is somewhat smaller, the high kinetic destructive force will likely be greater because of the accuracy. On an overall view this system gives a tremendous boost to armed forces of India by indigenous development of these kind of systems our country achieves technological advancement globally than the developed countries. This paper gives a complete study of design parameters and propellant analysis with flow-based calculations, the prototype is also developed for the given design.

Keywords– Ramjet system, Guided artillery shells, Rocket assisted projectile, Ducted-solid motor design conditions, Aluminized solid propellant, HTPB Fuel, Shell structural analysis, Ramjet Solid propellant combustion, Flame zone analysis, Boundary layer and erosive burning theoretical analysis, Flow analysis, Fabrication technique.

1. Introduction

The ramjet system hybridization with the artillery projectile shell is a game changer to artillery system as improving the range up to 120km to 150km, unlike a base bleed or a rocket artillery this system has fuel rich propellant (up to 100%) and the ambient air as an oxidizer for the propellant combustion.

A. The Basic Schematic of this System

Since 1657 the friction-oriented rocket iron propulsion systems have been thought by many inventors. But in the year of 1913 the actual ramjet engine prototypes were made for rocket propellant impaired by stove pipe combustion.

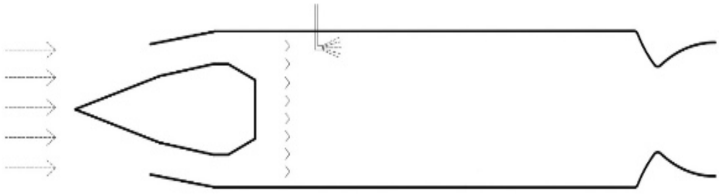

Figure 1: Schematic of ramjet engine

B. Artillery Shell

A **shell** is a payload-carrying projectile that, as opposed to a solid round-shot, contains an explosive, incendiary or other chemical filling, though modern usage sometimes includes large solid kinetic projectiles properly termed **shot**. Solid shot may contain a pyrotechnic compound if a tracer or spotting charge is used. Originally it was called a **bombshell**, but "shell" has come to be unambiguous in a military context.

All explosive- and incendiary-filled projectiles, particularly for motors, were originally called *grenades*, derived from the French word for pomegranate, so called because of the similarity of shape and that the multi-seeded fruit resembles the powder-filled, fragmentizing bomb. Words cognate with *grenade* are still used for an artillery or mortar projectile in some European languages.

Shells are usually large-caliber projectiles fired by artillery, armoured, fighting vehicle (e.g., tanks, assault, guns and motor carriers), warships and some ground attack airship (gunship). The shape is usually a cylinder topped by an ogive-tipped nose cone for good aerodynamic performance, and possibly with a tapered boat tail but some specialized types differ widely.

C. Guided shells

Guided or "smart" ammunition features some method of guiding itself post-launch, usually through the addition of steering fins that alter its trajectory in an unpowered glide. Due to their much higher cost, they have yet to supplant unguided munitions in all applications.

Figure 2: Prototype of 155mm pseudo ramjet artillery projectile

D. Base Bleed Projectile with Guidance

Base bleed is a system used on some artillery shells to increase their range, typically by about 20–35%. Since base bleed extends the range by a percentage, it is more useful on longer range artillery where an increase of approximately 5–15 kilometres (3.1–9.3 mi) can be achieved. Until the late 1980s the small gains in range were not considered worthwhile for field artillery. Base bleed shells are becoming more common in units equipped with modern artillery which have far greater range than the old ones, but are usually only used at close to, and beyond, normal maximum ranges due to the higher cost per shell.

Most (50–60%) of the drag on an artillery shell comes from the nose of the shell, as it pushes the air out of its way at supersonic speeds. Shaping the shell properly can reduce this drag but it is difficult to remove.

However, another powerful source of drag is the low-pressure area left behind the shell due to its blunt base. Base bleed can reduce this drag without extending the base of the shell. Instead, a small ring of metal extends just past the base, and the area in the rear of the shell is filled with a small gas generator. The gas generator provides little to no thrust, but fills the vacuum in the area behind the shell with an inflow of gas, dramatically reducing the drag. The lessened turbulence also turned out to produce tighter grouping due to the projectiles having a more consistent trajectory. The only disadvantage, apart from a higher price per shell, was a small loss in explosive payload in older shells due to some of the space.

Figure 3: Schematic of ramjet shell along with base bleed unit.

2. Non-Isentropic Design Conditions for Shell (Conceptual)

The schematic of the complete blueprint of design 1 and 2 for Ramjet Artillery System is given below,

$$ds = \frac{\delta q_{rev}}{T} + (\delta q)\ Irr \neq 0$$

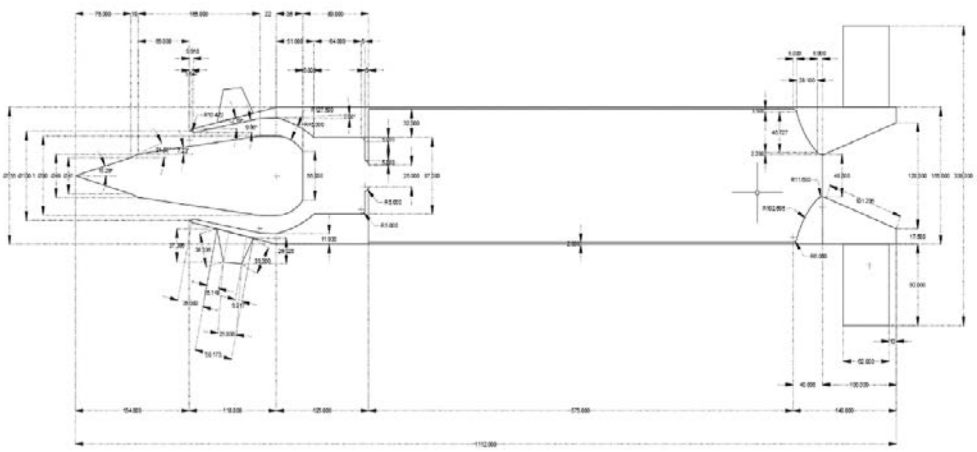

Figure 4: Complete Blue Print Image of Design 1

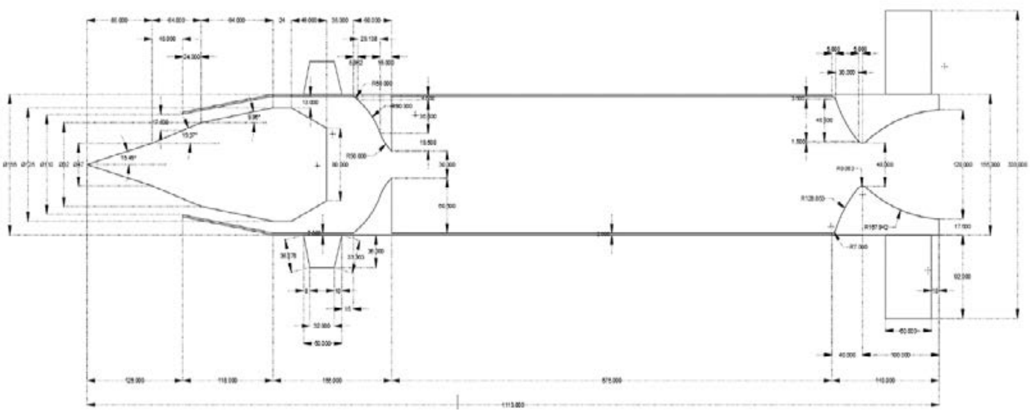

Figure 5: Complete Blue Print Image of Design 2

Note: The dimensions of blue print of both these design are subjected to the designers rights, kindly refer this for an example dimensional view.

When we say non-Isentropic condition there is a drop in pressure with respect to upstream condition compared with downstream value. Thus, this condition suits for flow a shock wave where the entropy is not constant since there is an irreversible addition of heat $\delta q_{irr} \neq 0$ thus the entropy value exists. Thus, there will be a drastic change across a shock wave when compared to small change in flow in subsonic conditions due to any disturbance. Thus, the isentropic relation won't be used for supersonic disturbance thus the design of supersonic structure needs the calculation of the oblique shock and normal shock relations with respect to pressure.

The isentropic equation from the basic fluid mechanics changes as follows.

$$\text{Mass: } \frac{\partial \dot{\rho}}{\partial t}+\nabla.(\rho\vec{u})=0$$

$$\frac{\partial \dot{\rho}}{\partial t}+\vec{u}\nabla\rho+\rho\nabla\vec{u}=0$$

Where,

$$\frac{\partial\rho}{\partial t}+\vec{u}\nabla\rho=\frac{D\rho}{Dt}.\text{ Total derivative,}$$

$$\frac{D^{\rho}}{D^{t}}+\rho\nabla\vec{u}=0\rightarrow(1)$$

Momentum

$$\frac{\rho\partial\vec{u}}{\partial t}+\rho(\vec{u}\nabla)\vec{u}+\nabla\rho=\rho\vec{F}+\nabla_{\tau}$$

Where $F_{B=}$ Body force per unit mass

τ = shear force.

For isentropic condition equations the body force and shear force of the fluid element is neglected, But in real case it won't.

Net Energy

$$\frac{\rho D h_0}{Dt}=\frac{\partial\rho}{\partial t}+\rho\vec{F}\vec{u}+\nabla\cdot(\tau\vec{u})-\nabla\cdot\vec{q}$$

Where the change in energy, h_0= u +PV for Non-Isentropic condition say its equal to sudden unsteady pressure rise across a shock (NSW or Expansion wave), bulk fluid force work on the system increases the energy,

Shear stress doing work increases the energy and divergence heat losses the energy of the system or $(-\nabla).q$ is convergence of heat which in turn increases the energy for Non-Isentropic condition. Thus, these basic conservative equations are used for making calculations of a Non-Isentropic real case condition. Thus, this equation illustrates the mechanism by which the mass, momentum and energy of fluid can be changed for a Non-Isentropic flow.

A. Calculations for Ramjet Artillery Shell Intake (Design 1)

The intake of the ramjet shell is installed with shock cone which is designed to produce a certain strength of oblique shock for a given inlet velocity. The downstream velocity depends upon the shock strength which is created for the given particular deflection angle. The calculation are as follows,

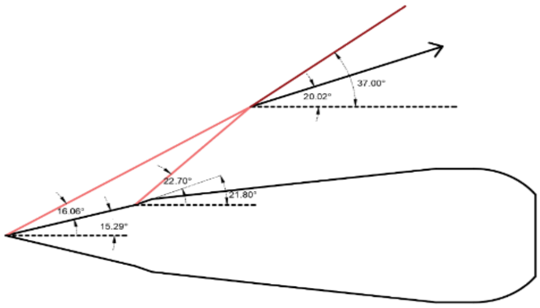

Figure 6: Oblique shock formation for Design 1

For $M_1 = 3.12$ $\theta = 15°$
$M_2 = 2.327$ for weak shock where $\beta = 31.53$

Compression in supersonic flow is non-isentropic. Generally, they take place through shock waves and are non-isentropic. But there are certain cases, for which the compression is isentropic. For the designed inlet cone the compression takes place through series of compression point of variable deflection angle which is individually a weak oblique shock their shocks pave a way for continuous turning of flow with combination of two or more weak shock which coalesce to form a strong or weak oblique shock at the outer section of the shell as shown in fig. Thus, the flow entering the inlet clearance will be turned by two or more weak shocks before overlapping into strong shock thus creates an oblique shock flows, the shock coalesces away from the wall of inlet spike to form a strong shock. Thus, the entropy increase across a weak wave is of the order of third power of deflection angle.

From the entropy change relation with the deflection angle,

$$\Delta s = \theta^3$$

$$\frac{P2 - P1}{p} = \frac{\Delta p}{p_1} \approx \frac{\gamma M_1^2}{\sqrt{M^2 - 1}}\theta$$

$$\frac{P2}{P1} = 1 + \frac{2\gamma}{\gamma + 1}\{M_1^2 \sin^2\beta - 1\}$$

$$\tan\theta = 2\cot\beta\left[\frac{M_1^2}{M_1^2}\frac{\sin^2\beta - 1}{(\gamma + \cos 2\beta)}\right]$$

$$M_1^2 \sin^2\beta - 1 = \frac{\gamma + 1}{2} M_1^2 \frac{\sin\beta \sin\theta}{\cos(\beta - \theta)}$$

We can say that for first order change of pressure, temperature and density with respect to (Δs), gives only as third order change of entropy. That is, weak shock produces a nearly isentropic change of state.

So, the design for the inlet compression gives high efficiency by reducing the heat addition thus the warhead material is prevailed form increment in temperature,

But the Downstream much number obtained from the initial wedge with a horizontal length 75mm can only produce M_2=2.327 thus the conventional Armament design step has been done which is used in major ballistic ammunition systems, i.e., a sudden increment of deflection angle θ_2, for a given horizontal distance of shock up to a certain distance which gives an effective but nearly isentropic flow across the weak shock near the wall that is formed over θ_2 the calculations are as followed,

For, $M_{2=}2.327$, $\beta = 3.53$
Where $\theta = 15°$
We have, $M_3 = 1.710$, $\beta = 39.64$
Similarly, $\theta = 7.17$, $M_3 = 1.710$
$\beta = 39.64$, $M_4 = 1.459$
$\beta = 43.31$
Thus, the air entering the inlet clearance with Mach 1.459 or 1.46 approx. for the design.

The shock at the inlet clearance over the external surface is cluster of inlet cone shocks which coalesce with the each other and form a strong oblique shock away from wall which has downstream Mach number($M<1$) less than 1. i.e., subsonic condition.

B. Calculations for Aft Compression Slit for Subsonic Air Entering the Combustion Chamber

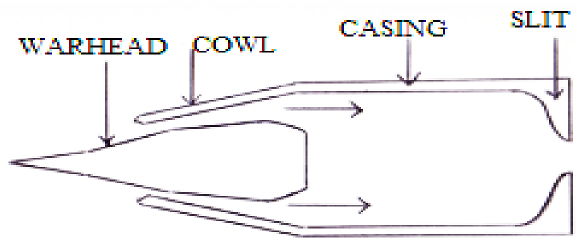

Figure 7: Inlet slit setting for Design 2

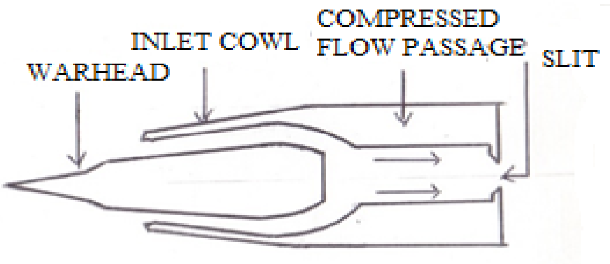

Figure 8: Inlet slit setting for Design 1

The aft compression slit is installed for prior compression of the subsonic air entering the combustion chamber. The air entering the percolation zone after the inlet cone is ruched into the pre cc zone at a velocity of 270m/s(approx.) which is 0.8 Mach this is almost a high subsonic velocity at which there is minor variation of entropy not as much as obtained from strong shock value but a considerable amount of entropy shifts as able to see in weak oblique shock flow. Thus, the reduction in area for a higher range subsonic flow for which there is a minor edge in the entropy has reduction in its velocity up to lower extents but costly and advantageous for combustion chamber conditions thus a reduced area (slit) is designed through with the compressed air is compressed further and a reduction in velocity is also occurred simultaneously along with the temperature increase and pressure decrease. Further the compression of the higher subsonic flow is continuous and smooth through a curved slit design.

3. Combustion Chamber Design and Thermal Insulations

The post air compression slit is the location of combustion chamber where the chamber is of 150 mm inner diameter with insulation and liners therefore there is sufficient movement for the propellant (in this case fuel) spacing integration as shown below,

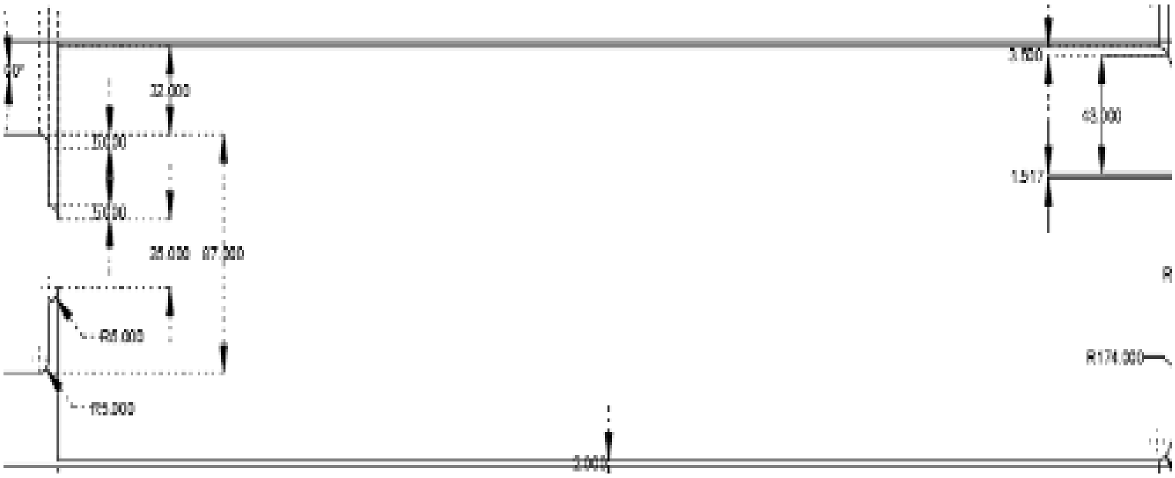

Figure 9: Standard combustion chamber casing dimensions

The metal casing used has a high entropy alloy material like Al, Ti, Ni, Co and Fe material alloy composition with respect to the heat transfer due to the propellant burning across the insulation surfaces and liners. The combustion chamber is axisymmetric and can accommodate the solid fuel motor for producing high efficiency without any material failure.

A. Insulation

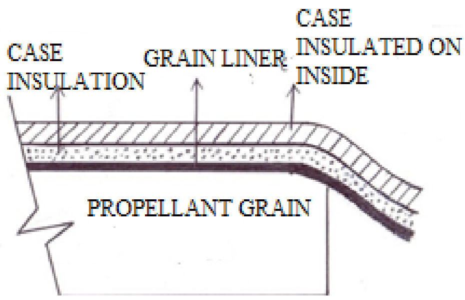

Figure 10: Combustion chamber insulation.

The liner, insulation must be chemically compatible with the propellant and each other to avoid migration or changes in material composition they must have good adhesive strength so that they bonded to the propellant.

Properties of an insulation material,

- They should have a low specific gravity,
- Thus, reducing inert mass.

Example:

- Neoprene (specific gravity 1.23)
- Butyl rubber (0.93)
- Synthetic rubber (EPDM) (0.86) (or)
- Binder used in propellent such as polybutadiene (0.9 to 1.0)
- There values are low compressed to propellant S.G ranging from (1.6 to 1.8)

Whereas the liner should be soft stretchable rubber. Type thin material (typically 1mm thick with 200 to 450% elongation) to allow relative movement along the bond line between grain and casing. This differential expansion occurs because of the thermal coefficient of expansion of the grain typically an order of magnitude higher than that of the case. The liner will also real the fibre wound of the case (particularly thin cases), which are often porous, so the high-pressure hot gas cannot escape. A typical liner for a tactical guided missile is polypropylene glycol (about 57%), a titanium oxide filler (about 20%) a di-isocyanate crosslinker (about 20%) and minor ingredients such as an anti-oxidant.

The insulation liner should be erosion resistant, particularly in the insulation of motor oft end or blast tube which has high exposure time erosion rate thus the thickness depends on,

$$d = t_e r_e f$$

f=safety factor which ranges 1.2 to 2.0 or simply we can also follow the insulation depth in twice the burnt(chassed)depth.

B. Inhibitor

An inhibitor is usually made of the same kinds of materials as internal insulators. They are applied (bonded, moulded, glued or sprayed) to grain surface that should not burn 'The usual common inhibitor materials are poly butadiene and EPDM (Ethylene Propylene Diene Monomer) or some butyl, Rubber composition.

To prevent the effect of migrants from the solid propellant in form of chemical species in Al based propellant EPDM (ethylene propylene diene terpolymer) i.e., used as thin liner to enhance bond strength, a polyurethane burner to prevent migration of plasticizer into the EPDM liner and HTPB liner to prevent burning next to the case interface.

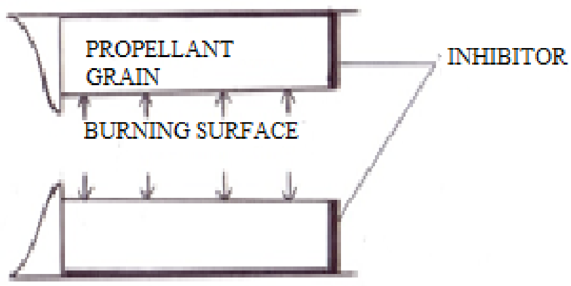

Figure 11: Propellant Grain configuration

4. Calculations for Real Case Nozzle Design

The losses that are carried for a conical nozzle design is overcome by using a bell nozzle which reduces the divergence loss, the current design of the artillery shell nozzle of ramjet system has a non-steep contour with a low inlet to outlet divergence angle ($\frac{\alpha_i}{\alpha_e}$)the design of the current nozzle is illustrated along with the design calculations for to nozzle variants.

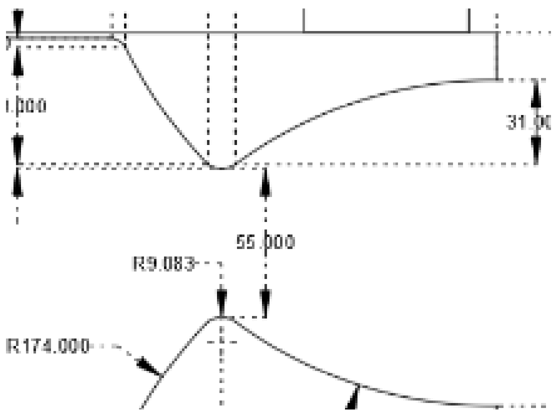

α_i= 25°, α_e= 8°

Figure 12: Bell nozzle dimension Design 2

This type of nozzle is highly performable at a high altitude since the actual to idea thrust ratio is low for bell nozzle as the altitude decreases, since λ=0.98 very low divergent loss

Steady flow through the nozzle of artillery shell takes place when mass flow through the throat is equal to the mass that is produced by burning of propellant

$$\frac{\alpha_i}{\alpha_e} = 3 \cdot 125.$$

For which λ=0.995 thus the divergence loss is neglected

To overcome the $\frac{F_{actual}}{F_{ideal}}$ value we have to obtain a greater amount of thrust at atmospheric pressures.

The design (1) of the bell nozzle can perform altitude greater than 3km or more since we have, p_a at 3km as 70108.54 pa. The expansion pressure for the design nozzle should be greater than p_a at a given altitude,

For chamber pressure, $P_C \geq$ 70 bars then the flow gets chocked at the throat and this makes the expansion of the flow at nozzle for which the pressure should not decrease than p_a at given altitude. The simulations for off design condition can be done for design (1) after the propellant analysis.

$$\frac{F_{actual}}{F_{ideal}} = 0.6 \text{ to } 0.85 \text{ for the designed nozzle (1).}$$

Design (1) for nozzle,

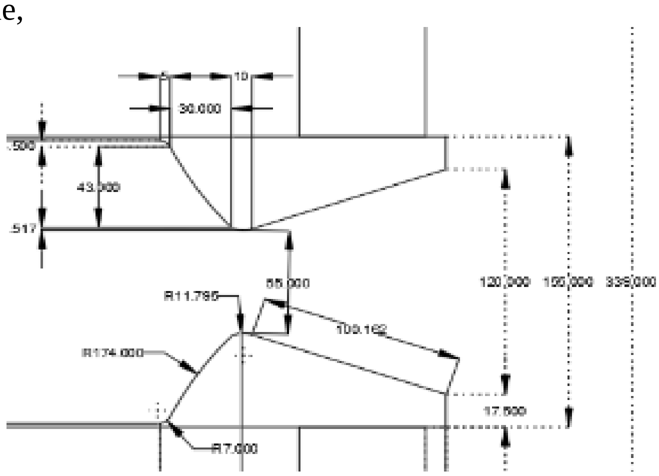

Figure 13: Straight nozzle dimension Design 1

$$\theta_i = 20, \theta_e = 19.65$$

$$\lambda = \cos^2\left(\frac{\alpha}{2}\right), \lambda = 0.9698$$

This design has considerable divergence loss but can perform well at low altitudes within 3-4 km.

5. Internal Ballistics Design in Context of Hybrid Rocket Motor

The theme of this artillery-based ramjet projectile is to simplify but same time to hybridize the solid fuel and oxygen from ram effect to increase the range of the projectile to produce 100% solid fuel propulsion by using unlimited oxidizer intake offered by the design. Thus, this kind of combustion comes under hybrid rocket (Air Breathing) propulsion using ramjet system producing higher safely during fabrication, storage and operation.

If we consider solid rocket propellant

$$\dot{m} = \rho_p A_0 a P_c^n$$

For Liquid rocket

$$\dot{m} = n_f C_d A_{in} j f \sqrt{2^{\rho} f^{(\Delta p)} \square inj} \;, f$$

$$\dot{m}_{0x} = \eta_{0x} C_d A_{in_J:0x} \sqrt{2\rho_{0x}} \Delta P_{inj,ox}$$

Where, n_f and n_{ox} are number of fuel and oxidizer injectors, and C_d is the coefficient of discharge

The combustion of fuel in the port of fuel is completely diffusion dominated then the pressure index (n=0),

$$\dot{r} = \rho_p A_b a p_c^0$$

The burn rate of propellant (fuel-oxidizer) is independent of pressure (or) less dependent on pressure.

$$\dot{r}_f = a G_{0x}^n$$

Where, G_{ox} = mass flux of oxidizer

a = burn rate at unit mass flux.

$$G_{0x} = \frac{\dot{m}_{Ox} \times 4}{\pi d_P^2}$$

dp = port diameter

$\dot{m}_{0x}$ = mass flow rate of oxidizer

$$\dot{m}_f = \rho_P A_b a G_{0x}^n$$

$\dot{m}_f$ (since the burning efflux is diffusion based)

$$n = \frac{d \ln \dot{r}}{d \ln G_{0x}}$$

For n≤0.5 the $\dot{m}$ ↑(or) constant with increase in port diameter d_p to get maximum constant or increasing I_{sp} to maximum.

$$\dot{m} = \rho_p \pi d_P L \cdot a \left(\frac{4\dot{m}_{0x}}{\pi d_p^2} \right)^n$$

$$\dot{m}_{Ox} = \rho_{ox} A_s U_{0x}$$

The Inlet velocity of oxidizer U_{ox} is ranging from 0.6-0.8 Mach number at high pressure and temperature density of gaseous oxidizer is depending upon the compression point due to slit compression of the subsonic air. From the design the slit diameter of oxidizer inlet is 25mm.

The value of chamber pressure exponent(n) is independent as the burn rate is low and almost depends upon the diffusion base solution. Thus, the value of burn rate (or) regression rate coefficient (a) and burn rate exponent n can be determined experimentally for a given solid fuel composition by using a standard burner(or) Internal ballistic testing equipment like a Crawford bomb.

For a given composition of propellant a, and n can be determined,

From which,

$$\dot{r}_f = a G_{0x}^n$$

Can be determined as,

$$G_{0x} = \frac{\dot{m}_{Ox} \times 4}{\pi d_P^2}$$

$$\dot{m}_{Ox} = \rho_{ox} A_s U_{0x}$$

$\rho \to 0$, Since temperature increases thus the specific weight decreases to zero.

From which the fuel burn rate can range from 1.5-2.2m/s which would be efficient for the Al & HTPB solution.

6. Methods to Mitigate Problems of Hybrid Solid Rocket Motor

One of the major problems in using hybrid solid rocket system is that it produces low burn rate thus low I_{sp} for a given mission (i.e., to attain high altitude). If we improve this barrier the ramjet artillery projectiles can be made to hit targets up to 150km easily. Though their effect of erosive burning it is healthier until existing in initial few seconds.

A. Burn rate

To produce higher I_{sp}, the mass flow rate of oxidizer should be higher which increases the overall fuel mass flow ratio increasing the I. This is obtained for an artillery ramjet projectile by using mixed oxidizer i.e., AP integrated fuel but not more than 20% for standard maintenance pf the fuel rich composition. The oxidizer flow injected through slit creates eddy flow at the fuel block walls by creating subsonic vortex formation leads to increase in actual burning surface area thus increase r and I_{sp}.

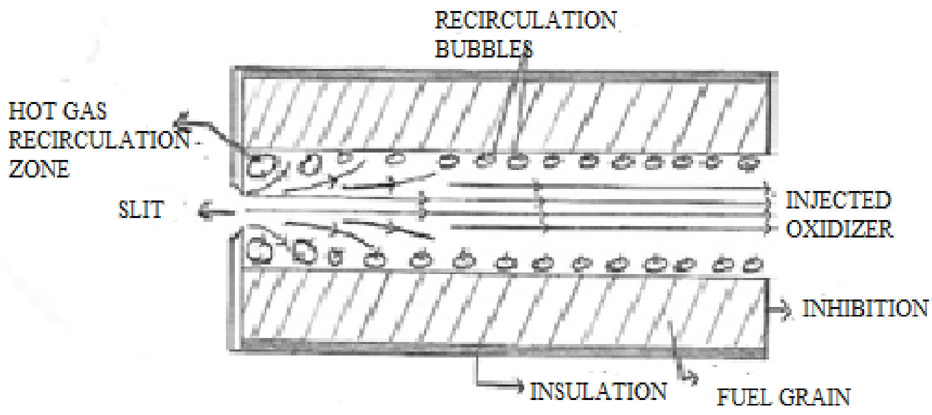

Figure 14: Flow characteristics within the port passage

Also, the fluid swirl eddies near the fuel block wall tries to stick the walls, so the actual velocity profile close to the wall is low allows high burn rate due to recirculation.

Fuel that can burn on its own can be used to increase the burn rate such as glycol azide polymer (GAP), The additional polymer of same density is used to minimize the burning of fuel on its own when the supply of oxidizer is cut off thus, this type of polymer used as additive along GAP to minimize the automatic burning is known Poly Ethyl Glycol

B. Combustion Zone Analysis

Q_C is the heat that is being converted to the propellant surface due to eddy heat flux.

$$Q_c = h(T_c - T_S)$$

Where, h- convective heat transfer coefficient

T_C- Combustion Chamber

T_s -Temperature at the surface of propellant block.

$$Q_c = k_c \frac{dT}{dy} + \rho_P \dot{r} Q_s$$

$$Q_c = \rho_\infty \dot{r}[C_P(T_s - T\infty) + Q_s]$$

$$h_v = C_P(T_s - T\infty) + Q_s$$

$$Q_c = \rho_\infty \dot{r} h_V$$

Similarly, between momentum &Energy gives

Stanton number= $C_h = \frac{h}{\rho_e u_e C_P}$

h- heat transfer coefficient

ρ_e, u_e- density and velocity behind boundary layer.

c_P- Specific heat at constant pressure.

From Reynolds Analogy,

$$C_h = \frac{C_f}{2} Pr^{-2/3}$$

C_f – Skin friction coefficient

Pr = Prandtl number, $P_r = 1$, for gases

$$C_h = \frac{C_f}{2}$$

$$C_h = \frac{h}{\rho_e u_C Cp} \frac{(Tc - T_s)}{(T_c - T_s)}$$

$$Q = h(T_C - T_s)$$

$$Q_s = \rho_P \dot{r} h_V$$

From heat balance at surface, $Q_C = Q_S$

$$\rho_{\dot{P}} r h_V = h(T_c - T_s)$$

Form, $C_h = \frac{h}{\rho_e u_C Cp} \frac{(Tc - T_s)}{(T_c - T_s)}$

$$\frac{c_f}{2} = \frac{\rho \dot{r} h_v}{\rho_e u_e \Delta h}$$

$\frac{c_{f0}}{2} = 0.0296 R_{ex}^{-0 \cdot 2}$ (Without blowing for turbulent flow)

$$\frac{c_f}{c_{f_0}} = 1.27 \beta^{-0 \cdot 77}$$

For skin friction with blowing where, β= Blowing coefficient where $\{5 \leq \beta \leq 100\}$

$$\beta = \frac{\rho_p \dot{r}}{\rho_c ue\, 0.5 c_f} = \frac{mass\ flux\ out\ from\ surface}{mass\ going\ through\ the\ port}$$

$$\frac{\Delta h}{h_V} = \beta$$

$$\dot{r} = \frac{c_f}{2} \frac{\rho_e u_e}{\rho_p} \frac{\Delta h}{h_V}$$

$$\dot{r} = 0.036 \left(\frac{\rho_c u_e x}{\mu}\right)^{-0 \cdot 2} \frac{\rho_e u_e}{\rho_P} \beta\text{^}(0.23)$$

$$\rho_P \dot{r} = 0.036 G^{0.8} \left(\frac{x}{\mu}\right)^{-0.2} \beta^{0.23}$$

$$\dot{r} = a G_{0x}^{n}$$

As we go from head end to nozzle end r increases as it depends on $\frac{G^{0.8}}{x^{0.2}}$.

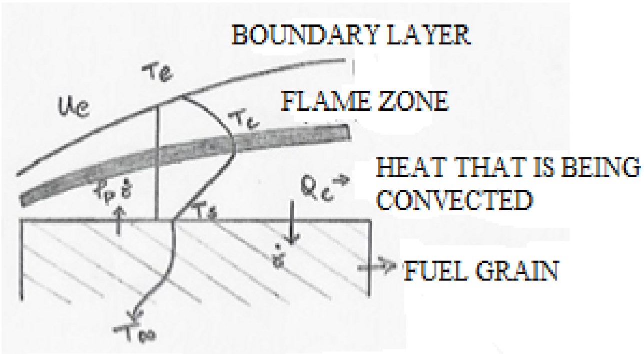

Figure 15: Combustion zone boundary layers

Q_C is the heat that is being converted to the propellant surface due to eddy heat flux.

$$Q_c = h(T_c - T_S)$$

Where, h- convective heat transfer coefficient

T_C- Combustion Chamber

T_s -Temperature at the surface of propellant block.

$$Q_c = k_c \frac{dT}{dy} + \rho_P \dot{r} Q_s$$

$$Q_c = \rho_\infty \dot{r}[C_P(T_s - T\infty) + Q_s]$$

$$h_v = C_P(T_s - T\infty) + Q_s$$

$$Q_c = \rho_\infty \dot{r} h_V$$

Similarly, between momentum &Energy gives

Stanton number= $C_h = \frac{h}{\rho_e u_e C_P}$

h- heat transfer coefficient

ρ_e, u_e- density and velocity behind boundary layer.

c_P- Specific heat at constant pressure.

From Reynolds Analogy,

$$C_h = \frac{C_f}{2} Pr^{-2/3}$$

C_f – Skin friction coefficient

Pr = Prandtl number, $P_r = 1$, for gases

$$C_h = \frac{C_f}{2}$$

$$C_h = \frac{h}{\rho_e u_C Cp} \frac{(Tc - T_s)}{(T_c - T_s)}$$

$$Q = h(T_C - T_s)$$

$$Q_s = \rho_P \dot{r} h_V$$

From heat balance at surface, $Q_C = Q_S$

$$\rho_{\dot{P}} r h_V = h(T_c - T_s)$$

$$\text{Form, } C_h = \frac{h}{\rho_e u_C Cp} \frac{(Tc - T_s)}{(T_c - T_s)}$$

$$\frac{c_f}{2} = \frac{\rho \dot{r} h_v}{\rho_e u_e \Delta h}$$

$\frac{c_{f0}}{2} = 0.0296 R_{ex}^{-0 \cdot 2}$ (Without blowing for turbulent flow)

$$\frac{c_f}{c_{f_0}} = 1.27 \beta^{-0 \cdot 77}$$

For skin friction with blowing where, β= Blowing coefficient where $\{5 \leq \beta \leq 100\}$

$$\beta = \frac{\rho_P \dot{r}}{\rho_c ue\, 0.5 c_f} = \frac{mass\ flux\ out\ from\ surface}{mass\ going\ throug\,h\ the\ port}$$

$$\frac{\Delta h}{h_V} = \beta$$

$$\dot{r} = \frac{c_f}{2} \frac{\rho_e u_e}{\rho_p} \frac{\Delta h}{h_V}$$

$$\dot{r} = 0.036 \left(\frac{\rho_c u_e x}{\mu}\right)^{-0 \cdot 2} \frac{\rho_e u_e}{\rho_P} \beta^\wedge(0.23)$$

$$\rho_P \dot{r} = 0.036 G^{0.8} \left(\frac{x}{\mu}\right)^{-0.2} \beta^{0.23}$$

$$\dot{r} = a G_{0x}^n$$

As we go from head end to nozzle end r increases as it depends on $\frac{G^{0.8}}{x^{0.2}}$.

7. Propellant Analysis

The performance for the given hybrid projectile motor propellant can be equated out by using chemical equilibrium application (CEA) for hybrid rocket settings for given composition

8. Experimental Techniques to Determine Burn Rate Coefficient and Exponent

Burning rate data are usually obtained in three ways- namely, form testing by;

A. Standard strand burners often called Crawford burners

A strand burner is a small pressure vessel (usually with windows) in which a thin strand or bar of propellant is ignited at one end and burned to the other end. The strand can be inhibited with an external coating so that it will burn only on the exposed cross-sectional surface. The diffusion rate of oxidizer and pressure is fixed for initial condition and there by the r is obtained for hybrid rocket motor and this is carries for various values to fix required burn time and rates respectively. The schematic representation of the strand burner is shown in the below figure which consist a transparent test section.

B. Small-Scale ballistic evaluation motors

Small Scale ballistic evaluation motor usually are not preferred for this type Artillery ramjet projectile which is of 155mm since the burn rate treasured is lower because of scaling factor.

C. Full-Scale motors with good instrumentation (Full Scale motors 155mm Hybrid ramjet motor for artillery shell)

During development of a new or modified solid propellant, it is tested extensively or characterized. This includes the testing of the burn rate (in several different ways) under different temperatures, pressures, impurities, and conditions. It also requires measurements of physical, chemical, and manufacturing properties, ignitability, aging, sensitivity to various energy inputs or stimuli (e.g., shock, friction, fires), moisture absorption, compatibility with other materials (liners, insulators, cases), and other characteristics. It is a lengthy, expensive, often hazardous program with many tests, samples, and analyses. The burning rate of propellant in a motor is a function of many parameters, and at any instant governs the mass flow rate rh of hot gas generated and flowing from the motor (stable combustion).

9. Precision Guided Kit (PGK)

To achieve the range of the given solid fuel motor the ramjet artillery shells the aerodynamic stability of the trajectory should be stabilized with tail stabilizing unit and air guidance system.

One of the main thrusts of modern military technology is accuracy improvement for the most basic form of missilery, the free flight rocket.

A. Tail Stabilizing Unit

The wrap-around fin (WAF) is used to provide missile performance equal to flat fins. The WAF has unique aerodynamic characteristics, particularly in roll, that are different from other types of stabilizing devices. The flight path for Ramjet Artillery Shell is free flight thus fins of the stabilizer assembly are canted to give the required spin to the rocket for minimizing the effect of thrust misalignment and dynamic imbalance along with the roll stability.

B. Tail Stabilzer Fins

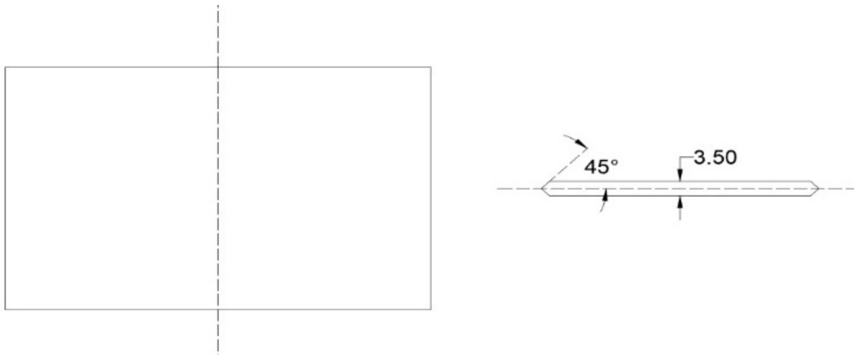

Figure 16: Side view and top view of tail stabilizer unit (from left to right)

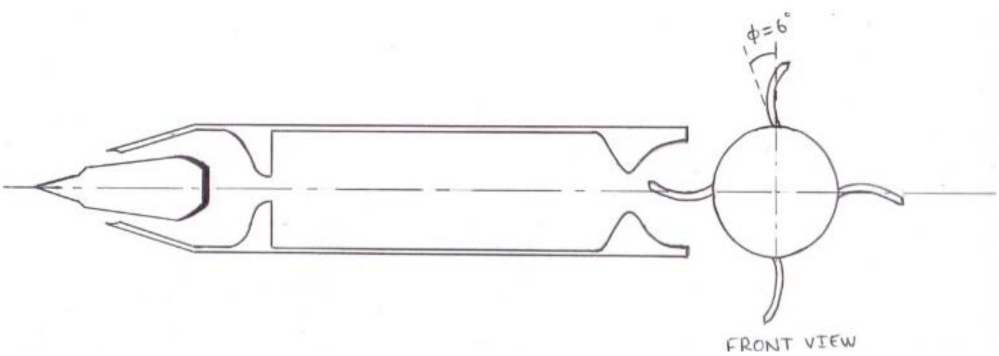

Figure 17: Cross sectional view of tail stabilizer unit (from left to right)

C. Inlet Air Guidance

The high-speed air inlet guidance fins are located at the front portion of the artillery shell to guide the speed of air for continuous stabilized flow.

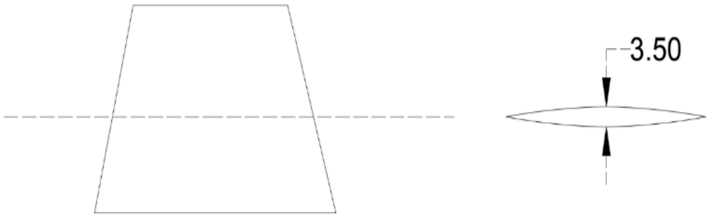

Figure 18: Side view and top view of inlet air guidance fin

The designed fin is operated best at Mach number ranging from 0.7 to 1.45 Thus, the weak shock wave is formed with respect to the divergence wedge angle and thus, the air is reduced to lower supersonic flow downstream the shock for supersonic condition which does not exceed above, Mach 1.45, in case of higher subsonic flow at 0.8-0.9 ranging, this guides the air according to the flow direction.

The inlet air guidance and tail stabilizer unit are a complex part unlike the other machinable system component these systems should has to be installed and monitored for proper deployment of the inlet guidance and stabilizer unit. The fins at the tail end of the stabilizer are fixed with spring system with open tension through a torsional spring system, since it is a WAF system the deployment is easily detected when the projectile system is ejected out form the base of the artillery gun due to torsion produced by torsional spring. Whereas the inlet fine has to be deployed once the projectile is on flight mode at atmosphere through a control ejection system of locked fin at inlet. The location of fine in Design (1) and (2) vary where design (2) has more air Guidance performance which improves the precision of terminal ballistics.

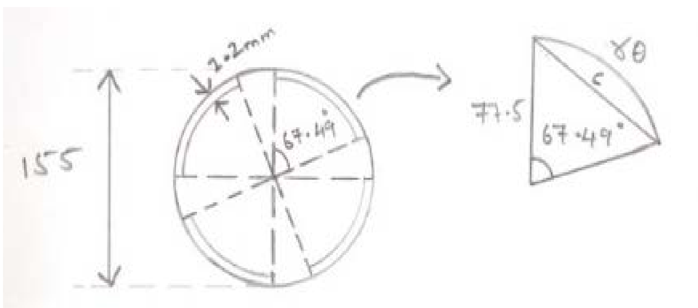

Figure 19: Tail stabilizer design calculation for given dimension

$$r\theta = (77.5) \times (67.49) \times \frac{\pi}{180}$$
$$r\theta = 91.289mm$$
$$C = \frac{\theta}{360} \times (2\pi r)$$
$$C = \frac{67.49}{360} \times (2\times\pi\times77.5) = 91.289$$

Thus, the chord length of tail stabilizer is determined.

D. Propellant Design and Study Analysis

The propellant grain integration into the insulated casing is of cartridge-loaded type, i.e., the grain is manufactured separately from the case by extrusion or by casting into a cylindrical mould or cartridge and then loaded into (or)assembled into the insulated casing.

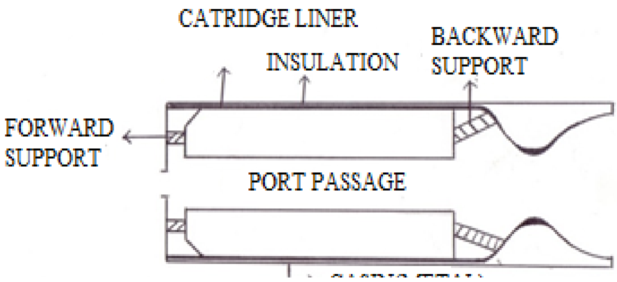

Figure 20: Internal support for the solid propellant grain.

E. Propellant Composition and Manufacturing for Cartridge Type Composite Propellant For Ramjet Artillery Shell [Fuel Based]

The propellant in any aerospace Non-Air-breathing engine consists of fuel and oxidizer together but for Air breathing engines, the fuel is mixed with atmospheric compressed air which is rushed into the combustion chamber. Unlike gas turbines the ramjet into the combustion chamber. Unlike gas turbines the ramjet air breathing Engine do not have any moving parts in it but uses a gas dynamical compression spike since operating in supersonic conditions and the air is reduced to subsonic condition for stabilized combustion of fuel air mixture the complete combustion of solid fuel in artillery ramjet depends upon the diffusion rate of air per unit area of the solid fuel (G_{OX}), and also determines the burn rate of fuel. For higher performance and to prevent losses due to two phase flow, the grain size of the solid fuel is made finer like nano Al particles will be best for higher performance.

Compositions that can be used for air breathing ramjet solid propellant will be 100% fuel solution thus the propellant burning time is increased and produces higher performance. The combination of fuel in Artillery ramjet can use Al as mother fuel (ranging 5-20mm) and HTPB as fuel Binder as it acts a high structural strength material and for its higher bonding rate with high density property. The aluminium during combustion form as aluminium oxide (Al_2O_3) (or) alumina as we know. And their oxide particles tend to agglomerate from larger particles. The aluminium increases the heat of combustion, the propellant density the combustion temperature, and thus the specific impulse. The other fuel particulate metals like Boron, Beryllium, (AlH_3) Aluminium hydride and beryllium hydride (BeH_2) have high melting point, high toxic powder ejection, manufacturing difficulties and deteriorate chemically during storage with loss of hydrogen respectively Some amount of AP is added typically below 20% to increase the burn rate of ramjet hybrid motor which is taken in account.

The HTPB has been the favourite hinder in recent years, because it allows a somewhat higher solid fraction (88 to 90% between Al) and relatively good physical properties at the and modifiers temperature limits.

Some burn rate modifiers can also be used in the fuel composition to decrease or increase the burning rate (monthly reduce due to erosive burning effect) Like or lithium fluoride (to reduce burning rate). The modifiers are effective because they change the combustion mechanism.

A curing agent or cross liker causes the pre-polymers to form longer chains of larger molecular mass and inter locks between chains. Even though these materials are present in small amounts (0.2 to 3%), a major change in the percentage will have major effect on the propellant physical properties, manufacturability, and aging. It is used only with composite propellants. It is the ingredient that causes the hinder to solidify and become hard. The curing agent that can be used are methyl axiridinyl phosphine oxide (MAPO), Toluene-2,4-diisocynate (TDI), Hexamethylene diisocyanatos (HMDI) and Isophorone diiscynate (IPDI).

Plasticizer is usually a relatively low- viscosity liquid organic ingredient which is also fuel. It is added to improve the elongation of the propellant at low temperatures and to improve processing properties, such as low viscosity for casting or longer pot life of the mixed but uncured propellant. The common plasticizers used for composite propellants are Dioctyl phthalate (DOP), Dioctyl adipate (DOA), Dioctyl sebacate (DOS), Isodecyl perlargonate (IDP) and Dimethyl phthalate (DMP).

Fuel that can burn on its own can be used to increase the burn rate such as glycol azide polymer (GAP), The additional polymer of same density is used to minimize the burning of fuel on its own when the supply of oxidizer is cut off thus, this type of polymer used as additive along GAP to minimize the automatic burning is known Poly Ethyl Glycol.

The standard Al particle size is preferred which is 5-15 micro meters but to increase the burn rate of the hybrid ramjet motor nano Al particles are preferred where the flip side of it is high cost, say fifty thousand per kilogram and it also increases the volumetric loading making the structure week and more viscoelastic in nature.

Table 1: Composition percentage of propellant mixtures and their type

INGREDIENT	WT%	ACRONYM	TYPE
Aluminium powder (5 to 15μm)	0-70	Al	Fuel
Hydroxy Terminated Polybutadiene	0-30	HTPB	Binder
Ammonium Perchlorate	0-20	AP	Burn rate modifier (oxidizer base)
MAPO-tartaric acid- adipic acid condensate	>0.1	MT-4	Bonding agent
Diphenylamine phenyl-naphthylamine	>0.5	DPA	Bonding agent
Glycol azide polymer	0-25	GAP	Fuel Composition
Poly Ethyl Glycol	0-25	PEG	Binder used to minimize the effect of GAP

10. Prototype Design and Manufacturing Technique Used

The complete ramjet artillery projectile prototype is fabricated as assemble system using thread type rotation assemblage, it offers easy component change thus the correction in the design of prototype can be changed easily. The fabricated model is done for Design (1) which is fully completed the Design (2) is on process for which the inlet spike part is completed.

A. Manufacturing Techniques for Each Parts

The moto of manufacturing is to maintain the physical property and to produce the designs dimensional output which has been done exceptionally for achieving cutting edge technology in defence products.

The material used in Ramjet artillery shell prototype is stainless steel material of 304 Grade alloy.

B. Inlet Spike Fabrication (War Head)

The spike is machined by master lathe in which the step dimensions for given deflections are achieved and operated by turner who has minimum experience. The CNC is also operated to fabricate their kind of machining but results in high cost thus traditional method of lathe processing is opted.

The outer turning is initially functioned through taper turning process for given diameters and lengths mentioned in diagram then it is bored to obtain the mentioned wall thick for the war head. The spacing is given for war head design which is not induced with fuze since it is a prototype.

Figure 21: Manufacturing of warhead spike

C. Inlet Area Variation and Air Slit Passage

The design (1) and (2) variants show major variation in the inlet area reduction with respect to the war head location for effective compression. The manufacturing procedure for the slit reduction of Design (1) is followed by simple lathe turning of given radius dimension and the velocity is further reduced form high subsonic to mild subsonic range.

Figure 22: Inlet slit setting for Design 1

For Design modification (2) we have a reduction in area where the area constantly decreases along with the trailing part of the war head spike at the intake zone, and after a given dimensional length it maintains constant diameter of here with reduced area flow and terminates the flow further to a minimized slit area before entering the combustion chamber as shown above.

D. Combustion Chamber Fabrication

The combustion chamber of the Ramjet artillery shell is a 155mm solid fuel motor of length 575mm which is the highest of any other part thus the fabrication of casing is done by a seamless pipe production through dye mould technique of 55 alloy material. The thread is made at the trailing ends of the solid fuel motor for easy removal to load the cartridge type propellant inside the casing and supported through a rubber block at front and near portion of the motor at both ends line the fuel is cartridge loaded type.

E. The C-D Nozzle Design and Nozzle Design Variation

The C-D Nozzle is the key element of the Ramjet Artillery which produces high through (kinetic energy) in form of increase in momentum of the mass flow. Thus, the converging dust is lower in length than the expansion unit (Nozzle)since to produce the effective chocking of gas by rapid chamber pressure increment. The C-D part fabrication is operated with SS 304 rod of dia 155mm and length as mentioned in blue mint through the lathe turning operation with nearly zero error defect as seen in the prototype. The Divergent nozzle has two variants, Design (1) has a lower contour radius dimension with a considerably high divergent angle than the usual (which is 2 to 5°). The divergent angle $\alpha°=8°$ for the fabricated nozzle thus the contour is not too steep as a regular high performing bell nozzle which is operated at high attitude, therefore the nozzle used in artillery shell will not expand the gas less than the atmospheric conditions at heights above 3km (best used) given a higher expansion value with greater I_{SP} at given attitude.

The Design (2) of nozzle variation has a straight nozzle of reduced length of given area ratio, this design produces greater thrust with increased loss of divergence than Design (1) usually preferred at h<3k. Both straight and bell nozzles are fabricated using the turning operation in master lathe machine which has polished surface finish to reduced viscous drag and Non-isentropic effects at the throat to nozzle.

Figure 23: Manufacturing of bell nozzle in lathe

F. Precision Guided Kit (PGK) System Fabrication For Prototype

The inlet air guidance and tail stabilizer unit are a complex part unlike the other machinable system component these systems should has to be installed and monitored for proper deployment of the inlet guidance and stabilizer unit. The fins at the tail end of the stabilizer are fixed with spring system with open tension through a torsional spring system, since it is a WAF system the deployment is easily detected when the projectile system is ejected out form the base of the artillery gun due to torsion produced by torsional spring. Whereas the inlet fine has to be deployed once the projectile is on flight mode at atmosphere through a control ejection system of locked fin at inlet. The location of fine in Design (1) and (2) vary where design (2) has more air Guidance performance which improves the precision of terminal ballistics. The manufactured PGK system with respect to the design is given in below figures.

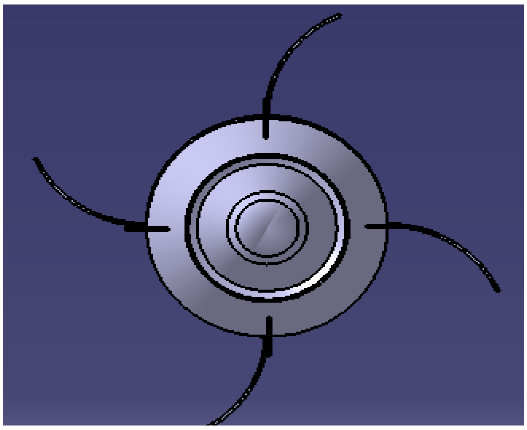

Figure 24: Front view of the projectile

Figure 25: Retraction torsional spring unit

11. Analysis of the System

The study of flow through Ramjet Artillery shell with respect to the above calculations are done through Ansys Fluent which shows the P_o difference and velocity domain for compressible flows. This analysis can be cross checked through various experimental flow techniques as mentioned in above section.

A. SOLUTION AND POST-ANALYSIS

The Pre-CFD conditions are checked and updated for further downstream projection of the program thus the solution setup is initialized before the optimum conditions of the experiments are feed in. The solution type adopted is series which is default setting and the other setup elements are also left as normal bias. The solution CFD fluent solver is opened and the solver conditions has to be set initially the solver base is density based and the flow conditions are absolute and study.

The equation models are fixed next for which the energy and viscous state equations are on for which the study of temperature, and viscous effects are posted. The cell zones are kept default as mentioned in the geometry naming and meshing part of analysis thus we directly move to boundary conditions where the inlet, outlet, and wall conditions are fixed. The momentum equation conditions are fixed first for which the supersonic conditions are opted where the inlet flow velocity is 1150 m/s, the thermal conditions are changed with respect to the ambient condition with respect to the flight altitude condition.

The outlet conditions are kept constant with respect to the ambient conditions, and also the wall is fixed as symmetry for all the dimensions which gives more likely a quick solver solution for given equation to get converged. A series of images are given for illustrating the procedure followed in the solution combined with the resulting images of various conditional parameters.

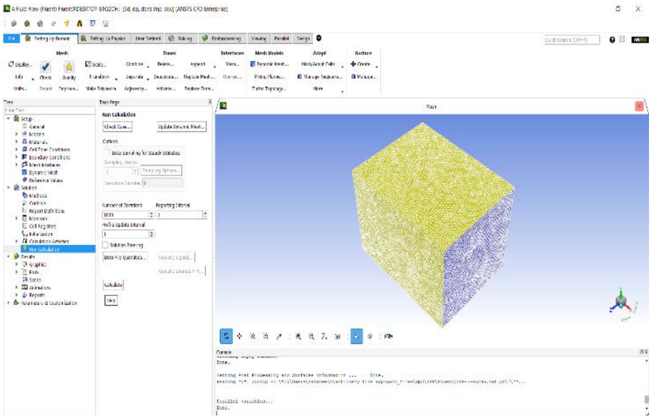

Figure 26: Induction of mesh grid to solver setting setup

As we see in the above figure the mesh file is updated in the fluent and the following steps as mentioned above like solver setting and boundary conditions are induced to the solver as given in the left dialogue box of the solver.

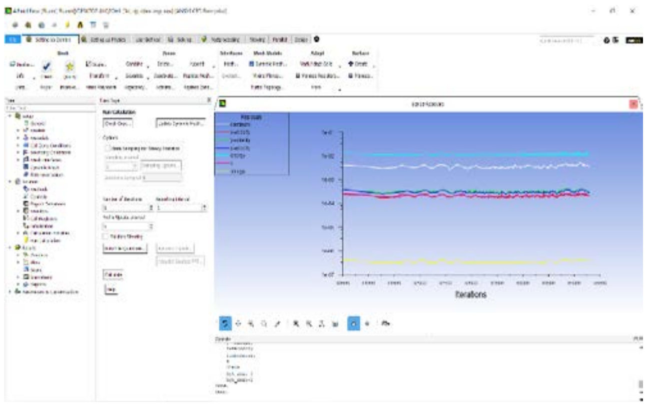

Figure 27: Solver residuals and console evaluation for given number of iterations.

After correcting the flow conditions the solution is initialized and the calculation tool bar is opened for calculation run for which a particular number of solution iteration is made, say five hundred initially for better convergence if the solution is converged for the given number of iteration then we can save it and move on to post result analysis of CFD if it is not converged repeat the iteration until the approx. value of flow is matched.

The effective resultant values match the design conditions as given in theoretical calculations in above initial sections of the journal. Values of the following results for velocity and temperature is shown in below figures for given compressible settings in density-based fluent solver as mentioned in above topics.

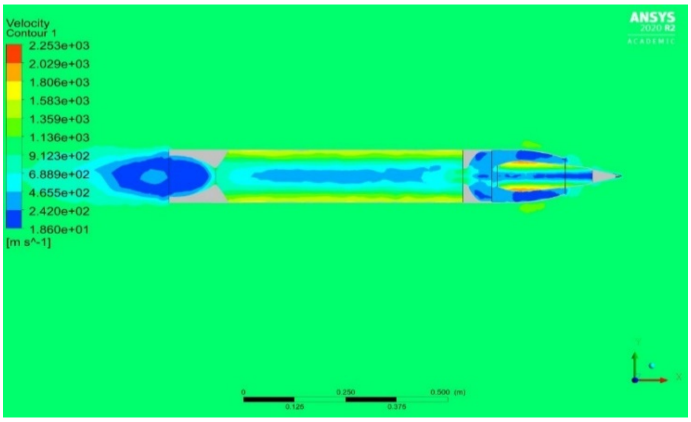

Figure 28: Result of velocity variation within the projectile at high speed M=3.4, Post analysis check for XY-Plane in plane 1 in given contour. The velocity variation is given in contour scale for which the change in velocities is shown for one lakh twenty five thousand iteration value which is cut down to approx value.

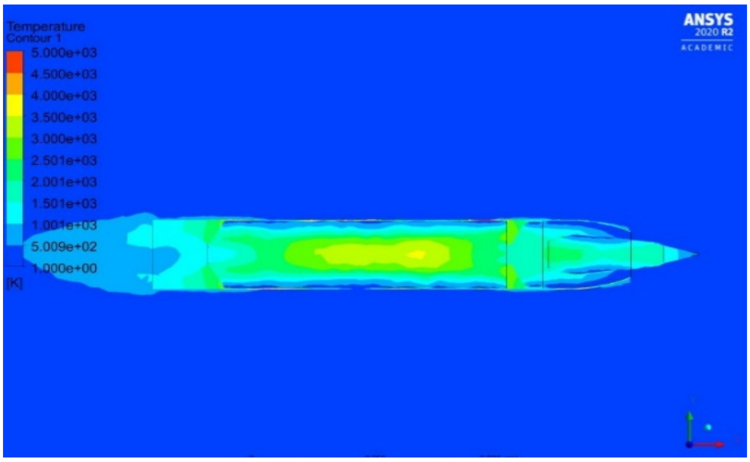

Figure 29: Result of temperature variation within the projectile at high speed M=3.4, Post anlysis check for XY-Plane in plane 1 in given contour. The temperature variation is given in contour scale for which the change in temperature is shown for one lakh twenty five thousand iteration value which is cut down to approx value.

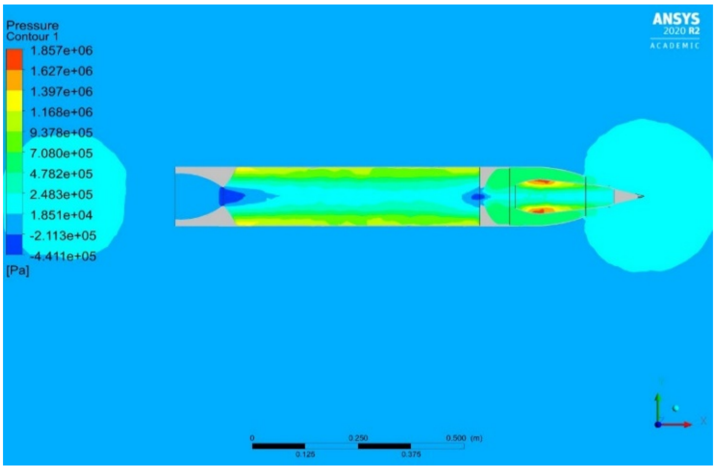

Figure 30: Result of pressure variation within the projectile at high speed M=3.4, Post anlysis check for XY-Plane in plane 1 in given contour.

12. Conclusion

Throughout this work we have illustrated we have complete concept and design for development of an Artillery Ramjet Projectile which includes

- Internal ballistic design and calculation {Includes Propellant science}
- Exterior ballistics {Armament projectile design with PGK}
- And the lethality effects and terminal ballistic science up to some extent conceptually

Thus, the above fields must be chosen for a successful development of the Ramjet Artillery Shell by testing trials and has to be improved further for high range efficiency of the projectile.
Truly the Ramjet Artillery Projectile used in ATGS system will be a huge turnover for India Army strength and respect among the world. Indigenous development of this system will give boost to our research and development combining the academics for India’s growth towards self-reliance.

13. Future Development of the Project Work

The fabrication of design 1 and design 2 for the given blue print is completed and submitted as the prototype fabrication system along with dummy PGK system and warhead installation the combustion chamber casing is done with stainless steel alloy which is 304 in its grade category which with stand about 1200 degree Celsius. The nozzle design is purely based on the blue print where the contour bell nozzle as well as the straight nozzle is made. The system can be easily removed into parts and can be integrated again with thread system where the cartridge type solid propellant can be easily installed for the projectile system.

Further development in this project includes manufacturing and testing sample composite propellant base from where the multiple testing has to be done with the 155mm solid fuel base to fix the chamber pressure and initial condition. These testing has structural base analysis for combustion chamber material and solid propellant. Along with which the environmental safety and manufacturing safety precautions must be followed. After the propellant analysis the study for propellant and metal casing adhesion is studied with criterion for choosing the liner and insulator component most commonly this is done while the study of propellant testing for better resultant I_{sp}. For thermobaric warhead fabrication along with fuze integration the study of conventional warhead mechanism and the kinetic impact of the ballistics has to be studied. The free projectile without propellant and warhead is projected from the ATGS guns for trail check analysis for target hit zone verification. After which the cartridge propellant is installed within the shell and loaded for real time parameter testing also known as Initial level of range check and the results can be cross checked with various static stimulation calculation. At least of 250-300 testing is necessary to fix the result for high range which include internal ballistic properties change at every consecutive check for better improvement in overall output.

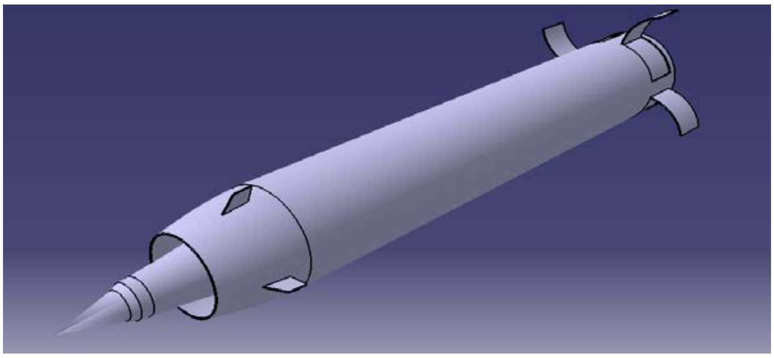

Figure 31: Isometric design view

Figure 32: Fabricated prototype of the projectile

14. References

[1] Ballistics: Theory and Design of Guns and Ammunition, By Donald E. Carlucci & Sidney S. Jacobson.
[2] Rocket Propulsion Elements by George P. Sutton (Author), Oscar Biblarz (Author).
[3] Tactical Missile Design, Second Edition by E. Fleeman.
[4] Tactical Missile Aerodynamics General Topics (Progress in Astronautics and Aeronautics) by Michael J. Hemsch.
[5] Conventional Warhead Systems Physics and Engineering Design (Progress in Astronautics and Aeronautics) by R. Lloyd.
[6] Artillery rocket system DRDO Technology focus.
[7] Gas Dynamics, Volume 1, 1976 by Joe D. Hoffman (Author), Maurice J. Zucrow (Author).
[8] Gas Dynamics, 2014 by Rathakrishnan E (Author).
[9] Guided Missiles published in the year 1990 DRDO publications.
[10] https://www.nammo.com/story/closing-the-range-gap/, Nammo closing the range gap development of ramjet assisted projectile and missile systems.
[11] Solid fuel ducted ramjet engine by DRDO, PIB Editorial.
[12] Combustion, Fifth Edition by Irvin Glassman, Richard A. Yetter, Nick G. Glumac.
[13] Principles of Combustion by Kenneth Kuan-yun Kuo.
[14] Engineering Design Handbook - Elements of Aircraft and Missile Propulsion.
[15] Physics of Direct Hit and Near Miss Warhead Technology by R. Lloyd.
[16] Design of guidance and control systems for tactical missiles by Defu, Lin Zaikang, Qi.
[17] Design and manufacturing process of ballistic missiles Sebastian Marian Zaharia* Rareş Ioan ŞTEFĂNEANU**.18. Fleeman, E.L. & Schetz, J.A. (2012). Missile Design and System Engineering, Reston, VA: American Institute of Aeronautics and Astronautics.
[18] Carter, A.B. & Schwartz, D.N. (1984). Ballistic Missile Defense, Washington, D.C.: Brookings Institution.
[19] Experimental Aerodynamics by Stefano Discetti, Andrea Ianiro (eds.).
[20] Tactical Missile Aerodynamics Prediction Methodology by Michael R. Mendenhall.
[21] Hirsch C. Numerical Computation of Internal and External Flows.Volume1-Fundamentals of Computational Fluid Dynamics (Elsevier,2nd edn,2007).

[22] High Performance Synthetic Fibers for Composites (Publication (National Research Council (U.S.)), No. 458.) by Committee on High Performance Synthetic Fibers for Composites.
[23] Modern Exterior Ballistics by Robert L. McCoy.
[24] High Entropy Alloys by B.S. Murty, Jien-Wei Yeh and S. Ranganathan (Auth.).
[25] Aircraft Propulsion and Gas Turbine Engines by Ahmed F. El-Sayed.

Mathematical Modelling and Kinetic Analysis of the Breech Block Operating Mechanism for Next Generation Main Battle Tank (NGMBT)

Davinder Kumar
Armament Research & Development Establishment
Pune
dev.ghorela@gmail.com

Karun Roat
Armament Research & Development Establishment
Pune
karun.roat@arde.drdo.in

P.H. Lankennavar
Armament Research & Development Establishment
Pune
paraslanknr@arde.drdo.in

A.K. Roy
Armament Research & Development Establishment
Pune
akroy@arde.drdo.in

***Abstract*—This paper describes the motion state and forces required to operate the Breech Mechanism of NGMBT. The major functions of Breech Mechanism in tank guns are to close/open the barrel chamber, extraction of spend cartridge case and in-housing of firing mechanism with required safety mechanism. The decreasing response time in Warfield called for higher rate of fire. To enhance the rate of fire there is requirement to speed up its operational speed (i.e. opening. closing, and extraction). This calls for kinetic analysis of breech mechanism so that defect free operation of mechanism at higher speed can be obtained. The paper deals with mathematical modeling and kinetic analysis of horizontal sliding type breech block operating mechanism for NGMBT. The breech mechanism related components were modelled in solid works and imported in Adams software for MBD analysis. The study also includes generation of free-body diagrams and kinetic analysis of individual components of the mechanism. Mathematical model has been established to calculate the torque required to open the breech end. Closing of breech end is assisted by Semi-Automatic (SA) spring mechanism. After simulating the mechanism with calculated torque in Adams software, it is found that it take 0.4192 second to open the breech end. Furthermore, this analysis can be useful in reducing the efforts to open the breech end when operated manually.**

***Keywords*— NGMBT, Breech Ring, Breech Block, SAGR, SAGC, Torque requirement**

1. Introduction

The basic principle of war is based on protection, mobility and firepower [1]. The decreasing response time and increasing lethality of the future Warfield make higher firepower, reliability and intelligence inevitable for the system to survive and win the war. The fire power has always shown its superiority over other parameters of the Gun. In tank gunnery to defeat the target at longer range and with maximum lethality there is a requirement of higher muzzle velocity. To achieve higher muzzle velocity there is requirement of higher chamber pressure. The breech mechanism plays vital role. In tank gunnery, withholding the very high pressure generated from propellant gases for a very short interval of time. The function of breech mechanism are as follows as: (i)To close the breech end of the gun and to withstand the rearward thrust of propellant gases, (ii) To trigger the firing mechanism, (iii) to Provide Inherent safety mechanism, (iv) to Extract the spent cartridge case, (v) to make the system to be accessible for auto-loading. To enhance the fire power of the gun, it requires quick Breech Mechanism operations (i.e. opening. closing, locking and reloading). The high rate of fire needs minimum operating time for Breech opening and closing. The Breech Mechanism has two major components (a) Breech Ring and (b) Breech Block. Breech Block moves in Breech Ring to close the breech end of the barrel.

It is essentially large heavy piece of steel that covers or seal the beech end. There are generally two types of Breech Mechanism in use in tank gunnery: (i) Horizontal Sliding wedge block mechanism, and (ii) Vertical Sliding wedge block mechanism due to limited operational space availability. The vertical type Breech Mechanism offers limited angle of elevation to the gun whereas horizontal type Breech Mechanism give compactness to the tank gun system and make amenable to high rate of fire and automation of ammunition loading. Sliding blocks slides in the breech ring under the action of crank mechanism. The Breech Mechanism of NGMBT is designed for either semi- automatic or automatic horizontal sliding-wedge type operation. Sliding Breech Block Mechanism in its simplest form has the breech block sliding along the key ways to open or close the barrel chamber during firing cycles to facilitate loading/unloading of rounds. Breech Mechanism is accommodating different sub-assemblies for various aforementioned functions. Such as breech block assembly, semi-automated gear, firing mechanism with firing circuit, safety device, and extractor assembly. These are mechanically coupled with each other. For automatic operation of the Breech mechanism, there is need to carryout kinetic analysis of the operating mechanism so that the effort and time can be minimized and higher rate of firing can be achieved. For kinetic analysis a definite relation must be maintained between motion of the various subcomponents of the breech mechanism, motion and firing mechanism. High velocity and accelerations of components are required to meet the desired firing rates. A thorough mathematical modelling and kinetic analysis have been done to ensure satisfactory operations of Breech Mechanism. Generally, three types of operations can be employed [4]. (i) Hand operated, (2) Semi-automatic (Closing of the breech end is assist by semi-automatic gear rod assembly), (3) Fully Automatic.

The automatic or semiautomatic operation of a Breech Mechanism put stringent requirements on the kinetic analysis of breech components which is concerned with action of unbalanced forces acting on a body and motion produced by these forces. A mathematical modelling and kinetic analysis of the breech operating mechanism with time constrained has been solved and logical outputs in the forms of the torque required for the opening and closing with manageable velocity and acceleration for the components to achieve 6-8 rds/min firing from NGMBT has been worked out in this paper.

2. Description of Breech Mechanism

The mechanism consists of crank with roller and semi-automatic gear assembly and both are mounted on the splined crank shaft. The power input is given to the crank shaft. As the crank rotate, roller slides over the slotted path that pushes the breech block and makes it to slide inside the breech ring. The main objective of kinetic analysis is to assure the opening of breech block for given torque input and to make sure that designed SA spring has enough stiffness to close the breech end quickly as the new round is loaded. The SA spring assembled on semi-automated gear rod assembly get compressed during opening of breech end. This stored spring energy is used to close the breech block. Major components of Breech mechanism are as follow as:

- Breech ring(BR): Grounded part.
- Breech block(BB): slides inside the slot of BR, having a mass of 71 kg approx.
- Crank with roller: Roller rolls and pushes the Breech Block to slide it.
- SAGC: Semi-Automatic gear cam.
- SAGR: Semi-Automatic gear rod.
- Crank shaft: SAGC and Crank make a rigid link with crank shaft through spline.
- Link: joining link between SAGC and SAGR.
- Extractor cam: assembled on breech block.
- Extractors: to latch and unlatch the breech block in open condition.

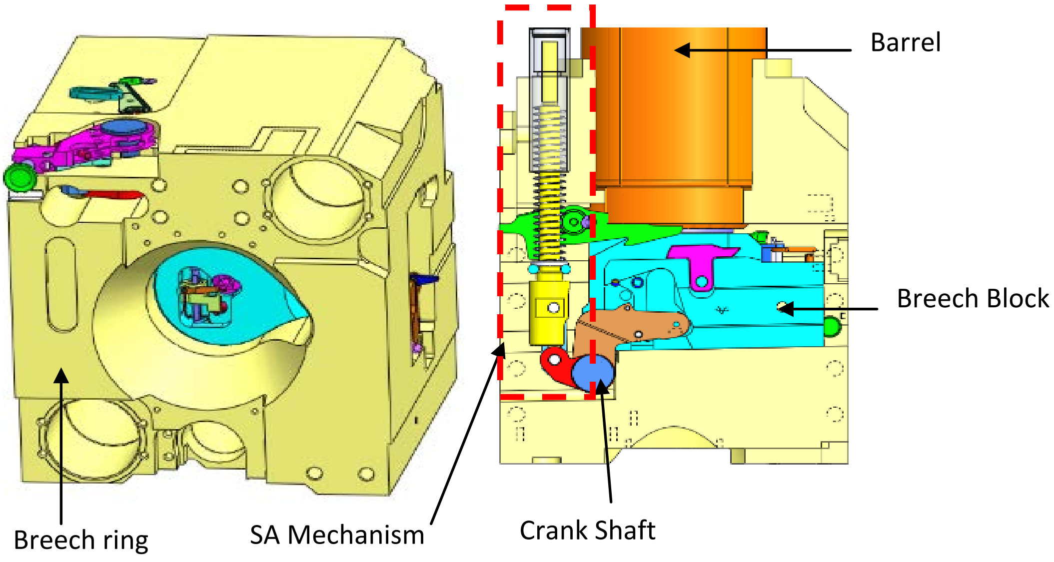

Fig. 1 Breech Mechanism for NGMBT.

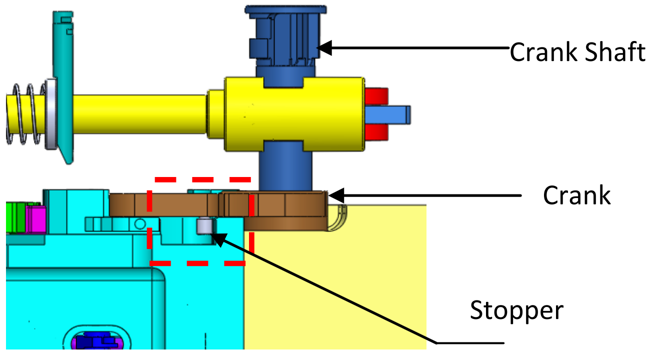

Fig. 2 Stopper to limit the displacement of block during opening of breech end.

3. Methodology

Simplified geometry has been taken to reduce the complexity. The Adams software can make it intuitionistic to study the multi body dynamics of the mechanism [2]. 3D solid models of the breech mechanism have established and the assembly of the various components is completed in Solid Works. After importing in Adams software, constraints are added in for the MBD analysis. Each part is assumed as a rigid link. Friction is assumed to be neglected on all joints and contact surfaces except for breech ring and breech block contact surface. Static coefficient of friction is assumed to be 0.3 between the breech block and breech ring contact surface. Total no of links is 14. The Spring Model used in ADAMS has been explained by Jiajun YAOa & Jisheng MA [3] is given below:

$$F_w = -\mathrm{k}(\mathrm{l}-\mathrm{l_o}) - \mu\frac{\mathrm{dl}}{\mathrm{dt}} + \mathrm{F_o}$$

F_0, F_w: pre-load and working spring force,
k: Spring stiffness, 10.23 N/mm,
l_0: pre-loaded length of the spring,
μ: damping coefficient, is neglected,

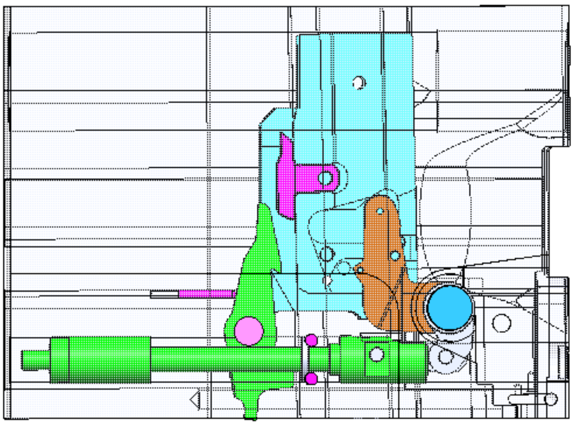

Fig. 3 The simplified Breech Mechanism assembly.

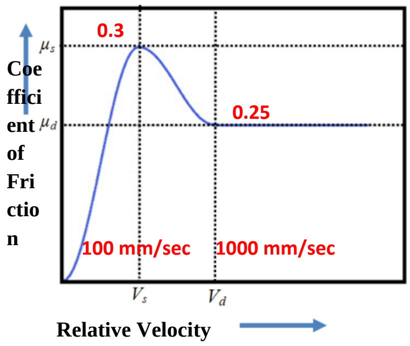

Fig. 4 Friction coefficient and relative velocity for contact surfaces**.**

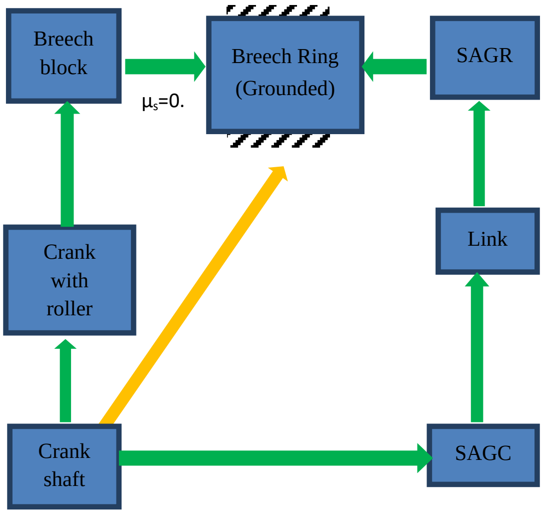

Fig 5. The Graphical topology among Breech Mechanism components.

A. Mathematical Approach

Mathematical model has been developed to calculate Total torque requirement. It has two components. Torque obtained from both components is superimposed to get the total torque.

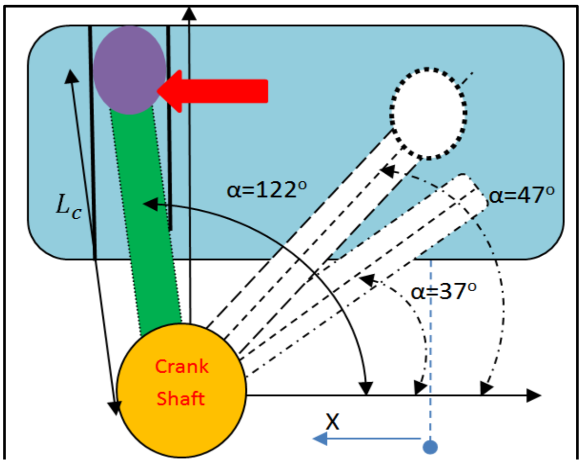

Fig.6 Crank arm rotation during breech opening operation.

1) *Component- I:* Breech Block Sliding torque.

Force required to displace the breech block to approx. 175.5 mm in 0.4 seconds taking μs=0.3 has been calculated using D Alembert's principal.

$$\sum F_{net} = m\ddot{x}$$

$$F - F_r = m\ddot{x} \qquad (1)$$

F_r= frictional force
m= Breech block mass
$\ddot{x}$ = linear acceleration of breech block

From Geometric equations for constant angular velocity (ω=3.708 rad/sec) of crank shaft, displacement, velocity, and acceleration of breech block are given below respectively.

$$x = 0.682L_c - L_c \cos\alpha \qquad (2)$$

$$\dot{x} = \omega \times L_c \times \sin\alpha \qquad (3)$$

$$\ddot{x} = \omega^2 \times L_c \times \cos\alpha \qquad (4)$$

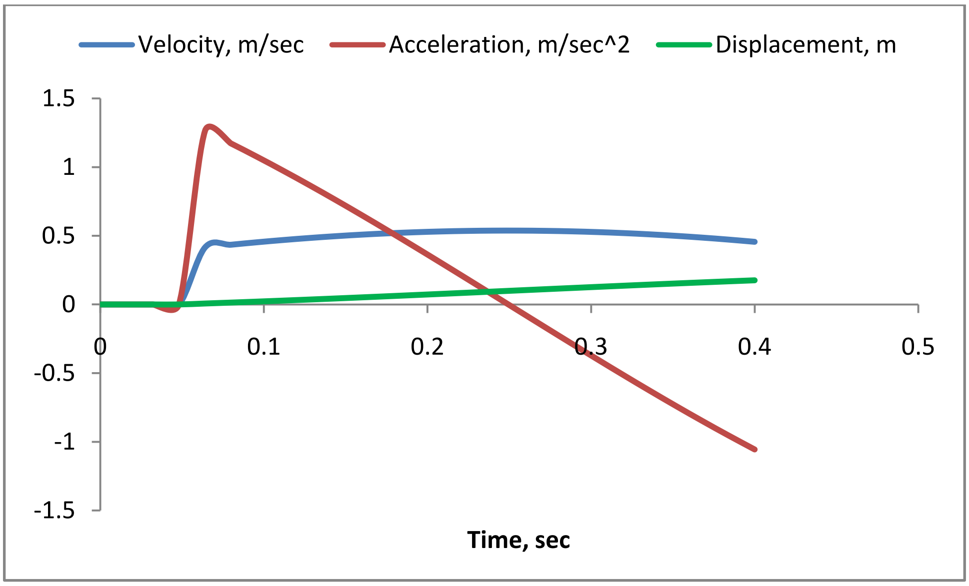

Fig. 7 Breech Block motion analysis.

Force required to slide the block has been calculated using equation 1 & 4. Further, torque required only to slide the Breech Block is calculated using free body diagram given in Fig. 6 is given by,

$$T_1 = F \times L_c \times \sin\alpha \qquad (5)$$

Where,
α is crank arm angle in degree
F is calculated from equation 1,
L_c, length of Crank Arm Length, mm,
Total crank arm rotation is 85°. but for initial 10-degree rotation (37^0 to 47^0) of crank shaft there is no displacement of breech block.

2) *Component ii*: Torque required against the SA spring compression.

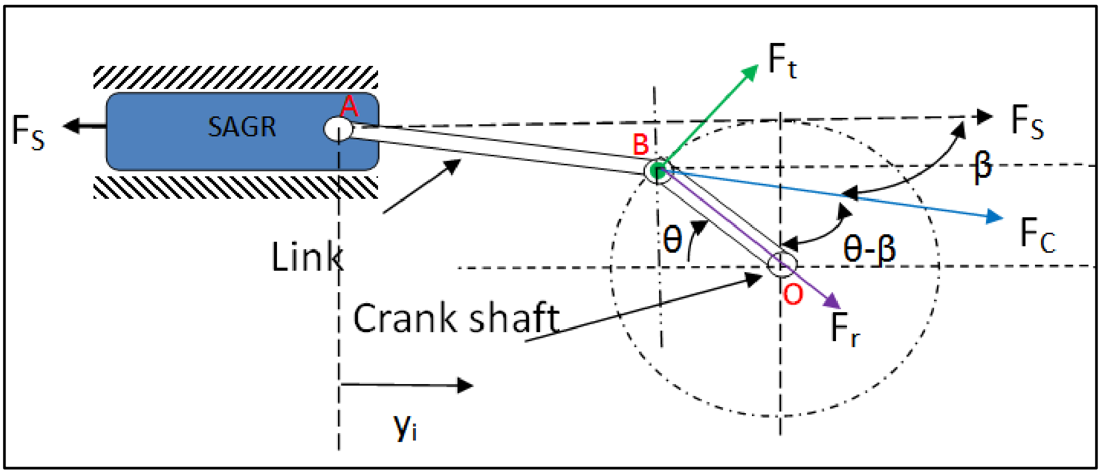

Fig. 8 Kinetics of SA mechanism.

Mathematical model to compute the torque required to rotate the crank shaft has been developed. This torque is required to overcome the SA spring force. In this the SA spring is preloaded to 1136 N and SAGC arm (OB) is assumed to rotate 85 degrees (θ_i=84^0, θ_f =169^0).
F_S = SA spring Force, N
F_C = Force acting along the link AB, N
F_t = Force acting normal to arm (OB), N
Δy = SA spring compression, mm
R = Length of link OB, mm

$$\Delta y = [90.27 - (L \times \cos\beta + R \times \cos\theta \qquad (6)$$

$$F_C = \frac{1136 + k.\Delta y}{\cos\beta} \qquad (7)$$

$$F_t = \frac{(1136 + k.\Delta y) \times \sin(\theta - \beta)}{\cos\beta} \qquad (8)$$

Where, β is angle between AB link and horizontal reference, degree (CW),
θ is angle between link OB and horizontal reference, degree (CW), and
L is length of link AB

$$\beta = sin^{-1}\frac{R - Rsin\theta}{L} \qquad (9)$$

$$\text{Torque, } T_2 = F_t \times R, \text{ (N-mm)} \qquad (10)$$

This is the torque required against the compression of SA spring during rotation of crank shaft.

$$\text{Total torque required} = T_1 + T_2 \qquad (11)$$

This torque is required to open the Breech block mechanism. After 85^0 rotation of crank shaft breech block get latched with extractors as shown in fig. 9. Stored energy in Compressed SA spring is utilised when the Breech Block is unlatched by new round. The torque calculated using mathematical approach has been validated using Adams software. Results and comparison are discussed subsequent Para.

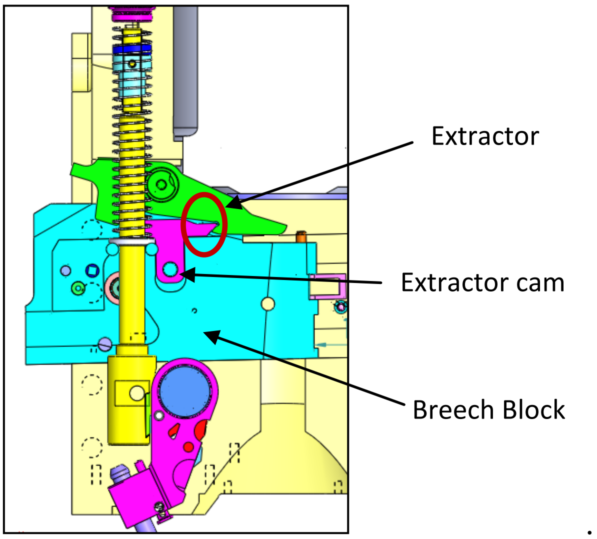

Fig. 9 Latched position of Beech block with extractor

4. Results and Discussion

After performing the MBD analysis, it is found that torque requirement for the displacement of breech block is 117 N and time taken for complete opening of breech end is 0.419 sec. The torque requirement also depends on variation of torque at Crank Shaft with respect to time. From the closed form solution, it is found that the out of total torque required major portion of torque requirement is consumed to overcome the SA spring compression which is approximately 70- 80% of total torque requirement. Velocity and displacement graph w.r.t time are given in fig. 10. Closing of breech end is done by SA mechanism when extractors are tipped by a force or a new round. This data became very useful to determine the rate of fire and to further improvements in fig. 10. Closing of breech end is done by SA mechanism when extractors are tipped by a force or a new round. This data became very useful to determine the rate of fire and to further improvements in it.

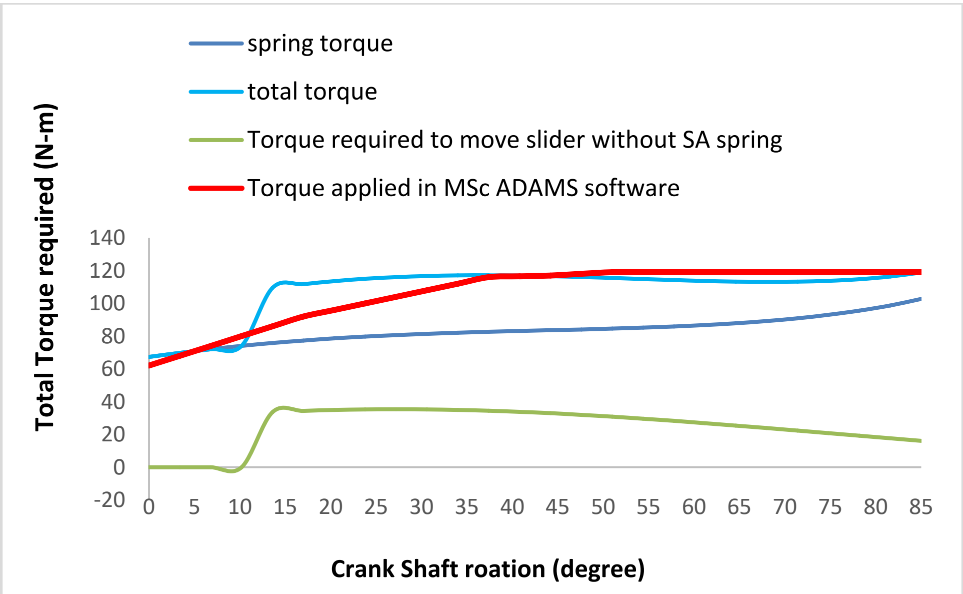

Fig. 10 Torque variation w.r.t. Crank Shaft angle.

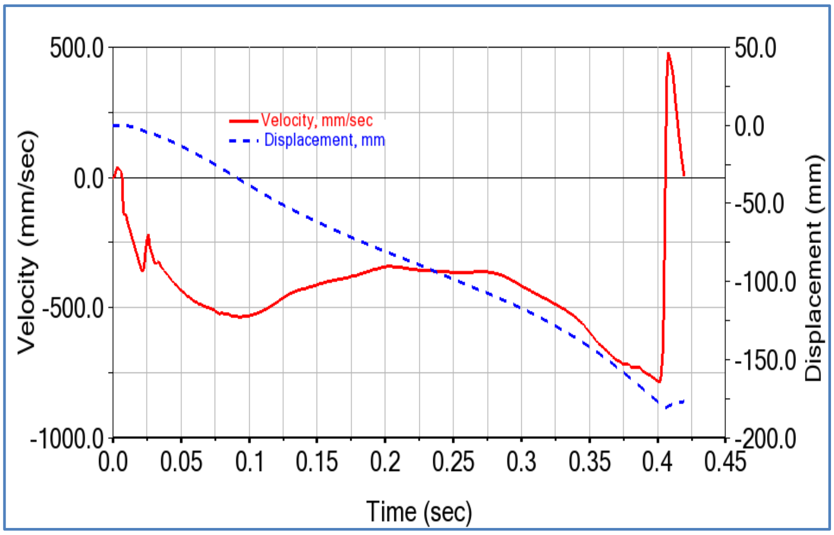

Fig. 11 Velocity& displacement diagram w.r.t. time.

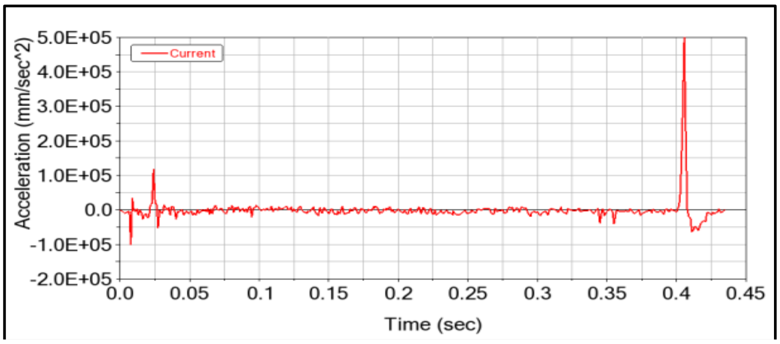

Fig. 12 Acceleration diagram w.r.t. time.

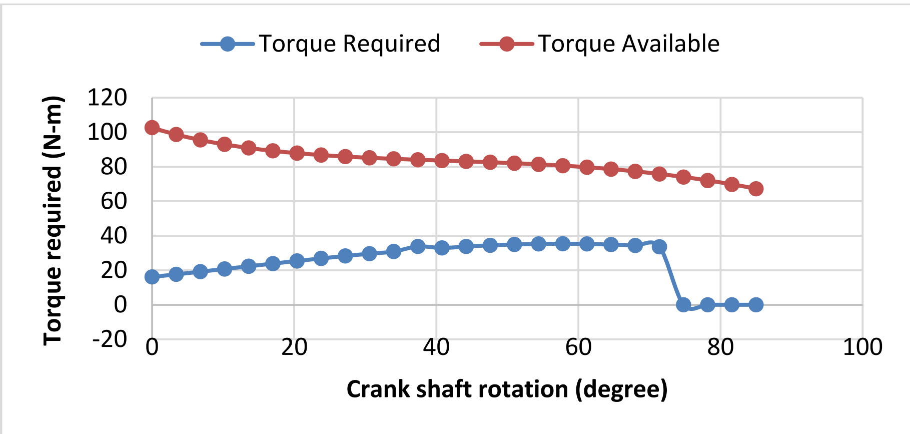

Fig. 13 Torque available from SA Spring for closing of breech end.

5. Conclusions

A very few literature is available for the kinetic analysis of Breech Mechanism with SA mechanism. The higher rate of fire in tank gun system has become feasible due to better kinetics of breech mechanism. The analysis is useful to designer to calculate the power source requirement for the opening of Breech Mechanism and to design the spring for closing of breech mechanism. The analysis has also helped us to optimise the design parameters (SA spring rate, crank arm length) to reduce the human effort if operated manually. Analysis will be further extended to simultaneous cocking action of firing mechanism during the breech opening and closing mechanism. A series of trials will be carried out for validation of the same.

6. Acknowledgement

Authors are grateful to Director ARDE for providing continuous support and motivation to complete this paper.

7. References

[1] A.K. Roy, P.H. Lankennavar, and V.S. Ghadge, Present and Futuristic Trends in Weapon System. Defence Science Journal. 2017; 67:401-406.

[2] Luo AN, Hu SH & Liu HP, Simulation and analysis of Breech Block mechanism. Journal of material science and application. 2006; 5:48–52.

[3] Jiajun YAOa & Jisheng MA, A Study on Design of a Breech Mechanism Test-platform Drive, Advanced Materials Research. 2010, 139-141: 1018-1021.

[4] Engineering Design Handbook-Breech mechanism Design, US Army Material and readiness Command, 1979.

Survivability and Terminal Performance Evaluation of Ammunition System for Triggering of Avalanche using Explosive

Rajeev Prakash
Armament Research and Development Establishment
Pune
rajeevprakash@arde.drdo.in

Ajay Vora
Armament Research and Development Establishment
Pune
ajay.vora001@gmail.com

Gyanendra Kumar
Armament Research and Development Establishment
Pune

RS Rao
Armament Research and Development Establishment
Pune

Dr S V Gade
Armament Research and Development Establishment
Pune

***Abstract*—Snow avalanches hamper the movement of army and civilians in high-altitude regions extensively and cause heavy mortalities. To mitigate this risk, a special ammunition is proposed for artificial triggering of snow avalanche to clear the passage. This paper discusses the details of its design i.e. configuration, structural analysis and estimation of blast peak over pressure. The results of numerical study carried out using ANSYS highlights that the shell can withstand the launch induced stresses. Further, data from static field trials is included which indicates that the proposed ammunition is able to satisfy the prime objective of generating sufficient overpressure.**

1. Introduction

The objective of artificial release of avalanche is to remove unstable snow from potential avalanche fracture zones and hence minimize the risk of an unforeseen occurrence of an avalanche in the region. Firing in the slopes in snow bound areas is an economical as well as practical method of triggering controlled avalanche and is being used by many nations worldwide [1]. The blast of ammunition creates a shock wave, which raises the pressure in the shockwave region above atmospheric pressure, which is termed as Peak Over Pressure (POP). This pressure breaks the weak ice sheet on which snow is accumulated and hence, avalanche gets triggered.

Along similar lines, efforts have been made to meet the requirement of artificial release of avalanche, in which an existing 84mm HE ammunition was modified to increase the HE content by ARDE (DRDO). Based on dynamic evaluation, a new ammunition is proposed to be configured and developed which has much higher explosive content [2].

2. Numerical Investigation

A. Configuration

The configuration that has been worked out for the ammunition is shown in Figure 1(a). The ammunition consists of shell body, Fuze, high explosive, driving band and sealing ring. This configuration is designed to accommodate more explosive content than the one designed earlier by ARDE [2]. Earlier design accommodated 530g of explosive, however this newly designed ammunition can accommodate 1.11g of explosive. This increase in explosive content is aimed at obtaining a POP of 3.5 kPa at MSL, which is considered sufficient for artificially triggering of avalanche. The old ammunition is shown in Figure (1b) for comparison.

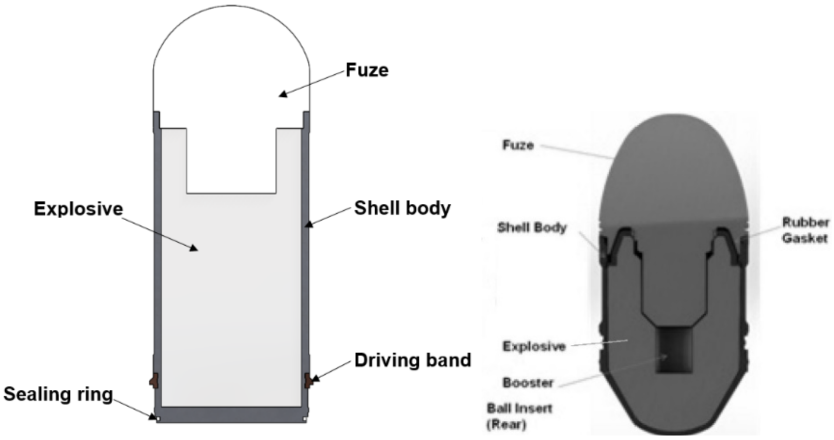

(a) (b)

Fig 1: (a) New Configuration (b) Modification of existing HE ammunition

B. Survivability of Projectile during Launch

Finite Element Analysis was performed using ANSYS 'Static Structural' module to evaluate the stress distribution and identify critical regions in the proposed design. D'Alembert's principle was employed to analyze the ammunition body during in-bore travel. For simplicity, the Fuze assembly is assumed as a solid block of same mass. The shell body is made of high strength Al alloy. Driving band and sealing ring are made of copper alloy and rubber respectively. The boundary conditions employed on the 3-D model and the mesh of the model are as shown in the Figure (2).

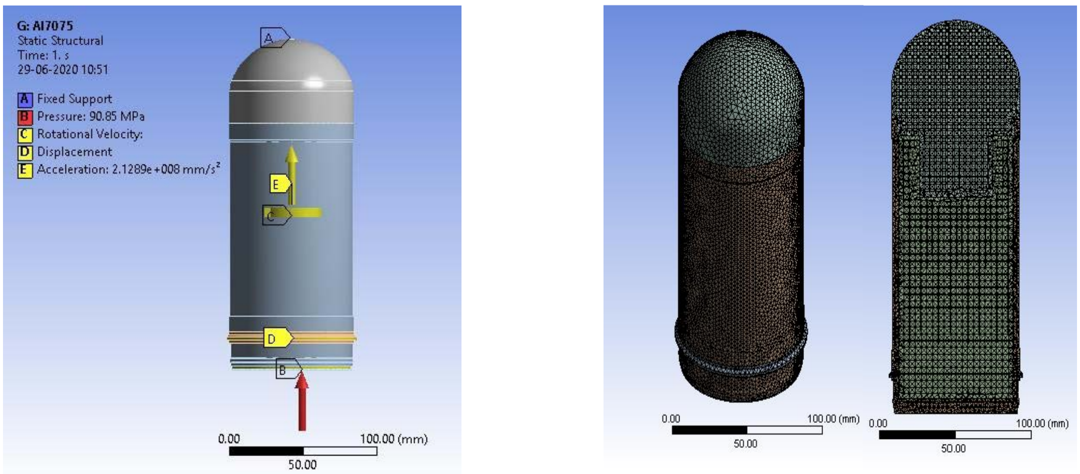

(a) (b)

Fig 2: (a) Boundary conditions (b) Mesh of the model

The major inputs required for the quasi-static structural analysis of the ammuniton are (i) pressure acting at the base of the ammunition and (ii) rotational velocity of the ammunition. Using these, the accelaration of the ammunition is calculated which is used to obtain the inertia force acting on the ammunition. The inertia force thus obtained is then used as an input. In this way, a dynamic problem is converted to a quasi-static one.

Using such a methodology, stress and strain solutions are obtained, which is shown in the following figures:

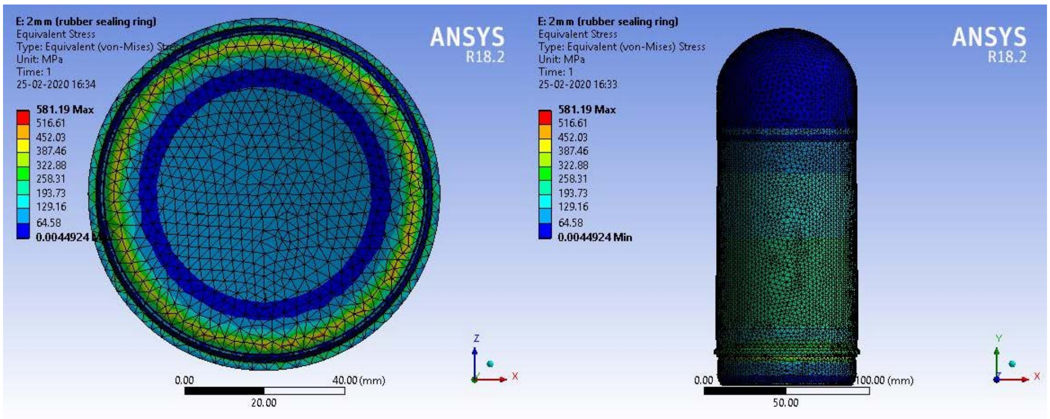

Fig 3: Equivalent stress results

In Figure 3, the equivalent stress is shown at the base of the projectile, since maximum stress occurs at the base only. The maximum stress that occurs is present only along a thin line along the circumference of the base. Factor of safety obtained in the shell is as shown in the table below:

Table 1: FOS calculations

Component	Material	Eq. Von Mises	Yield Strength	FOS
Shell	Aluminum Alloy 7075_T6	416 MPa	505 MPa	1.2

C. Terminal Performance

Blast POP has been estimated by empirical and numerical methods at varying distances from point of initiation. For performing numerical analysis, Autodyn software was used. A 2D wedge shaped geometry with spherical symmetry was used. The geometry and the mesh used is as shown in the figure 4.

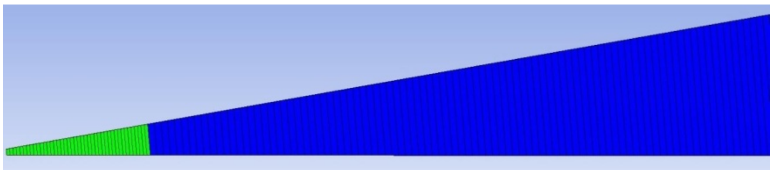

Fig 4: Geometry and mesh for POP calculation

In the numerical analysis, 1kg TNT (green) is blasted in air(blue). JWL EOS is used for TNT and air at standard atmospheric conditions is used. The calculated POP is matched with many empirical relations. The empirical relations used have been taken from the references [3][4]. For representation purposes, the comparison between calculated POP and two empirical relations is as shown in the table below:

Table 2: Comparison of POP data from Autodyn and empirical relations

R (m)	Autodyn (kPa)	Kinney-Graham (1.0 kg); kPa	Error (%)	Henrych, (1.0 kg); kPa	Error (%)
23	3.361	3.718	9.619	3.538	5.025
25	3.018	3.401	11.261	3.196	5.573
27	2.732	3.135	12.762	2.914	6.128

Thus, it was ascertained from numerical analysis and results from empirical formulae, that the required POP can be attained using the ammunition. To finally validate these results against experiments, static firing of filled ammunition was carried out. The filled ammunition was placed at a height from the ground to avoid reflection of pressure waves and hence measure the correct blast POP. For blast POP measurement, piezo based pressure sensors were placed in a straight line at varying distances (4m, 8m, 12m and 16m) from the center of shell. The shell configuration used in the firing trial and the layout of the pressure sensors is as shown in the figure below:

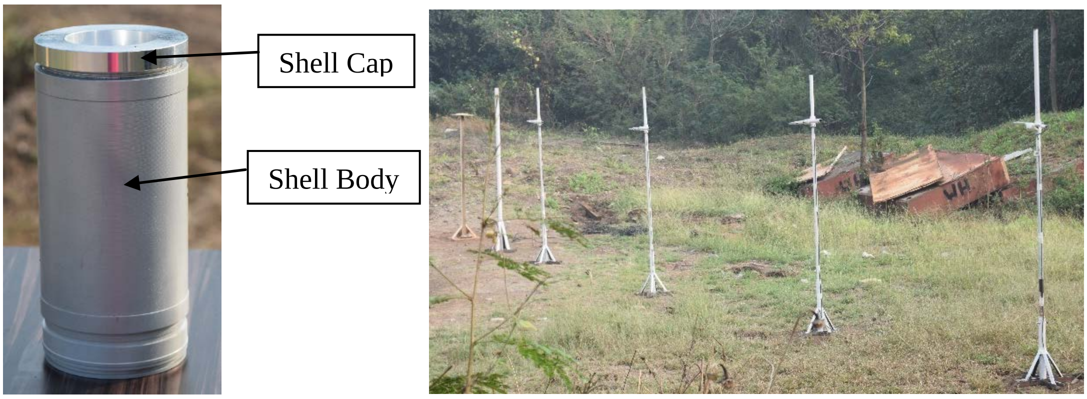

(a) (b)

Fig 5: (a) ammunition used for static trials (b) arrangement of pressure sensors

Blast POP values have been obtained by firing a number of shells. The POP values measured are as shown in the table below:

Table 3: PoP vs distance data

Location of sensor	**Pressure measured (kPa)**			
	Shell 1	**Shell 2**	**Shell 3**	**Shell 4**
7.70 m	21.0	19.0	20.7	18.0
15.60 m	10.8	10.7	10.4	10.3
19.87 m	7.1	7.7	7.2	8.1
25.00 m	5.7	6.0	6.2	6.3

Thus, it can be seen from the above data, that the POP required of 3.5 kPa at MSL is achieved by the proposed ammunition configuration. Hence POP data calculated using Autodyn and empirical relations was validated against actual experimental data.

3. Conclusions

The proposed shell ammunition has demonstrated its capability in generation of required peak over pressure. The values of PoP obtained are on an average 1.4 times the theoretical estimates and well above the required value. This indicates that there is no uncertainty associated with its output. Moreover, the results of numerical investigation indicate that the shell has a good structural integrity and it will not be compromised during the critical launch phase.

4. References

[1] G. Eason, Gubler, Wyssen, Kogeinig, Guidelines for Artificial Release of Avalanches, 2012
[2] RP Pandey, Rajeev Prakash, Vivek Soni, Dr K M Rajan, International Symposium on Snow Avalanches and Mitigation Strategies (SAMS-2019), Chandigarh, 2019
[3] Henrych J. The Dynamics of explosion and its use. Amsterdam and New York: Elsevier Scientific Publishing Company; 1979.
[4] Kinney GF, Graham KJ. Explosive shocks in air. second ed. 1985.

Design of Elevation mechanism for Telescopic Sight of 84mm Recoilless Launcher Weapon System

Ajay Vora
Armament Research and Development Establishment
Pune
ajay.vora001@gmail.com

Gyanendra Kumar
Armament Research and Development Establishment
Pune

Praveen Kumar
Armament Research and Development Establishment
Pune

Rajeev Prakash
Armament Research and Development Establishment
Pune
rajeevprakash@arde.drdo.in

R S Rao
Armament Research and Development Establishment,
Pune

Abstract—**Avalanches pose a grave threat to the lives of Indian Army personnel in snow clad regions of Himalayas. To mitigate this peril, avalanches are triggered artificially by bursting explosive above weak snow. 84mm RCL weapon is selected for firing such ammunition. However, the elevation mechanism of the existing sight caters for a maximum elevation of 17° which is suitable for obtaining a range of 1.3 km. However, considering the safety of the troops firing 84mm ammunition, a range of at least 2km is required to be achieved. For this, a new elevation mechanism for providing the weapon an elevation of 20° is designed. This paper discusses the aforementioned new proposed mechanism for enhancement of range.**

1. Introduction

The existing 84mm RCL weapon uses a telescopic sight that can provide a range of 0.6 km for HEAT and 1.3 km for HE ammunition. It employs a force-closed, radial cam and follower mechanism. The radial cam is connected to a range drum and a flat faced follower is hinged and connected to the telescopic sight. It provides appropriate movement/ inclination to the mounted telescope. A schematic diagram is shown in Figure 1.

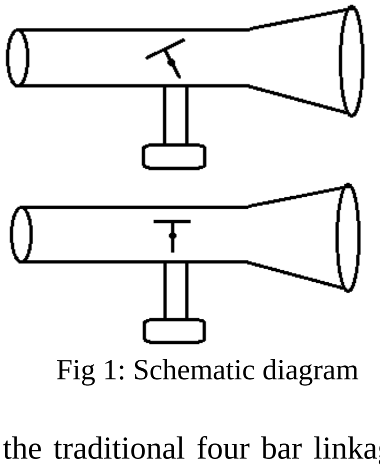

Fig 1: Schematic diagram

Cams are a modification of the traditional four bar linkage mechanism except that they have a variable length coupler link. They form a closed kinematic chain and provide the user with a controlled output as per design. Owing to their simplicity, flexibility and multiple modes of available outputs (translation, rotation or user-defined oscillation) they find application in multiple areas from automobiles to manufacturing plants. The cam mechanism employed in the existing sight provides an oscillating output that aids in the sight's movement.

Data from range table obtained by ballistic study suggests that an elevation of 20° is required for achieving desired range of 2.1 km. Since the present mechanism does not cater to our requirements, the cam has been re-designed. This paper discusses the design of the same.

2. Design of cam mechanism

For the design of cam-follower mechanism, the s-v-a-j (displacement, velocity, acceleration and jerk) variation of follower with respect to rotation of cam are primary requirements. Moreover, the fundamental law of cam design states that across the entire interval of 360 degrees rotation of cam, the cam function must be continuous through first and second derivatives of displacement. This principle assumes continuous rotation of cam. However, in this case, cam is just used to provide discrete angular displacements to the flat faced follower. Thus, only the displacement of the follower is of concern here.

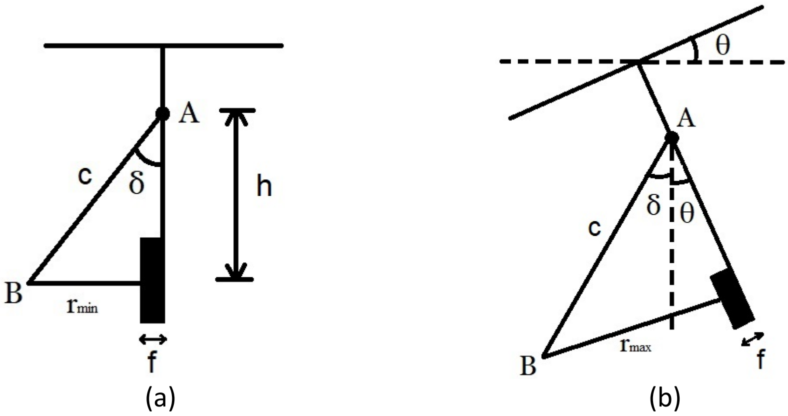

Fig 2: (a) Zero position of cam (b) Final position of cam

Figure 2(a) denotes the zero position of telescopic sight. The cam rotates about point B and the telescopic sight is hinged about point A. The final position is shown in Figure 2(b). Here the angular displacement of the sight occurs due to the rotation of cam which presses the black coloured flat faced follower. The profile of cam used in this calculation is spiral. Due to the minimum radius of the cam, the telescope rests at zero degree dip. However, due to the maximum radius of the cam, the flat faced follower gets displaced from its initial position and hence a maximum dip of telescopic sight is obtained.

The new cam is to be designed to fit inside the existing housing in which the existing cam is fitted. Thus, a minimum number of quantities required to design the new cam, which are 'c', 'h' and 'f', were measured from the existing housing. These quantities are as shown in Figure (2). Following trigonometric and geometric relations were used to create formulations for minimum and maximum radius of cam.

$$\delta = \cos^{-1}\frac{h}{c} \tag{1}$$

$$\sin(\delta) = \frac{r_{min} + f}{c} \tag{2}$$

$$\sin(\delta + \theta) = \frac{r_{max} + f}{c} \tag{3}$$

$$r = a\theta + b \tag{4}$$

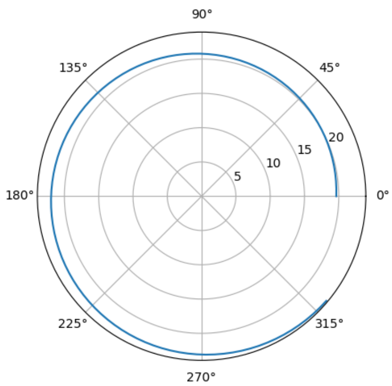

Fig 3: Spiral curve depicting continuous cam

Using equations, (1)-(3), r_{min} and r_{max} are calculated. These were then fitted on a spiral with equation (4). The continuous spiral thus obtained serves as the outline of the cam on which discrete steps are to be created. The spiral obtained using above mentioned methodology is shown in Figure (3).

Different values of ‘θ’ and ‘r’ are calculated using equation (4). Values of ‘θ’ in steps of 2° are shown in the table below:

Table 1: Elevation for different radius of curvature of cam

θ (degrees)	r (mm)
0	19.63
2	20.18
4	20.71
6	21.20
8	21.66
10	22.09
12	22.48
14	22.84
16	23.17
18	23.47
20	23.73
22	23.96
24	24.16

For obtaining, stepped cam, radii as mentioned in Table (1) are drawn from centre of spiral, shown in figure (3). Then lines normal to all the radii are drawn. Using this methodology, discrete steps are created on the spiral cam profile obtained earlier. The stepped cam thus obtained is shown in Figure (4).

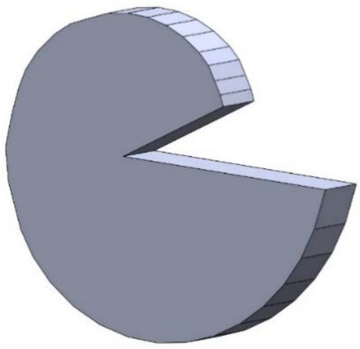

Fig 4: New stepped cam for sight elevation mechanism

To obtain a clear impression of the developed cam, the real cam used in the elevating mechanism of existing sight is shown in figure (5a). Also, an image of the partially assembled elevation mechanism along with a telescopic sight mounted on it is shown in figure (5b).

(a) (b)

Fig 5: (a) Stepped cam in use in existing sight elevation mechanism (b) Partially assembled Sight and elevation mechanism

3. Discussion and conclusion

Existing elevation mechanism of sight fitted with 84mm RCL launcher caters only for a maximum elevation of 17°. However, a new ammunition under development, which is to be used for artificial triggering of avalanches, requires elevation in excess of that. For that purpose, certain dimensions were measured from the housing of the existing cam. Using these dimensions, a new cam is designed which caters for maximum elevation of 24° and also for elevation angles in between 17° and 24°. The new cam is designed to fit inside the existing housing of elevation mechanism. Thus, by replacing the existing cam with the new cam, existing elevation mechanism can be used for achieving higher elevation for 84mm RCL without any other modifications.

4. References

[1] Norton, Cam Design and Manufacturing Handbook, 2009

[2] K D Deodhar, R B Varpe, 84 mm LIGHT WEIGHT LAUNCHER Provisional Illustrated Spare Parts List (ISPL), Armament Research and Development Establishment Pune, 2002

Investigation of the Flight of Tank-Fired Proof Shots with Two Different Shapes

B M Sethi
Proof & Experimental Establishment,
Defence Research & Development Organisation
Chandipur
b.sethi@pxe.drdo.in

A Banerjee
Proof & Experimental Establishment,
Defence Research & Development Organisation
Chandipur
a.banerjee@pxe.drdo.in

***Abstract*—Proof Shots are basically economic substitutes of actual projectiles fired from various weapon platforms in warfare. They are used for non-combat purposes viz. generating the ballistic parameters like proof pressures inside the gun barrel required for dynamic testing of different weapon components, evaluating the ballistic performance of gun propellants etc. Due to their typical shape, the proof shots experience high aerodynamic drag and hence, have a very small range. Thus, the aerodynamic behavior of proof shots is the subject of very few studies. In this work, Computational Fluid Dynamics (CFD) tools have been used to analyse the flow field and aerodynamics of two different designs of Proof Shot fired from a typical Main Battle Tank. The aerodynamic drag co-efficients simulated for the Design I at different velocities (Mach Numbers) were found to match quite agreeably with experimental data. However, significant variations between the simulated and experimental drag coefficients were observed for Design II. From an analysis of the variation of the simulated drag co-efficient with the angle of attack, it appears that the Proof Shots of Design II have a tendency to experience wide fluctuations in the angle of attack during flight. This can be attributed to the peculiarity in Design II that has been corroborated by study of the flow field around the Proof Shots.**

Keywords— Proof Shots, Drag Coefficient, Wake, Muzzle Velocity, Main Battle Tank

1. Introduction

Four methods are prevalent for predicting the aerodynamic forces and moments on a projectile in flight and the study of the flow of the medium past it [1]. The empirical method attempts to aerodynamically describe the projectile with a set of geometric properties. The database of aerodynamic coefficients as functions of geometric features is obtained from wind tunnel or spark range testing. The data are fit to multi-variable equations to create generic models. A typical example is PRODAS. Though it is a general method applicable to any projectile, it is the least accurate, particularly for new configurations.

The second method is the wind tunnel testing where the projectile under test is mounted at various angles of attack and the aerodynamic forces and moments are directly measured using sting balance. Modestly expensive, this method is very accurate, though dynamic derivatives viz. pitch and roll damping, Magnus force and moment coefficients are difficult to ascertain.

In the CFD simulations technique, the fundamental fluid dynamics equations are solved for a specific configuration. It is a general method valid for any configuration and is computationally expensive.

Finally, in the spark range testing, a projectile is fired through an enclosed building and at a discrete number of points, the state of the projectile is measured using spark shadowgraphs. This technique is the most accurate method for projectile aerodynamic coefficient estimation.

However, it is also the most expensive method and valid for only the particular projectile configuration [1].

Predictive capabilities using computational techniques for solving the N-S equations have been developed and applied to an extensive number of projectile configurations by Sturek et al. [2]. Silton [3] undertook a computational study to predict the static aerodynamic, Magnus moment and roll damping coefficients of a standard spinning projectile using N-S flow solver over a wide range of Mach Numbers to include subsonic, transonic and supersonic regimes. Good predictive capabilities were found for the static aerodynamic coefficients throughout all the flight regimes. Guidos et al. [4] conducted numerical and wind tunnel experiments for tangent ogive-cylinder projectile with pointed, spherical and flat nose tips at supersonic regime, M = 2.95. Two predictive approaches techniques were used to compute the flow fields of interest. The first method computed the flow in the vicinity of the blunt nose tip and provided inflow conditions for the second method that computed the flow over the remainder of the body excluding the base region. The nose tip flow structure, surface pressure distribution and turbulent boundary layer velocity profiles were found to be within the measurement accuracy. Algorithm and computing advances have also led to coupling of CFD codes to projectile RBD codes for simulation of free flight motion of projectile in a time accurate manner. The ability to simulate the flight of projectile using first principles has led to the notion of "virtual fly outs" where the simulation tools are used to replicate spark range test [5]. The understanding of flow over bluff bodies has been a topic of substantial significance. The major characteristic of the flow over the bluff body is the development of a turbulent wake with a recirculation that has a principal effect on the drag acting on the bluff body [6].

An example of a typical bluff body used in the field of defence is the proof shot projectile that is basically an economic version of the actual projectile fired from Tanks, Guns and Howitzers. Proof Shots have same mass as that of the actual projectile and are used for "proof" or testing of the weapon or ammunition components by generation of desired gun chamber pressures. Due to their typical shape, they experience high drag as they come out of the barrel of the weapon and can reach relatively small ranges. Due to their specific applications, analysis of their aerodynamic behavior is not readily available in the open literature. In this work, the aerodynamic behavior of two different designs of proof shot used as substitute of typical long rod projectiles fired from Battle Tanks has been investigated through CFD simulations technique. The predictions from the simulation have been validated by data available from limited dynamic firing experiments. The zero yaw drag coefficient in the subsonic to supersonic regimes has been estimated for each of the designs and compared. Furthermore, the flow around the two designs of projectile has been studied and the suitability of the designs has been compared.

2. Numerical Simulation

The projectiles under study are basically two designs of proof shot having maximum diameter 120mm and meant to be fired from the same weapon. Design I has a cylindrical front body followed by a tail plug of lesser diameter. Design II has a truncated ogive fore body followed by a saddle shaped mid-section and a tail plug at the rear. Projectiles of both the designs have the same mass. Geometric modelling of the projectiles has been done in ANSYS Design Modeller as shown in Fig. 1.

The rectangular shape domain modelling around the projectiles has been done in ANSYS Design Modeller. Upstream and the downstream lengths of the domains are taken as 5 times and 15 times the projectile length while along the radial inlet/outlet it is 10 times the projectile length as shown in Fig. 2.

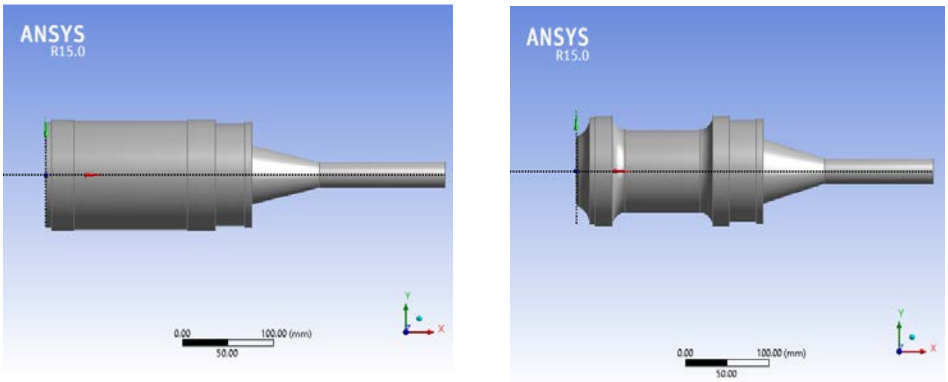

(a) (b)

Fig 1: Geometric model of proof shot (a) Design I and (b) Design II

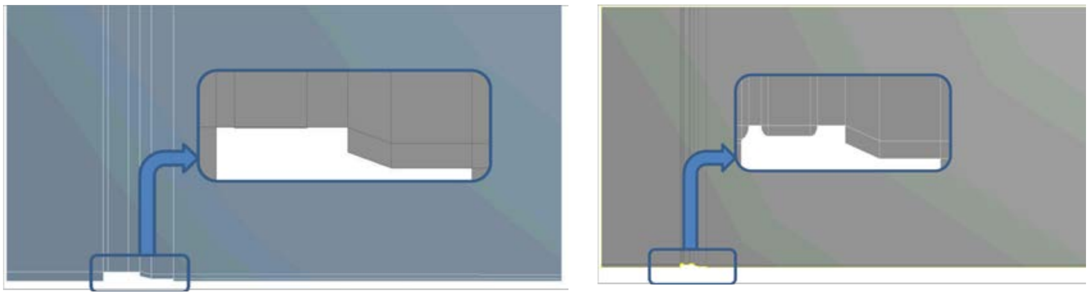

(a) (b)

Fig 2: Domain modeling around proof shot (a) Design-I, (b) Design II

Whole domain has been divided into finite number of sub-domains blocks. The above-mentioned distances are found sufficient to impose the inflow and the outflow boundary conditions at the extremities of the domain. This was done so that the flow around the geometry does not affect the free stream boundary conditions. This is followed by domain meshing presented in Fig 3.

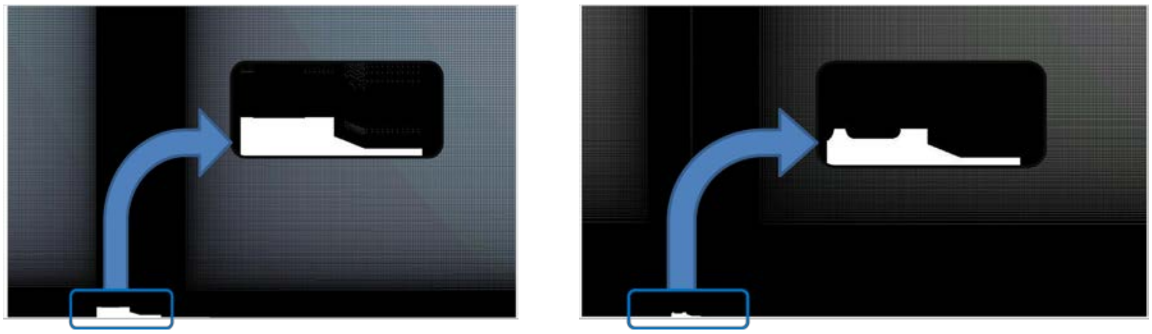

(a) (b)

Fig 3: Domain meshing of proof shot (a) Design I (b) Design II

The structural meshing of the computational domain around the projectiles has been done in ANSYS meshing. Each sub domain has been divided into finite number of control volumes with suitable edge sizing. Face meshing with quad type elements has been selected to obtain the better quality meshing. Near wall meshing has been resolved with suitable bias factor to capture the viscous effect accurately.

Pressure-far field boundary condition has been utilized for a rectangular domain. Pressure far field is a boundary condition that models the free-stream conditions at infinity, using the free stream Mach number and static conditions such as temperature. FLUENT extrapolates the flow variables inside the domain starting from the free stream conditions. Adiabatic wall boundary condition with no slip was used for the shell geometry.

Mach number is varied from subsonic region to supersonic region for both configurations of projectile models. The grid generated models are imported and boundary conditions are defined as mentioned in Table I. Solution iterations are carried out until the stabilized results are obtained. The convergence criterion was set to residuals of 1e-6 units. All the simulations were performed in parallel on system with double precision options. The steady state calculations took approximately 2-3 seconds of CPU time per iteration.

Table 1: Solution Setup

Parameters	Sub-parameter	Boundary
General parameters	Solver type	Density- based
	Time	Steady
Viscous model type	k-ω	SST
Flow fluid (Air)	Density	Ideal-gas
	Specific heat	1006.43 (J/kg-K)
	Thermal conductivity	0.0242 (W/m-K)
	Viscosity	1.7894e-05 (kg/m-s)
	Mol-weight	28.966 (kg/kmol)
Pressure Far-Field	Pressure	101325 Pa
	Temperature	300 K
	Mach Number	Subsonic to Supersonic velocity

3. Results & Discussion

A. Proof Shot, Design I

From the results of the numerical simulations of the air flow around the Proof Shot, Design I having zero angle of attack, the aerodynamic drag co-efficient, C_{D0} was obtained against different Mach number, M values. The variation of C_D vs. M is presented in Fig 4. It is seen that the C_{D0} values increase steadily with Mach number in the subsonic zone, attains peak value in the supersonic zone and thereafter, becomes more or less constant. The simulated results have been validated with limited experimental data. Proof Shots of Design I were assembled with appropriate propulsion units and dynamically fired from Tank platform. RADAR, working on the principle of Doppler shift in frequency was deployed to record the muzzle velocity (MV).

The drag co-efficient, C_D was obtained by post-processing the data generated by RADAR. Due to the use of fixed head RADAR, the proof shots could be tracked up to a limited range when the remaining velocities were still in the supersonic regime. Thus, experimental data for C_D were available only in the supersonic regime. A comparison of simulated C_{D0} and experimental C_D values is given in Table II. The error is found to be less than 10 %.

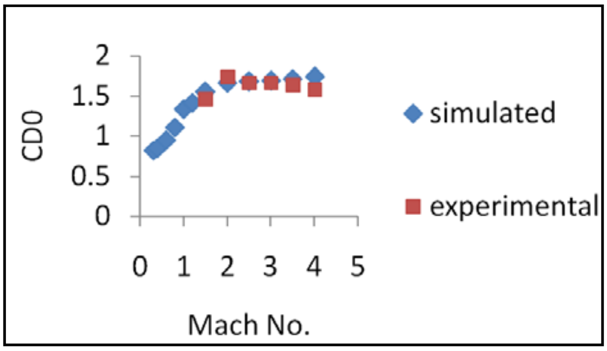

Fig 4: Simulated &Experimental C_{D0} vs. M data for Proof Shot, Design I

Table 2: Comparison of simulated C_{D0} and experimental C_D values for Proof Shot, Design-I

M	C_{D0} (Simulated)	C_D (Experimental)	Error (%)
1.5	1.553	1.465	5.97
2.0	1.664	1.739	4.33
2.5	1.681	1.668	0.77
3.0	1.691	1.668	1.34
3.5	1.712	1.640	4.33
4.0	1.739	1.581	9.93

B. Proof Shot, Design II

Numerical simulations have also been carried out for the Proof Shot, Design-II. It is seen from Fig 5 that for proof shot Design II, the value of C_{D0} varies with M in a similar pattern as that of Design I. The simulated C_{D0} vs. M profiles for both designs of the proof shot are presented in Fig 5. It is also observed that the C_{D0} values for Design-II are lesser than those for Design-I over the entire range of Mach numbers when moving at zero angle of attack. The decrease in aerodynamic drag coefficient, C_{D0} is evidently due to the change in the shape of the Proof Shot Design-II. Thus, it appears that Design II is aerodynamically more efficient than Design I. Limited experimental data for C_D vs. M were also generated for the Proof Shot, Design-II. The experimental C_D values obtained and compared with the simulated values are plotted in Fig 6. The comparative data of Fig. 6 indicate a significant variation between the simulated and experimental C_D values for Proof Shot, Design II. The experimental value is considerably higher than the simulated values for the Design-II. This is distinctly different from the case of Design I.

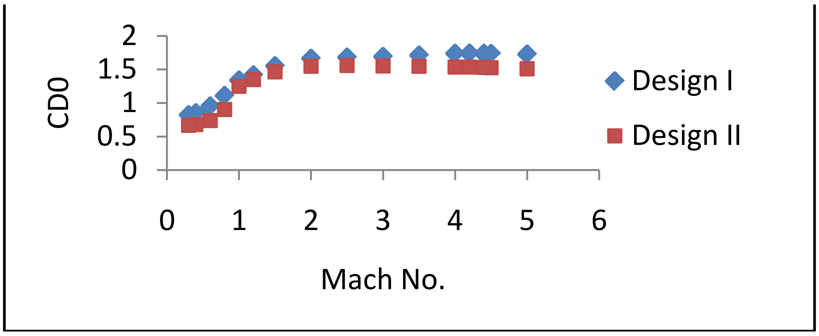

Fig 5: Simulated C_{D0} vs. M for Design I and Design II

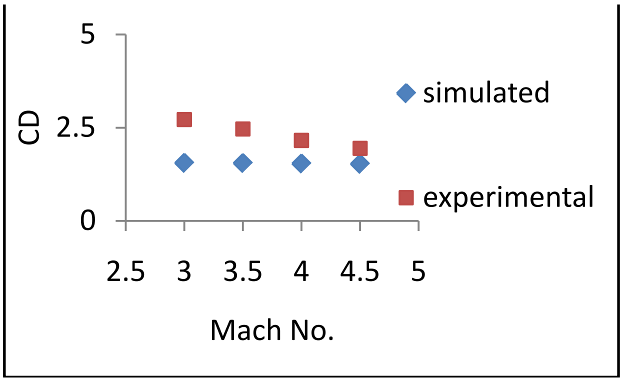

Fig 6: Comparison of simulated C_{D0} and experimental C_D values for PS, Design II

4. Simulation of C_D at different Angles of Attack (AoA) for Design II

The numerical model of Proof Shot, Design II was used to simulate the air flow over the projectile flying with different angles of attack with different velocities. The values of aerodynamic drag coefficient at different angles of attack, $C_{D\,(AoA)}$ were generated. The plots of simulated values of $C_{D(AoA)}$ vs. AoA at different Mach numbers for the Proof Shot, Design II are presented in Fig. 7 that indicate an increase of C_D values with AoA at each Mach number. Table III presents the comparison of C_D values of experimental and simulated at 0^oAoA (C_{D0}) and the AoA at which the simulated $C_{D\,(AoA)}$ approaches the experimental data for the proof shot, Design II. From analysis of data given in Table III, it appears that the Proof Shot, Design II may have experienced continuous changes in attitude (AoA) during flight. The continuous variations in the angle of attack of the PS Design II in flight may be attributed to its shape that is more prone to instability.

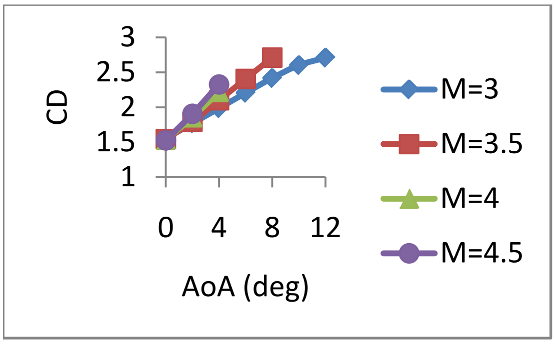

Fig 7: Simulated $C_{D(AoA)}$ vs. AoA at different M for PS, Design II

Table 3: Experimental and simulated C_D values for Proof Shot, Design II

MACH	Experimental C_D	Simulated C_{D0} (at 0^oAoA)	AoA at which simulated $C_{D(AoA)}$ approaches experimental C_D
4.5	1.950	1.528	2^o
4.0	2.157	1.537	4^o
3.5	2.467	1.550	6^o
3.0	2.722	1.554	12^o

To verify this, the contours of turbulence and vorticity for Proof Shot, Designs I and II have been studied at various Mach Numbers and compared.

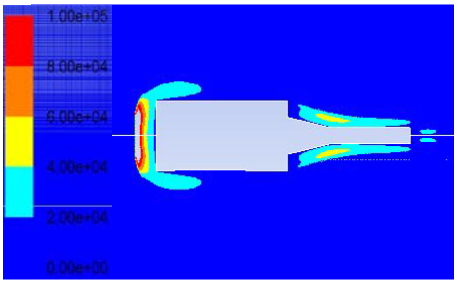

(a)

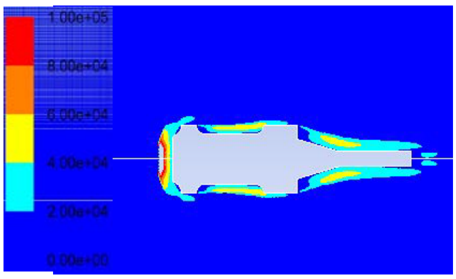

(b)

Fig 8: Turbulence contours of proof shot (a) Design I (b) Design II

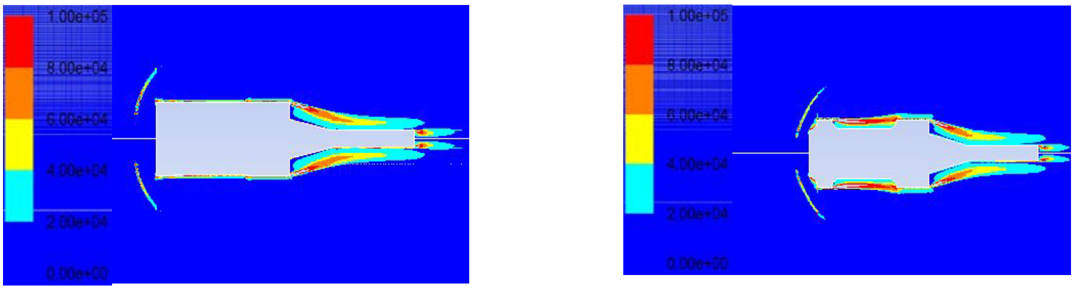

(a) (b)

Fig9: Vorticity contours of proof shot (a) Design I (b) Design II

A typical comparison of turbulence and vorticity profiles at Mach 3.5 is shown in Fig. 8 and Fig. 9. The proof shot, Design II is found to experience more the effects of turbulence and vorticity as compared to Design I. This leads to higher tendency of instability for proof shot, Design II that may experience frequent changes in angle of attack during the flight.

5. Conclusion

The aerodynamic behavior of two different designs of Proof Shots has been investigated through numerical simulations. The axial drag coefficient of blunt cylinder shaped design was found to be more for the range of speeds studied as compared to that for the other design. However, the latter design is prone to instabilities due to its shape and hence the angle of attack may vary during its flight.

6. Acknowledgement

The authors are thankful to Shri R D Misal and team of ARDE, Pune for valuable inputs and Radar & Sensor group of PXE led by Dr S Padhy for generating the experimental data used in this work. The authors are grateful to Director, PXE for kind permission for publishing this work.

7. Reference

[1] J Kokes, M Costello and J Sahu, Generating an aerodynamic model for projectile flight simulation using unsteady time accurate computational fluid dynamic results, Proc. 31stIntSymp Ballistics, India, 2019, 31 – 54.

[2] W Sturek et al, Applications of CFD to the aerodynamics of army projectiles, J Spacecraft and Rockets, 31 (2), 186-199, 1994.

[3] S Silton, N-S computations for a spinning projectile from subsonic to supersonic speeds, J Spacecraft and Rockets, 42 (2), 223-231, 2005.

[4] B J Guidos et al, N-S computations for pointed, spherical and flat-tipped shells at Mach 3, J Spacecraft and Rockets, 42 (2), 223-231, 2005.

[5] J Sahu, Time accurate numerical prediction of free-flight aerodynamics of a finned projectile, AIAA-2005-5817, AIAA Atm Flight MechConf, 2005.

[6] P Kumar, S K Singh, Flow past a bluff body subjected to lower subcritical Reynolds number, Journal of Ocean Engg. &Sc, Article in press

Development of High-Velocity Oxy-Fuel (HVOF) Thermal Spray Coating of Fe-Based Amorphous Powder to Enhance the Wear Life of MBT Arjun Gun Barrel

V. M. Nimbalkar
NMRL, Ambernath
vijayn@nmrl.drdo.in

A K Roy
ARDE, Pune
akroy@arde.drdo.in

D S Gowtam
NMRL, Ambernath
satyag@nmrl.drdo.in

S Prasad
ARDE, Pune
satendradrdo@gamil.com

Mahesh Mohape
NMRL, Ambernath
m.mohape@rediffmail.com

G Mahanta
NMRL, Ambernath
gagendramahanta1@gmail.com

S G Pandav
NMRL, Ambernath
shivdaspandav@gmail.com

T Latalwar
NMRL, Ambernath
tikaram.tnlg@gmail.com

Abstract- **The gun barrel wear is caused due to thermal, mechanical, and chemical wear. Before World War II the barrel life was dictated by the fatigue life of the barrel. But the development of clean steel, during World War II, has increased the fatigue life of steel by manifold but the wear life has not increased to the extent [1]. Thus, the present gun which uses clean steel ESR steel (VIM + VAR steel, etc.) for gun barrel manufacturing is condemned based on its wear life due to remaining fatigue life. To enhance the service life of the gun barrel there is a need to enhance its wear life. Presently Hard Chrome Plating (HCP) is in-vogue for the higher calibre gun barrel to enhance its wear life but chromic acid used in the HCP process makes it hazardous to the people involved in the process. Also, it reduces the fatigue life of the barrel due to micro-cracks formed during hydrogen de-embrittlement. There is a need for a paradigm shift in the surface engineering process to enhance the wear life of the gun barrel without compromising its characteristics. To enhance the wear resistance without compromising the characteristics of the gun barrel, HVOF thermal spray deposition is one of the suitable coating processes for higher calibre gun barrels. Generally, commercial powders like WC powder, Cr_3C_2 powders are being used in HVOF coating applications. NMRL developed (N2) Fe-based amorphous powder has been used for coating on steel used for MBT Arjun gun barrel applications. A cut piece of MBT Arjun gun barrel of length 50 mm and OD and ID 187 mm and 125 mm respectively has been coated by HVOF process with NMRL developed powder and around 300 µm coating thickness has been achieved. Adherent and dense coatings were obtained after optimizing the coating process parameters such as the size of the powder (25 – 45 µm), oxygen flow rate, kerosene flow rate, spray distance (350 mm) & spray rate (10 lbs/hrs.), etc. These coatings possess an amorphous/nanocrystalline microstructure, which imparts high hardness & better corrosion resistance.**

For better wear life coatings on the gun, barrel substrate should possess low wear resistance, low coefficient of friction, high adhesion strength, good surface finish & high corrosion resistance. Subsequent structure-property evaluation of the HVOF coatings studies indicated high hardness (≥ 750 VHN), low porosity (2%), high good adhesion strength (≥ 60 MPa) & low surface roughness (Rs≤ 1.6 µm), etc. These coatings have been characterized for evaluating the wear resistance using the pin-on-disc method. It was found that the coatings possess a low wear rate (1.923 X 10-7 X mm3/mm) & low coefficient of friction (µ ≤ 0.3) which is better than commercially available WC powder & other comparable surface engineering processes.

Keywords - High calibre gun barrel, High-velocity oxy-fuel (HVOF), thermal barrier coating, wear rate, coefficient of friction, adhesion strength, surface roughness

1. Introduction

The wear, an unacceptable loss of material that occurs on the forcing cone or bore of the barrel, is caused either by the action of the hot propellant gases passing over them at high velocity (a process called erosion) or by the projectile moving through the bore and interacting with the internal surface of a gun barrel, which typically has thermal, chemical and/or mechanical bore degradation components) [1]. Typical erosion rates are in the range of 0.1 - 200 μm per firing, with the worst damage usually occurring near the commencement of rifling (C of R) position or, for smooth-bore barrels, at the analogous location. The present production of the gun barrel is made of low carbon alloy steel and maintains the other alloying elements of less than 6 – 8 %. The made gun barrel is coated by hard chromium or HVOF coating of tungsten carbide powder to enhance their wear resistance and life. Some of the gun barrels have been carried out by cobalt-based line to reduce the erosion of gun barrel metal but this liner coating process is not formed the metallurgical bonded between liner and base material of gun barrel. During the firing of propellants, the temperature of the flame more ≥ 2000^0C are generated as well as high energy or high velocity are effect on the rapid succession with bursts from the gun barrels materials. The present high calibre gun barrel has limited life due to the thermal stress the extreme loss of wear at the internal surfaces of the gun barrel.

One of the most useful surface treatments such as hard chrome electroplating [2] and electrolytic hard chrome [3] is applied on the gun barrel materials' internal surfaces, this immensely helps for enhancing the wear resistance [4]. As per the guideline of the environmental protection agency, chromium metal is on the list of toxic materials [6]. In the electrolytic process, electrolytic contains large amounts of Cr^{6+} ions, and that Cr^{6+} ion is spread in the air and it also difficult to deception in drains and filters [6]. The current guidelines of environmental legislation restrict the use of chemicals containing hexavalent chromium ions and also suggested an alternative route for coating processes to be less harmful to the air atmosphere. Other than the air atmosphere issues, some metallurgical problems occur such as hydrogen environment and also non-homogeneity in the microstructure [7,8]. The hard chrome coating substrate is found some micro-cracks and tensile stresses, that affect the delamination of the chromium layers and also decrease the gun material's fatigue life [9,10].

The thermally sprayed HVOF coating process is an optioned for electroplating hard chrome to enhance the wear life of gun barrel materials [11,12]. A lot of materials are coated by various processes such as high-velocity oxy-fuel (HVOF), plasma, flame electric arc spraying, etc in the application for gas turbine and also for electronics industries. The above all processes and hard chrome All of them have been able to change over to high-velocity oxy-fuel (HVOF) [9], which is an immense help for good highly adherent coatings, with low porosity (< 1%) and good corrosion resistance [13].

A lot of papers on HVOF thermal sprayed coatings of WC-10Co-4Cr and this is also the well-known composition of HVOF thermal spray coatings [14]. Some of the papers examined the microstructure, corrosion resistance, and wear resistance study, and also carried out as-sprayed surfaces and that is indicated the high and low surface roughness values of the coated gun barrel substrate [13,15,18].

The aim of the present work activities is to carry out microstructure analysis, porosity measurement, surface roughness measurement, tribological behaviour, adhesion strength, and salt spray test, etc. of commercially available tungsten carbide & NMRL developed amorphous nanocrystalline Fe-based powder **(N2)** HVOF spry coating on higher calibre gun barrel MBT Arjun tank, the substrate was (ID 125 mm, OD 187 mm & 50 mm length). The HVOF thermal spray coated substrate shows the roughness values ≤ 1 µm (Ra) and this achievement is more constructive than the polished coated substrate and also avoids the extra mechanical processes.

2. Experimental

A. Gun Barrel Base Material

The chemical composition of the gain barrel base material is 3NiCrMoMn (VIM + VAR Process) used in this work is as shown in Table 1**.** The steel is cast, forged, heat-treated (Q&T), machined, boring & compressive strength generated steel. The gun barrel base material substrate surface roughness (Ra) value was found at 1.137 µm. A square sample with 50 X 50 mm & 30 mm thick. were cut it from (ID 125mm, OD 187mm & 50 mm length) substrate.

Table 1: Chemical Composition of VIM + VAR steel used for Coating:

Chemical Composition: As per DEF-STAN-10-13/2 H95									
% Elements	C	Si	Mn	Ni	Cr	Mo	V	S	P
Specified	0.25 0.45	0.10 0.35	0.30 0.70	2.7 3.3	0.7 1.2	0.4 0.7	0.25 Max.	0.15 Max.	0.15 Max.
Received Gun Barrel	0.42	0.22	0.54	2.77	0.71	0.69	0.12	0.016	0.013

B. High-Velocity Oxy-Fuel (HVOF) Coating

HVOF thermal spray coating trials were conducted by using a gun of make: Praxair-TAFA HP-HVOF JP5000 for gun barrel length of 152 mm. For conducting the trials were used two types of powder such as commercially available WC-10Co-4Cr (WOKA 3652, -45 +15µm, spherical, agglomerated and sintered), & NMRL developed amorphous nanocrystalline Fe-based powder (N2) 55Fe20Cr15Mo5W2Mn (20– 45µm, spherical shape) gas atomized powder was employed. The spraying distance was maintained at 350 mm. The HVOF thermal spray coating parameters are as shown in Table 2**.**

Table 2: HVOF Coating Parameters

Sr No.	**Parameters**	**Commercial WC**	**NMRL Developed (N2) Fe-Based**
01	Aspersion Rate (g/min.)	90	90
02	Kerosene Flux (l/min.)	23	23
03	O_2 Flux (l/min.)	875	87
04	Kerosene Pressure (bar)	11.5 (-/+1)	11.5 (-/+1)
05	O_2Pressure (bar)	10.0 (-/+ 0.3)	10.0 (-/+ 0.3)
06	Combustion Pressure (bar)	7 (-/+ 0.3)	7 (-/+ 0.3)
07	Temperature (^{o}C)	850 - 900	850 - 900
08	Spray Rate (lbs/hrs)	10	10

C. Sample Characterization

The microstructure of the coated substrate was evaluated by optical and scanning electron microscopy (SEM) microscope. Samples for microstructure and SEM analysis were cut by using MetcoBaincut – HSS make machine, cutting speed and feed rate were maintained between 100 – 3400 RPM and 1.2 mm/min respectively. Polishing was carried out by using 120 to 800 grits in SiC abrasive paper with 1 µm alumina suspension. Etching of the polished surface was used 2% Nital solution to revolve the phases.

Microstructure analysis evaluated by using carl Zeiss microscope and SEM analysis was carried out with field emission scanning electron microscope (Carl Zeiss, Sigma IV, & 1-nanometer accuracy, field emission filament) & EDS were carried out with Bruker (Solid-state detector). Microhardness tests were performed by using Vickers hardness tester (Make: Struers) applied load at 300 gm (Hv/0.3) at a dwell time of 10 seconds. Microhardness10 indentations were taken on the base material to the coating region for performing the hardness profile.

X-ray diffraction studies were performed by using make: Bruker D8 apparatus with copper tube and Mo Kα of (1.54060 A) radiation over a 2θ range of 10-100. The phase identification of coated substrate by using X'Pert high score PAN analytical.

D. Tribological Behaviour

The tribological behaviour gun barrel base material and coated substrate were carried out as per ASTM G-99 standard and using Pin – On – Disc method for experimental purposes. The test specimens of wear test were cleaned by alcohol and measured surface roughness (Ra) of the base material of gun barrel and & coated substrate, which were found ≤ 1 µm. Two specimens of base material and coated substrate were performed by Pin –on Disc method and the following parameters were used during testing as testing at room temperature (25°C), test load 40 N, sliding speed 0.1 m/s, sliding distance 1500 m, and track radius 25 mm. cylindrical specimens with 6.0 mm diameter and 30 mm length were used for testing and rotating disc were used of SAE 52100 of hardness 60 HRC. The test specimens were weighed before and after each experiment in a digital weighing balance with an accuracy of 0.0001 gm. Two average readings of weight loss of specimen were recorded to determine the amount of wear rate. The wear rate was calculated by weight loss of specimen converted into volume loss of specimens with density 7.8 g/cc and divided by the total sliding distance. Wear worn surface of base material and coated substrates specimens were investigated by SEM.

E. Coefficient of Friction

The coefficient of friction study was carried out of based higher calibre gun barrel, WC & N2 coated substrate by using pin on disc method. Roughness values (R ≤ 1 µm were found in the test samples of base & coated substrate. The coefficient of friction was calculated from the data received from the software.

F. Adhesive Strength Measurement

Pull-off adhesion tests were carried out according to ASTM D4544/ISO 4624 standard. The adhesive strength was performed on two sets of specimens of gun barrel base material and coated substrate. The adhesion test was carried out with these parameters: PosiTest automatic tester with dolly 20 mm, epoxy adhesive EP11HT with the strength of 37 MPa (5500 Psi), room temperature (25 °C), etc. Two reading were captured to record directly by equipment.

G. Salt Spray Tests

Salt Spray (Fog), was used for analyzing the corrosion rate of the base materials and coated substrate exposed in climatic conditions in a controlled environment. Salt spray tests were carried out according to the ASTM B-117 standard. Two tests were performed for each sample condition. The salt spray test was carried out with this parameter such as fog chamber, salt solution reservoir, fog atomized rate 1.0 – 2.0 ml/hrs, cabinet internal temperature 35°C (+/- 2^{0}C), pH range 6.5 to 7.2, salt concentration 5 % NaCl (3.5 Nacl + 95 parts of water) and the test is continuous for 48 hrs. duration of the entire test period.

3. Results and Discussion

A. Chemical Analysis

One sample for chemical composition was taken from the HVOF coated of WC & N2 substrate. The test was carried out as per ASTM E 478. The chemical composition of both the coated materials substrate is as shown in Table 3 (a-b).

Table-3 (a): Chemical Composition of HVOF WC Powder Coated Substrate

% El	Tungsten Carbide	Cobalt	Chromium
WC Coated Substrate	86	10	4

Table-3 (b): Chemical Composition of N2 Coated Substrate

% El	Fe	Cr	Mo	W	Mn	P	V
N2 Coated Substrate	54.86	19.55	13.48	4.95	1.80	0.35	0.10

B. Microstructure

The microstructural examination was done on the samples cut from suitable locations of coated gun barrel samples by using the HVOF process on WC and N2 coated substrate. Metallographic specimens were prepared as per standard ASTM E 112. The WC coating thickness obtained after HVOF coated process was 225 ± 25 µm and N2 substrate coating thickness obtained after the HVOF process was 325 ± 25 µm. The microstructure of coating thickness of WC & N2 coated substrate are as shown in Figure 1 (a-b).

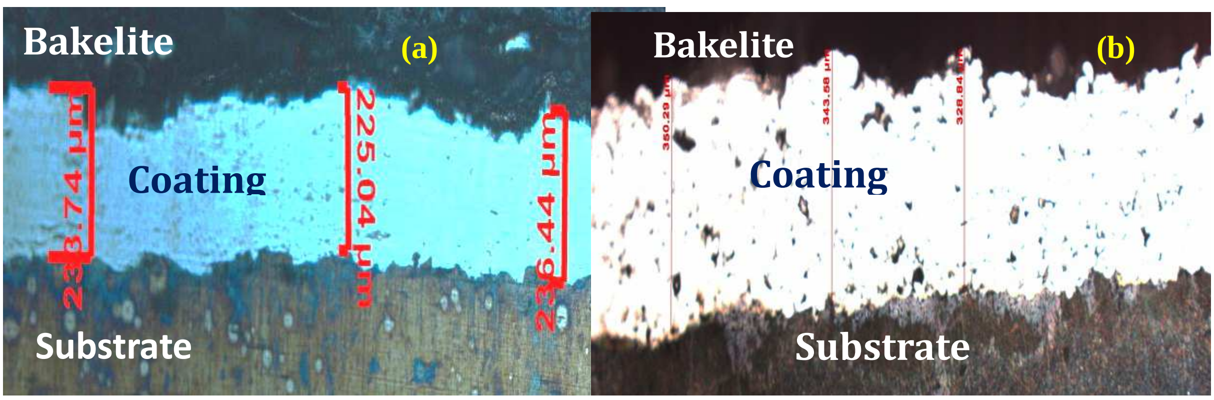

Fig.1 (a) HVOF Coated WC Substrate Coating Thickness: 225 (+/- 25 µm)

Fig. 1 (b) HVOF Coated N2 Substrate Coating Thickness: 325 (± 25 µm)

C. SEM Analysis

SEM studies were carried out with field emission scanning electron microscope (FESEM) of HVOF coated of WC & N2 substrate. SEM studies indicated that the light grey colour phase of the WC and CoCr phase is present in the coated substrate matrix and N2 substrate showing dense amorphous nanocrystalline structure with low porosity (≤ 2%) in the coating-substrate interface are as shown in Figure 2 (a-b).

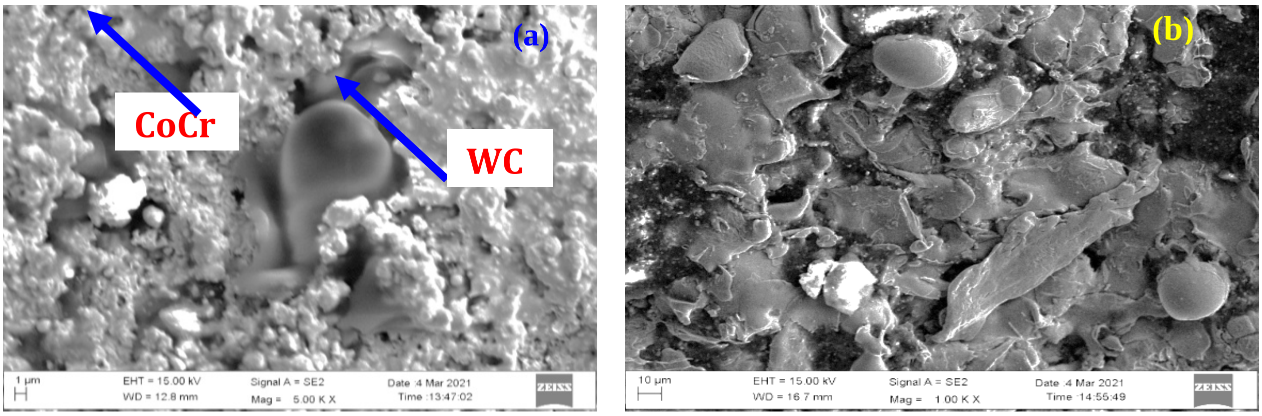

Fig. 2(b) N2 Coated Substrate Showing Fe, Mo, Cr & WC & CoCr Particles in Matrix W Particles in Matrix

D. EDS Analysis

EDS analysis was carried out with Brukar (Solid-state detector) of HVOF coated of WC & N2 substrate. EDS technique indicated the oxygen-free coating and meeting the exact stoichiometry composition of each element in HVOF coated WC & N2 on gun barrel substrate, results are shown in Figure 3 (a-b).

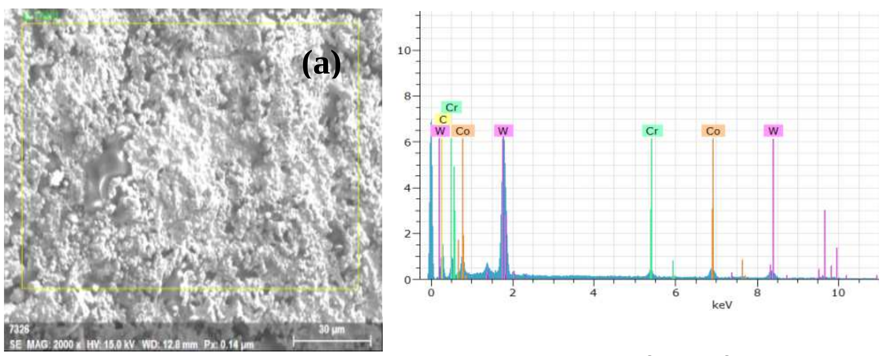

E1	AN	Series	Wt.%
W	74	L Series	61.26
C	6	K Series	22.79
Co	27	K Series	11.91
Cr	24	K Series	4.84
		TOTAL	100

Fig. 3 (a) EDS Analysis on the Coated Surface of WC substrate

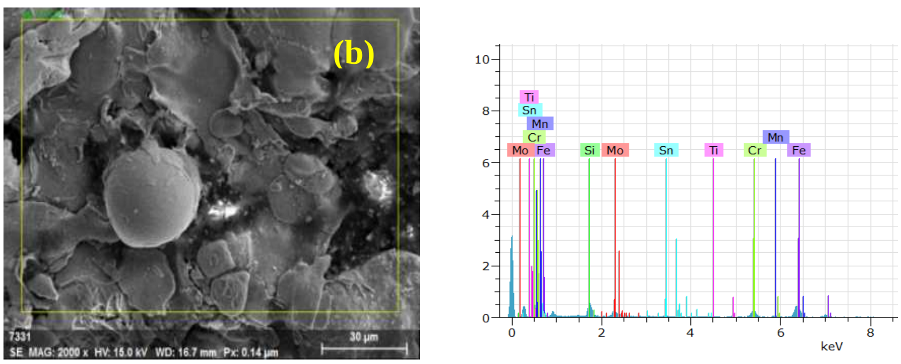

E1	AN	Series	Wt.%
Fe	26	K Series	58.67
Cr	24	K Series	18.40
Mo	42	K Series	10.29
Si	14	K Series	9.59
Mn	25	K Series	1.97
Sn	50	K Series	0.84
Ti	22	K Series	0.25
		TOTAL	100

Fig. 3 (b) EDS Analysis on the Coated Surface of NMRL Developed Fe-based Substrate

E. XRD Analysis

XRD patterns for WC powder & HVOF coated WC and N2 coatings on MBT gun barrels are shown in Figure 4 (a-b). HVOF coated of WC substrate showing a presence of the WC phases in the matrix[19] and as well as the angles between 30^{o} and 50^{0} a cobalt and chromium phases were also observed in the matrix[20,21]. N2 substrate showing 100% amorphous material. Amorphous hump (wide) component and crystalline component (narrow peaks) are as shown in Figure 4b**.** X-ray diffraction results of HVOF coated substrate.

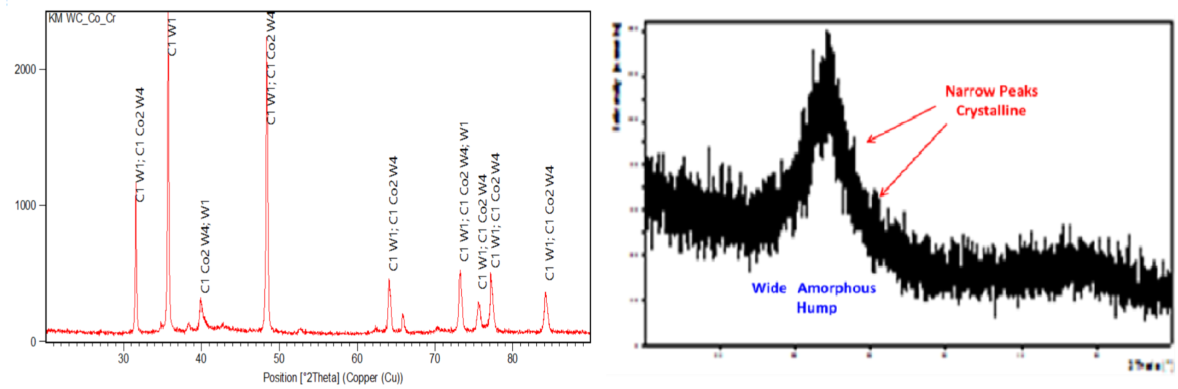

(a) WC Coated Substrate (b) N2 Coated Substrate

Fig 4 (a-b) X-Ray diffraction patterns of WC coated and N2 Coated on higher calibre gun barrel Steel

F. Micro Hardness Profile

The Microhardness profile of WC coated substrate and N2 coated substrate were shown in Figure 5. Ten hardness indentations were taken from the coating region to base material and the average hardness value of the coated region is as shown in Figure 5. The hardness value of the WC & N2 coated substrate region increases significantly due to the high velocity and high temperature of the powder particles. It was also observed that the coating particles are hotly deformed and collide with the surface of the gun barrel base material, which affect the increase the hardness of both the thermal HVOF sprayed coated substrate [24]

Microhardness values obtained were 1660 ± 50 VHN and 750 ± 20VHN of WC and N2 HVOF coated respectively. The average hardness of the substrate was 305 ± 10VHN.

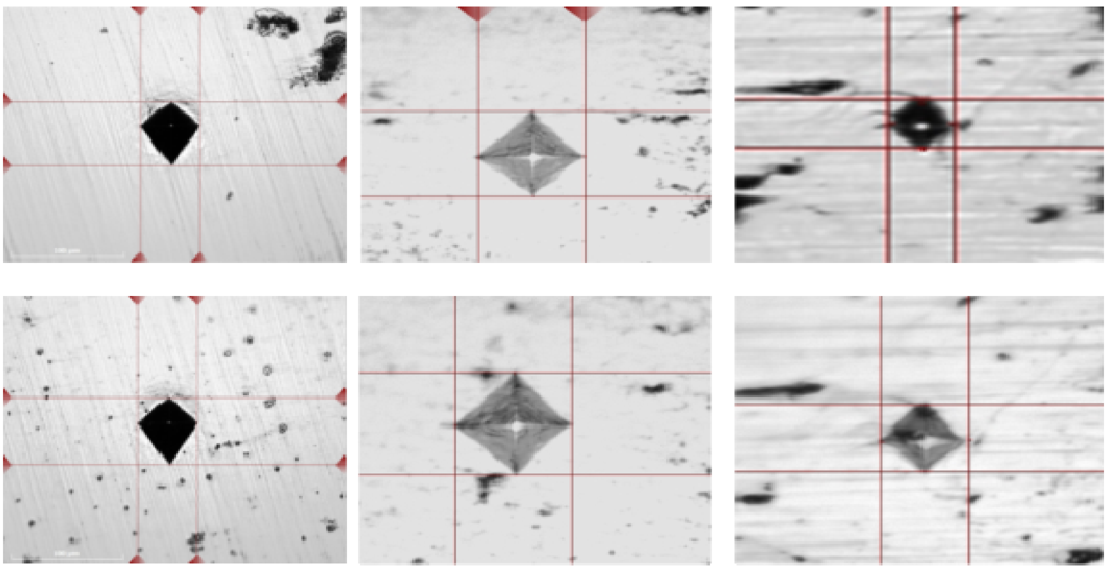

Fig. 5 Vickers Indentations (a) Gun Barrel (b) WC Coated & (c) N2 Coated Substrate

The higher dispersion of the microhardness values obtained for the thermally sprayed coated WC is due to the heterogeneity of the HVOF sprayed coating since each point of the indentation may be located in different phases, in this case, carbides, oxides, inclusions, and the matrix itself [20,21].

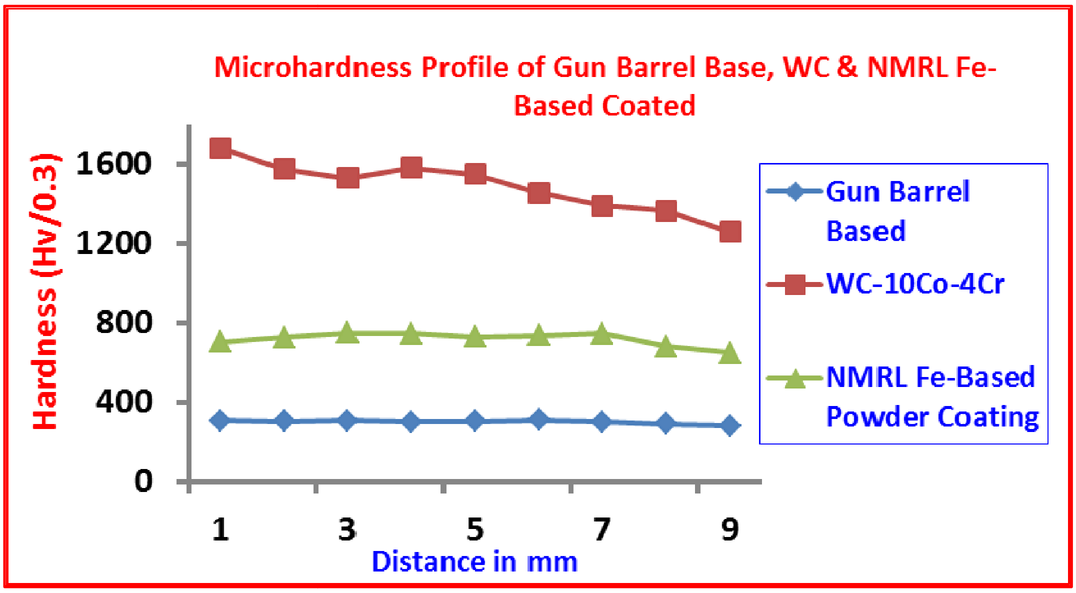

Fig 6: Microhardness profiles of Gun Barrel Base & HVOF Coated Substrate

G. Tribological Behaviour

The wear rate of gun barrel base, WC & N2 HVOF spray-coated is shown in Figure 7**.** N2 coated substrate showing approximately 3 times lower than WC coated substrate and 40 times lower than a higher calibre of MBT gun barrel steel.

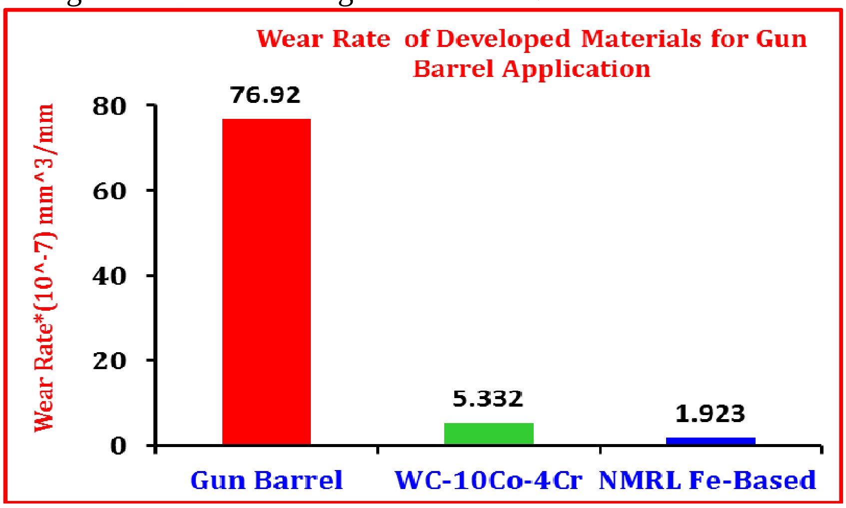

Fig.7: Wear rate of Gun Barrel Base, WC & N2 coated substrate

The wear rate values were 76.92x10^{-7}mm^3/mm for gun barrel steel, 5.332x10^{-7}mm^3/mm for WC coated, and 1.923x10^{-7}mm^3/mm for N2 coated respectively. On the other hand, the HVOF WC coated achieved excellent hardness but a higher wear rate (low wear resistance) than the N2 coated substrate. In the case of the N2 coated substrate showing low wear rate (high Wear resistance) because nano-crystalline particles homogeneously distributed with low porosity on the gun barrel substrate due to the high velocity and temperature of the HVOF process [13, 22]. HVOF coated N2 wear-tested specimens showed a very low amount of material removed from the coating surface and WC-coated wear-tested specimens showed a high amount of material removed from the surface of coating materials.

The wear track of higher calibre gun barrel-based material, WC coated and N2 coated are shown in Figure 8 (a, b). The grinding marks were observed in the gun barrel base materials in the sliding direction and the same is as shown in Figure 8a. These grinding marks are due to the plastic deformation or friction of the test specimen with contact rotating disc of SAE 52100. The relatively low hardness of the gun barrel base materials and compared to the coated substrate for determining factor for this behaviour. The white arrow is as showing the sliding direction of the wear test specimen. Wear test specimen of higher calibre gun barrel material showing severe delamination wear mode. Subsurface analysis by SEM in transverse direction indicates deep crater (≥ 45 mm) in wear-tested high calibre gun barrel material specimen.

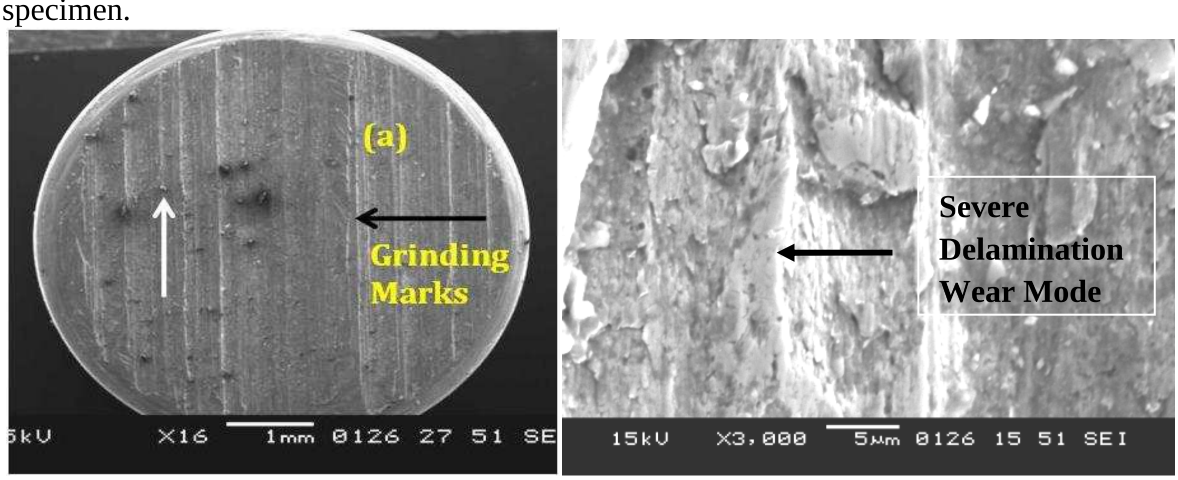

Fig. 8 (a & b) SEM images of the wear track of higher calibre gun barrel substrate

WC coated wear-tested specimen, also showing severe delamination wear mode Figure. 9 (a) with correspondingly high wear rate than gun barrel base materials. Subsurface analysis by SEM in transverse direction indicates shallow marks (≥ 35 mm) in WC-coated wear-tested specimens.

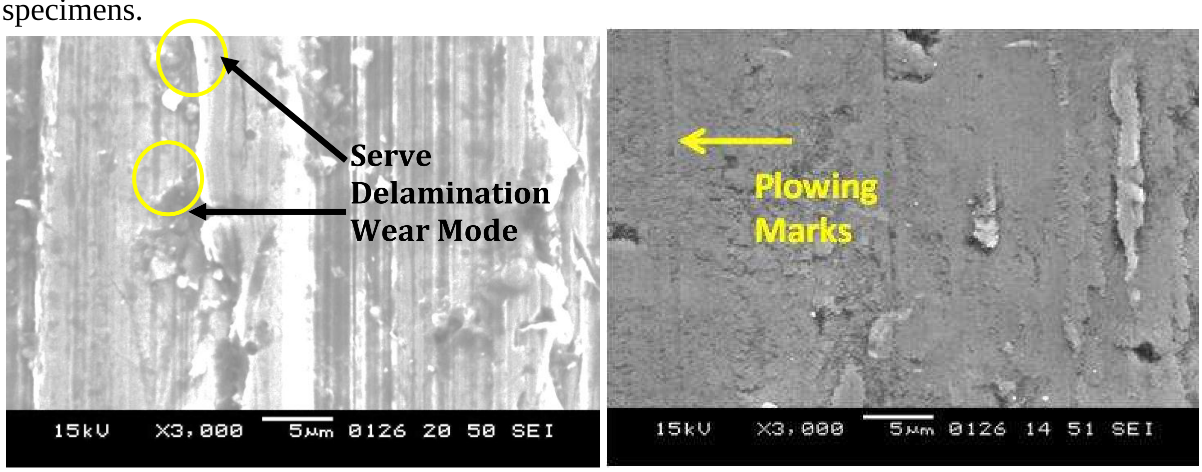

Fig.9 (a) SEM images of the wear track of WC (b) Wear track of N2 Coated

The wear track analysis of N2 coated samples is shown in Figure 9 (b). The worn surface analysis of the N2 coated samples showing mild wear mode with correspondingly low wear rate (high wear resistance) is as shown in Figure 9b, whereas other WC coated and high calibre gun barrel materials show severe delamination wear mode **(**Fig.8 b & Fig. 9 a**)** with correspondingly high wear rate (low wear resistance). SEM analysis of the subsurface on the transverse direction of wear tested samples of N2 coated samples, which shows the shallow marks (≤ 2 mm) and is as shown in fig 9 (b). When the harder amorphous nano-crystalline structure[23] is present against a ductile matrix iron during the sliding contact, the plastic deformations occur in the matrix, which is shown in the form of plowing marks and was shown in the Figure 9b.

It can be clearly seen from these micro-graphs that the typical wear ridges in the case of HVOF spray N2 are smoother as compared to received barrel & WC coated substrate. There was no evidence of gross particle pullout was observed indicative of strong particle-matrix bonding in the case of HVOF spray N2 coated. This enables nano-crystalline particles retention on the surface during dry sliding wear test and thereby resisting shear deformation beneficial in promoting wear resistance of these composites.

H. Coefficient of Friction

The coefficient of friction of based higher caliber gun barrel, HVOF spray-coated WC& N2 substrate. The structure of WC was showing WC & W^2C, which is a hard phase but lesser effects were found in the coefficient friction. Coefficient of friction results of HVOF coated N2 showing very good coefficient of friction other than base higher caliber gun barrel and WC coated substrate.

The values of three different materials were found to be 0.69µ (Based gun barrel, 0.54µ (WC) and 0.29µ (N2). The coefficient of friction results represents a ≥ 57 % decrease in coefficient of friction than based on higher caliber gun barrel. The results of the coefficient of friction are shown in Figure 10.

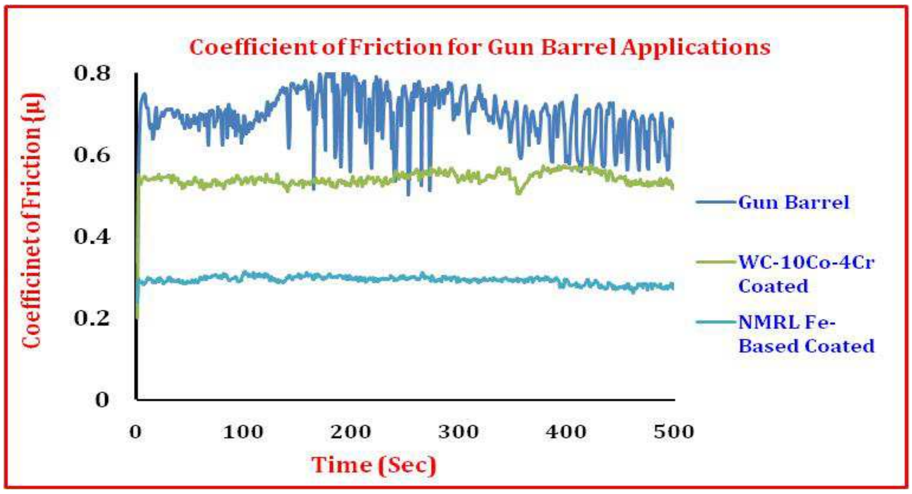

Fig 10: Coefficient of Friction of Base Gun Barrel, WC Coated & N2 Coated

I. Adhesive Strength Measurement

Pull-off adhesion tests were carried out according to ASTM D4544/ISO 4624 standard. Two tests were performed for each sample condition. The adhesion strength of the WC coated sample was found to be 30.09 MPa and the adhesion strength of the N2 coated substrate was found to be 26.50 MPa. The cohesive fracture was observed in WC coated substrate and glue failure was observed in the N2 coated substrate.

The pull of adhesion tests set – up is as shown in Figure 11 and test results of pull of adhesion test is as shown in Figure -12.

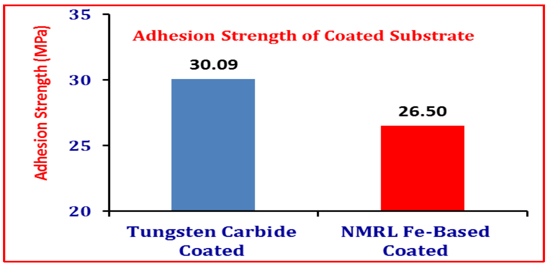

Fig. 11: Pull of Adhesion test Set –Up   Fig. 12 Test Results of Adhesion Strength

J. Salt Spray Tests

Salt spray tests were carried out according to the ASTM B117 standard. Two tests were performed for each sample condition. The salt spray test of higher calibre gun barrel, WC coated and N2 coated substrate was carried out in salt spray fog apparatus is as shown in Figure -13 with 48 hrs. After specified time samples were taken out from the fog apparatus and inspection was carried out in 10X magnification. The test results were showing salt spray effects (corrosion) were found on the higher calibre gun barrel substrate such as pitting and other samples were found satisfactory. The test specimens before and after the salt spray are as shown in Figure 14.

Materials	Before Salt Spray Test	After Salt Spray Test (48 Hrs.)
As Received Gun Barrel		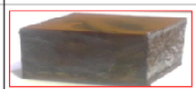
Tungsten Carbide Coating		
NMRL Powder Coating		

Fig. 13: Set –up for Salt Spray Test   Fig. 14: Test Specimens before & after Salt Spray Test

4. Conclusions

The wear behaviour of 3NiCrMoMn (ESR or VIM + VAR) gun barrel steel coated by the HVOF process was investigated. Samples were without ground prior to sliding tests and the following conclusion on the base of the experimental results:

- Surface roughness (Ra) was achieved ≤ 1 µm without grinding after coating.
- The wear rate of the HVOF-sprayed coating N2 was found to be about 40 times slower than the wear rate of the base 3NiCrMoMn (ESR or VIM + VAR) gun barrel steel.
- The high hardness associated with the formation of a wear-resistant tribo-layer enhances the wear behaviour of HVOF coated N2 better than HVOF-sprayed coated WC & base gun barrel steel.
- It can be clearly seen from these micro-graphs that the typical wear ridges in the case of HVOF spray-coated N2 materials are smoother as compared to received barrel & WC coated substrate.

- There was no evidence of gross particle pullout was observed indicative of strong particle-matrix bonding in the case of HVOF spray-coated of N2 materials. This enables nanocrystalline particles retention on the surface during dry sliding wear test and thereby resisting shear deformation beneficial in promoting wear resistance of these coated materials.
- The coefficient of friction results was representing a ≥ 57 % decrease in coefficient of friction than the higher caliber gun barrel steel.
- The adhesion strength of N2 coated shows better adhesion strength than WC coated materials.
- The HVOF coating of N2 has passed the Salt spray test without pitting (corrosion) on the samples.
- As per the feasibility study, HVOF spray-coated of NMRL developed Fe-Based substrate is a promising candidature process for futuristic higher calibre gun barrel ID coating for MBT Arjun Tank for enhancing their wear life without affecting their characteristics.

5. References

[1] AK Roy, M Srikanth, AV Suryavanshi, VS Ghadge & SV Gade, Hard Chrome Plating: A Practical Approach, National Seminar on Futuristic Combat Vehicle held at CVRDE, Chennai in Mar 2017

[2] Houdková Š, Zahálka F, Kašparová M, Berger LM. Comparative Study of Thermally Sprayed Coatings Under Different Types of Wear Conditions for Hard Chromium Replacement. Tribology Letters. 2011;43(2):139-154.

[3] Bolelli G, Cannillo V, Lusvarghi L, Riccò S. Mechanical and tribological properties of electrolytic hard chrome and HVOF-sprayed coatings. Surface and Coatings Technology. 2006;200(9):2995-3009.]

[4] Almotairi A, Warkentin A, Farhat Z. Mechanical damage of hard chromium coatings on416 stainless steel. Engineering Failure Analysis. 2016; 66:130-140.

[5] Ibrahim A, Berndt CC. Fatigue and deformation of HVOF sprayed WC-Co coatings and hard chrome plating. *Materials Science and Engineering: A*. 2007;456(1-2):114-119.

[6] Liang A, Li Y, Liang H, Ni L, Zhang J. A favourable chromium coating electrodeposited from Cr(III) electrolyte reveals anti-wear performance similar to conventional hard chromium. *Materials Letters*. 2017; 189:221-224.

[7] Brooman EW. Wear behaviour of environmentally acceptable alternatives to chromium coatings: cobalt-based and other coatings. Metal Finishing. 2004; 102(10) :42-54.

[8] Legg KO. Hard chromium replacements. In: 4^{th} International Chromium Conference*;* 2004 May; St. Etienne, France.

[9] Souza RC, Voorwald HJC, Cioffi MOH. Fatigue strength of HVOF sprayed Cr_3C_2-25NiCrand WC-10Ni on AISI 4340 steel. Surface and Coatings Technology. 2008; 203(3-4):191-198.

[10] Voorwald HJC, Padilha R, Costa MYP, Pigatin WL, Cioffi MOH. Effect of electroless nickel interlayer on the fatigue strength of chromium electroplated AISI 4340 steel. *International Journal of Fatigue*. 2007;29(4):695-704.

[11] Picas JA, Punset M, Baile MT, Martín E, Forn A. Tribological evaluation of HVOF thermal-spray coatings as a hard chrome replacement. *Surface and Interface Analysis* 2011;43(10):1346-1353.

[12] Gong T, Yao P, Zuo X, Zhang Z, Xiao Y, Zhao L, et al. Influence of WC carbide particle size on the microstructure and abrasive wear behavior of WC-10Co-4Cr coatings for aircraft landing gear. *Wear*. 2016;362-363:135-145.

[13] Singh J, Kumar S, Mohapatra SK. Tribological analysis of WC-10Co-4Cr and Ni-20Cr_2O_3 coating on stainless steel 304. *Wear*. 2017;376-377(Pt B):1105-1111.

[14] Bolelli G, Berger L, Bonetti M, Lusvarghi L. Comparative study of the dry sliding wear behaviour of HVOF-sprayed WC-$(W,Cr)_2$C-Ni and WC-Co Crhardmetal coatings. *Wear*. 2014;309(1-2):96-111.

[15] Hong S, Wu Y, Wang B, Zheng Y, Gao W, Li G. High-velocity oxygen-fuel spray parameter optimization of nanostructured WC-10Co-4Cr coatings and sliding wear behavior of the optimized coating. *Materials & Design*. 2014; 55:286-291.

[16] Wu Y, Wang B, Hong S, Zhang J, Qin Y, Li G. Dry Sliding Wear Properties of HVOF Sprayed WC-10Co-4Cr Coating. *Transactions of the Indian Institute of Metals*. 2015;68(4):581-586.

[17] Wu D, Liu Y, Li D, Zhao X, Liu Y. Tribo-corrosion properties of WC-10Co-4Cr coating in natural silt-laden waters when sliding against Si3N4. *International Journal of Refractory Metals and Hard Materials*. 2016; 58:143-151.

[18] Zoei MS, Sadeghi MH, Salehi M. Effect of grinding parameters on the wear resistance and residual stress of HVOF-deposited WC-10Co-4Cr coating. *Surface and Coatings Technology*. 2016;307(Pt A):886-891.

[19] Guilemany JM, Espallargas N, Suegama PH, Benedetti AV. Comparative study of Cr_3C_2-NiCr coatings obtained by HVOF and hard chromium coatings. *Corrosion Science*. 2006;48(10):2998-3013.

[20] Kang AS, Grewal JS, CheemaGS.Effect of thermal spray coatings on wear behavior of high tensile steel applicable for tiller blades. *Materials Today Proceedings*. 2017;4 (2 Pt A):95-103.

[21] Picas JA, Punset M, Baile MT, Martín E, Forn A. Properties of WC-CoCr Based Coatings Deposited by Different HVOF Thermal Spray Processes. *Plasma Processes and Polymers*. 2009;6(Suppl 1): S948-S953.

[22] Schwetzke R, Kreye H. Microstructure and properties of tungsten carbide coatings sprayed with various high-velocity oxygen fuel spray systems. *Journal of Thermal Spray Technology*. 1999;8(3):433-439.

[23] Lee CW, Han JH, Yoon J, Shin MC, Kwun SI. A study on powder mixing for high fracture toughness and wear resistance of WC-Co-Cr coatings sprayed by HVOF. *Surface and Coatings Technology*. 2010;204(14):2223-2229.

Automated Mine Burying Mechanism

Jagat Prakash Singh
Research and Development Establishment (Engrs.)
Defence Research & Development Organisation
Pune
jagatprakashsingh@gmail.com

Anil Kumar Upadhyay
Research and Development Establishment (Engrs.)
Defence Research & Development Organisation
Pune
akupadhyay@rde.drdo.in

Ajay Kumar Gupta
Research and Development Establishment (Engrs.)
Defence Research & Development Organisation
Pune
akgupta@rde.drdo.in

***Abstract* – The work presented in this paper highlights the design & development of Automated Mine Burying Mechanism. The mechanism is the key assembly of mine laying equipment known as "Self-Propelled Mine Burier". Armed mines are fed into the mechanism and then burying of mine at pre-determined depth & distance is achieved with the help of the mechanism automatically. After burying, mines are camouflaged through a camouflage attachment which is also a part of this mechanism. The design of mechanism renders it capability from surface laying to burying of mine to a desired depth as per the requirement. Automation has been achieved with the help of hydraulic actuators, sensors and an onboard controller. With this mechanism the maximum laying rate of 220 mines per hour at inter-mine spacing of 6 m can be achieved by the equipment "Self-propelled Mine Burier". The equipment "Self-Propelled Mine Burier" has been developed for Indian Army.**

Keywords— Automation, Burying, Digging tool, Mine burier (key words)

1. Introduction

A mine laying equipment "Self-Propelled Mine Burier" (SPMB) has been designed & developed to lay/bury the mines in plains, semi-desert and desert terrain. The mechanism has been designed in such that equipment can lay six types of anti-tank mines namely available in the inventory of Indian Army. The equipment can bury/lay the mines at any selected Inter-mine distance (in the step of 3m) and depth. Mines are stored in four containers. During mine laying operation mines are taken out from the containers and conveyed up to the arming station with the help of a conveyor. At arming station mines are armed manually and fed into the mine burying assembly through a chute attached with the digging tool of the mine burying assembly. The mine burying mechanism bury/lays the mine at desired depth and further camouflaged it with the help of camouflage attachment at the rear of the equipment. Thus, mine burying mechanism includes the activities like sensing of ground level before laying of mine, adjusting the mine burying assembly to dig a pit at required depth, placement of mine into the pit, retrieving the digging tool, and camouflaging of the mine. To achieve all these operations automatically, no. of proximity sensors and hydraulic actuators are used, which are operated with the help of onboard controller. The spacing between mines are maintained with the help of distance measuring device and GPS. Self-propelled mine burier is developed on BEML Tatra 8x8 carrier vehicle.

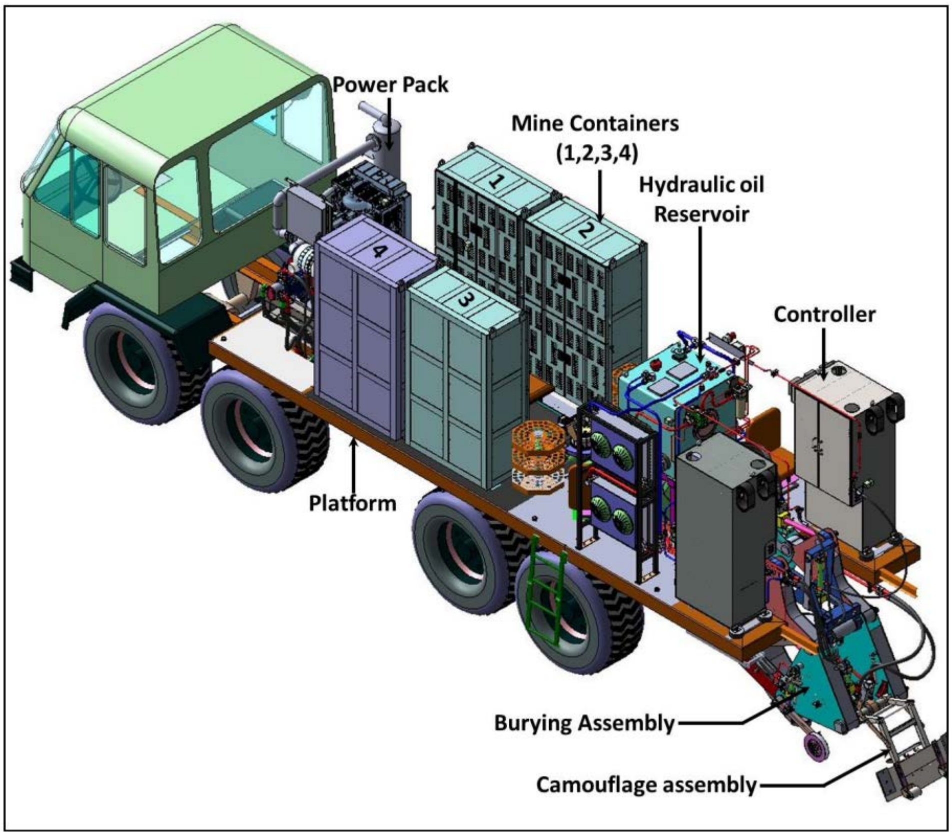

Fig. 1: Self-Propelled Mine Burier

2. Mine Burying Mechanism

A. Description

The mechanism is shown in Fig 2: Various components of the mechanism are as follows:

(i) Lift lower assembly (2 Nos.)
(ii) Digging tool assembly (1 No.)
(iii) Push tool assembly (1 No.)
(iv) Camouflage assembly (1 No.)
(v) Ground level sensing assembly (1 No.)
(vi) Mine counting sensor assembly (1 No.)
(vii) Connecting chute (1 No.)
(viii) Mounting bracket (2 Nos.)

As shown in Fig. 2 & 3 the Mine burying mechanism, consists of duplicate mechanisms of lift lower assembly (six bar mechanisms, 1-6), one digging tool assembly (four bar mechanism, 1- 4’) and one push tool assembly (four bar mechanism, 1 – 4”). These mechanisms operate independently in a particular sequence to bury the mine in the soil. Lift lower assemblies are mounted on two brackets which are mounted on the platform at the rear side as shown in Fig. 1. The chute is connected with the digging tool assembly. The kinematic diagram of the mechanism is shown in Fig. 3. The mine burying mechanism is configured in such a way it can assume two positions i.e. transport mode and burying mode. The dimensions of various links of the mechanisms are found through mechanism synthesis using graphical method.

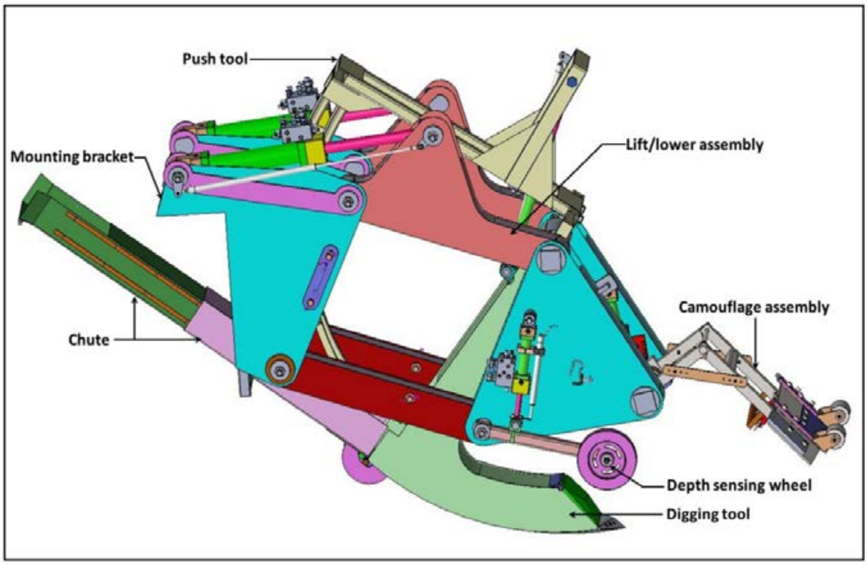

Fig. 2: Components of mechanism

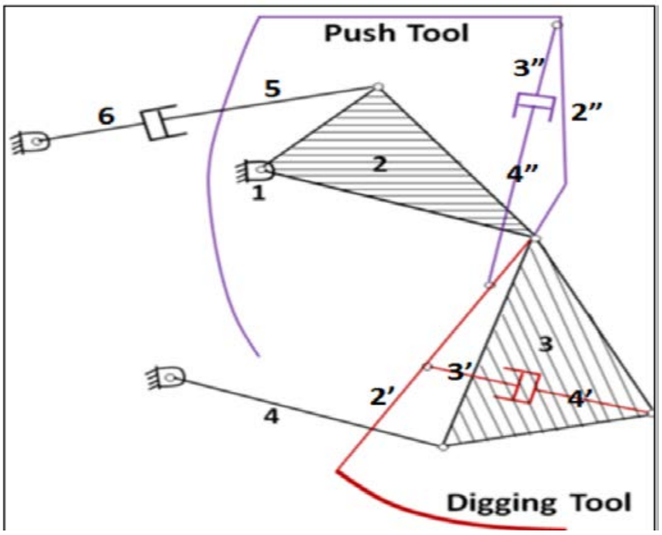

Fig. 3: Kinematic diagram of the Mine Burying Mechanism

B. Sequence of Operation

(i) **Controller input**: Before the start of operation following inputs are fed into the controller.

- Depth at which the mine is to be laid
- Distance between mines

(ii) **Sensing of ground level and adjustment of lift lower assembly**: At the start of operation the burying mechanism takes up the home position (burying mode) and the ground level sensing wheel is in fully open condition as shown in Fig. 4.

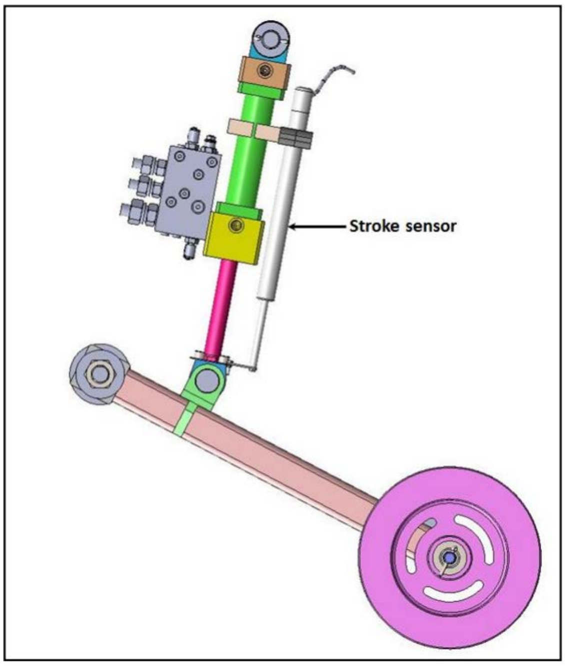

Fig 4: Ground level/depth sensing

The ground level sensing assembly consists of a hydraulic actuator a stroke sensor and a ground level sensing wheel. During the operation the hydraulic actuator remains in float mode and thus ground level sensing wheel is free to go up/down. At home position of mine burying assembly the hydraulic actuator is in fully open condition. When the mine laying/burying operation starts the lift/lower assembly is brought down with the help of hydraulic actuators (refer Fig 2 & 3) such that the ground level sensing wheel touches the ground, which is sensed by the stroke sensor. Based on the stroke sensor input the lift/lower assembly is further adjusted so that the digging tool can create the pit of required depth as already fed into the controller (Since the digging tool is attached with the lift/lower assembly, the depth of the pit created can be controlled).

(iii) **Digging of Pit**: After the lift/lower assembly is brought in the final position the digging tool is operated by the controller to dig into the ground. The digging tool is a hollow tool configured in such a way that all six types of mines can be laid/buried.

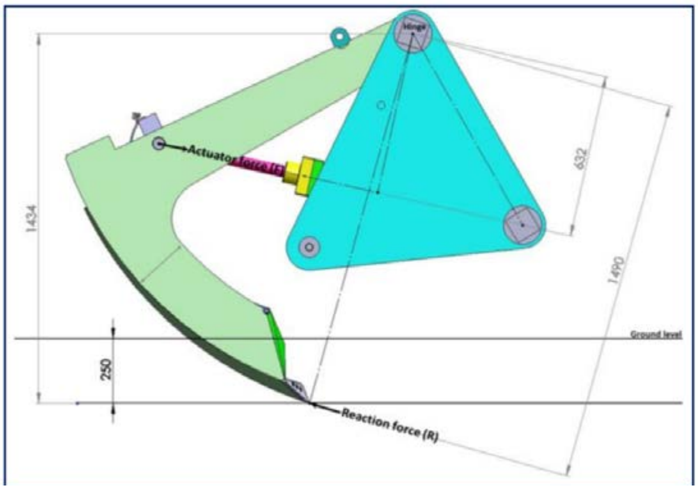

Fig 5: Digging tool digging 250 mm deep pit

Isolated image of digging tool is shown in Fig. 5. The digging tool is operated by a hydraulic actuator. The pit of required depth is dug by closing the hydraulic actuator fully at the final adjusted position of lift/lower assembly corresponding to ground level thus forcing the digging tool to dig into the soil.

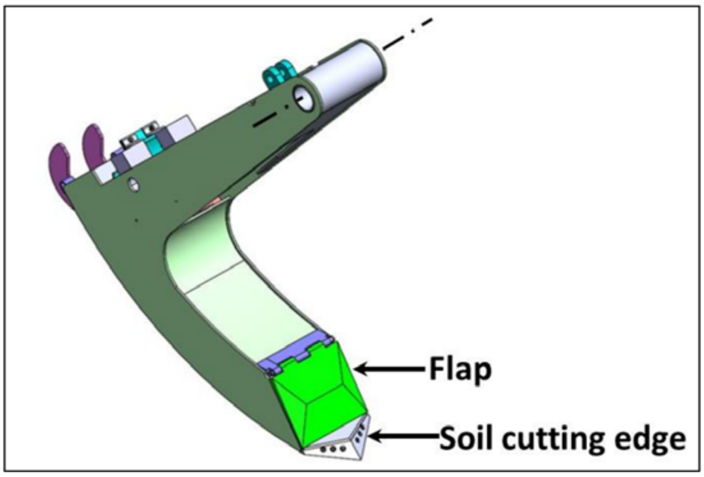

Fig 6: Digging tool

The digging tool is shown in Fig. 6. It has a flap at the end to avoid soil/dust entering inside the tool.

(iv) **Burying of Mine**: At this point when digging tool is fully inside the soil armed mine is slid into the chute as shown in Fig. 7 (refer Fig. 2 also).

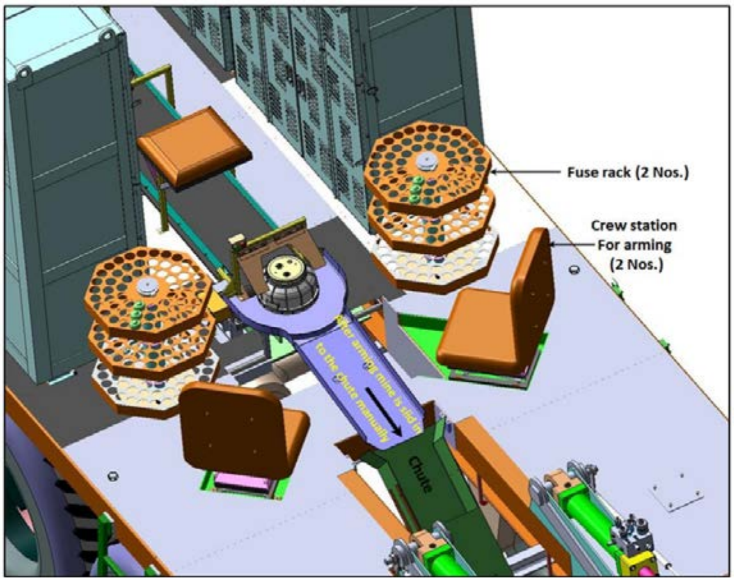

Fig. 7: Mine is slid into the chute after arming at arming station

Since the chute is directly connected with the digging tool as shown in Fig. 2 mine slid into it slides to the end of digging tool and hits the flap.

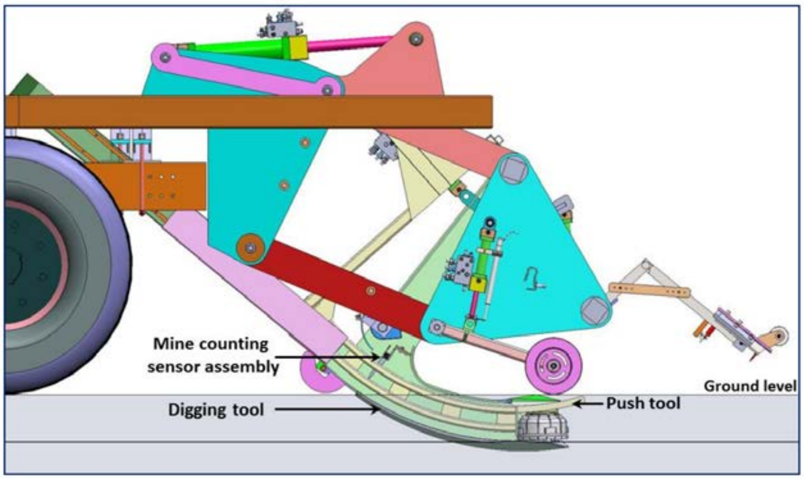

Fig. 8: Mine is being buried

During the travel of the mine into the digging tool it encounters through a mine counting sensor assembly. This sensor has dual purpose first to count the number of mine being laid and thus getting recorded in the controller and secondly to signal the push tool to operate, refer Fig. 3 & Fig. 8. The push tool is shown in Fig 9.

Fig. 9 Push tool

The push tool is operated through a hydraulic actuator such that it opens up the flap of the digging tool and just touches the mine (refer Fig. 8). At this point the digging tool is retrieved slightly thus mine is out of the digging tool, subsequently both digging tool and push tool is retrieved simultaneously. The mine is thus placed into the pit created by the digging tool.

(v) **Camouflaging of Mine:** After placing the mine into the pit the mine is camouflaged by the camouflaging attachment. The camouflage assembly is basically a scrapper which scrapes the soil while being dragged on the ground and fills into the pit thus covering the mine.

The camouflage assembly is operated through hydraulic actuator and can be operated either in float mode or pressure mode. When the mine is to be laid on surface it is raised hydraulically from the ground surface to the height such that it don't interfere with the laid mine, while in case when mine is laid below the ground surface it is operated in float mode.

(vi) **Recording of Mine**: Mine retrieval is very important aspects to be kept in mind when minefields are created. Without the record of location of mine being laid it become very cumbersome task to retrieve the mine hence the record of lat. long. of each buried mine is very crucial. The controller of SPMB record the lat. and long of each mine being laid.

Fig.10: SPMB in operation

3. Finite Element Analysis

Mine burying mechanism of SPMB is a combination of three mechanisms one six bar mechanism and two four bar mechanism. These mechanisms are operated independently to bury the mine into the soil. It can be observed that when digging tool is operated or when push tool is operated the remaining mechanisms are completely locked and thus has been designed as a structure. Based on the estimated design loads for various components FE analysis was conducted and sections were finalized. In the subsequent sections FE analysis of various components of the mechanism has been discussed.

A. Static analysis of digging tool

As shown in Fig. 5 the pit is created with the help of digging tool. The digging tool is pulled by the hydraulic actuators and thus forced into the soil for digging. To cut the soil a cutting edge is provided in front of the tool which shears through the soil. The maximum force required to shear the soil with the digging tool is estimated through experimentation (not discussed here). Thus, during the operation, the digging tool is subjected to a reaction from the ground. Based on it the size of the hydraulic cylinder and operating pressure was finalized which can apply the necessary force at the tip of digging tool. Stress plot of digging tool is shown in Fig. 11.

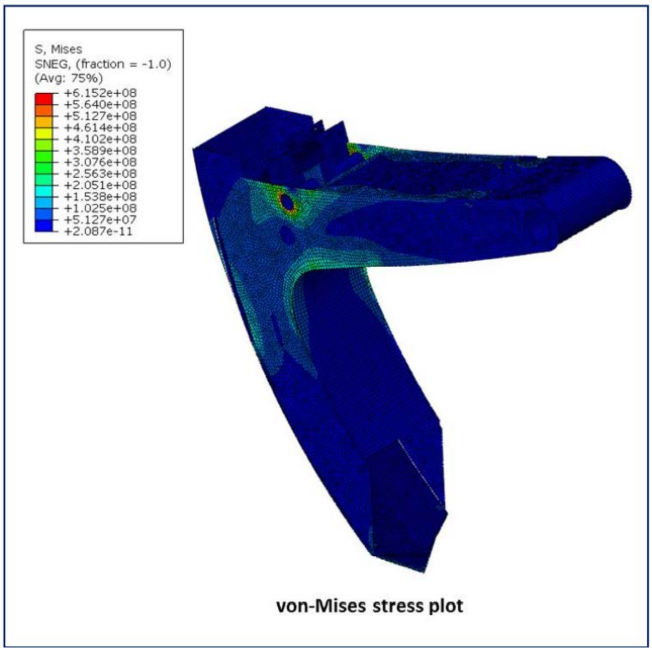

Fig. 11: FE analysis of the digging tool

B. Static analysis of Link 3
As shown in Fig. 2 & Fig 5.

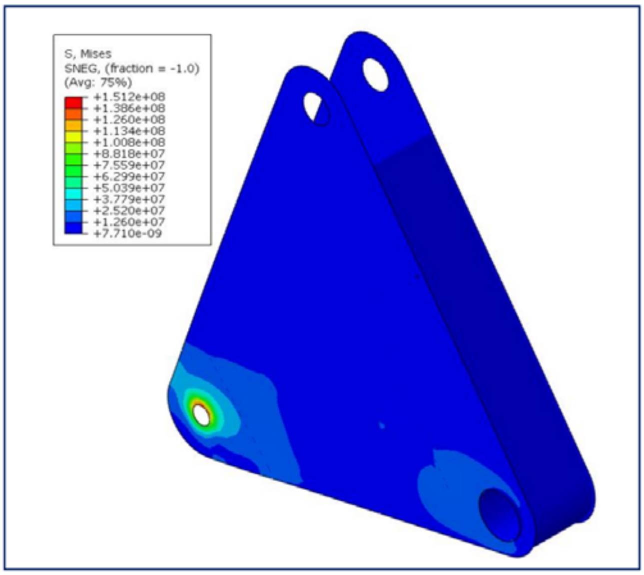

Fig. 12: FE analysis of the Link 3

The triangular bracket is connected with two other links while at the mid portion it supports the hydraulic actuator of the digging tool. Based on the configuration and loads coming onto the triangular bracket FE analysis was carried out and the stress plot is shown in Fig. 12.

C. Static analysis of Link 2
Stress plot of Link 2 is shown in Fig. 13

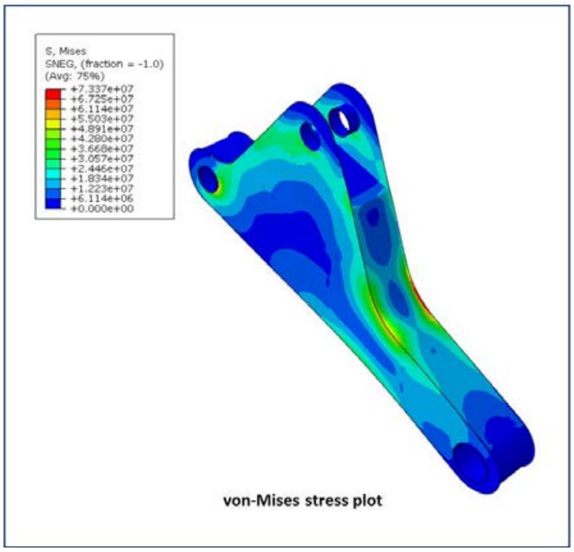

Fig. 13: FE analysis of the Link 3

D. Static analysis of mounting bracket

Stress plot of mounting bracket is shown in Fig. 14.

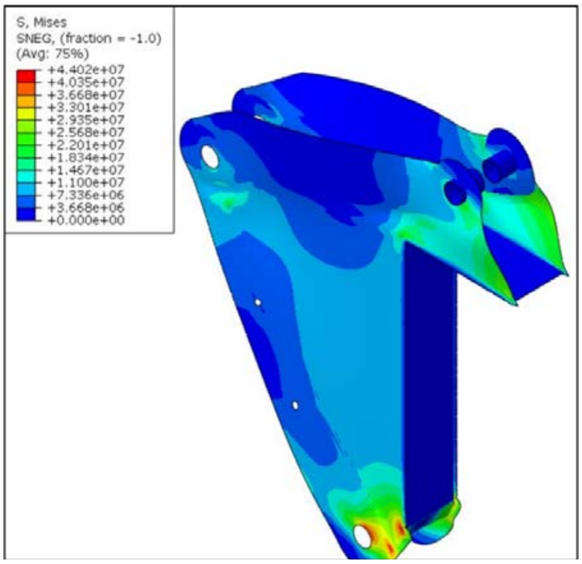

Fig. 14: FE analysis of the mounting bracket

4. Conclusion

The purpose of the paper was to present the concept of automated mine burying mechanism for the equipment Self-propelled mine burier. Since each anti-tank mine may carry 6-8 kgs of explosive, design of automated burying mechanism should be extremely safe considering the fact that five crew members are on-board on the equipment storing maximum up to 350 nos. of mines.

The conceptualization of the mechanism is based on the philosophy that during complete laying operation mine should be handled with extreme precaution by the burying mechanism so that the crew can operate the equipment safely. The equipment “Self-propelled mine burier” has completed the field trials successfully and thus recommended for induction into the services.

5. Acknowledgment

Authors gratefully acknowledge the guidance and encouragement given by Shri VV Parlikar DS & Director R & D E (E), in carrying out this work.

6. References

[1] Abaqus 10 software & documentation

[2] B. Robert Cook, "Concept and Applications of Finite Element Analysis", Fourth Edition, John Wiley & Sons Pub,2002.

Effect of Mass Imbalance on the In-Bore Motion of Projectile

Tapas Ranjan Panda
Proof and Experimental Establishment
DRDO
Chandipur
tr.panda@pxe.drdo.in

Arkadeb Banerjee
Proof and Experimental Establishment
DRDO
Chandipur
a.banerjee@pxe.drdo.in

Abstract - **The motion of a projectile inside gun barrel is affected by many factors. The lateral motion of the projectile inside the bore, called balloting, is undesirable. It has been shown that a radial shift in the centre of gravity (CG) of the projectile leads to imbalance in the in-bore motion. In this paper, the effect of different values of radial shift of CG on the in-bore motion for a typical 155mm artillery shell has been investigated through numerical simulations. A 3D finite element model has been developed for the simulation of the in-bore motion of a projectile. The lateral velocity, barrel exit angle and motion of the projectile inside the gun bore have been compared for the different values of radial shift in CG. It is shown that the degree of unbalanced in-bore motion of the projectile is proportional to the radial shift in CG and may lead to undesirable consequences during gun firing.**

Key words—internal ballistics, balloting, gun barrel interaction

1. Introduction

In a typical gun system, propellant burns in a confined chamber to generate high temperature and high volume of gases that propel a projectile along the barrel. The major factors that contribute to the in-bore velocity of the projectile are the temporal variation of the chamber pressure, base pressure, interaction between projectile and gun barrel rifling and the temperature generated. As the duration of the entire internal ballistic phenomena is in the order of milliseconds and the interaction between projectile and barrel extremely dynamic, the prediction of the dynamic phenomenon is extremely difficult.

A 3D finite element model was developed by Deng et al. [1] to simulate the in-bore motion and behavior of a 9 mm pistol bullet. Analytical method was used for the calculation of chamber and base pressures. Computational results were verified using experimental set up. The difference in muzzle velocities calculated by the numerical technique and experiments was in the order of 2.56%.

A two-dimensional contact-impact finite element model of projectile-barrel interaction was developed by Ge et al. [2] for rifled bore and smooth bore barrels. Elasto-plastic material model was used for modelling of the driving band of the projectile. The analysis result of rifled bore model was compared with that of smooth-bore model and it was concluded that the impact of contact of rifling and driving band has a great effect on flight attitude of the projectile.

A geometric modelling method for gun barrel and a finite element meshing strategy for the worn barrel were proposed by Ding et al. [3] that involved the combined use of Python code and ABAQUS software. A transient thermo-mechanical finite element model was developed to compute the interior ballistics parameters and plastic deformation of rotating band.

During the dynamic firing of artillery shells from guns and howitzers, a typical problem may arise i.e. the balloting motion of the shell inside the bore. It is the transverse or wobbling motion of the projectile inside the barrel. There are several reasons for which this phenomenon can occur. Kelly D Laughlin [4] listed out a number of factors responsible for the balloting viz. manufacturing tolerances, concentricity of the engraving of the rotating band, lack of concentricity of the projectile and tube deformation, asymmetric obturation of the propellant gases, rotating band wear, location of the centre of gravity of the projectile both radially and axially, axial location of the rotating band, and length of the wheel base (distance between centring bands) of the projectile. Manufacturing defects leading to eccentricity of the centre of gravity of the shell from the centre of geometry, driving band of insufficient strength and gun barrel wear may cause a transverse or wobbling motion of the projectile. In the study, various parameters were identified and their effect on the projectile motion studied and it was concluded that the variation of centre of gravity (CG) position in radial direction was the most significant contributor to balloting, followed by the variation in axial direction, the projectile body geometry variation, the wheel base length and lastly the band location.

Walker [5] showed that the effects of excessive balloting can be detrimental to the safety and stability of the shell. Ansari and Baugh [6] conducted a study on the energy growth due to balloting. In this work, a mathematical model of the projectile and gun tube system was developed. The effects of obturator flexibility and projectile impact with the gun bore at the bourrelet were included in the analysis.

Modelling of the in-bore motion in a large calibre rifled gun is not easily found in the open literature. In an earlier work by Panda and Banerjee [7], the balloting of artillery shells of high calibre due to mass imbalance was investigated.

In this work, attempt has been made to numerically simulate the effect of variations in the radial shift of CG of high calibre artillery shell on the resulting balloting motion. Different radial shifts in CG have been modelled and their effects on the in-bore motion of the projectile have been investigated for typical artillery shell of 155mm calibre.

2. Finite element model

A three-dimensional finite element model for the typical 155mm gun system has been developed. Necessary geometric model, material models, boundary and loading conditions have been taken and are described subsequently.

A. Geometric Modelling

The internal diameter of the Gun barrel has been taken as 155mm which is its calibre. Total Length of the barrel is approximately 5054mm with pitch of rifling 3100mm. 48 grooves have been cut on the inner surface of the barrel. Fig 1 (a) shows the rifling on a small cut portion of the barrel.

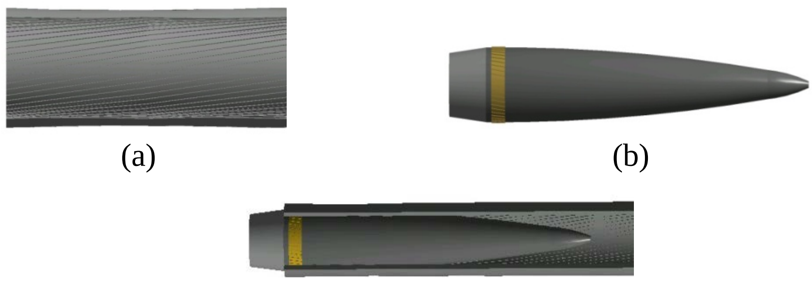

(a) (b) (c)

Fig 1: Geometric modelling of (a) cut section of barrel with rifling, (b) projectile with DB and BT and (c) engaged position of projectile

A typical 155mm shell consists of shell body, ogive section, boat tail (BT) unit and driving band. Geometric model of the shell with driving band and BT unit has been developed. Hollow section of the shell has been filled with material having density of the high explosive. Fig1 (b) shows the geometry of the typical 155mm shell. The driving band engages with the barrel during the ramming process and then slides over the driving edge of the barrel to give rotational motion of the projectile. To simplify the model, the rifling grooves have been pre-cut on the driving band and projectile and barrel has been engaged before application of the force. Fig 1 (c) shows the assembly of the gun and projectile system.

B. Geometric Modelling of Mass Imbalance

The mass imbalance i.e the radial shift in CG has been modelled as described in an earlier work7. The filling material which represents the High Explosive (HE) was divided in two parts as shown in Fig 2. Then the parts have been assigned two slightly different densities in such a way that the total mass of the projectile remains same and a radial shift in CG of desired magnitude can be achieved.

Fig 2: Modelling the filling of shell

C. Meshing

An optimum mesh size has been chosen to achieve reasonable accuracy and optimum computational time. The complete system is meshed with mixture of hexahedral and tetrahedral elements, so that curvature and proximities are meshed properly without compromising the mesh quality. Mesh quality has been rigorously checked so that numerical error can be minimised. The details of the elements are available in ANSYS documentation [8].

D. Contact

To accurately represent the motion of projectile inside the rifled barrel, frictional contact with a coefficient of friction, 0.05 was modelled between the driving band and the barrel such that driving band slides on the driving edges of the rifling that provides the rotational and translation motion to the projectile. The filling material and shell as well as boat tail unit and shell share faces. The nodes at the shared faces have been tied to restrict the relative motion between the pairs. A bonded type contact [8] has been applied to the driving band and shell surfaces disallowing any sliding motion between the two.

E. Material Modeling

Keeping in view the area of interest of the problem and negligible deformation that actually occurs in the barrel, the barrel including rifling bands has been assumed to be rigid. The shell body made of steel, boat tail made of aluminium alloy and driving band made of copper have been assigned elasto-plastic material property with appropriate material-specific values for the model constants. Filling material of the shell represents explosive therefore, it has been assigned mechanical properties of a typical explosive material. The values of the material model constants were taken from ANSYS material library [8] and are same as used in the previous work [7].

F. Boundary and Loading Conditions

For simplification of the problem, no aerodynamic forces are considered inside the gun barrel. Also, the barrel has been constrained against any degree of freedom. The shell is initially engaged with barrel rifling and has zero initial velocity.

The gun chamber pressure as a function of time is experimentally measured by internal piezo gauges placed at the rear part of the gun chamber. This pressure, also known as breech pressure is different from the pressure that acts at the base of the shell that is a little ahead of the breech. A semi-empirical relation [9] exists between the breech pressure and the base pressure. It is used to derive the base pressure that acts as the load on the shell. A typical breech pressure vs. time profile as determined by piezo gauge and the derived base pressure vs. time is shown in Fig 3.

In the simulations, it is observed that the motion of the projectile with a noticeable velocity starts a finite time after the application of the loads. This time is that required for development of shot start pressure [10]. After that, the projectile velocity increases rapidly and it starts to move with significant velocity. To reduce the computational time, the input loading pressure curve is slightly modified without significantly affecting the internal ballistics phenomenon. The time at which the velocity of the projectile becomes 1m/s is taken as the initial time in the simulations.

After application of material model, boundary and loading conditions, the model is decked to the ANSYS solver for solution.

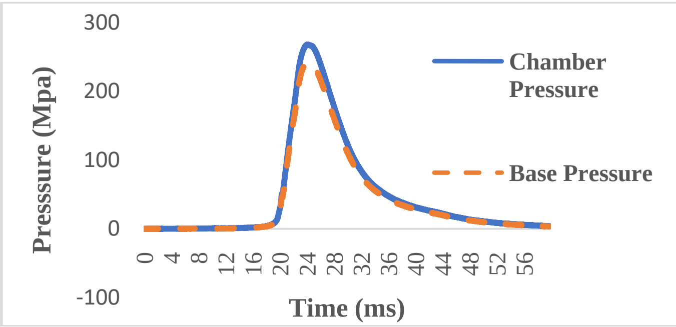

Fig 3: Variation of chamber and base pressure with time

3. Results and discussions

The problem was solved using ANSYS AutoDyn solver over a run time of 30ms. The translational and rotational motions of the projectile have been simulated for various values of radial shift of CG. In the simulations, 3D Global co-ordinate system has been taken for the calculation purpose. Y is the direction of the projectile movement along the barrel axis and is taken as the longitudinal axis. X and Z are the lateral axes. The radial shift in CG was taken radially along lateral X axis.

The validation of the simulated axial velocity at muzzle exit, bore travel time and projectile spin for different input pressure vs. time conditions with experimental data has been described in detail in the earlier work [7].

From the simulations, it was evident that the mass imbalance due to radial shift in CG has a significant effect on the in-bore motion of the projectile. The lateral velocity, barrel exit angle and motion of the projectile inside the gun chamber were compared for the different values of radial shift in CG. The damage area and stress distribution on the shell and driving band area for each case have been studied.

In the study, it has been found that the magnitude of the lateral velocity increases with the radial shift of the CG. This implies higher tendency of offset motion of the projectile inside the gun barrel. Also the longitudinal velocity decreases due to the interaction of projectile with the barrel. Table 1 shows the increase of lateral velocity and decrease of longitudinal velocity with the increase in radial eccentricity of CG.

Balloting motion of the projectile also causes the change in exit angle (angle between the projectile axis and the bore axis) of the projectile from the muzzle end. The bore axis is the line passing through centre at the breech end and at the muzzle end. Projectile axis is the line joining the geometric center of the projectile and the center at the base of the projectile. The co-ordinates with reference to the global co-ordinate systems have been taken for the above-described points.

Table 1: Comparison of Axial and lateral velocities (absolute values)

Shift in CG (mm)	**Bore travel time (ms)**	**VXmax (m/s)**	**VYmax (m/s)**	**VZmax (m/s)**
0	1.21	0.369	759	0.23
0.5	1.22	3.857	756	4.09
1.0	1.22	4.836	754	5.32
1.5	1.23	3.342	753	6.28
2.0	1.35	4.658	744	8.06

The angle between the lines has been calculated with point-slope formula. The exit angles for the different radial shifts in CG have been calculated and presented in Table 2. The exit angle depicts the inclination of the projectile about the concerned axis at the muzzle exit. From the results, it is clear that with the increase in radial shift of the CG, the projectile axis makes a marked departure from the barrel axis at the muzzle.

Table 2: Comparison of exit angles

Shift in CG (mm)	**θX (deg.)**	**θY (deg.)**	**θZ (deg.)**
0	89.97	0.07	90.06
0.5	90.10	0.10	90.00
1.0	90.24	0.33	90.22
1.5	89.95	0.95	89.05
2	89.14	1.17	89.22

The maximum stress and stain values developed on the shell body for different values of radial shift are presented in Table 3.

Table 3: Comparison of maximum equivalent stress and strain developed on shell body

Shift in CG (mm)	Maximum Eq. Stress (Mpa)	Maximum Eq. Strain
0	1186	0.125
0.5	1316.8	4.74
1.0	1158.9	4.78
1.5	1199	5.03
2	1172.3	3.6

A. Damage Area Assessment

The damage area is the representation of the material removed from the shell body after its exit from the muzzle. In the simulation, the element for which the equivalent stress exceeds the maximum set stress is deleted. The deleted elements represent the damage area occurring as a result of balloting of the projectile inside the gun barrel and interaction with the bore surface. Fig 4 shows the deleted elements due to failure of the material of the shell just above the DB groove due to a radial shift of CG of magnitude, 1.0mm.

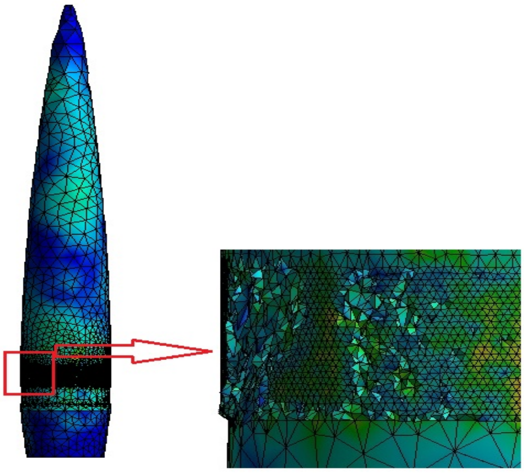

Fig 4: Damaged area on shell body

The damage areas presented in Table 4 are approximately calculated by taking the 2D projection of the curvature on an image. The damaged area has been enclosed with a polygon. The left-hand bottom corner pixel of the image has been assigned as origin of the cartesian co-ordinate system. The co-ordinates of the polygon have been found out by calculating the pixels of the image. Then the areas of the polygons have been computed by shoelace algorithm [11]. The damage area calculated in this method is given in the Table 4.

Table 4: Damage area on the shell body due to mass imbalance

Shift in CG (mm)	Damage Area (mm^2)
0	0
0.5	14113
1.0	18138
1.5	20835
2	21584

It is evident from Table IV that damage area steadily increases with the radial shift in CG indicating increase in balloting motion and thereby more and more undesirable interaction between the projectile surface and the bore.

4. Conclusion

The in-bore motion of a typical artillery shell of calibre, 155mm has been simulated and the effect of radial shift in CG, in other words, mass imbalance on the motion has been studied through numerical simulations. It has been found that as radial shift in CG increases, the projectile axis fails to remain in line with the barrel axis leading to balloting motion. Due to increased interaction between the shell surface and the bore, the stresses in the shell rise that may lead to material removal from the shell. Such occurrences are highly undesirable for safety during gun firings.

5. Acknowledgements

The authors express gratitude to the Director, PXE for permission for publication of the work.

6. References

[1] Deng S, Sun HK, Chiu CJ, Chen KC. Transient finite element for in-bore analysis of 9 mm pistols. Applied Mathematical Modelling. 2014, 38(9-10):2673-88.

[2] GE JL, YANG GL, CHEN YS, Xu W. A study on projectile-barrel coupling problem based on elastoplastic contact/impact model. Journal of Ballistics. 2008, 20(3):103-6.

[3] Ding C, Liu N, Zhang X. A mesh generation method for worn gun barrel and its application in projectile-barrel interaction analysis. Finite Elements in Analysis and Design. 2017, 124, 22-32.

[4] Laughlin KD. Characterization of the parameters that affect projectile balloting using finite element analysis (Doctoral dissertation, University of Oklahoma).

[5] Walker EH. Yawing and Balloting Motion of a Projectile in the Bore of a Gun with Application to Gun Tube Damage. ARMY BALLISTIC RESEARCH LAB ABERDEEN PROVING GROUND MD; 1974.

[6] Ansari KA, Baugh Jr JW. Dynamics of a balloting projectile in a moving gun tube. Battelle Pacific Northwest Labs Richland WA; 1988.

[7] Panda TR, Banerjee A. Numerical Simulation of the In-Bore Motion of a Typical Artillery Shell and Investigation of Balloting. 31st International Symposium on Ballistics. 2019.

[8] Documentation, ANSYS Mechanical APDL. "Release 15.0. SAS IP." 2015.

[9] Kankane DK, Ranade SN. Computation of In-bore Velocity-time and Travel-time profiles from Breech Pressure Measurements. Defence Science Journal. 2003, 53(4):351-356.

[10] Sudarsan N, Sarsar R, Das S, Naik S. Prediction of Shot Start Pressure for Rifled Gun System. Def Sci J. 2018;68(2):144. doi:10.14429/dsj.68.12247

[11] Hamberg CL, Vavrinek R, Rectangle WX. Shoelace Algorithm. Illinois Mathematics and Science Academy IMSA Math Journal, Fall. 1993.

Failure Analysis
&
Case Studies

Damage Behavior of Crack-patch Repair System with Material Tailored Bondline

Atul Khode
Vehicles Research & Development Establishment
DRDO
Ahmednagar

Sunil Nimje
Department of Mechanical Engineering
DIAT
Pune
sunilnimjediat@gmail.com

***Abstract*—Aircraft structures during their service life are subjected various loads, which causes damage to the structure. To increase life and structural integrity, composite patch bonded repair is mostly employed. In the present study finite element analyses have been carried out on single side patched repairs for inclined centre crack in aluminium alloy panel subjected to tensile load. Presence of defect in the panel cause stress gradients in the bondline. This reduces the performance of the patched panel. The important & potential characteristics of tailored material used for crack patch repair systems are explored in order to enhance the structural integrity of the system. This has been achieved by smoothening/relieving stress distribution over the entire bond area by introducing the concept of material tailored adhesive in-lieu of conventional mono-modulus adhesive. Bi-adhesive is a combination of flexible and stiff adhesive. Bi-adhesive can reduce the stress gradients in the panel. Fracture parameters such as stress intensity factor (SIF) & J-Integral have been used as characterizing parameters for assessing damage growth in the crack patch repair system. Crack patch repair system with material tailored bondline shows significant reduction in damage growth driving forces compared to that of mono-modulus adhesive.**

Keywords*— Single sided repair, material tailored bondline, inclined crack panel, composite patch, damage growth

Nomenclature

E	Modulus of elasticity	G	Shear modulus
ν	Poisson's ratio	K_{IC}	Critical SIF for mode I
σ_y, σ_u	Yield & ultimate strength respectively	K_I, K_{II}	Stress intensity factor (SIF) for mode I & mode II respectively

1. Introduction

Most of the aircraft structures that damaged during service are repaired by bonded joints. However adhesively bonded joints haveissues like high stress gradients at the overlap ends. This cause stress concentration which reduces the joint performance. For efficient bond design and longevity of structures, one has to reduce these stress concentrations and ensure uniform stress distribution along the bondline. Functionally graded adhesives (FGA) are the tailored adhesives which have varying mechanical properties along the preferred dimension, allowing a more uniform stress distribution along the bondline. [1]Bi-adhesive joint is also called as mixed adhesive joint, consists of combination of two adhesive, one is stiff adhesive and another is flexible adhesive. Mixed adhesive joint gives better strength as compared to stiff adhesive alone. Mixed adhesive joint can be considered as primary version of functionally graded adhesive.

S Kumar et al. [2] observed material tailoring of bondline significantly reduces peak adhesive stresses. The strength and life of the repaired structures can be significantly improved by introducing graded bondlines. RJC Carbaset al.[3] concluded that graded joints can be used to improve strength and reliability of repaired beams.E.A.S. Marques et al. [4] observed, joints with dual adhesives have strength comparable with that of joints with a stiff adhesive alone and at the same time more flexible and ductile. This can be useful especially for the dynamic loading. B BachirBouiadjraet al. [5] studied composite patch repair of edge crack specimen. He noticed that there is significant reduction in fracture energy due to presence of two adhesive bands. Conventional mono-modulus adhesively bonded structures employs stress peaks in the bondline which can be reduced with functionally graded adhesives. S V Nimjeet al.[6] carried out interfacial failure analyses of laminated composite tee joint. He observed by use of functionally graded adhesive in tee joint structure reduces damage growth parameters as compared to mono modulus adhesives.

In numerical analysis of composite crack patch repair system, requires the stress analysis of panel, adhesive layer and patch. It also requires estimation of fracture parameters and the nature of the stress state near the crack tip. Reduction in stress intensity factor (SIF) near the crack tip is effective in delaying the crack growth, which increases the life of the component. In present study aluminium alloy panel with centre inclined crack, subjected to tensile load is considered. This panel is repaired with composite patch. This patch is bonded in crack region with bi-adhesive. Comparison is made based on fracture parameters such as SIF & J-Integral at crack front between bi-adhesive & mono-modulus adhesives.

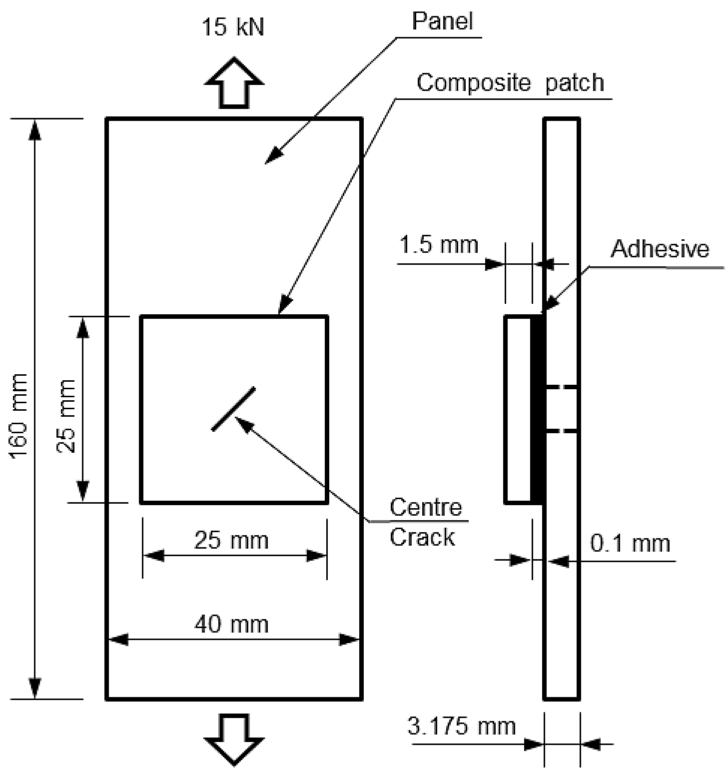

Fig. 1. Bonded Patch Repair

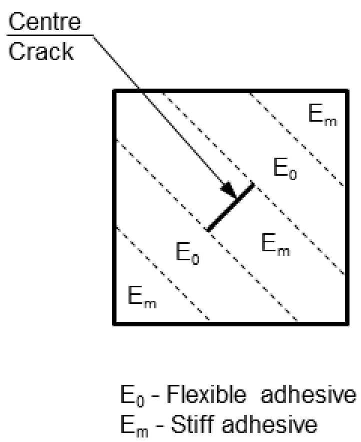

Fig. 2. Gradation scheme for multi-modulus adhesive

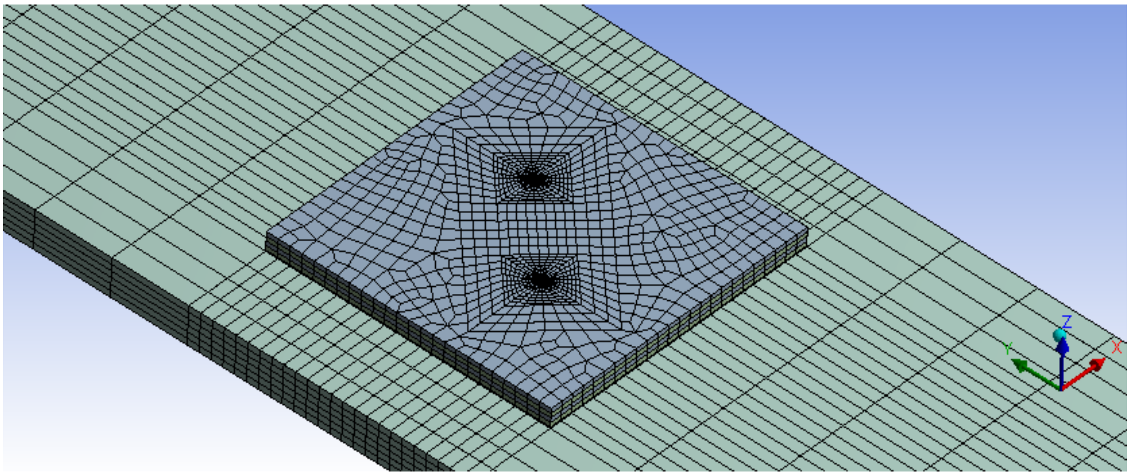

Fig. 3. Meshing scheme of bonded patch repair

2. Geometry & configuration of bonded patch repair

Numerical simulation is carried out for centre inclined cracked panel. Fig. 1 shows the geometry considered for simulation. Panel is made of aluminium alloy 2024 -T3. Material properties are given in Table 1. The width of the panel is 40 mm, length is 160 mm & thickness is 3.175 mm. It contains through thickness centre crack of length 10 mm & inclined at an angle of 45^o with the loading direction. The size of the patch is 25 mm x 25 mm x 1.5 mm thick. It is made of boron/epoxy composite laminate. Orthotropic material properties in principal material directions of boron/epoxy lamina are given in Table 2. The four layers of composite laminate with layup sequence [-45/45/-45/45] is used. Patch is bonded with panel by using adhesive of constant thickness of 0.1 mm. Here, stiff adhesive and flexible adhesive are used in combination to carry out bi-adhesive grading (fig. 2). Elastic properties of adhesive are given in Table 3.The complete assembly is subjected to uniform tensile load of 15 kN as shown in Fig. 1.

Table 1. Material properties of panel [7]

E	71.02 GPa
ν	0.33
σ_y	320 MPa
σ_u	480 MPa
K_{IC}	25 MPa$\sqrt{m}$

Table 2. Layer wise orthotropic material properties of boron/epoxy composite lamina in principal material direction [8]

E_x	208.1 GPa
$E_y = E_z$	25.44 GPa
$\nu_{xy} = \nu_{xz}$	0.1677
ν_{yz}	0.36
$G_{xy} = G_{xz}$	7.2 GPa
G_{yz}	4.9 GPa

Table 3. Material properties of adhesive [9]

	Stiff adhesive	Flexible adhesive
E	2.9 GPa	0.5 GPa
ν	0.34	0.34

3. FE Analysis of Bonded Patch Repair

FE analysis have been carried out for centre inclined cracked specimen bonded with composite patch. Fracture parameters such as SIF & J-Integral are used for comparison. The twenty noded brick elements called SOLID 186 from ANSYS, is used for discretization of the geometry. Structural SOLID 186 element is used for discretization of panel & adhesive. Layered SOLID 186 element is used for composite patch. Composite patch is defined with four layers across the thickness to define composite lamina layup sequence. Panel is having 6 elements across thickness to capture fracture parameters across the crack front. Adhesive layer is having single element across the thickness. For computing stress gradients near crack tip fine meshing has been made in the vicinity of crack tip. Convergence study is carried out to get optimised size of mesh. Validation is done with the available literature to establish present FE model. SIF and J-Integral are used as fracture characterizing parameters to access the damage growth in graded crack-patch repair system. Fig. 3 shows views of FE model of the geometry. Similar mesh is carried out at the panel to adhesive interface and adhesive to patch interface. It is assumed that panel, adhesive layer and composite patch are bonded perfectly with each other. Hence interface nodes between their interfaces are coupled by assigning contact between them. In this study it is assumed that plate is subjected uniform tensile load of 15 kN.

4. Results and discussion

Numerical simulation is carried out for three different adhesive configurations.

(i) Mono-modulusstiff adhesive
(ii) Mono-modulus flexible adhesive
(iii) Bi-adhesive by using combination of stiff & flexible adhesives

Comparison is made based on fracture parameters like SIF and J-Integral values at the crack front. Variations of these parameters are plotted against thickness of the panel for all above three configurations. Fig. 4 shows graphical output for J-Integral value along crack front. This value is smaller at patched surface while it goes on increasing at unpatched surface. Similar trend is found in literature [7]. Fig.5 & Fig. 6 shows graphical comparison for variation of SIF for mode-I & mode-II (K_I & K_{II}) respectively. From Fig.5 we can see that for flexible adhesive, value of K_I is higher while it is lower for stiff adhesive. For bi-adhesive, values of SIF are comparable to that of stiff adhesive. At panel-adhesive interface, K_I is smaller for bi-adhesive compared to that of both the mono-modulus adhesives. There is reduction of 8.4% as that of for stiffer adhesive. This indicates that there will be delay in crack growth in this area which may further increase the life of the component. As we move away from this adhesive panel interface along crack front by 27% of the panel thickness, the value of K_I is same as that of for stiff adhesive. We can see in fig. 6, for mode-II value of SIF, K_{II} is slightly more than that for stiff adhesive. Hence here we can say that bi-adhesive grading scheme implemented here will help to reduce K_I only. Fig.7 shows variation of J-Integral for 3 different configurations along crack front. Here similar to K_I, the value is smaller as compared to stiff & flexible adhesive. For bi-adhesive there is reduction of 7.7% in J-Integral value.

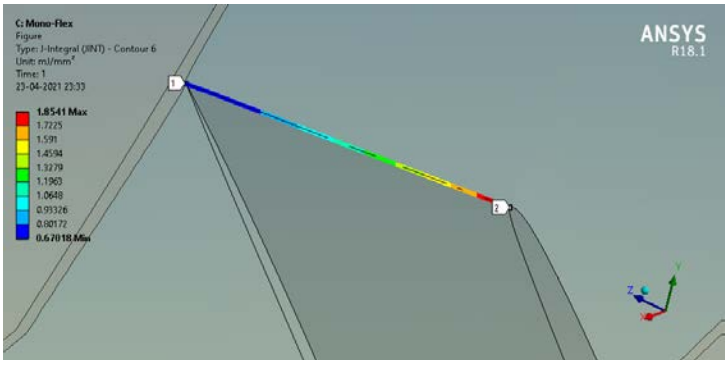

Fig.4. Variation of J-Integral along crack front

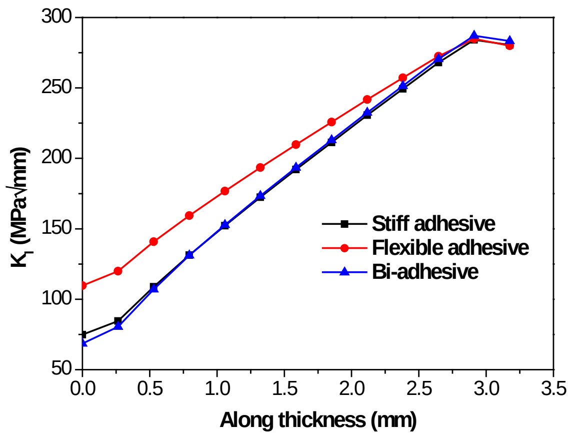

Fig.5. Variation of K_I along crack front for different adhesives

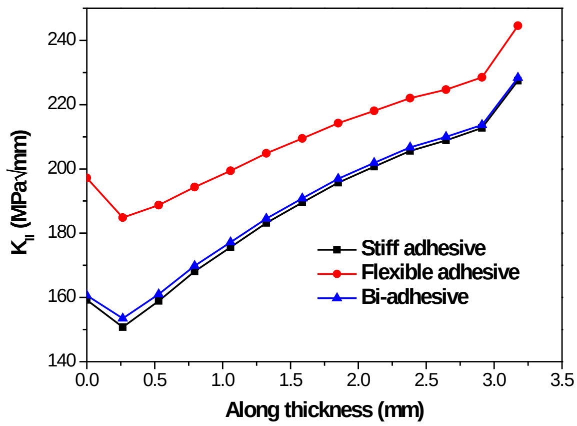

Fig.6. Variation of K_{II} along crack front for different adhesives

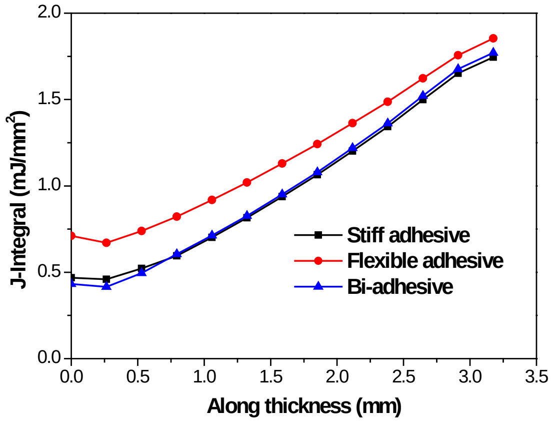

Fig.7.Variation of J-Integral along crack front for different adhesives

5. Conclusion

The following specific conclusions have been made from this present research.

- Due to patching in damaged area there is drastic reduction in SIF in the panel around the defect.
- For single sided repair, values of SIF & J-Integral are smaller at patched surface and it goes on increasing at unpatched surface.
- For mono modulus adhesive, value of SIF & J-Integral are smaller for stiffer adhesive compared to that for flexible adhesive
- As compared to mono-modulus adhesive, bi-adhesive shows reduction in value of SIF (K_I) by around 8% at patched surface, which can help for delaying crack growth in the panel.
- For mono-modulus adhesive, adhesive stresses are not uniform due to presence of crack in the panel. Proper gradation of adhesive will reduce peak adhesive stress.

6. References

[1] J.B. Marques, A.Q. Barbosa, C.I. da Silva, R.J.C. Carbas& L.F.M. da Silva (2019): An overview of manufacturing functionally graded adhesives – Challenges and prospects,The Journal of Adhesion, DOI: 10.1080/00218464.2019.1646647

[2] M. A. Khan & S. Kumar (2018) Interfacial stresses in single-side composite patch-repairs with material tailored bondline, Mechanics of Advanced Materials and Structures, 25:4, 304-318, DOI: 10.1080/15376494.2016.1255824

[3] R. J. C. Carbas, G. M. S. O. Viana, L. F. M. da Silva, G. W. Critchlow, Functionally Graded Adhesive Patch Repairs of Wood Beams in Civil Applications, Journal of Composites for Construction / Volume 19 Issue 2 - April 2015, DOI:10.1061/(ASCE)CC.1943-5614.0000500

[4] E. A. S. Marques & Lucas F. M. da Silva, Joint Strength Optimization of Adhesively Bonded Patches, The Journal of Adhesion,2008, 84:11, 915-934, DOI: 10.1080/00218460802505275

[5] B. BachirBouiadjra, H. Fekirini, M. Belhouari, B. Boutabout, B. Serier, Fracture energy for repaired cracks with bonded composite patch having two adhesive bands in aircraft structures, Computational Materials Science, Volume 40, Issue 1, 2007, Pages 20-26, ISSN 0927-0256, https://doi.org/10.1016/j.commatsci.2006.10.016

[6] S.V. Nimje, S.K. Panigrahi, Interfacial failure analysis of functionally graded adhesively bonded double supported tee joint of laminated FRP composite plates, International Journal of Adhesion and Adhesives, Volume 58, 2015, Pages 70-79, ISSN 0143-7496, https://doi.org/10.1016/j.ijadhadh.2015.01.002.

[7] M Ramji, R Srilakshmi, Design of composite patch reinforcement applied to mixed-mode cracked panel using finite element analysis, Journal of Reinforced Plastics and Composites, 2012, 31: 585, DOI: 10.1177/0731684412440601

[8] LinxiaGu, Ananth Ram MahanthKasavajhala, Shijia Zhao, Finite element analysis of cracks in aging aircraft structures with bonded composite-patch repairs, Composites Part B: Engineering, Volume 42, Issue 3, 2011, Pages 505-510, ISSN 1359-8368, https://doi.org/10.1016/j.compositesb.2010.11.014

[9] Fan-Rong Kong, Min You & Xiao-Ling Zheng (2008) Three-Dimensional Finite Element Analysis of the Stress Distribution in Bi-Adhesive Bonded Joints, The Journal of Adhesion, 84:2, 105-124, DOI: 10.1080/00218460801952791

Application of Fibre Bragg Gratings as Strain Sensor in the Health Monitoring of Ring Laser Gyro Inducted in INS

T. Ezhilarasi
Advanced Inertial Sensors Group
ISRO Inertial Systems Unit
Trivandrum
ezhilaraj@gmail.com

Karthigai Selvan
Advanced Inertial Sensors Group
ISRO Inertial Systems Unit
Trivandrum

Paul Pandian S
Advanced Inertial Sensors Group
ISRO Inertial Systems Unit
Trivandrum

***Abstract* – This work presents the concept of development of Optical Fiber Bragg gratings (FBG) based distributed strain sensors for the health monitoring in ring laser gyros inducted in Inertial Navigation Systems (INS). Strain measurement is one of the critical parameters to be measured in the Structural health monitoring systems (SHM). To verify the performance of this FBG strain sensor, an analysis was carried out in strain measurement using FBGs embedded in the top cover of the ring laser in the analysis of the hermiticity of the sensor. These experimental results demonstrate that the distributed sensing capability can be effectively used in the SHM of ring laser gyroscope inducted in INS.**

Keywords– Ring Laser Gyro, Fiber Bragg gratings, Path length control system, SHM

1 Introduction

Optical fiber-based Fiber Bragg grating (FBG) strain sensors are gaining increasing attention in stress analysis in Health monitoring systems. Fiber Bragg grating is an optical element that exhibits a lot of advantages such as small size, light weight, high sensitivity and insensitivity to electromagnetic interference. Added advantage of FBG is the distributing sensing capability with more than one sensor to measure a parameter like strain at different locations but single acquisition end. To verify its performance, an analysis was carried out with FBG based strain sensors in the detection of hermiticity of the sealing of the ring laser gyroscope.

A. Description

Ring Laser Gyroscope (RLG) is a single axis optical sensor used to measure the rotation rate in inertial navigation systems. It works on the principle of Sagnac effect. The schematic figure of ring laser gyroscope with four total internal reflecting prisms forming the resonator cavity is shown in the figure 1. He-Ne laser is the active medium.

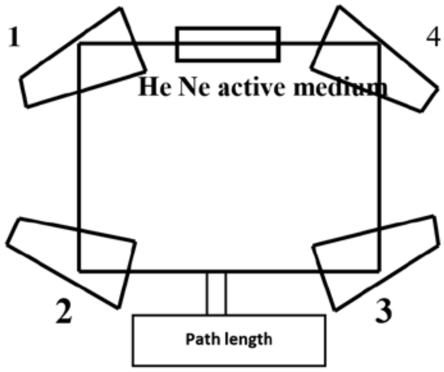

Figure 1: Schematic figure of resonator with prims

There are four channels forming the cavity resonator. One channel is filled with He Ne gas, adjacent two channels are vacuum sealed with prisms & prism covers and the fourth channel is connected to the path length control drum (PLC) by a silaxane tube. Path length modulation to sustain the lasing at single mode inside the cavity is done with a 1 atm. pressure filled N2 gas inside this unit. Top volume enclosing the resonator connected to PLC by silaxane tube is also hermetically sealed with 1 atm. pressure N2 gas as the silaxane tube is not good in hermiticity. Maintenance of 1 atm. pressure inside the volume is critical and any reduction in pressure will affect the operation of laser in single mode. Hermetic sealing of the sensor is as shown in the figure 2.

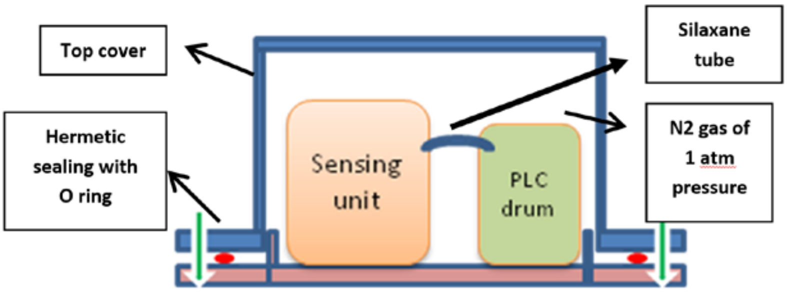

Figure 2: Hermetic sealing of ring laser

The hermiticity of ILG top cover has to be cent percent ensured by conducting vacuum test. During the vacuum test, the sealed sensor is kept inside the vacuum chamber and the vacuum environment is created externally. A pressure difference of 1 atm. pressure will be felt across the top cover. Since the top cover is only 1mm thick, due to the pressure difference it will deflect out. If the interface leaks, pressure difference will not be stable across the top cover as deflection will reduce. Hence by measuring the deflection of the top cover, leak in the joint can be estimated. So, a method was devised to detect the leak in the sealing.

To measure this strain on the top cover, a method is devised by inducting optical fiber-based FBG strain sensor used to evaluate the hermiticity of the sensor. Based on the Finite Element analysis, the center portion of the top cover is found suitable for strain monitoring.

2 Experimental Setup

An experiment is proposed to simulate the same condition of the sensor under vacuum testing. For this, a baseplate is identified and sealed with a top cover with a vent without the optical resonator and ensured with $5*10^{-10}$ mbar l /sec leak rate using He leak detector as shown in the figure 3. Now vacuum is felt inside the sensor while outside there is 1 atm. pressure. This condition is just the reverse condition of vacuum testing of the sensor.

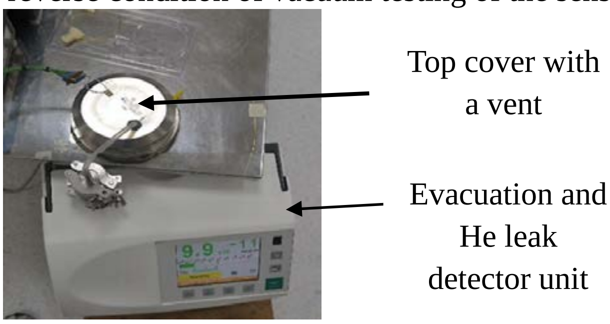

Figure 3: Experimental setup with vent

To measure the strain, a strain gauge (SG) and a FBG based strain sensor are bonded adjacently on the top cover with the cyanoacrylate exactly at the center as shown in the figure 3. A single axis foil type resistive strain gauge with a gauge factor of 2.08 is connected to the

LabVIEW data acquisition system and FBG is connected to the interrogator to acquire strain data. Both FBG and SG data were captured at a sampling rate of 1 Hz. A pressure gauge is also connected to the vent to measure the pressure at any instant.

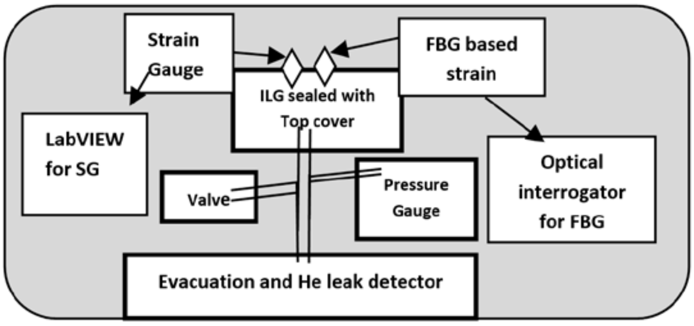

Figure 4: Schematics of the Experimental setup

Evacuation of the closed volume, causes change in inside pressure and the top cover deflects accordingly to the pressure change which is measured as strain. This strain change is sensed by both the strain sensors bonded on the top cover. This experiment started with controlled evacuation in 50 mbar in steps from 1 atm. pressure. Once the evacuation reached $1*10^{-10}$ mbar inside pressure, this condition is held for 15 minutes to check the stability of the measurement. Then the filling of filtered air in steps of 100 mbar up to 1 atm pressure was carried out. Once vacuum is removed the strain value return to zero and this experiment was repeated. Change in strain values of both the sensors due to the pressure change inside the top cover during evacuation and filling processes with respect to time is plotted.

3 Results and Discussions

A maximum value of 386 micro strain is measured by FBG and 368 micro strains by strain gauge to attain the vacuum level. These difference in the strain values may be due to the location of the sensor also. The strain due to the temperature can be eliminated in FBG sensors is the additional capability. The plot in the figure 5 gives the strain measurement related to hermiticity of the sensor without leak. As per this plot, the measured strain value is related to the vacuum level of the inside volume. If there is any leak, then the strain values measured by FBG sensor with and without leak will be remarkably different. But in strain gauge sensor, strain measurement is the composition of tensile force and temperature effect. So accurate leak estimation can be done by FBG based sensor.

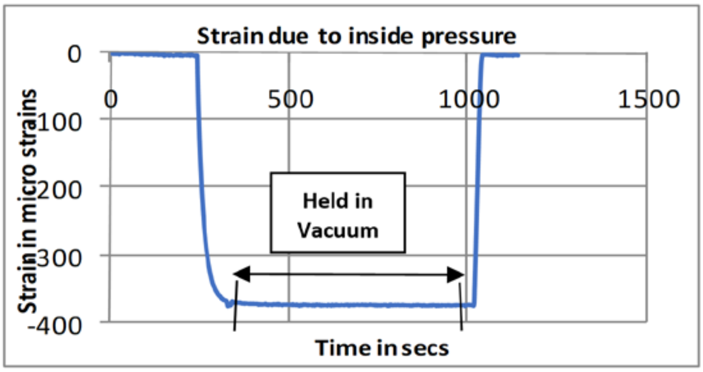

Figure 5: Strain value vs Vaccum level

The result shows that FBG based strain sensors are applicable for this hermiticity analysis. By fitting the linear regression for both the plots, we get regression value as 0.998 & 0.994 respectively.

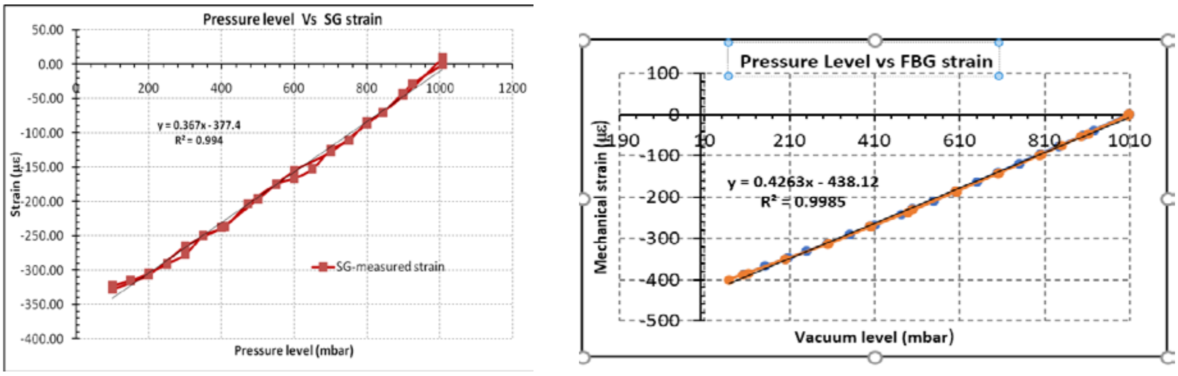

Figure 6: Pressure level with strain measurements

From the data acquired, the hysteresis and linearity of the both sensors are plotted as shown in figure 7 & 8 respectively. This shows the repeatability of the data is better in using FBG based strain sensors.

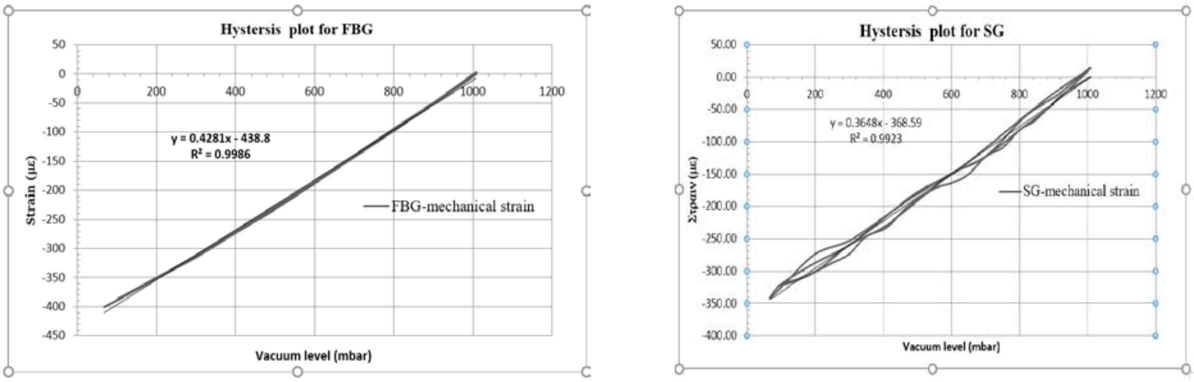

Figure 7: Hysteresis of both sensors

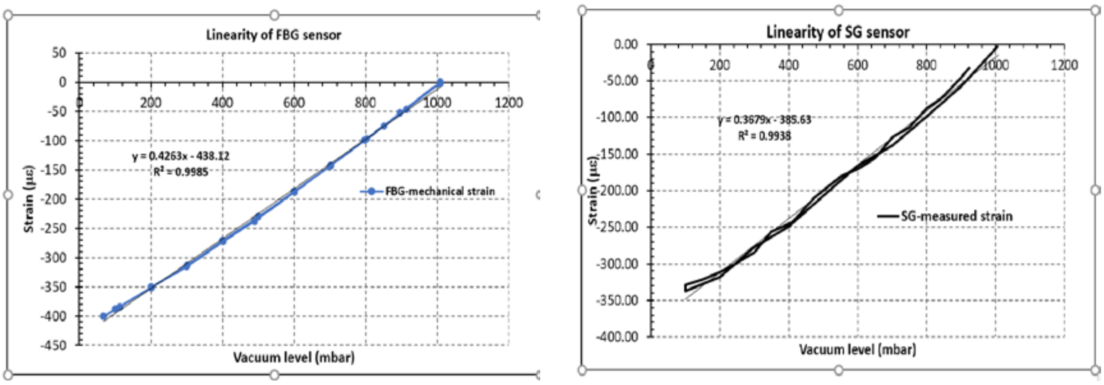

Figure 8: Linearity of both sensors

4 Future Work

Inertial navigation system (INS) is the device uses gyroscopes and accelerometers to continuously calculate by dead reckoning the position, the orientation, and the velocity of a moving object without the need for external references. Single system comprises of more than one ring laser gyroscope and accelerometers. Schematics of distribution sensing technique with FBGs to measure strain is as shown in the figure 9

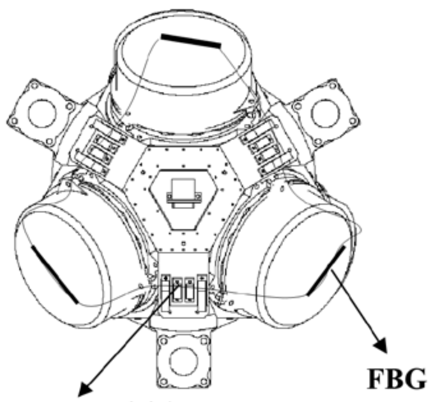

Figure 9: Distributed sensing of FBGs embedded on ring laser gyroscopes in INS

5 Conclusion

Experimental results show that FBG based strain sensor have excellent linearity, low hysteresis and noise level of 1 micro strain only. Thus, effective use of the FBG based strain sensors in the evaluation of the hermeticity of the sealing in ring laser gyro was demonstrated. This leads to the scope of employing distributed sensing technique of FBG sensors for health monitoring in the ring laser gyroscopes inducted in INS in future work.

6 References

[1] Application of B & K Equipment to Strain Measurements by John Vaughan
[2] Farrar C.R., Worden K. An introduction to structural health monitoring. Philos. Trans. R. Soc. A. 2007; 365:303–315. doi: 10.1098/rsta.2006.
[3] Bakht B., Mufti A. Bridges. Springer; Cham, Switzerland; New York, NY, USA: 2015. Structural health monitoring; pp. 307–354.

Investigation of Shock Signatures Observed in a Flight during Stage Separation at Electronic Package Bay: A Case Study

Narendra Nath
Space Transportation System
Vikram Sarabhai Space Centre
ISRO
Thiruvananthapuram
narendra2232in@gmail.com

Venkateswaran KP
Space Transportation System
Vikram Sarabhai Space Centre
ISRO
Thiruvananthapuram
kpv.isro@gmail.com

Dr. Sundararajan T
Space Transportation System
Vikram Sarabhai Space Centre
ISRO
Thiruvananthapuram

Dr. Geetha S
Space Transportation System
Vikram Sarabhai Space Centre
ISRO
Thiruvananthapuram

***Abstract*—Staging is the most crucial event in a launch vehicle. An efficient separation system should impart minimum disturbance to the ongoing stage / satellite by separating the lower stage without any re-contact. This paper discusses about one of the missions, wherein an unexpected shock signature was seen at a critical navigation package location situated on electronic package bay during one of the stage separations of the launch vehicle. Various onboard shock sensors and separation events were investigated to find the source and for similar signature in previous flights. It was noticed that similar signatures were seen in some of the flights and could not be noticed easily as the primary shock used to be comparatively high. A hypothesis was brought out and a transient analysis was done to prove the hypothesis and found that all the measured frequencies were present if the proposed phenomenon takes place. Proposed hypothesis considered the frictional release of energy from the fork and groove joint situated close the bay which might have initiated the second shock while in flight.**

Keywords- Shock, shock response spectrum, separation system, accelerometers

1. Introduction

Aerospace industries like launch vehicle, missiles, fighter planes are demanding numerous actuation devices for either separation of stage or actuation of deployment mechanisms. In contrast, it is also expected to be of compact size, least weight, highly reliable, high power to weight ratio and cheap in cost. Pneumatic and hydraulic actuators are reliable and testable, but they are bulky in size, weight and simultaneous actuation cannot be relied upon. The best preferred option currently available is pyrotechnic actuation which could meet all the requirement but it induces high shock levels.

Launch vehicle and missile stages have to be separated after the stage performance and commonly used separation system is pyrotechnic. These pyros have advantages like instantaneous ignition providing simultaneity, long storage life, compact size and less cost. Even though pyros are widely adopted in launch vehicles and missiles where single shot operations are needed, pyro shock can be fatal to electrical relay chains, adjacent structures, electronic packages, satellites or onboard payloads. During the pyro operation, detonation generates the high energy explosive gases which either sever the structure or actuate the separation mechanism resulting in sudden release of strain energy of the pre-strained separation joint. Explosion as well as strain energy release together generates a shock pulse which makes the environment hostile for the mechanical structures as well as sensitive onboard electronics packages.

Pyrotechnic shock is a very complex phenomenon to understand, especially in launch vehicles. Shock transmissibility and attenuation by structures is not yet fully understood. Launchers are generally 40 to 50 meters in length and are made up of various tankages, inter stages, truss structures and sometimes composite structures. Flange joints, hinge joints, spherical bearing joints, tongue and groove joints are commonly used joint between the structures. It is quite cumbersome to predict the shock at different locations of launch vehicle. In one of successful flight of the launch vehicle, an unexpected additional shock signature was seen after 140ms from the primary shock which was measured 14m away from the initiation point. Shock response spectrum (SRS) of both the shock shows different peaks i.e. it has different frequencies contents. This paper would be discussing the investigation for the cause of the second shock and brought out a hypothesis which could have occurred during flight.

2. Background

There were two shock sensors mounted in the launch vehicle, one was close to satellite interface and another one was on the electronic package bay (EPB) below the navigation package. Second shock signature was measured in EPB shock sensor exactly 140ms after the primary shock which occurred during one of the staging events of the launch vehicle. Shock signature time line plot is shown in figure-1 and it clearly shows two distinct shock signatures of the same order. Trimmed timeline to 200ms and corresponding SRS is plotted in figure-2. Red and fluorescent green curve in right hand plot of figure-2 shows satellite shock specification and blue is the SRS/Q of measured data. It is further evident that flight measured shock levels are well within the environmental shock specification but the source of second shock must be known. SRS plot is cumulative and could not show the peak response contribution of each shock. The shock sensor details are given in table-1 and filter cutoff (fc) was 1500Hz.

Table 1: Shock sensor details

Location	Range	Direction
EPB	+/- 100g	Axial

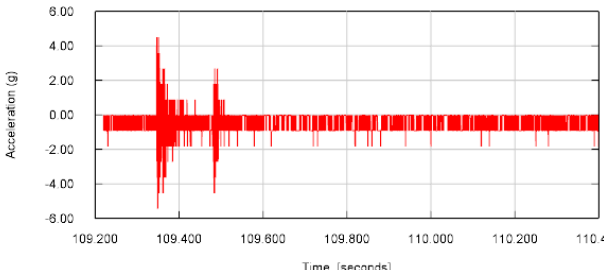

Figure-1. Timeline plot of shock signature measured at EPB.

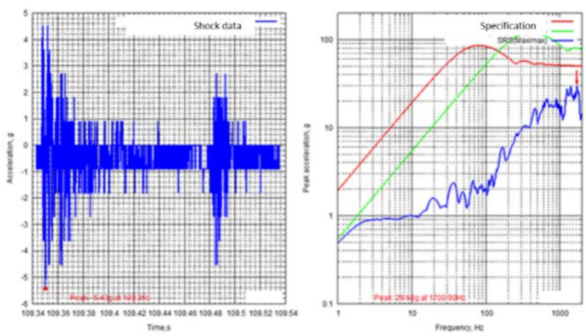

Figure-2, Trimmed timeline plot (200 milli-seconds) of shock signature and it's SRS/Q plot comparing with specifications measured at EPB.

Upper stage configuration of launch vehicle is shown in figure-3. Sensor locations at EPB is shown in Figure-4.

Figure-3, Upper stage configuration of the launch vehicle showing details of all the elements.

SRS of both the shocks are compared in figure-5. Higher responses in low frequency (<1000Hz) range are seen in primary shock however, response levels due to the second shock are less in low frequency range. The peak response in First shock is around 29g at the frequency 1400Hz. Second shock has two peak responses, one is 27g at 1250Hz frequency and second of 29.5g at 1700Hz frequency. First and second shock signatures are not matching with each other, it means the excitation to both the shocks can be from the different source.

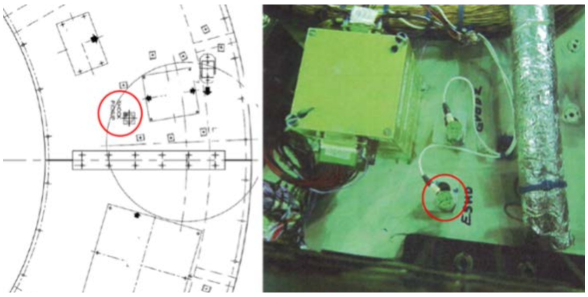

Figure-4, Shock sensor location sketch as well as actual onboard picture.

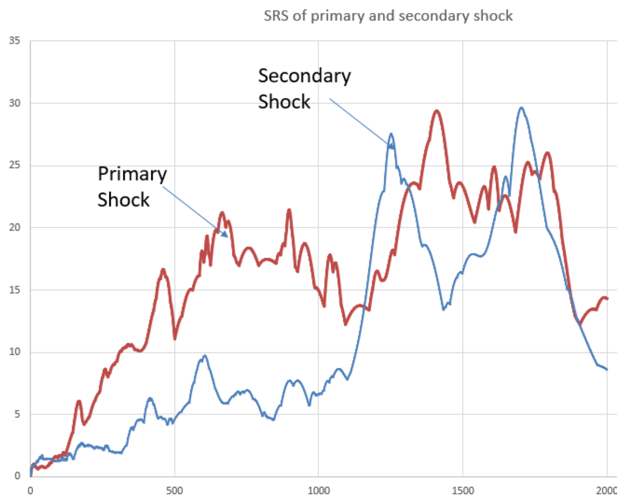

Figure-5, SRS of first as well as second shock separately.

3. Investigations

Various flight parameters were investigated to find out that any other sensor has picked up the similar response or could have showed any signature of source. The detailed investigations are brought out here.

A. Bending Moment Measurement Accelerometers response

Bending moment measurement accelerometers(BMMA's) were generally positioned at different locations of the launch vehicle to measure the bending mode of the launch vehicle throughout the flight. Four BMMA's located at various locations along the length of the vehicle are plotted in Figure 6. All the four BMMA's responded to the first shock event and suffered saturation due to the high acceleration levels (usual phenomenon). The sensors revived only after the time of occurrence of the second shock. Hence, the second shock signature could not be captured in any of the BMMA's.

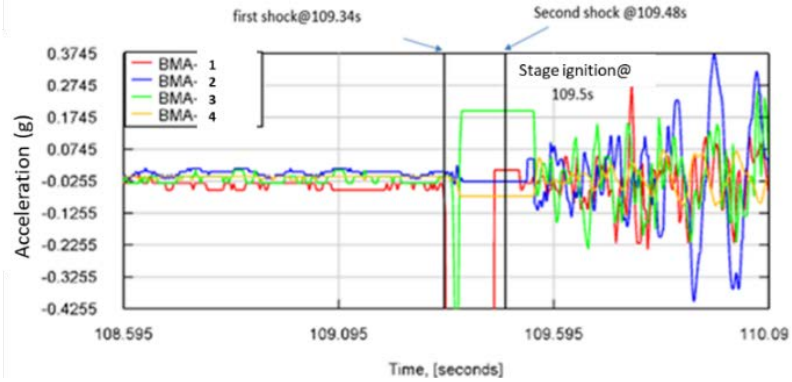

Figure 6: BMMA at thrust frame (1), PA (2), PLF (3) and third stage (4) responses are plotted. BMMA saturation/data loss observed after the first shock event, hence, second shock could not be captured.

B. Payload adapter (PA) shock sensor response

Spacecraft is the most critical article in the launch vehicle and continuous monitoring of the launch environment used to be done using vibration, shock, axial and bending mode measurement accelerometers. PA shock during separation events were measured by the shock sensor which was mounted at payload adapter fore-end. Shock sensor measured timeline data is plotted in Figure-7 for the stage separation event and 4.92g is the peak acceleration recorded wherein the second shock signature was not noticeable. This means that either the second shock did not get transmitted to the spacecraft or was not a real shock at all. Trimmed data and it's SRS for the same is plotted in Figure-8 which shows that levels are well within the environmental test levels.

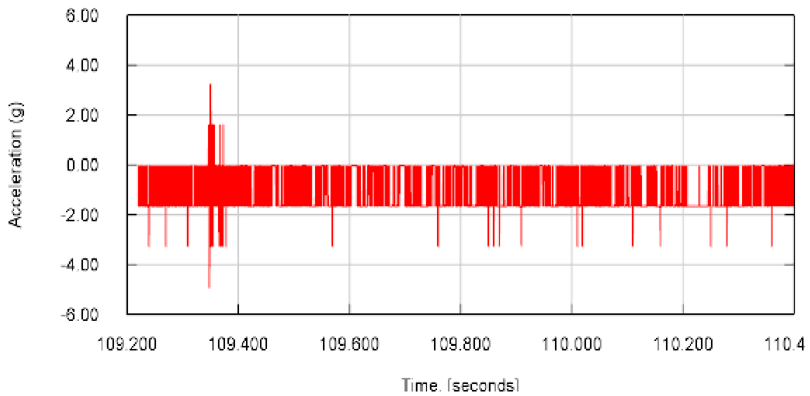

Figure 7: PA shock measurement timeline during stage Separation (1 or 2 bit data only)

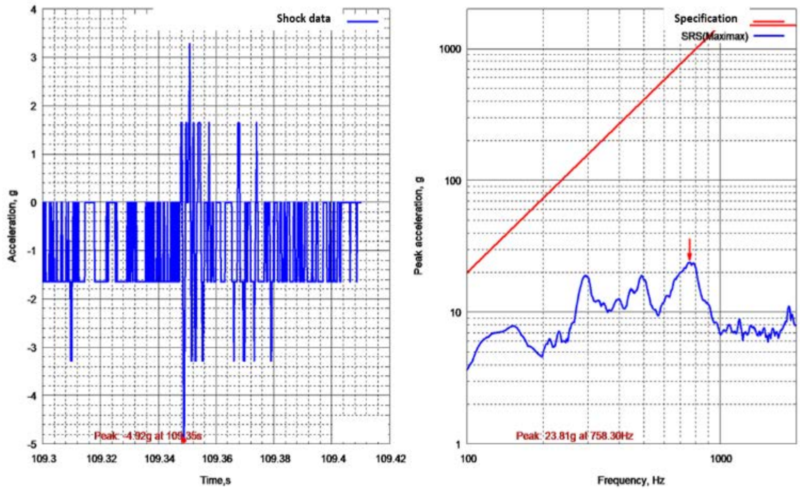

Figure 8: SRS of PA shock measured during stageseparation shows its very benign.

C. Previous Fight Shock Comparison at EPB

A detailed shock analysis was done for around 40 flights and compared to understand if similar signature existed. Because of space constrains all the plots cannot be brought out in this paper. Some of the flights, a second shock like signature was noticed and one among them is plotted for more clarity in figure-9. Furthermore, the charge density of the linear shaped charge (LSC) were also compared to see if it is a function of the charge density, but all the charge densities were well within the specifications and could not find any relation with shock signature.

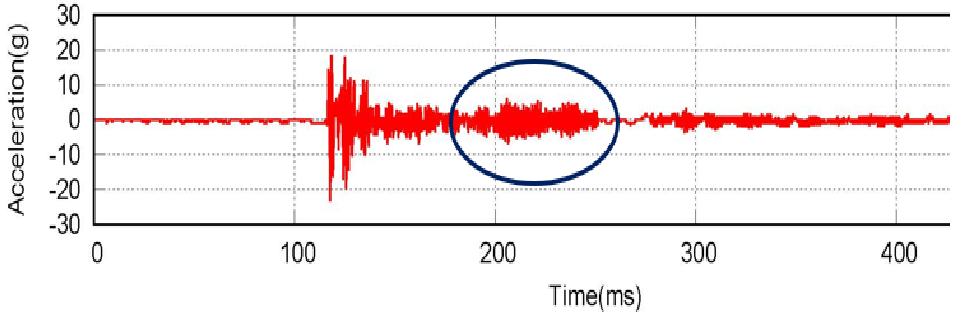

Figure 9: PA shock measurement timeline during stage Separation (1 or 2-bit data only)

Based on all the flight shock data analysis, the following conclusions were drawn. From the data analysis, it was evident that unusual shock signatures were recorded in some of the earlier flights also. In this flight, the primary separation shock and second shock levels were comparable in amplitude, hence it could be easily identified as an anomaly. Usually, first shock used to be greater than 10g, but in this flight, first shock amplitude was only 5.43g. LSC average charge density and peak shock co-relation could not be established. SRS of all the flights are within the ETL specification except higher frequency exceedance in some of the flights.

In a similar incident where a second shock like signature was compared with the current second shock signature along with FFT in Figure 10. A single frequency (approx. 700Hz) content is seen in earlier flight; however, in this flight multiple frequency contents are seen. This single frequency content was seen in most of the flights, but multiple frequency content is seen in this flight only.

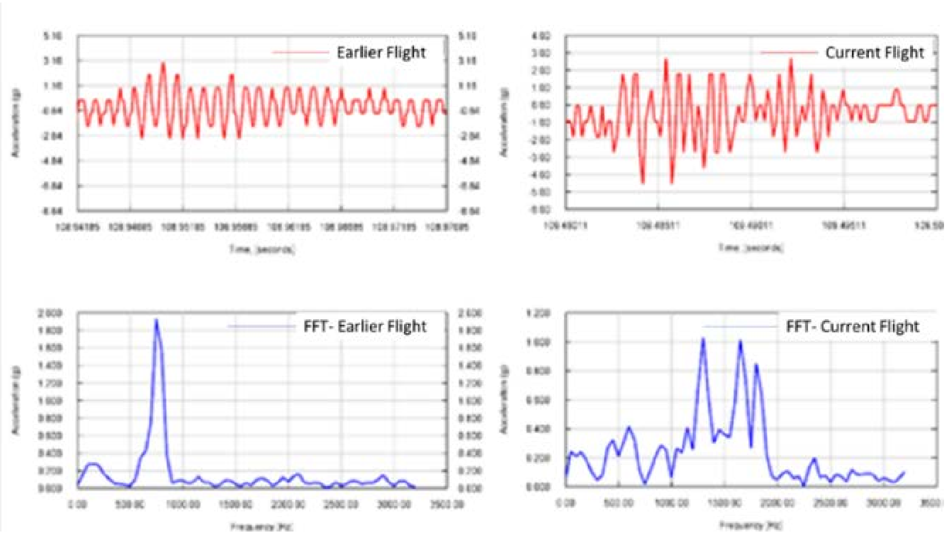

Figure 10: Earlier and current flights second shock signature after 140ms from the primary shock is plotted along with FFT. Earlier flight has single frequency however current flight shows multiple frequencies.

D. Payload Fairing Separation Event Shock Analysis

Payload faring separation event shocks were also analysed for the all the previous flights and found that the almost 50% of the flights, an additional shock was seen at the order of 2-5g at around 140 to 180ms from the first shock event. Connector snap-off time for the PLF separation system is only 35-50ms and there is no physical event during 140ms. One of the typical shock signatures is shown in Figure 11, where second shock signature is clearly evident. The second signature looks like single frequency.

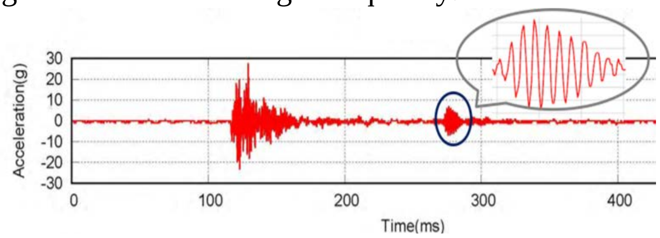

Figure 11: EPB shock measurement timeline during PLF Separation event.

E. Re-contact of Separating Stages

Second shock could be due to the re-contact of separating body and it was necessary to rule-out any re-contact. Ongoing vehicle body rates were compared in pitch, yaw and roll axes. Figure 12, shows all the three-body rate comparison for the current flight in red line, previous flight in green and second last flight in blue. All these body rates show no sudden change in the ongoing vehicle body rates, which confirms that there was no re-contact after the separation event. Further, dynamic pressures, tail-off thrust and angle of attacks were very benign in this flight which also strengthen the conclusion of no re-contact, which could cause the second shock at EPB.

F. Object falling on EPB

There could be a possibility that an object can fall from the above tank ages or wrapped solar panels due to stage separation shock. Considering the relative velocities of falling object and ongoing vehicle which were moving in same direction, an object should fall from 10-15mm above the EPB plate which can produce second shock after 140ms. There were no object sitting at 10-15mm from the EPB plate. Moreover, the LVUS underwent flight acceptance vibration test at ground before the flight which would have brought out if any loose article integrated to the stage. Hence, this possibility can be ruled out.

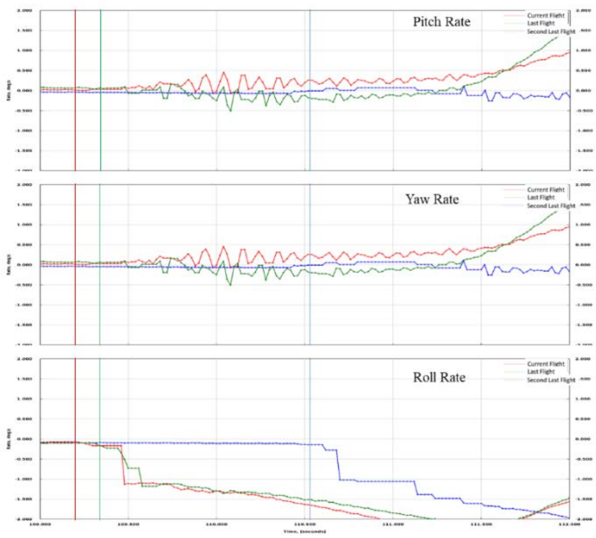

Figure-12, Navigation system measured pitch, yaw and roll rates during the stage separation.

G. Sympathetic detonation of LSC

Stage separation mechanism in this case was through linear shaped charge (LSC) severing the structure which connects the separating stage with the ongoing stage. For redundancy, two initiating devices were used to initiate LSC at two locations. It was suspected, that if delay in separation between two chains could cause the second shock phenomenon.

The initiation commands were issued together and travel time from the initiation device to the LSC squib was computed to be ~300 micro-seconds. Further, delay in the LSC squib initiation was only ~5-6 milli-seconds and travel time of this initiation and severance of connecting plate takes only ~30 micro-seconds. Adding all together, the whole separation events got completed in ~5.3-6.3 milli-seconds which was well away for the second shock duration of 140 milli-seconds.

Secondly, the sympathetic detonation i.e., delayed detonation of one LSC due to mechanical shock from the detonation of other LSC, was suspected and a test was done to demonstrate. Two LSC detonation ends were connected close by and one LSC was detonated and checked if other LSC got initiates because of first LSC shock. The test showed that other LSC could not initiated, hence sympathetic detonation was less likely.

H. Electrical chain measurement

Shock sensor measurements were taken only when the events were planned i.e., shock sensor measurements were not taken throughout the flight, however, the measurements initiated just before the scheduled shock events and closed after the separation events. These shock data used to be stored in the onboard storage and telecasted multiple times. So, there were a chance of overlapping of data while telecasting or stray data telecasting.

Electrical teams had actively gone through the measurement chain and data handling of onboard software. They concluded that current measurement was having no lacuna.

4. Hypothesis

From the above investigations, there were no firm conclusion that can be drawn because the phenomenon was quite random. It appeared in some of the flights and disappeared in most of the flight. Now, a hypothesis was proposed considering all other parameters did not created the second shock.

EPB is normally attached with conical adapter and upper stage tank. This conical adapter is attached to the vehicle end called propulsion adapter ring (PAR) using struts. These struts are having fork and groove joint at the ends. PAR end of the strut is having vertical groove and fork joint, however conical adapter end is having horizontal fork and groove joint. PAR is having two band joint interfaces; fore end of the ring has payload fairing band joint and aft end is having second stage separation system band joint. These bands are tensioned to 100kN and 80kN respectively. Further, PAR fore end has to carry payload fairing static and dynamic loads due to aerodynamics. PAR middle where struts are connected has to carry upper stage tankages, engine, propellant, upper stage adapters like; payload adapter, satellite adapters, double satellite adapters, electronic package bay etc. and spacecraft masses.

All these upper stages inertial load has to pass to the PAR through the struts. PAR end of the strut is having freedom to move axially due to the inertial loads, however, conical adapter end cannot move axially as it has freedom in tangential direction only. Band tension applied to the fore and aft end of the PAR, will try to make ring oval which further stress the conical adapter end of the strut. This cumulative effect of the loadings could have eaten away the fork and groove clearances which could have resulted the frictional contact between the fork and groove.

It has been seen that the additional shock signature was noticed some of the flights during stage separation events, second stage separation events and several fights during payload fairing separation events measured at EPB. The second shock could be the release of this frictional coupling between the fork and groove. Tribological stick and slip could lead to induce shock which could be of the order of 3-4g. This release of frictional energy would be like transient to the system and excite the stage.

Certain fight data further strengthens this hypothesis. This second shock signature is seen only once among all the separation events. It happened because, once the frictional coupling is released the joint get relaxed and it would not re-appear for any of the separation event. Second shock signature has only high frequency content i.e., above 500Hz. High frequency content could be generated either by pyros or through sudden release of mechanical energies like strain energy or frictional energies.

5. Analysis & Results

A finite element model was generated to simulate the launch vehicle during the stage separation using beam, shell and solid elements as shown in Figure 13. Various transient excitations cases were tried at the strut joining location to study if the peak frequencies could be reproduced through FE transient analysis[1][2]. Various combinations were studied by changing the transient as well as location of the excitation. Among all, the best combination of location is plotted in Figure 14 which produces almost all the frequencies present in the measured first and second shocks.

A 0.1 milli-second triangular pulse with 2g peak amplitude was given at the excitation location and response SRS/Q at sensor location is plotted in Figure 15.

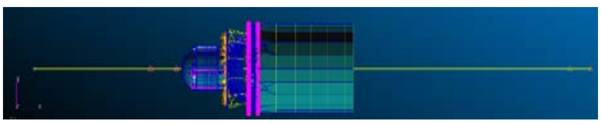

Figure-13, Finite element model of the launch vehicle after the stage separation.

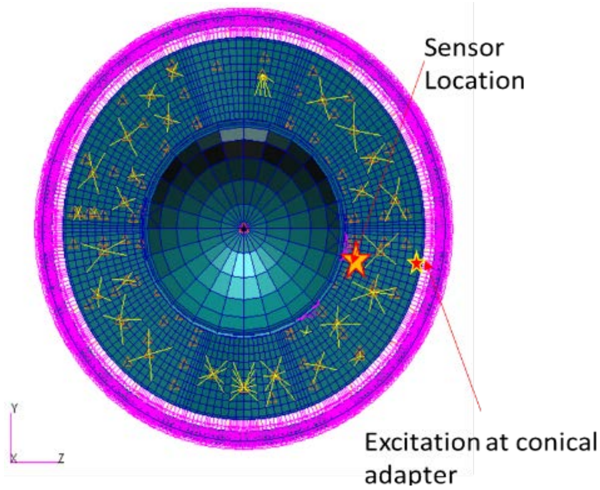

Figure 14, EPB FE model showing the excitation and shock sensor location for the best combination of the response.

6. Discussion

Both the measured shock signature plot shown in Figure 5 shows four major peaks for the primary shock at ~450Hz, ~600Hz, ~900Hz and 1400Hz, however, second shock has two distinct peaks at ~1250Hz and ~1700Hz.Transient analysis result SRS/Q plot shown in Figure 15 shows peaks ~450Hz, ~525Hz, ~1350Hz, ~1450Hz, ~1650 and ~1925Hz.Excitation at different locations yielded different combinations of high frequency responses. This shows that there is a possibility that joint relaxation at different locations could give rise to different second shock every time. Thus, it is possible that closest to the measurement location, a strut joint might have relaxed due to the far away separation event causing a second shock.

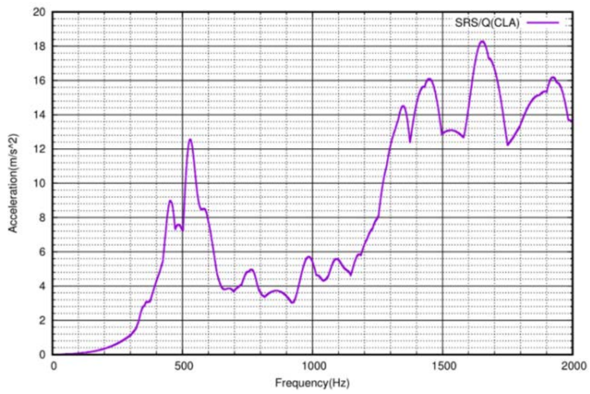

Figure 15, SRS/Q of the analysis response at the sensor location showing all the peak frequencies.

7. Conclusions

A detailed investigations of launch vehicle onboard sensors were brought out in the search of source or similar signature of the additional shock measured at a very critical location during one of the stage separations. After investigating several flights as well as separation events, it was found that this is not a unique signature but due to low amplitude of first shock, this seemed to be problematic however, these shock levels were benign and well within the environmental test levels of the critical package. A hypothesis was proposed and to prove the hypothesis a transient analysis was done which concluded that all the measured frequencies were present in the analysis response signalling that proposed phenomenon might have happened.

8. Acknowledgment

We would like to extend my sincere gratitude to Director, VSSC who has given opportunity to publish this paper. We are thankful to the internal reviewer as well as VSSC editorial board for their guidance. It will be our pleasure to acknowledge project team for the inputs.

9. References

[1] MD NASTRAN 2010 Dynamic Analysis User's Guide,2010. MSC Software Corporation
[2] MD NASTRAN 2010 Quick Reference Guide,2010. MSC Software Corporations
[3] Internal reports

Life Cycle Study of Composite Propellants based systems for Rockets and Missile Propulsion and Control Mechanisms

Pravin Kumar Mehta
O/o DG(ACE)
Pune

A Kumaraswamy
Deptt of Mechanical Engineering
DIAT(DU)
Pune

V.K. Saraswat
Member, Niti Ayog
Delhi

Himanshu Shekhar
O/o DG(ACE)
Pune
himanshushekhar@hqr.drdo.in

Ehtasimul Hoque
Advanced Centre for Energetic Materials
Nasik

Chandra Shekhar Pant
Advanced Centre for Energetic Materials
Nasik

Sushanta Das
Advanced Centre for Energetic Materials
Nasik

Srinivasan Seshadri
Advanced Centre for Energetic Materials
Nasik

***Abstract*—The health of naturally aged non-catalyzed and catalyzed HTPB/Al/AP based composite propellant was investigated by monitoring residual antioxidant content in the propellants by High Performance Liquid Chromatography (HPLC) technique. The study categorically showed that the depletion rate of antioxidant with ageing was substantially high for propellant samples containing transition metal oxides as compared to that of the non-catalyzed one. Simulated depletion of antioxidant in the presence of iron oxide (Fe_2O_3) and copper chromite ($2CuO.Cr_2O_3$) delineated that copper chromite exhibited higher generation of labile radicals due to degradation of polymeric binder than iron oxide. In addition, the surface hardness and degradation in mechanical property data were found to be aligned with the residual antioxidant content in the propellants. Naturally aged propellants with meager amount of residual antioxidant displayed significant surface hardening and deterioration in mechanical property due to the unavailability of adequate thermo-oxidative protection by antioxidant. Furthermore, these analytical results provided pivotal information for establishment of health monitoring schemes for rocket motors based on HPLC techniques, and it also described the plausible deleterious consequences on the depletion of antioxidant as well as mechanical properties by the presence of transition metal oxide burn rate modifiers.**

Keywords*—Composite propellant, Health monitoring, Antioxidant, Transition metal oxides

1. Introduction

The assessment of health of composite propellant is of significant interest to determinate the safe service life of rocket motors. During in service time period, the rocket motors have to endure variety of applied stresses in the form of thermal, UV, mechanical, electrical etc. exposures. These loads deteriorate the overall health of the rocket motor, and influence the failure mechanism[1–4].

In present days, composite solid propellants for rocket motors are primarily based on ammonium perchlorate (AP), aluminum (Al) and hydroxyl terminated polybutadiene (HTPB) based polymeric binders to accomplish better structural integrity and ballistic performances. In addition, to meet the requirements of high burning rate, in some instances these propellants were filled with transition metal oxide burn rate modifiers. For the most part, these rocket motors are relatively invulnerable to ageing as compared to their double base counterparts. Nevertheless, it has been reported that composite propellants may degrade their properties during storage and handling. The reasons for the loss of properties were attributed to the oxidative degradation of polybutadiene matrix if the antioxidant is not protective enough, loss of plasticizer and dewetting between the binder and filler. Furthermore, the incorporation of transition metal oxides in the propellant compositions might have adverse ageing effects in terms of catalyzing the breakdown of polymeric binder [5–11].

Considering the chemical aspect, it has been well apprehended that the efficacy of the antioxidant in the composite propellant is of paramount importance for the long-term resilience of the rocket motor. The antioxidant traps or inhibits the oxygen based radical species, and interrupts the autoxidation of polymeric binder, and therefore protects the propellant. In other words, determination of residual antioxidant content in the composite propellant may provide information pertaining to protection capacity of the antioxidant, and consequently the useful life of the rocket motor. The most common analytical method involves extraction of antioxidant from the composite propellant, and quantification of the antioxidant present in the extract. In this study, antioxidant of our interest is N-phenyl-β-naphthylamine (PBNA) which was incorporated in propellant compositions investigated in this study.

Herein, we wish to demonstrate the extent of depletion of antioxidant content i.e. percentage residual antioxidant as a health indicator for naturally aged non-catalyzed and catalyzed HTPB/Al/AP composite propellants. The effect of transition metal oxide burning rate modifiers: iron oxide (Fe2O3) and copper chromite (2CuO.Cr2O3) on the depletion of antioxidant was further elaborated using accelerated ageing simulation equivalent of five years of natural ageing. In addition, the degradation in mechanical property and surface hardness were evaluated as complimentary data set for health monitoring.

2. Experimental

A. Propellant Formulations

The naturally aged HTPB/Al/AP-based composite propellant samples were obtained from our own sample storage facility. In this study, the propellant samples were broadly classified in two sub categories; P01: non-catalyzed composition and P02: transition metal oxides catalyzed compositions. The propellant formulations of both the categories were commonly based on HTPB polymeric binder system, and they contained oxidizer ammonium perchlorate (AP), aluminum as fuel, DOA as plasticizer, N-phenyl-β-naphthylamine (PBNA) as antioxidant and toluene diisocyanate (TDI) as curing agent with about 86 % solid loading. Moreover, P02 composition contained 0.35 % oftransition metal oxide burn rate catalyst; a combination of iron oxide and copper chromite.

All the propellant formulations of same class were originally processed under controlled near identical conditions at different time intervals during the last nine years. Following curing, the propellant samples were stored in sealed polyethylene drums with silica gel desiccant, and naturally aged under identical temperature-controlled storage conditions. Table 1 summarizes the natural ageing time of propellant samples which were investigated during this study.

Table 1. Summary of the naturally aged composite propellant samples subjected to study.

Categories	Description	Natural ageing (Years)
P01	HTPB/Al/AP (Non–catalyzed)	9, 6, 5, 4, 2, & 0
P02	HTPB/Al/AP (Catalyzed)	7, 6, 4, 3, & 0

B. HPLC Method for Measurement of PBNA Content in Propellant

The two categories of propellant formulation: P01 and P02 contained about 0.1% of PBNA. High performance liquid chromatography (HLPC) was explored for quantitative determination of residual antioxidant PBNA in naturally aged propellant samples. Column purified sample of PBNA (Original make: Sigma Aldrich) was used as HPLC calibration standard.

5 gm of propellant specimen was taken out from a propellant block after removing the exposed surfaces. It was cut into small pieces of 2-3 mm, and extracted with 50 ml methanol with agitation under sealed condition for 12 hrs. The extracts of the PBNA was allowed to settle, and 10 ml to 15 ml of the supernatant solution was centrifuged at 2800 rpm for 6 minutes to obtain a perfectly clear solution. For analysis, 10 µl of the solution was injected into the HPLC, and the result was expressed as the percentage of PBNA remained in the composite propellant [12].

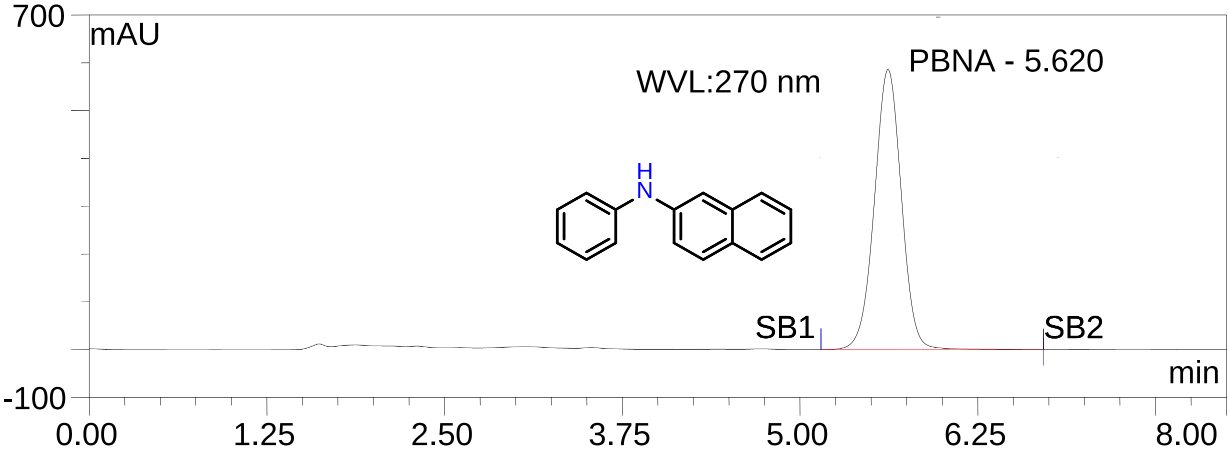

Figure 1. Reverse Phase HPLC chromatogram of PBNA.

All experimental HPLC runs were performed in Dionex Ultimate_3000 HPLC system fitted with a Rheodyne manual injector with a 10 µl loop, photo diode array detector and chromeleon 6.80 chromatography management software. Lichrophere® RP-18 endcapped 5 µm 4.6 X 150 mm reverse phase column was used as stationary phase. The isocratic mobile phase consisted of 80% methanol/20% water (v/v), and the flow rate was maintained at 1 ml/minute. PBNA was eluted as a sharp peak at approximately 5.6 minutes (Figure 1) as confirmed by the analysis of standard PBNA solution.

C. Simulated Depletion of PBNA by Accelerated Ageing

To elucidate the effect of transition metal oxide burn rate modifiers: iron oxide (Fe2O3) and copper chromite (2CuO.Cr2O3) on the oxidative degradation of HTPB binder during storage, accelerated ageing conditions were simulated. In view of this, three representative compositions were prepared as given in Table 2. The average particle size of the metal oxides ware 1-2 μ having volatile matter limited to maximum 0.2 %. The ageing conditions were formulated considering the storage environments of rocket motors. Since, weather-sealed rocket motors are practically stored in confinement, and essentially deprived from atmospheric air, one set of experiment (Exp 1) was carried out in closed lid airtight container and another in open lid conditions (Exp 2) which will allow a constant ingress of atmospheric oxygen. The main objective of this simulation experiment was to recognize the plausible adverse effect of transitional metal oxides in catalyzing the oxidative degradation of binder matrix.

The principle of Thermal Equivalent Load (TEL) as per Generalized van't Hoff rule (GvH) was employed to simulate 5 years of natural ageing condition. Hence, all the mixes were aged at 85 °C for 7days [13,14].

Table 2. Summary of representative compositions (in parts).

ID	HTPB	PBNA	Iron Oxide	Copper Chromite
Mix 1	10.0	0.1	---	---
Mix 2	10.0	0.1	1	---
Mix 3	10.0	0.1	---	1

After completion of the accelerated ageing experiment, the residual amount of PBNA in each of the mixes was extracted in 50 ml of methanol under agitation for 1 hour, and subsequently analyzed in HPLC as discussed in section 2.2.

D. Measurement of Shore A Hardness and Mechanical Properties of Composite Propellant

Shore A hardness of the propellant samples was measured in Shore-A durometer apparatus. Three consecutive measurements were taken for each sample with a minimum distance of 5 mm from each other, and the Shore A hardness was reported on the apparatus after 3 seconds.

The mechanical property analysis was performed on Universal Tensile Test Machine (Tinius Olsen) using standard dumbbell shaped test specimens (ASTM-D638D-type-IV) obtained from propellant cartons. Prior testing, propellant dumbbells were preconditioned for at least 4 hours at 24 °C and RH < 50%. The samples were pulled to failure and the tensile strength, % elongation and modulus were computed using Q-Mat software. For each propellant batch, five repetitive measurements were carried out to obtain a reliable test result.

3. Results and Discussions

A. Extraction and Measurement of Residual PBNA Content in Propellant

To begin with, we evaluated the precision of the method which consisted of extraction and determination of PBNA content. Propellant samples from a single propellant block were cut, extracted, and analyzed for PBNA content by HPLC. The standard deviation for the % residual of PBNA from the samples was obtained as 0.6, and this advocated the satisfactory reliability of the whole method.

Table 3. Residual PBNA in P01 (HTPB/Al/AP-non-catalyzed composition) after different years of natural ageing

Sr. No.	Natural ageing time (years)	% Residual of PBNA in propellant
1	0	92
2	2	87
3	4	92
4	5	88
5	6	92
6	9	86

HPLC analysis of naturally aged HTPB/Al/AP based composite propellant manifested that there was a distinct difference in the rate of depletion of PBNA antioxidant for the P01: non-catalyzed composition and P02: catalyzed composition. Table 3 summarizes the residual antioxidant level in P01 propellants as analyzed by HPLC.

Considering the experimental limitations and minor changes in purity of PBNA source, it is evident that none of the naturally aged samples of non-catalyzed P01 compositions showed significant decay of antioxidant level, even after 9 years of ageing (Figure 2). It indicated to the fact that the oxidative degradation of polymeric binder is substantially low for non-catalyzed propellant compositions. Besides it is of great interest to note that higher amount of residual antioxidant level signifies greater thermo-oxidative protection along with extended life period for propellant.

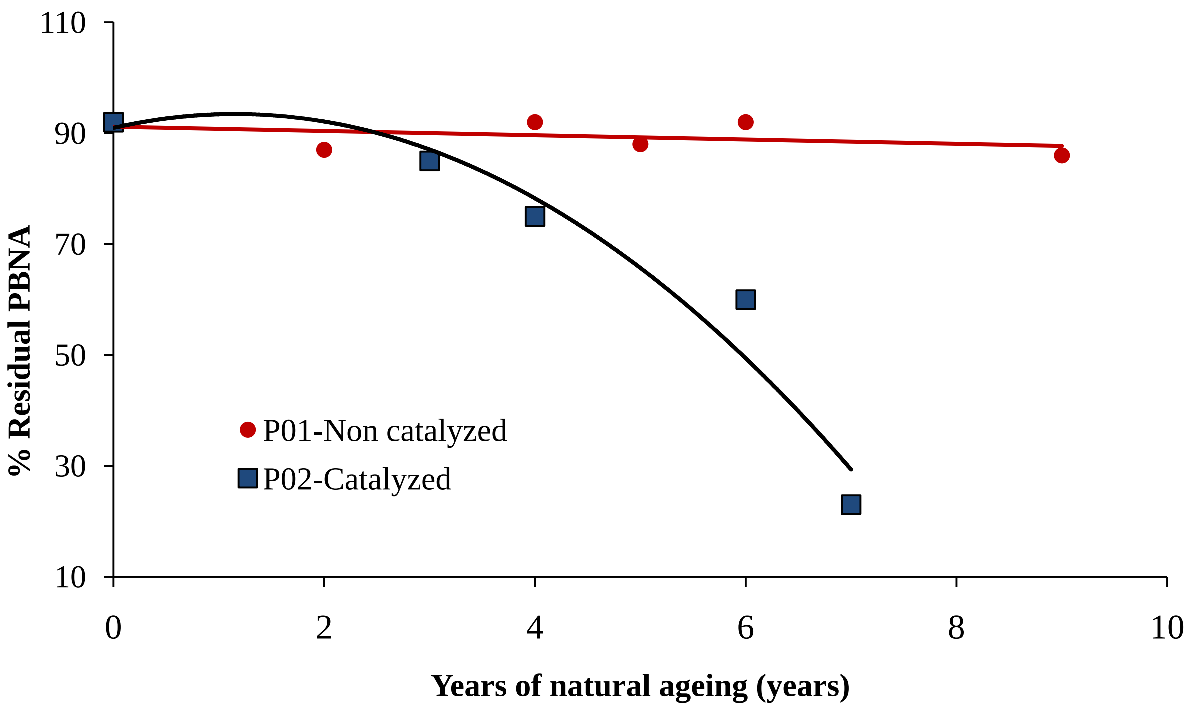

Figure 2. % Residual PBNA for naturally aged non-catalyzed P01 & catalyzed P02 propellant compositions. There was a significant depletion of PBNA for catalyzed P02 compositions whereas for non-catalyzed P01, there was practically no decay in PBNA concentration.

The propellant composition P02 contained 0.35 % of transition metal oxide burning rate modifiers iron oxide and copper chromite, and HPLC analysis of P02 propellant compositions showed a hyperbolic downward trend in % residual PBNA content with natural ageing. For instance, after seven years of natural ageing, only 23 % of antioxidant PBNA remained in the propellant for protective action against oxidative degradations. This is indicative of generation of high concentration of radicals, and ensuing sacrificial quenching of radicals by PBNA.

Table 4. Residual PBNA in P02 (HTPB/Al/AP-Catalyzed by Fe_2O_3& $2CuO.Cr_2O_3$ composition) after different years of natural ageing

Sr. No.	Natural ageing time (years)	% Residual of PBNA in propellant
1	0	92
2	3	85
3	4	75
4	6	60
5	7	23

Table 4 represents the HPLC results for P02 propellant composition, and the ageing profile of PBNA depletion is depicted in Figure 2.

Ranby and Rebeck [15] showed that oxides of transition metals act as catalyst for the degradation of polymeric systems. Now for P01: non-catalysed composition it can be hypothesised that due to the steady state nature of the classical anti-oxidant activity; there is a long induction period [16]. Therefore, the rate of antioxidant depletion was very low for non-catalysed P01 compositions even after 9 years of natural ageing.

Unlike P01 composition, the antioxidant depletion rate was very high for transition metal oxide catalysed P02 composition. The origin of this aggravated rate of antioxidant depletion can be presumed to be the increased concentration of labile free radicals generated by catalytic degradation of polymeric binder HTPB by transition metal oxides.

B. Simulated Depletion of PBNA by Accelerated Ageing

The simulated experiments of section 2.3 mimicked 5 years of natural ageing condition of composite propellant. The results of this study corroborated with the observed trend in depletion of PBNA in composite propellant in the presence of transition metal oxide mainly iron oxide (Fe2O3) and copper chromite (2CuO.Cr2O3). Table 5 displays the experimental results.

Table 5. Residual PBNA after simulated depletion under accelerated ageing equivalent to 5 years in the presence of Fe2O3&2CuO.Cr2O3

ID	% Residual of PBNA in mixes	
	Closed container	Open container
Mix 1	92	92
Mix 2 (IO)	59	74
Mix 3 (CC)	15	26

Specifically, Mix 1 which did not contain any burning rate catalyst resulted in a 92 % residual PBNA content even after accelerated ageing equivalent to 5 years. It comprehensively advocates the existence of steady state condition, and the very slow radical initiation reaction for non-catalyzed compositions. Furthermore, it was found thatthe depletion rate of PBNA was much higher for the Mix 3 as compared to that of Mix 2. This observation clearly indicates that copper chromite has a more catalytic effect in the oxidative degradation of polymeric binder than iron oxide. For instance, after thermal equivalent load of 5 years of ageing the % residual PBNA was as low as 15 % for Mix 3, whereas it was 59 % for Mix 2.

Mayo et al. accounted that besides catalytic nature in oxidative degradation; iron oxide exhibited antioxidant nature, and retarded the degradation of polymers containing double bonds (Scheme 1) [17,18].

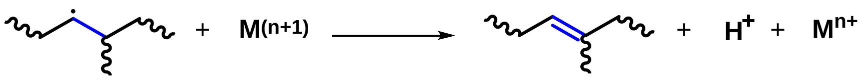

(1)

Scheme 1. Inhibition of Chain Carrying Radical

Perhaps it is due to this competition between the antioxidant activity and catalytic nature in polymer degradation, the oxidative degradation of polymeric binder by iron oxide was not as effective as copper chromite.

Of a particular note, it was observed that the % residual PBNA was higher for the closed container (Exp 1) than the open container (Exp 2) condition for the mixes with transition metal oxides (Mix 2 & Mix 3). It is presumed that for open container there is a decrease in concentration of radicals as volatile radicals might have escaped, but for closed container, no such occurrences could have happened.

C. Evaluation of Shore A Hardness and Mechanical Properties of Composite Propellant

Practically, naturally aged non-catalyzed P01 propellant compositions did not show any hardening due to ageing phenomena. On the other hand, the Shore Hardness increased about 25 % for the 7 years old catalyzed P02 propellant sample, although up to 5 years of ageing there was no significant enhancement in hardness even for P02 compositions.

Similar trend was also noted for mechanical properties of the composite propellant, and the results are demonstrated in Table 6.

Table 6. Degradation in mechanical properties of naturally aged propellants in terms of % change

ID	Years of natural ageing	% Change in		
		Tensile strength	Elongation (%)	Modulus
P01	6	17	-4	6
	9	13	-10	15
P02	4	-3	-23	27
	7	67	-36	130

The results suggested that the rate of degradation of propellant properties was significantly higher for transition metal catalyzed P02 compositions than its non-catalyzed counterpart. Intriguingly, as long as higher concentration of antioxidant PBNA is available, the rate of deterioration remains slow for both the compositions. However, due to rapid depletion of antioxidant for catalyzed compositions, there was an accelerated degradation in properties (Table 6).

4. Conclusion

To summarize, it can be concluded that the rate of depletion of antioxidant is considerably higher for naturally aged transition metal oxide catalyzed P02 propellant composition as compared to non-catalyzed P01 composition. The results from the simulated accelerated ageing conditions reinforce these observations: transition metal oxides (iron oxide, copper chromite) increase the radical concentration in the system which in turn enhances the rate of antioxidant depletion. Additionally, we are encouraged to observe that the copper chromite has a more catalytic effect as compared to iron oxide in the binder degradation reaction. Furthermore, the surface hardness and mechanical property degradation data reveal that the presence of transition metal oxide burn rate modifiers certainly has deteriorating ramifications, and these are the outcome of compromised thermo-oxidative protection due to high depletion of antioxidant.

Moreover, the HPLC quantification of residual antioxidant content for HTPB/Al/AP based composite propellants might have profound implications for implementation of modern analytical methods into health monitoring programs of solid rocket motors.

5. References

[1] S. Cerri, M.A. Bohn, K. Menke, L. Galfetti, Aging of HTPB/Al/AP rocket propellant formulations investigated by DMA measurements, Propellants, Explos. Pyrotech. 2013, 38, 190–198.

[2] R.B. Walter, J.F. Johnson, Analysis of Antioxidants in Polymers By Liquid Chromatography, J. Polym. Sci. Macromol. Rev.1980, 15, 29–53.

[3] R. Bogusz, P. Magnuszewska, The Aging Studies of the Low HCl Content Composite Rocket Propellant, Propellants Explos. Pyrotech. 2019, 44, 1193–1198.

[4] T. Tao, X. Sui, S. Li, N. Wang, A Study on Consumption and Characterization of Stabilizer Content of NEPE Propellant via FTIR, Propellants Explos. Pyrotech.2019, 44, 1–8.

[5] J.L. De La Fuente, M. Fernández-García, M.L. Cerrada, Viscoelastic behavior in a hydroxyl-terminated polybutadiene gum and its highly filled composites: Effect of the type of filler on the relaxation processes, J. Appl. Polym. Sci.2003, 88, 1705–1712.

[6] M. Celina, J.M. Skutnik Elliott, S.T. Winters, R.A. Assink, L.M. Minier, Correlation of antioxidant depletion and mechanical performance during thermal degradation of an HTPB elastomer, Polym. Degrad. Stab.2006, 91, 1870–1879.

[7] M.D. Judge, An investigation of composite propellant accelerated ageing mechanisms and kinetics, Propellants, Explos. Pyrotech.2003, 28, 114–119.

[8] K.N. Ninan, K. Krishnan, R. Rajeev, G. Viswanathan, Thermoanalytical investigations on the effect of atmospheric oxygen on HTPB resin, Propellants, Explos. Pyrotech. 1996, 21, 199–202.

[9] M. Celina, L. Minier, R. Assink, Development and application of tools to characterize the oxidative degradation of AP-HTPB-Al propellants in a propellant reliability study, Thermochim. Acta.2002, 384, 343–349.

[10] Tijen Seyidoglu, Manfred A. Bohn, Characterization of Aging Behavior of Butacene® Based Composite Propellants by Loss Factor Curves, Propellants Explos. Pyrotech.2017, 42, 1–13.

[11] W. Wu, C. Chen, X. Fu, C. Ding, G. Wang, The Correlation between Chemical Stability and Binder Network Structure in NEPE Propellant, Propellants Explos. Pyrotech.2017, 42, 1–7.

[12] STANAG- 4581: Explosives, Assesment of Ageing Characterstics of Composite Propellants Containing an Inert Binder, NATO Standardization Office, Brussels, Belgium 2006.

[13] S. Cerri, M. Bohn, L. Galfetti, K. Menke, Ageing Behaviour of HTPB Based Rocket Propellant Formulations, Cent. Eur. J. Energ. Mater.2009, 6, 149–165.

[14] M.A. Bohn, Prediction of Equivalent Time-Temperature Loads for Accelerated Ageing to Simulate Present in-Stroage Ageing and Time Temperature Profile Loads, 40th Int. Annu. Conf. ICT, Karlsruhe, Germany, June 23-26, 2009.
[15] B.G. Ranby, J.F. Rabek, Photodegradation, Photoxidation and Photostabilization of Polymers, Wiley-VCH, New York 1975.
[16] K.T. Gillen, J. Wise, R.L. Clough, General solution for the basic autoxidation scheme, Polym. Degrad. Stab. 1995, 47, 149–161.
[17] F.R. Mayo, K. Egger, Katherine C. Irwin, Accelerated Oxidation of Polyisoprene. I. Metal-Catalyzed Oxidation In Solution, Rubber Chem. Technol.1968, 41, 271–288.
[18] G.G. De Barros, N.M.P. Ricardo, V.W. Vieira, Effect of iron oxides on the thermal degradation of natural rubber from Manihot glaziovii, J. Appl. Polym. Sci.1992, 44, 1371–1376.

Application of Root Cause Analysis for Failure Monitoring & Control of Lighter-Than-Air (LTA) System

Arvind Kaushik
ADRDE
DRDO
Agra
arvind_kaushik@adrde.drdo.in

Kamlesh Kumar
ADRDE
DRDO
Agra

Arun Kumar Saxena
ADRDE
DRDO
Agra

Abstract — **Failures and problems are undesirable and unavoidable part of human life. We face failures and problems both in personal as well as in professional life. The same is true for an engineering system. Every engineering system is designed and developed to perform some intended function and objective. Failure is the state or condition of not meeting a desirable or intended objective for an engineering system. Various types of failures, faults and problems occur during the operation of an engineering system in its operational life. To solve a problem, the first and foremost important step is to identify and understand what is causing the problem. Several case studies have been conducted in industries, which show that root cause is the most basic reason for an undesirable state (fault or failure) in an engineering system. If the root cause of a failure or problem is not identified, then failure or problem will repeatedly occur during the operation of the system. This paper seeks to examine the Root Cause Analysis (RCA) for Lighter-Than-Air (LTA) system. This paper highlights about the approaches, which can be used in root cause analysis of LTA system. The selection of appropriate approach is one of the most important aspect for root cause analysis, because without selecting perfect approach it is not possible to analysis the actual root cause for a system failure.**

Keywords- Aerostat, Cause, Detection, Envelope, Failure, Fault, Maintenance, Occurrence, Prevention, RPN, Severity

1. Introduction

A root cause is defined as a factor that caused a non-conformance, fault, error or failure and should be permanently eliminated through design, configuration and process improvement. Root Cause Analysis (RCA) is defined as a collective term that describes a wide range of approaches, tools, and techniques used to uncover causal factors and root causes of failures/problems. Some RCA approaches are geared more toward identifying true root causes than others, some are more general problem-solving techniques, and others simply offer support for the core activity of root cause analysis. It's important to note that root cause analysis in itself will not produce any results; it must be made part of a larger problem-solving effort for system/product quality improvement.

Failure root cause identification is an important aspect in research and development project for new product development life cycle. An engineering system/product such as LTA system is usually consisting of several mechanical, electrical and electronic subsystems working in a coherent sequence to fulfill the intended objective and function.

ADRDE is a pioneer establishment for design & development of Lighter-Than-Air (LTA) systems. Lighter-Than-Air (LTA) systems are airborne platforms that overcome the gravity force by means of buoyancy force acting on them due to a lighter-than-air gas (usually helium) enclosed in one or more compartment of an inflatable system. There are two basic types of LTA systems – aerostat and dirigibles. Aerostats are tethered balloon and ground pilot can only control the flying altitude. In aerostat, the balloon is holding on ground (during flying & ground maintenance) by ground winch and mooring system. On the other hand, Dirigibles, often called airships, are usually powered balloon and ground pilot can control the flying altitude as well as can steer the balloon. Both types of LTA system can be used for military application such as for intelligence, reconnaissance and surveillance as well as for commercial application such as product/service advertisement.

The most important subsystem in LTA system is airborne platform i.e., helium inflated balloon or envelope. The useful payloads are mounted on balloon and inflated balloon is flying at some predefined altitude. The main subsystems of helium inflated balloon (envelope) are – hull, ballonet, fins, patches, handling lines and supporting accessories like manometer, gas valves, health monitoring & control system. The size and shape of balloon is decided on the basis of flying environment, flying altitude, payload capacity (surveillance cameras, radar etc.) and endurance [1]. A pictorial view of flying LTA aerostat designed and developed by ADRDE has been shown in Figure 1.

LTA being a multidiscipline system; the identification, detection and prevention of failure's root cause is a prime requirement both for safety as well as for reliable operation of the system. According to Doggett [2]; various techniques and procedures like Fault Tree Analysis (FTA), Common Cause Failure Analysis (CCFA), Failure Mode & Effect Analysis (FMEA), Cause-and-Effect Diagram (CED), Interrelationship Diagram (ID), Current Reality Tree (CRT) and Why-Why Analysis may be used for identifying root causes in system failure. He has added that Why-Why analysis is the most simplistic root cause analysis tool whereas current reality tree is used for possible failures of a system and it is commonly used in the design stages of a project and works well to identify causal relationships.

However, this paper will cover the CED and FMEA approach for root cause analysis of LTA airborne platform (aerostat balloon/airship envelope).

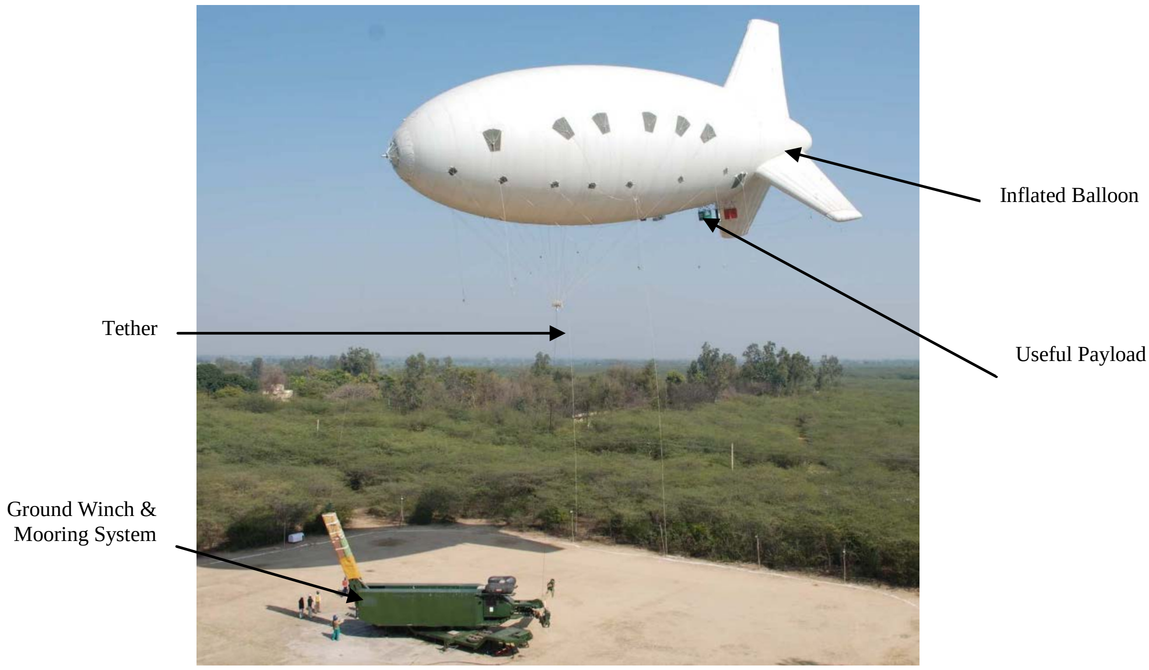

Figure 1: Pictorial View of LTA Aerostat System [1]

2. Objective Of RCA

Every system failure is associated with some defect or imperfection either in a system itself or in its associated system or process. We usually called this imperfection as a fault in system. An error is the manifestation of a fault and a failure occurs, when the component's/system's behaviour deviates from its specified behaviour [3]. Figure 2 shows the functional relationship between fault, error and failure. Fault detection for a given failure effect or mode is a reactive process. Usually, a failure has occurred and it needs to identify which component/subsystem or process is the root cause. Once the root cause has identified, it has to be either isolated or repaired/replaced/modified so that system can perform and fulfilled the intended function and objective. An RCA investigation discovers the cause-and-effect trail from the end failure back to the root cause (top-down approach). The main objectives of RCA include:

- Identification of permanent solutions to a failure (problem)
- Prevention of recurring failures
- Introduction of a logical approach for compliance of nonconformities

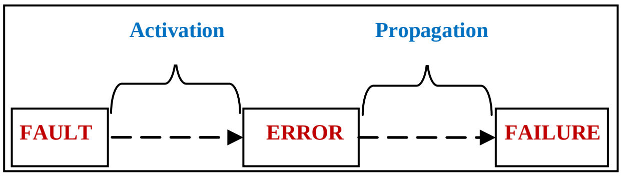

Figure 2: Functional Relation of Fault with Failure

The operation of LTA aerostat system involves airborne balloon system, which holds on ground by an electro-mechanical cable (tether) and ground winch & mooring system. The root cause identification is a critical area to prevent various possible failures during the operation of an LTA system. Here in this paper, we focused only on airborne balloon (envelope) system. Cause-and-Effect Diagram (CED) and Failure Mode & Effect Analysis (FMEA) may be used for identification and prevention of failure root causes [4] along with total quality control for airborne balloon operation. Both CED and FMEA are qualitative tools performed on the basis of system's data base management knowledge. The correct identification of possible failures, their root causes, detection and action to prevent these failures are essentials for continuous 24×7 hrs surveillance operation of LTA system. Methods like standard of preparation, inspection schedule, scheduled maintenance, preventive maintenance and provision of various sensors etc are suggested in the analysis for failure avoidance & failure detection in airborne balloon operation. This results in lower failure occurrence rate or early failure detection which results in high system up-time. The CED and FMEA have been performed on system hardware level (System-Assembly-Component) in combination of system functional level (functional block diagram).

3. Steps and Approach To RCA Process

The selection of correct RCA approach results in actual root cause identification. The RCA is a team exercise which consists of designer, serviceman, QA person, manufacture, management and some time the product user as a team member. Andersen and Fagerhaug [5] suggest a seven-step RCA flow chart as shown in Figure 3. The 7 steps and their application for airborne balloon are as follow:

A. Failure Understanding

The objective of this step is to understand the failure and its effect on airborne balloon operation. Qualitative Requirements (QR) are used to evaluate (compare) the balloon current performance and its importance for overall mission. Low lift of airborne balloon may be considered either as the loss of primary function or as the degradation of primary function depends on the mission qualitative requirements for balloon lift.

B. Failure Cause Brainstorming

The objective of this step is to explore the possible issues that may be causing the failure in airborne balloon. For this purpose, we applied unstructured Brainstorming, which is a technique where the team members verbally suggested all possible causes, they could think of, which was immediately noted on a whiteboard and summarized together at the end. For example, the low lift of airborne balloon may be due to leakage in balloon or due to low quality helium gas (impurities in gas) or due to cyclic change in environmental temperature (change in gas density).

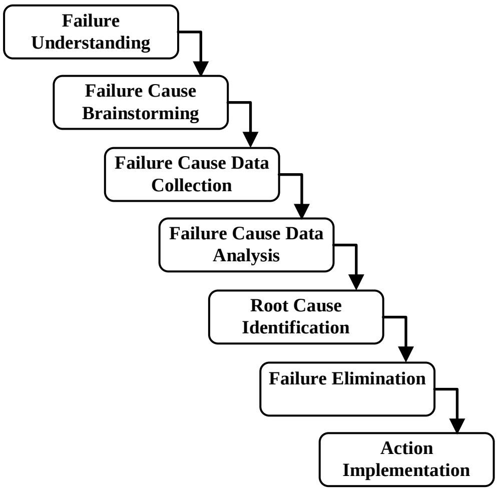

Figure 3: Seven Step Process for RCA Flow Chart [5]

C. Failure Cause Data Collection

The main goal of this step is to collect failure cause data for RCA. The various ways for data collection are literature survey, study of similar airborne balloon, the logbook entry of airborne balloon, expert opinion, acceptance test report & pre flying inspection report of balloon etc.

D. Failure Cause Data Analysis

The objective of this step is to analyses the cause data as collected in previous steps. Variety of statistical data analysis (pie chart, Pareto chart etc.) methods can be used for this purpose. For example, the pie chart is used in our study to bring out the proportion of possible causes (balloon leakage, helium purity, diurnal temperature variation etc.) for low lift in airborne balloon. FMEA uses a qualitative ranking technique for failure severity, occurrence and detection to calculate the possible risk (Risk Priority Number: RPN) for a particular class of failure cause in airborne balloon. The RPN can be used to prioritize the failure causal factors. The technical review board and failure review board (team exercise usually headed by subject field expert) play a vital role in driving conclusion from cause data analysis.

E. Root Cause Identification

The objective of this step is to identify the root cause(s) of the failure. For this, CED use Cause-and-Effect chart (Fishbone diagram) which is a tool for identifying the major causes of a failure, together with the secondary causes/factors influencing the failure. For example, the main cause for balloon low lift is helium leakage from fabric joints and secondary cause is inability of balloon health monitoring system to give an alarm (alert signal) to ground operator during initiation of leakage. Similarly, FMEA use the system hierarchy tree to drive Why-Why causal factors up to '5-Why level' for identification of root causal factor.

F. Failure Elimination

The objective of this step is to propose solutions to deal with the root causes of the failure. The solutions are concern with method, man, machine, material and management related to that system. If we talk about low lift (failure) of airborne balloon; the solutions are – leak detection using soap solution on air inflated balloon during ground test (method), the adequate training to ground operator (man), the ground simulated testing of balloon health monitoring system (machine), the use to UV treated adhesive for fabric joint (material) and the modification of standard operating procedure for balloon flying trial (management).

G. Action Implementation

The goal of this step to identify the project phase & key person for implementation of RCA recommendation. The post-trial review may be conducted to evaluate the benefits of recommendation on availability (up-time) and for compliance of qualitative requirements for airborne operation of balloon.

So, we have seen that Root Cause Analysis (RCA) is a structured investigation that aims to identify the real cause of a failure and the actions necessary to eliminate it. It is important to note that both CED and FMEA follow the similar RCA flow chart but in a different way to each other. However, the soul of analysis will more or less remains the same in both the approaches.

4. CED Approach And Its Application For Airborne Balloon Failure

CED is an analysis tool that provides a systematic way of looking at effect (failure, imperfection and defect) and the causal factors that create or contribute to that effect (failure, imperfection and defect) [6] [7]. Japanese quality guru Dr. Kaoru Ishikawa invented the idea of CED (also known as fishbone diagram or Ishikawa diagram) for solving problems at the Kawasaki shipyards in the 1960s.

The diagram looks just like a fish's skeleton with the problem (failure, imperfection) at its head and the causes for the problem feeding into the spine. Once all the causes that underlie the problem have been identified, we can start looking for solutions to eliminate or minimize the probability of problem recurrence.

Table 1 shows the industry types, recommended CED approach and applicable causal categories for failure RCA. We can also opt the customized CED approach (like 4 Ms, 6 Ms, 4Ms-2Ps etc) based on our own system requirements.

Table 1: Industry Vs CED Approach

Industry	CED Approach	Causal Categories
Manufacturing	8 Ms	Material
		Machine
		Method
		Man Power
		Measurement
		Milieu (Environment)
		Maintenance
		Management

Marketing	8 Ps	Product
		Price
		Promotion
		Place
		People
		Process
		Packaging
		Physical Presence
Service	5 S	Suppliers
		Systems
		Standard Documentation
		Skills
		Surroundings

For airborne balloon platform, the Qualitative Requirement (QR) states about flying of balloon at some particular altitude (AMSL) for a specified period of time with integrated surveillance payload (camera, radar). So, any helium leakage or low lift is considered as a failure for airborne balloon (nonconformance to QR). The causal factors for this failure have been decided on the basis of Pareto Analysis principle [8] – Few causes account for most of effects (Or in terms of quality improvement, a majority of failures (≈80%) are produced by a few key causes (≈20%)). Based on our development experience, the main causal factors of balloon low lift (failure) are categorized as follows:

(i) Methodologies – Standard Of Manufacturing (SOM) during fabrication, Standard Operating Procedure (SOP) during handling, inflation and flying.
(ii) Machinery – The working of balloon health monitoring & control system (air discharge valve, gas discharge valve, blower, differential pressure sensor etc) and support accessories.
(iii) Materials – The balloon base fabric properties, quality of gas barrier coating on base fabric, joint preparation, UV resistance of coated fabric & adhesive, balloon handling line.
(iv) Measurements – The functioning of pressure gauge, manometer, temperature and altitude sensor.
(v) Environment – The balloon storage condition, trial location with respect to mean sea level, trial team skills.

As discussed earlier in this paper, the sources of data collection are literature survey, study of similar airborne balloon, the logbook entry of airborne balloon, expert opinion, acceptance test report, ground air inflation report & pre flying inspection report & observation of balloon etc. The Figure 4 shows the CED for airborne balloon failure (leakage or low lift) using “4 Ms” approach.

This diagram graphically illustrates the relationship between balloon failure (leakage or low lift) and all the factors that influence the leakage or low lift and hence to identify the possible root causes i.e. basic reasons for balloon leakage or low lift.

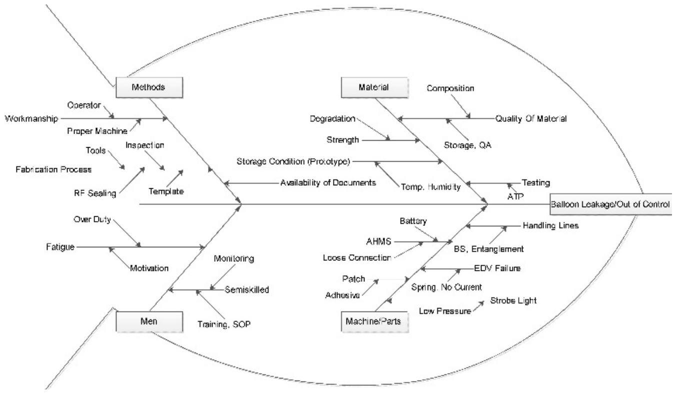

Figure 4: Fishbone Diagram Illustrating Contributing Causes to Airborne Balloon Leakage or Low Lift

Other failure modes like balloon burst, dynamic instability, fabric joint failure etc. can also be investigate in similar manner as described above for low lift (leakage) failure.

5. FMEA Approach And Its Application For Airborne Balloon Failure

FMEA was developed in the USA and published in 1949 as the MIL-STD-1629A [9] "Procedure for Performing a Failure Mode, Effects and Criticality Analysis". FMEA is commonly defined as "a systematic process for identifying potential design & process deficiencies and failures before they occur, with the intent to eliminate them or minimize the risk associated with them". This analysis can be done for a process (PFMEA), for a design (DFMEA) and for a product (Product FMEA). Several literatures are available for highlighting the importance of FMEA in identification of root cause for a system failure. Nadia Belu, Nicoleta Rachieru, Emil Militaru and Daniel-Constantin Anghel have elaborated the importance of FMEA to identify the causal factors and prevent the recurrence of failure during product development life cycle [10].

In FMEA, the risk associated with a failure cause is estimated by a Risk Priority Number (RPN), which consists of Severity (S), Occurrence (O) and Detection (D) rating values. As the risk increases, the values of the ranking rise. Most risky causal factor of the design/process/system can be finding out by targeting high value RPNs. RPN can be obtained on the basis of the following equation:

$$RPN = S \times O \times D \tag{1}$$

Severity (S) refers to the magnitude of end effect of any failure on the operation of the system & its surrounding. According to the MIL-STD-1629A, Severity is a numerical measure in the range of (0; 10). Occurrence (O) is a value that determines the frequency a failure is likely to occur. It is concerned with the component's failure rate. A quality classification of occurrence can also be done in a range of (0; 10). Detection (D) is a probability that the potential failure will be detected before it recurrence. The occurrence can also be classified in the range of (0; 10). A high value of all this above-mentioned scale represents a poor score for a particular aspect (i.e. catastrophically severe, very frequent occurrence and all most impossible to detect). However, all these rating are qualitative.

In our study, FMEA analyzes different failure modes, their severity and effect on performance of airborne balloon. The effect of failure root cause is depending on the functional relationship between the subsystems. The functional relation shows how the subsystems interact with each other to achieved system goal. For example, how the working of balloon health monitoring & control system affecting the differential pressure and aerodynamic shape of airborne balloon. FMEA is a "bottom-up" approach for failure analysis and investigation of root cause [11]. In FMEA, we consider possible failure mode in each component (smallest level) of the system and analyzing the effect of each corresponding failure mode on its next subsystem or system level performance. We used this functional relationship in FMEA to conclude a "Why-Why" relationship up to "5-Why" level for identification of failure root cause. The ranking process of the FMEA can be accomplished by utilizing existing failure data or by a subjective ranking procedure conducted by a team of people with an understanding of the LTA system. The FMEA process flow chart has been shown in Figure 5.

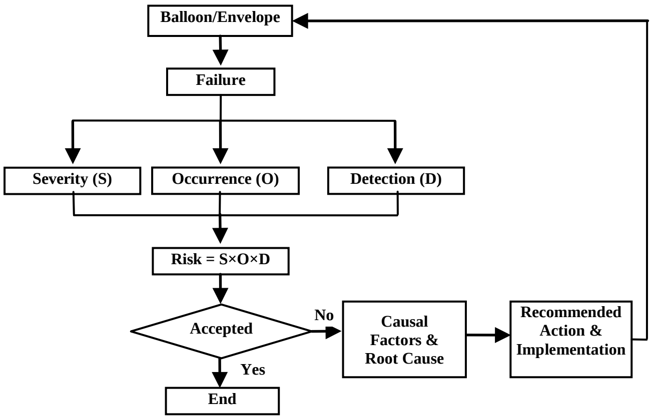

Figure 5: FMEA Flow Chart for Airborne Balloon

This flow chart is similar to as shown in Figure 3. The common root cause categories for various failures in airborne balloon have been summarized in Table 2. This table includes the causal factor for balloon and associated accessories used during FMEA.

Table 2: Failure Common Root Cause Categories: Balloon

Mechanical	**Electrical**	**Wear & Environment**
Design Deficiency	Loose Connections	Corrosion
Installation Error	Electrical Overload	Fatigue, Creep
Manufacturing Fault	Insulation Failure	Elastic Deformation
Maintenance Fault	Electrical Shorts	Leakage, Blow Holes
External Damage	I/P Power Loss	Insufficient Lubrication
Vibrations, Misalignment	Calibration Faults	Plastic Deformation
Stress Concentration	Actuator Overheating	Foreign Contaminants, Moisture
Material Degradation	Excess Bush Wear	UV Resistance
Mechanical Defect	Electrical Surge	Ground Staff Skills

The FMEA of airborne balloon was done on functional cum hardware approach. The failures causes associated up to component level were considered keeping in the view of system objective and qualitative requirements. Analysis shows the effect of each cause and failure on the mission objective. Some failure causes were Key Leading i.e. these failures will leads to other failures if not attained on time. For example, the malfunction of air deflation valve may lead to over pressurization of balloon which further may results in bursting of balloon. Corrective actions also suggested in the form of prevention to avoid any internal failure causal factors. For example, the foreign contamination in balloon fabric joints may be avoided by controlled environment & proper SOP during fabrication. Adequate measures in design were taken to avoid any critical failure. For example, the provision of ballonet (air compartment within balloon) in balloon helps to maintain the balloon differential pressure against change in atmospheric temperature and flying altitude to avoid over pressure and further balloon bursting.

Some of the high priority causes for airborne balloon failure based on literature survey & FMEA outcomes are as follows:

(i) Confluence Line - Low breaking strength of lines, entanglement of lines, high tension on line due to air gust
(ii) Balloon Hull - Abrupt rise in balloon pressure, EDV and pressure sensor failure of balloon health monitoring & control system
(iii) Gore and Panel Strips - Poor peel strength of fabric, sealing in uncontrolled machining condition
(iv) Ballonet - Poor sealing of joints, degradation of joints with time
(v) Payload Cord - Fraying and environmental degradation of cordage
(vi) Nose Cradle and Flange – Weld defect (cracks, porosity etc) in cradle assembly

FMEA Type	System	FAILURE MODE AND EFFECTS ANALYSIS Balloon System		Page	Appendix 'D'
Item	1 - Balloon System				22 of 40
Product	Model Year(s)/Program(s)	Responsibility	Release Date	Prepared By	Document Number
Balloon	Aerostat	Trial Team, QA Rep	----	Arvind Kaushik	----

Function	Failure	Effect	Si	Classification	Cause	Oi	Control	Control Type	Di	RPNi
1 - Balloon System										
1.1 - Balloon Hull										
Hull is an aerodynamically shaped body which provides optimum surface area for given volume and minimum drag to minimize the blow by. It contains helium gas, which give the balloon its lifting capability.	Balloon burst.	Mission failure, loss of payloads.	8	C	Abrupt rise in balloon pressure, EDV and pressure sensor failure of APCHMS.	1	Constant monitoring of balloon differential pressure.	Prevention	3	24
							Reading of pressure sensor unit of APCHMS.	Detection		
	Leakage in balloon - hull fabric.	Loss of helium gas and decrease in balloon lift.	5	KI	Tear / cut in hull fabric during operation.	2	Proper handling of balloon during inflation so that it will not strike with sharp edges.	Prevention	3	30
							Reading of pressure sensor and altitude sensor.	Detection		
	Under pressurization of balloon hull.	Aerodynamic shape of balloon get disturbs.	4	KLd	Ballonet unable to inflate, failure of APCHMS, failure of load curtains / ballonet - hull connection cordages.	2	Proper maintenance of APCHMS, ballonet connection curtains.	Prevention	1	8
							By visual vision of balloon shape, reading of APCHMS pressure sensor unit.	Detection		
	Hull joint failure.	Gradual decrease in balloon lift and loss of helium.	6	KLd	Poor sealing of joints, degradation of joints with time.	2	Proper sealing process should be followed at the time of sealing, selection of high quality adhesive with anti degradation property.	Prevention	3	36
							Reading of APCHMS pressure sensor unit.	Detection		

Figure 6: Sample FMEA: LTA Balloon with initial RPN

In FMEA, the qualitative risk limit for a particular failure may be decided mutually by system designer, project coordinator, users and subject expert. High risk limit and low risk limit are controlled by severity and occurrence ranking combination. For our study, we had chosen high priority risk limit for (S, O) as (9, 8); whereas low priority risk limit for (S, O) as (7, 4). Occurrence-severity matrix for LTA balloon based on initial risk ranking is shown in Figure 7.

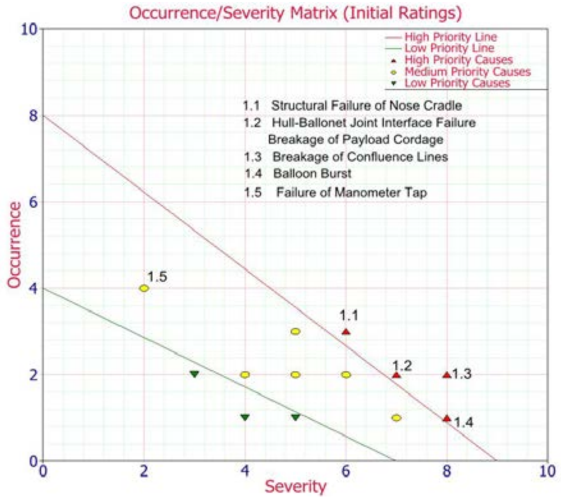

Figure 7: Severity Matrix Based on Initial RPN: LTA Balloon

Analysis shows that about 20% of failure modes are falling above the high risk priority line (severity as degradation of primary function or loss of primary function or failure to meet safety norm) but all these failure modes have low occurrence (O≤ 4; i.e. 0.1 failure per thousand items). Counter provision like air blower, gas discharge valve, emergency deflation valve, and detection techniques like temperature sensors, pressure gauges etc are used to counter/detect any predicted failures before their recurrence.

6. Conclusions

RCA is an effective approach for qualitative analysis of failure, its detection & prevention for LTA system. To be effective; RCA must be performed systematically, with conclusions and causes backed up by literature evidence and records. In case of LTA system, there is usually more than one root cause for any given failure. To be effective, the analysis must establish all known causal relationships between the root cause(s) and the failure under study. The selection of correct RCA approach plays a vital role for failure investigation. Both CED and FMEA are very useful for identification of failure root causes. Even the outcome of CED may be used as an input for FMEA.

In order to properly diagnose a failure in LTA system; it is necessary to review design, configuration, start inspecting raw materials, investigate all manufacturing steps, stage inspection, final inspection as well as the environment factors like skill of ground staff.

With the help of well developed RCA, we can focus on high impact failures. Failure recurrence can be controlled by assigning proper preventive action during design (material), manufacturing (process) and operational (maintenance) phases of product development life cycle.

7. References

[1] Preliminary Design Documents of medium size aerostat, ADRDE Agra

[2] Doggett, A. M. (2004):. A statistical Comparison of Three Root Cause Tools. Journal of Industrial Technology, 20(2), 1-9

[3] Algirdas Avizienis, Jean-Claude Laprie, Brian Randell, and Carl Landwehr: Basic Concepts and Taxonomy of Dependable and Secure Computing. IEEE Transactions on Dependable and Secure Computing, 2004

[4] Joymalya Bhattacharya: Root Cause Analysis – A Practice to Understanding and Control the Failure Management in Manufacturing Industry. International Journal of Business and

Management Invention ISSN (Online): 2319 – 8028, ISSN (Print): 2319 – 801X www.ijbmi.org Volume 3 Issue 10 ‖ October. 2014

[5] B. Andersen and T. Fagerhaug: Root cause analysis: simplified tools and techniques. ASQ Quality Press, 2006.

[6] Dalgobind Mahto, Anjani Kumar: Application of root cause analysis in improvement of product quality and productivity. Journal of Industrial Engineering and Management,2008.

[7] https://tallyfy.com/definition-fishbone-diagram/

[8] Lalit Kumar and D. R. Prajapati: Root Cause Analysis of Defectives of a Manufacturing Industry. Proceedings of National Conference on Advancements and Futuristic Trends in Mechanical Engineering, Oct-2014.

[9] MIL-STD-1629A Military handbook for conducting Failure Mode Effect and Criticality Analysis

[10] Nadia BELU, Nicoleta RACHIERU, Emil MILITARU and Daniel-Constantin ANGHEL: Application Of FMEA Method In Product Development Stage; Academic Journal Of Manufacturing Engineering, Vol. 10, Issue 3/2012

[11] http://www.weibull.com/basics/fmea.htm

Effective Utilization of "DFMEA" to Identify Design Issues, Thereby Making a Robust Safety Arming Mechanism

PY Borse
Armament Research and Development Establishment
DRDO
Pune
pyborse@arde.drdo.in

AK Singh,
Armament Research and Development Establishment
DRDO
Pune

RS Deodhar
Armament Research and Development Establishment
DRDO
Pune

Mehul Sirohi,
Armament Research and Development Establishment
DRDO
Pune

PW Sonawane
Armament Research and Development Establishment
DRDO
Pune

***Abstract*—Safety Arming Mechanism (SAM) is one of the most critical sub-systems of a kill mechanism that appropriates functioning of kill mechanism (Warhead)and also provides safety during handling, transportation, storage, launch and flight phases. In a Missile system, SAM is a key link that ensures safety of the missile and detonates the warhead as and when required based on the end game requirements. It is therefore crucial to ensure that SAM design incorporates all the safety features as well as trigger mechanism to ensure safety as well as functionality of SAM at desired place and time. Although, Electro-Mechanical type of SAM is a proven technology for missile systems, SAM design intricacies significantly changes as per space allocation in warhead, target of the missile, trigger signal to initiate SAM, modes of warhead detonation etc. and for these reasons it is pertinent to have fault-less and fail-safe SAM design. This paper explains utilization of Design Failure Mode Effect Analysis (DFMEA) to understand various failure modes of SAM for New Generation Anti-Radiation Missile (NGARM) so that corrective actions can be taken on critical failure modes to ensure robust SAM design.**

Keywords—DFMEA, SAM (Safety Arming Mechanism), NGARM (New Generation Anti Radiation Missile), Warhead.

1. Introduction

SAM assembly in study as shown in Figure 1 has got two subsystems, Electronic Control Unit (ECU) and Arming and Detonating Mechanism (ADM). The ECU generates the required logic for functioning of SAM and issues firing pulses to ADM for initiation of squib and igniters as per mission requirement. ADM houses all the explosive elements, impact sensors and arming mechanism in it. For successful mission, the SAM must initiate the warhead which in-turn conflicts with the target to cause desired damage to it. The purpose of New Generation Anti-Radiation Missile (NGARM) is to neutralize RF radiating targets. The missile will be launched from fighter aircraft like SU-30MKI, Jaguar etc. The primary targets against which the missile will be deployed are ground based RF emitters, early warning radar systems, ground control intercept radars, weapon control radars, surveillance radars, tracking radars etc. The success of the mission is completely dependent on the performance of the SAM. Hence it is important to understand various failure modes of SAM and therefore, conducting DFMEA is helpful.

There are two approaches in FMEA:

(i) Hardware Approach – When Hardware is identified, this approach is utilized. This is a bottom up approach.

(ii) Functional Approach – When Hardware is not known and only functions are known, this approach is utilized.

The approach is decided based on the stage at which the design is progressing. If hardware is known and drawings are made, hardware approach can be utilized. Both the above approaches are similar in nature in the sense that eventually they find out failure modes based on functions.

This study adapted the functional approach for developing DFMEA for SAM for NGARM. The failure mode probability and model failure rate is determined using charts from IS Standard 15550:2005 [1] and rankings in the ReliaSoft software. For severity and detection method IS standard is referred. Effects for individual failure are grouped and effect with highest severity number is considered for calculating RPN.Corrective actions were recommended for failure modes having RPN above 80.

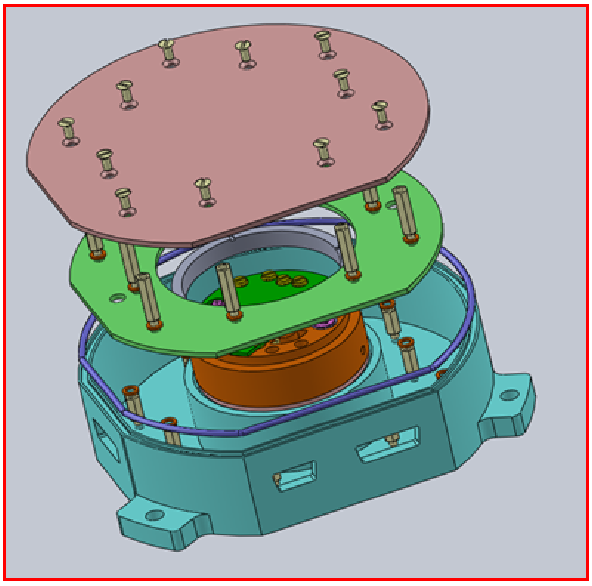

Figure1. Solid Model of SAM NGARM

2. DFMEA Methodology

Design Failure Mode and Effect Analysis is undertaken to understand various failure modes in the product during the design phase. It tries to identify as well as prevent potential failures by reviewing historical failures and anticipated customer uses and abuses, as well as current design practices with similar parts. It is an effective technique to foresee failure modes. Once failure modes are identified, its effects are determined to understand repercussion on the product. A detailed cause analysis is done to understand various causes that might have generated failures.

DFMEA originally was intended to be utilized as a bottom up approach where components of sub-systems were analyzed for the manner they would fail. The effects of those failures were investigated to understand or measure the risk to the main system [2]. It is a systematic approach of documenting all the design issues involved and taking corrective actions so that failures do not occur with end users. Information from DFMEA helps designers prioritizes risky aspects of a design so as to modify them and improve the reliability of the product.It is important to understand that reliability plays crucial role in satisfying and delighting the end users.

DFMEA has many advantages; few major ones are [1]:
(i) Design improvement –Prevent potential failures.
(ii) Pro-active approach to understand design effects on customers in case of failure.
(iii) Identify potential risks.
(iv) Encourage multi-discipline participations.
(v) Disclose safety hazards, liability problem, or non-compliance with regulatory requirements.
(vi) Facilitates the team's suggestions of any test criteria, test plans, or experimentations.
(vii) Supports the decision for reliability test, simulations, and design of experimentations.

DFMEA follows a typical pattern to identify severity of the failure mode, effects of the failure, and causes of the failure and is carried out from the early stages of the design. A multidiscipline team is formed that brainstorms on various functions of a component or sub-assembly or an assembly and accordingly identify failure modes. Team members can be from various areas but mostly should have one person from design, quality, reliability, and manufacturing discipline. A Risk Priority Number (RPN) is identified for each cause of the failure modes and accordingly corrective actions are recommended to reduce the risk priority number, ultimately mitigating the risks associated with the design. The most obvious outcome of DFMEA process is documentation of the collective knowledge of cross functional teams [3]. It is important to note that one of the most important factors for the successful implementation of DFMEA is timelines.

James Kotterman [4] explains that time frame requires to complete a typical DFMEA depends on the depth of analysis used by the team to perform DFMEA. He also mentions that the team should not dig too deep and the scope and level of analysis should be determined by the team, especially by the owner or requester with the help of FMEA team leader and a quality leader. Time spent properly in completing DFMEA at the initial stages of design, when product changes can be most easily and inexpensively implemented, can minimizes late changes crises and saves cost and time.

3. DFMEA for SAM

Safety and Arming Mechanism (SAM) is a vital link between missile and its warhead. It ensures safety of warhead and missile during flight, storage and handling. SAM has two major functions, first arming and second detonation of warhead as per the mission requirement at desired time and place. In general a missile system is a 'System of Systems'. In such a complex system, reliability of each subsystem should be very high to attain necessary reliability figure for the complete system. To meet this requirement, SAM should always function without fail. Hence SAM should be very safe and highly reliable. Safety and Reliability of SAM are complicated to achieve and hence pose a very challenging task for the design engineers. To meet high reliability requirement, there should be minimum number of failures in the design.

DFMEA technique is utilized for identification of failure modes in SAM. During the initial stage of SAM design, DFMEA provided an opportunity to the designer to optimize the design to meet both the requirements of safety and reliability by minimizing the failure modes either by reducing the occurrence and severity value by design optimization. NGARM

DFMEA team has chosen functional approach for the DFMEA study of SAM NGARM instead of hardware approach. The hardware approach is a better option when detailed design is available and all individual components can be listed out uniquely. It is more comprehensive approach since failure mode of each component is analyzed individually. In contrast to this, functional DFMEA approach is more advantageous when analyzing complex systems. Functional DFMEA of complex system analysis is based on most significant contributors in each level of analysis based on the various functionalities of the sub-systems/system. Functional approach is chosen since SAM NGARM is a complex sub system of the missile and detailed design was not available at initial design phase.

DFMEA of SAM has also provided the necessary measures to detect any failures in the system before the assembly of SAM with the missile. All the failure modes were identified based on functions of the SAM. Effects of failure modes on the functionality and causes of the failure modes were identified. Control method is also identified and accordingly RPN number is calculated based on severity of the effect, occurrence of the failure modes and detection of the causes. The team decided to take corrective actions for those causes associated with failure modes having high RPN value. Table 1 gives detail of failure modes having RPN value more than 80.

4. Discussion

System reliability can be greatly improved if DFMEA is done thoroughly and at proper stages of design starting from the conceptual stage of the design. DFMEA at conceptual stage can yield results that would benefit the designers to conduct design of experimentations to ensure robust design at subsequent stages. It also brings out potential failure modes that can be rectified to get fault free design. It is imperative that corrective actions are implemented and followed up, to calculate revised RPN for clearly understanding the benefits of DFMEA.

This paper explains details of DFMEA being conducted on one of the subsystems of NGARM Missile, i.e., SAM. SAM plays an important role in ensuring safety of the missile and hence it is imperative that the design of SAM is faultless. There is no better tool than DFMEA to identify failure modes during design stages, which includes conceptualized stage to prototype. DFMEA resulted into identification of causes of various failure modes and its effect. The team subsequently worked to implement solutions to reduce the RPN of high priority risk failure modes.

DFMEA has been performed for the first time on SAM for any missile projects in India. DFMEA on SAM for NGARM has given vital inputs to the design team for improvement of both the reliability and safety of the missile subsystem. It has also provided a platform on which future designs of SAM for various projects can be analyzed and a fail-safe design of SAM can be achieved.The improved design of SAM NGARM has given foundations for development of SAM for Quick Reaction Surface to Air Missile (QRSAM) and Akash NG missile systems. The design has shown consistent performance in QRSAM missile dynamic trials in 2019 and 2020. DFMEA is now an essential part of the design process in all the future designs of SAM.

5. Conclusion

Some of the important causes for failure of SAM identified during DFMEA analysis are listed below:

(i) Contact resistance increases due to oxidation/water vapor/dust particle in the Rotor Locking Mechanism.

(ii) Pressure generated by squib is not sufficient to shear the shear wire in the Rotor Locking Mechanism.
(iii) Explosive aging due to improper storage conditions of the Squib.
(iv) Change in resistance of conducting composition in the igniter.
(v) Unintentional firing pulse from ECU in the Squib Firing circuit.

Corrective actions were identified to reduce the occurrences of the causes and improve the detection method. At one instance, design change is also recommended to reduce the severity of the failure mode.All the corrective actions were implemented immediately to improve the design of SAM NGARM and other SAMs which share the same design platform.

Table 1: Analysis of failure modes with RPN equal to or greater than 80

SN	Item Name	Function	Failure	Effect	Si	Cause	Oi	Di	RPNi	Recommended Action
1.	Rotor Locking Mechanism	Short igniter through spring probes	Not shorting the igniters	Safety compromised	9	Contact resistance increases due to oxidation/water vapor/dust particle	5	3	135	Tolerances on "cavity for spring probe" to be reviewed and modified.
2.	Rotor Locking Mechanism	To rotate the rotor to align the explosive train after receiving arming signal	Rotor is not rotated	SAM failure	8	Pressure generated by squib is not sufficient to shear the shear wire	2	8	128	Test should be conducted to establish the relationship between the shear strength of wire and quantity of explosive used
3.	Rotor Locking Mechanism	To rotate the rotor to align the explosive train after receiving arming signal	Rotor is not rotated	SAM failure	8	Squib not fired at all	2	7	112	Root cause analysis of Squib not firing to be performed
4.	Rotor Locking Mechanism	Short igniter through spring probes	Not shorting the igniters	Safety compromised	9	Depth of spring probe cavity is greater than required	4	3	108	100% check of depth by depth gauge should be mentioned in QAP
5.	Rotor Locking Mechanism	To rotate the rotor to align the explosive train after receiving arming signal	Rotor is not rotated	SAM failure	8	Frictional force between the rotor and the rotor cavity wall more than the force due to the bending moment of the torsion spring	4	3	96	Geometric tolerances to be considered

6.	Squib	To break 'shear wire' to unlock rotors (During the specified life time)	Shear wire does not get sheared when required	Arming does not take place (SAM failure)	8	Explosive aging due to improper storage conditions	4	3	96	Bare squibs and integrated missiles to be stored in controlled atmosphere
7.	Igniter	To convert electric pulse into flash	Flash is not generated/igniter is not fired	SAM Failure	8	Change in resistance of conducting composition	4	3	96	Insitu measurement during tests need to be carried out
8.	Rotor Locking Mechanism	To hold rotor in misaligned position till arming signal is received	Rotor locking mechanism not holding the rotor in misaligned condition	Unintentional arming takes place. Safety compromised	9	Sleeve is not properly fitted	3	3	81	Visual indication for arming may be provided.
9.	Squib	To break 'shear wire' to unlock rotors (During the specified life time)	Shear wire gets sheared when not required	Safety compromised	9	Unintentional firing pulse from ECU	3	3	81	Microcontroller health should be checked at regular interval through watchdog timer or otherwise.

6. Acknowledgement

Authors are grateful to the Director, ARDE and Group Director, SAM for encouragement and motivation.

7. References

[1] Bureau of Indian Standards. Indian Standard on Failure Mode and Effects Analysis. IS 15550:2005. New Delhi, India. 2005.

[2] S. Muthukumar, N. SankaraNarayananan, Deepak Agarwal, Adalat Ali, "Failure Mode and Effect Analysis (FMEA) of Deployable Window System of a Flight Vehicle – A Case Study", 248-253, ARMS2012-MRM-05.

[3] Potential Failure Mode and Effects Analysis (FMEA), AIAG, Reference Manual, Fourth Edition, June 2008.

[4] James R. Kotterman, "Narrow(er) Focus – Tapping into a powerful new method to better identify potential failure modes", Quality Progress, p 23-28, January 2015.

Pad Abort Test for Manned Mission - Launch Pad Safety and Mission Success: FMEA Aspects

M Sunoj
Systems Reliability
Vikram Sarabhai Space Centre
Thiruvanathapuram

SS Maruthi
Systems Reliability
Vikram Sarabhai Space Centre
Thiruvanathapuram

Mahendra Kumar Joshi
Systems Reliability
Vikram Sarabhai Space Centre
Thiruvanathapuram

Mathew Tom
Systems Reliability
Vikram Sarabhai Space Centre
Thiruvanathapuram

PK Sreekumar
Systems Reliability
Vikram Sarabhai Space Centre
Thiruvanathapuram

Dr V Murugesan
Systems Reliability
Vikram Sarabhai Space Centre
Thiruvanathapuram

***Abstract*—Pad abort test (PAT) for manned mission program is planned with the objective of demonstrating crew rescue capability at launch pad in case of any exigency followed by safe recovery of crew module employing a dedicated crew escape system. In such cases, the crew module will be taken to a safe altitude by firing crew escape motors and will be recovered using a parachute based deceleration system. Present study is aimed towards identifying the critical failure modes which can be catastrophic to mission.**

FMEA is a systematic and analytical quality planning technique at the product, design, processing and service stages assessing what potentially can go wrong so as to aid fault diagnosis. The objective is to classify all possible failures according to their effect, measured in terms of severity, occurrence, and detection. This shall help in finding solutions to eliminate or minimize them.

This paper brings out the findings of FMEA studies carried out considering the launch pad safety as well as mission success of pad abort test. Single point/potential failure modes of various sub-systems and corrective actions for each are addressed to ensure mission success. Mission studies were carried out under various off-nominal conditions and failure mode cases for the same were identified as well.

Verification requirements and redundancy aspects to ensure reliable functioning of all crew escape system elements were brought out. Similarly, to ascertain end to end mission success, all the failure scenarios related with crew module separation and deceleration system were addressed in detail.

Detailed assessment related with design margins, fault tolerance system requirements, testability and verification requirements for the systems associated with PAT mission were brought out.

Keywords—FMEA, Launch pad, crew module, Jettisoning motor, crew escape system, Low altitude escape motor, high altitude escape motor, head end mounted safe arm (HMSA), Motor case, chamber pressure, parachute, crew module fairing, pilot parachute and drogue parachute.

1. Introduction

Pad Abort Test (PAT) is aimed towards demonstrating the crew escape system operation in case of a mission abort at launch pad. It envisages taking the crew module safely from launch pad to a specified altitude (nearly 2.2 km) followed by separation of the crew module and descending to a specified splash down point with the help of deceleration systems.

FMEA was carried out considering two major aspects; (a) launch pad safety in case of malfunctioning of the solid motors employed in crew escape system and (b) failures in crew module separation or deceleration system elements that may lead to a failure in safe recovery of the crew module.

Various failure modes related with each system and design provisions addressing the same along with verification requirements are studied in detail. Necessary design modifications/corrective actions to be implemented are also brought out.

2. FMEA Aspects: Launch pad safety

Launch pad safety includes the safety of personnel, various systems/facilities established in and around the launch pad, in case of malfunctioning of any of the subsystems at launch pad or immediately after the lift off.

As part of FMEA study, following critical parameters/systems are considered for analysis and failure modes. Effects and corrective actions were also addressed in detail.

A. Mission

The mission planning has been executed such that crew module should impact at a safe distance of minimum 500m away from the launch pad in sea even for the lower bound performance of escape motors. Four types of solid motors are planned based on mission studies to enable the satisfactory functioning of crew escape system.

Motor for low altitude escape – L1 type, four motors for high altitude escape, H1-4, motor for jettisoning the crew escape system, C1 and a pitch motor, P1. As part of FMEA studies, impact assessment related with any one motor failure and various combinations of failure cases were carried out and the crew module impact point was estimated.

The study was carried out with the mission sequence as given below:

L1 motor Ignition	- T0 sec
H1-4 motors Ignition	- T0 sec
P1 Motor Ignition	- T0+0.9 sec

Failure Modes: Following failure modes related with solid motors employed in PAT mission are addressed w.r.t the non-ignition considering launch pad as well as range safety;

- Pitch motor, P1 failure
- High altitude escape motors H1-4 failure
- Pitch motor and H4 motor failure (Y-side, towards land side)
- Pitch motor and two H1 & H2 motors failure
- L1 motor one nozzle blockage
- H1motor and one nozzle blockage in L1motor
- Crew module jettisoning - C1 motor failure

Mission studies were carried out with no wind and with 10m/sec wind conditions. Out of the various failure mode cases studied, it is evident that any one motor failure is detrimental to mission success. However various combination of failure cases is studied to assess the extent of impact on range

Following are the major findings based on FMEA study carried out considering failure of motors independently or in combination.

- Range safety criteria of minimum 500m away from land are not met for any of the failure cases in motors except for C1 motor failure

- Of all the failure mode cases, H4 (Y- side) failure is giving the most negative downrange

Except for two cases, P1 and L1-motor non- ignition, analysis showed that the CES/CM separation and C1 motor ignition occur few seconds after impacting the ground. This may lead to serious issues with respect to launch pad and mission safety.

Failure modes in various subsystems in PAT which can directly affect the launch pad safety are addressed in detail and compensating provisions/safety defences proposed in each system are brought out.

B. Motors (L1, H1-4, C1 & P1)

Four types of solid motors are planned PAT mission with specific objectives. In case of pad abort requirement, simultaneous firing of L1 motor and H1-4 motors can ensure that crew module is taken to a safe altitude wherein deceleration system can be initiated to ensure safe touchdown at sea.

Major failure modes and safety measures against the potential failure modes of motors are addressed below.

Failure Modes: Major failure modes w.r.t the escape motors which are detrimental to Launch pad, Range and Mission safety

- Command failure
- Motor / Igniter Pressure pick up interface failure (joint leak)
- Propellant system failure
- Pyro circuit failure
- Premature closure bursting
- Motor case or segment joints failure
- Motor burst at lift-off due to higher chamber pressure

Safety Defences: The possibility of non-ignition of motor or premature bursting of nozzle closure is thought to be very remote due to the presence of following mechanisms:

- TMR logic based command sequencing system
- Adequate qualification through static tests
- QA/QC checks during processing, assembly and testing
- NDT of motors and associated Pyros
- Batch acceptance testing of nozzle closures
- FCD identification and verification
- Proof pressure testing of motor cases & Igniter cases
- VOQ (verification of qualification)
- for Pyro elements
- NDT of propellant system

Safety defences for the above failure modes are in-line with operational launch vehicles. Adequate structural margins are established through testing. All operational procedures are done as per the approved operation document and ensured through online QC/QA participation.

Following points are also implemented to ensure satisfactory initiation and functioning of all solid motors with improved reliability.

- Adequate margin of safety is ensured in motor and igniter cases and given below in table.1&2.
- High altitude escape motors are very critical with respect to range safety from mission studies.H1-4 motors are provided with safe arm for ignition as well as improved interfaces.

Table 1: Design Margin for Motor cases

Motor	MEOP level
L1	1.25
H1	1.25
P1	1.25
C1	1.25

Table 2: Design Margin for Igniter

Igniter	MEOP level
L1	1.5
H1	1.5

Further, adequate number of series breaks is provided onboard, to avoid any inadvertent initiation. All ground ignition chains are configured with three series breaks and on board ignition chains are configured with five series breaks.

C. Crew Module (CM) Fairing – Service Module (SM) separation system

The Crew module, CES along with CM fairing will be attached to the SM simulator ring at launch pad to take care about the launch pad loads using a merman band based separation system.

Prior to lift -off, the separation will be achieved. Major failure modes and safety defense mechanisms present are given below.

Failure Modes:

- Command system failure
- Failure in cutters
- Inadvertent release of joint separation system
- Joint system not getting released on command and subsequent initiation of motors due to incorrect connector status.

Safety defences:

- T& E of check-out systems
- Margins/safety of systems are confirmed in-line with launch vehicle procedures. Acceptance testing of all components is done prior to assembly.
- Redundancy in separation systems
- VOQ testing of Pyro systems
- All critical system elements are proof loaded to 1.25 times limit load

- Monitoring of joint release status through redundant connectors and motor firing command is issued based on satisfactory connector demating status from both sides.

D. Grid fin Deployment Mechanism

Four grid fins are attached to CM fairing aft end to ensure aerodynamic stability for the CES in the ascent phase. The Grid fins will be initially in stowed condition and will be deployed on command at the specified time using pyro thruster and held in position using hydraulic damper and locking mechanism after deployment.

In PAT, deployment of all four Grid fins is planned at ground itself and will be kept in locked condition before Automatic Launch Sequence (ALS) initiation. Deployment and locking of all the four fins shall be ensured prior to the initialization of ALS. As full deployment and locking shall be ensured prior to the ignition of solid motors, this doesn't pose any concern with respect to launch pad and mission safety.

Failure Modes:

- Command system failure
- Failure in Pyro thrusters
- Inadvertent release of Grid fins
- No locking of Grid fins after deployment

Safety defences:

- Redundant initiation for Grid fin deployment
- Margins/safety systems are confirmed in-line with launch vehicle procedures.
- Acceptance testing of all components is done prior to assembly.
- Grid fin deployment and satisfactory locking will be ensured prior to ALS.

E. Stability at Launch Pad

The Crew escape system along with Crew module will be assembled to launch pedestal using band joint and will be separated at T-10 sec. The band system shall be capable of withstanding the launch pad loads till separation and PAT module should be stable till ignition of the escape motors.

Following points are considered pertaining to stability of PAT module at launch pad.

Failure Modes:

- CM-CES module may become unstable after separation of the CM-SM band joint due to wind loads
- Structural failure of band system
- In-advertant initiation

Safety defences:

- Stability of the CM-CES module was assessed for free standing condition at launch pad with a maximum expected wind velocity and found stable.
- Band system elements are proof loaded to 1.25-time launch pad loads
- Band system separation command is issued only at T0 - 10sec.
- Adequate number of breaks in ground check-out system

3. Summary of findings of FMEA: Launch Pad Safety

Failure Modes, effects analysis of mission critical systems for PAT is carried out considering the launch pad as well as range safety. All the major failure modes of safety critical systems are addressed along with defensive mechanism present. Salient points are given below;

- Failure modes of motors individually and in combination were also assessed with respect to the launch pad and range safety. Failure of any motor except C1 motor may lead to violation in range constraint and could not be tolerated.
- Firing circuits of motor ignition are configured with sufficient number of breaks
- Stability of the CM-CES module is assessed for a free standing condition with maximum possible wind velocity and found stable

4. FMEA Aspects: Mission Success

Apart from the normal functioning of all system pertaining to launch pad safety, successful functioning of few more systems is essential for the mission success.

Critical failure modes of those systems which are responsible for ensuring the satisfactory separation of CES followed by the descending and safe touchdown of the module are addressed in detail.

The compensating provisions implemented against critical failure modes are also examined critically.

A. CM-Shroud Aft joint separation system- Explosive nut based system

Crew module is connected to CM shroud at multiple locations at aft side using separation nut and stud assembly. Separation is achieved by severing the nuts on command.

Failure Modes:

- Non Initiation
- Inadvertent Initiation
- Structural failure
- Failure in capture system

Safety defences:

- Batch qualification tests give adequate confidence
- End -to end redundancy in pyro chain
- Pyro circuit breaks in line with launch vehicle applications
- Adequate design margins. Proof loading of explosive nut assembly
- Capability demonstration through tests. Proof loading/testing of capture system

B. CM-Shroud FWD joint separation system – Band system

At fore-end side, Crew module is connected to CM fairing by a band system. Separation is achieved by severing the connecting bolts using redundant bolt cutters.

Failure Modes:

- Non Initiation
- Inadvertent Initiation
- Structural failures of critical systems

Safety defences:

- Batch qualification tests gives adequate confidence

- Pyro circuit breaks in line with launch vehicle applications
- Redundancy in device and pyro chain
- Adequate design margins.
- Proof loading of band assembly

C. Apex cover separation system

Apex cover is used to protect the parachutes inside the compartment and has to be separated and jettisoned prior to the initiation of deceleration system. Separation and jettisoning is achieved using multiple numbers of pyro thrusters.

Failure Modes:

- Non initiation of pyros
- Inadvertent Ignition
- Failure/Entanglement of pilot parachutes
- Structural failure
- No deployment of pilot chutes due to large rates on CM
- Collision of apex cover with CM

Safety defences:

- Batch qualification tests gives adequate confidence
- Pyro circuit breaks in line with launch vehicle applications
- Redundant bolt cutters for initiation
- End to end redundancy in pyro chain
- Adequate design margins. Proof loading of band assembly

D. Deceleration system

A dedicated deceleration system is planned is PAT to bring down the touch down velocity of crew module within acceptable limits for the safe recovery of crew. Two stage fully redundant deceleration system using drogue chutes and main parachutes are planned in PAT.

Failure Modes:

- Structural failure
- Failure of parachutes
- Failure of reefing system
- Inadequate time available for completing the parachute opening sequence in case of one chain failure
- Parachute release system failure modes -

Safety defences:

- Adequate design margin for all parachute system elements
- Redundancy is provided for all parachute related systems. System performance established through sufficient number of tests.
- Redundancy is provided for initiation. Performance verified through system level tests.
- Mission analysis is carried out and ensured that sufficient time is available for completing the parachute opening well before touchdown in case of one chain failure.
- Mission sequence is finalized such that angle of attack during design drogue chute deployment is well below critical limits.
- Protection sleeve also implemented to safe guard the drogue chute riser in case of any interference with crew module.

5. Summary of findings of FMEA: Mission Success

Regarding the mission success, apart from the systems analyzed considering launch pad safety, FMEA was carried out for other separation systems of PAT module and Deceleration system. Salient points are given below;

- Adequate structural/functional margins were ensured through testing wherever possible and for non –testable items margins were ensured through analysis. Following points are also ensured;
  - Structural elements are load tested to minimum 1.1 times the maximum expected load.
- All parachute systems are tested to minimum load of 1.25 times the maximum load expected All the pyro elements are processed as per the process document and accepted after satisfactory batch acceptance testing. Following points are also ensured.
  - For pyro elements, multi-point electrical initiation redundancy ensured.
  - Device/cartridge/initiator level redundancy is ensured for multipoint release systems.
- Mission design and sequencing of parachute opening timings finalized to have sufficient time for full deployment and descending to terminal velocity. Analysis carried out by assuming one parachute chain is totally failed and confirmed the adequacy of mission sequence.
- Crew module rates during apex cover separation were estimated and separation dynamic analysis carried out to ensure collision free separation in worst case.
- With respect to parachute release command at touchdown, acceptable time windows are finalized considering failure of one of the pilot/drogue/main parachutes.
- Considering the large rates immediately after the jettisoning of CES, deployment test for the pilot chutes were carried out for inclination up to the maximum expected angle based on simulation studies.
- Angle of attack for the crew module during drogue chute deployment is ensured to be well within the prescribed limits through analysis and protective sleeve is implemented to avoid rubbing of riser with CM structure in case of any eventuality.

6. Conclusions

Failure Modes, effects analysis of mission critical systems for pad abort test is carried out considering the launch pad as well as range safety. All the major failure modes of safety critical systems are addressed along with defensive mechanism present.

Based on the above it is concluded that adequate safety mechanism/compensating provisions are built into the system design to prevent any catastrophic event that can impact the mission success for the Pad Abort Test.

7. Acknowledgment

The authors thankfully acknowledge the support received from Shri U A Subramanian, GD, ASMG and Shri Sheeju Chandran, Head, OAED/ASOE for his valuable suggestions. The authors also thankfully acknowledge the encouragement provided by Smt Athula Devi S Deputy Director (SR), VSSC during preparation of this paper.

Futuristic Mechanisms

Influence of Polyurethane Foam on the Vibration Isolation Characteristic of Nano-Satellite Transportation container (NSTC)

Dr. Rajeev Chaturvedi
U.R.Rao Satellite Centre
ISRO
Bangalore
rajeevc@ursc.gov.in

Atul Nigotia
U.R.Rao Satellite Centre
ISRO
Bangalore

Mohammad Ali
U.R.Rao Satellite Centre
ISRO
Bangalore

A Sekar
U.R.Rao Satellite Centre
Indian Space Research Organization
Bangalore

Rajeev Bangrao Badagandi
U.R.Rao Satellite Centre
Indian Space Research Organization
Bangalore

***Abstract* -Present article focuses on the vibration isolation offered by polyurethane (PU) foam. Article begins with the determination of mechanical properties of PU-foams, which finds extensive application in automotive industry. Viso-elastic properties of foam are addressed by measurement of damping force during compression test in UTM. Further, Vibration Isolation properties of PU-foam are addressed by road transportation tests. Experimental results demonstrate that PU-foam isolate significant levels at 6.0Hz and further above 100 Hz and hence protects the satellite hardware during transportation.**

Keywords- Polyurethane foam, Random vibration, Damping, cushioning material

1. Introduction

Open cell polyurethane (PUR) foam has become the first choice for automotive seats cushion construction. When compared to traditional steel spring seat support spring system it provides a significant decrease in weight/performance ratio and pro- vides cost effective solution. PUR foams provides both static (posture) and dynamic (vibration). Open cell PUR foam consist of polymer matrix, this matirx is responsible for entrained gas. The gas is able to flow through the polymer matrix under the ac- tion of imposed load. This movement of gas through the matrix affect the mechanical properties of the foam.

Polyurethane foams are cellular structures whose mechanical, chemical and physical properties are experimentally determined, and are reported in the published literature [1, 2]. PUR foam consist of polymer matrix which are significantly porous. Mechanical properties of the PU foam under compressive loading is affected by the cellular structure and air contained in the cells. During compression air escapes from cell and cell walls are bent, during unloading the air is again sucked in the foam [3, 4, 5]. This permeability is responsible for improved damping characteristics in the foam. Major applications of PUR foams are against compressive loading [6]. Therefore, it is important PUR foams behavior under compressive loading. Foam density, strain rate and temperature affect the compression performance of polyurethane foam [7, 8, 9].

The mechanical behavior of foams is highly non-linear with a large visco-elastic deformation and recovery, subsequent sections discuss these behaviors in details.

A. Measurement of mechanical properties of foam under static compression

Mechanical properties of PU foam ($\rho = 28\ \frac{kg}{m^3}$) was determined using quasi-static compression [10]. Test was done on the foam having dimension 250 x 250 x 75 mm. Figure-1 shows the PU-foam sample under compression in UTM machine.

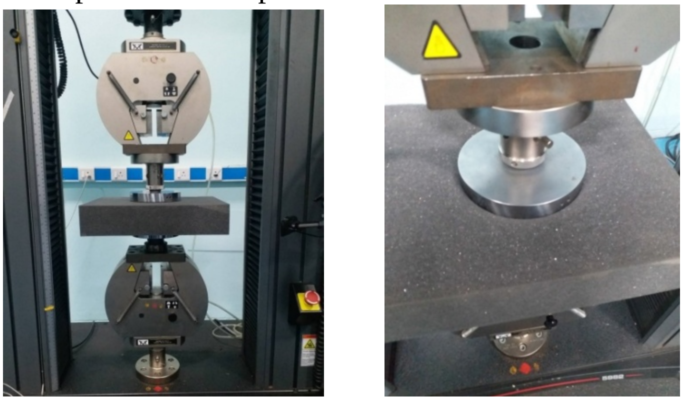

(a) (b)

Figure 1: Polyurethane foam under quasi-static compression: (a) Front view; (b) Top view

B. Quasi-static test results

Quasi-static test results are shown in Figure 2. Stress vs strain characteristic as shown in Figure 2(a), is non-linear in nature. It can be seen from the Figure 2(a) that compressive behavior of polyurethane foam can be preliminary divided into three stages; Stage-1 is a linear elastic range where stress is proportional to strain, Stage-2 plateau stage where the stress is nearly constant as strain increases and Stage-3 is a densification stage where the stress increases exponentially with increasing deformation. Under impact and compression loads the performance of foam material mainly depends on the energy absorption capacity in plateau region [11]. Dynamic compression of PU foam specimen by harmonic excitation for one period leads to a hysteresis course of the measured total force as shown in Figure 2(b).

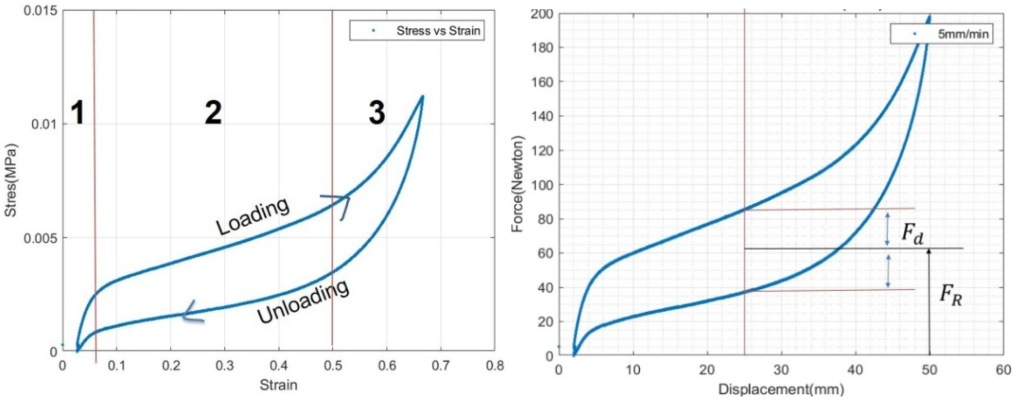

(a) (b)

Figure 2: Quasi-static test results: (a) Stress vs Strain; (b) force vs displacement

The Damping force F_d is distributed symmetrically along the skeleton curve of hysteresis loop. This skeleton curve represents the restoring force F_R which in non-linear in character and shows hardening behavior with increasing excitation frequency. In Figure 3 shows the plot of variation of damping force F_d vs displacement x. The profile looks like a typical pear like structure. Work of damping (dissipated energy) is given as a curve integral of damping force F_d with respect to x:

$$W_d = F_d\, dx$$

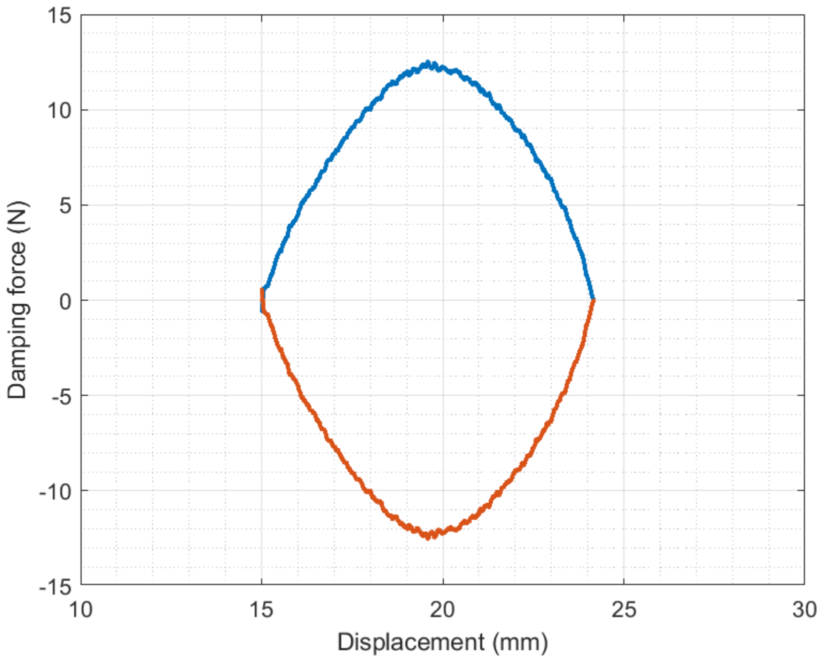

Figure 3: Damping force vs displacement

2. Experimental set up

A. Road test set up details

Figure 4 shows the road transportation test set up. Here NSTC is loaded into vehicle, PU-foam was laid over the vehicle bed and on this container was kept and fastened to vehicle using slings. NSTC has a total mass of 130 kg which includes dummy mass of 25.0kg.

(a)

(b)

Figure 4: Road transportation test set up: (a) NSTC loading in the vehicle; (b) Dummy mass

B. Measurement and Recording parameter

SAVER-9X vibration data recorder shown in Figure-5 was used to acquire vibration signals during the road transportation. Before starting the measurement, the data recorder is configured with following settings: an event trigger threshold of 0.2g, a sampling rate of 1000 Hz, a recording time of 2.0s and a signal pre-trigger of 25% for signal triggered data.

Figure 5: SAVER-9X vibration data recorder

3. Results

Figure 6 shows the comparison between the vehicle response to transmitted response to NSTC. Results shows that vehicle low frequency response at 6Hz is attenu- ated by PU foams, further above 100Hz it successfully attenuates vehicle response at 220 Hz, 362 Hz, 483 Hz, 632 Hz. Over all vehicle response was 1.005 Grms which was attenuated by PU foams and transmitted levels observed to be 0.608 Grms. Hence shows 40% effectiveness in isolating the road transportation levels.

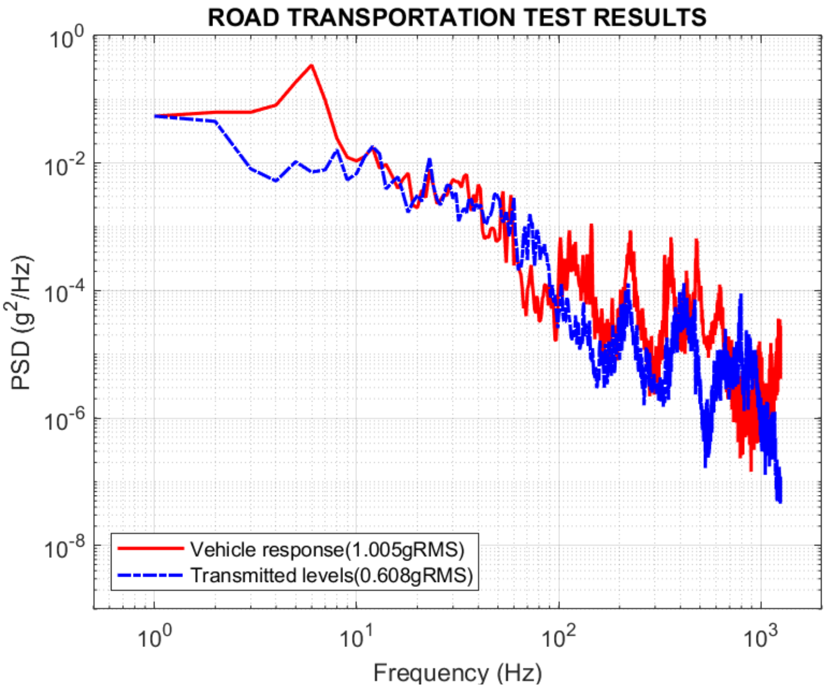

Figure 6: Experimental road transportation test levels

4. Conclusions

In this paper, cushioning properties of PU foams are studied under road transportation condition (random vibration). Paper provides information about the non-linear force vs deflection characteristic of PU foam. The non-linearity present in PU-foam helps in providing suitable cushioning to NSTC during the road transportation tests.

5. References

[1] M. Petr, O. Nov´ak, Measurement and numerical modeling of mechanical properties of polyurethane foams, Aspects of Polyurethanes (2017) 73–109.

[2] M. R. Kinkelaar, B. L. Neal, G. Crocco, The influence of polyurethane foam dynamics on the vibration isolation character of full foam seats, Technical Report, SAE Technical Paper, 1998.

[3] Cirkl, Modelling of damping force of dynamically loaded specimen of polyurethane foam in dependence on its density, Shock and Vibration 17 (2010), 373–381.

[4] W. Patten, S. Sha, C. Mo, A vibrational model of open celled polyurethane foam automotive seat cushions, Journal of Sound and Vibration 217 (1998) 145–161.

[5] Qiu, Y. He, Z. Yu, Investigation on compression mechanical properties of rigid polyurethane foam treated under random vibration condition: An experimental and numerical simulation study, Materials 12 (2019) 3385.

[6] L. J. Gibson, Cellular solids, Mrs Bulletin 28 (2003) 270–274.

[7] M. Saha, H. Mahfuz, U. Chakravarty, M. Uddin, M. E. Kabir, S. Jeelani, Effect of density, microstructure, and strain rate on compression behavior of polymeric foams, Materials Science and Engineering: A 406 (2005) 328–336.

[8] T.-R. Kim, J. K. Shin, T. S. Goh, H.-S. Kim, J. S. Lee, C.-S. Lee, Modeling of elasto-viscoplastic behavior for polyurethane foam under various strain rates and temperatures, Composite Structures 180 (2017) 686–695.

[9] O. Weißenborn, C. Ebert, M. Gude, Modelling of the strain rate dependent deformation behaviour of rigid polyurethane foams,Polymer Testing 54 (2016) 145–149.

[10] Cirkl, T. Hrus, Simulation model of polyurethane foam for uniaxial dynamical compression, Vibroengineering Procedia 1 (2013) 53–58.

[11] Linul, D. A. S¸erban, L. Marsavina, T. Sadowski, Assessment of collapse diagrams of rigid polyurethane foams under dynamic loading conditions, Archives of Civil and Mechanical Engineering 17 (2017) 457–466.

Gravity-based Transverse Mode Piezo Energy Harvester for Fusing System of Artillery Gun Munitions

Tejkaran Narolia
Rabindranath Tagore University
Raisen

Vijay Kumar Gupta
PDPM Indian Institute of Information Technology
Design and Manufacturing
Jabalpur

Abstract – **In this paper a gravity-based transverse mode piezo energy harvester for fusing system of artillery gun munitions has been proposed to harness the power from spinning of munitions. Free rotation of munitions about self-axis during the firing is converted into power through PZT patch, magnetic force and gravitational force. Analytical and Finite Element models are formulated to compute the harvested energy. Effect of geometrical and process parameters on the output power is studied. Average electrical power of 0.03 mW is calculated on application of 1.8 N of magnetic force and spinning speed of 1000 rps. The results from the mathematical model and finite element model is plotted to obtain the optimum results.**

Keywords – Gravity-based energy harvester; Piezoelectric material; Piezoelectric patch; Suspended lever; Rotary hub

1. Introduction

With enhancement of the technology in the area of defense, the munitions are becoming more and more smarter. All advance smart munitions are battery-operated to perform the electronics diagnostics, sense the objects, guide the direction, fuse the munitions, etc. A little amount of power is consumed by the munitions to execute these operations. However, replacement of battery is a major challenge. Life of the munitions can be increased by replacing the batteries with an alternative power source. A better option is to convert the self-kinetic energy into electric power. The broad power range, operating environment, safety, reliability and self-life of the munitions are the main issues facing by the designer and show that no single technology able to solve all issues for optimal designed of recent and coming applications.

Parameters and specifications of power sources such as discharge rate, charge and leakage at the time of storage, activation mode and levels of acceleration at the time of initiation of firing of munitions varies application to application. Thus, munitions need compatible and reliable supplies of power.

Conversion of waste environmental energy into electricity by piezoelectric material and other materials is not a new concept. Piezoelectric materials are considered as one of the most popular mode of energy harvesting [1]. Piezoelectric materials have property that make them useful to convert mechanical vibration or force into electrical energy or vice versa [2].

Various researchers worked in the area of harvesting energy from rotational kinetic energy. Xie et al. [3] proposed ring rotary type piezoelectric energy harvester, excited by high frequencies repulsive magnetic force. The highest power of 5274.8 W was calculated to be harvested from the device. Guan and Liao [4] designed and developed a new device to convert the angular kinetic energy into electrical power through PZT material. Experimental results were conducted by them and they reported that maximum power of 825 µW can be harvested at a rotational frequency of 13.5 Hz. This amount of power is able to run wireless transmitter. Zhang et al. [5] proposed a rotary table based energy harvester with impact on beam to harvest the energy. They used PVDF material for harvesting. They reported to harvest maximum power of approximately 2.56 mW at a wind velocity of 14 m/s. Tao et al. [6] presented a d_{33} mode piezoelectric wind turbine energy harvester, converting the rotational motion into linear vibrations through scotch-yoke mechanism. The maximum power of 150 W was analytically computed corresponding to 1 m radius of blades at a wind speed 7.2 m/s, and the designed angular velocity of 50 rad/s. Narolia et al. [7] proposed a novel design of piezo based energy harvester based on the principle of repulsive magnetic force to excite the harvester in vibrating mode. A mathematical model was formulated and highest power of 113.6684 W was calculated corresponding to rotational speed of 1835.59 RPM. Rastegar et al. [8, 9] design and developed piezoelectric based energy harvester to harvest the energy from the High G acceleration developed at the time of gun-firing. Willemin et al. [10] demonstrated that 20000G shock is developed at the time of gun-firing and it can be used to harvest the energy using spring-mass system with the coil-magnet transducer.

The objective of the present research is to design and develop a new mechanism for extracting energy from the gun fired rotary munitions projectiles during the flight. It is expected that the designed piezoelectric energy harvester is capable of accomplishing the need for low and medium power.

2. Design and Modeling

To fulfil the need of low and medium power, a harvester has been designed. In the proposed mechanism, rotary motion of the projectile about its own axis during the flight time is converted into vibration of a cantilever piezoelectric energy harvester. A mathematical model is developed and results are validated with FEM simulation and experimentally.

A. Mechanism for Harvesting Energy

Figure 1 shows the configuration of the device. The main components of the harvester are a hub and a support of radius R. Near the periphery of the hub n, number of PZT patches of dimensions $l_p \times w_p \times t_p$ mm3 are attached. Equal number of magnets of same sizes is mounted on the PZT patches. A lever of length equivalent to radius R is freely suspended on the shaft with the help of frictionless bearing. The lever remains suspended in vertical direction under the effect of gravity due to the mass attached at the end of the lever. A magnet of same dimension of the PZT is mount on the lever end such that, at the time of the rotation of the hub along with munitions, a repulsive magnetic force is induced between the magnets. This repulsive force induces strain in the PZT patches causing the generation of charge on the surfaces of the PZT. d33 mode of the piezoelectric has been explored in this work.

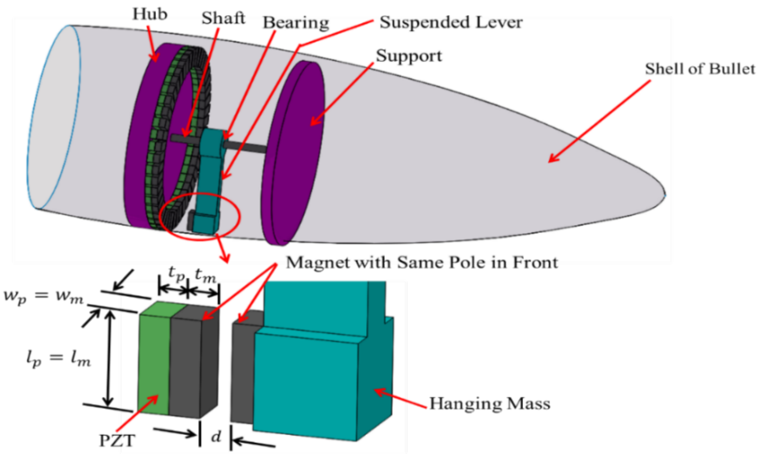

Figure 1 Pictorial view of the Energy Harvester:

B. Analytical Model

Spinning of hub with munitions shell exerts a sinusoidal compressive force, $F_m \sin(\omega t)$ on the PZT patches due to repulsion of magnets mounted on the lever and PZT patches. The magnitude of the force, F_m between both the magnets (dimensions $l_m \times w_m \times t_m \ mm^3$) can be represented as [11], [12]:

$$F_m = l_m w_m t_m^{1/3} B_r \left|B(d)\right| f(d) \tag{1}$$

where,

B_r = magnetic residual flux density,

$B(d)$ = flux density field of magnets and,

$f(d)$ = empirical function of decay of magnetic force.

For a cuboid shape of magnets, $B(d)$ and $f(d)$ can be given as [1], [2],

$$B(d) = \frac{B_r}{\pi}\left[\begin{array}{l} \tan^{-1}\left\{\dfrac{l_m w_m}{2d\sqrt{4d^2 + l_m^2 + w_m^2}}\right\} - \\ \tan^{-1}\left\{\dfrac{l_m w_m}{2(t_m+d)\sqrt{4(t_m+d)^2 + l_m^2 + w_m^2}}\right\} \end{array}\right] \tag{2}$$

$$f(d) = \left[1.749 + 1.145e^{\left(-\frac{d}{d_0}\right)}\right] \times 10^6 \left(\frac{kg}{s^4 m^{\left(\frac{4}{3}\right)}}\right) \tag{3}$$

where, d_0 = 1 mm,

This varying force develops strain in the PZT patches and hence generation of electric charge in poling direction. The generated electric displacement is given by [3]:

$$D_{33} = d_{33}\tau_{33} + \epsilon_{33} \ E_3 \tag{4}$$

where,

D_{33} = surface charge-density displacement on the electrodes surface;

d_{33} = strain coefficient;

τ_{33} = working stress on the PZT patches;

ϵ_{33} = dielectric constant and;

E_{33} = electric field in the PZT.

Charge Q_g^i on the i[th] PZT patch surface, due to applied force in time t, can be given as:

$$Q_g^i(t) = D_{3i}A = \left[d_{33}\tau_{33i}(t) + \epsilon_{33}E_3\right] l_p w_p \tag{5}$$

where,

D_{3i}(t) = piezoelectric charge-density on the i-th patch;
$\tau_{33i}(t)$ = normal stress applied on the i[th] patch;
A= area of the surface of PZT patch.

Considering, V as the voltage difference on the surface of the PZT patch along the poling direction, the electric field can be depicted as:

$$E_{33} = -\frac{\partial V}{\partial z} = -\frac{V}{t_p} \tag{6}$$

Using Eqs. (5) and (6) charge Q can be written as:

$$Q_g^i(t) = D_{3i}A = \left[d_{33}\tau_{33i}(t) - \epsilon_{33}\frac{V}{t_p} \right] l_p w_p \tag{7}$$

Since, the normal stress, $\tau_{33i}(t)$ is function of time t, and depends on the magnetic force and can be given as:

$$\tau_{33i}(t) = \left| \frac{F_m \sin(2 n_1 \pi t)}{l_p w_p} \right| \tag{8}$$

where n_1 is the frequency of excitation in cycles per second.
Time varying charge on the i^{th} PZT patch at time t, can be expressed as:

$$Q_g^i(t) = d_{33}F_m \sin(2n_1\pi t) - \epsilon_{33}\frac{V}{t_p} l_p w_p \tag{9}$$

As we know that charge, voltage and current are time dependent function and the current flow through the resistance can be given as surface charge variation with time, the current can be written as:

$$I = \omega Q_g^i(t) = \omega \left[d_{33}F_m \sin(2n_1\pi t) - \epsilon_{33}\frac{V}{t_p} l_p w_p \right] \tag{10}$$

Considering harvester as an electric system as depicted in Fig.3, with pure resistive external load and 90-degree phase deference in the current flowing through load and the PZT patch, hence the Eq. (10) can be written as:

$$I = \omega Q_g^i(t) = \omega \left[d_{33}F_m \sin(2n_1\pi t) - C_p(jIR) \right] \tag{11}$$

where, $C_P = \epsilon_{33}\ l_p w_p / t_p$ and $V = IR$

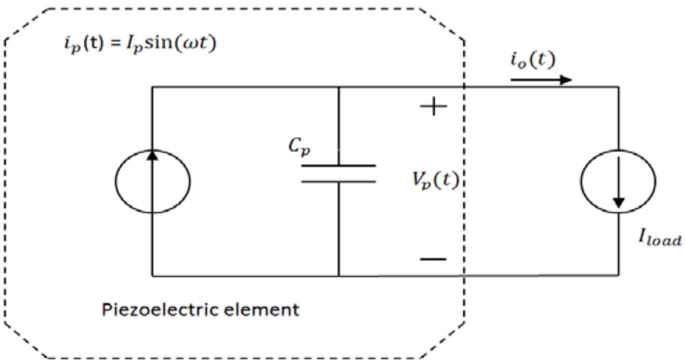

Figure 2 The equivalent circuit of harvester

Current and voltage across the external resistance can be written as:

$$I = \frac{\omega d_{33}F_m \sin(2n_1\pi t)}{\sqrt{1 + (\omega C_p R)^2}} \tag{12}$$

$$V = \frac{\omega d_{33} F_m \sin(2 n_1 \pi t)}{\sqrt{1 + (\omega C_p R)^2}} R \tag{13}$$

The RMS power output can be given as:

$$P_{RMS}(t) = VI = \left[\frac{\omega d_{33} F_m \sin(2 n_1 \pi t)}{\sqrt{1 + (\omega C_p R)^2}} \right]^2 R \tag{14}$$

If n number of PZT patches are mounted on hub periphery then the average power can be calculated as:

$$P_{av} = n.\left(\frac{2\sqrt{2}}{\pi} \right)^2 .P_{RMS}(t) = n.\left(\frac{2\sqrt{2}}{\pi} \right)^2 .\sqrt{\frac{1}{\tau} \int_0^\tau P(t) dt} \tag{15}$$

Numerical simulations are carried out using the MATLAB to study the effect of various parameters. Parameters considered for the study are summarized in Table 1, 2 and 3.

Table 1 Dimensions and Piezoelectric properties of PZT (PZT-5A).

d_{33} (C/N)	c_{55}^E (N/m^2)	l_p (mm)	w_p (mm)	t_p (mm)
3.74e-10	21e9	1-5	2-6	1-5

Table 2, Dimension and properties of magnets (Neodymium iron boron N5311).

Density (kg//m^3)	B_r (T)	d (mm)	l_m (mm)	w_m (mm)	t_m (mm)
7500	1.45	1-5	1-5	2-6	2

Table 3 Material properties and dimensions of hubs and lever (Al).

E_{al} (N/m^2)	Density (kg//m^3)	R (mm)	h_t (mm)	l_s (mm)
70e9	2700	32	2	12

C. Modeling For Estimation of Mass of Suspended Lever

The rotation of hub induces the force of repulsion between the magnets on the lever and the hub. The magnetic force has two components i.e. normal component and tangential component. The normal component of magnetic force is responsible to induce the strain into the PZT patches while the tangential component tends to rotate the suspended lever with the hub. In order to stop the rotation of suspended lever a sufficient amount of mass m, is attached to lever as shown in Fig. 3. The maximum resistive torque due gravitational force works on the suspended lever when the lever is in the horizontal position and can be given as:

$$T_R = mgl_s \tag{16}$$

Where g is the gravitational acceleration and l_s is the distance of mass from the axis of rotation,

The torque produced by the tangential component of the magnetic force will be:

$$T = F_T l_s \tag{17}$$

$$m = F_T / g \tag{18}$$

From Eqs. (16) and (17) the minimum amount of mass that can be attached to the lever can be given as:

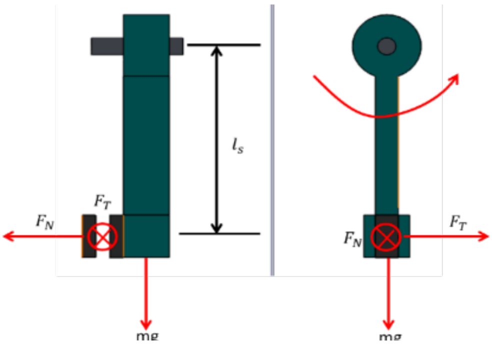

Figure 3 Magnetic Force and Gravitational Force on Piezoelectric Lever

D. FEM Modeling

Three-dimensional Finite Element (FE) model of the PZT patch as shown in Fig.4 is developed to study the electromechanical behaviour. COMSOL Multiphysics 5.3 FEA environment is chosen for the simulations. In the FE modeling the upper face of the PZT patch is considered as floating terminal while lower face is considered as ground. An electrical resistance '*R*' is inserted between the terminals of the PZT. The upper face of the PZT patch is selected for application of the magnetic force and lower face of the PZT patch is fixed. PZT is meshed with 3986 tetrahedral elements. The meshing is controlled by the inbuilt physics in the COMSOL package. Electric potential is generated between the electrodes of PZT patch due to the application of the magnetic force and can be measured in the simulation software.

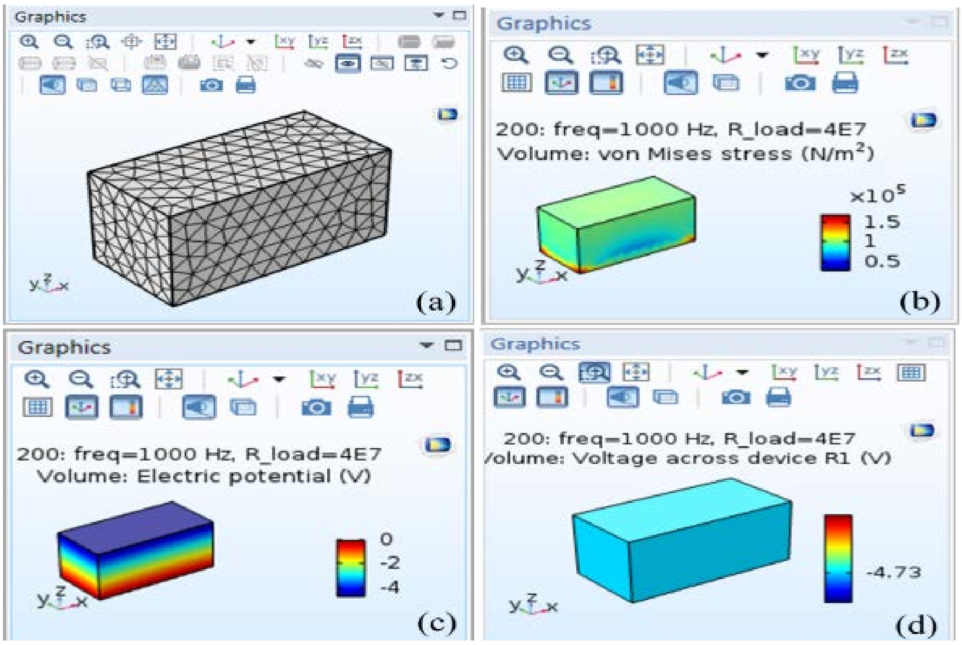

Figure 4 a) meshing of PZT patch, (b) deformation of PZT patch (c) electric potential on PZT patch and (d) voltage across the resistance

3. Results and Discussion

First of all, the magnitude of the tangential component of the magnetic force is determined and ensuring that it must be less than resistive force due to mass attached to the piezoelectric lever. Fig.5. shows the variation in the magnitude of the magnetic normal force, F_N, tangential force, F_T, and Resistive force, F_R, due to mass 160 gm attached at the end of lever, when the gap between the magnets d = 1 mm, from the starting of engagement of magnets to the end of engagement. Considering the tangential distance between the magnets is 8 mm. The tangential force and the normal force vary in sinusoidal way as shown in Fig.5. From the figure it can be observed that the resistive force always dominant the tangential force causing the relative motion between the rotary hub and piezoelectric lever thus producing the time variant force in the PZT to produce the charge.

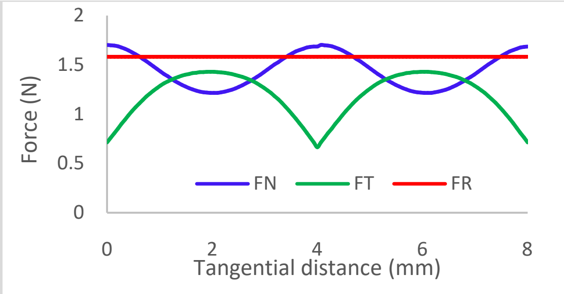

Figure 5 Variation in magnetic forces during interaction of magnets

Effect of various parameters, such as width, length and thickness of PZT patches, length and width of magnets, spin of munitions, space between magnets and electrical load on the harvested power has been studied. For the study, following geometric parameters are selected:

Radius of hub, R=32 mm,

Thickness of PZT, $t_p = 2$ mm,

Length of PZT and magnets, $l_m = l_p = 4\ mm$

Thickness of magnets $t_m = 2$ mm, Number of PZT patches= $12 - 37,$

Rotation Speed Munitions $= 1000\ rps,$ Resistance $R = 1210\ k\Omega$

Distance between magnets $d = 1\ mm.$

Fig. 6 shows the variation in electrical power with the variation in the width of the PZT patches and magnets. With the increasing width, power increase up to 4 mm and then starts to decrease. This is because with the increase in the width, the number of PZT patches decrease along the periphery of the hub. Maximum power of 0.13 mW is observed in this case.

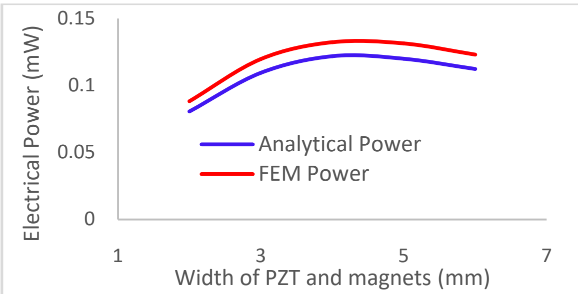

Figure 6 Power at various width of PZT and magnets

Fig. 7 shows the effect of the thickness of the PZT patch on the harvested power. Power increase linearly with increasing thickness of the PZT patches. Maximum power of 0.3 mW obtained corresponding to the 5 mm thickness of the PZT patches. The parameters considered in this case are:

Radius of hub, R=32 mm, length of PZT and magnets, l_m =l_p =4 mm, thickness of magnets t_m = 2 mm, number of PZT patches=18, width of PZT and magnets, w_p = w_m=4 mm, rotational speed of munitions=1000 *rps*, and d=1 mm.

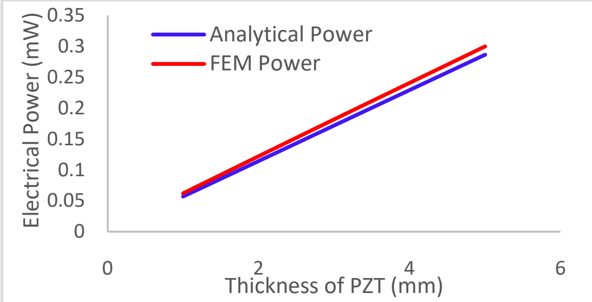

Figure 7 Variation in power with thickness of PZT

Fig. 8 shows the effect of the length of the PZT patches and magnets on electrical power. As the length increases, generated power increases due to the increase in the magnetic force. The variation is non-linear in nature. Thus, one needs to select the optimum length of the PZT patches and magnets for proper working of the harvester. A length of 4 mm is observed to be optimum.

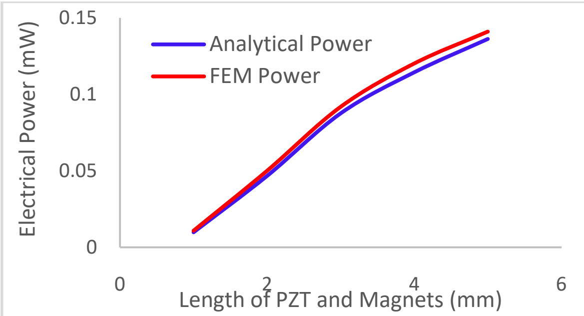

Figure 8 Variation in power with length of PZT and magnet

The effect of the speed of the munitions on the output power is next studied. It is observed that as the speed of the munitions increases, the working frequency of the force working on the PZT patches increase and hence power increase linearly as shown in Fig. 9. The dimensions and parameters of the harvester considered as: radius of hub, R=32 mm, length of PZT and magnets, $l_m = 4\,mm, l_p = 4\,mm,$, thickness of magnets t_m = 2mm, number of PZT patches=18, width of PZT and magnets, $w_p = 4\,mm, w_m = 4\,mm, d = 1\,mm.$

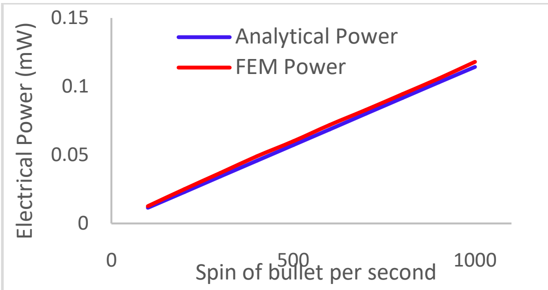

Figure 9 Power versus speed of munitions

The effect of the space between the magnets on the electric power is shown in the Fig. 10. As the space between the magnets increases, the magnitude of the magnetic force decreases causing reduction in the power. The maximum power of 0.013 mW is calculated at 1 mm space. Taking the following parameters: radius of hub, R=32 mm, length of PZT and magnets, $l_m = 4\,mm, l_p = 4\,mm,$ thickness of magnets t_m =2mm, number of PZT patches= 18, width of PZT and magnets, $w_p = 4\,mm, w_m = 4\,mm, R = 1210\,k\Omega,$

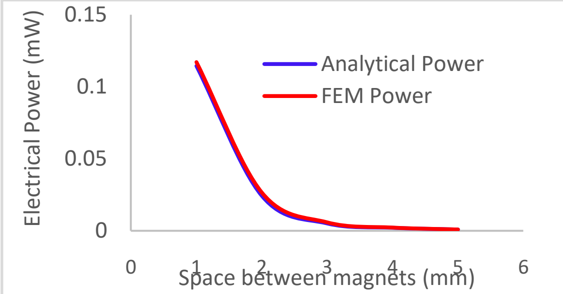

Figure 10 Power versus space between magnets

Fig. 11 shows the pattern of variation in electrical power with electrical load. With increase of the electrical load, power increase up to 2.01 M Ω and then start to decrease. The internal impedance of piezoelectric patches should be $= \left(\frac{1}{\omega C_p}\right) = R$, to get the optimum power (Maximum power theorem [14]). Hence, the power drastically increased at this value of resistive load. The power decreases slowly after this as shown in Fig.11. The parameters considered in this case are: R=32 mm, length of PZT and magnets, $l_m = 4\ mm, l_p = 4\ mm,$ thickness of magnets $t_m = 2$ mm, number of PZT patches= 18, width of PZT and magnets, $w_p = 4\ mm, w_m = 4\ mm,\ d = 1\ mm.$

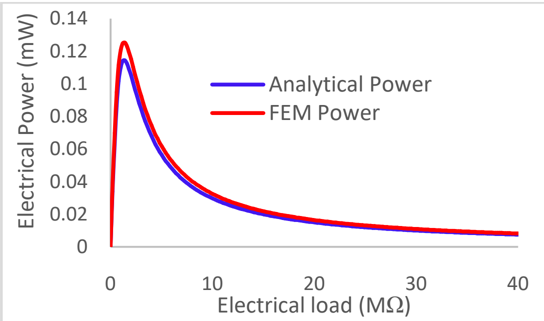

Figure 11 Power versus electrical load

4. Conclusion

In this paper, a gravity-based piezoelectric energy harvester to harvest the energy from the spinning of munitions of artillery gun is developed for fusing system of the gun. The harvester works in the d_{33} mode of the piezoelectric. Magnets are used to convert the angular kinetic motion into time varying compression of the PZT patches to generates the power. A mathematical model is developed and compared with the FE model. Effect of various parameters of the harvester is discussed. Maximum generated average power of 0.13 mW is observed corresponding to magnetic force of 1.8 N, external load R of 1.6 $M\Omega$ and rotation speed of munitions as 1000 rps. Analytical and FE models results agree with each other.

5. Reference

[1] T. Eggborn, "Analytical Models to Predict Power Harvesting with Piezoelectric Materials," *Masters Thesis, Virginia Polytech. Inst. State Univ. VA Frederick, A. A., Clark, W. W., Hu, H,* vol. 5, no. May, p. 11, 2003.

[2] J. Ajitsaria, S. Y. Choe, D. Shen, and D. J. Kim, "Modeling and analysis of a bimorph piezoelectric cantilever beam for voltage generation," *Smart Mater. Struct.*, vol. 16, no. 2, pp. 447–454, 2007, doi: 10.1088/0964-1726/16/2/024.

[3] X. D. Xie, Q. Wang, and N. Wu, "A ring piezoelectric energy harvester excited by magnetic forces," *Int. J. Eng. Sci.*, vol. 77, pp. 71–78, 2014, doi: 10.1016/j.ijengsci.2014.01.001.

[4] M. Guan and W.-H. Liao, "Design and analysis of a piezoelectric energy harvester for rotational motion system," Energy Convers. Manag., vol. 111, pp. 239–244, 2016, doi:

10.1016/j.enconman.2015.12.061.

[5] J. Zhang, Z. Fang, C. Shu, J. Zhang, Q. Zhang, and C. Li, “A rotational piezoelectric energy harvester for efficient wind energy harvesting,” Sensors Actuators, A Phys., vol. 262, pp. 123–129, 2017, doi: 10.1016/j.sna.2017.05.027.

[6] J. X. Tao, N. V. Viet, A. Carpinteri, and Q. Wang, “Energy harvesting from wind by a piezoelectric harvester,” Eng. Struct., vol. 133, pp. 74–80, 2017, doi: 10.1016/j.engstruct.2016.12.021.

[7] T. Narolia, V. K. Gupta, and I. A. Parinov, “A novel design for piezoelectric based harvester for rotating objects,” in Springer Proceedings in Physics, 2019, vol. 224, doi: 10.1007/978-3-030-19894-7_45.

[8] J. Rastegar, D. Haarhoff, C. Pereira, and H.-L. Nguyen, “Piezoelectric-based energy-harvesting power sources for gun-fired munitions,” Smart Struct. Mater. 2006 Sensors Smart Struct. Technol. Civil, Mech. Aerosp. Syst., vol. 6174, p. 61740W, 2006, doi: 10.1117/12.657441.

[9] J. Rastegar, R. Murray, C. Pereira, O. Partners, B. Shore, and N. York, “Energy-Harvesting Power Sources for Very-High-G Gun-Fired Munitions,” vol. 7643, pp. 1–7, 2010, doi: 10.1117/12.847777.

[10] T. R. J. Willemin1, 2, S. Boisseau1, 2, L. Olmos1, 2, M. Gallardo1, 2, G. Despesse1, 2, “20000G shock energy harvesters for gun-fired munition,” *J. Phys. Conf. Ser.*, 2016, doi: 10.1088/1742-6596/773/1/012084.

[11] K&J Magnetics, “www.kjmagnetics.com/calculator.asp” 2011. .

[12] W. Al-Ashtari, M. Hunstig, T. Hemsel, and W. Sextro, “Frequency tuning of piezoelectric energy harvesters by magnetic force,” Smart Mater. Struct., vol. 21, no. 3, 2012, doi: 10.1088/0964-1726/21/3/035019.

[13] D. Damjanovic, “Ferroelectric, dielectric and piezoelectric properties of ferroelectric thin films and ceramics,” Reports Prog. Phys., vol. 61, no. 9, p. 1267, 1998.

[14] C. S. Kong, “A General Maximum Power Transfer Theorem,” IEEE Trans. Educ. VOL. 38, NO. 3, vol. 38, no. 3, pp. 1993–1995, 1995.

Perching of Nano-quadrotor on Vertical Wall using Periodic Event-Triggered Control

Sandeep Gupta
Department of Electrical Engineering
Indian Institute of Technology Kanpur
sngupta@iitk.ac.in

Padmini Singh
Department of Electrical Engineering
Indian Institute of Technology Kanpur

Laxmidhar Behera
Department of Electrical Engineering
Indian Institute of Technology Kanpur

Nishchal K. Verma
Department of Electrical Engineering
Indian Institute of Technology Kanpur

Abstract — **This paper proposes perching of nano-quadrotor on vertical wall using periodic event-triggered sliding mode control. Quadrotor is a highly unstable system, which has twelve states and four control inputs. A finite time tracking controller is developed for nano-quadrotor. A recursive finite- time stable manifold has been designed for the convergence of the error states to zero in finite-time. Next, from the designed stable sliding manifold, sliding mode control laws for all the control inputs are derived. Furthermore, from the Lyapunov stability theory, periodic event-triggering conditions are derived to minimize resource utilization. Periodic event-trigger controller provides the control laws next trigger time.**

Keywords*— *Event-Trigger control; Nano-quadrotor; Perching on wall.

1. Introduction

Though lots of theory has been developed for path tracking of quadrotor but for perching application there are still lots of scope. Thus, there is a need for controllers to drive the system to a particular position when new applications are to be developed in unknown or critical situations. One such application is surveillance inside a room from the surface of a vertical wall or capturing some images from the vertical wall.

For the alignment of the quadrotor on vertical wall, forces are needed towards the direction of the wall such that the top sideof the quad-rotor perches on the wall.Several linear and non-linear control techniques have been discussed in literature to achieve path tracking [1], [2], [3] and perching task [4]. Sliding mode controller is one of the popular non-linear control techniques because it offers robustness against disturbances [5]. Now a days event trigger control technique is gaining popularity [6] [7] because it reduces the utilization of the controller action.

Fig 1: Crazyflie quad-rotor configuration

Instead of consistently transmitting the control signal to the plant, it sends the control signal whenever the plant states diverge from a certain boundary value. Further reducing the computation, the concept of periodic event-trigger control came which exempts the continuous monitoring of the states [8]. In periodic event-trigger control, the controller is triggered based on the triggering sequence update law. The key contributions of the paper are summarized as follows:

(i) Stable finite-time sliding manifold has been designed so that the perching task on vertical wall can be achieved in finite-time.
(ii) Using Lyapunov stability criterion periodic event-triggering conditions are derived to reduce the controller effort.
(iii) Experimental results are presented, for perching of quadrotor on two different scenarios.

2. Dynamic Modelling and Problem Formulation

Fig.1 represents the pictorial view of the crazyflienano-quadrotor designed in our laboratory. It is verylight in weight hence can be easily used for theperching application.

The governing dynamics of the quadrotor in 3-dimensional space is taken from [4]:

$$\begin{aligned}
\ddot{\emptyset} &= \dot{\theta}\dot{\Psi}\left(\frac{J_y - J_z}{J_x}\right) + \frac{u_2}{J_x} \\
\ddot{\theta} &= \dot{\emptyset}\dot{\Psi}\left(\frac{J_z - J_x}{J_y}\right) + \frac{u_3}{J_y} \\
\ddot{\Psi} &= \dot{\emptyset}\dot{\theta}\left(\frac{J_x - J_y}{J_z}\right) + \frac{u_4}{J_z} \\
\ddot{z} &= \frac{u_1}{m}(\cos\emptyset\cos\theta) - g \\
\ddot{x} &= \frac{u_1}{m}(\cos\emptyset\sin\theta\cos\Psi + \sin\emptyset\sin\Psi) \\
\ddot{y} &= \frac{u_1}{m}(\cos\emptyset\sin\theta\sin\Psi - \sin\emptyset\cos\Psi)
\end{aligned} \tag{1}$$

where, $(\theta, \emptyset, \Psi)$are attitude angles, represents roll, pitch and yaw respectively and (x, y, z) are position co-ordinates. $m$is the mass, J_x,J_y,$J_y$are the inertial values in respective coordinates. $u_1$is force and u_2,u_2, u_3 torques when, quadrotor align in perching mode the governing dynamics will become [4].

$$\begin{aligned}
\ddot{\theta}_p &= \frac{u_{3p}}{J_y} \\
\ddot{z}_p &= \frac{u_{zp}\cos\theta_p}{m} - g \\
\ddot{x}_p &= \frac{u_{xp}\sin\theta_p}{m}
\end{aligned} \tag{2}$$

For the non-linear model represented in (2), for the 3-dimensional tracking, objective is to track the desired path in presence of delay. $x_d, y_d, z_d, \theta_d, \emptyset_d, and\ \Psi_d$are the desired values of the states of the system. Desired values of pitch and roll are;

$$\emptyset_d = \sin^{-1}\left(u_x \sin\Psi_d - u_y \cos\Psi_d\right) \tag{3}$$

$$\theta_d = \sin^{-1}\left(\frac{u_x \cos\Psi_d - u_y \sin\Psi_d}{\sqrt{\left(1-\left(u_x \sin\Psi_d - u_y \cos\Psi_d\right)^2\right)}}\right) \tag{4}$$

For position control two virtual control inputs are considered and are termed as:

$$\begin{aligned} u_x &= \cos\emptyset \sin\theta \cos\Psi + \sin\emptyset \sin\Psi \\ u_y &= \cos\emptyset \sin\theta \sin\Psi - \sin\emptyset \cos\Psi \end{aligned} \tag{5}$$

In the case of perching (2), the desired states are $\theta_{pd}, x_{pd}, and\ z_{pd}$. Position control of x can be done by taking the virtual control input as:

$$u_{xp} = \sin\theta_p \tag{6}$$

Control inputs $u_1, u_2, u_3, u_4, u_x, u_y, u_{1p}, u_{2p}$ and u_{xp} has to design for relative degree two type of subsystems. Fig. (2) represents the overview of the problem objective. The paper addresses the problem of communication channel delay. Here, periodic event-trigger controller is designed for saving the effort of the actuator. For mitigating the effect of delay the transmitted information is encrypted using wave-variable [9]. The error dynamics for which the controller has been designed is discussed below.

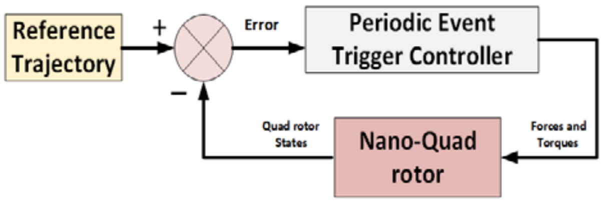

Fig 2: System architecture

A. Error Dynamics

In first part altitude dynamics are considered, let us take $z = z_1$ and $\dot{z} = z_2$ then attitude dynamics will become:

$$\begin{cases} \dot{z}_1 = z_2 \\ \dot{z}_2 = \dfrac{u_1}{m}(\cos\emptyset \cos\theta) - g \end{cases} \tag{7}$$

To fulfill the objective z achieves z_d then error equation for attitude is

$$\begin{aligned} e_{z_1} &= z_1 - z_d \\ \dot{e}_{z_1} &= e_{z_2} = \dot{z}_1 - \dot{z}_d = z_2 - \dot{z}_d \\ \dot{e}_{z_2} &= \dot{z}_2 - \ddot{z}_d = \frac{u_1}{m}(\cos\emptyset \cos\theta) - g - \ddot{z}_d \end{aligned} \tag{8}$$

Likewise, the same procedure is followed toobtain the error dynamics forthe position, roll, pitch, yaw, and perching states.

3. Periodic event-trigger sliding mode controller design

Let us take sliding manifold for the error dynamics defined in eq. (8) states as:

$$s_z = \dot{e}_{z_1} + \varepsilon_1 e_{z_1}^{\delta_1} + \eta_1 e_{z_1}^{\beta_1} \tag{9}$$

where, $\varepsilon_1, \eta_1 > 0$ and $\delta_1 < 1, \beta_1 < 1$. when sliding surface will become zero the reduced error dynamics will be like:

$$\dot{e}_{z_1} = -\varepsilon_1 e_{z_1}^{\delta_1} - \eta_1 e_{z_1}^{\beta_1} \tag{10}$$

For, the proper choice of $\delta_1$and β_1, the reduced error dynamics will converge to zero in finite-time. If δ_1 and $\beta_1$is rational with odd integers of numerators and denominators, then when $e_{z_1}$is far away from zero than the governing dynamics will be $\dot{e}_{z_1} = -\eta_1 e_{z_1}^{\beta_1}$ and when e_{z_1} is near to zero than the governing dynamics will be $\dot{e}_{z_1} = -\varepsilon_1 e_{z_1}^{\delta_1}$ which shows that the convergence of error is fast and takes place in finite-time. Likewise, the same procedure is followed to obtain the sliding surface for the position, roll, pitch, yaw, and perching states.

Now, control law and periodic event triggering conditions are derived using error dynamics of the quadrotor. Now, taking the derivative of sliding surface s_z (9).

$$\dot{s}_z = \dot{e}_{z_2} + \varepsilon_1 \delta_1 e_{z_1}^{\delta_1 - 1} e_{z_2} + \eta_1 \beta_1 e_{z_1}^{\beta_1 - 1} e_{z_2} \tag{11}$$

Now, substituting $\dot{s}_z = -k_z sign(s_z)$where k_z is some positive constant and putting the value of e_{z_2} from eq.(8) in eq.(11)

$$u_1 = \frac{m}{\cos\theta \cos\emptyset}\left[g + \ddot{z}_d - \varepsilon_1 \delta_1 e_{z_1}^{\delta_1 - 1} e_{z_2} - \eta_1 \beta_1 e_{z_1}^{\beta_1 - 1} e_{z_2} - k_z sign(s_z)\right] \tag{12}$$

For$k_z > 0$,

$$s_z \dot{s}_z = -k_z |s_z| \tag{13}$$

which shows that the reaching phase is finite time. It is to be noted that singularity may happen because of the term $e_{z_1}^{\delta_1 - 1}$, but under the condition $2\delta_1 > 1$, the control input u_1 will be bounded. Likewise, control input for position, roll, pitch, yaw and perching states can be obtained. The control inputs are:

$$u_x = \frac{m}{u_1}\left[\ddot{x}_d - \varepsilon_1 \delta_1 e_{x_1}^{\delta_1 - 1} e_{x_2} - \eta_1 \beta_1 e_{x_1}^{\beta_1 - 1} e_{x_2} - k_x sign(s_x)\right] \tag{14}$$

$$u_y = \frac{m}{u_1}\left[\ddot{y}_d - \varepsilon_1 \delta_1 e_{y_1}^{\delta_1 - 1} e_{y_2} - \eta_1 \beta_1 e_{y_1}^{\beta_1 - 1} e_{y_2} - k_y sign(s_y)\right] \tag{15}$$

$$u_2 = J_x\left[-\dot{\theta}\dot{\Psi}\left(\frac{J_y - J_z}{J_x}\right) + \ddot{\emptyset}_d - \varepsilon_1\delta_1 e_{\emptyset_1}^{\delta_1 - 1} e_{\emptyset_2} - \eta_1\beta_1 e_{\emptyset_1}^{\beta_1 - 1} e_{\emptyset_2} - k_{\emptyset} sign(s_{\emptyset})\right] \tag{16}$$

$$u_3 = J_y\left[-\dot{\emptyset}\dot{\Psi}\left(\frac{J_z - J_x}{J_y}\right) + \ddot{\theta}_d - \varepsilon_1\delta_1 e_{\theta_1}^{\delta_1 - 1} e_{\theta_2} - \eta_1\beta_1 e_{\theta_1}^{\beta_1 - 1} e_{\theta_2} - k_{\theta} sign(s_{\theta})\right] \tag{17}$$

$$u_4 = J_z\left[-\dot{\emptyset}\dot{\theta}\left(\frac{J_x - J_y}{J_z}\right) + \ddot{\Psi}_d - \varepsilon_1\delta_1 e_{\Psi_1}^{\delta_1 - 1} e_{\Psi_2} - \eta_1\beta_1 e_{\Psi_1}^{\beta_1 - 1} e_{\Psi_2} - k_{\Psi} sign(s_{\Psi})\right] \tag{18}$$

And for perching control laws are:

$$u_{3p} = J_y\left[\ddot{\theta}_{pd} - \varepsilon_1\delta_1 e_{\theta_{p1}}^{\delta_1 - 1} e_{\theta_{p2}} - \eta_1\beta_1 e_{\theta_{p1}}^{\beta_1 - 1} e_{\theta_{p2}} - k_{\theta_p} sign(s_{\theta_p})\right] \tag{19}$$

$$u_{zp} = \frac{m}{\cos\theta_p}\left[g + \ddot{z}_{pd} - \varepsilon_1\delta_1 e_{z_{p1}}^{\delta_1 - 1} e_{z_{p2}} - \eta_1\beta_1 e_{z_{p1}}^{\beta_1 - 1} e_{z_{p2}} - k_{z_p} sign(s_{z_p})\right] \tag{20}$$

$$u_{xp} = \frac{m}{\sin\theta_p}\left[\ddot{x}_{pd} - \varepsilon_1\delta_1 e_{x_{p1}}^{\delta_1 - 1} e_{x_{p2}} - \eta_1\beta_1 e_{x_{p1}}^{\beta_1 - 1} e_{x_{p2}} - k_{x_p} sign(s_{x_p})\right] \tag{21}$$

A. Stability Analysis

In this section event-triggering condition is derived using Lyapunov stability theory. Event-triggering conditions are derived for altitude controller. At event-triggering condition control input is constant in the interval $[t_i\ t]$ and is defined by:

$$\begin{aligned} u_1(t_i) = \frac{m}{\cos\theta(t_i)\cos\emptyset(t_i)}\Big[g + \ddot{z}_d(t_i) - \varepsilon_1\delta_1 e_{z_1}^{\delta_1 - 1}(t_i) e_{z_2}(t_i) \\ - \eta_1\beta_1 e_{z_1}^{\beta_1 - 1}(t_i) e_{z_2}(t_i) - k_z sign(s_z(t_i))\Big] \end{aligned} \tag{22}$$

Theorem 1: For the system (8) if the control update law (22) is held constant in the interval $[t_{i+1} t_i]$ then the system remains finite-time stable if it holds following event-triggering condition:

$$|e_{z_1}(\Delta)| < \frac{k_z}{L_A} \tag{23}$$

Proof 1: Let us take a Lyapunov function:

$$V = \frac{1}{2}s_z^2 \tag{24}$$

Taking the derivative of the Lyapunov function

$$\dot{V} = s_z\dot{s}_z \tag{25}$$

Substituting the value of $\dot{s}_z$from eq. (11) in eq. (26).

$$\begin{aligned} \dot{V} &= s_z\left[\dot{e}_{z_2} + \varepsilon_1\delta_1 e_{z_1}^{\delta_1 - 1} e_{z_2} + \eta_1\beta_1 e_{z_1}^{\beta_1 - 1} e_{z_2}\right] \\ &= s_z\left[\frac{u_1(t_i)}{m}(\cos\theta\cos\emptyset) - g - \ddot{z}_d + \varepsilon_1\delta_1 e_{z_1}^{\delta_1 - 1} e_{z_2} + \eta_1\beta_1 e_{z_1}^{\beta_1 - 1} e_{z_2}\right] \end{aligned} \tag{26}$$

Let us consider $b(\theta,\emptyset)=\frac{m}{\cos\theta\cos\emptyset}$. In our application positions are constants hence its derivative will die out. Substituting the value of $u_1(t_i)$ from eq. (22) in eq. (26)

$$\dot{V}=s_z\left[\frac{b(\emptyset(t_i),\theta)}{b(\emptyset,\theta)}\left[g+\ddot{z}_d(t_i)-\varepsilon_1\delta_1 e_{z_1}^{\delta_1-1}(t_i)e_{z_2}(t_i)-\eta_1\beta_1 e_{z_1}^{\beta_1-1}(t_i)e_{z_2}(t_i)-k_z sign(s_z(t_i))\right]-g-\ddot{z}_d+\varepsilon_1\delta_1 e_{z_1}^{\delta_1-1}e_{z_2}+\eta_1\beta_1 e_{z_1}^{\beta_1-1}e_{z_2}\right] \quad (27)$$

Let us consider that $\frac{b(\emptyset(t_i),\theta)}{b(\emptyset,\theta)}=\varsigma$ and is bounded$|\varsigma|\le\bar{\varsigma}$. Now eq. (27) will become

$$\dot{V}=s_z\left[\varsigma\left[g-\varepsilon_1\delta_1 e_{z_1}^{\delta_1-1}(t_i)e_{z_2}(t_i)-\eta_1\beta_1 e_{z_1}^{\beta_1-1}(t_i)e_{z_2}(t_i)-k_z sign(s_z(t_i))\right]-g+\varepsilon_1\delta_1 e_{z_1}^{\delta_1-1}e_{z_2}+\eta_1\beta_1 e_{z_1}^{\beta_1-1}e_{z_2}\right] \quad (28)$$

Let us assume $g\cong\varsigma g$ and from Lipschitz continuity following assumptions are made:

$$\begin{aligned}\varepsilon_1\delta_1 e_{z_1}^{\delta_1-1}e_{z_2}-\varsigma\varepsilon_1\delta_1 e_{z_1}^{\delta_1-1}(t_i)e_{z_2}(t_i)&=\varepsilon_1\delta_1 L_1\left|e_{z_1}-e_{z_1}(t_i)\right|+\varepsilon_1\delta_1 L_2\left|e_{z_2}-e_{z_2}(t_i)\right|\\ \eta_1\beta_1 e_{z_1}^{\beta_1-1}e_{z_2}-\varsigma\eta_1\beta_1 e_{z_1}^{\beta_1-1}(t_i)e_{z_2}(t_i)&=\eta_1\beta_1 L_1\left|e_{z_1}-e_{z_1}(t_i)\right|+\eta_1\beta_1 L_2\left|e_{z_2}-e_{z_2}(t_i)\right|\end{aligned} \quad (29)$$

Let us take event- triggering error as $e_{z_1}-e_{z_1}(t_i)=e_{z_1}(\Delta)$and $e_{z_2}-e_{z_2}(t_i)=e_{z_2}(\Delta)$. Now, substituting the value from eq. (29) in eq. (28)

$$\dot{V}=s_z\left[\varepsilon_1\delta_1 L_1\left|e_{z_1}(\Delta)\right|+\varepsilon_1\delta_1 L_2\left|e_{z_2}(\Delta)\right|+\eta_1\beta_1 L_1\left|e_{z_1}(\Delta)\right|+\eta_1\beta_1 L_2\left|e_{z_2}(\Delta)\right|-k_z sign(s_z(t_i))\right] \quad (30)$$

Rewriting eq. (30) and assuming $sign\big(s_z(t_i)\big)=sign(s_z(t))$ and assuming Lipschitz continuity on$\left|e_{z_2}(\Delta)\right|=L_a\left|e_{z_1}(\Delta)\right|$.

$$\dot{V}\le\Big[\big[\varepsilon_1\delta_1 L_1|s_z|\left|e_{z_1}(\Delta)\right|+\varepsilon_1\delta_1 L_2 L_a|s_z|\left|e_{z_1}(\Delta)\right|+\eta_1\beta_1 L_3|s_z|\left|e_{z_1}(\Delta)\right|+\eta_1\beta_1 L_4 L_a|s_z|\left|e_{z_1}(\Delta)\right|-k_z|s_z|\big]\Big] \quad (31)$$

$$\dot{V}\le|s_z|\Big[\big[(\varepsilon_1\delta_1 L_1+\eta_1\beta_1 L_3+\varepsilon_1\delta_1 L_2 L_a+\eta_1\beta_1 L_4 L_a)\left|e_{z_1}(\Delta)\right|-k_z\big]\Big] \quad (32)$$

Let us assume,$L_A=\varepsilon_1\delta_1 L_1+\eta_1\beta_1 L_3+\varepsilon_1\delta_1 L_a L_2+\eta_1\beta_1 L_a L_4+\lambda_z L_a$. For stability following condition should hold:

$$\left|e_{z_1}(\Delta)\right|<\frac{k_z}{L_A} \quad (33)$$

B. Periodicity of the Controller

In this section next triggering instant $t_{i+1}$is calculated using the current triggering instant t_i.

Theorem 2: When the control law (22) is applied at the t_i^{th}instant to the error states (8) under event-triggering condition (23), then the next triggering instant t_{i+1} will be

$$t_{i+1}=t_i+\frac{1+L_a}{L_B-L_A sign\big(s_z(t_i)\big)} \quad (34)$$

Proof 2: Again revisit eq. (8) and expanding it in terms of triggering instant t_i and next triggering instant t_{i+1}.

$$\frac{e_{z_1}(t_{i+1}) - e_{z_1}(t_i)}{t_{i+1} - t_i} = e_{z_2} \tag{35}$$

$$\frac{e_{z_2}(t_{i+1}) - e_{z_2}(t_i)}{t_{i+1} - t_i} = \frac{u_1(t_i)}{m}(\cos\theta\cos\emptyset) - g$$

Now take $t_{i+1} - t_i = \xi$ and $e_{z_1}(t_{i+1}) - e_{z_1}(t_i) = e_{z_1}(\Delta)$.

$$e_{z_1}(\Delta) = \xi e_{z_2}$$

$$e_{z_2}(\Delta) = \xi \frac{u_1(t_i)}{b(\theta,\emptyset)} - \xi g \tag{36}$$

Now, adding $e_{z_1}(\Delta)$ and $e_{z_2}(\Delta)$ from eq. (36)

$$e_{z_1}(\Delta) + e_{z_2}(\Delta) = \xi e_{z_2} + \xi \frac{u_1(t_i)}{b(\theta,\emptyset)} - \xi g \tag{37}$$

After, substituting the value of $u_1(t_i)$ from eq.(22) in eq.(37) results in:

$$\begin{aligned} e_{z_1}(\Delta) + e_{z_2}(\Delta) \\ = \xi \Big[e_{z_2} \\ + \varsigma \Big[g - \varepsilon_1\delta_1 e_{z_1}^{\delta_1-1}(t_i) e_{z_2}(t_i) - \eta_1\beta_1 e_{z_1}^{\beta_1-1}(t_i) e_{z_2}(t_i) \\ - k_z sign(s_z(t_i)) \Big] - g \Big] \end{aligned} \tag{38}$$

Again, from Lipschitz continuity following assumptions are made:

$$\begin{aligned} e_{z_2} - \varsigma\varepsilon_1\delta_1 e_{z_1}^{\delta_1-1}(t_i) e_{z_2}(t_i) - \varsigma\eta_1\beta_1 e_{z_1}^{\beta_1-1}(t_i) e_{z_2}(t_i) \\ = L_5\left|e_{z_1} - e_{z_1}(t_i)\right| + L_6\left|e_{z_2} - e_{z_2}(t_i)\right| \end{aligned} \tag{39}$$

Putting the Lipschitz assumption from (39) in (38).

$$e_{z_1}(\Delta) + e_{z_2}(\Delta) = \xi\left[L_5\left|e_{z_1} - e_{z_1}(t_i)\right| + L_6\left|e_{z_2} - e_{z_2}(t_i)\right| - k_z sign(s_z(t_i))\right] \tag{40}$$

Now assuming $L_B = L_5 + L_a L_6$ in eq. (40) and further solving,

$$\xi k_z sign\big(s_z(t_i)\big) = [\xi L_B - L_a - 1]\left|e_{z_1}(\Delta)\right| \tag{41}$$

$$\left|e_{z_1}(\Delta)\right| = \frac{\xi k_z sign\big(s_z(t_i)\big)}{[\xi L_B - L_a - 1]}$$

Solving for next $\xi = t_{i+1} - t_i$ from eq. (33) and eq. (41), next triggering instant t_{i+1} is:

$$t_{i+1} = t_i + \frac{1 + L_a}{L_B - L_A sign\big(s_z(t_i)\big)} \tag{42}$$

Eq. (42) represents the periodicity of the triggering instants. Hence it completes the Proof.

4. Experimental Results

Experiments are conducted for perching task using ROS running on Linux operating system. Quad-rotor initial position is taken as $[x = 0\ y = 0\ z = 0]$, all distance is measured in meters and initial roll, pitch and yaw angles are $[\emptyset = 0\ \theta = 0\ \Psi = 0]$. The experimental set-up is shown inFig. (3). The host computer is used to run python script consisting of proposed algorithm which sends the actuator commands. It communicates with crazyflie quadrotor via crazyradio PA USB dongle in full duplex mode. The crazyflie quadrotor has onboard communication radio module (nRF24LU1 without PA).

Parameters for crazyflienano-quadrotor are taken as: length of the arm $l = 0.010\ m$, mass $m = 0.040\ kg$, inertial parameters in 3D are $J_x = 1.112951 * 10^{-5} kg/m^2$, $J_y = 1.114361 * 10^{-5} kg/m^2$and $J_z = 2.162056 * 10^{-5} kg/m^2$ respectively. Two experiments are performed on the quadrotor.

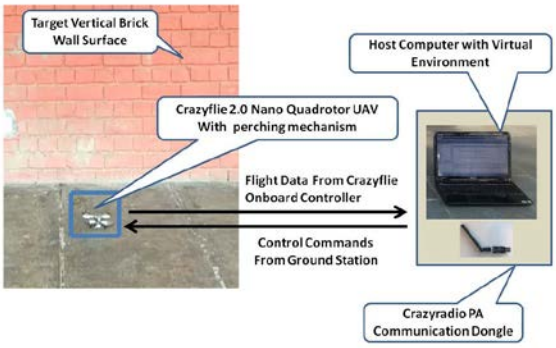

Fig 3: Experimental working environment

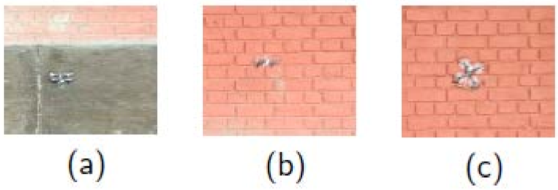

Fig 4: Tapped images of perching in fixed position

Case 1: Perching in fixed position. The desired position is $[x = 1\ y = 0.5\ z = 1.5]$ and desired angles for pitch is $\theta_d = 1$ radian. During perching states of the quadrotor changes from 3-D space to 2-D space. Perching in the fixed position of quad-rotor can be used for surveillance purpose on high rise transparent wall. Using event triggering strategy computation effort can be saved. Fig. (5) shows the evolution of states using event-trigger strategy. Fig. (4) shows the tapped images of fixed position perching.

Case 2: Perching and Pose changing in fixed position. The desired position is $[x = 1\ y = 0.25\ z = 1]$ and desired angles for pitch is $\theta_d = 1$ radian. Perching and pose changing in the fixed position of quad-rotor can be used for capturing the images from a high-rise building. Fig. (6) shows the tapped images and Fig. (7) shows the evolution of states.

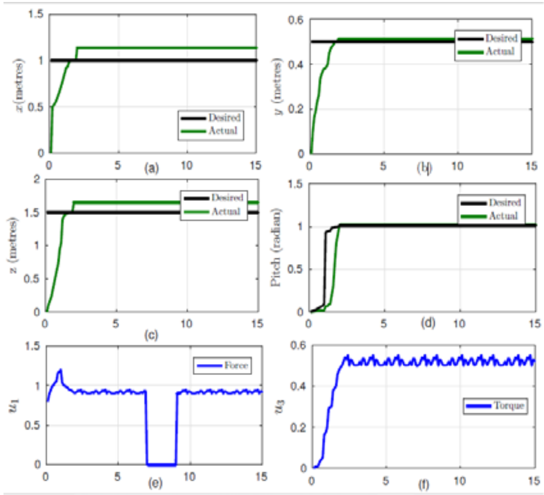

Fig 5: Evolution of system states (a) x position (b) y position (c) z position (d) pitch (e) position force (f) pitch torque

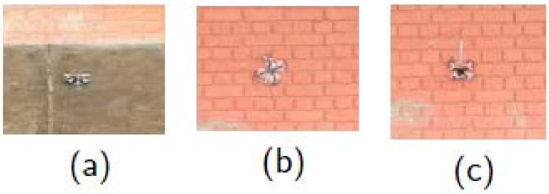

Fig 6: Tapped images of perching and pose changing from perching to hanging position.

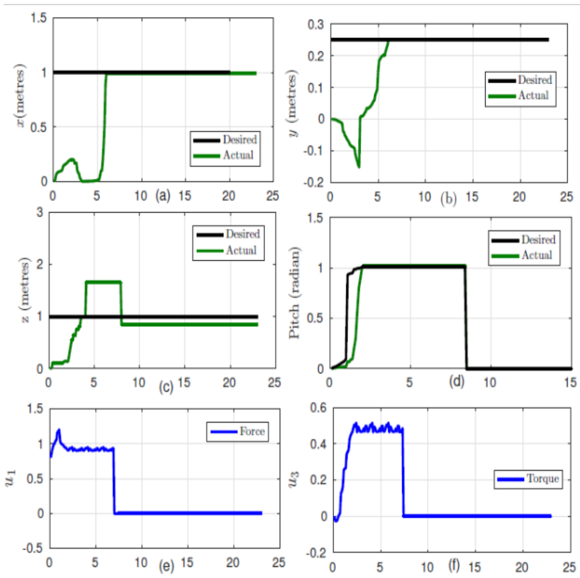

Fig 7: Evolution of system states (a) x position (b) y position (c) z position (d) pitch (e) position force (f) pitch torque

5. Conclusions

The article presents a perching application of nano-quadrotor using finite time sliding mode controller in presence of disturbances on vertical wall. Event-trigger conditions are derived for the proposed controller for reducing the computation effort of the controller. Experiments are performed for two different scenarios to validate the proposed theory. The future range of the job will concentrate on climbing and taking off of quadrotor for surveillance and image capturing application.

6. References

[1] Y. Yu, S. Yang, M. Wang, C. Li, and Z. Li. High performance full attitude control of a quadrotor, 2015 *IEEE International Conference on Robotics and Automation (ICRA). IEEE*, 2015, pp.1698-1703, doi:10.1109/ICRA.2015.7139416

[2] Das, K. Subbarao, and F. Lewis. Dynamic inversion with zero dynamics stabilization for quadrotor control. *IET control theory &applications*, vol. 3, no. 3, pp. 303-314, 2009, doi:10.1049/iet-cta:20080002

[3] G. Silano, E. Aucone, and L. Iannelli. CrazyS: a software-in-the loop platform for the crazyflie 2.0 nano-quadcopter. *In 2018 26th Mediterranean Conference on Control and Automation (MED). IEEE*, 2018, pp. 1-6. doi:10.1109/MED.2018.8442759

[4] P. Singh, S. Gupta, L. Behera, N. K. Verma, and S. Nahavandi. Perching of nano-quadrotor using self-trigger finite-time second-order continuous control. *IEEE Systems Journal*, pp. 1-11, 2020. doi:10.1109/JSYST.2020.3021579

[5] F. Chen, R. Jiang, K. Zhang, B. Jiang, and G. Tao. Robust backstepping sliding-mode control and observer-based fault estimation for a quadrotor UAV. *IEEE Transactions on Industrial Electronics*, vol. 63, no. 8, pp. 5044-5056, 2016.doi:10.1109/TIE.2016.2552151

[6] V. Kumar, S. R. Mohanty and S. Kumar. Event Trigger Super Twisting Sliding Mode Control for DC Micro Grid with Matched/Unmatched Disturbance Observer. *IEEE Transactions on Smart Grid*, vol. 11, no. 5, pp. 3837-3849, Sept. 2020. doi**:** 10.1109/TSG.2020.2990451

Lateral Thrust based Course Correction Mechanism

Sangeeta Sharma Panda
Armament Research and Development Establishment
DRDO
Pune
sangeeta_eca@arde.drdo.in

A. Anandaraj
Armament Research and Development Establishment
DRDO
Pune
aanandaraj@arde.drdo.in

***Abstract*— Major portion of Infantry battalion of Indian ARMY depends on long range indirect fire artillery shell for front line defence. These artillery shell are unguided with circular error probable (CEP) of around 1.3 cal at 20 km and 1.76 cal at 30 km which is required to be brought down to within 0.3 cal or less for better engagement of target.**

To improve its accuracy to 0.3 cal or less, GPS INS enabled Precision and Guidance kit is promising concept. Existing unguided artillery shells can be fitted with fuze with GPS INS enabled Precision Guidance (PG) kit and can be used for better terminal accuracy.

PG kit can utilizes concepts such as squibs or thrusters, drag brakes, movable nose, movable inertial mass, canards with dual spinning body, etc. Out of many such innovative control mechanisms, this work explores the feasibility of course correction with the application of thrust force with roll decoupled guidance module.

Mathematical simulations are performed on an indirect fire artillery projectile using the GNC module of PRODAS. This study is aimed to find out suitable thruster configuration to have better control on accuracy at the target end wrt time of application, thrust force magnitude, control direction, moment arm and number of thrusters etc. To carry out the study, a mathematical control mechanism for the control of spinning projectiles using impulse thrusters is developed in PRODAS software. All influential parameters discussed above are varied and their effect on range and mainly on drift is observed. It is observed that impulse thruster should be located forward of the

center of gravity for greater drift correction for a given thruster magnitude. It is seen that that when the thruster is located forward of the center of gravity, the yaw cycle oscillation following the impulse is in a direction opposite to the desired correction direction.

Along with this, from the point of view of application time of thruster, it is seen right after the vertex along the trajectory of the projectile, the earlier the thrust control is applied the more drift correction can be achieved.

Nomenclature
F_{SQB} = Lateral Thrust Force
CP_{SQB} = Axial Location of thruster from nose
φ_{USER} = User directed Control force application
γ_{SQB} = Orientation of squib or thruster w.r.t. to orientation
CGCG = ($CG - CP_{SQB}$) projectile's longitudinal axis

1. Introduction

Six-degree of- freedom (6-DOF) computations are carried out applied to the actual parameters of a generic 155-mm artillery shell. Efforts were made to observe the effect of impulse thrusters' capacity in terms of applied thrust magnitude, duration, time of application, moment arm & other related parameters to achieve the greatest amount of correction on the projectile trajectory.

2. RBD Mathematical model with Lateral thrust

Six-degree-of-freedom (6-DOF) rigid body dynamic model is used to simulate the trajectory of a projectile. Equation of motion are modified to include the effect of lateral thrust in body reference frame.

In GNC module of PRODAS three options are given to apply control direction for lateral thrust application.

1. Roll option 1 - Earth Fixed without spin influence ,$\Phi_{\mathbf{sqb}} = \varphi - \varphi_{user}$
2. Roll option 2 - Earth Fixed with spin influence, $\Phi_{\mathbf{sqb}} = \varphi - \varphi_{user} - \pm\dot{\emptyset}(\Delta t)$
3. Roll option 3 - Body Fixed, $\Phi_{\mathbf{sqb}} = \varphi$

For the present work, Body fixed roll option was chosen. Aerodynamic force and moments acting on the projectile when lateral thrust is applied is given by following set of equations:

$$\begin{bmatrix} X \\ Y \\ Z \end{bmatrix}_{BRF} = F_{SQB} \begin{bmatrix} \mathrm{Sin}\Gamma_{SQB} \\ \mathrm{Cos}\Gamma_{SQB}\,\mathrm{Sin}\emptyset_{SQB} \\ \mathrm{Cos}\Gamma_{SQB}\,\mathrm{Cos}\emptyset_{SQB} \end{bmatrix}$$

$$\begin{bmatrix} L \\ M \\ N \end{bmatrix}_{BRF} = \begin{bmatrix} 0 \\ Z * CGCP + X * \frac{d}{2} * \cos\emptyset_{SQB} \\ -Y * CGCP + X * \frac{d}{2} * \sin\emptyset_{SQB} \end{bmatrix}$$

3. Guidance and Control (GNC) Algorithm

The trajectory simulations were performed using the GNC module of prodasversion 3.6.11. The impulse thrusters' parameters include the start time, the duration, the thrust, the axial location, the orientation and roll angles were varied one by one.

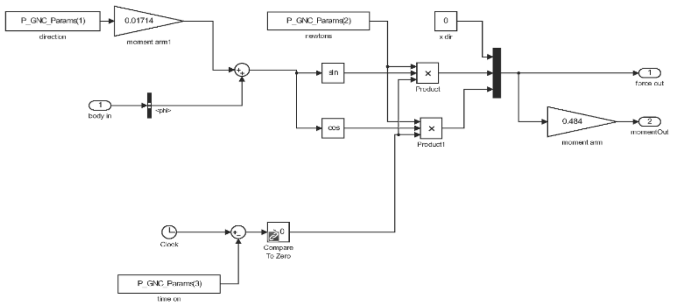

Figure 1: GNC algorithm for thruster based control

4. Results and Discussions:

As mentioned earlier, one of the main goals of this study is to establish the optimum configuration for thrusters mounted on an artillery projectile. All parameters such as thrust capacity, thrust duration, time of application and moment arm, number of thrusters were varied and their effect on range and drift was observed.

A. Case I: Thrust Variation

(i) **Moment arm = 3 Cal from nose**

(ii) **Control Direction = 270 deg**

(iii) **Time of application of thrust = 30 sec**

Effect on projectile's drift by varying magnitude of thrustisstudied first by using impulse thruster of 20 N, 30 N, 40 N, 50 N and 60 N capacity. The impulse thrusters are set off at a flight time of 30 seconds out of total flight time of 85.6 seconds. Thruster are kept on for the duration of five seconds .The results of the study are presented in Figures 2(a) & (b).

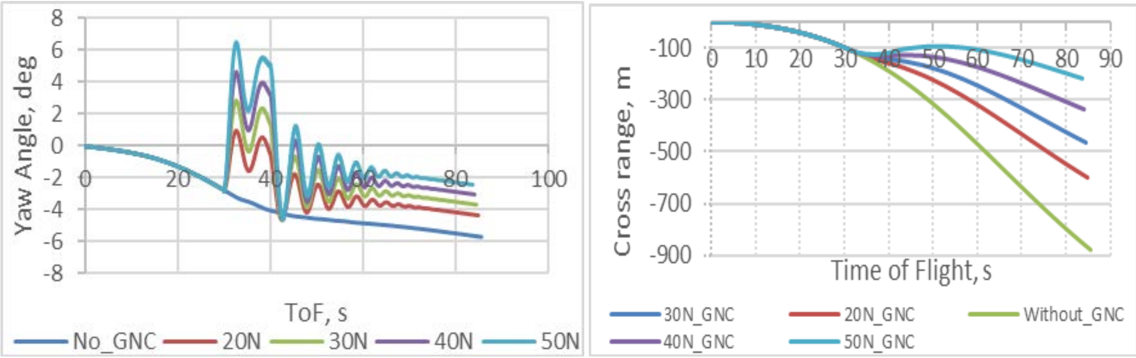

Fig 2(a) & (b): Yaw angle variation with the application of varying capacity of thrusters during flight; Cross range vs time of flight

The effect of the thrust magnitude on the trajectory correction is estimated. It is observed that projectile has a tendency to yaw when disturbed by the application of control force as shown in figure 2(a).

Fig 2(b) shows, the drift correction achieved with the 20 N thruster. Referring to Figure 2(b), for a single 20 N thruster located behind the center of gravity at 3 calibers from the nose tip, a drift correction of about 145 m can be obtained in either directions.

B. Case II: Time of application of Thrust during Trajectory

(i) **Moment arm = 3 Cal from the nose**

(ii) **Thrust = 20 N**

(iii) **Control direction = 270 deg**

Case II corresponds to application of spontaneous thrust at different point of time of flight during trajectory. Thrust was applied after 30 sec, 35 sec, 40 sec, 45 sec, 50sec, 55 sec and 60 sec after the launch of the projectile from the muzzle. Duration of thrust application was kept5 sec for all runs.

From the figure 3(b), it can clearly be seen that the time at which the thrust is applied also affects the drift correction achieved significantly. It was observed that after the vertex, the earlier the thrust control is applied the more drift correction can be achieved.

Not much change was observed in the range with the variation in point of application of thruster during flight.

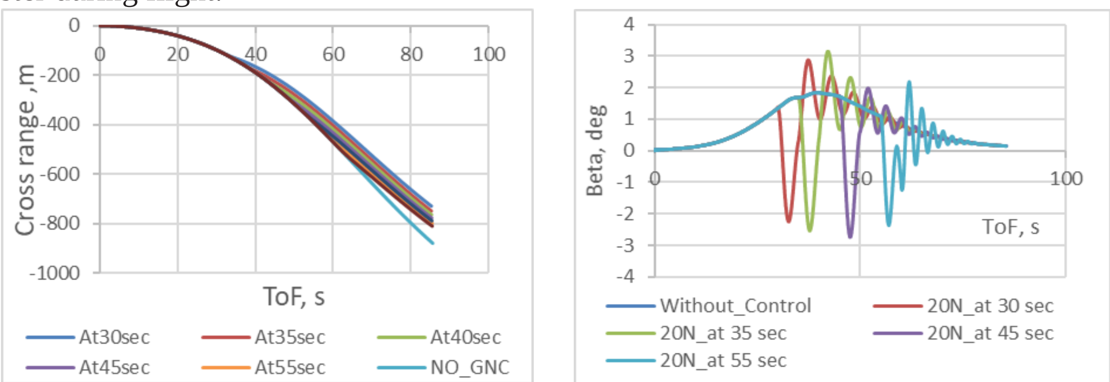

Fig 3(a) & (b): Variation in cross range & side slip angle with time of application of thrust

C. Case III: Moment Arm Variation
   (i) **Control direction = 315 deg**
   (ii) **Thrust = 20 N**
   (iii) **Time at which force is applied = 30 sec for 5 sec**

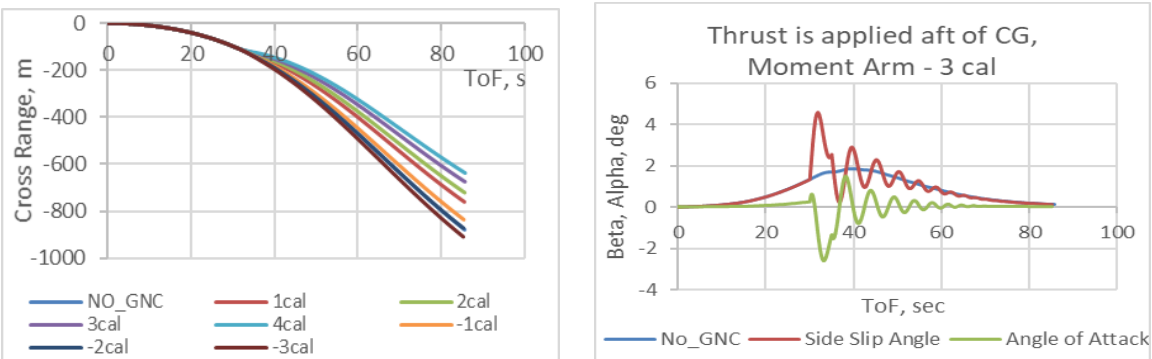

Fig 4(a) & (b): Variation in cross range & side slip angle with Moment arm variation

Case III studies the effect of moment arm variation or effect of location of thrusters along the longitudinal axis of the projectile. It was observed that the efficiency of the thruster in terms ofattainabletrajectory correction, increases when it is positioned forward to the CG of the projectile body.

It is observed that literally negligible amount of drift correction is obtained when the thruster is located close to 3 calibers aft of the center of gravity whereas sizeable correction is obtained when it is located 3 calibers forward of the center of gravity. This is explained by the fact that when the thruster is located forward of the center of gravity, the yaw cycle oscillation following the impulse is in a direction opposite to the desired correction direction as shown in Fig 5(a) & (b).

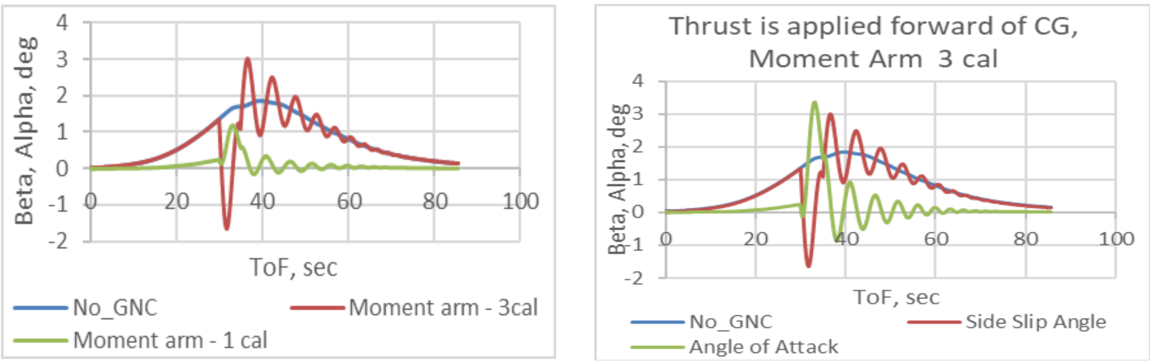

Fig 5(a) & (b): Yaw and Pitch cycle oscillation with the variation in Moment arm aft & forward of CG

D. Case IV: Thrust Duration Variation
   (i) **Control direction = 0 deg**
   (ii) **Thrust = 20 N**
   (iii) **Moment Arm = 3 cal**

It was observed that time of application of thrust affects the trajectory in both range and line to great extent. Figure 6 shows the drift correction that can be expected from a 20 N thruster fired for varying length of time before the impact. It is observed that duration plays a crucial role in the estimation of attainable correction.

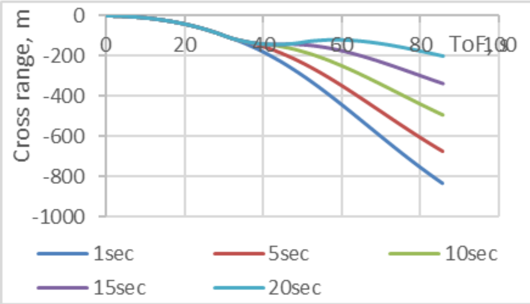

Fig 6: Cross Range variation wrt Thrust duration

Therefore, in the terminal phase of the trajectory, the thrusters can be used to make fine adjustment to the final impact point. Whereas, if thrusters can be initiated for 10 or more seconds from the impact time, a sizable drift correction is obtained.

E. Case V: Multiple Thrusters

By setting off more than one thruster along the projectile trajectory, it will be possible to achieve much greater course correction. This can be seen from Figure 7,which shows the cross range history of the projectile as a function Time of Flight.

Trajectories are shown for the cases where no thrusters were used and for the cases where 1, 2, 3, and 4, 20 N impulse thrusters are detonated. Each thruster contributes to drift correction of about 150 m. The five thrusters are initiated at flight times of 30, 35, 40, 45 and 50 seconds respectively. The setting off time of all the thruster was kept 5 sec. Figure 7 presents drift correction generated by a single thruster, located 3 calibers from the nose tip. It is observed that that the drift correction varies almost linearly with the impulse thruster magnitude. It also appears that an impulse thruster with a burning intensity of 20 N could give acceptable coursecorrections.

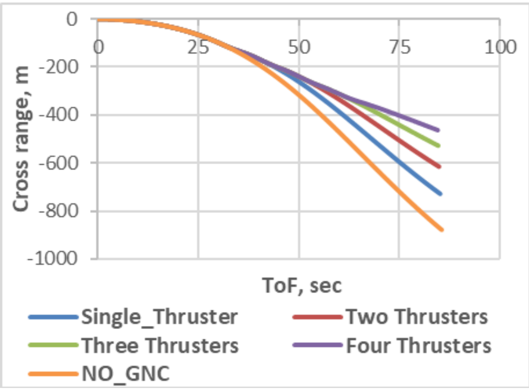

Fig 7: Cross Range variation wrt Number of Thrusters

5. Conclusion

Mathematical simulations were performed on an indirect fire artillery projectile using the GNC module of PRODAS. The aim of this study is to determine the suitable configurations of an impulse thruster which can provide the greatest amount of correction on the projectile trajectory. It is concluded that locating the impulse thruster forward of the center of gravity provide greater drift correction for a given impulse magnitude. It is also shown that impulse thrusters with a burning intensity between 20 and 30 N would provide adequate course correction for artillery projectile under consideration. Efficacy of usage of series of impulse thrusters along the trajectory of the projectile was investigated which helped to increase the amount of correction achieved in drift substantially. Validation of uncontrolled flight trajectory is done with the flight trial data.

6. Reference

[1] Guidos, B.; Cooper, G. "Closed Form Solution of Finned Projectile Motion Subjected to a Simple In-Flight Lateral Impulse", AIAA-2000-0767, *38th AIAA Aerospace Sciences Meeting and Exhibit*, Reno, NV, 2000.

[2] Likins, P. W. Attitude, "Stability Criteria for Dual-Spin Spacecraft" *Journal of Spacecraft and Rockets* 1967.

[3] Cloutier, G. J. Stable Rotation States of Dual-Spin Spacecraft. *Journal of Spacecraft and Rockets* 1968.

[4] Hall, C. D.; Rand, R. H. Spinup Dynamics of Axial Dual-Spin Spacecraft. *Journal of guidance, Control, and Dynamics* 1994.

[5] Cochran, J. E.; Shu, P. H.; Rew, S. D. "Attitude Motion of Asymmetric Dual-Spin Spacecraft", *Journal of Guidance, Control, and Dynamics* 1982.

[6] Tsuchiya, K. Attitude Behavior of a Dual-Spin Spacecraft Composed of Asymmetricbodies. *Journal of Guidance, Control, and Dynamics* 1979.

[7] Yang, H. X. Method for Stability Analysis of Asymmetric Dual-Spin Spacecraft. *Journal of Guidance, Control, and Dynamics* 1989.

[8] Viderman, Z.; Rimrott, F. P. J.; Cleghorn, W. L., "Stability of an Asymmetric Dual-Spin Spacecraft with Flexible Platform". *Journal of Guidance, Control, and Dynamics* 1991, *14*.

[9] Stabb, M. C.; Schlack, A. L. "Pointing Accuracy of a Dual-Spin Satellite due to Torsional Appendage Vibrations." *Journal of Guidance, Control, and Dynamics* 1991.

[10] Costello, M.; Peterson, A. "Linear Theory of a Dual-Spin Projectile in Atmospheric Flight" *Journal of Guidance, Control, and Dynamics* 2000.

[11] Mccoy, R. L. *Modern Exterior Ballistics*; Schiffer Publishing Ltd., Atglen, PA, 1999.

[12] Horwath, T. G., and Barnych, G., "Low Cost Course Correction (LCCC) Technology Applications," National Defense Industrial Association (NDIA) International Armaments Technology Symposium, Parsippany, NJ, 2004.

[13] Magnotti, P. J., Terhune, J., and Barnych, G., "Low Cost Course Correction (LC3) For Mortars Information Briefing," 38th Annual Gun, Ammunition and Missiles Symposium and Exhibition, Monterey, CA, 2003

[14] Burchett, B., Peterson, A., and Costello, M., "Prediction of Swerving Motion of a Dual-Spin Projectile with Lateral Pulse Jets in Atmospheric Flight," Mathematical and Computer Modelling, Vol. 35, No. 7, 2002.

[15] Guidos, B. J., and Cooper, G. R., "The Effect of a Simple Lateral Impulse on Kinetic Energy Projectiles in Flight," U.S. Army Research Laboratory, ARL-TR-2076, Aberdeen Proving Ground, MD, Dec. 1999.

[16] Wey, P., and Corriveau, D., "Trajectory Deflection of Fin- and Spin- Stabilized Projectiles Using Paired Lateral Impulses," Proceedings of the 24th International Symposium on Ballistics, New Orleans, LA, edited by S. Bless, and J.Walker, Vol. 1, Destech Publ., Lancaster, PA, 2008

[17] Ollerenshaw, D., and Costello, M., "On the Swerve Response of Projectiles to Control Input," U.S. Army Research Laboratory, ARLCR- 0604, Aberdeen Proving Ground, MD, April 2008.

Making of Solar Powered UAV and Increasing its Endurance (Time) with the Help of TEG (Thermo Electric Generator)

Shailesh kumar sah
School of Robotics
Defence Institute of Advanced Technology
Pune
kumarsahshailesh@gmail.com

Prajakta Koratkar
School of Robotics
Defence Institute of Advanced Technology
Pune
koratkarpv@gmail.com

***Abstract*—The paper briefly explains various advantages and problems of energy restrictions of UAV. The solution to all these problems is a renewable and clean energy i.e solar energy is discussed. Along with history of solar UAV, the type of UAV which should be used for solar mounting is also discussed. Not only that we have seen the major components of solar UAV in this paper. Selection and justification of c60 solar cells is given. After all these we know that the efficiency of solar cell can be increased to a limit that might be whichever solar cell, so we have one other power producing device other PV cells i.e. TEG (thermoelectric generator) which is a direct conversion device hence no movable parts nothing is required just waste heat or temperature difference. We discussed various positions where TEG can be used in brief and we have seen cad model of solar UAV with TEGs mounted on it. Also conducted experiment on TEG SP1848-27145, observations were recorded and subsequent graph between temperature differences vs voltage generated was plotted.**

Keywords- solar UAV, TEG, c60 solar cells, solar energy

1. Introduction

Now a days UAV benefits is not limited to military personal use, it has spread its leg in the life of civilian also for various purpose. Although UAV have various advantage the important thing is that it had reduce the risk

Of human life mostly in military application in case of war or surveillance in enemy territory, etc. It has open doors for new areas where earlier it was not possible for human to go that can be easily done with the help of UAV. Recently in last decade the use of UAV has highly increased due to its advantage in different areas like surveillance, remote sensing, natural disaster relief operation, etc. As with great power comes great responsibilities hence it should stand in competition and make its system more open-ended and resilient in terms of their potential.

Even though UAV gives so many aids, power restriction is a major issue which needs to be solved. As power source of UAV is fixed either it be fuel or battery as both have limits, like if we take example of battery once the UAV is off ground battery starts discharging with time and no other power source is there so for charging either it has to land on ground or it has to be dependent on other UAV. More number of batteries is not a solution to this problem as it will increase weight of the UAV and we know increase in weight in inversely proportional to endurance (time). same goes with the fuel type UAV as for more endurance more fuel is required and more fuel means more weight and more weight means less endurance.

With the implementation of solar cells on UAV, the UAV would be able to amass and store solar energy by the sun to be used for the flight.

The main motivation came from the environmental challenges that we are facing in our day-to-day life as the fossil fuels are limited in nature and polluting, even other power sources like a battery, etc provides limited endurance, so solar energy is the most abundant and clean energy among all the renewable sources of energy that can be used for this purpose.

It is made better with zero emission of solar energy than non-renewable energy and power sources. Another problem is although we have made Solar UAVs from small (toys) to larger UAVs up to 72m wingspans (Team Solar Impulse) and 2300kg aircraft, then also the endurance (time) is still the main issue. Solar PV Cells have a limit to maximum efficiency even after using the costliest solar material which gives the highest efficiency.so to overcome the challenges some other power producing devices should be used in addition to solar cells to increase endurance or efficiency.

2. History of Solar UAV

The very first flight of aircraft with solar power provision flew on 4th nov, 1974 in California, dry lake at camp. It was designed by R.J. Boucher with a contract with ARPA, flying sunrise I for 20 min at 100 m app. Altitude for its inauguration having wingspan of 9.76 m, weighing 12.25 kg. With the net output power of 450 W with 4096 solar cells.

Now today we can claim that we have made significant progress since the first solar aircraft on 4th Nov 1974 till today. Recent example of the round the world attempt that was done by team of solar impulse having the wingspan of 72m and having weight of 2300 kg. It is observed that a lot of work is successfully done in large wingspan (which is considered above 20 m) that is categorized as high-altitude long endurance, called as Hale class of the aircrafts powered by solar than the category of low altitude long endurance class called LALE. Ample of attempts were performed for a 48 hrs continuous flight with 3.2 m wingspan Sky Sailor [11]. On which 72 hrs long flight was performed using the updrafts. Also 5.6 m wingspan Unmanned Aerial Vehicle was developed for search and rescue missions on Atlantik solar.

A. Indian Solar UAV

The very first solar powered unmanned aerial vehicle, that is MARAAL-1 is a low altitude with long endurance solar powered UAV that increases the endurance with additional usage of solar cells in combination with batteries to power it.

Fig : 1 MARAAL 1

Specifications of MARAAL 1	
Weight	16 kg
Power Required to Cruise	- 210 Watt
Solar Power Extraction	-170 Watt (Avg, 1st March 2016)
Service- Ceiling	500m AGL
Endurance-	11 Hrs
Gliding -Ratio(L/D)	18
Payload-	5 kg

Fig 2: MARAAL-2

Specifications	
Weight	12 kg
Power Required to Cruise	160 Watt
Solar Power Extraction	245 Watt (Avg, 5th March 2017)
Service Ceiling	1000m AGL
Endurance	18 Hrs
Gliding Ratio(L/D)	20
Payload	7 kg

3. Selection of Type Of UAV

It is the most important thing before going to solar cells. UAVs are mainly of two types rotary and fixed wing. We have selected fixed wing type of UAV for solar implementation because we require large area to mount solar cells and also fixed wing UAV are generally more stable and have more efficiency in terms of flight time as compared to rotary ones.

4. Major Components of Solar UAV

- Solar Cell
- Electronic Speed Controller (ESC)
- Electric Motor
- Propeller
- Electrochemical Batteries
- Maximum Power Point Tracker

A. Solar cell

Solar cell basically consists of a p-n junction that generates emf when solar radiation falls on the it. The principle of working of it is photovoltaic effect as the photodiode, except that no external bias is applied and the junction area is kept much larger for solar radiation to be incident because we are interested in more power.

We will see about solar cells in a nutshell to understand its types and cost.

Types of solar cells: There are broadly three types of solar cells

(i) I GENERATION that is silicon wafer based.
(ii) II GENERATION that is thin film
(iii) III GENERATION that is latest technology emerging

I GENERATION: as its name suggests these are used from long time and of two types monocrystalline and polycrystalline.

II GENERATION: these are divided into three parts Cadmium Telluride, Amorphous Silicon, and Copper Indium Gallium Di-Selenide. These are have very thin light absorbing capability.

III GENERATION: These are mostly under research and not available for purchasing. The solar cells which falls under this category are Nano crystal based, Polymer based, Polymer based, Concentrated solar cells, Perovskite, etc.

B. Electronic Speed Controller (ESC)

It is used to control the speed of the brushless motor. Its rating is specified by the maximum current supplied to brushless motor. The common speed control method is PWM.

C. Electric Motor

In UAV we basically use two types of motor

Brushless DC motor: It is used in propeller for thrust

Servo motor: It is used to change the direction of UAV

D. Propeller

It is a mechanical device consisting of rotary blades to provide thrust.

E. Electrochemical Batteries

To store the energy generated by solar power for emergency situation.

F. Maximum Power Point Tracker

It the most important component of solar UAV as it gives the optimum power to the battery from solar cells. It is connected between solar cell and battery.

5. Solar Cell Selection for UAV

Type of solar cells	Max efficiency achieved
Si Monocrystalline (C60)	22.9 ± 0.6
Si Polycrystalline	18.5 ± 0.4
Si Thin film	8.2 ± 0.2
GaAs thin film	28.9 ± 1.0
CIGS	15.7 ± 0.5
CdTe	17.5 ± 0.7

After doing all the market survey in detail about which solar cell to be used, we finally came to a solution of using C60 SunPower solar cells as its efficiency is about 23% and it is cheaper in cost as compared to GaAs thin film which is about 30%. As C60 is monocrystalline it is far better than polycrystalline solar cells.

C60 Sun Power Specifications:-

Parameter	Value
Peak Power	3.63 Watt
Efficiency	23.7 %
Peak Voltage (Vmpp)	0.55 Volt
Peak Current (Impp)	6.6 Amp
Open-circuit Voltage (Voc)	0.649 Volt
Short-circuit Current (Isc)	6.996 Amp
Length	125 mm
Width	125 mm
Thickness	0.165 mm

Fig :3 C60 solar cell

It has a peak power of 3.63 watt with **23.7%** efficiency, Super light (**7 grams**) so it does not significantly increase the weight of the UAV that is good thing for UAV as it is itself lightweight, super thin (**0.165 mm**) this is important as it does not affect the shape of wing, flexible up to **30°** so that it can be easily get adjusted with the shape of wings .So all these characteristics makes it suitable to be used for Solar UAV.

6. Thermo Electric Generator (TEG)

Thermo electric effect is a phenomenon by which electrical energy is directly converted from thermal energy and vice-versa. As it is direct conversion device no moving parts or working fluids well for that matter is required. There are different methods in which solar radiation can be used for power generation other than PV cells, TEG is one of them others are not useful because either very high temperature difference is required or they convert solar radiation to thermal only.

Thermoelectricity was first discovered in 1821 by Thomas Johann Seebeck. He accidentally found that if we took a metal bar and if there is a temperature gradient across that metal bar, then he was able to show that there is actually a voltage that existed between the 2 ends of the bar. Seebeck also showed that we can write this e.m.f that is created is directly proportional to the temperature difference ΔT and the proportionality constant was named as Seebeck Coefficient.

Seebeck coefficient, **S = ΔV/ΔT**
where **ΔV** is the potential difference in V
ΔT is the temperature difference in K.

In 1834, Jean Charles Athanase Peltier discovered Peltier effect. Peltier effect is the reverse of Seebeck effect which means that if a direct current flows through a pair of junctions of dissimilar materials, then a temperature difference is created across the 2 junctions resulting in heat flow.

Qpeltier = (Π1 – Π2)I
where Π1 and Π2 are Peltier coefficients
I is the current from point 1 to 2 in A
Qpeltier is the heating or cooling rate of junctions in J.

Relationship between Peltier coefficients and Seebeck coefficient

Π1 – Π2 = S1-2 T
Where, T is the absolute temperature of the junction that we are talking about.

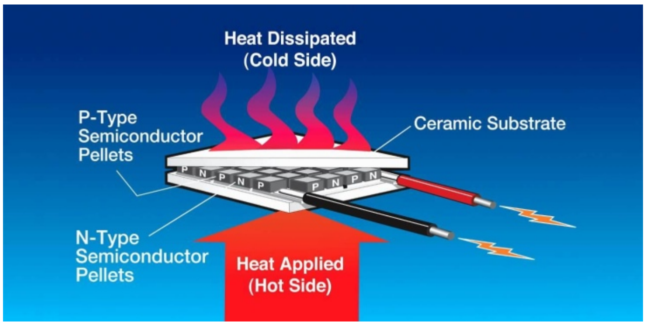

Fig 4: working of TEG

However, the use of metals and metal alloys as conductors the in thermoelectric modules limited its application. In the late 1930s, thermoelectricity as a source of electrical power received and renewed interest with the development of synthetic semiconductors which has a better Seebeck coefficients at 5 % thermal to electrical conversion efficiency. In 1950s, with improved thermal to electrical conductivity ratio led to even higher conversion efficiencies to up to 10 %. This was possible by alloying semiconductor materials with isomorphous elements.

A. Testing of TEG (thermoelectric generator)
Experimental Setup: It consist of**:**
- TEG SP1848 27145 SA
- Digital thermometer
- DMM
- Two metallic container, one empty and other with water inside it.

In this experiment first we have joined the connections of DMM with the TEG to measure the voltage. After that we have placed TEG (cold side) on empty metallic container at room temperature.

After that we have boiled the water in second metallic container which we will be kept at the top of the TEG (hot side). After that we have measured the temperature and corresponding voltage generated.

Fig 5- experimental setup

Fig 6 - measurement of voltage

TEG used: SP1848-27145

Fig 7: TEG SP1848-27145

Model	SP1848-27145
Open Circuit Voltage (V)	4.8
Operating Temperature (°C)	0 to 150
Maximum Temperature(°C)	150
Wire Length(mm)	350
Length (mm)	40
Width (mm)	40
Height (mm)	3.6
Weight(gm)	30

Table I: Observation Table of TEG Experiment

SR NO	TEMP DIFFERENCE (DEG C)	VOLTAGE GENERATED (VOLTS)
1	73	0.66
2	53	0.42
3	43	0.34
4	33	0.26
5	23	0.18
6	19	0.15
7	15	0.11
8	13	0.09
9	11	0.06
10	9	0.05
11	7	0.04
12	5	0.02
13	3	0.0198
14	2	0.0064
15	1	0.0028

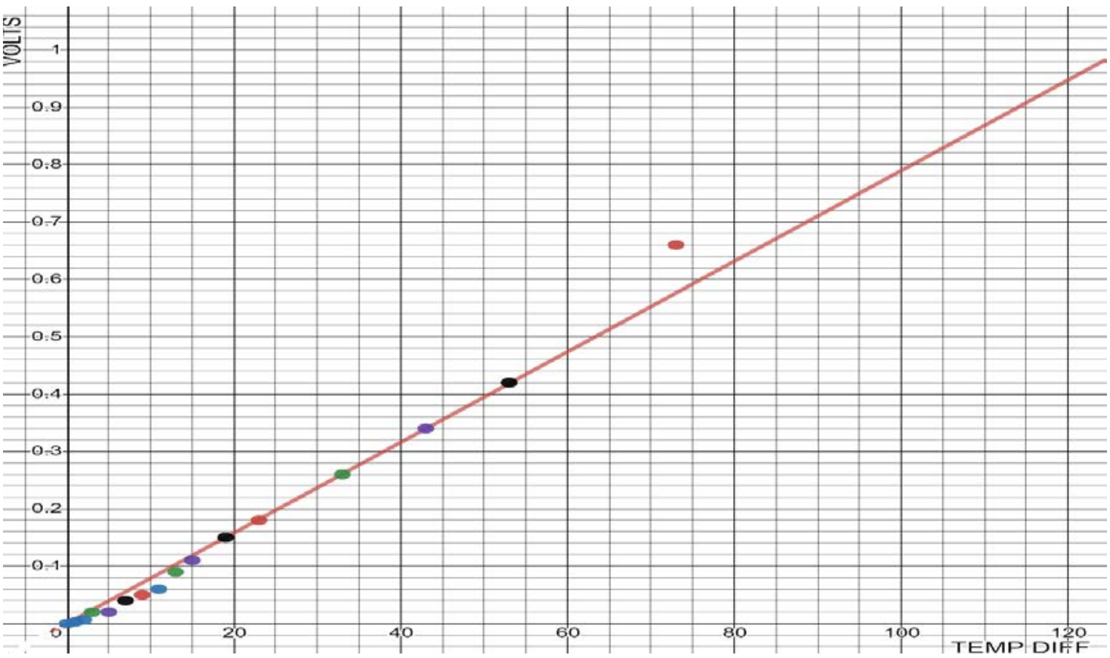

Fig 8: graph 1 of volt vs temp diff of TEG SP1848-27145

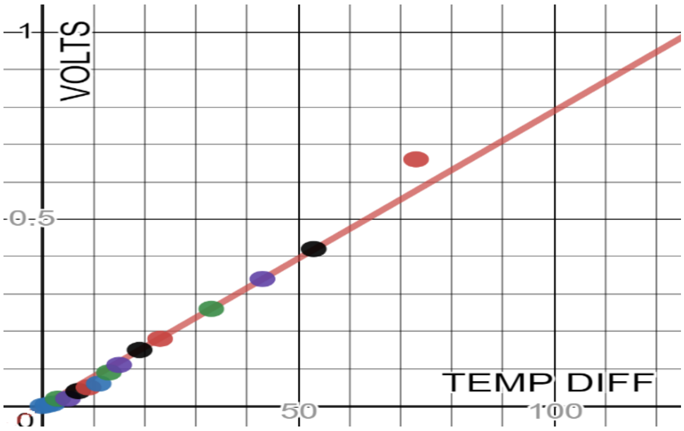

Fig 9: graph 2 of volt vs temp diff of TEG SP1848-27145

- From this graph we can see the graph is almost linear
- It has slope of m=0.007894
- From these graphs and table we can see that a very high temp difference is required for a considerable amount of voltage generation.
- The value of voltage generated for a particular temp difference varies for different models of TE

B. TEG in Solar UAV Model

As we know TEG converts heat (temperature difference) directly into electricity so we can install TEGs where heat is dissipated in UAV like motors, electronic components, etc. we have proposed one model where we have used TEG below the surface of solar cells (back side) and inside the wing as shown in figure so that the heat from solar cells can be used as energy. The advantage of this model is that a large number of TEGs can be used so that a good amount energy can be generated from waste heat.

We have purposely kept back side of wing open so that placement of TEGs can be seen easily.

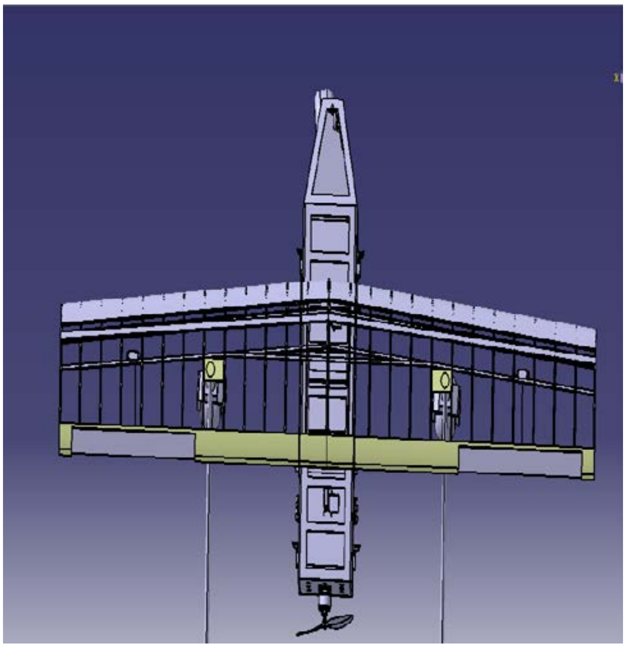

Fig 10: UAV without solar cells and TEGs mounted.

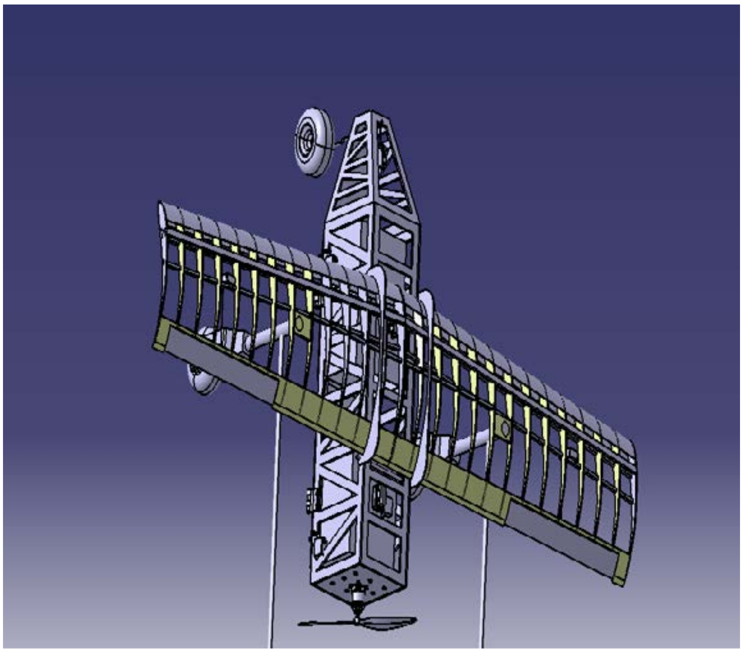

Fig 11: Different view showing UAV without solar cells and TEGs mounted

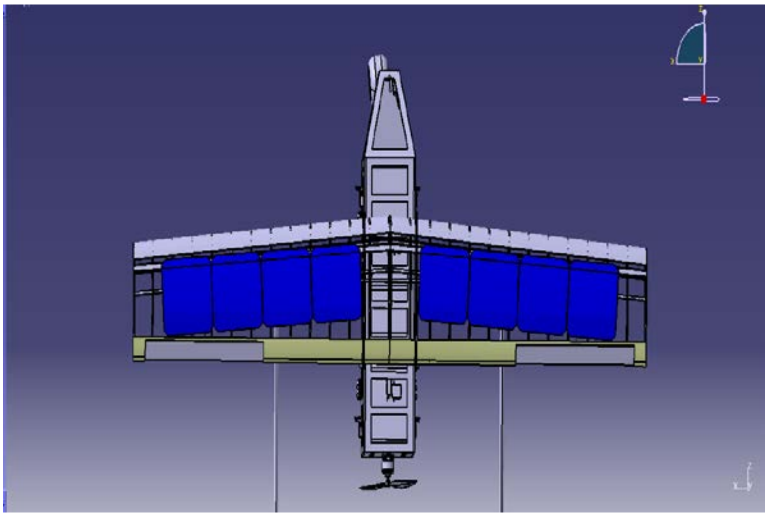

Fig 12: top view of solar UAV

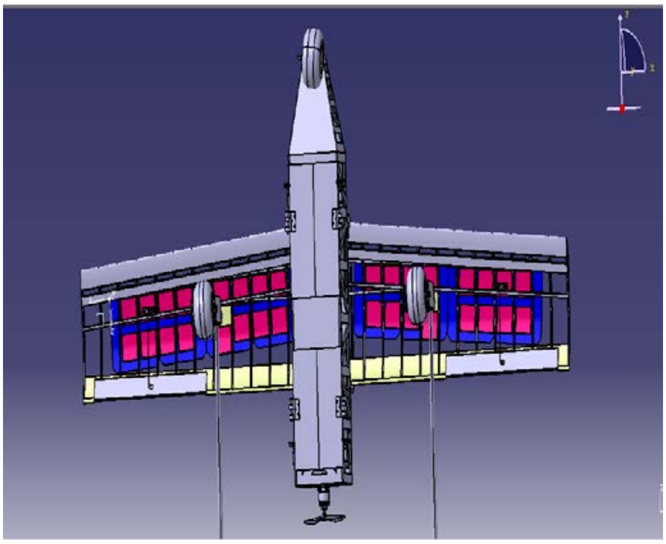

Fig 13: back side of solar UAV showing TEGs

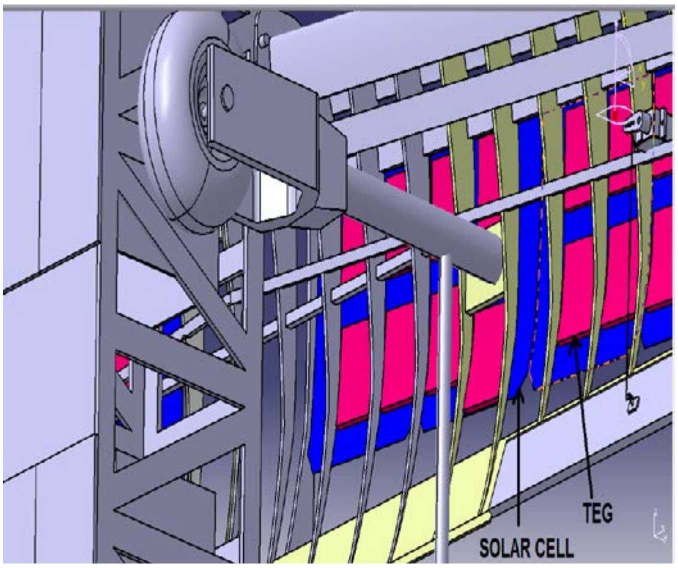

Fig 14: Showing of TEGs and Solar cells

7. Conclusion

For increasing the endurance of solar UAV some power sources other than PV cells is required. TEG is among them, should be studied in more detail in future. other methods than TEG should also been seen for increasing endurance.

8. References

[1] Baljit Singh Bhathal Singh, PhD thesis, Power Generation from Solar Pond Using Thermoelectric Generators
[2] NPTEL lectures on Energy Conservation and Waste Heat Recovery, Prof. Prasanta Kumar Das and Prof. Anandaroop Bhattacharya, Department of Mechanical Engineering Indian Institute of Technology, Kharagpur
[3] Shruti Sharma1, Kamlesh Kumar Jain1, Ashutosh Sharma2* CMD College, Bilaspur, India 2Materials Science and Engineering, University of Seoul, Seoul, South Korea Solar Cells: In Research and Applications—A Review
[4] Semiconductor Electronics: Materials, Devices and Simple Circuits, class XII physics NCERT
[5] H. Bahrami Torabi, M. Sadi, A. Yazdian Varjani, Solar Power System for Experimental Unmanned Aerial Vehicle (UAV); Design and Fabrication
[6] Vijay Shankar Dwivedi, Jay Patrikar, Amulya Addamane, A.K. Ghosh MARAAL: A Low Altitude Long Endurance Solar powered UAV For Surveillance and Mapping Applications, Indian Institute of Technology, Kanpur
[7] Vijay Shankar Dwivedi, Prashant Kumar, A.K. Ghosh, G. M. Kamath, Selection of Size of Battery for Solar Powered Aircraft
[8] https://www.google.com/url?sa=i&url=https%3A%2F%2Fwww.youtube.com%2Fwatch%3Fv%3DYhynSkFlJOs&psig=AOvVaw0f6LHoTBAcD7GCegN55W88&ust=1619375676358000&source=images&cd=vfe&ved=0CAIQjRxqFwoTCKjd9NrCl_ACFQAAAAAdAAAAABAE
[9] https://www.iitk.ac.in/aero/maraal

AI Enabled Voice Assistant for Aircraft Maintenance

RK Mohapatra
Defence Institute of Advanced Technology
Pune
rajmail.rajesh@gmail.com

Saurav Kumar
Defence Institute of Advanced Technology
Pune
sauravkumaree@gmail.com

Sanket Mohanty
Defence Institute of Advanced Technology
Pune
sanket_mohanty@diat.ac.in

CRS Kumar
Defence Institute of Advanced Technology
Pune
suthikshnkumar@diat.ac.in

Abstract — **Aircraft maintenance is a very critical task that demands thorough professionalism of the maintenance crew. Every maintenance activity is mentioned in the form of Standard Operating Procedures (SOPs) which are generally provided in the form of voluminous printed manuals or e-documents in a handheld device, such as a tablet or PDA. An air warrior is required to follow the instructions in the manual while undertaking any activity on the aircraft. This compels the air warrior to engage his working hand for holding the manual/PDA. As an approach to provide a hands-free solution to refer to the maintenance manual while undertaking any aircraft maintenance activity, it is proposed to implement an AI-enabled voice assistant. Augmented Reality/Virtual Reality devices are now becoming inherent tools for aircraft maintenance activities. Thus, using an AI-enabled voice assistant integrated with these devices will facilitate the usage of maintenance manuals in audio-visual mode, rather than using a book or PDA. Sufficient development has been done in the field of Automatic Speech Recognition (ASR) and Natural Language Processing (NLP) to develop a voice assistant for aircraft maintenance works. This paper brings out various developments made in the said domain and also discusses how different subsystems can be combined to develop and implement a voice assistant for aircraft maintenance.**

Keywords—chatbot, voice assistant, NLP, aircraft maintenance

1. Introduction

Aircraft maintenance is a very critical activity which is to be performed exactly as mentioned in corresponding manuals. An air warrior is required to use his/her hands to hold and read through the procedure while working on the aircraft. Referring to the SOP in the manual incurs a considerable amount of time for the activity performed and, therefore, causes an increase in downtime. If the procedures can be made available through an interactive audio interface on a wearable device, then the maintenance crew need not refer to the document/PDA frequently and will have his/her both hands-free to work on the aircraft. This will not only ease the working condition of an aircraft but also, increase the productivity of the maintenance crew.

Apple Siri, Google Assistant, and Alexa, etc. have made interaction with ICT devices enjoyable. There have been significant advances made in the field of Artificial Intelligence wherein an interactive voice assistant can be developed with a much less error rate. An AI-enabled voice assistant will comprise of an ASR engine in the input module to receive user query in the form of audio commands and perform speech to text, a chatbot that can text user queries as input and output text response, and finally a text to speech module that converts the response text to an audio signal to be delivered to the user. Among these three modules, text-to-speech conversion is not very difficult and can be achieved easily without any error. The critical modules are speech recognition and a chatbot for response generation.

2. Basic Components of the Proposed System

A. Automatic Speech Recognition (ASR)

Automatic Speech Recognition (ASR) [1-3], which is aimed to enable natural human–machine interaction, has been an intensive research area for decades, especially after the development of Deep Learning technology. The basic architecture of an ASR system is depicted in Figure-1.

An ASR can generally be divided into four modules: a pre-processing module, a feature extraction module, a classification model, and a language model. Pre-processing module is responsible for reducing the signal-to-noise ratio of the input audio signal. After pre-processing, the clean speech signal is then passed through the feature extraction module. Features are usually the predefined number of coefficients or values that are obtained by applying various methods to the input speech signal. The feature extraction module should be robust to different factors, such as noise and echo effect. The most commonly used feature extraction methods are Mel-frequency cepstral coefficients (MFCCs), linear predictive coding (LPC), and discrete wavelet transform (DWT). The classification model is used to predict the text corresponding to the input speech signal. The classification models take input of the features extracted from the previous stage to predict the text. Like the feature extraction module, different types of approaches can be applied to perform the task of speech recognition; Hidden Markov Model (HMM)- Gaussian Mixture Model (GMM) is the most famous classification model. This model uses joint probability distribution formed using the training dataset, and that joint probability distribution is used to predict the future output. Language models consist of various types of rules and semantics of a language. Language models are necessary for recognizing the phoneme predicted by the classifier; and is also used to form n-grams, words, or sentences using all of the predicted phonemes of a given input. The performance of an ASR system is evaluated by its Word Error Rate (WER) and Real-Time Factor (RTF).

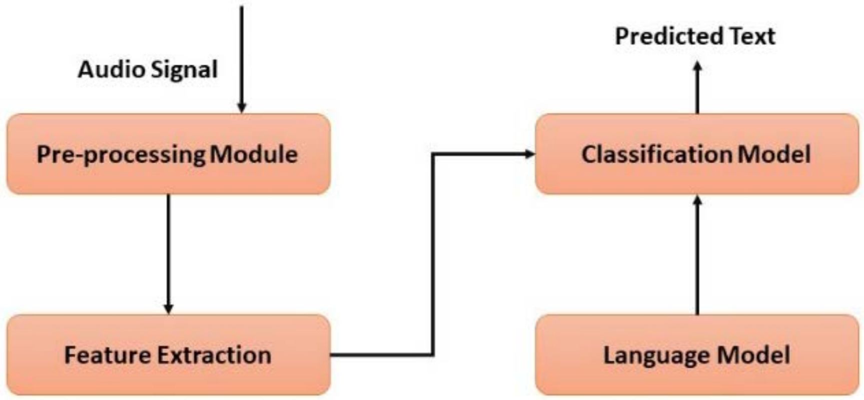

Fig 1: Basic structure of ASR system

B. Chatbot

Chatbot is nothing but a machine that is intelligent enough to understand your request and then formulate your request in such a way that is understandable by other software systems to request the data you need, fetch the response, and output it to the user. The usage of chatbots has seen a sudden growth in popularity in all sectors of businesses. It is predicted that 80% of businesses are projected to integrate some form of chatbot system by 2021 [4].

Effective usage of chatbots can be seen on e-commerce platforms, banking websites, messaging platforms, etc. The aviation industry is yet to see its usage in assisting in aircraft maintenance works. Chatbots are of two types; firstly, closed domain – having a limited dataset to perform a task and limited by the domain knowledge, secondly, open domain – where the whole internet serves as a dataset for response generation. There are three types of tasks performed by a chatbot:

(i) Question & Answer
(ii) Information Retrieval
(iii) Transactional

The basic structure of a chatbot is as shown in Figure-2. A user query is an input as text to the bot. From this input, the system identifies the intent (intent classification) of the user and also, performs entity extraction (Named Entity Recognition). Based on the intent and entities, action (Q&A or Information Retrieval or Transactional) to be performed is decided. Based on the action, a suitable response is generated and output to the user. The two most challenging tasks here are, intent classification and Named Entity Recognition (NER). There are different approaches to perform these tasks efficiently. An overview of the latest methodology of performing these tasks is given subsequently.

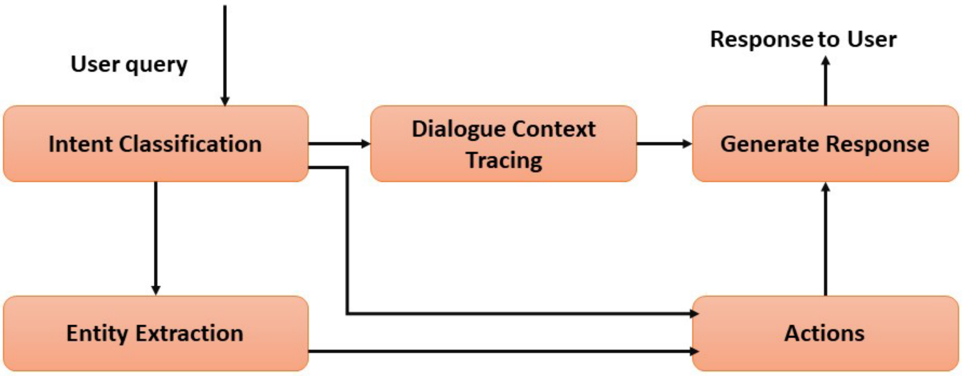

Fig 2: Basic structure of Chatbot

3. Related Work

Since the development of ELIZA [5] in 1966, chatbots have been developed for some specific applications and this has seen a sudden surge in the last decade. In 1995, the chatbot ALICE was developed which won the Loebner Prize, an annual Turing Test, in years 2000, 2001, and 2004. It was the first computer to gain the rank of the “most human computer”. ALICE [6] relies on a simple pattern-matching algorithm with the underlying intelligence based on the Artificial Intelligence Markup Language (AIML). Chatbots, like Smarter Child in 2001, were developed and became available through messenger applications. The idea of Watson was coined in 2006 was being designed to compete on the TV show “Jeopardy”. In its first pass, it could only get about 15 percent of answers correct, but later Watson was able to beat human contestants regularly. In 2010 Siri, an intelligent personal assistant was launched as an iPhone app and then integrated as a part of the iOS. In 2012, Google launched the Google Now chatbot. It was originally codenamed “Majel” after Majel Barrett, the wife of Gene Roddenberry and the voice of computer systems in the Star Trek franchise; it was also codenamed as “assistant”. 2014 saw the release of Amazon Alexa. The word “Alexa” has a hard consonant with the X, and therefore it can be recognized with higher precision. This was the primary reason Amazon chose this name. Cortana, a virtual assistant created by Microsoft in 2015. Cortana can set reminders, recognize a natural voice, and answer questions using information from the Bing search engine. The Artificial Intelligence Markup Language

(AIML) was created from 1995 to 2000, and it is based on the concepts of Pattern Recognition or Pattern Matching technique. It is applied to natural language modeling for the dialogue between humans and chatbots that follow the stimulus-response approach. It is an XML-based markup language, and it is tag-based. Following AIML, various other techniques such as Latent Semantic Analysis (LSA), Chatscript, Rivescript, etc. were also used in the chatbot development before usage of Natural Language Processing (NLP) and Natural Language Understanding (NLU). Text classification using NLP was achieved by Bag-of-Words (BoW) model and this was improved by using Word2Vec model. Currently, there are state-of-the-art language models like BERT [7] (Bidirectional Encoder Representations from Transformers). Further, there have been many approaches to fine-tune performance using BERT models and recently, Microsoft's DeBERTa [8] (Decoding-enhanced BERT with disentangled attention) has outperformed humans in Natural Language Understanding.

Similar to chatbot technology, many advances have been made in the field of speech recognition. The conventional speech recognition systems are based on representing speech signals using Gaussian Mixture Models (GMMs) that are based on hidden Markov models (HMMs). Also, some studies9 show that Deep Neural Networks yield better results than classical models. There are several commercial and open-source systems available that can be used for this task. Google speech API, Microsoft API speech, Alexa API, IBM Watson are a few of the ASR systems available to be used online with an API. Similarly, to build customized ASR systems, open-source systems such as Kaldi [12], ESPNet [13], OpenSeq2Seq [14], and wav2letter++ [16] are also available. CMU Sphinx is also a popular ASR system developed at Carnegie Mellon University (CMU). Currently, CMU Sphinx has a large vocabulary, speaker-independent speech recognition codebase, and its code is available for download and use. Various studies have been conducted to show the comparison of these ASR systems, be it commercial or open-source.

4. Comparison of ASR Systems

Microsoft has focused on increasing emphasis on speech recognition systems and improved the Speech API (SAPI) by using a context-dependent deep neural network hidden Markov model (CD-DNN-HMM) [11] to reach speech recognition of human parity. Google has improved its speech recognition by using new technology in many applications with the Google App such as Goog411, Voice Search on mobile, Voice Actions, Voice Input (spoken input to keypad), Android Developer APIs, Voice Search on desktop, YouTube transcription, etc. Google too employs various Deep Learning models to improvise its speech recognition engine. Code of Microsoft API speech and Google speech API is not available for download, these ASR systems can be used online only. CMU Sphinx, on the other hand, has made its code available for download and can be used offline. Sphinx has many versions available for download. A study [10] on comparison of Sphinx-4, Microsoft API, and Google API by using some audio recordings that were selected from many places with the original sentences showed that Sphinx-4 achieved 37% WER, Microsoft API achieved 18% WER and Google API achieved 9%. Thus, Google speech API is the best ASR system available to be used online.

Apart from these, there are many open source ASR systems available built on frameworks like PyTorch and Tensorflow using open-source tensor libraries. A recent study by Facebook AI has developed **wav2letter++,** built mostly using Arrayfire [15] tensor library. The study also brings out a comparison of Kaldi, End-to-End Speech Processing Toolkit (ESPNet), OpenSeq2Seq, and wav2letter++ models. The study [16] incorporated a comparison of using both Convolutional Neural Network (CNN) and Deep Neural Network

(DNN) based architectures. It concluded that wav2letter++ performs better than the other available systems with a Word Error Rate (WER) of approximately 4.92% which is even better than human performance.

5. Chatbot for Aircraft Maintenance

Aircraft maintenance activity can employ a type of Q & A chatbot that takes the user's query for any maintenance procedure as text and fetch corresponding response accurately. This task involves two of the most important operations in a chatbot, i.e, intent classification, and Named Entity Recognition (NER). These tasks involve the processing of natural language text and trigger the system for necessary action based on the understanding of the language. The user is free to input a query for a single intent in multiple ways that cannot be fully documented, therefore, a language model is used to process the user input and classify it to most likely intent. There are many language models available, but very recently BERT and its derivatives have shown promising performance beyond human parity. Also, BERT works well when the number of training examples for a classification work is higher, more than 100. However, for aircraft maintenance purposes, the number of training examples for intent classification will be very small, approximately 10. In this case, BERT model can be finetuned to match the expected performance. So far, there are no open-source dataset existing that can be used to finetune the BERT model for aircraft maintenance-related query handling. Thus, a specific dataset is required to be built for this task.

Any activity related to aircraft maintenance is mentioned in the form of standard operating procedures (SOP) that lists all the activity to be performed step by step. Thus, the task of the chatbot is just to match the user query to a particular task and thereafter, fetch the complete SOP and respond to the user in a step-by-step fashion. Here, pauses for response can be incorporated by using regular expressions to recognize paragraph change. Thus, the whole of the manuals need not form the part of the dataset for intent classification or NER, rather, only the index of the manual will do. Figure-3 shows a detailed architecture of the AI-enabled voice assistant system for aircraft maintenance.

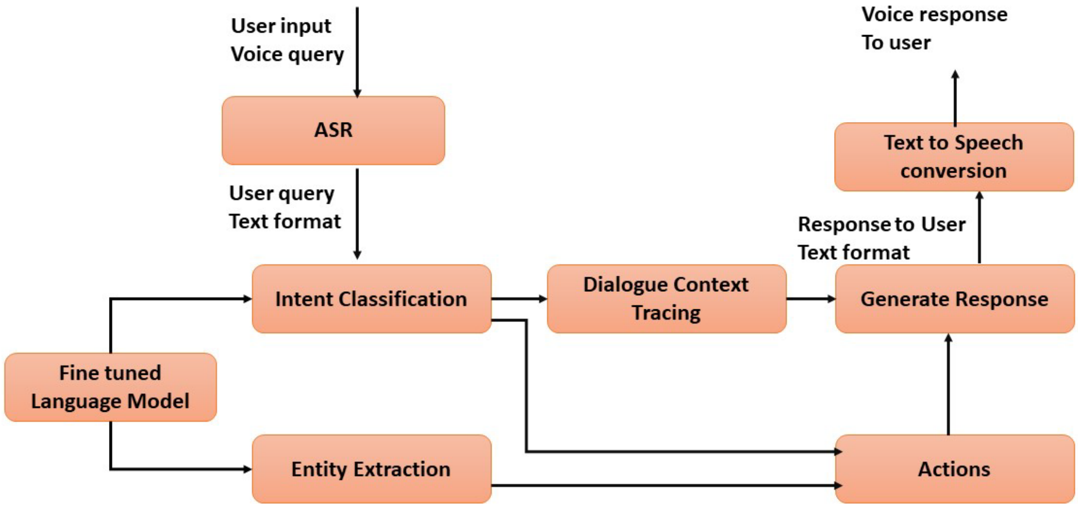

Fig 3: Proposed structure of AI-enabled Voice Response System

6. Evaluation Criteria

The performance of an ASR is evaluated based on two metrics: firstly, Word Error Rate (WER) [18]. WER is calculated using the following formula:-

$$WER = (S+D+I)/ N = (S+D+I)/(S+D+C)$$

Where,

S is the number of substitutions,

D is the number of deletions,
I is the number of insertions,
C is the number of correct words,
N is the number of words in the reference (N=S+D+C)

Secondly, Real-Time Factor (RTF) is also a good measure of speech recognition systems. It is useful to consider the speed at which you receive your transcript after submitting your file. This is called the real-time factor (RTF) and is measured by dividing the time taken to transcribe the audio file by the duration of the audio. The more time it takes to transcribe, the worse it is.

Precision, accuracy, and F-measure are good measures of NLP techniques, however, when it comes to evaluating a chatbot, a more comprehensive measure is a BLEU [17] (Bilingual Evaluation Understudy), which is a score for comparing a candidate translation of the text to one or more reference translations.

7. Steps In Implementation

It has been seen so far that many open-source systems are available for the said task. However, when it comes to implementing this for specific task of aircraft maintenance, there are some critical steps involved. Python is the popular programming language for development of AI systems. Many open-source packages for speech recognition and NLP are available for the said task. The frameworks like Tensorflow and PyTorch make the task of developing a solution much easier. The major challenge is the non-availability of a dataset specific to the domain of aircraft maintenance. Thorough care has to be made to prepare this dataset that will be used to finetune the language model which will be used for both ASR and chatbot. Secondly, for finetuning the speech recognition module, a large set of audio samples specific to the domain of aircraft maintenance should be used. Finally, the database for the chatbot response should be crafted carefully covering all maintenance activities for which the proposed system is intended to be used.

8. Conclusions

Many businesses intend to incorporate a chatbot in their processes because of the promising results shown by the latter. An AI-enabled voice assistant for aircraft maintenance will not only bring in the application of Artificial Intelligence in aircraft maintenance but also, help the maintenance crew perform their task more efficiently when the whole manual is available hands-free. Usage of such a system will also minimize human error in aircraft maintenance activities. Considering the criticality involved and accuracy requirement in aircraft maintenance, it is suggested that during the development of such a system, necessary care must be given to choosing a base model of speech recognition for ASR and a language model for both ASR and chatbot. A carefully prepared dataset will not only render a higher level of performance but also will be an effective aid for aircraft maintenance.

9. References

[1] Dong Yu, Li Deng: Automatic Speech Recognition A Deep Learning Approach. ISBN: 978-1-4471-5779-3
[2] Wang, Y.Y., Yu, D., Ju, Y.C., Acero, A.: An introduction to voice search. IEEE Signal Process.Mag.25(3), 28–38 (2008)
[3] Mishaim Malik, Muhammad Kamran Malik, Khawar Mehmood, Imran Makhdoom: Automatic speech recognition: a survey. Multimedia Tools and Applications-2021 80(3):1-47, Springer. DOI:10.1007/s11042-020-10073-7
[4] https://linchpinseo.com/chatbot-statistics-trends/ [accessed on 24 Apr 2021]

[5] J.Weizenbaum, "ELIZA — A Computer Program For the Study of Natural Language Communication Between Man And Machine", Commun. ACM, vol. 9, no. 1, pp. 36–45, 1966. DOI: 10.1145/357980.357991

[6] Wallace, R.S.: The anatomy of A.L.I.C.E. In: Epstein, R., Roberts, G., Beber, G. (eds.) Parsing the Turing Test: Philosophical and Methodological Issues in the Quest for the Thinking Computer, pp. 181–210. Springer, Cham (2009). DOI:10.1007/978-1-4020-6710-5_13

[7] Jacob Devlin, Ming-Wei Chang, Kenton Lee, and Kristina Toutanova. 2019. BERT: Pre-training of deep bidirectional transformers for language understanding. In Proceedings of NAACL. arXiv:1810.04805

[8] https://www.microsoft.com/en-us/research/blog/microsoft-deberta-surpasses-human-performance-on-the-superglue-benchmark/.[Accessed on 24 Apr 2021]

[9] Ali Bou Nassif, Ismail Shahin, Imtinan Attili, Mohammad Azzeh, And Khaled Shaalan.: Speech Recognition Using Deep Neural Networks: A Systematic Review. IEEE Access, Feb 2019. DOI: 10.1109/ACCESS.2019.2896880

[10] Veton Këpuska, Gamal Bohouta. Comparing Speech Recognition Systems (Microsoft API, Google API And CMU Sphinx). Int. Journal of Engineering Research and Application. International Journal of Engineering Research and Applications 2248-9622(3):20-24. DOI:10.9790/9622-0703022024

[11] Frank Seide, Gang Li, Dong Yu.: Conversational speech transcription using context-dependent deep neural networks. In: Proceedings of Annual Conference of International Speech Communication Association (INTERSPEECH-2011), pp. 437–440

[12] Daniel Povey, Arnab Ghoshal, Gilles Boulianne, Lukas Burget, Ondrej Glembek, Nagendra Goel, Mirko Hannemann, Petr Motlicek, Yanmin Qian, Petr Schwarz, et al., "The kaldi speech recognition toolkit," in IEEE 2011 workshop on automatic speech recognition and understanding. IEEE Signal Processing Society, 2011, number EPFL-CONF-192584. ISBN: 978-1-4673-0366-8

[13] Shinji Watanabe, Takaaki Hori, Shigeki Karita, Tomoki Hayashi, Jiro Nishitoba, Yuya Unno, Nelson Enrique Yalta Soplin, Jahn Heymann, Matthew Wiesner, Nanxin Chen, et al., "Espnet: End-to-end speech processing toolkit", 2018. arXiv:1804.00015

[14] Oleksii Kuchaiev, Boris Ginsburg, Igor Gitman, Vitaly Lavrukhin, Carl Case, and Paulius Micikevicius, "Openseq2seq: extensible toolkit for distributed and mixed precision training of sequence-to-sequence models", 2018. arXiv:1805.10387

[15] Chris McClanahan Vishwanath Venugopalakrishnan Krunal Patel John Melonakos James Malcolm, Pavan Yalamanchili, "ArrayFire: a gpu acceleration platform," Proceedings of SPIE - The International Society for Optical Engineering, 2012. DOI:10.1117/12.921122

[16] Vineel Pratap, Awni Hannun, Qiantong Xu, Jeff Cai, Jacob Kahn, Gabriel Synnaeve, Vitaliy Liptchinsky, Ronan Collobert.: "wav2letter++: ICASSP 2019 - 2019 IEEE International Conference on Acoustics, Speech and Signal Processing (ICASSP). DOI: 10.1109/ICASSP.2019.8683535

[17] Papineni, K.; Roukos, S.; Ward, T.; Zhu, W. J. (2002). BLEU: a method for automatic evaluation of machine translation. ACL: 40th Annual meeting of the Association for Computational Linguistics; 2002, pp. 311–318.

[18] Klakow, Dietrich; Jochen Peters (September 2002). "Testing the correlation of word error rate and perplexity". Speech Communication. 38 (1–2): 19–28. DOI:10.1016/S0167-6393(01)00041-3

Foot Trajectory Planning for Legged Robot: A Linear-Cubic Curve Approach

Vijay Kumar Haldiya
Defence Institute of Advanced Technology
Pune
vijay_haldiya@hotmail.com

Pankaj Kumar Sharma
Defence Institute of Advanced Technology
Pune
pankaj_sharma@diat.ac.in

Abstract—**Robots are becoming more popular, more useful and one of the most researched topics with advancement in associated technologies. Legged robots, due to their all-terrain capabilities, are more popular among researchers. Foot trajectory planning is one of the areas in which lot of work still needs to be done. In this paper work related to foot trajectory planning based on linear-cubic curve is presented. A generalized equation time interval dependent is derived and implemented for trot and walking algorithm for quadruped robot.**

***Keywords*—Legged robot, foot trajectory, path planning**

1. Introduction

Era of personal robotics has begun. Initially limited to industrial robots, to assist or replace workforce in mass production, and with technology advancement which is available at relatively low cost and easily accessible, a shift is seen towards development of commercial and personal robots. A major research topic for robots is type of locomotion i.e. wheel, leg etc. Wheel and leg locomotion are equally popular among researchers but being more work needs to be done in the area of legged robots, such robots are attracting more scholars. The main reason of it is flexibility and adaptability in unstructured environment or difficult terrain.

First of its kind research work in the area of legged robotics that was first fully computer-controlled robot "Phoney Pony" was done by University of Southern California in 1966 [1] paved the way. Since then, a large number of walking robots, such as BISAM [2], WARP1 [3], KOLT [4], Tekken [5], HuboDog [6], p2 [7], HyQ [8], BigDog [9], Cheetah [10], ANYmal [11] etc., have been developed.

One of the key aspects in the legged robot locomotion is foot trajectory planning. Trajectory [12] of foot of a robot can be of various types such as elliptical based [15], compound cycloid [17], cubic-linear [16], parabolic [12], higher order polynomial [12], [13], Bezier Curve [14] etc. In all the above papers the trajectory generated for one leg into swing phase while other legs are in stance phase. There is a clear knowledge gap about how to add a balancing phase between two phases: one leg touches the ground and other leg goes into swing phase. The idea is to reduce computation load of balancing on controller by ensure balancing of robot before lifting of any leg for swing phase but no balancing computation during the swing phase of the leg.

In this paper we have derived cubic-linear foot trajectory equations which will allow the controller to provide a stability phase. This phase is part of stance phase but no swing phase of any other leg is allowed during this phase. These equations then applied to the robot to achieve walking and trot gait on plane surface.

2. Foot Trajectory Planning

As the contact between leg of the robot and ground changes the contact force also changes. The efficient motion is achieved when this force is minimized. A complete legged robot can be divided into two major structures first mainframe and second legs. While mainframe needs to be stabilized during motion or to follow a pre-determined motion strategy and legs should take any disturbance caused due to ground contact or any other disturbance caused by the environment including the mainframe. Thus, the foot trajectory planning should be such that the leg moves with continuous path and velocity profile. However, the acceleration profile may be discontinuous. In order to achieve smooth motion, the mainframe should follow continuous path, velocity and acceleration profiles.

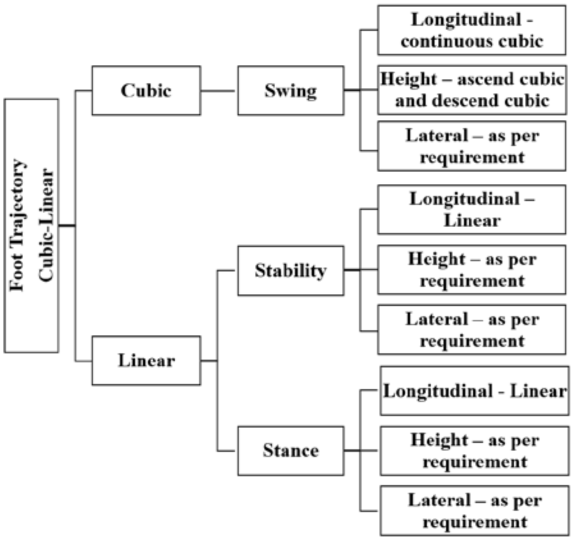

Fig 1: Foot Trajectory Planning

The foot trajectory planning has thus three phases of each leg; Swing, Stability and Stance (Figure 1). In real world scenario each leg may require to move in at least two directions, i.e., longitudinal (direction of desired motion) and height. Movement in lateral direction (perpendicular to height and direction of motion) should be considered as per initial design and stability criteria of the robot. Each phase of a leg has three path components, i.e., longitudinal, height and lateral. The robot achieves stable movement due to leg's stance phase and stability phase. The stance phase moves the robot as per planned by the controller so the robot should move in linear path thus achieves a constant velocity profile. So, the longitudinal component is linear, height and lateral components are zero for motion on plane surface. The stability phase which is prior to stance phase also moves the robot as to be moved during stance phase but the posture of the robot is corrected in case any changes occurred due to environmental disturbances including error caused by actuators. The controller thus gets the time to correct and modify further course of action. Initially it is assumed that the error is nil and no environmental disturbance is present thus for motion on plane surface the longitudinal component is linear, height and lateral components are zero. The swing phase of a leg has no role in moving the robot but may play an indirect role to control CG of the robot and thus may help to some extent to achieve stable movement. The longitudinal path of the foot in this phase has to move along with the robot so it is a continuous cubic curve but the height phase has to first lift the leg and the touch the leg so we have two cubic curve which are height ascend and height descend curve. For simplicity we take the lateral path similar to height path profile but lateral swing may be different than foot height. The continuous foot trajectory thus has the constraints to generate it. It needs to be understood here that each leg will have its own loop. This loop cannot overlook the contribution of other legs for walking of robot thus must consider that part also.

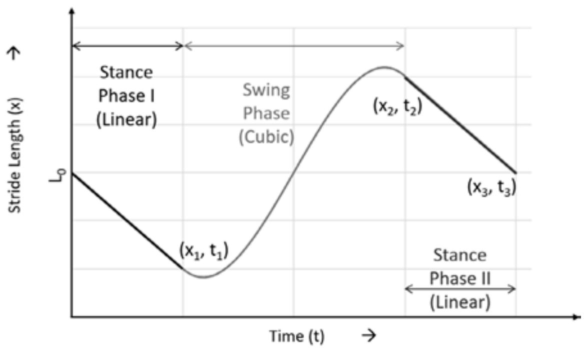

Fig 2: A generalized linear-cubic curve

For motion on plane where surface irregularities are minimal one can consider constant role of each leg. Thus, robot starts the loop with constant velocity for duration, say t_1 as per requirement. Thereafter swing phase starts and last up to time t_2, or duration $t_i = t_2 - t_1$, then stability phase starts which last as per program requirements. Finally, stance phase ends at time t_3, which is normally unit time.

Figure 2 shows a generalized linear-cubic curve with two linear segments first prior to swing phase and second next to swing phase. To maintain a continuous path profile at both merger points velocity is same. Thus, Stance phase I, Swing phase and Stance Phase II can be derived as follows

$$x_{st1} = a_1 t + b \ldots\ldots (1)$$
$$x_{sw} = c_3 t^3 + c_2 t^2 + c_1 t + c_0 \ldots\ldots. (2)$$
$$x_{st2} = a_1 t + b_1 \ldots\ldots\ldots. (3)$$

Following are the constraints

(i) at $t = 0, \quad x = L_0$ and
at $t = t_3, \; x = L_0$
where L_0 is initial offset

(ii) Robot speed $= \frac{L_s}{T}$
where L_s is stride length and,
T is time period for the loop

$$iii) \; \frac{dx_1}{dt} = \frac{dx_2}{dt} = \frac{dx_{st1}}{dt} = \frac{dx_{st2}}{dt} = -L_s/T$$

Here -ve sign is used to show velocity of the leg, moving in opposite direction w.r.t. the robot. Thus, we can solve equations (1), (2) and (3) and can be written as

$$x_{st1} = L_0 - \frac{L_s}{T} t \; \ldots\ldots..(4)$$

$$x_{sw} = \frac{L_s}{T}\left[-\frac{2t_3}{t_i^3}t^3 + \frac{3t_3(t_2+t_1)}{t_i^3}t^2 - \left(1 + \frac{6t_1 t_2 t_3}{t_i^3}\right)t + \frac{t_3 t_1^2(3t_2 - t_1)}{t_i^3}\right] + L_0 \ldots..(5)$$

$$x_{st2} = L_0 + \frac{L_s}{T}(t_3 - t) \; \ldots\ldots..(6)$$

Equations (4), (5) and (6) can be simplified further and can be made loop time period independent by putting

$$t_1 = t_b T, t_2 = (t_b + t_i)T, t_3 = T$$

$t_i = t_i T$ and $t = tT$

Thus, final equations for motion on plane in longitudinal direction are

$$x_{st1} = L_0 - L_s t \quad \dots\dots\dots\dots\dots.(8)$$

$$x_{sw} = L_0 + L_s\left[-\frac{2t^3}{t_i^3} + \frac{3(t_i + 2t_b)t^2}{t_i^3} - \left(1 + \frac{6t_b(t_i + t_b)}{t_i^3}\right)t + \frac{t_b^2(3t_i + 2t_b)}{t_i^3}\right] \dots\dots\dots.(9)$$

$$x_{st2} = L_0 + (1 - t)L_s \quad \dots\dots\dots\dots\dots \quad (10)$$

Here,

(i) all t's are unit less time quantity

(ii) t_b is start of cubic curve

(iii) t_i is interval of cubic curve

(iv) $t \in [0,1)$

The trajectory so plotted by eq (8), (9) and (10) are completely time period independent or in other words a modulus trajectory curve is obtained where total time elapsed is represented as follows:

$$t_{total} \equiv t \ (mod \ T)$$

The swing phase of the cubic part is now time interval, t_i, dependent and this can be used to introduce stability phase in stance phase II or in stance phase-I.

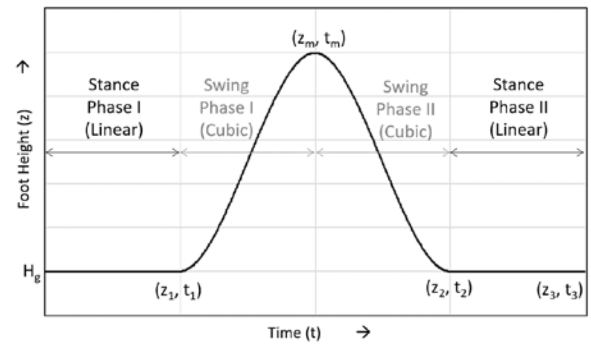

Fig 3: Foot Height Trajectory

Foot height trajectory is also consisting of both linear and cubic segments. In order to implement stable movement, the height of the robot mainframe w.r.t. ground is constant. Figure 3 shows the different segments used to draw the complete foot height trajectory.

It is divided into four segments two for stance phase and two for cubic curve phase. The two cubic phases are taken since the foot height goes to maximum and the return to its initial position this changes the slope of the curve thus two cubic curves are required.

Following are the constraints for motion on plane surface

(i) at $t = (t_1, t_2, t_3)$, $z = H_g$ and

at $t = t_m$, $z = H_g + H_f$

where H_g is Initial Height and,

H_f is max foot height

(ii)

$$\frac{dz_1}{dt} = \frac{dz_m}{dt} = \frac{dz_2}{dt} = 0$$

Thus, we obtained

$$z_{st1} = H_g \dots\dots\dots\dots\dots\dots (11)$$

$$z_{st2} = H_g \dots\dots\dots\dots\dots.(12)$$

$$z_{sw1} = H_g - \frac{4H_f}{t_i^3}[4(t-t_1)^3 - 3t_i(t-t_1)^2] \dots\dots\dots..(13)$$
$$z_{sw2} = H_g - \frac{4H_f}{t_i^3}[4(t_2-t)^3 - 3t_i(t_2-t)^2] \dots\dots\dots..(14)$$

The foot trajectory in xz plane can be plotted which is shown in Figure 4:

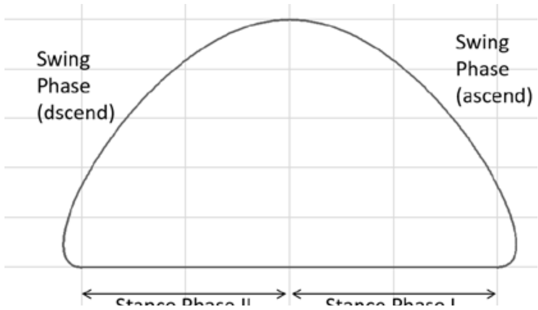

Fig 4: Foot Trajectory in xz plane

3. Discussion

The trajectory equations derived above for both longitudinal and height components, i.e. x and z directions respectively, are swing phase time interval dependent.

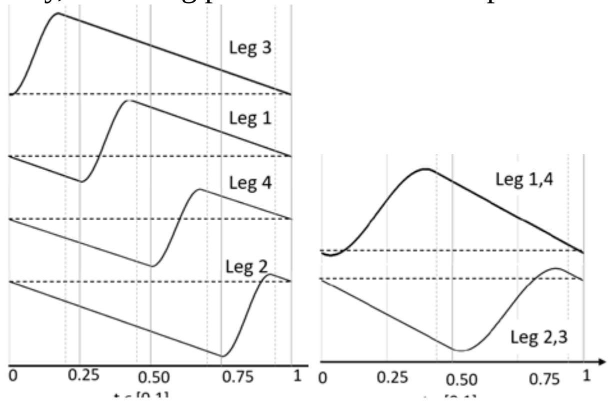

(a) (b)
Fig 5: Foot Trajectory (x) (a) Walking (b) Trotting

Fig 5 shows the longitudinal foot trajectory with leg sequencing for walking gait and trot gait of a quadruped robot. Four legs of a quadruped when moved in a sequence then the robot can move and two such motion patterns i.e. walking and trotting are shown in Figure 5(a) and 5(b) respectively. Under walking gait leg 3 first goes at any point of time in swing phase while all the other legs are on ground and firmly pushing the robot. The swing phase ends and then all the legs are in stability phase. Next leg 1 perform swing phase and rest other legs are in stance phase and as soon as swing phase of leg 1 is over than stability phase starts where again all the four legs are pushing the robot in same direction. The same procedure is then repeated by leg 4 and then leg 2 thus one cycle of operation is completed and then next cycle begins. The benefit of the stability phase is that any error detected by controller can be rectified before one leg goes into swing phase and hence the robot is in static stable environment. Under the trot gait the two diagonal opposite legs are in swing phase and rest two are in stance phase. This gait is dynamically stable gait and hence the robot getting disoriented may require extra time for posture correction but due to swing phase time interval dependency it already has the provision to correct its posture during the stability phase.

4. Conclusion

A set of equations for foot trajectory planning for a leg when goes for linear-cubic curve implementation with time interval dependency is derived. Each leg has three phases stance, swing and stance-stability. This extra phase should help controller to correct the errors or to adjust the various leg constants such as mainframe height from ground, H_g, foot height, H_f, stride length L_s etc. Thus, it should help in achieving the robot stable movement.

5. References

[1] S. M. Song and K. J. Waldron, Machines that walk: The adaptive suspension vehicle, MIT Press, Cambridge (1989).

[2] K. Berns and W. Ilg, Mechanical construction and computer architecture of the four-legged walking machine BISAM, ASME Transactions on Mechatronics, 4 (1) (1999) 32-38.

[3] C. Ridderstom and J. Ingvast, Quadruped posture control based on simple force distribution-a notion and a trial, IEEE Conference on Intelligent Robots and Systems, Mad, Hawaii, USA (2001) 2326-2331.

[4] L. R. Palmer III and D. E. Orin, Quadrupedal running at high speed over uneven terrain, Proceedings of the IEEE/RSJ Conference on Intelligent Robots and Systems, San Diego, USA (2007) 303-308.

[5] H. Kimura, Y. Fukuoka and A. H. Cohen, Adaptive dynamic walking of a quadruped robot on irregular terrain based on biological concepts, The International Journal of Robotics Research, 22 (3-4) (2003) 187-202.

[6] J. W. Chung, I. W. Park and J. H. Oh, On the design and development of a quadruped robot platform, Advanced Robotics, 24 (2010) 277-298.

[7] T. J. Kim, B. So, O. Kwon and S. Park, The energy minimization algorithm using foot rotation for hydraulic actuated quadruped walking robot with redundancy, the 6th German Conference on Robotics, Munich, Germany (2010) 786-791.

[8] C. Semini, HyQ - Design and development of a hydraulically actuated quadruped robot, PhD dissertation, University of Genoa, Italy (2010).

[9] M. Raibert, K. Blankespoor and G. Nelson et al., Bigdog, the rough-terrain quadruped robot, International Federation of Automation Control, Seoul, Korea (2008).

[10] Bledt, Gerado et al. "MIT Cheetah 3: Design and Control of a Robust, Dynamic Quadruped Robot." IEEE International Conference on Intelligent Robots and Systems, October 2018, Madrid Spain, Institute of Electrical and Electronics Engineers, January 2019. © 2018 IEEE

[11] Bellicoso, C.D.; Bjelonic, M.; Wellhausen, L.; Holtmann, K.; Günther, F.; Tranzatto, M.; Fankhauser, P.; Hutter, M. Advances in real-world applications for legged robots. *J. Field Robot.* 2018, *35*, 1311–1326.

[12] John J.Craig, Trajectory generation, Introduction to Robotics – Mechanics and Control, Third Edition, Pearson Education International, 201-229.

[13] I-ChihSu, (1994), Kinematic Analysis of Walking Machine Foot Trajectory, Oregon State University, Eugene, Oregon, US.

[14] D. J. Hyun, S. Sangok, L. Jongwoo and K. Sangbae, "High speed trot-running: Implementation of a hierarchical controller using proprioceptive impedance control on the MIT Cheetah," The International Journal of Robotics Research, vol. 33, no. 11, pp. 1417-1445, 2014.

[15] Kim, K.-Y.; Park, J.-H. Ellipse-based leg-trajectory generation for galloping quadruped robots. J. Mech. Sci. Technol. 2008, 22, 2099–2106.

[16] Rong, X., Li, Y., Ruan, J. *et al.* Design and simulation for a hydraulic actuated quadruped robot. *J Mech Sci Technol* 26, 1171–1177 (2012).

[17] Y. Sakakibara, K. Kan, Y. Hosoda, M. Hattori and M. Fujie, "Foot trajectory for a quadruped walking machine," EEE International Workshop on Intelligent Robots and Systems, Towards a New Frontier of Applications, Ibaraki, Japan, 1990, pp. 315-322 vol.1, doi: 10.1109/IROS.1990.262407.

Design and Performance Analysis of Robotic Jellyfish for Underwater Surveillance Manufactured as a Soft Robot

Rushikesh Pachghare
College of Engineering
Pune
pachgharerp18.mech@coep.ac.in

Mihir Deshmukh
College of Engineering
Pune

Dr. S. S. Ohol
College of Engineering
Pune

Abstract— **Soft-robotics is a sub-branch of robotics that deals with breaking this traditional perspective of rigid robots by making the robot more compliant and inspired by nature. This paper aims to design and analyses a soft robotic jellyfish for surveillance of small water bodies and sea shores. This robot is based on bio-mimicry of actual jellyfish. As like real jellyfish, this robot navigates by rowing with its tentacles. Rowing action of tentacles is quiet and unnoticeable compared to traditional auvs based on propellers and motors. By this way, robot navigates with less displacement of water and doesn't disturb aquatic life. The robot has six actuators which are radially symmetrical with radius of 100mm. Actuators in the robot are designed based on the volume change rate due to pressure change. At the end of the actuator there is a circular disk as a flap which helps in rowing action. Bending of tentacles rely on changing the pressure, inside the cavity between them, with the help of three small DC water pumps with maximum discharge flow 3 LPM. The robot can navigate through water either by remote operation or can be programmed in a way that it can work autonomously to detect suspicious underwater activities. Sensors such as temperature sensors, vision based sensors, pressure sensors, etc. Can be attached to the robot for navigation and surveillance. All the electronics and rechargeable battery pack is embedded in a waterproof body of the jellyfish. Fabrication of actuators is done using a PDMS casting process in 3D printed molds and other body parts are also 3D printed. Soft robotics is comparatively new topic and various researches and development work is being conducted throughout the world. This paper has a scope of static study of the actuator for the jellyfish robot on ABAQUS using hyper-elastic material model to acquire desired thrust force while actuation.**

Keywords— Soft Robotic, Underwater Robotics, Bio-mimicry, Jellyfish, Static study (FEA)

1. Introduction

Soft robotics is that the specific sub-field of robotics coping with constructing robots from extremely compliant/flexible materials, the same as those found in living organisms [1]. Soft robotics attracts heavily from the manner throughout that living organisms move and adapt to their surroundings. In distinction to robots engineered from rigid materials, soft robots leave inflated flexibility and adaptableness for accomplishing tasks, additionally as improved safety once operating around humans [2].

Plant and animal cells can produce hydrostatic pressure inside the cell due to change in solute concentration between fluid inside the cell i.e. Cytoplasm and fluid surrounding the cell [3]. This increase in pressure can change volume and shape of the cell. This is the working principle of pressure system used in many soft robots. These systems are composed of body made of soft resins containing single or multiple fluid cavities/sacs with network of connecting tubing for transportation of fluid [5].

Biomimetic robots have better camouflage effect to explore the seabed by mimicking the swimming pattern of aquatic animals [4]. They produce fewer disturbances in the aquatic system than any artificial underwater vehicle. Jellyfish usually propel it either by rowing or by jetting. Also, jellyfish are remarkably efficient, using less energy for locomotion than any other sea creature [5,6].

In this paper, aims to design and analyze a soft robotic jellyfish which will be propelled by rowing movement by its tentacles with further discussion on material selection process. Hydraulic pressure system is considered as a base for working principle and design of the robot.

2. Working Principle

Rowing motion of the jellyfish is done by moving of tentacles along with flaps attached to it. This motion is usually coupled with the jet coming out of the bell like body. This make the jellyfish the most efficient in locomotion among all aquatic creature [3,4]. In general, Jellyfish has thick, elastic, jelly-like body. The body of a jellyfish exhibits radial symmetry with an umbrella like bell shaped body from where tentacles are hangs down.

In this paper, six soft bending actuators or tentacles were designed symmetrically around three central pumps arranged on a 3D printed body with modification to accommodate electronics and battery inside a small capsule. The design of bending actuators or tentacles contains multiple cavities forming a Pneunet [7] Structure with different layer thickness to obtain bending motion. These tentacles, after giving the pressure from a 12V impeller pump, bends toward the thick side and perform the rowing motion. To make this elastic body silicon rubber [9] of different shore hardness were considered for molding into the shape of tentacles.

CAD design of version-I is shown in the figure 1. This design contains a 3D printed capsule to accommodate electronics and batteries, three 12V impeller pumps to actuate two pneunet [7] tentacles each. So, three pumps will give us three different controlling parameters on two tentacles each. Through this design the robot was supposed to mimic underwater propulsion seen in nature [8].

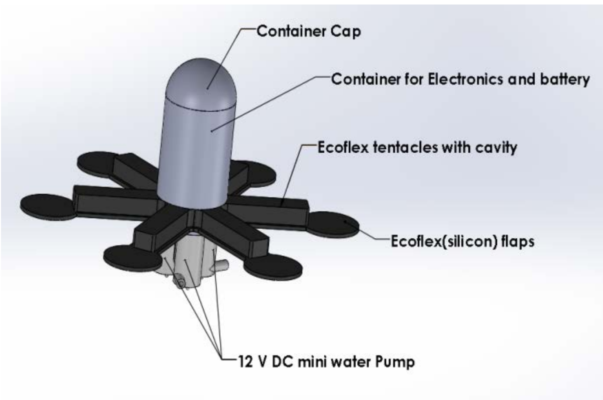

Fig 1: Design of the jellyfish
(Version-I).

The actuator used as a tentacle in this jellyfish is based on actuator design developed by Harvard University [10]. To create the bending deformation, bottom layer is generally made inextensible by adding paper or PDMS (Polydimethylsiloxane) in the layer or the bottom layer is made from material with higher shore hardness which will have less elongation than the upper body portion [14]. We are using a layer of piece of cotton fabric. This single cavity structure has an opening for water to flow. When the pump is turned on, water flows into the cavity building hydraulic pressure acting on the inner surface of the actuator. This pressure deforms the actuator as shown in figure 2(A to E). This is how the bending motion in a desired direction occurs due to pressure. Bending at Maximum pressure (1Bar) was 98 degree.

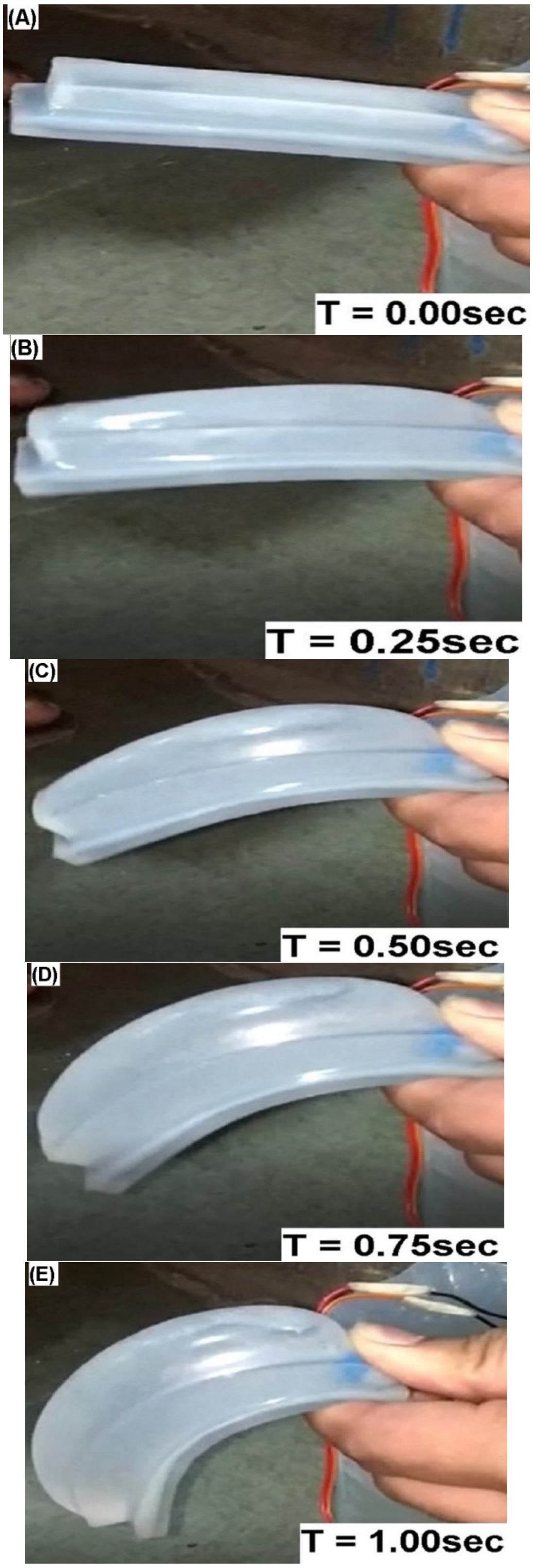

Fig 2: Deformation of single tentacle (A to E) (Max. Pressure = 1Bar)

3. Design

This cavity structure was fabricated and tested in a water container with 1.0bar pressure from each three 12V DC pumps to actuate two tentacles. Because of the shape of the actuator which is a single cavity structure, the rate at which the tentacle/actuator deforms when water is filled in the actuator cavity was less than or equal to the rate at which the water comes out due to the potential energy from stretching of the wall when the pump is turned off. This results in thrust in opposite direction when the pump is off. So, the movement of the robot, in the complete cycle of turning the pump on and off was canceling out each other. Figure 3 shows the testing of prototype based in primary design with tethered electronics and power connection.

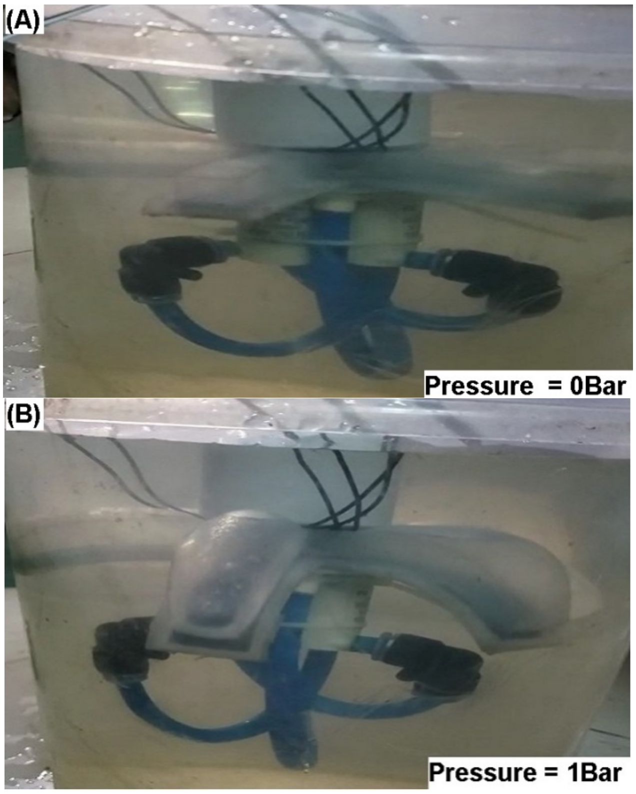

Fig 3: Testing of prototype based on version-i design (a: pressure = 0bar) & (b: pressure = 1bar)

To solve this problem, pneunet [5] actuator was taken under consideration. Pneumatic networks or pneunets are a class of actuator developed by Harvard university [10]. They are a series of chambers and channels inside an elastomer. When these chambers are pressurized they create desired motion. Because of the series of chambers instead of one single cavity, the potential energy stored in the side walls in less which reduces slows down the movement of the tentacle when the pump is off. Hence this structure is able to perform the rowing action effectively. FEA analysis of this improved version-II design is shown in section 4.2

4. Simulation

A. Selection of Material

Silicon rubber is an elastomer containing silicon with other polymers. Mechanical properties of these elastomers are measured on the basis of durometer or shore durometer hardness [11]. Durometer has different scales like 00, a, c, etc. Each durometer scale ranges from 0 to 100 which are unit less numbers to represent relative hardness between different materials with similar elastic properties. In this application, material stiffness affects the amount of pressure required and speed of retraction of the actuator. But, the material should also be hard enough to withstand the reaction force (thrust force) applied by surrounding water to the to the robot body. Lower durometer materials which have high strain can be operated at low pressure and they also have low retracting speed which minimizes the reverse thrust generated while retracting. For the fabrication of the robot silicone rubber of 30A hardness (Elastosil M4601 silicone rubber) was selected based on its properties. It comes under the category of extra soft rubbers. This rubber has tensile strength of 6.5MPa and elongation at break ~700% [12].

B. Finite Element Analysis

This selected rubber material was studied using FEA (Finite Element Analysis) method. FEA method is widely used as a design tool to determine design parameters and structural behaviors after application of load [13,14]. Cad model was built on SolidWorks 2020 and Abaqus 2020 was used for the FEA. This study was conducted with ramp input load pressure of 1bar on the internal wall of the cavity of tentacles/actuators. A hyperplastic yeah model was selected to mathematically simulate the behavior of Elastosilm4601 silicone rubber [15]. Figure 4 shows the deformation of the silicon body of Version-II cad design when 1bar ramped pressure load was applied after application of constant gravitational load along downward direction.

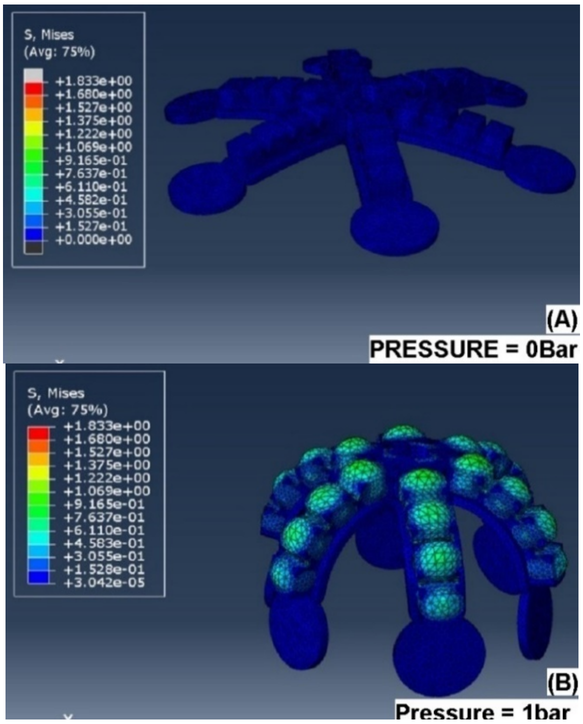

Fig 4: Deformation of the silicon rubber body (a: 0% deformation) & (b: 100% deformation)

In Abaqus, yeah hyper-elastic material was defined. The density of Elastosil M4601 silicone rubber is 1130kg/m^3. The material was assumed isotropic with yeah strain energy potential defined by coefficient c10=0.11 and c20=0.02 [14]. This method was used to validate the design and material selection by insuring the deformation after application of pressure on the inner wall of the cavity.

5. Results and Discussion

To understand the behavior of the actuator/tentacles, we plotted the y–displacement of the centroid of the disk shaped flap structure at the end of the actuator with respective to time when the pressure is applied. This plot is shown in figure 5. As the loading condition specified, the pressure is ramped from 0bar to 1bar in 1 sec and figure shows the plot from 1sec which is when pressure starts to 0.8sec.

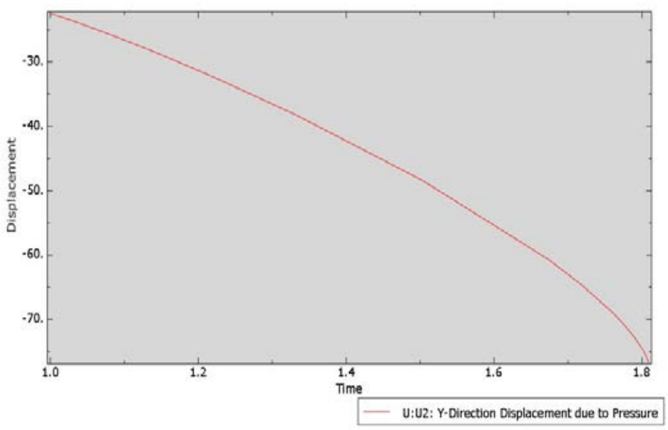

Fig 5: Y-displacement of the centroid of flap

This plot shows the displacement of flap in y direction from -30mm where it is displaced due to gravity and then from -30mm to ~ -75mm due to pressure. From slope of this graph, we can find the velocity the flap in –y direction and ultimately we can find the thrust force for one flap. This design can be further fabricated using 3d printed mold and experimental setup can be made to find actual thrust and velocities. Further to improve design parameters and select better material to optimize pressure values and hence power.

A small microcontroller system with 12V buck is used to control the robot. Additional to that, flex sensors can be added to measure the bending of the tentacles to form a closed loop for better controlling. Further, more sensors such as pressure sensor, temperature sensor vision based sensors can be added for surveillance purposes.

This kind of soft robots can be used in various applications in aquatic surveillance and sample collection. Jellyfish being the most efficient in underwater locomotion can inspire new such designs which will also be power efficient. The rowing motion of this fish creates less turbulence in water than propellers which does not disturb the aquatic life. As this robot is based on bio-mimicry, the robot can hide in its environment. Hence this robot design is better for surveillance in military applications.

6. Conclusion

A design based on inflatable structure was discussed in this paper based on the review of inflatable structure found in nature such as jellyfish. We designed silicone rubber based elastomeric actuator and examine the bending characteristics of the structure. The robot jellyfish has 200mm diameter and was made of ElastosilM4601 silicone rubber with 3D printed cylindrical body to accommodate the electronics and battery.

7. References

[1] Trivedi D., Rahn C. D., Kier W. M., & Walker, I. D. (2008). Soft robotics: Biological inspiration, state of the art, and future research. Applied Bionics and Biomechanics, 5(3), 99-117.

[2] Yao R, Daniela T, Michael T. (27 May 2015). "Design, fabrication and control of soft robots". Nature. 521 (7553): 467–475.

[3] Li Suyi, Wang K. W. (1 January 2017). "Plant-inspired adaptive structures and materials for morphing and actuation: a review". Bioinspiration & Biomimetics. 12 (1): 011001. Bibcode:2017BiBi...12a1001L. doi:10.1088/1748-3190/12/1/011001

[4] Wang S., Chen Z. “Modeling of jellyfish-inspired robot enabled by dielectric elastomer.” Int J

Intell Robot Appl (2021). https://doi.org/10.1007/s41315-021-00192-1.

[5] S. P. Colin and J. H. Costello, "Morphology, swimming performance and propulsive mode of six co-occurring hydromedusae," The Journal of Experimental Biology, pp. 427-437, 2002.

[6] Rathi, Akshat (15 May 2014). "Jellyfish are the most energy-efficient swimmers, new metric confirms" Ars Technica, PNAS, 2014. DOI: 10.1073/pnas.1310544111

[7] Souhail Amir & Vessakosol, Passakorn. (2018). “PneuNets bending actuator design and fabrication using low cost silicones”.

[8] Nawroth J., Lee H., Feinberg, A. *et al.* “A tissue-engineered jellyfish with biomimetic propulsion”. *Nat Biotechnol* 30, 792–797 (2012). https://doi.org/10.1038/nbt.2269doi: 10.1016/j.matpr.2019.05.110.

[9] F. Ilievski, A. D. Mazzeo, R. F. Shepherd, X. Chen, and G. M. Whitesides, “Soft robotics for chemists,” Angewandte Chemie, vol. 123, pp. 1930–1935, 2011..

[10] B. Mosadegh, et al., “Pneumatic Networks for Soft Robotics that Actuate Rapidly,” Advanced Functional Materials, 2013.

[11] Qi H. & Joyce K & Boyce M. (2003). “Durometer Hardness and the Stress-Strain Behavior of Elastomeric Materials. Rubber Chemistry and Technology”. 76. 419-435. 10.5254/1.3547752.

[12] Alici Gursel & Canty Taylor & Mutlu Rahim & Hu Weiping & Sencadas Vitor. (2017). “Modeling and Experimental Evaluation of Bending Behavior of Soft Pneumatic Actuators Made of Discrete Actuation Chambers. Soft Robotics”. 5. 10.1089/soro.2016.0052.

[13] Yilin Sun, Qiuju Zhang, Xiaoyan Chen, Haiwei Chen, “An Optimum Design Method of Pneu-Net Actuators for Trajectory Matching Utilizing a Bending Model and GA”, Article in Mathematical Problems in Engineering, published October 2019, doi: 10.1155/2019/6721897, pub.1121826357.

[14] P. Polygerinos *et al*., "Towards a soft pneumatic glove for hand rehabilitation," *2013 IEEE/RSJ International Conference on Intelligent Robots and Systems*, 2013, pp. 1512-1517, doi: 10.1109/IROS.2013.6696549.

[15] https://softroboticstoolkit.com/book/pneunets-variation-material (28 Sept 2020).

Dual Function Spin Decay Safe Arm Mechanism

Prabhakar Kumar
Armament Research and Development Establishment
Pune
pkumar@arde.drdo.in

SS Uppin
Armament Research and Development Establishment
Pune
shivanand uppin@gmail.com

S Rambabu
Armament Research and Development Establishment
Pune
srambabu@arde.drdo.in

Abstract – **The low caliber ammunitions show significant non-functioning rounds against targets like hard, soft or marshy grounds. Many designers have provided an additional function mode like self-destruction along with the impact function to enhance the reliability of these ammunitions. This paper presents the working principle, mathematical basis and design of fuze along with its safety arming mechanism, which requires spin and setback to operate. It functions on impact and has a novel mechanism for additional mode of functioning based on spin decay principle.**

Keywords – Safe Arm Mechanism, Spin Decay, Ammunition, Explosive Train, Setback, Spin, Reliability

1. Introduction

The fuzes for low caliber ammunition require safety and arming mechanisms with adequate safety features, reliable functioning and configured in minimum space. These ammunitions are used in variety of situations and have to function on impact against targets like hard, soft or marshy grounds. These have led to a significant number of non-functioning rounds and adversely affected the reliability of these ammunitions. Many designers have provided an additional function mode like self-destruction along with the impact function to enhance the reliability of the ammunition. The Self destruction is incorporated using either pyro delay or electronically, where if the ammunition has not functioned on impact, then after a preset time the ammunition shall function in self-destruct mode. The pyro delay-based self-destruction systems are low in testability while electronic circuits require provision of power and increase the cost of ammunition. This paper presents configuration and design of fuze along with its safety arming mechanism which requires spin and setback to operate and functions on impact. It has a novel mechanism as additional mode of functioning based on spin decay principle.

2. Operating Principle

On launch, the ammunition experiences setback and spin which arms the safety and arming mechanism. Subsequently, the ammunition hits the target, the fuze striker initiates the detonator and further explosive train. In case, the ammunition does not function in impact mode, an optimized mechanism for spin decay mode function is incorporated in the fuze. The mechanism will store the energy during setback phase of ammunition and will continuously sensing the spin of the fuze. Post- impact, on rapid decay of spin of ammunition, the spin decay mechanism will initiate the explosive train. The spin decay mechanism consists of metallic components, hence life, cost and testability of the system is not affected.

3. Configuration of Fuze

The fuze is configured as base fuze with the main charge filling. The main subsystems and components of fuze are safety arming mechanism (1), balls (2), housing (3), conical spring (4), striker assembly (5), striker housing (6) and booster (7). The conical spring is assembled with the striker housing along with steel balls in radial grooves of striker housing. The striker assembly is then positioned in the striker housing followed Safety Arming Mechanism Assembly.

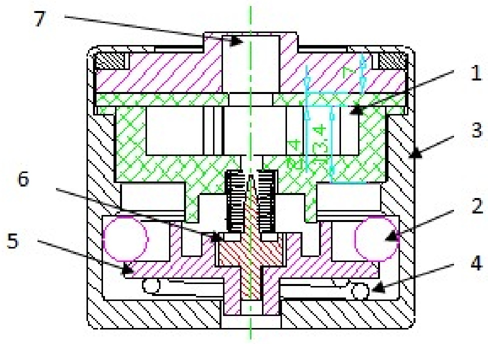

Figure 1: Configuration of Fuze

The SAM assembly, refer Fig.2, consists of percussion detonator (8), rotor (9), detent (10), Pallet Escapement (11) and housing (12).

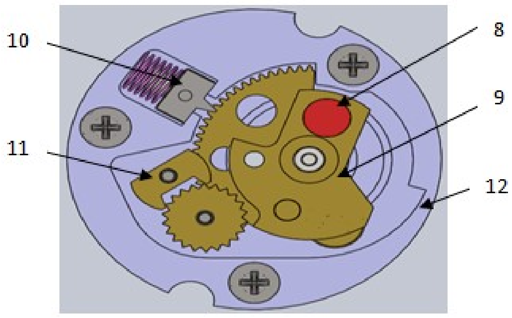

Figure 2: Model of SAM

An Asymmetric rotor is mounted on a pivot of the SAM housing. The rotor has a gear plate which drives a pallet escapement mechanism to provide arming delay. A detent holds the rotor and acts as a centrifugal lock, which prevents the rotor to arm before a pre-specified spin is not achieved. A percussion detonator is placed in the rotor and kept in offset position in safe condition.

4. Sequence of Function

In storage and pre-launch condition the fuze is kept in unarmed condition with two safety interlocks. First, the striker is assembled against a biased spring, which engages a cavity in the rotor and restrains it till it does not retract.

Second, a detent is assembled with a spring in radial direction, which engages the rotor Plate and prevents to rotate.

Once, the ammunition is launched the striker assembly retracts under the effect of launch forces. Subsequently, Spin is imparted to the ammunition during launch and radial detent retracts when adequate spin is experienced by the ammunition. Under the effect of sustained spin, the Safety arming mechanism arms the fuze after delay.

Consequently, once the ammunition hits the target the striker moves forward and hits the percussion detonator and initiates the explosive train. In case the impact is not sufficient or non-functioning of fuze. The ammunition loses spin quickly after repeated impact with ground. The balls will sense the decay of spin and free the striker assembly. The compressed conical spring will push the whole striker assembly into the percussion detonator and the fuze will detonate the main filling of the ammunition in spin decay mode.

5. Design of Fuze

The launch environment of typical low calibre ammunition can have of peak acceleration is more than 10,000 g and spin in excess of 4000 RPM. The safety and arming mechanism is designed to operate within these environments with adequate safety margins.

The striker retracts from the rotor when sufficient launch acceleration is experienced, it pushes the striker assembly against the conical spring.

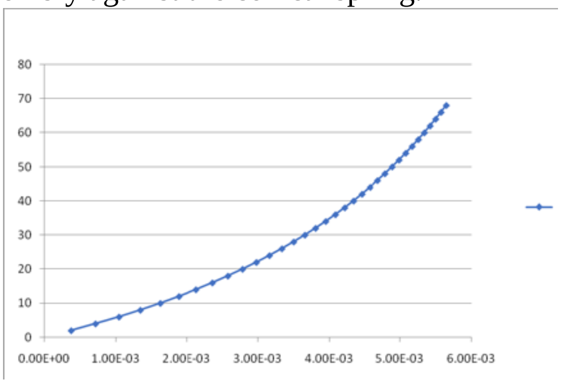

Figure 3: Force vs Deflection

The setback load on which the lock is released is given by following expression

Fs = K * x/Mst ------ (1)

Where,

Fs= Setback Load, K= Striker spring rate

x = displacement of striker required

Mst = Mass of striker assembly.

The rotor is yet not free to arm, as the detent is obstructing its rotation. The following equation determines the minimum spin required to allow arming

N = Ksp *Δ*30/π*m*r --------- (2)

N = Spin in RPM m = mass of detent

Ksp = Spring Rate r = radial distance

Δ = deflection

Putting various parameters in the equation 2, the minimum spin required for arming is determined. Once the safety interlocks of the rotor are removed, it starts to rotate under the effect of the spin as it is mounted offset to the axis of the rotation of the fuze. The torque on the rotor is given as

$Tr = rp*(M*\omega^2*ra)$ -------- (3)

Where,

Tr = Radial torque, M = mass of Rotor

Rp = radial distance of rotor CG to Pivot

Ra = radial distance of C.G from spin axis

ω = angular velocity

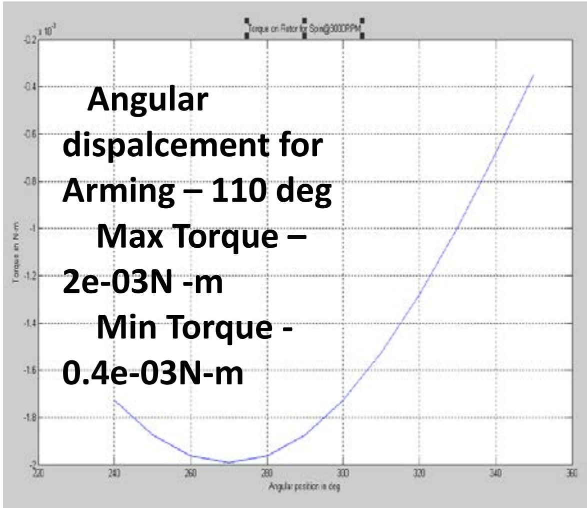

Figure 4: Torque vs Deflection

The Fig 4 represents a torque vs deflection graph computed using the equation 3. There graph shows the availability of a torque throughout the rotor arming.

The ball lock is designed to provide spin decay mode functioning of fuze. It stores energy during setback phase of the ammunition launch. Once setback is finished, the striker housing is locked to main housing with ball locks due to spin.

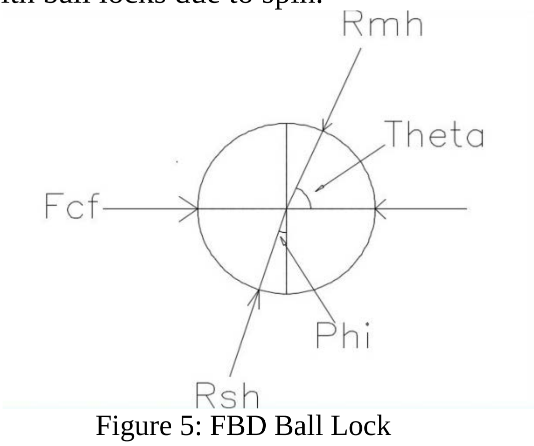

Figure 5: FBD Ball Lock

The fig 5 shows the free body diagram of the ball lock. It motion is governed by following equations

Rmh cos (theta)- Rsh sin(phi) < Fcf – (4)

Rmh cos (theta)- Rsh sin(phi) > Fcf – (5)

Where, Fcf = centrifugal force of ball

Rmh = Reaction force ball and housing

Rsh = Reaction force striker and ball

The reaction force on the ball is computed using the conical spring load values and different geometric parameters of the housing and striker assembly along with the steel balls.

Using the equations derived from the force body diagram of the ball locks. The fig. 6 shows the graph of computed values of the centrifugal forces at different spin values.

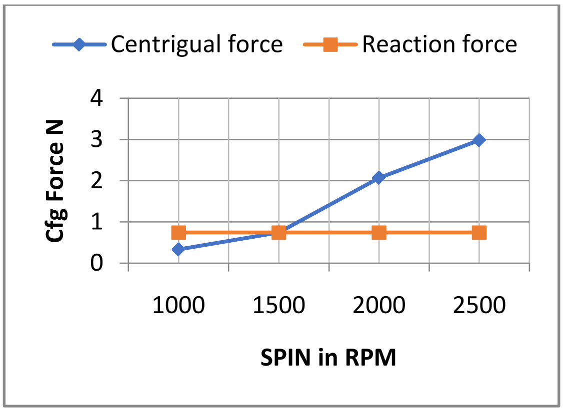

Figure 6: Centrifugal Force vs Spin

It is observed the ball will be locking the striker till its centrifugal force is more than the balance of the reaction on the ball by housing and striker assembly. The orange line shows the net reaction forces on the ball. Prior, to impact in flight Spin Decay mode of functioning of fuze is as follows, the striker is kept locked by the ball when the SAM is armed condition in flight condition Fig.7.

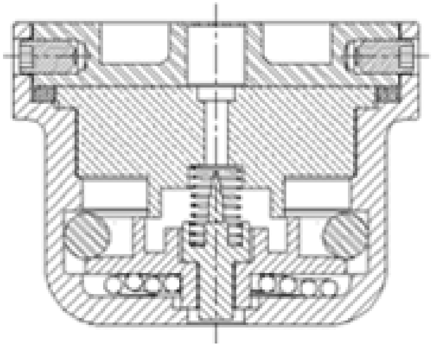

Figure 7: Striker Locked by Ball

In this condition the spin is sufficient as seen in fig.6 the blue line is above the orange level. After the impact, if the fuze has not functioned in impact mode its spin decays rapidly. Consequently, the centrifugal force on the ball also reduces quickly. When the blue line is below the orange line, reaction forces overcome centrifugal forces and the ball lock is removed. The striker assembly is free and the compressed spring pushes the striker into the detonator

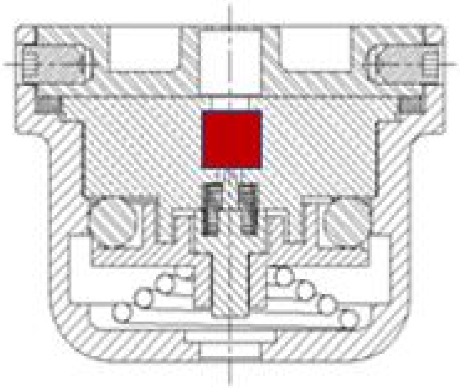

Figure 8: Function in Spin Delay Mode

6. Conclusion

This paper presents a conceptual and design of fuze along with its safety arming mechanism, which requires spin and setback to operate and functions on impact. It brings out details of a novel mechanism for additional mode of functioning based on spin decay principle. It also presents the working principle, mathematical basis and sequence of operation of the mechanism.

The spin decay mechanism provides an excellent dual mode of functioning for ammunition with spin. Unlike pyro Self destruction it does not reduce life or reduce testability of the ammunition. It can be a cost effective, rugged and reliable way to minimize number of blinds on many types of ammunition.

7. Reference

[1.] Budyness- Nisbett, Shigley Mechanical Engineering Design, Eigth Edition, The McGraw-Hill.

[2.] Avallone A. Eugene, Baumister III Theodre, Sagdeh M. Ali, Marks' Standards Handbook for Mechanical Engineers, Eleventh Edition, The McGraw-Hills.

[3.] Mehul Sirohi, Prabhakar Kumar, Rambabu Sala, Depth Sensing Switch for Safety and Arming Device for Torpedoes.

[4.] MIL-STD-1316E, Fuze design, Safety Criteria", July 1998.

[5.] J. E. Shigley, C. R. Mischke and T. H. Brown, Jr, "Standard Handbook on Machine Design", 3rd ed US: The McGraw- Hill 1994.

Mechanism for Automatic Creation of Pit and Bury the Object into Pit

Jagat Prakash Singh
CE Group
Research and Development Establishment (Engrs.)
DRDO
Pune
jpsingh@rde.drdo.in

Chandrakant Supare
CE Group
Research and Development Establishment (Engrs.)
DRDO
Pune

Ganesh Mutkule
CE Group
Research and Development Establishment (Engrs.)
DRDO
Pune
mutkuleg@rde.drdo.in

Vishwanath Ovhal
CE Group
Research and Development Establishment (Engrs.)
DRDO
Pune

Abstract – **The work presented in this paper demonstrates the conceptualization, design & development of a mechanism for automatic creation of pit and burying the desired object into the pit. Indian Army has tactical requirement to create pit of various dimensions and bury objects of different dimensions into the pit. The pit creation needs to be done in different terrains which can be plains of Punjab, desert/ semi-deserts of Rajasthan or mountainous terrain.**

Currently the task is done manually which is risky, time-consuming and laborious task. To cater to this need of Indian Army, a mechanism has been conceptualized to carry out following tasks through remote operation: (i) To create pit of desired dimensions, (ii) To align object with pit and place object inside pit, (iii) To camouflage the object.

1. Introduction

R&DE (E) has successfully developed object laying equipment which can be operated by 3 or 4 crew members. But considering future requirement, unmanned object layer is being conceptualized which will be completely automatic and will not need any human intervention to execute object laying operation.

The unmanned object layer will be operating in different kinds of terrains which include desert, semi-desert, plains and mountainous region. The soil can hard or soft and spacing between objects can be 1m to 6m.

To realize unmanned object layer, different experimental set-ups have been planned to validate the design of different sub-systems of equipment.

So initially experimental setup for automatic pit creation and placement of object into pit has been designed and developed to validate the functionality of the concept.

The experimental set-up has been designed for digging a pit at required location and placing object into the pit. The pit will be created at intermittent locations based on spacing requirement between objects. The set up will be mounted on wheeled trolley which will be towed to a carrier vehicle to take it to the digging site.

The experimental set-up has been planned for laying object 1 and object 2 with following dimensional details:

1	Object 1 	Shape: Circular	Size: - Dia 288 x 167 mm ht Wt: - 7.3 Kg.
2	Object 2 	Shape: Circular	Size: - Dia 88 x 51 mm ht Wt -200 gm.

Since both objects are having dimensional difference, the pit of different size will be created and accordingly two tools of different size will be used. The dimension of pit for object 1 will be 350 mm dia. X 225 mm depth while that for object 2 will be 120 mm dia. X 80 mm height.

2. Subsystems

The Subsystems/Operations in Unmanned Object Laying System comprises of following.

(i) Remotely Operated Vehicle Platform
(ii) Stacking and auto conveying of objects to arming station
(iii) Arming of Object
(iv) Digging of Pit
(v) Placing of object into pit
(vi) Camouflaging

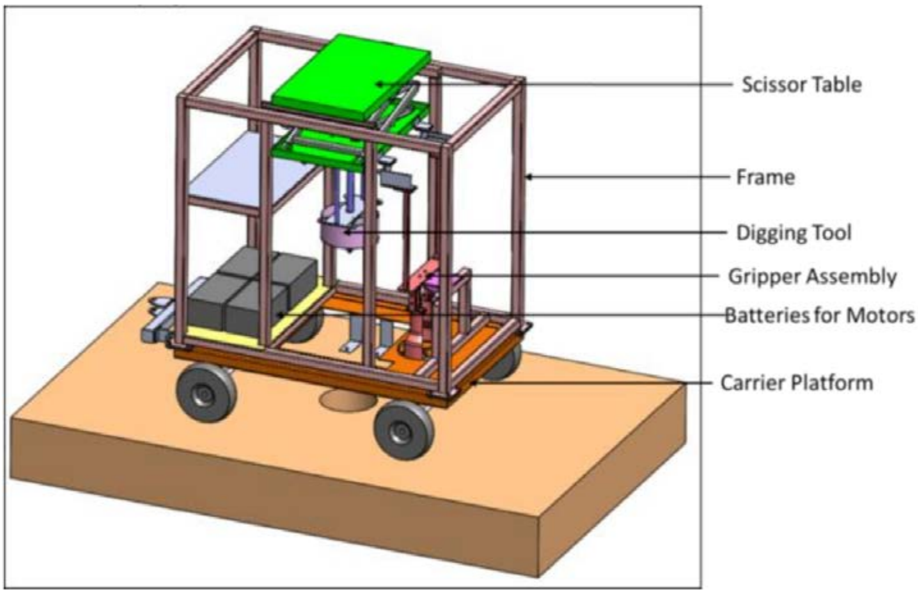

Figure 1: Experimental Set-up

A. Carrier platform:

The mechanism is mounted on carrier platform which can be remotely operated to drive it to desired digging location.

B. Frame:

The frame is mounted on carrier platform and supports the components of mechanism.

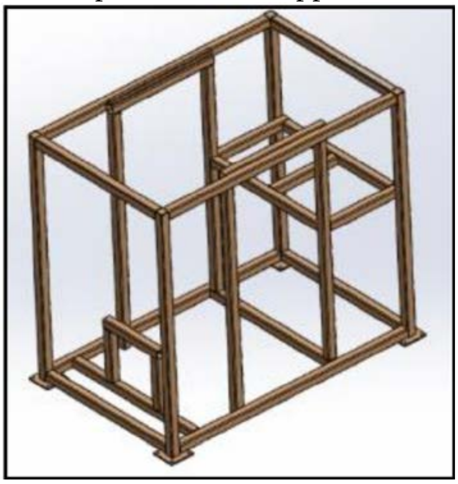

Figure 2: Experimental Set-up

C. Scissor table assembly:

The scissor table is fitted on frame and the digging tool is mounted on scissor table. The scissor table lowers or lifts the digging tool based on requirement. The depth of pit is controlled by adjusting scissor table height. The scissor table helps to accommodate the mechanism within compact size. Scissor table specifications are as follows:

Power = 1500 W, Torque = 60 Nm, Speed = 240 rpm

Lead screw of dia. 40 mm and pitch 10 mm has been finalized for scissor table.

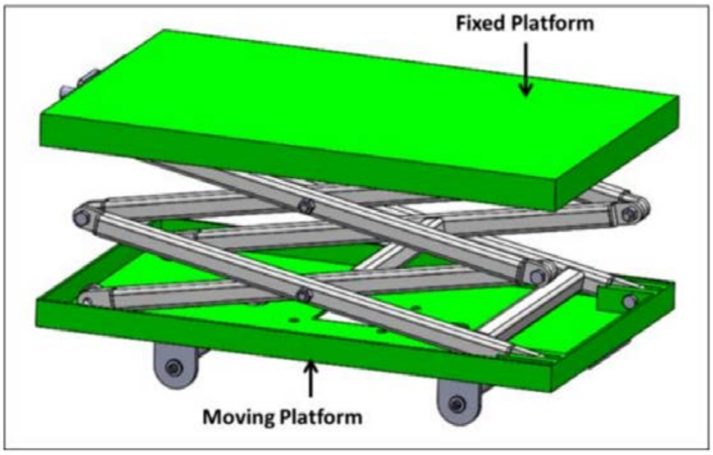

Figure 3: Scissor Table

D. Digging tool assembly:

The various digging tools have been experimented to create the pits of desired size. But Augur based tool with pointed teeth bolted at bottom has proved to be effective since the tool creates the pit as well as guides the loose soil to surface of ground. Since the tool guides loose soil to the ground surface, the cutting force to create pit is reduced also soil is available for camouflaging the object. The Augur tool has been designed to optimise power required for creating pit in minimum time of 2 to 3 seconds. The geometry of tool has been finalised based on literature and extensive experiments carried out on tool. The cutting teeth are bolted on circumference of augur tool so that worn out teeth can be replaced easily without need of replacing complete augur tool. The digging tool can be changed based on size of pit required. The digging tool is rotated by the BLDC motor which is powered by 48V D.C. batteries.

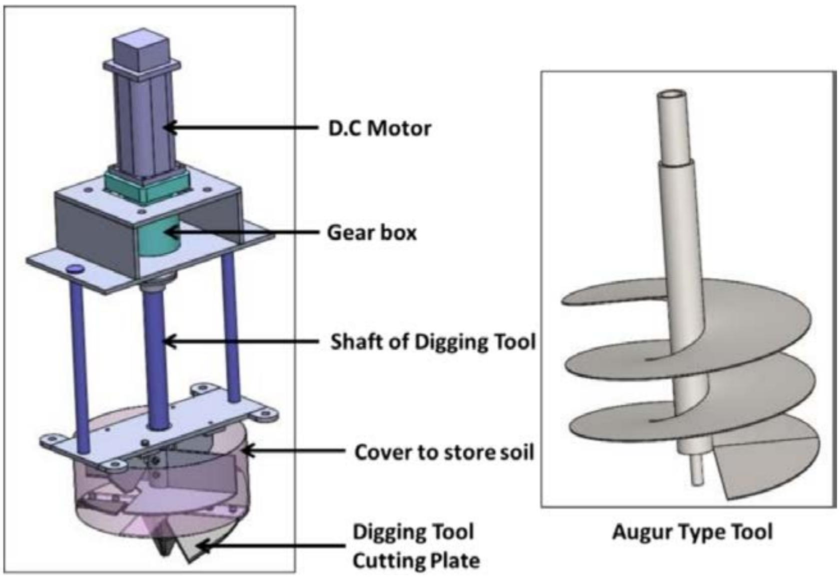

Figure 4: Digging tool assembly

E. Force calculation for digging tool

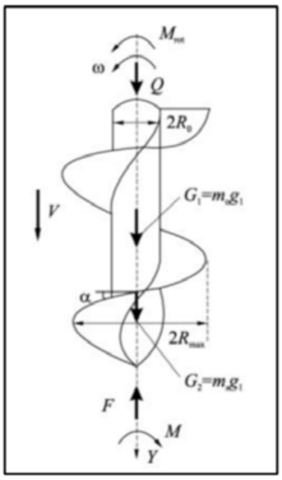

Figure 5: Forces on Digging Tool

Table 1. Properties of Soil of Different Terrains

Soil	**Soil Density λ (kN/m^3)**	**Cohesion of soil c (kN/m^2)**	**Angle of soil friction Φ (degree)**
Plains	21	185	24
Semi-desert	18	20	34.5
Desert	16	5	35.5

The force to dig the soil F is calculated as

$$\mathbf{F = (\lambda d^2 N\lambda + cdNc + qdNq + \lambda v^2 dNa) * w}$$

Here

$$N\lambda = (\cot \rho + \cot \beta) / 2*[\cos(\rho+\delta) + \sin(\rho+\delta) * \cot(\beta+\varphi)]$$

$$Nc = \{1 + \cot\beta * \cot(\beta+\varphi)\} / [\cos(\rho+\delta) + \sin(\rho+\delta) * \cot(\beta+\varphi)]$$

$$Nq = (\cot \rho + \cot \beta) / [\cos(\rho+\delta) + \sin(\rho+\delta) * \cot(\beta+\varphi)]$$

Where,
F : Resistive force experienced at the blade,
λ : Soil density
d : Tool depth below the soil
q : Surcharge pressure acting vertically on soil
α : Angle of entry of tool inside soil
β : Angle between the failure surface & horizontal
δ : Angle of friction between soil and tool Φ: Angle of soil friction
N**λ**, Nc, Nq are factors which depend on the soil frictional strength, the tool geometry and soil tool strength properties.

Depending on geometrical parameters of the bit and its friction ratio over soil there exists a minimum drill bit rotation rate that ensures non-stop soil movement up to the surface. This critical rotation speed has been found as follows.

Analytical solution for auger tip resistance in soils is presented. It involves several drilling parameters:

Torque, axial force, rotation speed, linear velocity. Tip resistance to auger drilling can be used to soil strata identification and to interpretation mechanical properties of soils in the same way as is done for cone penetration test.

As is known soil moves against the auger. The drilled soil moves to the auger flanges and due to centrifugal forces presses against the borehole cylindrical wall. The friction and gravity forces somewhat slow down a soil particle movement against the auger surface i.e. it rotates with lower angular speed than that of the auger.

The final equation for minimum auger rotation frequency, required to lift soil is as:

$$\omega_{rot} \geq \sqrt{\frac{g\left(\sin\alpha + \tan\varphi_{ag}\cos\alpha\right)}{K_1 R_{max}\tan\varphi_s\left(\cos\alpha - \tan\varphi_{ag}\sin\alpha\right)}}$$

or in rotations per second (Hz):

$$N_{rot} \geq \sqrt{\frac{g\left(\sin\alpha + \tan\varphi_{ag}\cos\alpha\right)}{4\pi^2 K_1 R_{max}\tan\varphi_s\left(\cos\alpha - \tan\varphi_{ag}\sin\alpha\right)}}$$

tanϕs = friction coefficient soil- soil;
tanϕag = friction coefficient soil- steel; and
K1 = soil-against-soil friction ratio

Based on calculations specifications of digging tool motor are as follows:
Power: 4600 W, Speed: 300 rpm
Toque: 14 Nm

F. Gripper assembly

Once the pit is created the object needs to be placed precisely into pit. Gripper assembly has been designed to serve this function reliably in short time. The gripper assembly grips the object and aligns itself with the pit. The gripper assembly is then lowered to the pit with scissor table to place the object into pit. The gripper assembly is designed such that the object of any size can be gripped and placed into pit. The gripper is actuated with lead screw mechanism which when operated with D.C. motor grips or releases the object into pit.

Gripper Motor specifications: Power: 1500 W, Torque: 60 Nm, Speed: 240 rpm

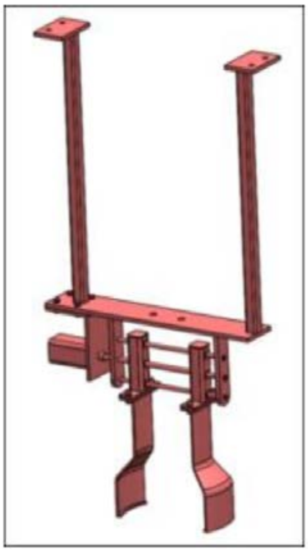

Figure 6: Gripper Assembly

3. **Sequence of operation**
   Timing sequence of each operation for burying object is as follows

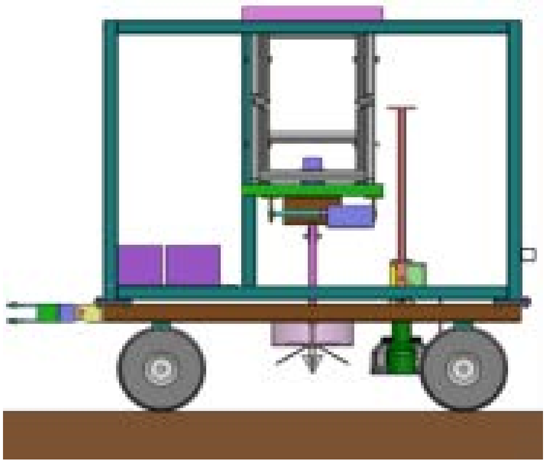

Figure 7: Home position for Cutting Tool and Gripper assembly

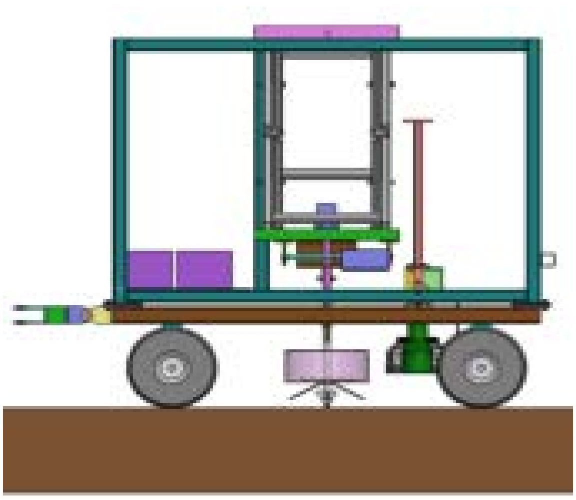

Figure 8: Tool lowered to the ground. Cutting of soil started

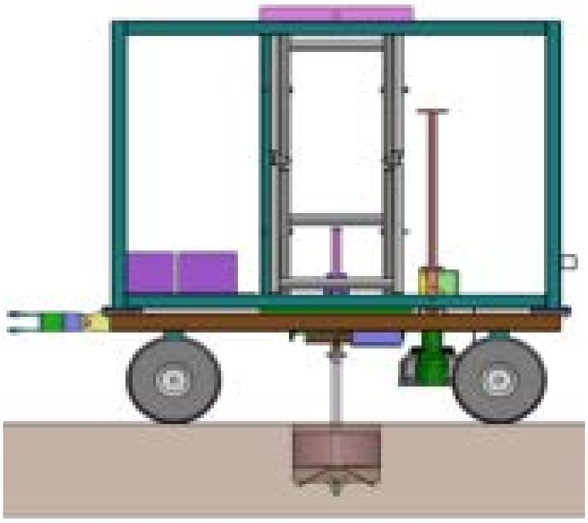

Figure 9: Digging of soil completed

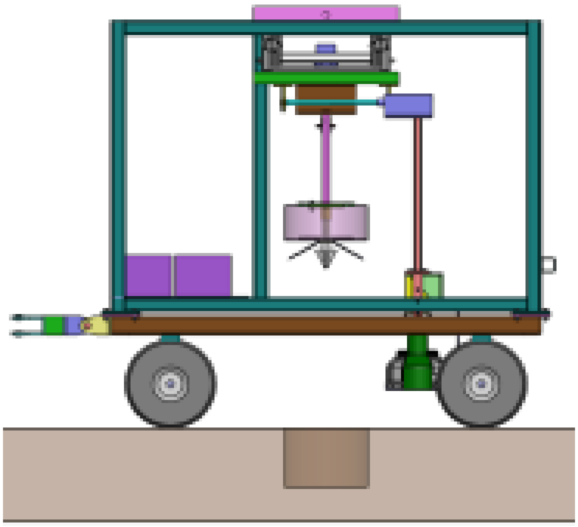

Figure 10: Scissor table lifted up and engaged with Gripper assembly

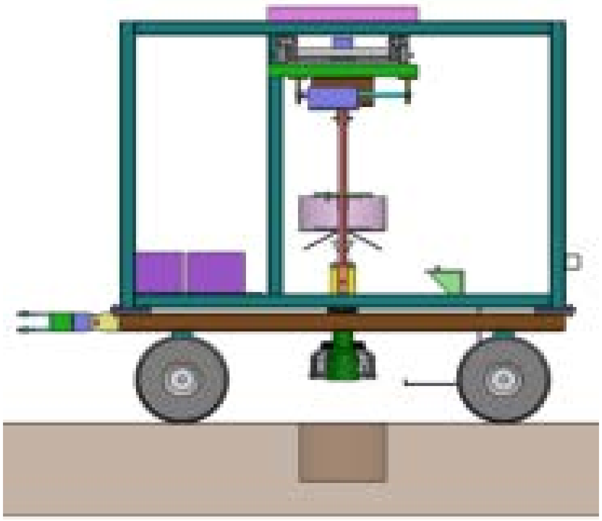

Figure 11: Gripper assembly aligned with Pit

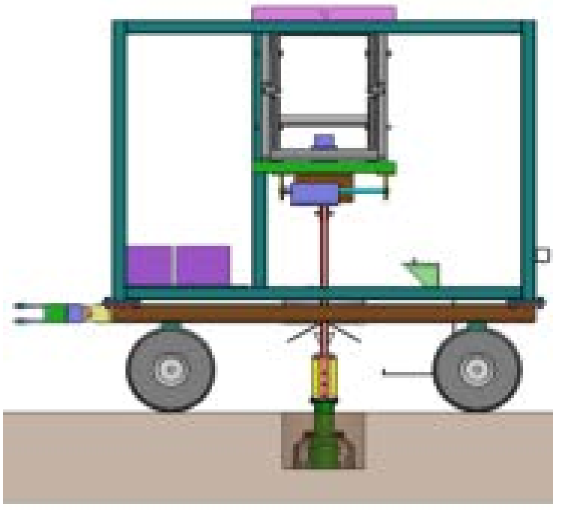

Figure 12: Gripper assembly lowered in Pit by lowering scissor table

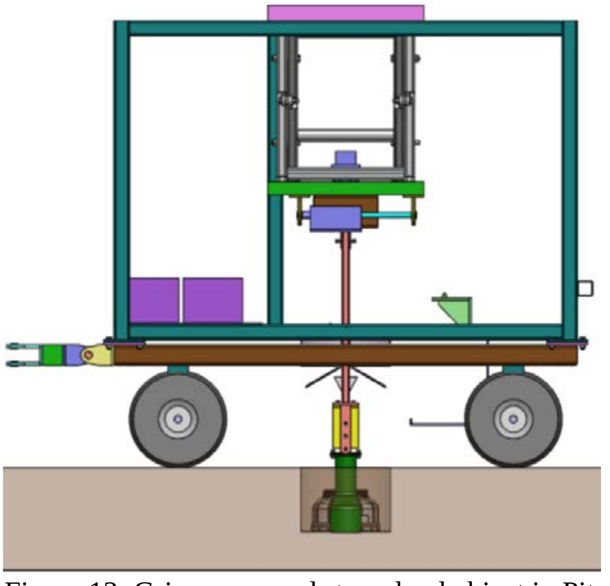

Figure 13: Gripper expands to unload object in Pit

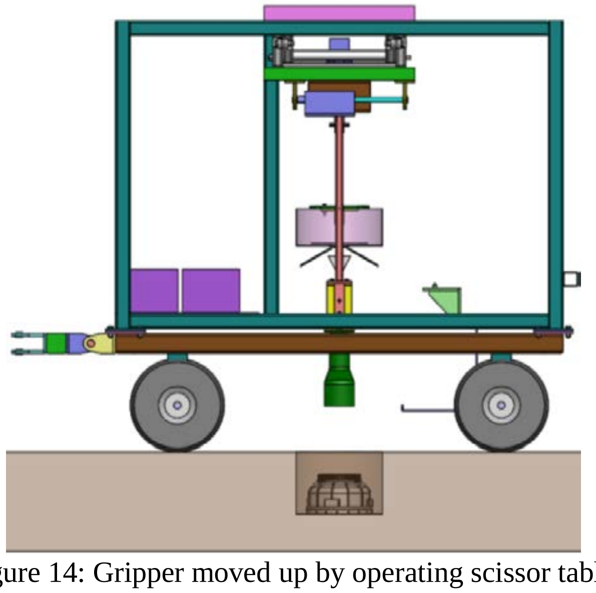

Figure 14: Gripper moved up by operating scissor table

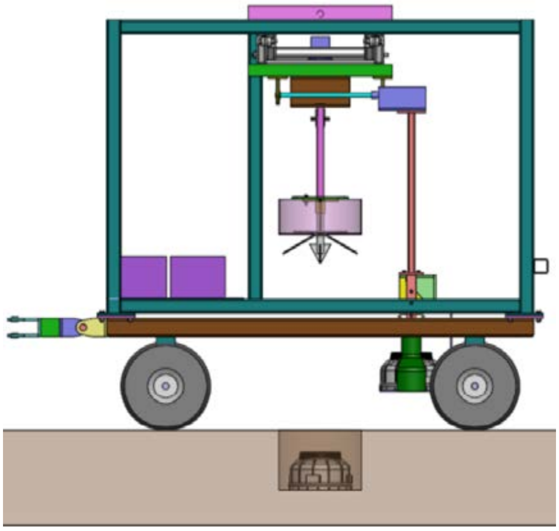

Figure 15: Gripper moved to home position and Vehicle ready to move to next pit location

4. Experimentations

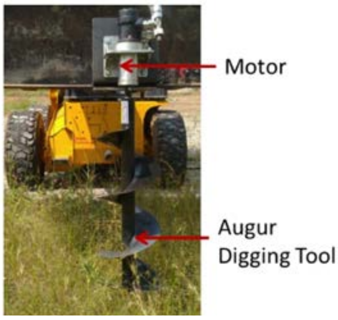

Figure 16: Experimental Set-up

Figure 17: Pit Creation and Mine Placed into Pit

Experimentation to validate the concept are under progress. The tool has been operated in different terrains and power requirement is matching with theoretical power calculated. The time sequence of activities has also been checked for compliance. The concept has been validated and will be used in Unmanned Object Laying equipment.

5. Acknowledgment

Authors gratefully acknowledge the guidance and encouragement given by Shri V V Parlikar, Director R&DE(E) and Shri A K Patel, Associate Director, R&DE(E) in carrying out this work.

6. References

[1] G.G. Boldyrev & G.A. Novichkov, "Evaluation of Tip Resistance to Auger Drilling", International Journal of Machine Learning and Computing, Vol. 2, No. 4, August 2012

[2] Bhaveshkumar P. Patel and J. M. Prajapati "Evaluation of Resistive Force using Principle of Soil Mechanics for Mini Hydraulic Backhoe Excavator", International society for soil mechanics and geotechnical engineering, 2016

[3] Arne Lislerud, "Principles of Mechanical Excavation", December 1997

Fuze Mechanisms and MEMS

Simulation and Analysis of Mechanical Timer for Five-minute Arming Delay for Fuze Mechanism of Land-Based Munitions

SR Parmar
Armament Research &
Development Establishment
Pune
suhagsindur@gmail.com

PK Choudha
Armament Research &
Development Establishment
Pune

Haribhau Markale
Armament Research &
Development Establishment
Pune

VK Dixit
Armament Research &
Development Establishment
Pune

Mahesh Wakchaure
Armament Research &
Development Establishment
Pune

Abstract – **Accurate measurement of time is one of the challenging problems throughout the history. Different methods are invented for measuring the time with accuracy and complexity involved in it. Timers are used for various military, domestic and industrial applications. To initiate the timing-based functioning of fuse the timer is used. For the different military application, the mechanical, electronic and pyro delay timer can be used as per environmental condition, accuracy required, timing duration etc. The research is already carried out on mathematical modelling, simulation of clockwork mechanism, evolution of clockwork, finite element model for clockwork mechanism, erosion of clockwork mechanism etc.**

For the land-based munition, the arming delay of 60 minutes was required and for that munition, the mechanical timer was already developed and it is in use in the munitions. For a different application, the mechanical timer of 5 minutes is to be developed. Instead of manufacturing a new timer, this existing timer was analyzed to convert into a 5 minutes timer without major modification and complexity.

This paper describes the achieving of the 5-minute timer from existing 60-minute timer gear train. For achieving the new arming time, from existing timer many alternatives have been studied by increasing the spring torque, by modifying the weight of pallet wheel, by changing the material of pallet wheel and by decreasing the gear ratio etc. Finally, reduction in gear ratio as an option was selected to conceptualize the new timer design. Further, factors affecting the arming delay of this new timer are analysed and presented in this paper. Timer mechanism is simulated using ADAMS multi body dynamic analysis tool, to study dynamic behaviour of timer. Variations in distance between Ratchet and Pallet, Diameter of pallet pins, Pallet pins and Spring torque are presented for their effect on timing of timer

Keywords: Mechanical timer; Escapement mechanism; Effect of tolerances; Arming delay; Clockwork simulation

1. Introduction

The mechanical timer was firstly introduced in the industrial application for automation and various time-based cycles with better precision. Most of the mechanical timers and clocks adopt clockwork that includes gear train, springs, an escapement mechanism and oscillator. The clockwork mechanism is important mechanism for estimating the time which was invented long ago. The history and qualitative analysis of evolution in escapement mechanism was carried out by Miodrag [1] et al. and is being used in different commercial and military applications even today. F Badrakhan [2] carried out the study of dynamic behaviour of oscillator, to generate new form of equation to estimate the natural frequency of escapement. Robuschi [3] et al. evaluated the damping characteristics of the oscillating system.

In ancient time, tower clock in Europe used dead weight as potential energy. John Wagner [4] et al. prepared theoretical model and got it verified by experimental result for deadbeat escapement. Aaron S. Blumenthal and Nosonovsky [5] brought out the importance of invention of the pendulum that had created much more accurate clock than ever before. Ji-hun Jeong [6] et al. designed the miniature mechanical safety arming devices for munition that works on escapement mechanism.

Time accuracy of clockwork mechanism is depending upon many environmental, manufacturing, material and design factors. These factors are also to be studied and analyzed to achieve the time accuracy within specified range. Signature analysis was carried out for mechanical watch movements to identify the various malfunctions in the clockwork by S. Su and R Du [7]. Design variables and manufacturing tolerances were also studied to check its effect on arming time by SR Parmar [8] et al.

Escapement mechanism is heart of clock mechanism ever invented. It controls the release of energy in controlled manner and thereby controls the motion of main shaft or cam. It allows intermittent movement of the last gear and provides uniform movement for the first gear. Variety of escapements mechanism with diverse operating principles is in use depending on the accuracy of timing device. The wear at the escapement and its effect on timing was studied by J. Rolland [9] et al. Finite element analysis, rigid body simulation and mathematical model were developed for analysis of clockwork mechanism before realizing the actual hardware by J. Rolland [10] et al. and Mayuri and Piyush rode [11].

2. Timer Modification

Timer mechanism is used in munition to initiates the fuze at proper time. In land-based munition, this arming delay is used for controlling the motion of sensitive fuze parts which can be aligned for proper function after specified time. This arming delay in current munition is of 60 minutes. The cam is connected to the timer for performing the specified function after the specified time duration as shown in Fig. 1. Central shaft connects the cam with the central gear. Spiral spring which imparts the torque to the timer is attached to the central gear. This torque is to be reduced through the gear train of proper gear ratio

Figure 1 Cam and Timer (60 Minutes)

In this mechanism, at the end of gear train there is a pallet wheel, having two pins mounted on it, to create oscillation and to control the ratchet by coming in contact alternately. Pallet wheel acts as an energy dispenser and keeps rotation of central shaft under control and also the loss of energy of the torsion spring. A 60 minutes duration timer was simulated, realized and tested successfully and now in current use for different safety arming devices.

It was required to create the mechanical time delay of 5 minutes for different application for different munition. To meet the requirement of 5 minutes arming delay mechanical timer with similar rotation of cam i.e. 270^0, alternatives are analyzed. Torque of a spring, size and material of the pallet wheel and gear ratio are studied for this. Study of combination of above modification is also carried out to achieve final timer of 5 minutes.

Finally, the new timer was achieved by changing the design of existing timer as shown in fig. 2 & 3. To achieve this, existing gear train ratio was modified by removing one gear-pinion set from the gear train as shown in fig. 2. The new design of timer is as shown in fig. 3 without much modification and complexity involved in it. This was simulated using multi body dynamic simulation using ADAMS, to check the arming time. After removing one gear, the gear ratio is changed from 4007 to 534 which increases the speed of the central gear which is connected with cam.

After achieving the basic time and rotation requirement of cam, further sensitivity analysis of this new timer is carried out before realization of actual hardware.

Figure 2 Existing Timer (60 Minutes)

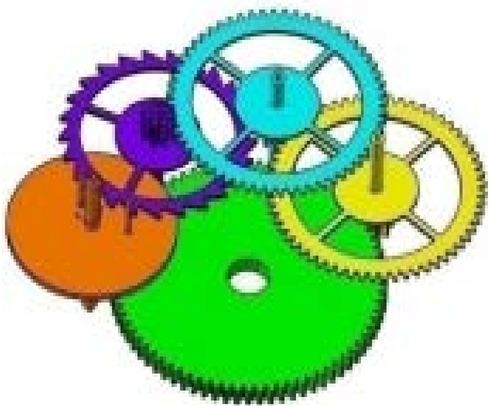

Figure 3 New Timer (5 Minutes)

3. Simulation

After carrying out the study of new timer to check the arming delay, further study was carried out to check the severity of the different parameters on the arming time. The critical, major or minor factors like manufacturing tolerances which can affect the arming time are studied further here. Timer mechanism is simulated for variations in Pallet pins distance, Pallet pin diameter, Ratchet - Pallet distance and spring torque. Following are the input parameters for the simulation.

Table 1 Input Parameters

No.	Parameter	Parameters
1	Angular Rotation of Cam	270°
2	Input Torque	0.0053 N.m
3	Radius of Pin	0.4 mm
4	Central Gear	76
5	N1-Pinion	8
6	N1-Gear	60
7	N2-Pinion	8
	N2-Gear	60
8	N3-Pinion	8
9	Distance: pin1&2	4.95 mm
10	Distance: Ratchet-Pallet	7.69 mm

The results were generated from the simulation and are discussed below.

4. Results & Discussion

Simulation result for rotation of cam of 60 minutes & 5 minutes timer respectively are as shown in fig. 4 & 5. Angular velocity was 0.075 deg / sec for old timer and 0.9 deg / sec for new timer. It is clear that for old timer, the time required about 60 minutes to rotate the cam for 270° and for new timer this time is 5 minutes.

Figure 4 Cam Rotation vs Time (60 Mins. timer)

Figure 5 Cam Rotation vs Time (5 Mins. timer)

Now, the critical factor for this timer is studied to finalize the design of new timer.

A. Variation in distance between Ratchet and Pallet

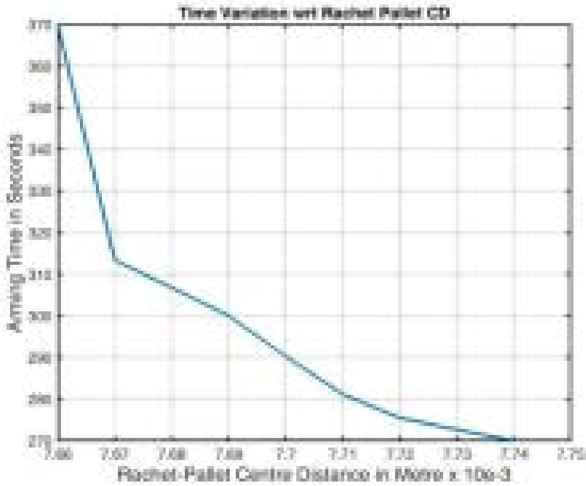

Figure 6 Effect of Pallet-Ratchet Distance

The distance between the shaft of ratchet and Pallet is 7.69 mm. The 270 deg. of rotation of a central gear in 5 min is achieved with the basic dimensions of gear. The effect of variation in ratchet and pallet distance change in arming time as follows.

If the distance between ratchet and pallet increased beyond 7.79 mm then there is no contact between ratchet and pallet. it didn't create escapement therefore allowed the ratchet to rotate freely. Also, if distance between ratchet and pallet decreased beyond 7.65 mm pallet gets locked with ratchet. It is clear that, distance between ratchet and pallet should lies between 7.67 mm and 7.70 mm for effective working of timer with the variation of 10 seconds.

B. Variation in distance between pallet pins

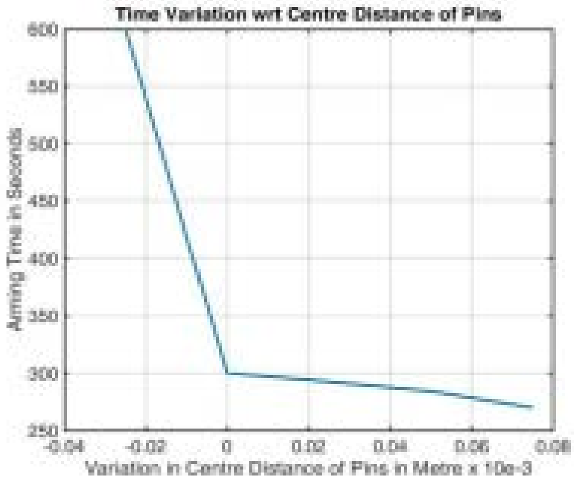

Figure 7 Effect of Distance between Pallet Pins

From the fig. 7, It can be evaluated that if distance between a pallet pins is increased then it allows cam for faster rotation and vice versa. The effect of increasing a distance is not as severe as decreasing a distance. If the distance between pallet pins decreased then arming time increased very rapidly. For the decrement of the distance between the pin just by 25 microns, the arming time increased from 5 to 10 minutes.

It is observed that, if centre distance between pallet pin 1 and pin 2 decreased by 75 microns then ratchet will be locked by pins and will not be allowed to rotate the timer.

C. Variation in Torque

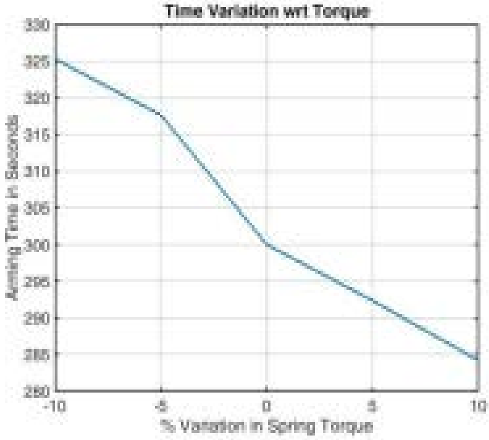

Figure 8 Effect of Variation in Torque

Torsion spring is used to provide torque to the timer. In manufacturing, tolerance is always to be considered by designer to keep the clock speed within specified limit. Here, torque is varied by ±5% of theoretical value to check the performance. The arming time can be varied by 15 seconds for the variation in spring torque of 10% as shown in fig 8. Therefore, spring torque is not much severe parameter as others.

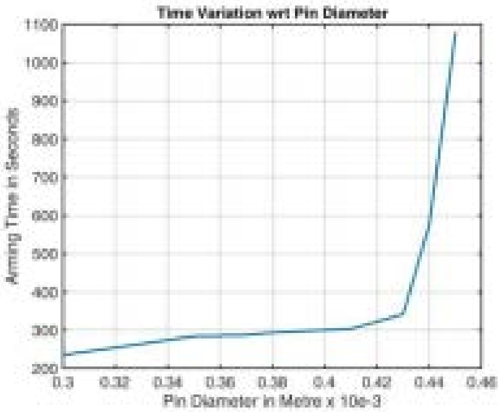

Figure 9 Effect of pallet pin diameter

D. Variation in pallet pin diameter

Fig. 9 shows the variation of arming time w.r.t. pallet pin diameter. From the result, it can be evaluated that by increasing the pin diameter, arming time increased significantly as it slowed down the rachet and vice versa.

If the pallet pin diameter increased from 0.4 mm to 0.45 mm than arming time came to 18 minutes. If a pallet diameter increased to 0.5 mm, then pallet pin will lock the ratchet. It is also observed that, by decreasing pallet pin diameter from 0.4 mm to 0.3 mm, timer time decreases linearly from 5 min to 3.91 minutes.

5. Conclusion

From the above result it is clear that the 5-minute timer can be prepared from already existed timer of 60 minutes.

This new 5-minute timer has a sensitive parameter are Centre distance between two pins and Ratchet-Pallet distance. Pin diameter is also a much severe parameter for arming time. Torque variation of spring doesn't affect the timing severely.

6. Acknowledgment

We would like to thank the Director, ARDE for the encouragement and guidance extended to the team to carry out this study. We also appreciate the effort of all our team members.

7. Reference

[1] Miodrag Stoimenov, Branislav Popkonstantinović, Lyubomir Miladinović, Dragan Petrović. Evolution of Clock Escapement Mechanisms, Faculty of Mechanical Engineering, Belgrade, Vol. 40, No 1, 2012, 17-23.

[2] F. Badrakhan, Dynamical behaviour of an oscillator sustained by an intermittent mechanism, Journal of Sound and Vibration (1983) 88(l), 27- 36.

[3] N. Robuschi a, F. Braghin a, A. Corigliano b, A. Ghisi b, A. Tasora c. On the dynamics of a high frequency oscillator for mechanical watches. Mechanism and machine theory 117 (2017) 276-293.

[4] John Wagner, David Moline, Eugene Vold. Model of a Mechanical Clock Escapement. Am. J. Phys. 80 (7), July 2012.

[5] Aaron S. Blumenthal, Michael Nosonovsky. Friction and Dynamics of Verge and Foliot: How the Invention of the Pendulum Made Clocks Much More Accurate. Appl. Mech. 2020, 1, 111–122.

[6] Ji-hun Jeong, Junseong Eom, Seung S. Lee1, Dong Wan Lim, Yong Ik Jang, Kyoung Woong Seo, Seong Soo Choi, Chun Jae Lee, and Jong Soo Oh. Miniature mechanical safety and arming device with runaway escapement arming delay mechanism for artillery fuze. Sensors and Actuators A: Physical (2017) DOI: https://doi.org/10.1016/j.sna.2018.05.

[7] S. Su, R. Du. Signature analysis of mechanical watch movements. Mechanical Systems and Signal Processing 21 (2007) 3189–3200.

[8] SR Parmar, SD Budhia, Pankaj K Choudha. Effect of Design Variables in Timing of Timer Mechanism for the Arming Delay in Land Based Munition. 2nd National Conference on Advances in Armament Technology 282-284.

[9] J. Rastegar, R. Murray, C. Pereira, O. Partners, B. Shore, and N. York, "Energy-Harvesting Power Sources for Very-High-G Gun-Fired Munitions," vol. 7643, pp. 1–7, 2010, doi: 10.1117/12.847777.

[10] J. Rolland, H. Walter-Le Berre, A. Saulot, Y. Berthier. Instrumentation of a contact with the Finite Element Method and experimental coupling: The case of the Swiss lever escapement mechanism. Tribology International 111 (2017) 176–183.

[11] Mayuri P. Rode, Mr. Piyush P. Rode. Computer Simulated & Mathematical Modeling For Mechanical Timer by using Runway Escapement Mechanism. IJSART - Volume 2 Issue 12 – December 2016. Issn [Online]: 2395-1052

Theoretical Model of Latching Switch Assembly for Fuze

Mehul Sirohi
Armament Research & Development Establishment
Pune
mehulsirohi100@gmail.com

Prabhakar Kumar,
Armament Research & Development Establishment
Pune

S. Rambabu
Armament Research & Development Establishment
Pune

***Abstract* – In this paper, the mathematical model has been proposed to analyze the motion of a plunger with zig zag slot against a fixed guided pin of Latching Switch Assembly. The Latching Switch is a setback switch that provides a permanent contact on sensing the setback acceleration during the launch of a missile or rocket. The mathematical model for the existing design is simulated for an external excitation assuming a half sine wave of a certain amplitude and frequency. The results of the simulation have been analyzed and presented in the paper.**

Keywords: Fuze, Latching Switch Assembly, Setback Plunger

1. Introduction

Safety is one of the most critical aspect in the design of a weapon system. Fuze is a vital subsystem of any missile, rocket or artillery which provides the required safety for crew during transportation, storage, handling and launch. Fuze shall incorporate minimum two independent safety features to prevent unintentional arming, each derived from different physical environments [1]. Setback force is experienced during the launch phase and is one of the prominent physical environments which is sensed by the Fuze.

The mechanical setback switches are commonly designed only as a spring mass system. The switches though offer simplicity during the design and assembly yet there is a drawback in the design i.e., the time response is almost instant. Therefore, it is important from safety aspect that the switches should function only after a sustained acceleration to distinguish launch event from crew operations such as handling and transportation. Latching Switch incorporates the design feature i.e., a setback plunger with a zig zag slot to increase the response time of the switch allowing it to operate after a sustained acceleration. It is therefore essential to evaluate the response time of the switch.

The Setback Plunger moves under the effect of external excitation where its motion is obstructed as the fixed pin engages with zig zag slot. The interaction during collision of the fixed pin with the zig zag slot is analyzed and equations of motion of Plunger for each collision are formulated. The vertical displacement as a function of time can be derived using the equations of motion. Subsequent vertical displacements can be evaluated by analyzing the velocity after each collision and the geometry of the slot profile. The time period can be deduced for each displacement.

The velocities at each collision can be derived from the corresponding displacement function and time period. The mathematical model therefore helps to evaluates the overall time response for the setback Plunger during the dynamic condition.

2. Switch Mechanism

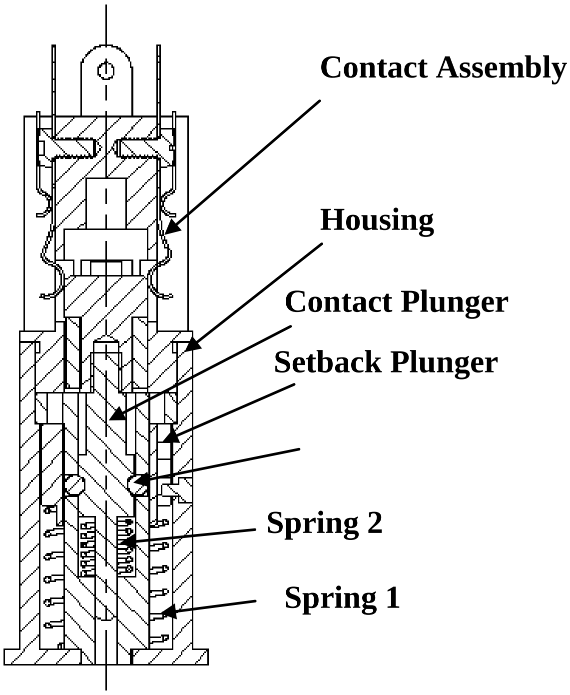

Figure 1: Latching Switch Assembly

Figure 1 shows the configuration of Latching Switch Assembly. The Switch comprises of a Housing with a press fitted pin, zig zag profile Setback Plunger, Spring 1, Contact Plunger, Spring 2, Contact Assembly and two steel balls. The Contact Plunger is made of stainless steel with nylon bush and brass body press fitted to the bottom end of the Contact Plunger respectively. The Contact Plunger is initially locked by the two steel balls. The steel balls are held in the slot of the Contact Plunger on one end and with the Setback Plunger on the other end. The Setback Plunger and contact plunger are assembled against helical compression springs i.e., Spring 1 and Spring 2 respectively. The Contact Assembly consists of a Contact Housing made of nylon, four metallic brass Contact Strips and two stainless steel pressure pads. The Contact Strips are pressed by the Pressure Pads that are fastened with the Contact Housing with the help of screws. The Pressure Pads thus ensure positive contact with the contact strips. The Housing, Setback Plunger and the Contact Strips are all gold plated to ensure proper electrical contact. The Setback Plunger moves against the Spring 1 when the setback acceleration reaches the design threshold value. The ball lock on the Contact Plunger is released and the Plunger moves due to the spring force of Spring 2. The initial contact of the Contact Strips is with the non-metallic part of the Contact Plunger i.e., Nylon. The forward movement of the Contact Plunger latches the metallic brass body with the Contact Strips and the closure of the switch is sensed. The switch therefore maintains a firm permanent contact even after operation and functions after sustained acceleration.

3. Mathematical Model

The Plunger starts its motion when the fixed pin is inside the zig zag groove. The forces acting on the Plunger as it moves under external excitation and coordinate system is shown in the Figure 2. The model is simplified under the assumptions: a) The weight of the Plunger is negligible compared to the external force and spring force hence it has been neglected; b) The collision between the setback plunger and the fixed pin is assumed as collision between an ideal cylinder and plain surface [2]; c) The components analyzed during collision are assumed as rigid bodies.

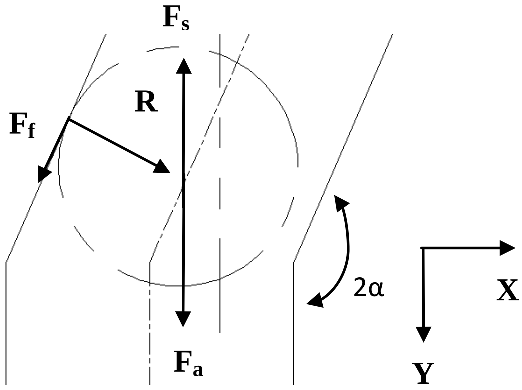

Figure 2: Forces on Plunger with fixed pin in the slot

Figure 2: Forces on Plunger with fixed pin in the slot

The mass of the plunger is assumed ‘m’, K is the stiffness of the spring. ‘μ’ is the coefficient of kinetic friction between the Plunger and the pin, ‘α’ is the half angle of the slot and ‘L’ is the length of the groove for one segment of slot.

‘Fa’ is the external excitation, ‘Fs’ is the spring force, ‘R’ is the force due to Normal reaction and ‘F_f’ (μR) is the force due to friction and ‘t’ is the time period of motion.

The external force excitation is assumed to be a half sine wave

$$Fa = A_m \sin (w*t) \tag{1}$$

Where ‘w’ is the angular frequency of excitation
‘A_m’ is the amplitude of excitation

Assuming ‘w_n’ as the natural frequency of spring mass system

$$w_n = \sqrt{\frac{K}{m}}) \tag{2}$$

‘

x’ is assumed as the horizontal displacement and ‘y’ as the vertical displacement

The force equation will be as

$$mx'' = R (\sin \alpha - \mu \cos \alpha) \tag{3}$$

$$my'' = Fa-Fs-R (\cos \alpha + \mu \sin \alpha) \tag{4}$$

The equation (4) can be written as

S $$my'' = m\, Am \sin (w*t) - K y - R (\cos \alpha + \mu \sin \alpha) \tag{5}$$

ince the Plunger moves in the slot throughout its motion after each collision, hence

$$\frac{y''}{x''} = \tan(\alpha) \tag{6}$$

Solving equations (3), (5) and (6) we obtain

$$y'' = \frac{Am\sin(wt)}{1+\frac{\cos(\alpha)+\mu\sin(\alpha)}{\tan(\alpha)(\sin(\alpha)-\mu\cos(\alpha))}} - \frac{Wn^2y}{1+\frac{\cos(\alpha)+\mu\sin(\alpha)}{\tan(\alpha)(\sin(\alpha)-\mu\cos(\alpha))}} \quad (7)$$

The equation (7) can be rewritten as

$$y'' + ay = b\sin(w\,t) \quad (8)$$

where,

$$a = \frac{Wn^2}{1+\frac{\cos(\alpha)+\mu\sin(\alpha)}{\tan(\alpha)(\sin(\alpha)-\mu\cos(\alpha))}} \quad (9)$$

$$b = \frac{Am}{1+\frac{\cos(\alpha)+\mu\sin(\alpha)}{\tan(\alpha)(\sin(\alpha)-\mu\cos(\alpha))}} \quad (10)$$

Let v_{i-1} be the final velocity of Plunger just before ‘i^{th}’ collision and u_i as the initial velocity of Plunger just after ‘i^{th}’ collision in the y direction and t_i as the time period for ‘i^{th}’ collision.

The initial conditions for displacement and velocity respectively are
$y(t=0) = 0$ and $u_0\,(t=0) = 0$

Substituting the above values of u and y, the particular solution of equation (8) is obtained as

$$y = \frac{b\left(\sin(wt) - \frac{w\sin(\sqrt{a}\,t)}{\sqrt{a}}\right)}{a-w^2} \quad (11)$$

The equation (11) is the displacement function with respect to time before the first collision.

The displacement before the first collision can be evaluated from the initial position of the pin in the zig zag slot and the geometry of the slot. Hence, the time period for the motion before the first collision can be deduced from the equation (11)

The final velocity before the first collision can be also be obtained as

$$v_0 = \frac{dy}{dt} \quad (12)$$

When the collision occurs, the component of the final velocity ‘v’ normal to the surface of collision will change to e v sin θ, assuming ‘e’ as the coefficient of restitution and ‘θ’ the angle between the velocity vector and the impact surface.

Hence, the velocity after the collision can be deduced by adding the resultant velocity vector components. Accordingly, the direction of velocity after collision can also be deduced.

The displacement function, time period for each displacement and velocity function for each collision can be evaluated.

The total time period 'T' taken for 'n' number of collisions will be

$$T = \sum_{i=1}^{n} t_i \tag{13}$$

4. Results and Conclusions

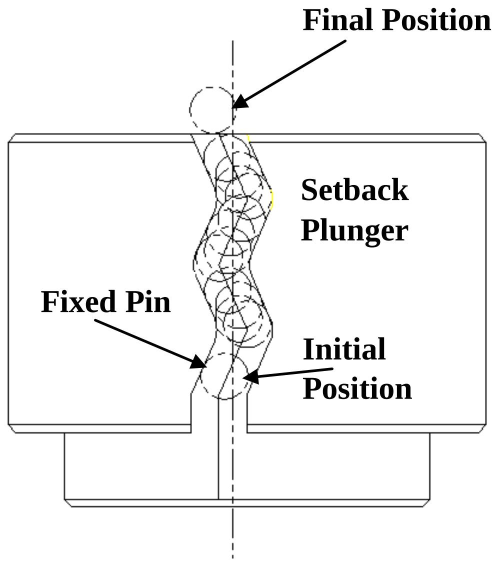

Figure 3: Collision of Plunger

The model of Setback Plunger for Latching Switch Assembly is simulated for an external excitation amplitude of 30 'g' and time period of 50 msec. The mass of the Plunger is 0.005 kg and the stiffness is 100 N/m. The coefficient of kinetic friction between the Setback Plunger and the fixed Pin is assumed as 0.44 [3]. The angle 'α' is 66.5° and the length of each segment of slot is 1.69 mm. The coefficient of restitution is assumed as 0.6 [4].

The collision pattern is shown in the Figure 3 after evaluating the displacement function, time period and velocity function for each collision. A total of 12 collisions are observed before the fixed pin finally disengages from the zig zag slot of the Setback Plunger.

The equations of motion for each collision are analyzed in MATLAB and graphs for the displacement and velocity functions in the 'y' direction are obtained as shown in the figure 4 and figure 5 respectively.

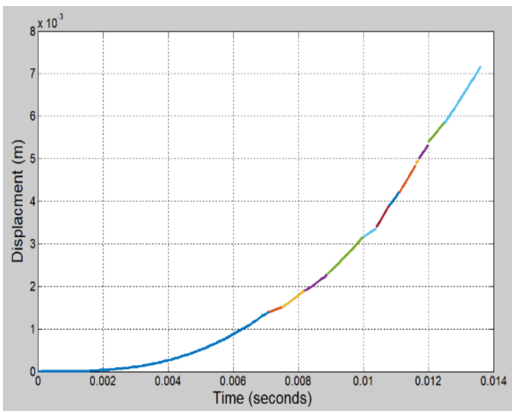

Figure 4: Displacement functions

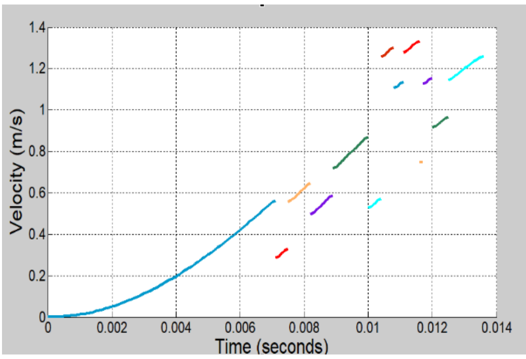

Figure 5: Velocity functions

The setback plunger disengages from the fixed pin after a total displacement of 7.2 mm as per the design. Hence, the total time period for the disengagement is evaluated as 13.6 msec.

The total time period also depends on the half angle and the length of each segment of the slot. The time period of motion increases with increase in the length of each segment and decreases as the half angle of the slot is increased.

The direction of velocity after each collision is also depends on the angle 'α' i.e., the half angle of the slot which determines the total number of collisions.

The initial position of the pin in the zig zag slot is important as it determines the collision profile of the pin in the slot.

The effect of the zig zag slot can be observed in the Figure 5. The velocity does not continuously increase under the effect of external excitation. The switch therefore operates only after a sustained acceleration ensuring the safety of the crew.

5. Reference

[1] Military Standard 1316-F Fuze Design and Safety Criteria.

[2] Wei-rong NIE, Zhan-wen XI, Wei-qing XUE, Zhi-jian ZHOU Study on Inertial Response Performance of a Micro Electrical Switch for Fuze.

[3] Dudley D Fuller Coefficients of friction.

[4] C.S. Sandeep, K. Senetakis, D. Cheng, CE. Choi, Y. Wang, M.R. Coop, C.W.W Ng Experimental Study on the coefficient of restitution of grain against block interfaces for natural and engineered materials.

All ways Quick Response Impact Sensing Mechanism

Prabhakar Kumar
Armament Research and Development Establishment
Pune
pkumar@arde.drdo.in

SS Uppin
Armament Research and Development Establishment
Pune
shivanand_uppin@gmail.com

S Rambabu
Armament Research and Development Establishment
Pune
srambabu@arde.drdo.in

***Abstract* – Considerable efforts have been put to develop a low cost and rugged impact sensing mechanism, which would reliably function under normal and graze situations. Variety of impact sensing mechanism has been developed, these are of mechanical, electronic, piezo based systems. This paper presents a novel rugged, low cost and all direction mechanical impact sensing mechanism. The paper brings out the configuration, design principle and evaluation methodology of the mechanism including shock and SDTA Testing.**

Keywords – All ways, Impact Sensing Mechanism, Standard Drop Test Apparatus, Shock Testing, Super Quick, Response time, Multidirectional

1. Introduction

Many types of ammunition are required to function on impact with the target. Normally, the impact of the ammunition is expected to be normal to target but it has been widely observed in trials and field use, the impact may be shallow or even ammunition may graze with target. So, considerable efforts have been put in the fuze design to enhance the capability of impact sensing mechanism for reliable functioning of the ammunition under diverse situations.

Variety of impact sensing mechanism has been developed for the purpose, these are of mechanical, electronic and piezo based systems. Many of these systems have been successfully integrated in ammunitions but are highly directional, costly or bulky and hence may not be suitable for use in small calibre ammunitions or where possibility of impact at non-normal situation is significant. This paper presents a rugged, low cost and all direction impact sensing mechanism.

2. Operating Principle

The mechanism presented is a novel concept, where the motion of contoured plunger against a biased non-linear spring is used to close and open spring leaf contacts.

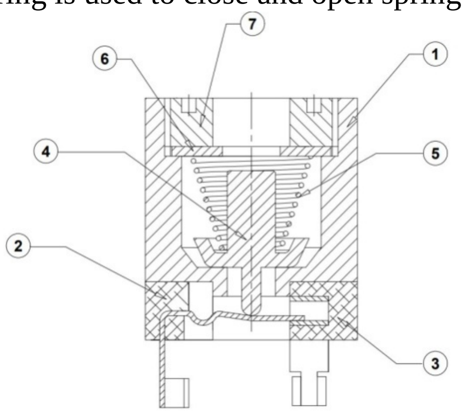

Figure 1: Configuration of Switch

It acts a mechanical inertia switch which senses impact when ammunition hits the target. The ammunition will rapidly decelerate on impact; however, the plunger of switch due to its inertia will be moving forward and pushes the spring further. As the plunger retracts, the contact strip will move and change the state of the switch. The switch will also operate in case the impact is not normal.

3. Configuration of Mechanism

The configuration of the switch is shown in Fig 1. It consists of Switch Housing (1), contact1 (2), Contact2 (3), Inertia Plunger (4), Conical Spring (5), Plate (6) and Lock nut (7). The Switch housing is metallic housing in which two contact are fixed. The contacts are plastic components with in situ metallic strips for electrical contacts. One of the contacts has leaf strip, which acts like a thin cantilever beam. The other contact has two fixed metallic plates one at the top and another bottom separated by a small distance. Upon the assembly of contacts in the housing, the leaf strip of contact1 due to its shape rests on the top plate of contact 2 (Fig. 2). The Inertia plunger is cylindrical shaped metal plunger with tapered feature.

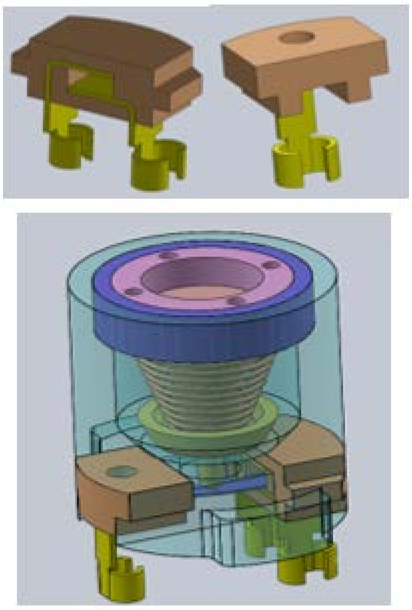

Figure 2: Models Impact Switch

It also has recess for assembly of the conical spring. A plate is positioned over the spring and the switch is closed using a lock nut. The conical spring gets compressed and pushes the plunger to deflect the leaf strip, which contacts the bottom plate of contact 2.

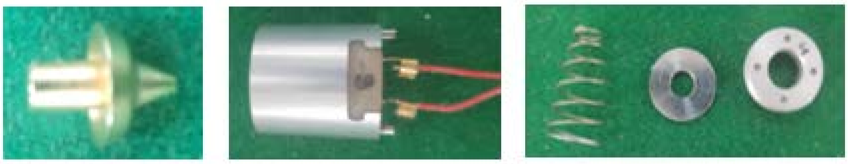

Figure 3: Impact Switch Components

4. Sequence of Operation

The switch is usually assembled in the nose portion of the ammunition. The switch is electrically integrated with fuze unit of the ammunition through wires soldered on the strips of the contacts.

The electrical status between one pair of terminals will be short, while it will be open for the other pair. Once the ammunition impacts with the target, it rapidly decelerates along with subsystems assembled inside it. However, the inertia plunger which is held against a conical spring will continue to move forward under the effect of inertia. Consequently, the leaf strip of first contact will move from bottom to top contact. This change of state of switch is sensed by the fuze and used to detonate the ammunition in impact mode.

In case the impact of ammunition to target is not normal but sideways, the ammunition will experience sideways deceleration. The side way deceleration will tilt the inertial plunger. The plunger shape is optimized to allow tilting about the tapered corners. This will lift the plunger nose from the leaf strip, which will move from bottom to top contact. In this the switch is capable of sensing impact in all directions and imparts all ways functioning capability to the ammunition.

Another important aspect in the functioning of the impact switch is its time taken to sense the impact. A very small time of functioning is preferable as the ammunition can detonate without any significant deterioration and cause maximum damage to the target. The order of response time of switch is expected in tens of micro seconds.

5. Testing and Evaluation

The testing and evaluation of impact switch requires subjecting it to adequate impact levels and measuring of the two parameters switch closure and response time of switch.

A. Shock test

The testing of switch was carried out at shock machine, where the closure of the switch at different angles of impact was checked. A special fixture, see fig 4, was designed which allowed the mounting of the switch at various angles to the shock axis on the machine. This simulated the different impact scenarios from normal to graze impact.

Figure 4: Shock Fixture Variable Mounting

The impact switch was subjected to a half sine wave shock pulse (fig 5) of amplitude 100 ‘g’ and pulse width of 10 msec. The closure of the switch was monitored through wires electrically connected to a oscilloscope.

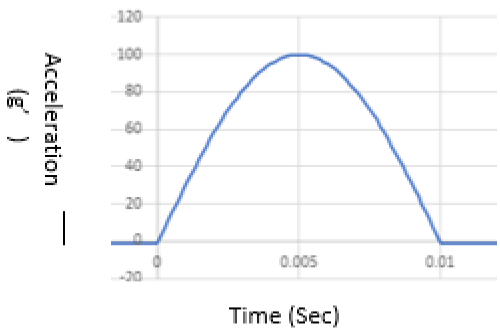

Figure 5: Half Sine Shock Pulse

The closure of the switch was observed for different orientation with respect to the axis of shock. The switch was able to sense normal impact as well as under graze condition also. The function of the switch was successfully evaluated in shock machine.

B. SDTA Test

The other parameter to be measured was the response time of the switch under impact condition. The duration impact obtained in shock machine is of the order of 10 milliseconds and magnitude of 100 ‘g’ however this does not represent actual impact situation. The impact in real case may typically reach in order to thousands of ‘g’ for duration of the order of milliseconds. So, a more realistic impact situation is needed to evaluate the performance of the switch. A standard drop test apparatus (SDTA) can be used to generate 10000 of g levels for duration of 100 of microseconds. The switches were tested on a Standard drop test apparatus and their functioning parameters were monitored.

Figure 6: Standard Drop Test Apparatus

The measurement of response time required precise determination time for impact, with reference to whom switch function delay shall be measured. For this purpose, an off the shelf high precision shock sensing accelerometer was used.

The test was carried out for five samples which were randomly subjected to drop test from various height ranging from 4 feet to 10 feet. The standard drop apparatus was remotely operated, the anvil with fixture having the switch and accelerometer were lifted with an electromagnet vertically along the structure see fig.6. After reaching the required height, the electromagnet was de-energised and the fixture drops under the effect of gravity and impacts on the anvil resulting in severe impact.

Table 1: SDTA Test Results

Unit No	Drop ht (ft)	Peak ‘G’& duration	Resp time (microsec)
16	4	11529	46
09	8	18735	49.8
25	10	17534	53.5
11	12	24400	37.5
04	11	22167	48.9
29	10	19868	47.3

The fig.7 shows screenshot of such test sample on the oscilloscope. The Table 1 summarizes the result of SDTA test of impact switches.

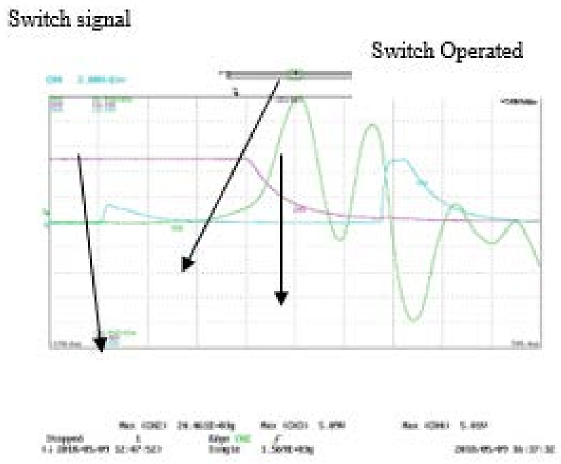

Figure 7: Oscilloscope Graph

The pink line in Fig.7 represents the switch voltage, which is high in initial condition and the green line is monitoring accelerometer output. Once the SDTA fixture impacts the anvil, the voltage output of accelerometer is seen in the oscilloscope and the switch operates which is evident by transition from high to low in switch signal is observed. The response of the accelerometer is a typical half sine curve observed in impact situation, the impact reference time is taken from point equivalent to 200 ‘g’ on the curve. Also, the transition of high to low of the switch delay of certain duration, a cut off voltage of 1V was decided, below which switch was accepted as functioned and response time was measured.

6. Conclusion

The paper presents the design of a rugged, low cost and all direction impact sensing mechanism. The prototypes of the mechanism were realized and tested on Shock machine and Standard drop test apparatus. The multidirectional functioning of the impact mechanism has been verified on shock machine using a special angularly indexed fixture. The switch will function in direct as well as graze condition if it experiences sufficient shock. The response time of the switch was also evaluated on a SDTA apparatus. The switches has been subjected to impact in the range of 10000 ‘g’ to 25000 ‘g’ and the response time was found to be 45±10 micro seconds, which would sufficient to detonated the ammunition in precise and effective manner. The paper has brought out the configuration, design principle and evaluation methodology of the mechanism including shock and SDTA Testing of an All ways Quick Response Impact Sensing Mechanism.

7. Reference

[1.] Thomson W T, Dahleh M D, Padmanabham. C, “Theory of vibrations with Applications”,5th ed US: The McGraw-Hill, 2008.

[2.] Avallone A. Eugene, Baumister III Theodre, Sagdeh M. Ali, Marks’ Standards Handbook for Mechanical Engineers, Eleventh Edition, The McGraw-Hills.

[3.] Sirohi Mehul, Kumar Prabhakar, Rambabu Sala, “Depth Sensing Switch for Safety and Arming Device for Torpedoes”, 10th National Symposium and Exhibition on Aerospace and Related Mechanisms, Thiruvananthapuram, Kerala, ARMS-2016-121.

[4.] MIL-STD-1316E, Fuze design, Safety Criteria”, July 1998.

[5.] J.E. Shigley, C.R. Mischke and T.H. Brown, Jr, “Standard Handbook on Machine Design”, 3rd ed US: The McGraw- Hill 1994.

Development of a MEMS Threshold G-Switch with Enhanced Contact Time

Murugappan R
Centre for Nano Science and Engineering
Indian Institute of Science
Bangalore
murugappan@iisc.ac.in

Prof. Prosenjit Sen
Centre for nano Science and Engineering
Indian Institute of Science
Bangalore
prosenjits@iisc.ac.in

Prof. Rudra Pratap
Centre for nano Science and Engineering
Indian Institute of Science
Bangalore
pratap@iisc.ac.in

Dr. Rajkumar
Armament Research & Development Establishment
Pune
rajkumar@arde.drdo.in

Abstract — **We report the design, fabrication, and testing of a MEMS g-switch. The switch is designed to close on experiencing an acceleration impulse of 250g. The fabricated switch is tested by giving impulses of varying magnitudes to determine the g-level at which the switch turns ON. The device is fabricated on an SOI wafer using the handle layer as the proof-mass to reduce its out-of-plane bouncing. The novelty in design is in increasing the contact time of the switch by simply increasing the electrode area. An increased contact area increases the adhesion between the proof-mass and the electrodes which in turn prolongs the release of the proof-mass.**

Keywords— Threshold accelerometer; MEMS g switch; proof-mass; shock input.

1. Introduction

MEMS g-switches are a special class of MEMS accelerometers that trigger some downstream action upon sensing a prespecified acceleration level, typically specified terms of a multiple of g (acceleration due to gravity) such as 100g. These accelerometers do not record anything until the threshold acceleration value is reached. Typically, the attainment of the threshold value results in some contact or latching between two electrodes, thus completing an electrical circuit and transmitting a signal that the threshold value has been reached. This is why they are called g-switches. Since any action follows only after the switch turns ON, there is no power consumption until then and, unlike their regular counterparts, these accelerometers do not consume power. Although they have a huge advantage of very low power consumption, g-switches have a few drawbacks. The acceleration profile has to be prespecifed (duration of the impulse, and the magnitude of acceleration, also called the g-level, where g is the acceleration due to gravity). The g-switch accelerometer can only be designed for this prespecified threshold g-level, while general accelerometers can sense acceleration over a range of magnitude and frequency bandwidth.

There are four types of g-switches: (i) latch type (ii) non-latch type (iii) bistable threshold g-switches and (iv) micro-fluidic inertial switches. This work is dedicated to non-latch type g-switches. Non-latch type g-switches make contact with a stationary electrode on experiencing the threshold acceleration but return to their original configuration once the external acceleration is removed. On experiencing the threshold acceleration, the movable electrode makes contact with the stationary electrode, closing an external circuit. Therefore, we know if the required acceleration level is reached. Compliant bistable switches have two equilibrium states, where the first stable state is the initial open position, and on experiencing the appropriate acceleration, the device transitions to the second stable state [1, 2, 3, 4]. A micro- fluidic inertial switch uses a liquid metal droplet that moves under the action of the applied acceleration, making contact with a pair of fixed electrodes and closing the external circuit. Since these switches have a liquid-solid contact as compared to the solid-solid contact of the other three types, they do not suffer from wear and high contact resistance [5, 6]. However, they need an actuation mechanism to move the liquid droplet back to its original position [7]. This work is targeted at realizing non-latch type and latch type MEMS g-switches for defense applications. We have designed and fabricated non-latch type switches for two threshold values, 200g and 500g. We have considerably improved the contact resistance, and the contact time, the two main performance parameters for non-latch type g-switches. . Zhuoqing Yang *et al*. [8] proposed a bridge type compliant electrode to increase the contact time, Tadao Matsunaga *et al*. [9] reported a device with squeeze film damping to prolong the contact time and Haogang Cai *et al*. [10] designed a flexible proof-mass that gradually increases the contact area over the duration of impact. Here, we propose and implement perhaps the simplest design to enhance the contact time by simply increasing the electrode area.

2. Modeling of MEMS g-Switches

The schematic design of the device is shown in Fig. 1. The light coloured portion is anchored to the substrate, and the dark coloured portion is suspended. The device essentially consists of a proof mass suspended by a set of four folded beams that support the proof mass. In Fig. 1, *m* is the effective mass of the structure, and *k* is the effective stiffness of the folded beams. Each serpentine spring has the fixed-guided boundary condition, $12EI/L^3$ is the stiffness of one beam in each serpentine spring, where *L* is the length of each beam, *E* is Young's modulus of the beam material, and *I* is the area moment of inertia of the cross-section of the beam. The two-fold serpentine beam in each suspension spring is in series, and all the four suspension springs are in parallel; therefore the effective spring constant is given by,

$$k = \frac{p}{n}\frac{12EI}{L^3} = \frac{p}{n}\frac{Etb^3}{L^3} \quad (1)$$

where *p* is the number of beams in parallel (equal to 4), *n* is the number of beams in series (equal to 2), *b* is the width of each beam, and *t* is the thickness of the device.

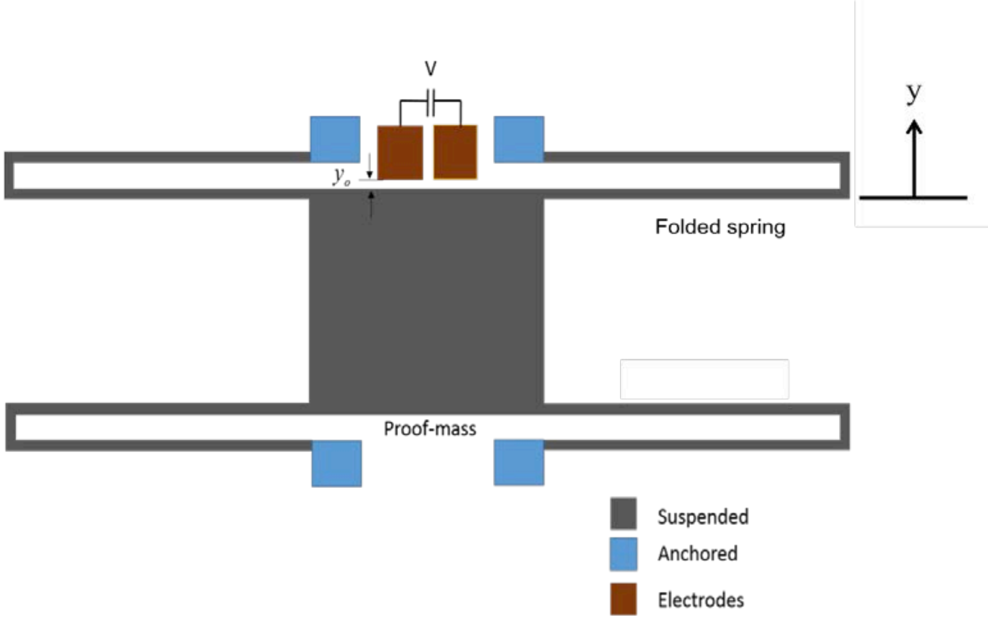

Fig. 1: Schematic of the fabricated non-latch type g-switch.

The governing equation of the device is given by,

$$m\ddot{y} + ky = ma(t) \qquad 0 \le t \le t_{contact} \tag{2}$$

where *a(t)* is the acceleration experienced by the device, and t_{cont} is the time at which contact is established between the proof-mass and the electrodes.

Since the acceleration in most cases will be an impact, *a(t)* is a non-linear shock impulse that cannot be readily used in simulation (equation 2). To obtain an analytical solution for the model, the actual acceleration pulse signal is approximated with a Fourier series as shown in Fig. 2. Here, the blue (continuous) curve is the actual triangular pulse, and the red (dotted) curve is its Fourier representation with 30 frequency terms. The Fourier series representation approximates the real profile well. This gives an analytical expression for the acceleration, *a(t)*, as a function of time. The acceleration function is given by,

$$a(t) = a_o + a_n \sin(\omega_n t) + b_n \cos(\omega_n t) \tag{3}$$

The Fourier coefficients of the acceleration profile *a(t)* are a_n , b_n and a_o. The n^th^ frequency is ω_n equal to $n\pi/T$, n is the number of frequency terms that make up the Fourier series, and T is the length of the impulse signal. Here a triangular profile is represented, but any arbitrary shape of the profile can be recreated using this approach. It can be seen from Fig. 2 that the real signal is recreated very well using the Fourier series approach.

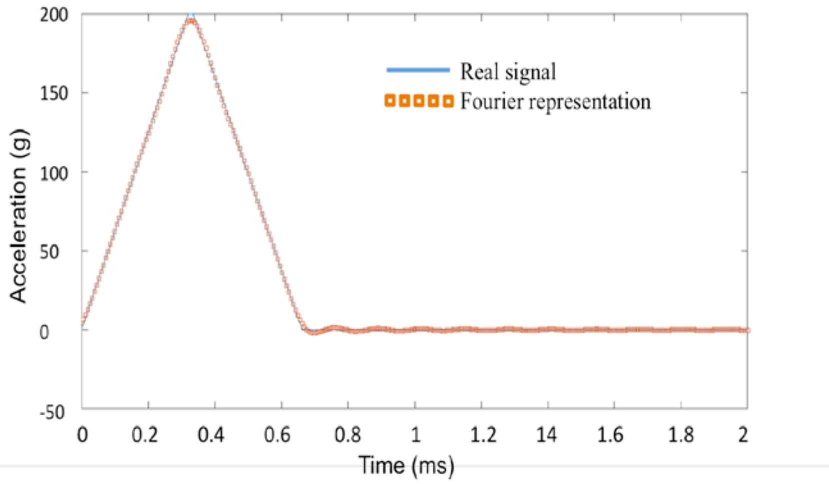

Fig. 2: A Fourier series representation of the input acceleration

The solution to the model for an input of any arbitrary acceleration profile is given by,

$$y(t) = A\cos(\omega t) + B\sin(\omega t) + \sum_n \frac{a_n}{\omega^2-\omega_n^2} sin(\omega_n t) + \sum_n \frac{b_n}{\omega^2-\omega_n^2}\cos(\omega_n t) + \frac{a_o}{\omega^2} \tag{4}$$

Equation (4) represents the displacement of the proof-mass and *v(t)* is the velocity profile of the proof-mass (time derivative of equation (4)) on experiencing the acceleration *a(t)*. The natural frequency of the suspended structure in its in-plane mode (plane of actuation) is ω. The viscous damping effect is neglected, as the proof-mass only completes one-fourth of a complete cycle and the energy dissipated in that interval is not significant compared to the other energy terms. A and B are constants that depend on the initial conditions of the proof mass. They are given by,

$$A = -\sum_n \frac{a_n}{\omega^2-\omega_n^2} - \frac{a_o}{\omega^2} \tag{5a}$$

$$B = -\frac{1}{\omega}\sum_n \frac{a_n\omega_n}{\omega^2-\omega_n^2} \tag{5b}$$

The device parameters chosen for an acceleration level of 250 g, and a half-sine shock profile of 1 ms pulse-width is shown in table 1.

Table 1: Optimal design parameters for a non-latch type device for a constant acceleration of 200g.

Parameter	Symbol	Value
Effective stiffness of folded spring	k	474 N/m
Mass of the suspended structure	m	4.57 mg
Initial separation distance	y_o	27 μm

3. Fabrication Methodology

A typical SOI MUMPS process flow is used in the fabrication of the G-switches. It consists of (i) patterning of device layer using lithography, (ii) DRIE to etch the device layer silicon, (iii) Patterning the handle layer and making a trench by etching (a through-hole from the backside of the device), (iv) etching the buried oxide by wet etching, and finally (v) using a shadow mask to sputter metal on the selected area of the electrodes and on the side-walls of the device. However, to reduce the size of the proof mass and to reduce the out-of-plane bouncing of the device, the handle layer silicon can also be used as the proof mass. The fabrication process flow is shown in Figure 3. Lithography pattern transfer is done on the bottom side of the SOI wafer using an MJB4 mask aligner allowing the handle layer of the wafer to be used as the proof mass in addition to the device layer. Positive photo-resist, AZ4562, is used here as this thick resist can withstand the etching of the deep handle layer. DRIE etching is done to land on the BOX layer (step b). When the handle layer is also used, it reduces the out of plane bouncing of the device that is encapsulated within a glass boning. A 500/300 nm composite layer of Cr/Au (Chrome/Gold) is sputtered on the device layer, and lithography is performed to pattern the metal on the electrodes and the proof mass. Wet etching (buffer HF solution with 69 nm/min etch rate) is done to remove Cr/Au from the remaining part of the device (step c). Lithography is done on the device layer (AZ4562E image reversal photo-resist is used) to pattern the structure of the device followed by DRIE etch to land on the BOX layer (step d). Wet etching etches the BOX layer and releases the device (step e). A shadow masking technique is used to deposit 500/400 nm Al/Au on the side-walls of the electrode and the proof mass where contact happens (step f). The shadow mask has a large tolerance and is aligned with the wafer on a microscope manually. This shadow mask protects the electrodes from forming a continuous metal connection that may cause shorting. Fig. 4 shows the SEM of the fabricated device.

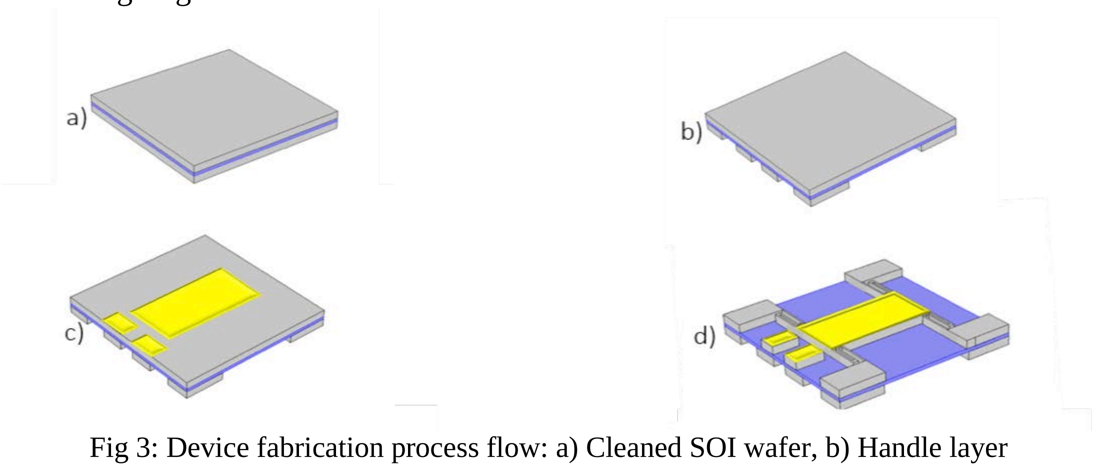

Fig 3: Device fabrication process flow: a) Cleaned SOI wafer, b) Handle layer patterning followed by DRIE, c) Patterning sputtered Cr/Au on the anchor pads and proof-mass, d) Device layer lithography followed by DRIE

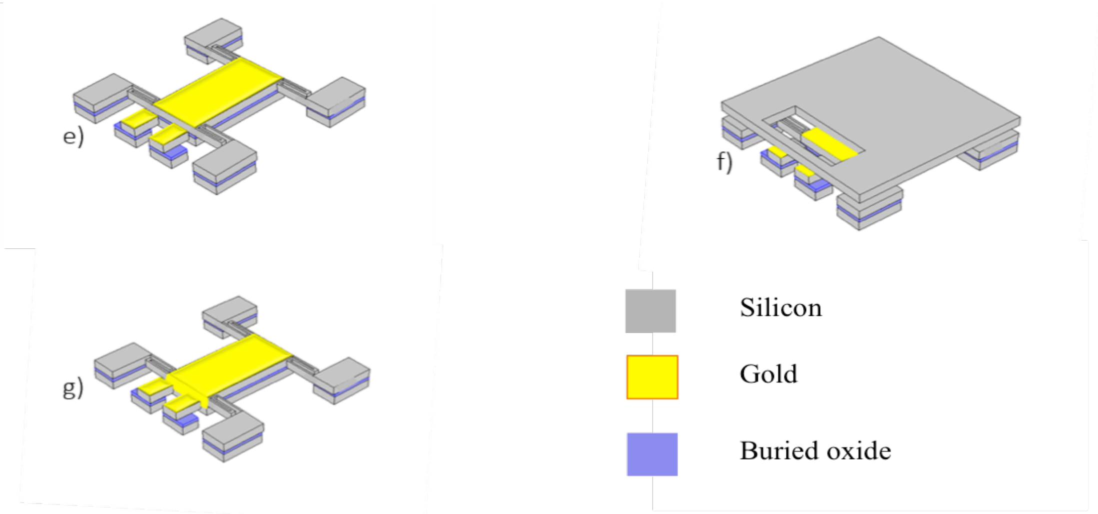

Fig 3: Device fabrication process flow: e) Wet etch of BOX to release device, f) Shadow masking to sputter Al/Au on the device side wall, g) Final device.

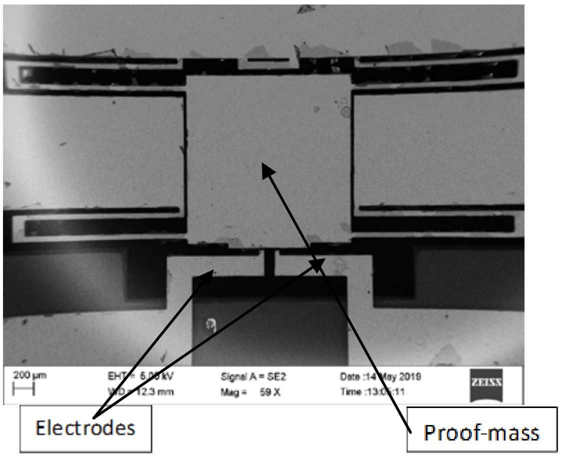

Fig. 4: SEM image of a fabricated switch

4. Sensor testing

The device essentially consists of a proof-mass suspended by four folded beams. Two stationary electrodes are at a distance y_o from the proof-mass as shown in Fig.1. On experiencing a sudden acceleration, the proof-mass moves through this distance, touches the electrodes and thus closes an external circuit. This circuit closing or *switching* indicates if the threshold acceleration is reached. The device is mounted on a spring manipulator that is subject to an impact loading. The magnitude of this impact acceleration is measured using a laser vibrometer (LDV). The voltage drop across the device is measured using a Data Acquisition module. The MEMS switch is designed to turn ON at 250*g*. A half sine wave shock pulse of approximately 1 ms pulse-width is generated using a spring manipulator. The initial separation distance y_o is chosen to be 27 µm. One of the fabricated devices is shown in Fig. 4. Figure 5 shows two different electrode designs: (a) the original design and (b) the enhanced electrode area design. The contact time increases from an average of 18µs to an average of 40µs (>100% enhancement) as shown in Fig. 7, the time of striking of the impulse can also be seen from the second graph of these figures. The overall switch resistance reduces drastically from an average of 45.8KΩ to an average of 11.5mΩ (a reduction of 75%).

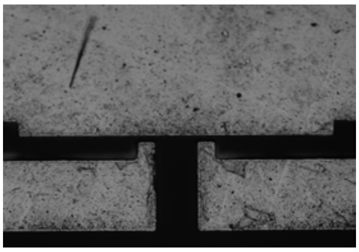
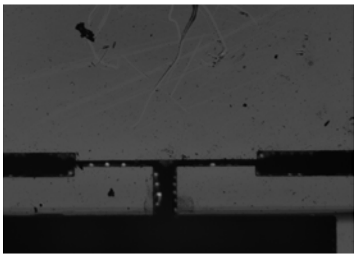

a) Small electrode area($4000\mu m^2$) b) Increased electrode area ($28000\mu m^2$)
Fig. 5: Different electrode area configurations, the area increases by a factor of 7.

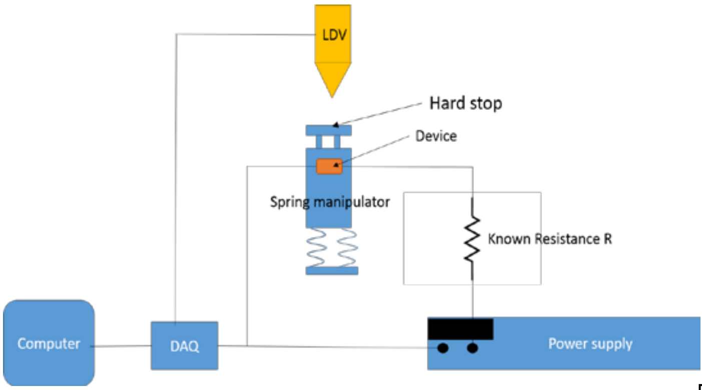

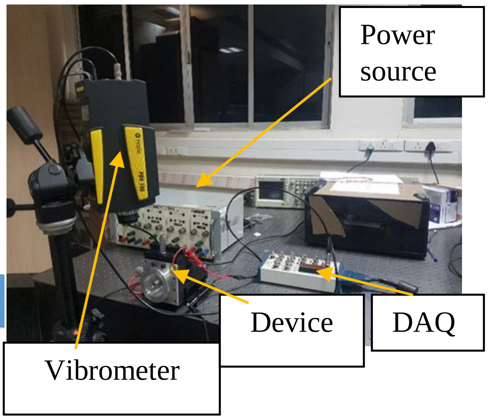

(a) Schematic of the experimental setup (b) The setup used to generate the impulse
Fig. 6: Description of the methodology used in the device testing.

The schematic of the test setup is shown in Fig. 6 (a). The spring manipulator is pulled down and released. The movable part hits a hard stationary block and this produces a shock acceleration to the proof mass. The setup is shown in Fig. 6 (b). Although the device is designed to close at $a \geq 250g$, in experiments the switch closes for $a \geq 225g$. The pulse width of the impulse generated using the spring manipulator is 0.7ms to 1.2ms.

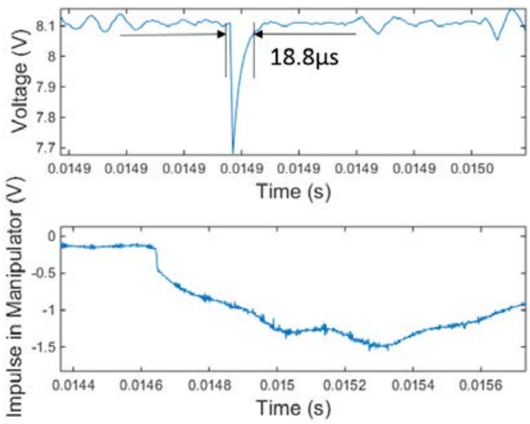

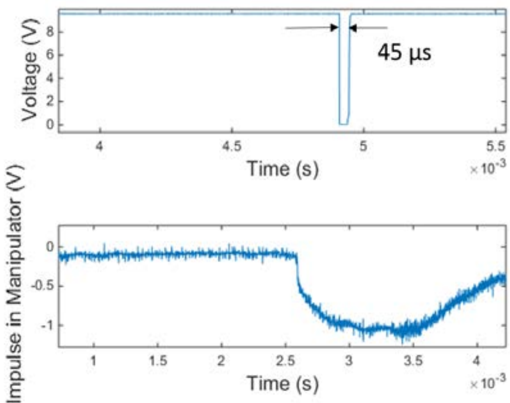

(a) Voltage drop in the switch with small electrode with a contact time of 18.8μs.
(b) Voltage drop in switch with large area electrode area with a contact time of 45μs.
Fig. 7: The measured data showing the enhancement of contact time with the two electrode designs.

5. Conclusion

We have developed a closed-form expression for the response of the latch and non-latch type devices from their governing equations for an impressed acceleration impulse. This is achieved by expressing the acceleration shock profile analytically as a function of time using Fourier series. This allows a profile of any waveform to be used as the acceleration term *a(t)* in the governing equation. A process flow to use the handle layer apart from the device layer of the SOI wafer to realize the proof mass is employed to fabricate the devices. This has the advantage of reduced size and reduced lateral bouncing effect of the proof mass. The contact duration of the device is increased by increasing from 18 μs to 40 μs by increasing the electrode area by a factor of 7.

6. References

[1] J. P. Lynch and K. J. Loh, “A summary review of wireless sensors and sensor networks for structural health monitoring,” The Shock and Vibration Digest, vol. 38, no. 2, pp. 91–128, March 2006.

[2] M. Abdo, Structural Health Monitoring, History, Applications and Future. A Review Book. Open Science, 01 2014.

[3] P. Cawley, “Structural health monitoring: Closing the gap between research and industrial deployment,” Structural health monitoring, pp. 1–20, 2018.

[4] D. S. E. J. A. M. J. W. Wittwer, M. S. Baker, “Mems passive latching me- chanical shock sensor,” in Proceedings of the ASME 2008 Inter- national Design Engineering Technical Conferences Computers and Information in Engineering Conference. ASME, 2008, pp. 1–7.

[5] W. N. C. X. Q. Sun, S. Zhou, “Surface micromachined latching accelerometer,” in International Conference on Solid-State Sensors and Actuators, vol. 2, 1997, pp. 1189–1192.

[6] A. Frangi, B. De Masi, F. Confalonieri, and S. Zerbini, “Threshold shock sensor based on a bistable mechanism: Design, modeling, and measurements,” Journal of Microelectromechanical Systems, vol. 24, no. 6, pp. 2019–2026, 2015.

[7] Y. Peng, Z. Wen, D. Li, and Z. Shang, “A low-g silicon inertial micro-switch with enhanced contact effect using squeeze-film damping,” Sensors, vol. 17, no. 2, p. 387, 2017.

[8] Zhuoqing Yang, Guifu Ding, Haogang Cai, and Xiaolin Zhao, “A MEMS Inertia Switch With Bridge-Type Elastic Fixed Electrode for Long Duration Contact”, IEEE Transactions on Electron Devices, Vol. 55, No. 9, Sep. 2008.

[9] Tadao Matsunaga, Masayoshi Esashi, “Acceleration switch with extended holding time using squeeze film effect for side airbag systems ”, Sensors and Actuators A, Vol. 100, pp. 10-17, Jan. 2002.

[10] Haogang Cai, Guifu Ding, Zhuoqing Yang, Zhijuan Su, Jiansheng Zhou and Hong Wang, “Design, simulation and fabrication of a novel contact-enhanced MEMS inertial switch with a movable contact point ”, J. Micromech. Microeng., Vol. 18, No. 11, pp. 10, Oct. 2018.

Performance Enhancement of Safety Arming Mechanism (SAM) with a Triple Lock System for Electro-Mechanical Impact Fuze for 40mm Grenade

N R Gawali
Armament Research and Development Establishment
Pune
nrgawli@arde.drdo.in

Rahul
Armament Research and Development Establishment
Pune

Jaihind
Armament Research and Development Establishment
Pune

S Rambabu
Armament Research and Development Establishment
Pune

Abstract – **Safety Arming Mechanism (SAM) is a device which prevents an unintended functioning of explosive train of the warhead and allows it to operate at the right time and place. Also, SAM prevents accidental activation of the munition during shipping, handling and storage by keeping the main detonator out of alignment with the initiating element of the explosive train. The explosive train is a sequential arrangement of explosive elements in decreasing order of sensitivity & increasing order of shock/power. Safety Arming Mechanism (SAM) ensures safeties to the munition during handling, transportation, launching, on firing and during flight. The SAM provides the Arming Delay in Fuze to achieve the muzzle safety. When not armed, the detonator and the squib are kept in misaligned position by a safe distance. The configuration of SAM with three independent safeties is chosen in such a fashion, that it must guarantee arming of the SAM only after ejection of grenade from the launcher and at the same time withstand the stresses structurally at the maximum possible ejection velocity.**

The basic aim of performance improvement of SAM was to evolve a miniature mechatronic design of SAM, which would ensure all necessary safeties & function reliably on impact. Thus, improving the performance of the system. This paper highlights the salient features of modified SAM for Electro-Mechanical Impact Fuze for 40mm Grenade. The modification carried out in SAM was validated in static and dynamic condition by realizing the hardware.

Keywords – Grenade, Warhead, SAM, Explosive Train, Rotor, Gear, Spring, Detonator

1. Introduction

Many of the military systems uses, high energy materials as a part of the ordnance called ammunition. The same will be initiated at the desired time at the terminal end, with the help of a device called “FUZE”. In general, in order to make ammunition to be effective against a target, two events are important. First to deliver the right quantity of high energy material at right place and second to trigger the high-energy material under right conditions. The first event is controlled by the fire & control system while the second event is controlled by the FUZE/Timer fitted in the ammunition. These high-energy materials shall be kept safe during handling, transport, processing & up to a limited distance from the launch point. This role is played by the FUZE. A FUZE is a mechanism or device designed to initiate ammunition and to function an item of ammunition at the time & under the circumstances desired. With the development of projectiles, it became necessary to produce devices for activating them. A

FUZE is a sort of brain traveling along with the projectile and controlling its actions; considered from that standpoint, it is most important part of the projectile; although each part of ammunition has its own mission to perform for proper projectile functioning. Fuze is an important part of the ammunition to achieve precision aim and efficient damaging ability. No ammunition is complete without the fuze, which has a pivotal role in keeping the ammunition safe during launch, arm it and initiate the lethal mechanism when needed.

Each fuze will have Mechanical Safety & Arming (MS&A) Device in addition to other Triggering Mechanisms. Once certain conditions such as rotary speed have been reached, the Safety and Arming (S & A) device must arm reliably and the fuze enters the state of readiness. Also, SAM prevents accidental activation of the munition during shipping, handling and storage by keeping the main detonator out of alignment with the initiating element of the explosive train. Safety Arming Mechanism (SAM) ensures safeties to the munition during handling, transportation, launching, on firing and during flight. The SAM provides the Arming Delay in Fuze to achieve the desired arming distance. When not armed, the detonator and the squib are kept in misaligned position by a safe distance. The configuration of SAM with three independent safeties is chosen in such a fashion, that it must guarantee arming of the SAM only after ejection of grenade from the launcher and at the same time withstand the stresses structurally at the maximum possible ejection velocity.

The explosive train is a sequential arrangement of explosive elements in decreasing order of sensitivity & increasing order of shock/power. Detonator and the squib are kept in misaligned position by a safe distance. The configuration of SAM with three independent safeties is chosen that guarantees arming of the SAM only after ejection of grenade from the launcher.

The miniaturization of the S & A device for fuzes contributes a lot to the system control of munitions, because weapons with S & A devices of a smaller size can provide more space for other devices. The application of micro technology can deal with this problem efficiently, which should bring a significant influence to the development of fuze. Most miniaturized S & A devices are through the environmental forces to be arming. The miniaturized S & A devices are safely armed through the setback and centrifugal forces. In addition, most of the setback and centrifugal insurance mechanisms in miniaturized S & A devices are made of elastic beam and mass block.

This paper highlights the salient features of Safety Arming Mechanism (SAM) for Electro-Mechanical Impact Fuze for 40mm Grenade. The modification carried out in SAM was validated in static and dynamic condition by realizing the hardware.

In this paper, we designed a high-reliability miniaturized S & A device in the small caliber projectile platform based on the expected design criteria. The size of the centrifugal insurance mechanism is determined theoretically, and the centrifugal insurance mechanism is studied under different conditions by simulation. Finally, the experimental results are presented, and the corresponding theoretical and simulation models are verified quantitatively.

2. Electro-Mechanical Fuze for 40mm Grenade

Fuze for 40mm grenade shall be electromechanical type which primarily functions on Impact of Grenade. Fuze will also have self-destruction (SD) as back up mode in case Impact switch does not function. Followings are the main components of Fuze:

A. Electronic Module:

Microcontroller based electronic module is used for functioning of Fuze in SD mode. Microcontroller will issue firing command at the end of set SD time. Electronic module shall be having Power regulators for Microcontroller and charging of firing capacitor. Electronic module also has firing circuit which fires Squib on Impact of Grenade or at the set SD time.

B. Power Source:

Fuze electronics shall be powered by Primary batteries. Mechanical Centrifugal switch is required to connect batteries to the electronics.

C. Safety & Arming Mechanism:

The Fuze shall be having Safety & Arming Mechanism (SAM) for providing mechanical safety to the Fuze during transportation, handling, storage and during launch of projectile. Explosive train will be misaligned through SAM till the launch of Grenade. Once the Grenade is launched, SAM senses ‘g’ & spin forces of projectile and aligns Detonator with Squib after a safe distance from the launch point with required arming delay.

D. Impact Switch:

Impact switch is designed to ensure functioning of Fuze on impact of Grenade considering the range of angle of fire and different type of target terrain.

E. Explosive Train:

The explosive train is a sequential arrangement of explosive elements in decreasing order of sensitivity & increasing order of shock/power.

3. Safety Arming Mechanism (SAM)

A. Need of Safety Arming Mechanism (SAM)

The fuze is safe in storage, handling and operation and ensures the safe and reliable function of grenade in all weather conditions.

The fuze has the following safety arrangements.

(i) Before firing rotor is held in unarmed condition by setback pin and centrifugal pin, which in turn provides detonator safety.
(ii) SAM aligns explosive train after sensing setback and spin force with a minimum delay corresponding to muzzle safety distance.
(iii) Centrifugal switch connects the power source with Fuze electronic after sensing spin of the projectile. d) Charging of firing capacitor is done with RC network from launch which gives additional electronic safety to Fuze.
(iv) Impact switch is used for Fuze functioning on Impact of the projectile against the ground targets.
(v) Microcontroller issues firing command in Self destruction (SD) mode in case of Impact switch does not function. SD time is factory settable.

In view of above-mentioned safety arrangements, Fuze provides all the necessary safeties to the grenade during its all phases including on firing & during flight provided the round does not get stuck and eject smoothly from the weapon barrel. This fuze has two modes of functioning viz. DA or Impact mode as primary mode of fuze functioning and Self Destruction (SD) mode as secondary mode for demolition of grenade. When the round is fired, the arming process starts due to setback & spin. On impact, a spring-loaded deceleration sensor closes its contacts on experiencing set forward force. This closure of impact switch causes triggering of firing circuit to generates a firing pulse which initiates explosive train.

In case of failure of sensing impact, micro controller generates a trigger signal at predetermined time to initiate explosive train results in detonation of grenade.

B. Functions of Safety Arming Mechanism (SAM)

There are three basic functions of Safety Interlock; namely

(i) Safety-Safety Interlock provides safety during manufacture, handling, transportation, storage, assembly, in a gun bore as well to avoid an accident during flight.

(ii) Arming- Arming of a device means it is a stage at which the required time delay is created, and the projectile is ready to blast in threat prone radius by aligning the det for passage of high voltage charge for initiating the detonator.

(iii) Functioning- Functioning depends upon the end use of the ammunition for which is employed like blast, incendiary, tracer etc.

C. Design Principles for Safety Arming Mechanism

The explosive train is the detonation or deflagration train beginning with the first explosive element and terminating in the main charge. In other words, the explosive train is that part of the S&A device that transfers a detonation wave from the most sensitive explosive element (usually a detonator) to the least sensitive explosive element (usually the warhead).

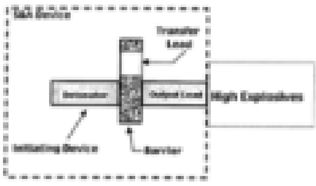

Figure 1: Explosive Train

Design principles used for this Safety Arming Mechanism are as follows:

(i) It is a mechanical time delay unit, it provides delay in rotor movement and alignment at required position with time delay and also it is a safety mechanism during transportation, handling and storage etc.

(ii) The arming energy used to move the rotor from the safe position can be derived directly from the arming stimulus-a configuration that ensures arming energy is derived from the post-launch environment (i.e. spin). Additionally, the movement of the rotor can serve as verification that the arming stimulus is present.

(iii) Acceleration profiles in these applications are of sufficient magnitude and duration that safe separation distance can be verified prior to final commitment to enable arming of the explosive train.

D. Configuration of Safety Arming Mechanism (SAM)

It is proposed a miniaturized SAM for use in small caliber projectile as shown in Figure 2. Due to the limited size of small caliber projectile (The caliber is 40 mm), the size of the device is designed as Ø32.4 x 13mm. Therein, and the explosion-proof rotor is held in unarmed condition by setback pin and centrifugal pin. The star wheel assembly and pellet assembly control the motion of rotor and gear assembly to ensure safe arming distance. A top plate is provided with two screws to enclose (cover) the Safety Arming Mechanism.

Previous design of SAM (Assembly without Top plate)
Figure 2Configurastion of Safety Arming Mechanism

4. Working of Safety Arming Mechanism (SAM)

Under the launching state of the grenade, the SAM experiences the setback and centrifugal force. During the launching state, when the 'g' forces reach to minimum required value, floating pin & floating cup spring sets downwards and then rotor movement takes place. Due to centrifugal force on centrifugal pin with a specified spin, the spring gets compressed. The locking of centrifugal pin gets unlocked. When the spin and axial acceleration took place the two safety locks get unlocked. The rotor gets aligned in position. There is a third safety lock provided to hold the armed rotor in position after impacting the grenade at the target. This is a spin-based lock consists of a lock pin and compression spring with a lock lid to hold it in position. Due to spin of grenade this lock pin also moves inwards by compressing the spring and removes the obstruction of the rotor. When the grenade experiences impact against target or ground, the rotational motion (spin) vanishes and the lock pin is pushed forward under the spring force and get engaged in the cavity provided on the rotor. In this way, the rotor gets locked positively in the armed position.

Unarmed Condition Armed Condition
Figure 3: Modified SAM with triple lock system (Assembly without Top plate)

5. Theoretical Analysis

The triple lock system for Safety Arming Mechanism is designed and its design scheme as shown in Figure 3. Accordingly, the design criteria of the Safety Arming Mechanism need to meet the following conditions. First, the rotor can reliably arm the fuze when the rotary speeds are in the specified limits. Meanwhile, the rotor is limited by the setback pin and centrifugal pin Second, when the grenade experiences setback accidently, the centrifugal pin could effectively lock the rotor to ensure the safety of fuze. In order to meet these conditions, we conducted the theoretical, simulation, and experimental studies of the Safety Arming Mechanism (SAM).

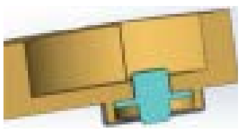

Setback pin
Figure 4: Setback pin assembly

Force, F = Mass X Acceleration
i.e. F = mXa ……….. (1)

From the above equation, value of acceleration is found and with known value of pin displacement S, response time of pin displacement is calculated from the equation,

$S = at^2/2$ ……….. (2)

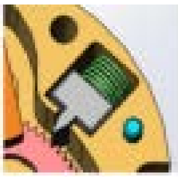

Centrifugal pin

Figure 5: Centrifugal pin assembly

Centrifugal Force acting on spring is calculated as,

Centrifugal Force = $m\ r\ \omega^2$ ……….. (3)

where, m= Mass of rotating member

r= radius of rotation

ω= (2ЛN/60) ……….. (4)

As the Centrifugal Force is greater than maximum spring force, the SAM operates at minimum spin.

6. Experimental Analysis

A. Static Tests:

(i) Spin test:

Since during static test no setback force is experienced so the spin test is to be conducted without setback pin assembly. Figure 6 shows the experimental setups for spin test of the Safety Arming Mechanism (SAM) / Safety Interlock. When the rotary speed reaches about 2500 rpm, the compression spring gets compressed by 1.5 to 2.0 mm. The locking of centrifugal pin gets unlocked and rotor gets aligned in position and held in this position by spin-based lock pin.

Figure 6: Setup for spin test

(ii) Sealing proof test:

Sealing proof test also known as detonator safety test is carried out to ensure safety of the fuze i.e. while handling, assembling or transportation in case of accidental initiation functioning of the detonator should not initiate subsequent explosive train components. This test was carried out by keeping the rotor with main detonator in misaligned condition with respect to the other explosive components of the explosive train and initiating the first fire element of the explosive train. This test was carried out successfully.

Before test

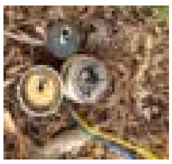

After test

Figure 7: Scaling Proof test

B. Dynamic Firing:

The old adage “the proof of pudding is in the eating” was never truer than when applied to ammunition. The development of fuzes is complicated by the fact that the only completely reliable test is the proof test; i.e., testing the fuze in the munition for which it was designed but under simulated combat conditions. The adequacy of out of line elements must also be determined by tests. Firing for recovery gives valuable information when it is important that the action of a certain element is to be determined. Recovery of firing gives the designer indispensable information. These tests are also carried out to generate data for compilation of Range Tables.


Grenade in terrain Explosive train functioned
Figure 8: Dynamic trial conducted

Few numbers of dynamic trials are carried out to evaluate the grenade performance.

7. Conclusion

In this paper, we designed, Safety Arming Mechanism (SAM) with a triple lock system for Electro-Mechanical Impact Fuze for 40mm Grenade, which is designed theoretically, and verified by experimental methods. When the rotary speed is over the minimum limit, the fuze was safely armed and through the spin-based safety interlock it gets locked in armed condition for positive initiation of the grenade. The modification carried out in SAM was validated in static and dynamic condition by realizing the hardware. Finally, this design culminated in the successful development of Safety Arming Mechanism that has enhanced the performance with satisfactory functioning of grenade.

8. Acknowledgement

Authors are thankful to Director, ARDE for continuous encouragement and other support. The authors are also thankful to all Project Team Members of 40mm Grenade for the support provided in manufacture and testing of the grenades to assess the performance of the Safety Interlock as well as complete grenade.

9. Reference

[1.] AMCP 706-210: Engineering Design Handbook; Ammunition Series, Fuzes.
[2.] Glossary of Ammunition Handbook.
[3.] Preliminary Design Review (PDR) Document of PDSD Fuze for LV Grenade -40mm UBGL/MGL of December 2020.
[4.] IS:4454; 2001.

All Weather, Rugged Proximity Fuze for Detection of Land Targets

P N Chine
Armament Research and Development Establishment
Pune
pnchine@arde.drdo.in

Abstract – **Several applications of Artillery and Infantry Ammunition require an Air Burst (AB) of the round fired. Especially, in the case of Pre-fragmented (PF) Warhead, the AB enhances lethality manifolds. A proven technique to achieve an AB is to detect the presence of the ground by electronic means using the RADAR principles and initiate the warhead at the desired distance from ground. The RADAR involves sending electromagnetic signals towards the target, picking up the reflected signal and extracting the beat frequency signal resulting from the mixing of the two. This requires a compact trans-receiver using a common antenna for transmit and receive. The extraction of the beat frequency poses a challenge because the transmitted signal is very large in amplitude as compared to the received signal owing to scattering, reflection and refraction of the transmitted signal at the target. In order to overcome these limitations, a trans-receiver working in the L-Band, with a single antenna was designed and pulsed RADAR principles were adopted to extract the beat frequency, the operating frequency of the trans-receiver was identified taking into consideration all necessary parameters such as antenna footprint, target reflectivity, spurious and undesirable reflections from clouds, hail, rain drops etc. The pulsed signal was processed through digital algorithms running on a microcontroller and distance measurement was carried out. Six fuzes were fired from 130mm Artillery Gun at PXE, Balasore. Two fuzes functioned in AB mode. The trial report is available. This exercise has resulted into establishment of a Land Target detection system based on a compact, rugged electronic Proximity Fuze.**

Keywords – Proximity Fuze, Land Target Detection

1. Introduction

It was an outcome of the dire survival needs during the World War II when the proximity fuze was invented to improve the lethality of aircraft bombs. The initial version of the proximity fuze used valves and discreet inductances and capacitances to realize oscillators, mixers, amplifiers, etc. Hence the size and power requirements were very high nonetheless the strategic advantage of surprise and improved effectiveness. Later on, with miniaturization of semiconductor devices and with the availability of advanced, safer power sources for the fuze, complex electronic functionalities could be realized on board resulting into more accurate target detection. Ruggedization of the fuze electronics made it possible to adapt the proximity fuze to a variety of artillery shells.

The developments in RADAR signal processing and incorporation of various stealth features tempt to use of Frequency Modulated Continuous Wave (FMCW) techniques for target detection with adequate accuracy and Electronic Counter Counter Measures (ECCM) features for protection against jamming in the proximity fuze.

2. Working Principle

A low noise Voltage Controlled Oscillator (VCO) generates a Frequency modulated Carrier wave which is amplified and transmitted via the antenna. The reflected signal is picked up by the same antenna and amplified before applying to the mixer. The beat frequency is filtered and the desired band is extracted. This is applied to the decision-making algorithm in order to compare the threshold and arrive at the decision of presence of target.

A single antenna is preferred because of space limitations. Isolation between the transmitted and received signal is achieved by switching the antenna between transmitter and receiver synchronously. The switching times are chosen so as to cater for range of detection and modulating frequency., details of which are shown in Fig 1.

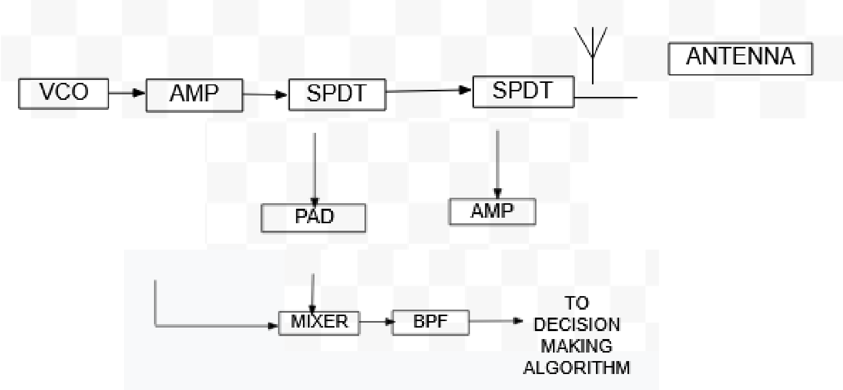

Figure 1: Block Diagram

3. Design of Antenna

The artillery shell travels with a high rate of spin and hence the antenna radiation pattern is required to be virtually omnidirectional. Due to shape and size constraints, it is not feasible to accommodate antenna with high gain. A balun fed, dipole antenna having an almost omnidirectional radiation pattern was designed. A theoretical model of the antenna is shown in Fig 2.

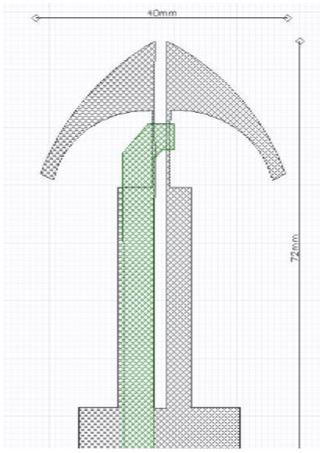

Figure 2: Antenna Model

The theoretical return loss plot is shown in Fig. 3.

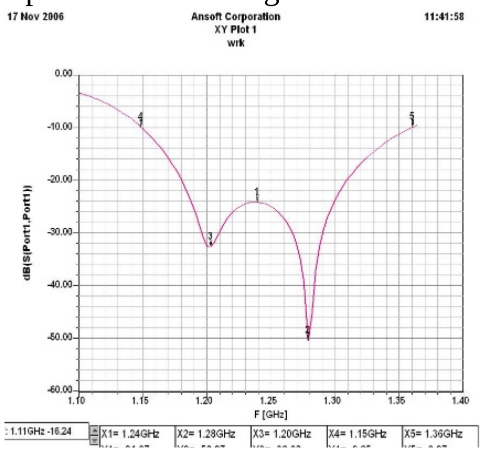

Figure 3: Return Loss Plot

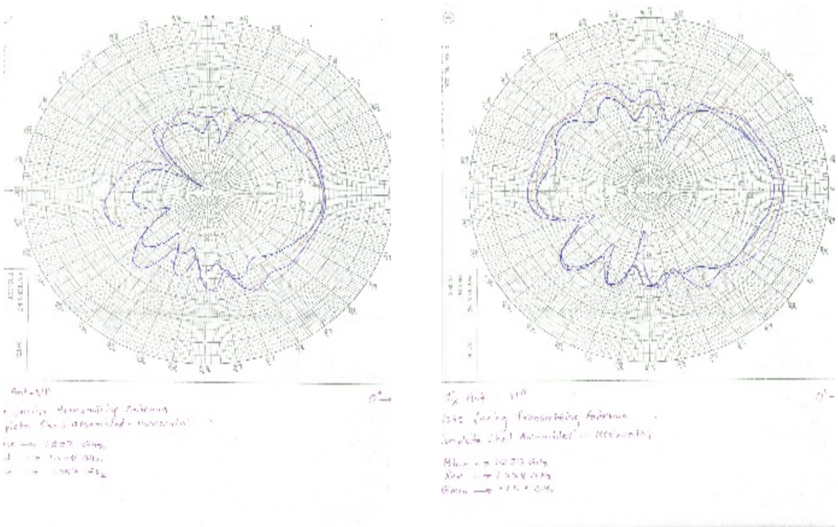

Figure 4: Measured Radiation Pattern

The measured radiation patterns with the presence of the artillery shell is available in Fig 4.

The antenna was further modified for manufacturing and assembly purposes. A novel packaging material was identified and incorporated for strengthening the antenna in order to withstand the firing forces.

4. Power Source

A rugged, energy efficient, compact reserve battery was realised to act as a safe and reliable power source with high shelf life. With porous, light lithium as electrode and thionyl chloride as the electrolyte, the batter was designed to deliver 370 mA current at 12V for a duration of 30 seconds. A picture showing the structure of the battery is available at Fig. 5.

Figure 5: Reserve Battery

5. Field Testing and Fuze Characterisation

The working conditions of the proximity fuze, especially the velocity, the spin and the reflection free environment, are almost impossible to realize for characterization of the fuze. A practically viable, low budget arrangement was adopted to study the field behaviour of the fuze. This set-up, called the hoist gear facility, is shown in Fig. 6.

In this method, the fuze is raised to a known height, powered on and then allowed to fall freely. The beat frequency generated during this descent is recorded in a data logger in a digital form and retrieved on to a computer for analysis. Several such exercises were carried out in order to arrive at the decision-making data pattern. A camera flash gun was then connected to the firing pulse output and the flash was checked for confirmation of proper functioning of the fuze.

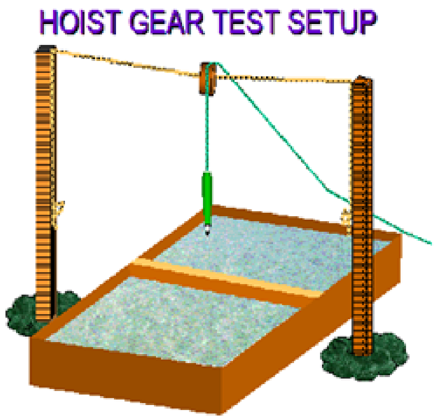

Figure 5: Field test Apparatus

6. Results

The development was carried out under a task project. Six prototypes were finally identified for subjecting to dynamic trials. The order of firing the units was decided according to the characteristics exhibited by the units during field testing. The six proximity fuze units were fired from 130mm IFG with flash filled charges.

Firing Schedule: 130mm Artillery Gun at Charge III and Range 12 km

Total No. of Fuzes fired: 09.

First 3 were fired as sighters (2 in time mode and one in impact mode) initially and functioned as per the set mode.

6 fuzes fired in proximity mode

2 functioned in air at 23m and 13 m respectively!!!

Remaining 4 fuzes resulted into blind.

7. Conclusion

Advanced techniques for land target detection were tried and exciting results were obtained in the way of functioning of fuzes. An ECCM feature as an added, strategic advantage was also demonstrated. The sensitivity and target dectivity can be further improved from the experience gained during this development.

8. Reference

[1.] Closure Report: Task Project No. ARDE/Task/43/2007.

Satisfactory Development of Post Impact Delay Fuze for Hard Targets

P N Chine
Armament Research and Development Establishment
Pune
pnchine@arde.drdo.in

Dr Virendra Kumar
Armament Research and Development Establishment
Pune

D N Joshi
Armament Research and Development Establishment
Pune

Abstract – **Runway Denial Penetrating Submunition (RDPS) for PRITHVI Warhead consisted of a number of submunitions, each capable of creating a crater big and deep enough to render the runway unusable. The submunition is initiated after a predetermined delay after impact by a post impact delay fuze which is located at the base and is equipped with Safe and Arming mechanism (SAM), impact sensor and an electronic delay generating mechanism. Designed to function in extremely high 'g' environment, all the mechanisms in the fuze are arranged in such a way so as to accommodate in a compact and constrained space. The fuze was trial evaluated under dynamic conditions and satisfactory results were obtained.**

Keywords – Hard Target Fuze. Electronic Delay, Safety and Arming Mechanism, Missile Warhead

1. Introduction

The RDPS Warhead for PRITHVI Missile was one amongst the many variants of warheads developed for this Surface-to-surface missile system. It consisted of several submunitions arranged axially symmetrically and stacked along the length as shown in Fig 1.

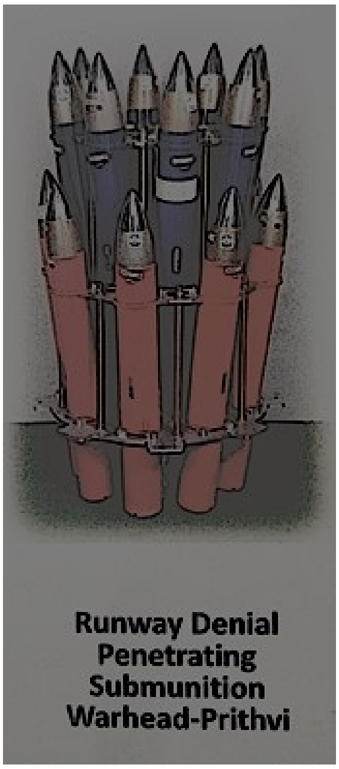

Figure 1: RDPS Warhead

All the submunitions were ejected simultaneously. Each submunition was capable of creating a crater big and deep enough to render the runway unusable. The submunition acquired a very high speed after ejection and by virtue of the high strength casing, the projectile would penetrate hard targets. The RDPS comprises of Kill Mechanism, Rocket Motor, Stabilization System and Impact Delay Fuze. The impact delay fuze is a base fuze, located next to the main charge and is shown in Fig 2.

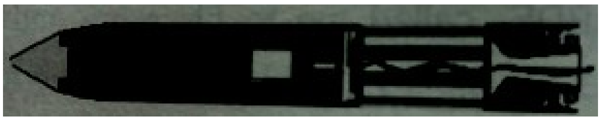

Figure 2: RDPS

The fuze experiences high level of shock and vibrations, both during the flight of the missile, during ejection and at the target end. It is required to be ruggedized enough to sustain the high level of shocks. A predetermined delay is desired to be set into the fuze for post impact functioning.

2. Fuze Configuration

The Fuze is basically equipped with Safety and Arming mechanism (SAM), impact sensor and an electronic delay generating mechanism. An impact switch works as a time reference since it closes almost instantly when the submunition experiences impact with the ground. The electrical pulse that the submunition receives during separation from the mother carrier is utilised to power the electronic delay circuit as well as to initiate the safe and arming mechanism. Arming takes place almost instantaneously when this electrical pulse is received by the submunition. As soon as the impact switch closes, the delay is initiated and after the elapse of the pre-determined delay, the main charge gets initiated. The arrangement and interconnectivity is shown in the block diagram in Fig. 3.

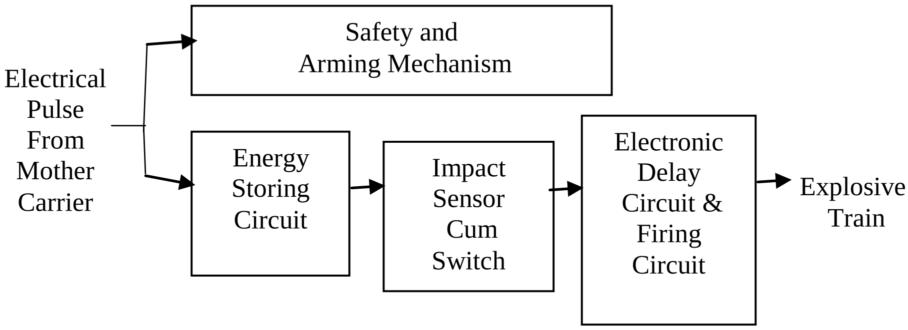

Figure 3: Configuration Block Diagram

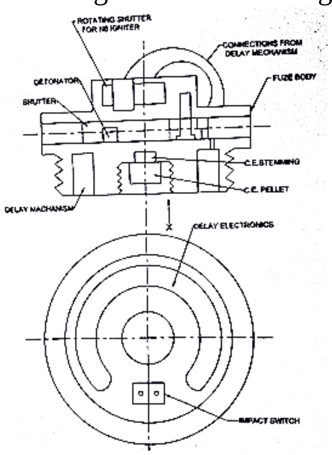

Figure 4: Assembly of Impact Delay Fuze

A. Safety and Arming Mechanism (SAM)

The SAM was realised by a pivoted, rotating lever carrying the igniter at its free end which would align with detonator after arming. The explosive train consisted of an N8 Igniter followed by 132 mg RZY Detonator followed by a CE Stemming and then a Booster Pellet. Safeties were incorporated by keeping the N8 Igniter shorted and misaligned with the detonator until arming command is issued by the mother carrier. The detonator was kept off centre during safe mode and would come to the centre for alignment with the igniter when the fuze is armed by initiation of a pyro device during separation of the submunition. This arrangement is shown in Fig. 4

A spring-loaded lock plunger would secure the position of the shutter carrying the detonator. The sealing plug would ensure that the gases released due to functioning of the pyro device do not leak.

This is shown in Fig 5.

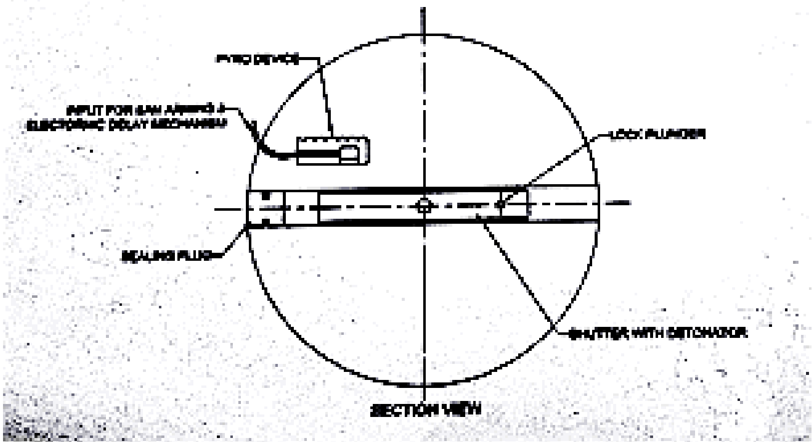

Figure 5: SAM: Detonator Shutter Arrangement

B. Impact Sensor

A latching type compact, rugged impact sensor was incorporated in the fuze housing. The impact sensor/switch has a dual role to play. It acts as impact sensor thereby giving a timing reference for generating the pre-determined delay and makes electrical power available to the firing circuit only after the impact. The arrangement of the impact sensor was such that the sensor could be reassembled after its functioning. This enabled several iterations of testing to be carried out with fewer prototypes. The firing capacitor would charge only after the impact sensor would close (connect) an otherwise open contact after sensing the impact.

C. Electronic Sub-system

As shown in Fig 3, the electrical pulse received from the mother carrier is applied to an energy storing circuit equipped with mechanically rugged tantalum capacitors. The capacitors hold the charge until impact. On impact, the impact switch closes and connects this section to the delay circuit and the firing circuit. The delay is initiated and parallelly the firing capacitor gets charged. The time required for charging of firing capacitor is very small as compared to the pre-determined impact delay. After the pre-determined delay is elapsed, the N8 igniter is initiated by the firing circuit and the fuze blows off. The electronic circuits were wired on a horse-shoe shaped Printed Circuit Board (PCB) and the assembly was accommodated in the fuze housing. Circuits were hardened by potting with polymeric compounds and interconnections were embedded in tiny slots on the fuze hardware. A three-dimensional view of the fuze is shown in Fig. 6.

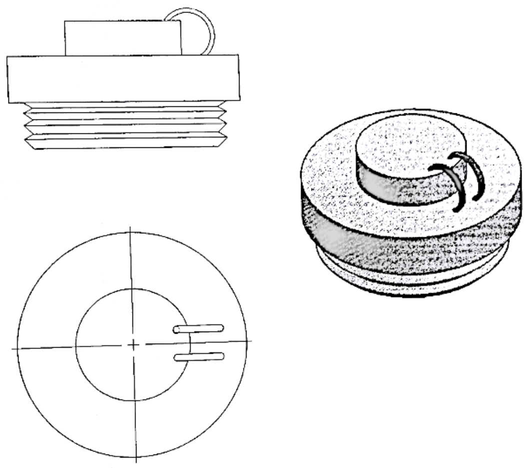

Figure 6: Isometric View of the Fuze

3. Testing and Development

The fuze was initially rigorously tested on the Standard Drop Test Apparatus (SDTA) for achieving the functional requirements. This involved conduct of several iterations and improvements in the various sub-systems as and when found necessary. A delay of 40 milliseconds was set in the fuze and recorded through instrumentation. The fuze was drop tested for extremely high values of ‘g’. After achieving satisfactory results in the testing at SDTA in ARDE, the fuze was subjected to dynamic trials.

4. Trial Evaluation

At RTRS in TBRL, Chandigarh, three prototypes were subjected to dynamic testing against LCN 60 targets. The fuze was loaded with CE Stemming and the submunition was filled with HES. A picture showing the assembly of the test configuration is available in Fig.7. The submunition was test fired on a sledge mounted on the rails with the help clamping shoes. An explosive bolt would initiate at the appropriate position on the rails and separate the submunition from its mounting.

Figure 7: RTRS Trial Assembly

5. Trial Results

The fuzes functioned satisfactorily showing a post impact blast. The delay set was 45 milliseconds. The events of impact and functioning were recorded using high speed video. Record No. 94 of round No. 2 is presented here. In Fig 8, the impact is seen at a time tag of 01.21.540. The resolution of this frame is 5 milliseconds.

Figure 8: Round Impact with the Target

The frame showing the blast is available in Fig 9. Here, the time tag is **01.21.585.**

Figure 9: Fuze Functions Post Impact

The time difference of 45 milliseconds in the two frames is the desired delay pre-set in to the fuze.

6. Conclusions

This development effort established a design and process for post impact delay fuzing against hard targets. Additional, advanced features such as bunker counting, extended delays, smart sensing can be incorporated on this basic design. The technique of ruggedizing the electronics and the SAM in order to suite this unique application is an achievement and needs to be further explored.

7. Reference

[1.] R L Boylestad, Electronic Devices and Circuit Theory, 11th Ed. Pearson Education Limited.

Launch Mechanisms

Cooling Shutter Mechanism in Payload Fairing of a Launch Vehicle and its Effect on Compartment Venting

B Venkat Shivaram Jadav
Aero Combustion Modeling Division
Vikram Sarabhai Space Centre
ISRO
Thiruvananthapuram
shivaram_jadav@vssc.gov.in

Manokaran K
Vikram Sarabhai Space Centre
ISRO
Thiruvananthapuram

Dipankar Das
Vikram Sarabhai Space Centre
ISRO
Thiruvananthapuram

Vidya G
Vikram Sarabhai Space Centre
ISRO
Thiruvananthapuram

M M Patil
Vikram Sarabhai Space Centre
ISRO
Thiruvananthapuram

Ashok V
Vikram Sarabhai Space Centre
ISRO
Thiruvananthapuram

***Abstract*—Cooling shutter mechanism in the payload fairing of a launch vehicle is used to cool the satellite bay area and maintain the temperature within allowable limits. At liftoff this mechanism should be closed and intact, so that the aerodynamics around the payload fairing shouldn't disturb the internal arrangement. This system has been implemented in the existing launch vehicle and flown in all successful missions. During one of the ground test (design qualification vibration testing), for supplying the system to new launch vehicle, it was observed that the flap of the cooling shutter mechanism can open up in adverse conditions. Therefore the mechanism has been modified such that it doesn't open up even in the worst scenario. The present case study corresponds to the opening of flap during the flight regime and its implication on the compartment venting. Differences between the compartment pressure values with and without opening of the flap/shutter mechanism is presented in this paper.**

Keywords—Cooling shutter mechanism, Payload fairing, compartment venting, internal pressure, Rocker Clamp mechanism, Cool air inlet, Transonic Mach number, Supersonic Mach number, Differential pressure

1. Introduction

Payload fairing in the launch vehicle comprises of many systems and subsystems to support the smooth functioning of payload sitting inside it. After integration of payload fairing with the vehicle, the satellite and the other systems related to it will be, in general, at atmospheric pressure i.e at 1bar. The heat generated due to functioning of vehicle systems, during ground operations till lift-off, may result inincrease of temperature inside PLF. Hence cooling air will be pumped inside the PLF through cooling umbilical shutter mechanism as seen in Fig 1 to bring down the temperature levels to allowable limits. Vent system in the payload fairing is a process to maintain the internal pressure within allowable limits to withstand the loads across the structure, by relieving air from compartment during flight (NASA standard [1]). Vents are provided in the cylindrical portion of the payload fairing as seen in the Fig 1.

Fig 1: Cooling shutter mechanism in payload fairing

Primarily meant for maintaining the required temperature setting on the launch pad, the cooling inlet is closed by a shutter clamp mechanism at the time of lift off. Once closed, this mechanism is supposed to be intact till the payload fairing separation takes place. During one of the vibration tests for qualification for new launch vehicle application, it was observed that the shutter clamp mechanism got opened due to the vibration felt across the structure. Details of the shutter mechanism and the failure associated with it are studied by Murugesan[2] et al. similar studies related to opening of pressure relief doors is done by Peter Pratt[3] et al. If the cooling shutter mechanism is opened instead of being intact all the time during flight, it will act as a venting path apart from the existing vents provided in the cylindrical portion. The possibility of such opening during the flight and the effect of this opening on the compartment venting and details of the compartment pressure levels due to venting, with and without opening this cooling shutter mechanism is the case study presented here.

2. Cooling shutter mechanism

Vehicle half assembly consists of a preloaded shutter which closes the cut-out opening on the PLF after ground half separation and shutter will be locked by two shutter clamp mechanisms at 120° apart as seen in Fig2. This mechanism is called rocker clamp mechanism.

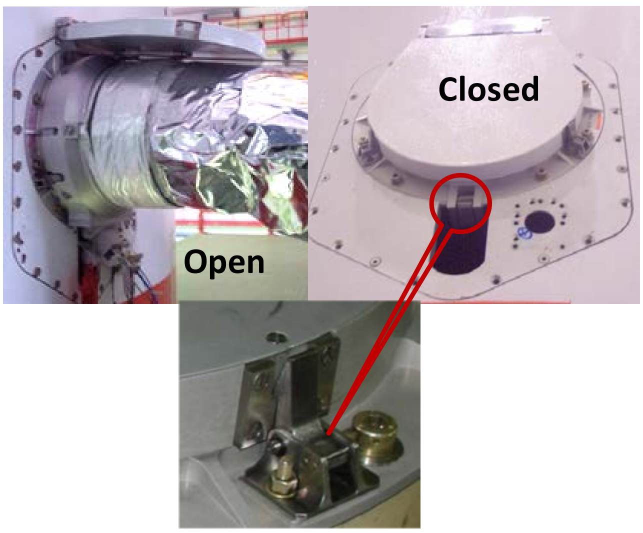

Fig 2: Shutter clamp mechanism mounted in PLF

The main function of the clamp mechanism is to hold the shutter in closed condition during the launch phase. The rocker clamp mechanism has the following parts namely shutter locking pad, spring loaded clamp as seen in Fig3.

A. Rocker clamp mechanism

Shutter locking pad: Assembled to the side face of the shutter at 120° apart having 10 ° taper interfaces.

Spring loaded clamp: Assembled to the shutter mounting ring. It consists of a spring loaded clamp hinged to a bracket.

Functioning: Clockwise moment generated by shutter force will be opposed by anti clock wise moment due to spring force and friction while the horizontal force will be provided by tapered interface.

Due to the forces acting on the shutter clamp, the anticlockwise moment is higher than the clockwise moment, which resulted in the opening of the shutter.

In order to reduce the anticlockwise moment acting on the shutter, the clamp mechanism has been modified by having a projected landing face. Details of the modified rocker clamp mechanism are as given below.

B. Modified rocker clamp mechanism

Shutter locking pad: Modified pad with projected landing face for clamp as seen in Fig3, assembled to the side face of the shutter at 120° apart having 10º taper inter face.

Spring loaded offset clamp: Assembled to the shutter mounting ring. It consists of a spring loaded clamp hinged to a bracket.

Functioning: Shutter force will pass through the hinge of clamp such that no opening moment is created.

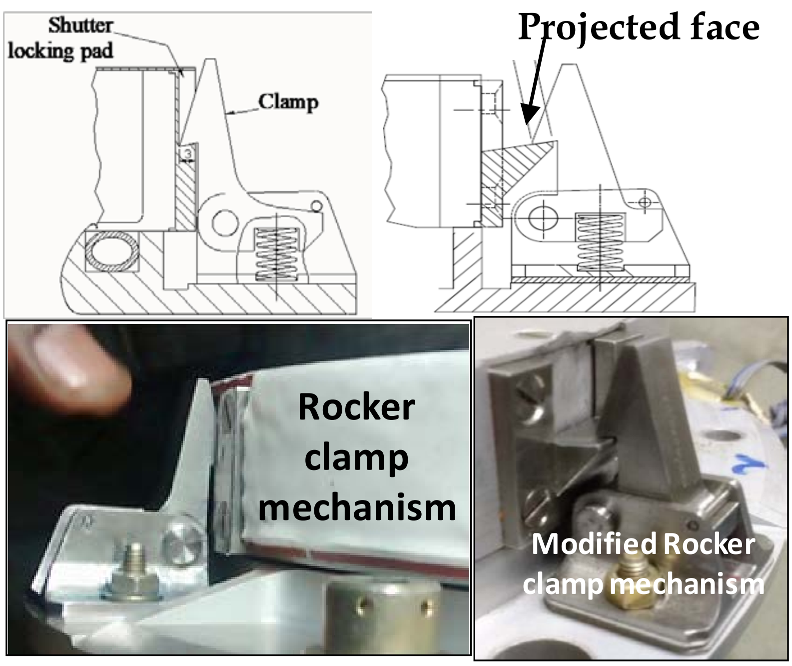

Fig 3: Shutter clamp mechanism (Existing and modified) (Ref.2)

3. Compartment Venting

Venting plays an important role in relieving the entrapped air inside the compartments to outside during the ascent phase of launch vehicle. Extent of possible opening and mass flow rates associated with the possible area opening during the flight and change in the compartment pressure levels with this effect is studied in detail. Details of compartment venting for a typical ISRO launch vehicle compartments was carried out by B. Venkatshivaram Jadav [4]et.al. Compartment pressure values across the compartment are calculated by solving the following equation (1).

$$\frac{dP_c}{dt} = \sum_k C_{d_k} \frac{A_k}{V} \sqrt{P_c \rho_c} \sqrt{\sqrt{\frac{2\gamma}{\gamma-1}} \left[1 - \left(\frac{P_e}{P_c}\right)_k^{\frac{\gamma-1}{\gamma}}\right] \left(\frac{P_e}{P_c}\right)_k^{\frac{2}{\gamma}}} \gamma \left(\frac{P_c}{P_e}\right)_k^{\frac{\gamma-1}{2\gamma}} . P_c \qquad (1) \text{ (Ref. 4)}$$

Where P_c is Compartment pressure, γ is specific heat ratio- (Cp/Cv)-(1.4), $C_d$is Discharge coefficient, A is Vent area, ρ is Density, V is the Volume of air in the compartment, dt is the time step (seconds), k is a constant representing multiple no. of vents, P_e isexternal pressure.

Compartment pressure computation is directly proportional to the mass flow rate across the total vents, total area, and free air volume of the compartment and discharge coefficient across the vents.

The differential equation for the compartment pressure is integrated using RK4 method.

4. Analysis

The shutter clamp mechanism tested during vibration test was employed in the existing launch vehicles of ISRO. Based on the observation, the clamp mechanism has been modified in the subsequent flights. This had an implication on the compartment pressure levels where it was deployed.

The cooling shutter is located near to the cone-cylinder junction as seen in Fig4, where the aerodynamics of the shape has a major contribution towards the aerodynamic properties like pressure coefficient and local Mach number.

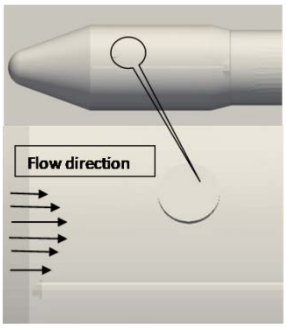

Fig 4: Cooling shutter mechanism in PLF

Cp variation for three typical Mach numbers over the payload fairing is shown in Fig 5.

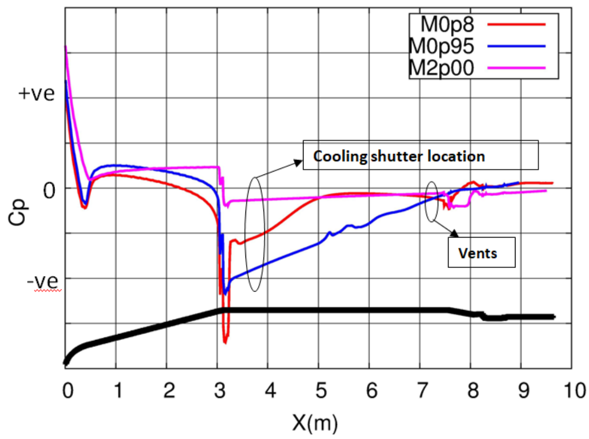

Fig 5: Cp variation over the PLF and Cp values at the cooling shutter mechanism

Cp variation is very low (highly negative) at cone-cylinder junction and further down the cylinder, as the flow expands, the pressure recovers along the length of the cylinder with change in Mach number.

As the free stream Mach number increasesfurther (still less than sonic speed), the flowlocally expands to a supersonic pocketterminated with shock. Shock thusgenerated interacts with the boundary layer and makes the flow separate. Furtherincrease in free stream Mach number leads to further expansion leading to theformation of supersonic pocket after the cone–cylinder junction which is a region ofstrong expansion[5]. Cp palette for M=0.95 is seen in the Fig6. Cp value is low and is negativein the aft end portion of the shutter mechanism. They are as low as -0.9 to -1.0 for M=0.95, whereas at the vent locations Cp values is around -0.2 to -0.18.

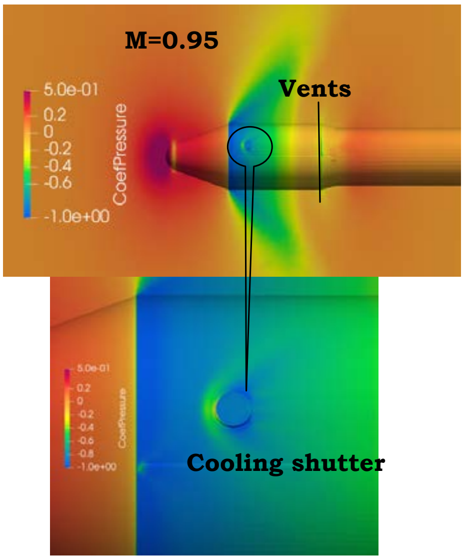

Fig 6: Cp palette over PLF for M=0.95 and Cp at aft-end of cooling shutter mechanism

For M=3.0, a strong shock is observed in the payload fairing compartment. Supersonic flow is characterizedby shock and expansion waves depending on the flow turning angle and theflow over the vehicle is generally smooth. Similar observation of M=0.95 is there for supersonic Mach number M =3.0, where the cp variation at the aft-end of cooling shutter is around -0.2 to -0.1 and the Cp value is in between 0 to 0.05 at the vent locations as seen from the Fig 7.

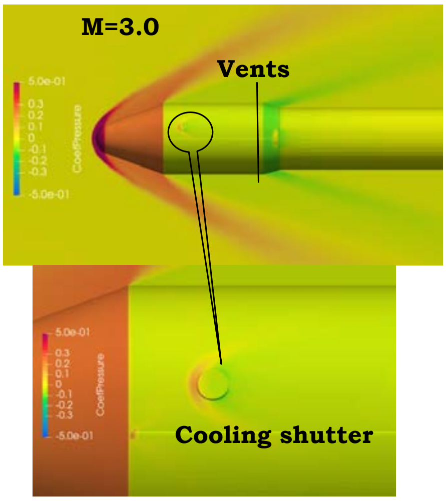

Fig 7: Cp palette over PLF for M=3.0 and Cp at aft-end of cooling shutter mechanism

5. Results

Low pressure values correspond to high suction through openings/vents which aids in the quick relief of air that can lead to drop in the compartment pressure levels. With the existing shutter clamp mechanism, the shutter got opened by 2 to 3mm and it acted as un-intentional opening during the transonic regime of the flight. The 3mm opening created a vent area in the form of radial gap of approximately $100cm^2$. Vent area being in the high suction zone, the discharge coefficient through this gap is as high as 0.6-0.8 as seen in Fig8.

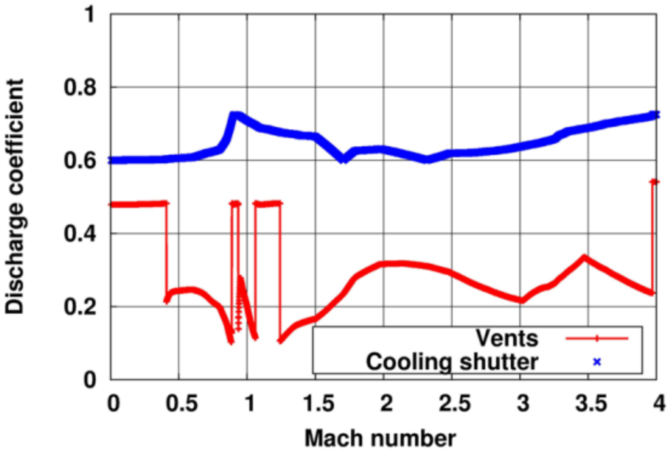

Fig 8: Discharge coefficient across Vents and cooling shutter opening

Due to the combined phenomenon of low pressure and high discharge rate, the mass flow rate from the payload fairing during transonic Mach number was as high as 2.5kg/s, which lead to the drop in compartment pressure values. But the modification in the rocker clamp mechanism in the cooling shutter didn't open up which constrained any leakage through it during the entire flight regime due to which the mass flow rate across the payload fairing dropped to 1.5 kg/s as seen in Fig 9.

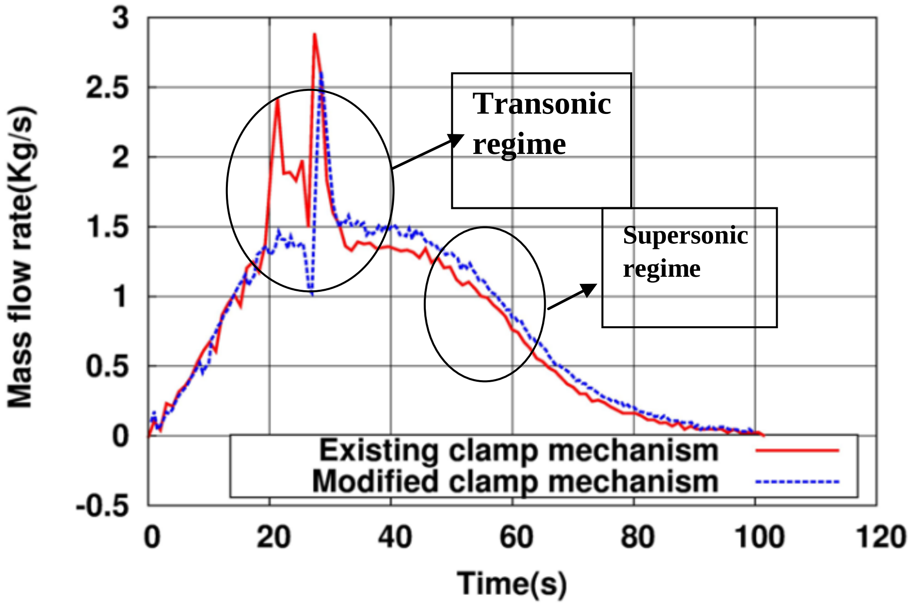

Fig 9:Mass flow rate across payload fairing with and without change in clamp mechanism

The compartment pressure levels due to the change in the shutter mechanism were higher in the transonic regime against the pressure values obtained from the existing clamp mechanism as seen in Fig 10.

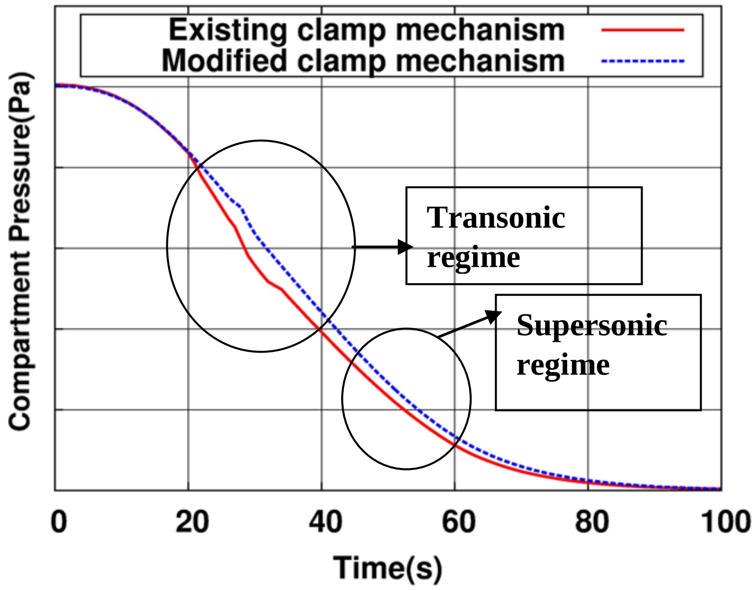

Fig 10:Compartment pressure values with and without change in clamp mechanism

Similarly the comparison of differential pressure values across the payload fairing compartment with and without modification of shutter clamp mechanism showed the same difference as compartment pressure values. The peak differential pressure values in this case didn't exceed the design specification of p_c-p_{inf} of ±10kPa as seen in Fig 11.

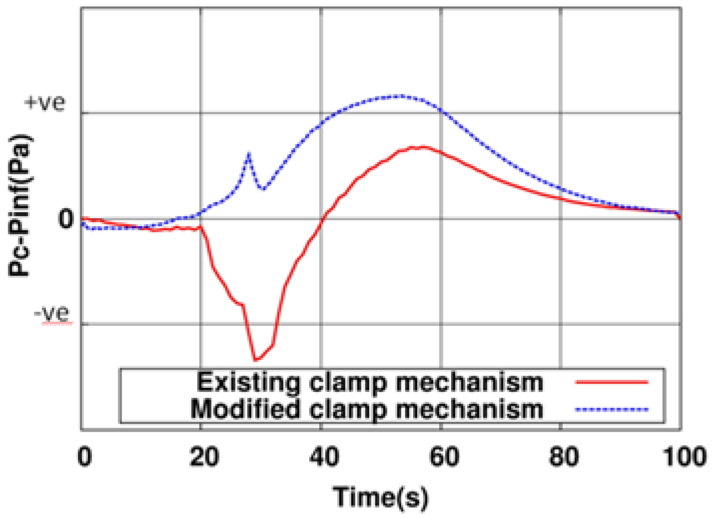

Fig 11:Differential pressure values with and without change in clamp mechanism

6. Conclusion:

Effect of change in the cooling shutter mechanism on the compartment venting through venting studies was brought out in this paper. Because of the anti clockwise moment generated due to the spring force and friction is higher than the clockwise moment of shutter, the shutter flap opened during the flight regime, which lead to the fast depletion of compartment volume of air through it. This fast depletion is also due to the positioning of shutter in a highly expansion zone on the payload fairing, where the suction pressure is higher in the aft-end side of the shutter. A radial gap area of approximately 100cm^2 was formed causing the mass flow rate of nearly 2.5kg/s during the transonic phase of the flight.With the modification of the rocker clamp mechanism in the cooling shutter, the mass flow through the radial gap ceased and thereby leading to increase in the compartment pressure values.The modified cooling shutter mechanism is being used in all existing and new launch vehicles of ISRO.

7. Acknowledgements

Authors would like to acknowledge the contribution of PSLV project team in the form of technical support and guidance during this activity. Also, acknowledgement is due to various internal review forums. Thanks, are also due to Dr. S. Geetha, PD, STS for reviewing this paper.

8. References

[1] NASA space vehicle design criteria (Structures), NASA SP-8060, “Compartment Venting”, Nov 1970.

[2] Murugesan et. al, “Failure Analysis of a Launch Vehicle Umbilical Shutter mechanism during Vibration Qualification”, J Fail. Anal. and Preven. (2018) 18:457–464.

[3] Peter Pratt et al, “Computational and Experimental Studies of Pressure Relief Doors in Ventilated Nacelle Compartments”, Integrating CFD and Experiment Symposium, Glasgow, UK, Sep 2003.

[4] B.Venkat Shivaram Jadav et al, “Venting system design and analysis for a typical launch vehicle compartment”, 27th NCAE, Nov 08-09, 2013.

[5] B.N Suresh, K. Sivan, chapter 10.2 (Aerodynamic flow characteristics), Integrated design for Space Transportation (Springer, New York, 2015), pp. 397–398.

Design of a Pneumatic System for Stage Jettisoning for Improving Payload Capability of a Launch Vehicle

Mridul Songara
Vikram Sarabhai Space Centre,
ISRO, Thiruvananthapuram
songaraspcm@gmail.com

Shiju G. Thomas
Vikram Sarabhai Space Centre,
ISRO,
Thiruvananthapuram

Manu V. Unnithan
Vikram Sarabhai Space Centre,
ISRO,
Thiruvananthapuram

Abraham Varghese
Vikram Sarabhai Space Centre,
ISRO,
Thiruvananthapuram

U A Subramanian
Vikram Sarabhai Space Centre,
ISRO,
Thiruvananthapuram

***Abstract*— A pneumatic system is designed for replacing currently used solid motor based jettisoning systems for spent stages of a launch vehicle. Advantages of pneumatic jettisoning system over solid motor based system are explained. A mathematic model is developed for predicting the performance of the system and is used for the system design and selecting operating parameters. A test plan is also proposed to verify the functionality of the system.**

Keywords—Gas Strut, Stage Jettisoning, Pressure Cylinder, Vent, Stroke

1. Introduction

A pneumatic system is proposed as an alternative to currently used retro rockets to jettison spent stages of a launch vehicle. Once the stages are separated, the high pressure gas in the system expands and pushes the two stages apart. The system is based on a pre-charged gas strut with metering pin to control the force with respect to stroke. For Aries I launch vehicle, replacement of the existing Retro motors with such a pneumatic jettisoning system gives a payload benefit of 227kg [1]. Since the factors involved are same, payload benefit is expected for any launch vehicle by replacing a retro rocket with a gas strut system. While the quantitative analysis can be carried out for any stage to get the exact number, this study focuses on the design aspect of the system. The current study is based on using a variable cross section rod instead of a vented rod proposed for Aries I.

2. Advantages of Replacing Retro Motors with Gas Strut

A. Flexible with mission requirements

Gas strut based jettisoning systems can be tailored as per the mission requirements. Required performance can be achieved by changing the pressure of the gas in the two chambers and the piston stroke. Also, rods with different vent area profile can be used as per the mission requirement.

B. Reliability and Reusability

Gas strut system flight hardware can be tested before launch as opposed to the solid rocket motor based jettisoning systems which can be used just one time. The reusability aspect can also be exploited in a reusable launch vehicle stage.

C. Reduction in aerodynamic drag

Solid motor based retro rockets have to be placed externally in any launch vehicle. Gas strut systems can be placed inside a stage because there is no exhaust from the system; this reduces the projections on a launch vehicle. Reducing projections will result in lesser drag compared to drag in a similar launch vehicle with retro systems. [1]

D. Momentum to the ongoing stage

Retro rocket systems push the spent stage down and no momentum is imparted to the ongoing stage. Gas strut based jettisoning system pushes the ongoing stage and spent stage apart by exerting a force between them. This results in a ΔV addition to the ongoing vehicle also (Figure 7), which increases the payload capacity.

E. Separation dynamics

A gas strut system acts as a spring. During stage jettisoning, if any lateral rate is induced, it would cause differential strokes on the individual gas struts, which in turn would provide differential forces opposing the rate. This rate correction provides better clearance and collision avoidance is possible [1].

3. System Description

The system consists of a piston cylinder arrangement – where the piston is also a cylinder containing gas at a pressure higher than that of the outer cylinder. A rod with linearly varying cross section is attached to the inside of the outer cylinder (Figure 2). In the initial condition the rod project inside the piston through an axial opening and the two cylinders are sealed using O-rings.

The force acting between the stages is given by equation①. This force can be varied by adjusting the pressure in the chambers. Once the connection between the two stages is severed, the initial force causes relative displacement between them. This results in mass flow between piston and cylinder. As the inner cylinder (Piston) moves relative to the outer cylinder allowing an annular area for transfer of gas, the force rises to the maximum and further reduces due to the adiabatic expansion of the gas, giving the required force displacement profile (Figure 4).

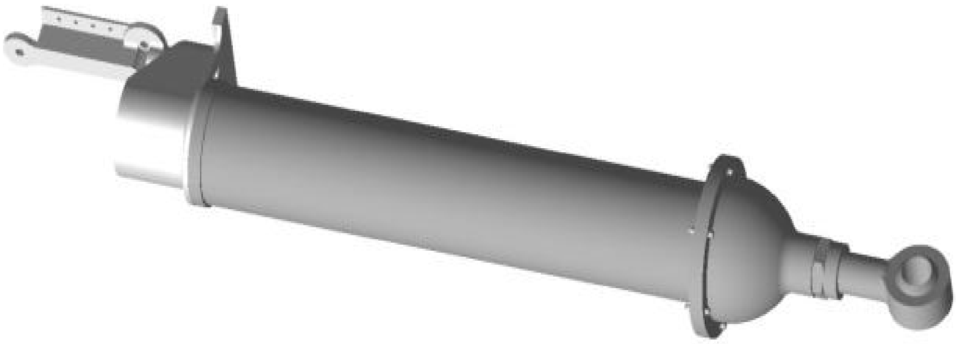

Figure 1: 3D Model of the Stage Jettisoning System

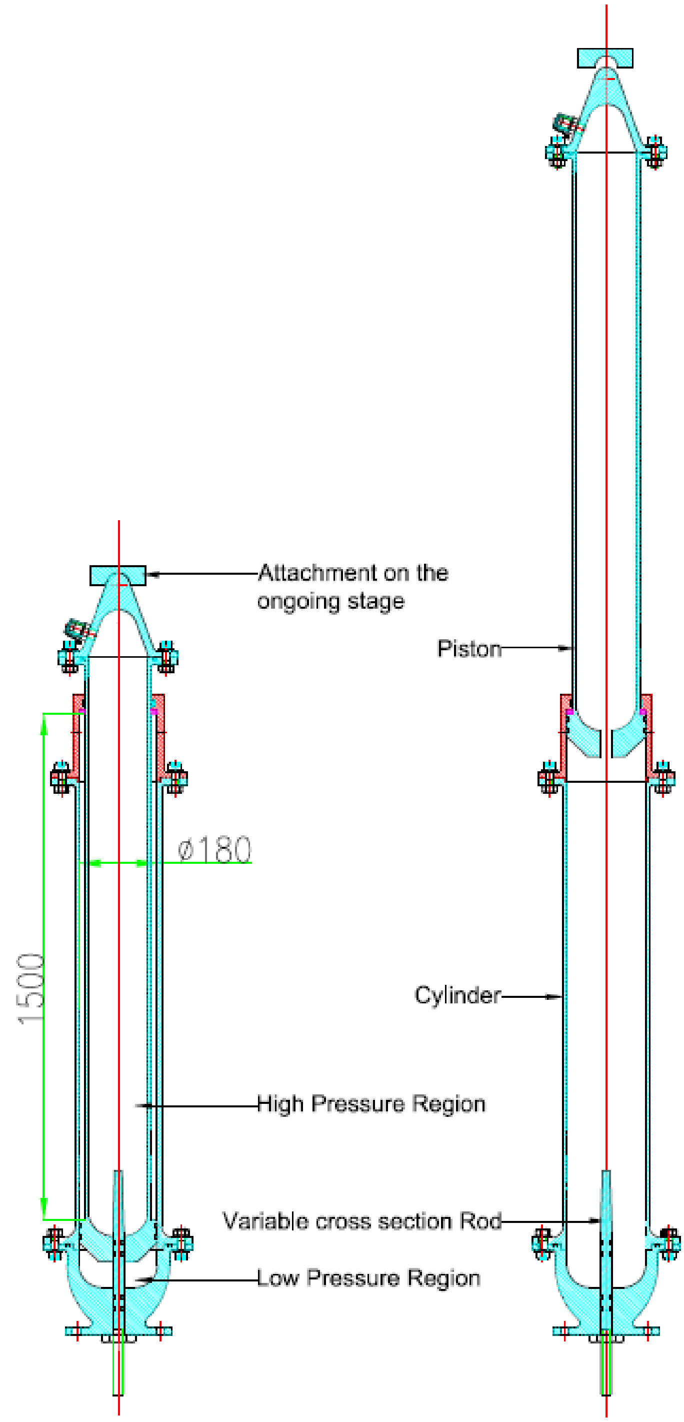

Figure 2 Cross Section of Pneumatic Stage Jettisoning System in closed condition (left) and after jettison (right)

4. System Design

A mathematical model is generated to evaluate the performance of the system. The results are generated by a code developed in MATLAB R2014a using the model as per the flowchart below.

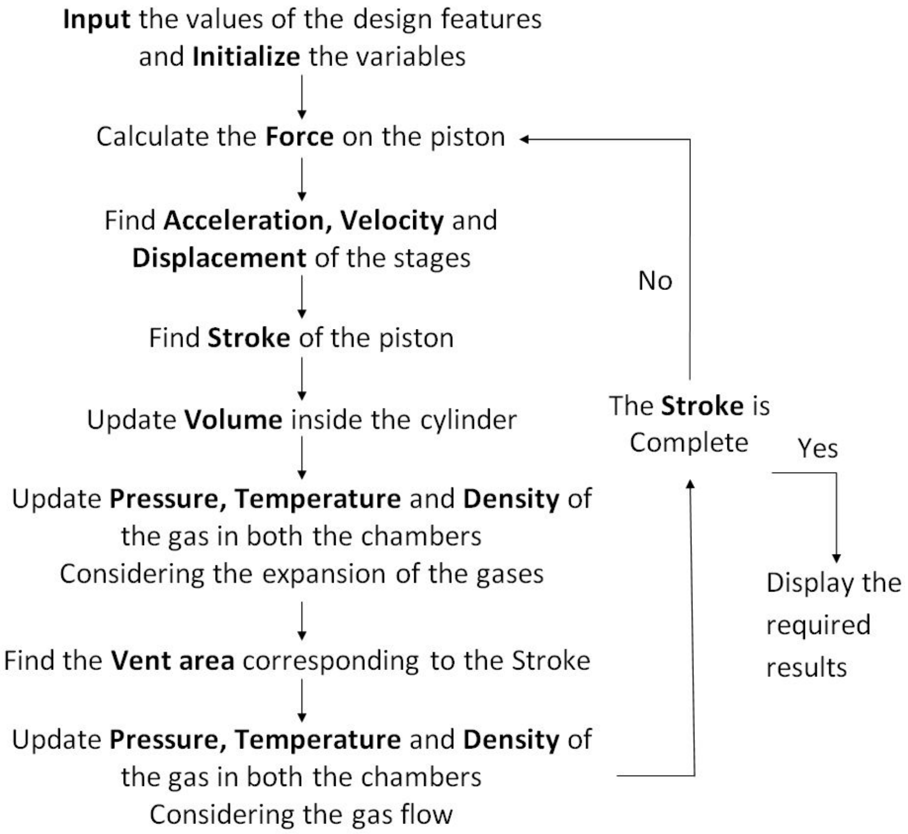

Figure 3 Flowchart to evaluate the System Performance

Following is a description of the steps mentioned in Figure 3

A. The design features and the variables are
   a. Design features
      i. Mass of ongoing stage
      ii. Mass of spent stage

   b. Design variables
      i. Inner diameter of the Cylinder
      ii. End diameters of the Rod
      iii. Length of the Rod
      iv. Volume inside piston (inner cylinder)
      v. Maximum Stroke
      vi. Initial volume of Gas in the Cylinder (outside the Piston)
      vii. Gas pressure in both chambers
      viii. Gas temperature in both chambers

B. Calculation of the Force F
   Using

A_r	=	Cross section area of the rod as a function of stroke
$A_{r,max}$	=	Maximum cross section area of the rod
P_p	=	Pressure of the gas inside the Piston
A_{an}	=	Outer Cross Section Area of the Piston – Area of the axial opening in the Piston for the Rod
P_c	=	Pressure of the gas inside the Cylinder

$$F = A_{r,max} \times P_p + A_{an} \times P_c - (1)$$

C. Acceleration, Velocity and Displacement of the Stages

$$\text{Acceleration} = \frac{\text{F}}{\text{Mass of the stage}}$$

Velocity is calculated by integrating the acceleration over time
Displacement is calculated by integrating velocity over time

D. Stroke of the Piston
Stroke is calculated from the relative displacement of the two stages.

E. Volume inside the two chambers
Using
A_c = Inner Cross section area of Cylinder
For cylinder,

$$\text{Volume}(t + \Delta t) = \text{Volume}(t) + (A_c - A_r) \times \text{Stroke}(\Delta t)$$

For piston, the change in volume is very small compared to the initial volume and may be neglected.

F. Pressure, Temperature and Density – Change due to gas expansion
Adiabatic expansion of the gases is assumed.
For,
γ =Ratio of the specific heats of the gas

$$\text{Pressure}(t + \Delta t) = \text{Pressure}(t) \times \left(\frac{\text{Volume}(t)}{\text{Volume}(t + \Delta t)}\right)^{\gamma}$$

$$\text{Temperature}(t + \Delta t) = \text{Temperature}(t) \times \left(\frac{\text{Pressure}(t + \Delta t)}{\text{Pressure}(t)}\right)^{\frac{\gamma - 1}{\gamma}}$$

$$\text{Density}(t + \Delta t) = \text{Density}(t) \times \left(\frac{\text{Pressure}(t + \Delta t)}{\text{Pressure}(t)}\right)^{\frac{1}{\gamma}}$$

G. Vent Area
Venting is through the annular area between the rod and the opening in the piston. Since the variation in the cross section area of the rod (A_r) is known
Vent area = Area of the Opening in the Piston for the Rod – A_r

H. Pressure, Temperature and Density – Change due to gas flow For
m =Mass of the gas in a chamber
A =Vent Area
Vel = Velocity of the gas flow at the orifice
C_d = Coefficient of discharge of gas through the orifice
P_c = Pressure of the gas in the chamber
P_e = Pressure of the gas at the orifice
V = Volume of the gas in the chamber
ρ_c = Density of the gas in the chamber
ρ_e = Density of the gas at the orifice
M_e = Mach no. of the flow at the orifice
R = Gas Constant
T = Temperature of the gas at the orifice

$$\frac{dm}{dt} = \rho_e \times A \times \text{Vel} \times C_d - ②$$

$$\text{Vel} = M_e\sqrt{\gamma \times R \times T} - ③$$

$$\frac{dm}{dt} = \frac{d\rho_c}{dt} \times V - (4)$$

For Adiabatic Expansion

$$P_c \times V^{\gamma} = \text{constant}$$
$$P_c = \text{constant} \times \rho_c^{\gamma} - (5)$$
$$\frac{dP_c}{dt} = \text{constant} \times \gamma \times \rho_c^{\gamma-1} \times \frac{d\rho_c}{dt}$$
$$\frac{d\rho_c}{dt} = \frac{\rho_c}{\text{constant} \times \gamma \times \rho_c^{\gamma}} \times \frac{dP_c}{dt}$$

Using (4) and (5) with the above equation

$$\frac{dm}{dt} = \frac{\rho_c \times V}{\gamma \times P_c} \times \frac{dP_c}{dt}$$
$$\frac{dP_c}{dt} = \frac{\gamma \times P_c}{\rho_c \times V} \times \frac{dm}{dt}$$

Using (2) and (3) in the above equation

$$\frac{dP_c}{dt} = \frac{\gamma \times P_c}{\rho_c \times V} \times \rho_e \times A \times M_e \sqrt{\gamma \times R \times T} \times C_d$$

For isentropic flow, M_e can be calculated from the following equation

$$\frac{P_c}{P_e} = \left(1 + \frac{\gamma - 1}{2} \times M_e\right)^{\frac{\gamma}{\gamma-1}}$$

If

$$\frac{P_e}{P_c} < 0.528$$

the flow is choked and $M_e = 1$

5. Configuring the Gas Strut System for replacing the retro motors

A configuration is finalized for the gas strut systems (Table 1) which results in performance as shown in Table 2.

Table 1 Design variables for computing gas strut performance

Design Variable	Value
Inner diameter of cylinder	180 mm
Rod maximum diameter	33 mm
Rod minimum diameter	22 mm
Rod length	60 mm
Stroke	1500 mm
Outer Cylinder Pressure	1 bar
Inner Cylinder Pressure	100 bar

Parametric studies are completed for rod parameters (Figure 5 and Figure 6). Other parameters decided for the analysis shall be based on the impulse requirement and constraints such as – Inner diameter of cylinder shall be limited by the available envelop, Stroke shall be limited by the available fabrication technique, and Pressure shall be limited by safety concerns and structural limitation.

6. Result And Discussion

Following is the result obtained using the MATLAB code

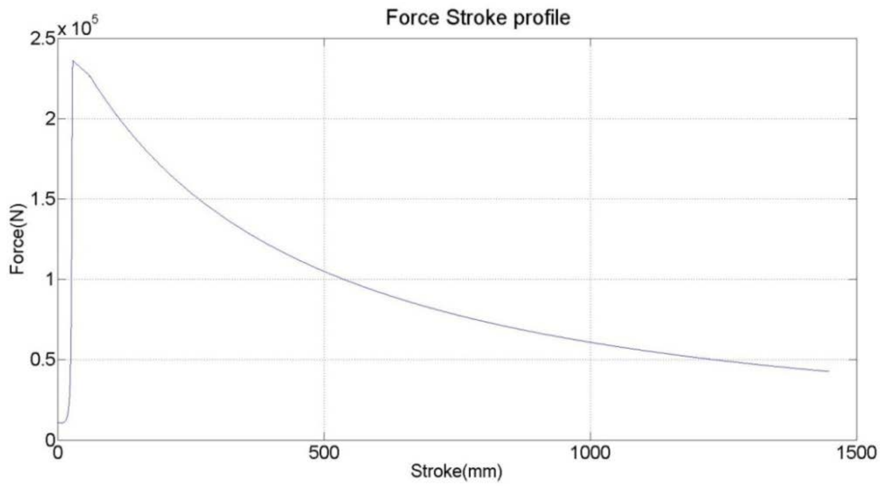

Figure 4 Force Stroke profile of the System obtained from the mathematical model

The force delivered by the system during the initial stroke is very low (Figure 4), since there is no gas flow between the piston and the cylinder. After the initial stroke an annular area between the rod and the axial opening in the piston allows the gas to vent to the cylinder resulting in sudden increase in force which further reduces due to expansion of gas in the cylinder as the stroke increase. The expansion of gas is assumed to be adiabatic in the model as is visible from the typical adiabatic P-V curve in the Force-Stroke profile.

A. Parametric Study

Analyses are run by varying the rod lengths and varying the end diameters, without changing any other dimension.

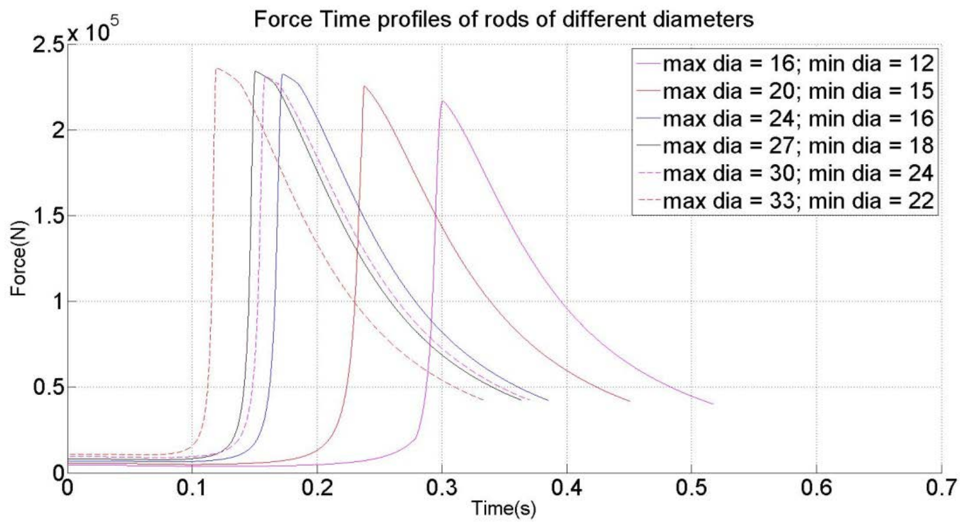

Figure 5 Force Time profiles of 60 mm length rods of different end diameters

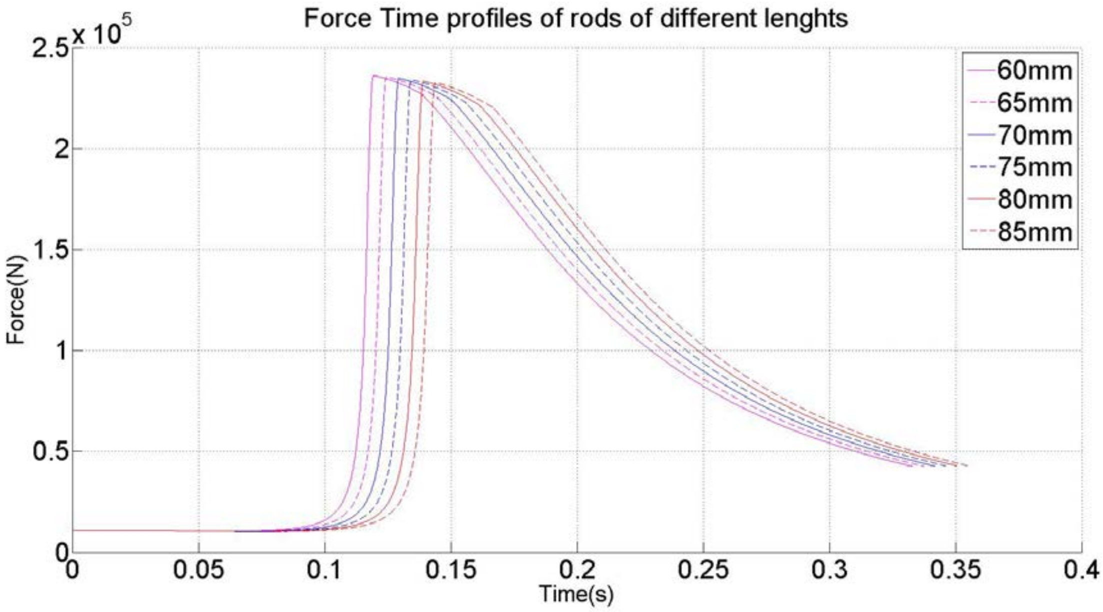

Figure 6 Force Time profiles of rods of different lengths with end diameters of 33mm and 22mm

Figure 5 and Figure 6 shows the effect of varying rod taper on system performance. The performance plots show us that steeper the taper of the rod, higher is the peak force achieved. 60 mm long rod with maximum diameter 33mm and minimum diameter 22mm gives maximum peak force. Also, the peak force is achieved quicker as the taper is increased. Another observation is related to the rate of increase of force i.e. the slope of the curve increases if the rod taper is increased. This presents conflicting requirements for rod design, since we want a system which provides less shock and high peak force.

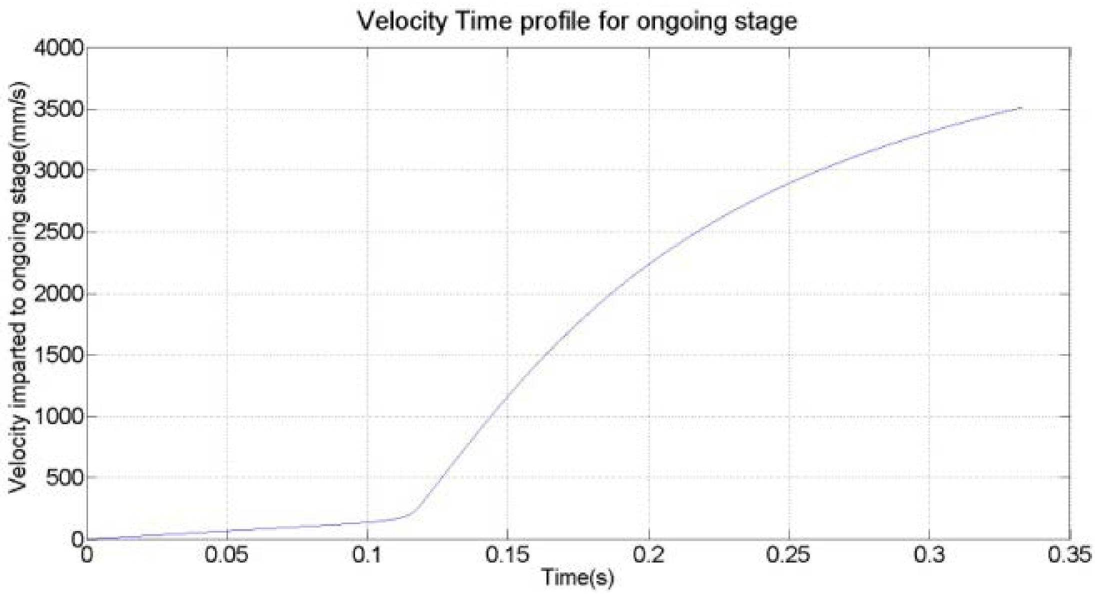

Figure 7 Velocity Imparted to the Ongoing Stage

Four units of the proposed system on a launch vehicle can impart a ΔV of around 3.5 m/s (Figure 7) to an ongoing stage of 32 tons.

B. Comparison with available system

Gas strut system delivers a peak force of more than five times compared to that of available retro system.

Table 2 Comparison of the two jettisoning systems on the basis of different parameters

Parameter	Gas Strut (as per Table 1)	Retro Motor
Time for Stage Clearance(4.45m Pull–out length)	0.79 s	1.01 s
ΔV to the ongoing stage	3.5 m/s	0
ΔV to the spent stage	6.3 m/s	8.8 m/s

The system shall be explored further in future studies, using detailed separation dynamic analysis for an exhaustive comparison with the existing jettisoning system.

7. Test Scheme

A test scheme is proposed for proof of concept of the pneumatic jettisoning system.

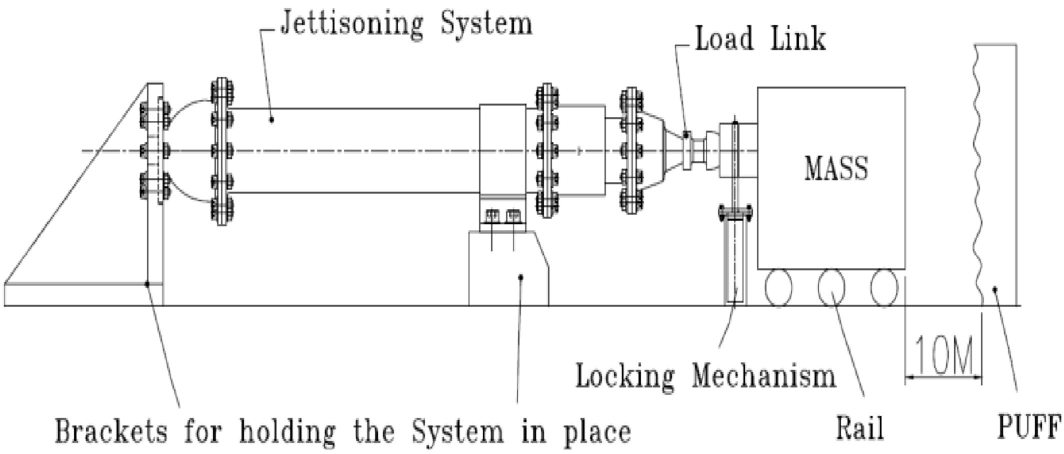

Figure 8 Set Up for Testing the Pneumatic Jettisoning System

The locking mechanism simulates the stage separation system. Upon release, the jettisoning system activates and pushes the mass. The load link reading can be recorded to evaluate the system performance and compare with the available retro rocket performance.

8. Conclusions

A pneumatic system for jettisoning a spent rocket stage is designed as alternative to currently used retro rocket motors. A comparison of the two systems and advantages of using a gas strut system is discussed. A mathematic model is generated and the algorithm to evaluate the system performance is also discussed. Preliminary studies and parametric studies are done to choose a suitable design. A test scheme is proposed for proving the concept of pneumatic jettisoning system.

9. References

[1] Brian Floyd and James Owens, Gas Strut Separation Alternative for Ares I, Proceedings of the 39th Aerospace Mechanisms Symposium, NASA Marshall Space Flight Centre, May 7-9, 2008

Advancement in Development of Controller for Road Mobile Launchers

Jatinkumar Janshali
Vehicle research & Development Establishment
DRDO
Ahmednagar
jatinjanshali@vrde.drdo.in

GRM Rao
Vehicle research & Development Establishment
DRDO
Ahmednagar

***Abstract* – Electronic controller is an integral part of any launching mechanism. The role of controller has changed drastically in past decades from a simply display panel to advance control system with state of art HMI (Human machine Interface). The degree of automation required in launching systems increasing day by day. VRDE is involved in design and development of Road mobile launchers for various programs/ projects. All launchers developed by VRDE are equipped with electronic controller system which carries out all launcher operations in fully auto mode to facilitate easy, safe and reliable launcher operations within predefined time limits. The major role of electronic controller on launchers is stabilization and leveling of launcher platform and articulation of long and heavy article within specified boundary conditions and safety margins with the help of advance control algorithms.In addition to aforementioned functionality, controllers are also being used to carry out automation of other assemblies of launcher such as cup support, sliding operations, locking and unlocking of hydraulic cylinders. Since the launchers are important part of crucial warfare, all its subsystems must be robust as well as accurate. VRDE has continuously evolved the design of controller system for launchers from traditional system with analog sensor and actuator interface to fully digital system with network-based sensor and actuator interface to meet stringent requirements. The control logic also evolved from simple on-off control to close loop multistage PID controls for the launcher operations. The system architecture of both controller systems is presented in this paper. The selection criteria of sensor and actuator network are discussed. The performance evaluation of both type of controller system architecture for various design criteria such as hardware design and optimization, software design, ease of installation and maintenance, advance diagnosis capability, future expandability are discussed and summarized**

Keywords–Network based controller system, Analog vs. Digital HMI, Performance evaluation of Analog and digital network-based controller system, Electro hydraulic controller system

1. Introduction

Launchers are required for transportation, positioning and launching of articles. The design of launcher varies according to type, size and configuration of articles.The positioning of the article is carried out with the help of hydraulic or electrical actuators. For achieving safe, precise and easy operation, electronic controller system is used in launcher which carries out the positioning of the article. Electro hydraulic controller systems developed by VRDE to carry out launcher operation are considered in this paper for performance evaluation.The controller system consists of four subsystems as hardware, software, sensors and actuators. The main focus of this paper is to show the two approaches taken by VRDE for development of controller system to carry out the identical task. The evaluation of both controller systems is not straight forward as well as not limited to the speed of Central processing unit (CPU) and type of operating system but also depends on parameters such as hardware complexity, reliability, adaptability and maintainability. Evaluation of both controller system based on aforementioned parameters are discussed and summarized.

2. Controller system type & objective

VRDE has developed following two types of controller systems for launchers:

(i) Analog Network based Controller (ANC)system
(ii) Digital Network based Controller (DNC) system

The functional objective of both controller systems is shown in Table 1.

Table 1: Functional Objective of Controller

Operational Constraint	Time of operation	No of hydraulic actuators	No of sensors
Auto leveling Pitch angle: Accuracy: in arc min Roll angle: Accuracy: in arc min	3 minutes	6	10
Articulation (0 to 90 degree & back) Max Tilt Cylinder velocity:75 mm/sec Max Tilt Cylinder acceleration: 75 mm/sec^2	5 minutes	2	11
Positioning of load Load: In ton Accuracy: In arc min	2 minutes	2	10

The simplified representation of electro hydraulic controller system as shown in figure 1:

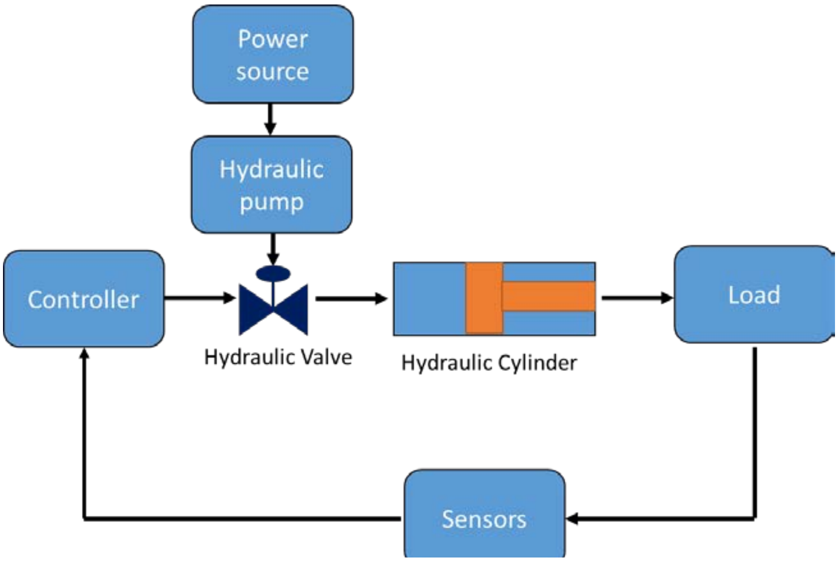

Figure 1 Electro hydraulic controller system

The controller receives the inputs from various sensors and switches mounted on launcher and generate the output based on control algorithm. This output controls the flow of hydraulic fluid flowing through valve which in turns controls the movement of cylinder which is connected to load.

The details of two type of controller system are as below:

A. Analog network-based controller (ANC) system:

The architecture of ANC system developed by VRDE is shown in figure 2.

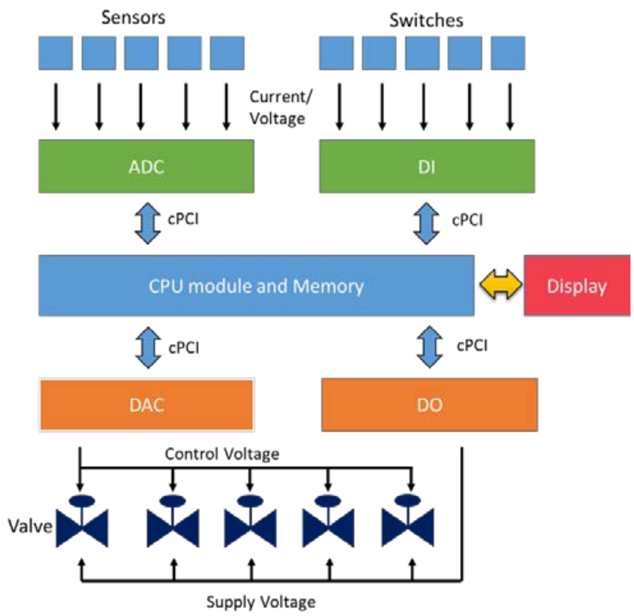

Figure 2: Architecture of ANC controller system

In this architecture all sensors generate analog signal (voltage/ current) which receives and converted into digital form by Analog to Digital Convertor (ADC) module, similarly all switches shall be interface with Digital Input (DI) module. This ADC and DI module interface with CPU via Compact Peripheral Component Interconnect (cPCI) bus defined by PCI Industrial Computers Manufacturers specification[1]. The software runs within CPU and process the digital inputs according to control algorithm as well as operation selected by user. The output generated by control algorithm is in digital form which is converted into analog form with the help of digital to analog convertor (DAC) module. The Supply to the valve is controlled by Digital Output (DO) module. In this system all interface of controller system with the sensors and actuators are in analog form. Therefore, this system is called analog network-based controller system. However, it is to be noted here that the communication between ADC, DAC DI, DO and CPU is in digital form.

B. Digital network-based controller (DNC) system:
   The architecture of DNC system is shown in Figure 3.

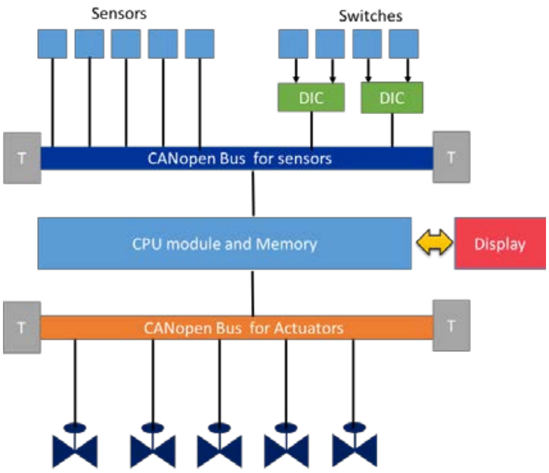

Figure 3: Architecture of DNC system

As shown in Figure 3, CANopen based network has been used for sensors and actuators. CANopen is higher layer protocol based on Controller Area Network (CAN). The CAN is robust, non-destructive arbitration-based broadcasting protocol and defined by ISO 11898[2] standard. The branch architecture mentionde by Wolfhard[3] is used.The switches are connected to the Digital Input to CANopen convertors (DIC). The DICs are connected on the network. All Sensors and actuators are treated as a node on the network. 127 independent nodes can be connected on one CANopen network. The network must be terminated with 120-ohm resistance (T) at both extreme ends. The CPU module also interfaced as a node on CANopen network. All communication between CPU, Sensors, Switches and actuators is in digital form.

.

3. Evaluation Criteria

Evaluation of both controller systems is not straight forward due to difference in architecture. For evaluation of ANC and DNC system, following criteria are selected:

(i) Performance
(ii) Hardware size and complexity
(iii)Software size and complexity
(iv)Cable harnessing
(v) Advance diagnosis

The evaluation carried out against the aforementioned criteria is described hereafter.

A. Performance

As shown in Figure 2 and Figure 3, the system architecture for both controller systems is different.Moreover, i7 based CPU[4] has been used in analog network-based controller system and ARM Cortex A8 based CPU[5]has been used in digital network-based controller system. Both CPU are having entirely different architecture as well as performance. The key differences identified between these two processors by Alghuraibi[6] are summarized in Table 2.

Table 2: CPU Comparison

Parameters	i7 CPU	ARM Cortex A8 CPU
Speed	2.93 GHz	1 GHz
Level I cache	8 MB	3 KB
MMU	Available	Available
Power	25 watts	≤ 300 mill watts

It is clear from above that the performance of both the CPU is quite different. However, the only CPU performance is not the deciding factor for controller system. The combined performance of all components shown in figure 1 should be the criteria for evaluation of both the controller system. The evaluation should also be done based on functional requirement of launchers. The functional requirements of the launchers for two main operations are given in Table 3.

Table 3: Operational requirements of controller system

Operation	Response time
Leveling	≤ 200 milliseconds
Articulation	≤ 150 milliseconds

The response time is inclusive of sensor data acquisition, signal processing and conversion, control algorithm execution time, output signal processing and conversion, hydraulic valve response time and cylinder response time.

The response time for sensors, hydraulic valves and hydraulic cylinders with load are same for both type of controller system. Therefore, only the response time of controller system is required to be derived for performance evaluation.

I. Response time of ANC system.

Following test setup has been prepared to measure the response time of ANC system.

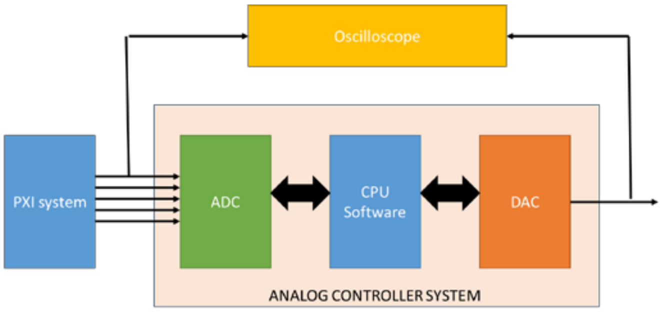

Figure 4: Test setup for ANC system

PCI extension for Instrumentation (PXI) based system has been used to generate the sensors signals and fed to controller system. The same system is also interfaced with oscilloscope. The controller system processes the signals and based on control algorithm of selected operation generates the output which is measured with the same oscilloscope and time difference between input signal and output signal has been measured. The results are given in Table 4.

Table 4 Response time of ANC system

Operation	Response time (millisecond)		
	ANC system	Hydraulic system & sensor	Total
Leveling	16	130	146
Articulation	19	110	129

II. Response time of DNC system

Test setup shown in Figure 5 has been prepared to measure the response time of DNC system.

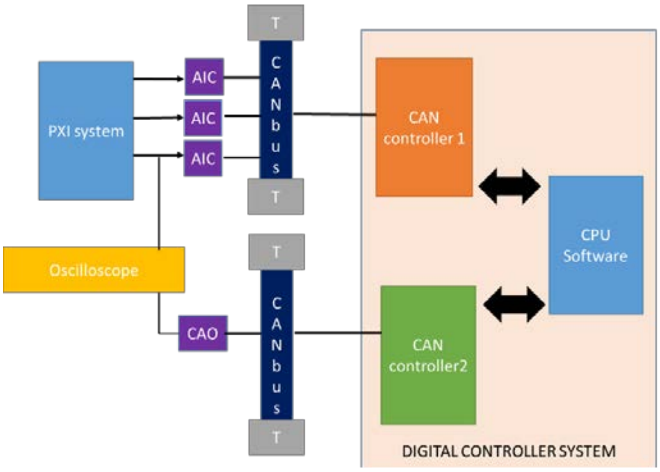

Figure 5: Test setup for DNC system

As shown, the CAN network has been used for sensors and actuator interface to controller system in digital controller system. The baud rate of both networks has been selected as 250 Kbps with 11-bit CAN identifier and bus load analysis7 carried out. The PXI system generates analog signals which are fed to Analog Input to CANopen convertor (AIC). Each AIC is connected as an independent node on CAN bus. The CPU also connected on two CAN bus with the help of 2 no's of CAN controllers. The output generated by the control algorithm asserted on CAN bus 2. The CANopen to Analog output convertor (CAO) converts the output signal in analog voltage which is fed to oscilloscope. The time duration between changes of input to change of output is measured in oscilloscope. The results are given in Table 5.

Table 5: Response time of Digital Controller System

Operation	**Response time (millisecond)**		**Total**
	DNC system	**Hydraulic system & sensor**	
Leveling	20	130	150
Articulation	25	110	135

B. Hardware complexity

Hardware complexity matters when the size, reliability and stringent requirements are prime concern. The controller system is very crucial system and must have high reliability to reduce the risk of failure. ANC as shown in Figure 2 consists of large amount of the hardware compare to DNC system shown in Figure 3 for identical functional requirements. The hardware details of both controller systems are given in Table 6

Table 6 Hardware complexity details

Module	**ANC system**	**DNC system**
CPU unit	1	1
cPCI backplane	1	0
CAN controller	0	2
ADC module	1	0
DAC module	1	0
DI module	1	0
DO module	1	0
Field power supply	1	1
Connectors	15	2
Weight	50 kg	10 kg

Apart from more numbers of hardware modules, the connectors and cabling requirements of ANC system are also huge. It is clear from above table that ANC systems are having significantly large amount of hardware modules and connectors which increase the chances of failures as well as possesses the difficulty to maintain the thermal requirement, Electromagnetic compatibility requirement and vibration /shock requirements of launcher system.

C. Software size and complexity

Software architecture of ANC system is different for both type of controller system.

I. Software architecture of ANC

Software architecture of ANC system is shown in Figure 6.

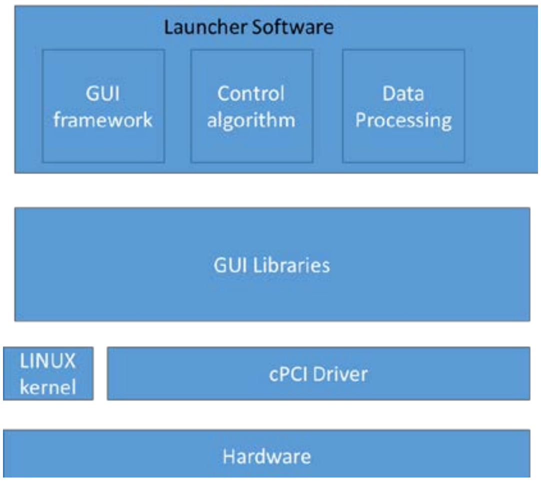

Figure 6:Software architecture of ANC system

For ANC system, only the measured data are communicated to the controller which are converted into digital form and provided to application software through the cPCI device drivers. Since there are no additional information other than process value provided by sensors and actuators, the minimal data processing is required at software level. The application software mainly performs three functionalities of Graphical User interface (GUI) handling, Control algorithm execution and data processing. The software complexity is very low for ANC system.

II. Software architecture of DNC

Software architecture of DNC system is given in Figure 7. The CANopen protocol8 supports various functionalities for node management such as Process Data Object (PDO) communication, Service Data Object communication, Error handling, Network Management (NMT). All these functionalities must be handled by software. The CANopen stack implements the functionality of CANopen protocol for all CANopen buses connected with system. Apart from process value, the node on CANopen network sends heart beat signals as well as node specific details and state of node. Each node sends the error messages in case of deviation of any node on the network as well as node itself. Therefore, role of the software is not just limited to processing of measure value but complete network managements needs to be done. Therefore, software complexity of DNC system in high compare to ANC system.

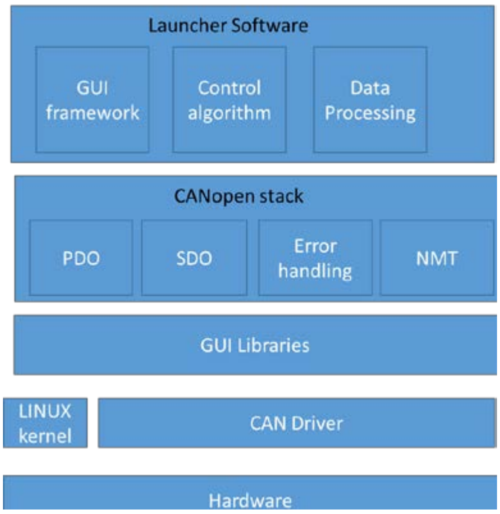

Figure 7: Software architecture of DNC system

III. Bus load optimization

CANopen protocol supports various baud rates from 10 Kbps to 1 Mbps. The selection of baud rate depends upon parameters such as response time, bus length, bus load, number of nodes active at a given instance. The baud rate finalization requires careful design of the network. For design of CANopen network and optimization of bus load for launcher controller following network configuration method is adopted:

(a) During any operation, node related to running operation shall be in operational (Active) mode and those nodes only communicate with controller. All nodes related to other operations shall be in preoperational (inactive) mode.
(b) All nodes shall be configured in time triggered mode. That is each node has assigned a time stamp. After elapsing a time stamp, node send a data to controller.
(c) Node with a fast cycling time shall be configured with lowest priority so that it will not take over entire bus.
(d) All nodes shall be configured for 11-bit identifier frame.
(e) Bus load must be less than 50% in any case.
(f) Bus load is calculated for message having 64 bits data length but in actual all sensor nodes are having a data length of 4 bits only.

Based on above, the busload has been calculated for leveling and articulation operation at 250 kbps baud rate and measured using a software tool CAN analyzer from VectorInfornatik[9]. The bus loads measured are shown in Figure 8 and Figure 9

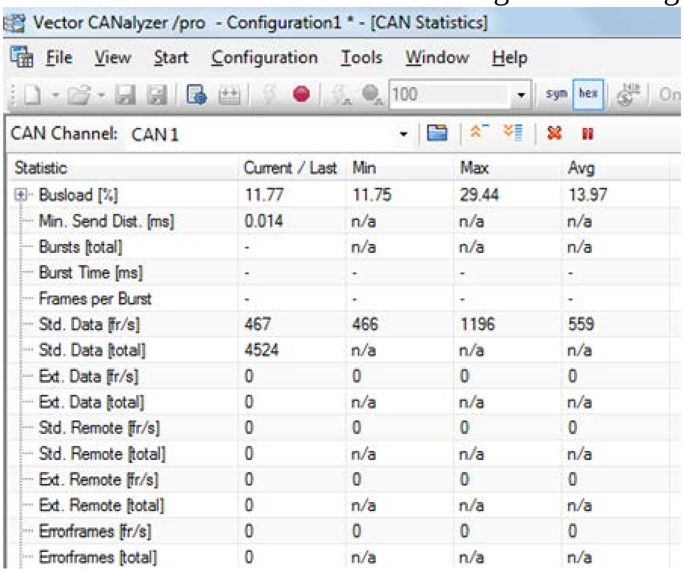

Statistic	Current / Last	Min	Max	Avg
Busload [%]	11.77	11.75	29.44	13.97
Min. Send Dist. [ms]	0.014	n/a	n/a	n/a
Bursts [total]	-	n/a	n/a	n/a
Burst Time [ms]	-	-	-	-
Frames per Burst	-	-	-	-
Std. Data [fr/s]	467	466	1196	559
Std. Data [total]	4524	n/a	n/a	n/a
Ext. Data [fr/s]	0	0	0	0
Ext. Data [total]	0	n/a	n/a	n/a
Std. Remote [fr/s]	0	0	0	0
Std. Remote [total]	0	n/a	n/a	n/a
Ext. Remote [fr/s]	0	0	0	0
Ext. Remote [total]	0	n/a	n/a	n/a
Errorframes [fr/s]	0	0	0	0
Errorframes [total]	0	n/a	n/a	n/a

Figure 8 Bus load simulation for leveling operation

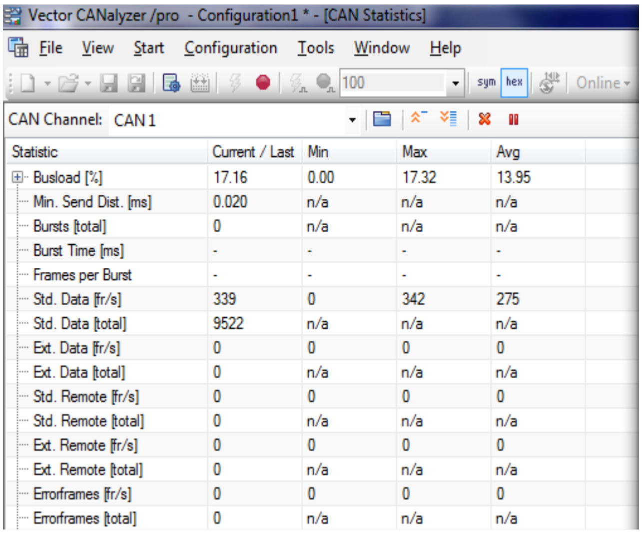

Figure 9: Bus load simulation for Acceleration operation

The summary of result is given in Table 7 below:

Table 7: Bus load results

Operation	No. of nodes	Cycle time (milliseconds)	Theoretical bus load (%)	Practical bus load (%)
Leveling	16	50	21.16	29.44
Articulation	13	30	13.8	17.32

The bus load calculated for payload of 64 bits. For both the operation the busload achieved is less than 50 % which is good for future expandability of the bus.

D. Cable harnessing scheme

Cable harnessing plays important role for the controller system which is mounted on launchers. The simple cabling scheme provides good maintainability as well as ease of trouble shooting. Further, there are always space limitations for vehicle-based application for cabling. Following objectives must be fulfilled by cable harnessing scheme:

a. The length of cable and no's of connectors must be minimized
b. Utilization of same type of cables and connectors wherever possible to reduce the inventory
c. There must be provision for addition of sensors/actuators and actuators without major change in cabling scheme
d. The replacement of faulty cable /connectors must be easy and less time consuming
e. Fault confinement as well as fault isolation methods must be considered during cabling to continue the operation in case of local failures in sensors/actuator/cable
f.

Two different type of cabling scheme has been implemented for both controller systems.

I. Cable harnessing scheme of ANC system

The cable harnessing scheme of ANC system is shown in Figure 10.

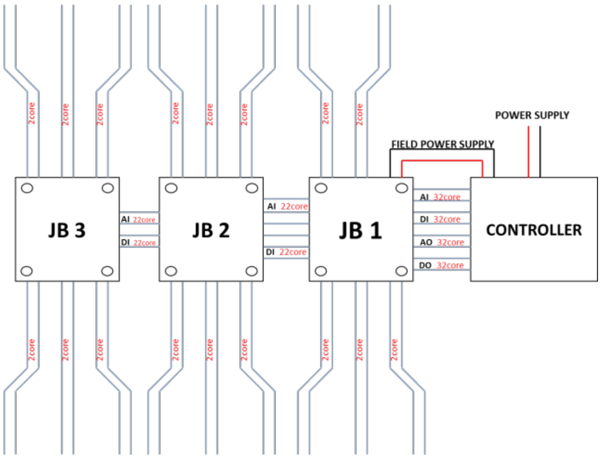

Figure 10: Cabling system for ANC system

As shown in Figure 10, in ANC system, every sensors and actuator independently connected to controller system. Therefore, the amount of cabling increases with increase in sensors and actuators quantity. There is major change is required for addition of any sensor/actuator in the system. The Junction Boxes (JB) are used to distribute the signal as well as to provide checkpoints for cabling in case of any fault. Further there are various type of signals are used such as Analog Input (AI), Digital Input (DI), Digital output (DO) and Analog output (AO) in the scheme. For distribution of signals cable with different numbers of core are used as shown in Figure 10. The advantage of this scheme is fault isolation. In case of cable cut or damage for any sensors/ actuators, the other components will not have any issue. However, addition of any components requires complete change in cabling scheme

II. Cable harnessing scheme of DNC system

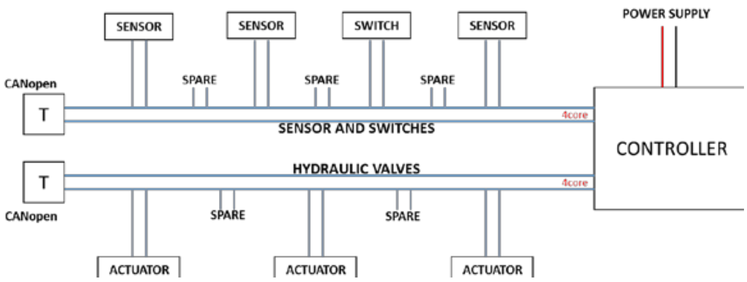

Figure 11 Cabling scheme of DNC system

In DNC system, every sensors and actuator connect on the network as a node. The cable of the node does not need to run up to the controller. All nodes sends CAN messages on the bus so there is no missed signals are required. Therefore, the cable is identical for entire network and only one type of cable with 5 cores is used. Therefore, uniform connector and cable requires for all nodes which drastically reduces the efforts for cabling and replacement of the cable and connectors. The main drawback of this scheme is the failure of the network in case of the cut/damage of main bus cable. The addition of the nodes is very easy in this scheme. The maximum cable length allowed for CAN bus with baud rate 250 Kbps is 250 meters.

E. Advance diagnosis

Advance diagnosis includes vast aspect starting from boundary checks to advanced fault prediction. The main aim of diagnosis is to reduce system down time as much as possible which increases the system reliability. The diagnosis capability of the system depends on the architecture of the system as well as advancement incorporated in sensors and actuators. The diagnosis capabilities for both controller systems are summarized in Table 8.

Table 8 Advance diagnosis capability of controller

Diagnosis type	**ANC system**	**DNC system**
Boundary check	Yes	Yes
Health monitoring of Nodes	No	Yes
Node guarding in case of controller failure	Yes	Yes
Data integrity check	No	Yes
Data validity check	Yes	Yes
Self-isolation due to internal error of node	Manual	Automatic
Data validation by actuator node	No	Yes
Health check of neighbour node[10] for synchronized operation of actuator	No	Yes
Self-health check of node	No	Yes

4. Conclusion

Controller system is a crucial part of any launchers. The architecture of two type of controller system along with evaluation criteria are described in this paper. The summary of evaluation for both controller system carried out is given in Table 9.

Table 9: Summary of evaluation of controllers

Evaluation criteria	**ANC system**	**DNC system**
Performance	Excellent	Good
Hardware complexity	High	Moderate
Software complexity	Moderate	High
Cable harnessing	Complex	Simple
Advance diagnosis	Limited	Good

Apart from evaluation criteria mentioned in Table 9, the cost and development time of ANC system when the large numbers of sensors and actuators are required is high compare to DNC system. Therefore, the selection of controller system depends on the size of the system, cost, development time and requirement of advanced features. As a general guideline the ANC system can be selected for the system wherein the count of sensors and actuators are less and fixed in future and advance diagnosis features are not required. This will reduce the software complexity and cost overhead. The DNC system is a good option where the minimum hardware size, advance diagnosis capability and network expansion capability are prime concern.

5. Acknowledgment

The author expresses gratitude to Shri Sangam Sinha, Director, and VRDE for publication of the article. Author also acknowledges the support given by his team for data generation and analysis.

6. Reference

[1] Compact PCI short form specification, PCI Industrial Computers Manufacturers Group, November 1,1995.

[2] Road vehicles - interchange of digital information - controller area network (CAN) for high-speed communication. ISO 11898, 1993.

[3] Wolfhard, L. (2014). CAN system Engineering (2nd ed.). Springer.

[4] CP3003-SA Datasheet. (n.d.). Retrieved from www.kontron.com.

[5] AM335x Sitara Processor datasheet. (n.d.). Retrieved from www.ti.com.

[6] Alghuraibi, A. (2016). ARM Cortex-A8 and Intel core i7. International Journal of Scientific & Engineering Research, 7(5).

[7] Marco Di Natale, H. Z. (2012). Understanding and Using the Controller Area Network Communication Protocol.

[8] Olaf Pfeiffer, A. A. (n.d.). Embedded Networking with CAN and CANopen (First ed.). Copperhill Technologies Corporation.

[9] CANalyzer. CANopen product information. Retrieved from www. Vector.com.

[10] Technical Information Proportional Valves PVED-CC, Series 5 CANopen. (2015, December). Retrieved from www.powersolutions.danfoss.com.

Parametric study of Initial Yaw & its Rate induced by In-bore Dynamics for FSAPDS Ammunition

Sangeeta Sharma Panda
Armament Research & Development Establishment
Pune
sangeeta_eca@arde.drdo.in

LK Gite
Armament Research & Development Establishment
Pune
lkgite@arde.drdo.in

A.Anandaraj
Armament Research & Development Establishment
Pune
anandaraaj@arde.drdo.in

Abstract – **The dynamic state of a projectile at muzzle exit is determined by the in-bore launch disturbances imparted to the projectile when it travels inside the launch tube or barrel. Contributing factors are initial misalignment of the projectile's principal axis, centre of gravity (CG) offset with respect to the bore centre-line, tube-droop, bore profile, etc. Moreover, at the time of firing the projectile, axial travel of the projectile and propellant gas pressure imparts forces on the gun for recoil and induces slight bending in the barrel. This creates a situation where projectile's motion inside barrel is governed by instantaneous lateral and longitudinal shape of barrel and response of non-rigid barrel to this motion. Path thus generated, gives start to 'projectile balloting' inside the barrel. First maximum yaw experienced by projectile at muzzle exit and yaw dispersion at target end are initiated due to this balloting motion, primarily. It has been observed that projectile's target end performance in terms of penetration, consistency and accuracy hugely depends upon initial yaw angle & yaw rate at muzzle end. Thus, for desired consistency and accuracy, initial yaw and yaw rate not only need to be quantified but also demanded to be curbed to as minimum as possible.**

In-Bore Balloting Motion analysis for FSAPDS is presented in this work, which provides estimates regarding first maximum yaw & yaw rate of FSAPDS projectile at muzzle exit. In this analysis, effects of variations in initial projectile orientation, barrel's & projectile's material, manufacturing tolerances, perturbed internal ballistics variables, etc. are dealt in detail. The output of the paper provides crucial estimates for the initial conditions required for dispersion studies of the ammunition. Results are validated experimentally in terms of yaw rate and yaw angle

Keywords: FSAPDS, In-bore balloting, initial maximum yaw, In-bore dynamics, Monte Carlo simulation, residual spin, yaw rate

1. Introduction

A long-rod, kinetic energy (KE), anti-tank ammunition is a projectile travelling with hypersonic velocity. It is fin stabilised projectile. During its travel in air, it develops angle of attack in both horizontal and vertical plane. Resultant of these two angles is termed as yaw angle. Target end effect of this projectile is the depth to which it can penetrate enemy tank. If penetrator/projectile reaches to the target with high yaw angle, a significant decrease in penetrator performance in terms of depth of penetration is observed. Moreover, a yawing projectile possesses a higher retardation than a well-launched one. This leads to the yawing projectile generally ranging shorter and dispersed [6].

Therefore, detailed study to quantify the parameters affecting initial yaw imparted to the projectile while travelling inside the bore, is required. In-order to quantify and analyse the initial yaw/pitch rate and yaw angle, a detailed in-bore dynamics analysis is carried out. All in-bore parameters inducing initial yaw/pitch rate are investigated and optimal combination of values of parameters for desired end effect is quantified for ammunition under consideration.

The balloting analysis program, BALANS, from Arrow Tech Associates, is utilised for this study.

A. FSAPDS Ammunition

The fin stabilized armour piercing discarding sabot (FSAPDS) ammunition under consideration is a hypersonic kinetic energy projectile fired from a rifled bore gun as shown in Fig. 1. Rifled bore provides initial spin to the ammunition. However, the spin rate of an FSAPDS round must lie within limits set by the requirement to keep the spin low enough to avoid Magnus problems and high enough to keep inaccuracy due to fin unit asymmetries down to a low level [3]. A slipping driving band is fitted to the sabot when firing FSAPDS from a rifled gun to reduce the spin rate of the projectile at the muzzle exit.

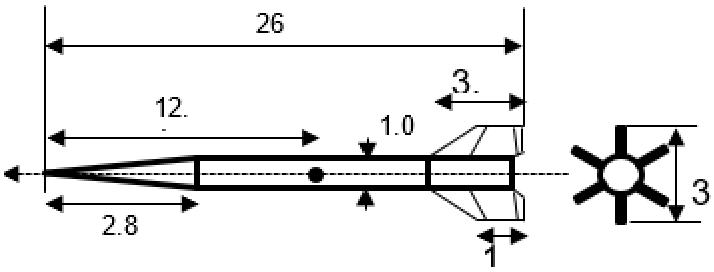

Figure 1: FSAPDS geometrical details (All dimensions in calibre)

2. Modelling And Simulation

Single/Nominal in bore balloting analysis & internal ballistics (IB) analysis are carried out to estimate yaw angle and yaw rate at muzzle exit. After that, to obtain realistic set of data, statistical in bore balloting analysis & internal ballistics analysis is done using Monte Carlo simulation.

A. Internal Ballistics Analysis

Baer- Frankle analysis is carried out using internal ballistics (IB) module of PRODAS. Spin, velocity and acceleration are computed and are used to calculate Centrifugal & axial forces experienced by projectile while travelling inside barrel is estimated using motion parameters such as, velocity, acceleration and spin. In-bore balloting analysis is performed to estimate lateral force primary source generating yaw rate and angle.

B. In Bore Balloting Analysis

BALANS is a module of PRODAS software which includes the effects of a curved bore profile [8] & used to perform in bore balloting simulation. This, in bore balloting simulation requires output of the Internal Ballistics simulation and CG Offset calculations.

Time history of instantaneous location of projectile and lateral and axial loads experienced by it during travel are observed. The resulting yaw angle, angular rate, and transverse velocity at muzzle exit are then analysed. Fig. 2 & 3 shows the balloting analysis model of the FSAPDS projectile & barrel.

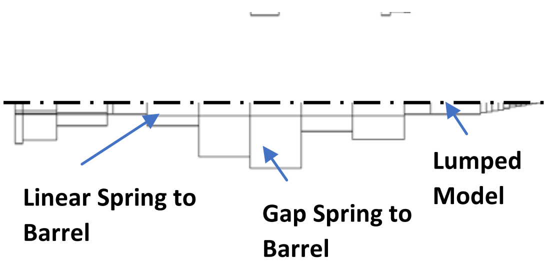

Figure 2: Schematic of penetrator and sabot assembly for Existing design

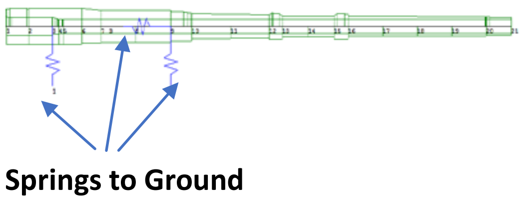

Figure 3: Schematic of barrel

i. Inputs Variables:

Following projectile, internal ballistics and barrel parameters are considered to evaluate the sensitivity of each parameter on yaw /pitch rate.

Table 1: Inputs of MV and Maximum Chamber Pressure used for stochastic analysis

Parameter	**unit**	**Nominal Value**
MV	(m/s)	1650
Charge Mass	*(kg)*	7.2348
BB Rate	*(cm/s/bar)*	0.086051
B Exponent	-	0.67
Impetus	*MJ/kg*	0.9774

ii. Nominal Run Output

Nominal geometrical parameters for the projectile, internal ballistics and barrel are considered to estimate maximum yaw & yaw / pitch rate at muzzle exit.Fig. 4 and 5 shows yaw angle and yaw rate variation with respect to travel of projectile inside barrel.

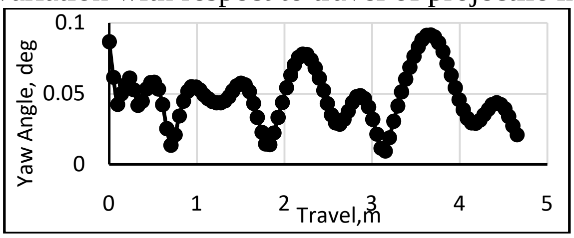

Figure 4: Yaw angle vs barrel length

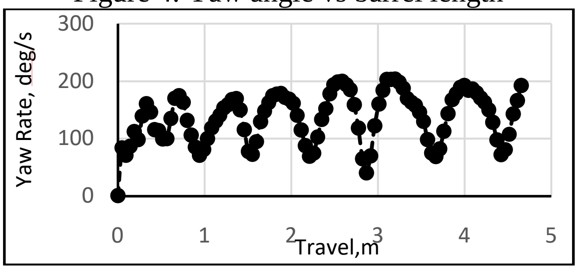

Figure 5: Yaw rate history in barrel

Table 2: Output of Single / Nominal Run In bore balloting analysis

Parameters	Unit	Value @ Muzzle
Time	sec	0.00563
Travel	m	4.652
Yaw Angle	deg / mils	0.021 / 0.37
Yaw Rate	deg/s	106.2

Lateral motion inside non-rigid barrel affects the development of yaw angle significantly. Ideal estimate for yaw angle, time of travel inside barrel, travel distance & yaw rate for controlled/designed motion of projectile inside barrel is presented in Table 2. Any designer would wish to have full control on design parameters for consistent performance of ammunition at target end, but manufacturing tolerances, barrel wear, material deformities, charge mass variations, etc. put constraint to get idealistic set of combination of all variables all the times. Hence, to get realistic estimates, Monte Carlo analysis is performed, where all influencing parameters are varied randomly and effect of all these variation on yaw angle and yaw rate is quantified.

iii. Monte Carlo Simulation

In Monte Carlo Simulation initial conditions are randomly selected and in-bore balloting analysis is performed to determine the probability of occurrence of the outcome [8]. Fig. 6 shows the flowchart used for stochastic analysis of in - bore balloting behaviour of FSAPDS ammunition.

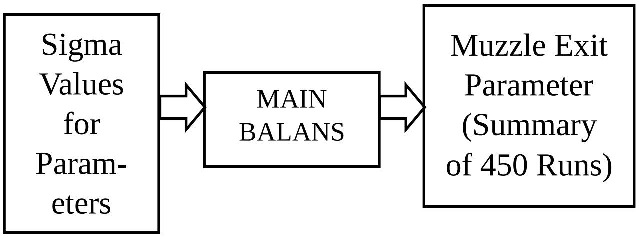

Figure 6: Flow chart used for BALANS

Value of each influential parameter normally distributed is varied between ±3σ. 450 Number of samples of such values are taken. Parameter analysis is performed with respect to time. Average of these 450 runs gives output of balloting analysis in the form of averaged muzzle exit yaw rate.

3. Result & Discussion

For a given weapon system, a projectile with better yaw/pitch rate dampening characteristics has lesser dispersion and vice-versa [3]. Not only yaw/pitch dampening characteristics but also less initial yaw rate at muzzle end itself will be beneficial in terms of improved consistency and less dispersion. Initial condition at muzzle exit for yaw angle and yaw rate are quantified by doing detailed in-bore balloting studies conducted using statistical/Monte Carlo in bore balloting analysis, results of which are discussed below in detail.

A. Yaw Rate due to Internal Ballistics (IB) Parameters

Internal ballistics parameters such as burn rate coefficient, charge mas, impetus, BB rate are varied between ±3σ and variation in Muzzle velocity, chamber pressure, acceleration, temperature and resistance to motion are estimated by IB Monte Carlo analysis keeping other parameters constant. This is done to see the effect of IB variations only on yaw rate at muzzle exit.

Table 3: Yaw rate variation with respect to IB parameters' variation

Yaw Rate	**Nominal**	**Due to ±3σ variation in IB parameters**
Average, deg/s	106.2	110.9
Standard Deviation, (deg/s)	-	104.2

It is observed that the average yaw rate increases to 110.9 deg/ s due to variation in IB parameters

B. Yaw Rate due to Barrel Id & Front Bore Rider's Outer Diameter Variation

Due to manufacturing inaccuracies or due to wear of the barrel there may be variation in the inner diameter of the barrel and in the outer diameter of the front bore rider. Both of these parameters are varied one by one and their effect on developed yaw rate at the muzzle can be seen in Fig. 7 andFig. 8.

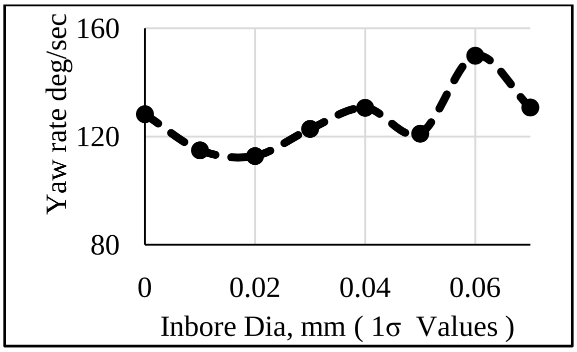

Figure 7: In-bore Dia (1σ values) vs. Yaw Rate

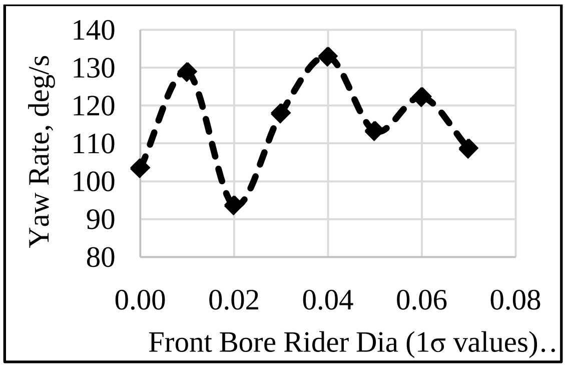

Figure 8 Front Bore Rider Dia (1σ values) vs. Yaw Rate

It is a well-known fact that in the design of fin-stabilized projectiles, the radial stiffness of the sabot front bore-rider has a significant impact on the projectile's dispersion characteristics and is therefore, an important design consideration. If variations in Stiffness and Young's Modulus ±10% for bore rider and barrel is the yaw rate is not affected much and is show in Table 4

C. Yaw Rate due to Wheel Base and Clearance

The yaw rate observed due to wheel base and clearance is show in Table 5. Reduction in wheel base increases the yaw rate and increases in clearance contribute towards increase in yaw rate.

Table 4 Yaw Rate due to wheel base and clearance

Yaw Rate Parameters	**Nominal**	**Wheel Base (- 30mm)**	**Clearance (+.05mm)**
Average (deg/s)	106.2	124.5	125.1
Standard Deviation (deg/s)	-	194.0	190.0

D. Yaw Rate due to Mass & Inertia Properties of Projectile & its Contribution to Dispersion

Variation in Mass and Inertia properties is taken as $\pm$20% of the Nominal value. Increase in mass and transverse inertia reduces the yaw rate.

It is observed that variation due to stiffness barrel and projectile riders, wheel base, clearance, inertia, velocity and pressure profile and obturator have less effect on yaw rate.

Table 5: Yaw Rate due to wheel base and clearance

Yaw Rate Parameters	**Nominal**	**Mass**	I_{xx}	I_{yy}
Average, (deg/s)	106.2	105.2	107.4	101.2
Standard Deviation, (deg/s)	-	134.0	133.2	120.4

E. Yaw Rate due to Twist in Barrel

Being a rifled barrel, the spin generated in-bore serves to be the most important parameter in yaw/pitch rate analysis. It is observed that, the yaw rate depends linearly on number of twists per caliber as shown in Fig. 9. The yaw rate becomes double if residual spin if residual spin changes from 5% to 15%.

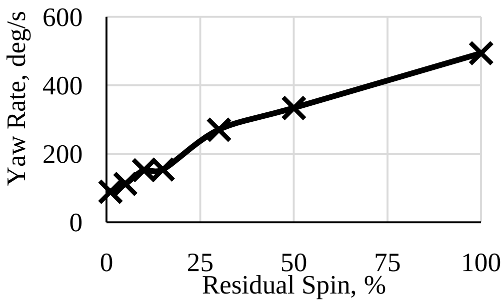

Figure 9 Effect of in-bore spin on yaw rate

4. Conclusion

It is observed that variation due to stiffness of the barrel and projectile riders, wheel base, clearance, inertia, velocity and pressure profile and obturator have effect on yaw rate. The most important parameter on which yaw depends is in-bore spin. To minimize the yaw rate initial spin should be optimum. This study suggests that the optimum initial spin should be between 5 to 10% for normal yaw rate and better consistency.

5. Acknowledgement

Authors are grateful to Shri RD Misal & entire Aero- CFD & External Ballistics team of ARDE for their valuable guidance and support & to Shri Rohit Bhandari & Shri Prashant Patil for providing essential data for this study.

6. Reference

[1] "Text Book of Ballistics & Gunnery" Vol 1, Her Majesty's Stationery Office 1987.
[2] Thomas P. Erline and Alan F. Hathaway, "Dispersion Analysis of the XM881 Annor-Piercing, Fin-Stabilized, Discarding Sabot (FSAPDS) Projectile", ARL-MR-433, January 1999.
[3] Peter Plostins, "Launch Dynamics of FSAPDS", 8th International Symposium on Ballistics, Orlando, Florida, October 23-25 1984.
[4] W.J. Rossouw, "On the influence of yaw and yaw rate (magnitude and orientation) on dispersion", 19th International Symposium of Ballistics, 7-11 May 2001, Interlaken, Switzerland.
[5] Alan F. Hathaway and John R. Burnett, "Sabot Front Borerider Stiffness vs. Dispersion: Finding the Knee in the Curve", U.S. Army Symposium on Gun Dynamics, McLean, Virginia, 17-19 Nov 1998.
[6] Peter Plostins, Ilmars Celmins and Jonathan Bornstein, "The effect of sabot wheelbase and position on the launch dynamics of fin-stabilized kinetic energy ammunition", 12th International Symposium on Ballistics, 30 October-1 November, 1990 San Antonio, Texas.
[7] Dr Stephen Wilkerson, "The impact of lnterior ballistics on kinetic energy projectile accuracy", 15th International Symposium on Ballistics, Vol.2, Jerusalem, Israel, 21-24 May 1995.
[8] "Arrow Tech associates, PRODAS Version 3.2, User's Technical manual", south Burlington, VT, March 2016.

Assessment of Numerical Simulation of Store Separation from Fighter Aircraft using Instrumented Flight

Sunil Hiwale
Armament Research and Development Establishment
DRDO
Pune
sbhiwale@arde.drdo.in

Sangeeta Sharma Panda
Armament Research and Development Establishment
DRDO
Pune
sangeeta_eca@arde.drdo.in

AS Badrinarayanan
Armament Research and Development Establishment
DRDO
Pune
badrinarayanas@arde.drdo.in

Abstract- **Store separation is very crucial from safety aspects of aircraft when the store is released from the parent aircraft. The behavior of the store should not be abrupt in proximity of the aircraft. Therefore, safe separation studies are very important for flight clearance of the store. In present work, a case study of store separation is presented for a canard-tail guided store using overset meshing approach of the commercial software CFD++ [7]. Similar store separation study was carried-out earlier with dynamic meshing approach of ANSYS Fluent [1] Software. In this study, the store is attached to the mid-board weapon station of the aircraft, Numerical simulation of store separation is carried out with the help of CFD coupled 6-DOF approach and results are obtained. An instrumented flight trial was carried out for the same operating condition and the comparison of the numerical data with flight data is carried out. The performance of the store in vicinity of the aircraft and the safe separation studies performed using CFD is presented in the paper. CFD++ is an in-viscid solver used for flow simulation and the trajectory of the store is modeled with the help of a 6-DOF based rigid body dynamics module coupled to the flow solver. It employs overset meshing technique for solving flow problems involving relative motion between the rigid bodies. Initially, the methodology is validated with 'Eglin Wing Store Separation' test case, to ensure that the predicted results are reasonably accurate. Subsequently, the same methodology is extended to simulate separation of the given store from the aircraft. Unstructured mesh is generated over the flow domain and In-viscid flow simulation is carried out at transonic Mach No. 0.85 for release altitude of 9.8 km. The over-set meshing approach has been used to handle the mesh of moving zone in accordance with the store movement. Trajectory parameters such as CG position, body rates, body orientations and store velocities etc., are estimated. These flight parameters are compared with the measured flight data obtained in the store release trial to assess the separation phenomenon of store from aircraft. This study has helped to gain confidence in the numerical simulation of store separation using CFD and predict the store dynamics accurately in vicinity of aircraft to ensure safe separation.**

Keywords - store separation, CFD, overset mesh, dynamic meshing, In-viscid flow, 6-DOF

1. Introduction

The safety of parent aircraft is an utmost concern during release of any store. The behavior of the store has to be studied and analyzed critically before the actual release. Detailed 6-DOF coupled unsteady CFD simulations are carried out to obtain various flight parameters such as CG location, body orientations, body rates, body velocities etc., for the required release time. But the validity of the data needs to be proven to build confidence over the adopted methodology to simulate flight of store in close proximity of the aircraft. The present paper focuses on the use of overset meshing approach of CFD++ software for simulating the separation of the store from the aircraft. The store separation methodology is validated initially with the benchmark case of Eglin wing store separation. Using similar simulation analogy, store separation for guided store is carried out at Mach 0.85 (AOA=1.5º), when the store is released from aircraft and instrumented store release trial was also carried out at similar operating conditions. Flight Parameters including accelerations and body rates of the store were obtained with the help of onboard IMU sensors. Parameters such as velocity components, position of CG, body rates, orientations are obtained by post processing the measured sensor data. An assessment of the numerical data with the instrumented flight data was carried out and the results are presented in this paper.

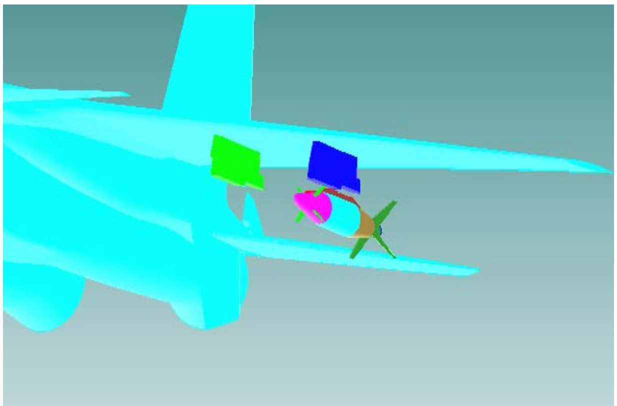
Fig. 1: Representative picture of store with aircraft

2. Dynamic Mesh Aapproach vs Overset Mesh

This store separation study has been attempted earlier using dynamic mesh approach of ANSYS FLUENT Software [1]. Dynamic mesh approach does re-meshing in the computational domain around movable zone boundaries as per the movement of the store. During the movement of store, the poor cells are clubbed into a group and then the mesh of the group is modified. Depending on the skewness of the cells, re-generation of cells or spring-based smoothing is done [8]. During this process of re-meshing, the dynamic mesh is highly prone to generation of negative cells in the simulation and very high cell count. This approach is hence highly un-predictable and un-reliable in-terms of convergence and completion. This issue is overcome in recent times by the overset meshing approach wherein separate meshes are used for the different rigid bodies in the flow domain and the data across the different meshes is transferred through zonal boundary condition. Overset meshing approach is available in ANSYS FLUENT and CFD++. However, in this study, over-set approach of CFD++ software has been used to carry out the separation simulation. CFD++ solver uses the overset algorithm to handle 6-DOF coupled CFD simulation to solve store separation. Overset mesh method facilitates the robustness in the mesh generation during the store movement. The present work focuses on the over-set mesh application to obtain numerical simulation of store separation and the assessment of simulation results with the flight data.

3. Validation of CFD++ Software

A. Geometry and Grid Generation

Eglin test case results for transonic release condition (Mach=0.95, Altitude 26000 ft) is used to validate the CFD methodology used for store separation studies. Geometrical parameters of the wing and store are obtained from Ref [2-5]. Wind tunnel set up consists of wing configuration with the store made of a tangent-ogive fore-body, clipped tangent-ogive after-body and cylindrical central body. The attachment of store with the wing is shown in Fig 2. An unstructured mesh was generated over the computational domain with help of IMIME tool of CFD++. Small domain containing component mesh over the store was created of 0.8 million cells. Similarly, a bigger domain of total cell size 2.6 million was created to represent the computational domain as background mesh for the overset approach. The background mesh remains stationary during transient simulation, while the domain consisting the store, will travel through it. Cutting and blanking operations are performed to accommodate newer position and orientation of store which is estimated by the in-built 6-DOF rigid body dynamics solver. The data is transferred into meshes through zonal boundary condition. A sectional view of mesh with the smaller domain over the store is shown in Fig 3.

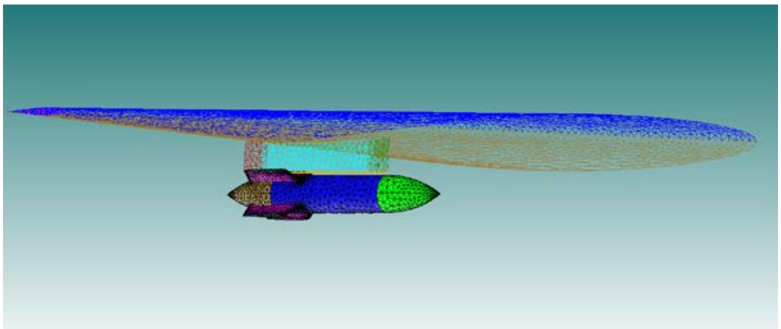

Fig. 2: Attached store with wing

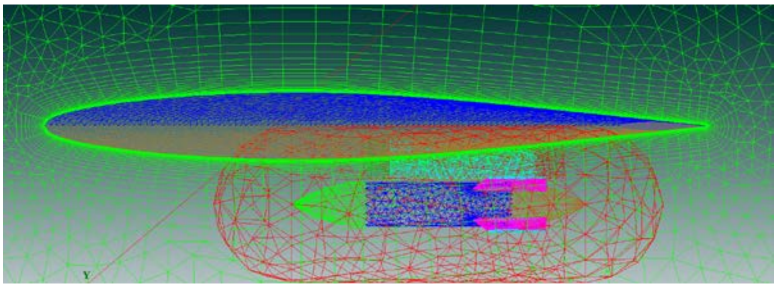

Fig 3: Mesh sectional view

B. Simulation Results for validation

An inviscid simulation is carried out for the flight Mach No. 0.95 at 0º angle of attack. Initially, steady state CFD simulation is carried out and subsequently transient solution is obtained. Transient CFD simulation is carried out with the help of 6-DOF coupled solver and various flight parameters are obtained such as displacement of CG location, body attitudes, body rates, store velocities etc. Flight parameters such as displacement of CG location and orientation is compared with the data reported in Ref [3]. The results are presented with respect to Body Coordinate System (BCS). The BCS has an origin located at CG, positive X is pointing towards tail of the store, positive Y is pointing to right if the store is seen from back and positive Z is pointing downwards. A plot of displacement of CG location and Euler angles of the store are shown in Fig 4 and Fig 5 respectively. It is observed that X, Y and Z displacements of center of gravity location are in close agreement.

In Fig.5, it is seen that the Roll, Pitch and Yaw angles follows the trends very well with respect to the wind tunnel data. Minor differences are noted in roll angle computed by CFD as against the experimental data. This difference in roll is expected and attributed to the sensitivity of variation of axial moment of inertia which results into higher changes into roll angle. The same has also been reported by several other researches in various literatures.

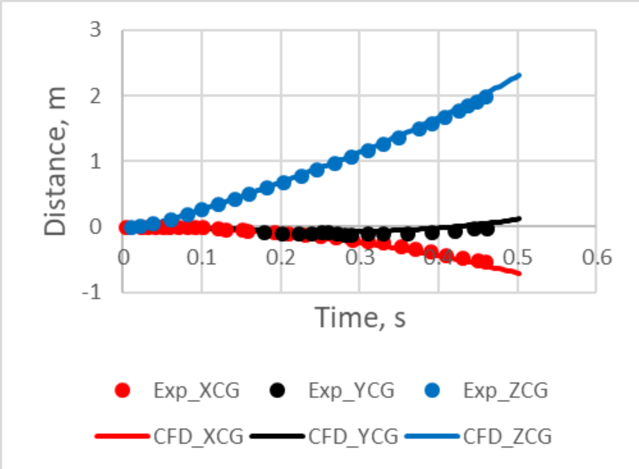

Fig 4: Center of Gravity location displacement

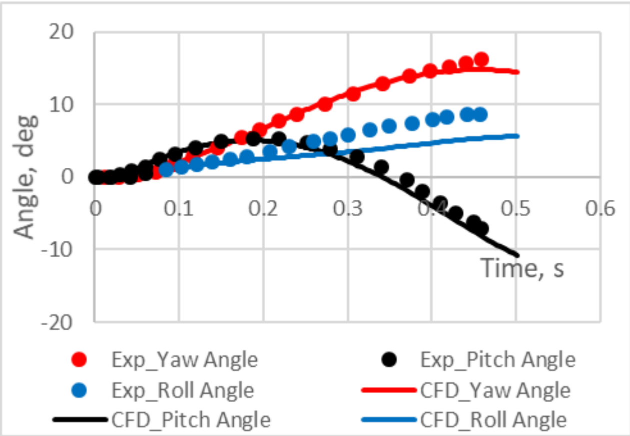

Fig 5: Euler angles- Orientation of store

4. Numerical Simulation For Guided Store

An un-structured mesh was created over the computational domain. The computational domain is divided into two parts; one consisting the background mesh and the second a smaller domain around the store. The total cell count is around 12 million for both domains. The domains interact with each other in overset fashion during transient simulation. Inviscid flow solver is used to obtain the numerical CFD simulation. Free stream air properties at 9.8 km altitude are used as Pressure Far Field boundary condition. Converged steady state simulation is used as initial solution to the coupled CFD 6-DOF simulation. The initial time step of the solution was 1 millisecond which was gradually increased to 5 milliseconds as the separation distance increases. Convergence was monitored and ensured for residuals and aerodynamic forces. Trajectory parameters such as displacement of CG location, body rates, attitudes and store velocities are obtained. These parameters are discussed in subsequent section.

5. Assessment of Numerical Results with Flight Data

The store was released from an altitude of 9.8 km at flight Mach of 0.85. This flight trial was conducted with measuring instruments and flight data was transmitted by the on-board telemetry unit to the ground station. An onboard Fiber Optic Gyros based IMU-GPS unit (FINGS) is used to measure linear accelerations and angular rates. This FINGS unit can measure position, velocity, accelerations and body rates very accurately. The flight data has been processed to obtain displacement of CG position, velocity components, Euler angles and body rates of the store for the separation event of 1 sec.

Variation of Euler angles and body rates with time is shown in Fig 6 and Fig 7 respectively. The Euler angle and body rates are chosen for the comparison purpose as the estimation of aerodynamic moments play an important role in assessment of the accuracy of the CFD solver. Meticulous estimation of all three aerodynamic moments such as roll, pitch and yaw mainly decide the trends of the selected flight parameters viz; Euler angles and Body rates. It is observed that the trends of roll angle, pitch angle and yaw angles match very well. The store has tendency to increase roll in the positive direction. The CFD has predicated lesser roll as compared to roll measured in flight. Maximum of 19.5º roll is computed by CFD while in actual case the roll is attained by store is 22.5º in 1 sec of separation time. Pitch and yaw angle trends are also match fairly well but there are minor differences in maximum angles achieved by the store. CFD has predicted higher maximum value of pitch as compared to the value in flight. In case of yaw angle, the maximum angle predicted by CFD is higher than yaw achieved in flight. It is observed that the response of store is faster in CFD simulation than the actual release trial with respect to lateral direction dynamics.

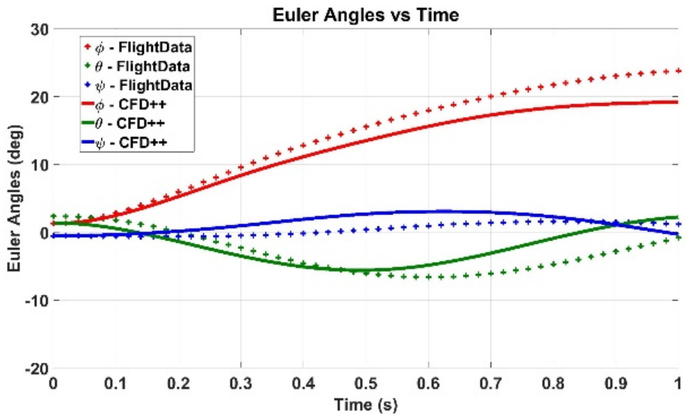

Fig 6: Variation of Euler angles

Fig 7 shows the variation of body rates with respect to time. Trends for roll rate, pitch rate and yaw rates match very well with the flight data. The maximum body rates predicted by CFD are very close to the body rates measured in flight. It is also observed that the CFD predictions indicate faster response of the store. CFD predictions indicated that the store completed one cycle of pitch rate but in actual flight the store had just reached its peak in positive direction of pitch rate and started to decrease. Similarly, CFD predictions indicated that the yaw rate positive peak reached earlier whereas it occurred at around 0.45 sec in actual flight. There is a Delay Of 0.1 Sec To Achieve Maximum Yaw Rate.

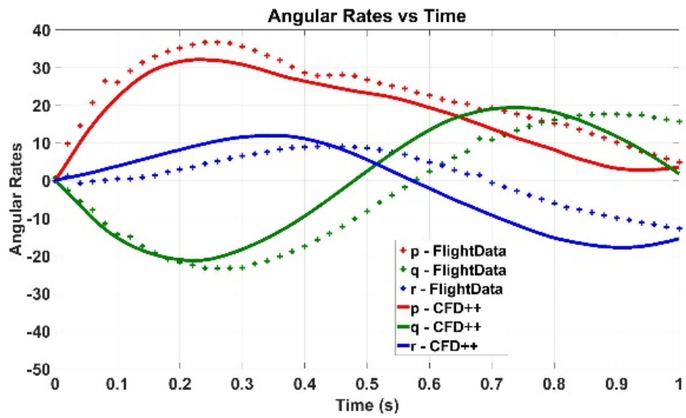

Fig 7: Variation of body rates

The dynamic response of the store predicted by CFD seems faster than the behavior of the store in actual flight. This can be attributed to variations in parameters such as ejector forces with locations, inertial properties, aerodynamic forces estimation etc. Axial and transverse moment of inertia properties also play a major role in capturing the dynamics of the store. The difference in flight parameters in lateral direction could be due to variation in the transverse moment of inertia parameters of the store. Therefore, it is further required to conduct some numerical experiments by varying transverse moment of inertia within given range to bridge gap between the CFD and actual flight trial.

6. Conclusion

The overset meshing approach of CFD++ software has been effectively used to establish a methodology for carrying out store separation study of a store. Overset mesh approach provides good flexibility in mesh generation and helps to prevent generation of negative volume cells during transient phase of solution.

An assessment of numerical simulation with flight data is carried out in the present work. It is found that the trends for Euler angles and body rates are predicted very well and the values are within the close range. But the response reported by CFD is faster than the actual flight trial and it can be attributed to the variations in inertial properties of the store. Therefore, numerical experiments like in [6] are essential to be carried out to investigate the effect of variation of inertial properties within the allowed range in future.

7. Acknowledgment

We are thankful to Dr VV Rao, Director ARDE for providing opportunity and resources for completion of this work. We would like to express our sincere thanks to Group Director Shri. RD Misal for his valuable guidance and Division Head Shri. Anandaraj A for his support. We are also very thankful to Division Head (Control and Guidance) Shri. Kishore Jadhav for the providing critical details of the instrumentation. We take the opportunity to appreciate the support provided by Division Head (Telemetry) Ms. Shyamala Kulkarni, for the telemetry data. We are thankful to our teammates Shri. RS Chopde and Shri. NY Patil, who have given valuable suggestions for successful completion of this work.

8. References

[1] SB Hiwale, PP Parkhi " Numerical Simulation of store separation of guided projectile" , NCAAT, June-2018, pp.285-290

[2] Heim, R.R., "CFD Wing/Pylon/Finned Store Mutual Interference Wind Tunnel Experiment," AEDC-TSR-91-P4, 1991

[3] Yunus Emre Sunay, Emrah Gülay & Ali Akgül, "Numerical Simulations of Store Separation Trajectories Using the EGLIN Test", Scientific Technical Review, 2013,Vol.63,No.1,pp.10-16

[4] Deryl O.Snyder, Evangelos K.Koutsavdis, John S.R. Anttonen, "Transonic Store Separation Using Unstructured CFD with Dynamic Meshing", AIAA 2003-3919, 33rd AIAA Aerospace Sciences Meeting and Exhibit, 23-26 June 2003

[5] Elias E. Panagiotopoulos and Spyridon D.Kyparissis, "CFD Transonic Store Separation Trajectory Predictions with Comparison to Wind Tunnel Investigations", International Journal of Engineering(IJE), Volume(3), Issue(6), June 2010, pp 538-553.

[6] SB Hiwale, PP Parkhi and Mahendra Jha " Perturabation studies for separation dynamics of store during release from aircraft" , International Ballistics Symposium, Sept-2017

[7] " ICFD User Manual 2015" Metacomp Software Ltd, USA

[8] "ANSYS FLUENT MANUAL 2015" ANSYS Ltd, USA

Understanding the Generation of Rolling Moment Coefficient for Typical Launch Vehicle using CFD

J Sreenivasulu
Vikram Sarabhai Space Centre
Trivandrum

Sanjoy Kumar Saha,
Vikram Sarabhai Space Centre
Trivandrum

Dr. Patil M M
Vikram Sarabhai Space Centre
Trivandrum

V Ashok
Vikram Sarabhai Space Centre
Trivandrum

Abstract – **Understanding the generation of rolling moment and its control is very important for designing of launch vehicle. This paper presents the details regarding cause of rolling moment coefficient generation for a typical launch vehicle and studies carried out to reduce the rolling moment. Towards this CFD simulations have been carried out over the launch vehicle configuration using in house developed code PARAS-3D. Configuration consists of various wire tunnel options and simulations carried out at various Mach numbers (M=1.2 and 1.6) and roll angles (φ=0° to180°) at an angle of attack of 40. It is noticed that main reason of experiencing higher rolling moment is the presence of long wire tunnel. Removal and reshaping of protrusions (wire tunnel) reduces rolling moment. Segmenting the wire tunnel suitably into different components help to reduce rolling moment at some roll angles. In order to reduce rolling moment various studies are attempted. CFD simulations over cone cylinder configuration with 1, 2, 3 and 4 wire tunnels have been carried out for Mach number 1.2 and 1.6 at various roll angles and at θ=4°. Compared to configuration with 1, 2 and 3 wire tunnels, 4 wire tunnel configuration experiences lesser rolling moment.**

Abbreviations

D - Diameter of the vehicle, m
M - Mach number
C_{RM} - Rolling moment coefficient
CFD - Computational Fluid Dynamics
CFL - Courant-Friedrichs-Lewy number
RCS - Reaction Control System
ϕ_w - Wind plane angle (deg)
θ - Total angle of attack (deg)
WT - Wire tunnel

1. Introduction

Aerodynamics play a very significant role in designing of a launch vehicle. Steady and unsteady forces are generated on a launch vehicle due to relative motion between the vehicle and surrounding air during atmospheric flight phase of the vehicle. Depending on the shape and size of the different components of launch vehicle, this forces and moment vary. The different components of structure are needed to be designed to take care of this aerodynamic disturbances. Which peaks at transonic Mach numbers and maximum dynamic pressure condition.

The vehicle considered here is having a cylindrical in shape with diameter 'D'. There are some protrusions like wire tunnel, cowling, retro motor etc. are added on the outer surface. These protrusions will cause an unbalanced force which will give rise to rolling moment.

Launch vehicles with low inertia about the roll axis are susceptible to large roll rates and roll angle errors due to aerodynamic rolling moments. Hence, either the inherent rolling moment has to be reduced or appropriate roll control system to counter the disturbing rolling moments has to be incorporated. The configuration studied here has a long wire tunnel running along the length of the vehicle. Numerical analysis has been carried out to understand the rolling moment generation and ways to prevent it. Analysis shows that use of symmetric protrusion reduces the rolling moment. More over dividing the long wire tunnel into smaller pieces also helps in reduction of CRM. All the analysis is presented here in this paper.

2. Configuration Details

Launch vehicle configuration with wire tunnels are shown in Figure 1. Total length of the configuration is 16.9D, conical nose of 200 and 150 flare. Where 'D' is diameter of the launch vehicle. It consists of 2 wire tunnel each 180° apart.

3. Flow Solver

Flow simulation has been carried out using in house developed code PARAS-3D [1,2]. It is versatile tool for analyzing various types of flows with multiple free streams. It solves the Reynolds Averaged Navier-Stokes (RANS) equations. The turbulent flows are simulated using k-ε model in association with modified wall function. The time stepping is done for each cell based on local CFL criteria while the fluxes at the interface of the cells are computed by means of an approximate Riemann solver. The explicit scheme used is second order accurate in space and of TVD type, which is achieved by means of min-mod limiter. As the solution proceeds, the flow can be refined by adding more grids in regions of high flow gradients and at the same time removing extra cells around regions of low flow gradients.

4. Grid generation

The in house developed PARAS code uses the cartesian mesh. An adaptive mesh technique used for the grid generation. The nose of the vehicle has been fixed as the origin. The flow domain [2] is 50 times diameter as upstream, downstream is 100D and remaining sides are 60D for Mach number <1.0 condition. For Mach >1, upstream domain reduced to 10D, remaining sides kept same. The initial grid contained nearly 23.2 million cells and the final refined grid turned out to be between 31 to 46 million cells for various Mach numbers. In order to capture the flow features, appropriate clustering was used to make finer grid near the body. Figure 2 (a) shows the section view of 3D grid for subsonic Mach numbers. Close up view of the computational grid of the configuration is shown in Figure 2 (b). Final grid after refinement is shown in Figure 2(c). For Mach<1, upwind boundary conditions are used for inward flow and pressure for all remaining sides. For Mach>1, upwind boundary conditions are used for inward flow and shift (zero flow gradients) for all remaining surfaces.

5. Simulation details, boundary condition and convergence

Analysis of trajectory data show that the vehicle experiences maximum dynamic pressure at supersonic Mach numbers. Turbulent flow simulations carried out at Mach number 0.8 to 2.5 for 2 wire tunnel configurations (base line configuration). Based on the observation from the results various configuration options are considered for further studies. The roll angles considered for the simulations are 0 to 180^0 at an angle of attack of 4^0 at various Mach numbers. Typical C_{RM} convergence at Mach 0.8 and 1.2 is shown in Figure 3. It is observed that, the solution is converged well

6. Baseline configuration C_{RM}

Variation of C_{RM} with Mach number for φ_W of 45^0 is given in Figure 4. Even though magnitude is small, control of this rolling moment is must in the launch vehicle during the flight. In order to understand the contribution due to various components of vehicle on total C_{RM}, the variation of cumulative C_{RM} along vehicle length is plotted (Figure 5) at different Mach numbers. As expected, being axisymmetric PLF does not produce any C_{RM}. Once, the protrusions starts, vehicle starts experiencing C_{RM}. It is observed that about 80% of the total C_{RM} at any Mach number is generated from the wire tunnel. It is also observed that the variation of C_{RM} along vehicle length is almost same for all Mach numbers till 4.5D. After 4.5D, significant difference in C_{RM} is noticed. This may be because, as the free stream Mach number changes, contribution of the protrusions and other cowlings of vehicle to C_{RM} alters. The maximum C_{RM} occurs at Mach number 0.8. It is noticed that, the existing propulsive control model is not sufficient to control the vehicle at this $C_{RM.}$

7. Different concepts to reduce C_{RM}

A. Single wire tunnel concept

Subsequently, in order to reduce the rolling moment, different changes were made in the configuration. Stringers were removed in all inter-stages. RCS thruster cowlings were removed in equipment bay, and payload fairing shape also modified to ogive and one wire tunnel also removed. For this configuration (Figure 6), flow simulations have been carried out at various Mach numbers at $\alpha=4^0$. It was observed that maximum C_{RM} has come down by 22%. Above M=1.2, the variation in C_{RM} with Mach number is less (Figure 6). But still this is very high value of C_{RM} as compared to the RCS capability of vehicle especially off nominal case (with dispersion band).

B. Splitting of wire tunnel

As the length of the wire tunnel is main reason for this high values of C_{RM} (Figure 4), to reduce C_{RM} further, split wire tunnel has been introduced instead of one wire tunnel running continuously throughout the length. Wire tunnel has been split into two and three segments (Figure 7) to minimize C_{RM} value. For two segment wire tunnel configuration, wire tunnel was split at 5.5D (end on second stage) and placed 90^0 away from current wire tunnel. Simulations are carried out Mach 0.8, $\varphi=45^0$ and $\theta=4^0$. It is observed that, compared to without segmentation, two segment wire tunnel reduces the C_{RM} significantly. Cumulative rolling moment coefficient plot for different segmented WT configurations are shown in Figure 8. It is observed that, 2 segment wire tunnel reduces the C_{RM}, but not to a very low value. To reduce C_{RM} further, wire tunnel was split into 3 segments (by observing the C_{RM} data of 2 wire tunnel configuration, wire tunnel split into one more segment so that C_{RM} becoming zero). This reduces the C_{RM} to near zero. For 3 segment wire tunnel configuration, wire tunnel was split at 5.5D (and placed 90^0 away from current wire tunnel) and 11.25D length (placed back in same plane). This split wire tunnel concept is to reduce C_{RM}~0, worked for 45^0 roll angle at M=0.80. For other roll angles and Mach numbers it may produce slight C_{RM}. This also can be avoided by making wire tunnel in spiral shape i.e., wounding circumferentially. But implementation of this wire tunnels are difficult in the flight configuration. So, this option is ruled out.

C. 4-Wire tunnel concept

Earlier analysis of flow field data show that, the reason of C_{RM} generation is due to the asymmetric pressure distribution due to presence of protrusions and wire tunnels. To further reduce the C_{RM} in the flight, 4 wire tunnels (3 dummy wire tunnels placed each at 90^0 apart) is proposed to mount on launch vehicle instead of 1 wire tunnel (Figure 9). CFD simulations are carried out at various Mach numbers. As maximum C_{RM} occurs at 22.5^0 interval for these kinds of configurations, flow simulations are carried out at roll angle of22.5^0. It is observed that 4 wire tunnel configuration reduces the C_{RM} by 70-80% as compared to 1 wire tunnel configuration across Mach number range as shown in Figure 10. In addition, C_{RM} has become almost Mach number independent. But, with dispersion, the available RCS is not enough to control this rolling moment.

8. Aerodynamic analysis of CRM for 1, 2, 3 and 4 wire tunnel geometry

Earlier analysis shows that increasing number of wire tunnel to four, vehicle faces the least C_{RM} and 2 WT configuration has the highest. But in all cases, the C_{RM} is generated in presence of cowling, protrusions and wire tunnels. To understand the C_{RM}behavior in presence of wire tunnels alone, clean cone (20^0) cylinder (dia. D) geometry with 1 wire tunnel (Figure 11), 2 wire tunnels (180^0 apart), 3 wire tunnels (120^0 apart) and 4 wire tunnels (90^0 apart) has been considered for study. Typical sectional view of body with 1, 2, 3 and 4 wire tunnels and their position with flow direction are given in Figure 12. Simulation matrix (Table 1) is decided such a way that for all roll angles ($\leq 360^0$), C_{RM} data can be computed based on vehicle symmetry. Variation of C_{RM} for 1, 2, 3 and 4 wire tunnel configurations at M=1.2 and $\theta=4^0$ is given in Figure 13. It is observed that, as the number of wire tunnel increases, peak magnitude of C_{RM} decreases. Out 4 configurations, configuration with 4 wire tunnel gives the least C_{RM} at various roll angles as expected.

To understand further, C_{RM} variation with roll angle for each wire tunnel of 3 WT and 4 WT configuration is estimated and plotted in Figure 14 and Figure 15 respectively. It is observed that all wire tunnels does not contribute same way to C_{RM}. For 3 WT configuration, as the roll angle increases, the wire tunnel which is 240^0 away comes under leeward side of the flow. Hence, it experiences lesser C_{RM} as compared to 0^0 and 120^0 WT.

For 4 WT configuration, it is observed that WT which is 0^0 and 180^0 generator does not contribute any C_{RM} at 0^0 roll angle, whereas 90^0 and 270^0 generator WT generate maximum and are of almost same magnitude but opposite in nature. This is as per expectation. With the increase of vehicle roll angle, the contribution of 0^0 WT increases and 180^0& 270^0 WT decreases. The change of other WT is less. At 45^0roll, the contribution of 0^0 and 90^0 WT is same but opposite in magnitude. Similar observation is seen for 180^0 and 270^0 WT also. As a result, net C_{RM} is 0.

Comparison of cumulative C_{RM} for 1, 2, 3 and 4 WT configuration at M=1.2 and $\varphi=30^0$ is shown in Figure 16. It is clearly observed that, at a given roll angle (30^0), 4 WT configuration experiences the least C_{RM} as compared to 3WT, 2WT and 1WT configuration. C_P palette at X=10D for 1, 2, 3 and 4WT configuration at $\varphi=30^0$ shows in Figure 17. From Cp palette, it is observed that, flow over 0^0 WT is similar for all 4 configurations. Hence, C_{RM} for 0^0 WT for all 4 configurations is same for 30^0 roll angles (Figure 18).

Variation of C_{RM} for configuration with 1, 2, 3 and 4 wire tunnel at M=1.6 and $\theta=4^0$ is given in Figure 19. Here also, configuration with 4 WT experiences, less C_{RM} compared to 2 and 3 WT configuration. At Mach number 1.6, the difference in C_{RM} between 3 and 4 WT configuration is less compared to M=1.2.

9. Conclusions

CFD simulations have been carried out over launch vehicle configuration with various wire tunnel options at various Mach numbers to control C_{RM} generation. It is noticed that, reshaping of wire tunnel and protrusions reduces the$C_{RM.}$ Though split wire tunnel configuration reduces C_{RM} at some roll angles, its implementation in the flight is difficult. Compared to 1 and 2 wire tunnels, 4 wire tunnel configuration reduces C_{RM} significantly. CFD simulations over clean cone cylinder configuration with 1, 2, 3 and 4 wire tunnelshavebeencarriedout at Machnumber1.2and1.6atvariousrollanglesandat $\theta=4^0$. It is clearly understood why, compared to configurations with 1, 2 and 3 wire tunnels, 4 wire tunnel configuration experiences the least $C_{RM.}$

10. Acknowledgement

Authors are thankful to Sri. Harichand for his support during simulation work. Authors thankful to Shri. T Sivamurugan, Deputy Project Director, Test Vehicle Project for kindly agreeing to review the paper and for the valuable suggestions.

11. Reference

[1.] Harichand M V., "Acceleration of an Adaptive Cartesian Mesh CFD Solver in the Current Generation Processor Architectures", 25th International conference on High Performance Computing (HIPC-2018), Bangalore.

[2.] J Sreenivasulu, Sundeep Epuri and Dr. Patil M M., “Estimation of Surface and Base Pressure Coefficient over Launch Vehicle, with Reverse Flow Nozzles using CFD", 17th Aesi CFD Symposium, August 11-12, 2015, Bangalore, India.

Table 1: Simulation matrix for cone cylinder with various wire tunnel geometry configuration

M	Roll angle (deg)			
	1 WT	2 WT	3 WT	4 WT
1.2 and 1.6	0, 15, 30, 45, 60, 70, 80, 90, 120, 150 and 180	0, 15, 30, 45, 60, 70, 80 and 90	0, 10, 20, 30, 45 and 60	0, 10, 20, 30 and 45

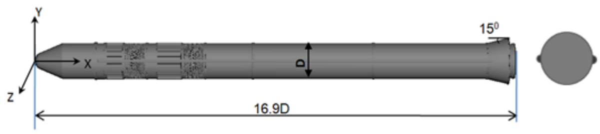

Figure 1: Launch vehicle configuration with wire tunnels

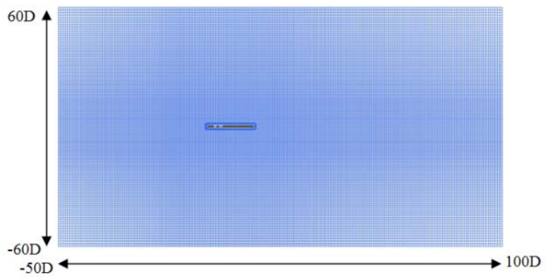

Figure 2(a): Initial grid over the geometry along with simulation domain

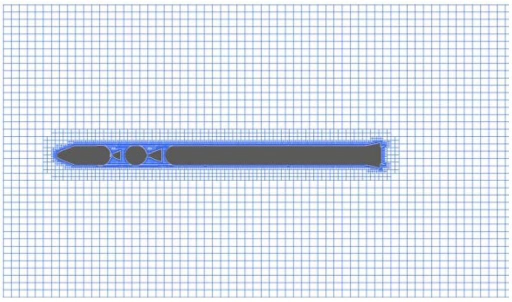

Figure 2(b): Close up view of initial grid

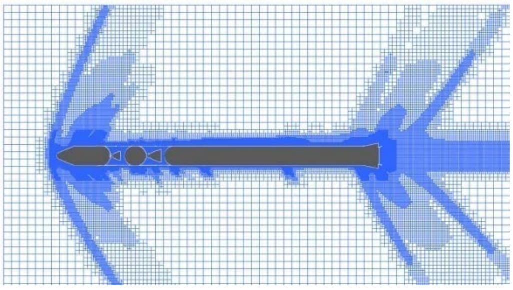

Figure 2(c): Grid after refinement

Figure 2: Grid details and Domain

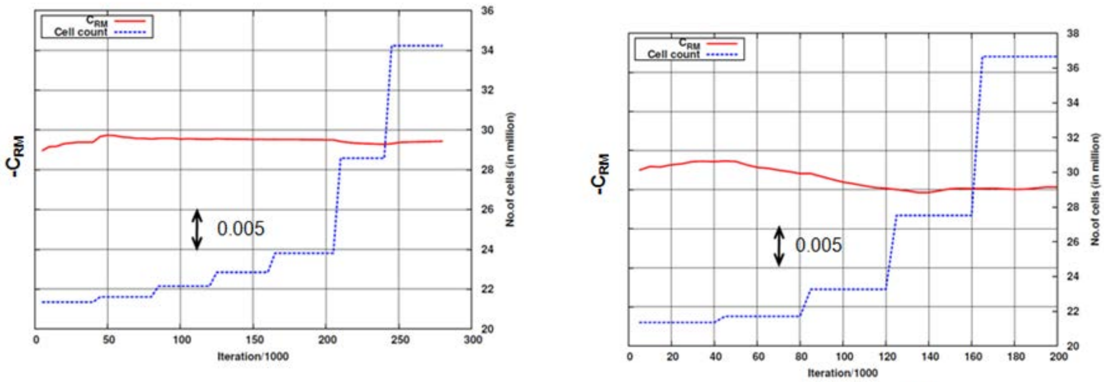

(a) M=0.8 (b) M=1.2

Figure 3: C_{RM} convergence at Mach 0.8 and 1.2 at $\varphi_W=45^0$ and □$=4^0$

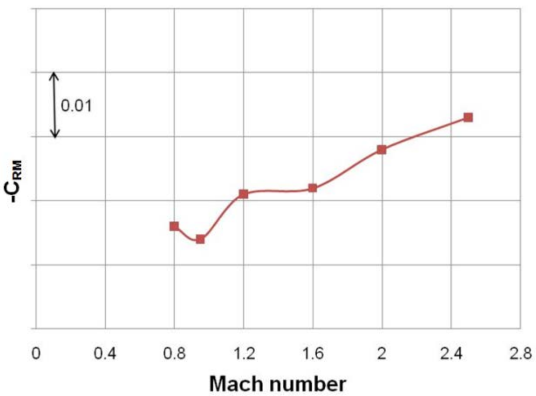

Figure 4: Variation of C_{RM} for two wire tunnel configuration at $\varphi_W=45^0$

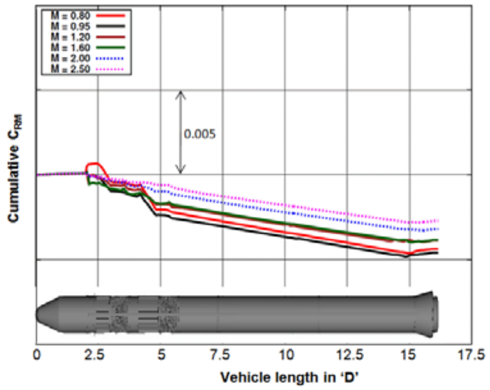

Figure 5: Variation of C_{RM} along the vehicle length of the launch vehicle configuration

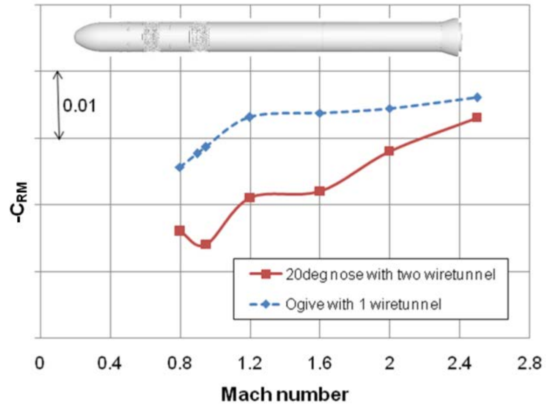

Figure 6: Variation of C_{RM} for two wire tunnel and one wire tunnel configuration

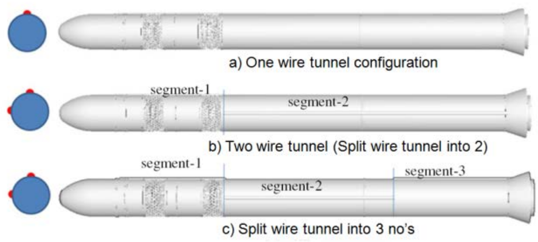

Figure 7: Different wire tunnel configurations

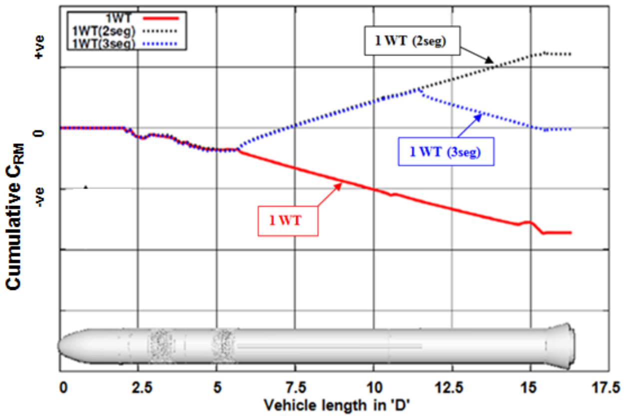

Figure 8: Variation of cumulative rolling moment for various wire tunnels at M=0.8

Figure 9: Configuration with 4 wire tunnels (placed 90^0 apart)

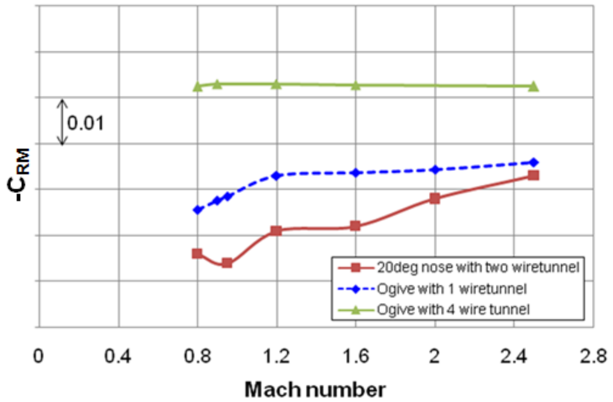

Figure 10: Comparison of C_{RM} for configurations with 1, 2 and 4 wire tunnels

Figure 11: Cone cylinder geometry with 1 wire tunnel

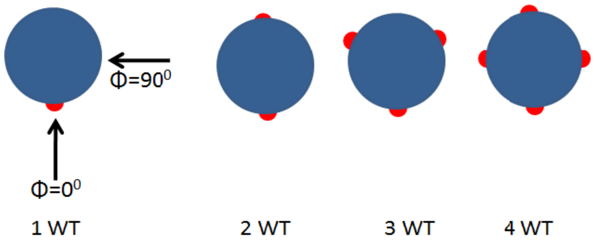

Figure 12: Typical section view of 1, 2, 3 and 4 wire tunnel geometries

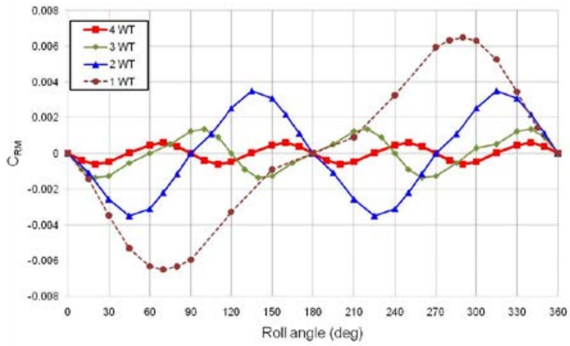

Figure 13: Variation of C_{RM} for configuration with 1/2/3 and 4 wire tunnels at M=1.2 and $\theta=4^0$

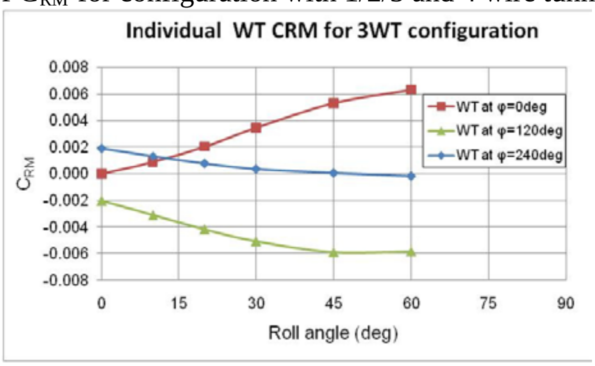

Figure 14: C_{RM} variation with roll angle for individual wire tunnel of 3 WT configuration at M=1.20

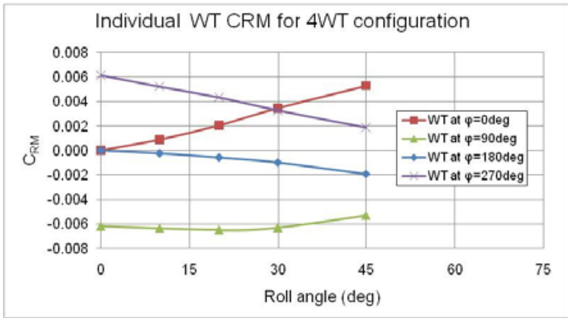

Figure 15: C_{RM} variation with roll angle for individual wire tunnel of 4 WT configurations at M=1.20

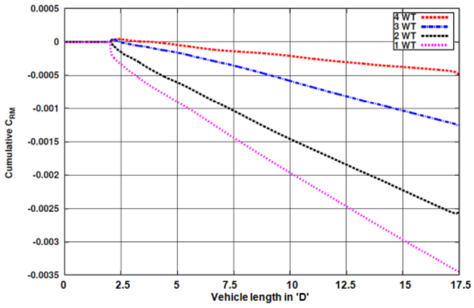

Figure 16: C_{RM} variation with roll for individual wire tunnel of 4 WT configuration at M=1.2

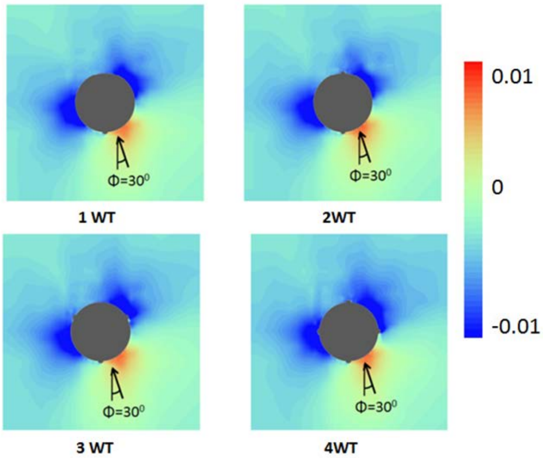

Figure 17: C_P palette at X/D=10 for 1, 2, 3 and 4 WT configuration at Mach 1.2, $\phi=30^0$ and $\theta=4^0$

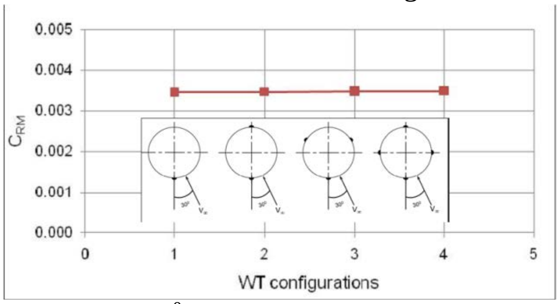

Figure 18: C_{RM} generated by 0^0 WT for 1, 2, 3 and 4WT configuration at $\varphi=30^0$

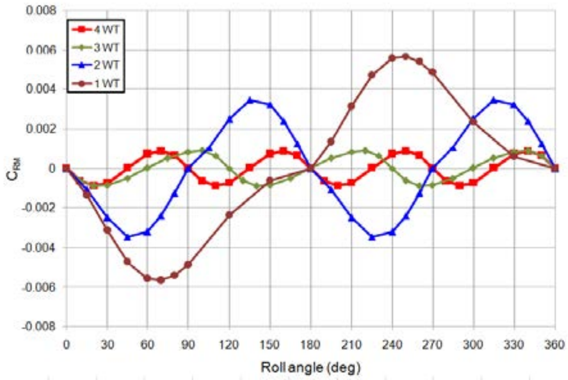

Figure 19: Variation of CRM for configuration with 1/2/3 and 4 wire tunnel at M=1.6 and =40

Computation on Effect of Retro and Ullage Plumes During Launch Vehicle Stage Separation

Ankur Nagpal
Aero Combustion Modeling Division
Vikram Sarabhai Space Centre
Thiruvananthapuram
ankur_nagpal@vssc.gov.in

Amit Kumar Singh
Aero Combustion Modeling Division
Vikram Sarabhai Space Centre
Thiruvananthapuram

Harichand M V
Aero Combustion Modeling Division
Vikram Sarabhai Space Centre
Thiruvananthapuram

G. Vidya
Aero Combustion Modeling Division
Vikram Sarabhai Space Centre
Thiruvananthapuram
g_vidya@vssc.gov.in

M.M. Patil
Aerodynamics Design and Synthesis Group
Vikram Sarabhai Space Centre
Thiruvananthapuram

V. Ashok
Aero Entity
Vikram Sarabhai Space Centre
Thiruvananthapuram

***Abstract*– A typical launch vehicle stage separation is usually assisted by a number of small rockets considering various mission requirements. Resulting aerothermal environment, due to multiple plumes and their interaction with freestream, is a strong function of separation altitude. Detailed CFD analysis is carried out during first stage separation of a typical satellite launch vehicle. The flow field resulting due to four ullage and eight retro rocket plumes at two typical altitude values 55km and 70km is analyzed in detail with emphasis on gap region between separated bodies. Distinct differences are observed in the external flow field at two altitudes and interestingly the flow field inside the gap region is not affected strongly due to altitude.**

Keywords – Retro jet, Ullage jet, pressure ratio, plume interaction, stage separation

1. Introduction

The stage separation process of a launch vehicle is typically assisted by several rocket motors. The sizing of these motors is governed by separation requirements which in turn depend on propulsion system of separated and ongoing stage, configuration of separation interfaces, pull-out requirements and control availability. Ullage rockets are used for the ongoing liquid rocket stage mainly to provide and maintain positive acceleration till man engine thrust build-up occurs. Retro rockets are used to decelerate the separated stage thereby aiding in collision free separation considering fast pull-out requirements [1], [2]. The accurate prediction of aerothermal environment, during stage separation due to multiple plumes at typical separation altitude, is essential for predicting thermal behaviour of housed components. The interaction between freestream-jets flow fieldand jet-jet flow field can lead to complex flow dynamics, hence necessitating detailed analysis. The parameters influencing these types of complex flows are investigated by Klopfer et al [3].

In this study, numerical computations are carried out for a launch vehicle 1st stage separation of a typical satellite launch vehicle with retro and ullage plumes. Separation altitudes studied are 55km and 70km and details of conditions are given in subsequent sections. Figure 1 shows the launch vehicle configuration being studied, representing stages separated by 0.32D, where D is the diameter.

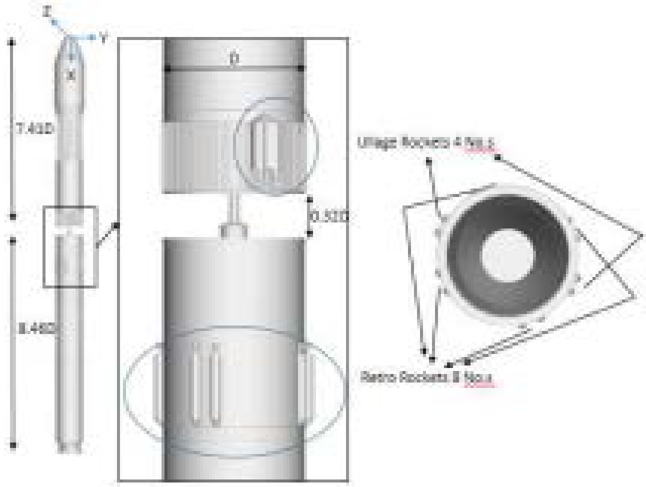

Figure 1: Launch Vehicle configuration with separated stage, retro, ullage rocket

2. Computational Details

Navier Stokes simulations are carried out using in house developed code PARAS 3D [4]. The tool usage has been established for various types of flows including multiple jets for launch vehicle applications. Reynolds Averaged Navier-Stokes (RANS) equations are solved using k-ε turbulence closure model with modified wall function. Inviscid fluxes at the cell interface are computed with an approximate Riemann solver and local time stepping based time marching approach is employed. Four-level multi-grid is used for faster convergence. Flow gradient-based grid refinement and unrefinement is carried out at fixed iteration intervals. Multi-species version with three species is used for the present work. The software runs on a Linux cluster with MPI for parallel computing.

For 55km altitude simulation, the domain used is 32.1D in axial direction and 21.4D in lateral directions. The initial mesh is 45.1 million cells and with solution based adaptive refinement, the cell count goes to 72.9 million cells after 3 refinements. For 70km altitude case, based on the upstream travel of the shock, the domain was increased to 89.3D axially and 35.7D in lateral directions. For this case, the initial mesh is 52 million cells and the final mesh is 103 million cells.

The final mesh is shown in Figure 2 and the solution-based refinement is limited to 2.8D distance from the body in all directions. The run conditions corresponding to a typical trajectory are 55km altitude and Mach number 7.54 corresponding to jet pressure ratio (Exit pressure to free stream pressure ratio) 6615 for retro rockets and 2516 for ullage rockets as tabulated in Table 1. Simulations are also carried out for another typical trajectory i.e. 70km altitude, Mach 6.59 corresponding to jet pressure ratio 59062 for retro rockets and 22468 for ullage rockets. The effect of altitude variation is studied for jet and free-stream flow interaction. All simulations have been carried out for angle of attack 0˚ and angle of side slip 0˚.

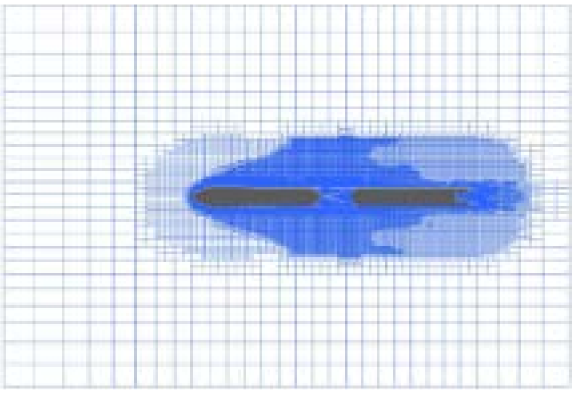

Figure 2: Final computational mesh for 55km simulation

Table 1: Simulation conditions at separation instant

Altitude (km)	Mach No.	Jet Pressure Ratio	
		Retro	Ullage
55	7.54	6615	2516
70	6.59	59062	22468

3. Results and Discussions

Figure 3 shows the Mach contour in z=0 plane for retro + ullage firing corresponding to 55km altitude conditions. In Figure 3(a), nose cone oblique shock pattern is altered by retro jet effect. Figure 3(b) shows a zoomed view of Mach contour in the region where bodies are separated. Jet boundary and jet shock are clearly visible near the body. The highly underexpanded jet interacts with incoming hypersonic flow [5] resulting in the shock pattern shown. It is observed that a low speed re-circulating flow field inside the gap exists.

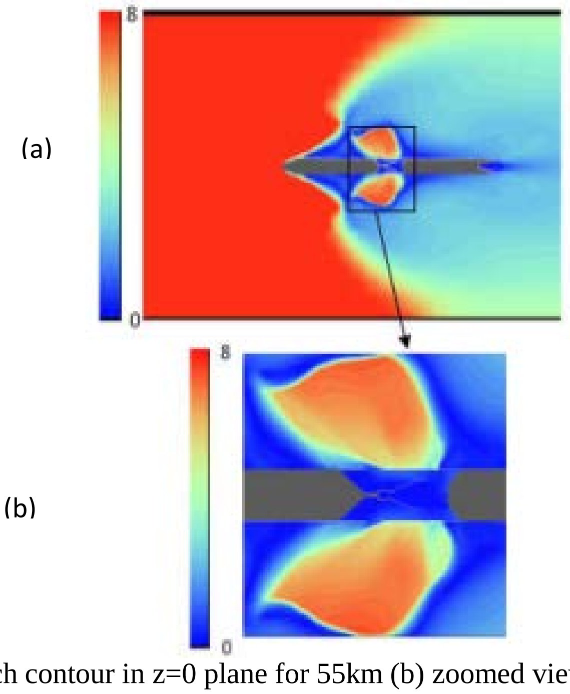

Figure 3: (a) Mach contour in z=0 plane for 55km (b) zoomed view near the gap region

The extent of flow field with pure retro jet gas can be seen in Figure 4. The flow field upstream of nosecone shock is pure air and within the retro jet boundary is pure retro jet gas. The upstream influence caused by retro jets is a strong function of jet pressure ratio.

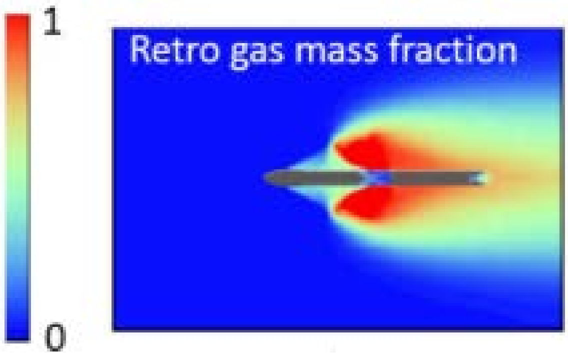

Figure 4: Retro gas species mass fraction in z=0 plane for 55km

Figure 5 shows retro and ullage mass fraction in the zoomed view showing species in the gap region. Interestingly, the ullage gas enters the gap region despite higher pressure ratio for the retro jets. The reason behind this is the relative placement of the retro and ullage nozzles and their complex interaction. It can be seen in Figure 1, that the ullage rockets are placed very near to the gap developed due to separation.

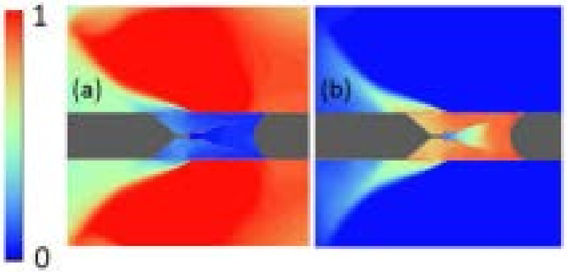

Figure 5: Species mass fraction distribution in the gap region at 55km altitude (a) retro gas (b) ullage gas

Figure 6 shows the temperature contour in the gap region for 55km. Stagnation temperature for the solid rockets is in excess of 3500K.

The temperature of recirculating gas inside the gap is close to stagnation temperature of ullage rocket gas as shown. Also, the post shock free-stream temperature is higher than jet static temperature.

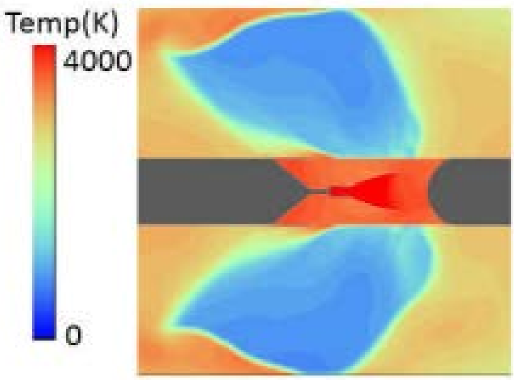

Figure 6: Temperature contour in the gap region at 55km

Figure 7(a) shows the Mach contour in z=0 plane for retro + ullage firing corresponding to 70km conditions. The nose cone shock pattern is altered by retro jet effect. In this case, due to much higher-pressure ratios, the nosecone shock is pushed upstream of the nose cone and results in an upstream normal shock. Figure 7(b) shows the Mach contour in zoomed view of gap region. Despite external flow field being very different from that at 55km, the internal flow field is similar with low speed flow. The flow field upstream of nosecone shock is pure air and within the retro jet boundary is pure retro jet gas.

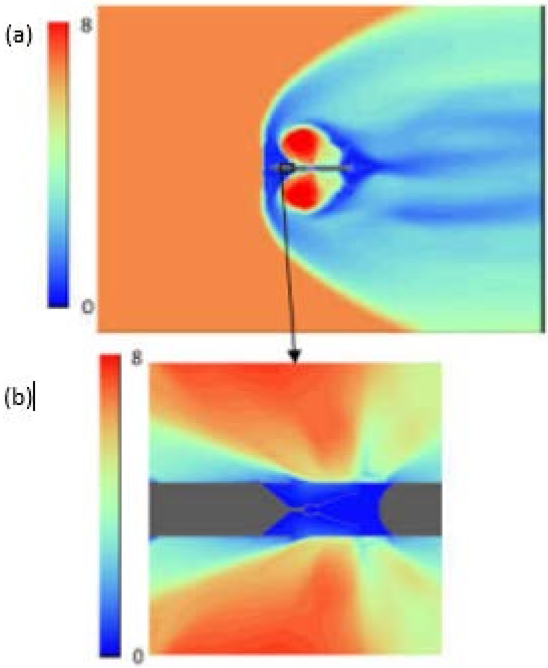

Figure 7(a) Mach palette in z=0 plane for 70km (b) zoomed view near the gap region

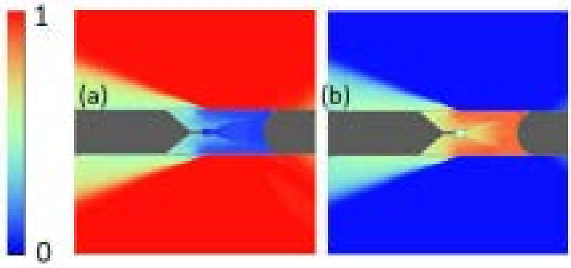

Figure 8 Species mass fraction contour in the gap region at 70km (a) Retro gas (b) Ullage gas.

Figure 8 shows the species mass fraction contour in the gap region at 70 km. Here again, interestingly the gap region is filled with ullage gas due to the same reasons as explained earlier. Figure 9 shows the temperature contour in the gap region for 70km. Higher temperature is observed for the recirculating gas inside the gap. In this case, due to higher pressure ratio, the jet boundaries are extended as compared to 55km. The relatively hotter freestream post shock flow is observed outside jet boundaries.

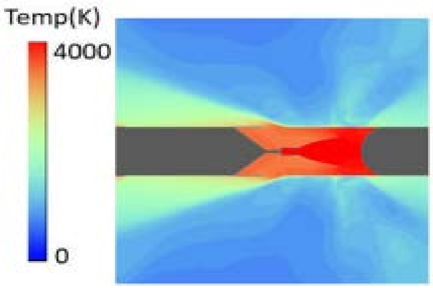

Figure 9: Temperature contour in the gap region at 70km

4. Conclusions

Flow field analysis has been carried out during first stage separation process of a typical satellite launch vehicle at two typical altitude values 55km and 70km. The retro jets interact with free-stream and alter the nose cone shock shape. The plume-freestream interaction is found to be strong function of the pressure ratio. Flow field inside the gap between separated stages has been studied for the aerothermal environment on housed components. Interestingly, ullage gas enters the gap region at both altitude conditions despite having lower jet pressure ratio as compared to retro jets. Low speed recirculating flow has been observed in the gap region with temperature nearing stagnation temperature of ullage rockets.

5. Acknowledgement

Authors acknowledge the experience shared by Shri Babu C, HSFC/ISRO in carrying out similar simulations earlier. Authors also thank Shri Sowmianarayanan L, STS/VSSC/ISRO for the critical review of this paper.

6. Reference

[1] B. N. Rao, D. Jeyakumar, K. K. Biswas, S. Swaminathan, E. Janardhana, “Rigid body separation dynamics for space launch vehicles”, The Aeronautical Journal, Vol 110, Issue 1107.

[2] Sivasakthi R, N Radha, C Ravikumar, Abhay Kumar, “Separation Dynamics Analysis of a Spent Solid Stage during its Thrust Tail-off”, ARMS 2016, Thiruvananthapuram.

[3] Goetz h. Klopfer, James E. Kless, Henry C. Lee, “Validation of overflow for computing plume effects during te Ares I stage separation process”, 49th AIAA Aerospace Sciences Meeting including the New Horizons Forum and Aerospace Exposition, 4-7 January 2011, Orlando, Florida.

[4] Harichand M V., "Acceleration of an Adaptive Cartesian Mesh CFD Solver in the Current Generation Processor Architectures", 25th International conference on High

[5] Sanjoy Kumar Saha, G Vidya, “Effect of retro jet firing on the aerodynamics of a wing body configuration at instant of separation”, International heat and mass transfer conference (IHMTC 2017), December 2017, Hyderabad.

Release Basket Computation for Air to Surface Guided Weapon

Shweta Dadarya
Armament Research and Development Establishment
DRDO
Pune
sdadarya@arde.drdo.in

Richa R Jaitly
Armament Research and Development Establishment
DRDO
Pune

Deepak Maurya
Armament Research and Development Establishment
DRDO
Pune

Kishore B Jadhav
Armament Research and Development Establishment
DRDO
Pune

Abstract-- **The purpose of evaluating the release basket in real time is to provide mission critical decision of when to release the weapon to the pilot for the designated target. A Release Basket defines the predicted maximum and minimum engagement ranges as well as the no escape zone for the target. These values are calculated continuously in real time during flight with respect to a tracked target while the weapon is still attached to aircraft. The Release Basket information is displayed to the pilot via a heads up display (HUD), allowing the pilot to make informed decisions when launching a guided weapon. A guided aerial weapon can be launched for against any target falling within its range bracket. In the present work, the algorithm design, its mapping to Human Machine Interface (HMI) and its implementation in on board computer is focused on. The algorithm runs on the On Board Computer of the weapon and takes the current target location and orientation, aircraft location, orientation and its speed into account when determining the range capability. The designed Release Basket Algorithm (RBA) is loaded in the weapon itself making it platform independent. Prior to launching weapon, only RBA algorithm runs in the OBC and subsequent to launch only Guidance and Control algorithm runs on the OBC, thus time multiplexing the available on board computational resource.**

Keywords – RBA, DLZ, LAR, Aerial Weapon, SixDof, WEZ

Nomenclature

DLZ	Dynamic Launch Zone
FCIEU	Flight Control & Interface Electronics
GnCalgo	Guidance and Control Algorithm
GPS	Global Positioning System
ICD	Interface Control Document
HMI	Human Machine Interface
INS	Inertial Navigation System
LAR	Launch Acceptability Region
RBA	Release Basket Algorithm
SixDOF	Six Degree of Freedom
WEZ	Weapon Engagement Zone

1. Introduction

A Release Basket/ Dynamic Launch Zone (DLZ) defines the predicted maximum and minimum engagement ranges as well as the no escape zone for the target to be engaged from an aircraft launched weapon. These values are computed continuously in real time during flight with respect to a designated target while the weapon is still attached to aircraft. The Release Basket information is displayed to the pilot via a heads up display (HUD), allowing the pilot to make informed decisions when launching weapon. The algorithm runs on the weapon OBC (On Board Computer) and takes the current target location and orientation, aircraft location, orientation and its speed into account when determining the range capability.

The important outcome parameters include weapon range, time of flight, time to enter launch basket, time left in the basket depending on the launch condition (altitude, mach, pitch, and heading) of the aircraft.

Release Basket calculation can be done in two ways for notional weapon models.

- The first method performs continuous real time simulation of the approximated weapon model [1].
- The second and more widely used method executes simulated trajectories offline and then creates a lookup table utilizing the pre-generated truth data. A form of interpolation is then used in real time during the computation of DLZ algorithm [1]. For more number of varying inputs artificial neural network is also used [4].

Here, second method is used with linear interpolation. In this case, release basket algorithm (RBA) is loaded in the weapon itself because, firstly, it makes the pre-launch computations independent of the aircraft where it is attached. Secondly, it doesn't load the aircraft mission computer (MC) since MC has to do extensive computations for multiple weapons attached to it. Prior to launching weapon, only DLZ algorithm runs in the OBC and subsequent to launch only guidance and control algorithm runs on the OBC, thus time multiplexing the OBC computational resource.

2. Release Basket Engagement Scenario

Case 1: Aircraft carrying weapon is approaching the release basket: In this case the parameters of interest are current range of aircraft from the designated target and also time to go i.e. time to enter the basket. Fig 1 depicts the approaching scenario and the respective release basket in terms of its minimum and maximum achievable range for given launch condition.

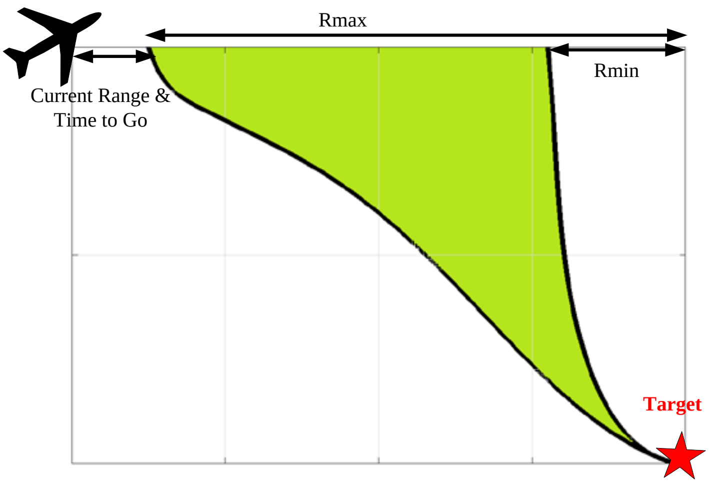

Fig 1: Aircraft carrying weapon is approaching the basket

Case 2: Aircraft carrying weapon is inside the release basket: In this case the parameters of interest are current range of aircraft from the designated target, time left in the basket and time of flight (if weapon is dropped at the given instant). Fig 2 depicts the scenario and the respective release basket in terms of its minimum and maximum achievable range for given launch condition.

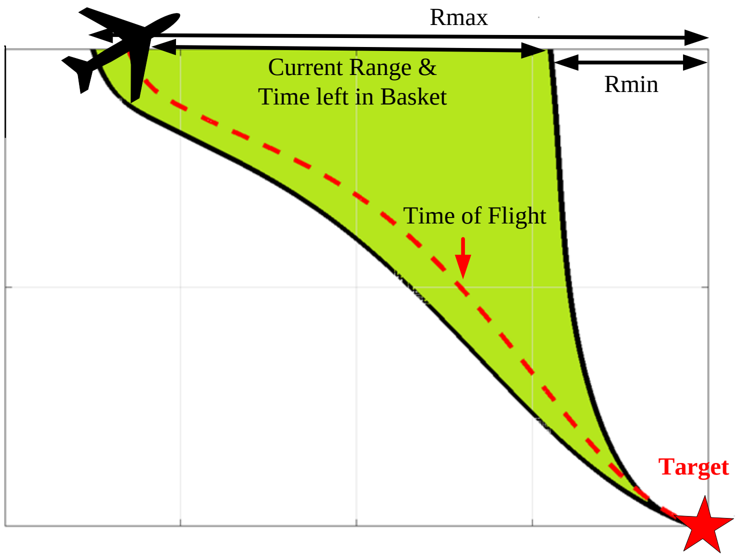

Fig 2: Aircraft carrying weapon is inside the basket

Case 3: Aircraft carrying weapon is ahead of the release basket: In this case the parameters of interest are current range of aircraft from the designated target. Time to go/time left in the basket and time of flight becomes invalid, so need not be displayed. Fig 3 depicts the scenario and the respective release basket in terms of its minimum and maximum achievable range for given launch condition.

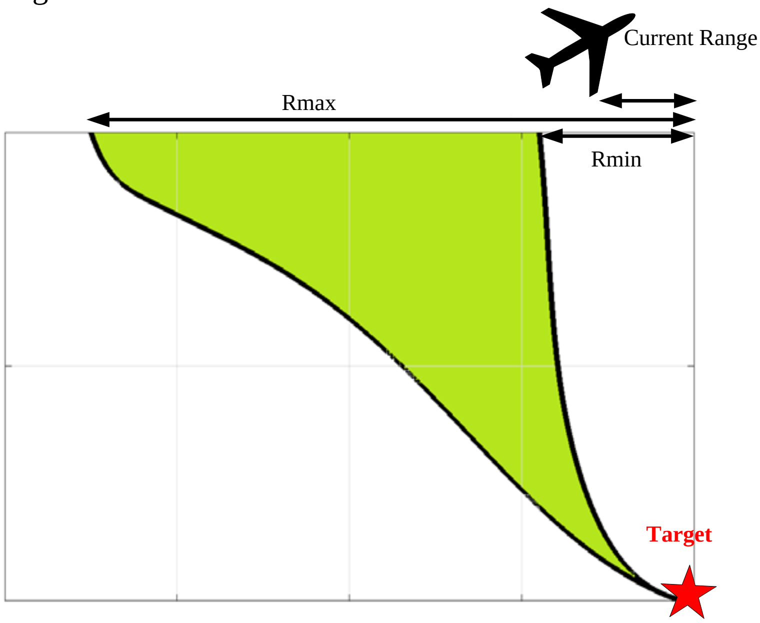

Fig 3: Aircraft carrying weapon is ahead of release basket

3. Display in Aircraft

Human Machine Interface (HMI) Display inside the cockpit of the aircraft is employed for display of release basket to the pilot. Typically, two types of HMI Display are used in aircraft:

- **Vertical Situation Display (VSD):** Refer Fig 4 for symbolic representation of VSD page.

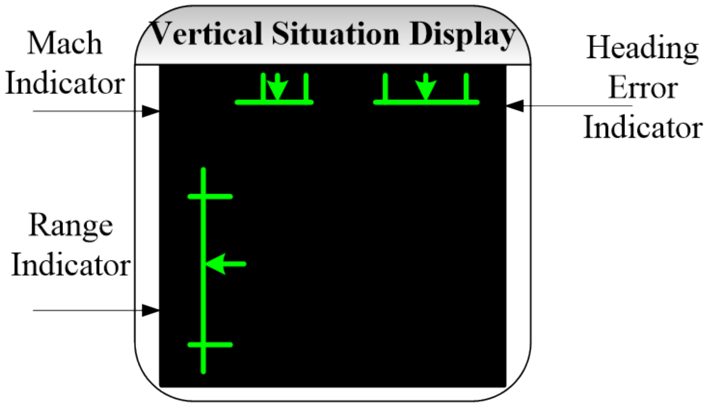

Fig 4: Symbolic representation of VSD

- **Tactical Situation Display (TSD):**

TSD is basically a polar plot in which the respective points and its location are specified in terms of r $\angle\theta$ as depicted in Fig 5.

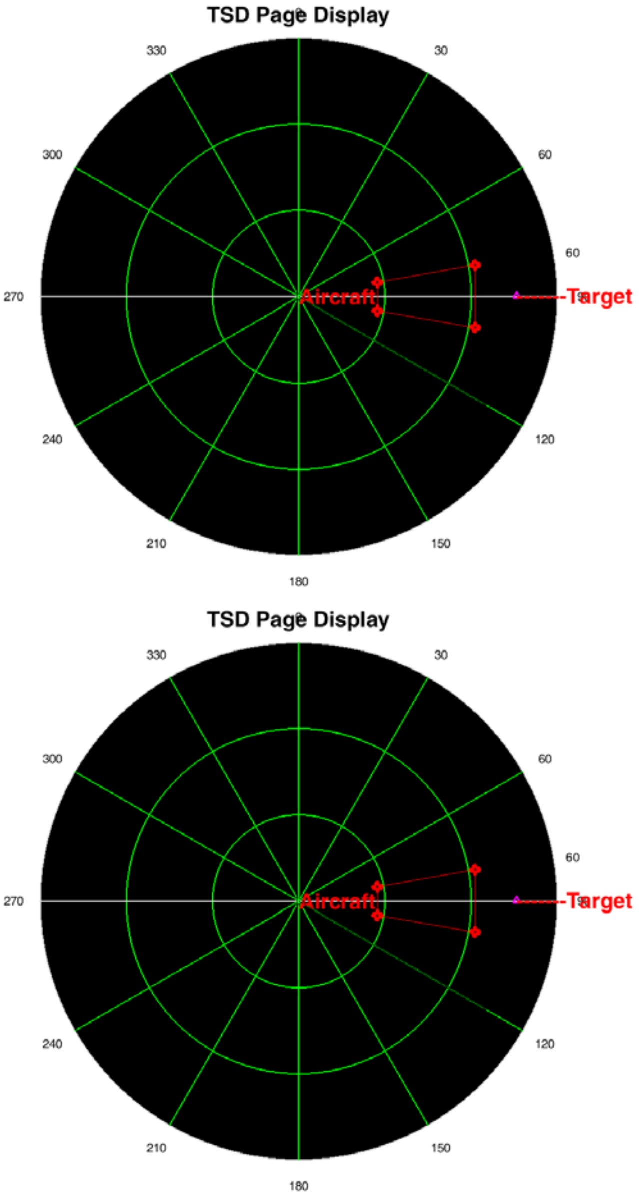

Fig 5: Symbolic Representation of TSD

4. Problem Formulation

A. Approach

The weapon range capability can be computed online or derived from a database kept on board. Here, the second approach is used i.e. the minimum and maximum range and its respective flight duration are stored on board with varying launch conditions such as launch altitude, mach no in form of lookup table. This range capability is then mapped w.r.t target and subsequently the release basket is generated in terms of feasible range and heading error. The critical parameters such as time to enter the range basket, time left in the basket once weapon enters into the basket and flight time are evaluated. The parameters depicted on the HMI display are as shown in Fig 6.

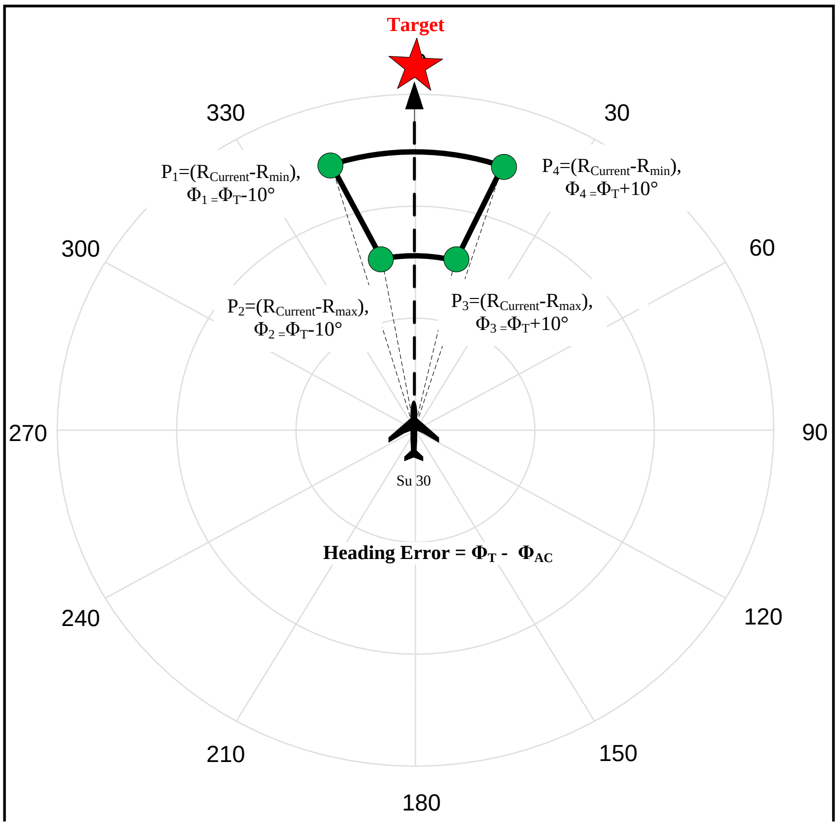

Fig 6 Release Basket Schematic on Tactical Situation Display (TSD) page

B. Model Considerations:

SixDOF was considered for the overall exercise with the following assumptions.

Assumptions made:

- The INS is error free.
- All subsystem performed nominal.
- Only Midcourse guidance is present
- Miss distance < 10m for acceptable cases.
- Lat/Long to range calculation is done using haversine formula due to unavailability of ECEF positions from Master INS to FCIEU.
- Wind is considered absent.

C. Database Generation

For present study, database is generated for **level flight** condition. The pitch, yaw and roll are limited to zero in the SixDOF and then the minimum and maximum achievable ranges are evaluated along with their corresponding flight time. The tables generated are:

(i) Minimum Range
(ii) Time of flight for minimum range
(iii) Maximum Range
(iv) Time of flight for maximum range

The above mentioned tables are 2 dimensional. Row variation is the release altitude and column variation is the release mach.Linear Interpolation is used for 2Dimensional and 1Dimensional interpolations. The release envelope for the weapon is subset of the carriage envelope of aircraft. So the minimum and maximum mach number allowed with respect to launch altitudes are also stored as lookup table on board. Bunch of successful trajectories for maximum and minimum ranges are as shown in the Fig 7 and Fig 8.

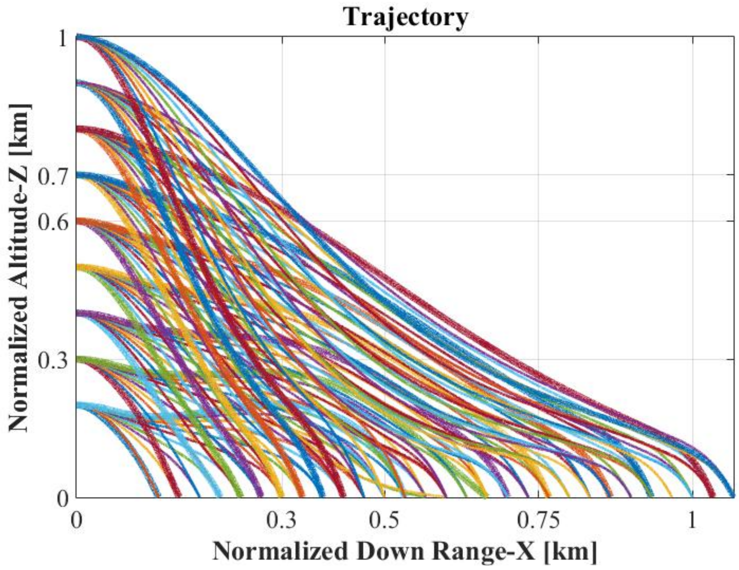

Fig 7 Maximum Range for all height and mach combination

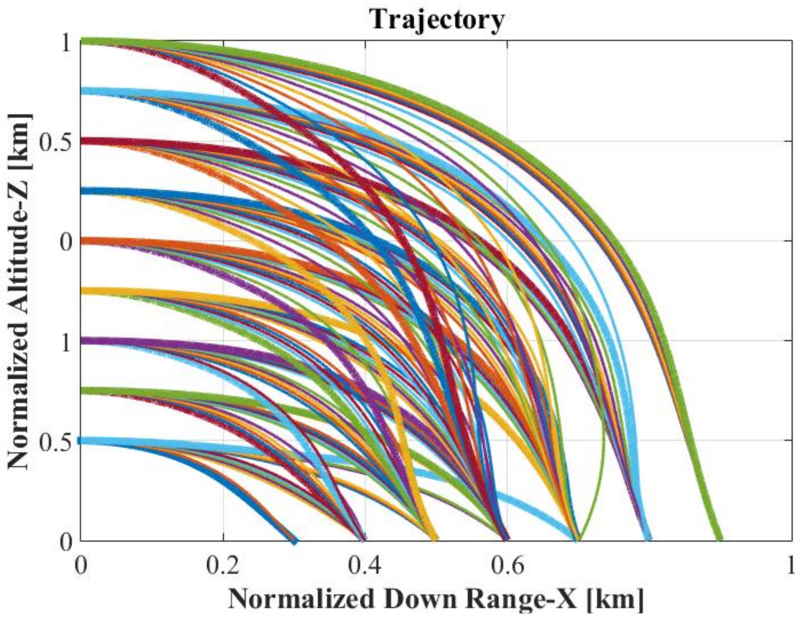

Fig 8 Minimum Range for all height and mach combination

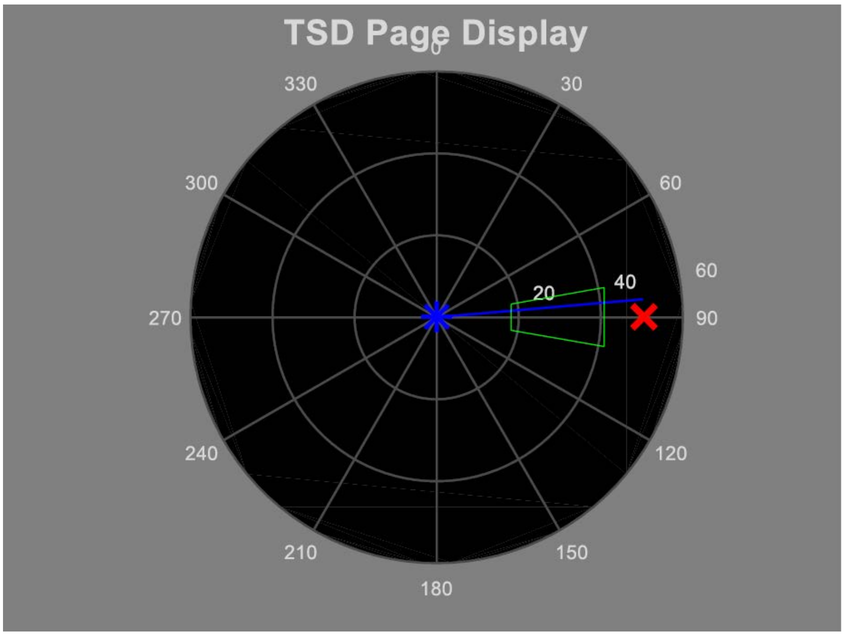

Fig 9 Typical case for No Launch Permit Condition

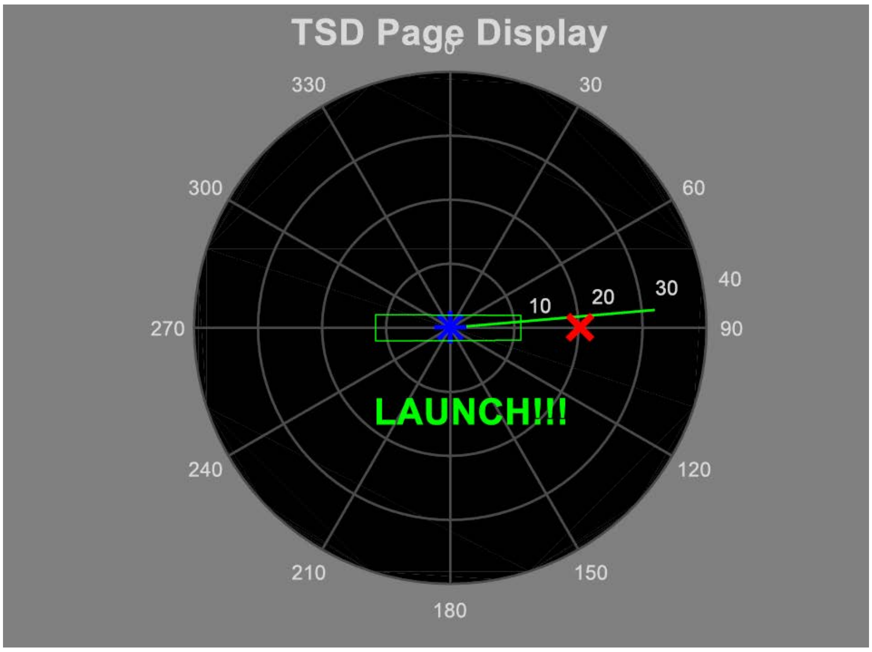

Fig 10 Typical case for Launch Permit Condition

5. Implementation Aspects:

A. Parameters required as per Interface Control Document

The input parameters to the RBA which runs on FCIEU are derived from Master INS placed in the aircraft and the computed output parameters are sent to Mission Computer (MC) of aircraft. MC then presents the values to HMI in the cockpit for display. All this communication is through 1553B. Fig 11represents the input and output parameters.

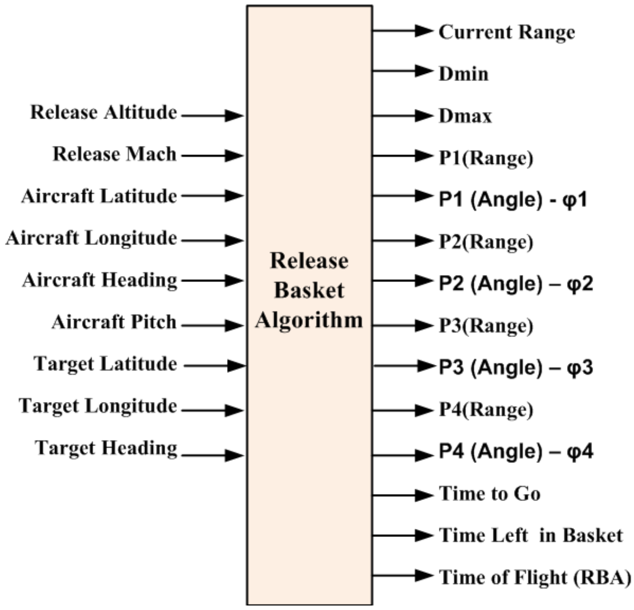

Fig 11 input and output parameters as per Interface control document

B. Validity Condition for Release Basket

The valid condition for release basket is mainly derived from the release envelope of aerial weapon. The minimum and maximum acceptable value of various parameters for valid release basket are applied on Release Altitude, Release Mach, Heading Error, Current Range, P1,P2, P3, P4 range, Dmax, Dmin, Impact Angle, Impact Velocity.

C. Implementation

Release Basket is run in real time application to validate the algorithm performance. In this case, the range basket was continuously updated based on varying launch conditions for feasible regions. OBC has MIL 1553B interface to communicate with Aircraft where it is configured in RT mode to exchange RBA data. This RBA data includes Aircraft Navigation data i.e LLA info, euler angles, velocities, Mach no etc and target LLA .The OBC is computing max and min permissible ranges, time of flight and other required parameters at 80ms using the stored lookup tables in OBC for aircraft current height and mach no along with valid pitch, roll and yaw limits of aircraft for designed weapon separation. These validity limits assist pilot to maintain required aircraft orientation before weapon release once the aircraft is in basket and weapon is ready to fire.

6. Conclusion

This Paper brought out the simplified approach to define release zone for guided weapon to be applied for stationary ground target. This design ensures time domain performance of guided aerial launched weapon at different launching conditions withacceptable accuracy of trajectory prediction in the environment where the dynamic coupling between operating condition and engagement scenario makes design more challenging within the constraint. Also, the presented implementation further simplifies the computation burden on Master Computer of Mother Aircraft and made it platform independent.

7. Acknowledgements

The authors also like to express their deep sense of gratitude to Associate Director and Director ARDE for giving motivation and opportunity to work on this problem.

8. References

[1] *George M. Siouris*, “Missile Guidance and Control Systems”, Springer, 2004, pg339-345

[2] *SR Mohan*, “Fundamentals of guided missile”, Defence Research & Development Organisation, 2016,pg

[3] *Zarchan P*, “Tactical and Strategic Missile Guidance (Sixth edition)”, American Institute of Aeronautics and Astronautics, 2013, pg 107-135.

[4] *Kun Su Yoon, Jae Hyun Park, In Gyu Kim, Kwang Su Ryu*,” New Modeling Algorithm for Improving Accuracy of Weapon Launch Acceptability Region”, *Korea Aerospace Industries, Ltd., Sacheon-City, Gyeongnam, 664-710, South Korea.*

Mechanisms in Automation & Robotics

Design of a Space-Qualified 6-DoF Anthropomorphic Robotic Arm for Half-Humanoid

Dileep Rajendran
Mechanisms and Advanced Actuators Section,
ISRO Inertial Systems Unit
ISRO
dileeprajendran90@gmail.com

Abhilash Mony
Mechanisms and Advanced Actuators Section,
ISRO Inertial Systems Unit
ISRO
abhilash.mony@gmail.com

Joji J Chaman
Mechanisms and Advanced Actuators Section,
ISRO Inertial Systems Unit
ISRO

***Abstract*—As ISRO is preparing for Gaganyaan mission, along with the development of systems needed for launching astronauts; the development of robotic systems which can support and assist them gains equal importance. From simple inspection, routine activities and easy assembly tasks, they can perform a variety of activities as demonstrated in the international Space Station (ISS). Performance of extra-vehicular activity and crew rescue if they are incapacitated and performing various higher level intelligent functions are now in the conceptual stage. Unlike conventional industrial robotic arms, a space-qualified robotic arm has to sustain and survive the severe launch vibrations prior to the start of actual on-orbit operation. Consequently, in addition to other basic functional requirements, design features like hold-downs are needed for the arm. Since the crew module returns after its mission, the arm is also planned to be recovered and reused. As a result, the arm should sustain loads at both the ascent and descent phase. It should also be capable to operate both on-ground (1-g) and on-orbit (0-g) condition as desired. A 6-DoF robotic arm- with 3-DoF intersecting shoulder joint axes, 1-DoF elbow and 2-DoF wrist with a 5 fingered end-effecter is configured. Two such arms fixed to the torso becomes part of the half-humanoid. The designed structure has low mass, high stiffness and sufficient structural safety factors to sustain launch loads. The final configuration was realized through a combination of additive manufacturing and final finish machining at critical locations. The right arm was assembled and preliminary testing is completed. The final arm characterization and testing is in progress.**

Keywords- space robotics, robotic arm, anthropomorphic arm, 6-DoF arm, humanoid arm, hold-down, electro-magnetic lock

1. Introduction

India is preparing for its human in space program. In this context along with the systems needed for launching and safely bringing back astronauts, the development of robotic systems to aid and assist them gains equal importance. These robots can perform autonomously or under supervision. ISRO is developing a half-humanoid which is proposed to be flown in the initial unmanned flight of the Gaganyaan program. The robotic system has a head, torso and two 6-DoF arms with a 5-fingered end-effecter. It also has a posture change mechanism to change the half-humanoid from the launch to the operational position.

Robotic arms are developed by various agencies across both industries and academia throughout the world. However, space qualified robotic arm requires a different design philosophy. The ability to meet all functional requirements as specified in the orbital phase after surviving launch vibrations is the most critical factor guiding the mechanical design. In addition, the ability to function after sustaining the re-entry phase environment puts additional design constraints. But it makes the system reusable for future mission, thereby reducing overall cost and increasing utilization. Another challenge in space robotics is the ability of the arm to function on ground as well as in-orbit. While the former gives the full effect of gravity on the system where as the latter demands operation under micro-gravity environment.

Thus, the design of a robotic arm for outer space applications entails many complications which are not faced for ground operation like ability to sustain launch vibration loads, lack of ability to service the robotic arm and requirement of high reliability and long life in the harsh environment of outer space. Wenfu XU et al. has studied theoretical modelling of dual robotic arms for capturing a moving target. The authors use a novel "Area Oriented Capture" algorithm to capture a non-cooperative moving target, eg: space debris [1]. Robert. O. Ambrose et al. from NASA Johnson Space center has built a humanoid with two arms having human form and scale. The authors propose a 5-DoF robotic arm with gripper for performing lower-skilled works, for assisting the astronauts. The robotic arm uses brushless dc motor with harmonic gear reduction [2]. Ravi Kiran et al. proposed a robotic arm for planetary soil collection and pick and place operations on top of a 4-wheel rover. The robotic arm is designed with 6 DoFs with a two fingered gripper and manufactured using conventional methods [3]. Chunguang Fan et al. have developed a 6-DoF robotic arm system with visual feedback which can be remotely controlled from ground for performing on-orbit maintenance operations [4].

In this paper, the configuration and design of a space qualified human-like (anthropomorphic) robotic arm is given. The functional and design requirements of the arm are given in Sec. 2. Sec. 3 explains the arm design starting from the forward kinematics based link-length selection and joint arrangement based on meeting the basic workspace requirement. This is followed by the preliminary dynamic analysis for actuator selection. The structural design of the robotic arm is explained in Sec. 4. The strength and stiffness based design covers in detail the design methodology and engineering done for surviving the launch loads and meeting the control-bandwidth requirement. The arm realization aspects are also included here. Sec. 5 concludes the paper and gives scope of future work.

2. Functional And Design Requirements

A. Functional Requirement

The functional requirements of the robotic arm was identified for three stages of the half-humanoid mission- ascent phase, orbital phase and descent phase and are listed as given below[5]:

(i) The robotic arm should be able to attain a hold-down configuration (stowed) in ascent and descent phase of the crew module so that it is able to survive the launch and re-entry vibrations
(ii) In the on-orbit phase, the arms should perform the task assigned to it within its workspace such as switch panel operations, replacement of carbon dioxide canisters, perform gestures while speaking e.t.c
(iii) The arm should be able to attain a safe mode configuration in case of exigency
(iv) The robotic arm must have human like shape with anthropomorphic proportions
(v) The arm should meet the functional requirements at both on-ground and on-orbit conditions

B. Design Requirements

The above functional requirements are translated as the following design requirements for the arm.

(i) The arm should have an electro-magnetic lock (EM lock) which can be enabled during the ascent and descent phase to hold-down the arm to increase its natural frequency
(ii) The link lengths are to be chosen such that the arm meets the planned work space requirement on-orbit
(iii) Safe mode configuration of arm to be attained using EM-lock
(iv) The joint arrangement is made similar to that of a human arm and the link design and lengths are proportional to the size of the designed torso
(v) The joint torque capability is chosen such that the arms can function both on-ground and on-orbit

C. Additional Features

In addition to the above requirements, the arm is proposed to have these additional design features:

(i) First three-joints are made intersecting for utilizing a closed form inverse kinematic solution for such configurations [7]
(ii) Light weight structure is proposed to minimize mass and inertia so that the joint actuator torques are minimized without compromising the overall stiffness
(iii) The arm structure and joint actuator bearings must sustain launch vibration and shock loads during ascent and descent phase.
(iv) First natural frequency of arm in launch configuration should be > 100 Hz so that the structure is not excited due to the severe sine input vibration from launch vehicle. This will be achieved by EM-lock based arm hold-down .
(v) The arm must have only one hold down point during launch to avoid differential loading
(vi) First natural frequency of arm in fully extended condition (least stiff configuration) should be at least 5 times more than the control bandwidth to avoid control structure interactions

3. Arm Design

The functional and design requirements of the robotic arm were discussed in Sec.II. The details of various aspects of the arm design are explained in this section. The configuration starts with the kinematic design based on the workspace requirement. This is followed by the preliminary selection of actuators based on initial torque estimates. After this, structural design and optimization is done which is followed by the EM lock design. Finally, an integrated finite element analysis with torso is done to complete the design.

A. Kinematics Based Design

The basic design of the robotic arm starts from assigning the link-lengths, assignment of number of degrees-of-freedom and joint arrangement. It was understood that a human arm has 7-DoF (degrees-of-freedom) [8-9]. In addition, a minimum of 6-DoFs are needed to reach a point in three-dimensional space [6]. In addition for a 6-DoF arm with revolute joints, if any three consecutive joints are intersecting, there exists an analytical closed form inverse kinematic solution [6-7]. Considering all these aspects, it was decided to configure an arm with 6-DoF. The joint arrangements were chosen as 3-DoF shoulder with intersecting axes, a 1-DoF elbow and a 2-DoF wrist. The link lengths are chosen so that the final configuration is able to meet the work-space requirement needed for performing the final operation. The number of degrees of freedom, joint arrangement, link lengths and shape are chosen and configured to meet these requirements.

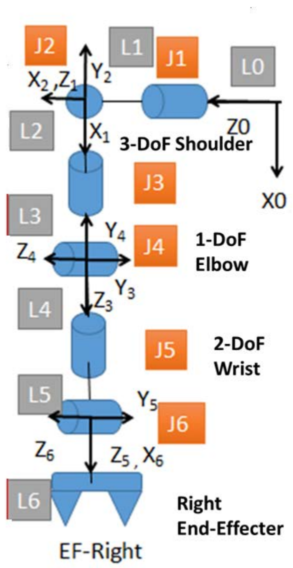

Figure.1 Kinematic arrangement of the 6-DoF with DH coordinates. Here L1 to L6 represents length and J1-J6 the joints. X0Y0 is the fixed co-ordinate on the torso

The kinematic arrangement of the 6-DoF arm assigned with modified DH parameters (for a tutorial definition for modified DH parameters, refer [6]) is shown in Fig.1. Using this, the forward kinematics of the arm can be derived. It should also be noted that the length of the end-effecter which is attached to the wrist joint is also considered in the final transformation matrix. The forward kinematics of the arm can be used to compute the work-space. In this case, the arm work-space should accommodate the switch panel on which it is planned to perform operations within the crew-module. The computed work-space of the left and the right arm with respect to the base coordinate on torso is shown in Fig.2. The projections on the y-z and x-y plane are given, confirming that the chosen link lengths meet the requirement.

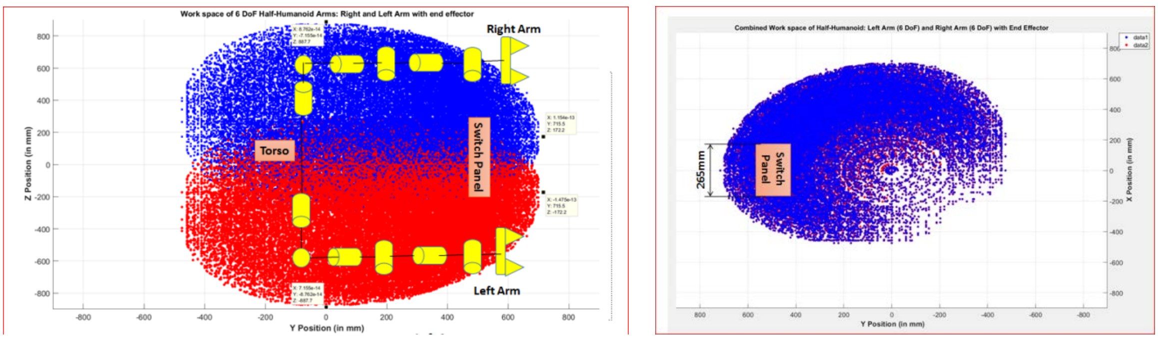

Figure.2 Work-space of the two6-DoF robotic arms computed based on forward kinematics. The switch panel is seen to be within the workspace. The top-figure shows the y-z plane and bottom figure shows projection on the x-y plane.

B. Actuator Selection and Arm Configuration

During the initial design phase, only the link lengths and joint arrangements of the arm will be known. Knowledge regarding the mass and inertia properties will be available only after the completion of structural design. Ironically, the structural design cannot be started without knowing the estimated mass of the joint actuators. This is a real conundrum while designing robotic arms. The problem is tackled using heuristics and engineering judgement rather than using conventional design methodology. It is logical to assume that the first two joints of the robotic arm (at the shoulder) will demand the largest torque (on-ground). In addition, the bearings within all the actuators should have sufficient load capability to withstand launch loads. The torque and the bearing loads decrease as we move away from the shoulder joints. In addition, the use of bulky actuators away from the shoulder will result in an enormous increase in mass and resultant inertia felt at the shoulder joints. Also, the wrist joint feels the mass and inertia of the end-effecter only. Hence this can be assigned with a low torque joint with smaller bearings.

The structural design is done based on the length and actuator mass values computed as shown earlier. It was seen through inverse dynamic analysis that, that the chosen output torque capability of the actuators are higher than the torque demanded while performing arm operations (for brevity these are not covered in this paper).

The 6-DoF robotic arm with the selected joint arrangement, link lengths and actuators is shown in Fig.3. The high torque actuators are used in the first two joints. The end-effecter, which is similar to a human arm, is also shown. In order to reduce mass and for better thermal conductivity, the material for arm structure is chosen as an aluminum alloy. Being a complicated structure, it is proposed to realize the structural elements through additive manufacturing. Hence AlSi10Mg is chosen as the type of aluminum alloy.

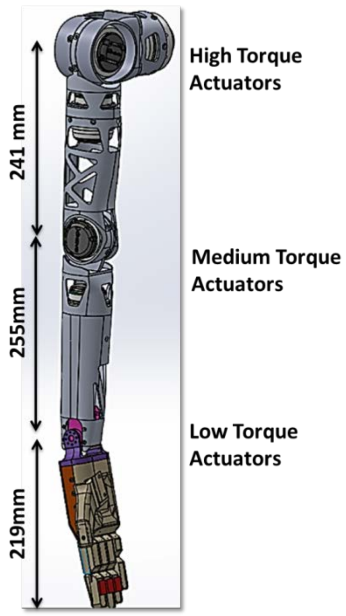

Figure.3 Configuration 6-DoF robotic arm with actuators and end-effector

The functional requirements for the arm are switch operation, carbon canister replacement and gesticulation while speaking. None of these activities are highly dynamic and time critical. Hence the arm operation is proposed to be done at a slow rate of 1-3 mm/s for the end-effector. Considering this, the angular acceleration requirement would be approximately 10/s2 and torque due to acceleration will be several orders of magnitude lower than that of the torque required for overcoming the moment due to the self-weight of the arm. An estimate of the torque due to self-weight and friction felt at each joint is computed and listed in Table 1.

Table 1: Estimated Torque Due to Self-weight and Friction

Joint Name	Estimated Torque due to self-weight and friction (N.m)	Rated Torque of the Actuator (N.m)
Joint 1	8.1	12
Joint 2	8	12
Joint 3	0.8	3.6
Joint 4	3.0	3.6
Joint 5	0.7	3.6
Joint 6	1.1	1.5

From Table 1, it is clear that the estimated torque due to self-weight, an acceleration of $10/s^2$ and an estimated friction of 0.5 N.m per joint is well within the rated torque capability of the chosen actuators. Even though joints 3 and 5 appear to be having a large margin, they were chosen because of their higher bearing load capacity. This is because compared to the torque-output capability, the load capability of joint bearings is more critical for sustaining the launch loads. In addition, there was a need for limiting the type of actuators to be used in the arm.

Considering all these aspects the joint actuators are chosen as follows. Joints 1 and 2 are assigned high torque joints with 12 N.m nominal and 30 N.m peak torque capability. Joint 3-5 are assigned with an actuator with 3.6 N.m nominal and 6.8 N.m peak torque capability. The wrist joint is assigned with a 1.5 N.m low torque actuator. The bearing load capacities of these joints are 3000N, 1800N and 100N respectively. The masses of the joints are 600g, 400g and 100g respectively. The final configuration of the arm is shown in Fig. 3.

Details of the mass break-up of one arm are shown in Fig. 4. The mass optimized arm has a total mass of 4 kg out of which 60% of the mass is contributed by the actuators. The structure accounts for only 28% of the total mass.

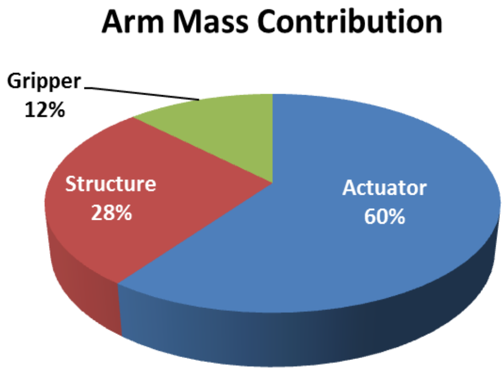

Figure.4 Mass break-up of robotic arm

C. Need for Arm Hold-Downs

The main difference between an industrial and space robotics becomes evident in this section. Unlike conventional robotic manipulators, the arms which operate in outer space must be capable of surviving the severe launch vibrations. This is incorporated in the design as a structural factor of safety and by increasing the natural frequency. The former is attained by providing adequate sections at critical locations while the latter is achieved using increase in structural stiffness, lowering of mass and provision of hold-downs.

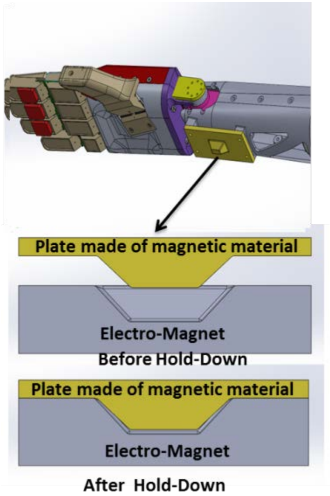

Figure.5 Electro-Magnetic (EM) lock used for hold-down of robotic arm. Configuration before and after hold-down

The severe sine vibration input from the launch vehicle used by ISRO due to slosh, pogo, stage separation and other effects is found to be below 100 Hz. So, it is desirable to keep the first mode of natural frequency greater than 100 Hz. The arm is having a total mass of 4 kg with a length of 715 mm. Hence it is theoretically impossible to attain a high natural frequency. In order to stiffen the arm, the simplest way is to provide additional support to reduce its length. This will naturally increase the frequency. But the support should be removable and re-usable for aiding multiple hold-down and release at various stages of operation. Consequently, it is decided to provide hold-down for the arm during the ascent phase of the mission.

After on-orbit operation, the crew module returns to earth and is recovered. Hence, the arms can be recovered and reused. As a result, it is proposed to hold-down the arm during the descent phase as well. In addition, the arms can also be locked in case of attaining a safe mode of operation on-orbit. As a result, the hold-downs shouldn't be permanent and should be easily removable before commencement of the on-orbit operation. It shouldn't be a one-time-deployable design, but must be reusable during the operational period. All these functional requirements, eliminates the use of conventional wire-rope and plunger-based hold-downs. This is because in these mechanisms, the wire ropes are cut by means of a pyro device for deployment and can thus be used only once. As a result, it is decided to use an electrically actuated hold-down.

D. Electro-magnetic Locks

The electro-magnetic locks (EM-locks) are electrically actuated hold-down systems which works based on the magnetic force. The arm is attached with a magnetic material and the place for arm hold-down (in this case the half-humanoid torso) is provided with the electro-magnetic coil. If the plate attached to the arm is held close to the coil, it locks due to electro-magnetic force. For 'unlocking', the electric current is switched OFF and the coil is demagnetized to remove residual magnetic field.

EM-lock is capable of generating force only normal to the clamping surface. This means that in the in-plane direction, there will only be a frictional resistance. In order to develop a large in-plane frictional force, the normal force has to be increased even more. This will result in a bulky EM lock design which consumes higher electrical power and gives higher thermal dissipation. In order to avoid this, the plate attached to arm is given a profiled projection and a corresponding cavity is given at the EM coil housing. This will give a mechanical constraint in the in-plane direction during arm vibration. The mechanical configuration of the EM-lock is shown in Fig.5. The plate attached near arm wrist is shown along with the configuration of the EM-lock before and after hold-down. The profiled projection for in-plane locking is also shown. As explained in the previous section, this can be locked and un-locked multiple times, thus meeting all the functional requirements.

E. Hold-Down Configurations

The need for re-lockable hold-downs leads to the use of EM-locks. Now for the arrival of an optimum hold-down configuration for the dual arms is essential. The half-humanoid has two arms with end-effecter attached onto the torso. In order to avoid multiple EM-locks and to avoid differential displacements, it is planned to choose an arm hold-down configuration using a single EM-lock (per arm) at the wrist without providing an additional lock for the end-effecter.

The hold-down configuration of dual-arms on torso is shown in Fig. 6. The plate made of magnetic material is attached near arm wrist. The EM coils are attached onto the torso. The two arms are folded such that the location near wrist gets locked. Simultaneously, a portion of the end-effecter palm comes in contact. This act as an additional constraint and provide Coulomb damping when subjected to vibration. Thus with a single hold-down location per arm both the arm and the gripper are locked to increase stiffness.

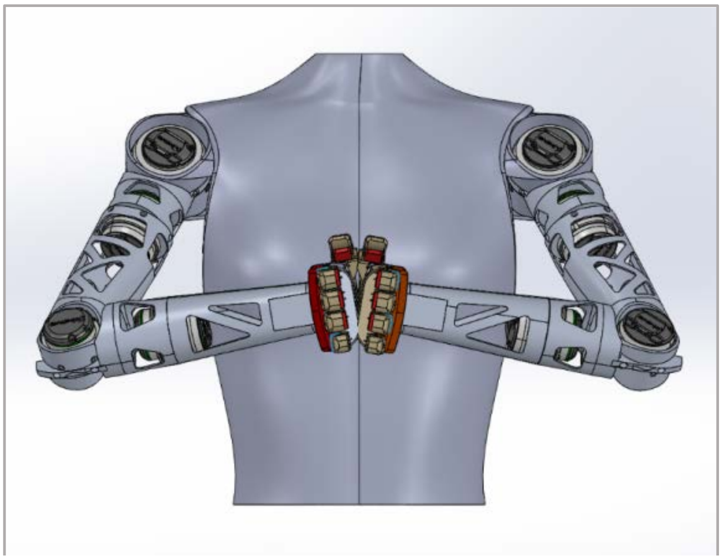

Figure.6 Dual arm hold-down configuration on torso. Both arms are arrested at the wrist by attaching onto the torso. A portion of the end-effecter palm is in contact providing Coulomb damping.

4. STRUCTURAL DESIGN

The configuration of the robotic arm and its hold-down design was discussed in the previous sections. In this section, its structural design aspects are explained. Both stiffness and strength based design are described and the various criteria to be satisfied are elucidated. Initially the modal analysis results of the arm is given in which both the hold-down and worst case deployed frequencies are computed. The stress analysis is done after applying an estimated quasi-static load of 25g about the x, y and z axes. The structural model of the arm is shown in Fig. 7.

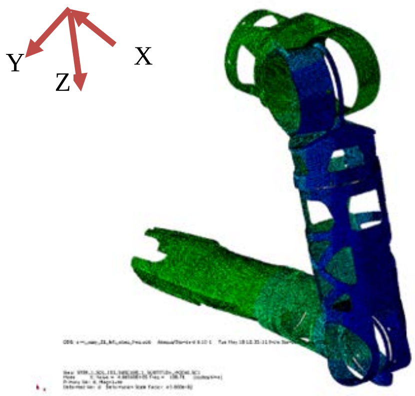

Figure.7 Structural modal of the robotic arm. The finite element modal where the hold-down locations are constrained is used for modal and strength analysis.

A. Modal Analysis

The finite element model of the robotic arm is made and constraints are given at the base and the hold-down locations to evaluate the natural frequency. Several design iterations were conducted so that the first natural frequency (mode shape in Fig. 7) at hold-down condition is well way from 100 Hz. The salient results are listed in Table 2.

Table 2: Modal Analysis Results

Mode No.	Option 1: Frequency (Hz)	Option 2: Frequency (Hz)	Mode Shape
1	108	143	Shoulder bending
2	229	270	Shoulder + wrist bending-1
3	273	303	Shoulder + wrist bending-2

Option 2, after stiffening of the shoulder structure, gave higher natural frequency at arm hold-down condition. It should also be noted that the stiffening was done only at critical locations resulting in only a minimum mass increase. The deployed natural frequency of the arm is equally critical as it should be well away (at least > 5 times) the control bandwidth of the arm. This will help to avoid control-structure interactions during arm operation. As the arm has a length of > 700 mm and a total mass of 4 kg, with distributed actuator locations resulting in inertia increase, it is indeed a challenging task to satisfy this requirement. A worst-case minimum frequency estimate of the arm at fully deployed condition was studied. This is because, at different orientations, the arm will have different natural frequencies.

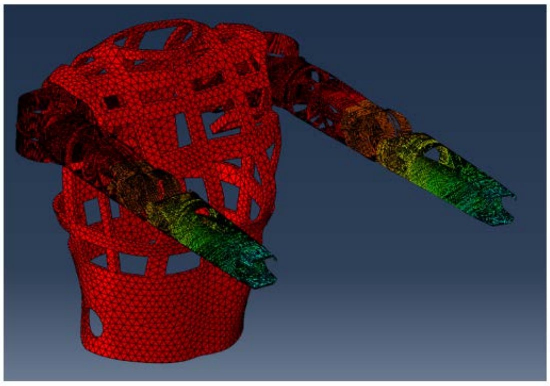

Figure.8 Deployed modal analysis of the arms when attached to torso and after inclusion of joint flexibilities

The deployed modal analysis was done at various stages. In the first stage the deployed frequency of the arm was computed in the stand-alone condition. Then both the left and right arms were integrated with the torso structure to study the drop in frequency. It was seen that due to the stiff design of the torso, the drop in frequency was insignificant. Lastly the flexibility of the bearings and harmonic drive in each of the joint actuators were also included to get an estimate as close to reality as possible. The salient results are listed in Table 3. The last column gives a condition as close to the reality as possible. The first mode is 18.8Hz which is > 5 times the control bandwidth (3 Hz). This is selected and the stress analysis of the same is done to evaluate the structural factor-of-safety (FoS).

Table 3: Modal Analysis: Deployed Condition

Mode No.	Frequency of Arms on Torso before stiffening of arm (Hz)	Frequency of Arms on Torso after stiffening of arm (Hz)	Frequency of Arms on Torso after stiffening of arm and inclusion of joint flexibilities (Hz)
1	14	21.4	18.8
2	22	26	19.8
3	80	82	84

B. Strength Analysis

The strength analysis of the model (which satisfied the frequency requirements during both hold-down and deployed condition) was done for verifying the structural factor of safety. The arm were assumed to be held-down by the EM-lock and 25-g quasi-static load was applied about the x, y and z axes. The maximum von Mises stress at critical locations were noted and studied. The maximum stress values and the FoS available, considering AlSi10Mg as the base material is given in Table 4. The structure has minimum factor of safety of 2 and the design is acceptable. The primary design was done to meet the stiffness requirement. If we try to lower the FoS to 1.2 or 1.5, though it may result in a lower mass, it will lead to the violation of the frequency requirements.

In addition to the stress analysis, an estimate of the reaction forces acting at the EM lock interface locations was also computed. These are given as input to the EM lock designers for sizing. The reaction forces computed are given in Table 5.

Table 4: Stress Analysis Results

Direction of Applied Load (25-g).	Maximum Stress (MPa)	Factor of Safety
X	68	3.3
Y	84	2.7
Z	115	2.0

Table 5: EM Lock Reactions

Direction of Applied Load (25-g)	Reaction along –X – in plane (N)	Reaction along –Y- out of plane (N)	Reaction along –Z-in plane (N)
X	539	33	2.5
Y	59	501	131
Z	117	66	422

The reaction forces at the EM lock shows a requirement of >500 N in both in-plane and out-of-plane directions. However, the EM locks are capable of developing forces only along the out-of-plane direction. The in-plane forces have to be generated by friction. Assuming a coefficient of friction of 0.2, for an in-plane force of 540 N, the normal reaction should be 2700 N. This means that the size, power and volume of the EM-lock will increase many folds for generating this higher normal force. Hence as explained earlier in Sec.II D, it was decided to lock the in-plane movement through mechanical constraint and obtain an out-of-plane reaction of > 540 N from it.

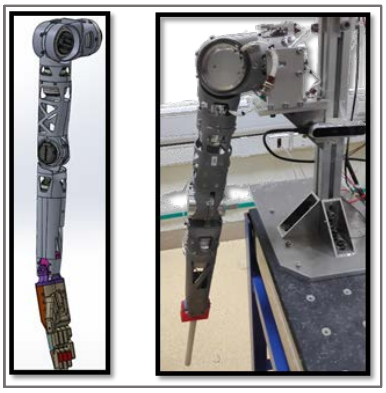

Figure.9 6-DoF robotic arm: realized structural elements integrated with actuators. The 3D model of the arm is also shown

C. Realization of arm

After the completion of the analysis, the arm structural elements were realized. Due to the complicated shape of the links, the arm was realized through additive manufacturing by using the 3D model of individual elements using AlSi10Mg alloy. After this, the finish machining of the elements was done at the actuator mounting locations. The requirement for precise diametric clearance, control of center-to-center length, perpendicularity between adjacent actuators bores were realized in finish machining. Thus these crucial dimensions which affect the forward and inverse kinematics were controlled during finish machining by assigning appropriate dimensional and geometric tolerances at the required locations. The realized structural members were assembled with the joint actuators and was tested (refer Fig.9). The steps for calibration of the arm for characterizing its systematic, repeatable errors are in progress.

5. Conclusion

The configuration and design of a 6-DoF anthropomorphic robotic arm for a half-humanoid is covered in this paper. The joint arrangements and link lengths are fixed based on the kinematic requirements. The joint actuators are chosen for their ability to overcome arm self-weight and with bearings having sufficient load capability. Unlike other industrial arms, the space qualified robotic arm must have design features like hold-downs for sustaining the severe launch vibrations. The initial mechanical design was guided by the requirement for launch and deployed configuration natural frequency requirements. The former is achieved with both structural stiffening and with the re-usable electro-magnetic locks. The latter is kept more than five times away from the control bandwidth through judicious addition of ribs to stiffen the structure. The strength analysis showed adequate factor of safety for the structural members. The inputs required for EM lock sizing and the mechanical design features for in-plane arresting of the lock is explained. The mechanical locking feature results in reducing the EM lock force requirements by 80%. The designed arm was realized by a combination of additive manufacturing and finish machining at critical locations. The testing and calibration of the arm for characterizing its systematic, repeatable errors are in progress. After this, the full level testing of the arm for performing the required functional requirements will be verified.

6. Acknowledgment

The authors would like to place on record their sincere gratitude to Dr. D Sam Dayala Dev, Director IISU for his whole hearted support, vision and guidance. We would also like to acknowledge the entire team members of the Robotics Lab at IISU without whose efforts; the project would not have materialized. We also acknowledge VSSC team, who designed and supplied the 5-fingered end-effecter.

7. References

[1] Wenfu XU, Lei YAN, Zhonghua HU, Bin LIANG. “Area-oriented coordinated trajectory planning of dual-arm space robot for capturing a tumbling target”

[2] Robert O.Ambrose, Hal Aldridge, R.Scott Askew, Robert R. Burridge, William Bluethmann, Myron Diftler, Chris Lovchik, Darby Magruder and Fredrik Rehnmark. “Robonaut: NASA’s Space Humanoid”

[3] Ravi Kiran Bollineni, Sidharsh S Menon, Ganesha Udupa. “ Design of Rover and Robotic Arm”. IConAMMA 2018. Materials Today: Proceedings 24(2020) 1340-1347

[4] Chunguang Fan, Yuanfei Zhang, Zongwu Xie, Zhiqi Li, Chongyang Li and Hong Liu. “ Design of Space Robotic Arm-Hand System and Operation Research”. In Proceedings of 2018 IEEE International Conference on Mechatronics and Automation August 5-8, Changchun, China

[5] Report for Half-Humanoid for Gaganyaan Mission, Internal Design Report ISRO Inertial Systems Unit, 2020

[6] Craig.J., John., Introduction to Robotics: Mechanics and Control, Third Edition, Pearson Education International, 2005

[7] Pieper, Donald, “ The Kinematics of Manipulators Under Computer Control”, PhD Thesis, Stanford University, 1968

[8] Wang, Zhiming, Zhenglong Cai, Lizheng Cui, and Changfu Pang. "Structure Design And Analysis Of Kinematics Of An Upper-limbed Rehabilitation Robot." In MATEC Web of Conferences, vol. 232, p. 02033. EDP Sciences, 2018.

[9] Kim, Hyunchul, Levi Makaio Miller, Aimen Al-Refai, Moshe Brand, and Jacob Rosen. "Redundancy resolution of a human arm for controlling a seven dof wearable robotic system." In 2011 Annual International Conference of the IEEE Engineering in Medicine and Biology Society, pp. 3471-3474. IEEE, 2011.

Reactionless Manipulation of Dual 3-DoF Robotic Arms on a 1 U CubeSat

Gaurav Sharma
BITS
Pilani
f20170532@pilani.
bits-pilani.ac.in

Karthik B Nair
BITS
Pilani

Devashish V. Gupta
BITS
Pilani
bits-pilani.ac.in

N. Sai Kiran
BITS
Pilani

Abhilash Mony
ISRO Inertial Systems Unit
Trivandrum
abhilash.mony@gmail.com

Dileep Rajendran
ISRO Inertial Systems Unit
Trivandrum

Joji J Chaman
ISRO Inertial Systems Unit
Trivandrum

***Abstract* — The modelling and dynamics of robotic manipulators is well established for pick-and-place operations and other repetitive tasks during their operation on earth. For the operation of robotic arms attached to a freely floating spacecraft, the effect of arm dynamics on platform stability is highly critical. In this paper, the reactionless manipulation of dual 3-DoF robotic arms attached to a 1U CubeSat for performing pick and place operations is analysed. The kinematic model of the arm is developed using modified DH parameters. The arm dynamics equations are derived based on the Iterative Newton-Euler method. The coupled dynamics equation during the dual arm operation are derived for an arbitrary trajectory. During arm motion, the acceleration of the centre of mass of the arm-CubeSat system is considered and included in the dynamic equations. The problem is then numerically simulated based on a defined pick-and place trajectory for the left arm. Using the coupled dynamics equations of both the arms, a right arm trajectory is computed and executed. The achieved right arm trajectory is found to nullify the residual reaction torques transferred to the CubeSat while operating the left arm, resulting in a stable spacecraft attitude.**

Keywords — Reactionless manipulation, Dynamic Analysis, Space Robots, Dual Robotic Arm

1. Introduction

Robotic devices are finding more use in space applications as they are required to aid or even replace astronauts in performing mundane and sometimes dangerous activities like repair, maintenance and exploration. Controlling such freely floating robots in space, in contrast to industrial robotics, can be quite complex owing to the absence of a stable platform for support. The lack of such a platform is a cause for concern as the satellite itself moves when it tries to operate its attached arms. If not properly controlled, the motion of the robotic arms can impart high undesirable disturbance onto the spacecraft. Hence, various methods of disturbance-less, or rather, reactionless manipulation have been explored in the past.

The studies conducted for a solution to reactionless manipulation problem can be classified into two categories. In the first category, the manipulator is designed such that reactionless manipulation is achieved with the use of parallel manipulators [1], [10]. Some studies use counterweights and auxiliary parallelograms [2], [11], while others use counter-rotation of flywheels to cancel reaction torques [3]. The second category mainly involves the use of path planning. Reaction Null Space (RNS) based Zero Reaction Maneuvers (ZRM) has been used in [4].

The RNS method uses those trajectories of arm joint angles which makes the base reactions zero. Hence, there will be no change in the angular momentum due to the arm motion and consequently the attitude remains undisturbed. This method has also been used in the path planning and trajectory generation for a 2-DoF manipulator in [5].

The cancellation of reaction torques for a 9 link 3-DoF parallel manipulator was explored in [6]. Reactionless manipulation for dual planar manipulators was studied in [15]. Based on the RNS concept, a simulator ReDySim was developed and used to study a dual 3 DoF planar manipulator in [7], [14]. An energy optimal reactionless control was also implemented in these papers. A composite control law was proposed based on RNS concept with a manipulator system in [8]. An adaptive reactionless control algorithm in a post capture scenario to minimize the reactions on the base was proposed in [12]. Reactionless motion control on a 7-DoF redundant manipulator and three practical maneuvers were explored in [13].

This study is novel as the coupled dynamic equations of 3 DoF non-planar dual arms, derived based on Iterative Newton-Euler formulation have been used to compute the reactionless trajectory. Moreover, this method can be easily extended to any spacecraft with a pair of n-DoF manipulators.

The system under study here is a 1U CubeSat with dual 3-DoF robotic arms. Each arm has DoFs as yaw (shoulder), pitch (elbow) and roll (wrist). Out of these, only the shoulder and elbow joint angles determine the position of the end effector. The wrist joint affects only the orientation of the end effector. Both the arms are identical and have the same inertia properties and link lengths.

The aim of this study is to nullify the disturbances on the satellite caused by the moving arm. To attain this, it has been assumed that all tasks can be implemented using one hand alone, say, the left arm. Hence, a trajectory is specified beforehand, for the left arm alone. The objective is to find the trajectory of the right arm to balance the reactions on the satellite due to the motion of the left arm. Since the CubeSat is required to maintain a steady attitude, it is the reaction torques which are nullified. Since only less DoFs are available to balance the reaction forces, there is a residual acceleration on the CubeSat. This couples the dynamics of the dual arms attached to it and is thus included in the reactionless manipulation formulation.

The rest of the paper is organised as follows: Sections 2 deals with the forward kinematics of the robotic arms. The mathematical formulation of the dynamics of the robotic arms using the iterative Newton-Euler Method is described in Section 4. Verification of these equations is done using MSC ADAMS, a commercial multi-body dynamics simulation package. The algorithm followed to cancel reaction torques is explained in Section 5. Section 6 contains the results obtained through numerical simulations and discussion of Section 7 concluded the paper.

2. Forward Kinematics

In any forward kinematics problem, the aim is to determine the position and orientation of the end effector, parameterized by the joint angles. The robotic arm has 3 DoFs, out of which only 2 DoFs (shoulder and elbow) change the position. The wrist changes the orientation of the end-effector. The Modified Denavit-Hartenberg (DH) convention [9] has been followed for deriving the forward kinematics.

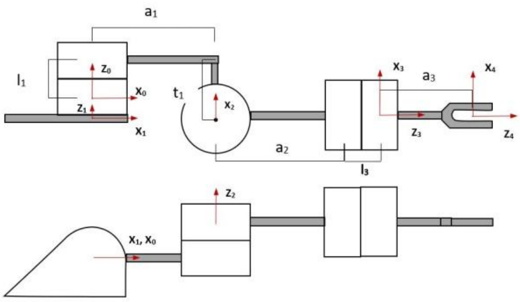

Figure 1: Schematic diagram of left arm

The schematic of the left arm is given in Fig. 1. The modified DH parameters of the left and right arm are given in Table 1.

Table 1: DH Table for Left arm (L) and Right arm (R) (all angles are in degrees)

i	a_{i-1}		α_{i-1}		d_i		θ_i	
	L	R	L	R	L	R	L	R
1	0	0	0	0	$l_1 - t_1$	$l_1 - t_1$	θ_{1L}	θ_{1R}
2	a_1	a_1	90	90	l_2	$-l_2$	$90 + \theta_{2L}$	$90 + \theta_{2R}$
3	0	0	90	90	$a_2 + l_3$	$a_1 + l_1$	θ_{3L}	θ_{3L}

Using homogeneous transformations [15], the transformation from end-effector frame to the base frame is given as,

$$T_4^0 = T_1^0 \cdot T_2^1 \cdot T_3^2 \cdot T_4^3 \tag{1}$$

Where T_i^{i-1} is given as,

$$T_i^{i-1} = [c\theta_i \ -s\theta_i \ 0 \ a_{i-1} \ s\theta_i c\alpha_{i-1} \ c\theta_i c\alpha_{i-1} \ -s\alpha_{i-1} \ -s\alpha_{i-1}d_i \ s\theta_i s\alpha_{i-1} \ c\theta_i s\alpha_{i-1} \ c\alpha_{i-1} \ c\alpha_{i-1}d_i \ 0\ 0\ 0\ 1\ ] \tag{2}$$

Where, s$\theta = sin\theta$ and $c\theta = cos\theta$.

The x, y, z coordinates of the end effector for the left arm obtained from the final transformation matrix are,

$$X_L = a_1 c\phi + l_2 s\phi + c\phi c\psi(a_2 + l_3) + a_3 c\phi c\psi \tag{3a}$$
$$Y_L = a_1 s\phi - l_2 c\phi + s\phi c\psi(a_2 + l_3) + a_3 s\phi c\psi \tag{3b}$$
$$Z_L = l_1 - t_1 + s\psi(a_2 + l_3) + a_3 s\psi \tag{3c}$$

Where, $\varphi = \theta_{1L}$ and $\psi = \theta_{2L}$

Orientation of the end effector of the left arm is given by the following rotation matrix,

$$R_{4L}^0 = [s\theta_{1L}s\theta_{3L} - c\theta_{1L}s\theta_{2L}c\theta_{3L} \ s\theta_{1L}c\theta_{3L} + c\theta_{1L}s\theta_{2L}s\theta_{3L} \ c\theta_{1L}c\theta_{2L} \ -c\theta_{1L}s\theta_{3L} - s\theta_{1L}s\theta_{2L}c\theta_{3L} \ -c\theta_{1L}c\theta_{3L} + s\theta_{1L}s\theta_{2L}s\theta_{3L} \ s\theta_{1L}c\theta_{2L} \ c\theta_{2L}c\theta_{3L} \ -c\theta_{2L}s\theta_{3L} \ s\theta_{2L}\ ] \tag{4}$$

The constraints on the joint angles of left arm from the CAD model are $-120 < \theta_{1L} < 40$, $0 < \theta_{2L} < 136$ and $0 < \theta_{3L} < 360$ (all the angles are in degree). The orientation of the end-effector for the right arm can be computed by substituting l_{2L} as$-l_{2R}$ and θ as $-\theta_{1R}$ in Eqs.(3) and (4).

3. Inverse Kinematics

The inverse kinematics problem for a general robotic manipulator requires finding the joint angles resulting in a particular end-effector position and orientation. If the arm is to be moved from one point in space to another with minimal reactions, inverse kinematics has to be implemented beforehand. This is because the joint space information of the manipulator is required for implementing the algorithm for cancelling reaction torques. An analytical method is followed here to obtain a closed form solution for the inverse kinematics problem.

Let the desired position and orientation of the end-effector of the left arm be the function of the joint angles which are given by the following matrix.

$$T = [r_{11}\ r_{12}\ r_{13}\ X_L\ r_{21}\ r_{22}\ r_{23}\ Y_L\ r_{31}\ r_{32}\ r_{33}\ Z_L\ 0\ 0\ 0\ 1\ ] \tag{5}$$

And the rotation matrix as observed from the above transformation matrix is:

$$R = [r_{11}\ r_{12}\ r_{13}\ r_{21}\ r_{22}\ r_{23}\ r_{31}\ r_{32}\ r_{33}\ ] \tag{6}$$

Comparing Eq. (4) and Eq. (6), it is found that $r_{31} = c\theta_{2L}c\theta_{3L}$ and $r_{32} = -c\theta_{2L}s\theta_{3L}$. This implies,

$$\theta_{3L} = tan^{-1}\left(\frac{-r_{32}}{r_{31}}\right) \tag{7}$$

From Eq. (3c),

$$sin\theta_{2L} = \left(\frac{Z_L - l_{1L} + t_{1L}}{a_{2L} + a_{3L} + l_{3L}}\right) \tag{8}$$

Squaring and adding Eqs. (3a) and (3b), and then solving for $cos\theta_{2L}$,

$$cos\theta_{2_L} = \frac{-a_{1_L} \pm \sqrt{X_L^2 + Y_L^2 - l_{2_L}^2}}{a_{2_L} + a_{3_L} + l_{3_L}} \tag{9}$$

The value of θ_{2L} which satisfies both Eqs. (8) and (9) is chosen. Henceforth, θ_{1L} can be determined from Eqs. (3a) and (3b) as,

$$s\theta_{1_L} = \left(\frac{X_L l_{2_L} + Y_L \cdot \left(a_{1_L} + \left(a_{2_L} + a_{3_L} + l_{3_L}\right) \cdot c\theta_{2_L}\right)}{((a_{1_L} + (a_{2_L} + a_{3_L} + l_{3_L}) \cdot c\theta_{2_L})^2 + l l_{2_L}^2}\right) \tag{10}$$

$$c\theta_{1_L} = \left(\frac{s\theta_{1_L} \cdot \left(a_{1_L} + \left(a_{2_L} + a_{3_L} + l_{3_L}\right) \cdot c\theta_{2_L}\right) - Y_L}{l_{2_L}}\right) \tag{11}$$

$$\theta_{1_L} = tan^{-1}\left(\frac{s\theta_{1_L}}{c\theta_{1_L}}\right) \tag{12}$$

Similarly, the joint angle for the right arm can be computed by substituting θ_{1L} as $-\theta_{1R}$ and l_{2L} as $-l_{2R}$ in Eqs. (7) - (12).

4. Dynamics

The basic premise of dynamics of a robotic arm is to find the torques required to be applied at each joint, such that the end effector traces a prescribed trajectory in 3D space. The joint torques are obtained by providing the joint angles as a function of time. Dynamics for the robotic arm was performed using iterative Newton-Euler Method and was later verified using MSC ADAMS.

A. Iterative Newton Euler Method

The Newton-Euler method [15] is based on Newton's third Law and Euler's equation. It has two sets of iterations, namely outward and inward. Outward iterations (from 0th link to (n−1)th link) are used to compute velocities and accelerations of each link. The inward iterations (from nth link to 1st link) are performed to calculate joint forces and torques for each link. The forces and torques obtained from these iterations are given by,

$$f_i^i = R_{i+1}^i f_{i+1}^{i+1} + F_i^i \tag{13}$$

$$n_i^i = N_i^i + R_{i+1}^i n_{i+1}^{i+1} + P_{C_i}^i \times F_i^i + P_{i+1}^i \times R_{i+1}^i f_{i+1}^{i+1} \tag{14}$$

where, F_{i+1}^{i+1} is the inertial force acting at the centre of mass (CoM) of link $i+1$ w.r.t. the frame $i+1$.
N_{i+1}^{i+1} is the inertial torque acting at the CoM of link $i+1$ w.r.t. the frame $i+1$
f_i^i is the force exerted on link i by link $i-1$.
n_i^i is the torque exerted on link i by link $i-1$.
R_{i+1}^i is the rotation matrix from frame $i+1$ to frame i.
$P_{C_i}^i$ is the vector from frame i to CoM of link i expressed in frame i.
P_{i+1}^i is the vector from frame i to frame $i+1$ expressed in frame i.

The complete equations for the iterative Newton-Euler method are given in Appendix A.

5. Reactionless Manipulation

The dual 3-DoF robotic arms analysed so far are integrated to the 1U CubeSat and this robotic system performs a pick and place operation. For the purpose of simplicity, it has been assumed that the robot does not carry any load while moving its arms. Even in this case, the actuation of the robotic arms in space causes disturbances in the attitude as well as the position of the satellite. The main objective of this study is to nullify such disturbances caused on the 1U CubeSat by cancelling out the reactions caused by one arm with the help of the other. The exploded view of CubeSat and robotic arm system is shown in Fig. 2.

In this study, only one arm is used to perform a task, say, a pick and place operation. Here, the left arm is used as the working arm and has to follow a specific trajectory. Hence, the joint angles and its derivatives are predefined for the left arm as functions of time;

$$\Theta_L = \left[\theta_{1_L}\ \theta_{2_L}\ \theta_{3_L}\ \right] = \left[f_1(t)\ f_2(t)\ f_3(t)\ \right] \tag{15}$$

The objective is to obtain Θ_R,

$$\Theta_R = \left[\theta_{1_R}\ \theta_{2_R}\ \theta_{3_R}\ \right] \tag{14}$$

Such that the reactions on the CoM of the CubeSat are zero. The joint forces and torques required for the arms to perform tasks causes reactions at the base joint of the robotic arm, i.e., the joint between the CubeSat and the arm. These are reactions on the CubeSat, because it is not supported by any means, causes it to accelerate. These accelerations cannot be neglected as it affects the trajectory of both the arms. Balancing the reaction forces and torques on the CubeSat is accomplished by solving 6 non-linear differential equations (f_x, f_y, f_z, n_x, n_y and n_z). These 6 equations for forces and torques contain only 3 variables (the joints of right arm: θ_{1R} , θ_{2R} and θ_{3R}) for which finding a solution is not possible. Since the left arm is the working arm, its trajectory is predefined, and its joint angles cannot be used to aid reactionless manipulation. Hence, it was decided to balance the torques (n_x, n_y and n_z), to get a unique solution for the right arm trajectory. The reason for this was that the CubeSat was required to point in a desired direction and any attitude disturbance will prevent it from doing so. It is impractical and expensive to operate thrusters throughout the motion of the space robot for tasks which may extend for a long duration as the CubeSat has very limited supply of fuel for operating the cold-gas thrusters. Hence, while the arm operates, the resultant forces on the satellite are not balanced and the thrusters are deactivated. The forces can be balanced only if 3 more degrees of freedom are available.

The satellite can be assumed to be made of two systems: The CubeSat and the dual robotic arms (Fig. 2).

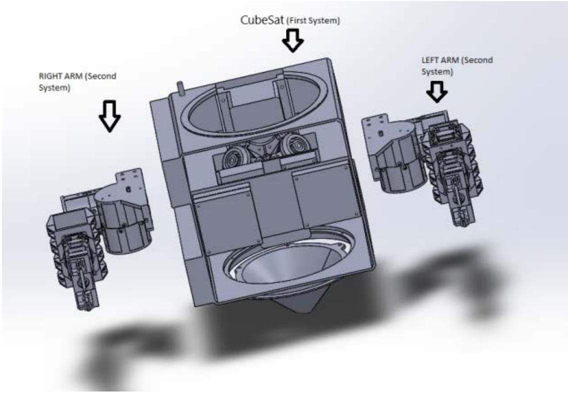

Figure 2: The exploded view of CubeSat and the robotic arms

The mass of the CubeSat is $\mathrm{m_{sat}}$ and the mass of left and right arm are $\mathrm{m_L}$ and $\mathrm{m_R}$ respectively. Since there is no net force on the combined system of the 2 bodies:

$$F_{net} = 0 \tag{17}$$

This implies,

$$m_{sat} a^U_{sat} + m_L a^U_L + m_R a^U_R = 0 \tag{18}$$

where, $\mathrm{a^U_{sat}}$ is the acceleration of CubeSat with respect to orbital frame of the satellite (U) which has the same orientation as the CubeSat frame. It has been assumed that the orbital effects are negligible due to the arm operating only for a short period of time. $\mathrm{a^U_L}$ is the acceleration of the left arm with respect to U. $\mathrm{a^U_R}$ is the acceleration of the right arm with respect to U. Eq. (18) can also be written as,

$$m_{sat} a^U_{sat} + m_L(a^{sat}_{cm_L} + a^U_{sat}) + m_R(a^{sat}_{cm_R} + a^U_{sat}) = 0 \tag{19}$$

where,
$\mathrm{a^{sat}_{cm_L}}$ is the acceleration of the CoM of the left arm with respect to CubeSat frame. $\mathrm{a^{sat}_{cm_R}}$ is the acceleration of the CoM of the right arm with respect to CubeSat frame.

The acceleration of the CubeSat with respect to U can be obtained and is given by:

$$a^U_{sat} = -\frac{m_L a^{sat}_{cm\,L} + m_R a^{sat}_{cm\,R}}{m_L + m_R + m_{sat}} \tag{20}$$

Using Eqs. (32) - (35) in Appendix A, the acceleration for each link in the CubeSat frame (assuming that the orientation of the base frame of both arms and the CubeSat frame remains the same) is given by,

$$(a^{sat}_{cm_i})_j = (R^0_i \dot{v}^{i}_{C_i})_j \tag{21}$$

Where i varies from 1 to 3.
$(a^{sat}_{cm_i})_j$ is the acceleration of the center of mass of the i^{th} link of the j^{th} arm with respect to CubeSat frame.
$\dot{v}^{i}_{C_i}$ is the acceleration of the CoM of the i^{th} link with respect to i^{th} frame.

Using Eq. (20) and Eq. (21),

$$a^U_{sat} = -\frac{\sum_{i=1}^{3} \quad (m_{iL}(a^{sat}_{cm\,i})_L + m_{iR}(a^{sat}_{cm\,i})_R)}{m_L + m_R + m_{sat}} \tag{22}$$

The dynamics of the arm is affected by this acceleration and Eq. (36) of the outward iteration (Appendix A) is modified as,

$$F_{i+1}^{i+1} = m_{i+1}(v_{C_{i+1}}^{i+1} + R_0^i a_{sat}^U) \quad (23)$$

Using Eq. (23) in Eqs. (37) - (39) (Appendix A), the reaction forces and torques on link 1 can be obtained as:

$$f_{1j}^1 = M_{f_j}(\Theta_L, \Theta_R)\ddot{\Theta}_j + V_{f_j}(\Theta_L, \dot{\Theta}_L, \Theta_R, \dot{\Theta}_R) \quad (24a)$$

$$n_{1j}^1 = M_{n_j}(\Theta_L, \Theta_R)\ddot{\Theta}_j + V_{n_j}(\Theta_L, \dot{\Theta}_L, \Theta_R, \dot{\Theta}_R) \quad (24b)$$

where, the sub-subscript j denotes the left and the right arm, i.e., $j = L, R$ and,
$f_{1_j}^1$: force exerted by base frame (frame 0) on link 1 (R^3).
$n_{1_j}^1$ is the torque exerted by base frame on link 1 (R^3).
$M(\Theta)$ is the mass matrix ($R^{3\times3}$).
$V(\Theta, \dot{\Theta})$ is a vector of centrifugal and Coriolis terms (R^3) (note that the effect of gravity is negligible in space, and hence the gravity terms are zero).

Here subscript f corresponds to matrices in the equation for computing force and subscript n corresponds to matrices in the equation for computing torque. Since the base frame (frame 0) has no inertial properties, the force and torque in the base frame of jth arm are given as:

$$f_{0j}^0 = R_1^0 f_{1j}^1 \quad (25a)$$
$$n_{0j}^0 = R_1^0 n_{1j}^1 + [P_{1j}^0 \times] R_1^0 f_{1j}^1 \quad (25b)$$

For the j^{th} robotic arm:
f_{0j}^0 is the force exerted by CubeSat on base of robotic arm.
R_1^0 is rotation matrix from frame 1 to base frame (frame 0).
n_{0j}^0 is the torque exerted by CubeSat on base of robotic arm.
P_{0j}^0 is vector from frame 0 to frame 1 expressed in frame 0.

For a general vector $a = [a_1 \;\; a_2 \;\; a_3]^T$

$$[a\times] = [0 \; - a_3 \; a_2 \; a_3 \; 0 \; - a_1 \; - a_2 \; a_1 \; 0\,]$$

The vector from center of mass (CoM) of the CubeSat to the base frame of jth arm is r_j. Since there is no reaction torque on the CubeSat, the orientation of the CubeSat's frame of reference (located at the CoM of the CubeSat), base frames of reference of the left and right arm are fixed and don't change with time. Based on this, the net torque acting on the CoM of the CubeSat due to jth arm is computed as,

$$\tau_{Net_j} = n_{0j}^0 + [r_j \times] f_{0j}^0 \quad (26)$$
$$\tau_{Net_j} = R_1^0 n_{1j}^1 + ([P_{1j}^0 \times] + [r_j \times]) R_1^0 f_{1j}^1 \quad (27)$$

Using Eq. (24) in Eq. (27), if the net reaction torque on the satellite is to be cancelled:

$$\tau_{Net_L} + \tau_{Net_R} = 0 \quad (28)$$

On simplification, a coupled non-linear differential equation can be obtained of the form:

$$M_L(\Theta_L,\Theta_R)\ddot{\Theta}_L + M_R(\Theta_L,\Theta_R)\ddot{\Theta}_R + V(\Theta_L,\dot{\Theta}_L,\Theta_R,\dot{\Theta}_R) = 0 \tag{29}$$

where,

$$M_L = R_1^0 M_{n_L} + \left([P_{1_L}^0 \times] + [r_L \times]\right) R_1^0 M_{f_L}$$
$$M_R = R_1^0 M_{n_R} + \left([P_{1_R}^0 \times] + [r_R \times]\right) R_1^0 M_{f_R}$$
$$V_L = R_1^0 V_{n_L} + \left([P_{1_L}^0 \times] + [r_L \times]\right) R_1^0 V_{f_L}$$
$$V_R = R_1^0 V_{n_R} + ([P_{1_R}^0 \times] + [r_R \times]) R_1^0 V_{f_R}$$

As Θ_L is known as functions of time, Eq. (29) is integrated with ode45 in MATLAB™ to obtain a trajectory for the right arm for cancelling the net reaction torques on the spacecraft. In the simulations conducted, a 3-DoF manipulator is used and only reaction torques could be balanced. When the robotic arm has more DoFs, it is possible to balance reaction torques and reaction forces using Eq. (29). For a case where the acceleration of the CoM of the CubeSat is balanced using thrusters, Eq. (29) becomes decoupled and can be given as,

$$M_L(\Theta_L)\ddot{\Theta}_L + V_L(\Theta_L,\dot{\Theta}_L) + M_R(\Theta_R)\ddot{\Theta}_R + V_R(\Theta_R\dot{\Theta}_R) = 0 \tag{31}$$

6. Numerical Simulation

This section has two parts. In the first part, the dynamic model is verified using MSC ADAMS. The numerical simulation of reactionless manipulation is demonstrated in the second part. The following assumptions were considered for the simulations:

(i) Effect of friction has been neglected in the joints.
(ii) Attitude dynamics for the CubeSat is not considered.

The link lengths and link offsets which were used in the dynamics simulation are:
$a1 = 66.8\,mm,\ a2 = 276.3\,mm,\ a3 = 10\,mm,\ l1 = 36.0\,mm,\ l2 = 56.90\,mm,\ l3 = 40\,mm,\ t1 = 12.2\,mm.$

The MoI, mass and CoM vectors which were used in the simulations are specified in Table 2. The mass of the CubeSat (m_{sat}) was taken as 13480 g.

The vector from CoM of CubeSat to the base frame of leftarm (r_L) is $[20.72, -133.21, -24.76]^T$ mm.

The vector from CoM of CubeSat to the base frame of right arm (r_R) is $[20.72, 133.21, -24.76]^T$ mm.

NOTE: The form of Inertia matrix to be used in Iterative Newton Euler Method is as described in Appendix A. Both arms are identical and have similar inertia properties.

A. Verification of Dynamics model with MSC ADAMS

The dynamics of the manipulator has been verified using MSC ADAMS, a multi-body dynamics package. The verification of the dynamic model instilled confidence for using Newton-Euler equations for reactionless manipulation. The input joint angles are: $\theta_1 = 0.01t^2$, $\theta_2 = \sin(t)$ and $\theta_3 = 0$. Fig. 3 shows the joint torques obtained through MSC ADAMS and Fig. 4 shows the joint torques obtained through MATLABTM. From Fig. 3 and Fig. 4, it is clear that MSC ADAMS and the model results are matching. Hence the dynamic model is verified.

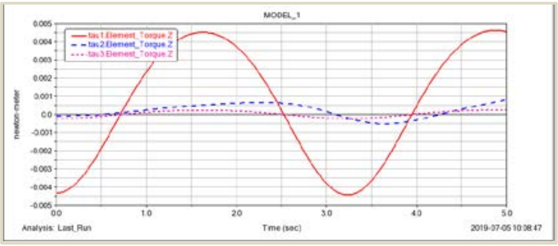

Figure 3: Joint Torques obtained from MSC ADAMS

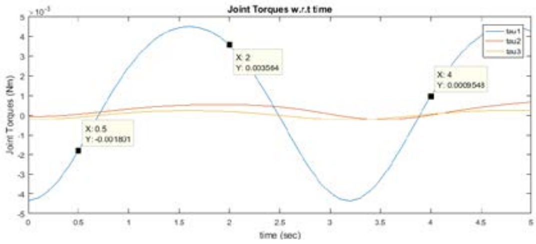

Figure 4: Joint Torques obtained from MATLAB

B. Reactionless Manipulation

The trajectory for the left arm was assigned as,

$$\theta_{1L} = 0.05t^3\, rad,$$
$$\theta_{2L} = \pi - 0.0873t\, rad,$$
$$\theta_{3L} = 0.0005t\, rad.$$

The initial conditions for the right arm are given as,

$$\theta_{1R}(0) = 0,\ \theta_{2R}(0) = \pi,\ \theta_{3R}(0) = 0,$$
$$\dot{\theta}_{1R}(0) = 0, \dot{\theta}_{2R}(0) = 0\,, \dot{\theta}_{3R}\,(0) = 0.$$

Table 2. Inertia properties obtained from CAD Software

i	$I_{CAD}\ (g\ mm^2)$	m_i (g)	$P_{C_i}^i$ (mm)
1	$\begin{bmatrix} 224876.16 & 170894.68 & 76216.72 \\ 170894.68 & 716567.68 & -25420.76 \\ 76216.72 & -25420.76 & 766421.84 \end{bmatrix}$	471.24	$[33.43\ \ -10.91\ \ 4.42]^T$
2	$\begin{bmatrix} 1935091.44 & 88107.44 & -3792.86 \\ 88107.44 & 217972.43 & 106290.26 \\ -3792.86 & 106290.26 & 1971729.36 \end{bmatrix}$	573.05	$[2.35\ -64.67\ \ 1.25]^T$
3	$\begin{bmatrix} 386535.65 & -98.11 & -2259.60 \\ -98.11 & 346720.03 & -39562.40 \\ -2259.60 & -39562.40 & 70053.61 \end{bmatrix}$	213.4	$[0.95\ \ 5.47\ \ 18.95]^T$

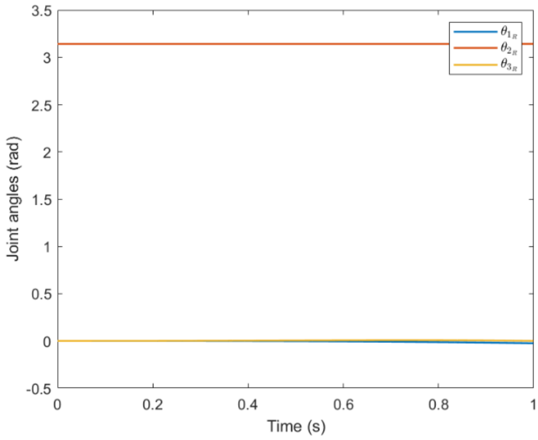

Figure 5: This figure shows the joint angles obtained for the right arm

The trajectory of the right arm is shown in Fig. 5 and the joint rates are shown in Fig. 6. The reaction force of each robotic arm is shown in Fig. 7 and from the figure it is clear that the torque exerted by right arm is opposite to that of the left arm. The residual forces and torques are plotted in Fig. 8 and Fig. 9, respectively. From the plot of reaction torques on the CubeSat (Fig. 8) it is clear that the reactionless manipulation algorithm is working perfectly. In the plot of joint velocities (Fig. 5), it is evident that the shoulder joint and the wrist joint are moving at higher joint rates to compensate for the trajectory provided. A future work would be to optimize the trajectory for the left arm to reduce these joint rates and also the reaction forces on the CubeSat.

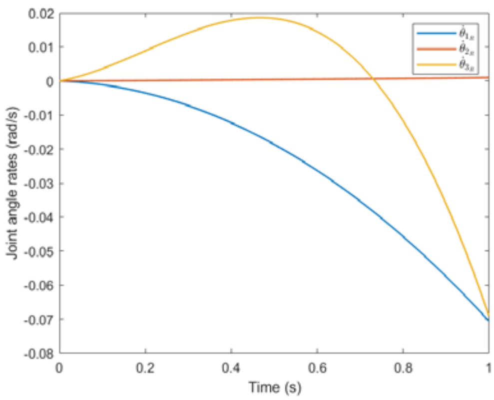

Figure 6: The variation in the angular velocities of the right arm for the given motion.

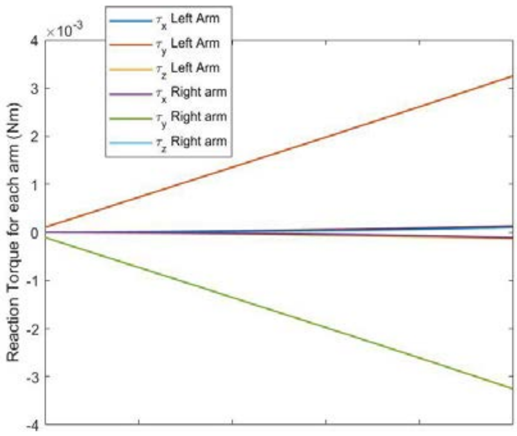

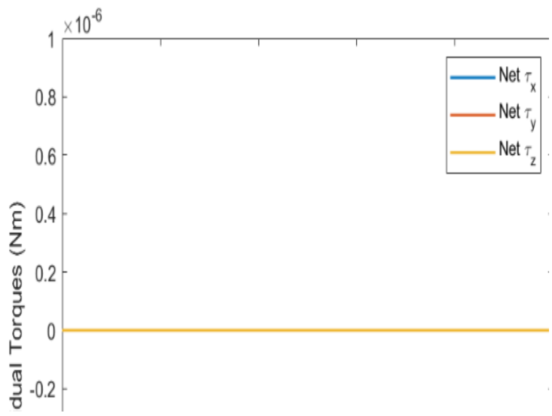

Figure 7: Reaction torque V/s Time

Figure 8: The net torque acting on the satellite

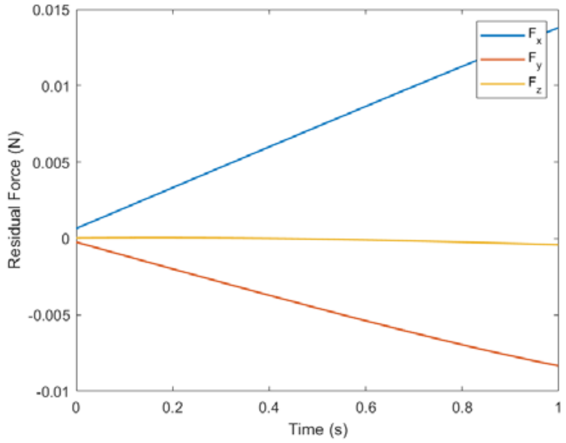

Figure 9: The net forces acting on the satellite.

7. Conclusion

In this paper the reactionless manipulation of a dual 3-DoF robotic arms on a 1U CubeSat is studied. The forward and inverse kinematics of the arms were derived using modified DH parameters. The dynamics of the arms was mathematically simulated using the Iterative Newton-Euler method to obtain joint torques required for the manipulator to move in a particular trajectory. These results were verified using MSC ADAMS, a commercially available multi-body dynamics package. Henceforth, an algorithm for reactionless manipulation was developed such that the left arm performs a task, and the right arm works in order to balance the reaction torques. This analysis was done for a simple 3-DoF arm which only balances the reaction torques on the CubeSat. The said method can also be used in a dual n-DoF system attached to a spacecraft. But a minimum of 6-DOFs is required to balance both the reaction forces and torques completely.

8. Appendix

A. Iterative Newton Euler Equations

The various terms used in iterative Newton Euler method are:

- ω_{i+1}^{i+1} is the angular velocity of link $i+1$ w.r.t. the frame $i+1$.
- $\dot{\omega}_{i+1}^{i+1}$ is the angular acceleration of link $i+1$ w.r.t. the frame $i+1$.
- $\dot{v}_{i+1}^{i+1}$ is the linear acceleration of link $i+1$ w.r.t. the frame $i+1$.
- $\dot{v}_{C_{i+1}}^{i+1}$ is the linear acceleration of the CoM (centre of mass) of link $i+1$ w.r.t. the frame $i+1$.
- F_{i+1}^{i+1} is the inertial force acting at the CoM of link $i+1$ w.r.t.the frame $i+1$.
- N_{i+1}^{i+1} is the inertial torque acting at the CoM of link $i+1$ w.r.t. the frame $i+1$.
- f_i^i is the force exerted on link i by link $i-1$.
- n_i^i is the torque exerted on link i by link $i-1$.

Outward Iteration (For these equations, i varies from 0th to 2nd):

$$\omega_{i+1}^{i+1} = R_i^{i+1}\omega_i^i + \dot{\theta}_{i+1}\hat{Z}_{i+1}^{i+1} \tag{32}$$
$$\dot{\omega}_{i+1}^{i+1} = R_i^{i+1}\dot{\omega}_i^i + (R_i^{i+1}\omega_i^i) \times \dot{\theta}_{i+1}\hat{Z}_{i+1}^{i+1} + \ddot{\theta}_{i+1}\hat{Z}_{i+1}^{i+1} \tag{33}$$
$$\dot{v}_{i+1}^{i+1} = R_i^{i+1}(\dot{\omega}_i^i \times P_{i+1}^i + \omega_i^i \times (\omega_i^i \times P_{i+1}^i) + \dot{v}_i^i) \tag{34}$$
$$\dot{v}_{C_{i+1}}^{i+1} = \dot{\omega}_{i+1}^{i+1} \times P_{C_{i+1}}^{i+1} + \omega_{i+1}^{i+1} \times (\omega_{i+1}^{i+1} \times P_{C_{i+1}}^{i}) + \dot{v}_{i+1}^{i+1} \tag{35}$$
$$F_{i+1}^{i+1} = m_{i+1}v_{C_{i+1}}^{i+1} \tag{36}$$
$$N_{i+1}^{i+1} = I_{i+1}^{C_{i+1}}\dot{\omega}_{i+1}^{i+1} + \omega_{i+1}^{i+1} \times I_{i+1}^{C_{i+1}}\omega_{i+1}^{i+1} \tag{37}$$

Inward Iteration (i varies from 3rd to 1st in descending order)

$$f_i^i = R_{i+1}^i f_{i+1}^{i+1} + F_i^i \tag{38}$$
$$n_i^i = N_i^i + R_{i+1}^i n_{i+1}^{i+1} + P_{C_i}^i \times F_i^i + P_{i+1}^i \times R_{i+1}^i f_{i+1}^{i+1} \tag{39}$$

The moment of inertia (MoI) used in Newton-Euler method is such that the off-diagonal terms are the negative inverse of those obtained from the CAD model (Solidworks). If the MoI obtained from the CAD model is,

$$I_{CAD} = \left[I_{xx}\ I_{xy}\ I_{xz}\ I_{xy}\ I_{yy}\ I_{yz}\ I_{xz}\ I_{yz}\ I_{zz} \right]$$

Then, the MoI used in the Newton-Euler method is,

$$I_i^{C_i} = \left[I_{xx}\ -I_{xy}\ -I_{xz}\ -I_{xy}\ I_{yy}\ -I_{yz}\ -I_{xz}\ -I_{yz}\ I_{zz} \right]$$

9. Acknowledgements

The authors would like to thank ISRO Inertial Systems Unit (IISU) for allowing the summer internship and the use of its facilities. We thank Dr. D. Sam Dayala Dev (Director, ISRO Inertial Systems Unit) for his encouragement and insightful comments on the work. We are grateful to Prof. S. Gurunarayanan (Dean, Practice School Division) for enabling this collaboration between BITS Pilani and IISU.

10. References

[1] Yangnian Wu, C. Gosselin, “Design of Reactionless3-DoF and 6-DoF parallel manipulators using parallelepiped mechanisms”, IEEE Transactions on Robotics, VOL. 21, NO.5, October2005.

[2] Remi Ricard, C. Gosseli, “On the development of Reactionless parallel manipulators”, ASME 2000 Design Engineering Technical Conferences and Computers and Information in Engineering Conference Baltimore, Maryland, January 2000

[3] Sunil Agrawal, Abbas Fattah, “Reactionless space and ground robots: Novel designs and concept studies”, Mechanism and Machine Theory, VOL.39, pp 25-40, January 2004.

[4] Sunil K. Agarwal, “Design and simulation of a class of spatial Reactionless manipulators”, Robotica, VOL.23, Issue 1, pp 75-81, January 2005.

[5] V.H. Arakelian, M.R. Smith, “Design of planar 3-DoF 3-RRR Reactionless parallel manipulators”, Mechatronics, VOL.18, Issue 10, pp 601-606, December 2008.

[6] K. Yoshida, K. Hashizume, S. Abiko, “Zero reaction maneuver: flight validation with ETS-VII space robot and extension to kinematically redundant arm”, Proceedings of the 2001 IEEE International Conference on Robotics and Automation, ICRA 2001, VOL.1, pp 441-446, January 2001.

[7] P. Piersigilli, I. Sharf, A.K. Misra, “Reactionless capture of a satellite by a two degree-of-freedom manipulator”, Acta Astronautica, VOL.66, Issue 1-2, pp 183-192, January–February 2010.

[8] E. Papadopoulos, A. Abu-Abed, “On the Design of Zero Reaction Manipulators”, Journal of Mechanical design, VOL.118, Issue 3, pp 372-376, September 1996.

[9] Sunil Kumar Agrawal, Shravan Shirumalla, ”Planning motions of a dual-arm free-floating manipulator keeping the base inertially fixed”, Mechanism and Machine Theory,VOL.30, Issue 1, pp 59-70, January 1995.

[10] S.V. Shah, Inna Sharf, A.K. Mishra, “Reactionless Path Planning Strategies for Capture of Tumbling Objects in Space Using a Dual-Arm Robotic System”, AIAA Guidance, Navigation, and Control (GNC) Conference, August 2013

[11] S. V. Shah, A. Gattupalli, A.K. Misra, “Energy Optimum Reactionless Path Planning for Capture of Tumbling Or-biting Objects using a Dual-Arm Robot”, AMM, India,2013

[12] Dragomir N. Nenchev, Kazuya Yoshida, Prasert Vichitkulsawat, Masaru Uchiyama, Reaction Null-Space Control of Flexible Structure Mounted Manipulator Systems, IEEE Transactions on Robotics and Automation, VOL. 15, NO. 6, December 1999
[13] Thai Chau Nguyen-Huynh, Inna Sharf, ”Adaptive Reactionless Motion and Parameter Identification in Post capture of Space Debris”, JGCD, VOL.36, Number 2, March2013
[14] Hiroki Sone, Dragomir N. Nenchev, ”On some practical Reactionless motion tasks with a free-floating space robot”, Proceedings - IEEE International Conference on Robotics and Automation, pp 2836-2841, June 2015
[15] John J.Craig, ”Introduction to Robotics: Mechanics and Control”, 3rd ed., Pearson, 2005

Automated Test Jig For Electrical Isolation Test Of Electrically Integrated Sections Of Aerospace Vehicles

Arvind kumar kushwaha
CAS
Hyderabad
arvind@cas.drdo.in

Praveen Tandon
CAS
Hyderabad
praveen.tandon@cas.drdo.in

Pramod Kumar Jha
CAS
Hyderabad
pkj@cas.drdo.in

Suresh Kumar Siripuram
CAS
Hyderabad
suresh.tweet@gmail.com

***Abstract*—An electrical isolation test is a direct current resistance test, that is performed between sub circuit common and subsystem chassis to verify that a specified level of isolation resistance is met. Isolation resistance measurements may be achieved using a high impedance ohmmeter, digital multi-meter (DMM). A minimum acceptable resistance value is usually specified. In aerospace where the isolation needs to be checked between high numbers of pins to chassis at various stage level is very cumbersome job. Since these connectors are densely populated and the manual isolation testing there is a possibility to damage connector pins while testing, due to poor workmanship and Apart from above difficulty the time duration of isolation test is very high. The automated test jig for isolation test is developed to come across these problems. This automated test jig is developed over NI platform with PXI chassis, Multiplexer and DMM cards and having an automated test and report generation features.**

Keywords—Isolation Test, Electrical Connector, LabVIEW, continuity.

1. Introduction

In aerospace vehicle industry electrical integration and testing of electrical cable harness are critical because the overall system performance depends on the healthiness of cable harness therefore ensuring the quality of the cable harness is necessary. The required quality and reliability of cable harness can be achieved by specifying the test and type of equipment to be used during cable harness acceptance.

The two most commonly measured parameters of electrical cable harness testing are isolation and continuity. Isolation measurements are carried during the assembly of cable harness as well as integration of assembled cable harness in to the sections.

Isolation testing is conducted between one or more electrical circuits of the same subsystem. The test often reveals problems that occurred during assembly, such as defective/wrong component, improper component placement/orientation and wire insulation defects that may cause inadvertent shorting or grounding to chassis, defect in connectors, cut in cable assembly in turn compromising electrical circuit quality and product safety& reliability. This paper is about the basic isolation test methods and its drawback and development of automated isolation test jig to overcome the drawback of traditional testing methods.

2. Isolation Test Description

A basic electrical diagram of connector is shown in Fig .1 and during cable harness testing, isolation is carried out at connector level to ensure that none of the connector pins are shorted to each other and verifies each connector pin have specified isolation resistance or not, because improper ground or pin Short of the connector will drastically affect the overall performance of the system.

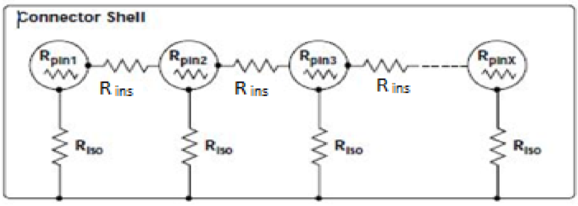

Figure1: Basic electrical connector with isolation resistance (R_{ISO}), insulation resistance (R_{ins}).

Isolation test done by applying a known voltage between the pin and connector body, thus allows current to flow and by measuring current, corresponding resistance value is obtained. The resistance value is compared with specified value of the resistance for particular pin of the connector with acceptable error value. If the obtained value is less than the specified threshold level, the connector pin fails to maintain the minimum isolation resistance. To take the necessary action to achieve the required isolation resistance value. Each pin of all individual connectors will undergo this test to qualify each connector pins are maintaining required level of isolation.

Isolation test of electrical connector is carried out manually using digital multi meter has following drawbacks.

(i) Possibility of connector Pin damage
(ii) Time consuming process
(iii) Prone to human errors

To overcome above drawbacks an automated Isolation test jig developed. Configuration of the required range of resistance measurement, and kept the minimum length of the cables for electrical connector, and required settling time was selected to obtain the accurate output in the automated test jig for the isolation test. and this paper is all about the development and features of the Automated Isolation Test Jig.

3. Automated Test Jig

Automated test jig for isolation check to test the connector pins of assembled and Integrated cable harness has been developed based on PXI digital multi meter (DMM) Card, multiplexer (MUX) Card and LabVIEW based GUI to control and operate the automated test jig.

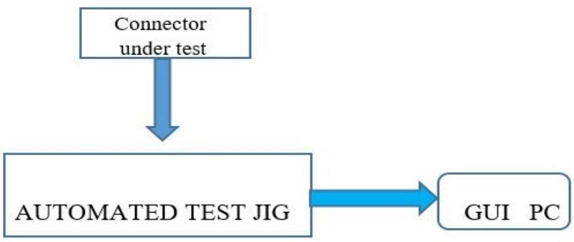

Figure 2:. Block diagram representation of automated test jig

A. Test system description

Automated Test Jig is designed and developed using NI PXI Technology.This Automated Test Jig is a bench top unit equipped with following mentioned hardware

- (i) NI PXI-1036-6 slot chassis with AC power supply and real time controller
- (ii) NI PXI-8360 Express MXI kit
- (iii) NI PXI-2575 196 channel multiplexer
- (iv) NI PXI-4065 6 ½ digit digital multi meter (DMM) And LFH connector bare wire switch cable

Operation of test jig is through GUI on controller PC and communication between controller pc and PXI chassis using a MXI card to control the PXI express systems.

B. Test setup

Test setup for isolation resistance measurement using above mentioned Hardware is shown in Fig 5. The detailed hardware description, software development will be discus further.

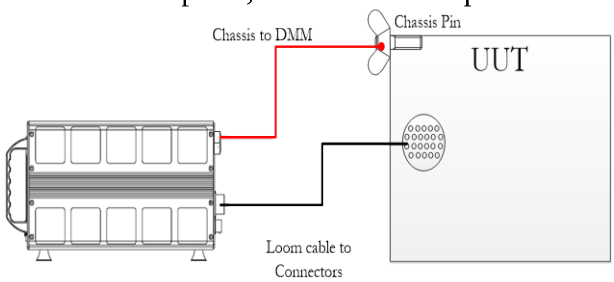

Figure 3: Test set up for isolation resistance measurement

Chassis ground pin of UUT is connected to High terminal of DMM Card and all the multiplexer output will be connected to connectors using the Loom cables.

4. Hardware Overview

Automated test jig for isolation test was developed using NI (National Instruments) hardware they are PXI chassis, controller, digital multimeter, multiplexer switch.

A. PXI -1036,6 slot 3U chassis

The National Instruments PXI-1036 is designed for remote control applications having five slots for measurement modules and one for controller. Its smaller package works with a remote controller. This low-cost, low-power chassis is ideal for remote, real-time, and data acquisition applications

B. NI PXIe-8360

The NI PXI e-Express Card 8360 in the controller PC is connected via an Express Card MXI cable to an NI PXIe-8360 module in slot 1 of a PXI Express chassis. The NI PXIe-8360 module implements a PCI Express-to-PCI Express switch that connects the cabled PCI Express link to the PCI Express bus that is used in PXI Express chassis.

C. PXI-4065 PXI Digital Multi-Meter (DMM) 6½-Digit DMM (300V,3A)

The 6½-digit PXI-4065 PXI digital multi meter (DMM) is a measurement module for measuring voltage, current, and resistance with ±300 VDC/Vrms of isolation, current measurements up to 3 A, and 2- or 4-wire resistance measurements.

D. NI PXI-2575 196 Multiplexer Switch

The National Instruments PXI-2575 is a high-density multiplexer switch module. the NI PXI-2575 is capable of routing hundreds of signals to measurement devices or from source units. Each channel of multiplexer uses electromechanical relays and is capable of switching up to 100 VDC/100 VAC or 1 A. With a scanning speed of up to 140 cycles/s, Switch card of multiplexer is configured to connect automated test jig to many test pins of connector under test. Each switch is controlled by main frame that can be programmed with desired test sequence. the system has built in trigger to allow the system switch between the various test pins of the connector.

5. Software Development Description

For Isolation test of the integrated cable harness assembly of aerospace vehicle, software developed on NI based LabVIEW platform. The software development architecture has been chosen such a way that any manual/human errors can also eliminated. Login screen will be the first screen confirming the identity of the user and their access level (Administrator or user). Administrator creates end users to perform Isolation test. After successful login, Home page on GUI will display a group of buttons that are clicked to activate another window and inter functions as shown in Fig 7.

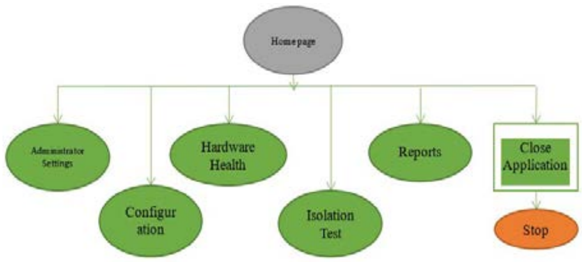

Fig 7. Architectural Design of home page

The development of software having inbuilt features for hardware health check. As soon as software application is open, first it will check the all hardware connected to it. If it health is found to ok of all Cards, then only software will be ready for further isolation test.

The isolation test window is designed in such way that the user has both manual control and automated isolation testing. All the pins of electrical connector which undergone isolation test has been configured in systems with standard value of isolation resistance for particular pins. The measured value of isolation resistance for each pin of electrical connector is compared with standard value of respected pin and the results will be displayed. For report generator suitable format has been identified and saved data can be reproduced back in required report format.

6. Isolation Test procedure

Automated test jig involves sequence of actions to complete the isolation test and generate the final test report. After the hardware health check is performed and it found to be ok isolation test is performed. Isolation test can be performed in two modes Auto& Manual mode, when requirement is for all pins of electrical connector select Auto mode or isolation is required on selected pins only then select Manual mode.

Isolation resistance measurement using NI PXI 4065 DMM card has resistance ranges Auto range or configurable resistance range of 100Ω, 1KΩ, 100KΩ, 1MΩ, 100MΩ. The accuracy of measurement can be improved by selection of suitable range of isolation resistance measurement. The Values Related to Open Terminal Voltage and Short Circuit current are Observed from The Isolation Test Jig Unit under different Resistances range of

DMM is shown below Tables. Table-1 is the range selection in DMM but no resistance is applied.

Table-1. Voltage, current measurement across DMM Resistance

S.NO	DMM RANGE	OPEN TERMINAL VOLTAGE	SHORT CIRCUIT CURRENT
1	Auto range	2.5 - 4.8V	0.6mA -0.74mA
2	100MΩ	2.53V	0.4µA
2	10MΩ	4.88V	0.4µA
3	1MΩ	6.02V	4.7µA
4	100KΩ	6.01V	9.6µA
5	10KΩ	11.64V	96.4µA
6	1KΩ	5.9V	964µA
7	100Ω	5.9V	965µA

Table 2. Voltage, current measurement across DMM measurement with fixed range and resistance applied

S.NO	DMM RANGE	APPLIED RESISTANCE	VOLTAGE	CURRENT
1	10KΩ	1KΩ	0.094V	87.6 µA
2		2.1 KΩ	0.208V	92.2 µA
3		3.2 KΩ	0.316V	93.6 µA
4		4.7 KΩ	0.45V	94.5 µA
5		5.5 KΩ	0.53V	94.4 µA
6		6.1 KΩ	0.59V	95 µA
7		7.4 KΩ	0.714V	95.3 µA
8		8.0KΩ	0.78V	95.4 µA
9		9.1 KΩ	0.87V	95.6µA

Table 3. Voltage Measurement across DMM with different Resistors with Different Ranges

Applied Resistance	Measured voltage		
	Auto Range	10MΩ Range	100MΩ Range
1KΩ	0.4V	0.4mV	5.2mV
1MΩ	0.4V	042V	0.42V
1.5MΩ	0.62V	0.62V	0.62V
2.2MΩ	0.88V	0.87V	0.74V
3MΩ	1.2V	1.2V	0.98V
4.7MΩ	1.6V	1.57V	1.06V
6.8MΩ	2.06V	2.05V	1.32V
10MΩ	2.56V	2.55V	1.67V

LabVIEW based GUI is developed to control the automated test jig for isolation checks is shown in Fig 8. The configuration of selected connector gives each pin with its isolation resistance. The test mode compares the measured isolation resistance of the specific pin with isolation resistance in the configuration. based on the test performance report will be generated and it Saved to PC.

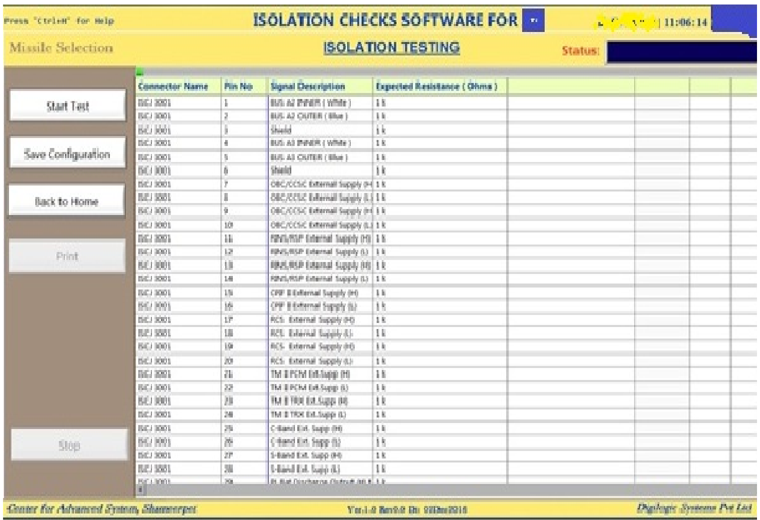

Fig 8. shows isolation test GUI window based on LABVIEW.

7. Simulation & Experimental Results

Test report generated after the completion of the isolation test. it gives the test status for each pin in standard report format as shown in Fig 9. The remark is also shown against each pin of the electrical connector. If the error percentage of isolation resistance is within allowable range, it shows as pass otherwise fail status. The test report can be download to PC.

Development of Automated test jig for Isolation resistance test ensured that isolation resistance test completed within less time and report was generated without any errors.

S.No	Channel No	Connector pin number	Resistance Value		Error (%)	Remarks (status)
			Expected resistance (Ω)	Measured resistance (Ω)		
1	CH1	1	1 k	980.8903	-1.9	Pass
2	CH2	2	1 k	980.9799	-1.9	Pass
3	CH3	3	1 k	981.6309	-1.8	Pass
4	CH4	4	1 k	985.5832	-1.4	Pass
5	CH5	5	1 k	987.3777	-1.3	Pass
6	CH6	6	1 k	983.1879	-1.7	Pass
7	CH7	7	1 k	984.4054	-1.6	Pass
8	CH8	8	1 k	989.042	-1.1	Pass
9	CH9	9	1 k	984.177	-1.6	Pass
10	CH10	10	1 k	983.9228	-1.6	Pass
11	CH11	11	1 k	985.8597	-1.4	Pass
12	CH12	12	1 k	981.2553	-1.9	Pass
13	CH13	13	1 k	985.5387	-1.4	Pass
14	CH14	14	1 k	980.5632	-1.9	Pass

Fig 9. Test report generated for the electrical connector.

8. Acknowledgment

Author would like to thank Dr. M Manickvasagam, Director CAS for permission and extended support to development of Automated test jig.

9. Refrence

[1] Data Card of Cable Harness
[2] Data Sheet of PXI-4065 PXI Digital Multi-Meter
[3] Data Sheet of NI PXI-2575 196 Multiplexer Switch
[4] Data Sheet of NI PXIe 8360
[5] Data Sheet of PXI 1036
[6] www.NI.com

SLAM based Autonomous Navigation of Differential Wheeled Robot using Laser scanner and Robot Operating System

Manish Pujari
Vehicles Research & Development Establishment
Ahmednagar
manishpujari@vrde.drdo.in

Ms. Prajakta V Koratkar
Defence Institute of Advanced Technology
Pune

Abstract — **In today's robotics era, dependency and necessity of robots in various applications such as Defence, Space, Medical, Automobile, Industrial etc. fields is increasing day by day. To cater this, robots with high degree of autonomy are very much essential. Our objective is to enable a differential wheeled robot to navigate in a structured environment autonomously. This requires mapping of unknown environment, localization of the platform and navigation in that environment without hitting any obstacle. The presented work describes how a small range laser scanner used with Robot Operating System (ROS) in a mobile robot for localization, mapping and autonomous navigation in a Lab environment. In this project work, standard mapping algorithms have been used for map generation and comparison of the maps generated for their accuracy.**

Keywords —Mobile, Robotics, SLAM, Mapping, Localization, Navigation, ROS, LiDAR.

1. Introduction

A fully autonomous robot will have the ability to acquire information about its environment through its sensors and will work in the environment avoiding situations that are harmful to its environment or to itself. An autonomous navigation system is an integrated suite of sensors and software modules that enables autonomous navigation capabilities. To develop truly autonomous navigation in a robot, SLAM is the first and foremost requirement.

The simultaneous localization and mapping (SLAM) problem says that, how a mobile robot, when placed in an unknown environment, incrementally builds its own map for the surrounding as well as simultaneously detects its own location in the map. The SLAM is more difficult problem where both map and pose of robot are unknown. There are several algorithms [2] known for solving it, Popular algorithms are based on the particle filter (Fast SLAM) and Kalman filter.

It was originally developed by Hugh Durrant-Whyte and John J. Leonard[1] based on their earlier work. SLAM is concerned with the problem of building a map of an unknown environment by a mobile robot while at the same time navigating the environment using the map.

The selection of SLAM algorithm depends on the available resources and robot platform. No SLAM algorithm is perfect but its performance varies depending on the environment. Various SLAM algorithms are employed in self-driving cars, unmanned aerial vehicles, autonomous underwater vehicles, rovers, etc.

Earlier waypoint based navigation was implemented in similar differential drive robot but because of GPS outage problem in the indoor environment it couldn't navigate in the indoor environment. To enable a mobile robot to traverse in the indoor environment without GPS data there was a requirement of development of software system that process odometry data and perception sensor data to generate map of surroundings and localize robot in this map. To address this problem, it was decided to develop indoor SLAM along with localization and path planning algorithm to enable autonomous navigation in indoor environment. Under this project, a small range Laser scanner with range of 10 meters, differential wheeled robot platform (FireBirdVI) along with ROS framework architecture[13] are used. Standard mapping algorithms like [18] [13] Gmapping and [13] Hector slam have been used for map generation and generated maps are compared for their accuracy. For localization purpose Monte Carlo Localization algorithm (MCL) is used because MCL is the most popular[3] approach to date. The MCL algorithm uses a particle filter to represent the distribution of likely states, with each particle representing a possible state, i.e., a hypothesis of where the robot is. For navigation purpose, [13] ROS navigation stack is used.

2. Related Work

In this article [1] SLAM Problem is explained starting from the history and SLAM structure explained along with the existing solutions to the SLAM problem like EKF based and Particle filter-based Algorithms with their respective mathematical equations. In this paper [2] an superior approach to generate 2D maps with RBPF is presented. In this paper, most recent data and odometry data along with the scan matching process are used for the generation of more accurate proposal distribution. This led to a reduced number of samples. In this paper [4] Gmapping SLAM with Hokuyo LiDAR is utilized to generate a map of the university campus. Authors tried combinations for indoor, outdoor, or combination and observed that the accuracy is good for the indoor environment but poor for an outdoor or mixed environment. In this article [5], the author has given a good explanations of SLAM technologies for mobile robots. Under paper[6], author have utilized the Robot Operating System (ROS) as software framework and utilized Navigation Stack along with Gmapping stack to enable the autonomous navigation. Researchers have used ultrasonic sensors and HD web camera as perception sensors. In this paper [7] OrthoSLAM algorithm is presented which was found that this is less time consuming and space consuming for small indoor environment. In this paper [8] authors have presented the SLAM algorithm based on digital camera and odometry data, which performed good in dynamic environments. Under this work [9] authors have used a model robot that is made using gazebo package and ROS framework architecture. Author made simulation in the rviz tool of ROS and also used a Gmapping algorithm. The Gmapping algorithm uses laser data to make the map. Under this [10] authors have used a mines rover platform which is a six-wheel platform along with URG 04 laser sensor. The team has developed 200 lines of small code for SLAM. In this paper [11] Gazebo simulation approach to simultaneous localization and mapping (SLAM) is described. Under this work [12] a Gazebo and ROS have been used for simulation of SLAM algorithm. In this paper [16] three 2D-SLAM algorithms namely Cartographer, Gmapping, and Hector-mapping were compared and evaluated and it is concluded that Gmapping algorithm gives best results in the typical indoor environment whereas Hector-slam performed good in long passages like environment, and Cartographer has more advantages in a complex environment. In the paper [17], An introduction and fundamentals of various path planning algorithms have been explained.

3. Development Methodology

Under this project, development of autonomous navigation system for a differential drive mobile robot (FireBird VI) using Robot Operating System (ROS) software framework architecture and small range perception sensor was done. While development of the autonomous navigation system the comparative analysis of two SLAM algorithms namely Gmapping SLAM and Hector SLAM is carried out in combination with Navigation Algorithm. For localization purpose Adaptive Monte Carlo Localization algorithm (ACML) was used because ACML is the most popular approach to date [3]. For navigation, ROS navigation stack has been used with a visualization tool called RViz tool to visualize the robot pose, map and goal. FireBird VI mobile robot platform was utilized for the experiment purpose.

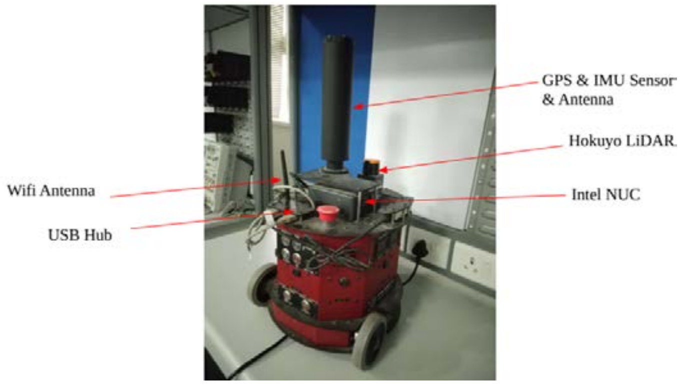

Figure 1. Robotic Test platform with sensors and controller

Experimental setup is shown in following figure, where a local controller running ROS master is communicating with Robot hardware with specified protocol.

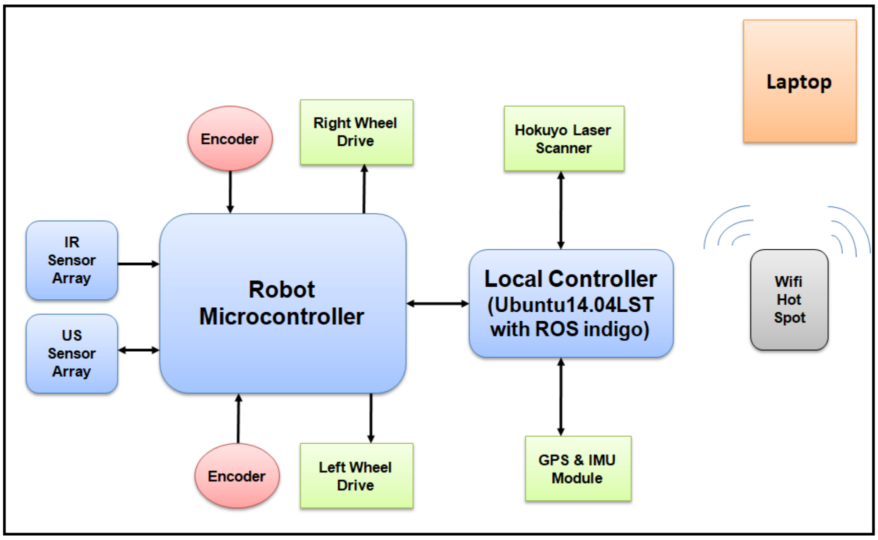

Figure 2. Block Diagram of autonomous mobile robot setup

In the block diagram shown in Figure 2, robot platform is having an independent microcontroller which is directly connected with wheel drives and encoders. Also, one intel NUC has been used for local controller.

4. Implementation

Local controller is connected over serial port with robot controller. Ubuntu 14.04 LTS along with ROS Indigo is installed on the local controller for all control software. Robot takes motion commands in the form of linear and angular velocities i. e. v and w. Hokuyo LiDAR (Laser scanner) UST 10LX has been used as perception sensor. This LiDAR scans for 270° with range of 10m. This is connected to local controller over Ethernet interface.

Power supply is provided through two 16.8V 1.5A batteries, one for robot and one for local controller.

Software development and deployment was done with ROS on the local controller. For laser scanner, standard ROS URG package was used with required configuration. ROS TF package was used to publish required transformations in the robot.

The standard ROS packages offer several features and in order to use these features, the current work utilizes readily available ROS standard package.

There are following major stages of development and testing were carried out in current work:

(i) Manual Mapping of environment using ROS Hector SLAM package : under this robot was tele-operated in the test environment and laser data recorded along with tf (transformation) data using rosbag feature of ROS. Thereafter, recorded data were parsed to hector slam node and map of unknown environment was generated.

(ii) Manual mapping using ROS Gmapping package: in this stage also robot was tele-operated using keyboard and laser data along with tf and odometry data recorded. Thereafter, using Gmapping node map was generated from the recorded data.

(iii) Comparison of maps generated from Gmapping and hector slam was done and found that Gmapping generated maps are more correct.

(iv) Localization of robot in the map using ROS amcl package: in this live laser data and odometry data were used to localize the robot in the map. Rviz tool of ROS was used to provide initial pose of the robot to amcl node. After some travel it gives precise location of the robot in the map.

(v) Navigation using ROS Navigation Stack: Once map of the environment is generated and we have localized our robot in this map, we can go for autonomous navigation. In this current work the move base package of navigation stack has been used for path planning and autonomous navigation.

5. Results and Discussions

Under these current work, 2D maps of different office environments have been prepared by manually operating the robot using keys. Maps of resolution of 0.05m has been generated for three different size environments.

Figure 3 (a) Test Environment – I

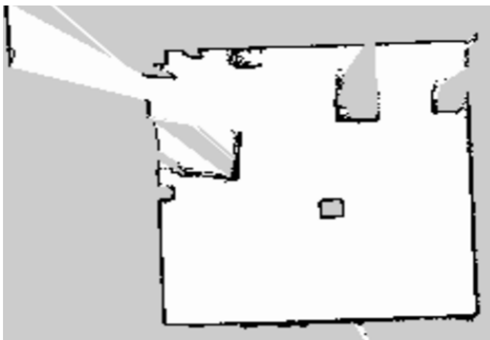

Figure 4 (b) Map generated from Hector SLAM

From the above results we can say, Hector mapping can generate decent map of the simple environments without using odometry data. Another test carried out at outside of lab that is a corridor as shown in the following Figure 4

Figure 5 Test Environment - Corridor

Under this environment straight passage with door opening, static objects, staircases, etc which created different shapes of obstacles. Under this environment when the angular and linear velocities are kept some higher (0.34rad/sec and 0.23m/s respectively) during testing in this environment. The map generated by hector mapping was distorted when at the T – junction a 'U'- turn was made whereas Gmapping generated map was more accurate as it used odometry data to correct robot's pose. Both the maps are shown in following figure:

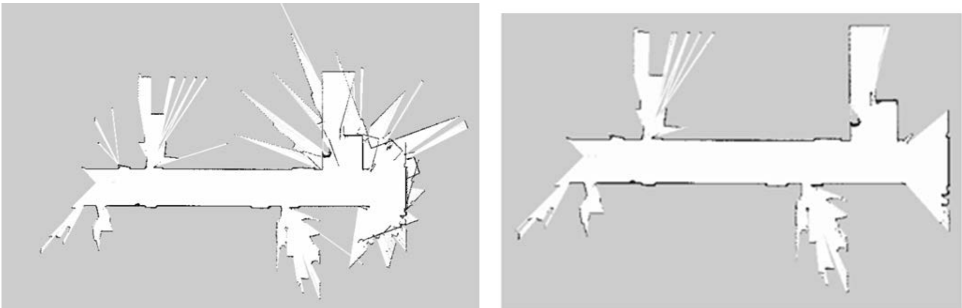

(a) (b)

Figure 6. Maps generated for Corridor (a) Hector SLAM and (b) Gmapping

Thereafter, a more complex environment with same angular and linear velocities was selected for mapping. The environment -3 and the map generated from the Hector SLAM are shown in following Figure 6

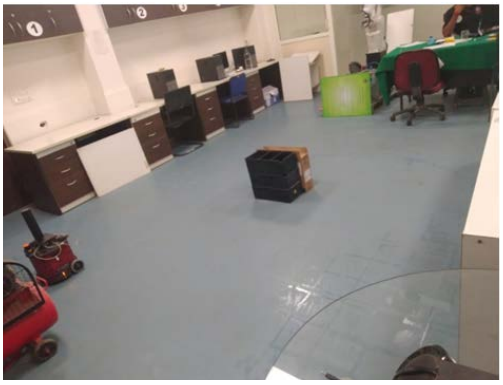

Figure 6 (a) Test Environment -3 Figure 7 (b) Map generated by Hector SLAM

From the above figures we can observe, as the complexity of the environment increases and if we operate robot on a bit higher angular speeds and frequent rotations then hector mapping gives lot of errors in the map generation. In the environment – 3, which is a relatively complex environment, the hector mapping fails to generate accurate, consistent and reliable map. The hector mapping doesn't use odometry data for map building thus it doesn't perform correction in map.

Now, in next stage, Gmapping was used for the same complex environment to build the map and resultant map is shown in Figure 7: As we can see, the map generated by Gmapping is more accurate, consistent and reliable. The ROS Gmapping package implements laser-based SLAM, through slam_gmapping node, which can create a 2-D occupancy grid map (like a building floor plan) from laser and pose data (odometry) collected by a mobile robot.

Figure 8. Map generated by Gmapping for Test Environment -3

Finally, the map generated by Gmapping was more accurate and reliable so it was selected for next stages of the autonomous navigation. For localization, standard ros package amcl package is used. The initial 2D pose estimate given through rviz refer Figure 8 and converged pose of the robot after some movement of robot using tele-operation is given in following Figure 9:

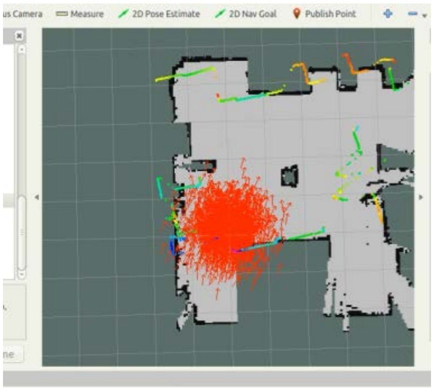

Figure 9. Initial pose of the robot given in rviz

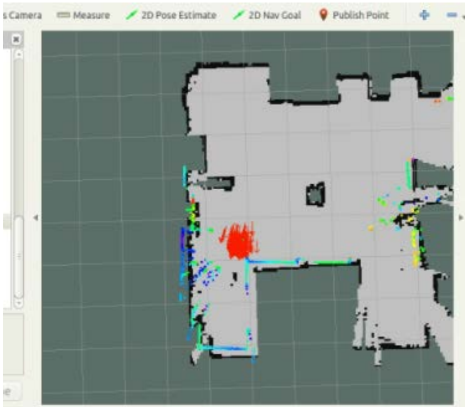

Figure 10. Converged pose of robot by AMCL

Once the robot is localized in the map we can perform autonomous navigation. For autonomous navigation ROS navigation stack[13] is used and move_base node is responsible for autonomous navigation using laser scanner data in the given map. The goal pose is given with the help of of 2D Nav Goal button of the rviz tool. Move_base node generate move command on “cmd_vel” topic in the form of standard message geometry_msgs/twist. Twist message is basically combination of linear and angular velocity. These commands are sent to robot microcontroller which further converts twist messages to motor speeds and run the motors.

6. Conclusion

The autonomous navigation of the differential wheeled robot in static indoor environment is achieved using ROS based software system. Two SLAM mapping algorithms named Hector mapping and Gmapping has been used to generate maps of various indoor environments and maps are compared for their accuracy. During this project, it has been observed that for simple environment and lower velocities Hector mapping generates decent maps, while for relatively more complex indoor environments and at some relative higher speeds it doesn't generate accurate map rather it generates distorted map. But the Gmapping generates good maps in conditions like complex environment, higher linear and angular velocities, etc. where Hector mapping fails because it also uses odometry data to correct the pose of the robot while generating maps. Finally, ROS navigation stack is used for autonomous navigation with Gmapping generated map and amcl localization of the robot in the map. From this research, it is observed that the robot performed good in terms of response time and time to achieve goal pose.

7. References

[1] H. Durrant-Whyte and T. Bailey, "Simultaneous localization and mapping: Part I," *IEEE Robot. Autom. Mag.*, vol. 13, no. 2, pp. 99–108, 2006.
[2] G. G, S. C, and B. W, "Improved Techniques for Grid Mapping with Rao-Blackwellized Particle Filters," *IEEE Trans. Robot.*, pp. 23–34, 2007.
[3] S. Thrun, "Probabilistic robotics," *Commun. ACM*, vol. 45, no. 3, pp. 52–57, 2002.
[4] W. A. Syaqur *et al.*, "Mobile Robot Based Simultaneous Localization and Mapping in UniMAP's Unknown Environment," *2018 Int. Conf. Comput. Approach Smart Syst. Des. Appl. ICASSDA 2018*, pp. 1–5, 2018.
[5] S. R. and M. R. Blas, "SLAM for Dummies," *Tutorial*, vol. 80, no. 4, pp. 699–705, 2000.
[6] M. K. N and T. Shreekanth, "Autonomous Robot Based on Robot Operating System (ROS) for Mapping and Navigation," vol. 6, no. 07, pp. 449–457, 2015.
[7] R. S. Viet Nguyen, Ahad Harati, "Ortho SLAM," pp. 12–19, 2007.
[8] N. Karlsson, E. Di Bernardo, J. Ostrowski, L. Goncalves, P. Pirjanian, and M. E. Munich, "The vSLAM algorithm for robust localization and mapping," *Proc. - IEEE Int. Conf. Robot. Autom.*, vol. 2005, no. April, pp. 24–29, 2005.
[9] R. Kannan Megalingam, C. Ravi Teja, S. Sreekanth, and A. Raj, "ROS based Autonomous Indoor Navigation Simulation Using SLAM Algorithm," *Int. J. Pure Appl. Math.*, vol. 118, no. 7, pp. 199–205, 2018.
[10] B. Steux and O. El Hamzaoui, "CoreSLAM: a SLAM Algorithm in less than 200 lines of C code," *Proceeding Int. Conf. Control. Autom. Robot. Vis.*, no. December, pp. 7–10, 2010.
[11] I. Afanasyev, A. Sagitov, and E. Magid, "ROS-based SLAM for a gazebo-simulated mobile robot in image-based 3D model of Indoor environment," *Lect. Notes Comput. Sci. (including Subser. Lect. Notes Artif. Intell. Lect. Notes Bioinformatics)*, vol. 9386, no. October, pp. 273–283, 2015.
[12] K. Takaya, T. Asai, V. Kroumov, and F. Smarandache, "Simulation environment for mobile robots testing using ROS and Gazebo," *2016 20th Int. Conf. Syst. Theory, Control Comput. ICSTCC 2016 - Jt. Conf. SINTES 20, SACCS 16, SIMSIS 20 - Proc.*, pp. 96–101, 2016.
[13] "ROS Tutorial, ROS Documentation, http://www.ros.org." .
[14] N. Robotics, "Hardware Manual," *Robotics*.
[15] C. Fairchild and T. L. Harman, *ROS Robotics By Example:* 2016.
[16] D. Shen, Y. Xu, and Y. Huang, "Research on 2D-SLAM of indoor mobile robot based on laser radar," *ACM Int. Conf. Proceeding Ser.*, 2019.
[17] N. Sariff and N. Buniyamin, "An overview of autonomous mobile robot path planning algorithms," in *SCOReD 2006 - Proceedings of 2006 4th Student Conference on Research and Development "Towards Enhancing Research Excellence in the Region,"* 2006.
[18] G. G. Cyrill Stachniss, Udo Frese, "www.openSLAM.org." .

Design and Construction of a Robotic Arm for Machining Solid Propellants

Venkattesh Kumar M
School of Mechanical Engineering
SASTRA Deemed University
Thanjavur

Manikandan K
School of Mechanical Engineering
SASTRA Deemed University
Thanjavur

Hari Krishnan R
School of Mechanical Engineering
SASTRA Deemed University
Thanjavur

Sreehari VM
School of Mechanical Engineering
SASTRA Deemed University
Thanjavur
sreehari_vm@mech.sastra.edu

***Abstract*—Due to the rapid development in defence and space technologies, usage of solid rocket boosters in spacecraft launches and missiles is getting increased attention. Prior to using solid propellant grains for thrust production, the propellant grains should be machined to get the desired size and shape for better combustion. Conventionally CNC machines have been used for machining process and it require more time and some manual operations like handling, feeding into the machine and so on. Nowadays a different composition of propellant with higher hardness materials is being used. Handling these materials may cause heath issues. So, there is a need for a new methodology to machine the solid propellants. The design and fabrication of a robotic arm for machining the solid propellant grains have been carried out in the present work. By using a robotic arm, the short comings of the conventional machining process can be overcome. The end effector consists of three main tools such as gripper, primary tool and secondary tool. Depending upon the operation, the respective tool will be ejected and performs the operations while the remaining tools will be held folded. The robotic arm employs a vacuum pump to collect the chips formed during the machining operations. The movement of the robotic arm is analysed by the forward kinematics formulated using Denavit-Haternberg (D-H) method. In this work, wax propellant is used to verify the machining operations using the robotic arm and to compare with the conventional machining methods. The conceptual design of the robotic arm with tool head, formulation of the forward kinematics using D-H conversion, verification of the performance characteristics of machining operation using the developed robot with conventional method are presented in this work.**

Keywords: Solid propellant grains, Conventional machining process, Robotic arm, D-H conversion, Wax propellant

1. Introduction

In present era, there is a huge race in the development of space technologies and military power such as exploration of new space missions, development of intercontinental ballistic missiles, etc. This development created the usage of solid propellant booster in larger amounts. Before using the solid propellants in space mission or in the missiles for thrust production, the solid propellant grains should be machined to attain desired dimension and shape for better combustion efficiency. [1] Conventionally, these propellant grains had to be machined in the CNC machines. But there are some disadvantages in this method, like it need some manual operations, it requires more time, and propellants with larger length cannot be machined easily and so on. Nowadays, the solid propellants with higher hardness have been used to produce the maximum amount of thrust in a short span of time to achieve the greater velocity in rockets, hypersonic and supersonic missiles. The propellant grains with higher hardness cannot be machined effectively and safely by the conventional method, so there is a need for a new methodology to machine the solid propellants [2]. Robotic arms can be employed to work in conditions like high temperature, polluted air zone, handling hazardous materials, etc. [3].

The present work discusses the designing of a robotic arm to overcome from the short comes of the conventional machining process and to implement the robotic arm to machine the solid propellant grains. The movement of the robotic arm is determined by the forward kinematics formulated using Denavit-Hartenberg(D-H) method. By using this data, the robotic arm will move and make the machining operation. The forces acting on the robotic arm have been calculated and used in the designing process. A prototype has been fabricated and functional verification have been carried out on wax propellant.

2. Design of Robotic Arm for Propellant Machining

A robotic arm has been designed with 6 degrees of freedom (DoF) so that, it can move freely to any coordinate positions within the workspace. The robotic arm is intended to set rigid joint bodies capable to take a different configuration and move between these configurations with prescribed limits on velocity and acceleration. Present robotic arm was designed with revolute joints. Some of the important robotic arm parameters considered in present work are: DoF: 6, Number of links: 5, Number of joints: 6, Joint speed: 0.2s/450, Hardware interface: 3 pin connector, Gripper opening: 12cm, Torque (motor): 10kg-cm. The specifications of robotic arm are given in Table 1 and the details of the joint are mentioned in Table 2.

Table 1. Weight and length of the robotic arm.

Name of the link	Weight of each link	Length of each linkage
Link1(base)	65g	12cm
Link 2 (shoulder)	125g	25.5cm
Link 3 (elbow)	72g	13.5cm
Link4 (wrist)	48g	9cm
Gripper link	65g	12cm

Table 2. Weight and rotation of the robotic arm joints.

Name of the joint	Weight of each joint	Length of each joint
Base Joint	45 g	180 degrees spin
Shoulder	90 g	120 degrees pitch
Elbow	90g	120 degrees pitch
Wrist	45g	150 degrees pitch
Gripper link	40 g	180 degrees roll

A. Robotic Arm Design

The robotic arm end effector consists of three main tools to machine the propellants such as gripper, primary tool and secondary tool. Each tool is designated with unique functionalities4. The primary tool is responsible for making the different thrust pattern, secondary tool will make the finishing operation and gripper will be used to lift and place the propellant grains in the pre-defined coordinate points. The robotic arm employs a vacuum pump to collect the chips formed during the machining process. Machining parameters have been considered and calculated for every propellant grains before the start of machining process.The present robotic arm design in AutoCAD is in Fig. 1and the block diagram of the functioning of robotic arm for propellant machining is shown in Fig. 2.

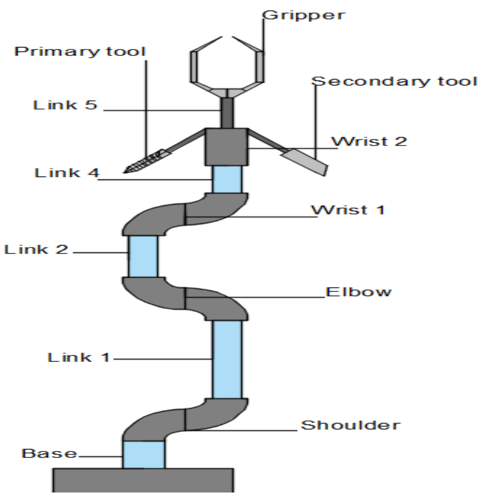

Figure 1. Robotic arm design done in AutoCAD.

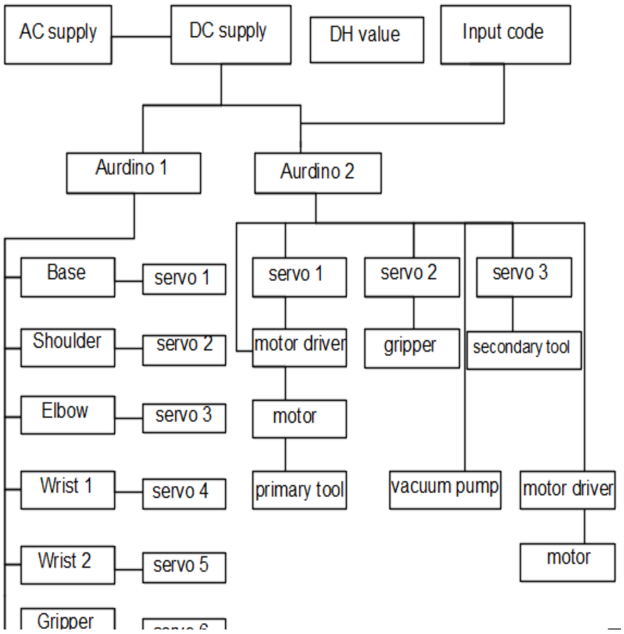

Figure 2. Architecture of present robotic arm.

B. Kinematics Study of the Arm using Forward Kinematics

Forward kinematics deals with the problem of finding end-effector pose (position as well as orientation) with given joint variables. Robotic arm kinematic structure is shown in Fig.3. Robotic arm links and joints are shown in Fig. 4. Generally, the forward kinematics is solved by using D-H conversion method5.This method depends on four parameters:ai-1 is the distance from Zi to ZI+1 measured along Xi,αi-1 is the angle from Zi to Zi+1 measured along XI, di is the distance from Xi-1 to Xi measured along Zi and Ɵi is the angle from Xi-1 to Xi measured along Zi. Using convention, each homogenous transformation (TI) is represented as a product of four transformation matrices.

$$T_i = Rot_{z,\Theta i} \times Trans_{z,di} \times Trans_{x,ai} \times Rot_{x,ai} (1)$$

$$T_I = \begin{bmatrix} C\theta & -S\theta & 0 & 0 \\ S\theta & C\theta & 0 & 0 \\ 0 & 0 & 1 & 0 \\ 0 & 0 & 0 & 1 \end{bmatrix} \times \begin{bmatrix} 1 & 0 & 0 & 0 \\ 0 & 1 & 0 & 0 \\ 0 & 0 & 1 & d \\ 0 & 0 & 0 & 1 \end{bmatrix} \times \begin{bmatrix} 1 & 0 & 0 & a \\ 0 & 1 & 0 & 0 \\ 0 & 0 & 1 & 0 \\ 0 & 0 & 0 & 1 \end{bmatrix} \times \begin{bmatrix} 1 & 0 & 0 & 0 \\ 0 & Ca & -Sa & 0 \\ 0 & Sa & Ca & 0 \\ 0 & 0 & 0 & 1 \end{bmatrix}$$

$$T_I = \begin{bmatrix} C\theta & -S\theta C\alpha & S\alpha S\theta & aC\theta \\ S\theta & C\theta C\alpha & -C\theta S\alpha & aS\theta \\ 0 & S\alpha & C\alpha & d \\ 0 & 0 & 0 & 1 \end{bmatrix}$$

This matrix is known as the general form of D-H matrix.

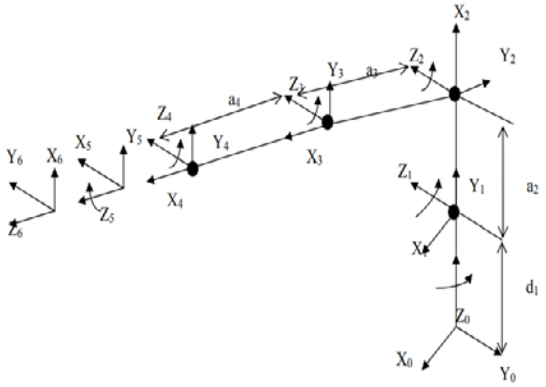

Figure 3.Robotic arm kinematic structure.

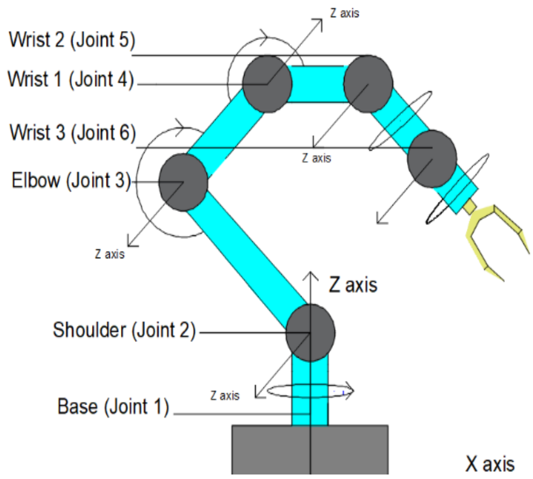

Figure 4. Robotic arm links and joints.

D-H parameter table

By using kinematic structure of the robotic arm Fig 3, the D-H values have been calculated. The homogenous matrices are,

$$^{0}T_1 = \begin{bmatrix} C1 & 0 & S1 & 0 \\ S1 & 0 & C1 & 0 \\ 0 & 1 & 0 & 21 \\ 0 & 0 & 0 & 1 \end{bmatrix}$$

$$^{1}T_2 = \begin{bmatrix} C2 & -S2 & 0 & 39.5C2 \\ S2 & C2 & 0 & 39.5S2 \\ 0 & 0 & 1 & 0 \\ 0 & 0 & 0 & 1 \end{bmatrix}$$

$$^{2}T_3 = \begin{bmatrix} C3 & -S3 & 0 & 27.5C3 \\ S3 & C3 & 0 & 27.5S3 \\ 0 & 0 & 1 & 0 \\ 0 & 0 & 0 & 1 \end{bmatrix}$$

$$^{3}T_4 = \begin{bmatrix} C4 & 0 & S4 & 21C4 \\ S4 & 0 & -C4 & 21S4 \\ 0 & 1 & 0 & 0 \\ 0 & 0 & 0 & 1 \end{bmatrix}$$

$$^{4}T_{5}=\begin{bmatrix} C5 & 0 & S5 & 0 \\ S5 & 0 & -C5 & 0 \\ 0 & 1 & 0 & 0 \\ 0 & 0 & 0 & 1 \end{bmatrix}$$

$$^{5}T_{6}=\begin{bmatrix} C6 & -S6 & 0 & 0 \\ C6 & S6 & 0 & 0 \\ 0 & 0 & 1 & 12 \\ 0 & 0 & 0 & 1 \end{bmatrix}$$

Where, $C_1=\cos\Theta_1$; $S_1=\sin\Theta_1$

Multiplying the matrices from $^{0}T_{1}$ through $^{5}T_{6}$ and setting the results equal to $^{0}T_{6}$,

$^{0}T_{6} = {}^{0}T_{1} \times {}^{1}T_{2} \times {}^{2}T_{3} \times {}^{3}T_{4} \times {}^{4}T_{5} \times {}^{5}T_{6}$(2)

Thus, the homogenous matrix for the 6 DoF robotic arm is obtained (0T6)by using the D-H value from the Table 3.

Table 3. D-H conversion value.

Axis	α_{i-1}	a_{i-1}	d_i	Θ_i
1	90	0	21	Θ_1
2	0	39.5	0	Θ_2
3	0	27.5	0	Θ_3
4	90	21	0	Θ_4
5	90	0	0	Θ_5
6	0	0	12	Θ_6

$$T_{i}=\begin{bmatrix} r11 & r12 & r13 & r14 \\ r21 & r22 & r23 & r24 \\ r31 & r32 & r33 & r34 \\ r41 & r42 & r43 & r44 \end{bmatrix}$$

Where,Orientation matrix $= \begin{bmatrix} r11 & r12 & r13 \\ r21 & r22 & r23 \\ r31 & r32 & r33 \end{bmatrix}$, Position vector $= \begin{bmatrix} r14 \\ r24 \\ r34 \end{bmatrix}$

The orientation matrix tells about the orientation of the robotic arm in the workspace region. The position vector gives information about the coordinates (x, y, z) in the workspace region.

Forces and torque

In general T = F× L, where T is torque, F is evaluated force and L is a distance from the pivot point6.From forward kinematics equations, partial derivative of x and y with respect to q1 and q2 yield matrix called Jacobian matrix. The Jacobian matrix will provide relationship between joint velocities and end-effector velocities. Revolute joint will contribute both linear and angular velocity.

$$\begin{bmatrix} v \\ w \end{bmatrix} = J\,(q_1, q_2, q_3, \ldots\ldots q_n) \begin{bmatrix} q1 \\ q2 \\ . \\ qn \end{bmatrix} \tag{3}$$

Where v= linear velocity and w = angular velocity.

C. Robotic Arm Workspace

From the kinematics study of present robotic arm design, the region through which the robotic arm can move is analysed and is shown in Figs. 5-6.

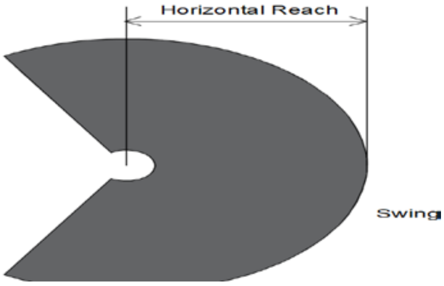

Figure 5. Horizontal workspace region.

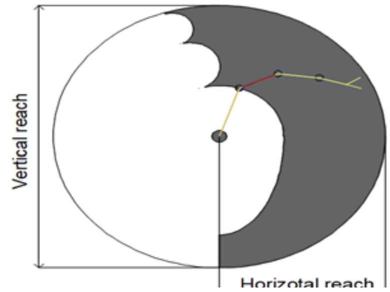

Figure 6. Vertical workspace region.

D. End Effector

The robotic arm end-effector (Fig. 7) consists of three tools such as gripper, primary tool and secondary tool. Each tool is separated by the angle of 1200. Depending upon the operation respective will be do the process other tools will be folded back.

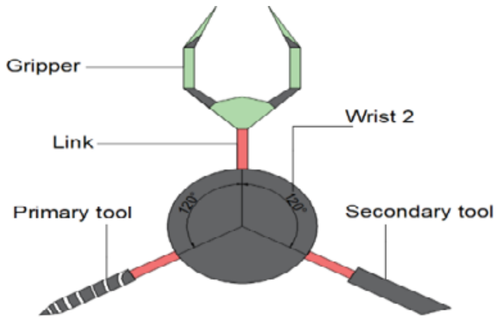

Figure 7. Robotic arm end-effector.

3. Results- Machining Process Using Robotic Arm

Wax propellant is used to verify the machining process of the robotic arm and to compare with conventional machining operations. Three machining parameters are identified which will decide the machining operations- Speed of the cut (VC), Feed (Vf) and Depth of the cut (t).

A. Speed of the Cut

The speed at which the work moves with respect to the tool and vice versa. Cutting speed $= (\pi\times D\times N)/1000$.

Where, D = diameter, N = spindle speed or RPM.

V_C (thrust pattern) $= (\pi\times6\times2000)/1000$

$= 37.68$ m/min

V_c (surface finishing) $= (\pi\times D_o\times N)/1000$

$= 160.925$ m/min

B. Feed

The distance travelled by the tool during one spindle revolution. Feed (Vf) = N × fz× Z, where, N = spindle speed, Fz = feed per tooth, Z = number of flutes.

V_f (thrust pattern) $= 2000 \times 0.017 \times 4$

$= 136$ mm/min

V_f (surface finishing) $= 1025 \times 0.015 \times 1$

= 15.375mm/min

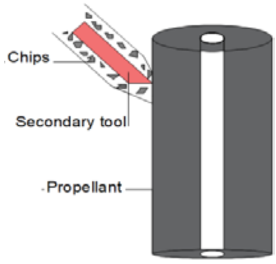

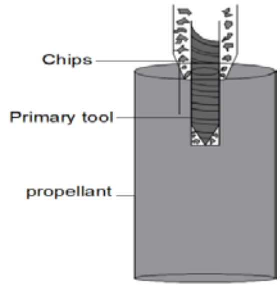

Figure 8.a. Surface finishing and chip collection. b. Milling and chips collection process.

The chips formed during the machining process will be collected by the vacuum pump to ensure the chips will not affect the machining process. Figs. 8a-8b shows the chips collection technique.

C. Depth of Cut
The amount of material removed per pass of the cutting tool. Depth of cut (t) = (DO-df)/2, where, Do = original diameter, df= final diameter.
Depth of cut (t) = (52 – 50) / 2= 1mm

D. Calculation of Machining Time of Propellant Using Robotic Arm
Numerically, Cutting time = L / (feed/rev × N)

Where, L = length of the machined propellant, feed/rev = feed of the tool per revolution.
Cutting time (thrust pattern) = 100 / (0.068×2000) = 43.8 sec (theoretical)
Cutting time (surface finishing) = 100 / (0.015 × 1025) = 390.24 sec (theoretical).

The prototype of robotic arm for propellant machining is constructed and a code is generated in Python for controlling the robotic arm movement and machining process. The calculated values of speed of the cut, feed and depth of the cut (as in Section 3.1-3.3) are given in the code. The robotic arm was employed to perform the machining operations on the manufactured wax propellant. Figs. 9 shows the difference in propellant, before and after machining process. Fig. 10 shows the developed prototype of robotic arm and Fig. 11 illustrates its operation.

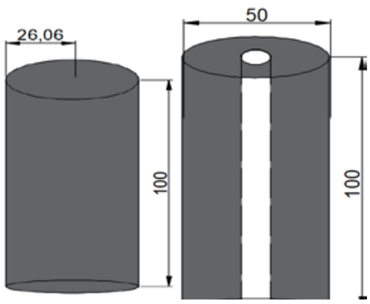

Figure 9a. Dimensions before and after machining

b. Wax propellant after machining with robotic arm.

Figure 10. Robotic arm prototype

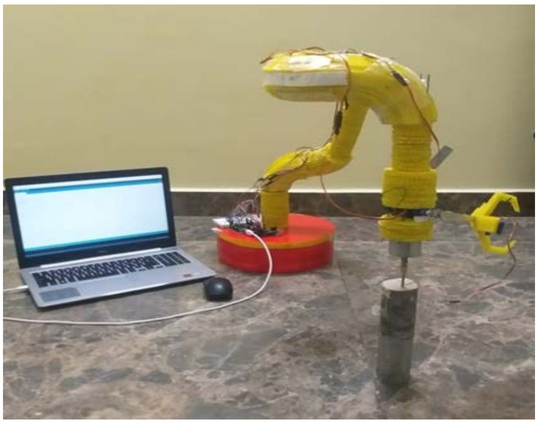

Figure 11. Machining of wax propellant using robotic arm

The observed values for the machining time in experimental study employing robotic arm are given below.

Cutting time (thrust pattern) = 42.58 sec (experimental)
Cutting time (surface finishing) = 390.108 sec (experimental)
For robotic arm, Total time (T) = Tm + Th.

Where, Tm = machining time, Th= time taken by the robotic arm links, joints and tool changing process (2 min).

T= Tm + Th= (42.58 + 390.108) + 120
= 552.68 sec or 9.21 minutes

Thus, by using robotic arm, the total machining process of the solid propellant is completed within 10 minutes and the experimental results are in correlation with the theoretical results.

But, in conventional machining process, four different times need to be considered. Standard time in conventional machining process (T) = Tm + Th+ Ts+ TF, where, Tm = machining time, Th = handling time, TS = service time, Tf = relax time. The machining of wax propellant was also carried out in CNC machine. It was observed that the total time required to machine one wax propellant was 25 minutes by this conventional machining process which was double the time taken by robotic arm. Thus, the present study on robotic arm for propellant machining is very significant.

4. Conclusion

A robotic arm to machine the solid propellant grains is designed and a prototype is constructed. The goal of present work is to create a new safer method to machine the solid propellant grains using the 6DoF robotic arm. Forward kinematics included in the robotic manipulator. Calculations for speed, feed and depth of cut are presented. Using these values, a code is generated in Python for controlling the robotic arm movement and done the machining process. The experimental results employing robotic arm were compared with the theoretical calculations. Also, the machining was done with CNC machine. It was observed that machining process can be done in lesser time using present robotic arm compared to conventional machining process. Thus, the employment of robotic arm for propellant machining is highly worthy due to its various advantages.

5. References

[1] Adde, Y. Alemayehu, Lulseged G. Solomon. Design of a solid rocket propulsion system. Int J Aeronautics Aerospace Res. 2020, 7(2), 224-229.

[2] Perez, R., Gutierrez Rubert, S.C., Zotovic, R.A. Study on Robot Arm Machining: Advance and Future Challenges, Proceedings of the 29th DAAAM International Symposium, 2018. pp.931-940, B. Katalinic (Ed.), Published by DAAAM International, Vienna, Austria.

[3] Razali, Z.B., Mohamed, M.M.A.K., Khoo,Z.Y., Daud, M.H., Design and analysis on robotic arm for serving hazard container. AIP Conference Proceedings, 2017,1885, 020208, doi: 10.1063/1.5002402

[4] Md. Anisur Rahman, Alimul Haque Khan, Tofayel Ahmed, Md. Mohan Sajjad. Design, analysis and implementation of a robotic arm- The animator. AJER 2013, 02(10), pp.298-307.

[5] Mittal, R.K. and Nagrath, J. Robotics and control, Tata McGraw-Hill Education, 2003.

[6] https://www.societyofrobots.com/robot_arm_tutorial.shtml.

Design And Simulation Of Novel Convertible Legged-Wheel Mobile Robot

Raageshver J Sood
School of Robotics
Defence Institute of Advanced Technology
Pune
raageshversood01@gmail.com

Savitha M Jakkula
School of Robotics
Defence Institute of Advanced Technology
Pune
savitha.mj@gmail.com

Prajakta Koratkar
School of Robotics
Defence Institute of Advanced Technology
Pune
koratkarpv@gmail.com

Ashish Singh Rajput
Blast Furnace Projects
Jindal Steel and Power Limited
ashishrajput09@gmail.com

***Abstract*—This paper discusses design, simulation and performance comparison of a novel legged/wheeled convertible mobile robot which can execute walking or rolling motions as required. While many hybrid platforms already exist with similar functionality, they require separate sets of parts and actuators to execute each kind of motion. The proposed design uses same set of parts and motors for actuation of walking or rolling. The transformation mechanism switches between morphologies of, bipedal legs, each with 3 DOF and wheeled rolling. Design consists of Torso-Cylinder, Disc-Thighs, Shanks, Slip-Rings, Feet connected through revolute-joints, actuated using servo motors. The design is tested for working of walking and rolling over a flat terrain. Kinematics of centre of mass has been discussed. Furthermore, ground-contact-forces are discussed.**

Keywords — Bipedal, convertible, Legged, mobile robot, wheel.

1. Introduction

As learned from search and rescue activities at disaster sites, the mobility of the mobile robot is of the greatest necessity [1]. This aim can be fulfilled via several mechanisms; for example, one-, four-, and six-legged locomotion or many layouts of wheeled locomotion however robots based on single locomotive forms lack crucial multi-terrain adaptivity or efficiency which prevents them from being used practically in stochastic environments, where much of human interaction takes place. This elaboration emphasizes on legged and wheeled locomotion. Biological Systems often tend to influence legged robot locomotion mechanisms, which have consistently proved their mettle in moving through a wide area of harsh environments. On the other side there is wheeled locomotion, they are a pivotal human invention and a highly sought-after locomotion concept in man-made vehicles.

The proposed mechanism intends to use advantages of wheel on flat surfaces and bi-pedal mechanism on rough uneven terrains, with its uses as diverse as Environmental Monitoring, Search and Rescue, Scientific

Exploration. A bipedal mechanism comprises of torso connected to thigh via hip joint, thigh and shank are connected via knee joint, and lastly ankle joint connects shank and foot. whereas in wheeled locomotion we need a pair of wheels connected via an axle. To satisfy both criterions i.e., for the leg and the wheel a disc femur is introduced, a disc femur replaces the femur, a rod like structure with a disc like structure. The disc femur enables hybrid usage such that it can be selectively used for executing wheeled rolling and bi-pedal walking.

A model based on above discussion was designed in CAD software and subsequently imported into MATLAB/SimScape Multibody to study its kinematics and dynamics using 3D simulation.

For the modelling of the Robot a reference was taken from MATLAB central file exchange [2].

Figure 1 shows this Reference Robot with Frames attached and COM represented.The robot comprises of a basic Bi-Pedal design which simulates walking motion on a flat surface. Additionally, libraries such as Contact force library [8] and Multi Physics-library were used [9].

A physical structure of a rigid body can be represented by a SimScape multibody model specified through some parameters like mass properties, geometric properties and kinematic relations between its components, from this representation it extracts an equivalent mathematical model [10], This paper presents a methodology for creating a model of a 9-link high mobility hybrid robot, with a proportional-integral-derivative (PID) control implemented to execute a chosen trajectory.

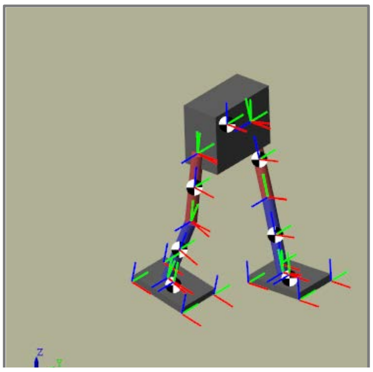

Figure 1: Reference Robot with Frames attached and COM represented

Section 2 introduces the design of the proposed system;it is followed by the methodology of execution of each kind of locomotion technique i.e., biped walking and wheeled rolling. Section 3 briefly discusses the simulation results. Section 4 concludes the paper.

2. Methodology

The robot can switch between 2 locomotion techniques, one being walking with 3 DOF for each leg and second being, Segway like rolling. Uniqueness of this robot is the description of Thigh.

When walking, we can roughly trace the motion of the thigh about hip joint as a circular arch with centre at hip-joint and knee at the periphery of disc. This observation inspired us to replace the traditional rod-shaped Thigh a with disc-shaped Thigh. By making such a change to Thigh's shape, the same framework of leg can now easily be manipulated to perform wheeled rolling. When configured for walking, the robot has 3 DOF in each leg, allowing it to perform several basic kinds of gaits. While when it is configured to roll, it behaves like a Segway robot, 2 wheeled rolling with inverted pendulum.

A. Design

Based on above description, the proposed design consists of following parts as shown in Figure 2:

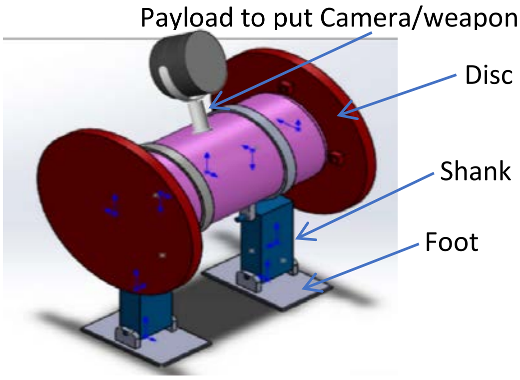

Figure 2: CAD Design

Torso Cylinder:

A cylindrical shell was designed, which acts as torso of the system. The ends of the cylinder are connected with disc femur using a simple revolute joint.This revolute joint makes the hip joint for walking and the axial for wheeled rolling.Two grooves have been cut out in the cylinder which house the slip rings.

Disc Femur:

The disc constitutes of a solid disc with a shaft at its centre, number square pockets have been placed near the periphery of the disc to engage the slip rings with the Disc femur for walking. We use a pair of it.

Slip Rings:

These are meant to engage the shank with the disc femur, for bipedal walking.These have a shaft at the lower end which connects to the shank acting as knee joint. Their disengagement will free the wheels for rolling motion. We use a pair of it.

Shank:

A long prismatic bar with two shafts at top and bottomends, for knee and ankle joints respectively. We use a pair of it.

Foot:

A flat prismatic block connected to the shank via the ankle joint, it the point of contact between the robot and the ground. We use a pair of it.

Based on choice of locomotion method to be selected, we choose necessary morphological changes as shown in Figure 3.

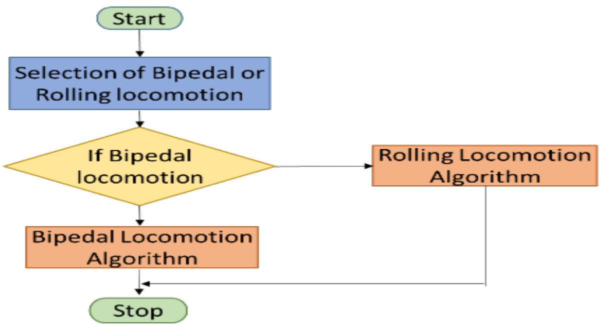

Figure 3: Flowchart to initialize Novel Convertible Legged-wheel Mobile Robot

B. Bipedal Walking

Bipedal walking is a topic of extensive research since decades and still under development. While the scope of its application is enormous, its execution is challenging. The configuration for bipedal walking is inherently unstable and requires active control for its stabilization. To prove that our design is capable of walking, the bipedal walking has been simplified for the simplest case of walking over a flat ground. For this case, we can safely assume the hip joint and ankle joint both have 1 revolute joint each. This assumption works well for simple gaits on flat grounds.

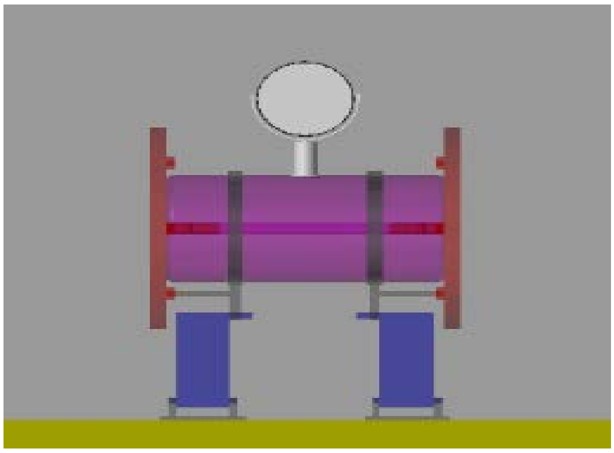

Figure 4: Novel Convertible Legged-Wheel Mobile Robot as a Biped

For walking, the slip rings and the Disc-Femur should be engaged for proper transfer of motion to the shank as shown in Figure 4. When inputs are given to hip-joint, the slip ring engaged at the periphery of the Disc-Femur transfers the motion to the shank via the keen joint. Further giving the inputs to the knee- joint and the ankle joint, the above-described simplified bipedal walking is achieved.

The architecture of the walking mechanism is an open loop, where we provide reference trajectory as input as shown in Figure 5.

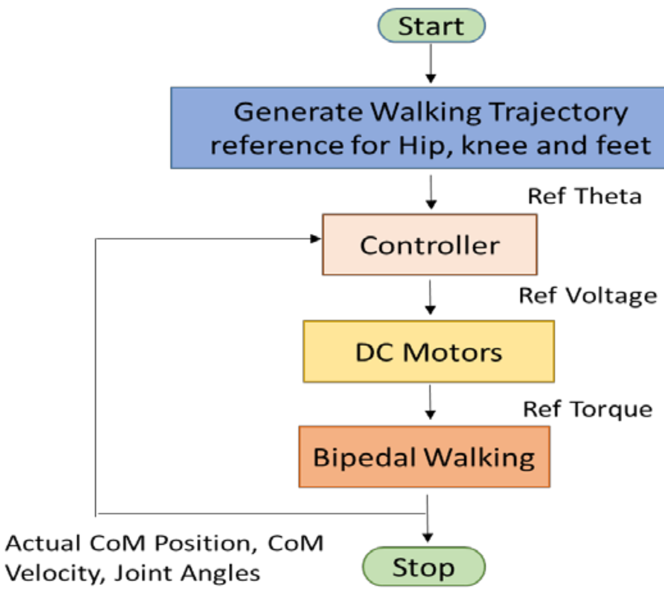

Figure 5:Flowchart of Bipedal Locomotion Algorithm

The trajectory is in terms joint angles to each of the 6 joins. The input provided to the right leg and left leg are same, inputs to the left leg are provided at a delayed time, the delay is half of the gait cycle time.

With these set of joint angles, we roughly achieve a straight walk on a flat ground. To ensure proper angles and smooth walking we use a PID controller for each motor. We provide reference angles as input to the PID controller, joint angles of each motor are completely observable, these are further fed back to the PID for error computation, based on the error controller computes the input torques to be provided to motor.

C. 2-Wheeled Rolling

For wheeled rolling, we first disengage the slip rings from the disc femur and arrest its rotation with respect to the torso-cylinder. This manipulation stops the transfer of motion between the Disc-Femur and the remaining parts of legs.

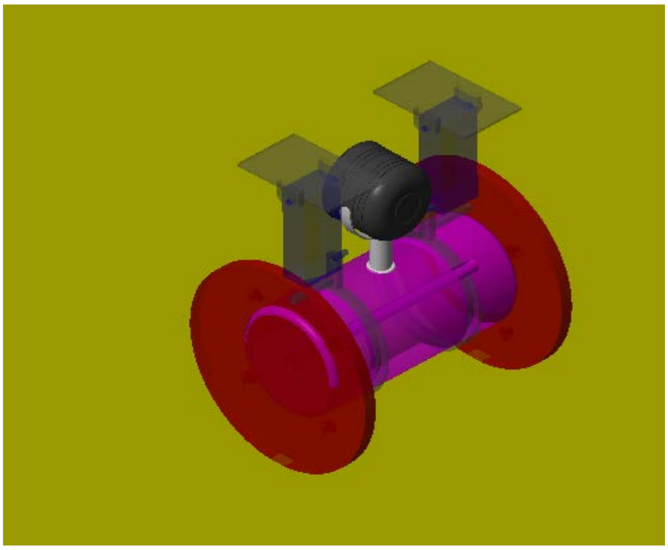

Figure 6: Novel Convertible Legged-Wheel Mobile Robot as a 2 Wheeled Robot

After this disengagement of the shank from the disc femur is done and feet need to be set into a configuration such that they do not interfere with the wheeled rolling or fall on the ground.

A suitable configuration is that of a 2-wheeled robot with inverted legs as shown in Figure 6, effectively assumed as 2-wheeled rolling with inverted pendulum. This configuration is very common, more popularly called Segway robot. The architecture of wheeled rolling can be described as shown in Figure 7. The execution of rolling is relatively simple. It can be executed without the need of closed loop controller. The challenge lies in keeping the legs inverted in vertically upwards configuration. This requires a closed loop control strategy. To balance the legs in this configuration, the same PID controllers can be used as in bipedal walking. From the plots (Fig 12) it shows the amount of torque required to keep legs in Segway condition. The reference input in this case will correspond to the angle for inverted leg configuration.

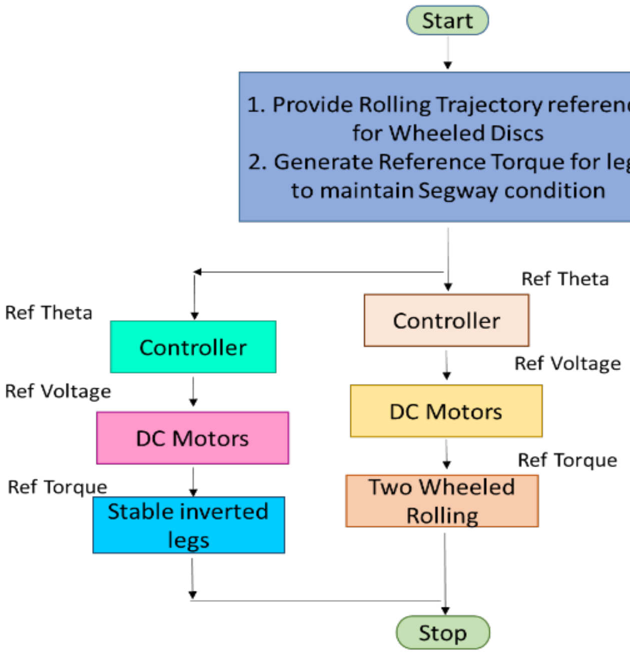

Figure 7: Flowchart of Rolling Locomotion Algorithm

3. Simulation of Robot Locomotions

In the previous section, by using SolidWorks and SimScape Multibody we built the hybrid model. In this section we present simulation and subsequent analysis. All simulations use ode15s (stiff/NDF) solver to solve nonlinear equations.

A. Biped Walking Simulation

Since the two legs actuate from the same input, with a phase difference, result of only one leg have been discussed. The simulation was run for 10 seconds, a gait cycle here executes in repeating tables of 0.8 seconds.

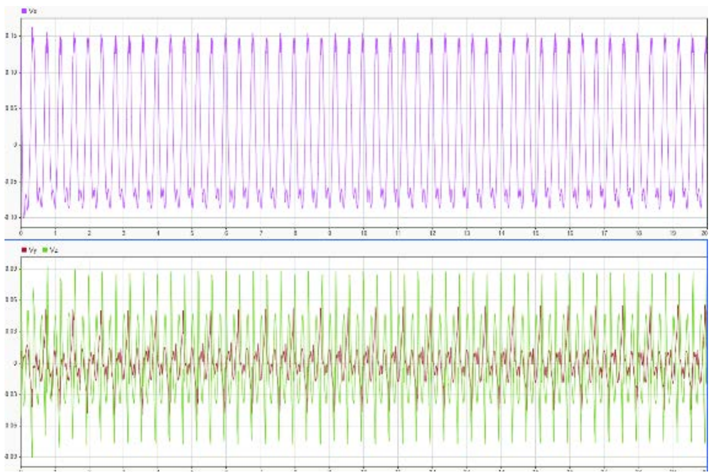

Figure 8: Plot of Bipedal Robot Velocity in X, Y and direction

In the plot (Fig 8) the velocity of the Centre of mass is plotted against time. We can clearly infer how slow this kind of locomotion is.In plots (Fig. 9-Fig. 11) shows how much torque is required for the actuation of each joint. While these characteristics look highly inefficient, one must not forget, while Bipedal walking is slow and inefficient, its advantage lies in its versatility opening many avenues for successful locomotion in highly stochastic environments.

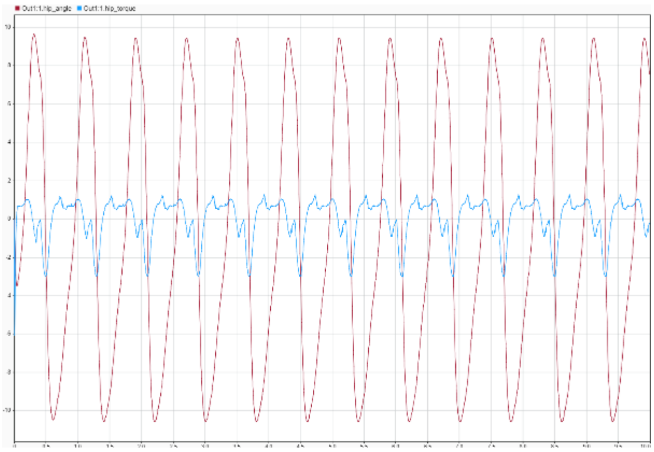

Figure 9: Plot of Bipedal Robot Hip Angle and Hip Torque

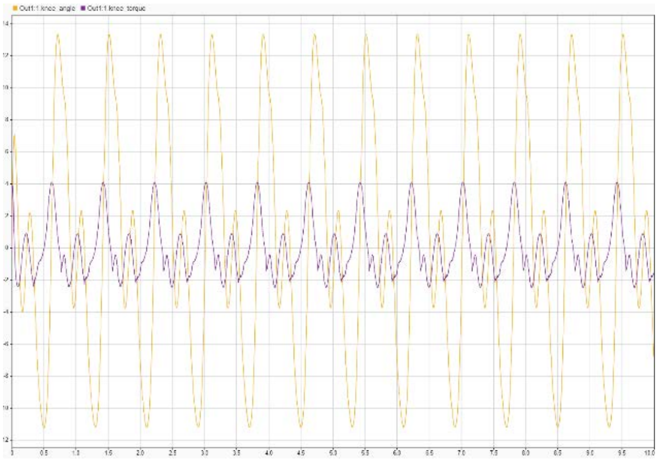

Figure 10: Plot of Bipedal Robot Knee Angle and Knee Torque

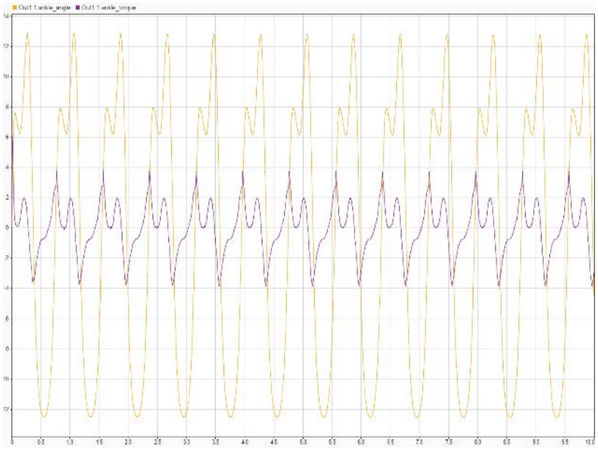

Figure 11: Plot of Bipedal Robot Ankle Angle and Ankle Torque

B. Wheeled Rolling Simulation

In this simulation we start with the legs in any arbitrary orientation. First the legs are pulled in the upward inverted position, then they are maintained at that angle. Then the wheeled rolling starts.

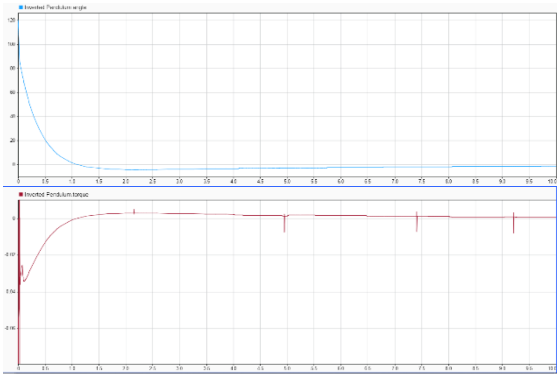

Figure 12: Plot of 2 Wheeled Robot Inverted Pendulum Angle and Torque

In the wheeled rolling plot (Fig 13) shows the velocity of CoM with respect to time. We can clearly see; this locomotion is fast. From the plots (Fig 14) we can also see it is very efficient as it requires less torque for forward motion. Undoubtably it's a fast and efficient form of locomotion, its major disadvantage lies in the fact, it requires a flat uniform surface for proper operation. If the surface is uneven or stochastic, its efficiency and speed drops dramatically, many a times, it cannot access a wide variety of outdoor terrains.

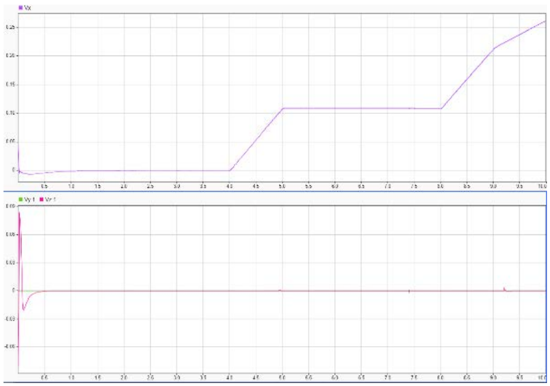

Figure 13: Plot of Wheeled Robot Velocity in X, Y and Z direction

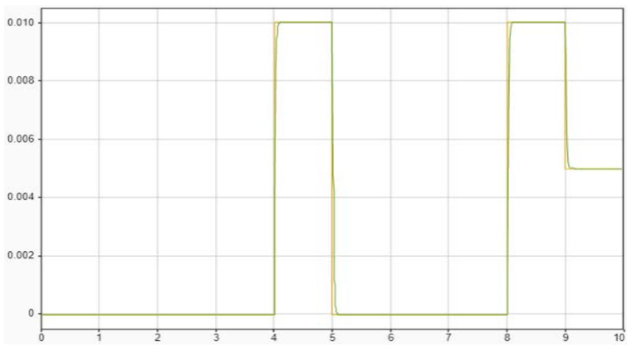

Figure 14: Torque Input to motors of 2 Wheeled Robot

4. Results and Discussion

With this paper we can certainly state that this kind of design modification enables us to execute both the kinds of locomotion methods and use each of them as and when suites. With this design we have been able to preserve the inherent advantage of both legged and wheel locomotion by keeping the principal functions of both in one robot. This design was tested in simulation from which we can clearly infer from the plot this and this, the seamless forward motion of CoM as shown in Figure 15 and 16 for both the locomotion methods, while trying to walk in a straight line. A comparative analysis was also done between two modes of locomotion, underlining the difference in characteristics of each locomotion form and they both have their own advantages and disadvantages. Many aspects such as Kinematics, Kinetics and Control were explored. The PID controllers were used, for smooth walking as well as balancing the legs in inverted position for wheeled rolling.

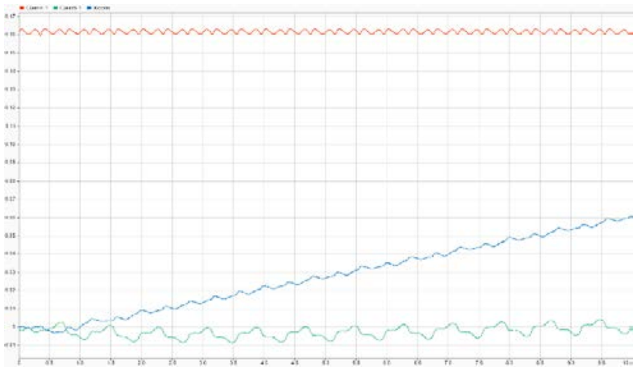

Figure 15: CoM Position for Biped Walking

With this paper we can certainly state that this kind of design modification enables us to execute both the kinds of locomotion methods and use each of them as and when suitable. We can clearly see from the plot this and this, the seamless forward motion of CoM for both the locomotion methods, while trying to walk in a straight line.

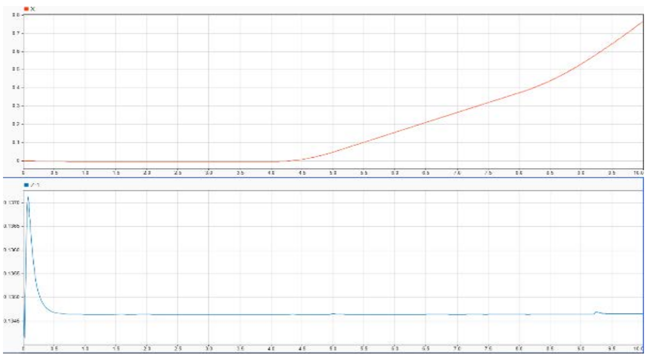

Figure 16: Plot of 2 Wheeled Robot CoM Position

The study can be further extended into developing a full-fledged high-mobility system which has calibre to perform wheeled-rolling and bipedal-walking individually giving it the special feature to work in indoor and outdoor surroundings, which can be exploited by inclusion of obstacle-avoidance.

5. Conclusion

The study can be further extended into developing a full-fledged high-mobility system which has calibre to perform wheeled-rolling and bipedal-walking individually giving it the special feature to work in indoor and outdoor surroundings, which can be exploited by inclusion of obstacle-avoidance. A robust control system which ensures stability of the robot in various terrains, the robot has achieved dynamic stability on a flat surface as well as rolling motion, however the study can be extended further to achieve general and local stability via overall closed loop control. Furthermore, modifications can be done to accommodate for sensors such as gyroscope and stability equations be generated via optimization methods like Lyapunov Method, Artificial Intelligence etc. The data obtained from simulations can be successfully used to make design changes so as to achieve desired results, for example: Changing the value of Input torque changes the time required to complete a gait cycle.

6. References

[1] Murphy RR. “An overview of robots from USA at Fukushima and the tsunami recovery”. Presented at: 2011 IEEE international conference on robotics and automation (ICRA’11). Shanghai, China 2011.

[2] MathWorks Student CompetitionsTeam“https://in.mathworks.com/matlabcentral/fileexchange/64227-matlab-andsimulink-robotics-arena--walking-robot

[3] Luxman Ramamoorthy, Zielinska Teresa, “Robot motion synthesis using ground reaction forces pattern: Analysis of walking posture” Presented at: International Journal of Advanced Robotic Systems 2017

[4] Introduction to Humanoid Robotics by ShuujiKajita, Hirohisa Hirukawa,Kensuke Harada, Kazuhito Yokoi

[5] Craig, J.J.: Introduction to Robotics: Mechanics and Control, 2nd edn. Addison-WesleyPublishing Company, Inc.

[6] Lim, B., Lee, J., Kim, J., Lee, M., Kwak, H., Kwon, S., Lee, H., Kwon, W., Roh, K.: Optimal gait primitives for dynamic bipedal locomotion. In: Proceedings of the IEEE/RSJ International Conference on Intelligent Robots and Systems, pp. 4013–4018 (2012)

[7] Balancing a Two-Wheeled Segway Robot by Maia R. Bageant

[8] SteveMillerhttps://in.mathworks.com/matlabcentral/fileexchange/47417-simscape-multibody-contact-forces-library

[9] SteveMillerhttps://in.mathworks.com/matlabcentral/fileexchange/37636-simscape-multibody-multiphysics-library

[10] Marlon Fernando Velásquez-Lobo, Juan Manuel Ramirez-Cortés, José de JesusRangel-Magdaleno. “Modelling a Biped Robot on Matlab/SimMechanics”. Presented at: CONIELECOMP 2013, 23rd International Conference on Electronics, Communications and Computing.

Formation Tracking of Chained form Nonholonomic Robotic System using Sliding Mode Control

AnujNandanwar
Department of Electrical Engineering
Indian Institute of Technology Kanpur
anujnand@iitk.ac.in

Vibhu Kumar Tripathi
Department of Electrical Engineering
Indian Institute of Technology Kanpur

Laxmidhar Behera
Department of Electrical Engineering
Indian Institute of Technology Kanpur

***Abstract*—This paper discusses the formation control problem of the chained form nonholonomic mobile robots in the presence of parametric uncertainty and external disturbances. A coordination transformation has been used to obtain the chained model of the nonholonomic mobile robot in order to reduce the complexity and to enhance the feasibility in the practical implementation. An integral nonsingular terminal sliding manifold is proposed to ensure the finite-time convergence while avoiding the singularity problem. Moreover, a modified power- rate reaching law has been utilities to improve the convergence speed of the system. Closed-loop stability has been proven using Lyapunov theory. The efficacy and effectiveness of the proposed controller are tested using Pioneer P3-Dx mobile robot in Gazebo simulator. The comparative analysis is done to tell the superiority of the proposed approach over existing methods.**

Keywords: Formation Control, Chained nonholonomic system, Sliding-mode control.

1. Introduction

The multi-robotic system (MRS) is prevalent and gained remarkable attention of the research community due to its several advantages compared to a single robotic system in diverse applications like surveillance and security to collaborative transportation. To solve the formation tracking problem of MRS, several control methodologies have been developed in the past for single and double-integrator model, linear and nonlinear MRS and deterministic and stochastic systems.

Previous work mainly focuses only on the nonholonomic mobile robot with the low-order model. However, many mechanical systems, i.e. wheeled mobile robot, the knife-edge, mobile vehicle with multiple trailers, and space robotics, can be described in the form of high-order chained structure using coordination transform [1]. In [2] introduced variable transform strategies for solving a cooperative control problem of chained-form high-order model with small communication delay. The consensus problem of multiple nonholonomic chained model has investigated when the reference input is persistently or not [3]. Using a model feature and finite-time control protocol, a cooperative controller is developed to handle the tracking problem of a high-order chained model in [4]. The finite-time distributed observer strategies have been designed to observe both control input and state of leader in undirected and directed communication graph [5]. However, these controller design only considered the multiple nonholonomic mobile robots without parametric uncertainty and external disturbance.

For considering the formation tracking problem of chained form nonholonomic robotics system with disturbances and external uncertainties, Sliding Mode Controller (SMC) is one of the best option. The SMC has gained much attention due to its robustness against parametric uncertainties, modelling inaccuracies and bounded external disturbances. In brief, the idea behind designing an SMC is to develop a suitable control law for the system that can make the system trajectory reach a predefined sliding manifold in finite time and keep the system trajectory on this surface thereafter. However, infinite time convergence of the tracking error and chattering phenomenon are the major issues in SMC. To tackle these issues, several variant of sliding variable and reaching laws are proposed in the literature. Terminal sliding manifold (TSM) [6]–[8] and fast terminal sliding manifold (FTSM) [9] are widely used for tracking problem of nonholonomic chained form to developed sliding mode controller that ensures the convergence of the tracking error in asymptotically [7], [9] and finite time [8]. However, both TSM and FTSM induces the singularity in the control laws. In [10], a generalized sliding mode disturbance observer is developed to observer the unknown disturbance in the chained form dynamics. Similarly, for avoiding the communication problem encounter by a distributed observer to observer the state information [11]. Finite-time tracking control problem of nonholonomic chained model with time-varying external disturbance and parametric uncertainties has been investigated in [12] using an anti-interference, chattering free SMC.

However, the controller design for nonlinear multi-robotics system has some limitation to implementation in multiple nonholonomic system due to their special structure. However, most of the approaches [13], [14] are based on the single integrator nonholonomic model of the mobile robot that results in the reduction of the control accuracy when extended to real-time implementation. Motivated by the above discussion, therefore, the main objective of this paper is to solve a formation tracking problem of chained-form nonholonomic system [4] in the presence of parametric uncertainties and external disturbances using finite-time sliding mode control.

2. Problem Formulation and Preliminaries

In this work, we consider the consensus problem of multiple nonholonomic systems with one leader and n followers.The communication connection between the robots are expressed by an edge set $\mathsf{E} \subseteq \mathsf{V} \times \mathsf{V}$ of a directed graph $\mathsf{G} = \{\mathsf{V}, \mathsf{E}\}$. The adjacency matrix $A = [a_{ij}] \in \mathbb{R}^{n \times n}$ is defined by $a_{ij} > 0$ if follower i can get information from robot j but not vice-versa and otherwise $a_{ij} = 0$. The pining matrix is denoted by $\mathsf{B} = diag\{b_1, \ldots, b_n\}$ where $b_i > 0$ if leader information is available for robot i otherwise $b_i = 0$. The Laplacian matrix $\mathsf{L}_f = [l_{ij}]$ and the degree diagonal matrix $\mathsf{D} = diag\{d_1, \ldots, d_n\}$ are expressed the same in [15].

A. Problem Formulation

Let us considern follower indexed as robot $i, \in \Gamma = 1, 2, \ldots, n$ and a leader indexed as robot 0 in nonholonomic chained-form. The system modelling of each follower $i^{th} (i \in \Gamma)$ is described as

$$\begin{aligned}
\dot{z}_{i,1} &= \tilde{n}_1 u_{i,1} + \delta_{i,1}(t, z_{i,1}); \\
\dot{z}_{i,2} &= \tilde{n}_2 z_{i,3} u_{i,1}; \\
\dot{z}_{i,3} &= \tilde{n}_3 u_{i,2} + \delta_{i,2}(t, z_{i,3})
\end{aligned} \tag{1}$$

Where $z_i = [z_{i,1}, z_{i,2}, z_{i,3}]^T$ and $u_i = [u_{i,1}, u_{i,2}]^T$ are the state and control input of robot i^{th} respectively. $\tilde{n}_1, \tilde{n}_2, \tilde{n}_3$ are the parametric uncertainties of the all robots; and

$\delta_{i,1}(t, z_{i,1}), \delta_{i,1}(t, z_{i,3})$ is the time-varying unknown nonlinear function. The leader is responsible for the generation of the reference trajectory, whose dynamics is described by

$$\begin{aligned} \dot{z}_{0,1} &= \tilde{n}_1 u_{0,1} + \delta_{0,1}(t, z_{0,1}); \\ \dot{z}_{0,2} &= \tilde{n}_2 z_{0,3} u_{0,1}; \\ \dot{z}_{0,3} &= \tilde{n}_3 u_{0,2} + \delta_{0,2}(t, z_{0,3}) \end{aligned} \tag{2}$$

Where $z_0 = [z_{0,1}, z_{0,2}, z_{0,3}]^T$ and $u_0 = [u_{0,1}, u_{0,2}]^T$ are the state and control input of leader, respectively; and $\delta_{i,1}(t, z_{0,1})$, $\delta_{0,2}(t, z_{0,3})$ is the time-varing unknown nonlinear function.

Formation Tracking Problem: For the multi-robot systems described in (1), (2), finite-time formation tracking can be achieved within time T with a control protocol $u_i(t)$ such that

$$\lim_{t->T} \| (z_{i,l} - z_{0,l}) - \Lambda_i \| = 0; \forall i, l \quad \text{where } i \in \Gamma, l = 1, 2, 3$$

Where Λ_i is a desired formation among the robots. Finally, the aim of this work is to design a control laws $u_{i,1}$ and $u_{i,2}$ for robot i modelled by (1), (2), such that the formation tracking can be established in the presence of parametric uncertainty $\tilde{n}_l$ and the external disturbances. The following assumptions and lemmas are as required to complete in the proof.

Assumption 1. There exist known constants $\underline{\tilde{n}}_l$ and $\bar{\tilde{n}}_l$ such that $\underline{\tilde{n}}_l \le \tilde{n}_l \le \bar{\tilde{n}}_l$

Assumption 2. For a known constant $\hat{\delta}_1, \hat{\delta}_2 > 0$ such that $| \delta_{i,1}(t, (z_{i,1}) - \delta_{0,1}(t, (z_{i,1}) | \le \hat{\delta}_1 | x_{i,1} - x_{0,1} |$ for $i \in \Gamma$, and $\delta_{i,2}(t, (z_{i,1}) | \le \hat{\delta}_2$ for $i \in \Gamma \cup \{0\}$.

Lemma 1. [16] For a matrix $\mathbf{R} \in \mathbb{R}^{n \times n}$\$, we have $(| z |_\pi^r)^T | \mathbf{R} |_\pi | w |_\pi^s \le \sum_{i=1}^{n} (\mu_i | x_i |^{r+s} + \bar{\mu}_i | y_i |^{r+s})$ where $x = [x_1, \ldots, x_n]^T$ and $y = [y_1, \ldots, y_n]^T$ are vectors and $\mu_i, \bar{\mu}_i > 0$ are some positive constants.

Lemma 2. [16] If there exists a continuous radially unbounded and positive definite function $V(x)$ such that

$$\dot{V}(x) \le -K_0 V^P - K_1 V^q \tag{3}$$

for some $K_0, K_1 > 0$, $p > 1, 0 < q < 1$, then the origin of this system is globally fixed time stable and the settling time function T can be estimated by

$$T = \frac{1}{K_0 (p-1)} + \frac{1}{K_1 (1-q)} \tag{4}$$

3. Design of finite-Time consensus tracking

Now, we proposed a robust finite-time consensus control design for the leader-follower multi-robotic system (1) and (2). The design of control law $u_{i,1}$ and $u_{i,2}$ will be developed individually.

A. Design of robust control law $u_{i,1}$

Let as considered the local relative tracking error for robot i is

$$e_{i,1} = \sum_{j\in\Gamma} a_{ij}(z_{i,1} - z_{j,1}) + b_i(z_{i,1} - z_{0,1}) \tag{5}$$

The compact form of eq. (5) is as follows

$$e_1 = (\mathsf{L}_f + \mathsf{B})\overline{z}_1 - \mathsf{B}\underline{\mathbf{1}}z_{0,1} = (\mathsf{L}_f + \mathsf{B})(\overline{z}_1 - \overline{z}_0) \tag{6}$$

Where $e_1 = [e_{1,1}, \ldots, e_{n,1}]^T$, $\overline{z}_1 = [z_{1,1}, \ldots, z_{n,1}]^T$ and $\overline{z}_0 = \underline{\mathbf{1}}z_{0,1}$. The time derivative of $e_{i,1}$ is as follows

$$\dot{e}_{i,1} = \text{ñ}_1\gamma_{i,1} + \sum_{j\in\Gamma} a_{ij}(\tilde{\delta}_{i,1} - \tilde{\delta}_{j,1}) + b_i\tilde{\delta}_{i,1} \tag{7}$$

where $\gamma_{i,1} = \left(\sum_{j\in\Gamma} a_{ij} + b_i\right)u_{i,1} - \sum_{j\in\Gamma} a_{ij}u_{j,1} - b_i u_{0,1}$ and $\tilde{\delta}_{i,1} = \delta_{i,1}(t, z_{i,1}) - \delta_{0,1}(t, z_{0,1})$ for $\forall i \in \Gamma$.

The compact form of eq. (7) is follows as

$$\dot{e}_1 = \text{ñ}_1\gamma_1 + (\mathsf{L}_f + \mathsf{B})\tilde{\delta}_1 \tag{8}$$

where $\gamma_1 = [\gamma_{1,1}, \ldots, \gamma_{n,1}]^T$,and $\tilde{\delta}_1 = [\tilde{\delta}_{1,1}, \ldots, \tilde{\delta}_{n,1}]^T$. For solving a finite-time formation tracking problem, the integral sliding surface is defined for each followers as

$$S_{i,1} = e_{i,1} + \text{ñ}_1\int e_{i,1}\,dt \tag{9}$$

Where $S_1 = [S_{1,1}, \ldots, S_{n,1}]^T$.

Theorem 1. For the multi-robotic network given by model (1),(2), if the graph G is connected, than the robust sliding mode controller $u_{i,1}$ is given by

$$u_{i,1} = \left(\sum_{j\in\Gamma} a_{ij} + b_i\right)^{-1}\left(\gamma_{i,1} + \sum_{j\in\Gamma} a_{ij}u_{j,1} + b_i u_{0,1}\right)$$

$$\gamma_{i,1} = -\frac{\text{ñ}_1}{\bar{\text{ñ}}_1}e_{i,1} - \frac{K_i}{\bar{\text{ñ}}_1}S_{i,1} - \frac{\sigma_0}{\bar{\text{ñ}}_1}|S_{i,1}|^{1-\text{ò}}\operatorname{sign}(S_{i,1}) - \frac{\sigma_1}{\bar{\text{ñ}}_1}|S_{i,1}|^{1+\text{ò}}\operatorname{sign}(S_{i,1}) \tag{10}$$

where $K_i > 0, \sigma_0 > 0, \sigma_1 > 0, \text{ò} \in (0,1)$ and $\varepsilon > 0$ are constants and sliding manifold is designed in (9).

Proof: First, we prove that the trajectory of first-order subsystem in (1) and (2) will reach the sliding manifold $S_i = 0\,(i = 1, \ldots, n)$ in a finite-time. Let us consider a Lyapunovfunction $V_1(S_1) = 0.5S_1^T S_1$. The time derivative of $V_1(S_1)$, we get as

$$\dot{V}_1 = S_1^T(\dot{e}_1 + \text{ñ}_1 e_1) = S_1^T(\text{ñ}_1\gamma_1 + (\mathsf{L}_f + \mathsf{B})\tilde{\delta}_1 + \text{ñ}_1 e_1)$$

With the help of Assumption 2 and Lemma 1, there exist constant $\eta_i > 0$ such that $S_1^T(\mathsf{L}_f + \mathsf{B})\tilde{\delta}_1 \le \sum_{i=1}^{n}\eta_i S_{i,1}^2$, Then, we get

$$\dot{V}_1 \le \sum_{i=1}^{n}\left(\text{ñ}_1 S_{i,1}\gamma_{i,1} + \eta_i S_{i,1}^2 + \text{ñ}_1 e_{i,1}\right) \tag{11}$$

By using (10), ineq. (11), we get

$$\dot{V}_1 \le -\sum_{i=1}^{n}\left(\sigma_0 \,|\, S_{i,1} \,|^{2-\grave{o}} + \sigma_1 \,|\, S_{i,1} \,|^{2+\grave{o}}\right) \tag{12}$$

With the help of Lemma 2, the sliding surface will converge to zero in finite time.

B. Design of robust control law $u_{i,2}$

To design a robust controller $u_{i,2}$, we have a consider second subsystem of actual system in (1)-(2). The equation of reduce subsystem is

$$\begin{aligned} \dot{z}_{i,2} &= \tilde{n}_2 z_{i,3} u_{i,1}, \\ \dot{z}_{i,3} &= \tilde{n}_3 u_{i,2} + \delta_{i,2}(t, z_{i,3}) \end{aligned} \tag{13}$$

and

$$\begin{aligned} \dot{z}_{0,2} &= \tilde{n}_2 z_{0,3} u_{0,1}, \\ \dot{z}_{0,3} &= \tilde{n}_3 u_{0,2} + \delta_{0,2}(t, z_0) \end{aligned} \tag{14}$$

Let as consider the tracking error is

$$e_{i,l} = \sum_{j\in\Gamma} a_{ij}(z_{i,l} - z_{j,l}) + b_i(z_{i,l} - z_{0.l})\; l = 2,3. \tag{15}$$

The combination of (13) and (14) leads to

$$\begin{aligned} \dot{e}_{i,2} &= \sum_{j\in\Gamma} a_{ij}(\dot{z}_{i,2} - \dot{z}_{j,2}) + b_i(\dot{z}_{i,2} - \dot{z}_{0,2}) \quad = e_{i,3} + \delta_{i,2}\dot{e}_{i,3} \\ &= \tilde{n}_3 \gamma_{i,2} + \sum_{j\in\Gamma} a_{ij}(\tilde{\delta}_{i,2} - \tilde{\delta}_{j,2}) + b_i \tilde{\delta}_{i,2} \end{aligned} \tag{16}$$

where $\delta_{i,l} \;= \sum_{j\in\Gamma} a_{ij}[(\tilde{n}_l u_{i,1} - 1) z_{i,l+1} - (\tilde{n}_l u_{j,1} - 1) z_{j,l+1}] \;\; + b_i[(\tilde{n}_l u_{i,1} - 1) z_{i,l+1} - (\tilde{n}_l u_{0,1} - 1) z_{0,l+1}]$ (17)

It is observer that the system model in (16) is not a pure-feedback form. Therefore, it is very challenging to design a proper sliding mode controller for this type of system. Now, the coordinate transform is used to transform system model in (16) to the pure-feedback form by represent:

$$\begin{aligned} \zeta_{i,1} &\triangleq e_{i,2} \\ \zeta_{i,2} &\triangleq e_{i,3} + \delta_{i,2} \end{aligned} \tag{18}$$

Now, differentiate the pure-feedback form in (18), we get

$$\begin{aligned} \dot{\zeta}_{i,1} &\triangleq \zeta_{i,2}, \\ \dot{\zeta}_{i,2} &\triangleq \tilde{n}_3 \gamma_{i,2} + \sum_{j\in\Gamma} a_{ij}(\tilde{\delta}_{i,2} - \tilde{\delta}_{j,2}) + b_i \tilde{\delta}_{i,2} + \dot{\delta}_{i,2} \end{aligned} \tag{19}$$

The compact form of (19) is represented by

$$\dot{\zeta}_1 = \zeta_2$$

$$\dot{\zeta}_2 = (L_f + B) u_2 - B 1_n u_{20} + \dot{\delta}_2 \tag{20}$$

where $\zeta_1 = [\zeta_{1,1}, \ldots, \zeta_{n,1}]^T$, $\zeta_2 = [\zeta_{1,2}, \ldots, \zeta_{n,2}]^T$, $u_1 = [u_{1,2}, \ldots, u_{n,2}]^T$, and $\tilde{\delta}_2 = [\tilde{\delta}_{1,2}, \ldots, \tilde{\delta}_{n,2}]^T$. For solving a finite-time formation tracking problem, the terminal sliding surface is defined for each followers as

$$S_{i,2} = \zeta_{i,1} + \tilde{n}_2 \zeta_{i,2}^{\alpha} \tag{21}$$

Now, the compact form of (21) is represented as

$$S_2 = c_1 \eta_2^{\alpha} + \eta_1 \tag{22}$$

Theorem 2. *For sub-system (13)-(14) with the non-singular terminal sliding manifold (21), if the controller is designed as*

$$u_2 = u_2^a + u_2^b + u_2^c + u_2^d \tag{23}$$

Where

$$u_2^a = (\mathsf{L}_f + \mathsf{B})^{-1} \otimes I_m (B 1_n u_{20})$$

$$u_2^b = -(c_1 \alpha)^{-1} (\mathsf{L}_f + \mathsf{B})^{-1} \otimes I_m (\eta_2^{2-\alpha})$$

$$u_2^c = -(\mathsf{L}_f + \mathsf{B})^{-1} \otimes I_m \dot{f}_2$$

$$u_2^d = -(\mathsf{L}_f + \mathsf{B})^{-1} \otimes I_m K_2 \operatorname{sgn}(diag(\eta_2^{\alpha-1}) S_2)$$

Proof. Due to space constraints, the similar step has follows [17].

4. Simulations Result

To show the tracking performance of the designed controller, Gazebo simulator [18], [19] is used for performing the numerical simulations. The Pioneer P3-Dx mobile model has been considered in the Gazebo simulator. There are three robots have been considered for the simulations in which one is acting as a leader and other two are acting as a follower. The kinematic model of the mobile robot is given by

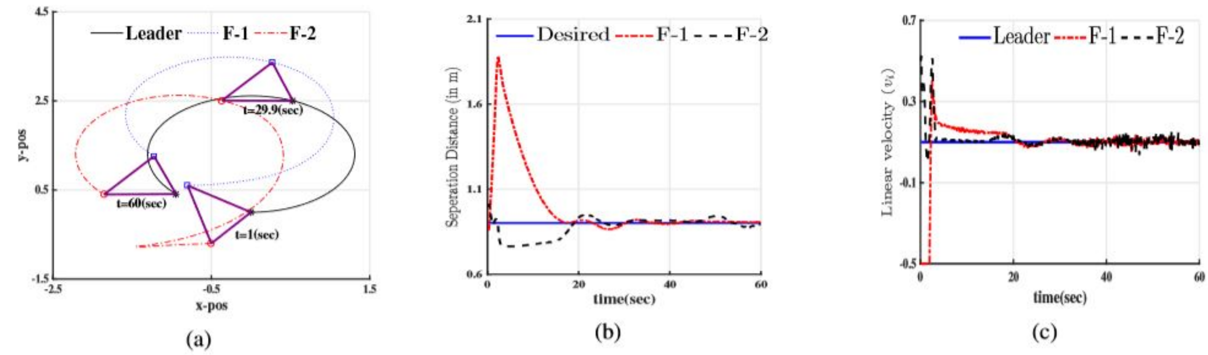

Figure 1: (a) Robots trajectory during circle formation in presence of the parametric uncertainties and disturbances (b) Relative distance of followers from leader and (c) Linear velocities of robots (v_i).

$$\begin{aligned} \dot{x}_i &= (v_i + d_i(t)) \cos\theta_i; \\ \dot{y}_i &= (v_i + d_i(t)) \sin\theta_i; \\ \dot{\theta}_i &= \omega_i \end{aligned} \tag{24}$$

where $i \in \Gamma \cup \{0\} = \{0,1,2\}$, $q_i = \{x_i, y_i, \theta_i\}$ is the position along with orientation, and v_i and ω_i are the linear and angular velocities of the robot i^{th}, respectively. It is assumed that the disturbance $d_i(t)$ is acting on the linear velocity v_i. Using the coordination transform, one can get

$$\begin{bmatrix} z_{i,1} \\ z_{i,2} \\ z_{i,3} \end{bmatrix} = \begin{bmatrix} 0 & 0 & 1 \\ \sin\theta_i & -\cos\theta_i & 0 \\ \cos\theta_i & \sin\theta_i & 0 \end{bmatrix} \begin{bmatrix} x_i - \Lambda_i^x \\ y_i - \Lambda_i^y \\ \theta_i \end{bmatrix} \tag{25}$$

$$\begin{bmatrix} u_{i,1} \\ u_{i,2} \end{bmatrix} = \begin{bmatrix} 0 & 1 \\ 1 & z_{i,2} \end{bmatrix} \begin{bmatrix} v_i \\ \omega_i \end{bmatrix} \tag{26}$$

On converting Eq. (28) into chained form, one can get

$$\begin{aligned} \dot{z}_{i,1} &= u_{i,1} + f_{i,1} \\ \dot{z}_{i,2} &= z_{i,3} u_{i,1} \\ \dot{z}_{i,3} &= u_{i,2} + f_{i,2} \end{aligned} \tag{27}$$

Where $f_{i,1} = 0$ and $f_{i,2} = d_i(t)$. The initial states of the leader and followers are selected as $q_0 = [0, 0, 0]^T$ and $q_1 = [-0.8, 0.6, 0.1]^T$, $q_2 = [-0.5, -0.7, 0.1]^T$ respectively. In order to achieve the circular shape, control input of the leader is selected as $v_0 = 0.1 m/sec$, $\omega_0 = 0.07 rad/sec$ and disturbance $d_0(t) = 0$. The disturbance and parametric uncertainties for followers are chosen as $d_i(t) = 0.9\sin t$ and $\tilde{n}_i = 0.2$ respectively. The desired time-varing deviation is defined as $[\Lambda_i^x, \Lambda_i^y] = [r\cos(\frac{7\pi}{5} - \frac{2i\pi}{5}), r\sin(\frac{7\pi}{5} - \frac{2i\pi}{5})]$, where $i = 1, 2$ and $r = 0.9m$.

The simulator result is shown in Fig. 1a. Fig. 1a shows the tracking response of each robots during the entire formation tracking. Initially, the follower-2 goes away from the leader to maintain the desired separation from the leader. It is evident from the Figs. 1b and 1c that the formation in MRS is achieved in finite time in the presence of disturbance and parametric uncertainties, which infers the controller robustness. The consensus is achieved within $15 - 20s$. A YouTube link of the video for simulation is given in [20].

5. Conclusions

Formation tracking control for nonholonomic chained- form systems are studied in this paper. The controller has been developed using nonsingular integral sliding manifold and modified power-rate reaching law. The stability of the closed-loop system has been analyzed using Lyapunov theory. A real-time simulation using Pioneer P3-Dx mobile robots has been performed to show the proposed controller tracking performance.

6. References

[1]. R. M. Murray and S. S. Sastry, “Nonholonomic Motion Planning: Steering using Sinusoids,” IEEE Trans. on Automatic Control, vol. 38, no. 5, pp. 700–716, 1993.

[2]. W. Dong and J. A. Farrell, “Cooperative Control of Multiple Nonholonomic Mobile Agents,” IEEE Trans. on Automatic Control, vol. 53, no. 6, pp. 1434–1448, 2008.

[3]. K.-C. Cao, B. Jiang, and D. Yue, “Consensus of Multiple Nonholonomic Chained Form Systems,” Systems & Control Letters, vol. 72, pp.61–70, 2014.

[4]. H. Du, G. Wen, Y. Cheng, Y. He, and R. Jia, “Distributed Finite-Time Cooperative Control of Multiple High-order Nonholonomic Mobile Robots,” IEEE Trans. on Neural Networks and Learning Systems, vol. 28, no. 12, pp. 2998–3006, 2016.

[5]. B. Ning and Q.-L. Han, “Prescribed Finite-Time Consensus Tracking for Multiagent Systems with Nonholonomic Chained-form Dynamics,” IEEE Trans. on Automatic Control, vol. 64, no. 4, pp. 1686–1693, 2018.

[6]. Y. Wu, B. Wang, and G. Zong, “Finite-Time Tracking Controller Design for Nonholonomic Systems with Extended Chained Form,” IEEE Trans. on Circuits and Systems II: Express Briefs, vol. 52, no. 11, pp. 798–802, 2005.
[7]. Y. Wu, R. Yuan, and X. Zheng, “Finite-Time Tracking Controller Design for a General Class of Nonholonomic Systems,” in Proceedings of the48h IEEE Conference on Decision and Control (CDC) held jointly with 2009 28th Chinese Control Conference. IEEE, 2009, pp. 4408–4413.
[8]. S. Khoo, L. Xie, and Z. Man, “Leader-Follower Consensus Control of a Class of Nonholonomic Systems,” in 2010 11th International Conference on Control Automation Robotics & Vision, 2010, pp. 1381–1386.
[9]. S. Mobayen, “Fast Terminal Sliding Mode Tracking of Nonholonomic Systems with Exponential Decay Rate,” IET Control Theory & Applications, vol. 9, no. 8, pp. 1294–1301, 2015.
[10]. F. Bayat, S. Mobayen, and S. Javadi, “Finite-Time Tracking Control of nth-Order Chained-Form Nonholonomic Systems in the Presence of Disturbances,” ISA Transactions, vol. 63, pp. 78–83, 2016.
[11]. Z. Zuo, B. Tian, M. Defoort, and Z. Ding, “Fixed-Time Consensus Tracking for Multi-agent Systems With High-Order Integrator Dynamics,” IEEE Trans on Automatic Control, vol. 63, no. 2, pp. 563–570, 2017.
[12]. H. Chen, B. Zhang, T. Zhao, T. Wang, and K. Li, “Finite-Time Tracking Control for Extended Nonholonomic Chained-Form Systems with Parametric Uncertainty and External Disturbance,” Journal of Vibration and Control, vol. 24, no. 1, pp. 100–109, 2018.
[13]. M. Ou, H. Du, and S. Li, “Finite-Time Formation Control of Multiple Nonholonomic Mobile Robots,” International Journal of Robust and Nonlinear Control, vol. 24, no. 1, pp. 140–165, 2014.
[14]. Y. Cheng, R. Jia, H. Du, G. Wen, and W. Zhu, “Robust Finite-Time Consensus Formation Control for Multiple Nonholonomic Wheeled Mobile Robots Via Output Feedback,” International Journal of Robust and Nonlinear Control, vol. 28, no. 6, pp. 2082–2096, 2018.
[15]. Q. Yang, H. Fang, M. Cao, and J. Chen, “Distributed Trajectory Tracking Control for Multiple Nonholonomic Mobile Robots,” IFAC- Papers OnLine, vol. 49, no. 4, pp. 31–36, 2016.
[16]. C.-C. Hua, X. You, and X.-P. Guan, “Leader-Following Consensus for a Class of High-Order Nonlinear Multi-Agent systems,” Automatica, vol. 73, pp. 138–144, 2016.
[17]. C.-E. Ren and C. P. Chen, “Sliding mode Leader-Following Consensus Controllers for Second-Order Non-Linear Multi-Agent Systems,” IET Control Theory & Applications, vol. 9, no. 10, pp. 1544–1552, 2015.
[18]. N. Koenig and A. Howard, “Design and Use Paradigms for Gazebo, “An Open-Source Multi-Robot Simulator,” IEEE/RSJ Int. Conf. on Intelligent Robots and Systems (IROS), vol. 3. IEEE, 2004, pp. 2149–2154.
[19]. A. Nandanwar, N. K. Dhar, D. Malyshev, L. Rybak, and L. Behera, “Finite-Time Robust Admissible Consensus Control of Multi-robot System under Dynamic Events,” IEEE Systems Journal, vol. 15, no. 1, pp. 780–790, March 2021.
[20]. Formation Tracking of Chained form Nonholonomic Robotic System using Sliding Mode Control. [Online]. Available: https://youtu.be/qb- VZCD9t6M.

Development of Robotic Arm Manipulator mounted on Self Balancing Two Wheeled Mobile Robot

Pranay Junare
College of Engineering Pune
Pune
junarepg18.extc@coep.ac.in

Shaunak Mahajan
College of Engineering Pune
Pune

PrithvishTaukari
College of Engineering Pune
Pune

Anirudh Nallawar
College of Engineering Pune
Pune

Dr. S. S. Ohol
College of Engineering Pune
Pune

Abstract— **Self-balancing robots are becoming increasingly popular now a days. They have better agility and are compact in size when compared to four-wheeled mobile robots. On the other hand, robotic arms are widely used in manufacturing units and industrial automation processes. But most of these robotic arms lack the navigation capabilities. Thus, to overcome these issues of mobile arm manipulation and performing swift locomotion in narrow dense areas, we have built a robotic system. It has two wheeled self-balancing mobile base and two 5DOF arms driven by servo actuators capable of mimicking the humanoid robot movement. For accurate state estimation of the robot, angles computed by implementation of MEMS sensor fusion algorithms is used. The Cascaded PID Controller is designed to realize the movement of the robot in forward and backward direction. Thus, the complete methodology used to maintain the robot upright throughout the unprecedented disturbance along with mechanical system design and mathematical modeling is mentioned in this paper. Later the simulation of the robotic system is done using Gazebo and ROS and finally verification of the simulation results is done by actual hardware implementation.**

1. Introduction

In today's world the application of two wheeled robots is difficult to limit to specific applications, since they can be used in numerous applications such as Segway, humanoid wheeled robots, service robots and surveillance in hazardous places. In the defense sectors, these robots can be used to train the soldiers as they can be made to act as insurgents, hostages or civilians. They can be used for visual surveillance in sensitive high-density areas as these robots are capable of moving on the streets just like humans. The design of the Self-balancing robot is based on the principle of the inverted pendulum which maintains the balance about zero moment point. Main challenge in these robots is to maintain the position of the robot upright. On the other hand, existing robotic arms are widely used in industries, warehouses, defense, manufacturing and hence combining it with mobile platforms which are compact and are capable of navigating in dense environments makes it one of the important areas of research. This paper presents the development of the Robotic arm manipulator mounted on the two-wheeled self-balancing mobile robot. The main advantage of using a two-wheeled mobile robot over the legged robot or four-wheeled robot is better mobility as well as the ability to rotate in small space. These robots are capable of moving faster than the legged robots. Two-wheeled self-balancing robots are intended to balance themselves by controlling the rotation of the wheel governed by the immediate response from the encoded motors. Also, this system computes the tilt angle of the robot and provides an optimal controlled feedback to motors using the efficient control algorithm.

The remaining sections of the paper are organized as follows: In Section 2 literature survey is done. Section 3 includes detailed Mechanical Specification and Mathematical modelling. Section 4 describes the methodology followed by us to control the built Robot system design by simulating it in the Gazebo environment. Section 5 describes the experimental results observed on the actual hardware implementation. Lastly section 6 includes the conclusions derived from the research work.

2. Related Work

Over the years, researchers have widely studied modelling and dynamic control of Two wheeled self-balancing robot. Robots such as JOE [1]- a mobile inverted pendulum robot developed in 2002, nBot[2] - which was featured as NASA's Cool Robot of the Week in 2003 &iBot[3] - a wheelchair capable of balancing on two co-axial wheels developed by Dean Kamen are some of the pioneering work. Multiple control strategies were proposed such as Pole Placement [1], Linear Quadratic Regulator (LQR)[4], Proportional Integral Derivative(PID)[5][6], Fuzzy control [7]. Since none of the single controller that performs efficiently on all the Self balancing robots so multiple control algorithms have been and will be proposed over the years. There have also been several attempts at developing two wheeled robots which had robotic arms mounted on them. Some of them include NASA's Robonaut and MIT's Cardea robot, both based on SEGWAY robotic mobile platform. One of the most recent and a notable mention is Handle Robot by Boston Dynamics, which is a two wheeled robot having robotic manipulator arm mounted on it.

3. System Design

A. Mechanical Structure

The mechanical model mainly consists of two robotic arm manipulators controlled by servos, namely MG996 for rotation of main joints and micro servo for 2 finger gripper. The arm is designed in such a way that it can mimic human hand movements and is mounted onto the torso which in turn is mounted on the main body of a two wheeled balancing robot. The basic test-based model was designed on CAD modelling software and was designed in accordance with the 3D prototyping capabilities. Hence, the material chosen was ABS which is a commonly used material for 3D prototyping. The wheels used were standard wheels available in the market and a 12V high torque encoded motor of 400 rpm was used for precise control of wheels to balance the robot. The torso and the lower body are acrylic laser cut and are joined together using bond glue and slots. The robotic arm mainly consists of 4 links to imitate human hand motion. The first link is attached to the torso which mimics the shoulder’s rotational movement in the vertical circle. The next link mimics the lateral motion of the robotic arm. Link 3 mimics the elbow movement of the arm and the last link mimics the wrist rotation. The last link is then connected to a servo actuated 2 fingered grippers. This gripper consists of a servo horn which is connected to two links at the end which has a restricted linear motion. The entire model has a maximum span of 1300 mm. It has a height of 800mm and has a width of 200mm.

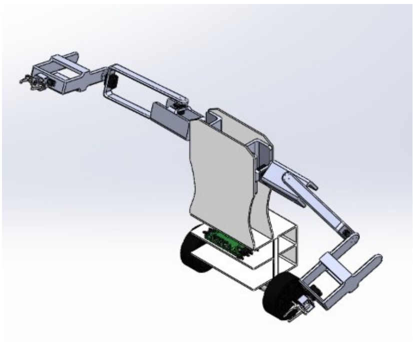

Fig. 1. CAD Design

B. Mathematical Model

Assumptions:

(i) The system is assumed to be rigid.
(ii) There is no net slip in wheels and ground.
(iii) Radius of both wheels are constant and don't vary.
(iv) Mass distribution in the body is uniform.

Table 1

Symbol	Name of the parameter	Values	Unit
r	Wheel radius	0.15	m
M_R	Mass of rotating system	0.52	kg
I_R	Moment of Inertia	0.0117	kgm^2
F_R	Friction Coefficient	0.2	$Nrad^{-1}s^{-1}$
M_B	Mass of main body	3.00	kg
I_B	MOI of main body	0.82	kgm^2
F_B	Friction coefficient of main body	0.002	$Nrad^{-1}s^{-1}$
l	Length measured from the wheel axis to COM	0.112	m
g	Gravity	9.8	ms^{-2}

The motion of the two-wheel-balancing robot can be obtained using Lagrangian dynamics.

The kinetic energy of the rotation system due to angular displacement is:

$$K.E. = \frac{1}{2} m_R v^2 \# \quad (1)$$

Here, x_i and y_i coordinates indicate the position of the center of gravity of the main body:

$$x_i = x + l \sin(\theta_b) \#(2)$$
$$y_i = -l sin(\theta_b) \#(3)$$

Here θ_b is the angle subtended by the vertical axis and the longitudinal axis of the two-wheel-robot.

Differentiating x_i and y_i with respect to time we have:

$$v_x = v + l cos(\theta_b); \#(4)$$
$$v_y = -l sin(\theta_b); \#(5)$$

Calculating the scalar quantity of total velocity;

$$|v^2| = v^2 + +2lv\omega \cos(\theta_b) + l^2\omega^2 \#(6)$$

Now the kinetic energy of the main body due to linear motion is:

$$K.E._B = \frac{1}{2} m_B v^2 + m_B l\omega v cos(\theta_b) + \frac{1}{2} m_b l^2 {\theta_b}^2 \#(7)$$

Hence, by adding all the K.E. we get the total energy as:

$$E_T = \frac{1}{2}(m_B + m_R)v^2 + m_B l v\omega \cos(\theta_b) + \frac{1}{2}(J_B + m_B l^2)\omega^2 \#(8)$$

Using Lagrangian equations [5], we find angular acceleration and linear acceleration for the linearized model as:

$$a = -\frac{m_B l}{m_B + m_R}\omega + \frac{1}{m_B + m_R}(T_w - f_R v) \#(9)$$

$$\alpha = \frac{m_B l}{J_B + m_B l^2} a + \frac{m_B l g}{(J_B + m_B l^2)}\theta_b \ \#(10)$$

4. Simulation in Gazebo

For verification, efficient testing, algorithm implementation and feasibility of the proposed robot model we first need to simulate it in a virtual environment. Thus, for this purpose out of numerous Robotics Simulator platforms such as Webots, Gazebo, V-REP, CARLA, AirSim, USARSim we choose Gazebo software due to its enormous features, flexibility and convenient integration with ROS. Gazebo is an Open-source 3D simulator which has an inbuilt physics engine, supports sensor manipulation and has a rich visualization. On the other hand, Robot Operating System (ROS) is a middleware that has numerous collections of libraries, drivers, and tools for building robotic systems.[9]

A. Simulation world

Gazebo was used to simulate the entire real-world environment. It allows us to create a 3D Virtual world with characteristics such as length, mass, joints, links, friction coefficients, etc[10,11]. Other parameters such as simulation step size, camera pose, lighting was configured according to our need. Finally, in this experiment for simulating the environment, a custom world file was written by specifying different parameters. (Fig. 2)

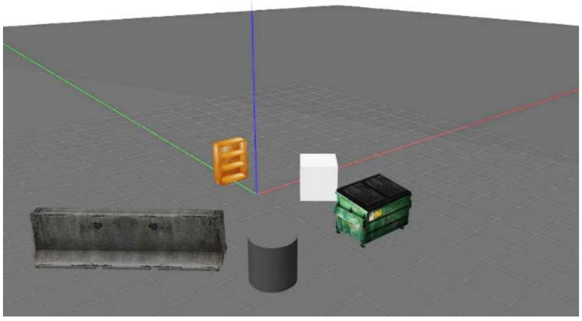

Fig. 2. The simulation world

Table 2: Parameters in Gazebo

Name of the parameter	**Values**
Gravity(m/s^2)	9.8
Density (kg/m^3)	1.1
Mass (kg)	3.6
Length of frame(mm)	1300
Width of frame(mm)	200
Height of frame(mm)	800

B. Modelling the robot

For building the robot model, SolidWorks was used and the built model was converted to URDF (Universal Robotic Description Format) using SolidWorks to URDF Exporter. URDF file only specifies the dynamic and kinematic [12] properties and hence further it was modified to add additional properties and simulation specific information to make it compatible with Gazebo. Some of the important parameters are listed in TABLE II. Our robot model has two robotic arm manipulators, two wheels, upper torso and a lower body chassis frame. Finally importing of robot model in the previously built Gazebo virtual environment was done. (Fig. 3)

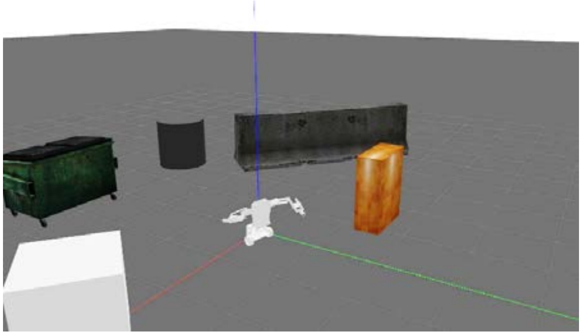

Fig. 3. The simulated robot model

C. State Estimation

To apply the control strategy on a Self-Balancing robot it is very important to estimate the dynamic current state of the robot. The state of the robot at any time t is represented by y(t) and is represented by the following eq 1.

$$y(t) = [\phi \ \ \theta \ \ x \ \ y] \#(11)$$

Where:
ϕ: pitch angle (Tilt angle)
θ: yaw angle
x: Position x of the robot
y: Position y of the robot

For measuring the pitch and yaw angles of the robot MEMS motion sensor is used. Further the raw values of accelerometer, gyroscope and magnetometer are fused using Sensor Fusion algorithms such as Complementary and Madgwick filters.

D. Cascade PID Control

Proportional-Integral-Derivative (PID) Controller is a feedback control mechanism used for controlling the process variable. It is used when the control systems are closed loops. PID Controller has three parameters: Proportional Gain, Integral Gain and Derivative Gain. Proportional component determines the system response to the current error value, Integral component determines the accumulation of overtime error value whereas Derivative Component is used to predict future error in the system. PID controller is represented by the following equation:

$$u(t) = K_p * e(t) + K_i \int_0^t e(t)\, dt \ + K_d * \#(12)$$

Where:
u: controller output.
E: Error = Setpoint – Process Variable
K_p: proportional constant gain.
K_i: integral constant gain.
Ki: derivative constant gain.

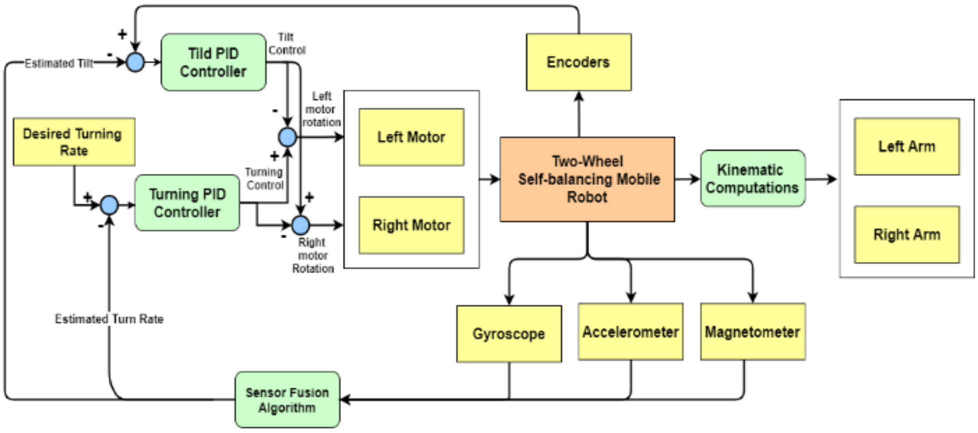

Fig. 4. Control System block Diagram

We implemented the cascaded PID controller in order to control the robot state. Cascaded PID controller is a control algorithm where output of the first controller provides the setpoint for the second controller. Such systems are able to give improved response to non-linear gains and disturbances. In our controller the inner PID loop is used to precisely control the encoded motors whereas the outer PID loop maintains the robot upright by controlling the tilt angle. The complete block diagram of the implemented Control System is as shown in Fig. 4.

5. Experimental Results

The proposed robot after mathematical analysis and simulation was implemented in hardware prototype. The developed robot having two robotic arm manipulators and balancing on two-wheels is shown in the Fig. 5. Thus, the proposed theory was experimentally verified.

6. Conclusion

In this paper, mathematical modelling and analysis of Self balancing mobile robot having Robotic arm mounted on it is done. Further the proposed model was simulated in Gazebo to test the feasibility and finally it was implemented in hardware. The experimental results show that for the robot having mechanical specifications as mentioned in the paper, Implemented Cascaded PID Controller is able to achieve stability.

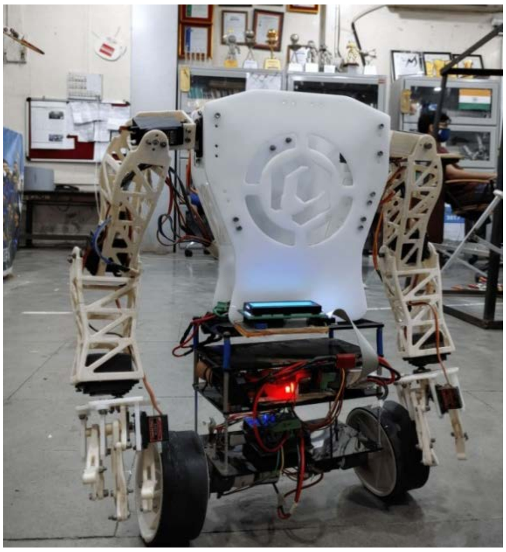

Fig. 5. Hardware Implementation

7. Acknowledgment

The authors would like to thank all the members of Robotics & Automation Laboratory COEP, for their valuable inputs. This research is supported by Robotics and Automation Laboratory of College of Engineering Pune.

8. References

[1] Grasser, A. D'arrrigo, S. Colombi, And A. C. Rufer, "Joe: A Mobile, Inverted Pendulum," Ieee Transactions on Industrial Electronics. 49, No. 1, Pp. 107–14, 2002

[2] P. Anderson. (2003, Aug.) nBot balancing robot. Online. [Online]. Available: http://www.geology.smu.edu/ dpa-www/robo/nbot

[3] L. Kamen, R. R. Ambrogi, R. K. Heinzman, C. C. Langenfeld, M. A. Nisbet, S. B. Smith (III), and T. A. Brindley, "Medical improvements to a personal vehicle", U.S. Patent 6,405,816, June 18, 2002

[4] S. Ahmad and M. O. Tokhi, "Linear Quadratic Regulator (LQR) Approach for Lifting and Stabilizing of Two-Wheeled Wheelchair," 2011 4th Int. Conf. Mechatronics, no. May, pp. 1–6, May 2011.

[5] T.-J. Ren, T.-C. Chen, and C.-J. Chen, "Motion control for a two-wheeled vehicle using a self-tuning PID controller," Control Eng. Pract., vol. 16, no. 3, pp. 365– 375, Mar. 2008.

[6] H. -S. Juang and K. -Y. Lum, "Design and control of a two-wheel self-balancing robot using the arduino microcontroller board," 2013 10th IEEE International Conference on Control and Automation (ICCA),2013, pp. 634-639, doi: 10.1109/ICCA.2013.6565146.

[7] Huang, W. Wang, and C. Chiu, "Design and Implementation of Fuzzy Control on a Two-Wheel Inverted Pendulum," IEEE Trans. Ind. Electron., vol. 58, no. 7, pp. 2988–3001, 2011.

[8] Fabián R. Jiménez, Ilber A. Ruge, and Andrés F. Jiménez, "Modeling and Control of a Two Wheeled Auto-Balancing Robot: a didactic platform for control engineering education", 18th LACCEI International Multi-Conference for Engineering, Education, and Technology:

[9] Player/Stage project. (2016) The Player Project. [Online]. Available: http://playerstage.sourceforge.net/

[10] http://wiki.ros.org/gazebo_ros_pkgs

[11] http://gazebosim.org/tutorials?tut=ros_plugins&cat=connect_ros

[12] Takaya, Kenta, et al. "Simulation environment for mobile robots testing using ROS and Gazebo." 2016 20th International Conference on System Theory, Control and Computing (ICSTCC). IEEE, 2016.

AI based Equipment Readiness and Combat Analysis for Formation Readiness State Automation

Ajay Kumar Gill
Defence Institute of Advanced Technology
Pune

Pooja Agrawal
Defence Institute of Advanced Technology
Pune
poojaa.diat@gmail.com

Abstract **—Wide range of vehicles/equipment are integrated part of Indian Army and are the backbone of the operations and logistics where they play both combatant as well as non-combatant roles. Thus, health and condition of vehicles/equipment is vital for the performance of duties optimally. As an approach to find an automated and efficient solution, automation of Formation Readiness State (FRS) and an AI based predictive maintenance model using ridge regression and classification has been proposed. The Ridge Regression provides L2 regularisation i.e., avoids over fitting and generalises the patterns. The proposed approach is based on past repair data trained using regression algorithms predicting the Remaining Useful Life (RUL) of the equipment. This paper adopts system's remaining useful life (RUL) as an indicator of the health status of the system by minimizing the set of maintenance costs that could be caused by a possible system failure. A further classification model can be obtained giving out the status of the equipment as non-critical, critical and very critical based upon the remaining useful life giving out decision rules for the further employment of equipment.**

Keywords— Formation Readiness State; Regression; Predictive maintenance

1. Introduction

Indian Army has, in its inventory, a wide range of vehicles/ equipment and therefore ensuring full mission capability at all times, in order to achieve the desired operational role, remains a challenge. Presently no real time flow of data and monitoring mechanism exist between the user and the repair agency for carrying out timely preventive maintenance and ensure improved serviceability state.

To address this, different repair methodologies are being followed viz. Corrective Maintenance and Preventive / Planned Maintenance. The former methodology results in increased maintenance efforts and longer non availability of vehicle, whereas the latter results in reduced usage life of parts being replaced and thus more expenditure on maintenance in anticipation of the fault. Hence, there is a requirement to cater for appropriate repairs at a time just before the occurrence of failure to maximise the equipment life and minimise the associated maintenance costs by predicting the likely faults.

These factors seeks to optimize and plan the maintenance strategy taking into account the automation of database and develop an AI based model for predictive maintenance. AI system with automation would address various issues pertaining to own operational preparedness as well as the engineering support voids with respect to equipment of the entire formation.

2. State readiness and technique

A. Formation Readiness State (FRS)

The basis for the equipment readiness is the monthly report known as Formation

Readiness State. It is generated by an EME battalion and higher headquarters. FRS states the varsity of equipment held in the formation covering various parameters under 19 appendices compiled manually consuming an average time of a week and prone to errors.

B. Regression Technique

A Ridge regression [1] is a way to create a sparing model when the number of predictor variables in a set exceeds the number of observations. By adding certain bias to the regression estimates, ridge regression reduces the errors and net effect will be to give estimates that are more reliable. Ordinary Least Squares regression uses the following formula to estimate coefficients:

$$\hat{B} = (X`X)^{-1}X'Y$$

If X is centred and scaled matrix, the cross-product matrix (X`X) is singular when the X-columns are highly correlated. Ridge regression adds a ridge parameter (k), of the identity matrix to the cross-product matrix, forming a new matrix (X`X + kI).

C. Predictive Maintenance

It aims at predicting the requirement of maintenance based on actual condition of the vehicle. Successful implementation of predictive maintenance [2] allows predicting failures and possibility of accurate diagnosis of such failure once predicted. The essential data sources required for implementation of predictive maintenance are fault history, maintenance/ repair history, vehicle Condition. Diagnostics and prognostics are the main methodologies of a predictive maintenance framework. Prognostics is meant to estimate the time remaining until such faults actually occur to determining the system's remaining useful life (RUL) [3]. The equipment is of high-cost, old vintage and specialist vehicles required to perform critical specialist tasks and aren't equipped with sensors or any equipment monitoring systems.

3. Related work

The present process is purely based on manual report and returns. The process being adopted is archaic and not in sync with the technological advances made. The book on predictive maintenance [5] gives an idea on the impact of maintenance on the business and describes various maintenance management methods like Run-to-Failure, Preventive Maintenance and the domain of predictive maintenance. The book on Applied Predictive modelling [6] is based on data analysis with a specific focus on the practice of predictive modelling using various techniques like machine learning, pattern recognition, and data mining. The book on The Elements of Statistical Learning [7] gives overview of the importance of statistical methods towards data mining techniques and extracting inferences to implement a predictive model. There doesn't exist any significant literature on deriving intelligence for predictive maintenance from the past repair. None of the literature highlighted the significance of the age, KM and cost expense combination in deciding the life of the vehicle.

4. Experimental design

Preprocessing of FRS is carried out by analysis of the report. It was found that the report needed a review and further refinement in order to avoid data redundancy and duplication of database which may further burdens the automation process. In this experiment, the data storage will be moderate but classified in nature and very limited users omitting any chances of the bottleneck. Although it is also feasible with Azure Cloud SQL server, local SQL server appears much more outstanding. This leads to understanding the data flow in the web application. Flow chart of the proposed approach is shown in Fig 1.

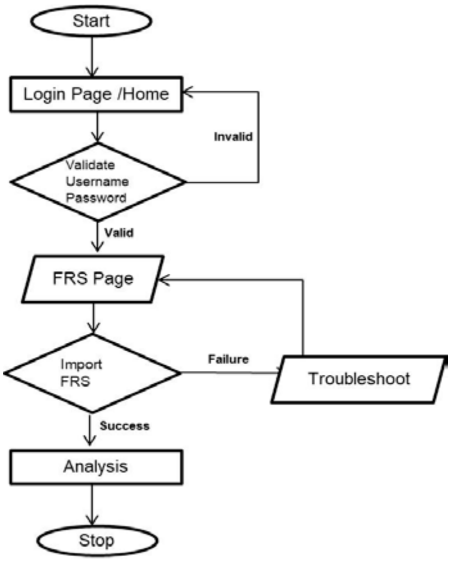

Fig 1. Flow Chart.

A. Login

Multiple users have been created with complex passwords to validate user and proceed to web page [8] as per the privilege of the user. Fig 2 shows the home page as the application is launched.

B. Data Import Platform

Once the user is logged in, it is directed to data import platform as per his privilege. Once the user clicks on any sub unit button then the user is directed to import its unit FRS page as shown in Fig. 3.

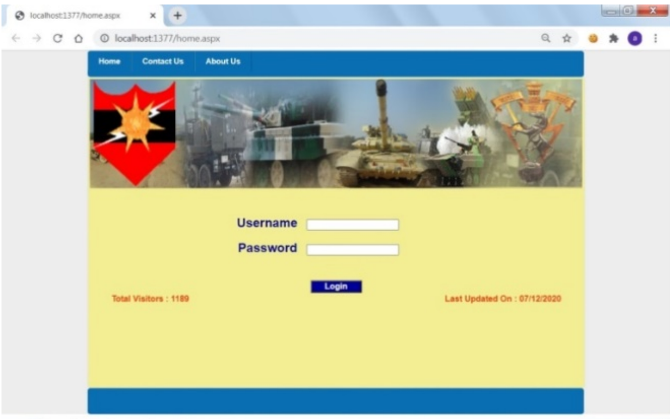

Fig 2. Login Page

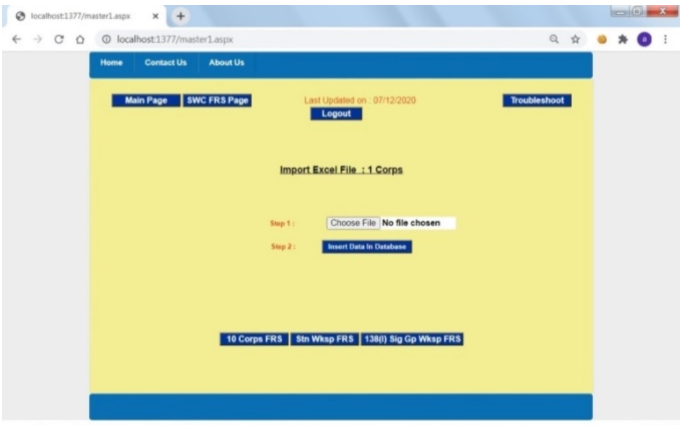

Fig 3. Sub Unit FRS

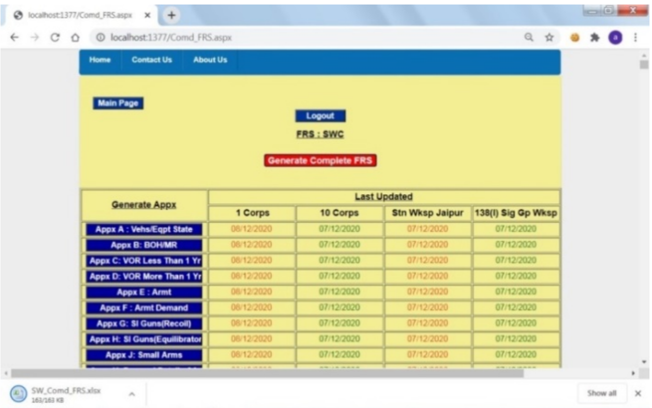

Fig 4. FRS Generated

C. Troubleshoot

Troubleshooting is needed once an error is shown during the import of the data.

D. FRS Generation

Once the error is rectified and subsequently the FRS of all sub units are imported successfully then the user may navigate to FRS page generation page by clicking on View Comd FRS button on import data platform page as shown in Fig 4.

E. Analysis

Equipment Readiness

The quantitative analysis based upon the FRS data is further sub divided into various critical categories as shown in Fig 5.

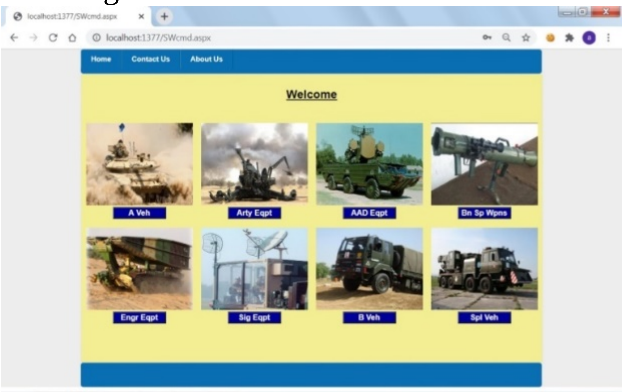

Fig 5. Quantitative Analysis

It out the percentage availability of equipment categorized as shown in Fig 5 in form of a dashboard. The dashboard figure cannot be shown due to sensitivity of the data.

Combat Analysis

To predict the life cycle of equipment Machine Learning (ML) based model is developed. A cost model [9] is developed based on past repair data trained using regression algorithms predicting the Remaining Useful Life (RUL) of equipment.

Data Augmentation: As the data was sensitive due to the critical nature of operations of the organisation, the same has been generated synthetically duly incorporating all the factors.

Creating Vehicle Database: Synthetic data was created with the dependencies in between the attributes and the requirements of the desired model.

(i) Assumptions: As per the common understanding on the subject various assumptions considered for the study are as below:

- The higher number of visits to the workshop indicates higher likelihood of repeat visits.
- The higher the age of the vehicle indicates greater probability of needing maintenance.
- The higher odometer indicates greater wear and tear probability and hence need for maintenance.
- The greater number of occurrences of repair type indicates higher probability of the recurrence.
- The higher average labour effort over 1 year suggests vehicle involves high cost and frequent servicing.
- The higher repair parts change indicates there is a higher wear and tear on the vehicle and hence likelihood of other parts failing.
- If there is high labour time in the last Job there could be larger problem in the vehicle and hence probability of vehicle needing further service is higher.
- All vehicles are serviceable to 100% state on first date of period under consideration. After repairs, the vehicle serviceability state is restored to 100%.
- All vehicles are subjected to similar exploitation and Geographical terrain.
- The efficiency and work procedure of maintenance echelon manpower is uniform.
- There exists uniformity in the operator's way of using the vehicles.

Volume of Dataset: The volume of dataset generated synthetically for various aspects as shown in Table.1.

Table 1: Datatype and corresponding volume

Data Type	Volume
Geog Locs	4
Units	117
Vehicles	1990 (Distributed in Geographical Locations)
Age	1970 to 2016
Categories	20 (distributed based on Age & Location)
Sub Systems	64
Job Cards	55,671 (Org in various type of exploitation randomly)
Job Date	2010 to 2017
Faults	693 (Sub System wise organised & Randomly distr)
Spares	10,339 (Randomly distributed in Jobcards)
Job _ KM	Distributed based on Age of vehicle

Cost Equivalence Model: Vehicle health monitoring [10] and maintenance are critical factors for every employing agency in order to optimise the work output from the vehicles and minimise the repair costs. The main objective of the study is to analyse the vehicle repairs in terms of Cost Effect and establish a means to quantify dependability of a vehicle for a known task/mission and assist decision making for vehicle repair/discard actions. All the repair activities of each vehicle are been converted to equivalent cost incurred as Work Value Cost, Cost of Spares & Repairs. The resultant plot of the data is shown in Fig. 6.

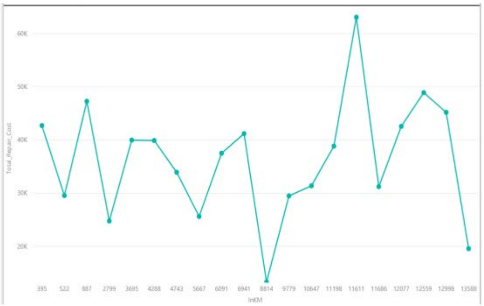

Fig 6. KM Vs Cost Plot

(ii) Linear Model: Based on Linear Model Theory, a linear Model with Least Sum of Squares Method was calculated, and the following equation of line was obtained:

y = .146368 * x + 35197.128

The plot of cost vs km using linear model is shown in Fig. 7.

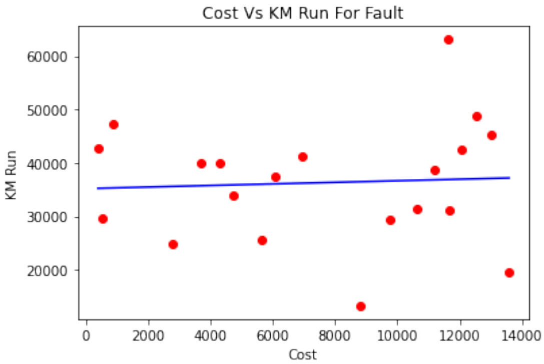

Fig 7. Plot of Cost Vs KM using Linear Model

(iii)Polyfit Model: Based on Polyfit **Model**[11] we can try building a model with all polynomial terms up to degrees ranging from 1 to n as shown below:

$$y = a_1 x_1 + a_2 x_1^2 + a_3 x_1^3 + .. a_n x_1^n + e$$

It can be observed from Fig. 8 that as we build models with more and more polynomial terms, the model starts to fit every data point in the training set which is a case of overfitting. The variation of RMSE of Train vs Test for model varying up to 15 degrees can be seen in plot shown in Fig. 9.

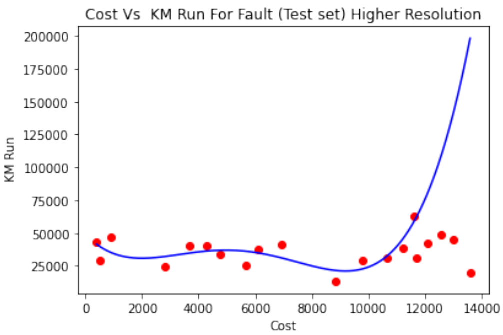

Fig 8. Polyfit KM vs Cost Plot

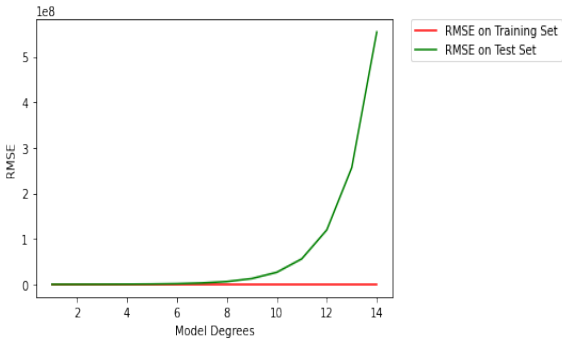

Fig 9. RMSE vs Model Degrees

(iv) Ridge Regression: One way to deal with overfitting is regularization. Regularization applies penalties on parameters if they inflate to large values and keeps them from being weighted too heavily.. The results of ridge regression applied to given data revealed the plot with 75 % training data as shown in Fig.10.

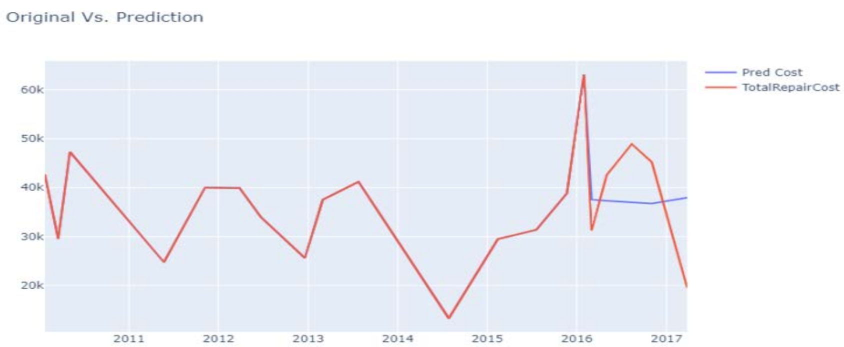

Fig 10. Ridge Regression Cost Vs KM

(v) Remaining Useful Life: The data analysis of the past and predicted expenditure data can result in valuable insights into the remaining useful **life**[11] of the vehicle based on the maintenance expenditure on the vehicle. Considering the threshold value as the original vehicle cost for lowest dependability, using the individual vehicle data, the following can be analysed for the sample set of vehicles under study with target cost prediction for a mission of 500 KM is shown in Fig. 11.

	RegnNo	Geog_Loc	Total_Expended	2017_Expended	Pred_tgt	Avg_Yly_Cost	Bal_Cost_Life	Bal_Age
0	00Y1866G	High Altitude (Plains)	871339	155890	[[35947.613312551795]]	108917.375	10.362543	7.000000
1	00Y1987D	Desert	726042	19563	[[37440.408154175304]]	90755.250	14.037293	13.000000
2	00Y3422G	Desert	1221491	241875	[[39331.204042123325]]	152686.375	5.098746	3.000000
3	00Y5215F	Desert	934533	135063	[[36209.2094406307]]	116816.625	9.120851	9.120851
4	00Z3656B	Desert	1056499	18147	[[32179.31287108315]]	132062.375	7.144359	6.000000
...	...	...	...	...	...	...	...	...
173	99Y4247C	Desert	1012394	85097	[[40139.299423603]]	126549.250	7.804124	7.804124
174	99Y6803E	Desert	1079913	275222	[[37766.80416713405]]	134989.125	6.816008	4.000000
175	99Z2632B	Desert	963684	164056	[[39189.4664040079]]	120460.500	8.602953	7.000000
176	99Z4098F	Plains	1145641	170339	[[30798.654927449174]]	143205.125	5.965981	7.000000
177	99Z5382C	Desert	778150	163597	[[30858.033878031885]]	105465.500	10.963547	6.000000

178 rows × 9 columns

Fig 11. Remaining Useful Life of Vehicle

(vi) Vehicle Criticality: The analysis can be used further to evaluate the criticality of condition of the vehicles, thus, facilitating the decision makers towards appropriate utilisation of the vehicles as per their criticality state. It is evident that the vehicles whose actual age is more and balance age is less are in critical state of operation and are likely to cause more expenses in the immediate future tasks and are close to the end of life calculated using the threshold value. The screen shot of analysis is shown in Fig. 12.

(vii) Rules for Employability of Vehicle: The above data can give valuable insights into decision making towards employability of the vehicle based on anticipated predicted costs of a vehicle in present given state. Depending on the likely predicted expenditure (which is dependent on the age and mileage of the vehicle) in various combinations of geographical location and exploitation, various conditions suitable for vehicle exploitation with lesser cost of repairs need to be identified in order to employ the vehicle effectively with minimal costs of maintenance. The said rules can be obtained as an output of a Machine Learning Classification Algorithm. Various classification techniques were applied to the grouped data for classification into high and low cost of repairs. In view of the results obtained, the Decision Tree Classification Algorithm is used to generate the rules for the employability of a vehicle. With three conditions each of Geographical Location, Exploitation, KM, Engine Hrs as mentioned below, the Cost prediction and rules are obtained:

- Geographical Location- Desert, High Altitude, Plains.
- Exploitation - Exercise, Operational, Routine, KM - High, Medium and Low.
- Engine Hrs - High, Medium and Low

The logic for generating understandable rules has been generated by creating reoccurring loops for each of the above conditions thus resulting in 81 Rules as mentioned in results section. These rules can be filtered for Low and High Expenditure costs to decide the exploitation of the vehicles.

```
There are  131 Non Critical Vehs,  3 vehs in Critical State and  44 vehs in Very Critical State

Vehicles in Very Critical State are :
       ['00Y3422G', '00Z4952C', '02Y4965E', '02Z3379G', '03Y4858F', '05Y6003E', '05Z3902G', '06Y3536G', '07Y4346D', '09Y1658F', '09Y4007A', '09Z3594A',
Vehicles in Critical State are :
       ['12Z3045E', '15Z3876B', '15Z6913E']

The status wise veh list is as below :
```

	RegnNo	Geog_Loc	Total_Expended	2017_Expended	Pred_tgt	Avg_Yly_Cost	Bal_Cost_Life	Bal_Age	Max_Age	VehicleStatus
0	00Y1866G	High Altitude (Plains)	871339	155890	[[35947.613312551796]]	108917.375000	10.362543	7.000000	8	Not_Critical
1	00Y1987D	Desert	726042	19563	[[37440.408154175304]]	90755.250000	14.037293	13.000000	8	Not_Critical
2	00Y3422G	Desert	1221491	241875	[[39331.204042123325]]	152686.375000	5.098746	3.000000	8	Very_Critical
3	00Y5215F	Desert	934533	135063	[[36209.2094406307]]	116816.625000	9.120851	9.120851	8	Not_Critical
4	00Z3656B	Desert	1056499	18147	[[32179.31287108315]]	132062.375000	7.144359	6.000000	8	Not_Critical
5	00Z4165A	High Altitude (Plains)	1408826	185682	[[33236.62512906898]]	176103.250000	3.356974	7.000000	8	Not_Critical
6	00Z4952C	Desert	1045193	158252	[[25961.958155305954]]	130649.125000	7.308178	5.000000	8	Very_Critical
7	01Y1819D	High Altitude (Plains)	966333	110413	[[38105.640253878504]]	120791.625000	8.557439	7.000000	8	Not_Critical
8	01Y2197A	Desert	655478	132048	[[27556.55313957812]]	81934.750000	16.409667	16.409667	8	Not_Critical
9	01Y2556A	Desert	898801	117196	[[20911.288387429644]]	112350.125000	9.801493	9.801493	8	Not_Critical
10	01Y565E	Desert	1105575	39128	[[31227.084177852854]]	157939.285714	5.663094	12.000000	8	Not_Critical
11	01Y6842A	Desert	918234	115815	[[23082.836994707868]]	114779.250000	9.424752	9.424752	8	Not_Critical
12	01Z366C	Desert	697686	78108	[[26389.997929339115]]	87210.750000	14.932953	12.000000	8	Not_Critical
13	01Z4495B	High Altitude (Plains)	1014200	226874	[[38407.689548472044]]	126775.000000	7.775981	7.000000	8	Not_Critical
14	02Y2629B	Desert	715002	106617	[[31874.727091774057]]	89375.250000	14.377560	19.000000	8	Not_Critical
15	02Y3915G	Plains	900385	115899	[[34823.43816808765]]	112548.125000	9.770176	8.000000	8	Not_Critical
16	02Y4141A	Desert	952093	56541	[[28216.580633845602]]	119011.625000	8.805081	8.805081	8	Not_Critical
17	02Y4265D	Plains	930749	69144	[[33580.29445348532]]	116343.625000	9.190456	9.190456	8	Not_Critical
18	02Y4965E	High Altitude (Plains)	1285167	273730	[[35994.64278089365]]	160645.875000	4.449744	3.000000	8	Very_Critical
19	02Y5458E	Desert	693741	167544	[[36112.78894352938]]	86717.625000	15.063362	12.000000	8	Not_Critical
20	02Y827E	Plains	993781	192735	[[46446.28538809333]]	124222.625000	8.100127	9.000000	8	Not_Critical
21	02Z3379G	Desert	1381243	189750	[[50156.44067882845]]	172655.375000	3.583769	4.000000	8	Very_Critical
22	02Z5924G	Plains	746099	0	[[41265.82414274557]]	106585.571429	11.764266	11.764266	7	Not_Critical
23	03Y1641F	Desert	971402	48038	[[31530.408002901084]]	121425.250000	8.471039	8.471039	8	Not_Critical

Fig 12. Vehicle Criticality Classification

5. Results

The Web Application provides a platform to view the equipment state and availability at a click of a button. For AI model it was observed from Fig 7 that the relation between *Cost* and *Km* is not linear and looks like some polynomial. It can be observed from Fig 8 and Fig 9 that as we build models with more and more polynomial terms, the model starts to fit every data point in the training set. This is the case of overfitting Hence Ridge Regression was used which regularized the overfitting to calculate RUL of the vehicles.

Remaining Useful Life (RUL): Based on the purchase cost, amount expended each year, and the balance life cost difference, the remaining life in terms of cost has been derived and the ridge regression has been applied on the yearly cost expenditure data to predict the future yearly cost. Knowing these metrics of balance life (cost) and likely cost for each future year, the balance age of each vehicle has been calculated.

Vehicle Criticality: The criticality of vehicle in terms of balance life has been calculated in a logical manner out of the balance life cost and age of the vehicle. Here, it is taken into account that the vehicles in the end of their life have reduced dependability factor and thus aren’t recommended to be deployed in important tasks.

Rules for Employability: Finally, the actionable insight from the analysis rests on the practical utilisation of the vehicle. The rules generated give the various combinations of vehicle status which may lead to high / low maintenance costs. Various classification techniques were applied to the grouped data for classification into high and low cost of repairs. The accuracy results obtained were as under:

- Logistic Regression Classifier - 64.51%
- Naïve Bayes Classifier - 64.51%
- K Nearest Neighbour Classifier - 62.76%
- Decision Tree Classifier - 64.93%
- Random Forest Classifier - 64.85%

In view of the above obtained results, the Decision Tree Classification Algorithm is used to generate the rules for the employability of a vehicle. With three conditions each of Geographical Location, Exploitation, KM, Engine Hrs, the Cost prediction and 81 rules are obtained.

6. Conclusion

This paper discussed the design of a Web-based Application, automating the compilation process in order to save time, provide a real time & error free data enabling commanders at various levels to assess the equipment availability and accordingly select the best suited equipment for a particular mission.

The cost analysis of the vehicle helps the owner choose the vehicles based on dependability factor for a mission as per its criticality and also fund availability. Furthermore, the same can be helpful in deriving remaining useful life of the vehicle (with reference to a defined threshold value) based on the expenditure pattern. The Decision Rules generated using the Decision Tree Algorithm give the set of conditions leading to high/low-cost expenditure on the vehicles. As a Future work, this model can be further fine-tuned along with onboard sensor data which would predict the failure of equipment and validate it with the cost analysis model.

7. References

[1] https://www.statisticshowto.com/ridge-regression.
[2] A Binding, N Dykeman, S Pang, Machine Learning Predictive maintenance on Data in the Wild, 2019 IEEE.
[3] Frisk, Krysander, Larsson, Data-Driven Lead-Acid Battery Prognostics Using Random Survival Forests, annual conference of the prognostics and health management society 2014, Conference, 2014.
[4] J Buddhakulsomsiri, A Zakarian, Sequential pattern mining algorithm for automotive warranty data, Computers & Industrial Engineering 57 (2009) 137–147, 2009.
[5] R. Keith Mobley, An introduction to Predictive Maintenance (Second Edition), Butterworth-Heinemann, USA, 2002.
[6] Max Kuhn, Kjell Johnson, Applied Predictive Modelling, Springer, USA, 2013.
[7] Hastie T, Tibshirani R, Friedman J, The Elements of Statistical Learning, 2008.
[8] Viswanathan, Viswa. Rapid web application development: IEEE 25.6 (2008): 98-106.
[9] Coble, Jamie Baalis, Merging Data Sources to Predict Remaining Useful Life – An Automated Method to Identify Prognostic Parameters. PhD diss., University of Tennessee, 2010.
[10] Machine Learning Using Python by Manaranjan Pradhan and U Dinesh Kumar.

Mechanisms in Electrical Systems

High Frequency Micro-Spherical Transducer for Underwater Sensing Mechanisms in Naval Armament

CM Lonkar
Armament Research and Development Establishment
DRDO
Pune
cmlonkar@arde.drdo.in

S.D. Shinde
Armament Research and Development Establishment
DRDO
Pune
shivdattashinde@rediffmail.com

B. Praveen kumar
Armament Research and Development Establishment
DRDO
Pune
praveenkumar@arde.drdo.in

I.R. Abisekaraj
Naval Scientific and Technological Laboratory
DRDO
Vishakapatnam
abisekaraj@nstl.drdo.in

Abstract— **High frequency underwater piezo-transducers enable high resolution imaging but then demands transducer size miniaturization which becomes challenging due to inherent brittleness of piezoceramics. Piezoceramic compositions viz' $Pb_{0.988}(Zr_{0.52}Ti_{0.48})_{0.976}Nb_{0.024}O_3$ (PZT type 5A) and $Pb_{0.98}La_{0.02}(NiSb)_{0.05}[(Zr_{0.52}\ Ti_{0.48})_{0.995}]_{0.95}O_3$ (La-PNS-PZT) were processed through solid state reaction route and used for development of hollow micro-spherical transducers of OD 4.7mm with wall thickness of 0.5mm. Both the compositions contain perovskite phases revealed from XRD analysis and possess dense microstructure with polygonal grain morphology indicated by Scanning Electron Micrographs. Piezoelectric and hydrostatic coefficients, those plays vital role in underwater performance, were superior for La-PNS-PZT. Underwater performance of the polyurethane moulded transducers (Hydrophones) was carried out in acoustic tank and compared with imported hydrophone of similar specifications (Make-Reson Model 4034). Resonance frequency and sensitivity for La-PNS-PZT was found superior compared to PZT type 5A hydrophone in the usable frequency range of operation. Further performance comparison of La-PNS-PZT hydrophone with Reson hydrophone shows, superior sensitivity and flat response over wider frequency band for La-PNS-PZT hydrophone. Indigenously developed La-PNS-PZT hydrophone shown promising performance over imported one.**

Keywords— Hydrophone, High frequency hydrophone, PZT, Micro-spherical transducer

1. Introduction

PZT based piezoceramics exhibits excellent electro-mechanical energy convertibility which makes them a promising candidate for underwater sensing mechanisms like hydrophone [1,2] wherein they produce proportionate electrical signal in response to underwater pressure variations generated due to acoustic signals [3]. Therefore, piezoceramics are considered as a heart of any kind of underwater weaponry system, communication system or navigation system. These systems include various types of SONAR, passive sonobouy, hydrophone, homing torpedo, towed arrays over large distances etc. [4].

Underwater performance of the sensing transducer mechanism is highly influenced by hydrostatic piezoelectric charge coefficient (d_h), hydrostatic piezoelectric voltage coefficient (g_h), and Figure of Merit ($d_{h*}g_h$) [5,6].. Strength of signal generated i.e. Receiving Sensitivity,(RS), indicated by M_o of the underwater transducer is given [3] by-

$$M_0 = g_h * t = (g_{33} + g_{32} + g_{31}) * t \quad ....(1)$$

Where, g_{ij} are piezoelectric voltage coefficient tensors. d_h and g_h parameters of piezo-ceramics are respectively proportional to piezoelectric charge coefficient (d_{33}) and piezoelectric voltage coefficient (g_{33}) [7,8]. Hence, piezo-ceramics with superior values of d_{33} and g_{33} are always looked-for underwater sensing mechanisms.

Underwater transducers are generally used for generating underwater acoustic signals for communication and imaging purposes. Piezoelectric based transducer is commonly used as underwater high frequency transducer for underwater detection and imaging. Because piezoceramics fabrication can be tailored easily for critical shapes and sizes based on the frequency requirements. Wavelength and thus frequency of sound wave is fundamental parameter which decides it's underwater distance of propagation and resolution of image. Low frequency waves can travel to larger underwater distances without much attenuation. Although, high frequency sound travel for shorter distances due to attenuation, it provides high resolution images. [9]. Owing certain advantages, usually, frequency of operation of a transducer is chosen below the resonance frequency. Since resonance frequency is inversely proportional to related dimension of excitation of transducer, size miniaturization of piezo-component becomes inevitable in high frequency transducer [8].

In our current study, a design of broadband spherical hydrophone is considered because of its uniform omni-directional characteristics over a wide frequency range of 10 Hz to 450 kHz. Miniaturization of component with smaller wall thickness and machinability was a challenge due to inherent brittle nature of piezoceramics. The miniaturized spherical piezo sensor transducers were developed from PZT type 5A & La-PNS-PZT piezoceramic compositions and were permanently encapsulated in acoustically transparent polyurethane rubber to ensure "matching acoustic impedance" with that of water and piezo transducer. Underwater performance of developed miniaturized hydrophones was evaluated and compared with imported hydrophone of Make- Reson Model- TC 4034.

2. Experimental

Ferroelectric compositions $Pb_{0.988}(Zr_{0.52}Ti_{0.48})_{0.976}Nb_{0.024}O_3$ (PZT type 5A) and $Pb_{0.98}La_{0.02}(NiSb)_{0.05}[(Zr_{0.52}\ Ti_{0.48})_{0.995}]_{0.95}O_3$ (La-PNS-PZT) in stoichiometry were selected and were processed through solid state reaction route using raw materials in the powder form of oxides of Lead, Zirconium, Titanium, Niobium, Nickel, Antimony, and Lanthanum. Mixtures were milled for 24 h using de-mineralized water medium. Solid state reaction was carried out at 1060 °C followed by wet milling for 24 h to obtain the fine powder of particle size about 1.2 ± 0.2 μm. Adding an appropriate binder, powders were granulated. Compaction was carried out by double ended die punch hydraulic machine to form the component in the form of one end closed cylinder there by maintaining the green density about 4.8 g/cc. Removing the binder, by components were machined on mini CNC lathe machine to obtain hemispheres. Sintering was carried out at 1270 °C for 30 min in the lead rich environment. Crystal structure was analysed from XRD patterns recorded using diffractometer Make- Bruker, Model-D8 advance. Microstructure of fractured samples was evaluated using high resolution scanning electron microscope Make- Quanta 200 FESEM of FEI. Silver electroded hemispehers were poled in heated oil bath. Capacitance (*C*), tan δ (measured at 1 kHz), resonance frequency (*fr*), anti-resonance frequency (*fa*), Impedance (*Zm*) were measured using Hioki Hi-tester (model 3532). Piezoelectric charge constant (d_{33}) was measured by d_{33} meter (PM 300 Piezo Test,UK). Standard mathematical relations were used to compute dielectric constant (K^T_3), voltage coefficient (g_{33}) and Figure of Merit

(FoM). Providing the electrical connections, hemispheres were assembled together using epoxy based adhesive. Stages of development of transducer are depicted in Fig.1. Further, these were moulded with acoustically transparent poly-urethane and cured for 72 h. to form hydrophones (Fig. 2). Hydrophones were tested in an acoustic tank for under water performance, at NSTL, Visakhapatnam using primary calibration method. All the three transducers were calibrated using primary calibration using NI based Hydrophone calibration system. Schematic of calibration setup is shown in Fig. 3.

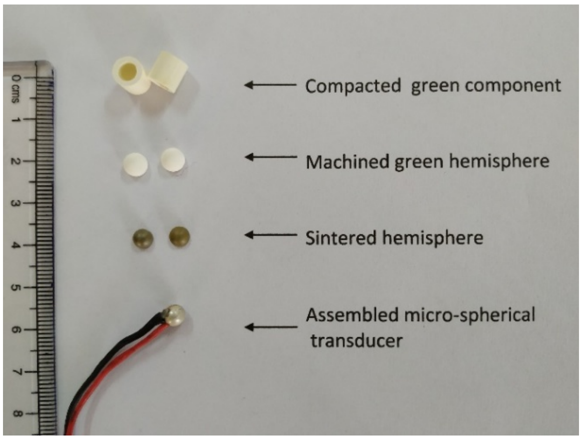

Fig 1: Stages of development of transducer

Fig 2: Stages of development of hydrophone from transducer

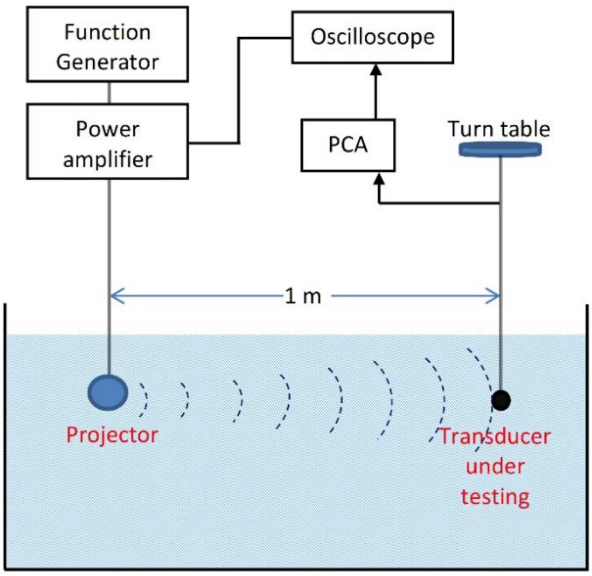

Fig 3:Transducer calibration set-up

3. Results and Discussions

A. Crystal Structure

X-Ray diffraction patterns recorded from 20° to 60° for 2θ positions for PZT 5A and La-PNS-PZT are shown at Fig.4. Sharp narrow peak patterns reveal the polycrystalline nature. A perovskite phase formation is indicated by intense peak for (110) plane in both the compositions [10,11]. The splitting in the peak intensity at triplet (200), (210) and (211) indicate the co-existence of both ferroelectric tetragonal (F_T) and ferroelectric rhombohedral (F_R) phases [11,12]. PZT 5A composition richer in F_R indicated by larger peak intensity at (200)R. La-PNS-PZT contains equal amounts of F_T and F_R phases indicated by identical peak intensity at (200)R and (200)T.

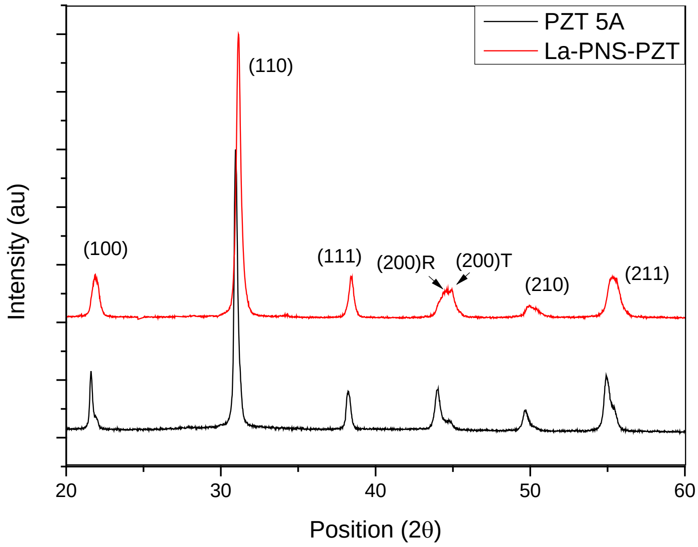

Fig 4: XRD patterns for PZT 5A and La-PNS-PZT

B. Microstructure

Fig. 5a and 5b represents the microstructure of the PZT 5A and La-PNS-PZT samples sintered at 1270ºC for 30 minutes. Compact microstructure with polygonal grain morphology observed in both the cases indicating appropriateness of sintering parameters. However, comparatively wider grain size variation observed in PZT 5A sample while uniform grain morphology observed in La-PNS-PZT. Grain size was measured by linear intercept method wherein five lines were drawn at the different places on micrograph. The number of grains cut by the lines was counted. The average grain sizes were calculated by dividing the length of the line in µm by the numbers of grain covered by the line. Average grain sizes were calculated to minimize the error. Averaged grain size was 1.4 µm and 5.3 µm for PZT 5A and La-PNS-PZT respectively

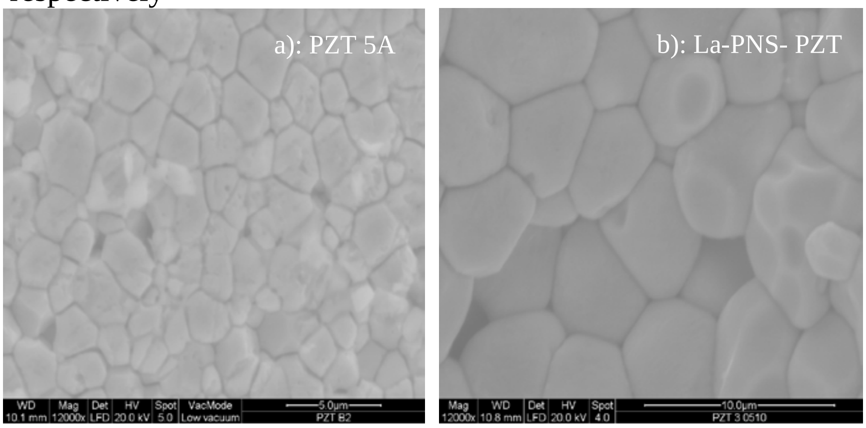

Fig 5: Microstructure for a) PZT 5A and b) La-PNS-PZT

C. Piezoelectric properties

Piezoelectric properties for both the compositions are listed at Table 1. Particularly properties like piezoelectric charge coefficient (d_{33}), piezoelectric voltage coefficient (g_{33}) and Figure of Merit plays significant role in underwater transducing performance were superior for La-PNS-PZT which is attributed to composition at MPB having compact, uniform microstructure and optimum grain size [13,14]. Acoustic emission power and sensitivity of the spherical hydrophone is highly dependent on piezoelectric properties. These hydrophones have exclusive vibrating mode of operation in broad frequency band and wide beam during high frequency action, that are essential characteristics for underwater acoustic detection mechanisms.

Table 1 Piezoelectric Properties required for underwater transducer application

Parameter	**PZT type 5A**	**La-PNS-PZT**
Piezoelectric charge coefficient, d_{33} $x10^{-12}$ (C/N)	318	410
Piezoelectric voltage coefficient, g_{33} $x10^{-3}$ (m.V/N)	25	29
Dielectric Constant, $K^T{}_3$	1428	1608
tan δ	0.018	0.017
Figure of Merit $x10^{-12}$ (m.v.C/N^2)	8	12

D. Receiving Sensitivity (RS)

Hydrophones were subjected to hydrostatic pressure of 10 bar for half an hour and then tested for receiving sensitivity and performance was compared with commercially available similar kind of imported hydrophone TC 4034 by M/s. Teledyne-Reson. Underwater receiving sensitivity measurements are shown in Fig. 6. In case of PZT 5A hydrophone, a large dip was observed till 200 kHz in the broad frequency zone up to 300 kHz with fall of sensitivity from -205db to -235 dB. Then there was flat response till 400 kHz and further reduced. Comparatively, Reson hydrophone has shown a good flat response in slightly parabolic profile upto 325 kHz with sensitivity about -223 dB. La-PNS-PZT hydrophone shown a good flat response among all the three hydrophones as shown in inset of Fig. 6 with usable frequency upto 375 kHz with improved sensitivity about -220 dB .

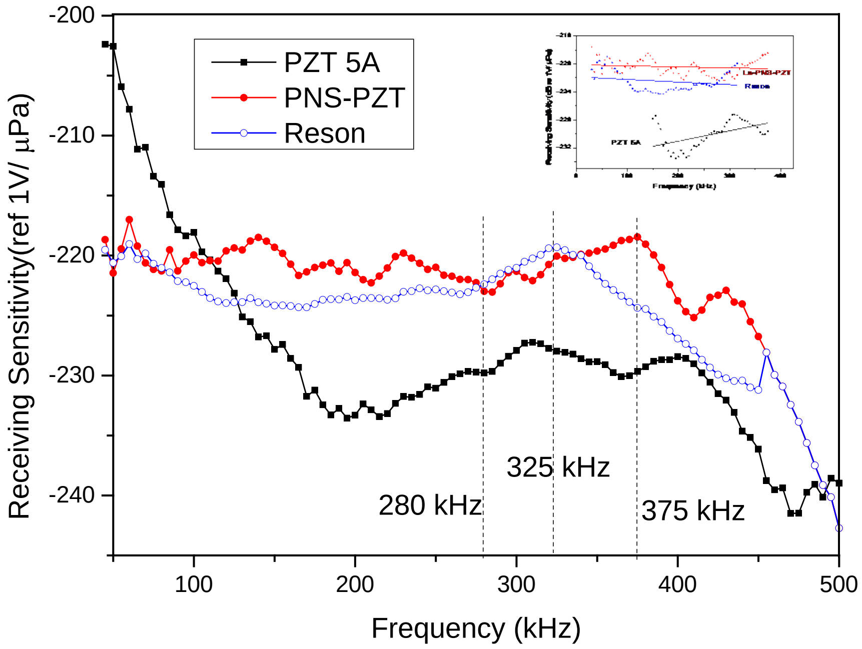

Fig 6: Underwater Receiving Sensitivity response

4. Conclusions

Hollow micro-spherical transducers of OD 4.7mm with wall thickness of 0.5mm were successfully developed from perovskite piezoceramic compositions viz' $Pb_{0.988}(Zr_{0.52}Ti_{0.48})_{0.976}Nb_{0.024}O_3$ (PZT type 5A) and $Pb_{0.98}La_{0.02}(NiSb)_{0.05}[(Zr_{0.52}\ Ti_{0.48})_{0.995}]_{0.95}O_3$ (La-PNS-PZT). Transducers were characterized for piezoelectric properties and underwater performance as a hydrophone. PZT 5A showed flat response in the narrow frequency brand approximately 275 – 400 kHz with sensitivity of -228 dB. Reson and La-PNS-PZT hydrophone shown better performance compare to PZT 5A hydrophone. La-PNS-PZT hydrophone have shown superior performance over Reson hydrophone TC 4034 in following respects-

- Better frequency independent i.e. flat response.
- Wider useful frequency band, 50-375 kHz, for operation in place of 50-325 kHz.
- Better receiving sensitivity ~-220 dB ref 1V/μPa in place of ~ -223 dB ref 1V/μPa.

A hydrophone made-up of La-PNS-PZT composition and jointly developed by ARDE and NSTL, Visakhapatnam is superior in all respect and can replace imported one. Miniaturization, highly smart and effectiveness will be the emphasis point for future research in the piezo mechanisms.

5. Acknowledgement

Authors express their sincere thanks to Director, Armament Research and Development Establishment (ARDE), Pune for giving permission to publish this work. Thanks, are also due to Director, NSTL, Visakhapatnam, for giving permission to carry-out the experiment. Our sincere thanks to TD (Homing), officers & staffs of Sensors Group and Rubber Technology Group, NSTL, Visakhapatnam for fabrication and testing of hydrophones.

6. References

[1]. J. F. Tressler, Piezoelectric Transducer Designs for Sonar Applications, edited by A. Safari & E. K. Akdoğan. Piezoelectric and Acoustic Materials for Transducer Applications, Springer Science+Business Media, New York, 2008. pp. 217-239.

[2]. Haertling, G.H. Ferroelectric ceramics: History and Technology, *J. Am. Ceram. Soc.* 1999, **82,** 797–818.

[3]. Lonkar C.M.; Kharat D.K.; Prasad S.; Balasubramanian K. Prasad N. Study of Pb (Ni1/3Sb2/3)O3-PbZrTiO3 Ceramic Sensors for Underwater Transducer Application *Def. Sc. J.,* .2012, 62 (4), 269-273

[4]. Tressler, J. F.; Alkoy S. & Newnham, R., Piezoelectric Sensors and Sensor materials, *J. Electromics*, 1998, 2(4), 257-71,

[5]. Moulson, A. J & Herbert, J.M., Electroceramics (2nd edition), John Wiley & Sons Ltd, London ,2003, 384 p.

[6]. Lonkar C.M.; Kharat D.K.; Prasad S.; Balasubramanian. K. Synthesis, Characterization and Development of PZT-based Composition for Power Harvesting and Sensors Application in hand book of "Nanoceramic and nano composite coatings and materials, Vol 1, Butterworth-Heinemann,2015,579-593p.

[7]. Zhaohui, L.; Aigen, H.; Guidong; L.; Jinduo, Z. Finite element analyzing of underwater receiving sensitivity of PMN-0.33PT single crystal cymbal hydrophone, *Ultrasonics,* 2006, **44**, 759-762.

[8]. Newnham, R.E.; Markley,D.C.; Tressler, J.F.; Zhang, J.; Uzgur, E.; Hennion, A.C. & Hughes,W.J. Size Effects in Capped Ceramic Underwater Sound Projectors. *IEEE Xplore Digital Library*, 2002, 2315-2321.

[9]. Webstar J. (ed). High frequency underwater sound in Wiley encyclopedia of electrical and electronics engineering, John Wiley & Sons INC, 2007, 1-4 p.

[10]. Tipakontitikul, R.; Anantha, S. A modified two-stage mixed oxide synthetic route to lead Zirconate Titanate powders, *Mater. Lett.,* 2004, **58**, 449-454.

[11]. Nasar, R.; Cerqueira, M.; Longo, E.; Varela, J.; Beltran, A. Experimental and theoretical study of the ferroelectric and piezoelectric behavior of strontium-doped PZT, *J. Eur. Ceram. Soc*., 2002, **22(2),** , 209 -218.
[12]. Boutarfafia,A.,Investigations of Co-existence region in lead zirconate titanate solid solutions:X-ray diffraction studies, *Ceram. Int.,* 2000, 26 (6), 583-87.
[13]. Kungl, H. & Hoffmann M.J., Effects Of Sintering Temperature On Microstructure And High Field Strain Of Niobium-Strontium Doped Morphotropic Lead Zirconate Titanate, *J. Appl. Phys*., 2010 **107(5)**, 054111
[14]. Ming Chen, Xi Yao, Liangying Zhang, " Grain Size dependence of dielectric and field –indiced strain properties of chemical prepared (Pb,La)(Zr,Sn,Ti)O3 antiferroelectric ceramics, Ceramic International ,2002, 28 (2)201-207

Design of Semiconductor Switching Mechanism for a 400 kJ module for Railgun Applications

Gaurav Kumar
Armament Research and Development Establishment
DRDO
Pune

Satyam Swarup
Armament Research and Development Establishment
DRDO
Pune

Shivam Rajput
Armament Research and Development Establishment
DRDO
Pune

Nomula A Prasanth
Armament Research and Development Establishment
DRDO
Pune

Pradeep Kumar
Armament Research and Development Establishment
DRDO
Pune

SK Nayak
Armament Research and Development Establishment
DRDO
Pune

***Abstract*—A Capacitor Bank is the most widely used pulsed power source for railgun applications. A capacitor bank is divided into many modules and the energy from the capacitor is switched into the railgun by means of a closing switch and the oscillations in the circuit are prevented by a crowbar switch. Advancements in semiconductor technology have allowed the use of semiconductor devices for use as switches in pulsed power applications. However a number of devices have to be used in series and parallel combination and operated at the peak of their surge rating to achieve the high peak current required. This paper discusses the use of Thyristor stack based main closing switch and Diode stack based crowbar switch for a 400 kJ Capacitor based pulsed power module**

1. Introduction

An electromagnetic railgun requires a large amount of current (in order of MAs) to be injected into the rails for operation. This current is sourced from a pulsed power source which stores energy over a period of time and releases it in the order of ms. A capacitor bank based pulsed power source is the most practical pulsed power source for railgun applications. A capacitor bank pulsed power source comprises of a number of pulsed forming units called modules. Each module has capacitors, an inductor and two kinds of high current high voltage switches to feed energy from the capacitors into the railgun. Out of this switches, one switch called the main switch is a triggered switch that switches energy from the capacitor into the railgun through the inductor. In order to prevent voltage reversal across the capacitor and to prevent oscillations in the current a second switch called the crowbar switch is used which turns on automatically once the voltage reversal across the capacitor starts. Traditionally these switches were made using spark gaps or ignitrons but these switches are not field worthy and require maintenance and conditioning.

Semiconductor based pulsed power switches have widely replaced the spark gap and ignitron in various pulsed power applications. In railgun the main switch can be a thyristor based switch (since it has to be triggered) and the crowbar switch can be a diode based assembly.

A single thyristor or diode device is however not suitable for handling the voltage and current levels required in pulsed power module. A number of such semiconductor devices have to be operated in series (to sustain the rated voltage) and parallel (to carry the rated current). The devices are operated at their peak surge ratings. The devices connected in series are held together by means of a clamp to apply the rated mounting force to form a string. It is necessary that a uniform contact pressure is applied on the device surface to ensure uniform current distribution. A number of these strings are connected in parallel to carry the rated current. In order to ensure equal distribution of static and dynamic voltages across each device snubber elements and balancing resistors have to be connected to each of the devices used in the assembly.

The selection of the devices (diodes and thyristors) is based on the peak voltage, current and action integral of switch required and the characteristics of the devices (such as leakage current, reverse recovery charge and turn on delay) must fall within a small window of variance to make an optimal design. The selection of snubber elements and voltage sharing network requires characterization of the devices to obtain a model and simulate the same in the circuit of the module. In order to trigger the thyristor switch, a high gate current is required to be given as input to each of the thyristors in the switch assembly at the same instant. This is sourced from a single gate drive circuit which is magnetically coupled to every thyristor gate in the assembly.

This paper presents the design of Thyristor main switch with its gate drive and Diode crowbar switch for a 400 kJ capacitor pulsed power module rated for 120 kA and 11 kV. The design uses Thyristors rated for 6500V and 65 kA for the main switch with a gate current of 10 A input to each device. The diodes used in crowbar are rated for 6500 V and 70 kA. The methodology for selection of devices, snubber elements and the thyristor gate drive is presented. A number of such modules can be used to generate the current required for the powering the Railgun.

2. Layout of a Pulsed Power Module

Fig.1 represents the layout of the module used in the design. It consists of a set of capacitors which are charged to hold the energy, the main switch, the pulsed shaping inductor, a crowbar switch and the load.

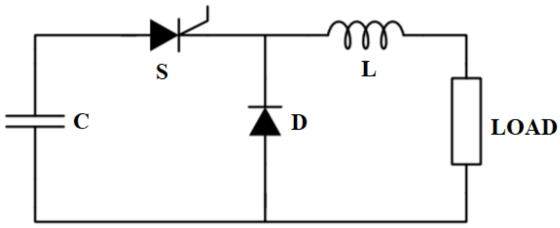

Fig 1: Layout of a single module

Here in the present case, the peak voltage of the capacitors is 11 kV with total capacitance of 6640 µF. The pulsed shaping inductor is 55 µH to give a peak current of about 120 kA. Thus the module will require a main switch and crowbar switch with rating of 120 kA. A typical current profile from the circuit is given in Fig 2. A minimum resistance of 2 mΩ is assumed as a series resistance in the circuit.

Table 1 gives the rating of the main and the crowbar switches. Based on these ratings Thyristor 5STP 26N6500 from ABB (peak current 65 kA, peak voltage6.5 kV) and diode 5SDD 50N5500 (peak current 73 kA and peak voltage 5.5 kV) from ABB have been chosen for use as switches in the pulsed power module described. The subsequent sections describe the design of snubber elements, static voltage equalization resistors and the gate drive for the thyristor switch.

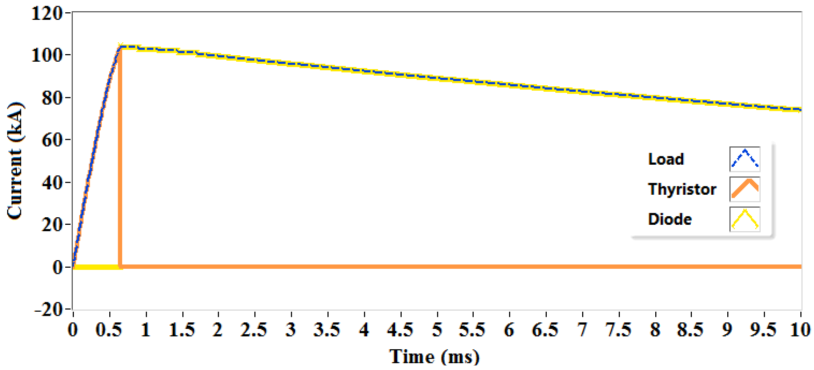

Fig2: Current through the main switch the diode and the thyristor

Table 1: Ratings of Thyristor Switch and Diode Crowbar

Rating	Thyristor Switch	Diode Crowbar
Peak Voltage	11 kV	11 kV
Peak Current	120 kA	120 kA
Peak di/dt	200A/µs	-
$\int I^2 dt$	7 MJ/Ω	93MJ/Ω

3. The Thyristor main Switch

The main switch comprises of two strings of series connected Thyristor devices. In order to increase the string reliability and reduce leakage current during off state five Thyristor devices (5STP 26N6500) are connected in series to form a string. In order to ensure equal voltage distribution during off state, a voltage sharing resistor is placed across each device. A Snubber circuit across each device ensures the Dynamic voltage equalization during the turn on and turn off transients. It is essential that all devices in the string are given trigger at the same instant so that all devices turn on simultaneously to ensure that the devices are not stressed and damaged. Fig 3 shows the components in the thyristor main switch

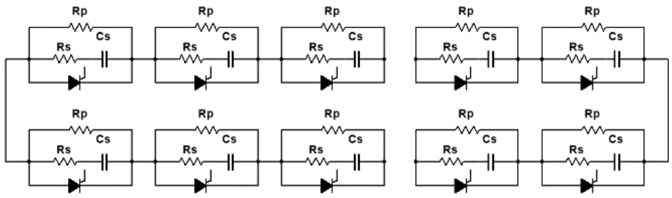

Fig 3: Components of the Thyristor main switch

The di/dt through the device is limited by limited by the pulsed shaping inductor L. The peak di/dt=V/L which is 200A/µs. The $\int I^2\, dt$ rating require per devices becomes 1/4th as the current through each device is half. So the $\int I^2\, dt$ rating is 1.75 MJ/Ω which is within the limit of 8 MJ/Ω for the device.

A. Voltage Sharing Resistor (R_p)

During the off state none of the devices conduct and the complete switch blocks the voltage of the capacitor and prevent it to discharge in the load. However a small leakage current flows through each device and because of mismatch in the devices, different thyristor may block different voltages due to different leakage current. In order to force the devices to share equal voltage, a voltage sharing resistor is put across each device. The voltage sharing resistor in series connected devices is given by [1]

$$R_p \leq \frac{mV_b - V_s}{(m-1)(I_1 - I_2)} \qquad (1)$$

where V_s is the voltage of the string of m devices and V_b is the rated blocking voltage of each device I_2 and I_2 are the maximum and minimum leakage current of the Thyristor respectively. The datasheet gives a maximum leakage current value of 600 mA at rated voltage.

Assuming a mismatch of 10% in the devices $I_1 - I_2$=60mAR_p comes as 89 kΩ.

B. Snubber Circuit for turn on transient Thyristor

It is necessary that when a switch is turned on all the devices turn on simultaneously otherwise the device turning last will experience the complete voltage of the capacitor and will get damaged due to overvoltage. Even if all the devices are given trigger simultaneously (zero delay), the gate of the devices do not turn on instantly and have a time called gate turn on delay t_{gd} after which the Thyristor actually turns on. This delay also varies with each device. So the device that turns last will actually see the complete voltage of the capacitor and may become damaged due to this transient voltage. In order to prevent this, an RC snubber is placed across each of the device. Initially when the capacitor is charged each device holds a maximum of 2.2 kV and so is the snubber capacitor (C_s) across each device. When the thyristors are triggered the voltage across them reduces to zero but the device that turns last will see the voltage across the capacitor. But current will start flowing through the snubber resistor, capacitor and the pulsed shaping inductor. The di/dt across the inductor will prevent the voltage across the thyristor to reach the peak voltage of the capacitor. Once the snubber capacitor is charged completely to 11kV, then only the device experiences the complete voltage of the capacitor. Using the snubber elements we must ensure, that the voltage across the device does not exceed the rated device voltage. Hence L/R_s>>Δt_{gd} and R_sC_s>>Δt_{gd} . Assuming a linear rise of voltage across the device (worst case), the overvoltage ΔV in time Δt_{gd} is given by [2]

$$\Delta V = V(m - \frac{1}{m})(\frac{R}{L}\Delta t_{gd}) \qquad (2)$$

t_{gd} is given as 3μs in the data sheet. For Δt_{gd} = 500ns, R_s=60 Ω, C_s is chosen as 0.1μF.

C. Gate drive circuit

In order to trigger the thyristor in the proposed configuration, it is necessary to give trigger to all the 10 thyristors simultaneously. The cathode of each thyristor is at different potential. So the cathode terminal in the gate drive for each of the thyristor should be isolated. One method is to use isolated gate drive triggered by a common input for each of the thyristors which will be quite cumbersome and may not be jitter free. Another method is to use a gate drive feeding a pulse transformer with single primary and multiple secondary. One secondary of the transformer will be connected to the gate and cathode of one thyristor and will be responsible to give the current to each of the thyristor. The data sheet recommends to give a current of about 7 to 10 A for high di/dt and to operate the thyristor at surge ratings so that the complete wafer of the thyristor conducts. The pulse duration of 5μs is sufficient for di/dt> 20A/ μs.

In order to achieve this a gate drive unit triggered by optical source drives a long loop of wire coupled magnetically to secondaries connected to each of the thyristors as shown in Fig. 4. After each secondary the pulse is conditioned by a small diode bridge rectifier to ensure that only positive gate pulse is applied to the gate terminals

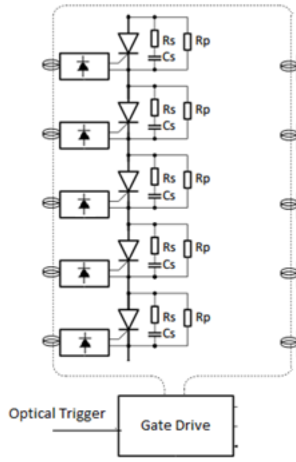

Fig 4 Gate drive Scheme

In order to drive the gate of each of the thyristors we have to generate a current of about 8 A in each of the secondary. Keeping the turn ratio as 1:10 the current through the primary is about 80A. This has to be injected into a long wire looping through each of the secondary. The primary will be energized by a capacitor precharged to a voltage V_G and triggered and discharged through the primary using a small thyristor as shown in Fig 5

When the thyristor is triggered the capacitor discharges through the primary and induces currents in each of the secondaries. Assuming that power is drawn from a capacitor of 20µF, and charged to 500 V, the voltage can be taken as divided into 5 thyristors in series. So in effect a voltage of 100 V drives the equivalent primary of each of the thyristor gate.

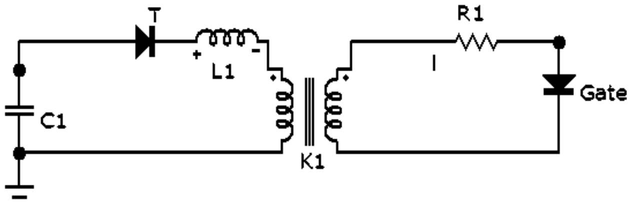

Fig 5 Gate Drive Circuit simulation

Fig 5 shows the simulation of gate current through one of the thyristors. It consist of C_1 charged to 100 V. The capacitor is connected to the transformer with turn ratio 1:10 through a thyristor T1. The coupling coefficient of the transformer K_1 is assumed to be 0.8 owing to the poor coupling between the long primary and multiple secondary. R_1 is the equivalent resistance of the windings. The gate of the device is modeled by a diode I series with each of the secondary Fig 5 shows the simulated gate current which extends to about 7 µs and is sufficient to drive the gate of the thyristor.

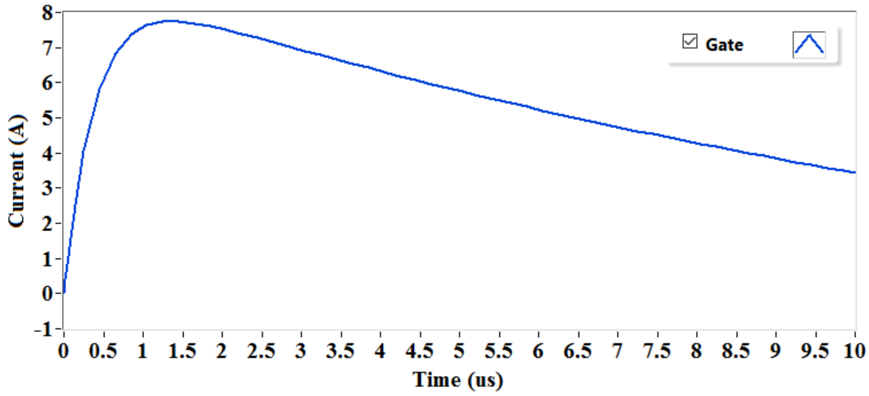

Fig 5 Gate Current through each thyristor

4. The Diode Crowbar

The crowbar switch comprises of two parallel strings of 5 series connected diodes (ABB-5SDD 50N5500). Only static voltage equalization is required in the case of diodes because diodes automatically turn on by application of forward voltage and do not require any protection during turn on. Also the current through them naturally falls to zero and there is no forced turn off or commutation exhibiting reverse recovery behavior and overvoltage transients. Fig 6 shows the configuration of the diode switch with total 10 devices and a resistance R_p across each of the devices. The value of R_p is given by (1). Evaluating R_p for a leakage current of 400 ma and 10% mismatch R_p comes out to be 133 kA.

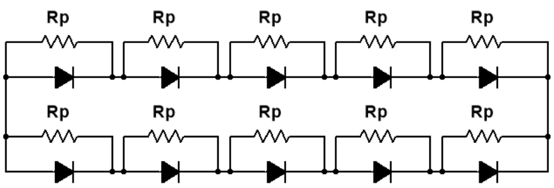

Fig 6 The diode crowbar

There is no limit on the di/dt required for the device and the di/dt is governed by the lead inductances in the crowbar circuit. The $\int I^2\,dt$ rating require per devices becomes 1/4th as the current through each device is half. So the $\int I^2\,dt$ rating is 23.25 MJ/Ω which is within the limit of 27.5 MJ/ Ω for the device

5. Conclusion

This paper presents the design and configuration of thyristor switch and diode crowbar for a 400 kJ capacitor bank based pulsed power module. The component selection, snubber circuit and the gate drive have been discussed. The design will be assembled and tested in the 400 kJ modules at ARDE

6. References

[1] B. Williams, Power Electronics: Devices, Drivers and Applications. London, U.K.: Macmillan education, 1987
[2] E. Spahn, G. Buderer, J. Wey, V. Wegner and F. Jamet, "The use of thyristors as main switches in EML applications," in IEEE Transactions on Magnetics, vol. 29, no. 1, pp. 1060-1065, Jan. 1993
[3] ABB 5STP 26N6 500 Datasheet, ABB Power Grids Switzerland Ltd. semicond., Lenzburg, Switzerland, 2014.
[4] ABB 5STP 5SDD 50N5500 Datasheet, ABB Power Grids Switzerland Ltd. Semicond., Lenzburg, Switzerland, 2014.

Development of Miniaturized & Ruggedized On-board Telemetry for Performance Evaluation of a Typical Laser Guided Missile

CP Singh
Armament Research and Development Establishment
DRDO
Pune

P Nagrale
Armament Research and Development Establishment
DRDO
Pune

SS Kulkarni
Armament Research and Development Establishment
DRDO
Pune

D Tilante
Armament Research and Development Establishment
DRDO
Pune

Jayashri Shikhare
Armament Research and Development Establishment
DRDO
Pune

DT Korade
Armament Research and Development Establishment
DRDO
Pune

SC Rana
Armament Research and Development Establishment
DRDO
Pune

BB Padhy
Armament Research and Development Establishment]
DRDO
Pune
bbpadhy2@gmail.com

***Abstract*—This paper describes the development and implementation of on-board telemetry unit (OBTU) for the performance evaluation of a typical Laser guided missile for anti-tank applications. Various aspects of telemetry sub-modules and selection criteria for sub-systems as per the design requirements and space availability are elaborated. Integration of standalone OBTU and its pre & post integration checks with the missile are also discussed. Various analog and digital parameters are monitored in real time using the developed telemetry unit. Bandwidth of transmitted signal is optimized against a baud rate of data. Operational aspects related to deployment of appropriate receiving antenna to ensure reception of RF signal from the missile while it is inside the metallic body of the tank gun are also discussed. Few typical telemetered results are presented.**

Keywords: **PCM Encoder, FM Transmitter, Bandwidth, Conformal Microstrip Antenna**

1. Introduction

During the developmental phase of any projectile, it is necessary to evaluate the performance in real time through flight trials. Various methods like EOTS, Radars and High Speed Cameras are available for measurement of designed parameters. However, they provide only qualitative measurements and are limited in their functional capabilities during adverse weather conditions. In presence of strong wind, rain, haze and fog etc., the performance parameters are not monitored properly by the above methods. In such scenario, telemetry becomes very vital for obtaining accurate and quantitative measurements in real time.

The article under evaluation here is a typical short-range Laser guided missile which can engage a target up to 5 km range. Miniaturised and ruggedized on-board telemetry unit has been developed and implemented which occupies a small space within the warhead section of the missile and can withstand shock level up to 700 ‘g’. Various design parameters are monitored in real time and the results are analysed to evaluate the performance of the missile and for further performance enhancement.

2. OBTU Description

The developed OBTU consists of built-in Sensors (IMU & Pressure Transducer), Signal Conditioning Module (SCM), FPGA based PCM Encoder with interface for analog and digital parameters, FM Transmitter, Microstrip Patch Antenna and Power Source. Biphase-L based encoding is used for generation of modulating signal which is passed through Bessel filter to limit the bandwidth of RF signal. A MEMS based IMU is used to measure 3-axis linear acceleration and three angular rates. A Piezo-resistive pressure transducer measures the pressure of the motor chamber. A VCO in close loop with PLL is used to generate a programmed carrier frequency which is passed through multiple levels of band pass filters & power amplifiers. An isolator is used between power amplifiers and antenna to restrict back reflections and ensure proper transmission. A conformal microstrip patch antenna has been designed to generate omnidirectional radiation pattern. Lithium-ion based power source is used to power the OBTU during the flight. The architecture and photograph of developed OBTU shown in figure 1.

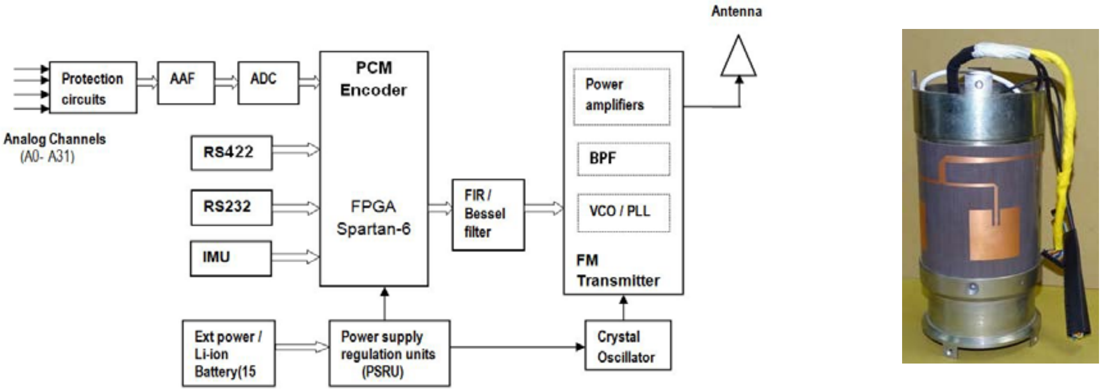

Fig.1. Block diagram and photograph of OBTU

The developed OBTU is placed inside the missile in the warhead section. A photograph of the missile with OBTU is shown in figure 2.

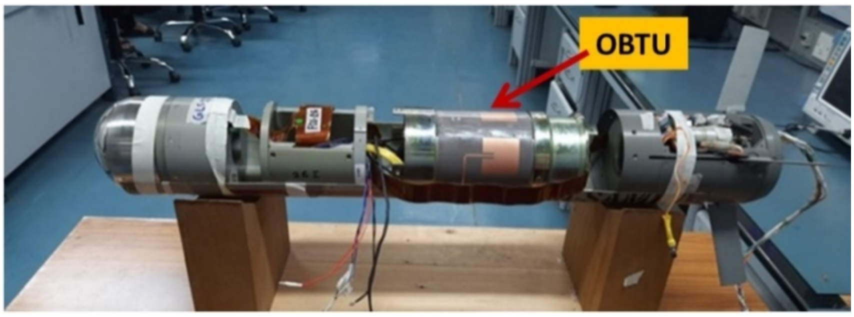

Fig.2. Placement of OBTU in the missile

A. Sensors

The data collection system is composed of sensors or transducers that convert a physical variable into an electrical signal. The OBTU has 32 analog input channels so, 32 different kinds of sensors can be incorporated in the design. In the initial trials, shock accelerometer is used to monitor the launch shock profile of the missile. In the present design, a pressure sensor is used to monitor the pressure profile of the motor chamber.

The OBTU has an inbuilt MEMS IMU sensor. IMU typically consists of accelerometers for providing specific force or acceleration, gyroscopes for providing angular rate and sometimes magnetometers for providing the measurement of magnetic field surrounding the system. IMU is a combination of triaxial accelerometer, triaxial gyroscope and triaxial magnetometer, typically used to manoeuvre a projectile. The acceleration in 3 axes and the angular rates in 3 axes give the orientation of the projectile in space. This helps the projectile to navigate to the target.

B. Signal Conditioning Module

Signal conditioning is the modification of a signal from a signal source to some final form. The signal is usually very small and must be buffered or amplified before being sent to the multiplexing block. Sometimes, the signal is large as compared with the succeeding system then it need to be attenuated for measurement. Modification steps can include amplification, filtering, sampling, digitization, data compression, digital formatting, correction factors, and conversion.

The signal conditioning module for OBTU of ATGM is a miniaturized (5cm x 5cm) complex PCB. It accommodates 12 analog channels. The placing of all the 12 parameters on a small single PCB requires a skilful design. The same PCB attenuates and monitors the telemetry battery voltage and also extends power to the pressure sensor.

C. PCM Encoder

The output of the signal conditioning module is fed into the encoder which is basically a multiplex system and is implemented in Spartan-6 FPGA. It is a highly efficient fast processing platform to acquire the data and multiplex them into a single bit stream. The encoder in OBTU uses time division multiplex pulse code modulation (PCM) technique. It samples the data from different sensors and timely stamps them into a PCM frame. The PCM frame is generally called major frame in which every sensor has been sampled at least once. The major frame comprises of one or more number of minor frames. Minor frames are identified with sub-frame identification number and frame sync word.

Some of the fast varying signals such as firing signals and pressure are sampled at a higher rate is called super-commutation. The slow varying signals such as battery voltage are sampled at a lower frequency called sub-commutation. The goal in creating a PCM format is to maximize the efficiency of the PCM stream by maintaining the minimum sampling rate for each parameter while keeping the bit rate as low as possible.

D. FM Transmitter

FM transmitter is selected for transmission of base band information because of constant amplitude of modulated signal. This facilitates the system designer to remove the noise from the received signal by use of limiter circuit at ground receiver system. The bandwidth of FM signal is controlled as well as optimized by eye diagram of received signal on the receiver screen. The amplitude of modulating signal is controlled by a DAC circuit with help of varying gain factor as shown in figure 3.

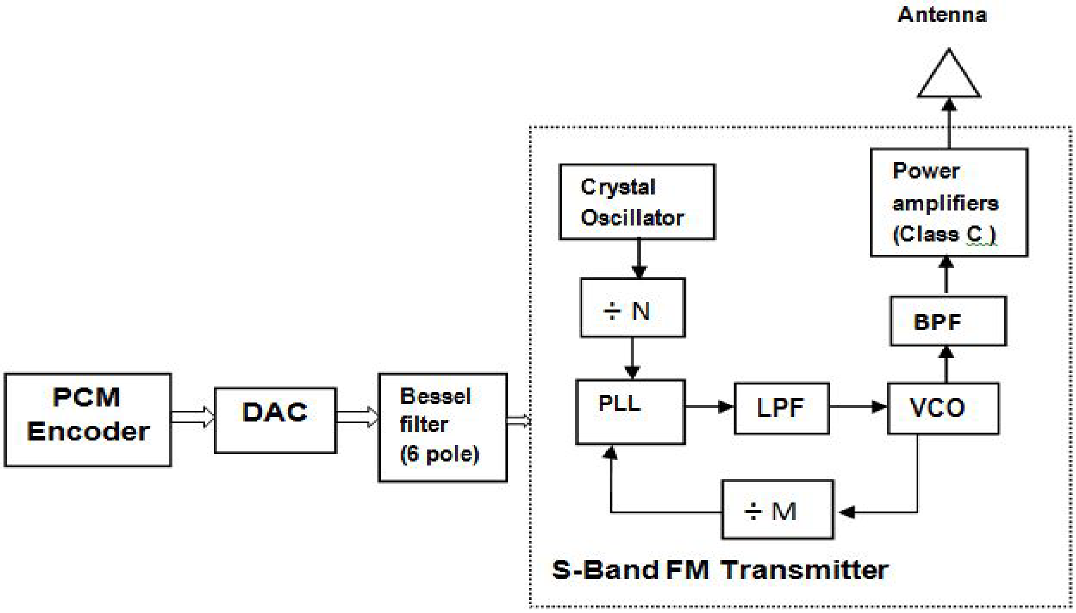

Fig.3. Block diagram of S-band FM Transmitter

A suitable gain factor is selected to optimize quality of received signal as well as bandwidth of RF signal. The Eye diagram and carrier frequency deviation against suitable gain factor is shown in figure 4.

Fig.4. Eye diagram and power spectrum of FM signal

E. Antenna

Antenna is a very important sub-system of telemetry chain. The RF power generated by transmitter has to be fruitfully delivered to space. This is only possible with the help of good design of antenna. Further, the proper selection of the location and orientation of transmit antenna has to be considered to maximize the uniform coverage of transmitted signal. The main electrical (radio frequency) parameters considered for antenna design are centre frequency, bandwidth, impedance, VSWR, beam width and gain.

A conformal microstrip patch antenna is designed for OBTU according to the flight dynamics of the Laser guided missile. Conformal Antenna is the most common form of antenna found on missiles, rockets, bombs and artillery rounds. It is built into the body of the missile and often is indistinguishable from the body itself. It is an array made up of several patch antennas that are fed through a power divider network in order to create the desired radiation pattern. Wrap-around or micro-strip antenna is used to preserve the aerodynamics of the missile and also to maintain space and weight.

The designed antenna has centre frequency of 2255.5 MHz & very good VSWR of the order of 1.04 to 1.1 and is successfully used in flight trials. A photograph of the antenna used for trials is shown in figure 5.

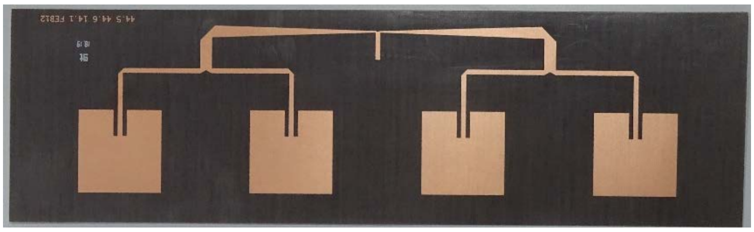

Fig.5. Photograph of wraparound microstrip antenna

3. Typical Results

The performance of OBTU is evaluated at various test stages such as: Standalone mode, Pre-integration & post-integration test and dynamic flight trial with missile. During standalone mode, all analog channels are given a fixed voltage and their corresponding values are checked on decom screen of receiving system. Digital parameters which are on RS422 or RS232 are tested with simulated data through docklight software with configured baud rate. For pre- & post -integration testing with missile, all sub-systems are interconnected and one sequence of operation is executed and data is logged with receiving station & processed to verify the transmitted parameters.

During dynamic flight trial, all analog & digital parameters are logged with two or more ground receiving stations. Some of the vital parameters are displayed in real-time and other data is immediately post-processed with MATLAB based GUI to generate test result plots for further analysis and performance evaluation.

The developed OBTU is capable of measuring all the analog and digital design parameters. Data integrity of the clean telemetered data is verified through Cyclic Redundancy Check (CRC). Typical result from a flight trial indicating the commanded & achieved fin deflections of the four fins is shown in figure 6.

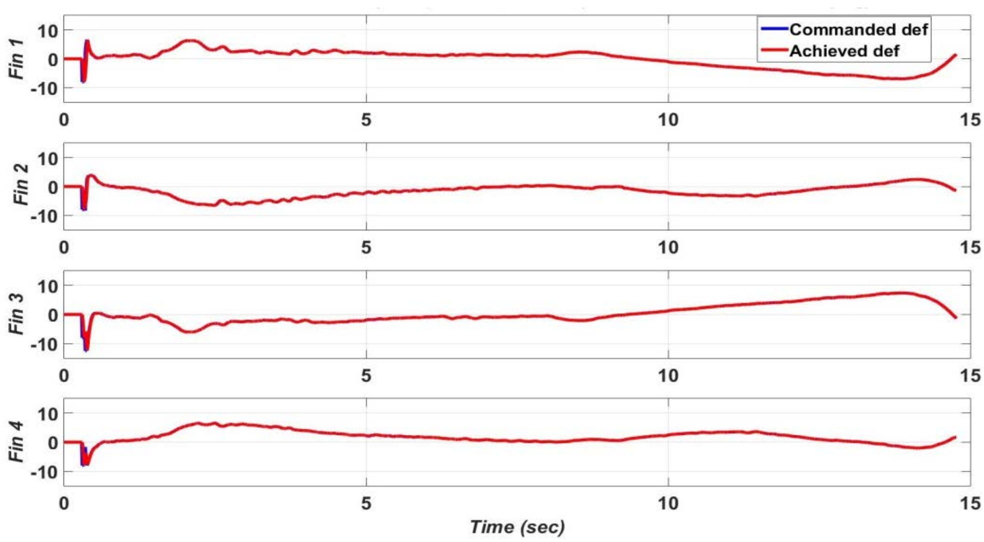

Fig.6. Result showing commanded and achieved fin deflections

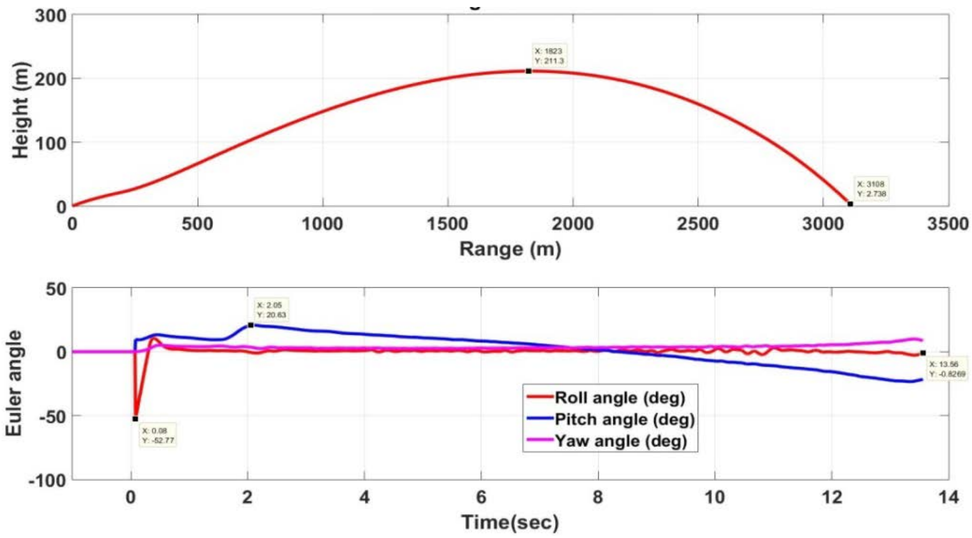

Fig.7. Result showing trajectory profile and Euler angle plots

Results indicating the trajectory profile and Euler angle plots during a dynamic trial are shown in figure 7.

4. Conclusion

A compact and ruggedized on-board telemetry unit has been developed and implemented successfully for the performance evaluation of a short-range Laser guided missile. Standalone mode, Pre-integration & post-integration tests are carried out in the Lab for qualifying the missile for flight trials. Pre-launch telemetry checks are also carried out at trial site to rule out any issues that might emerge because of transportation from Lab to the trial site. The developed OBTU has complied with RCC IRIG-106 standard and is capable of monitoring the real-time data throughout the flight duration. This has resulted in validating the design parameters, providing information regarding deviations from expected values and hence performance evaluation of the missile. The telemetered results have proved vital for performance enhancement of the guided missile system.

5. Reference:

[1] Carden F, Henry R & Jedlicka R, *"Telemetry systems engineering"*, Norwood: Artech House, 2002.
[2] Dash SP, *"Flight instrumentation for missiles"*, Hyderabad: Dharani Printers, 2018.
[3] Pozar DM, *"Microstrip Antennas"*, Proc. of IEEE, Vol. 80, No.1, 1992.
[4] Telemetry Group: *"Telemetry standards IRIG-106"*, New Mexico: Secretariat RCC, 2019.
[5] Kumar G & Ray K P, *"Broadband microstrip antennas"*, London: Artech House, 2003.

Design of GPS Microstrip Patch Antenna (MPA) for Guided Projectile Applications

Swapnil Narke
Savitribai Phule Pune University
Pune
swapnil.narke06@gmail.com

D C Gharpure
Savitribai Phule Pune University
Pune
br@gmail.com

C P Singh
Armament Research and Development Establishment
DRDO
Pune

Shyamala Kulkarni
Armament Research and Development Establishment
DRDO
Pune

BB Padhy
Armament Research and Development Establishment
DRDO
Pune

Abstract—**In the global positioning system (GPS), mitigation in the receiving signals because of the polarization losses in the ionospheric region, environmental losses or path losses required well specified antenna characteristics. In this paper, the circularly polarized aperture coupled rectangular microstrip patch antenna (AC-MPA) and proximity coupled microstrip patch antenna (PC-MAP) for GPS in the guided projectile applications. The reflection coefficient has been achieved < -15dB in AC-MPA as well as in PC-MPA design at 1.575GHz. The Right-hand circular polarization (RHCP) has been achieved by truncating the opposite corners of the microstrip patch antenna at resonating frequency. The gain of AC-MPA is 4.71dB and PC-MPA is 4.85dB gain in the zenith direction. Antenna design analysis is supported by simulation design in CST microwave studio software platform.**

Keywords— Global positioning system (GPS), Circular polarization (CP), axial ratio (AR), aperture coupled microstrip patch antenna (AC-MPA), proximity coupled microstrip patch antenna (PC-MPA)

1. Introduction

Microstrip patch antenna (MPA) have the vital role in the various applications such as in automobiles, wireless communication system, global positioning system (GPS) etc. [1]-[3] because of their low-profile configuration. In the unmanned aerial systems such as in missiles, in artillery shells, etc., require GPS for accurate position information. The space constraints in the projectile bodies demand physically smaller antennas with accurate antenna characteristics. The antenna characteristics are well specified according to the applications requirement such as for GPS applications require right hand circularly polarized (RHCP) antenna radiation pattern [4], for the telemetry applications antenna required wider half power beam width (HPBW) with circular polarization [3][5].

The MPA characteristics such as circularly polarized antenna radiation pattern, enhancement in the scattering parameters of the antenna, wider half power beam width (HPBW) are optimized using the various topologies of the antenna structure such as 3D ground structure for wider HPBW, single feed or double feed techniques for circular polarization (CP), slots in the antenna for better scattering performance, etc. [5]-[9]. The MPAs can be energized using direct feeding techniques as well as indirect feeding techniques. In direct feeding techniques the co-axial feeding, microstrip line feeding, coplanar wave guide feeding techniques are proposed in [8]-[9]. Whereas, in the case of indirect feeding techniques the aperture coupled and the proximity coupled feeding techniques are proposed in [8]-[10].

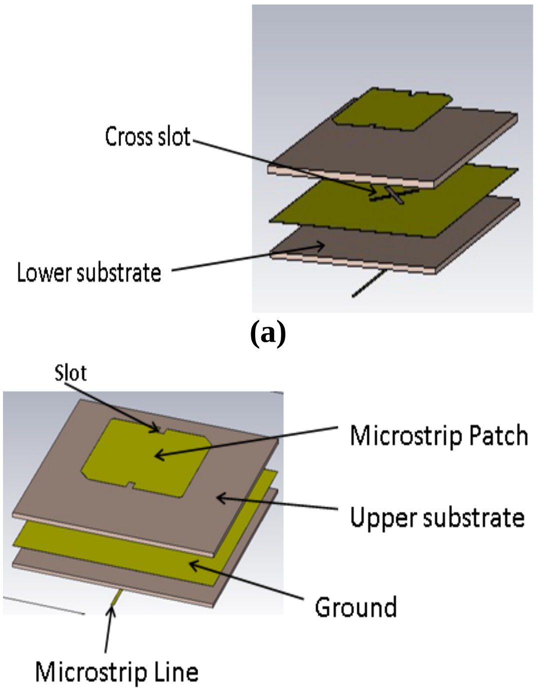

Fig.1 Geometry of aperture coupled Microstrip Patch Antenna (MPA)

Direct feeding technique generates higher order modes in the cavity of an antenna, whereas in the indirect feeding technique due to the non-conducting coupling between the microstrip line and patch of an antenna mitigates the higher order modes in the cavity which enhances the co-polarization to cross polarization ratio [8]. The bandwidth of an antenna is depending on the thickness of the MPA [8]. Therefore, the aperture coupled MPA (AC-MPA) or the proximity coupled MPA (PC-MPA) configurations are highly demanded for high bandwidth applications.

This paper presents the design and simulation analysis of I) aperture coupled MPA (AC-MPA) II) proximity coupled MPA (PC-MPA) for GPS (Global Positioning System) applications in guided projectiles. Both antennas are designed and simulated in CST microwave studio environment at resonating frequency 1.575 GHz. The designed MPA's are right hand circularly polarized (RHCP). The substrate material RT/duroid 6006 of dielectric constant (ε_r) 6.15 of thickness 1.27mm for AC-MPA design and 0.635mm for PC-MPA are used. The configurations of the proposed antenna designs are under fabrication.

2. Multilayered Microstrip Patch Antenna Design

In the multilayered MPA case, the RF signal is applied between the ground and microstrip line in the lower substrate using 50Ω *SubMiniature version-A* (SMA) connector is shown in Fig.1 and Fig.7.

A. Aperture coupled Microstrip patch antenna (AC-MPA)

In the AC-MPA design, the slotted conducting ground plane is sandwiched between two substrate materials of same or different dielectric constants. The microstrip patch is situated on the outer surface of the upper substrate material and the microstrip line is situated on the outer surface of the lower surface as shown in Fig.1.

Antenna design and simulation analysis: Design configuration of the AC-MPA is shown in Fig.1. The dimensions of the truncated patch of an antenna are 32.27 mm x 32.27mm along the length and along the width of MPA is shown in Fig.2. The corners of the MPA are truncated diagonally by 0.7 mm and 3.3 mm respectively which generates two orthogonal resonating frequencies. The right hand circularly polarized resonating frequency is the resultant frequency of the two orthogonal frequency components generated along the diagonals of an antenna [6]. The lower frequency component is 1.565GHz along the diagonal truncated by 0.7mm and the higher frequency 1.585GHz along the diagonal truncated by 3.3mm shown in Fig.2. The reflection coefficient at circularly polarized resonating frequency is ~ -15dB with impedance band width (BW) is ~ 29.2MHz. The patch of the antenna has slots of dimension 2.3mm x 2.66mm in width and length to enhance the reflection coefficient. Axial ratio (AR) of 1.66dB has been achieved at zenith position in the simulation. The AR have magnitude below 3dB over the ~160^o in the elevation plane. The realized gain of the antenna is 4.71dB with HPBW of ~98^o shown in Fig.6.

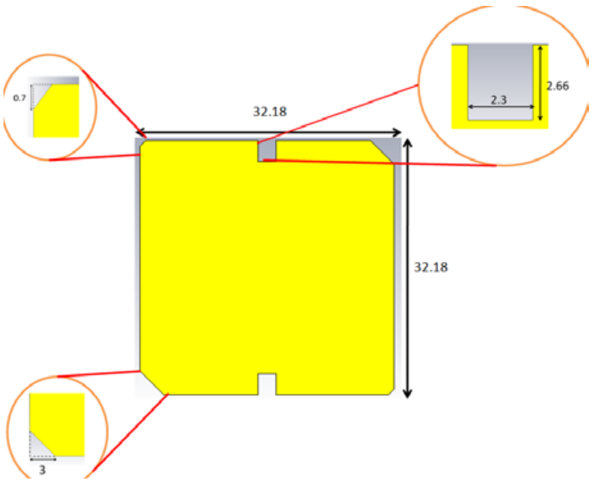

(a) Patch of an antenna

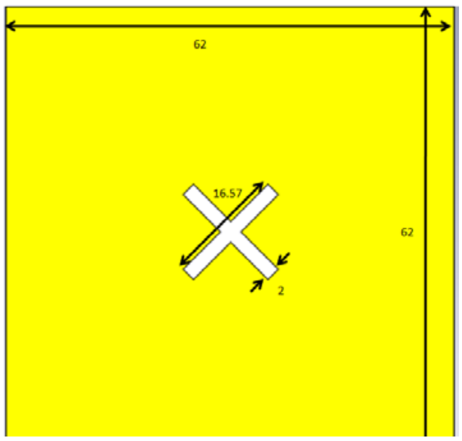

(b) Slotted ground of an antenna

Fig 2. Designed of the aperture coupled MPA

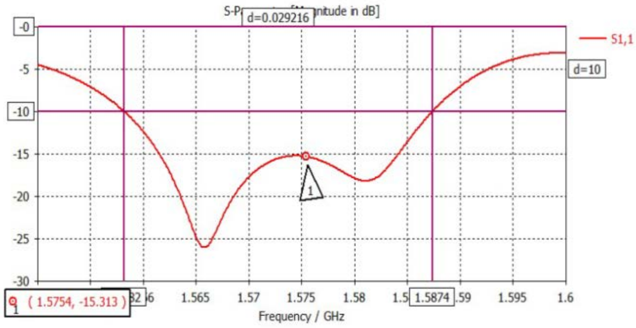

Fig. 3 Reflection coefficient

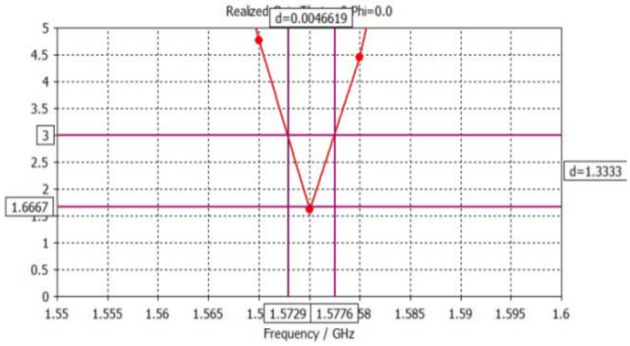

Fig. 4 AR vs Frequency

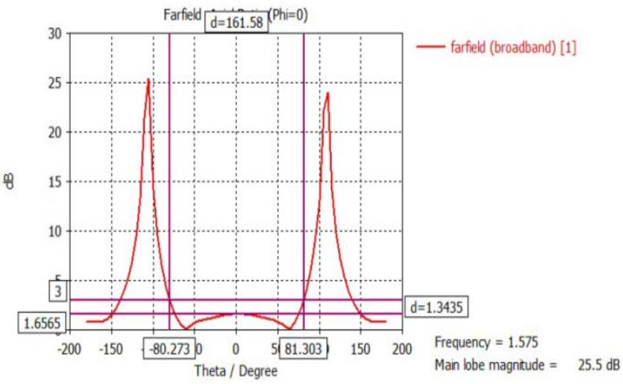

Fig. 5 AR vs Elevation angle

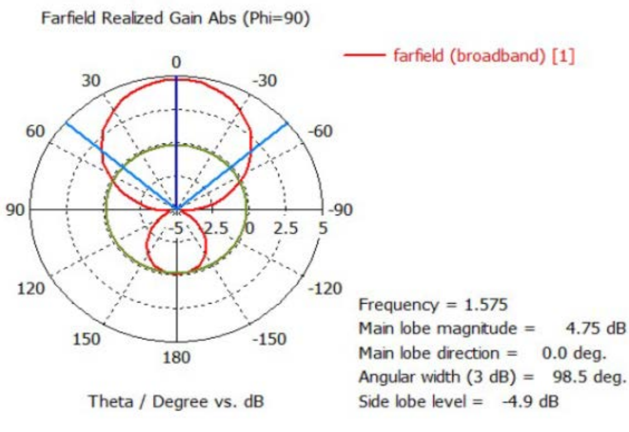

Fig.6 HPBW vs Elevation angle

B. Proximity coupled Microstrip Patch Antenna analysis

In the design and structure of the proximity coupled MPA the feeding microstrip line is sandwiched between the upper dielectric substrate and the lower dielectric substrate. The conducting ground of an antenna is pasted on the other side of the lower dielectric substrate is shown in Fig. 7.

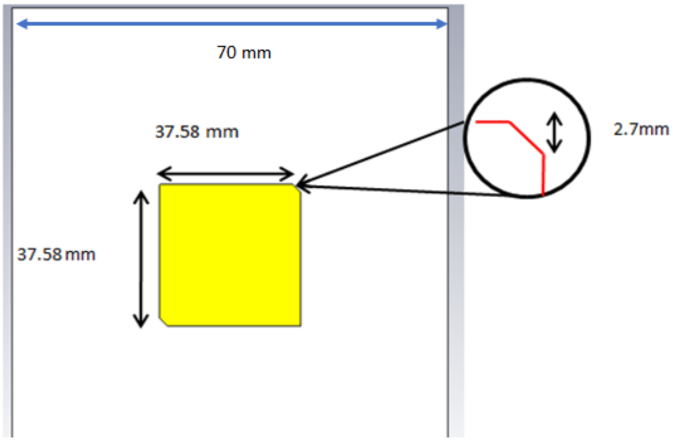

(a) Designed dimensions of an antenna

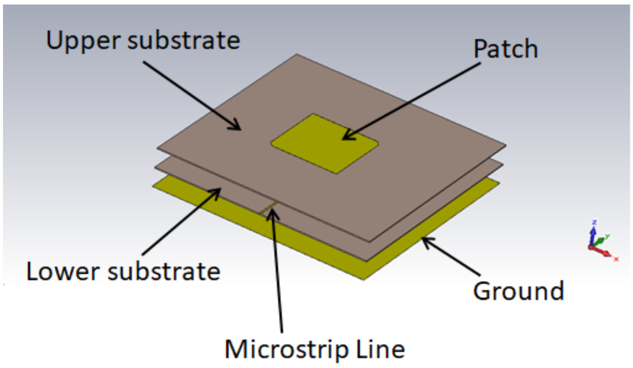

(b) Structure of an antenna

Fig.7 Geometry of Proximity Coupled Microstrip Patch Antenna (MPA)

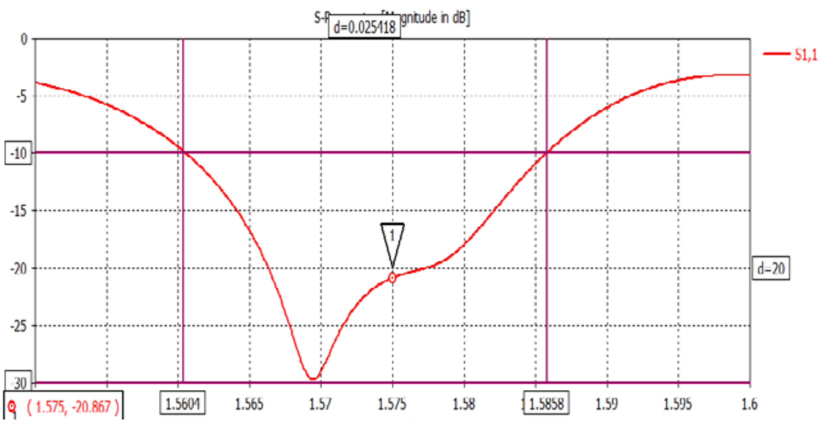

Fig. 8 Reflection coefficient

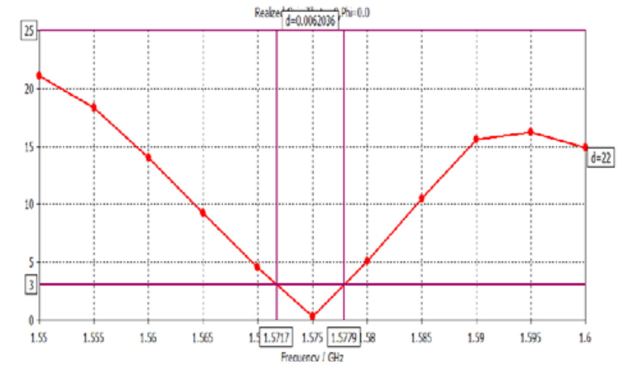

Fig.9 Axial ratio vs Frequency

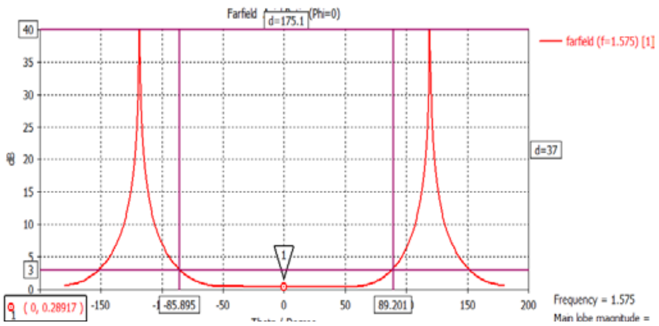

Fig.10 Axial ratio vs Elevation angle

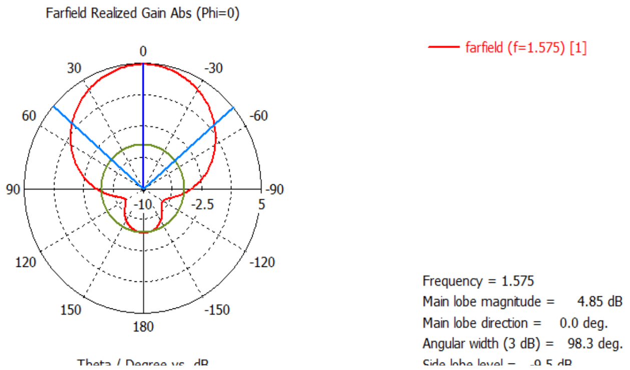

Fig. 11 Polar Plot of antenna radiation pattern

Antenna design and simulation: In the design of proximity coupled MPA, the dimensions of the patch are 37.19 mm x 37.19 mm. The RHCP has been achieved by truncating the diagonal corners of the patch by 2.7mm as shown in Fig. 7(a). The optimized reflection coefficient of the antenna is -20dB at CP resonating frequency (1.575GHz) with the impedance BW ~25 MHz is shown in Fig.8. The AR bandwidth is ~6.2MHz with minimum magnitude of 0.28dB at 1.575GHz shown in Fig.9. In Fog.10, the magnitude of AR below 3dB has been achieved over ~175^{o} in the elevation angle. The HPBW is approximately 86^{o} plotted in polar form shown in Fig. 11. The realized gain of the antenna is 4.85dB. The summary of the simulated designed antenna characteristics of AP-MPA and PC-MPA is given in the below Table.1.

Table.1. Summary of the designed antenna characteristics AP-MPA and PC-MPA

Antenna Characteristics	AC-MPA	PC-MPA
Reflection coefficient (S_{11}) (dB)	-15	-20
Impedance BW (MHz)	29.2	25
AR (dB)	1.64	0.28
AR BW (MHz)	4.6	6.2
AR beam-width	161^o	175^o
HPBW	98^o	86^o
Gain (dB)	4.71	4.85

AC-MPA: Aperture coupled microstrip patch antenna
PC-MPA: Proximity coupled microstrip patch antenna

3. Conclusion

The design of the aperture coupled MPA and the proximity coupled MPA have promising antenna characteristics for GPS application. Both antenna designs have the circular polarization characteristics over the wider beam-width. The axial ratio in proximity coupled antenna is 0.28dB where as in the aperture coupled MPA have 1.64 dB AR. HPBW in case of PC-MPA is 86^o and whereas in case of AC-MPA is 98^o. The optimized antenna dimensions are suitable for the onboard applications in projectile bodies.

4. Reference

[1] Ebenezer Abishek, Arun, Raaza, V. Rajendran, “Design and development of vehicular microstrip patch antenna for emergency vehicle”, *International journal of Engineering & Technology*, 7 (2.33), 2018, 473-476.

[2] G. Jegan; A. Vimala juliet; G. Ashok kumar, “Multi band microstrip patch antenna for satellite communication”, Recent Advances in Space Technology Services and Climate Change 2010 (*RSTS & CC-2010*), 13-15 Nov. 2010.

[3] Yoon-Kyoung Chae, Chan-Ho Lee, Jae-Ho Cha, Wan-Joo Kim, Bierng-Chearl Ahn," Design of a ceramic patch antenna for artillery projectile positioning applications", *Journal of KIIT*. Vol. 15, No.5, pp. 81-85, May 31, 2017.

[4] Brain J. Herting, “Analysis and design of electrically small, circularly polarized cylindrical microstrip antennas”, PhD thesis, University of Illinois at Urbana-Champaign, 2014.

[5] S. Narke, S. Ananthakrishnan and C. Bhattacharya, "Enhancement of axial ratio-beamwidth of X-band composite microstrip patch antenna with conical ground plane", *ELECTRONICS LETTERS*, 30th April 2020, Vol. 56 No. 9 pp. 419–421.

[6] C. Sharma and K C Gupta, “Analysis and optimized design of single feed circularly polarized microstrip antennas”, in *IEEE Trans. Antennas and Propagation*, vol. AP-31, no.6, November 1983.

[7] S.A. Malekabadi, A.R. Attari and M.M. Mirsalehi, “Compact and broadband circular polarized microstrip antenna with wideband axial-ratio bandwidth”, 2008 International Symposium on Telecommunications, Aug 2008, 106-109.

[8] C.A. Balanis, Antenna theory, John Wiley & sons, Inc., 2010.

[9] Girish Kumar and K.P. Ray, Broadband Microstrip Antennas, Artech House, 2003.

[10] Michael Paul Civerolo, Aperture coupled Microstrip Antenna Design & Analysis, MS thesis, California Polytechnic State University, June 2010.

Model-Based Sensored Field Oriented Control Implementation for Permanent Magnet Synchronous Motor using TI F28035 DSP Processor

Aakriti Srivastava
Armament Research and Development Establishment
DRDO,
Pune
ajaylohia@arde.drdo.in

Rounak Padgil
Armament Research and Development Establishment
DRDO,
Pune
rpadgil@arde.drdo.in

Abhishek Gupta
Armament Research and Development Establishment
DRDO
Pune

Ajay Lohia
Armament Research and Development Establishment
DRDO
Pune

N. P Nair
Armament Research and Development Establishment
DRDO
Pune

S.V Gade
Armament Research and Development Establishment
DRDO
Pune

Abstract - **As the world shifts from mechanized to maneuver advanced weapons, automation and control performs the essential role. The objective of this paper is to present the implementation of model-based sensored field oriented control algorithm (FOC) for controlling the permanent magnet synchronous motor (PMSM). The model-based design is a graphical specification and design of the system. This approach proves to be an effective and efficient means of understanding the product parts such as processors, algorithm and code for the working of whole dynamics of the system. It supports troubleshooting the real world problem in simulation environment that can occur in the complex systems. The beauty of model-based implementation lies in the verification and validation process of system and its operation without actual hardware which saves time and error possibility at product developmental stage. MIL, SIL, PIL and HIL testing come in the verification part of Model-based design approach after the required system modeled at simulation level and this is performed before model is deployed to hardware.**

The aim to implement FOC to control dynamics of PMSM is because of following advantages such as to produce maximum torque at zero speed, fast acceleration and deceleration and smooth operation of motor at all speed which is required for elevation and traverse movement of mechanical arm. The key element of vector control algorithm is the identification of rotor position with respect to the stator. In this sensored algorithm encoder is used to provide angle feedback. Excitation is provided on the winding of stator in such a fashion that it generates maximum torque by aligning net magnetic field vector of the stator perpendicular to the magnetic field component of the rotor. This is also known as rotor flux aligned field oriented control algorithm. The simulation verified and hardware experimental results of torque control loop, speed control loop, axis transformations and angle waveforms are shown in the paper.

Keywords: Permanent Magnet Synchronous Motor, Field oriented control, Model based design, Space vector pulse width modulation.

1. Introduction

The automation and control unit consists of driver circuit which excites motor and leads to the movement of mechanical arm of weapon. Motor is a transducer which converts electrical energy (excitation in form of voltage and current) into physical movement or mechanical motion. The stator part of PMSM is energized and phenomenon behind the movement of rotor (permanent magnet) with respect to stator is based on the torque experienced by rotor as a consequence of electromagnetic induction. There are several methods to govern the excitation on the windings of permanent magnet synchronous motor among which Field Oriented Control becomes more popular. FOC supports decoupling of torque current and the flux current through coordinate transformation in the equivalent two-phase rotating coordinate system [1]. Hence this control algorithm facilitates smooth operation of electric motor over the full speed range, generate full torque at zero speed and can deliver fast acceleration and deceleration of the motor. FOC technique have control over magnetic field and torque by controlling d and q components of stator current. This paper describes about the model based implementation of sensored FOC algorithm to control PMSM using F28035 processor. FOC algorithm use SVPWM for switching the voltage source inverter and switching frequency should be less than 20KHz. This frequency is required by the PS21765 inverter IC for switching the gate of its IGBTs. The PWM peripheral is in synch with ADC which triggers SOC pulse at the end of each PWM period.

This paper is focused on model based design of sensored FOC with encoder as the feedback for speed and torque control of PMSM motor. This algorithm is rotor flux oriented and based on cascade PI controllers. It is implemented on target hardware platform which is a fixed point DSP processor TMS320F28035. The embedded real time code for model based design of control algorithm is generated by MATLAB using embedded coder which reduces the effort and error to occur. Hence this work will add value in the field of automation and control and making system robust. The mechanism and implementation is described in this research paper.

2. Method

A. FOC Control Algorithm

This method has excellent dynamic performance, wide speed range and high precision. Using id= 0 as the method of FOC strategy enables control system to have many advantages such as small impulse and excellent torque characteristics [1]. In AC machines, the stator and rotor fields are not orthogonal to each other. The only quantity that can be controlled is stator current. The field oriented control is the technique used to achieve the decoupled control or have independent control of torque and flux. It is also referred as vector control algorithm and based on decomposition of stator current into two components one for magnetic field generation and other for torque generation. It is a rotor flux oriented control algorithm and works on the principle of aligning the net magnetic flux generated by stator winding to be perpendicular to the rotor flux i.e. the direction of resultant magnetic motive force is consistent with q axis [3]. For controlling the current on the stator winding FOC transforms feedback three phase stationary reference frame current(Ia,Ib,Ic) into two phase rotating reference frame Id and Iq. Id is flux producing component and Iq is torque producing component. In this control algorithm implementation for generating the maximum torque desired value of Id = 0. The torque and flux producing components are controlled with the PI controller, the controlled outputs which are the voltages, are then transformed back (inverse transformation) to the stator reference frame. Now these are fed into Space-Vector PWM generator. Space-Vector PWM generates switching period i.e compare register value of PWM peripheral which varies the duty cycle of PWM.

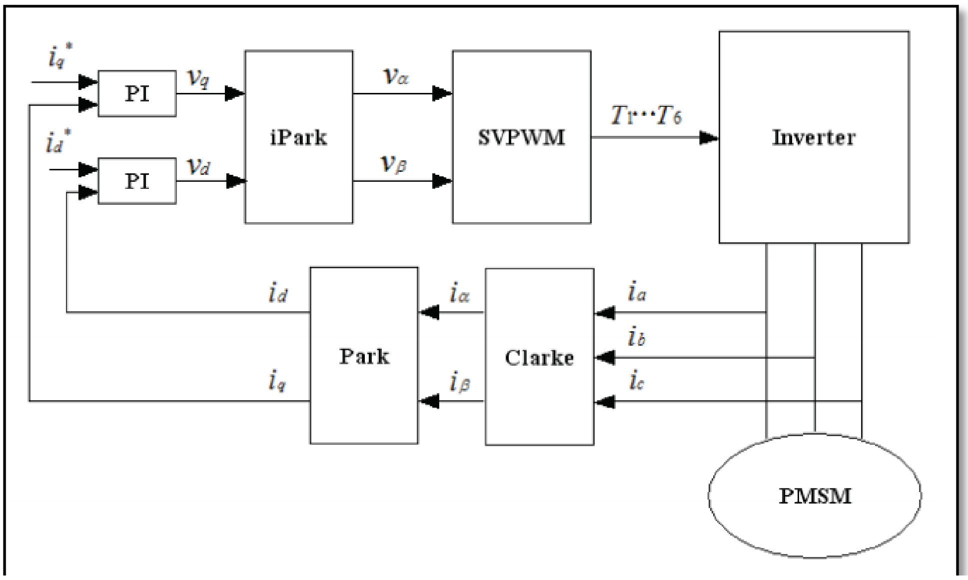

Fig 1: Block diagram of current closed-loop FOC system [1]

Mathematical equations involved:

Clark transform: The measured motor current is transformed from three phase reference frame to two axes orthogonal reference frame.

$$I\alpha = Ia \quad (1)$$

$$I\beta = (Ia+2*Ib)/\sqrt{3} \quad (2)$$

Park transform: The two-axis orthogonal stationary reference frame quantities are then transformed to two axis rotating reference frame.

$$ID = Id*\cos\theta+Iq*\sin\theta \quad (3)$$

$$IQ = -Id*\sin\theta+Iq*\cos\theta \quad (4)$$

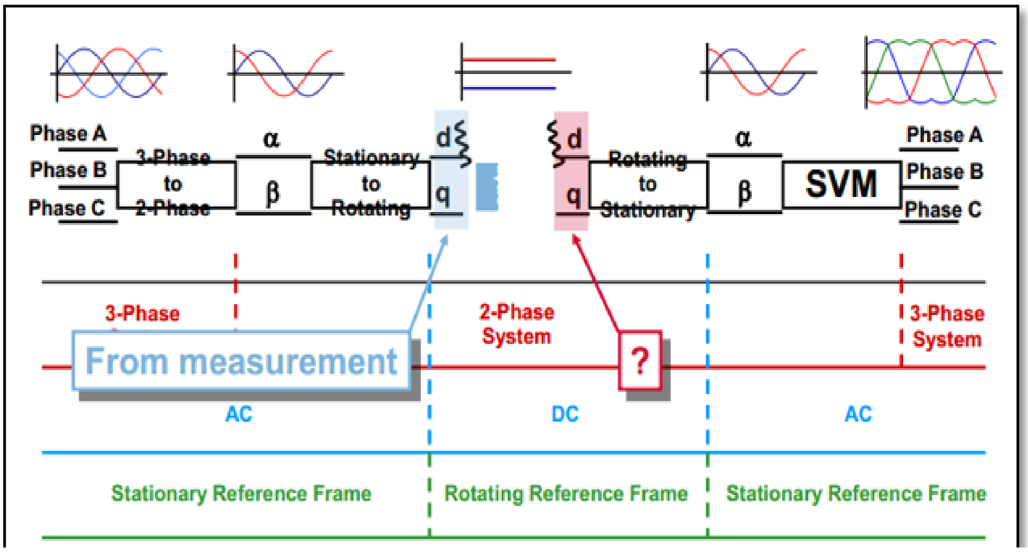

Fig 2: Transformations and reference frame [1]

B. Mechanism

For proper sinusoidal commutation, the absolute rotor position information is very important in order to produce the synchronized voltage waveforms to the motor. To get the fine position information, in this control algorithm encoder is used as feedback for position and speed estimation. It requires two control loops one for FOC control and other for speed control. The vector control of voltages and currents results in control of spatial orientation of the electromagnetic fields in the machine and it has led to the field, called field oriented control [4].

C. Speed control loop

Speed control loop consists of PID controller having desired speed (reference speed) and estimated speed (calculated from motor feedback) as an input and provides desired torque(Iq) value as an output.

D. Torque control

Sinusoidal permanent magnet synchronous motor does not have the damper winding, and rotor flux is constant [5]. Based on rotor flux oriented control method, in the d-q coordinate the motor mathematical model given as:-

$$\psi d = Ldid + \psi r \text{ and } \psi q = Lqiq \qquad (5)$$

Torque equation given by:

$$Te = Np(\psi diq - \psi qid) \qquad (6)$$

where ψd, ψq are stator flux in d-q coordinate; id, iq stator current in the d-q coordinate; Te electromagnetic torque of motor; Ld, Lq are d-q axis equivalent synchronous inductance; Np number of armature pole pairs [1]. For id= 0 current control method i.e to make rotor flux perpendicular to stator flux.

The torque equation becomes

$$Te = Np\psi riq \qquad (7)$$

In permanent magnet motors, one of the magnetic fields is created by permanent magnets and other is created by stator coils. The maximum torque is produced when the magnetic vector of the rotor is perpendicular to the magnetic vector of the stator. Since torque depends on iq hence can generate maximum torque by adjusting value of iq using PID controller.

3. Space Vector Pulse Width Modulation

Space vector pulse width modulation technique has become a prominent PWM generation technique for driving AC motors. The space vector method of analysis is originally developed as a vector approach to pulse width modulation (PWM) and it enables representation of the three phase quantities (voltages and currents) by a single complex vector [2]. PWM inverters makes it possible to control both magnitude and frequency of the voltage supplied to the motor. In SVPWM methodology the three phase quantities transformed to their equivalent two phase quantity in stationary or rotating reference frame [3]. The reference vector magnitude can be found from these two-phase components and are used for modulating the inverter output.

$$\begin{bmatrix} U\alpha \\ U\beta \end{bmatrix} = 2/3 \begin{bmatrix} 1 & -\frac{1}{2} & -\frac{1}{2} \\ 0 & \frac{\sqrt{3}}{2} & \frac{\sqrt{3}}{2} \end{bmatrix} \begin{bmatrix} Ua \\ Ub \\ Uc \end{bmatrix} \qquad (8)$$

Then, magnitude of rotating vector and its angle are:

$$|U| = \sqrt{U\alpha^2 + U\beta^2} \qquad (9)$$

$$\alpha = \tan^{-1}(U\alpha/U\beta) \qquad (10)$$

A. SVPWM Switching Period

The reference voltages are given by space voltage vectors and the output voltages of the inverter are considered as space vectors. There are eight possible output voltage vectors, six active vectors V1-V7 and two zero vectors V1,V8 [4] which is used to add dead time to the switching period. Each space vector at 60deg phase difference. The motive of the SVPWM is to apply the given voltage vector U to a three phased electric motor (PMSM). This is accomplished by determining the sector of reference voltage U and decompose it instantaneously by combination of the switching states corresponding the basic space vectors(V1-V8) which is given by

$$U(nT) = 1/T(T_1Vx + T_2Vx_{+60} + To(V_1orV_8)).$$

Hence for every PWM period T, U can be obtained by having the inverter in switching state Vx and Vx_{+60} for T1 and T2 duration of time respectively [2].

Switching period can be obtained by following equation and U makes and angle α with Vx, then

$$T1 = \sqrt{2}Tpwm1|U|\cos(\alpha+30°) \quad (11)$$
$$T2=\sqrt{2}Tpwm1|U|\sin(\alpha) \quad (12)$$
$$T0=Tpwm-T1-T2 \quad (13)$$

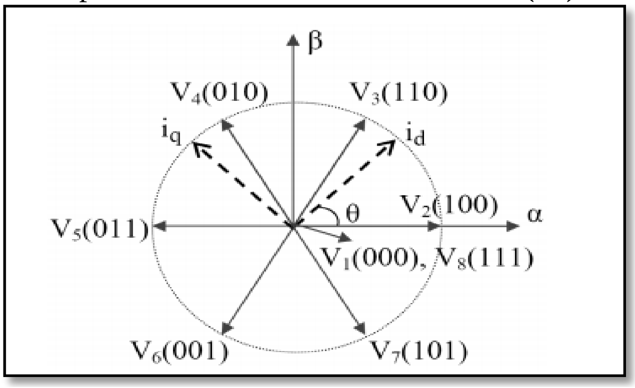

Fig 3: Output voltages represented as space vectors [4]

These switching periods are loaded into corresponding compare registers of PWM peripheral. Hence the space Space vector generator generates duty ratios for stator reference voltage. The modulated PWM optimize the operational characteristics of AC drive by minimizing the harmonics of the current.

4. Model Based Design In MATLAB

The model-based design is a way to create virtual representation of real world system. It helps to address various difficulties and complexities which arises during the life cycle of embedded application software through visual prototyping and simulation of models. While development of complex control system it is necessary to monitor application design processes at each step to optimize the overall system design. Field oriented control is a complex algorithm to control the system dynamics along with controller design for which model based design provides a virtual platform. This virtual platform supports offline verification of whole control mechanism by multiple iteration using sample input signal and tuning parameters to reach the desired response without hardware interface. Model-based design supports troubleshooting the real world problem in simulation environment that can occur in the complex systems. First stage is MIL (model-in-loop) testing in which controller and plant model is designed to test the control logic on simulated model of plant. Second stage is SIL(software-in-loop) testing where controller model is removed with controller block consisting generated corresponding c-code and run the simulation which is still a software model. In PIL (processor-in-loop) stage controller model is put onto an embedded processor and closed loop simulation is run on plant model to verify the system. In HIL (hardware-in-loop) testing stage plant model in our case PMSM motor is replaced with actual hardware and controller is in TI DSP board hence a real time testing of the complete control algorithm is verified.

Matlab facilitated with embedded code generation facility to generate C code as per designed model. Hence CCS project will be generated which can be imported to CCS Ide and code can be easily run and debugged on the hardware. The experimental setup and block diagram of model based FOC shown in fig.4.1 and 4.2 respectively.

A. Experimental setup

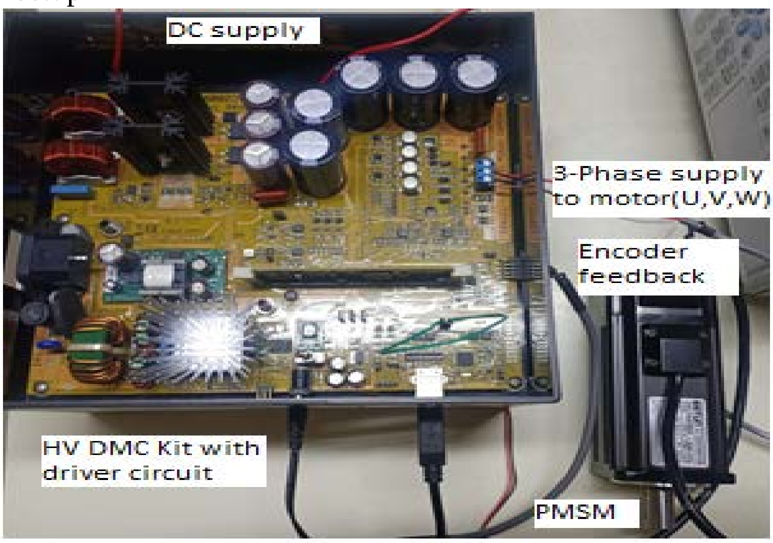

Fig 4.1: Experimental setup

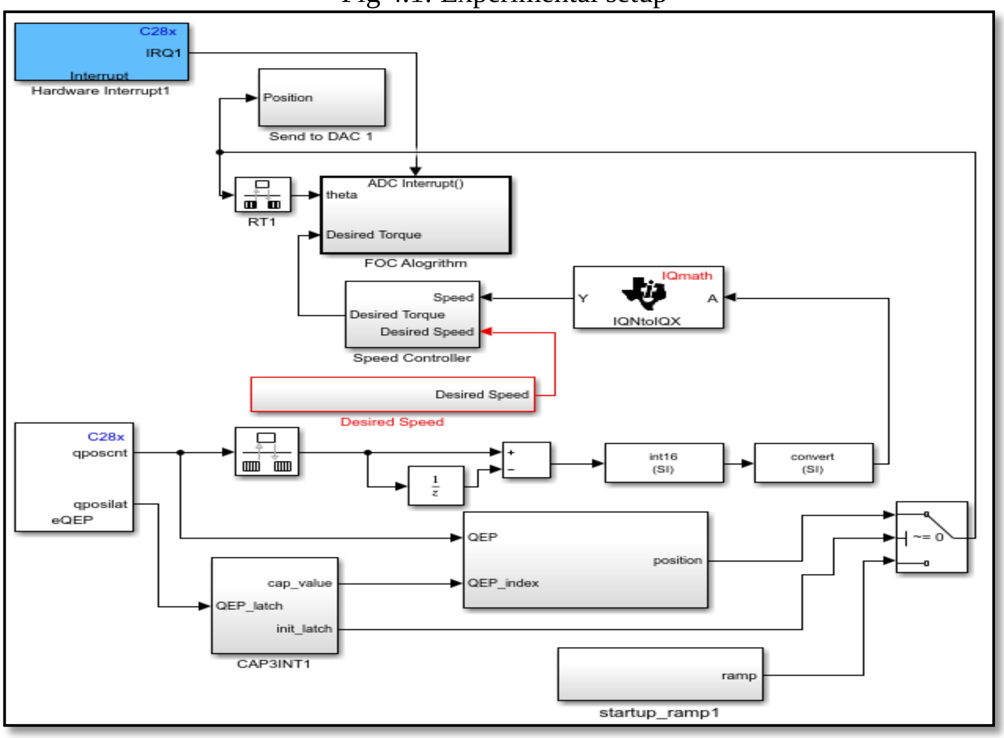

Fig 4.2: FOC model based design

5. Results & Discussion

A Sensored FOC algorithm is established with model based design technique with encoder as the feedback. The output waveform with hardware implementation satiates with the simulation results. Each waveform is discussed and described which shows the ability and usefulness of model based design technique for complex algorithm. The experimental results are obtained by running the setup i.e. PMSM with TI F28035 PICCOLO board HVDMC kit for 50sec.

The incremental encoder is used as position sensor to estimate rotor angle from the stator, it provides actual angular displacement of rotor with respect to stator only after the first indexing pulse (i.e. rotor aligned with stator phase A winding), hence to run algorithm initially angle value is provided by ramp generator. As a switchover can be seen in the fig. 5 between ramp input and evaluated angle from encoder feedback. Angle plays a crucial role in rotation of motor and determines its direction i.e for positive slope ramp motor turns anticlockwise and vice-versa.

θ(angle/radian)

Time axis [sec]

Fig 5: Angle waveform feedback from the encoder

Space vector PWM DMC block generates the switching period (Ton time period of PWM) corresponding to the input reference voltage. Matlab having feature of handling value within the range of (-1to 1), hence these on time period must be scaled and converted into uint16 bit to feed value to the compare register of PWM peripherals.

Voltage(5V/division)

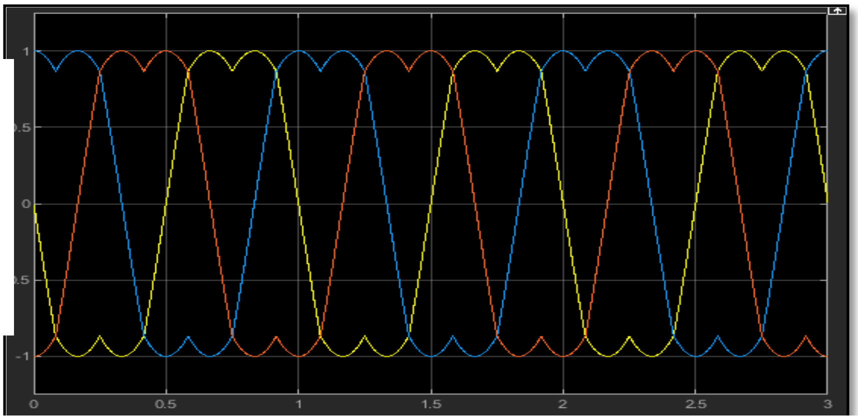

Time axis [sec]

Fig 6: Simulated SVPWM waveform with test values of Id and Iq

Voltage(5V/division)

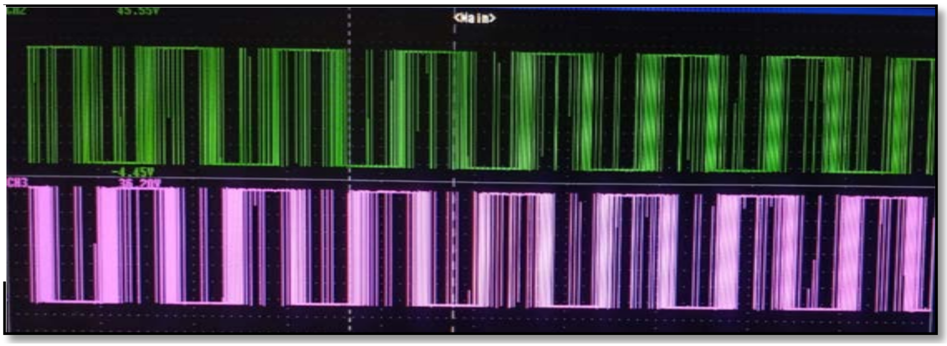

Time axis [sec]

Voltage(5V/division)

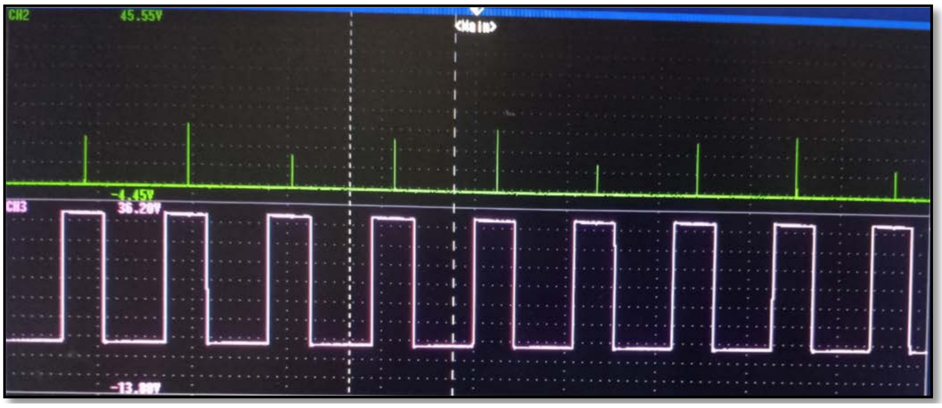

Time axis [μsec]
Fig.7: PWM waveforms

The output 3-phase current value from the motor is obtained using current probe and scopemeter having value of approximately 3.5A as shown in fig.7. Since current probe have scaling factor 1A/10mVhence 35mVcorresponds to 3.5A.

Voltage(mV)

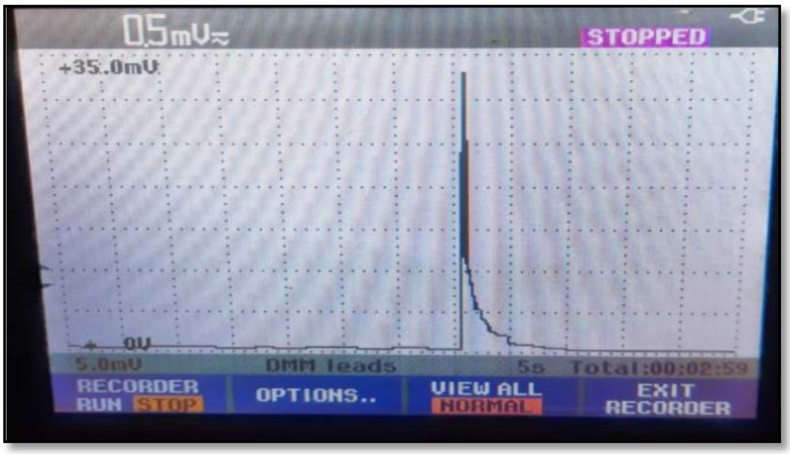

Fig 8: Measured Current

It is also found that by increasing the DC bus voltage current drawn by the motor winding increases. C2000 DMC Clark transform block transforms three phase current into balance two phase quadrature quantity as shown in waveform in below figure.

Time(sec)

Fig 9. Ialpha,& Ibeta

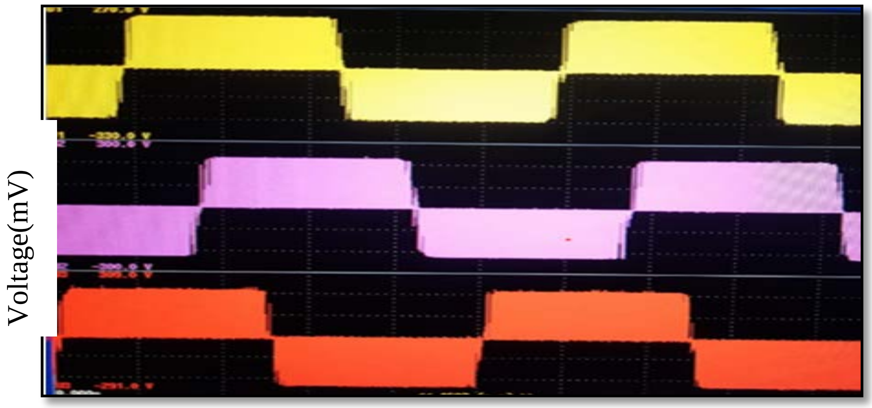

Time(sec)

Fig 10: 3-Phase voltage waveform

The measured speed and desired speed waveform is obtained on the DAC (digital to analog converter) of the board. The desired speed is obtained using IIR filter to avoid abrupt change in the desired speed. The first waveform is of desired speed and second is the feedback speed calculated from the encoder.

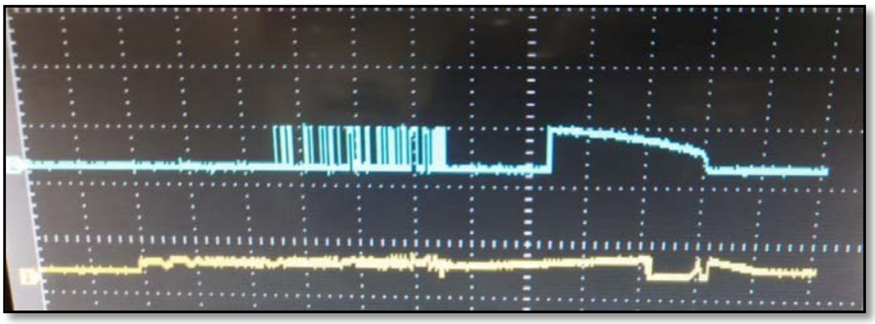

Fig.11: Desired speed and feedback speed

6. Conclusion

It has been shown and discussed that model based design methodology for implementing complex algorithm such as Field oriented control (FOC) makes automation and control of mechanical movement of system efficient and easy. Iteration for tuning and verification of system becomes handy at developmental stage. Each and every step is validated to avoid any fatality and probability of error before implementing the algorithm on actual hardware. The work also demonstrates ability of model based design to generate embedded real time C code and reduces the effort and software bug. The experimental results compared well with simulated results and present efficacy of the present methodology. This prove to be useful tool in early design process and later developmental stage.

7. References

[1] Xiangnan Zhang, Xiaohua Xie, Rongzi Yao, “Field Oriented Control for Permanent Synchronous Motor Based on DSP Experimental Platform”, Chinese Control and Decision Conference (CCDC), 2015.

[2] Ashish Gupta and Sanjiv Kumar “Analysis of Three Phase Space Vector PWM Voltage Source Inverter for ASD’S”, International Journal of Emerging Technology and Advanced Engineering, Volume 2, Issue 10, October 2012.

[3] S. Vasudevamurthy and Swetha, “Simulation and comparison of Space Vector Pulse Width Modulation for Three Phase Voltage Source Inverter”, International Journal of Engineering Research & Technology Vol.2 Issue 5, May-2013.

[4] M.B.B Sharifian, T.Herizchi, K.G.Firouzjah, “Field oriented Control of Permanent Magnet Synchronous Motor Using Predictive Space Vector Modulation”, 2009 IEEE Symposium on Industrial Electronics and Applications (ISIEA 2009), Kuala Lumpur, Malaysia.

[5] C. D. French, J.W. Finch and P.P. Acamely, “Rapid prototyping of a real time DSP based motor drive controller using Simulink”, 1998.

[6] A.Samat , P. Saedin, A.I Tajudin and N. Adni, “The implementation of Field Oriented Control for PMSM Drive Based on TMS320F2808 DSP controller.” 2012 IEEE International Conference on Control System, Computing and Engineering (ICCSCE), 2012, pp.612-616.

[7] M. S. Basar, M. M Bech, T.O Anderson, P. Scavenius and T.T Busar, “Comparison of sensorless FOC and SVM-DTFC of PMSM for Low-Speed Applications,” 4th International Conference on Power Engeneering, Energy and Electrical Drives, 2013, pp 864-869.

[8] Khalid Chikh, Abdllah S and Mohammad Khafallah, Driss Yousufi, “PMSM vector control performance improvement by using pulse width modulation and antiwindup PI controller”, IEEE International Conference on Multimedia Computing and Systems (ICMCS), 7-9 April 2011, pp1-7.

[9] T.S Kwon and S.K. Sui, “A novel flux weakening algorithm for surface mounted Permanent Magnet Synchronous Machine with infinite constant power speed ratio”, Proceedings of the International Conference on Electrical Machines & Systems, 2007, pp. 440-445.

[10] Pushpendu Maji, Prof. G K Panda, Prof. P K Saha, “Field Oriented Control of Permanent Magnet Synchronous Motor using PID controller”, International Journal of Advanced Research in Electrical, Electronics and Instrumentation Engineering, Vol.4, Issue 2, February 2015.

Mechanisms in Ejection Systems

Modeling and Analysis of Stage Separation Dynamics with Expanding Bellow System

Sivasakthi R
Aero Flight Dynamics Group
Vikram Sarabhai Space Centre
ISRO
Thiruvananthapuram
sivasakthi@vssc.gov.in

N Radha
Aero Flight Dynamics Group
Vikram Sarabhai Space Centre
ISRO
Thiruvananthapuram

C Ravikumar
Aero Flight Dynamics Group
Vikram Sarabhai Space Centre
ISRO
Thiruvananthapuram

Abhay Kumar
Aero Flight Dynamics Group
Vikram Sarabhai Space Centre
ISRO
Thiruvananthapuram

Abstract — **Designing of staging systems to separate and jettison apart the stages of a launch vehicle is important in the development of any new launch vehicle. The Design choice is made after critically considering over all mission and vehicle engineering requirements. A new launch vehicle is under development to cater to the small satellite industry. For this vehicle, a new and unconventional separation system is proposed for separation of second stage – Expanding Bellow System (XBS). This paper brings out the design and modelling efforts in shaping the system requirements to ensure a clean separation.**

Keywords-component: Separation dynamics, Small satellite launch vehicle, stage, expanding bellow system, Gap margin

Nomenclature

A_i	Area of zone i	Pi	Pressure in zone i
F	Separation force acting on the stages	r_i	Force acting point in zone i from respective stage c.g.
F_i	Force in zone i	s	Distance between the separating stages
I	Inertia of the stages	v	Separation velocity of the stages
M	Moment acting on the stages	vd	Detonation velocity
M_i	Moment in zone i	θ, ψ, φ	Euler angle of the stages
m	Mass of the stages	ω	Body rate due to separation on the stages

1. Introduction

Small Satellite Launch Vehicle (SSLV) is a threestage vehicle with an additional velocity trimming module to aid the precision injection and orbit raising maneuvers of satellite. SSLV was configured to capture the growing market of small satellites. An all-solid stage configuration was decided upon and the vehicle sizing was completed. Following this, the crucial aspect of vehicle staging was addressed. In launch vehicle design process, designing of staging systems is a major milestone. The feasible options for safe separation of stages were explored before finalization of separation systems.

A. Sizing of Separation System

From separation dynamics perspective, the critical aspects to be considered for sizing a stage separation system includes, mass and configuration of the separating stages, nature of the propulsive system in stages, the allowable coasting duration between stage transitions, tolerable no-control zone, residual errors in body rate due to control-OFF, tail-off thrust characteristics of spent stage, ignition characteristics of continuing stage, aerothermal requirements, mission specifications/ constraints and vehicle engineering specifications/ constraints. Based on the afore-mentioned factors, separation system is proposed and on acceptance further design details such as force levels, finalization of separation configuration, separation sequence, tolerable dispersions on design parameters are worked out.

A robust design that can cater to future modifications in the stage configuration, sequence of separation and varying mission profiles is always preferred.

B. Requirements of Second Stage Separation System of SSLV

The generic requirements of a separation system and its interaction with the other elements are discussed in Ref 2. The requirements which are specific to second stage separation of SSLV are as follows, [1] Vehicle Engineering: One fundamental requirement of SSLV is to have a clean external configuration. Thus, the choice of retro based separation system, which is the conventional separation system employed in other launch vehicles, was deemed to be infeasible. [2] The internal branching and hanging design of third stage requires a longer pull-out. The second stage separation system should result in minimum lateral disturbance on the separating stages. [3] Mission Requirement: The second stage being a solid stage, the tail-off characteristics requires a minimum combined coast duration before the separation. The separation system should allow for greater flexibility in the coasting duration between the stages, even after accounting for the possible dispersions in the tail-off thrust profile. [4] At the instant of second stage separation, the satellite is uncovered and the feasibility of a hot separation, as in the case first stage separation, does not exist.

C. Proposed Second Stage Separation System of SSLV

For the second stage separation of SSLV, Expanding Bellow System (XBS) was proposed. It is a new development. It is derived from the Linear Bellow System (LBS). The LBS has a pedigree of being used in the vertical separation of the payload fairing for all our Launch Vehicles. In the XBS, the rubber bellow is circularized and sandwiched between the separating stages (second and third stage) at the separation plane. The system performs both the severance and jettisoning functions.

D. Literature Review

The theoretical aspects of dynamics of separation of spent stages of launch vehicles were discussed by Ball and Osborne [1]. The requirements and design of separation systems were further elucidated by Suresh and Sivan [2]. Typical separation mechanisms – retro rocket, firing the upper stage, spring-based mechanisms – used in stage separation are explained in detail.

The separation dynamics of a spent liquid stage with a twin engine configuration was addressed earlier [3]. The axial pull-out length of the upper stage nozzle is about 5 m. The higher pull-out of 5 m is comparable to the present study. However, the inertia of the spent liquid stage is also comparatively high and aids in separation.

The separation dynamics of a spent solid stage very much comparable to the present problem, in terms of dynamical properties of the stages, is studied [4]. The study focused on the coasting requirements to be met. The stage is jettisoned by means of low energy springs resulting in relatively lower separation velocity and hence differs widely from the present problem.

2. System Description

A. Separation Configuration

The third stage follows an internal branching configuration and is supported by the adaptor at the top. The stage (both motor and nozzle) is encapsulated inside a closed interstage. The lateral clearance between the third stage motor and interstage is about 100 mm and the lateral clearance subsequently improves at the nozzle section, Fig 1.

Single-plane Separation: Since the nozzle is enclosed by the interstage, before the ignition of the third stage, the interstage has to be discarded. On separation, the interstage is separated along with the second stage and discarded. Any length of the interstage (above the nozzle and enclosing motor alone) that continues with the third stage is a penalty on the payload. Hence it is desirable to have the separation plane at the top of the adaptor from which third stage hangs.

Two-plane Separation: In the eventuality of collision with a single separation plane, there should be two separation planes. The first separation plane needs to be fixed at a height tolerable for safe separation, followed by the second separation plane at the top of the adaptor. However, two plane separation is a relatively complex design with increased number of mechanical systems.

Single-plane Separation with Guiding Systems: An alternate to the two-plane separation is providing a mechanism to guide the motion until the end of motor case. This results in a continuous contact between the bodies and transfer of forces and moments between them.

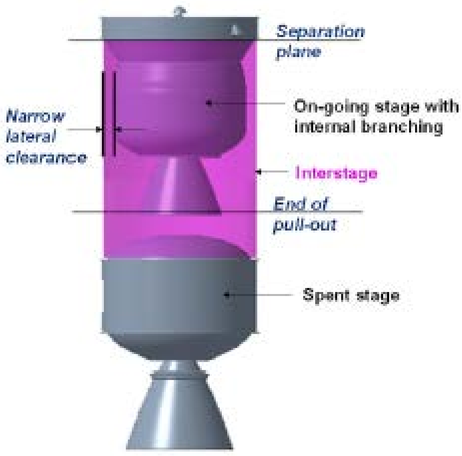

Fig 1. Separation geometry – Hanging internal branching of third stage and Interstage structure (highlighted) enveloping the third stage

B. Separation System

System Description: It has a piston cylinder assembly held together by rivets, with a folded rubber bellow between them, Fig 2a. Through the rubber bellow runs cluster of mild detonating cord (MDC). On separation command, MDC detonates releasing gas and causing the bellows to expand. In the pressure so generated, rivets are sheared (physical severance of stages) and the velocity is imparted to the separated stages (jettisoning of stages).

Cut-outs: The provision for initiator introduces break in XBS circuit. Also, from easiness of manufacturing a circularized attenuator tubes and assembling it, it is preferred that the XBS ring is made in two halves. This introduces two cut-outs in the XBS on opposite sides, Fig 2b. To ensure that separation forces are well balanced by design, the cutouts are to be diametrically opposite and of equal length.

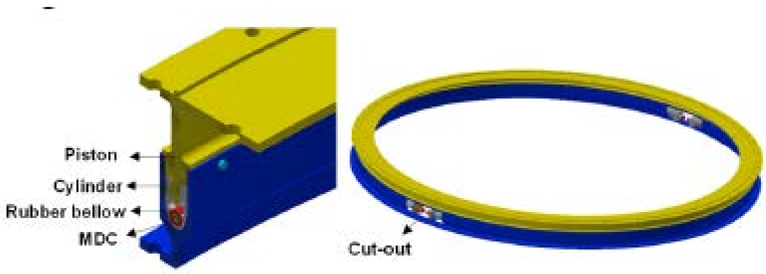

Fig 2. (a) Piston – Cylinder assembly with bellow (b) XBS with cut-outs

The system is located at the separation plane, sandwiched between stages. It acts as a primary load carrying member during flight and hence the energy required for physical severance is quite high – this is the same energy which later jettisons the system. Thus, the system is primarily characterized by an impulsive nature. The LBS is also impulsive by nature. However, by comparison, it is observed the pressure levels of XBS and LBS are quite different. Separation dynamics analysis of payload fairings using LBS is discussed elsewhere [5].

3. System Modelling and Design Nuances

A. System Modelling

The six degree of freedom equations of motion for rigid body are solved to obtain the translational and rotational motion of the bodies.

$$m\,[dv/dt + \omega \times v] = F \qquad (1)$$

$$I\,d\omega / dt + \omega \times I\omega = M \qquad (2)$$

The equations are solved for / and / and further integrated twice to obtain θ, ψ, φ and s. The XBS is discretized into zones and across a zone, pressure Pi(s) is constant and acts at the midpoint of the zone.

For each zone, i

$$F_i(s) = P_i(s) * A_i$$

$$M_i(s) = r_i * F_i(s)$$

The contact area, Ai is assumed to be constant and ri is the force acting point from c.g. of the respective bodies.

The force and moments of the expanding bellow system are modelled as follows,

$$F = \sum F_i \qquad M = \sum M_i$$

Pressure, P(t) is arrived from mathematical modelling or test data. The pressure is transformed to P(s). This conversion is valid since the test set-up is mounted on rollers and the total energy content of the system is translated into translational motion of the test masses. The significance of P(s) is that, it characterizes the energy of the system and is invariant of mass.

B. Design Philosophy

Design philosophy followed in separation dynamics is worst case design philosophy. To begin with a nominal case is performed – all parameters in nominal – to confirm the system behavior. The adequacy of the design was subsequently confirmed by synthesizing a worst-case analysis with off nominal conditions. In a worst case, all the parameters are perturbed in additive sense for the worst outcome.

C. Failure Case Studies

The system is provided with two initiators. Two failure cases identified, from separation dynamics perspective, are (a) complete failure of one initiator and (b) delay in initiation between the initiators. The failure cases are studied and addressed.

4. Results and Discussion

A. Scenario – 1

XBS – with two disconnected halves The initial development was the two halves of the bellow are separate entities such that the pressure developed in one half is independent of the pressure developed in another half. The pressure profile is given in Fig 3. The pressure difference of ~50% between the halves is considered for the study, Fig 3. In Fig 3, time is normalized against the action duration of nominal case and pressure is normalized against peak pressure of nominal case.

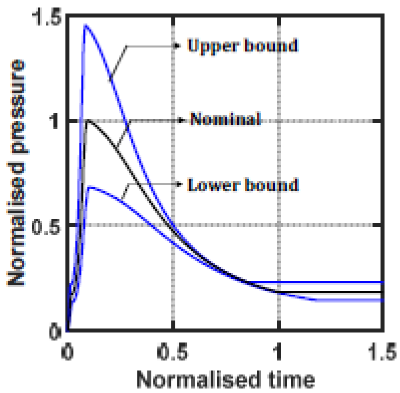

Fig 3. Pressure profile – nominal and bounds

Table 1(a). Nominal case results with two XBS halves

Case description	Relative velocity (m/s)	Lateral gap consumed at motor case clearance (mm)	Time taken for complete pull-out (ms)	Energy (kJ)
Nominal pressure	4.2	18	860	10
Upper bound pr.	3.7	19	760	13
Lower bound pr.	4.8	17	990	8

Nominal case – pressure in both the halves are same. It is observed the system performance does not vary with the pressure until the pressure in both the halves are same.

Table 1(b). Worst case results with two XBS halves

Case Id	Case description	Lateral gap consumed at motor case clearance (mm)
1	Nominal	18
2	Dispersions in inertia properties	33
3	LV body rate at the instance of separation	45
4	UB & LB pressure in two halves	350

Worst case synthesis shows that the system tolerates the dispersion in mass and inertia properties and body rate from launch vehicle at the instance of separation. However, the two halves having extreme possible pressure difference is not tolerable and leads to collision.
Criticality: (a) Pressure difference between the halves is not tolerable and leads to collision. (b) In case of failure to initiate at one side, the half will remain attached to on-going vehicle leading to failure.

Recommendations: (a) It is desirable to ensure uniform pressure between the halves (b) If not possible, the pressure to be contained within a tolerable range – 10% as compared to 50% - discussed in Scenario 2. (c) If pressure dispersion cannot be contained, then separation is to be guided to arrest lateral rate – discussed in Scenario 3.

B. Scenario – 2

XBS – with two connected halves The three major improvements after the initial study were, (a) the pressure levels and subsequently, dispersion between the upper bound and lower bound profiles were reduced (but contact area is increased to deliver more force), Fig 4. In Fig 4, time is normalized against the action duration of nominal case of initial profile and pressure is normalized against peak pressure of nominal case of initial profile. The difference in pressure is reduced from 50% to 20%. (b) two halves were connected to ensure uniform pressure between the bellow halves (c) inclusion of SMDC (as in payload fairing) to transfer pyro ignition between halves.

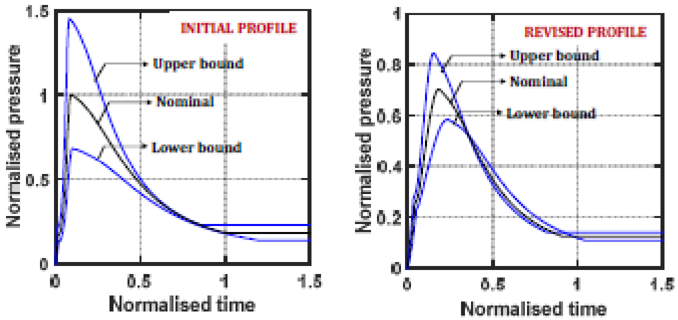

Fig 5z. Pressure profile – comparison between initial and revised profiles

The effect of increasing the contact area and decreasing the pressure levels resulted in a nominal relative velocity of > 5 m/s.

Outcome: The effect of the afore mentioned design modifications are given in Table 2. The effect of reducing the bounds of pressure improves the lateral gap, worst case(a). Further, ensuring uniform pressure leads safe separation with a better margin, worst case (b). One side initiation, enabled by SMDC, is studied and found to be safe (Section 4.4)

Table 2. Results with SMDC

Case description	Relative velocity (m/s)	Lateral gap consumed at motor case clearance (mm)	Lateral gap consumed at nozzle exit (mm)
Nominal	5.5	18	44
Worst case (a)	5.3	160	340
Worst case (b)	5.3	50	140

C. Scenario – 3

Guided Separation Design with two sets of rollers, to guide the separation, was studied. The rollers guide over the motor case, Fig 5 and arrest any relative lateral motion of the stage. The guides were modelled as rigid guides.

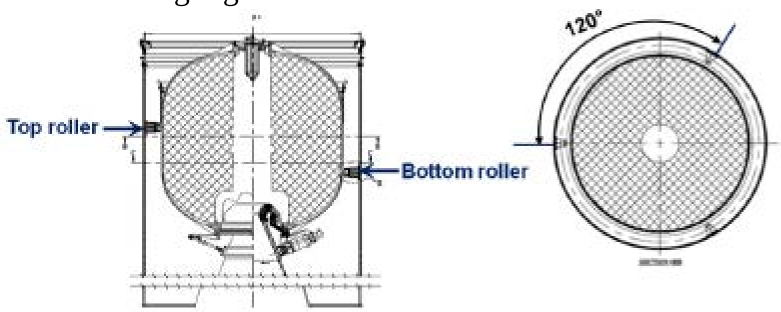

Fig 5. Roller configuration

The guiding effect continues for 200 ms from the begin of separation and at the clearance of motor case only 10 mm lateral gap is consumed. Inclusion of guiding mechanism in the Design was found to be beneficial.

D. Effect of One Side Initiation

If pyro ignition fails on one side, the detonation from other side will propagate to the other end through SMDC, Fig 6(a). Thus, the inclusion of SMDC in the Design prevents failure. Here, bellow pressure is modelled as Pi (si,vd).

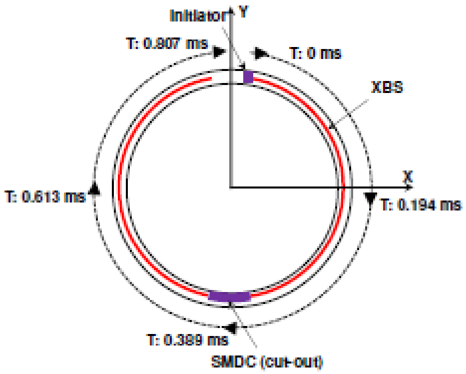

Fig 6(a). Schematic of one side initiation

Due to this phenomenon, (a) the lateral rate buildup on the stages involves a correction, Fig 6(b) and (b) the separation disturbance on the bodies are higher than the two-side initiation case. In Fig 6(b), time is normalized against the action duration of nominal case and body rate is normalized with peak rate component of second stage.

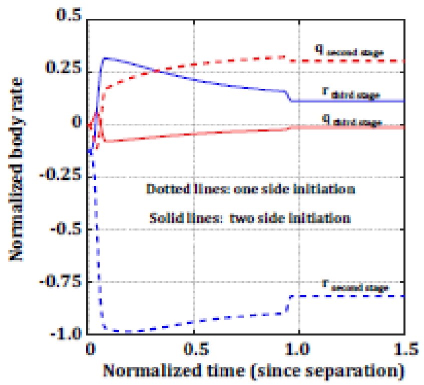

Fig 6(b) Body rate on second and third stage for one side initiation – Nominal case

Table 3. Results with one side initiation

	One side initiation		Two side initiation	
	Nom	WC	Nom	WC
Third stage lateral rate (°/s)	1.5	7.0	0.2	4.4
Second stage lateral rate (°/s)	4.5	20	1	12
Lateral gap consumed at motor case clearance (mm)	70	105	18	50

E. Effect of Delay in Initiation between halves of XBS

The delay ignition between the two halves introduces a staggering of action duration between the halves. The effects are studied and as expected is found to be a benign condition as compared to one side initiation, Table 4.

Table 4. Results with one delay in initiation – Nominal case

Delay in initiation (ms)	0	0.1	0.2	0.5
Third stage lateral rate (°/s)	0.2	0.2	0.2	1.0
Second stage lateral rate (°/s)	1	1.3	2.8	3.5
Lateral gap consumed at motor case clearance (mm)	18	20	23	55

From the on-going arguments, we can clearly see, any delay of more than a threshold value, will result in the pyro detonation transfer through SMDC from other side and is similar to one side initiation after 0.8 ms.The delay in initiation has a non-linear effect on the dynamics of the system as can be seen from Table 4.

F. System adaptability to Coasting Requirements

Mission design for SSLV requires a minimum coasting between second and third stage. The relative velocity of > 5 m/s, offers the flexibility to separate at a higher tail-off thrust. As compared to similar stage separation where spring-based separation system is employed, XBS allows the separation to be preponed by 35 s without any constraints/ additional requirements from other systems. And, if the ongoing stage can be ignited within 10 s of separation, an addition reduction 50 s is possible in the coasting duration.

5. Conclusion

The paper highlights the separation dynamics design explorations in arriving at a choice separation system for the second stage separation of small satellite launch vehicle. The requirements and constraints on the system are discussed in brief. Studies proved that newly developed expanding bellow system holds an edge as compared to the conventional flight proven systems used in stage separation. The design is similar to linear bellow system used in payload fairing separations of ISRO's launch vehicles.

The initial studies with XBS showed interference between the separating stages is inevitable. Analyses helped in identifying the critical parameter and tuning of system design. Also, the failure case studies brought out the system redundancy.

6. References

[1] K.J. Ball and G.F. Osborne, Space Vehicle Dynamics, Oxford University Press, 1967

[2] B.N. Suresh and K. Sivan, Integrated Design for Space Transportation System, Springer, 2015.

[3] Yuvaraja R, Dynamics of Separation of Liquid Stage with twin engine configuration from a longer pull out of Upper Stage, 11th National Seminar and Exhibition on Aerospace & Related Mechanisms (ARMS 2018).

[4] Sivasakthi R, Separation Dynamics Analysis of a Spent Solid Stage during its Thrust Tail-off,

10th National Seminar and Exhibition on Aerospace & Related Mechanisms (ARMS 2016).

[5] N Radha, Abhay Kumar, Separation Dynamics Analysis of a Large Full-scale CFRP Heat Shield Separation Test on Ground, National Seminar and Exhibition on Aerospace & Related Mechanisms (ARMS 2010).

[6] [6] Sivasakthi R, 'SS2/SS3 separation dynamics analysis with expanding bellow system – Level 2', VSSC/SDPED/TM-SSLV/009/2019.

[7] [7] Sivasakthi R, 'SS2/SS3 separation dynamics analysis with expanding bellow system', VSSC/SDPED/TM-SSLV/005/2019

Modelling and Simulation of Separation Dynamics of Twin Large Satellite Systems from Upper Stage of Launch Vehicle

Sivasakthi R
Vikram Sarabhai Space Centre
ISRO
Thiruvananthapuram
sivasakthi@vssc.gov.in

N Radha
Vikram Sarabhai Space Centre
ISRO
Thiruvananthapuram

C Ravikumar
Vikram Sarabhai Space Centre
ISRO
Thiruvananthapuram

Abhay Kumar
Vikram Sarabhai Space Centre
ISRO
Thiruvananthapuram

***Abstract*— The paper focuses on establishing the design space for safe separation of twin identical large spacecraft of mass 2.5 ton each and of height nearly 6 m subjected to constraints (tight clearance). Study of different possible sequences of separation brings outsequential and simultaneous separation is possible. The sensitive parameters for the relative dynamics of the spacecraft are identified and the tolerance limits are defined. Sensitive parameters for design are center of gravity (c.g.) of spacecraft and initial body rate at the beginning of separation. Under worst-case design, the tolerance limits on dispersion sources are arrived at. Also, the necessary conditions for a safe separation are brought out. An option to improve design space is increase the mounting inclination of spacecraft. This is achieved by means of reducing the adaptor length or re-configuring the payload fairing to have larger diameter.**

Keywords: Separation dynamics, twin satellite, spring-based separation system, lateral rate due to separation, launch vehicle

1. Introduction

In any launch vehicle mission, the final event that decides the success of mission is the precise and safe injection of satellite into orbit. This depends much on the safe separation of satellite from launch vehicle. The area of design and analysis of spacecraft separation dynamics focuses on providing solution towards safe separation and as well to accomplish the spacecraft mission requirements.

A. Dynamics of Satellite Separation

In general, the requirements of a satellite separation dynamics are safe separation. The separating satellites has to satisfy mission requirements ranging from orbit requirements, additional velocity on satellite due to separation to body rate constraints on separated satellites (at injection). For a safe separation, stage and satellite lateral body rates are equally critical parameter. Various satellite separations are summarized below.

(i) *Main-satellite separation:* In ISRO launch vehicles, typically payloads of mass more than 1000 kg are carried as single main satellite. The piggy-backs in these missions, if present, are mostly nano satellites and are mounted away from the main satellite deck. In such cases at the time of primary payload separation, there is no possibility of interference from any launch vehicle structures.

(ii) *Micro-satellite separation:* In the multiple payload missions, the main satellite deck or adaptor deck are shared by multiple micro-satellite and they are mounted in close vicinity. However, these satellites are of micro satellite class (< 500 kg). The presence of launch vehicle structures and/or co-mounted satellites pose a possibility of interference.

(iii) *Nano-satellite separation:* The requirements of nano-satellite separation are minimal, often limited to safe separation. By means of mounting configuration and guiding the separation to arrest any lateral rate arising from separation, the safe separation requirement is met.

B. Proposed Mission

For a future launch vehicle designated to carry more than 5 t payload to GTO, a twin satellite system was proposed as the payload. The satellites are identical with mass 2.5 t eachand co-mounted in the same deck.

C. Literature Review

The satellite separations so far studied are in a wide range. To meet the lateral rate requirements of satellite at separation, the strategy of using springs of different energy levels was studied, proposed and successfully implemented [1]. For two micro satellites mounted on EB deck the satellites had to clear the launch vehicle tank. To avoid interference with stage, simultaneous separation was recommended [2]. Since then, both these strategies are being used as a standard Design solution for satellite separation in ISRO's missions.

Separation dynamics of three near identical satellites of mass 500 kg and mounted with minimal clearance was analysed and design aspects were brought out [3]. Separation of multiple micro satellites mounted inside a constrained envelope have also been studied earlier [4].

In Ariane 6 launch vehicle used for injection twin tall satellites, dual launch structure is employed and satellites are stacked one above other. The sequential stacking is possible because of 20 m height of payload fairing [5].

2. Problem Formulation and Design Philosophy

A. Problem Formulation

The six degree of freedom equations of motion for rigid body are solved for the translational and rotational motion of the bodies in their respective body frame. The state vectors (position, velocity, attitude and attitude rate) are transformed to an Inertial (LI) frame. In the LI frame, the relative dynamics between the separated satellites are monitored to study the possibility of interference between the satellites. In the absence of collision, lateral gap between the satellites is worked out.

Forces on the satellites: The spring force is the only force acting on the separated satellite and it is modelled as function of displacement.

B. Design Philosophy

The design philosophy followed in satellite separation dynamics is worst case design philosophy. Initially, nominal case is performed – all the parameters in nominal value. Worst-case analysis is performed by cumulatively adding the dispersions on all parameters. This mode of perturbation brings out the worst outcome of the system. The system is cleared, if only all the mission requirements are met in worst-case or else, the system is re-designed to clear in worst-case.

3. Problem Description

A. System Configuration

Satellite configuration: The satellites are identical with mass nearly 2.5 ton each and length ~ 6m. The lateral moment of inertia is of the order of 1500 kgm^2. The satellites are mounted with a tight clearance among themselves (150 mm) as well as with the payload fairing, Fig 1(a).

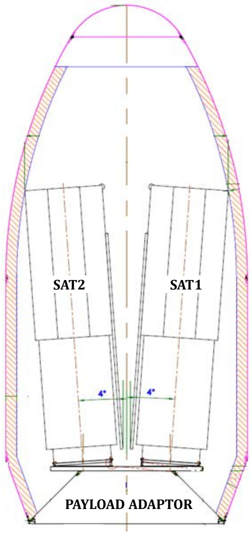

Figure1(a). Separation mounting geometry (at the time of separation, payload fairing would have been already discarded)

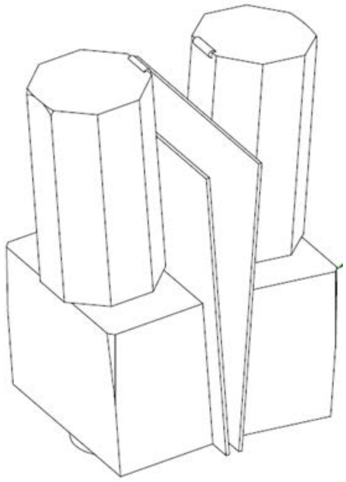

Figure 1(b). Separation geometry (adapter and stage not shown)

Separation geometry: The satellites are mounted on the payload adaptor. The separation system provides the interface between payload adaptor and satellite. The satellites are at equidistant from center. The separation system houses the springs. It also provides an inclination of 4º – the direction of jettisoning. A higher mounting inclination is rendered impossible by the tighter clearances between satellite and payload fairing at mounting. The separation geometry is given in Fig 1(b). The separated satellite has to clear the other satellite top.

Separation system: The jettisoning of the satellites is by means of convention helical compression springs that used in satellite separation.

Design variables: The c.g. of the satellite, being a generic design, was not restricted and considered as a design variable. The study considered the possibility of axial c.g. variation by about 1.6 m and tolerable lateral c.g. had to be concluded from the studies based on the necessary condition of safe separation. The choice of number of springs is again left-out as a design variable.

Dispersions on Design variables: The dispersions on design variables are critical because the system clearance is based on worst-case performance. Notable dispersions include lateral c.g. error, moment of inertia error, a possible 0.7 deg/s residual attitude rate at the instant of separation command (initial body rate – IBR).

4. Results and Discussion

The number of springs and energy delivered by the springs are fixed at the maximum possible limit to improve the relative velocity to the best possible limits. The energy delivered by the system is ~ 0.8 kJ (twice as much as in any other satellite separation).

A. Separation Sequence

Sequential separation: The satellites are separated sequentially and in between the separations control system of the stagecontrols and nearly nullifies the separation disturbance on the stage. The time interval between the separations is of the orders of tens of seconds. A sequential separation is characterized by,

(i) Relatively higher body rate on the stage (as compared to simultaneous separation)
(ii) Longer pull-outs (separated satellite has to pull-out and clear the length of satellites that continue with stage at that point)

In general, these are two factors work in tandem leading to collision. However, for the present case, the separation disturbance on the stage and satellite are benign – less than 0.5 °/s in nominal case. In the worst case, IBR dispersion leads to interference of separated satellite and sequential separation is not a feasible option, Table 1. In the cases described in Table 1, the dispersions are added and every row includes the effect of all dispersions mentioned up until then.

Table 1. Sequential separation – Worst case

Additional dispersion	**Body rate on satellite (°/s)**	**Body rate on stage (°/s)**	**Lateral gap available at pull-out (mm)**
Nominal	0.02	0.33	576
Satellite dynamic properties	0.71	0.34	386
Stage dynamic properties	0.71	0.38	336
Spring system	1.22	0.37	209
Initial body rate	1.72	0.87	collision

In worst case, collision occurs 0.7 m before the end of pull-out. IBR is the only source of higher rate on the stage. If the rate on the stage can be controlled to 0.3 °/s instead of 0.5 °/s, sequential separation will be feasible.

Near-simultaneous separation: The satellites are separated sequentially and in between the separations there is no control capture of the stage. The time interval between the separations is of the orders of milli-seconds. In simultaneous/ near-simultaneous separation, the stage dynamics is of no consequence in the pull-out of the satellites. The second satellite has to clear the first separated satellite. Also, the separation disturbance from first separation is carried onto the second satellite.

The relative velocity between the satellites is 0.24 m/s. The pull-out takes approximately 24s. To make feasible the near-simultaneous separation, the c.g. dispersion and inertia dispersion on the satellites are reduced by 50%. However, collision is observed on inclusion of SAT2 inertia, mass dispersion and initial body rate, Table 2.

Table 2. Near-simultaneous separation – Worst case

Additional dispersion	Lateral gap available at pull-out (mm)	Additional remarks
Nominal	1845	SAT1: 0.02 °/s; SAT2: 0.31 °/s
Stage disturbance from SAT1 separation	1281	stage rate: 0.47 °/s
Additional rate on SAT1	238	SAT1 rate: 0.85 °/s (c.g.: 5 mm, inertia: 5 %, spring system error)
Additional rate on SAT2	-108	SAT2 rate:0.74 °/s (c.g.: 5 mm)

Even with further tightening of c.g. dispersion to 3 mm, collision is still observed. Lateral c.g. error is found to be of more sensitive parameter for near-simultaneous separation (more than even sequential separation) and is not feasible. Axial c.g. offset is also a contributor for collision and is discussed in next section.

Simultaneous separation: The satellites are separated simultaneously. In simultaneous separation, the stage disturbance is of no consequence right from the beginning of separation. In the case of identical satellites undergoing simultaneous separation, as being discussed here, the behavior of the satellites is also identical in nominal case. There is no pull-out involved, in nominal case, as the satellites move laterally away from separation instant, Table 3(a).

Table 3(a). Simultaneous separation – Nominal case

	Between base of satellites	Between top of satellites
Initial gap by geometry (mm)	150	950
Lateral gap at 10 s (mm)	1015	1815
Lateral gap at 20 s (mm)	1881	2680
Lateral gap at 30 s (mm)	2746	3546

In the worst case, the effect of the lateral velocity is overcome by the rotational dynamics of the satellites. Three pull-out scenarios are identified and studied as follows,

(i) Base of one satellite clearing the top of other satellite: this situation is critical if both the satellites are having the same sense of rotation.
(ii) Base of one satellite clearing stations close to base of another satellite: this is critical if both the satellites exhibit a base closing tendency
(iii) Top of one satellite clearing stations close to top of another satellite: this is critical if both the satellites exhibit a top closing tendency

Tolerable rate for all three scenarios is worked out, Table 3(b). Simultaneous separation is a feasible mode of separation, if the rate constraints specified can be honored under worst case.

Table 3(b). Simultaneous separation –Worst case

	Tolerable lateral rate (°/s)
between base of one spacecraft and top of another	1
between base of one spacecraft and base of another	1.1
between top of one spacecraft and top of another	1.4

B. Effect of axial c.g. movement

Studies of separation sequence focused on the dynamics and the axial c.g. of the satellites are kept at 2.6 m from the base. The present section brings out the effect of axial c.g. variation with respect to lateral gap available and results are provided in Table 4(a) & (b).

Table 4(a). Effect of axial c.g. movement with respect to lateral gap available– Nominal case

Separation Sequence	Axial c.g. of satellite		
	2.6 m	1.5 m	0.9 m
	Lateral gap available (mm)		
Sequential	576	540	514
Near-simultaneous	1845	1694	1606
Simultaneous	1015 mm between satellites at 10 s		

In sequential separation, the rate on the stage varies with the axial c.g. of the satellite and hence with a lower c.g. satellite the lateral gap consumed is more. With axial c.g. movement, for the sequential separation to work, the initial body rate on the satellite further needs to be reduced to 0.2 °/s. Similar trend is seen in near simultaneous sequence also. The lower c.g. causes more lateral gap to be consumed.

The nominal case results do not vary with axial c.g. variation in simultaneous separation. In the worst case, the limit rates are critically constrained by the axial c.g. The axial c.g. is the parameter that limits the tolerable lateral rate on the separating satellites.

Table 4(b). Simultaneous separation – Worst case

Additional dispersion	Axial c.g. of satellite		
	2.6 m	1.5 m	0.9 m
	Tolerable lateral rate (°/s)		
between base of one spacecraft and top of another	1	1	1
between base of one spacecraft and base of another	1.1	2.2	2.7
between top of one spacecraft and top of another	1.4	0.9	0.7

In case1, the constancy of limit body for various axial c.g. can be understood as the gap lost by one satellite is gained by another satellite and relative dynamics doesn't alter. For case 2, as the axial c.g. moves close to base, the rotational effect is reduced and more rates are tolerable and vice versa for case 3. If the axial c.g. of the satellites are at 0.9 m, the tolerable lateral rate on the satellite from all the separations is only 0.7 °/s.

For the simultaneous separation to be feasible, the lateral rate on the satellites should not exceed 0.7 °/s from all dispersion sources, excluding initial body rate.

C. Tolerable dispersions on design parameters

The tolerable dispersion levels and further limitations in their nature are discussed here. The possible dispersion sources are,

(i) Physical severance of stage and satellite
(ii) Separation system dispersion
(iii) Dynamical property (lateral c.g., inertia and mass)

The dispersions from sources 1 & 2 are standard across satellite separation. In the dynamical property of the satellite, inertia and c.g. are critical for lateral dynamics. For a possible rate of 0.7 deg/s, the inertia dispersion should be limited at 5% and c.g. dispersion at 3 mm per axis (otherwise 4.25 mm in any quadrant). Additional c.g. dispersion can be tolerated at the expense of reduction in inertia dispersion.

*Tolerable nominal c.g. offset:*The choice of only 4.25 mm tolerable c.g. dispersion is very well justified as follows. Only the dispersion in limited to 3 mm per axis, with the strategy of spring tuning a nominal c.g. offset of 25 mm can be tolerated in any quadrant. Also, additional 5 mm lateral c.g. offset can be tolerated by appropriately removing springs. Both these strategies will ensure a nominal lateral rate on the satellite to be 0 deg/s (effectively no c.g. offset).

Relative velocity between the satellites: From the on-going discussion, it is understood in a simultaneous separation of identical satellites, the relative velocity between the satellites is zero. In the case of a non-zero relative velocity, the scenario transfers itself into near-simultaneous separation, which we observed is the most critical of all three sequences. The possible scenarios under which relative velocity may ensue are,

(i) Identicality is lost between the satellites,
  (a) Mass variation during realization
  (b) Large and different lateral c.g. requiring different spring tuning for the satellites
(ii) Unintentional delay between the separations (order of milli-second)

D. Effect of mounting inclination

Presently, the mounting inclination is 4 deg due to space constraint inside fairing. If this can be relaxed by means of increasing fairing diameter and mounting inclination increased by 1 deg (5 deg), the limit rate can be relaxed to 8 deg/s. This is equivalent to 5 mm lateral c.g. dispersion.

In the case of a sequential separation, additional initial body rate 0.1 deg/s can be tolerated. The inclination change is possible by two means,

(i) Reducing the adapter length at interface
(ii) Increasing the fairing diameter.

With reference to the later point, it is totally a feasible option as an operational launch vehicle of ISRO is recently designed with a fairing of diameter 4 m (as compared to the standard 3.4 m fairing). Flying the same vehicle with different fairings is also a standard practice across global space agencies.

5. Conclusion

This paper discussed in detail the feasible and infeasible options for separating twin identical satellites of mass 2.5 t each in a future mission. The necessary conditions are laid for safe separation, especially in terms of the separation sequence. The prime parameters that dictate the dynamics under various separations modes are discussed.

Of the two feasible separation sequences, sequential and simultaneous, simultaneous is preferred as it does not require any system change.

In cases which warrant a sequential separation – missions where satellites are to be injected in different orbits – sequential separation is possible, if initial rate at the beginning of separation can be constrained from its present value. This calls for a system level tuning of the stage.

The design discussed in this paper is generic and can cater to any satellite in this category. The axial, lateral c.g. offset and their dispersions are not fixed to a particular value and are allowed to undergo a large variation nominally – axial c.g. variation of 1.6 m.

Simultaneous separation is possible by constraining the lateral c.g. dispersion to 4.3 mm in any quadrant. This is over and above the 30 mm nominal c.g. offset in any quadrant. The design recommendations are easily implementable. Another mandatory requirement for simultaneous separation is the identicality of the satellites.

Relaxation on all the afore-mentioned dispersion limits is possible by increasing the mounting inclination of satellite. It requires a fairing of larger diameter. For future missions with heavier and bulkier payloads, launch vehicles should be able to take different fairings as per the need.

This paper attempts to bring out the design and analysis effort made during the separation of twin large satellites from spent upper stage of Launch Vehicle.

6. References

[1] N Radha & Abhay Kumar, 6-D Separation Dynamics Analyses for Reduction in Satellite Lateral Rotational Velocities by Employing Separation Springs of Different Energy levels, 4th National Seminar and Exhibition on Aerospace & Related Mechanisms (ARMS 2002).

[2] N Radha & Abhay Kumar, On Simultaneous Separation of Multiple Satellites from Spent Upper Stage, 7th National Seminar and Exhibition on Aerospace & Related Mechanisms (ARMS 2012).

[3] Sivasakthi R, N Radha, C Ravikumar and Abhay Kumar, Design Solution for Separation of a Constellation of Satellites of 500 kg Class, 10th National Seminar and Exhibition on Aerospace & Related Mechanisms (ARMS 2016).

[4] Sivasakthi R, N Radha, C Ravikumar and Abhay Kumar, Separation of micro-satellites from a constrained envelope, 11th National Seminar and Exhibition on Aerospace & Related Mechanisms (ARMS 2018).

[5] Ariane 6 User's Manual, Issue 1 Revision 0 March 2018.

[6] Sivasakthi R, Preliminary Separation Dynamics Analyses of Twin Spacecraft for a Future GSLV MkIII Mission (Level 1 Study), VSSC/FMD/TM-LVM3/096/20

Dynamical Study of Air Crew Ejection System

R B Sarsar
Armament Research and Development Establishment
DRDO
Pune
rahulbsarsar@arde.drdo.in

S D Naik
Armament Research and Development Establishment
DRDO
Pune

R S Kalaskar
Armament Research and Development Establishment
DRDO
Pune

***Abstract* — An ejection seat is used in an aircraft for safe escape of the pilot in case of an emergency where pilot has to abandon the aircraft. With the advent of modern aircraft with high speed and high performance, safe ejection from the aircraft is vital. The safe ejection of the pilot depends on the velocity/acceleration of the aircraft, rotation motion of the aircraft, type of motion of the aircraft at the time of ejection, complete motion of the seat and the relative motion of the seat with the aircraft. In this work, a mathematical model is developed using dynamical equations of motion of ejection seat, which is divided in four phases, viz., gun stroke phase, rocket motor phase, free flight phase and parachute deployment phase. The study has been carried out for safe ejection under different aircraft motion conditions like zero-zero ejection, steady and level flight, aircraft moving with constant sink rate. A MATLAB code is developed and simulation analysis has been carried out for all phases.**

Keywords — Ejection Seat, Equation of Motion, Trajectory, Ejection System, Simulation

Nomenclature

A	Acceleration due to gun stroke
C_D	Drag Force
g	Acceleration due to gravity
m	Mass of ejection Seat and Pilot
T	Thrust force of rocket motor
t	Time
V	Velocity of ejection seat
V_x, V_y, V_z	Velocity components direction in inertial frame
ϕ	Roll angles
θ	Pitch angle
Ψ	Yaw angle
O – XYZ	Inertial or earth fixed Frame
$C – X_{ac}Y_{ac}Z_{ac}$	Aircraft Frame
C – xyz	Ejection Seat Frame

1. Introduction

The conventional way of rescue for aircraft crew in emergency was to abandon the aircraft by coming out of the cockpit, open the personal parachute after free fall and land safely. Advent in technology has improved the performance of the aircraft, whereas, the escape at greater speed would be feasible only if the pilot is propelled to and clear the aircraft. This lead to the development of the ejection seat. The purpose of the ejection seat is to lift the pilot out of the aircraft to a safe distance, then deploy a parachute to allow the pilot to land safely on ground.

To study and understand the optimum pressure required for ejection of a particular mass from the aircraft and effect of this pressure on pilot, lot of research work is carried out [1-3]. A validation of the mathematical model of pneumatic ejection system for aircraft store is carried out by Param Ram et al. [4]. Apart from ejecting seat from aircraft during emergency, it is also important to remove the canopy safely so that pilot should not suffer from any injury during ejection. Dhanapal et al. has mentioned the role of canopy severance system in seat ejection for military aircraft [5]. This paper discusses the dynamical motion of ejection seat which is divided in four phases. The study has been carried out for safe ejection under different aircraft motion conditions like zero-zero ejection, steady and level flight and aircraft moving with constant sink rate. A MATLAB code is developed and simulation study has been carried out for all phases.

2. Seat Ejection Dynamics

The purpose of the ejection seat is to lift the pilot out off the aircraft to a safe distance, then deploy a parachute to allow the pilot to land safely on ground. An ejection seat works on initiation of ejection by pulling the seat firing handle, the sear is withdrawn from the firing unit in the seat pan. This action fires a cartridge and the gas pressure developed which moves the ejection seat along the guide rail. The aircrew seat is ejected and the drogue parachute is deployed after rocket burnt out phase with pre-defined delay. For the safe ejection of the seat, trajectory of the seat along with pilot needs to be analyzed. Analysis of the trajectory has been carried out for following phases as shown in Fig. 1:

A. Phase I: Movement of seat with gun stroke.
B. Phase II: Movement of seat with rocket thrust.
C. Phase III: Free flight till drogue deployment.
D. Phase IV: Flight with drogue deployed.

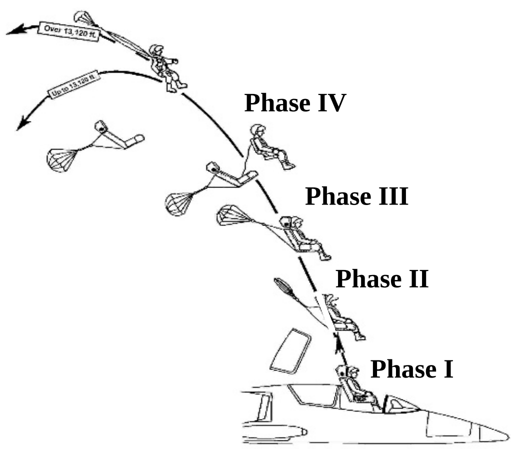

Fig 1: Phases of Seat Ejection

During Phase I, the ejection seat is moving along with the aircraft till it is ejected out with the gun stroke. Hence the initial velocity of the ejection seat is same as that of the aircraft. With gun stroke, it moves along the rails. Hence the velocity of the ejection seat is velocity of aircraft plus velocity of seat achieved due to gun stroke. At the end of gun stroke Phase II starts where rocket is fired, thrust will start affecting the motion of the seat. Once the burning phase is over, seat follows free flight path where only drag and gravity acts. In phase IV the drag component increases due to deployment of parachute.

During the motion of the seat, maximum acceleration and rate of change of acceleration achieved due to gun stroke needs to be calculated. It should not go beyond physiological limit of human body otherwise the pilot will suffer from heavy injuries. Safe ejection criteria is defined as maximum acceleration or rate of change of acceleration achieved due to gun stroke is bearable to pilot and ejection seat should cross dorsal fin safely. Keeping all above constraints for safe ejection, a mathematical model is developed, simulated and analyzed for safe separation of the pilot.

3. Mathematical Model for Trajectory of Ejection Seat

To study the dynamical motion of ejection seat a mathematical model has been developed using Newton's second law of motion. The equations of motion in vector form is given as follows [6].

$$m\frac{d\overline{V}}{dt} = m\overline{g} + \overline{C_D} + \overline{T} + \overline{A} \qquad \cdots(1)$$

Where, m is the mass of the seat and pilot, V is the velocity of the seat, CD is the drag forces acting on the seat, g is the acceleration due to gravitational force, T is the thrust force in phase II, A is acceleration force due to gun stroke in phase I of the motion.

The seat and pilot together is considered as point mass for the safe ejection study. The forces taken into consideration which act on the seat are gravity, drag, thrust in rocket phase and acceleration due to gun stroke. Equations of motion generated from above vector equations can be resolved in three different reference frames. Three reference frames have been defined inertial or earth fixed frame, aircraft frame and ejection seat frame. A mathematical model developed using above equations of motion for trajectory computation of ejection seat during the motion of seat and aircraft are transformed into inertial frame and motion of seat in aircraft frame for safe separation.

The reference frames used for analyzing the motion of seat relative to aircraft for safe separation are Inertial frame, Aircraft frame and Ejection seat frame which are defined as follows:

A. Inertial Frame (O-XYZ): Launch point is defined as origin O. XZ plane is the horizontal plane. XY is vertical plane of motion. X is along the initial direction of the aircraft, Y defines altitude i.e. in vertical plane and Z is perpendicular to X in horizontal plane.
B. Aircraft Frame (C-$X_{ac}Y_{ac}Z_{ac}$): Aircraft frame is fixed with respect to the geometry of aircraft. The origin for this frame is defined at centre of gravity aircraft. X_{ac} is along the axis of Aircraft. Y_{ac} is vertically upwards. Z_{ac} is normal to X_{ac} in yaw plane.
C. Ejection Seat Frame (C-xyz): The origin for this frame is defined at center of gravity ejection seat. C_x is direction of seat in front direction of pilot. C_y is vertically along the back of pilot seat. C_z is normal to x in seat plane (Along the side of pilot).

The relation between these frames has been established using transformation matrices. Transformation matrix from Inertial frame to aircraft frame consists of maximum three rotations and can be obtained as product of three rotation matrices. A_x (ϕ) denotes the rotation matrix obtained by applying rotation through the angle 'ϕ' about x-axis, similarly about y-axis and z-axis. The transformation matrix between aircraft frame and inertial frame is defined by eqn. (2).

$$\begin{bmatrix} x \\ y \\ z \end{bmatrix}_{AC} = A^x(\phi)A^y(\psi)A^z(\theta)\begin{bmatrix} X \\ Y \\ Z \end{bmatrix}_{inertial} \quad \cdots(2)$$

$$\begin{bmatrix} x \\ y \\ z \end{bmatrix}_{AC} = \begin{bmatrix} \cos\theta\cos\psi & \sin\theta\cos\psi & -\sin\psi \\ \sin\phi\sin\psi\cos\theta - \cos\phi\sin\theta & \sin\phi\sin\psi\sin\theta + \cos\phi\cos\theta & \sin\phi\cos\psi \\ \sin\phi\sin\theta + \cos\phi\sin\psi\cos\theta & \cos\phi\sin\psi\sin\theta - \sin\phi\sin\theta & \cos\phi\cos\psi \end{bmatrix}\begin{bmatrix} X \\ Y \\ Z \end{bmatrix}_{inertial}$$

Where, ϕ, Ψ and θ are roll, yaw and pitch and A_x (ϕ), A_y (Ψ) and A_z (θ) are rotation matrices in x, y and z direction respectively. $[x, y, z]^T_{AC}$ is vector in aircraft frame. $[X, Y, Z]^T_{inertial}$ is vector in inertial frame.

In the similar way, transformation matrix between aircraft frame and velocity frame and velocity frame and inertial frame can be obtained. Once the relation between different frames has been developed then each force is represented in given reference frame which is used to develop the equation of motion of ejection seat. The vector equation given in eqn. (1) is resolved in scalar form using transformation matrices in inertial frame as in eqn. (3).

$$\begin{aligned} m\dot{V}_x &= -D_x\cos\gamma\cos\delta + T_x\cos\theta\cos\psi + A_x\cos\theta\cos\psi \\ m\dot{V}_y &= -mg - D_y\cos\gamma\sin\delta + T_y\sin\theta\cos\psi + A_y\sin\theta\cos\psi \quad \cdots(3) \\ m\dot{V}_z &= D_z\sin\gamma - T_z\sin\psi - A_z\sin\psi \\ \dot{X} &= V_x \\ \dot{Y} &= V_y \\ \dot{Z} &= V_z \end{aligned}$$

Simulation study has been carried out in MATLAB. The equations of motion are integrated using forth order Runge-Kutta method.

4. Simulation and Results:

In this paper, an attempt has been made to develop the preliminary model of trajectory estimation. The data used for estimation of the trajectory is as follows: the mass of the seat along with pilot is 150 kg, gun stroke time is 0.15 s, velocity of the seat at end of gun stroke is 15.24 m/s, rocket motor thrust is 14500 N, rocket motor burn time is 0.31 s. Analysis of the trajectory has been carried out for following phases:

Phase I: Movement of seat with gun stroke starting from 0 to 0.15 s.
Phase II: Movement of seat with rocket thrust 0.15 to 0.46 s.
Phase III: Free flight till drogue deployment 0.46 to 0.50 s.
Phase IV: Flight with drogue deployed 0.50 to 1.50 s.

It should be noted that in any case of seat ejection, seat should not hit the dorsal fin of the aircraft. This gives the condition that when ejected seat travels the distance up to dorsal fin unit, its altitude from aircraft should be more that the height of dorsal fin unit. The aircraft considered for the simulation is having dorsal fin unit of 3m. Trajectory analysis for ejection seat is carried out for three different cases, zero-zero ejection, steady and level flight of the aircraft and aircraft moving with constant sink rate.

A. Zero – Zero Ejection:

In zero-zero ejection, it is assumed that the aircraft is grounded and pilot needs to be ejected due to emergency. It is observed that the trajectory taken by the ejected seat achieved the altitude of 27.88 m and 45.48 m range from the aircraft as shown in Fig. 2. The height of the seat at the time when it is above the dorsal fin unit is 15.63 m which is 12.63 m above the dorsal fin unit and time taken to achieve this height is 0.654 s as shown in Fig. 3. Hence it is a safe separation or ejection for pilot.

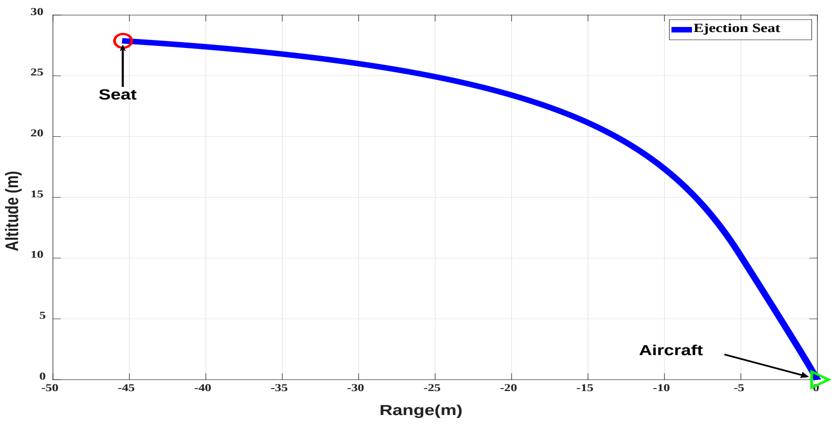

Fig 2: Flight Path of Ejection Seat for Zero – Zero Ejection Case

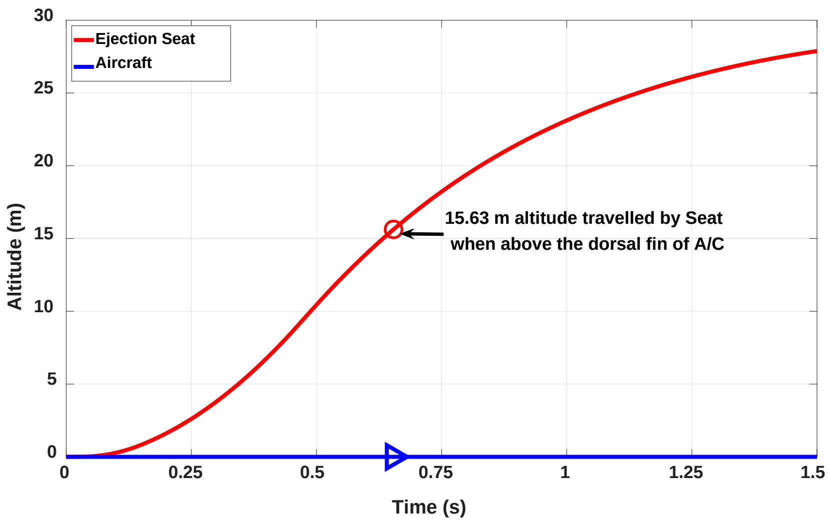

Fig 2: Position of Seat & Aircraft Vs Time

B. Steady and Level Flight Ejection:

In this case, it is assumed that the aircraft is travelling at a constant height 91m where seat ejection process has started. With the aircraft velocity of 77 m/s the seat is ejected at the 91m altitude and attend another 30m height i.e. the achieved 120.89 m altitude and travel 67.37 m in horizontal direction as shown in Fig. 4. The time taken to cross the dorsal fin unit is 0.644 s when ejected seat is 106.8 m altitude. The altitude difference between dorsal fin unit and seat is 12.41 m.

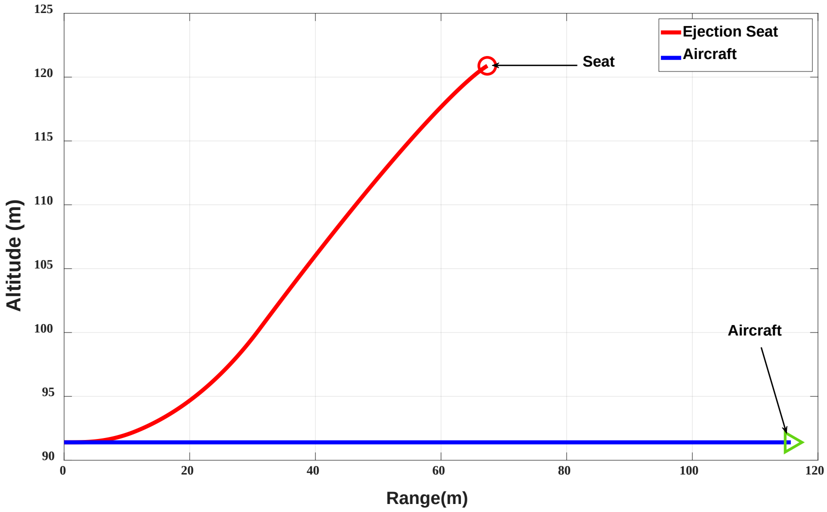

Fig 4: Flight Path of Ejection Seat for Steady & Level Flight Case

C. Aircraft with Constant Sink Rate Ejection:

In this case, it is assumed that the aircraft is coming down with constant sink rate of 50.8 m/s from an altitude of 91 m. The trajectory of the seat is shown in Fig. 5. At end of phase IV, seat has travelled and came down to altitude of 45.11 m from the 91 m while the horizontal range travelled by the seat is 68.35 m. The time when seat is above the dorsal unit is 0.642 s and difference between seat and dorsal fin unit altitude is 12.57 m as shown in Fig. 5.

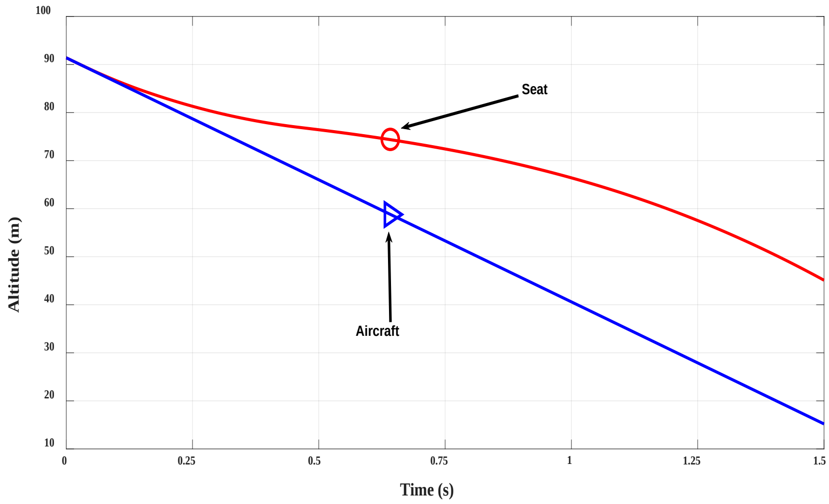

Fig 5: Flight Path of Ejection Seat for Steady & Level Flight Case

Table 1 shows position of aircraft and ejected seat along with velocity of the seat at the end of each phase from Phase I to Phase IV. It is observed that in all the cases the seat ejection is safe. There is sufficient distance between seat and aircraft when seat is above the dorsal fin unit in all cases.

Table 1: Phase wise Results for All Cases

Case	Time (s)	Range (m)	Altitude (m)	Vx (m/s)	Vy (m/s)	Remark
Zero-Zero Ejection	0.000	0.00	0.00	0.00	0.00	Initial Conditions
	0.150	-0.39	0.83	-6.47	13.87	End of Phase I
	0.460	-4.38	8.92	-19.32	38.39	End of Phase II
	0.500	-5.15	10.45	-19.34	38.02	End of Phase III
	0.654	-8.46	15.63	-23.90	29.40	Seat above Dorsal Fin. Vertical separation from dorsal 15.63 - 3 = 12.63 m
	1.500	-45.48	27.88	-66.14	5.12	End of Phase VI
Steady and Level Flight Ejection	0.000	0.00	91.40	77.17	0.00	Initial Conditions
	0.150	11.19	92.23	70.70	13.87	End of Phase I
	0.460	31.10	100.27	57.73	38.09	End of Phase II
	0.500	33.41	101.79	57.71	37.68	End of Phase III
	0.644	41.25	106.81	51.05	32.00	Seat above Dorsal Fin. Vertical separation from dorsal 15.41- 3 = 12.41 m
	1.500	67.37	120.89	9.11	2.62	End of Phase VI
Aircraft with Constant Sink Rate Ejection	0.000	0.00	91.40	77.17	-50.80	Initial Conditions
	0.150	11.19	84.61	70.70	-36.93	End of Phase I
	0.460	31.10	76.93	57.73	-12.54	End of Phase II
	0.500	33.41	76.42	57.70	-12.93	End of Phase III
	0.642	41.07	74.35	50.17	-16.36	Seat above Dorsal Fin. Vertical separation from dorsal 15.57- 3 =12.57 m
	1.500	68.35	45.11	18.96	-57.34	End of Phase VI

5. Conclusion

A mathematical model for aircrew ejection seat is developed and simulated for three different cases. It is observed that in all cases seat ejection in safe and achieved sufficient height for safe ejection. The dynamical model developed is very useful to study and analyze various conditions of aircraft motion, sequence of seat ejection as well as environmental factors for a particular aircraft. The simulation study will help the designer to define the safe criterion for ejection to the pilot.

6. References

[1] B. Etkin, "Dynamics of Atmospheric flight", John Wiley & Sons, Inc, 1972.
[2] "MK-14 High Technology Electronic Ejection Seat", Martin Baker Aircraft Co. Ltd, 1987.
[3] Air Force Wing précis on "Aircrew Ejection System – EJ 95", 1986.

[4] R. Paras, R. S. Khire, S. Akatti, “Validation of Mathematical model for aircraft store ejection mechanism”, 9th National Symposium and Exhibition on Aerospace and Related Mechanisms (ARMS 2015), pp. 449 – 458, 2015.

[5] M. Dhanapal, D. K. Kharat, “Role of Canopy Severance System (CSS) in Seat Ejection For Military Aircraft”, 8th National Symposium and Exhibition on Aerospace and Related Mechanisms (ARMS 2008), 2008.

[6] “Text Book of Ballistics and Gunnery”, Volume 1, 1987.

In-Orbit Thermal Management of Small Satellite Separation Systems

H M Ankita
STS
Vikram Sarabhai Space Centre
Thiruvananthapuram
ankitah9@gmail.com

P Ullekh
AERO
Vikram Sarabhai Space Centre
Thiruvananthapuram

M Ram Prabhu
AERO
Vikram Sarabhai Space Centre
Thiruvananthapuram

K K Raveendra Babu
STS
Vikram Sarabhai Space Centre
Thiruvananthapuram

L Sowmianarayanan
STS
Vikram Sarabhai Space Centre
Thiruvananthapuram

Abstract — **Separation systems of small satellites placed on launch vehicle decks are exposed to orbital thermal loads, radiation loss to deep space and thermal interaction with other stage elements, during the course of the launch vehicle mission. Prolonged exposure in long-duration missions could cause the separation system temperatures to breach their laboratory qualified ranges. Active or passive techniques of thermal management may be used in such scenarios to maintain the system temperatures within limits. This study evaluates the thermal management requirement of satellite separation systems for an extended duration launch vehicle mission. An integrated mathematical model of the final stage of the launch vehicle is developed in the commercially available NX software. The orbital thermal loads on the stage are computed with the help of sun and earth vectors based on launch date, time, vehicle trajectory and attitude. The adequacy of a passive thermal management scheme is computationally verified and is successfully demonstrated in flight.**

Keywords— thermal management, satellite separation systems, orbital loads

1. Introduction

The small satellite industry has expanded rapidly in the recent years. Numerous small satellites may be carried aboard a single launch vehicle as primary or piggyback payloads. Multiple satellites with different mission requirements often lead to extended mission durations with satellite separation and injection in multiple orbits.

Small satellite separation systems are designed to suit various sizes and configurations of satellites and are integrated with the final stage of the launch vehicle. In the course of launch vehicle ascent, the satellite separation systems are shielded from external thermal environments such as aerodynamic heating by encapsulation within the heat shield. However, post heat shield separation, the systems are subjected to direct Solar radiation, albedo, Earth emitted infrared (IR) radiation, radiation from stage elements and radiation loss to deep space. The systems are laboratory qualified for specific temperature ranges. Critical elements of the separation systems may reach temperature extremes due to prolonged exposure in extended duration missions. Temperature constraint violations may lead to failure in satellite separation due to thermo-structural or pyro component failures.

In this study, thermal assessment of small satellite separation systems has been carried out for an extended duration launch vehicle mission. The launch vehicle carries several small satellites alongside the main payload and injects them into multiple orbits using suitable separation systems. Thermal analysis of the separation systems is carried out for a duration from heat shield separation to satellite separation time. The performance of a passive thermal management technique is evaluated to maintain the temperatures of the satellite separation systems within the specified constraints. Adequacy of the technique is verified and the passive scheme is proposed for implementation in flight.

A. Satellite Separation Systems

In the present study, satellite separation systems used aboard the launch vehicle may be classified into two types – box type with a swinging door for radially separating satellites; and ring type with ball lock mechanism for axially separating satellites, as shown in Figures 1 & 2.

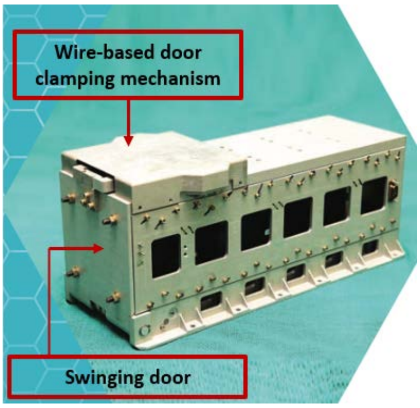

(a) Door-closed configuration

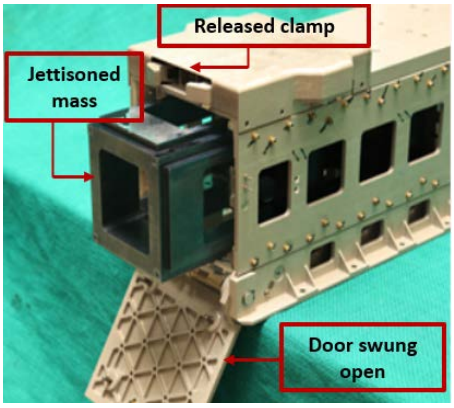

(b) Door-closed configuration

Fig 1. Box-type separation system [1,2]

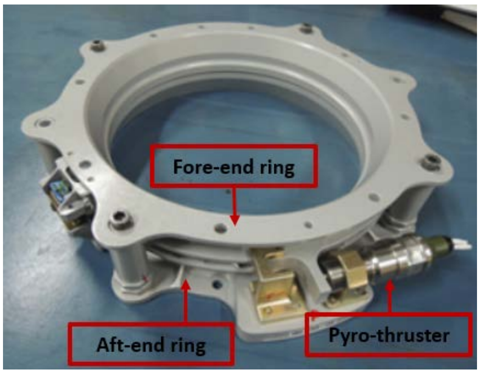

Fig 2. Ring-type separation system [1]

The box type separation system consists of a satellite kept inside a rectangular box and locked by a swinging door. The door is held in a locked condition with a wire-based clamping mechanism. A heating element causes the wire to fuse at separation time, thereby releasing the door. A compressed helical spring at the aft end of the box jettisons the satellite in a direction parallel to the mounting plane.

The ring type separation system consists of two rings held together by a ball-lock mechanism. The fore end ring is attached to the satellite while the aft end ring is mounted on a deck of the final stage of the launch vehicle. In addition, there exist a set of compressed springs parallel to the separation axis between the rings. A pyro-thruster mechanism releases the ball-lock hold at satellite separation time and the compressed springs are released, thereby providing a force in a direction perpendicular to the mounting plane for satellite separation.

The separation systems are mounted on a multi-satellite adapter (MSA) deck, which is integrated with the final stage of the launch vehicle as shown in Figure 3.

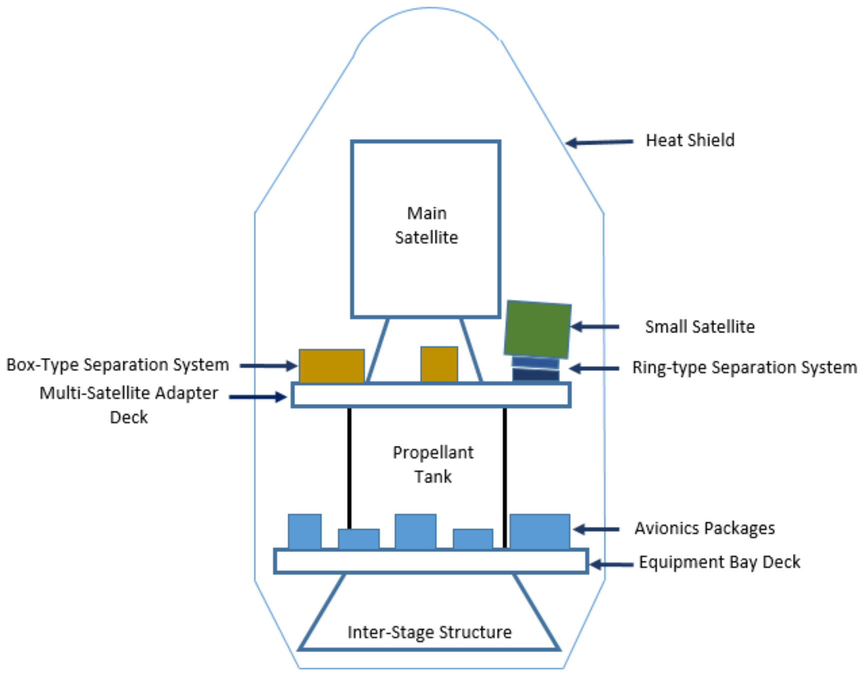

Fig 3. Schematic of small satellite separation systems integrated with launch vehicle stage elements

The separation system temperatures are required to be maintained within a temperature constraint of -10^{o}C to 60^{o}C. In the current study, an integrated model of the separation systems with the launch vehicle stage is developed, considering appropriate thermal mass, material and surface properties.

B. Thermal Management Systems

The choice of thermal management systems for various components aboard the final stage of the launch vehicle, such as, avionics packages, satellite separation systems and other structural elements, depends on several factors. Orbital thermal loads on the systems, power dissipation of components, thermal mass, material, surface optical properties and qualified temperature ranges of the systems play an important role in deciding the thermal management technique to be used.

Thermal management systems may be classified into active and passive types. Active systems rely on power for operation. Electrical resistance heaters and thermoelectric coolers are examples of active systems. Passive systems require no power source and may involve embedded heat pipes in equipment bay decks, selective surfaces such as low or high emissivity tapes, coatings, optical solar reflectors and multi-layer insulations.

The thermal management options in the current study consist of two techniques – a passive scheme, consisting of surface coatings to alter radiative exchange; and an active technique, consisting of stage re-orientation to alter orbital thermal load distribution. The second option, though not strictly active in nature, is classified as such, since it requires the use of the vehicle’s attitude control system. The choice between the two options is a trade-off between implementation feasibility, effect on downstream activities and mission requirements.

2. Thermal Environments

After heat shield separation, the final stage of the launch vehicle is exposed to (i) direct solar radiation, (ii) Earth albedo, (iii) Earth emitted radiation and (iv) radiation loss to deep space (at 4K).

The computation of orbital thermal loads requires continuous knowledge of the relative position of the launch vehicle stage w.r.to the Sun and the Earth. These relative positions, given by Sun and Earth vector in the vehicle reference frame, are dependent on the date and time of launch, the vehicle trajectory and the stage attitude. The attitude of the vehicle determines the direction of incidence of the solar and earth thermal loads on the stage.

The orbital loads on various stage elements are also affected due to shadowing by other stage components. Hence, for thermal assessment of the satellite separation systems, it is necessary to create an integrated thermal model of the stage. The view factors of the various stage elements with each other and w.r.to the Sun and the Earth are computed based on the stage configuration and the Sun and Earth vectors in the vehicle reference frame.

Material and surface optical properties, thermal mass and conductive couplings between various components also play a significant role in the thermal response.

3. Methodology

An integrated thermal model of satellite separation systems and the final stage elements of the launch vehicle is developed using NX software[3], as shown in Figure 4. The computed conductive thermal couplings between the separation systems and the MSA deck are defined as per the mounting interface scheme. The radiative interaction of the separation systems with deep space and with other stage elements is modelled using measured surface properties of various components. The time-varying sun and earth vector on the final stage of the launch vehicle and its geodetic altitude are computed using the launch vehicle trajectory, attitude, date and time of launch, using an in-house code. They are given as inputs to the NX model for computation of orbital thermal loads. The mass of the satellites housed inside the box-type separation systems and mounted over the ring-type systems is not modelled for a conservative temperature estimate. All components on the MSA deck are non-power dissipating in nature.

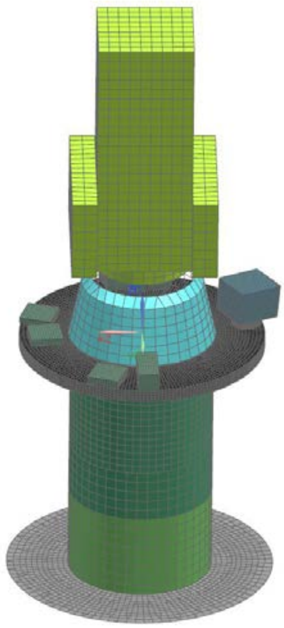

Fig 4: Integrated meshed model of final stage

Transient thermal analysis is carried out in the Space Systems Thermal module of NX software for a duration of 6800s, from the time of heat shield separation to the time of satellite separation.

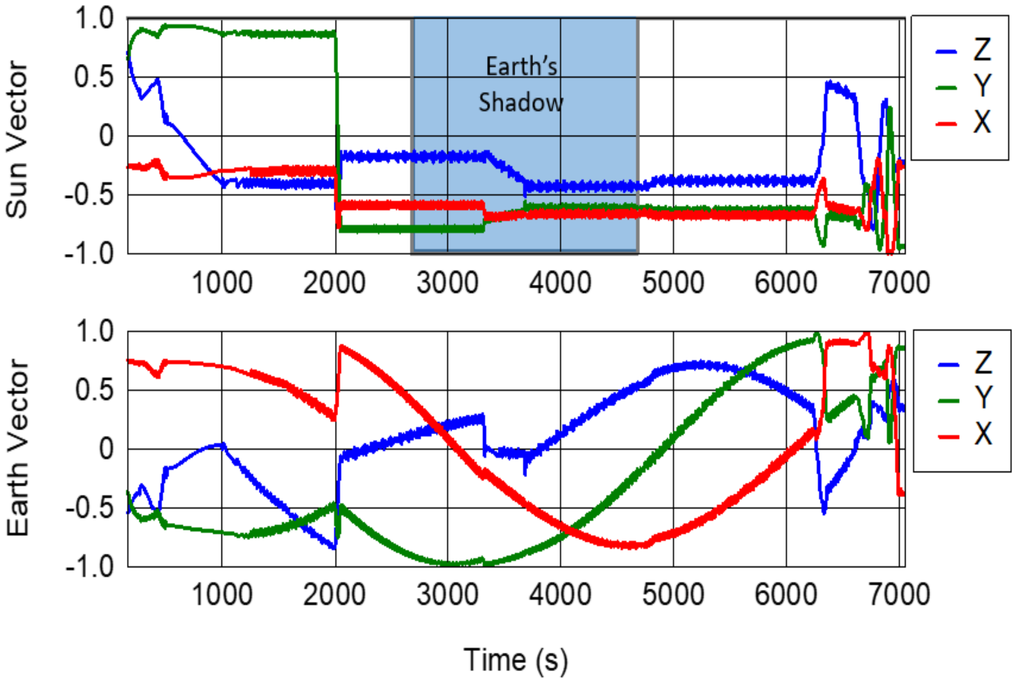

Fig 5: Computed Sun and Earth vectors in vehicle reference frame

4. Results and Discussions

The computed Sun and Earth vectors in the vehicle reference frame are as shown in Figure 5. The vehicle reference frame is as shown in Figure 6. The magnitudes of the Sun and Earth vector components indicate the direction of incidence of orbital thermal loads on the MSA deck.

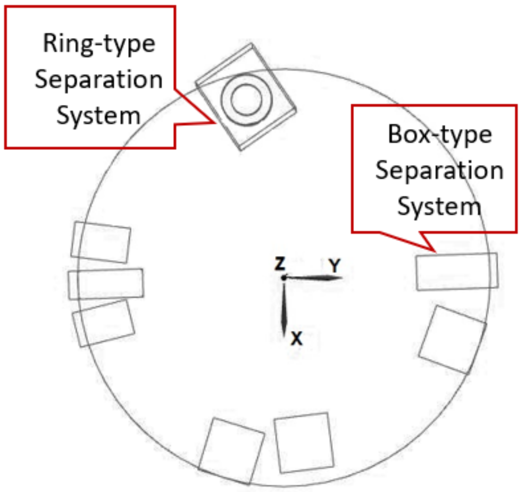

Fig 6: Top-view of MSA Deck

The preliminary transient thermal analysis indicates that certain separation system temperatures violate the lower bound constraint during the course of the mission. Considering the ease of implementation of a passive thermal management system in the current scenario, the application of a low-emissivity tape is examined as a viable first option. Analysis is carried out with the application of a low-emissivity tape on the bottom side of the MSA deck, under the separation systems.

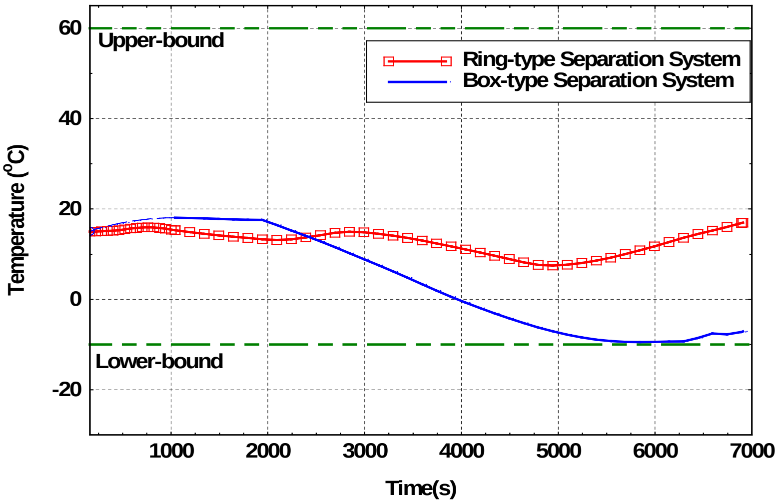

Fig 7: Computed in-orbit temperatures of small satellite separation systems

Adequacy of the proposed thermal management system is verified. The computed temperature variation of a typical box-type and ring-type separation system is as shown in Figure 7.

The application of low-emissivity tape (emissivity = 0.03) restricts the radiation loss to deep space from the bottom side of the MSA deck (emissivity=0.85), which is composed of a carbon fiber composite material. This prevents the temperature of the box-type separation system from falling below the lower bound constraint. It is to be noted that orbital thermal loads have a significant impact on the separation system temperatures, as is evidenced by the fall in box-type separation system temperature after the sun vector shifts to the diametrically opposite sector at about 2000 s. The low thermal masses of the systems in consideration lead to a relatively rapid response to changing orbital loads. The proposed thermal management scheme was implemented in flight and its satisfactory performance was demonstrated by the successful separation of all passenger satellites.

5. Conclusion

In-orbit thermal analysis of small satellite separation systems is carried out for an extended duration launch vehicle mission. A preliminary thermal analysis indicates the violation of lower-bound temperature constraints. Application of low-emissivity tape on the multi-satellite adapter deck is proposed to minimize radiative heat loss to deep space. The adequacy of the proposed thermal management scheme is verified through computation. The computed separation system temperatures are maintained within the acceptable limits.

The proposed thermal management scheme is implemented in flight and satisfactory performance is observed by successful separation of all passenger satellites. Analysis for future flights may be validated using on-board temperature measurements on satellite separation systems.

6. References

[1] New Space India Ltd., ‘*Separation Systems*’, www.nsilindia.co.in/payload-mechanism-separation-system
[2] Antrix Corporation Ltd., ‘Payloads Separation Mechanisms’, www. satsearch.co/products/antrix-inls-3u
[3] Siemens Product Lifecycle Management Software Inc. NX 9.0, 2012

Quick Ejection and Unfolding Mechanism of Deployable Systems

Amitabh Chakraborty
Advanced Systems Laboratory
DRDO
Hyderabad
asl_ac@rediffmail.com

Sachin Jain
Advanced Systems Laboratory
DRDO
Hyderabad

D Laxman
Advanced Systems Laboratory
DRDO
Hyderabad

Usha P Verma
Advanced Systems Laboratory
DRDO
Hyderabad

Dr. R Srinivasan Advanced
Systems Laboratory
DRDO
Hyderabad

Abstract —**Most of the space mission requires development of light weight structures which needs to be quickly ejected and deployed for its proper functioning. The requirement of the deployable system is to have a light weight structure and should be folded so as to accommodate in a small space confinement. Once released from the spacecraft / missile / aircraft, it should unfold or deploy other structures. The current design consists of an experimental deployable structure having two dihedral flaps, four fins folded in opposite directions. The opening torque of the fins and the flaps are provided by torsion springs. The material of construction of the deployable system is aluminum. The constraint of the design is to limit the weight of each deployable system to 1.5 kg. This paper documents a unique design and analysis of a deployable system hardware for a long range missile system and validation of analysis results with that of testing results.**

Keywords—Ejection Mechanism, Deployment Mechanism, Pyro Mechanism.

1. Introduction

Most of the modern day aerospace systems are required to carry sub systems which on completion of its intended function are required to be ejected out of the original vehicle. Some of these systems are required to be ejected from the main vehicle to perform its function only after separation from the mother vehicle. In addition, there is a lot of requirements to deploy small satellites in canisterised systems as well as deployment of other expendable systems. These ejection systems are also required in the field of deception technology like that of chaff ejection or ejection of decoy systems.

The original spacecraft vehicle is required to carry a lot of these deployable systems which has to be housed in a confined environment and on ejection seldom requires to be enlarged to a bigger geometry by unfolding of fins or panels. In addition, these deployable systems are required to have a light weight structure and are required to be folded so as to be confined in a small space. Once released from the original vehicle, it unfolds itself to a larger geometry. These systems require quick ejection from the original vehicle and should unfold quickly so as to function as a separate entity. These deployable systems are kept in initial position using locking mechanisms and on command, gets quickly ejected out of the original vehicle.

This paper contains the realisation and testing of a quick ejection mechanism for an experimental deployable system and its unfolding mechanism. The current deployable system configuration consists of two flaps and four fins folded in opposite directions. The driving torque for the fins and the flaps openings are provided by torsion springs. The material of construction of the deployable system is aluminum. These deployable system should be light in weight for quick ejection. Based on these constraints, a unique system has been designed which is rigidly mounted to base plate of the vehicle. The deployable system is initially a plate like structure which is housed inside a guide rail to ensure smooth ejection. The ejection force is given by a pyro cartridge which delivers high amount of energy per unit volume. The pyro force breaks the locking pin and ejects the deployable system from the vehicle.

Initial configuration of the deployable system was carried out and the fin unfolding time was calculated by solving conservation of angular momentum. The same system was also analyzed by using a commercial software for multi body dynamics (ADAMS) simulation. The theoretical calculations were then compared with those of experimental values which are closely matching. Two number of ejection tests were carried out to verify the theoretical values of the flap unfolding time as well as velocity of ejection. The experiment was carried out with the deployable system mounted on a plate and ejection of the plate captured through two numbers of high speed cameras. In addition, shock was also measured in the near field and far field shock regions. This paper documents the realisation, testing of the deployable system and comparison of experimental results with simulation.

2. Configuration and Material Selection

The current configuration consists of two numbers of dihedral flaps, four numbers of fins folded in opposite directions. The opening torque of the fins and the flaps are provided by torsion springs. The material of construction for the deployable system is aluminum.

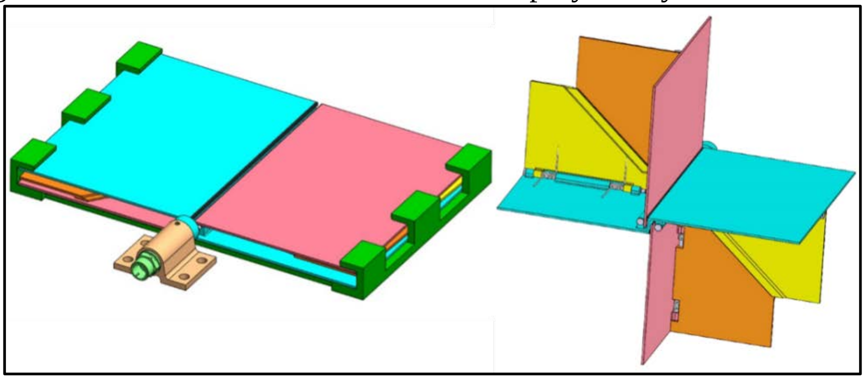

Fig 1: Configuration design of Deployable system in folded and in unfolded condition

Spring: The material used for helical spring is passivized SS 302 material. After multiple number of design iterations, the spring with cross section diameter of 1.5 mm and a mean diameter of 7 mm with 24 number of turns gives a bending stress of 872 MPa with factor of safety on maximum bending stress is 1.45. Due to geometrical envelope constraints, two torsional springs in parallel each with 12 turns has been chosen.

Shear Pin: The component is initially held in place by means of locking or shear pin. The shear pin is designed to take the loads coming during initial flight vibration as well as disturbance loads but on initiation of the pyro cartridge will shear off to facilitate the ejection of the deployment component. Shear pin is designed to withstand 750 Kg load during the operation. The material chosen is Brass.

3. Theoretical estimation of Ejection velocity

A. Ejection velocity calculation (Analytical)

Based on the total mass of the deployable system hardware and the pyros used, the pressure being generated within the available free volume was theoretically calculated. Knowing the geometry of the ejection system, the pyro ejection force was then calculated. The energy equation was then solved to give the resultant theoretical ejection velocity which is 24.94 m/s.

B. Ejection velocity calculation (Simulation)

Adams is the most widely used multi body dynamics and motion analysis software. Simulation of the ejection of the deployable system from the guiderail is carried out in ADAMS software. The deployable system has been subjected to a ramp force of 5600 N magnitude for 5 ms (input data calculated from pyro pressure calculations). The simulation is shown in Figure 2.

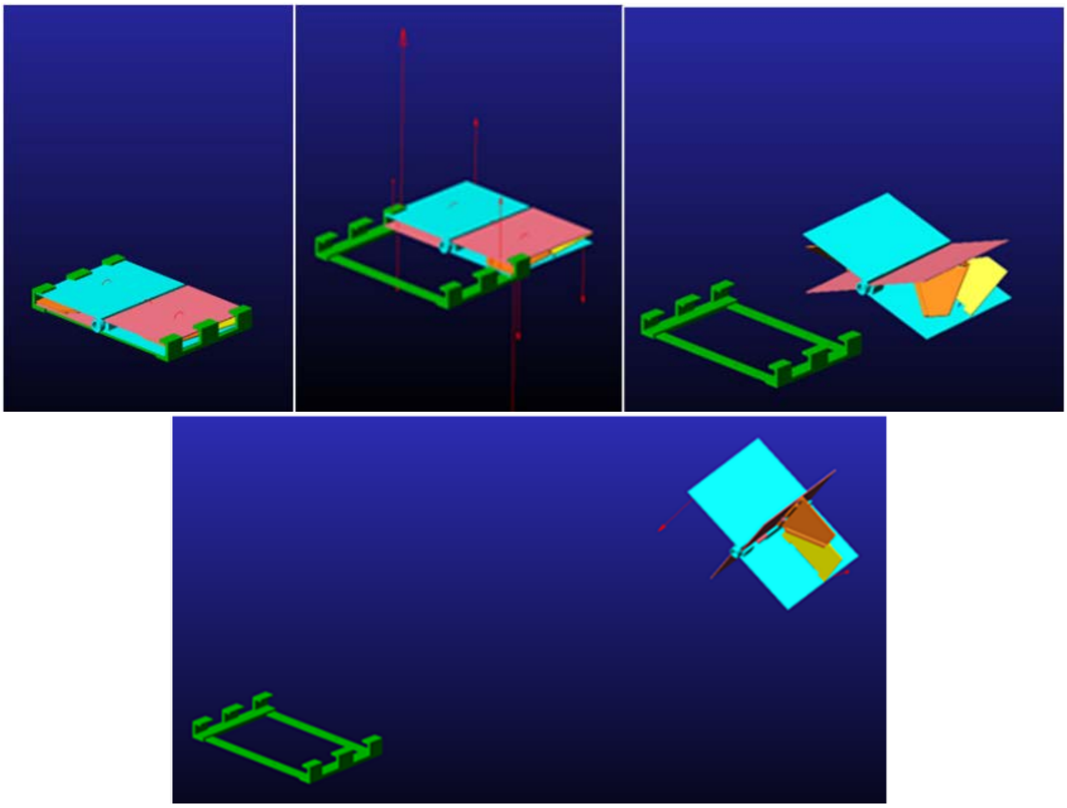

Fig 2: Sequence of analysis results of the deployable system ejection to full unfolding of fins

From the simulation it has been estimated that the ejection velocity is approximately ***28.5m/s*** which closely matches with the theoretical calculations.

4. Testing of deployable system releasing mechanism

The hardware has been realized to validate the design of ejection mechanism and deployment time. A limited number of hardware were realized for the ground test. The objectives of the test are to estimate the following parameters.

(i) Ejection Velocity
(ii) Deployable system unfolding time
(iii) Approximate Shock transmitted to deck plate
(iv) Interaction with deck plate (if any)

The details of test schematic is given in Figure 3. Deployable system assembly was mounted at a height of 2.5m above the ground. Expected ejection velocity is 20 – 30 m/s. Wire net has been placed at a distance of 2m so as to ensure that the full deployment of the article takes placed before the hardware is recovered. The wire net placed at a height of 0.8m above the ground so as to ensure no damage to the hardware.

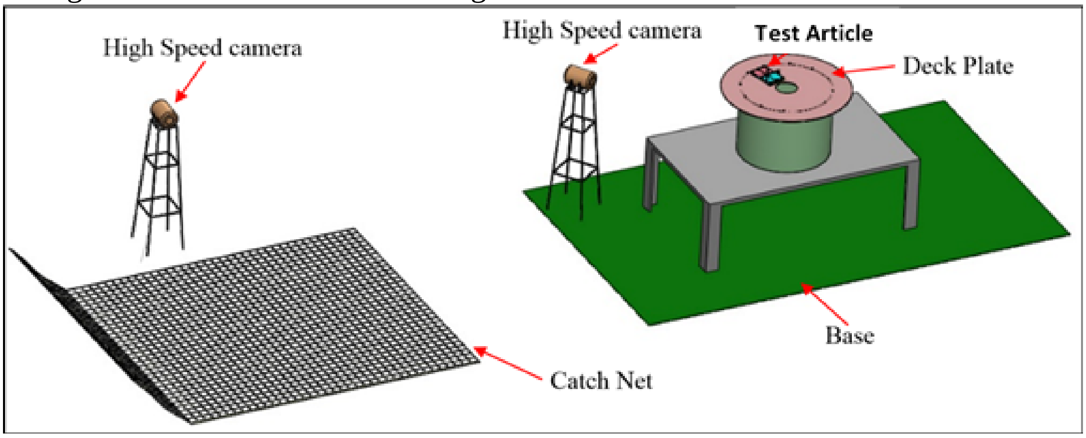

Fig 3: Test Set-up arrangement

Instrumentation Details: The test was planned with detailed instrumentation to capture the events of the ejection and deployment of the fins of the deployable system. A 4m long display with colored marking has been placed at perpendicular distance to the high speed videos to measure the distance along with frame rates from high speed camera. This enables to calculate the ejection velocity at different intervals. In addition, shock sensors were also mounted as the firing of the pyro cartridges are always associated with huge amounts of shock transmitted to the base structure. The following items and equipment were used in the test.

S.No	Parameters	Quantity (Nos.)
1	Deployable system hardware	01
2	Payload aft end plate	01
3	Pyro hardware (PC050DQ)	01
4	Instrumentation High Speed Camera (1000 Frames/s or higher) *Shock (1,00,000g or better)	 02 03
5	Power supply	01
6	Wire net to arrest deployable system after release	01
7	Mounting table	01

* Shock sensors were be placed in the following manner

- S1 at a distance of 200 mm from pyro
- S2 mounted on plate closer (within 50 mm distance) to deployable system assembly
- S3 on the guide rail location.

These shock sensors were mounted in a way to measure the shock at different fields, viz. near field, mid field as well as far field region from the shock source.

5. Test Results and Observations:

The deployable system was initiated with pyro cartridges which in turn has ejected the deployable system out of the deck plate. Upon clearing the deck plate, the torsional springs has immediately unfolded the fins and the whole structure got deployed, proving successfully the mechanism design. The following were the observations from the test.

(i) Deployable system is ejected as expected from the railing, by means of pyro thruster.
(ii) There are no visible scratch marks on the deck plate.
(iii) Deployable system assembly took about 25 ms to clear the deck plate of diameter 1.3 m.
(iv) Ejection velocity observed is 25 m/s.

The shock levels recorded at S1, S2 and S3 are given below.

Location/ ID	Peak shock level (g)	Duration (ms)
S1	22,760	0.1299
S2	29,113	0.13
S3	813	2.2

Figure 4. Start of Ejection of Deployable system from Guide Rail

Figure 5. Start of Deployable system Ejection and Deployable system clearing the deck plate

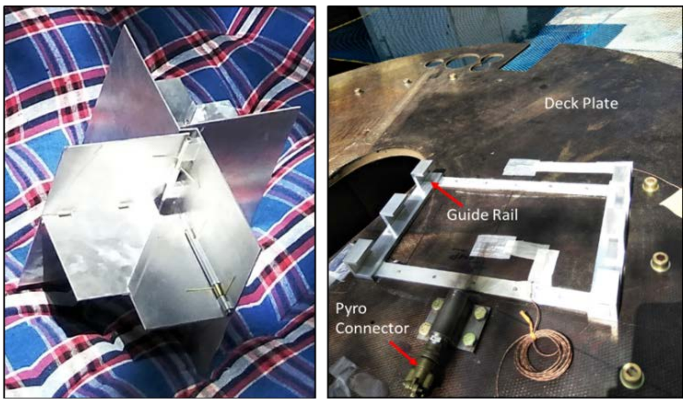

Figure 6. Post Test Hardware

6. Conclusions

The test parameters closely match with the predicted results and meets all the project requirements. It is observed that the sensors near to pyro component has given high shock. Hence for such systems it has to be ensured that no electronic or avionic components are placed in the vicinity of pyro cartridge.

Configuration and Analysis of Solar Array Deployment Mechanisms for Satellite Applications

Vijay Shankar Rai
Spacecraft Mechanisms Group
U. R. Rao Satellite Centre
ISRO
Bangalore
vijayrai@ursc.gov.in

K. Balaji
Spacecraft Mechanisms Group
U. R. Rao Satellite Centre
ISRO
Bangalore
kbala@ursc.gov.in

B.P. Nagaraj
Spacecraft Mechanisms Group
U. R. Rao Satellite Centre,
ISRO
Bangalore
bpn@ursc.gov.in

H.N. Suresha kumar
Spacecraft Mechanisms Group
U. R. Rao Satellite Centre
ISRO,
Bangalore
hns@ursc.gov.in

Abstract—**Geo-synchronous orbit provides an excellent opportunity for monitoring the earth and this orbit has been extensively used for meteorological observations. From GEO platform, it is possible to have continuous imaging of the earth or the region interest and thereby improving the resolution. It has become utmost important to have a solar panel which meets the power requirement and to have minimum CG variations in configuration so that it will provide stable platform for imaging during the spacecraft maneuvering. In this paper the solar array configuration study, finite element analysis and multi-body dynamic simulations results for solar array deployment has been presented. From the simulation, suitable damper was proposed to reduce the shock loads at the end of solar array deployment.**

Keywords—solar array; solar array drive assembly, multi-DOF model, dynamics simulation, latch-up loads

1. Introduction

As spacecraft becomes larger and more complex the need for stowing the spacecraft solar array within the dimension of the launch-vehicle becomes a challenging design constraint. Different solar array configurations with different numbers of panels will be required to meet the specified power requirement, stowed and deployed frequency and minimum spacecraft CG shift due to solar array deployment for the GEO-imaging spacecraft.

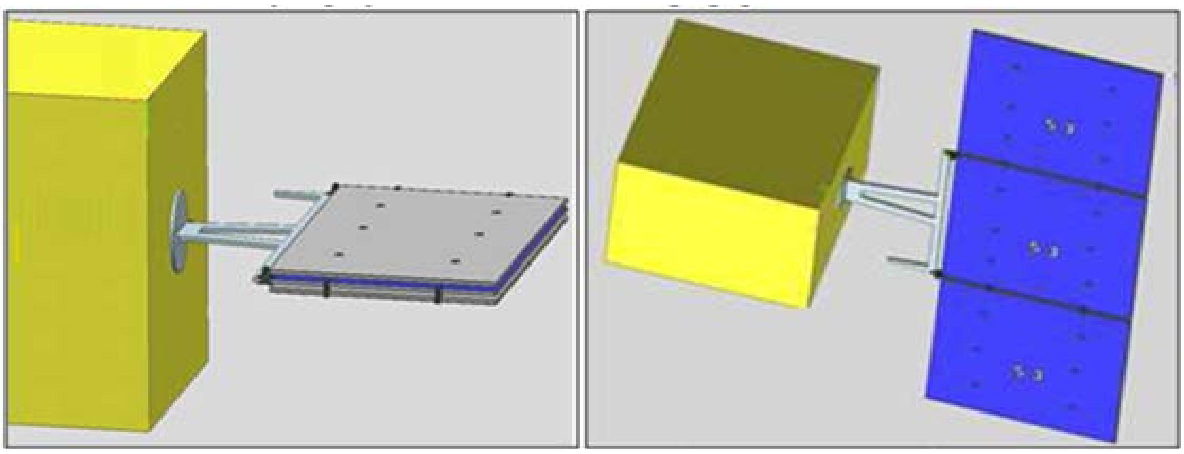

Fig 1: Solar array in primary and secondary deployed configuration along with spacecraft

This paper presents T type solar array configuration which meets the above requirements. The configured solar array consists of a yoke with main panel and two side panels which are the same size of main panel folded on either side of main panel such that outer panel cells always expose for the power generation. The array deployment will be carried out in two stages. Yoke and main panel with side panel's stack deploy in primary stage and two side panels deploy in secondary stage as presented in Fig-1.

2. Configuration Study

Large appendages like solar panels are stowed on to the spacecraft deck during the launch and deployed in the final orbit. The two wings of solar arrays are mounted symmetrically on either side of spacecraft to have zero CG offset and the CG will be along launch axis. If the requirement is have one wing and to mount on one side of the spacecraft, the gets shifted to deployed panel side. For an imaging satellite is utmost essential to minimize the disturbances due to appendages like solar array during the maneuvering of the spacecraft for better imaging or mapping. Hence, different configurations were studied. In option-1, T type yoke with two panels as shown in the Fig-2 and in option-2, Triangular yoke with two panels are selected as shown in Fig-3. Both the options do not meet the minimum CG shift after deployment and power requirement for the mission. Hence, as an option-3, yoke with main panel and two side panels as shown in the Fig-4 is considered. This option provide the minimum CG shift due to solar array deployment, but unable to meet the power requirement as panels are of smaller size. Hence, option-4 which is similar to the option-3 with large size of solar panel as shown in the Fig-5 is considered. This configuration provides minimum CG shift as well as meets the power requirement for the mission. This configuration required six hold down due to larger size panel in order to off load the launch loads and meets the desired stowed array frequency. Detailed static and normal mode analyses were carried out to ensure desired stiffness/frequency in stowed and primary and secondary deployed configurations.

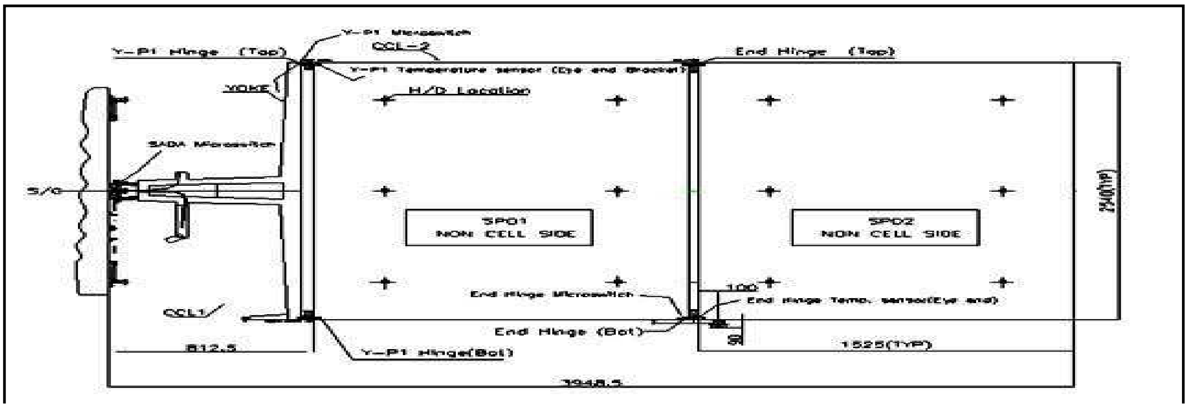

Fig 2: Option-1 T type yoke with 2 panels (2540X1525X20mm)

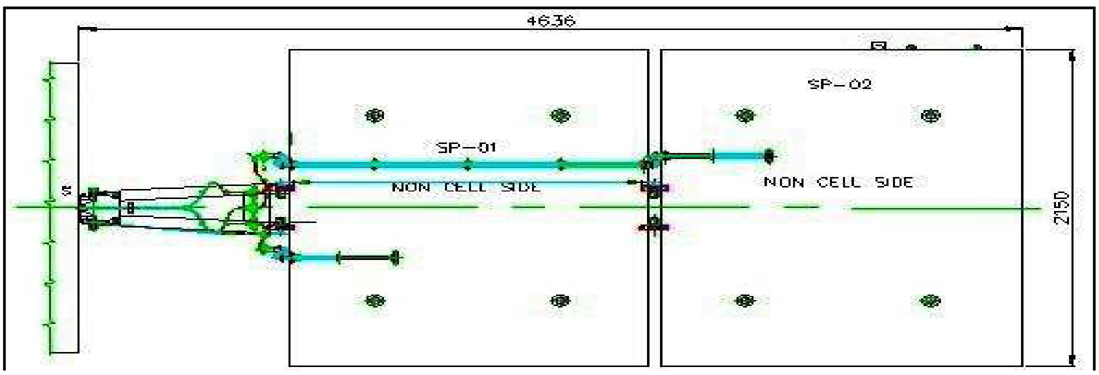

Fig 3: Option-2 Triangle type yoke with 2 panels (2150X1800X26mm)

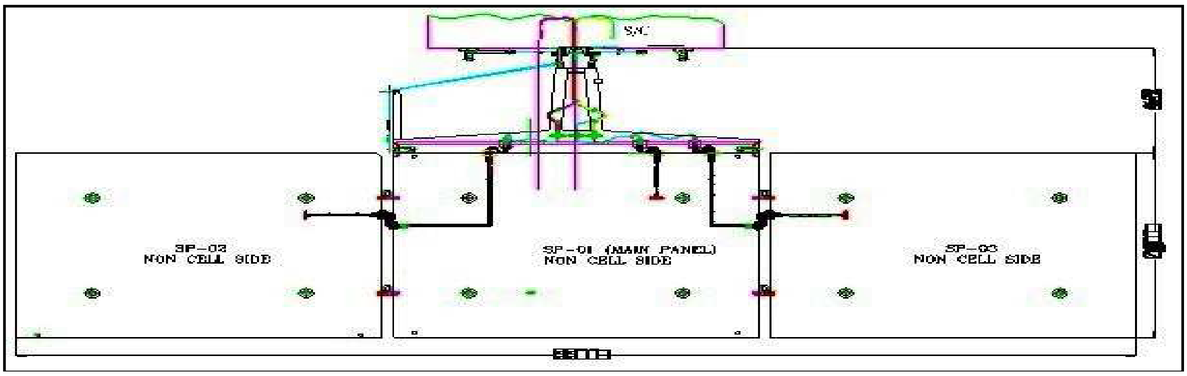

Fig 4: Option-3 T-type yoke with Main panel and 2 sides panel (1800X1400X20mm)

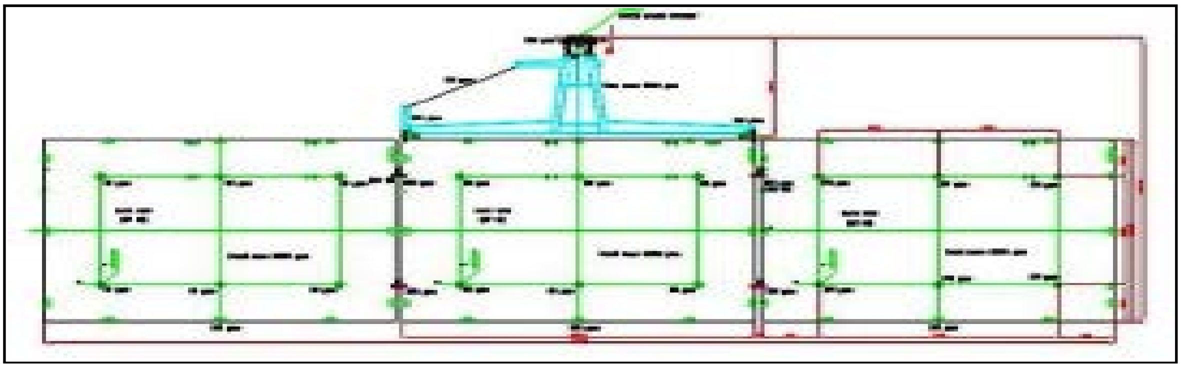

Fig 5: Option-4 T-type yoke with Main panel and two sides panel (2540x1525x20mm)

3. Mathematical Modelling

This section presents the finite element analysis of stowed and deployed configurations in MSC PATRAN/NASTRAN. Panels are modeled as QUAD-4 elements. Each solar panel size is 2.54 x 1.525 m. Hold-down and solar array drive assembly SADA is modelled as TET-10 elements. Hinges are simulated by using BUSH elements by allowing respective DOF along the hinge axis. The stowed solar array FE model is shown in the Fig-6. Fixed boundary condition is used at hold down base interface and SADA hinge interface. The number of hold downs and hold-down preload is arrived using the static analysis. The hold downs are required to off load the appendage loads to the spacecraft deck during the launch and provide sufficient stiffness for the stowed frequency. Hold-down base is provided with the fixed boundary condition. Thermal slippages are modeled at hold down and panel interface. During the transfer orbit, panel stack is exposed to thermal gradient, thermal slip helps in minimizing the stresses. Thermally induced loads will transfer to spacecraft deck as well as solar cell which may lead to damage or failure the solar cells. The hinge stiffness values are obtained experimentally and presented in the Table-1. Damper and other elements mass are simulated as point mass elements wherever required. Spacecraft deck stiffness is not considered in the simulation and assumed rigid. An iterative frequency analyses has been carried out for deployed configuration to meet the specified deployed frequency for an imaging satellite for geostationary-orbit.

Table 1: Hinge stiffness value in the bending direction for the yoke and inter panel hinges

Hinge Location	**Stiffness about hinge axis**	**Remark**
SADA –Yoke Hinge	16500 N.m/rad	Other direction stiffness can be one order higher compared to hinge axis stiffness
Yoke –Panle-1	5360 N.m/rad	
Panel-1-Panel-2& Panel-1-Panel-3	4100 N.m/rad	

4. Analysis Results and Discussion

Quasi Static and Normal mode analysis for launch configuration, primary and secondary deployed configuration has been carried out. Quasi-static analysis has been carried out for the all three axes. An inertial load of 30g is simulated about each axis independently for the stowed configuration. The pull out loads for 30g load at hold down location is ~3075N. Hence, hold down load preload of 5000N has been provided to have adequate design margin. The normal mode analysis results along with modal effective mass for stowed configuration is presented in the Table-2. The first frequency is 54 Hz which meets the stowed frequency requirement greater than 40 Hz. The mode shape for first mode is presented in the Fig-7. Finite element modelling of primary and secondary deployed configurations is presented in Fig-8 & Fig-9 respectively. The array deployed frequency for the primary configuration and secondary deployed configuration is found to be 1.04 Hz and 0.8 Hz respectively. The fundamental mode shape for the primary and secondary deployed configuration is presented in the Fig-10 & Fig-11 respectively.

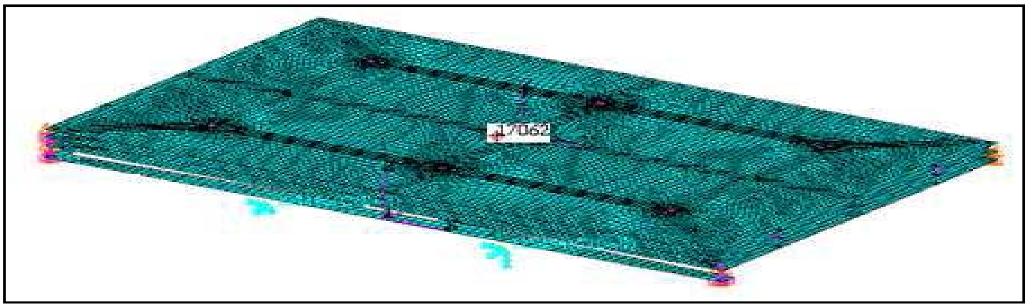

Fig 6: Stowed solar array configuration

Table 2: Normal mode analysis results for stowed Configuration

Modal Effective Mass				
Mode No.	**Freq. Hz**	**T1**	**T2**	**T3**
1	5.40E+01	2.95E-05	6.08E-03	4.92E+00
2	5.67E+01	6.56E-03	3.41E-04	1.69E-02
3	6.41E+01	4.95E-07	7.05E-04	2.12E-02
4	6.42E+01	1.15E-03	2.62E-04	3.40E-01
5	6.51E+01	1.29E-03	1.88E-08	9.71E-01
6	6.72E+01	2.67E-03	9.42E-04	1.44E+00
7	7.04E+01	1.58E-03	2.20E-04	9.67E-01
8	7.21E+01	5.41E-04	1.78E-04	3.83E-01
9	7.55E+01	8.82E-05	2.25E-07	7.47E-02
10	7.70E+00	1 6.27E-0	4 2.20E-0	3 1.53E-01

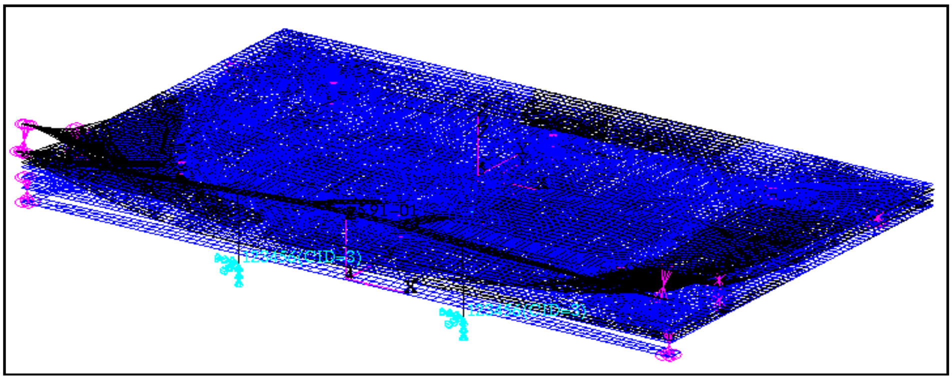

Fig 7: First mode shape of stowed configuration

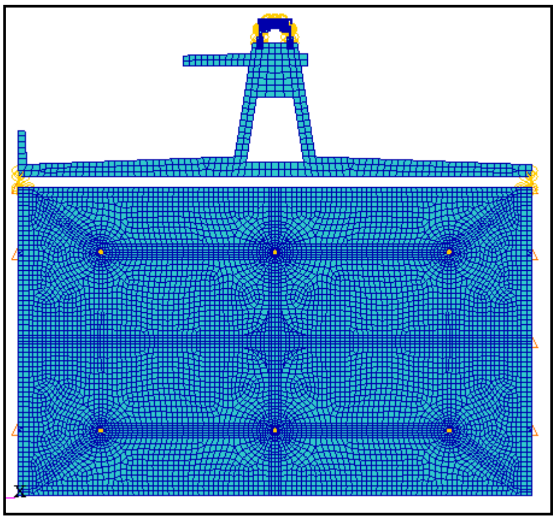

Fig 8: FE model of primary deployed array

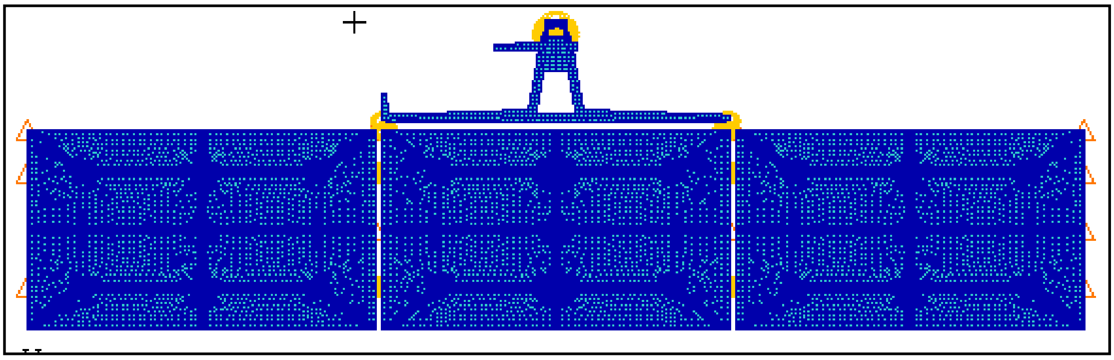

Fig 9: FE model of secondary deployed array

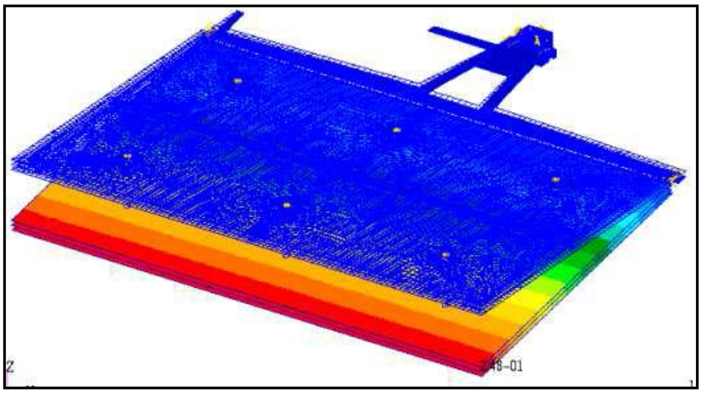

Fig 10: First mode shape of primary deployed array

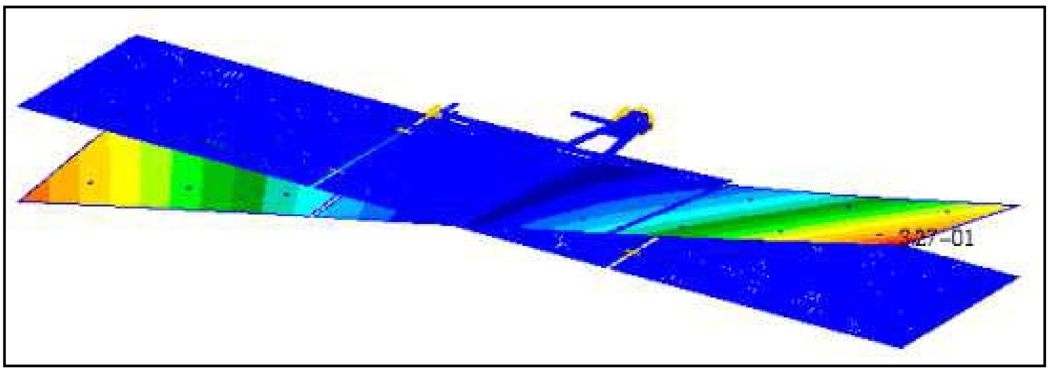

Fig 11: First mode shape of secondary deployed array

Transient dynamic analyses have been carried out to evaluate the loads at latch-up for the solar array at the end of primary and secondary deployment. The Velocity profile for the yoke and panels obtained at latch-up from ADAMS simulation is given as initial condition. The latch-up loads and moments are evaluated at the root hinge and inter panel hinge locations for root fixed boundary condition. Analysis has been carried out for the different latch-up velocities obtained from dynamic simulations. The evaluated loads are used as design inputs for the solar array interface and mechanism elements. The energy conservation has been checked and validated for the results obtained from simulation using dmap_energy card in MSC PATRAN. Deployment dynamics simulation carried out for the primary and secondary deployment of solar array for ground and on-orbit configuration in multi-body dynamics software ADAMS. In ground deployment air drag and zero g system has been modeled. Deployment time and latch-up velocity is important parameter to evaluate the mechanism performance during the deployment. Latch velocity used to predict the latch-up loads are one of the important design input for the mechanism and panel interfaces design. Dynamic simulation for primary deployment has been carried for different damping rates. To synchronize the motion of the panels approximately, close control loop (CCL) is mounted alongside yoke and panel [1-2], The CCL is modelled in ADAMS to generate near single degree of freedom (DOF). Damper is modelled in the simulation and its effect has been studied The simulation shows a high angular velocity for the primary deployment which results in higher latch-up loads at the mechanism and panel interfaces. The latch-up loads at root hinge is 450N.m and shear loads 700N. In order to reduce the latch-up loads an eddy current damper is used [3]. Damper is modelled in the simulation and its effect has been studied by varying the damping rate. Results are presented in the Table-3. The loads are reduced significantly with damper between yoke and panel-1 stack. The damper configuration is shown in Fig-12. This is a new type of configuration which is considered first time in this type of solar array deployment. The damping rate 0.21 N.m/rad/sec is considered from the study for solar cell and deployment mechanisms safety prospects.

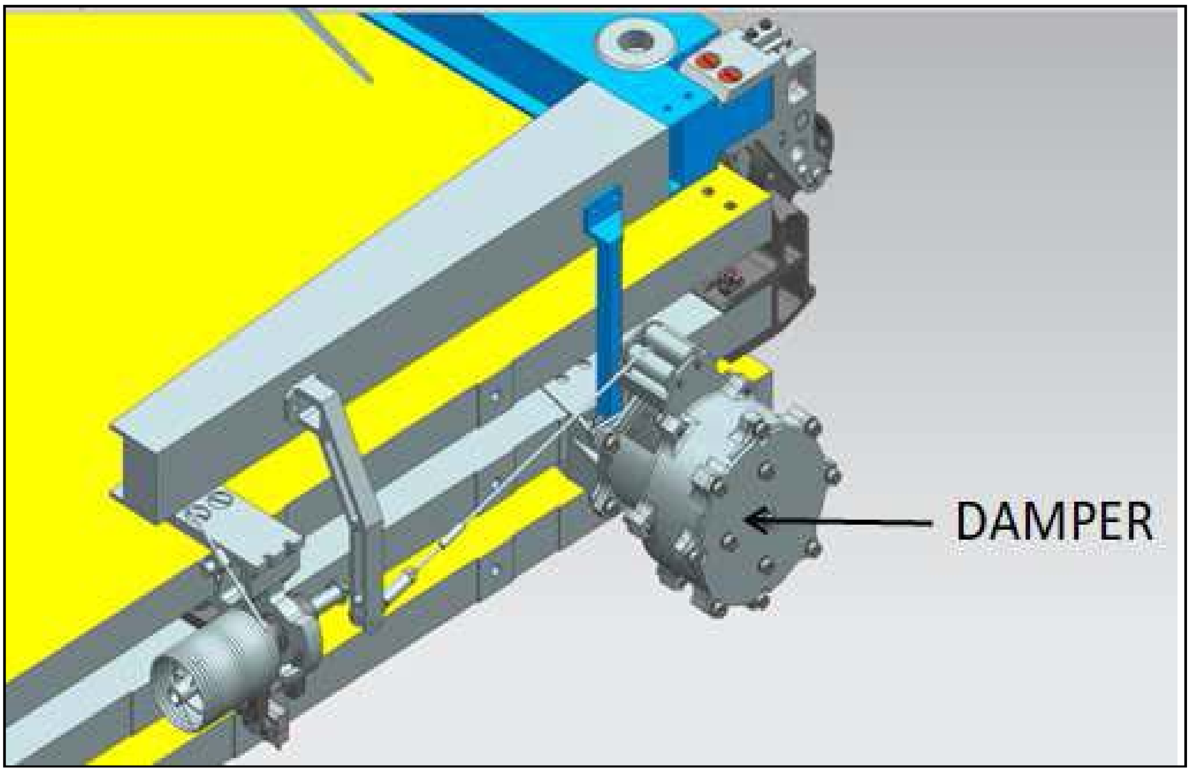

Fig 12: Damper model between yoke and panel-1

Table 3: Latch-up loads with different damping rates

Pre Rot. Angle (rad)	Damper kgf.cm/rad/sec	Latchup Vel (rad/sec)	Energy (N.M)	Depl. Time (Sec)	Moment (N.m) at SADA	Shear (N) at SADA
11.19	0.0	1.41	8.500	4.700	450	700
11.19	2.1	0.76	2.100	6.400	225	325
11.19	3.1	0.55	1.100	7.70	150	245
11.19	2.5	0.63	1.55	10.56	185	285
9.12	2.5	0.5	1.02	11.5	150	245
9.12	2.1	0.6	1.42	10.8	200	300

The predicted deployment time for primary and secondary deployment for ground is 7.5-11 sec and 14.2-17 sec and for on-orbit 7.0-9.5 sec and 12.5-15.5 sec respectively. The ground deployment test has been conducted and measured deployment time for primary deployment is ~10 sec and for secondary deployment is ~17 sec and matched well with predictions. The results are presented in the Table-4. The latch-up loads evaluated was well within the specifications. The deployment sequence of solar array is shown in the Fig-13. Deployment dynamics results for on-orbit deployment angle and deployment velocity for primary and secondary deployment are presented in the Fig-14 to Fig-17. Deployment time and latch-up velocity has been estimated for ground and on-orbit. Spacecraft body rate [4] for primary deployment is presented in the Fig-18. The solar array hardware has been realized. All ground tests has been performed and ground deployment performance are nominal.

Table 4: Results of deployment dynamics study

Parameters Predicted	On-orbit	Ground
Deployment time for primary deployment (sec)	7.0-9.5	7.5-11.0
Deployment time for secondary deployment (sec)	12.5–15.5	14.2-17.5
Latch-up velocity primary deployment (rad/sec)	0.5	0.48
Energy (Nm)	1.5	

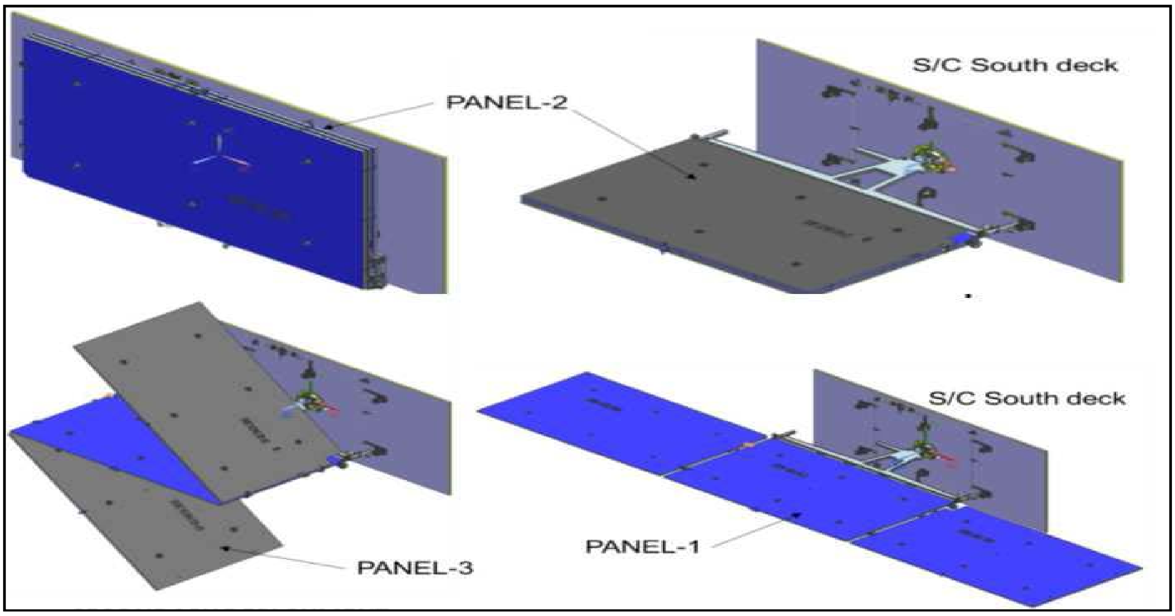

Fig 13: Solar array multi stage deployment

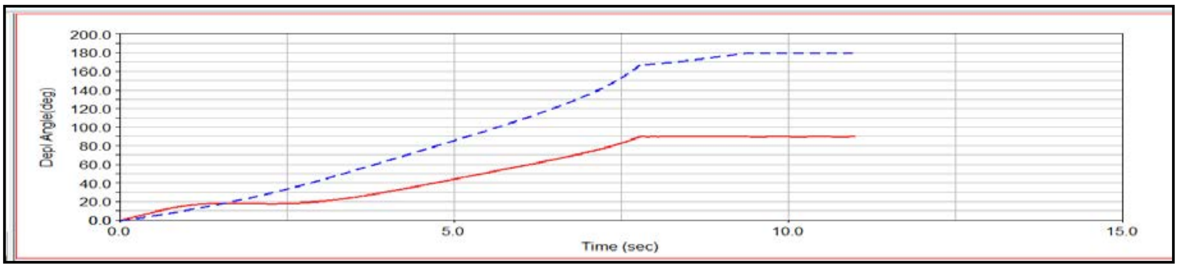

Fig 14: Angle of opening vs time for on-orbit first stage

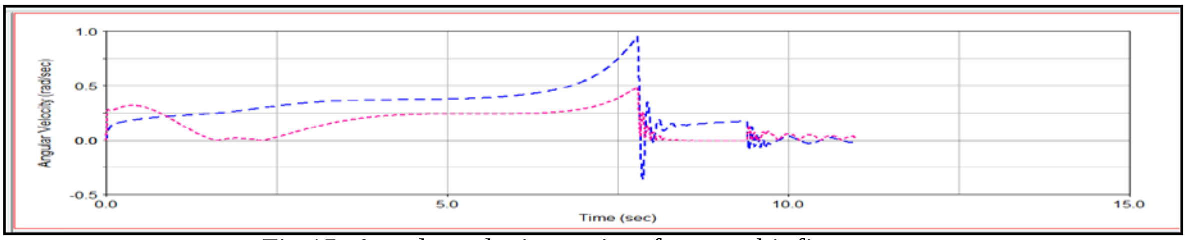

Fig 15: Angular velocity vs time for on-orbit first stage

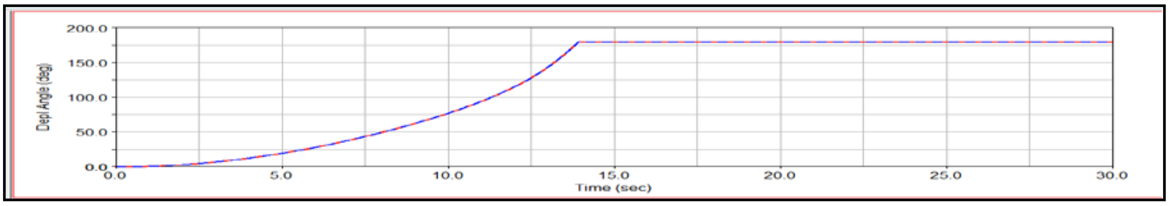

Fig 16: Angle of opening vs time for second stage

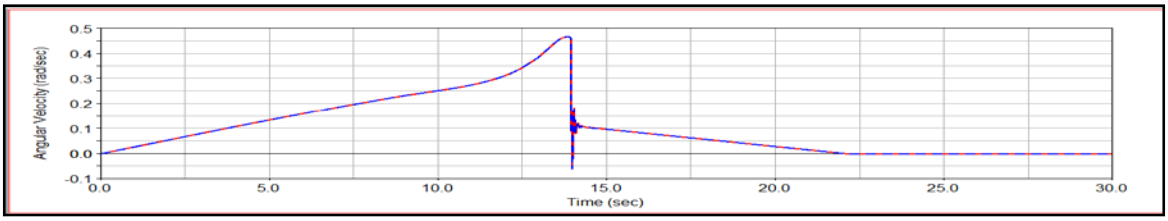

Fig 17: Angular velocity vs time for second stage

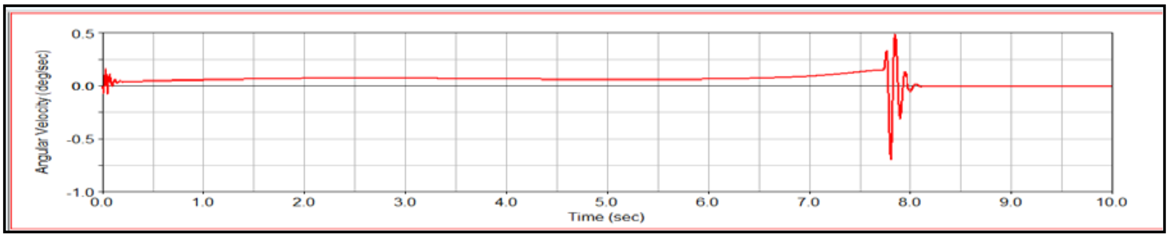

Fig.18: Spacecraft body rate for primary deployment

5. Conclusions

Analytical studies towards configuring a new concept of solar array deployment have been carried out. The parametric studies include the changing solar array configuration, varying number of panel and size of panel. The effects of the above on overall stowed and deployed frequency, minimize the CG shift for stowed to deployed configuration have been evaluated. Damper used between yoke and panel-1 to reduce the latch-up loads. Number of Hold down, location and preload in the hold down is arrived based on the study. Stowed and deployed frequency are estimated which meets the launch specifications. The solar array deployment time and deployment velocity are evaluated for the ground and on-orbit configurations. Analysis inputs are implemented realized and tested successfully.

6. Acknowledgment

The authors would like to thank Deputy Director, MSA and Director, URSC for their continuous support and encouragement.

7. References

[1] Fiore J, Kramer R, Larkin P, et al. Mechanical design and verification of the TOPEX /Poseidon deployment solar array. AIAA-1994- 1323-CP, 1994

[2] Kumar P, Pellegrino S. Deployment and retraction of cable-driven rigid solar array. AIAA-1995-1367-CP,1995.

[3] Nagesh G, Viswanatha N and Bhat N. C. "Eddy current damper for deployment control of spacecraft appendages", In proceedings of National Seminar on Aerospace and Related Mechanisms, MSC-14-18, 1996.

[4] Kwak M K, Heo S, Kim H B. Dynamics of satellite with deployable rigid solar arrays. Multi body System Dynamics 2008; 20(3): 271-286.

Design of Hold Down & Steering Mechanism for Science Payload Onboard Lunar Rover

Abhinandan Kapoor
Spacecraft Mechanisms Group
U R Rao Satellite Centre
Bangalore
akapoor@ursc.gov.in

Gaurav Sharma
Spacecraft Mechanisms Group
U R Rao Satellite Centre
Bangalore
gsrs@ursc.gov.in

Abhishek Kumar
Spacecraft Mechanisms Group
U R Rao Satellite Centre
Bangalore
abhishek@ursc.gov.in

A. Shankara
Spacecraft Mechanisms Group
U R Rao Satellite Centre
Bangalore

H.N.Suresha Kumar
Spacecraft Mechanisms Group
U R Rao Satellite Centre
Bangalore

***Abstract*— A Science payload mounted on the chassis of lunar rover is required to be steered so as to position it near the lunar terrain for taking measurements when the rover is stationary and to rotate it away from the terrain while the rover is moving. This is done to avoid any interference with obstacles and possible contamination during rover motion. During launch/ touchdown of Lander, the mechanism and payload have to withstand the vibration/shock loads while ensuring structural integrity. Therefore, a motor driven steering mechanism is planned together with a hold down bracket that connects the Science payload to the hold down and release mechanism of the rover and thus distributes the environmental dynamic loads among the motor drive and the rover hold down. Two design options have been studied viz. Motor drive connected to Science payload using an external bearing unit and Motor Drive connected to payload through a flexure coupling.**

This paper discusses in detail the design and analysis of the steering and hold down mechanism for both the options. Based on the study, mechanism hardware was developed and its performance was validated through ground tests.

1. Introduction

The Science payload on lunar Rover is driven using a steering mechanism mounted underneath the chassis of the rover. The steering mechanism is a motor driven mechanism which can steer the Science payload from stowed position (0^o) to deployed position (90^o) and vice versa. Fig. 1shows the Science payload mounted on the chassis of Rover and Fig. 2 shows the Science payload in stowed and deployed condition.

The mechanism is held during launch with the help of rover's front hold down mechanism through a hold down bracket that is assembled in between the upper and lower brackets of the rover front hold down mechanism (Fig.3). During launch Science payload will be subjected to launch loads which are withstood by the hold down and motor drive unit. The mechanism design should be stiff so as to provide a stable interface to payload when deployed and should be designed in such a way that the loads transferred to the motor bearing are within its design specification.

With the aforementioned design objective in mind, two design options have been studied in the present work.

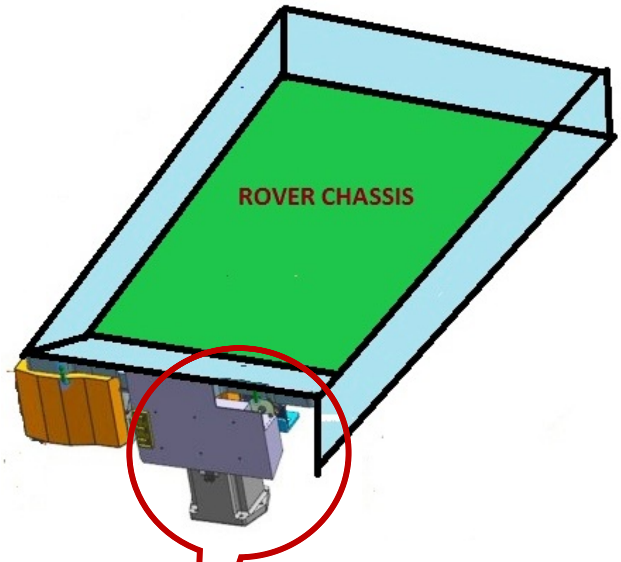

Fig 1. Science payload mounted on chassis of Rover

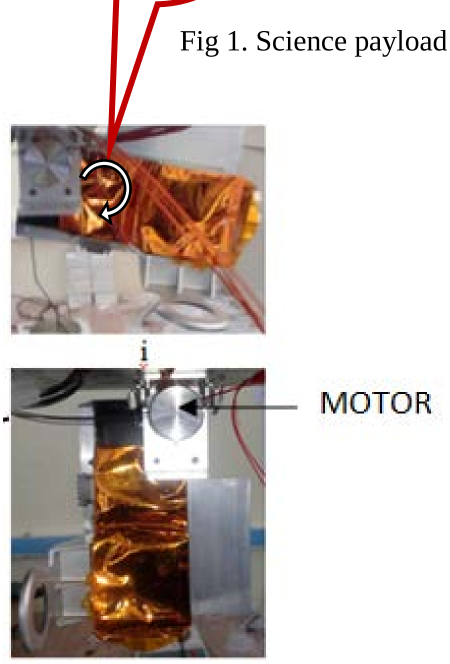

ii)

Fig 2. Stowed (i) & Deployed (ii) Configuration of the Science payload.

In option 1, the load induced on the motor drive is withstood by an external bearing unit whereas option 2 incorporates a flexure coupling to reduce the launch loads transferred to the motor bearings. The merits/demerits of both have been assessed. Section II presents the mechanism design requirements, Section III discusses the option studies, Section IV explains the analysis and Section V concludes with important findings of the study.

2. Mechanism Design Requirements

The design requirements for Science payload hold down and steering mechanism are discussed below.

The mechanism should keep the payload in stowed condition during launch and steer the payload by 90^o and vice versa upon release. Hold down mechanism should provide adequate support during launch and be stiff so that more of the launch loads get transferred to it.

Mechanism should allow multiple operations and should provide a stiff interface to the payload so that it does not deflect under the influence of lunar gravity while in stowed/ deployed condition. Motor should be able to drive against torque due to harness and lunar gravity and with a margin of greater than 1 for the drive module output torque. Subsequent to release of rover's hold down mechanism, the steering mechanism's hold down bracket should not interfere with the rover's front hold down brackets. In addition, the two extreme positions of the mechanism should be confirmed through limit switches. These switches will work as safety mechanism to switch off motor when activated. The stowed indication also acts a release indication for hold down

The mechanism specifications are shown in Table1.

Table 1. Mechanism design specifications

Operation	Motorised movement of the Science payload Assembly	
Angular Range	90 ±1 deg	
Telemetry(Stowed and Deployed)	Limit Switch	
Material (Mechanisms)	AL6061, Ti 6Al 4V and SS 304.	
Mass of Mechanism	~500 grams	
Frequency of Operation	1 Lunar day (approx. 200 cycles)	
Temperature Requirements	Operating Range	0 to 40^{o} C
	Storage	-50^{o} to 60^{o} C
Distance from Ground (at 90^{o} position)	70 mm (approx.)	
Science Payload Position information	By Hall Sensor (in built in BLDC Motor)	
Hold Down Release Mechanism	Frangibolt Actuator of Rover Front HDRM(Hold down release Mechanism)	
Mass of Science Payload	1 kg (approx.)	

3. Option Studies

This section discusses in detail the design trade-off carried between options pursued for the mechanism design. Features common to both the options are: -

(i) The mechanism consists of a BLDC motor with Gearhead to drive Science payload.
(ii) The motor housing is connected to the chassis of the Rover.
(iii) Angular Rotation of the Science payload on lunar surface after hold down release: 90^{o} ±1 degree.
(iv) The motor is connected to the Science payload housing via a L bracket, which has two extensions for indicating the start and end position of the motion of the mechanism. Also to avoid possible damage to the limit switches hard stoppers are provided which will restrict the over travel of the limit switches' leaf within nominal range.
(v) Hold down Mechanism
(vi) Microswitch and Safety features: Telemetry indication switch indicates the stowed and deployed position of Science payload during operation.

A. Option 1: Motor drive with a bearing unit

A motor drive module is connected to the Science payload housing at one end via a coupler shaft, which in turn is supported on a bearing unit with higher load capacity to withstand the launch loads hence keeping the motor bearings safe. The hold down bracket is connected at suitable interface end of the Science payload housing and the other end is sandwiched between the brackets of the rover's front hold down and release mechanism (Fig.3)

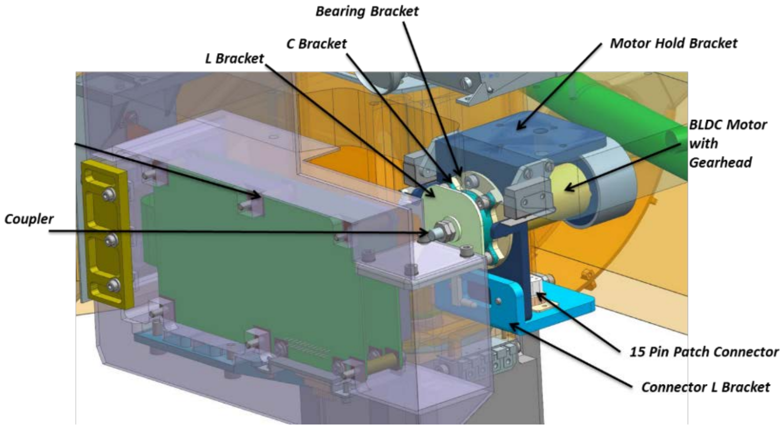

Fig. 3. Option 1: Motor drive connected to Science payload using an external bearing unit

Salient features of option 1 are: -

(i) Loads induced on the motor bearing during launch are reduced using an external bearing unit with higher load capacity.

(ii) External bearing's outer and inner races are arrested and preloaded using two brackets namely C bracket and bearing bracket with a circlip and a washer.

(iii) Telemetry indication switch indicates the stowed and deployed position of Science payload during operation.

The mass details of the mechanism are shown in Table 2 and the specifications of the external bearing [1] are shown in Table 3.

Table 2 Mass Details for Option 1

Component	**Mass (gms)**
Mechanism brackets (Al 6061) and fasteners (Ti6Al4V)	270
Limit switch	60
BLDC motor with gearhead	220
Bearing mass	12.3
Total Mechanism Mass	520

Table 3 Bearing Specifications

Parameter	**Value**	
Type	Deep Groove Ball Bearing	
Load - Static	Radial	113 kg
	Axial	208 kg
Weight	12.3 g	
Lubricant	Braycote 601 EF grease	

B. Option 2: Motor Drive connected with a flexure coupling

Motor drive module attached to the Science payload housing via a flexure shaft coupling is shown in Fig.4. The hold down mechanism and the telemetry interfaces are the same as in the previous option.

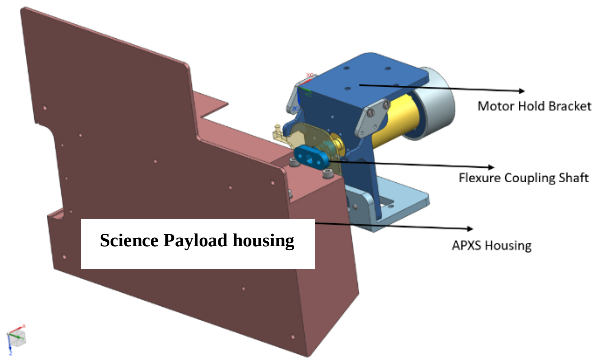

Fig. 4. Option 2: Motor Drive connected to Science payload using a flexure coupling to reduce launch loads transferred to motor bearings

Salient features for option 2 are: -

(i) Loads induced on the motor bearing during launch are reduced due to the good amount of load absorption at the flexure shaft coupling, instead of an external bearing.

(ii) Incorporating flexural coupling reduces the number of parts used, thereby making the assembly simpler.

Mass details for option 2 are shown in Table 4:

Table 4. Mass Details for Option 2

Component	Mass(gms)
Mechanism brackets (Al 6061) and fasteners (Ti6Al4V) with flexure	200
Limit Switch	60
BLDC Motor with Gearhead	220
Total Mechanism Mass	480

Design requirements that the flexural coupling should meet are:

(i) Possess low axial and bending stiffness so to reduce the loads induced on the motor bearing during the launch.

(ii) Have high torsion stiffness for proper torque transmission and stability (to prevent the payload from sagging under lunar gravity) during mechanism's operation.

(iii) Should be dimensionally optimized to fit in the given geometric constraints.

(iv) The coupling should be strong enough to keep the generated stresses below the yield strength.

The requirements listed above under (i) and (ii) conflict each other; therefore the flexure is designed iteratively.

Two limit switches are used to indicate the initial and final position of the mechanism. The limit switches are fixed to the limit switch bracket, which in turn is connected to the motor hold bracket, to provide the information for the initial and final position of the Science payload movement. The extensions from L bracket interact with the limit switches at the start and end position. A schematic of limit switches in stowed and deployed position is shown in Fig. 5.

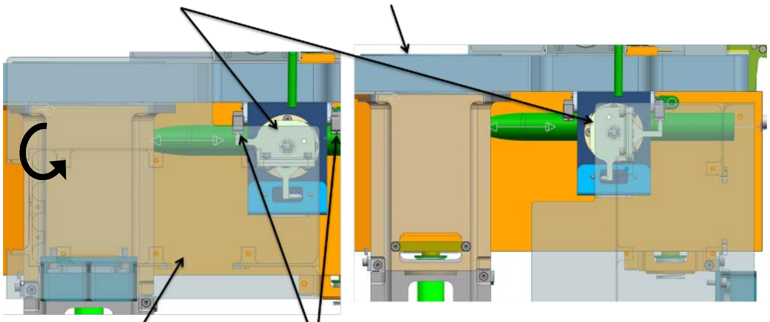

Fig. 5. Initial (Left) and Final (Right) Configuration

Specification of the BLDC motor used are shown in Table 5.

Table 5. Motor Drive Specifications [2]

Parameter		Value
Resistive Torque	Gravity torque(Max.) on Lunar Surface*	0.34 Nm
	Bearing Friction Torque	5 mNm (Negligible)
	Harness Torque	0.15 Nm
Detent Torque		3 Nm(approx.)
Max. Continuous Torque		4 Nm
Nominal Current		0.5 A
Nominal Voltage		24 V
Output Speed		1 rpm
Margin(while driving)		7.16
Margin(while power off)		7.82

*Lunar gravity will aid as well as hinder depending upon the rotation; here the worst case scenario is taken.

4. Analysis

In this section, finite element analysis to assess the load induced in motor drive is presented for both options.

A. Option 1: Motor drive with a bearing unit

Finite element model of the mechanism is developed [3] using constituent CAD geometries (Fig.6) of the Science payload housing, hold down and release mechanism bracket and the L bracket.

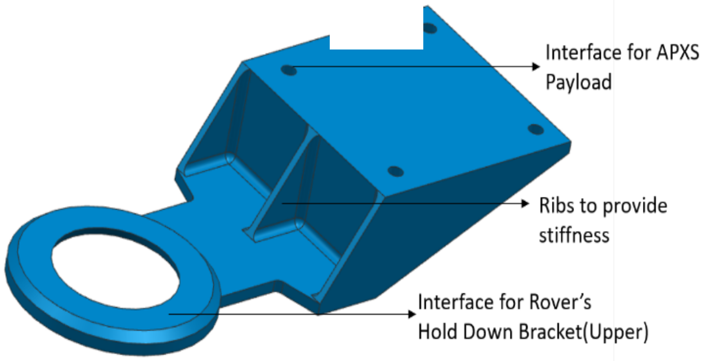

Fig 6. Isometric view of the hold down bracket.

Tet-10 elements are used for meshing and requisite boundary conditions are provided to connecting parts (Fig.7). The assembly is fixed at two places - rover front hold down via hold down bracket and to rover chassis through motor hold bracket. Launch loads experienced by the Science payload assembly will be shared between these two locations.

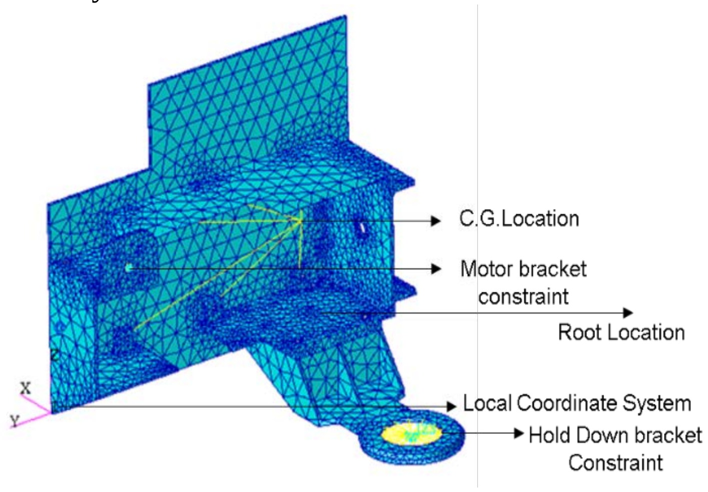

Fig. 7. FEM model of the mechanism

Quasi-static launch loads are applied individually along the three axes and the load distribution is estimated among the interfaces.

It is observed that despite the C.G. of the mechanism being closer to hold down location, load shared by the motor drive is more than the bearing capacity. This is due to lower stiffness of hold down bracket than the motor bracket and is verified by constraining the root of hold down bracket and estimating the load distribution as shown in Table 6.

Table 6. Load at motor and hold down interface

Loading direction	Motor (%)	Hold down (%)
Axial	66	34
Radial	44	56

Later the section thickness of the hold down bracket and the material (Al6061 to Ti6Al4V) is altered and appreciable increase in hold down stiffness is observed & therefore load on motor reduces as shown in table 6.1 below

Table 6.1. Load at motor and hold down interface

Loading direction	Motor (%)	Hold down (%)
Axial	8	92
Radial	21	79

Peak stress of 37 MPa is observed for ‘Z’ loading (Fig.8) and sufficient margins exists over the yield strength of Al-6061.

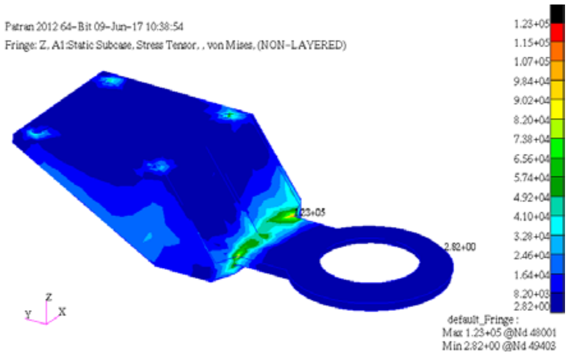

Fig. 8. Von Mises stress plot of hold Down bracket

B. Option 2: Motor Drive with a flexure coupling

The flexure has been designed iteratively through finite element analysis by first estimating the flexure stiffness then estimating the load distribution between the hold down end and motor bearing. Three different flexure configurations were considered. The dimensions of the three coupling are comparable. Titanium alloy (Ti-6Al-4V) is used for all the three couplings.

For modelling the flexural coupling Tet 10 solid elements were used, with a fixed boundary condition at motor end and application of load at the other end.

a) Flexure coupling 1:

The flexure coupling 1 (Fig.9) has a low bending stiffness about Y and Z axis but possesses high axial stiffness as shown in Table 7. Hence, the loads in axial (X direction) transmitted to the motor bearings are above its capacity (Table 8).

Table 7. Stiffness Table for Flexural Coupling Type 1

Direction	Stiffness (N/m)
X(In Plane)	2875×10^3
Y(In Plane)	458×10^3
Z(Out of Plane)	754×10^3

Table 8. Load distribution for Flexural Coupling Type 1

Loading direction	Motor (%)	Hold down (%)
X (Axial)	52	48
Y (Shear)	14	86
Z (Shear)	20	80

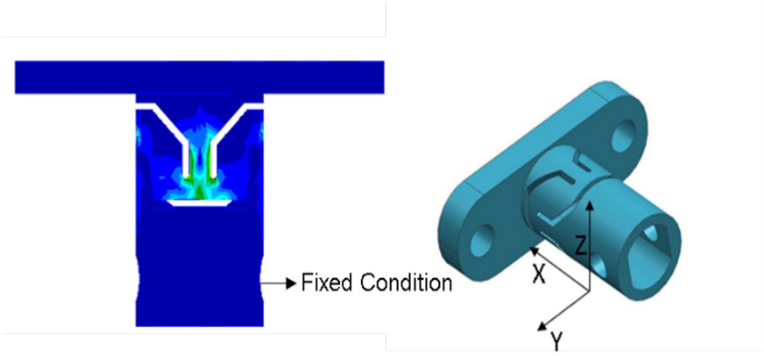

Fig. 9. Flexural Coupling 1: Finite element model (left) and CAD model (right)

b) Flexure coupling 2:

This Flexure Coupling (Fig.10) has low stiffness in all three directions in comparison to flexure coupling 1 but it also possesses a very low torsional stiffness which makes it unsuitable for the mechanism operation as the mechanism would sag under lunar gravity.

Stiffness of flexural coupling 2 and load distribution in three axes are shown in Table 9 and 10 respectively.

Table 9. Stiffness Table for Flexural Coupling Type 2

Direction	Stiffness (N/m)
X(In Plane)	16.25×10^3
Y(In Plane)	9.82×10^3
Z(Out of Plane)	9.87×10^3

Table 10. Load distribution for Flexural Coupling Type 2

Loading direction	Motor (%)	Hold down (%)
X (Axial)	5.0	95.0
Y (Shear)	2.0	98.0
Z (Shear)	3.0	97.0

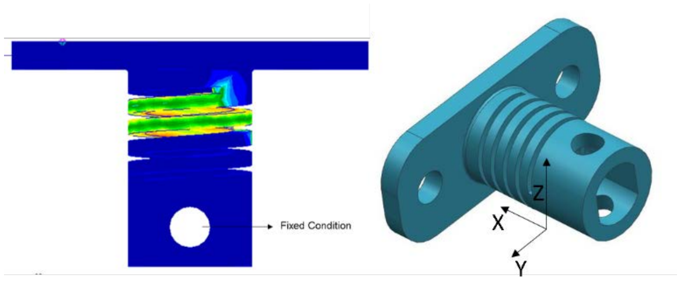

Fig. 10. Flexural Coupling 2: Finite element model (left) and CAD model (right)

c) Flexure coupling 3:

Flexure coupling 3 (Fig.11) has low bending stiffness in Y and Z axes. Its axial stiffness is slightly higher compared to flexure coupling 2 and its torsional stiffness is higher in comparison to flexure option 2. Stiffness of flexural coupling 3 and load distribution in three axes are shown in Table 12 and 13 respectively. Hence, this option is selected for present application.

Stiffness of flexural coupling 3 and load distribution in three axes are shown in Table 12 and 13 respectively.

Table 11. Stiffness Table for Flexural Coupling Type 3

Direction	Stiffness (N/m)
X(In Plane)	221 x 10^3
Y(In Plane)	26 x 10^3
Z(Out of Plane)	26 x 10^3

Table 12. Load distribution for Flexural Coupling Type 3

Loading direction	Motor (%)	Hold down (%)
X (Axial)	29	71
Y (Shear)	2	98
Z (Shear)	5	95

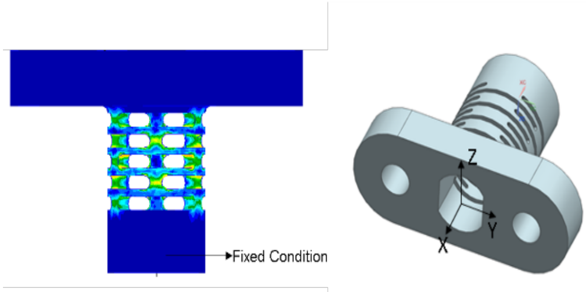

Fig. 11. Flexural Coupling 3: Finite element model (left) and CAD model (right)

Torsional stiffness of the flexural Coupling Type 3 is estimated as 1.265 Nm/deg, its deflection under lunar gravity is 0.258 deg, axial load during launch on motor bearing [2] is 56.9 N (within specification of 100 N) and radial load during launch on motor bearing is 11.7 N (within specification of 70 N). Peak induced Von mises stress under launch loads in flexural coupling 3 is 608 MPa which is within the yield strength (950 MPa) of Ti6Al4V. Therefore, flexure coupling design 3 is superior to coupling 1 and 2

5. Conclusion

Two design options have been studied to arrive at a suitable design configuration that meets the functional and structural requirements of the proposed mission. Option 1 reduces the load on the motor bearing by integrating an external bearing in the drive module. Option 2 makes use of flexural coupling’s lower stiffness to reduce the launch loads on the motor bearing. Hardware for both the options had been realized and the estimated performance was validated through ground tests. Even though test data for both options was promising, Option 1 with an external bearing was selected for implementation.

6. Acknowledgment

The authors would like to thank Deputy Director, MSA and Director, URSC for their continuous support and encouragement.

7. References

[1] High Precision Ball Bearings, ADR
[2] Nastran Quick reference guide, MSC Software combined documentation 2013.
[3] Maxon Motor Catalogue

Design of Effortless and Swift Detach Mechanism for Defence Systems

Abhilasha Kesarwani
Research and Development Establishment (Engrs.)
DRDO
Pune
abhilasha.kesarwani@rde.drdo.in

Sanjay Kumar
Research and Development Establishment (Engrs.)
DRDO
Pune

Ravi Tiwari
Research and Development Establishment (Engrs.)
DRDO
Pune

***Abstract*-Trawl Assembly mounted on tanks aims at developing a mechanical system to detonate underground buried anti-tank mines to create assault/vehicle safe lane (VSL) through minefield for forward movement of troops. Trawl roller assembly detonates pressure actuated anti-tank mines by simulating tank pressure. In war scenario, there may be a situation to detach the entire heavy trawl system from tank to increase the mobility of tank. To fulfil that requirement, an effortless and swift detach mechanism is designed. This mechanism has dual functions to perform: 1. To keep the entire trawl system connected with tank and in locked position while operation; 2. Provision to allow the entire system to be detached quickly and effortlessly. The mechanism is designed in such a way that the entire trawl assembly can be detached by pull of just one lever by a single person in a few seconds, which would have otherwise required many persons, crane, tool kit, long time and even risked the life of army men during battle time. Provision is given for both manual and remote operations.**

Keywords- Trawl, mine roller, mechanism, toggle position

1. Introduction

A minefield contains various type of anti-tank mines such as pressure actuated mines, influence mines etc. Since, these mines are generally buried under the ground therefore can't be seen with naked eyes. In order to neutralize these mines decoys are used very often. Also, it is very much essential to clear minefield to allow safe passage of friendly tanks and march forward through these minefields.

Mine trawl system is primarily used to create a Vehicle Safe Lane (VSL) for friendly tanks to pass by in minefield. The system utilizes roller assembly ahead of tank to detonate pressure actuated mines.

Generally, minefields are deployed at forward areas which are accessible to tanks mainly. Mine trawl system is attached at tank front side so that mines can be detonated at safer distance from tank body. The actuation methodology for pressure actuated mines are through weight and geometry of rollers which can simulate equivalent pressure of tank which therefore requires use of heavy weight rollers. Three such rollers are needed on each side of tank tracks to create the required width of safe lane for tanks to pass. Also, left and right parts are required to be kept independent of each other so that mine blast on one side does not affect the other side. The system is to be used in difficult terrains.

R&DE(E) has designed and developed Mine Trawl System for detonating pressure actuated as well as influence mines as shown in Fig.1. It also has a plough attachment which uproots leftover mines. A roller assembly is attached in front of tank so that during motion roller will come in contact with mine first and explode the mine by creating simulated pressure of tank on the pressure pad of mines. The mine trawl system is successfully developed. Since, these rollers are heavy and do effect the mobility of tank therefore a swift detach mechanism is required for easy and effortless removal of mine trawl system especially during wartime when the life of soldiers are at risk. Also, after release of mine trawl tank gets free and can act as a battle tank. In this paper we present design and analysis of an effortless swift mechanism for easy attachment/detachment of mine trawl system with tank.

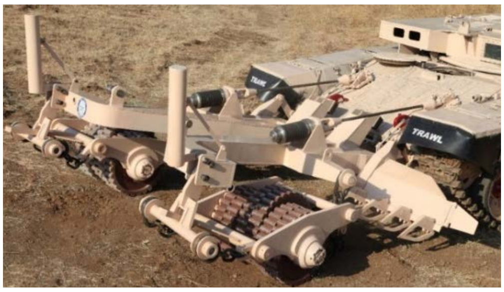

Fig. 1: Trawl assembly attached in front of tank

2. System Description

A swift detach mechanism is designed which connects the Trawl system with tank at two locations i.e. at upper bracket and lower brackets mounted on tank. The free body diagram of the Trawl assembly connection with tank is shown in Fig.2.

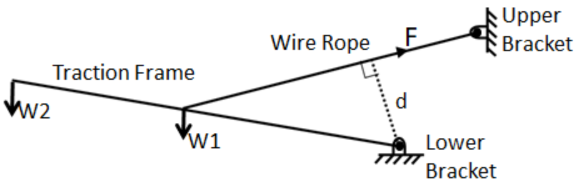

Fig. 2: Free body diagram

The connections on tank are designed in such a way that the blast energy can be easily released which can otherwise damage the system. In order to achieve it, the traction frame is given hinge connection with lower brackets on tank and the connection with upper bracket is made via wire rope so that the trawl assembly can rotate freely unless it reaches stoppers given at proper locations on tank.

The beauty of this mechanism is that it connects the entire system with tank without any permanent joints. The swift detach mechanism along with its attachment on tank is shown in Fig.3. The hinge connection between the traction frame and lower bracket assembly on tank is made in two halves with the help of link assembly free to rotate so that it can be opened and closed easily. The natural tendency of link assembly is to open under the action of gravity but is kept in locked position throughout operation with the help of two holds on latch shaft. The contact surfaces of the two holds are carefully designed. The latch shaft is operated with the help of locking rod assembly which is connected to the locking link integrated shaft of the upper bracket link assembly. The wire rope attached to traction frame on one side is given a socket on the other side which is inserted into the upper bracket pin and is prevented from coming out during operation with the help of the same locking link of the upper bracket link assembly which operates the latch shaft. Thus the lock/unlock at both locations can be controlled by controlling the motion of a single link. This locking link is kept in locked position throughout operation utilising the concept of four bar mechanism in over toggle position used in the upper bracket assembly. The design of mechanism ensures system release simultaneously from both attachment locations and that too only when the opening link of the mechanism is operated by giving external torque when desired.

Additional provision is given to insert pin between a projection on latch shaft hold and similar projection on the link assembly. It can be used when trawl is desired to be operated in very difficult terrains which lie outside the design scope. The pin can be removed when system release is desired and the mechanism can be operated.

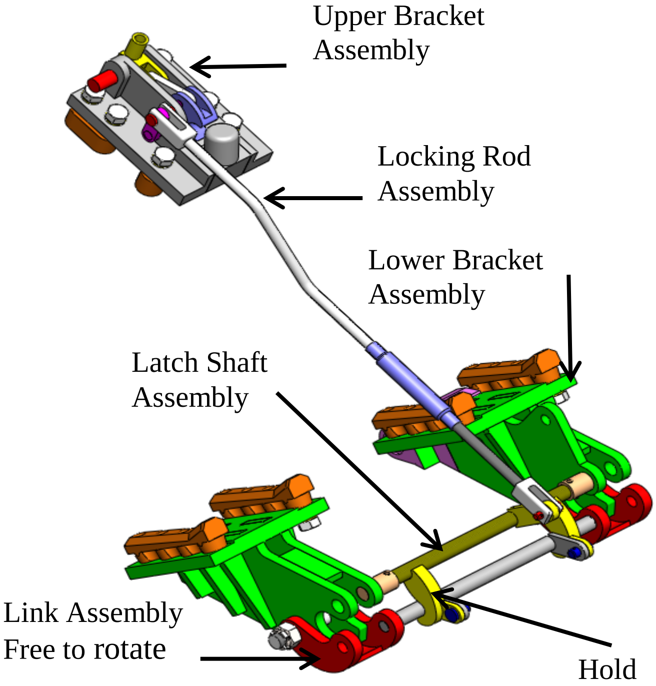

Fig. 3: Swift Detach Mechanism

3. Kinematic Analysis

The mechanism utilizes the concept of over toggle position in four-bar mechanism at upper bracket assembly as shown in Fig. 4a. The kinematic diagram of the linkage assembly at upper bracket is shown in Fig. 4b. The opening link/input link is numbered as 1 while the locking link is numbered as 3. The hold/release of the lower bracket link assembly has been coupled with that of the upper bracket with the help of additional links which makes it a six bar mechanism. The kinematic diagram of the entire mechanism is shown in Fig. 5.

The mechanism is designed in such a way that during lock condition the complete weight of trawl assembly act as a locking force which keep mechanism in lock position. During unlocking, an external torque has to be applied at the opening link to move the mechanism from toggle position. Then only the mechanism opens and releases the system. The configuration of trawl system and bracket design is carried out considering this locking-unlocking mechanism operation.

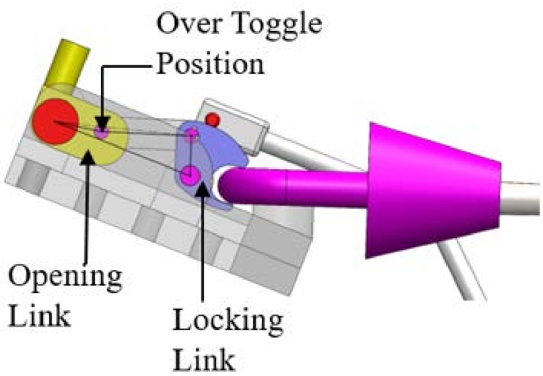

Fig. 4a: Upper Bracket Assembly

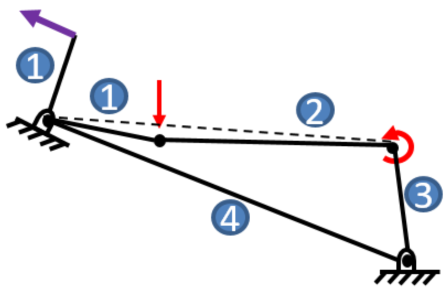

Fig. 4b: Kinematic Diagram at upper bracket

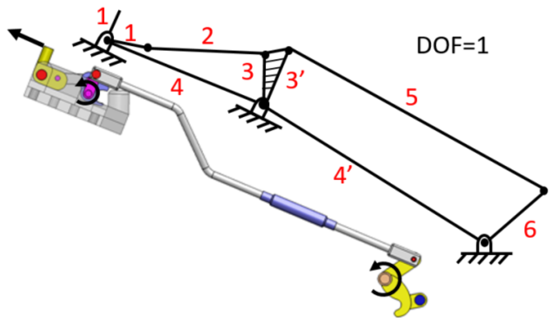

Fig. 5: Kinematic Diagram of full mechanism

4. System Design

The mechanism has been designed from basic principle of kinematics. The link length has been designed based on non-Grashof linkage configuration and necessary toggle position is achieved. Links shape, size and orientation are synthesised based on space availability on tank to ensure positive locking during operation and at the same time release the system with minimum efforts at the time of need. The input link is made in ‘L’ shape. Its bottom leg is used as a link of mechanism while top leg is made as hollow cylinder so that a rod can be inserted to open the mechanism and release the system manually when desired. An integrated shaft is provided with this link for remote operation. The first output link/locking link at upper bracket is given a ‘C’ shape to keep the wire rope socket in position. It has been given proper clearance at bottom side so that it can rotate freely. The link lengths have been synthesised to minimize the opening torque value.

A force diagram on mechanism is drawn in Fig. 6 to show that trawl system weight generates toque on locking link which keeps mechanism in toggle position only. To open the mechanism a positive force/torque is to be applied at the opening link (Link 1).

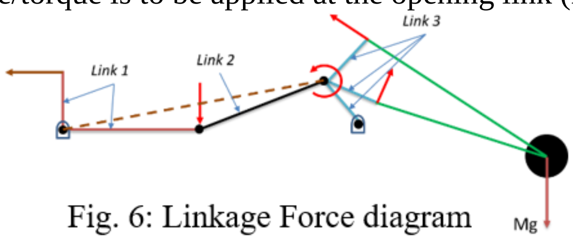

Fig. 6: Linkage Force diagram

The sections are designed considering forces in worst case they will experience. The contact length of the latch shaft hold is optimized based on simulation results so that the mechanism does not open at its own during trawl movement or operation but at the same time the system can be detached by a single person’s effort. The positive locking of mechanism has been verified for all terrain mobility as required including trench through motion simulations software. Also, the opening torque and release operation are estimated and verified.

5. Motion Simulation

The mechanism has been designed by analytical method and also a simulation study has been performed in multi-body dynamics software. The complete trawl system has been modelled in simulation software and motion simulation has been performed to evaluate mechanism performance while movement on different terrain conditions. Solid model of trawl system with tank is given in Fig. 7 while the simulation model of mine trawl system along with the mechanism is shown in Fig. 8.

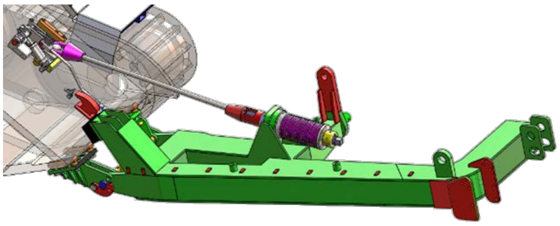

Fig. 7: Trawl System model with tank

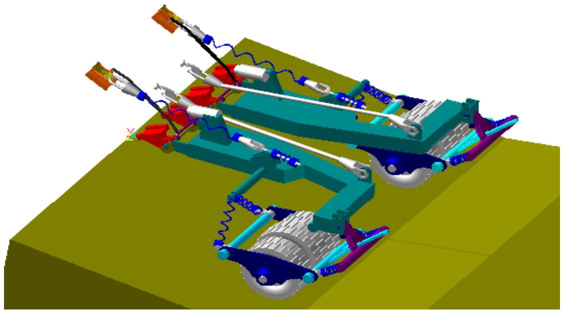

Fig. 8: Simulation model of Trawl System

The mechanism has been simulated for its opening and closing operation. The linkage configuration in locked and open positions are shown in Fig. 9 & Fig. 10 respectively. The ‘C’ shape link keeps the system locked at both attachment locations. When opening torque was given to the opening link (link 1), the complete trawl system got released from tank and fell down allowing the tank to move freely.

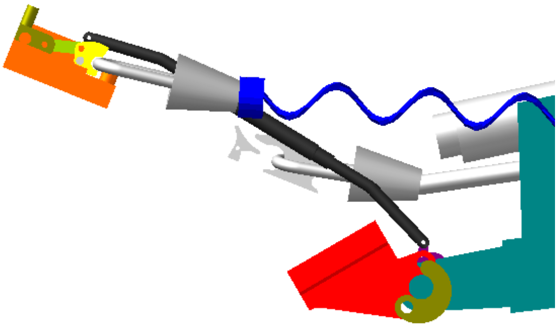

Fig. 9: Mechanism in lock position

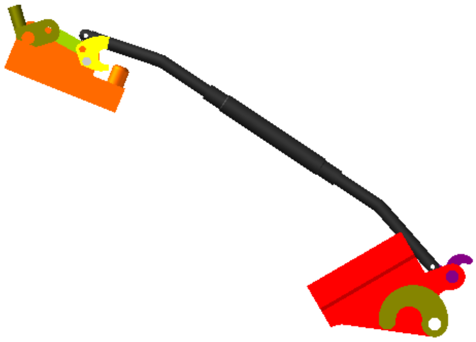

Fig. 10: Mechanism in open position

6. Results and Discussion

The simulation study of mechanism is presented in this section. The simulation has been run for 2sec and opening torque was provided to the input link on one side of trawl system while other side of trawl unit was kept stationary to compare the position and force values at joints. The stationary unit of trawl system has position almost stationary during simulation.

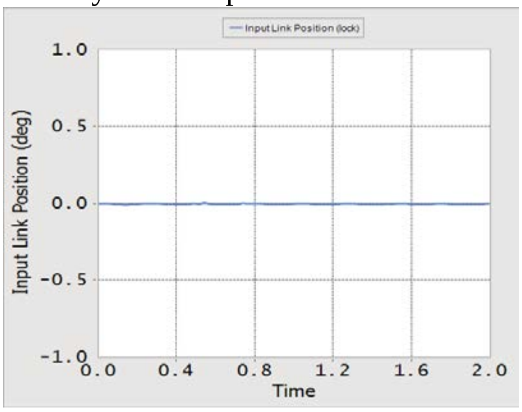

Fig. 11: Input link position in lock condition

It can be seen in Fig. 11 that the input link does not rotate during lock condition keeping the mechanism in lock position, regardless of forces exerted by trawl system, because it is kept in over toggle position.

The left side of trawl assembly input link is provided with a time variable torque to validate the opening torque value. The position of input link is presented in Fig. 12. It shows that during the unlock operation the input link rotates about 40deg to open the mechanism. Since, torque is provided to the opening link therefore it is able to move the mechanism out of the toggle position.

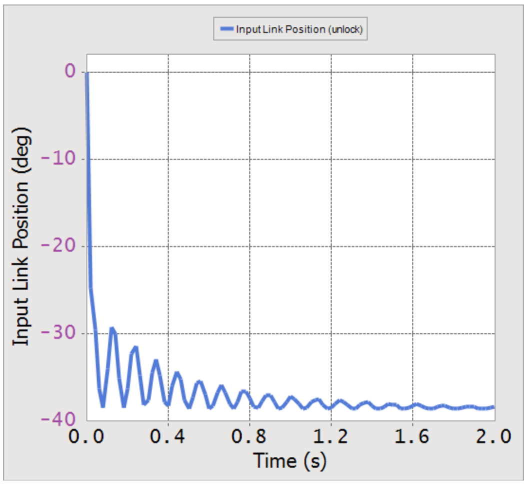

Fig. 12: Input link position during unlock

A time variable input toque is provided to input link to find out torque requirement at input link. The graph shown in Fig.13 presents the opening torque required at the input link which is coming approximately 22Kg-m and the mechanism opens quickly.

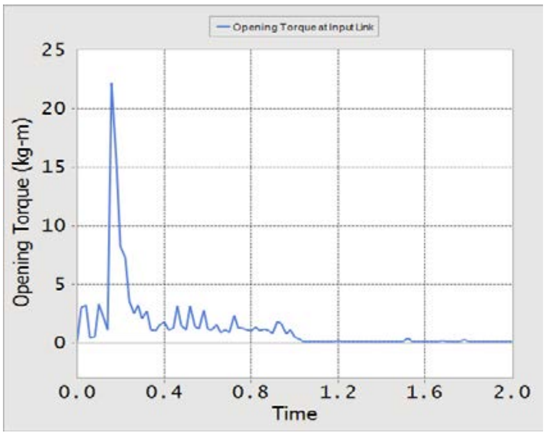

Fig. 13: Input Torque at input link

Based on this, it can be seen that with the use of the designed mechanism, it requires very less force and time to detach the entire heavy trawl assembly. This force can be provided via manual handle with appropriate lever arm or remotely. The mechanism has been realized and a trial was also conducted to validate the design. The designed mechanism is fitted in T-72 tank as can be seen in Fig. 14. A hydraulic cylinder has been used to operate the mechanism and measure the torque requirement. The experimental result is matching with simulation result. Manual operation is also validated.

Fig. 14: Mechanism fitted with T-72 Tank

7. Conclusion

The Mine Trawl system is an essential system for creating a vehicle safe lane for friendly tanks. The mine trawl system utilizes mine rollers for detonating pressure actuated mines. Since, after creating safe lane tank should be freed to increase its mobility or use it as battle tank during wars therefore an effortless and swift detach mechanism has been designed and developed.

The mechanism requires approximately 22Kg-m torque for opening which can be provided manually with appropriate lever arm. Provision is also given for remote operation which can be operated by hydraulic or pneumatic power by army men sitting inside the tank. This can prove as life saver during war time. Also, the mechanism keeps the trawl roller assembly in position and does not open during regular motion of the system which has been verified by motion simulation software and also validated during trials.

In overall the designed mechanism is effortless and swift operation type. In the absence of such mechanism it would have required many persons, crane, tool kit, long time and even risked the life of army men during battle time. The mechanism has been realized and fitted with a tank. Also, the effortless swift release feature of the mechanism has been tested for its manual as well as remote operation which was successful.

8. References

[1] Norton, R. L. (2011). Design of machinery: an introduction to the synthesis and analysis of mechanisms and machines. Boston: McGraw-Hill Higher Education.

[2] Rattan, S. S. (2014). Theory of machines. Tata McGraw-Hill Education.

[3] Yang, Z., Anderson, T., Crawford, V., Ju, Y., & Schweinzer, P. (2016). Journal of Mechanism and Institution Design Volume 2, Issue. Journal of Mechanism and Institution Design, 1(1), 1.

[4] Wandling Sr, G. R. (2000). Synthesis of mechanisms for function, path, and motion generation using invariant characterization, storage and search methods.

[5] Erdman, A. G., & Sandor, G. N. (1997). Mechanism design analysis and synthesis (Vol. 1). Prentice-Hall, Inc..

[6] Beran, J., Bílek, M., & Žabka, P. (Eds.). (2016). Advances in mechanism design II: Proceedings of the XII International Conference on the Theory of Machines and Mechanisms (Vol. 44). Springer.

Separation Dynamics Analysis of a Human Rated Launch Vehicle Fairing

Ashis Kumar Samanta
Aerospace Mechanisms Group
Indian Space Research Organization
Thiruvananthapuram
ashis_joy@rediffmail.com

Shiju G Thomas
Aerospace Mechanisms Group
Indian Space Research Organization
Thiruvananthapuram

Gopakumar M
Aerospace Mechanisms Group
Indian Space Research Organization
Thiruvananthapuram

Damodaran P
Aerospace Mechanisms Group
Indian Space Research Organization
Thiruvananthapuram

Subramanian U A
Aerospace Mechanisms Group
Indian Space Research Organization,
Thiruvananthapuram

Abstract—**In human rated launch vehicle, the Service Module Fairing (SMF) protects the service module from aerodynamic, thermal and acoustic loads during the atmospheric regime of flight. The separation of SMF is executed subsequent to separation of Crew Escape System (CES). SMF is a cylindrical metallic isogrid shell structure made in two halves and located between the launch vehicle and orbital vehicle. SMF has to be separated and jettisoned from the vehicle once the vehicle crosses the atmosphere, and to avoid collision with the on-going vehicle, it is planned to be separated and jettisoned laterally in to two halves. For achieving this, a vertical separation system called Linear Bellow Actuation (LBA) is assembled between two halves. Both halves of the fairing are made of metallic isogrid construction, and the flexibility and elastic deformation of the halves during separation and jettisoning have to be considered critically to achieve a collision free separation. So, a separation dynamics analysis considering the flexibility of structures is required at the design stage itself for ensuring successful functioning of the system.**

After the preliminary design of the structure, a separation dynamics analysis is carried out using ADAMS software. Initially a 3D FE model of fairing halves with all the subsystem mass a modal analysis is carried out in ANSYS software for generating the model neutral file (MNF). This MNF file and forcing function generated by the vertical separation system i.e LBA are the inputs for ADAMS analysis. The acceleration of vehicle at the instant of separation and necessary interfaces which are critical from point of view of collision are also included in the analysis. The result of the analysis indicated sufficient clearance of the separating fairing halves with the on-going vehicle. This paper describes the methodology and results of separation dynamics analysis carried out for SMF of a Human rated Launch Vehicle.

***Keywords— Service module fairing, Separation dynamics, Rigid and Flexible body motion*.**

Nomenclature

CMF	Crew Module Fairing	AE	Aft end
LBA	Linear Bellow Actuation	FE	Fore end
SMF	Service module fairing	MNF	modal neutral file.

1. Introduction:

In the launch vehicle used for human space programme, systems for carrying crew are the payload instead of satellite. The payload consists of Orbital Module (OM), Crew Escape System (CES), Crew Module Fairing (CMF) Ejection systems and separation mechanisms. Service Module Fairing (SMF) interconnects the OM and the launch vehicle. SMF covers the service module and protects it from aerodynamic, thermal and acoustic loads during the atmospheric regime of flight and it is separated once vehicle crosses the same.

Fairing of service module is three meter tall cylindrical iso grid shell structure, made of aluminium alloy. Two cylindrical metallic halves are joined in vertically by vertical separation system called linear bellow system (LBA) and horizontally by two clamp band separation mechanism (One in forward and one in aft ends). Figure-1 shows the configuration for Orion, where SMF is made of three pieces. In the system studied here, it is made of two halves instead of three. The separation of fairing halves is executed subsequent to separation of CES at near to vacuum condition. Both the fairing halves are unique structures due to the difference in cut out locations and subsystems attached with structure. Hence, both the halves have different offsets for centre of gravity (CG) in all directions. Due to the same reason, moment of inertia (MI) is also different for both halves. Since both the halves are half cylinder structures, optimised for thickness and strength, flexibility and elastic deflection of the structures need to be considered during the separation. The separation system should ensure clean and collision free separation from the on-going launch vehicle during its function. Hence even any minor offset in CG, change in MI and structure frequency, become critical from the separation point of view. Also both the separation mechanisms are actuated by individual electrical initiation with predetermined time delay. Even if the separation command would be initiated simultaneously, delay in relay, initiation of pyros and actuation time of the separation system would delay the actual separation event. Fairing halves are situated in upper stage of launch vehicle, so separation dynamics studies is needed for assessing possibility of collision and body rates imparted to the launch vehicle.

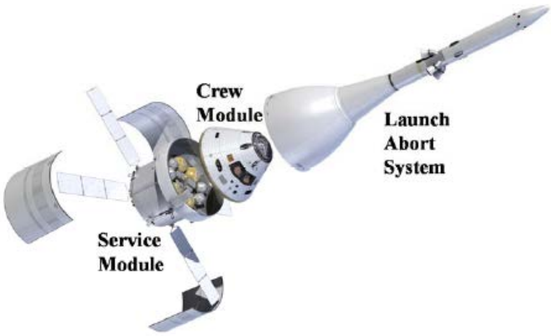

Fig 1: Schematic diagram of Orion [6].

After the preliminary design of the structure a separation dynamic analysis is also carried out using ADAMS software, to ensure that the flexibility of the structure is adequate for providing a clean separation. Initially a modal analysis of fairing halves with all the subsystem masses is carried out in ANSYS software for extracting the modal frequencies, mode shapes and model neutral file (MNF). This MNF file and forcing function generated by the vertical separation system are the inputs for ADAMS analysis. The forcing function is given as force versus displacement data of the LBA, as obtained from the panel level testing in ground. . The acceleration of vehicle at the instant and during separation affects the clearances and is included in the analysis. Necessary interfaces which are critical from point of view of collision are also included in the analysis. The result of the analysis indicated sufficient clearance for the separating fairing halves with the on-going vehicle.

In parallel to this analysis, same separation dynamics study was done using an in-house developed software, but it lacked the capability for visualization of separating bodies, accounting external protrusion of sub systems, intricate shapes etc., and these lacunae called for the present ADAMS analysis. Also these results would give additional confidence the in capability of the system. This paper describes the methodology and results of separation dynamics analysis of fairing halves for assessing the collision free separation of the system.

2. System Description:

Fairing halves are made of aluminium alloy with fore end ring, aft end ring, bulk head and isogrid panels. Both the cylindrical isogrid panels are joined together by vertical separation system, called linear bellow system (LBA) in diametrically opposite direction. Fairing halves are connected with two horizontal separation system i.e clamp band separation mechanisms with OM at forward end and with launch vehicle at aft end respectively.

The fore end horizontal separation system consists of clamp band separation system between fairing fore end rings and CES aft end ring as shown in Figure-2. Two rings are held together by wedge blocks and clamp bands are wrapped over the wedge blocks. These clamp bands are connected by connecting bolts and nuts at diametrically opposite directions and preload is provided by tightening the bolt and nut. Bands are separated along with wedge blocks and connecting bolts. Separation event is achieved by issuing separation command to electrically initiated pyro bolt cutter and subsequent severing of the connecting bolt. Wedge blocks along with bands are retracted by torsion springs and capture brackets, which are assembled at the fairing fore end rings.

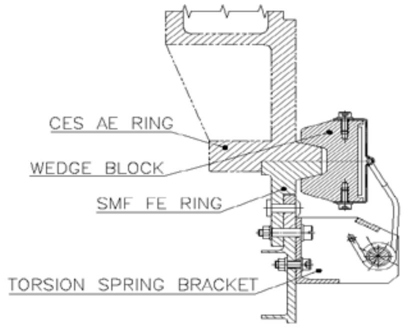

Fig 2: Fore end horizontal separation system

A different clamp band separation system is used for Fairing aft end separation. Here, band retention system is not provided and is free to separate along with connecting bolts, once the system is actuated. Wedge blocks are retained along with separating fairing halves. Aft end separation system is shown in Figure-3.

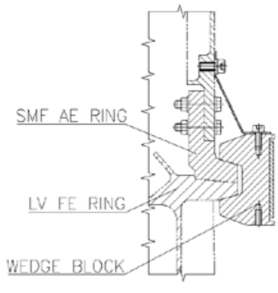

Fig 3: Aft end horizontal separation system

Linear bellow system is employed to provide lateral forces to separate the fairing halves away from the core vehicle. It is a Zip Cord based system where pyro charges kept inside a rubber bellow is placed along the vertical length of the fairings. LBA consists of piston and cylinder arrangement as shown in the Figure-4. One half of fairing is connected with piston and other half is connected with cylinder by fasteners. The mild detonator chord, attenuator tube and folded bellow are assembled inside the cylinder along the length. Piston and cylinder are joined together with uniformly pitched rivets, with are sheared during the separation event by the force generated by bellow. Two halves are pushed and jettisoned away from core vehicle due to pyro energy of separation system itself.

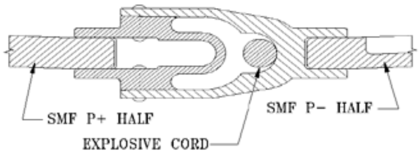

Fig 4: SMF vertical separation system.

3. Methodology:

Prediction of trajectories of separated halves can be generated in ADAMS software as the result of dynamic analysis in which the trajectory is computed based on combined effect of rigid body and flexible body motions and other inputs. A rigid body has six degrees of freedom i.e three rotational and three translation motions.

A. Coordinates and Reference of frame

A traditional Cartesian coordinate system consists of three orthogonal axes X, Y, Z of launch vehicle. Conventional pitch, yaw and roll axis of launch vehicle are used as X, Y and Z axis respectively. Launch vehicle motion is considered as a rigid body motion and aerodynamic forces are ignored, since separation occurs in space. Two coordinates systems are used in the analysis. The first one often called global or inertial frame of reference, which is fixed in space and time. Second one is the body reference frame. The body reference frame translates and rotates with the body and thus its position is changed in relation to the inertial frame of reference with time.

B. Position, Translation and Rotation

An arbitrary point or any article in the space can be positioned with three coordinates x, y and z and the position vector can be expressed as

r = xi + yj + zk ………………. (1)

Where i, j, k are the unit vector along the x, y, z axis.

The velocity vector is the time derivative and it can be express as

$v = \dot{r} = \frac{d}{dt}(r) = \dot{x}\, i + \dot{y}\, j + \dot{z}\, k$ ……….. (2)

And acceleration can be expressed as

$a = \dot{v} = \ddot{x}\, i + \ddot{y}\, j + \ddot{z}\, k$ …………….... (3)

These can be represented in matrix form as

$r = [x_1\ \ x_2\ \ x_3]^T$; $v = [\dot{x}\ \ \dot{y}\ \ \dot{z}]^T$ and $a = [\ddot{x}\ \ \ddot{y}\ \ \ddot{z}]$

A variable in space, u can be similarly formulated as $u = u_1\, i + u_2\, j + u_3\, k$. In the 3D space, six variables are needed to accurately specify the location and orientation of the body. Three for coordinate $r_i = [\ r_1^i\ \ r_2^i\ \ r_3^i\ ]^T$ and three for rotation $S_i = [\ \propto_1^i\ \ \beta_2^i\ \ \gamma_3^i\ ]^T$ where $\alpha,\ \beta$ and γ are the angle of rotation with respect to X, Y and Z axis. Velocity vector can be formulated as $v = v_1 i + v_2 j + v_{3k.}$ Body rotation can be accurately determined by specifying the angle of rotation and unit vector along the axis of rotation. The angular velocity (ω) can be expressed as ω= pi +qj + rk; where p, q and r are the components and i, j, k are the unit vector in pitch roll and yaw axis of body respectively. 3 x 3 rotational matrix presents one body rotation conventionally in a single matrix.

C. Formulation of Multi body dynamics

Multi body dynamics problems can be solved using three different methods:

(i) Classical Newtonian dynamics

(ii) Principle of Virtual work

(iii) Lagrangian dynamics.

The Lagrangian method is widely used in finding automated solutions for Multibody dynamic problems. This method is used in ADAMS for formulation. It is also called Scalar Variation Principles, which is based on scalar quantities such as work and energy as opposed to Newtonian method which operates with vectors such as velocity and force. It is a principle of least action, where, the solution moves in the direction where it requires or uses the least energy or work.

The Lagrangian is defined as L = T –V; where T is the kinetic energy and V the potential energy of the system. Once these energies have been calculated, L can be determined. Subsequently, equations of motion describing the system can be obtained from the equation given below.

$$\frac{d}{dt}\left(\frac{\partial L}{\partial \dot{q}_j}\right) - \frac{\partial L}{\partial q_j} - Q_j = 0 \quad \ldots\ldots\ldots\ldots\ldots\ldots..(4)$$

Where, q_j is generalized coordinate and Q_j corresponding generalized force.

D. Jettisoning force of LBA

Jettisoning force is exerted by LBA and it is quantified by a panel test data. The pressure imparted by the LBA is available as a function of relative displacement from this test. For the application of force, the LBA is considered as 46 segments along the vertical length and forces acting on these segments are estimated from the pressure and area of each segment. The forces acting on these 46 segments as a function of displacement are given as input jettisoning force during the simulation. Typical force verses displacement data at one of the 46 segments, derived from the test, which is used as input force is given in the figure-5.

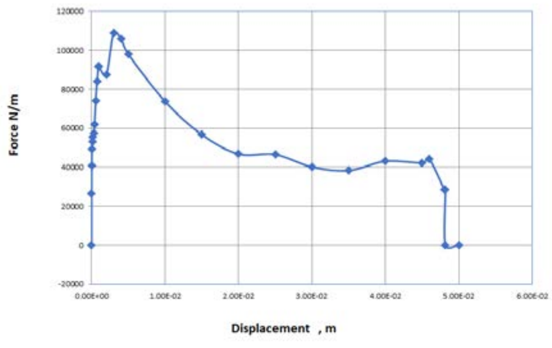

Fig 5: LBA force verses displacement graph

4. Model for ADAMS

3D finite element model of both halves of SMF is used for this analysis. Inertial properties like mass, centre of gravity and moment of inertia are defined as per global coordinate system and data are verified through different software.

A. Finite Element Model

A detailed 3D finite element model is generated in ABAQUS software for modal analysis. All elements which provide stiffness to the structure including panels, bulk head, rings, edge beam, cut out elements are modelled along with structural sub element like spacer, shear bolt, fasteners etc. Inertia properties of this detailed FE model are mentioned in Table-01. Piston half is referred as SMF P+ half and cylinder half is referred as SMF P- half. Between P+ half and P- half, properties are different due to difference in mass of sub systems and locations of them.

Table-01: Inertia Properties

Item	**Mass (kg)**	**CG Location from Aft end (mm)**			**MI about CG ($kg\text{-}m^2$)**		
		Roll	**Pitch**	**Yaw**	**I_{Roll}**	**I_{Pitch}**	**I_{Yaw}**
Piston Half (P+)	393	1720	-1235	2.9	1012	1323	654
Cylinder Half (P-)	428	1704	1142	19	1195	1502	737

Aim of modal analysis is to determine and solve the vibrational modes and frequencies of structure. These modes are mainly the results of inertial and elastic properties of structure. Since structure is flexible due to its shape and size, hence this modal analysis is important in separation dynamics. First six modes are rigid body modes which do not include flexibility. Though, mainly 7th mode to 12th mode only play the key role in flexibility during separation, modal analysis has been carried out up to 25th mode. Details of results of modal analysis are mentioned in Table-02.

Table-02: Modal analysis results

	Frequency in Hz		**Remarks**
	P+ Half	**P- Half**	**Mode**
7th mode	1.15	0.99	Torsion
8th mode	1.97	1.69	Flexing
9th mode	3.00	2.57	Torsion
10th mode	5.36	4.65	
11th mode	7.43	6.63	
12th mode	10.72	9.68	

B. Modal Neutral Files (MNF)

Modal Neutral Files (MNF) is in essence, modal descriptions of flexible bodies. This MNF files is the input to ADAMS software. MNFs contains following.

(i) Geometry including node location and connectivity. These nodes are generated from the mesh of the FEA program while constructing the MNF file.
(ii) Nodal mass and inertia.
(iii) Mode shape.
(iv) Generalized mass and stiffness for the mode shape.

The MNF file was generated in ANSYS software, where FE model of ABAQUS software is the input file. Inertial properties and modal analysis data are cross verified during FE model conversion time. Uniformity of units and coordinate system for specification of properties are verified even after importing the MNF file in ADAMS.

C. ADAMS Flex

ADAMS (Automatic Dynamic Analysis of Mechanical System) software is a widely used multi body dynamic simulation tool. Both the halves MNF files are imported separately to the ADAMS and cross verified the inertia properties, mode shape data, coordinate system and unit.

5. ADAMS Simulation

ADAMS model is shown in Figure-7. Both the fairing halves are geometrically positioned at the integrated locations and locked together to simulate the initial conditions. Following are the assumptions in the modelling of dynamics.

(i) The horizontal separations are not considered for this simulation, it is assumed that the horizontal separations occurred prior to the vertical separation.
(ii) Simulation starts once force is applied on the LBA halves.
(iii) LBA force is acting as a point load at the centre of pressure of 46 individual segments on each half.
(iv) LBA forces are deactivated once piston and cylinder distance crosses the critical distance.
(v) Pressure generation in the LBA is uniform throughout the length; hence LBA force is acting throughout the length.

In actual separation process the folded bellow within the piston cylinder assembly expands due to the pressurised gas generated by explosive and pushes the fairing halves till the bellow loses contact with the piston half. This distance at which the bellow is attached to the cylinder half and loses the contact with piston half is called critical distance, refer Figure – 6.

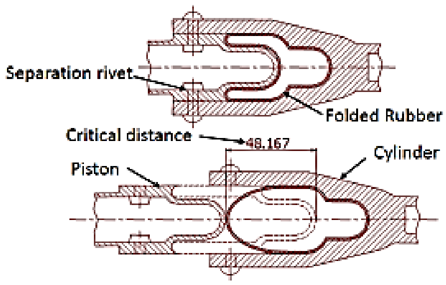

Fig 6: LBA before and after separation

This phenomenon is simulated in ADAMS model as follows. Each LBA force is made zero when the distance between the two halves at that location reaches critical distance. A Measure Function (ADAMS feature) is used to compute continuously the distance between the two halves at respective points of force application. This Measure Function is applied in each force location. In the simulation, Single LBA length is divided equally into 46 numbers of segments. Also total LBA force is segregated into 46 forces as discrete point forces on each side of LBA, hence 92 single point forces is applied per half. Each point force is applied with Force Function. This function is equation driven with boundary conditions, where force vs. displacement of actual LBA test data is taken as input. This force vs. displacement history is derived from the actual pressure-time curve from LBA test data.

6. Simulation Result and Discussion

Simulation was carried out with full coupling. This means that the Moment of Inertia and Centre of gravity of the bodies are dynamically updated to the corresponding flexible shape of the body at different time steps. Core vehicle acceleration of 13.5 meter per Second Square is applied during the simulation. During the jettisoning of flexible body, total energy is the sum of its translation kinetic energy, rotational kinetic energy and energy utilized of flexing. Flexing energy is the percentage of total energy, which indicates the level of flexing in particular structure. Summary of results are mention in Table – 03.

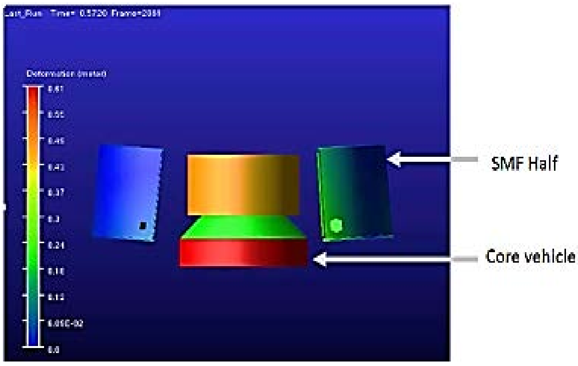

Fig 7: ADAMS model

Table – 03: Summary of results

Parameter	P+ half	P- half
Velocity (m/s)	5.31	4.94
Yaw rate (deg/s)	11.5	7.6
Strain Energy (kJ)	1.98	1.21
Total Energy (kJ)	7.48	6.58
Energy for flexing (%)	26	18
Closest approach to LV (mm)	155	206
Fairing flexing frequency (Hz)	1.97	1.69

During the process of separation, the traces of extreme points at fore end (AE) and aft end (FE) location of the SMF halves are plotted w.r.t the core vehicle, which are shown in Figure – 07 & Figure-08 respectively.

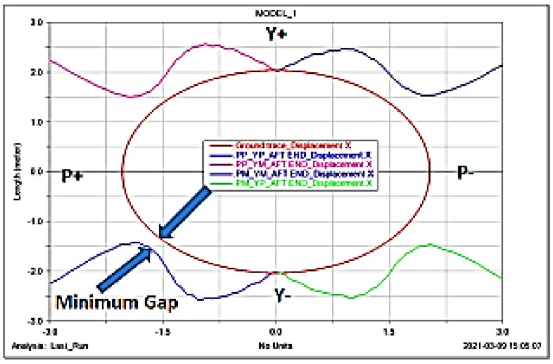

Fig 7: Traces of aft end points

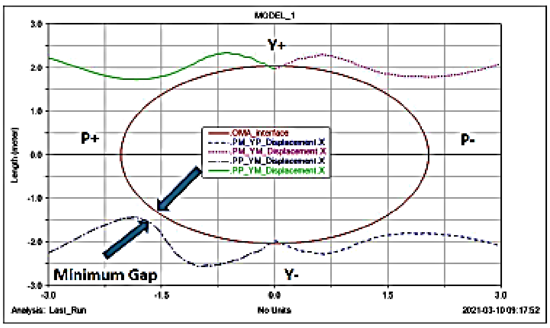

Fig 8: Traces of fore end points.

In figures 7 and 8, central circle refers the core vehicle, which is 4m diameter and each segment is 500 mm. Four lines represent the end traces passes through the space at the time of separation. From the analysis it was observed that the closest approach of the separated half is at P+ Y+ aft end location with a minimum gap of 155 mm. The results obtained from the simulation including energy, translational velocity of separated halves, body rates etc., in all three axes.

7. Conclusion

Flexible dynamic model for Service Module Fairing was generated. Integrated separation dynamics analysis with rigid body motion and flexible body motion was carried out by using ADAMS software. Yaw rate, translation velocity, jettisoning acceleration and body rate are within limit. Analysis result indicates a clean and collision free separation, which confirms the adequacy of the structural design from the functional point of view.

8. Reference

[1] Butcher J R, "The separation test in vacuum of Arian 4 fairing". In proceeding of fifteenth Space Simulation Conference on Support the Highway to Space through testing, November 1988, NASA CP – 3015.

[2] Narendra Nath, Venkateswaran KP, Biju G, Balakrishnan S, "Separation dynamic studies on dual satellite simultaneous separation". 11th National Conference an Exhibition on ARMS - 2018.

[3] N Radha, Abay Kumar, Madan Lal, "Separation dynamic Analysis of full scale Heat Shield separation test on ground". VSSC-MS-98-MS 567.

[4] Venkateswaran K P, A K Agarwal, P Damodaran, P Purushothaman, M Premdas, "Integrated dynamic analysis of a large CFRP payload fairing separation/jettisoning". National Conference and Exhibition ARMS – 2012,

[5] ZHAO Chunhaua, CHEN Shijun, LIU Xianming, ZHANG Jin, ZENG Jia, "Study on Modelling method of flexible body in ADAMS" IEIT Journal 2012.

[6] Yasmin Ali, Jesse D Chuhta, Michael P Hughes, "Forward body cover separation modelling and testing for the Orion multipurpose Crew Vehicle" American Institute of Aeronautics and Astronautics, 2015-00-3013

Design and Qualification of separation system for RLV Landing Experiment (LEX)

M. Harish
Aerospace Mechanisms Group
MVIT, VSSC,
ISRO
Trivandrum
harish_malepati@vssc.gov.in

Anjul Beohar
Aerospace Mechanisms Group,
MVIT, VSSC,
ISRO
Trivandrum
anjul_beohar@vssc.gov.in

Binoy M
Aerospace Mechanisms Group,
MVIT, VSSC,
ISRO
Trivandrum

Joby Mathew George
Aerospace Mechanisms Group,
MVIT, VSSC,
ISRO
Trivandrum

Manu V. Unnithan
Aerospace Mechanisms Group,
MVIT, VSSC,
ISRO
Trivandrum

Abraham Varghese
Aerospace Mechanisms Group,
MVIT, VSSC,
ISRO
Trivandrum

UA Subramanian
Aerospace Mechanisms Group,
MVIT, VSSC,
ISRO
Trivandrum

Abstract — **A single point separation system is required for the release of RLV from the helicopter during Autonomous Runway Landing Experiment (LEX) experiment will be conducted with a helicopter using RLV Interface System (RIS). The function of the separation system is to hold the RLV and RIS against the external inertial, aerodynamic loads and hoist preload acting during various phases of the flight. After reaching a predefined altitude and range, RLV will be released from RIS by separation system with minimum disturbances for landing experiment. A separation system is designed and qualified to fulfill the need of the above experiments. In this paper, various design features of the separation system catering to functional, structural and interface requirements are presented. The system has undergone a series of structural and functional tests (unit as well integrated level) as a part of qualification. The details of the tests carried out, tests results and validation with FE results are also presented.**

Keywords – RLV, LEX, system, ADAMS, FE analysis, ANSYS

1. Introduction

As a part of the Qualification program of Reusable Launch Vehicle (RLV) being developed by ISRO, a series of landing experiments (LEX) are planned to demonstrate the autonomous landing capability on runway. In these tests RLV winged body, along with an RLV interface system (RIS) is in combined phase lifted up by a helicopter from runway to a predetermined altitude and range (Figure 1). After reaching the required altitude, range and speed, the RLV will optimum configuration is a key for design of linear shaped charge based separation system. Also, due to lack of in-depth understanding and complexity of the problem, a combination of analytical calculation, software-based simulation and experimental studies is the most effective way to verify the effectiveness of the configuration.

The separation system developed is a single point, pyro initiated, initiated bolt cutting mechanism. The system is very compact and has an unique design to hold the separating parts by a single bolt and can be easily integrated with RLV using hook beam and shear plate. The system is built with redundancy in initiation and designed to minimize disturbance during release avoiding debris in operation. It is also designed to minimize the protrusion after separation and generates less shock to the RLV's avionics packages.

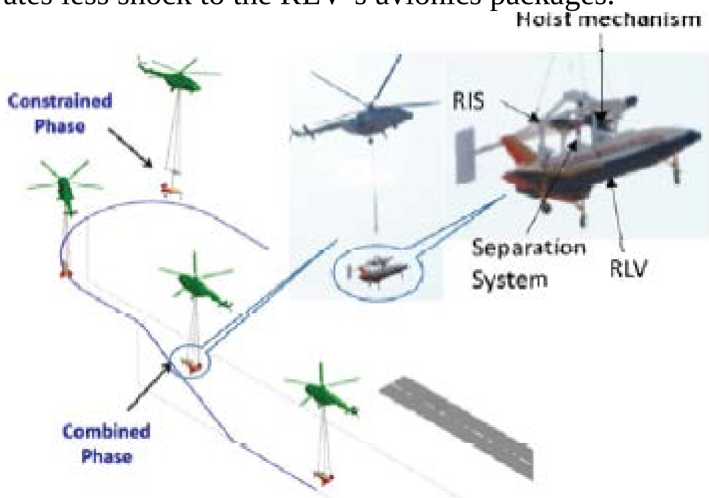

Fig 1: RLV - LEX

A. System Description

The separation system provides the interface between RLV and RIS through hoist mechanism. It is mounted on the RLV over hook beam at CG location and is connected to RIS using load cell adaptor of the hoist mechanism. RLV-LEX LEX separation system is configured with h cylindrical adaptor, shear plate, bolt support and hook beam preloaded together with a centrally mounted single tension bolt (refer Figure 2). In order to take the shear loads, system is assembled on the hook beam over the e shear plate plate, which is fixed to the hook beam through two shear pins. The required preload is applied to the system using hydraulic preloading fixture which gives clamping force to the joint.

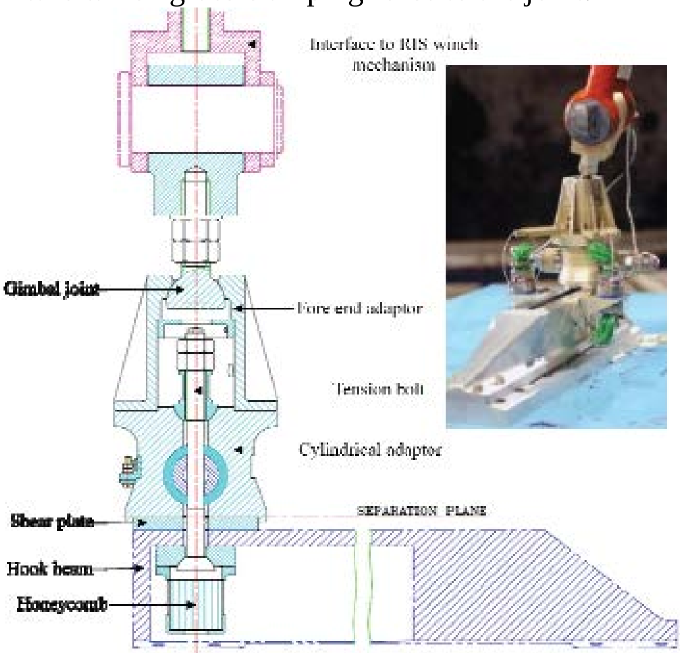

Fig 2: RLV-LEX separation system

Spherical washer is provided for better alignment of bolt during assembly. Calibrated load cell is provided in the bolt assembly to monitor the bolt tension. Fore end adaptor is assembled over the cylindrical adaptor and provides interface to load cell of RIS hoist mechanism via aft ball insert and wire rope terminal. A gimbal joint is provided to the fore end adaptor for providing alignment requirements. A pyro based bolt cutter is used for the severance of the bolt which in turn separates the RLV from RIS. After severance, both cut parts of the bolts are contained inside ide the system.

The lower half of the bolt is captured by the honeycomb in the container to avoid any rebound and contact with ongoing separating parts thereby by minimizing the disturbance during separation separation. The gap between the pyro cutter body and cylindrical adaptor is filled with rubber seal to prevent the bolt olt debris coming out. Two electrical connectors are provided and mounted on the hook beam for getting release configuration. Confirmation status after separation. System specifications are given in Table 1.

Table 1: System specifications

Parameters	Details
Type of separation system	Single point, pyro bolt cutter
Bolt interface	M14x1.5
Joint preload	90^{+3} kN
EAL	71.7 kN
Release confirmation	Separation connectors – 2 no.s
Release time	< 20 ms
Envelope	118 mm x 258 mm x 306 mm
Mass	$12^{\pm 5\%}$ kg
Redundancy	Device level
Operational temperature	5°C to 70° C

B. Design Details

Aerodynamic and inertial loads acting on RLV are considered for the design of separation system. . These aerodynamic loads are worked out using CFD simulations for the worst angle of attack and side slip angles. The inertial loads are worked out based on the worst acceleration (1 m/s 2 axial and 2g normal) found during helicopter trajectory simulations. Loads acting on the RLV separation system are classified into in four cases (refer Table 2).

Table 2: Load cases during RLV LEX

Phases	Cases	Details
Combined phase	Case-1	Take off condition
	Case-2	During motion
Constraint phase	Case-3	Start & end of lowering
	Case-4	During & after lowering

Aerodynamic loads are acting on the RLV in three directions – axial(X-X) X), lateral (Y-Y) and normal (Z-Z) as shown in figure 3 (refer figure 4 for sign conventions). In combined phase, the RLV is in hugged and preloaded condition with RIS, hence the separation system is not subjected to axial and lateral loads as these loads are directly transferred to the RIS by friction grip. Therefore, the loads acting on separation system during combined d phase are minimum compared to constraint phase. In constrained phase the maximum load acting on the system is in case-3 3 during start & end of lowering down of RLV where the inertial loads due to gravity prevails. Accordingly, the case-3, 3 loads are taken as design loads for the system. The maximum resultant load acting on the separation system during case - 3 is computed as 42.8 kN. The flight loads and additional hoist preload applied to RLV through hoist mechanism are considered for design calculations. Maximum EAL acting on the separation system is worked out as 71.7 kN for case-3 and preload to the system joint is fixed as 90 +3 kN with 1.25 margin.

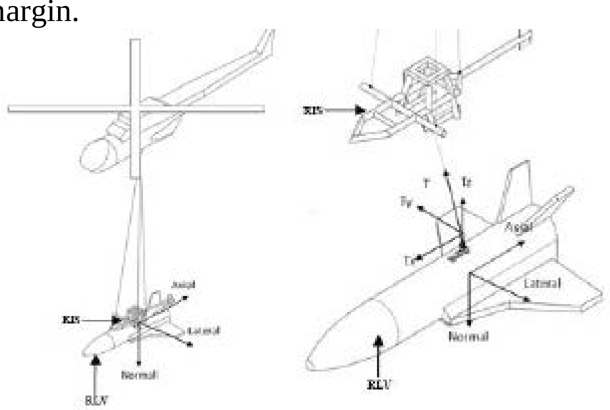

Fig 3: Combined & constraint phases

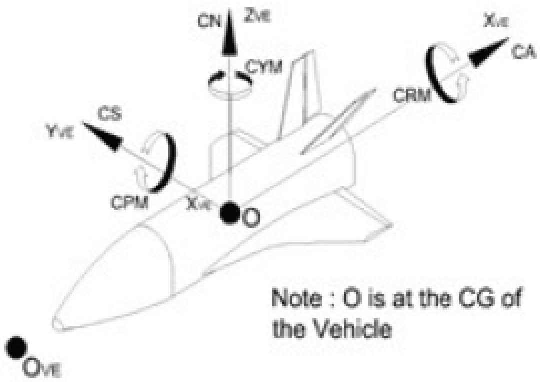

Fig 4: Sign conventions

C. System Preloading

The system is preloaded to 90 kN with a specially designed hydraulic preloading fixture set up (Ref figure 5) so as to avoid direct application of torque to the tension nut, which otherwise may cause damage the thread. Hydraulic pressure is measured me by pressure gauge and bolt preload is measured by a calibrated load spacer.

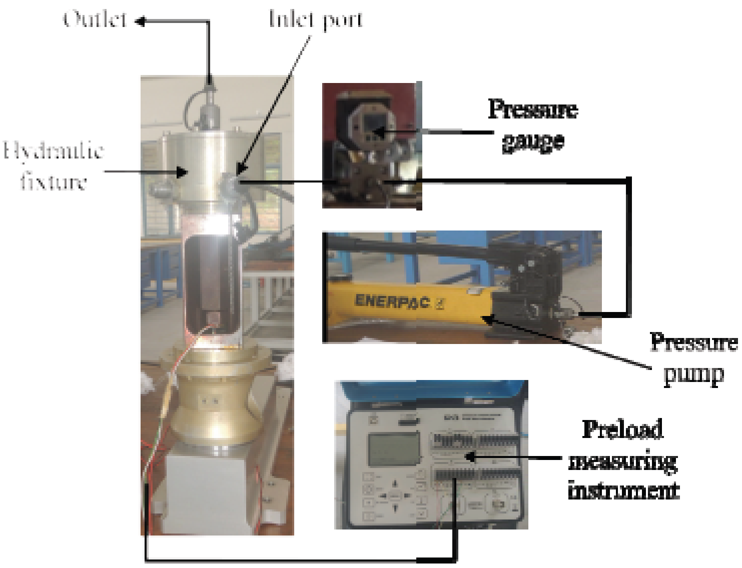

Fig 5: Hydraulic preloading fixture set up

D. FE Analysis

FE analysis is carried out in ANSYS Workbench to evaluate the stress & deformation patterns in the system components and also preload augmentation in tension bolt under worst load condition (case-3 loads). 3D model is created in Autodesk Inventor and exported to ANSYS for FE analysis (refer Figure 6).

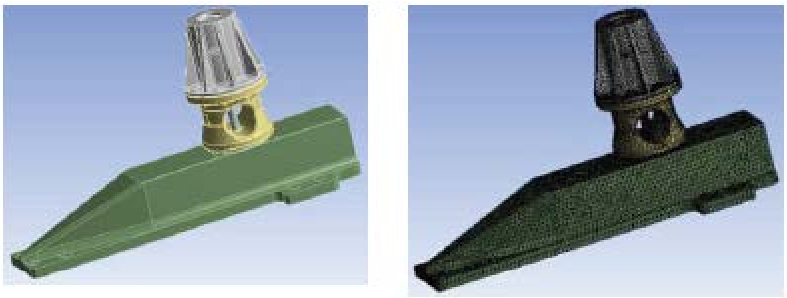

Fig 6: Geometric model

The analysis is solved in two load steps. In first load step, bolt preload is applied on tension bolt using pretension element. In second load step, the external loads (case-3) of constraint phase) are applied on spherical end of fore end adaptor. The stresses found are within the acceptable limits. Maximum stress of 1400 MPa (refer Figure 7) is observed in tension bolt (M250 yield: 1725 Mpa). . Bolt preload augmentation i is found within 10 % of the applied preload and is found acceptable.

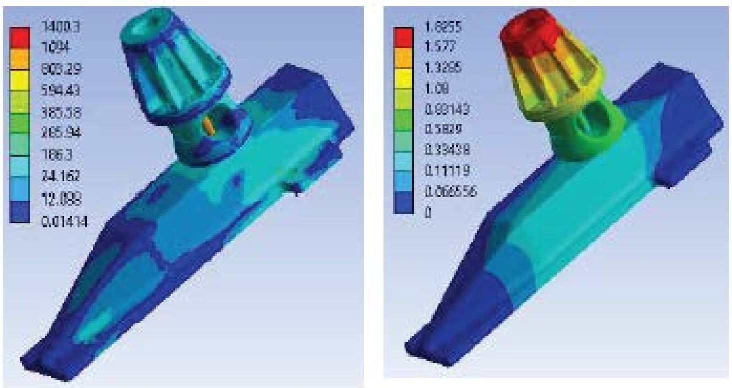

Fig 7: Stress & deformation patterns

E. Qualification Test Programme

As a part of Qualification test programme, following tests were proposed and all of them were conducted successfully.

Integrated Structural Test: Integrated structural qualification test with RLV flight model was conducted (refer Figure 8) to verify the structural adequacy of the system components under worst flight load conditions during case-3 of combined phase and test results are compared with structural FE analysis.

To measure strain at critical locations, two strain gauges are re mounted on cylindrical adaptor or and tension bolt’s preload i is also monitored by load spacer (refer Figure 9 9).

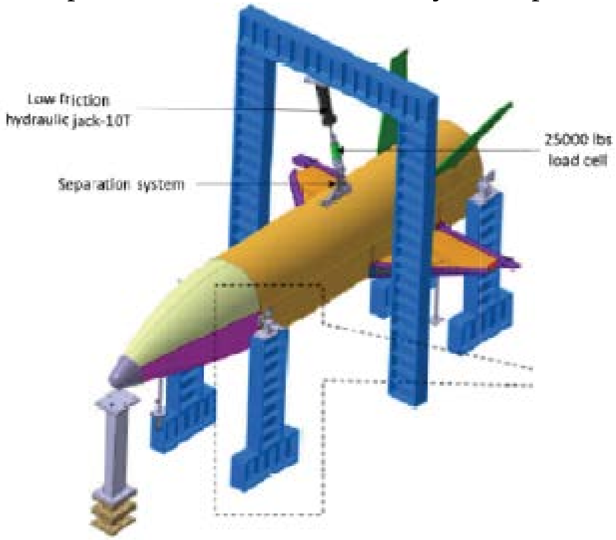

Fig 8: Test set up

Maximum strain values observed at strain gauge locations are found comparable with the FE analysis results (refer Table 3 & Figure 10) and well below the yield strain value (4000 µ for 15CDV6). Preload augmentation (refer Figure 11) is also found benign (within 10% applied preload). Posttest NDT of M250 components is carried out and found satisfactory.

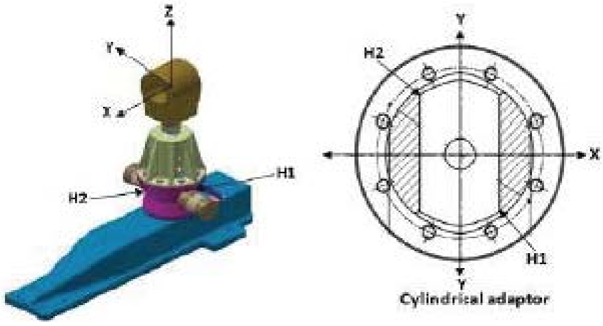

Fig 9: Strain gauge locations

Table 3: Test results

Parameters	Test values	FE analysis results
H1 (µ)	666	682
H2 (µ)	-141	-181
Preload Variation (kN)	1.87	4.83

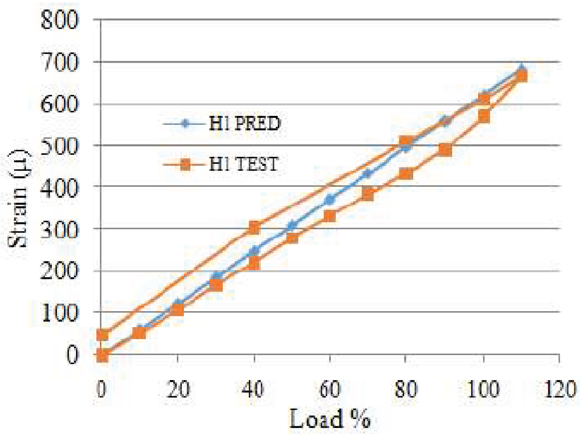

Fig 10: Load vs strain

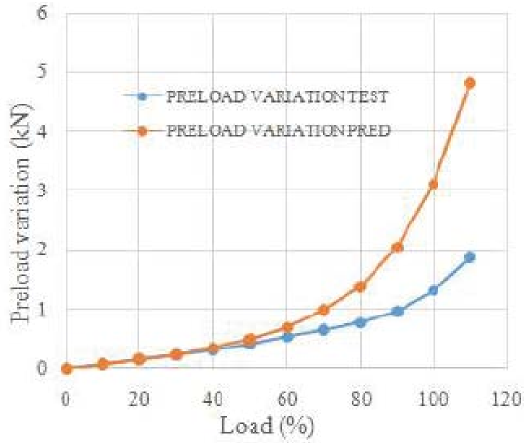

Fig 11: Load vs preload variation

I.

Unit Level Functional Test: Unit level functional qualification test was carried out to demonstrate the redundancy, clean and safe separation of the system under worst inclined load condition during case-4 of constrained phase. The test article consisted of RLV-LEX LEX separation system, hook beam, test adaptor and ground test fixture. The load of 25.5 kN is applied through a counter mass attached to the separation system by wire rope and pulleys at an angle, simulating worst loading direction (refer Figure 12). Two electrical connectors are used for monitoring the separation status and for demonstrating the redundancy. Test conducted by firing single side of pyro bolt cutter.

System separated satisfactorily within 10 ms from command and both the electrical connectors got de-mated mated within 18 ms (refer Figure 14) at 5 pull out angle (Acceptable limit is 15). Pull out angle is captured through test videos. Cut parts of the separated bolt (both upper and lower halves) are contained and captured inside the system (refer Figure 13).

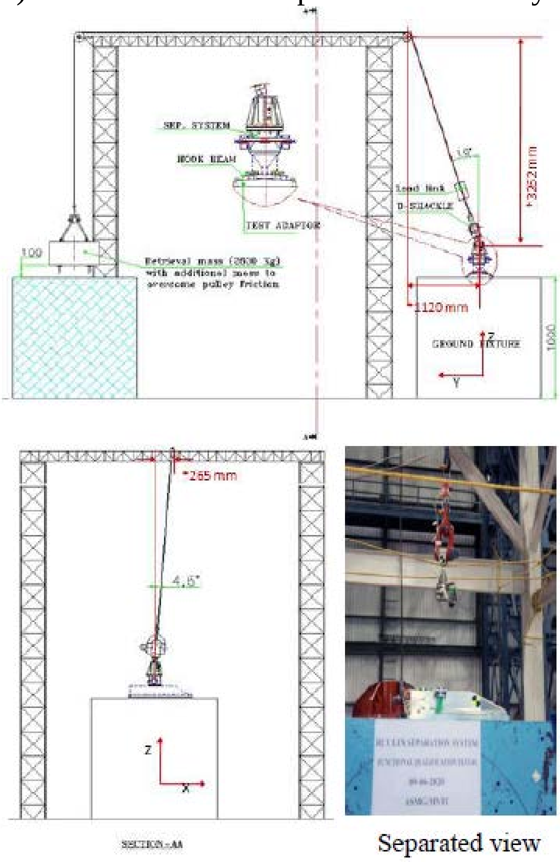

Fig 12: Test set up

The pull out angle is estimated through dynamic simulations using ADAMS and good correlation found with the test results.

Autodesk inventor and exported to ADAMS for separation dynamics analysis (refer Figure 15). Required material properties (steel &aluminum) are assigned to the components for simulating mass and inertia. Joints and contacts are modeled at required interfaces. . Wire rope tension (External load) at a required angle is simulated by modeling a spring of equivalent stiffness. Fixed joints are modeled initially between the separation parts (shear plate & cylindrical adaptor).

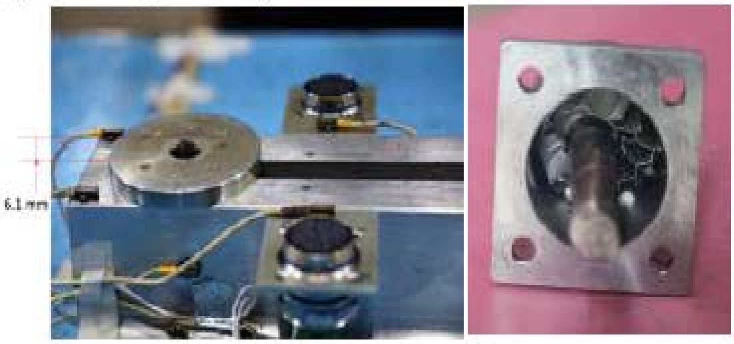

Fig 13: Honeycomb Capturing System

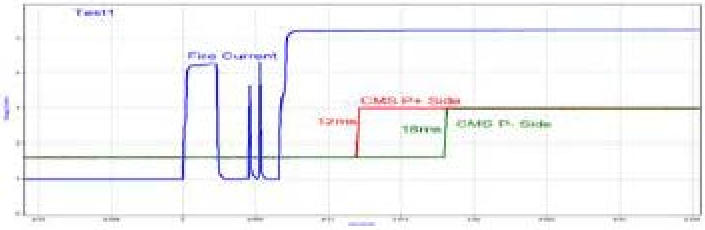

Fig 14: Pyro fire current & connector demating status

Simulation is carried out initially for 100ms to achieve static equilibrium and then separation event is simulated by deactivating the fixed joint. Impact load of cut bolt (upper half) is also simulated after separation. Dynamic analysis is further carried up to total time period of 200 ms. Pull out angle is measured by creating markers at connector and lanyard hinge locations. Pull out angle at the time of connector separation is obtained when the marker reaches to the position (89+10=99 mm) corresponding to the lanyard slackness of 10mm. From the analysis, the worst pull out angle of 5.7 degree is found in Y- side connector and is comparable with test result of 5 degree (refer Figure 16).

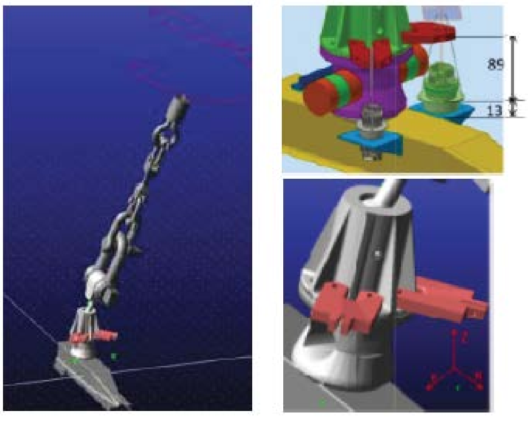

Fig 15: ADAMS simulation

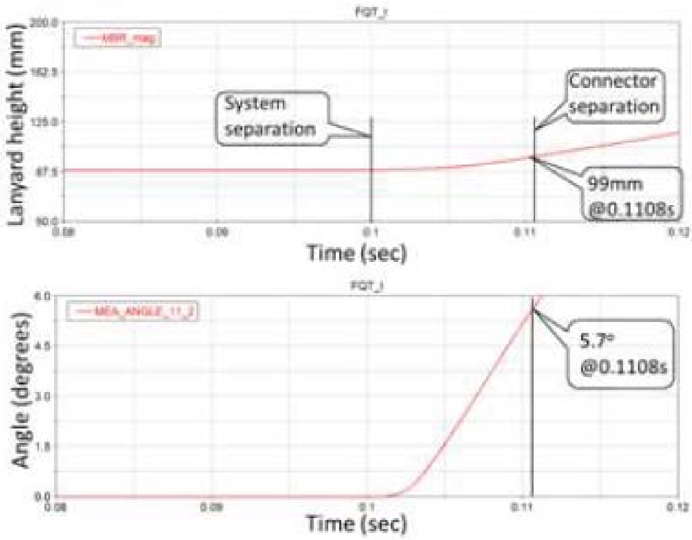

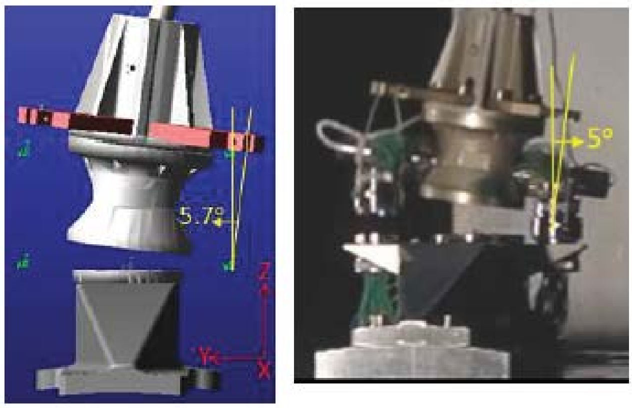

Fig 16: Connector pull out angle, Y- side simulation & test video result

Integrated Functional Test: Integrated level functional qualification test with RLV engineering model is carried out to assess the shock generated due to separation at various critical packages locations. The test article consisted of RLV- LEX separation system, hook beam and RLV engineering model hanging through the overhead crane via steel wire ropes and D-shackle connected to separation system (refer Figure 17).PUF is provided on the ground to capture RLV after release. In order to minimize e the impact, impact a free fall height of 50mm is provided over the PUF.

Fig 17: Test set up

Both sides of pyro bolt cutter are a fired for simulating the maximum shock condition. 11 numbers of shock sensors are a mounted on hook beam, connector brackets and at various critical package locations on RLV engineering model for measuring the shock levels during separation. System separated satisfactorily within 10 ms on giving command to both side pyro bolt cutter and both the electrical connectors de-mated within 18 ms (refer Figure 18). 18 Shock generated due to separation at various critical packages locations is measured and found to be benign (refer Figure 19).

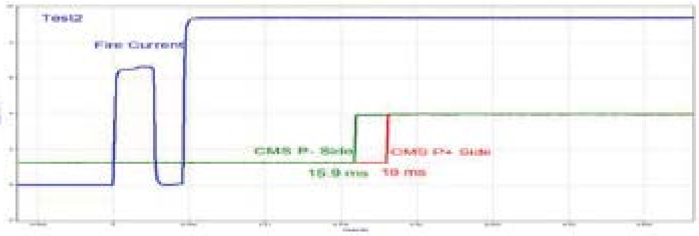

Fig 18: Pyro fire current &connector demating status

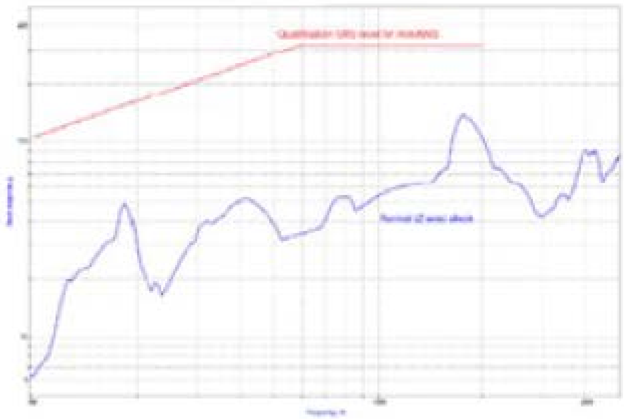

Figure 19: SRS computed for mini AINS

F. RLV-EMT trials

RLV engineering model test trials (EMT-1 & EMT-2) are carried out simulating the combined phase of landing experiment. Passive separation system (without pyro bolt cutter)is used for the trials (refer Figure 20). The maximum external load observed on the separation system during flight is 32.5 kN.

Fig 20: RLV-EMT trials

2. Conclusion

The separation system is designed and fully qualified to meet the structural and functional requirements of RLV-LEX mission. The passive unit of system is successfully demonstrated in the combined phase trials of EMT-1 & 2.

3. Acknowledgement

Authors gratefully acknowledge the continuous support and encouragement given by the members of Aerospace Mechanisms Group, VSSC. Authors are thankful to RLV project for providing relevant inputs for system design. Support provided by the ASMG facility team for carrying out the qualification tests is also highly appreciated.

4. References

[1] Requirement of TDV release system at C.G. location for Autonomous Runway Landing Test, Ref. no: VSSC/ASTS/RLV/Fab/26/17, dtd 09/10/2017.

[2] Critical Design Review document of RLV-LEX separation system, Doc. no: VSSC-MVIT-ASMG-SSMD-DR-1342- 2021, dtd 12/01/2021.

An Approach for Optimized Configuration of Linear Shaped Charge Based Separation Systems

Akhil Srivas KM
Aerospace Ordnance Entity
Vikram Sarabhai Space Centre
Thiruvananthapuram
akhil_sk@vssc.gov.in

Pramod R Nair
Aerospace Ordnance Entity
Vikram Sarabhai Space Centre,
Thiruvananthapuram
prnair.vssc@gmail.com

Mohammad Munis
Aerospace Ordnance Entity
Vikram Sarabhai Space Centre
Thiruvananthapuram

Piyushkanti Kar
Aerospace Ordnance Entity
Vikram Sarabhai Space Centre
Thiruvananthapuram

Alex Thomas
Aerospace Ordnance Entity
Vikram Sarabhai Space Centre
Thiruvananthapuram

Ramachandran V
Aerospace Ordnance Entity
Vikram Sarabhai Space Centre
Thiruvananthapuram

Baby Abraham
Aerospace Ordnance Entity
Vikram Sarabhai Space Centre
Thiruvananthapuram

***Abstract* —Linear shaped charge (LSC) based separation system is widely used in space transportation systems owing to its inherent advantages and reliability. They are quick, controllable and generally mass effective in nature, compared to its alternatives, which makes it one of the prime candidates for any separation system requirement. The challenging task of designing a Linear Shaped Charge (LSC) based separation system is to arrive at an optimum configuration which induces minimal shock to ongoing stage, least debris and avoidance of secondary cracks, meeting all the vehicle structural constraints. There was a requirement to develop an optimum configuration of separation system for a medium payload capacity launch vehicle with low shock transfer to ongoing stage, lower mass and a configuration aiding easy assembly thereby reducing integration time. Separation system was configured retaining the heritage of proven systems; at the same modifying certain system elements viz target, LSC support and LSC backup. Using stiffness based design, the support structure is configured to have minimum mass; maintaining post function hardware integrity. It can substantially reduce time & resources avoiding the traditional trial and error route. Geometry of target plate is also important parameter, which if not designed properly, can cause shock amplification leading to crack/debris post separation. Shock transferred to ongoing stage can be drastically reduced by judicial positioning of the LSC. Analytical tools such as hydrocode based softwares were also used for validating the design and confirming the design margins. An optimized configuration of LSC based separation system was arrived and optimized based on the test observations. The system was successfully tested functionally meeting all objectives.**

Keywords— Shaped Charge, Separation System, Secondary Crack

1. Introduction

Linear shaped charge (LSC) based separation system is widely used in space transportation systems owing to its inherent advantages and reliability. They are quick, controllable and generally mass effective in nature, compared to its alternatives, which makes it one of the prime candidates for any separation system requirement. However, the shock generated from pyro systems during functioning, debris and maintaining post fire integrity are few disadvantages of using these systems in launch vehicles and satellites.

Basic design requirements of LSC based separation system are to induce minimal shock to ongoing stage, post-test hardware integrity, joint stiffness, minimum tip-off rate, minimum disturbance to ongoing stage, collision free separation, avoidance of secondary crack and low system mass. Critical parameters of LSC based separation system viz Local mass, stiffness, target and other hardware configuration, joints etc. affects this shock wave absorption / propagation, debris and post fire integrity considerably. The explosive shock generated by LSC functioning is a high frequency wave pulse with high acceleration amplitude. Often electronic packages, relays, etc. don’t survive to this pyro shock, if placed close to the separation plane. Hence arriving at an optimum configuration is a key for design of linear shaped charge based separation system. Also, due to lack of in-depth understanding and complexity of the problem, a combination of analytical calculation, software-based simulation and experimental studies is the most effective way to verify the effectiveness of the configuration.

2. System Configuration

The system configuration includes (i) Target of separation system, which carries the flight load with required stiffness and has to be separated by LSC upon actuation, (ii) LSC Support which accommodates the LSC and (iii) the Backup element of LSC. Target plate should have enough stiffness to resist crack generation and propagation induced due to explosive driven shock. Target Geometry should be such that it doesn’t induce shock wave interference /amplification. A recess on target plate for LSC is normally provided, thereby eliminating, the need for a separate LSC support element. However, such design may lead to stress raiser points leading to secondary cracks. A separate support fastened to target can reduce shock transfer, as at each joints shock is attenuated. The backup for the LSC plays a crucial role in absorbing the explosive energy. Suitability arriving the thickness and cross section, the majority of the residual explosive energy of LSC can be diverted to bending of the backup structure resulting in minimal shock on to the primary structure. This reduces the probability of secondary cracks emerging on the primary structure which may lead to undesired debris formation. Using stiffness-based design, the support structure can be configured to have minimum mass however maintaining post functional hardware integrity.

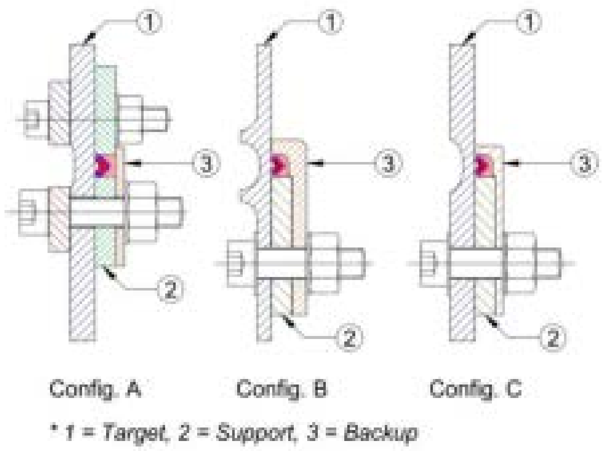

Fig 1. Cross section of System Configurations

Typical configurations of LSC based separation systems are given in figure 1. Configuration A is most common and used in space transportation vehicle and has very good heritage. Target plate is an Aluminium alloy having a curved groove at the location opposite to the LSC, for ensuring the fracture along the required plane. LSC is housed in cavity formed between top and bottom support. LSC support is held in position by fasteners assembled to Target plate. Backup plate made of stainless steel support LSC. Additionally, two external stiffener structures are also provided to improve stiffness of target and attenuate the shock response.

For launch vehicle of higher diameter and payload capacity, owing to higher cutting thickness requirement, LSC of higher charge caliber is necessary. For higher caliber LS based separation system the configuration A is best suited. Requirement was projected for designing LSC based separation system for medium sized launch vehicle. For this application a new separation system design, (Configuration B) which impart lower shock to ongoing stage, lower mass and which aids easy assembly (lower integration time) was envisaged. Configuration B gets rid of the upper Support element and the Backup is shaped to do that function. The external stiffeners are made integral to the Target. To reduce load on fasteners, backup thickness and Target thickness was maintained same. Flat panel level and ring level tests were carried out with configuration B. However, during ring level functional test secondary cracks and undesirable debris were noticed. Based on the observation and critical analysis, configuration C was envisaged. Subsequently flat panel test, curved panel test and ring level tests were conducted successfully meeting all objectives were carried out.

3. Results & Discussion

As per accepted development philosophy, initially flat panel tests were done with Configuration B and results were compared with configuration A. Clean separation achieved and no debris / secondary crack were observed. (Fig. 2 & 3).

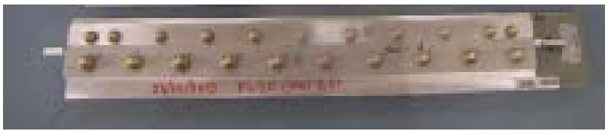

Before Test After Test

Fig 2. Flat Panel Test – Confign. A

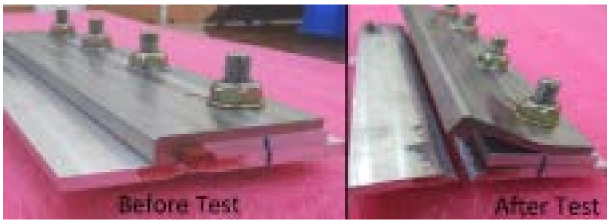

Fig 3. Flat Panel Test – Confign. B

Based on the confidence gained, test was done at ring level simulating actual flight requirement. (Fig. 4).

Test result shows severance of Target and separation, however breakage of separation rings with multiple fracture was observed. Debris of undesirable sizes were generated due to the multiple fracture and hence clean separation could not be achieved (Fig. 5).

Fig 4. Subscale Ring Level Test

Crack generated at the edge of inbuilt stiffener

Fig 5. Multiple fracture on Target

Post-test observation revealed the following. Jet penetration signature and shock severance pattern suggests normal functioning of LSC. However, after the severance, the pressure generated by the LSC has deformed the target as well as the washer of the fasteners holding target ring and backup. This was understood to be due to higher Stiffness of Backup; as the backup was made of Stainless steel and thickness same as target. Target ring, being of lower stiffness than backup, absorbed more energy and deformed considerably leading to multiple cracks.

Based on studies it is understood that stiffness ratio between target and backup is a key parameter that determines energy sharing and need to be addressed appropriately for design of LSC based separation systems. On calculation, it was noticed that Local stiffness ratio along the circumference, for configuration B was much higher compared to the Configuration A (Fig. 6). It is also found that local stiffness ratio frequency is directly proportional to fastener pitch and lower at the ends.

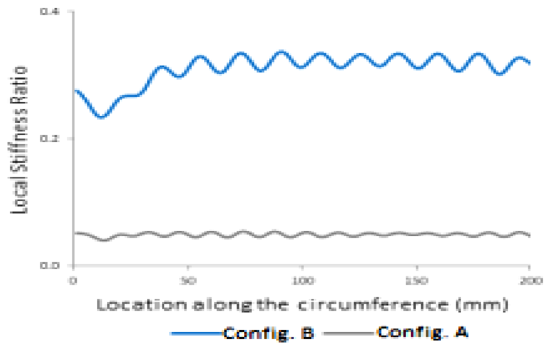

Fig 6. Stiffness Ratio variation

Another point was the understanding that design should be such that the backup should absorb maximum energy with minimum load on to the assembly fasteners. Studies also revealed that beyond certain limit of stiffness ratio, the energy transfer to Target becomes dominant and can result in secondary cracks in both separated structures.

Based on the studies, the stiffness ratio was optimized by reducing the thickness of backup and increasing the global thickness of the Target (configuration C). For initial trials, stiffness ratio was kept closer to config. A is a flight proven configuration (Fig. 8).

Also, critical analysis of posttest observation revealed generation of crack at the base of inbuilt stiffener provided on the target (Fig. 5). This shows that the discontinuity in the target structure near the separation plane leads to shock amplification leading to fracture. Hence for configuration C, inbuilt stiffness was avoided, smooth curve was provided on the cutting plane and global thickness was improved.

Based on the test observation configuration B was modified/ improved. Thickness of backup and global target thickness was modified based on stiffness ratio. It was also found that local stiffness of backup was much less at the ends. Thus, average Stiffness of backup was reduced by increasing backup segments. External stiffener on target was avoided. Refer configuration C (Fig. 7).

The Configuration C was tested in flat panel level, curved panel level, subscale ring level and full-scale ring level. Clean separation was observed in all cases. No debris or secondary cracks were noticed. Close observation of the fastener joint shows minimal load acting on it, compared to the generic configuration (Configuration A).

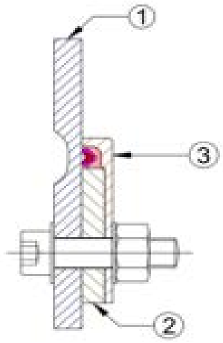

Figure 7. Configuration C

One of the main objectives was to design system which transfers minimum shock to ongoing stage. Analyses indicated that shock would be less for configuration C. This aspect was confirmed by shock measurement carried out to measure radial and axial shock and values were compared with configuration A.

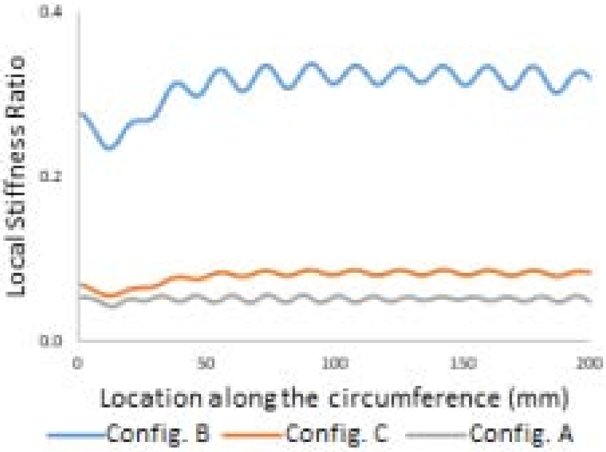

Figure 8. Stiffness Ratio of all 3 configurations

The test results clearly conclude a lower shock level (Fig. 9) to ongoing stage for Configuration C. This is due to fact that in configuration C, the support for LSC at the top is not a part of the target and is integral to the backup. Hence post separation, the shock pulse generated by LSC is not directly transferred to ongoing stage via top support. In configuration C, LSC top support is eliminated and LSC is housed between is bottom support and backup, hence the no element is connecting LSC to ongoing stage post separation. This is one of the main advantages of Configuration C.

Figure 9. Subscale test - Configuration C

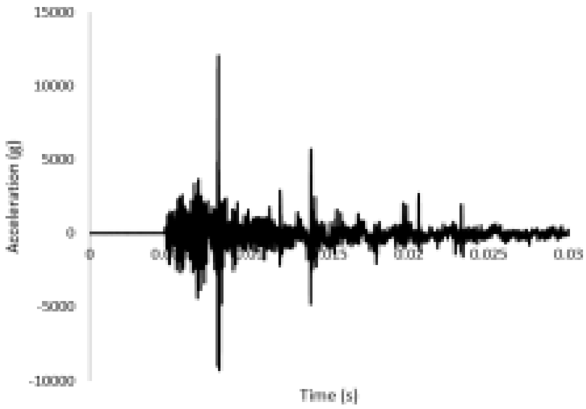

Figure 10. Shock data for Full Scale Test

4. Conclusion

A design of an optimum LSC based separation system which induces minimum shock to ongoing stage, lower mass and aiding easy assembly was arrived. From test results it can be concluded that the stiffness ration of backup to target is an important parameter to be addressed for design of separation system. It can substantially reduce time & resources avoiding the traditional trial and error route. Target geometry need to be suitably configured without discontinuity to avoid shock amplification. Shock imparted to ongoing stage can be reduced to a greater extends by suitably configuring the separation system components.

5. Acknowledgement

With great gratitude we would like to acknowledge Shri. Sheeju Chandran for his active role in reviewing the paper as well as valuable advice and feedback on the topic. Authors acknowledge the support from the Space Ordnance Test & Evaluation Division (STED) & Rocket Systems Testing Division (RSTD) of VSSC for providing necessary support for carrying out the experiments.

6. References

[1] Shete Mayuresh Kailas, “A Study on Target Material Grain Direction Sensitivity on Cutting Capability of FLSC for Rocket Stage Separation Applications”

[2] MIL-STD-810F, 1 January, 2000; “Test Method Standard for Environmental Engineering Considerations and Laboratory Tests” Sean P. Keon, 44th

[3] AIAA/ASME/SAE/ASEE Joint Propulsion Conference & Exhibit, “Pyrotechnic Shock Testing: Real Test Laboratory Experiences at EBA&D”, 21 - 23 July 2008, Hartford, CT

Modeling and Simulation of Mechanisms

Modified Transmission Map Estimation with Gradient Domain Guided Image Filtering for Single Image Dehazing

Anshal Sinha
Dept. of Electrical Engineering
Indian Institute of Technology
Kanpur
anshal.sinha.11@gmail.com

Teena Sharma
Dept. of Electrical Engineering
Indian Institute of Technology
Kanpur
tee.shar6@gmail.com

Pooja Agrawal
School of Robotics
Defence Institute of Advanced
Technology
Pune
pooja_agrawal@diat.ac.in

Nishchal K. Verma
Dept. of Electrical Engineering
Indian Institute of Technology
Kanpur
nishchal@iitk.ac.in

***Abstract*—A dependable vision system must be capable of dealing with adverse weather conditions like haze. The phenomenon of haze is observed when there is absorption and scattering of light because of the presence of turbid medium present in the atmosphere. Therefore, the ability to produce enhanced images while having a robust system to be able to tackle fickle and difficult weather conditions is paramount to scientific research and various Defense applications. A novel method for single image dehazing has been proposed in this paper for the removal of haze from the input images. First, the input hazy image which is in RGB domain is converted to the HSV domain. Simultaneously, an image prior, i.e., Dark Channel Prior (DCP) whose intensity gives an estimate of the thickness of haze, is employed on input hazy image. After calculating the DCP and HSV color channels, the modified transmission map function is estimated for the input hazy image considering the saturation and value channels. Furthermore, the Gradient Domain Guided Image Filtering (GDGIF) is utilized so that the details in the input image can be preserved. Once the image has been filtered, the global atmospheric light is calculated using DCP method. Thereafter, a haze-free image is obtained using the atmospheric scattering model upon which GDGIF is applied again. The experiments have been extensively performed on various benchmarked datasets. Through rigorous experimentation, it can be concluded that the proposed methodology effectively maintains the image details and visual realism while generating haze-free images**

Keywords: Image dehazing; Dark channel prior; Guided image filtering; Transmission map.

1. Introduction

Computer vision is widely utilized to gain high-level understanding from images and videos, such that their applications can automate the tasks performed by human visual system. In the field of Defense, it can help to gather and retrieve information that can be helpful in logistical and operational missions. For such applications, there is a need to extract accurate images. However, images in outdoor environment, exposed to adverse weather conditions, can lead to loss of information. One of them is haze. It is a phenomenon caused due to absorption and scattering of light by particles and droplets in the atmosphere, i.e., the turbid medium. A ray of light irradiated by a point of an image is attenuated before it reaches the camera lens, also along the path it is further blends with airlight, which is the light from the atmospheric particles. Since the scattering of light is subject to object distance from the camera, contrast and colour fidelity degrade due to loss of information while travelling the distance. A high-quality image is imperative for vision-based applications [1-16] for the Defense establishments.

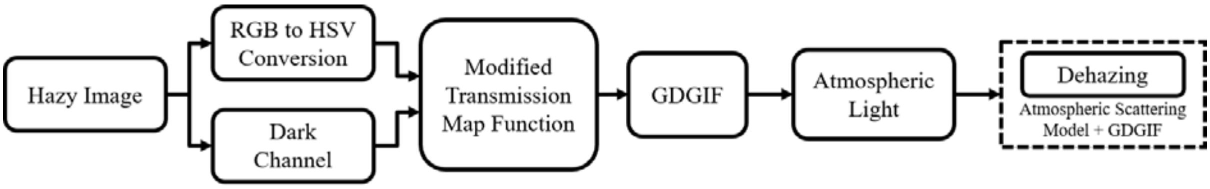

Figure 1. Flowchart: Proposed methodology

Image dehazing algorithms can be grouped together either on the basis of number of images or the requirement of images attributes; with each having their own merits and demerits. In the past, due to technical limitations, vision-based algorithms required multiple images to be able to generate desirable results. Among these methods, polarization method proposed by Schechner et al. [17,18], where researchers were able to recover the contrast and correct colour of the scene, by adjusting the polarizer and capturing multiple images was quite famous. Thereafter, many other popular methods were devised to obtain a haze-free image, like Narasimhan and Nayar [19,20], Kopf et al. [21], etc. Single image dehazing is a practical alternative as it requires less information, but that is what makes it a complicated process. Various such algorithms have been proposed which utilize certain attributes of the input images directly like saturation, contrast [22], and histogram [23]. Based upon certain priors, these algorithms estimate the true scene transmission. Narasimhan et al. proposed atmospheric scattering model which aimed at replicating how hazy images are formed. Fattal [24,25], Tan [26], He et al. [27], Meng et al. [28] are some of the other researchers who proposed methods to obtain transmission maps and dehazed images by utilizing certain priors. Outstanding success has been displayed by Convolutional Neural Networks (CNNs) in this field. Zhu et al. [29], Cai et al. [30], Ren et al. [31], Li et al., etc. have proposed CNN based dehazing models. Their drawback though, is that their architecture is complex, and heavily reliant on training datasets which are cumbersome and difficult to create.

A novel image dehazing technique has been discussed in this paper, and its initial step involves converting the colour domain of the input hazy image from RGB to HSV, while simultaneously DCP is calculated. After calculating the DCP and HSV colour channels, the modified transmission map function is estimated for the input hazy image. This function utilizes the saturation channel and the value channel, along with the dark channel. Need to modify the traditionally used transmission map function arose because it frequently resulted in overly saturated and dehazed images. Once the transmission map is calculated, the Gradient Guided Image Filtering (GDGIF) [32] is used to preserve the details of the image. Once the image has been filtered, the global atmospheric light is calculated using DCP method. Thereafter, the atmospheric scattering model is used to come up with a haze-free image. Finally, the GDGIF is applied again so that images are visually more appealing without losing the textural information, especially around edges.

2. Proposed Methodology

This section of the paper goes through the implementation of the proposed methodology in detail, and which has been shown in the flow chart at Fig. 1.

A. RGB to HSV Conversion

The colour domain of the input hazy image is converted from RGB to HSV image domain. In the proposed method, two channels, i.e., saturation and value from the HSV image domain have been considered to get accurate results. They have been considered because they are most susceptible to be influenced by presence of haze amongst the three channels. The amount of light reflected by an object is specified by the value channel which is greatly affected by attenuation. Whereas the purity of colour whose measurement is given by the Saturation channel, is reduced upon addition of another pigment to the foundational colour. Haze acts as that pigment, which results in decrease in the saturation. Considering an input image, I_h (ϕ), where ϕ stands for pixel location (m, n), with the intensity of its RGB image domain as $\{\mathrm{R}, \mathrm{G}, \mathrm{B}\} \in [0, E_{\alpha_0}]$ The value channel $\left(I_h^{\mathrm{V}}(\phi)\right)$ and saturation channel $\left(I_h^{\mathrm{S}}(\phi)\right)$ of the HSV colour space are obtained by

$$I_h^{\mathrm{V}}(\phi) = \frac{E_{\alpha_1}(\phi)}{E_{\alpha_0}} \qquad (1)$$

and

$$I_h^{\mathrm{S}}(\phi) = \begin{cases} \dfrac{E_r(\phi)}{E_{\alpha_1}(\phi)} & E_{\alpha_1}(\phi) > 0 \\ 0 & \text{otherwise} \end{cases} \qquad (2)$$

Where $E_{\alpha_1}(\phi) = \max(R, \mathrm{G}, \mathrm{B})$ and $E_r(\phi) = E_{\alpha_1}(\phi) - E_{\alpha_2}(\phi)$ for $E_{\alpha_2}(\phi) = \min(\mathrm{R}, \mathrm{G}, \mathrm{B})$ at pixel location (ϕ).

The thickness of haze is affected by depth. In areas of input image where there is fine haze the value of dark channel approaches zero. This is so because the areas with very little haze have a minimum intensity value close to zero. Whereas the saturation channel's intensity is nearly 1 as the haze is finer so there will be more impurity. Converse will be true for the values of dark channel and saturation channel in areas with greater haze. Consequently, if both channels are used together, a better insight about the thickness of the haze can be obtained.

B. Dark Channel

The DCP required for further calculations is obtained by

$$I_h^{dark}(\phi) = \min_{i \in K(\phi)} \left(\min_{L_c \in (\mathrm{R,G,B})} I_h^{L_c}(\phi) \right) \qquad (3)$$

Where, $L_c$represents {R, G, B} colour channels of input hazy image $I_h(\phi)$, and a local patch which is centred around pixel (m, n) is defined as K(ϕ), where ϕ stands for (*m*,*n*). A local patch of size 3×3 has been selected for this paper. Patch size affects the estimation of the transmission map, as a larger patch size would result in darker channel, and a smaller patch size would result in a more saturated recovered scene image.

According to dark channel, airlight is the determining factor for the intensity of dark or low pixels. This directly produces hazy transmissions, thus resulting in inaccurate image depth measurement. Therefore, utilisation of saturation and value channels is proposed to be able to estimate the haze more accurately.

C. Modified Transmission Map Function

Conventional atmospheric scattering model states that the transmission channel T(ϕ) is expressed as

$$T(\phi) \; = \; e^{-\beta . I_h^{dark} \, (\phi)} \qquad (4)$$

Where, β is the coefficient of scattering for the atmosphere and $I_h^{dark}\,(\phi)$ stands for the image scene depth. This function uses dark channel for the purpose of haze estimation, which is why the map obtained shows little variance in relation to the depth of the scenery. Therefore, haze thickness is exaggerated. On top of that it also involves a parameter β which requires manual adjustment depending on the images, requiring additional information to estimate haze thickness. As suggested in [29], the saturation and value channels of hazy input image are more affected than the hue channel. Thus, modified transmission map function is

$$t(\phi) = exp\left(-\frac{I_h^{dark}\,(\phi)}{exp\left(\left(I_h^{S}(\phi)\right)^{4} \times \left(I_h^{V}(\phi) + I_h^{S}(\phi)\right)^{0.01}\right)}\right) \qquad (5)$$

Where, $t(\phi)$ is the modified transmission map estimation function.

From the above section, it is known that the presence of haze in the scene image leads to reduction in saturation value, therefore such regions will have the value of saturation approximately zero, and the denominator value of (5) closer to one, thus hinging the estimation of transmission map on dark channel. Conversely, when estimating the transmission map for regions with fine haze, the saturation value will be higher. And that makes this modified transmission map more sensitive to the presence of finer haze, thus preventing over-enhancement of the image. The value channel is also present in this function where it maintains the colour fidelity and contrast information.

D. Gradient Domain Guided Image Filter

While using the DCP method, there are chances that halo may be encountered near the edges. The size of the patch dictates whether halo is encountered or over-saturation of the recovered scene image. In the earlier section modified transmission map estimation function was discussed which is capable of handling the over-saturation of image. This section discusses the usage of Gradient Domain Guided Image Filter (GDGIF) to take care of halo effects near the edges, thus preserving the edges of the recovered scene image. The resultant image upon the application of the filter is obtained using.

$$I_{Filter} \; = \bar{a}_{\phi} . G(\phi) + \bar{b}_{\phi} \qquad (6)$$

Where, $\bar{a}_{\phi}$ and $\bar{b}_{\phi}$ are the mean values of $a_{\phi'}$ and $b_{\phi'}$ in the window$\Omega_{\zeta_1}(\phi')$, centred around the pixel location ϕ and with the radius ζ_1, are calculated using

$$\bar{a}_{\phi} \; = \frac{1}{\left|\Omega_{\zeta_1}(\phi)\right|} \sum_{\phi' \in \Omega_{\zeta_1}(\phi)} a_{\phi'} \qquad (7)$$

$$\bar{b}_{\phi} \; = \frac{1}{\left|\Omega_{\zeta_1}(\phi)\,\right|} \sum_{\phi' \in \Omega_{\zeta_1}(\phi)} b_{\phi'} \qquad (8)$$

and, $\left|\Omega_{\zeta_1}(\phi')\,\right|$ is the cardinality of $\Omega_{\zeta_1}(\phi')$.

The filter is great at dealing with halo artefacts, and that is the reason why it has been used twice in the proposed method. An edge-preserved smooth image would be the output image obtained using the proposed method.

E. Atmospheric Light

The transmission map that was obtained using the modified function (5) is further utilized to obtain the atmospheric light (L_a) as

$$L_a = \max_{i \in ((\phi)|t(\phi)<t_0)} I_h(i) \qquad (9)$$

Where, t_0 is the is the threshold for medium transmission, which for the purposes of this paper has been chosen as 0.1

F. Dehazing

Attenuation and airlight, due to presence of haze, combined results in a hazy image, and is given as

$$I_h(\phi) = I_c(\phi)\,.\,t(\phi) + L_a\big(1 - t(\phi)\big) \; (10)$$

Where, $I_c(\phi)$ is the haze-free image. $I_c(\phi)\,.\,t(\phi)$ defines the attenuation, and $L_a(1 - t(\phi))$ defines airlight. These equations imply that both these factors are impacted by $t(\phi)$. Finally, to obtain a haze-free image (I_c), Eq. (10) is rearranged as

$$I_c(\phi) = \frac{I_h(\phi) - L_a}{t'(\phi)} + L_a \,. \qquad (11)$$

The output dehazed image is then passed through GDGIF to make sure that the images are visually more appealing without losing the textural information, especially around edges.

3. Results

After exhaustive experimentation, the results of the proposed method vis-a-vis other avant-garde methods has been enumerated in this section. The specification of setup used is Windows 10 64-bit Operating System, Intel (R) Core (TM) i5-7300 HQ CPU in MATLAB2021a. The avant-garde methods that have been selected as the comparative methods are Dark Channel Prior (DCP)

Table 1. Comparison on HSTS dataset [34]

Performance metrics	**DCP** [27]	**BCCR** [28]	**CAP** [29]	**DehazeNet** [30]	**GMAN** [31]	**Proposed Method**
PSNR [35]	18.9331	11.4926	11.8863	14.2192	10.0533	21.06526
SSIM [36]	0.6917	0.5971	0.6126	0.7334	0.5353	0.87679

Table 2. Comparison on SOTS indoor images from RESIDE dataset [34]

Performance metrics	**DCP** [27]	**BCCR** [28]	**CAP** [29]	**DehazeNet** [30]	**GMAN** [31]	**Proposed Method**
PSNR [35]	11.8304	17.0468	18.9634	21.1671	28.0794	20.1606
SSIM [36]	0.6346	0.7938	0.8524	0.8741	0.9664	0.8671

Table 3. Comparison on SOTS outdoor images from RESIDE dataset [34]

Performance metrics	**DCP** [27]	**BCCR** [28]	**CAP** [29]	**DehazeNet** [30]	**GMAN** [31]	**Proposed Method**
PSNR [35]	15.0527	15.5109	18.1236	21.760	18.8861	20.7125
SSIM [36]	0.6993	0.7575	0.7622	0.8570	0.8548	0.9020

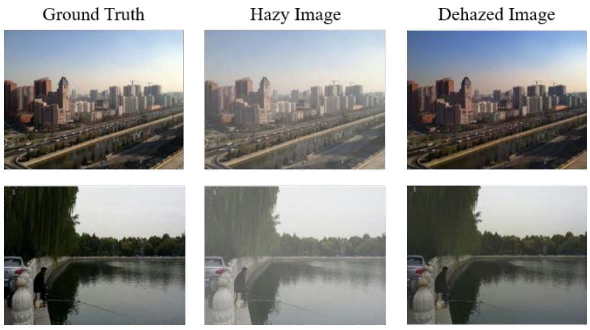

Figure 2. Dehazing results using proposed method.

Boundary Constraint and Contextual Regularization (BCCR), Color Attenuation Prior (CAP), DehazeNet, and Generic Model Agnostic Network (GMAN) [33]. Datasets that have been utilized for the experimental analysis, results, and the performance metrics used to compare the various methodologies have been explained in a detailed manner in the following subsections.

A. Datasets

The dataset that has been employed in this paper is the RESIDE [34] dataset. From the RESIDE dataset 500 indoor and outdoor Synthetic Objective Testing Set (SOTS) images, and 10 real-world synthetic hazy images of the Hybrid Subjective Testing Set (HSTS) have been utilised for experimentation.

Figure 3. Visual comparison of dehazing results on images from HSTS dataset [32].

B. Performance Metrics

The quality of images is a personal assessment measure which is based on the subjective analysis. For commensurate comparison, two performance measures have been used, i.e., Peak Signal to Noise Ratio (PSNR) [35] and Structural SIMilarity (SSIM) index [36]. PSNR is an image quality measure and its higher value suggests that the hazy image has been dehazed to match the clear image as closely as possible, and SSIM is the difference in the perception amongst the images. SSIM value ranging from 0 to 1, a higher value, provides the perceived similarity of luminance, contrast, and saturation.

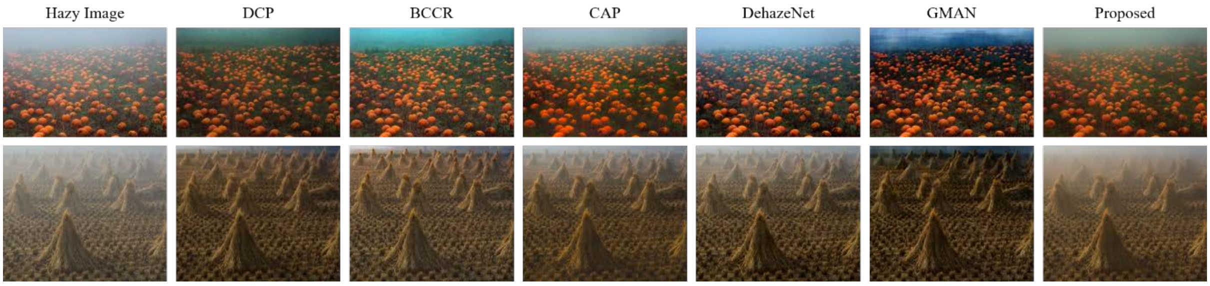

Figure 4. Comparison of results on naturally hazy images

C. Results

After performing exhaustive experiments with the proposed methodology, its benefits are abundantly clear vis-à-vis the other methods. Tables I, II, and III propound the results of the analysis performed on the proposed method while comparing it with the results of the other selected methods on the same dataset. Figs. 2 and 3 show the comparative visual results by showing the dehazed image obtained by the proposed method vis-à-vis the other methods. The comparative results on natural hazy images popularly used in literature is shown in Fig. 4. The comparative performance measures elucidated in Tables I-III establishes the superiority of proposed methodology over the methods being used hither to fore.

4. Conclusion

The proposed method utilizes an altered function based upon value, saturation, and dark channel to obtain a transmission map, and uses gradient domain guided image filter at multiple stages to retain the input details. Over-saturation or over-intensification effects are avoided while successfully extracting haze-free image. The finally obtained images are images which are visually more appealing without losing the textural information, especially around edges. Although results of deep-learning based models are comparable, the proposed method edges them by virtue of being an unsupervised method not necessitating training, which establishes the efficiency and thus its suitability in dehazing applications

5. Reference

[1]. Huang, S. C.; Chen, B. H. & Cheng, Y. J. An efficient visibility enhancement algorithm for road scenes captured by intelligent transportation systems. IEEE Trans. Intell. Transp. Syst., Oct. 2014, vol. 15, no. 5, pp. 2321–2332. doi: 10.1109/TITS.2014.2314696.

[2]. Chaudhry, A. M.; Riaz, M. M. & Ghafoor, A. A framework for outdoor RGB image enhancement and dehazing. IEEE Geosci. Remote Sens. Lett., Apr. 2018, vol. 15, no. 6, pp. 932–936. doi: 10.1109/LGRS.2018.2814016.

[3]. Shih, K-T. & Chen, H-H. Exploiting perceptual anchoring for color image enhancement. IEEE Trans. Multimedia, Feb. 2016, vol. 18, no. 2, pp. 300–310. doi: 10.1109/TMM.2015.2503918.

[4]. Wang, T.H.; Chiu, C-W; Wu, W-C; Wang, J-W; Lin, C-Y; Chiu, C-T & Liou, J-J. Pseudo-multiple-exposure-based tone fusion with local region adjustment. IEEE Trans. Multimedia, Apr. 2015, vol. 17, no. 4, pp. 470–484. doi: 10.1109/TMM.2015.2403612.

[5]. Li, S.; Tao, Z.; Li, K. & Fu, Y. Visual to text: Survey of image and video captioning. IEEE Trans. Emerg. Topics Comput. Intell., Aug. 2019, vol. 3, no. 4, pp. 297–312. doi: 10.1109/TETCI.2019.2892755.

[6]. Dua, H.; Sharma, T.; Agarwal, P. & Verma, N. K. An efficient algorithm for image haze removal in outdoor environment. In International Conference on Computational Intelligence: Theories, Applications and Future Directions (ICCI-2017), Springer, India, Dec. 6-8, 2017. doi: 10.1007/978-981-13-1135-2_25.

[7]. Sharma, T.; Rajurkar, S. K. D.; Molangur, N.; Verma, N. K. & Salour, A. Multi-faced Object Recognition in an Image for Inventory Counting. In International Conference on

Computational Intelligence: Theories, Applications and Future Directions (ICCI-2017), Springer, India, Dec. 6-8, 2017. doi: 10.1007/978-981-13-1135-2_26.
[8]. Sharma, T. & Verma, N. K. Adaptive Interval Type-2 Fuzzy Filter: An AI Agent for Handling Uncertainties to Preserve Image Naturalness. IEEE Trans. On Artificial Intelligence, May 2021. doi: 10.1109/TAI.2021.3077522.
[9]. Sharma, T.; Agarwal, I. & Verma, N. K. CSIDNet: Compact Single Image Dehazing Network for Outdoor Scene Enhancement. Multimedia Tools and Applications, Springer, July 2020, vol. 79, pp. 30769-30784.
[10]. Bhola, A.; Sharma, T. & Verma, N. K. DCNet: Dark Channel Network for Single Image Dehazing. Machine Vision and Applications (MVAP), Springer, March 2020, vol. 32, no. 62. doi: 10.1007/s00138-021-01173-x.
[11]. Sharma, T.; Shah, T. & Verma, N. K. A Review on Image Dehazing Algorithms for Vision based Applications in Outdoor Environment. In 49th Annual IEEE AIPR 2020: Trusted Computing, Privacy, and securing Multimedia, Washington D.C., U.S.A., Oct. 13-15, 2020. doi: 10.1109/AIPR50011.2020.9425261.
[12]. Sharma, T.; Agarwal, I. & Verma, N. K. Transmission Map Estimation Function to Prevent Over-Saturation in Single Image Dehazing. In International Conference on Deep Learning, Artificial Intelligence and Robotics, 2019, Malviya National Institute of Technology (MNIT), Jaipur, India, Dec. 07-08, 2019. doi: 10.1007/978-3-030-67187-7_16.
[13]. Bhanu T.; Sharma, T. & Verma N. K. Image Dehazing for Object Recognition using Faster RCNN. In 2018 IEEE World Congress on Computational Intelligence (WCCI 2018), July 8-13, 2018. doi: 10.1109/IJCNN.2018.8489280.
[14]. Sharma, T. & Verma, N.K. Estimating Depth and Global Atmospheric Light for Image Dehazing Using Type-2 Fuzzy Approach. IEEE Transactions on Emerging Topics in Computational Intelligence, 2020. doi: 10.1109/TETCI.2020.3032970.
[15]. Agrawal, P.; Sharma, T. & Verma, N. K. Supervised approach for object identification using speeded up robust features. International Journal of Advanced Intelligence Paradigms. Feb. 2020. vol. 15, no. 2, pp. 165-182. doi: 10.1504/IJAIP.2020.105142.
[16]. Sharma, T.; Verma, N. K. & Sudhakaran, S. Fuzzy based Pooling in Convolutional Neural Network for Image Classification. In International Conference on Fuzzy Systems (FUZZ IEEE 2019), JW Marriot New Orleans, June 23-26, 2019. doi: 10.1109/FUZZ-IEEE.2019.8859010.
[17]. Schechner, Y. Y.; Narasimhan, S. G. & Nayar, S. K. Instant dehazing of images using polarization. In Proc. IEEE Conf. Comp. Vis. Pattern Recognit., Kauai, HI, USA, Dec. 8–14, 2001. doi: 10.1109/CVPR.2001.990493.
[18]. Schechner, Y. Y.; Narasimhan, S. G. & Nayar, S. K. Polarization-based vision through haze. Appl. Opt., Jan. 2003, vol. 42, no. 3, pp. 511–525. doi: 10.1364/AO.42.000511.
[19]. Narasimhan, S. G. & Nayar, S. K. Chromatic framework for vision in bad weather. In Proc. IEEE Conf. Comput. Vis. Pattern Recognit., Hilton Head Island, SC, USA, Jun. 15, 2000. doi: 10.1109/CVPR.2000.855874.
[20]. Narasimhan, S. G. & Nayar, S. K. Vision and the atmosphere. Int. Journal of Comput. Vis., Jul. 2002, vol. 48, no. 3, pp. 233−254. doi: 10.1023/A:1016328200723.
[21]. Kopf, J.; Neubert, B; Chen, B; Cohen, M; Cohen-Or, D; Deussen, O; Uyttendaele, M & Lischinski, D. Deep photo: Model-based photograph enhancement and viewing. ACM Trans. Graphics (TOG), 2008, vol. 27, no. 5. doi: 10.1145/1409060.1409069.
[22]. Narasimhan, S. G. & Nayar, S. K. Contrast restoration of weather degraded images. IEEE Trans. Pattern Anal. Mach. Intell., Jun. 2003, vol. 25, no. 6, pp. 713–724. doi: 10.1109/TPAMI.2003.1201821.
[23]. Xu, Z.; Liu, X. & Ji, N. Fog removal from color images using contrast limited adaptive histogram equalization. In Proc. 2nd Int. Congr. Image Signal Process., Tianjin, China, Oct. 17-19, 2009. doi: 10.1109/CISP.2009.5301485.
[24]. Fattal, R. Single image dehazing. ACM Trans. Graph. (TOG), Aug. 2008, vol. 27, no. 3, Article ID 72.
[25]. Fattal, R. Dehazing using color-lines. ACM Trans. Graph. (TOG), Nov. 2014, vol. 34, no. 1. doi: 10.1145/2651362.

[26]. Tan, R. Visibility in bad weather from a single image. In Proc. IEEE Conf. Com-put. Vis. Pattern Recognition 2008, Anchorage, AK, USA, Jun. 23-28, 2008. doi: 10.1109/CVPR.2008.4587643.

[27]. He, K.; Sun, J. & Tang, X. Single image haze removal using dark channel prior. IEEE Trans. Pattern Anal. Mach. Intell., Dec. 2011, vol. 33, no. 12, pp. 2341–2353. doi: 10.1109/TPAMI.2010.168.

[28]. Meng, G.; Wang, Y.; Duan, J.; Xiang, S. & Pan, C. Efficient image dehazing with boundary constraint and contextual regularization. In Proc. IEEE Int. Conf. Comput. Vis. 2013, Sydney, NSW, Australia, Dec. 1–8, 2013. doi: 10.1109/ICCV.2013.82.

[29]. Zhu, Q.; Mai, J. & Shao, L. A fast-single image haze removal algorithm using color attenuation prior. IEEE Trans. Image Process., Nov. 2015, vol. 24, no. 11, pp. 3522–3533. doi: 10.1109/TIP.2015.2446191.

[30]. Cai, B.; Xu, X.; Jia, K.; Qing, C. & Tao, D. DehazeNet: An end-to-end system for single image haze removal. IEEE Trans. Image Process., Nov. 2016, vol. 25, no. 11, pp. 5187–5198. doi: 10.1109/TIP.2016.2598681.

[31]. Ren, W.; Liu, S.; Zhang, H.; Pan, J.; Cao, X. & Yang, M.-H. Single image dehazing via multi-scale convolutional neural networks. In Proceedings Eur. Conf. Comp. Vis., 2016.

[32]. Kou, F.; Chen, W.; Wen, C. & Li, Z. Gradient Domain Guided Image Filtering. IEEE Transactions on Image Processing., Nov. 2015 vol. 24, no.11, pp.4528-4539. doi: 10.1109/TIP.2015.2468183.

[33]. Liu, Z.; Xiao, B.; Alrabeiah, M.; Wang, K. & Chen, J. Single image dehazing with a generic model-agnostic convolutional neural network. IEEE Signal Process. Letters, Jun. 2019, vol. 26, no. 6, pp. 833–837. doi: 10.1109/LSP.2019.2910403.

[34]. Li, B.; Ren, W; Fu, D.; Tao, D.; Feng, D.; Zeng, W & Wang, Z. Benchmarking single-image dehazing and beyond. IEEE Trans. Image Process., Jan. 2019, vol. 28, no. 1, pp. 492–505.

[35]. Salomon, D. Data Compression: The Complete Reference. Springer Science & Business Media, Berlin, Germany, 2004.

[36]. Wang, Z.; Bovik, A.C.; Sheikh. H.R. & Simoncelli, E.P. Image quality assessment: From error visibility to structural similarity. IEEE Trans. Image Process., Apr. 2004, vol. 13, no. 4, pp. 600-612.

Design Optimization of Small Satellite Separation System using Differential Evolution

Partha Ajit Surve
Vikram Sarabhai Space Centre
Thiruvananthapuram
parthasurve1@gmail.com

KK Raveendra Babu
Vikram Sarabhai Space Centre
Thiruvananthapuram

L Sowmianarayanan
Vikram Sarabhai Space Centre
Thiruvananthapuram

Dr. Geetha S
Vikram Sarabhai Space Centre
Thiruvananthapuram

***Abstract*—Improving access to space has been a driving force in the aerospace industry for last few decades. Numerous innovations in launch vehicle technology has made it possible to inject multiple satellites in a single mission. The current paper studies one such spring-based separation system used for multiple satellite separation. The separation system intended to inject three satellites was modelled using MSC Adams. Due to the incompatible combination of springs it was found that there is an intermittent recontact occurring between the separating bodies during the jettisoning process. The contact between the bodies was modelled using the IMPACT model function in Adams. Subsequently, an optimization study was performed using Differential Evolution in order to determine the optimum spring combination so as to prevent recontact while achieving the mission requirements. The optimum configuration eliminated recontact entirely and there was no discontinuity in the relative separation velocities of the satellites.**

***Keywords*— Aerospace Hardware, Separation dynamics, Small Satellite, Differential Evolution, Optimization**

1. Introduction

In the recent years, small satellite market has flourished considerably, driven by factors, such as the growing demand for LEO-based internet services, Earth observation and orbital experiments. Large small satellite constellations like Dove by Planet Labs and Starlink by SpaceX have already established the edge over the existing Remote sensing and Internet service technologies. Numerous new constellations such as Guo Wang, OneWeb, Kuiper and Pixxel are also in the pipeline and will be fully established in the upcoming years.

Given the increasing demand in small satellite applications, constant efforts are made from the vehicle engineering perspective, to develop aerospace hardware that can accommodate maximum number of satellites in a single launch. This aids in reducing the cost to orbit for the customers. Commercially available dispensers such as EXOpod, Canisterized Satellite Dispenser (CSD) and ISRO Nanosatellite Launcher System (INLS) serve to accommodate satellites of various form factors. These separation systems are all spring based and can accommodate multiple satellites of varying sizes. The separation system mass plays a critical role here since it directly affects the payload fraction. This shortcoming has also led to many innovative separation mechanisms such as the one implemented for the Starlink satellites which are stacked for launch in a dispenser. Subsequently, the rocket's upper stage is spun causing the satellites to drift away from one another thus eliminating the need of heavy spring-based separation system and accommodating maximum satellites in a single launch. Though this approach is lucrative smaller satellites tend to favor spring-based separation system due to their robust nature and minimal tip off rates due to guided separation. The separation velocity imparted by these systems allows the satellites to steer clear from the upper stage and remaining satellites thus reducing the chances of collision.

The current study focuses on one of such spring-based separation system used to jettison three identical 1U satellites (10x10 cm). When the door opening command is issued, a single spring pushes out the combination of 3 satellites together as seen in Fig 1. The satellites are equipped with their own separation springs at the interface between two satellites which push them away from one another.

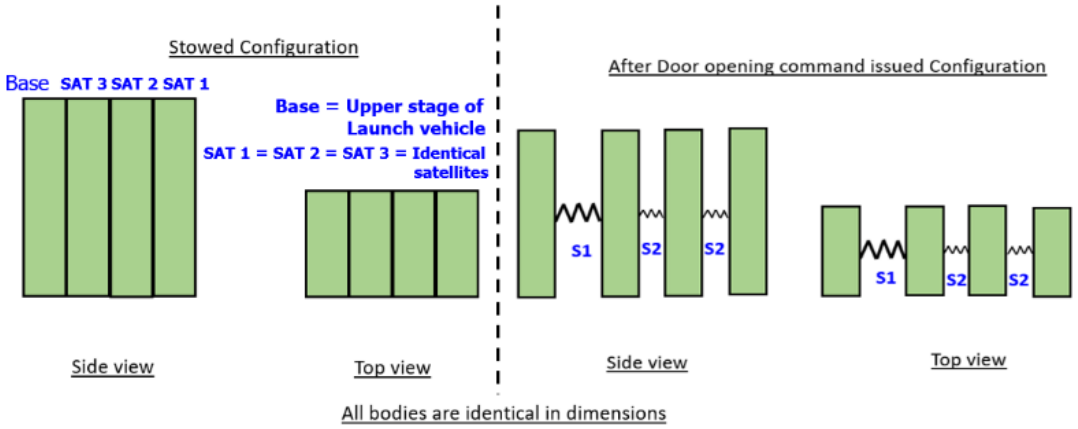

Figure 1: Schematic of the separation system

The separation dynamics of the above-mentioned system was modelled in MSC Adams in order to evaluate the force acting on each satellite along with the corresponding relative separation velocities and body accelerations. It was found that due to incompatibility in spring parameters of the main spring and the spring plungers, oscillatory motion of the middle satellite may persist, leading to an intermittent contact with the other satellite inside the separation system. A design optimization study of the spring parameters can eliminate such a scenario.

The literature review shows that there are a few existing studies that discuss about the optimization of spring-based separation system in order to reduce either the mass or the final tip off rates [2,3,4]. A prior study employs hierarchical optimization using Multi-Island Genetic Algorithm in order to reduce the system mass and separation angular velocity [2]. The optimizer led to reduction of compression spring catapult mass by 30.7%, and tip off rates which was further verified through, ground separation tests. Similarly, another study employs Genetic Algorithm in order to identify the spring locations and parameters in a given separation system [3] with the objective of minimizing the body rates imparted to the satellite at separation while meeting the mission requirements. The flight observed rate with the optimized spring configuration also indicated near zero body rates. In one of the recent studies, the separation dynamics of a CubeSat has been modeled in Adams with contact and collision [4]. Though the optimization scheme is unclear, the authors were able to achieve flight body rates < 2deg/s by tuning the mechanism parameters. Previous studies have almost exclusively focused on reduction of mass or tip off rates. So far, no study could be identified in literature which used optimization techniques in order to minimize the recontact force between the satellite. In the current study, design optimization of the spring properties was carried out in order to prevent re-contact between the satellites, while meeting the mission constraints.

The subsequent sections dwell upon the Differential Evolution algorithm and the IMPACT function employed in Adams. The modeling in Adams and the optimization problem statement are explained in section 4. Finally, section 5 and 6 elaborate on the results and conclusion drawn from the study.

2. Differential Evolution

Differential Evolution (DE) is a widely used stochastic numerical optimization algorithm put forth by Storn and Price [1]. It's an evolutionary optimization technique, which doesn't rely on gradient information to choose the search direction and can parallelly search the entire design space. It is initiated with a randomly generated population similar to other heuristic methods, after which the generations evolve through the process of mutation, crossover and selection. The performance of Differential Evolution (DE) heavily relies on the choice of parameters such as population size (NP), scale factor (F), crossover rate (CR) and the choice of the mutation and crossover strategy. The combination of these parameters can vary from problem to problem depending upon the dimensionality, accuracy required and the multi-modality of the design space.

In classic DE the control parameters remain constant throughout the optimization process. However, in the recent years, there have been many developments in the field of self-adaptive DE, where the control parameters are adjusted dynamically such as SaDE [5], jDE [6]. There have been many studies aiming to improve the performance of DE as well, Rahnamayan et al [7] have proposed opposition based differential evolution where they have demonstrated how simultaneously evaluating the opposite solutions can improve the convergence performance. A parallelized DE using a ring-network topology was proposed by [8] in order to improve the speed and convergence of the algorithm. In the last two decades, it has been employed in various domains, as an optimizer for minimizing the training loss and evaluating weights of an Artificial Neural Network [9]. DE has also been used for optimizing the size of ANN architecture for classification or regression applications [10]. It has also been applied in optimization of various real-life design problems [11,12,13].

Differential Evolution (DE) is an easy to code evolutionary optimization algorithm which is ideal for real valued problems but can also work with discrete variables. It operates on an NP x D design space, where NP is the population size and D is the dimension of the objective function. The design space is initialized using uniform distribution, $\mathbf{X_{i,G} = \{x^1_{i,G},...,x^D_{i,G}\}, i=1,...,NP}$, where G denotes the generation. All the individual $\mathbf{X_{i,G}}$ in the design space are referred to as target vectors. Corresponding to each target vector a mutant vector $\mathbf{V_{i,G}}$ is generated using the mutation scheme. The classic mutation strategy **DE/rand/1** is as follows

$$\mathrm{V}_{i,G} = \mathrm{X}_{r_1^i,G} + F * (\mathrm{X}_{r_2^i,G} - \mathrm{X}_{r_3^i,G})$$

Where, the $\mathbf{r_1^i, r_2^i, r_3^i}$ are randomly selected within the design space [1, NP] without replacement. The scale factor F is a positive value ranging between [0, 2]. After mutation the crossover operation is performed between the target $\mathbf{X_{i,G}}$ and mutant vector $\mathbf{V_{i,G}}$ elements to generate a trial vector $\mathbf{U_{i,G}}$ This aids in the diversity enhancement of the population. The binomial crossover operation is as follows

$$\mathrm{u}_{i,G}^j = \begin{cases} \mathrm{v}_{i,G}^j, & \text{if } (\mathrm{rand}[0,1] \leq CR) \\ \mathrm{x}_{i,G}^j, & \text{otherwise} \end{cases} \qquad j = 1, 2, ..., D$$

Where, the crossover rate CR is varied between [0,1]. After the crossover operation the fitness is evaluated for the trial vector $\mathbf{U_{i,G}}$ and it's compared with the corresponding target vector fitness $\mathbf{X_{i,G}}$. If found to be better, the $\mathbf{U_{i,G}}$ replaces the corresponding $\mathbf{X_{i,G}}$ in the upcoming generation. For a minimization algorithm it can de denoted as follows:

$$\mathrm{X}_{i,G+1} = \begin{cases} \mathrm{U}_{i,G}, & \text{if } f(\mathrm{U}_{i,G}) \leq f(\mathrm{X}_{i,G}) \\ \mathrm{X}_{i,G}, & \text{otherwise} \end{cases}$$

Algorithm 1 Differential Evolution Algorithm

Set generation counter G to zero
$\mathrm{P}^0 \leftarrow$ Initialize population (D, NP)
while stopping condition not met **do**
    for *individual* $= 1, 2, \ldots, NP$ **do**
        Evaluate the fitness $f(x_i)$
        Generate the trial vector $\mathrm{V}_{i,G}$ using the mutation operator
        Generate the offspring vector $\mathrm{U}_{i,G}$ using the crossover operator
        if $f(\mathrm{U}_{i,G}) \leq f(\mathrm{X}_{i,G})$ **then**
            $\mathrm{X}_{i,G+1} = \mathrm{U}_{i,G}$
        else
            $\mathrm{X}_{i,G+1} = \mathrm{X}_{i,G}$
        end if
    end for
end while

The Differential Evolution code was developed in Python with DE/best/1 (DE with one difference vector added to the Best individual) strategy which acted as a wrapper for the Adams solver.

The optimizer was also benchmarked with 8 test functions outlined by [1]. Subsequently, the spring parameter optimization problem was evaluated with Population size (NP) of 50, Crossover Rate (CR) of 0.9 and Scaling Factor of 0.9.

3. Contact Modeling in MSC Adams

MSC Adams is used extensively for motion analysis and multibody dynamics [14]. One of its key feature is the contact modeling between objects during multibody dynamics simulations which is essential while emulating real life scenarios. Given the discontinuous and non-linear nature of contact forces, Adams performs iterative calculations, the accuracy of which highly depends on user-defined values. There are three types of contact models available in Adams, namely IMPACT function, the POISSON restitution and the Coulomb friction. Given the nature of the problem in the current study, the recontact is modeled using IMPACT function which allows more control over the contact modeling compared to the POISSON restitution model.

The IMPACT function is derived from the Hertzian contact theory in which the reaction force is modelled as a non-linear spring force as follows

$$F = k(x_1 - x)^e$$

Where the reaction force depends on stiffness parameter(k_c), the penetration depth $(x_1 - x)$ and force exponent (e). The stiffness parameter is evaluated using both the materials' Young's Moduli and Poisson's Ratios, both objects' radii and the force pressing the objects together. The penetration depth deals with the overlap between the two objects. As the penetration depth increases so should the reaction force, the force exponent is used to account for this non-linear phenomenon. The deformation also leads to dissipation of energy; thus, the damping factor is also added in the IMPACT function [15]. In the current study, stiffness parameter used is 2.0E+08 N/m, damping of 2.0E+06 Ns/m, Force Exponent is 2.2 (Hard materials) and penetration depth provided is 1.0E-04 m. These values were arrived upon after literature survey of similar problems. Their authenticity was further verified with a parametric study of each individual parameter.

4. Methodology

The current section deals with the modeling aspects of the satellite separation system along with all the relevant assumptions. The optimization problem statement consisting of the objective function, design variables and constraints is also discussed in detail.

A. Modeling in MSC Adams

The satellites were modelled as cuboids with their respective mass (0.5 kg each) and appropriate Moment of Inertia. There is no lateral CG offset and since they are traversing in a guided separation system, they won't experience any lateral body rates either. The Adams model is shown in Fig 2. It can be noted that the left most block represents the upper stage of the launch vehicle.

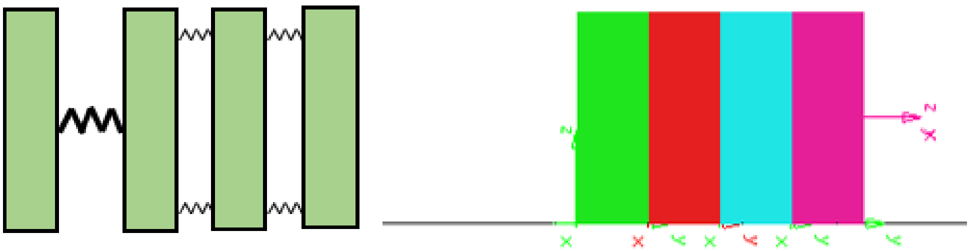

Figure 2: Adams model of the separation system

Once the door opens, the main spring shown on the left most side starts pushing the trio, subsequently the small spring plungers start relaxing. The spring plungers are located on diagonally opposite locations but in the current model they are considered to be acting at the center of satellite given that there is no lateral CG offset present. The spring forces were modelled using a STEP function considered to act at the geometric center of the satellites as shown in Fig 3 (Normalized w.r.t peak force).

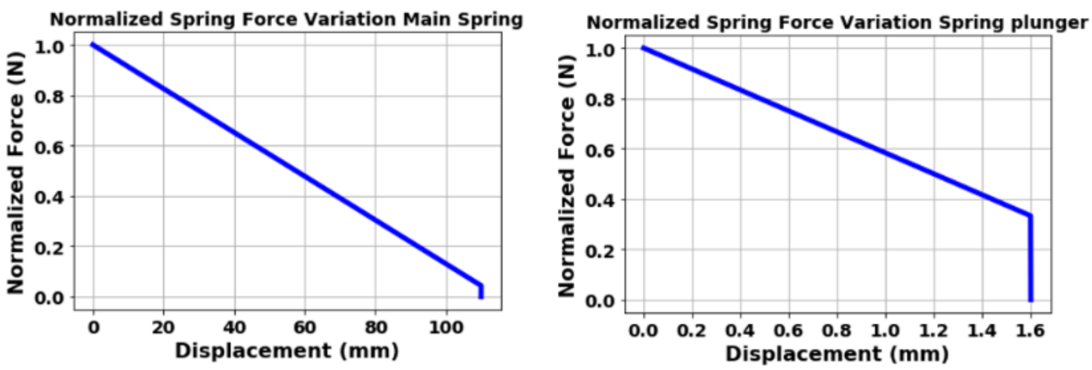

Figure 3: Baseline spring force modeled as a STEP function a) Main spring b) Spring plunger

As discussed earlier the contact between the satellites was modelled using the IMPACT function. The Adams model was parameterized and executed using an external Python optimization wrapper.

B. Problem statement

In the current study, design optimization of the spring properties was carried out in order to prevent recontact between the satellites, while meeting the mission constraints. The properties of each spring i.e. Initial force, Final Force and stroke were treated as design variables. The objective was to minimize the recontact force between the separated satellites. Appropriate constraints on relative separation velocities were also imposed. Differential evolution algorithm (DE/best/1/bin) was used as the optimizer. The summary of the optimization model is as follows-

Objective :

$$\text{Minimize} : \ \text{Force}_{\text{contact}}$$

w.r.t :

$$\text{S1}_{\text{initial}_i} \in [\mathbb{R} \ : \ (8\text{N}, 20\text{N})], \quad \text{where } i = 1,2$$
$$\text{S1}_{\text{final}_i} \in [\mathbb{R} \ : \ (0\text{N}, 6\text{N})], \quad \text{where } i = 1,2$$
$$\text{S2}_{\text{initial}} \in [\mathbb{R} \ : \ (15\text{N}, 22\text{N})]$$
$$\text{S2}_{\text{final}} \in [\mathbb{R} \ : \ (0\text{N}, 8\text{N})]$$
$$\text{S1}_{\text{stroke}} \in [\mathbb{R} \ : \ (1\text{mm}, 2.5\text{mm})], \quad \text{where } i = 1,2$$
$$\text{S2}_{\text{stroke}} \in [\mathbb{R} \ : \ (80\text{mm}, 130\text{mm})]$$

Constraints :

$$1.35\text{m/sec} \geq \text{V}_i \geq 1.1\text{m/sec}, \ \text{where } i = 1,2,3$$

Where, the contact force ($\text{Force}_{\text{contact}}$) and the relative separation velocities (V_i) are extracted from the Adams simulation.

5. Results and Discussion

The current section presents the results from the baseline study and optimized configuration. The root cause of the recontact in the baseline configuration has been discussed along with the improvement with the optimized configuration.

A. Baseline Configuration

Firstly, an analysis was carried out with the baseline configuration without the contact modeling. The overlap occurring between the satellite bodies during the separation process is shown in Fig 4. The overlap is evaluated by measuring distance between two adjacent satellite surfaces. As it can be seen, initially the satellites are flushed with each other hence the overlap is zero. Subsequently, when the spring plungers start relaxing an overlapping occurs in two distinct regions for SAT 2 and 3 (0-25 ms and 30 – 75 ms) i.e. distance between the surfaces becomes negative. The growing distances between satellites also indicate an oscillatory nature which can be related to the choice of spring parameters.

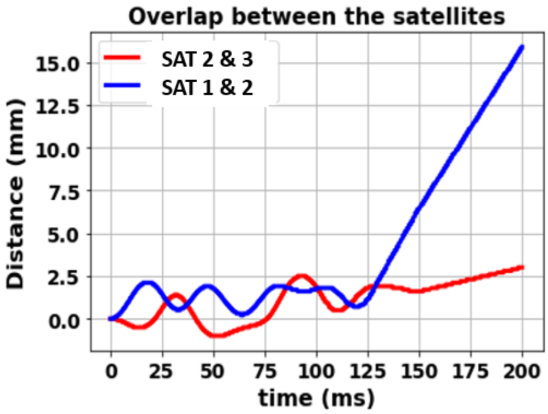

Figure 4: Overlap between the satellites during separation

This phenomenon can be understood by looking at the force body diagram of the separating bodies shown in Fig 5. The main pusher spring Force (F_1) is acting on SAT 3 while the reaction force acts on the upper stage. Similarly, the spring plunger forces (F_2) are acting on SAT 1 and 2. This leads to a momentary cancellation of forces on SAT 2 causing it to remain stationery while SAT 3 is pushed against it leading to the overlap (Fig 4).

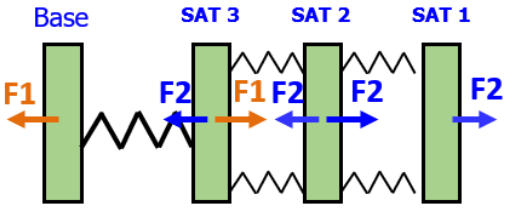

Figure 5: Force Body Diagram of the separating bodies

In order to prevent the overlap a contact has to be defined between the separating bodies. Upon adding the IMPACT function model, the overlap is prevented due to the additional reaction force acting on the bodies. The variation of the spring force during separation for all the three springs in the base line configuration is shown in Fig 6. The resultant body acceleration and separation velocities imparted to the satellites are shown in Fig 7 and 8 respectively.

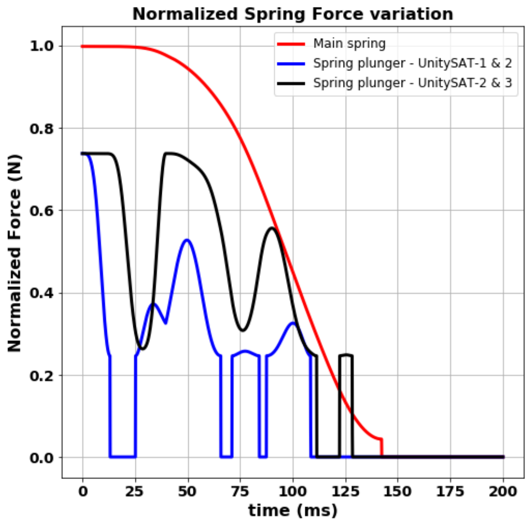

Figure 6: Spring force variation for the baseline configuration

It can be observed that the main spring relaxes over a period of 140 ms, while the intermediate spring plungers compress and relax during this duration.

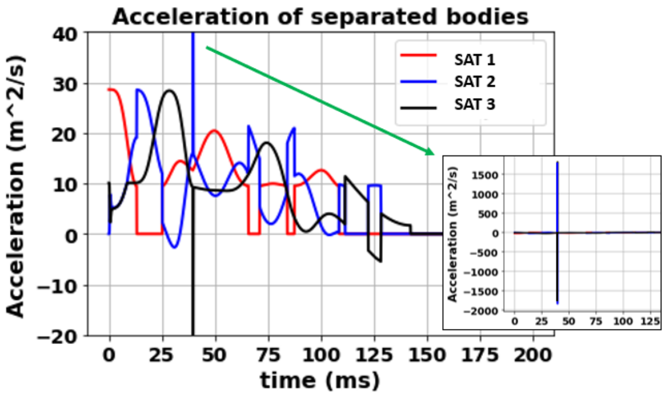

Figure 7: Body acceleration variation for the baseline configuration

This phenomenon leads to an intermittent contact between the satellite 2 and 3, leading to reaction force which is reflected as a jerk in the acceleration plot. The instantaneous jerk acts on both SAT 2 and 3.

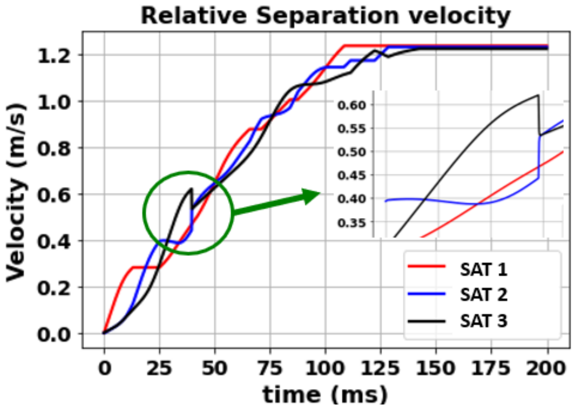

Figure 8: Relative separation velocity variation for the baseline configuration

The above jerk leads to sharp discontinuity in the separation velocity as seen in Fig 8 as SAT 2 gains velocity while SAT 3 loses it; the differential isn't identical given the damping coefficient present in the contact model. Upon studying the contact reaction forces plotted in Fig 9, it can be noted that the contact occurs at two instances. Firstly, when the bodies just begin to move under the action of the main spring and secondly when the SAT 3 traverses with higher velocity compared to SAT 2 and makes contact. The first contact can be categorized as butting between the bodies while the second can be classified as an intermittent contact.

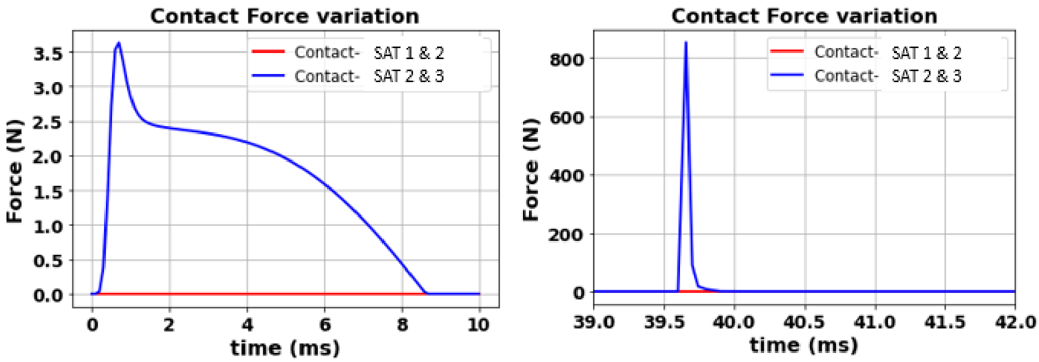

Figure 9: Contact Force variation for the baseline configuration

The severity of the second contact can be understood only with structural analysis of the colliding bodies, but that doesn't fall under the scope of the current paper. The current study aims at identifying the root cause and provide an optimum configuration in order to avoid such scenarios. The primary cause of the intermittent contact in the baseline configuration was due to the identical properties of the intermediate spring plungers. Since, the initial forces exerted by the springs on the middle satellite were identical, they had a tendency to cancel out, causing the SAT 2 and 3 to re-contact.

B. Optimum Configuration

The optimization results are compared with the base line configuration in Table 2. The values in bracket correspond to the base line configuration. In the optimum spring configuration, it is seen that the spring plungers have different initial forces i.e. Spring force between SAT 2 and 3 greater than between SAT 1 and 2.

Table 2: Comparison of Optimum and Baseline spring properties of the separation system

Spring	Initial Force (N)	Final Force (N)
S1: Base and SAT 1	16.5 (18.1)	3.0 (0.8)
S2: Satellite SAT 1 and SAT 2	14.3 (13.3)	0.5 (4.5)
S3: Satellite SAT 2 and SAT 3	13.6 (13.3)	5.2 (4.5)

The normalized spring force variation for the optimum configuration is shown in Fig 10. The relative separation velocities are plotted in Fig 11. No discontinuity was observed in the separation velocities. This can be attributed to the differential spring plunger force causing the middle satellite (SAT 2) to keep translating unlike the baseline scenario, thus preventing any scenario of re-contact.

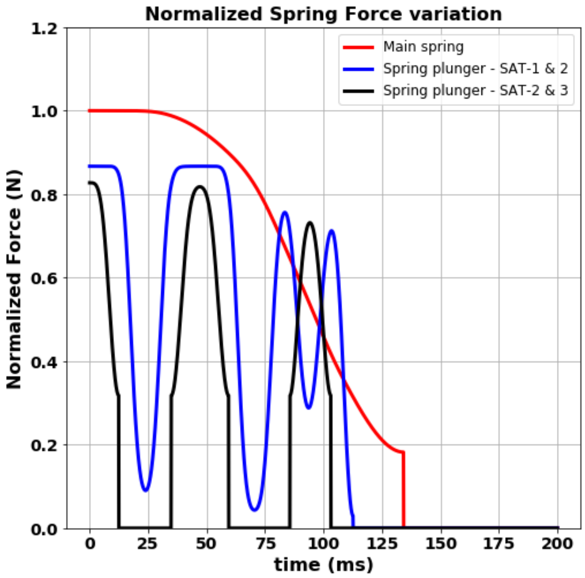

Figure 10: Spring force variation for the optimum configuration

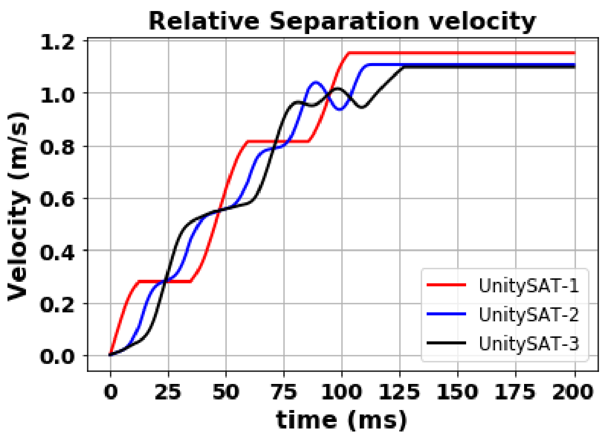

Figure 11: Relative separation velocity variation for the optimum configuration

6. Conclusions

An optimization design approach using Differential Evolution is proposed and demonstrated for small satellite separation systems, with the design objective of minimizing recontact between the satellites in the separation system. The separation dynamic analysis was carried out using MSC Adams, integrated with a Python wrapper for optimization. The constraints and design variables employed were in line with the mission requirements.

Optimization studies were carried out for three spring scenario. The resultant optimum configuration posed a differential spring plunger force between satellites thus eliminating intermittent contact entirely. Subsequently, a Finite Element analysis was carried out in order to estimate the structural loads due to the recontact, which is not covered in the current study. The optimum configuration wasn't implemented in flight because the recontact was reported to be benign. The structural sensor data from Post-Flight telemetry indicated a recontact between the satellites at 30 ms from the door opening status as predicted, thus validating the model.

The study in this paper can be used to enhance the design of satellite separation systems. Some related issues are worth further studying. Namely, the modeling of satellites with their lateral CG offsets and guide rails of the separation system in order to capture contact between them. Large body rates imparted by the system can cause the satellite to get jammed during deployment. Spring plungers between the satellites can be selected in order to minimize the rotation of the satellite inside the guides. Physical/fabrication constraints on the choice of spring parameters can also be employed to make the results implementable in real life applications.

7. Acknowledgments

The authors wish to thank Mr. Shiju G Thomas, Mr. Abraham Varghese and Mr UA Subramanian, VSSC for their critical advice on the modeling aspects in Adams.

8. References

[1] Rainer Storn and Kenneth Price, "Differential Evolution – A Simple and Efficient Heuristic for Global Optimization over Continuous Spaces",*Journal of Global Optimization* 11: 341–359, 1997.

[2] Xingzhi Hu, Xiaoqian Chen, Yong Zhao, Wen Yao,

[3] Optimization design of satellite separation systems based on Multi-Island Genetic Algorithm, *Advances in Space Research*, Volume 53, Issue 5, 2014, Pages 870-876,

[4] Surve P.A., Vamsi Krishna D., Madhavi K.R., Raveendra Babu K.K., Sowmianarayanan L., Ayyappan G.,

[5] Spring Tuning for Spacecraft Separation Dynamics Using Genetic Algorithm. *Advances in Systems Engineering. Lecture Notes in Mechanical Engineering.* Springer, Singapore, 2021

[6] J. Zhang, J. Zhou and Y. Deng, "CubeSat Separation Parameter Optimization," *2018 12th International Conference on Signal Processing and Communication Systems (ICSPCS)*, 2018, pp. 1-4, doi: 10.1109/ICSPCS.2018.8631745.

[7] Qin, A.K., Suganthan, P.N.: Self-adaptive Differential Evolution Algorithm for Numerical Optimization. *The 2005 IEEE Congress on Evolutionary Computation CEC 2005*, vol. 2, pp. 1785–1791. IEEE Press, Los Alamitos (2005)

[8] Brest, Janez & Zamuda, Aleš & Bošković, Borko & Maučec, Mirjam & Zumer, Viljem. (2009). Dynamic Optimization using Self-Adaptive Differential Evolution. *2009 IEEE Congress on Evolutionary Computation, CEC 2009*. 415 - 422. 10.1109/CEC.2009.4982976.

[9] Rahnamayan S., Tizhoosh H.R., Salama M.M.A. (2008) Opposition-Based Differential Evolution. In: Chakraborty U.K. (eds) *Advances in Differential Evolution. Studies in Computational Intelligence*, vol 143. Springer, Berlin, Heidelberg

[10] Plagianakos V.P., Tasoulis D.K., Vrahatis M.N. (2008) A Review of Major Application Areas of Differential Evolution. In: Chakraborty U.K. (eds) *Advances in Differential Evolution. Studies in Computational Intelligence*, vol 143. Springer, Berlin, Heidelberg

[11] M. Z. A. Bhuiyan, "An Algorithm for Determining Neural Network Architecture Using Differential Evolution," *2009 International Conference on Business Intelligence and Financial Engineering*, Beijing, 2009, pp. 3-7.

[12] Tasoulis, D.K. & Pavlidis, Nicos & Plagianakos, V.P. & Vrahatis, Michael. (2004). Parallel differential evolution. Proceedings of the 2004 Congress on Evolutionary Computation,

CEC2004. 2. 2023 - 2029 Vol.2. 10.1109/CEC.2004.1331145.
[13] Wang, Yong & Liu, Hao & Long, Huan & Zhang, Zijun & Yang, Shengxiang. (2017). Differential Evolution with A New Encoding Mechanism for Optimizing Wind Farm Layout. *IEEE Transactions on Industrial Informatics*. PP. 1-1. 10.1109/TII.2017.2743761.
[14] Abou El-Ela, Adel & Abido, Mohammed & Spea, S.. (2009). Optimal power flow using differential evolution algorithm. Electric Power Systems Research. 91. 878-885. 10.1016/j.epsr.2009.12.018.
[15] Arunachalam, Vasan & Simonovic, Slobodan. (2010). Optimization of Water Distribution Network Design Using Differential Evolution. *Journal of Water Resources Planning and Management*-asce - J WATER RESOUR PLAN MAN-ASCE. 136. 10.1061/(ASCE)0733-9496(2010)136:2(279).
[16] https://www.mscsoftware.com/product/adams
[17] Giesbers, Jochem. "Contact mechanics in MSC Adams-A technical evaluation of the contact models in multibody dynamics software MSC Adams." Bachelor's thesis, University of Twente, 2012

Separation Dynamic Analysis for Umbilical System in MSC ADAMS

Ashish Tomy
Vikram Sarabhai Space Centre
ISRO
Thiruvananthapuram
ashishtomy95@gmail.com

Surbhi Baghotia
Vikram Sarabhai Space Centre
ISRO
Thiruvananthapuram
surbhibaghotia@gmail.com

Anoop P P
Vikram Sarabhai Space Centre
ISRO
Thiruvananthapuram
anoop2p@yahoo.co.in

Damodaran P
Vikram Sarabhai Space Centre
ISRO
Thiruvananthapuram

Subramanian UA
Vikram Sarabhai Space Centre
ISRO
Thiruvananthapuram

***Abstract*— The space segment of any Human Space Programme consists of a Habitat Module (HM) for crew and a Service Segment (SS). An Umbilical system acts as a link between the HM and SS for various crew service fluid lines and electrical lines during the ascent and orbital phase. It also accommodates the fluid and electric connectors which disconnect all the transfer lines before re-entry. During nominal mission and abort scenarios, the upper half of the umbilical, the Fore end subassembly separates from the HM. During this separation, it should not collide with the Thermal Protection System in the Aft end dome of HM which would otherwise prove fatal to the mission during re-entry. With the help of springs at different locations, the Fore end subassembly of umbilical needs to achieve clean separation of the connectors with a required minimum translational velocity while imparting minimum rate to both the bodies. The challenge is to configure a jettisoning system to achieve the requirements to ensure positive separation gap from Aft end dome of HM. A study was conducted with different configurations of spring thrusters used for jettisoning the system with required velocity. These configurations were simulated in MSC ADAMS software and analysed for separation dynamics. Analytical calculations of various parameters were compared with the results. The configuration which met the criteria of collision free separation was finalised. This paper focuses on the separation dynamic analysis carried out in MSC ADAMS to finalise the jettisoning system and on the subsequent upgradations in design. Further improvements were proposed as a scope for future studies.**

Keywords—Human Space Program, Umbilical system, MSC ADAMS, Separation Dynamics

1. Introduction

The Human Space Programme envisages to send a crew to Low Earth Orbit and return them back to Earth. It consists of two major modules – Habitat Module (HM) and Service Segment (SS) (Figure 1). An umbilical system is incorporated to ensure a link for transfer of Crew Service fluids and electricity between HM and SS and disconnect from the HM before its re-entry. The functional requirements include:

- Separation of all Crew Service fluid and electrical lines within stipulated time under nominal mission and abort scenarios.
- Collision free separation with adequate clearance.
- Perform satisfactorily under all the environments envisaged.

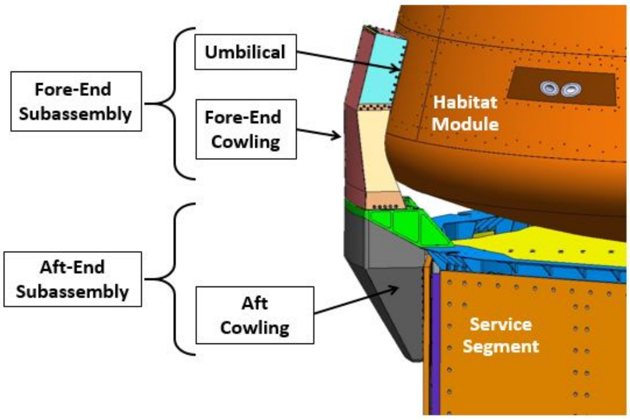

Figure 1: Umbilical System configuration

A. State of the art

All human spaceflight missions have incorporated umbilical connection between the Crew/Command module (CM) and Service Modules (SM).

The Apollo umbilical separation consisted of a pyrotechnically-activated guillotine with three pyrotechnic charges and four cutting blades [1]. The connections between CM and SM were packed into two rectangular blocks. The CM/SM guillotine cut the umbilical between the CM and the SM to allow the hinged umbilical boom to swing clear of the CM and permitted separation of the CM from the SM [2].

On the other hand, Orion crew-service module umbilical retention and release mechanism is a two-stage separation system with connector separation and boom deployment as the two stages. During the first stage, separation bolts are fired and the separation springs push the umbilical plates apart which in turn separates all the connections across the interface. The boom carrying the SM plates and connectors is then pushed away by actuators [1].

2. Separation instances for umbilical system

In a nominal mission, the Umbilical System separation is initiated just before the re-entry of HM.

Under emergency/abort situation, the Umbilical System separation might be required at launch pad or during the initial atmospheric phase or at high altitude. Under such situations, the response time of the umbilical is critical for a smooth separation.

This paper focuses on the separation dynamic analysis during nominal mission scenario assuming the HM to be stationary/fixed and under microgravity environment. However, the results with gravity are also analyzed.

The simulation is carried out using MSC Adams/View for the separation of Fore End sub-assembly from the HM. The results are presented in a graphical representation for the movement of the separated assembly. The displacement, velocity, acceleration, forces and moments of key components and points are also obtained.

3. Umbilical system for human space programme

The Crew Service fluid lines and cables for electrical power and data transfer are routed from the SS to the HM through the Umbilical system. At the umbilical interface, there are connectors which join the fluid & electrical lines. The umbilical connecting Fore End sub-assembly with the HM consists of a pair of umbilical plates clamped together using a preloaded pyro device.

A. Umbilical System Separation

The separation of Fore-end Subassembly from the HM takes place along the conical surface of HM. Umbilical separation with actuation of pyro device leads to jettisoning of Fore End subassembly consisting of Plate, Fore End cowling, all fluid hoses and electrical cables. The system incorporates spring thrusters to effectively jettison the Fore End sub-assembly with a specified velocity of 1m/s. Collision free and clean separation is vital to ensure the safety of HM under all mission conditions.

4. Mathematical formulation

To verify the design for separation mechanism of umbilical system, dynamic analysis was carried out in Adams view. The Adams model was verified using analytical calculations. The equations used for calculations were total energy conservation, and force and moment equation for a body having both rotation and translation [3].

The energy equation is,

$$E_{springs} = \frac{m v_x^2}{2} + \frac{I \omega_x^2}{2} \tag{1}$$

Here, $E_{springs}$ is the total energy of all the springs, 'm' is total mass, 'v_x' is the translational velocity, 'I' is the total moment of inertia and 'ω_x' is the rotational velocity of the Fore End sub-assembly.

The translational and rotational equations are,

$$ma + m\omega v = F \tag{2}$$

$$\frac{dL}{dt} + \omega L = M \tag{3}$$

'a'- translational acceleration
'F'- jettisoning forces
'L'- angular momentum
'M'- rotational moment

Equations 1, 2 and 3 are the governing equations for the separation dynamics of Fore end sub-assembly.

5. The separation mechanism model

The 3-D model used for dynamic analysis in MSC Adams/View was generated in Solidworks (Figure 2). This model consisted of HM, umbilical plates with connectors and pyro device, fluid and electrical lines, cowling, supporting ribs and fasteners. The mass, moment of inertia and centre of gravity (CG) data were estimated in Solidworks. This 3-D model was imported into Adams after due simplification by maintaining necessary profiles and the original mass properties were implemented in ADAMS.

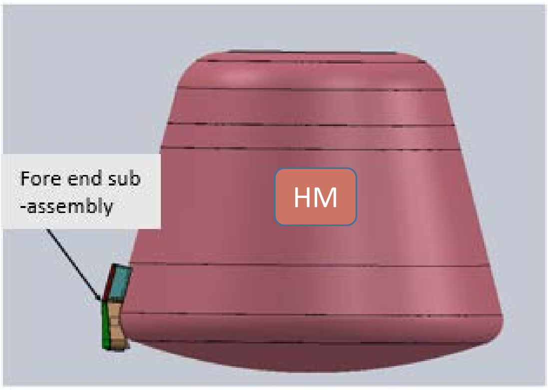

Figure 2: Solidworks model for Dynamic Analysis

The Fore End sub-assembly, which gets separated from the HM consists of umbilical plate at HM interface, line routings, cowling and cover plates. The total mass of the sub-assembly is 50 kg. The separated assembly is required to move away from the HM with minimum velocity of 1 m/s to meet the functional requirement. It should also avoid re-contact with the HM after separation for the safety of the HM.

When the separation command is received the pyro device is actuated releasing the ejection system and the ejection springs push the assembly away from the HM. The design of the springs is done to meet the jettisoning velocity requirement. The location of springs is important in order to control the rates of the separated assembly during all mission scenarios.

A. Configuration with ejection springs at corners of Umbilical plate

For the initial model, four ejection springs were designed and located at the four corners of Umbilical plate. However, the forces due to these springs act eccentric to the CG of the Fore End sub-assembly thereby generating a moment which results in rotation of the separated part. Therefore, out of these four, the two springs at the lower end of plate were designed with higher stiffness to provide greater force nearer to the CG to minimise the rotation after separation. The total mass of Fore End sub assembly to be ejected from the HM was taken as 50 kg. To meet the ejection velocity requirement of 1 m/s, the energy ‘E’ required for separation was estimated as following:

$$m = 50\ kg, v = 1\ ms^{-1}$$

$$E = \frac{1}{2}mv^2 = 25\text{ J}$$

Assuming frictional losses of the order of 20 % and a Factor of Safety of 1.5 on the energy requirement, the total energy requirement was calculated as 45 J.

Considering a stroke of 40 mm (from envelope constraint) and based on the CG offset of spring thrusters, the four springs were configured such that the two bottom springs provided 3 times the energy as that of the top two springs.

Hence, the energy provided by bottom springs:

$$E_1 = \frac{3}{4} \times E$$

Energy provided by top springs:

$$E_2 = \frac{1}{4} \times E$$

The stiffness of the springs was estimated based on these energy equations. Apart from these four ejection springs, there are springs present in the fluid connectors and they were also incorporated in the ADAMS model.

The volute springs present inside the electrical connectors were modelled to provide constant force. All the electrical connector springs provided a load of 250 N each and were deactivated after connectors lost contact.

6. Analysis and results

This section details the separation dynamic analysis carried out and the results obtained.

A. Analytical verification of model

An analytical verification of the design was carried out prior to the ADAMS analysis for a simplified case. Since gravity force was neglected for dynamic analysis, the same conditions were considered for the analytical calculations.

The initial accelerations, both translational and translational, were calculated analytically and compared with values from ADAMS model.

First, the translational acceleration of the Fore End sub-assembly was estimated by simulating all the loads due to ejection springs, fluid connector springs and electrical connector springs. Therefore, at the beginning of the simulation, the total loads were:

$$F_t = F_{ej} + F_f + F_{el}$$

Where F_t, is the total separation force, F_{ej} is the ejection spring force, F_f is the fluid connectors' force and F_{el} is the electrical connectors' forces.

Now $F_{ej} = 2 \times (K_t x + K_b x)$. Here x , is the stroke of the springs (40 mm).

So, F_e is estimated as $F_e = 2600\ N$

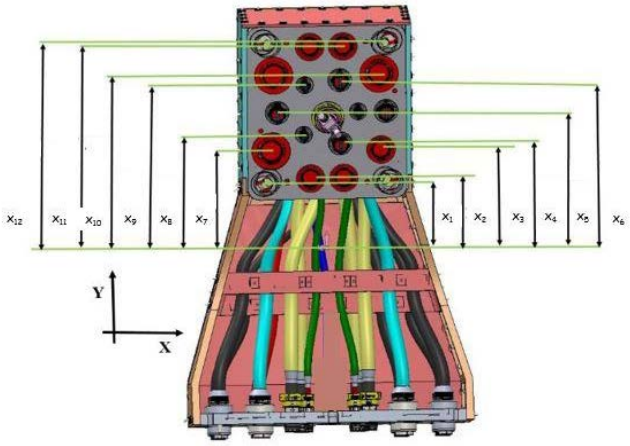

Figure 3: Connector forces and ejection spring force offset

F_f which is force due to fluid connectors is derived as

$$F_f = 1200\ N$$
$$F_{el} = 2000\ N$$
$$\text{So}\ \ F_t = \mathbf{5800\ N}$$

Considering the mass of Fore End sub-assembly, $m = 50\ kg$, under microgravity:

$$F_t = ma$$

Solving for acceleration 'a',

$$a_x = \frac{F_t}{m} = \frac{5800}{50} = \mathbf{116\ ms^{-2}}$$

Next, the rotational acceleration about X axis (α_x) of the Fore End sub-assembly was estimated by simulating all the loads due to ejection springs, fluid connector springs and electrical connector springs. It was assumed that rotation rates of umbilical system along other axes are zero.

The ejection springs and all the connectors are present at an offset from the C.G. in the Y axis (Figure 3). These offset forces generate a rotation of the separated Fore End sub-assembly about its C.G. The moments generated by these forces about the X axis are calculated below.

Moment due to electrical connector spring forces:

Force by each electrical connector is 250 N. Based on the offset distances (Figure 3), the moment due to electrical connectors' spring forces about the CG:

$$M_{el} = 2 \times 250 \times (x_2 + x_3 + x_{10} + x_{11})$$

Moment due to ejection springs:

Top ejection springs are located a distance of x_{12} and bottom springs at x_1 from C.G. (Figure 3) At the onset of separation, the top springs generate force, $F_{ts} = K_t \times 40$. Similarly bottom springs generate force $F_{bs} = K_b \times 40$. Therefore, moment due to ejection springs can be calculated as

$$M_e = 2 \times (F_{bs} \times x_1 + F_{ts} \times x_{12})$$

Moment due to Fluid Connector spring forces

Base on the locations of the Fluid Connector springs the moment due to Fluid Connector springs is,

$$M_f = f_1 \times (2 \times x_5 + x_6 + x_4) + f_2 \times (x_8 + x_9) + f_3 \times x_5$$

Where f_1, f_2 & f_3 are fluid connector spring forces.

Total moment is

$$M = M_{el} + M_e + M_f = 1100 \text{ Nm}$$

Moment of inertia of the Fore End sub-assembly along the Y axis obtained from 3D model is, $I_{xx} = 2.87\, kg\, m^2$. Hence, angular acceleration of the sub-assembly after separation will be,

$$\alpha_x = \frac{M}{I_{xx}} = \frac{1100}{2.87} = 383.28\, rad\, s^{-2} = 21945\, deg\, s^{-2}$$

B. Compilation of Model in MSC ADAMS

The models imported from Solidworks were given mass properties in Adams based on the data from Solidworks model. Due to the large mass & Moment of Inertia of HM as compared to Fore End sub assembly, the relative movement and rotation of HM was assumed to be negligible. Hence, HM was considered to be fixed to the ground for all the analysis conditions. The four ejection springs & fluid connector springs were modelled as spring forces.

Contact forces were modelled between the HM and the pistons of the four ejection springs as well as the pistons of fluid connectors & their corresponding mating surfaces on HM side plate. Frictional forces were neglected during the definition of contacts. All the normal forces due to contact were modelled with recommended values of contact parameters for metal to metal contact [4].

Electrical connector forces were modelled as constant force of 250 N which act until the connectors were in contact. Once the male and female parts of the connectors lose contact, the electrical force was deactivated in the analysis. For this, sensors were created in ADAMS model to turn off the constant force when contact between the connectors is lost during separation.

Two different cases were simulated i.e. one with gravity and another without gravity. For the initial 0.05 s, all the forces in the models were locked by creating a fixed joint at the pyro device location. This was done to ensure that the model reached an equilibrium position before separation. At 0.05 s, the fixed joint was deactivated and the separation was initiated.

C. Results

All the spring forces and deformations were plotted and it showed that the springs acted as expected. The acceleration along x axis curve of the separated Fore End sub-assembly (Figure 4) shows that it has an initial acceleration of about 116 ms^{-2}. This is close to the predicted value by the analytical model. The angular acceleration (α_x) is shown in Figure 5. The initial α_x predicted by analytical model matches with the Adams results. So by comparing both the initial accelerations, the Adams model was verified as the results were similar in analytical model and in Adams model.

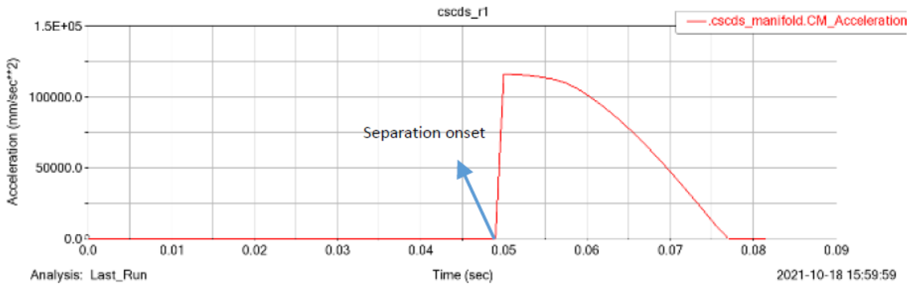

Figure 4: Translational acceleration for Configuration 1

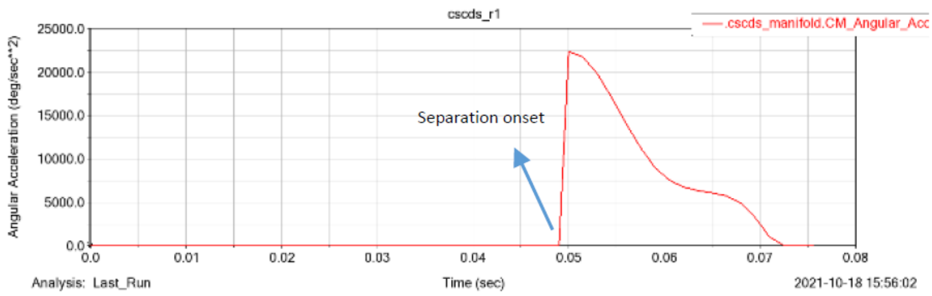

Figure 5: Rotational acceleration for Configuration 1

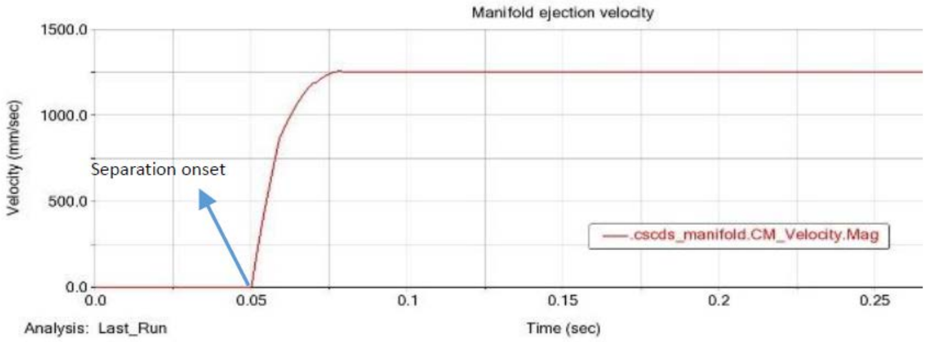

Figure 6: Fore End Sub-assembly ejection velocity

Now Figure 6 shows that the Fore End ejection velocity after separation is 1.25 m/s which is higher than the required translational velocity. Figure 7 shows that the angular velocity of the sub-assembly is 250 deg/s showing significant rotation.

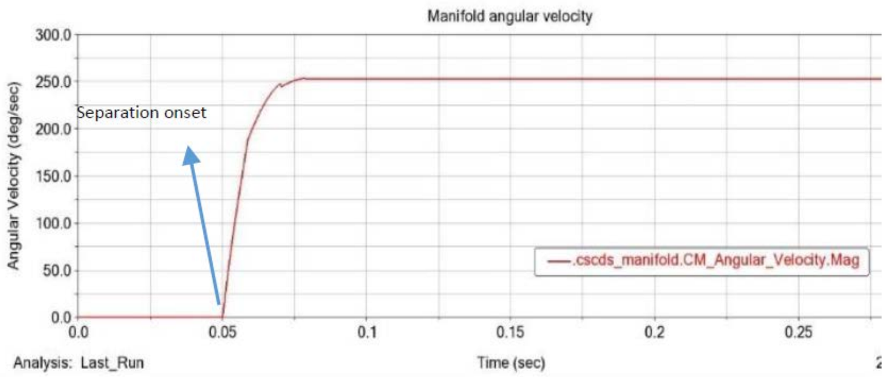

Figure 7: Angular Velocity of Fore End

The animation of the separation (Figure 8) & the clearance curve (Figure 9) from MSC ADAMS showed significant rotation of the Fore End sub-assembly about its C.G. The rotated assembly then collided with the HM at 80 ms after separation. This was observed under both gravity & without gravity conditions. The rotation was more for the zero-gravity condition.

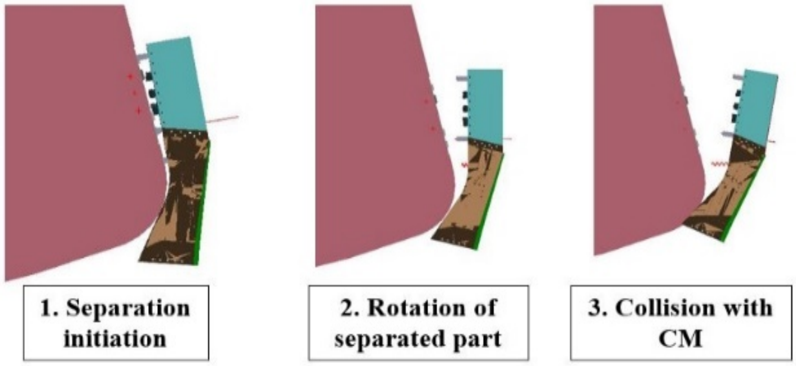

Figure 8: Separation Sequence animation in ADAMS

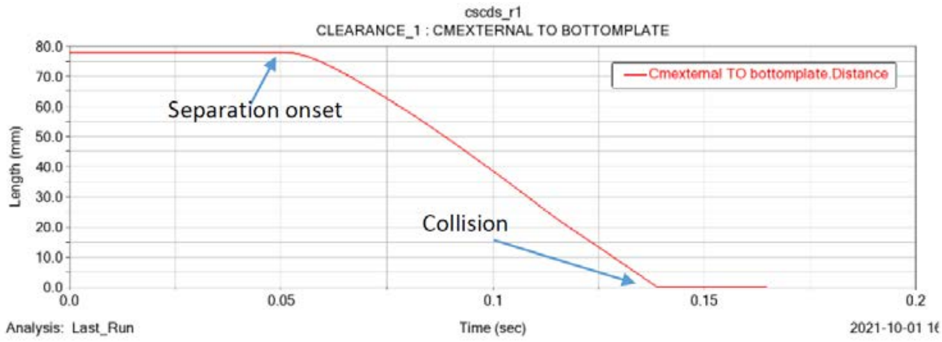

Figure 9: Clearance between HM & Fore End Sub Assembly for Configuration 1

The configuration with ejection springs located at the four corners of the plate does not meet the required condition of collision free separation. Different options were studied by varying the stiffness of the ejection springs. However, all these options resulted in similar observations. Hence, it was decided to provide two additional springs at the C.G. location of the Fore End sub-assembly for proper ejection with minimal rates.

7. Analysis of revised configuration with additional springs at C.G

To mitigate the rotation and subsequent collision as observed in the earlier configuration, a new configuration with two jettisoning springs placed at the C.G. of the Fore End assembly was proposed (Figure 10). This configuration was studied largely due to the following reasons:

- Reducing the energy of ejection springs and redistributing it to additional spring thrusters at CG will provide translational velocity without generating additional moment due to force.
- Envelope and reaction point constraints on HM.

A. Spring design

The two jettisoning springs in the model are in addition to the existing four springs located at the plate corners. The stiffness of four corner springs was reduced and made equal to aid the connectors for a near parallel separation.

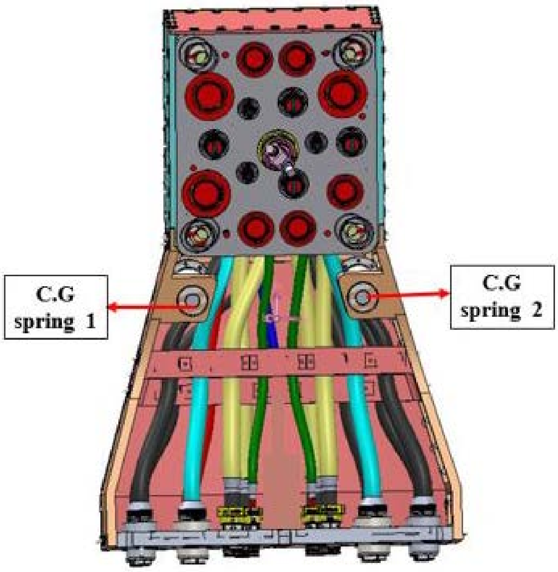

Figure 10: Two additional springs at CG Location

All the four ejection springs were modelled with stiffness, K_{ej}= 6.5 N/mm and preload of 130 N. The stroke of these springs were reduced from 40 to 20 mm. Thus, energy provided by these four springs is:

$$E_{ej} = 4 \times 0.5 \times K \times x^2 = 2 \times 6 \times 20^2 = 4.8\, J$$

The two jettisoning springs at C.G are required to be designed to eject the Fore End assembly with the velocity of 1 m/s. Hence, they need to provide additional energy of, $E_{cg} = 45 - E_{ej} = 45 - 4.8 = 40.2\, J$

Carrying out similar calculations as in the previous model, the spring stiffness was estimated at K_{cg} = 25.125 N/mm for a stroke of 40 mm.

B. Analytical verification of model

To determine the translational velocity of the ejected part, the separation forces need to be re-estimated taking into consideration the updated forces due to ejection springs. The new force is:

$$F_e = F_{cg} + F_{ej} = 2800\, N$$

So total separation force is, $F_t = F_e + F_f + F_{el} = 6000\, N$

Thus, the acceleration, 'a' is,

$$a_x = \frac{F_t}{m} = \frac{6000}{50} = 120\, ms^{-2}$$

It is observed that the translational acceleration has increased in the new configuration.

For estimation of the rotational acceleration, the moments due to ejection springs would reduce from the calculations carried out in the earlier configuration whereas the other moments remain the same. The C.G. springs don't contribute much to moments. The new moment about C.G. due to four corner ejection springs is,

$$M_e = 2 \times 6.5 \times 20 \times (x_1 + x_{12})$$

Total moment is : M = $M_{el} + M_e + M_f$ = 843.6 Nm

Revised angular acceleration and velocity is

$$\alpha_x = \frac{M}{I_{yy}} = \frac{843.6}{2.87} = 294\, rad\, s^{-2} = 16845\, deg\, s^{-2}$$

It is seen that the angular acceleration has been reduced from the first configuration. The dynamic analysis in ADAMS further verifies the model.

C. ADAMS analysis and results

Similar to previous configuration, dynamic analysis of this model was carried out in ADAMS. The spring properties of ejection spring on plates were modified. Two new springs for jettisoning were created at the CG location. The spring properties for these two springs were also defined. The remaining input forces and constraints were same as the previous analysis.

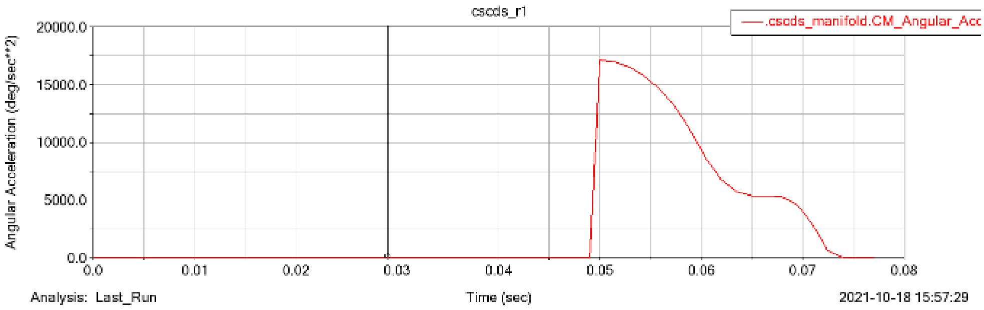

Figure 11: Translational acceleration for Configuration

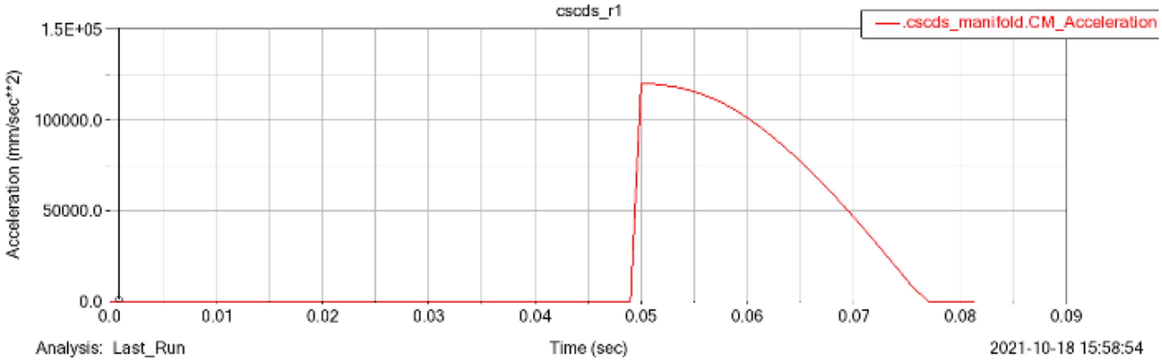

Figure 12: Rotational acceleration for Configuration 2

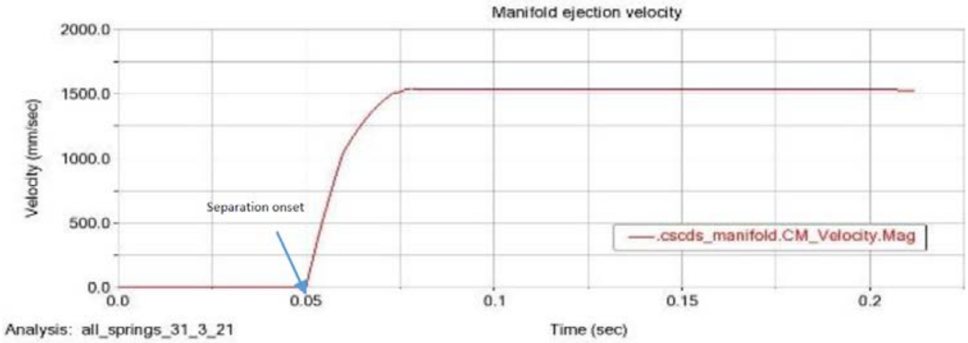

Figure 13: Fore End ejection velocity for new configuration

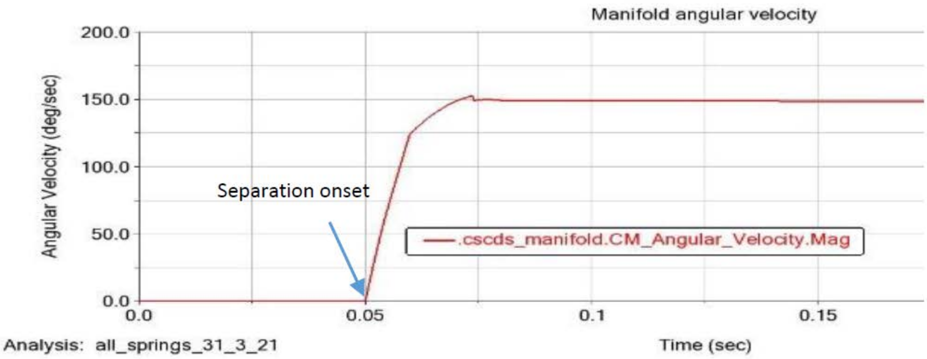

Figure 14: Fore End angular velocity for revised configuration

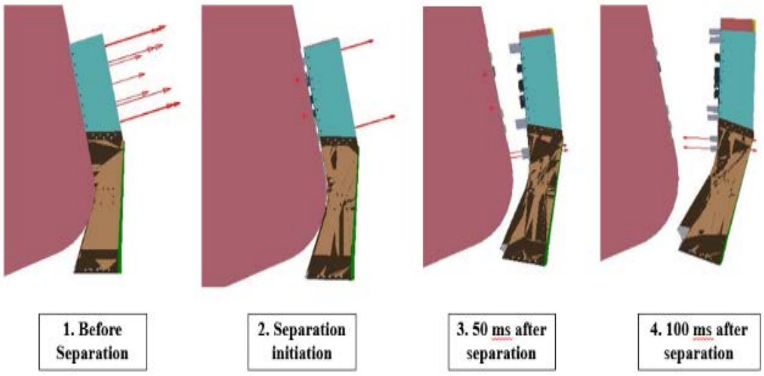

Figure 15: Separation sequence in ADAMS for revised configuration

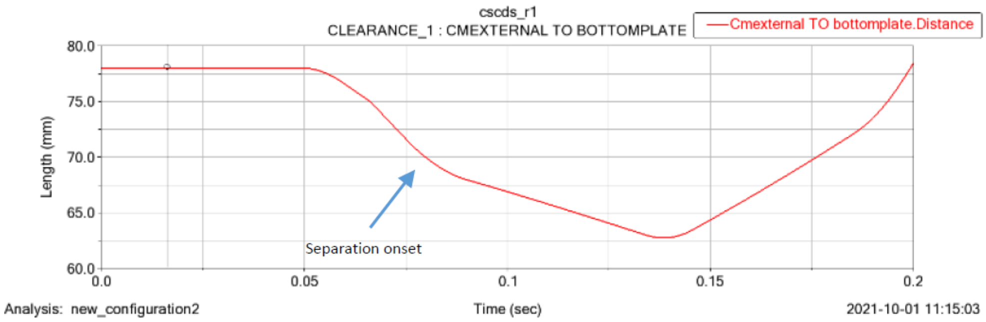

Figure 16: Minimum Distance between HM Aft end dome and Fore End Subassembly for revised configuration

Separation of Fore End sub-assembly was simulated with both gravity and zero gravity conditions. The results of zero gravity condition are shown here. The acceleration along x axis of the separated Fore End sub-assembly (Figure 11)shows that it has an initial acceleration of about 120 ms^{-2}. This is close to the predicted value by the analytical model. The angular acceleration (α_x) is shown in Figure 12. The initial α_x predicted by analytical model matches with the ADAMS results. Thus, the ADAMS model was verified for this configuration also. Figure 13 shows that the Fore End ejection velocity after separation is 1.5 m/s which is higher than previous configuration.

The angular velocity of the sub-assembly is shown in Figure 14, which is 150 deg/s which is lower than previous configuration. Figure 15 shows the separation sequence & Figure 16 shows the clearance curve for the configuration 2. It is observed that the Fore End sub-assembly moves away from the CM after separation ensuring a collision free separation.

8. Conclusion

The separation dynamics analysis of Umbilical System is brought out in this paper. The analytical results are compared with the ADAMS analysis. The offset in C.G. from the location of Fore End Plate Springs demand the introduction of C.G. springs. It is seen that the additional spring thrusters at C.G. along with springs at the Fore End plate provide the total separation velocity demanded for the mission.

The design based on springs located near C.G. also ensures that in addition to the required separation velocity, the rates built up due to the separation are limited to an extent that a collision free separation is ensured.

The rates built up can be further reduced by introduction of a suitable guided separation between the umbilical plates and can be explored in future studies.

9. References

[1] D. Delap, J. Glidden and C. Lamoreaux, "Development of the Orion Crew-Service Module Umbilical Retention and Release Mechanism," 15th European Space Mechanisms & Tribology Symposium, 2013.

[2] M. J, Falbo and R. L. Robinson, "Apollo Experience Report - Spacecraft Pyrotechnic Systems," NASA, 1973.

[3] N. Nath, V. KP, B. G and B. S, "Separation dynamic studies on dual satellite simultaneous separation," in ARMS, 2018.

[4] J. Giesbers, "A technical evaluation of the contact models in multibody dynamics software MSC Adams," Enschede, 2012.

[5] M. Hajžman, "Help text for an introduction to the basics of working with the system ADAMS".

Fractional Order Control Design for Unmanned Aerial Vehicle

Heera Lal Maurya
Electrical Engineering
Indian Institute of Technology
Kanpur
hlmaurya@iitk.ac.in

Padmini Singh
Electrical Engineering
Indian Institute of Technology
Kanpur

Subhash Chand Yogi
Electrical Engineering
Indian Institute of Technology
Kanpur

Laxmidhar Behera
Electrical Engineering
Indian Institute of Technology
Kanpur

Nishchal K. Verma
Electrical Engineering
Indian Institute of Technology
Kanpur

***Abstract*– Unmanned Aerial Vehicle (UAV) is a highly nonlinear unstable system. This work proposes a fractional order backstepping controller applied to quadrotor in the presence of uncertainties. A novel fractional order backstepping controller is designed which mitigate the effect of matched and unmatched uncertainty. The stability analysis of the controller is given using the Lyapunov stability theory and Barbalat's lemma. Simulation analysis shows the advantage of the proposed controller over existing backstepping controller.**

Keywords—Back-stepping Control, Fractional order control, Matched-Unmatched Uncertainty, Lyapunov Stability

1. Introduction

In the recent two decades, the UAV has gained popularity due to various real-time applications such as monitoring any task, obstacle avoidance, surveillance, border patrol, etc. The critical challenge is to seek a balance between the desire to complete a job and preserve network integrity in the presence of network uncertainties and disturbances. Fractional order control techniques [1] are now a days a area of advanced research as it gives flexibility in designing by adding some more parameters to the system. In the proposed work authors have used the concept of fractional order calculus for designing of the inner loop control and outer loop control of quadrotor [2].

Quadcopter is highly unstable system but it is very reliable, agile and maneuverable [3]. It has four propellers with two of them rotating in clockwise and the other in anti-clockwise direction. By varying the rotor speed, 6 Degrees of Freedom can be obtained during flight motion. With equal propellers speed the desired altitude of the quadcopter can be obtained either hold in steady hover (assuming no disturbance/uncertainty). If the rpm of CW or CCW spinning propellers are decreased or increased, a net torque is induced on the quadcopter which provide yaw motion. If rpm of one of the propellers is decreased or increased on the roll and pitch axis, a roll and pitch motion will occur respectively. The quadcopter dynamics is modeled with respect to two reference frame one is inertial frame which is related to the earth and other is body frame which is attached to the quadcopter itself. It is propelled by four rotors require proper control strategies [4]. Recently, with the advancement of digital technology and advanced processors, fractional order differentiation/integration gained much attention in the control community. It has been shown that the fractional order dynamics can exhibit non-classical phenomena than the integer-order dynamics and are a powerful tool to describe the structure of a complex dynamical system. A Fractional order controller provides an extra degree of freedom in terms of tuning parameters which are to be used for improved system performance [4]. This is very important from a robustness point of view where the additional design parameters can be used to enhance the performance of the controller.

The key contributions of the paper are summarized as follows:

A. A fractional order robust backstepping controller is designed, which compensates the matched and unmatched uncertainty.
B. Stability Analysis has been done using the Lyapunov stability theory.
C. Simulations are conducted to validate the proposed approach, and comparative study has been done in the presence of uncertainty.

2. Preliminaries

A. Fractional Order Derivative

The caputo fractional derivative of any function $f(\vartheta)$ is represented by [5]:

$$D^{\alpha}[f(\vartheta)] = \frac{1}{\Gamma(n-\alpha)} \int_{t_0}^{t} \frac{f^{(n)}(\tau)}{(t-\tau)^{\alpha-n+1}} d\tau \qquad (1)$$

where, $\Gamma(.)$ represents the Gamma function and $n-1 < \alpha < n \in N$.

3. Quadrotor Model and Problem Formulation

Fig. (1a) represents the pictorial view of quadrotors. It has four rotor arms. The direction of the forces acting on the four arms is shown in Fig. (1b).

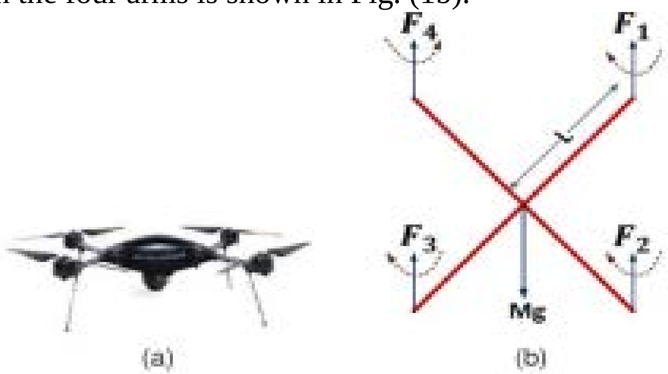

Fig. 1: (a.) Quadrotor (b.) Direction of Forces acting on Four arms

A. Quadrotor Mathematical Model

The quadrotor is an underactuated highly non-linear system, where its twelve states are controlled by four control inputs. There are three position (x,y,z) and three Euler angles $(\emptyset,\theta,\Psi)$ which are termed as roll, pitch and yaw respectively. The dynamics of the quadrotor is [6]:

$$\begin{aligned} m\ddot{x} &= -B_1\dot{x} + (\cos\phi \sin\theta \cos\psi + \sin\phi \sin\psi)u_1 \\ m\ddot{y} &= -B_2\dot{y} + (\cos\phi \sin\theta \cos\psi - \sin\phi \sin\psi)u_1 \\ m\ddot{z} &= -B_3\dot{z} - mg + (\cos\phi \cos\theta)u_1 \\ J_1\ddot{\phi} &= -B_4 l\dot{\phi} + l\tau_1 \\ J_2\ddot{\theta} &= -B_5 l\dot{\theta} + l\tau_2 \\ J_3\ddot{\psi} &= -B_6 l\dot{\phi} + l\tau_3 \end{aligned} \qquad (2)$$

where, m is the total mass of the quadrotor and l is the length of the arm. B_i is the damping coefficient for i = 1, . . . ,6. J_1, J_2, J_3 are the inertial constant. Here, $u1$ is the force applied for position tracking and $\tau1$, $\tau2$, $\tau3$ are torque applied for attitude tracking. Since quadrotor is an underactuated system, we consider virtual control inputs in x, y and z direction as:

$$u_x = \frac{u_1}{m}(\cos\phi\sin\theta\cos\psi + \sin\phi\sin\psi)$$
$$u_y = \frac{u_1}{m}(\cos\phi\sin\theta\sin\psi - \sin\phi\cos\psi) \tag{3}$$
$$u_z = \frac{u_1}{m}(\cos\phi\cos\theta) - g$$

Hence,

$$u_1 = m\sqrt{(u_x)^2 + (u_y)^2 + (u_z + g)^2} \tag{4}$$

In quadrotor for attitude controller desired values of roll and pitch are generated using virtual control input. Let us design desired values of roll and pitch are:

$$\phi_d = \sin^{-1}\left(\frac{m}{u_1}(u_x\sin\psi - u_y\cos\psi_d)\right) \tag{5}$$

$$\theta_d = \tan^{-1}\left(\frac{u_x\cos\psi_d + u_y\sin\psi_d}{u_z + g}\right) \tag{6}$$

B. Problem Formulation

Fig. (2) gives objective of the paper. The objective is to track the desired points and mitigate the matched and unmatched uncertainty. The designed controller is a novel fractional order backstepping controller where virtual control input mitigates the unmatched uncertainty, and real control input mitigates the matched uncertainty. Event-triggering condition relaxes the computation effort of the controller without disturbing the tracking performance of the plant.

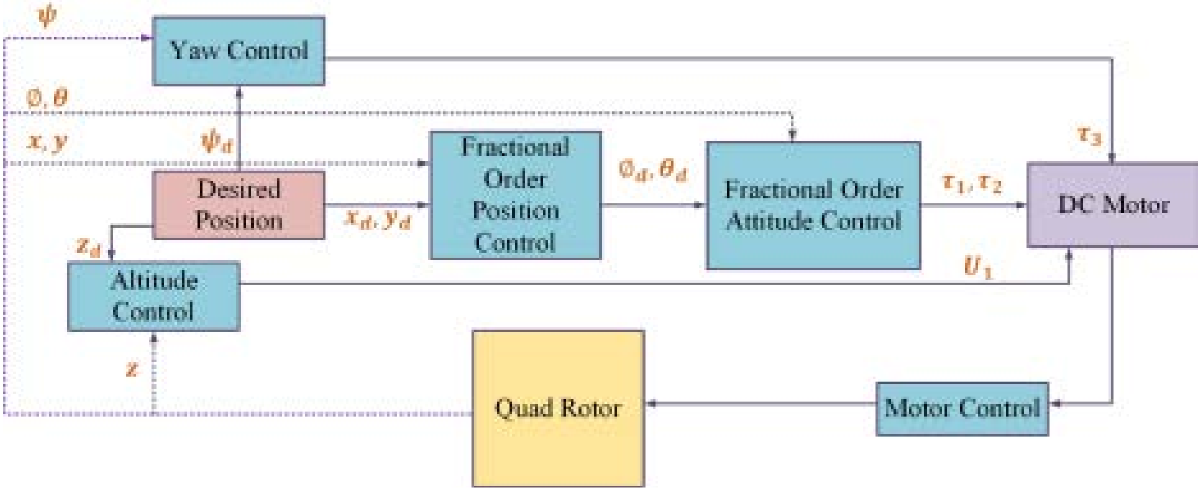

Fig. 2: Control Block Diagram of Quadrotor

Let's us take $x = x_1$, $\dot{x} = x_2$ then the quadrotor dynamics in x direction in presence of uncertainty is:

$$\dot{x}_1 = x_2 + \chi_{ux}$$
$$\dot{x}_2 = \frac{-B_1 x_2}{m} + u_x + \chi_{mx} \tag{7}$$

where, χ_{ux} is unmatched uncertainty and χ_{mx} is matched uncertainty. Likewise, considering $y = y_1$ and $\dot{y} = y_2$, $z = z_1$, $\dot{z} = z_2$, quadrotor dynamics for y and z positions in presence of uncertainty are

$$\begin{aligned}\dot{y}_1 &= y_2 + \chi_{uy} \\ \dot{y}_2 &= \frac{-B_2 y_2}{m} + u_y + \chi_{my}\end{aligned} \tag{8}$$

where, χ_{uy} is unmatched uncertainty and χ_{my} is matched uncertainty.

$$\begin{aligned}\dot{z}_1 &= z_2 + \chi_{uz} \\ \dot{z}_2 &= \frac{-B_3 z_2}{m} + u_z + \chi_{mz}\end{aligned} \tag{9}$$

where, χ_{uz} is unmatched uncertainty and χ_{mz} is matched uncertainty. For Euler angles considering, $\phi = \phi 2$, $\theta = \theta_1$, $\theta = \theta_2$, $\psi = \psi_1$ and $\psi = \psi_2$, dynamics can be written as:

$$\begin{aligned}\dot{\phi}_1 &= \phi_2 + \chi_{u\phi} \\ \dot{\phi}_2 &= \frac{-B_4 l \phi_2}{J_1} + \frac{l}{J_1}\tau_1 + \chi_{m\phi}\end{aligned} \tag{10}$$

where, $\chi_{u\phi}$ is unmatched uncertainty and $\chi_{m\phi}$ is matched uncertainty.

$$\begin{aligned}\dot{\theta}_1 &= \theta_2 + \chi_{u\theta} \\ \dot{\theta}_2 &= \frac{-B_5 l \theta_2}{J_2} + \frac{l}{J_2}\tau_2 + \chi_{m\theta}\end{aligned} \tag{11}$$

where, $\chi_{u\theta}$ is unmatched uncertainty and $\chi_{m\theta}$ is matched uncertainty.

$$\begin{aligned}\dot{\psi}_1 &= \psi_2 + \chi_{u\psi} \\ \dot{\psi}_2 &= \frac{-B_6 l \psi_2}{J_3} + \frac{l}{J_3}\tau_3 + \chi_{m\psi}\end{aligned} \tag{12}$$

where, $\chi_{u\phi}$ is unmatched uncertainty and $\chi_{m\phi}$ is matched uncertainty. Now objective is to design a robust controller u_1, τ_1, τ_2 and τ_3 such that desired position of x_d, y_d, z_d, ϕ_d, θ_d and ψ_d can be achieved and also matched and unmatched uncertainty can also be compensated.

4. Fractional Order Backstepping Control Design

A. Proposed fractional-order reaching law

For the novel fractional order backstepping controller design, a novel fractional order reaching law has been proposed in this paper, which is chattering free compared to existing super-twisting reaching law. Although it is well known that second-order super twisting reaching law reduces the chattering, chattering reduction of the proposed fractional-order reaching law is more significant. The proposed second-order reaching law is

$$\begin{aligned}\dot{s} &= -k_1\left[|s|^{\frac{2}{3}}\mathrm{sign}(s + D^{\alpha}|s|^{\frac{2}{3}}\mathrm{sign}(s)\right] + \mu \\ \dot{\mu} &= -k_2|s|^{\frac{1}{3}}\mathrm{sign}(s)\end{aligned} \tag{13}$$

where, k_1 and k_2 are positive gain parameters. The phase plot response of the proposed reaching law and time-response plot of the proposed reaching law is shown in Fig. (3).

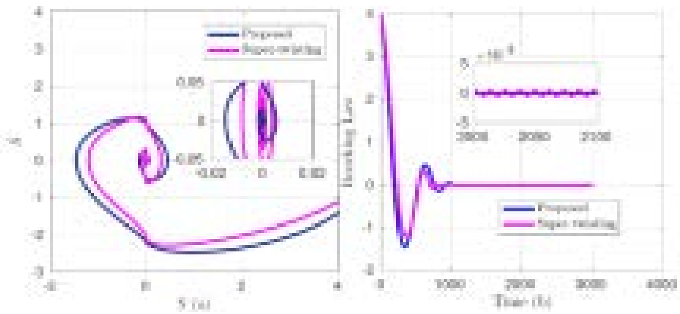

Fig. 3: (a.) Phase Plot (b.) Time-response Plot

From the response of Fig. (3), it is verified that the proposed fractional order reaching law reduces the chattering significantly. In next step procedure for the design of the backstepping controller using proposed reaching law is given.

Notation: Expressions like $-|\bullet|^{\alpha}$ sign($\bullet$), are expressed as $-\ulcorner \bullet \lrcorner^{\alpha}$ to compact the equations.

B. Backstepping Control Design

The dynamics of the quadrotor described in (2) is a combination of second-order subsystems as given in eq. (7), (8), (9), (10), (11), (12). Hence each subsystem is a relative degree two-type of subsystem. In backstepping control if the system can be written in the strict feedback form, then states of the system itself works as a virtual control input [7]. For designing of the backstepping controller let us again take the dynamics of x position.

$$\begin{aligned} \dot{x}_1 &= x_2 + \chi_{ux} \\ \dot{x}_2 &= \frac{-B_1 x_2}{m} + u_x + \chi_{mx} \end{aligned} \tag{14}$$

Now purpose is to design virtual control input x_2 such that state x_1 tracks desired value of x_{1d} and mitigate unmatched uncertainty χ_{ux}. Next from virtual control input x_2 desired value of x_{2d} is obtained and u_x is designed in such a way x_2 achieves x_{2d} and mitigate matched uncertainty χ_{mx}.

Remark 1. The matched and unmatched uncertainty are bounded by some prior known constant such that $\dot{\chi}_{ux} \leq \Delta_{x1}$ and $\dot{\chi}_{mx} \leq \Delta_{x2}$

Design Steps:

Step 1: A virtual control input x_2 is designed such that tracking error $e_{x1} = x_1 - x_{1d}$ and unmatched uncertainty χ_{ux} converges to zero. The proposed virtual control input is:

$$\begin{aligned} x_2 &= -k_{x1}[\ulcorner e_{x1} \lrcorner^{2/} + D^{\alpha}\ulcorner e_{x1} \lrcorner^{2/3} + \mu_{x1} + \dot{x}_{1d} \\ \dot{\mu}_{x1} &= -k_{x2}\ulcorner e_{x1} \lrcorner^{1/3} \end{aligned} \tag{15}$$

Now substituting the value of x_2 from (15) in (14a).

$$\dot{e}_{x1} = -k_{x1}[\ulcorner e_{x1} \lrcorner^{2/} + D^{\alpha}\ulcorner e_{x1} \lrcorner^{2/3}] + \mu_{x1} + \chi_{ux} \tag{16}$$

and defining a new variable $\nu_{x1} = \mu_{x1} + \chi_{ux}$ the error dynamics for e_{x1} will become

$$\begin{aligned} \dot{e}_{x1} &= -k_{x1}[\ulcorner e_{x1} \lrcorner^{2/} + D^{\alpha}\ulcorner e_{x1} \lrcorner^{2/3}] + \nu_{x1} \\ \dot{\nu}_{x1} &= -k_{x2}\ulcorner e_{x1} \lrcorner^{1/3} + \dot{\chi}_{ux} \end{aligned} \tag{17}$$

Hence when $\nu_{x1} = 0$ unmatched uncertainty can be completely mitigated.

Step 2: From virtual control input x_2 desired value of x_{2d} is derived. The desired value of x_{2d} is.

$$x_{2d} = -k_{x1}[\lceil e_{x1} + D^{\alpha}\lceil e_{x1} \rfloor^{2/3} + \mu_{x1} + \dot{x}_{1d} \tag{18}$$

Step 3: Control input u_x is designed such that tracking error $e_{x2} = x_2 - x_{2d}$ and matched uncertainty χ_{mx} converges to zero in finite time. The proposed control input u_x is:

$$u_x = \frac{B_1 x_2}{m} - k_{x3}[\lceil e_{x2} \rfloor^{2/} + D^{\alpha}\lceil e_{x2} \rfloor^{2/3} + \mu_{x2} + \dot{x}_{2d}$$
$$\dot{\mu}_{x2} = -k_{x4}\lceil e_{x2} \rfloor^{1/3} \tag{19}$$

Now substituting the value of control input u_x from (19) in (14b)

$$\dot{e}_{x2} = -k_{x3}[\lceil e_{x2} \rfloor^{2/3} + D^{\alpha}\lceil e_{x2} \rfloor^{2/3}] + \mu_{x2} + \chi_{mx} \tag{20}$$

Now defining a new variable $\nu_{x2} = \mu_{x2} + \chi_{mx}$ the error dynamics for e_{x2} will become

$$\dot{e}_{x2} = -k_{x3}[\lceil e_{x2} \rfloor^{2/3} + D^{\alpha}\lceil e_{x2} \rfloor^{2/3}] + \nu_{x2} \tag{21}$$

Hence when $\nu_{x2} = 0$ matched uncertainty can be completely mitigated. Same procedure is to be followed for designing the controller for y and z position tracking. If the desired trajectory for y positions are y_{1d} and y_{2d}, then the tracking error for position is $e_{y1} = y_1 - y_{1d}$ and velocity is $e_{y2} = y_2 - y_{2d}$. Likewise, for altitude if the desired values are z_{1d} and z_{2d}, then the altitude tracking errors are $e_{z1} = z_1 - z_{1d}$ and $e_{z2} = z_2 - z_{2d}$. Now considering the dynamics of (8), the designed backstepping controller is:

$$y_2 = -k_{y1}[\lceil e_{y1} \rfloor^{2/3} + D^{\alpha}\lceil e_{y1} \rfloor^{2/3}] + \mu_{y1} + \dot{y}_{1d}$$
$$\dot{\mu}_{y1} = -k_{y2}\lceil e_{y1} \rfloor^{1/3} \tag{22}$$

$$u_y = \frac{B_2 y_2}{m} - k_{y3}[\lceil e_{y2} \rfloor^{2/3} + D^{\alpha}\lceil e_{y2} \rfloor^{2/3}] + \mu_{y2} + \dot{y}_{2d}$$
$$\dot{\mu}_{y2} = -k_{y4}\lceil e_{y2} \rfloor^{1/3} \tag{23}$$

where, k_{y1}, k_{y2}, k_{y3} and k_{y4} are positive gain parameters. For altitude dynamics (9), backstepping controller is:

$$z_2 = -k_{z1}[\lceil e_{z1} \rfloor^{2/3} + D^{\alpha}\lceil e_{z1} \rfloor^{2/3}] + \mu_{z1} + \dot{z}_{1d}$$
$$\dot{\mu}_{z1} = -k_{z2}\lceil e_{z1} \rfloor^{1/3} \tag{24}$$

$$u_z = \frac{B_3 z_2}{m} - k_{z3}[\lceil e_{z2} \rfloor^{2/3} + D^{\alpha}\lceil e_{z2} \rfloor^{2/3}] + \mu_{z2} + \dot{z}_{2d}$$
$$\dot{\mu}_{z2} = -k_{z4}\lceil e_{z2} \rfloor^{1/3} \tag{25}$$

where, k_{z1}, k_{z2}, k_{z3} and k_{z4} are positive gain parameters. Likewise, for roll, pitch and yaw tracking if the desired values are ϕ_d, θ_d and ψ_d and tracking errors are defined as $e_{\phi1} = \phi_1 - \phi_{1d}$, $e\phi_2 = \phi_2 - \phi_{2d}$, $e_{\theta1} = \theta_1 - \theta_{1d}$, $e_{\theta2} = \theta_2 - \theta_{2d}$, $e_{\psi1} = \psi_1 - \psi_{1d}$ and $e_{\psi2} = \psi_2 - \psi_{2d}$ then the proposed backstepping controllers are:

$$\phi_2 = -k_{\phi1}[\lceil e_{\phi1} \rfloor^{2/3} + D^{\alpha}\lceil e_{\phi1} \rfloor^{2/3}] + \mu_{\phi1} + \dot{\phi}_{1d}$$
$$\dot{\mu}_{\phi1} = -k_{\phi2}\lceil e_{\phi1} \rfloor^{1/3} \tag{26}$$

$$\tau_1 = \frac{J_1}{l}\left[\frac{B_4 l\phi_2}{J_1} - k_{\phi 3}[\lceil e_{\phi 2} \rfloor^{2/3} + D^{\alpha}\lceil e_{\phi 2} \rfloor^{2/3}] + \mu_{\phi 2} + \dot{\phi}_{2d}\right] \tag{27}$$

$$\dot{\mu}_{\phi 2} = -k_{\phi 4}\lceil e_{\phi 2} \rfloor^{1/3}$$

$$\theta_2 = -k_{\theta 1}[\lceil e_{\theta 1} \rfloor^{2/3} + D^{\alpha}\lceil e_{\theta 1} \rfloor^{2/3}] + \mu_{\theta 1} + \dot{\theta}_{1d}$$
$$\dot{\mu}_{\theta 1} = -k_{\theta 2}\lceil e_{\theta 1} \rfloor^{1/3} \tag{28}$$

$$\tau_2 = \frac{J_2}{l}\left[\frac{B_5 l\theta_2}{J_2} - k_{\theta 3}[\lceil e_{\theta 2} \rfloor^{2/3} + D^{\alpha}\lceil e_{\theta 2} \rfloor^{2/3}] + \mu_{\theta 2} + \dot{\theta}_{2d}\right] \tag{29}$$

$$\dot{\mu}_{\theta 2} = -k_{\theta 4}\lceil e_{\theta 2} \rfloor^{1/3}$$

$$\dot{\mu}_{\theta 1} = -k_{\theta 2}\lceil e_{\theta 1} \rfloor^{1/3} + D^{\alpha}\lceil e_{\psi 1} \rfloor^{2/3}] + \mu_{\psi 1} + \dot{\psi}_{1d}$$
$$\dot{\mu}_{\psi 1} = -k_{\psi 2}\lceil e_{\psi 1} \rfloor^{1/3} \tag{30}$$

$$\tau_3 = \frac{J_3}{l}\left[\frac{B_6 l\psi_2}{J_3} - k_{\psi 3}[\lceil e_{\psi 2} \rfloor^{2/3} + D^{\alpha}\lceil e_{\psi 2} \rfloor^{2/3}] + \mu_{\psi 2} + \dot{\psi}_{2d}\right] \tag{31}$$

$$\dot{\mu}_{\psi 2} = -k_{\psi 4}\lceil e_{\psi 2} \rfloor^{1/3}$$

where, $k_{\phi 1}$, $k_{\phi 2}$, $k_{\phi 3}$, $k_{\phi 4}$, $k_{\theta 1}$, $k_{\theta 2}$, $k_{\theta 3}$, $k_{\theta 4}$, $k_{\psi 1}$, $k_{\psi 2}$, $k_{\psi 3}$ and $k_{\psi 4}$ are positive gain parameters.

5. Stability Analysis

Following lemma is used for the stability analysis of the fractional derivative:

Lemma 1. ([5]) Let x(t) ∈ R be a continuous and derivable function. Then, for any time instant t ≥ 0

$$\frac{1}{2}D^{\alpha}x^2(t) \leq x(t)D^{\alpha}x(t) \tag{32}$$

In this section stability analysis for the convergence of e_{x1}, v_{x1}, e_{x2} and v_{x2} is given. Let us select Lyapunov function as:

$$V = \frac{1}{2}|v_{x1}|^2 + k_{x2}\frac{3}{4}|e_{x1}|^{\frac{4}{3}} + \frac{1}{2}|v_{x2}|^2 + k_{x4}\frac{3}{4}|e_{x2}|^{\frac{4}{3}} \tag{33}$$

Taking the derivative of (33)

$$\dot{V} = v_{x1}\dot{v}_{x1} + k_{x2}|e_{x1}|^{\frac{1}{3}} sign(e_{x1})(\dot{e}_{x1}) + v_{x2}\dot{v}_{x2} + k_{x4}|e_{x2}|^{\frac{1}{3}} sign(e_{x2})(\dot{e}_{x2}) \tag{34}$$

From (17) and (21) substituting the value of $\dot{v}_{x1}$, $\dot{e}_{x1}$, $\dot{v}_{x2}$, $\dot{e}_{x2}$ in (34)

$$\dot{V} = k_{x2} \ulcorner e_{x1} \lrcorner^{1/3} \left[-k_{x1}\left[\ulcorner e_{x1} \lrcorner^{2/3} + D^{\alpha} \ulcorner e_{x1} \lrcorner^{2/3}\right]\right] + k_{x4} \ulcorner e_{x2} \lrcorner^{1/3} \left[-k_{x3}\left[\ulcorner e_{x1} \lrcorner^{2/3} + D^{\alpha} \ulcorner e_{x1} \lrcorner^{2/3}\right]\right] \tag{35}$$

Further simplifying and using lemma 1-

$$\dot{V} = -k_{x1}k_{x2}[|e_{x1}| + D^{\alpha}|e_{x1}|] - k_{x3}k_{x4}[|e_{x2}| + D^{\alpha}|e_{x2}|] \tag{36}$$

which is bounded and stable.

6. Simulation Results

For simulation parameters are taken as: length l = 6.65 cm, mass m = 0.07 kg, damping constants are B_i = 0.01 Ns/m for i = 1, . . . ,6. Inertia in x, y and z directions are J_x = 0.0552 kg.m^2, J_y = 0.0552 kg.m^2 and J_z = 0.1104 kg.m^2 respectively. Simulations are done to show the advantage of proposed fractional order controller over existing controller.

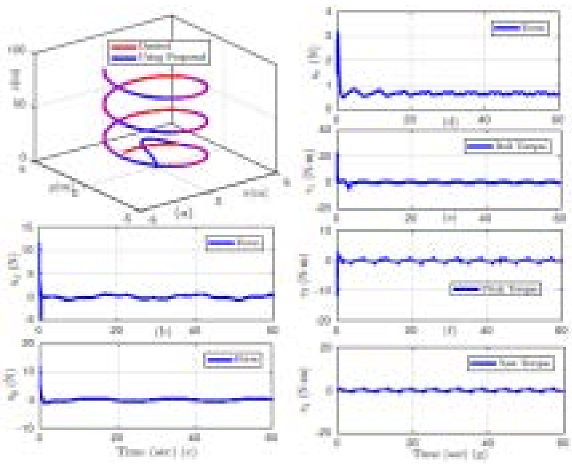

Fig. 4: Quadrotor tracking spiral-shaped trajectory in presence of uncertainties using proposed backstepping control

A. Scenario I:

The initial position is [x = 0 y = 0 z = 0], and desired position is [x = $3sin(0.3t)$ y = $3cos(0.3t)$ z = $1.5t$]. For simulation matched disturbance is taken as χ_m = $0.2sin(t)$ and unmatched disturbance is taken as χ_u = $0.2cos(t)$. Controller gains parameters values for virtual control inputs are between 1 to 2 and for real control inputs values are taken between 1.5 to 2.5. Fig. 4 shows the tracking of the desired path smoothly by the quadrotor in presence of uncertainties. From control inputs of Fig. 4, it is also verified that control inputs of the proposed method are smooth in presence of matched, unmatched uncertainty and are able to reject uncertainties nicely.

B. Comparative Analysis with Reference [8]

The controller given in [8] is applied to the proposed quadrotor. The design of the backstepping controller proposed in [8] will be as follows:

Step 1: The virtual control input for x position tracking will be:

$$x_2 = -k_{x1}e_{x1} + \dot{x}_{1d} \tag{37}$$

Now substituting the value of $x2$ from (37) in (14a)

$$\dot{e}_{x1} = -k_{x1}e_{x1} \tag{38}$$

Step 2: from virtual control input x_2 desired value of x_{2d} is derived. The desired value of x_{2d} is

$$x_{2d} = -k_{x1}e_{x1} + \dot{x}_{1d} \tag{39}$$

Step 3: control input u_x is designed such that tracking error $e_{x2} = x_2 - x_{2d}$ converges to zero. The backstepping control input ux is according to is:

$$u_x = \frac{B_1}{m} - k_{x3}e_{x2} + \dot{x}_{2d} \tag{40}$$

From virtual control input (37) there is no such term which mitigate unmatched disturbances and from (40) there is no such term which contract the matched disturbances.

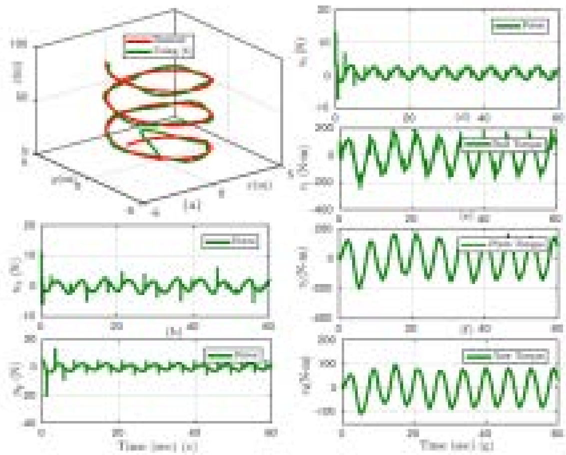

Fig. 5: Quadrotor tracking spiral-shaped trajectory in presence of matched-unmatched uncertainty backstepping control proposed in [8]

Hence theoretical and mathematical analysis proves that the proposed controllers provide more robustness towards uncertainty. Fig. (5) shows the tracking performance of the controller [8] in presence of matched unmatched uncertainty.

7. Conclusion and Future Scope

The paper proposes a novel backstepping controller for trajectory tracking of the quadrotor in the presence of matched and un matched uncertainty. Through simulation results, it is verified that the designed controller rejects the uncertainty nicely. The future scope of the present work is to extend the controller in the cyber-physical frame work.

8. References

[1] X. Shi, Y. Cheng, C. Yin, S. Zhong, X. Huang, K. Chen, and G. Qiu,“Adaptive fractional-order smc controller design for unmanned quadrotor helicopter under actuator fault and disturbances,” Ieee Access, vol. 8, pp. 103 792–103 802, 2020.

[2] Z. Odibat, “Approximations of fractional integrals and caputo fractional derivatives,” Applied Mathematics and Computation, vol. 178, no. 2, pp.527–533, 2006.

[3] G. Yu, D. Cabecinhas, R. Cunha, and C. Silvestre, “Nonlinear backstepping control of a quadrotor slung load system,” IEEE/ASME Transactions on Mechatronics, vol. 24, no. 5, pp. 2304–2315, 2019.

[4] P. Singh, S. Gupta, L. Behera, N. K. Verma, and S. Nahavandi, “Perching of nano-quadrotor using self-trigger finite-time second-order continuous control,” IEEE Systems Journal, 2020.

[5] N. Aguila-Camacho, M. A. Duarte-Mermoud, and J. A. Gallegos, “Lyapunov functions for

fractional order systems," Communications in Nonlinear Science and Numerical Simulation, vol. 19, no. 9, pp. 2951–2957, 2014.

[6] B. Zhao, B. Xian, Y. Zhang, and X. Zhang, "Nonlinear robust adaptive tracking control of a quadrotor uav via immersion and invariance methodology," IEEE Transactions on Industrial Electronics, vol. 62, no. 5, pp. 2891–2902, 2014.

[7] L. Behera and I. Kar, Intelligent systems and control principles and applications. Oxford University Press, Inc., 2010.

[8] Y.-C. Choi and H.-S. Ahn, "Nonlinear control of quadrotor for point tracking: Actual implementation and experimental tests," IEEE/ASME transactions on mechatronics, vol. 20, no. 3, pp. 1179–1192, 2014.

Drive Mechanisms for Internal Weapon Bay Systems of Fighter Aircrafts: Synthesis, Kinematic Analysis, and Optimization of Mechanisms

Ravi Yadav
Aeronautical Development Agency
Bangalore
raviyadav@jetmail.ada.gov.in

Ravi Jai Prakash
Aeronautical Development Agency
Bangalore
jaiprakash @jetmail.ada.gov.in

M. B. Angadi
Aeronautical Development Agency
Bangalore
angadi@jetmail.ada.gov.in

K. S. Nagesh
Aeronautical Development Agency
Bangalore
ks_nagesh@jetmail.ada.gov.in

Abstract - **In a typical 4th generation aircraft, external stores have major contribution in increasing RCS. However, one of the primary requirements of a 5+ generation Fighter Aircraft is 'Stealth' with very low Radar Cross Section (RCS). Stealth requirements of the Aircraft with very low RCS necessitates need to carry Weapons / Stores in an Internal Weapon Bay (IWB). This carriage and deployment of weapons from IWB over a wide range of flight speeds and maneuvering conditions, brings with it a world of challenges that need to be addressed in the design of IWB, ranging from, safe release, high acoustic loading in the bay, and fatigue life of the structure and thin walled members, to sensitive electronics in the bay due to highly unsteady flow in and around the weapons bay cavity.**

One of the most important challenges in the design of IWB is, design of Up-lock Mechanism, Door Actuation Mechanism and Stores Ejection Mechanism, all working in close conjunction. Challenging requirement in this whole business is that the entire sequence of store release cycle, i.e., Up-lock release, door opening, store release, door closing and Up-lock engagement, should occur in about 2.1 seconds.

This paper addresses the design of the kinematics mechanism of theInternal Weapon Bay Doors, based on 4-bar linkage. This configuration helps to minimize the RCS and aerodynamic drag due to external stores. Internal weapon bay (IWB) doors will open and close while ejecting/launching a store. In this paper, a reliable and robust kinematic mechanism designed for opening and closing the IWB doors simultaneously, is brought out.

Keywords— IWB (Internal weapon bay), Radar cross section (RCS), Four-Bar mechanism.

1. Introduction

Stealth is an essential requirement for a 5th generation aircraft. Stealth from the radar wave can be defined in terms of radar cross sectional area (RCS). RCS is defined as "RCS of an object is the cross-sectional area of perfectly reflecting sphere that would produce the same strength reflection as would the object". It is an effective area of an object that intercepts the transmitted radar power and then scatters that power back to radar receiver. Therefore, a 5th generation aircraft should have a minimum RCS for maintaining its stealth feature. To achieve the minimum RCS, the geometry of the aircraft is shaped in such a way that radar wave will not reflect back from the aircraft to radar receiver.

But a fighter aircraft should carry the stores for mission requirements.A typical 4th generation aircraft carries all the stores on externally mounted pylon. This external configuration introduces high radar cross sectional area (RCS) and aerodynamic drag. The RCS can be reduced by placing the stores inside the mother aircraft and the stores should not be visible from outside. A dedicated cavity is formed inside the fuselage of the aircraft to carry stores, named as Internal Weapon Bay (IWB). Consequently, the aerodynamic drag due to stores (external configuration) can be mitigated. Designing the IWB cavity and placing the stores inside the IWB throw many challenges. The designing part of the cavity will not be discussed here.The IWB should be closed during the operation and at the same time the aircraft should be capable of releasing the stores when needed. Therefore, it is required to put the doors to close / open the IWB cavity. In the present work, a mechanism is provided to for the IWB door operation. A four-bar mechanism is chosen for door operation becauseafour-bar mechanism has all revolute joints instead of sliding joint and has fewer number of links compare to other mechanisms. In the paper, synthesis of the four-bar linkage and its kinematic analysis are presented.

During flight operation, the aerodynamic forces are continuously acting on the doors therefore, it is necessary to hold the door in the closed position by a positive mechanism. To achieve that, an up-lock mechanism should be provided. Two doors are provided on both sides i.e. LH and RH sides. Therefore, up-lock mechanism should unlock both the doors simultaneously. During a store ejection, first up-lock unlock the doors and then the door actuating mechanism opens the door after that the store is ejected. The design and operating mechanism of the up-lock are also discussed in the paper.

2. Numerical Investigation

A. Four-bar linkage for door operations

The door operating mechanism is designed while considering the following requirements-

(i) The mechanism should be robust and reliable.
(ii) Aerodynamic loads on the door during opening should be minimum.
(iii) The full operating mechanism must have fewer number of links.
(iv) Any link of the mechanism should not interfere with any of the components of the aircraft.
(v) The total angle turned by the crank is ϕ.
(vi) The opening time of door is 1 sec so is the closing time.
(vii) In fully open condition, any component of the door or link should not be in the store ejection path.

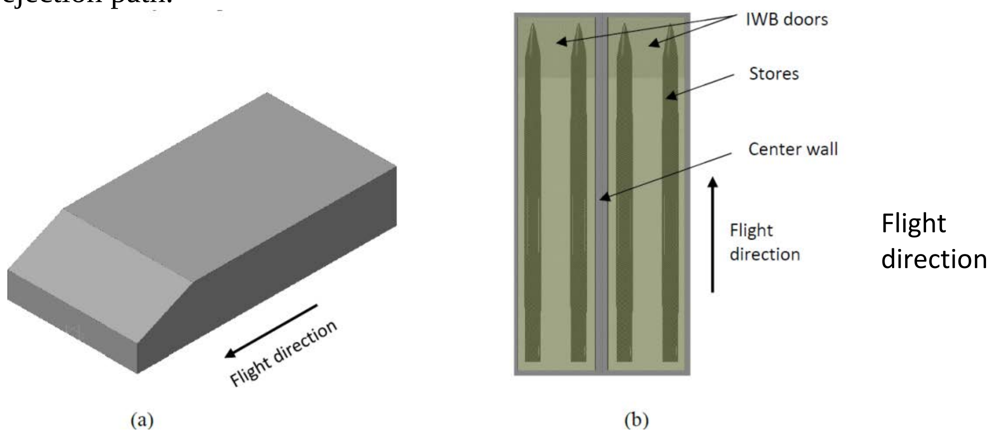

Fig. 1 Illustrative diagram of IWB cavity (a) Isometric View and (b) Bottom view

By looking at Fig. 1(b), it is clear that doors need to put to close the cavity. During the store ejection, the doors should open, otherwise these doors is in closed condition. Two doors are provided on both sides and each door is split in two parts, namely (i) Inboard door (IB door) and (ii) Outboard door (OB door), to minimize the aerodynamic drag on the door while opening. It can be seen from Fig. 2 that in the fully open condition the IB door is moved back and the total length of the door in the air is reduced. Fig 2 shows the front view of the IWB closed and fully open conditions. The main challenge is to design the hinge axis of the crank i.e. what should be the coordinate of the hinge so that the door should perfectly seal the cavity in closed condition without interfering with other aircraft components.

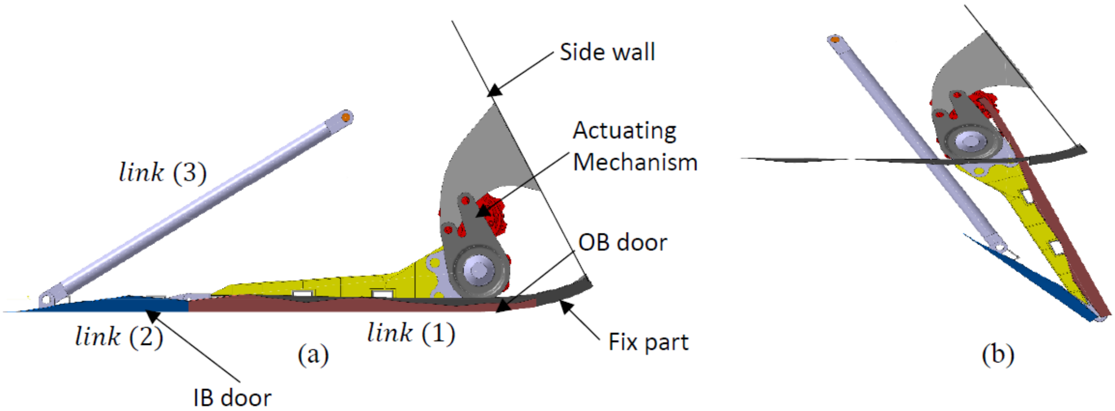

Fig. 2 IWB (a) open and (b) closed positions

Fig. 3 shows the line diagram for the OB door. It shows closed and opened position of the OB door. The objective here to determine x_0, y_0 and s in such a way that while closing the OB door should rest on the fixed part and in fully open condition the door should not interfere with the fix part and at the same time the locus of the end point of door (dotted circle) should have a minimum clearance (given) with the side wall of the IWB cavity. From the rule of geometry, we can write the equation of circle –

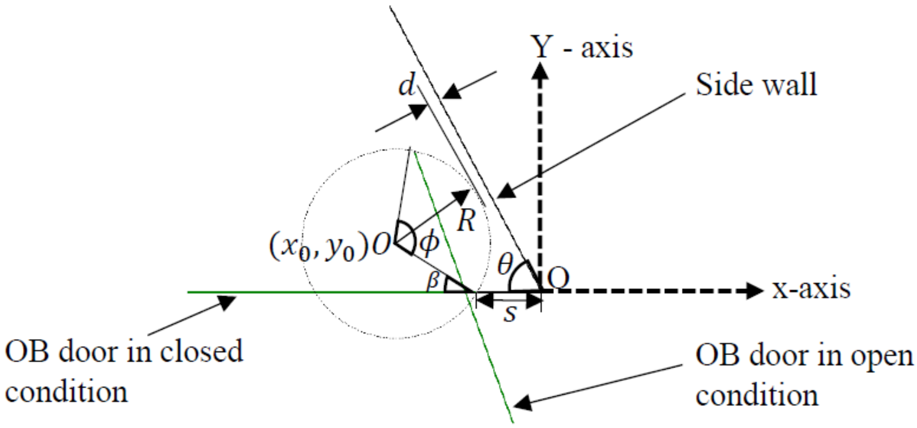

Fig. 3 Line diagram for the OB door rotation

$$(x - x_0)^2 + (y - y_0)^2 = R^2 \; and \; R^2 = (x_0 + s)^2 + y_0^2$$

Where,

R = radius of the circle (locus of the end point of door)
(x_0, y_0) = Hine point coordinate
ϕ = Angle rotated by the OB door or crank
d = minimum distance between the circle and side wall
s = distance from the origin (O) to point where the circle cuts the x-axis
θ = inclination angle between the side wall and x-axis

Equation of side wall –

$$y = -x(tan\theta)$$

The minimum clearance between the circle and side wall is –

$$d = \frac{|x_0 tan\theta + y_0|}{\sqrt{1+\tan^2\theta}} - R$$

After rotation of ϕ, the equation of the OB door –

$$(y - y_1) = (x - x_1)\tan(\phi)$$

The above equation intersects with x-axis when $y = 0$

$$x^* = -\frac{y_1}{\tan(\phi)} + x_1$$

And from the Fig. 2, it can be deduced –

$$s = x_0 - y_0 \tan(\beta)$$

The OB door should rest on the fixed part in closed condition. Therefore –

$$s = x^* = x_0 - y_0 \tan(\beta)$$

Now the three unknowns (x_0, y_0 and s) can be determined from the above three equations.

B. Calculation for computing the dimensions of the link –

The width of the OB door is fixed. Therefore, by fixing hinge axis or point (A), the length of link (1) or value of a is fixed. Now the goal is to determine the values of b, c and d. The value of b is determined based on the aircraft geometric constraint. After rotation of OB door for a given angle (ϕ), the IB door will also rotate with respect to the OB door. But the IB door should clear the weapon ejection path. The weapon ejection path is given and based on the ejection path the values of c and d are calculated. As we can see in Fig. 4, the point A and D are fixed and point B will move in the circle because point B is on the crank (AB). Now draw a circle passing through the point B and B′. This circle will be the locus of point B. Now again draw a circle passing from point C and C′ and this is locus of point C. Locus of the centre of the circle will be a straight perpendicular to the line joining C and C′.

Parameters for the calculations –
a = length of link (1) or AB
b = length of link (2) or BC
c = length of link (3) or CD
d = length of link (4) or AD

(x_0, y_0) = coordinate of point D (link (4) hinge point)
(x_1, y_1) = coordinate of point C
(x_2, y_2) = coordinate of point C' (after rotation)

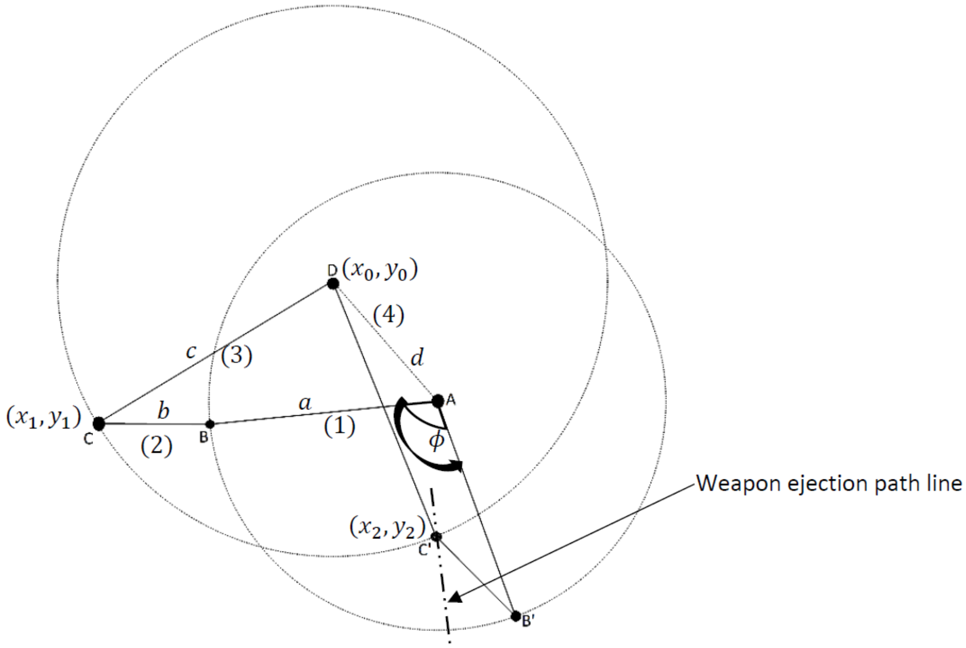

Fig 4. Line diagram of Four bar linkage for door opening / closing mechanism

The equation of the circle passing from C and C′ –

$$(x - x_0)^2 + (y - y_0)^2 = c^2$$

From the geometry we can write –

$$(x_1 - x_0)^2 + (y_1 - y_0)^2 = (x_2 - x_0)^2 + (y_2 - y_0)^2$$

After simplification –

$$y_0(y_1 - y_2) + x_0(x_1 - x_2) = \frac{1}{2}\left((x_1^2 - x_2^2) + (y_1^2 - y_2^2)\right)$$

This is an equation of a straight line. After full rotation of the OB door, there should be a positive angle between the link (4) and link (3), otherwise locking of the links may happen during closing the OB door. In this study arbitrarily 15^0 is chosen. After fixing this positive angle or transmission angle, the point D will be the intersection of the bisecting line of C and C′ and the line generated from the point C′. Once we know the point D, values of $c\ and\ d$ can easily be determined.

C. Up-lock linkage for locking the door –

The up-lock mechanism is designed while considering that both the doors (LH and RH sides) should unlock simultaneously i.e. synchronization must be there. Fig. 5 shows the up-lock mechanism. It is a combination of two four bar mechanisms. Both latched will be actuated by the actuation of link (1). Both the four-bar mechanisms are synchronised. For creating two four-bar mechanisms, we need three fixed points ($O, O^{'} and\ O$") and these points are determined using aircraft space constraints. The design is based on the fact that during operation the angular displacement of both the latches must be same.

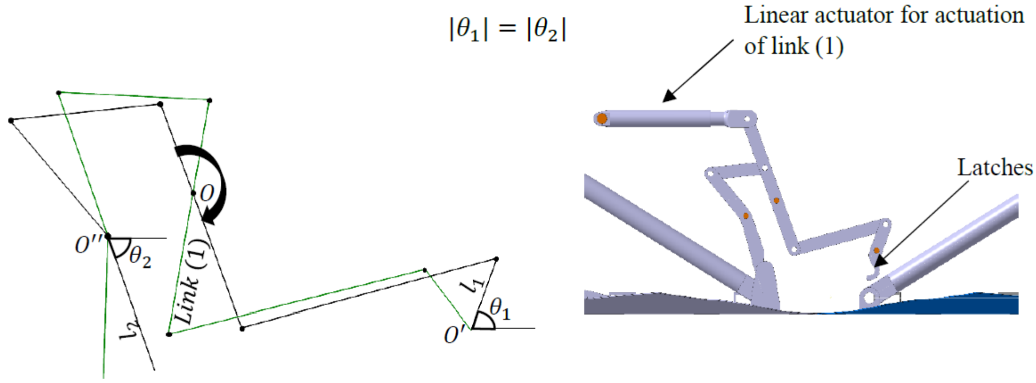

(a)Black lines indicate the initial position and green lines indicate the final position

(b) 3D – Diagram of Up-lock mechanism

Fig. 5 Up-lock mechanism

3. Results and Discussions

A. Door operations

In the present work, values of $a = 556\,mm, b = 275\,mm, d = 25\,mm,$ and $\beta = 26^0$. Based on these values $s = 118\,mm$ and (x_0, y_0) is $(229\,mm, 55.6\,mm)$. Value of $c = 670\,mm$. CATIA is used for creating 3D design and kinematic analysis. Fig. 6 shows the front view of the IWB closed, partially open and closed conditions.

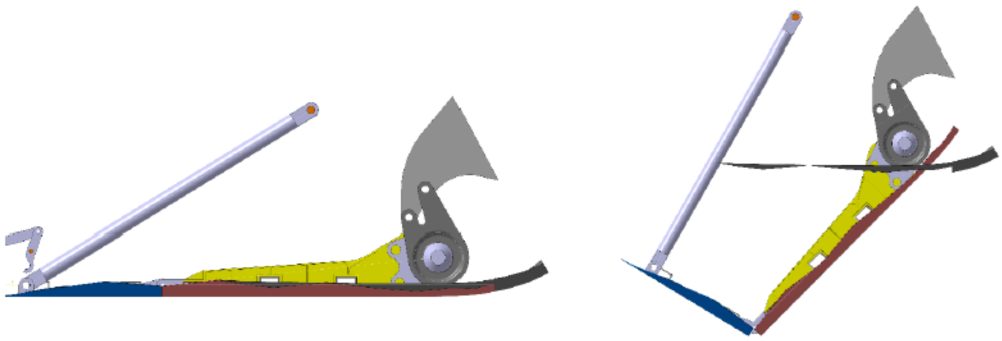

(a) Crank angle ($\phi = 0^0$)

(b) Crank angle ($\phi = 45^0$)

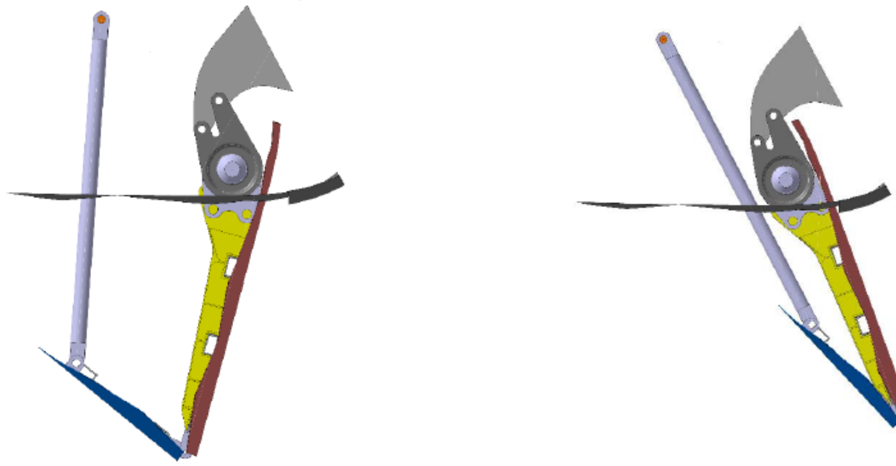

(b) Crank angle ($\phi = 80^0$)

(d) Crank angle ($\phi = 110^0$)

Fig. 6 Door operating mechanism

It can be seen from the above figure that the OB door (in Red color) rotates about the hinge line is such a way that it doesn't interfere with any of the structural component and in closed condition, it rests on the fix part.

B. Kinematic analysis of door mechanism –

In this section, the velocity and acceleration analysis of IB door is given. For kinematic analysis of IB door, a point on the IB door is required because the velocity and acceleration will be determined on that point only. Fig. 7 shows the magnitude of the acceleration of the mid-point on IB door.

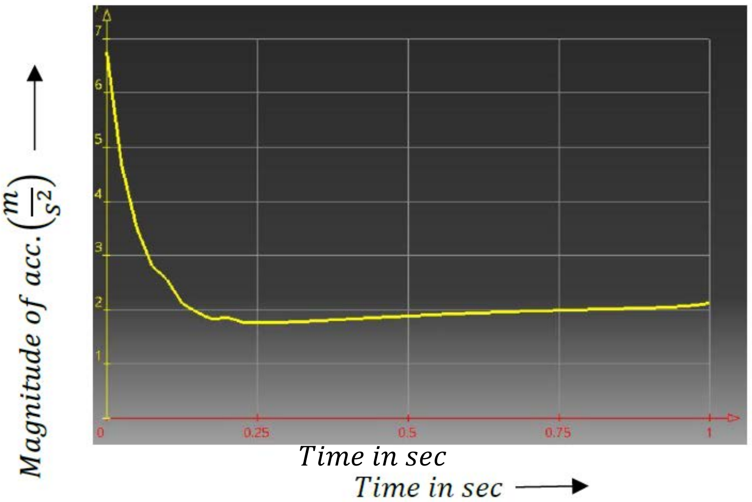

Fig 7. Acceleration of the IB door

The IB door experiences the maximum acceleration at starting or t = 0sec which is 6.5 m/s^2. While designing the door it is necessary to take care the inertia loads which the IB door will experiences. Fig. 8 shows the acceleration of mid-point of link (4).

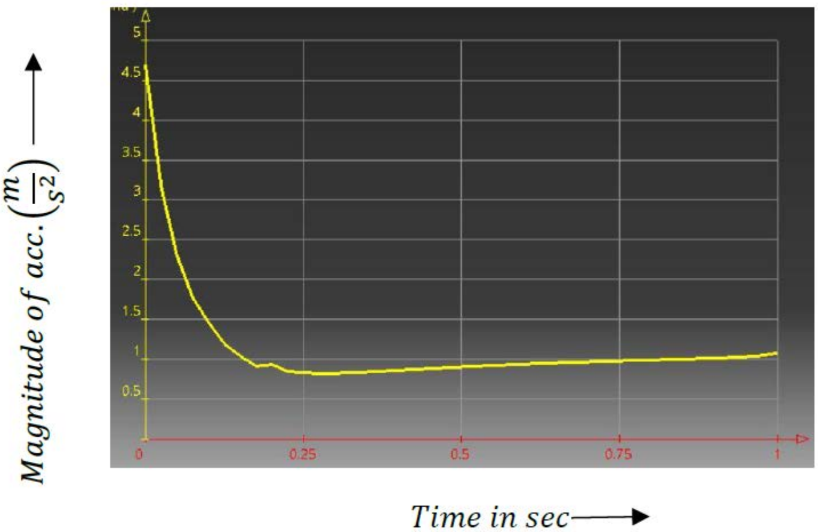

Fig 8. Acceleration of the link (4)

Both the curves show the similar behavior in a way that both have the maximum acceleration at t = 0 sec and then the acceleration gradually decreases. For designing the links, it is important to check for the inertia loading.

C. Kinematic analysis of Up-lock mechanism –

Fig. 9 and 10shows the initial and final positions of the up-lock mechanism and angular speed of the latches, respectively.

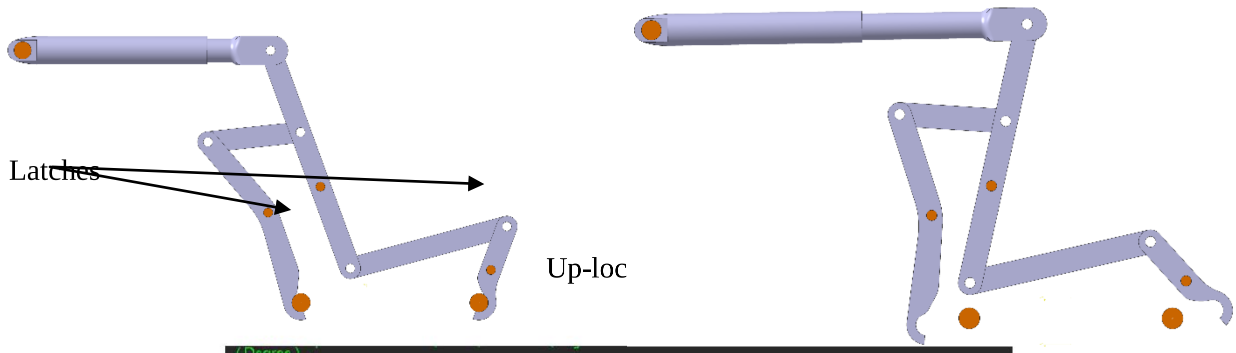

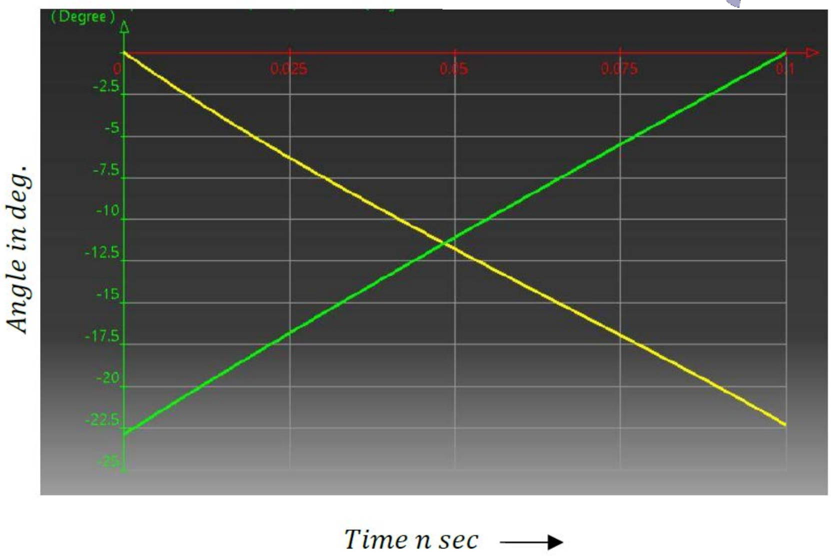

Fig. 10 Angular speed of latches

As we see in Fig. 10 the magnitude of angle turned in 0.1 sec by the latches are the same and this was the criteria for designing for the up-lock mechanism.

4. Conclusions

- The four-bar linkage for door operation opens the door in 1 sec. This four-bar linkage is a rocker-rocker kinematic inversion of a four-bar chain. The crank rotates through an angle of 110^0 in 1 sec. The acceleration of the IB door and link (4) are analyzed with respect to time and the maximum accelerations for IB door and link (4)are found to be 6.5 m/s^2 and 4.5 m/s^2, respectively.
- It is necessary to calculate the maximum acceleration for getting the inertia loads on the door. Both the door will experience the aerodynamic force as well as inertia loads. Therefore, for designing the door, the values of both the loads must be known with respect to time. Aerodynamic loads are not considered in this study.
- The up-lock mechanism is a combination of two four bar mechanism which work in a complete synchronization to unlock the both the door simultaneously. The operating time for up-lock mechanism is 0.1 sec. The linear speeds of the latches must be the same for synchronization and it is verified from the angular speed diagram.

5. References

[1] Internal Weapon Bay Door Actuation Mechanisms in contemporary aircrafts, viz. F-22 Raptor,YF 23, F-35, FGFA

[2] YF 23 Leading Edge Flap and Weapon Bay Door Hydro-mechanical Drive Systems, AIAA-93-1162

[3] Flight Manual YF 23A, NTM 1F-23(Y)A-1

[4] Norton R.L., Kinematics and Dynamics of Machinery, McGraw Hill India, 2010

[5] Ratan S.S., Theory of Machine, McGraw Hill India, 2019.

[6] Thoughts and Analysis of Some Problems in the Hydraulic Control System Design with theWBD, 2016 IEEE/CSAA International Conference on Aircraft Utility Systems (AUS), October10-12,2016

Experimental Modelling and Analysis of Acoustic Impingement on Propagating Fires

Bhushan Thombare
Department of Aerospace Engineering
SRM Institute of Science & Technology
Chennai
bp5463@srmist.edu.in

Saumya Shekhar
Department of Aerospace Engineering
SRM Institute of Science & Technology
Chennai

Vinayak Malhotra
Department of Aerospace Engineering
SRM Institute of Science & Technology
Chennai

***Abstract* – Space propulsion commands the essential understanding of engendering fires. For most terrestrial and extra-terrestrial systems, improving propulsive performance by regulating external factors has been a demanding topic of study. Understanding of fire propagation is needed for space propulsion. The majority of combustion processes are accompanied by sound, which has a significant impact on the process. Significant work has been done but the complexity problem has precluded further understanding due to heat and mass transfer. The aim of this research is to gain a physical understanding of the acoustic- thermal energy exchange and its consequences for diffusion combustion. Experiments were carried out with systematic variations in configurations, surface orientations, Number of External heat sources, variation in frequencies, and acoustic source distance. Work includes research on flame behavior in presence of external heat sources and heat sink sources, under varying configurations and orientations. Different configurations of external heat sources and heat sinks will be experienced under various conditions and changes in pilot fuel regression rates will be evaluated systematically. The outcomes from the research will be applied to increase fire safety and a better combustion process. The results are possible to assist an accurate energy prediction system via way of means of growing suitable correlations based on experimental and numerical results for efficient energy transfer prediction**

Keywords– Propagating Fires, Thermoacoustic, External Heat source, Forward Heat Transfer, Downward Spreading Fires.

1. Introduction

Fire is without a doubt one of humanity's greatest invention, and it has been constant source of human evolution. Engineering industrialization the practical environment, functional and operating structures in variety of domains have been benefitted from the efficient use of fire.

Figure 1: GSLV F06

Fire also has the potential to spiral out of control and be source of one of the world worst disasters that occurred in the forms of large-scale fires in industries, forest fires, building fires, Aircraft and Rocket crashes, which lead to illimitable loss of mankind, nature, resources, and every year an immense amount of money is being invested on research to prevent fires. In the records of human spaceflight, a few fire accidents are recorded which resulted in the loss of crew.

Figure 2. Indian Airlines flight 171

On-orbit, there has been a number of overheat incidents that were essential and represented a clear risk to the crew. Since a spacecraft cabin is an enclosed volume with limited no of resources for firefighting and options for crew response and escape, the severity of even small fire is increased. The main reason for the appearance of fire is the growth and spread of flames. Fire proliferation focused on this work. Through this combustion, the development speed of the flame, that is, the moving speed of the flame on the surface of the fuel, is determined.

Figure 3. Apollo 1 crash

As a result of the experiment, it's known that Acoustics excitation can improve the flame combustion efficiency because of the introduction of sound waves causing flame instability. Acoustic energy creates localized temperature, pressure, and velocity fields around the pilot fuel, which are affected by lead.

The principal issue with space fire is its propagating nature. Figure 1, 2 and 3 show the accidents because of fire propagation. Research efforts have extended over a century with Semenov [1] highlight the chemical mechanics and chemical reactions. Experimental work by Toong et al. [2] has shown observations based on diffusion flame and showed the evidence of both the suppression and the amplification of sound waves when they interact with a flame. Chiu et. al., [3] analyzed the turbulent combustion of droplets from premixed fuel and liquid fuel. Kampen [4] developed an effective numerical algorithm to test the sensitivity of the combustion system to thermoacoustic instability. Krivokorytov et. al., [5] estimated the effect of acoustic vibration on the characteristics of diffusion flames. Dowling and Mahmoudi [6] solved the problem of limiting combustion noise. Shafiq et al. [7] studied about one-dimensional premixed laminar methane flame, when subjected to sound acoustics and performed simulations of oncoming flow oscillations were performed for the heat release rate dynamics for ducted flames. Parallel results for the effectiveness of acoustic suppression were confirmed by Niegodajew et al. [8] and for the liquid line flame, the results were demonstrated by Friedman and Stoliarov [9]. Non-premixed flame sheet deformation was introduced by Yamazaki et al. [10] around 400 Hz sound frequency. All these previous researches were focused on the suppression of flame produced by stationary burner by acoustics. At different amplitudes and frequencies, the flame response with acoustics waves has been studied.

In the midst of significant scientific contributions, one factor that has yet to be thoroughly investigated is the effect of thermo acoustics on configurations of external heat sources and comparison of performance for various source locations. This is likely to have a major impact on the propagation phenomenon, which is reason to research and study fire propagation.

The work's specific objectives are to:

(i) To investigate the phenomenon of fire propagation in presence of acoustic source at different locations.

(ii) To investigate the effect of a number of external heat sources in the form of distinct configurations on the pilot fuel.

(iii) To fundamentally understand the role of key controlling parameters.

2. Experimental Setup And Solution Methodology

A basic experimental setup was upraised to investigate fire propagation. It was done this way so that more parameters could be varied and studied

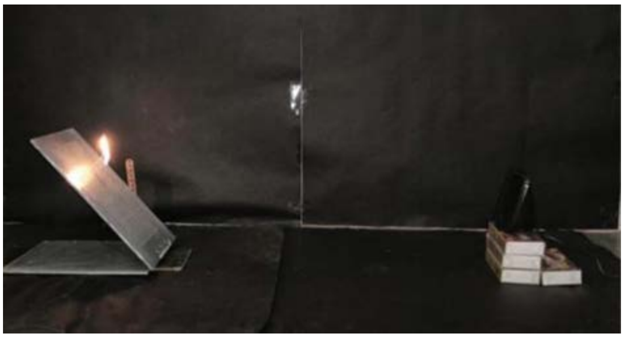

Figure 4. Complete Experimental Setup

Figure 5. External Heat Sources.

The Experimental Setup includes a) A matchstick Holder made of mild steel, b) Orientation change mechanism, c) a matchstick with uniform marking, and d) Speakers. The coordinate sticks are fixed at interval 0.5cm division marking followed by three 1 cm markings. A mild steel plate was used to settle the match sticks opposite to the base. The interspace distance between matchsticks is 0.5cm. A computer multimedia speaker 2.1 was utilized to emanate sound. For changing frequencies, NCH tone generator computer software was used. To study the different impacts of acoustic vitality on heat energy. matchsticks were fixed in 4 configurations: a) Unilateral b) Bilateral c) Trilateral (Y) and d) Quad-lateral (+) configuration.

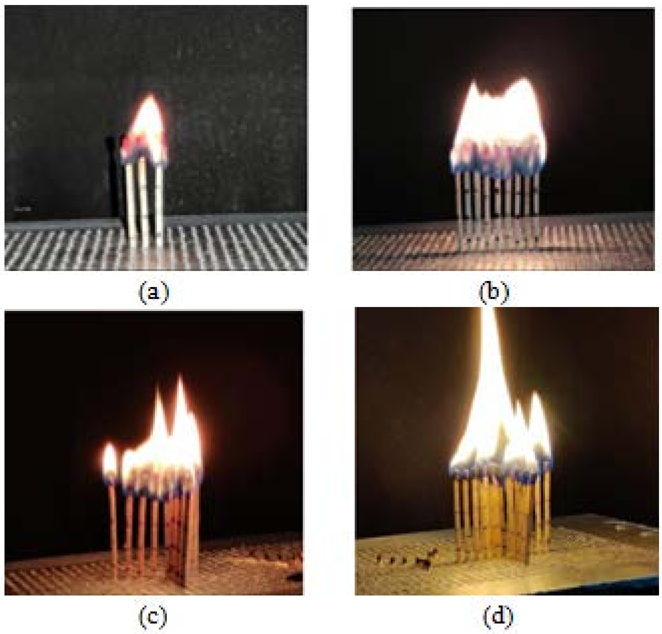

Figure 6. Four Different Configurations, (a) Unilateral, (b) Bilateral, (c) “Y” Configuration, (d) “+” Configuration

The speaker was set at a distance of 50 cm from the pilot fuel for all four cases. It was compared with the results of 100cm. [11] The essential objective was to carry out experiments when no acoustic source was placed. In each case, the fire spread rate was measured by noticing down the time taken to burn 1 cm of the matchstick marking. These values of fire spread rate make the base case for comparison. Taking after this a speaker was placed at 50 cm perpendicular to the pilot fuel and sounds of changing recurrence were created using the NCH Tone generator computer program. Repeatability of all experiments was guaranteed to third order. Pictures and recordings were taken to capture the extraordinary cases.

A. Forward Transfer Theory

From the Second Energy Equation we know that:

Energy Change = Energy produced – Energy lost

So,

$$\rho_s C_s V(dT/dt) = q_p - q_L \quad (1)$$

$$\text{where, } q_p = \Delta H_c V C_i A^* e^{(Ea/RT)} \quad (2)$$

$$q_L = hA(T - T_a) \quad (3)$$

Where,

ρ_s : Density of the solid fuel;

t : Thickness of the solid fuel;

V : Speed of sound in that medium;

$T_{surface}$: Temperature of the surface;
T_{∞} : Temperature of the surrounding;
dT/dt : Change in temperature;
q_p : Energy produced;
q_L : Energy lost;
A^* : Pre-exponential factor;
E_a: Activation energy;
R : Ideal gas constant;
T : Temperature in kelvin;
H : Thermal Conductivity constant;
A : Cross-sectional area of the material;
T_a : Ambient temperature;
q_{net} : Total Energy;
c_s : Speed of sound in the material

Hence, according to Classical Forward Heat Transfer Theory, the Flame spread rate (r) is given by:

$$r = \frac{\int q_{net}}{\rho_s \tau_s c_s (T_{surface} - T_{\infty})} \quad (4)$$

B. Measurement

The rate at which the surface burns is called the Flame spread rate which is linearly calculated as:

$$r = \frac{Distance\ burnt}{Time\ taken\ to\ burn\ that\ region} \quad (5)$$

The term is the difference between the energy generated and the energy lost.

The fire regression rate was calculated in each case where a speaker was utilized to transmit the sound of particular frequencies. The experiment was conducted at typical room temperature and readings were taken legitimately ensuring productivity and congruity in each case. It is imperative to know that each data shown here speaks to the repeatability and reproducibility of the third order.

3. Result and Discussion

The initial experiment was carried out to determine the base case values for the flame spread rate. It's worth noting that the flame spread rate of pilot fuel was measured from all orientations. Figure 7 shows a non-monotone pattern with a maximum burn rate of 5.142cm/min at 45 degrees.

Based on the results obtained, a novel equation model was formed as:

$$y = a.x^2 + b,x + c \quad (6)$$

Where, 'y' is the representation of fire propagation rate, 'x' detail te surface orientation and 'a, b and c' are equation coefficients and their values vary for different cases. At a fixed frequency and with varying surface orientation, the solution to this equation will extend details of the fire propagation rates. This necessary information of propagation rates would be very useful in signifying the appropriate control time, understanding the propagation and thus suppression action to be taken and in design of state art fire suppression system. Figure 8 represents the plot for single matchstick which denotes flame spread rate. As

$$y = -0.0004x^2 + 0.0384x + 3.5956 \quad (7)$$

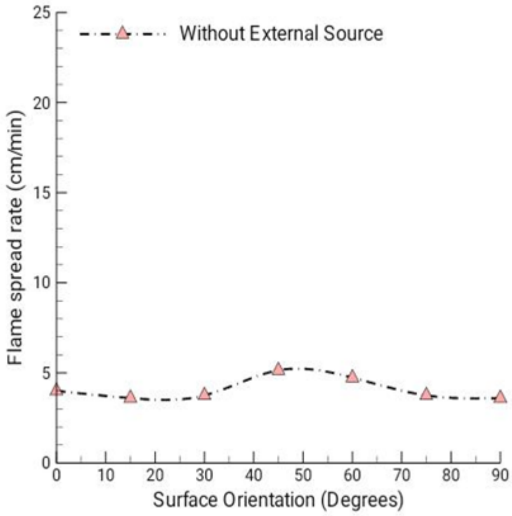

Figure 7. Single matchstick in absence of Acoustic

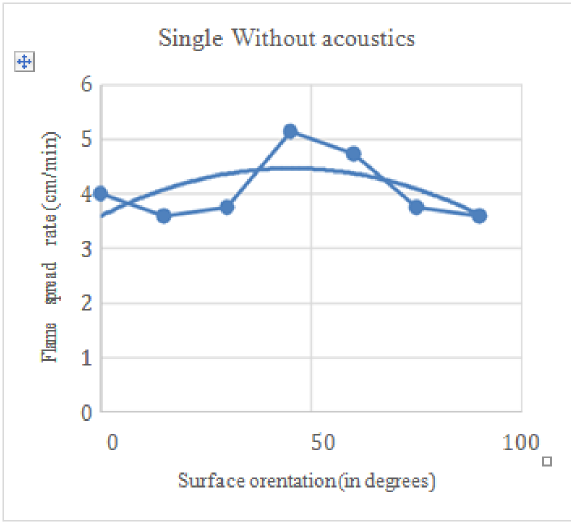

Figure 8. Single matchstick in absence of Acoustic (plot equation)

The result was checked using traditional heat transfer theory, and matched from Pratik et al, [12] it was found to be fairly accurate. The experiment was carried out to determine the fire regression rate's base case values. It's important to remember that the flame regression intensity of pilot fuel was calculated with and without acoustic interference at both orientations.

The recurrence frequency was adjusted from 3500Hz to 7500Hz. The drift is non-monotonic for all cases, with the most intense burn rate of **220%** at 75 degrees angle for 6500 Hz frequency, as shown in the plot (figure 9). These figures were used as a baseline for comparing fire rates for various configurations with external heat Sources. The coefficients of a, b and c for this case are 0.0001, 0.047 and 6.2407.

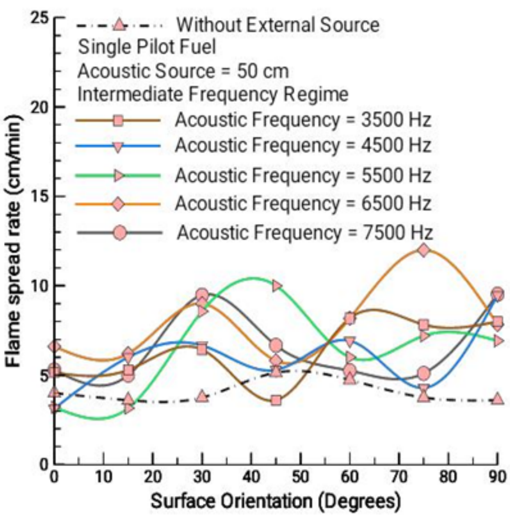

Figure 9. Pilot fuel with varying Frequency.

According to traditional heat transfer theory over thin solid fuels, the propagating front expands upstream through heat feedback (forward heat transfer) from burning to unburned solid fuel. This is manifested as an increase or decrease in regression rates. It is formed around the fuel surface due to the convective buoyant stream, localized speed, and temperature regions. High temperature smoke, where heat brings heat flowing parallel to the moving surface, provides additional energy and preheating. Fast regression rates can be due to high accumulated heat transfer from burned fuel to unburned fuel. The remaining results were split into two categories.

A. Stabilizing Effect:

The flame flickering stops in this effect, and the flame becomes steady under the influence of acoustics. The coupled energy conversion of acoustic and thermal energy is assumed to be the same, and there is no impact in pilot fuel.

B. Destabilizing Effect:

In this scenario, the flame begins glowing brightly due to acoustic impact, and the relapse rate changes as a result. The acoustic coupled thermal energy is dominant, or the thermal energy is prominent to the acoustic energy, as shown by an increase or decrease in the flame regression rate.

The effect further divides the result into three zones.

A. Heat Sink Zone:

Heat transfer decreases in this regime due to a reduction in the concentrated temperature around the pilot fuel. Because of acoustics, not enough oxygen enters to fume the pilot fuel. As a result, the regression rate for this situation is lower than for the pilot fuel.

B. Neutralizing zone:

In this case, the heat transfer is constant to that of the pilot fuel, so there is no acoustic effect i.e. the regression rate is the same as in the base case of pilot fuel.

C. Heat source zone: The total heat transfer dominates in this area due to buoyancy, which transports heat from burned to unburned fuel due to the external effects of acoustics. As a result, the regression rate for this situation is higher than for the pilot fuel.

The ratio of the flame spread rate at that particular orientation for a given number of external sources in the context of acoustics to that of the flame spread rate at that particular orientation for a defined number of external sources without acoustics is known as the Fire Stimulation number (FSN). Fire Stimulation Number is a Non-Dimensional number. The results are classified into various regimes. The heat sink zone is FS<1, the heat source zone is FS>1, and the neutralizing zone is FS=1. A non-dimensional number was calculated for each orientation. It was done to verify the configuration's efficacy and to assess the influence of positions, orientations, acoustics, and external sources in comparison to without acoustics.

$$FSN = \frac{(\ /\ )}{(\ /\ )}$$

Based on FS number new regime is formed.

A. FS-I: Potential Heat sink Effect - Here the ratio of FS number is less than 1. (FS<1) In this effect energy from external sources is absorbed by pilot fuel.
B. FS-II: Neutralizing Effect. Here the ratio of FS number is equal to 1. (FS=1). It does not take part in positive or negative heat sources.
C. FS-III: Heat source Effect. Here the ratio of FS number is greater than 1. (FS>1). In this Effect, energy is supplied to external sources by pilot fuel.

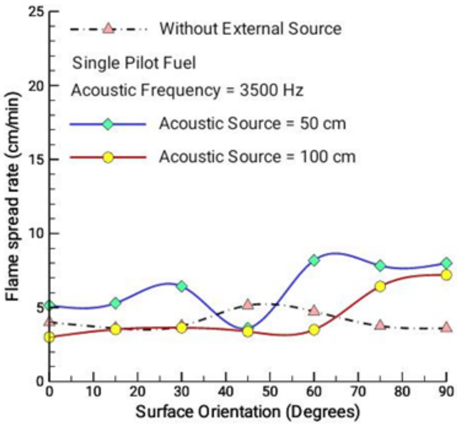

Figure 10. At 3500 Hz Frequency

The following graphs show the effect of acoustic source location in thermoacoustic fire propagation. From figure 10 and 11 it can be observed that increment in source distance results in drop of regression rate by 5.15% at 3500Hz for 60 degrees. In comparison to the acoustic effect with source placed at 50 cm, reduction in separation distance results in enhanced regression by 56.62% following a non-monotonic trend. The drop-in regression rate with increment in source separation distance indicates the drop in acoustic effect owing to enhanced interaction of rarefaction part. Similar to the compression front interactions and resultant localized field development. The additional rise in regression rate as source is bought closer to pilot fuel may be attributed to the development of strong gradients pressure, temperature and velocity flow field across immediate vicinity of ignition front. The interactions are likely to be more intensely associated to the compression front of the sound wave resulting in the acoustics effect dominance reflected in regression rate. Regression rate was seen for unilateral configuration at 45 degree angle. The coefficients of a, b and c for this case are 0.0029, -0.1603 and 7.3366. A few cases of blow off was seen for unilateral and Y configuration at 0 degrees. Most of cases comes under heat source zone due (seen from table 1) to of buoyancy that carries the heat from burnt to the unburnt fuel due to external influence of acoustic. It is interesting to that neutralizing effect was seen for Y and + configuration at 60 and 90 degree respectively

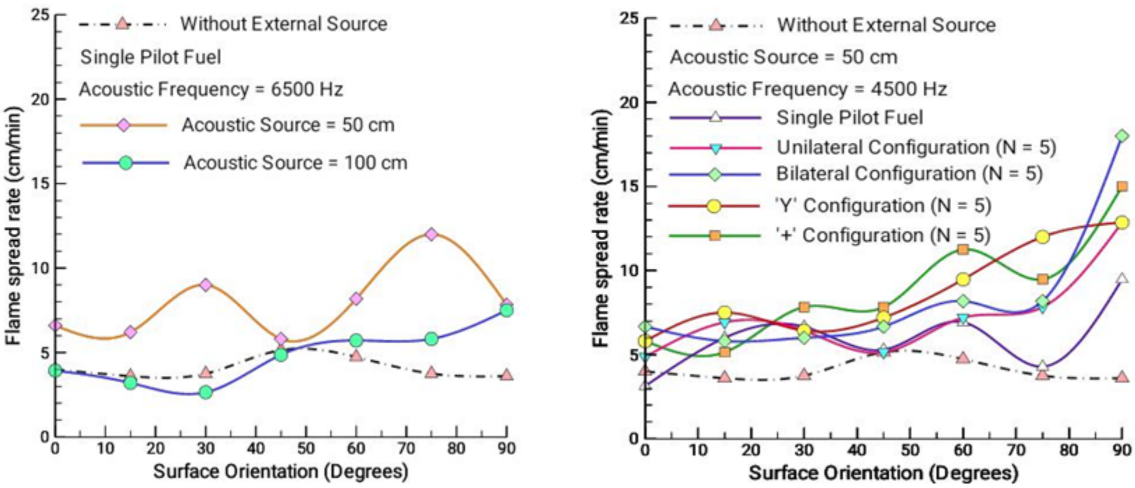

Figure 11. At 6500 Hz Frequency

Figure 12 represents case of 3500Hz when external sources was fixed at 4. From the graph it can be seen that all configuration follows non-monotonic trend. The highest regression rate was obtained for '+' configuration. The rise of around 316.66% (FS>1) was seen at 90-degree orientation. The coefficients of equation are 0.0011, -0.0067 and 6.1318. It was interesting to observe that no drop-in regression rate was seen for bilateral configuration at 45-degree angle. Blow off was dominant for 0 and 15 degrees for Unilateral, Bilateral and Y configuration. The FS number was less then1 for most of cases reason is heat transfer in this regime drops due to the decrease in the localized temperature around the pilot fuel. It is interesting to note that neutralizing effect was seen for Y and + configuration at 0 and 45 degree respectively

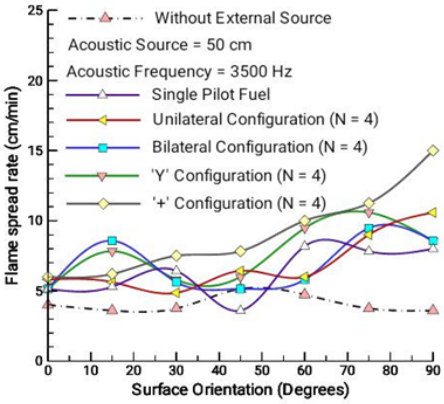

Figure 12. Different Configurations at 3500 Hz when N=4

Figure 13 represents case of 4500 Hz and when number of external sources was 5, the maximum rise in flame spread rate was seen for bilateral configuration with an increase of 400% (FS>1) for 90-degree orientation were as no drop-in

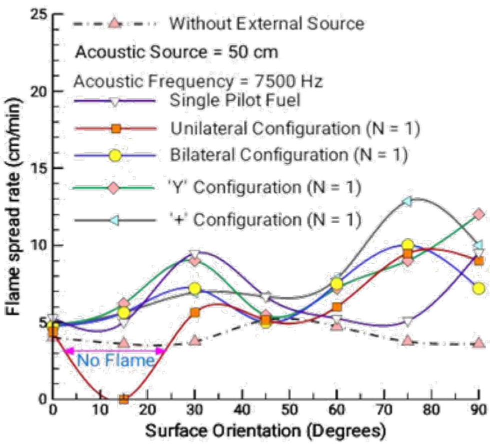

Figure 13. Different Configurations at 4500 Hz when N=5

Table 1. FS Number Variation for Bilateral Configuration when N=5

Orientation (in degree)	3500	4500	5500	6500	7500
0	1.125	1.33	1.058	1.40	1.090
15	1.29	1.290	1.379	1.142	1.290
30	1.40	1.167	1.289	1.667	1.207
45	1.065	1.22	1.056	1.501	1.138
60	0.852	1.046	0.885	0.639	0.676
75	1.135	1.228	0.885	1.818	0.931
90	1.263	2.4	1.6	1.263	1.33

The next set of plots shows the variation of thermoacoustic energy interaction for different configurations for 7500 Hz. It can be seen that all configuration follows non-monotonic trend. For figure 14 the number of external sources is fixed at 1. The highest regression rate was obtained for Y configuration at 90 degrees. The massive rise of around 233.33% (FS<1) was seen. The coefficients of equation are 0.0007, -0.0662 and 5.8029. The maximum drop was seen for unilateral configuration of around -100% (FS<1) at 15-degree orientation where the fire extinguished completely before reaching the first 1cm mark. The coefficients of a, b and c for this case are 0.0.0006, 0.0241 and 2.7945. It comes under blow off condition. Blow off was dominant for the unilateral and Y configuration for angles 0 to 15 degrees. For most of cases heat sink effect was seen because of thermal effect dominance with respect to acoustic energy. Appealing thing to observe is no neutralizing effect is seen

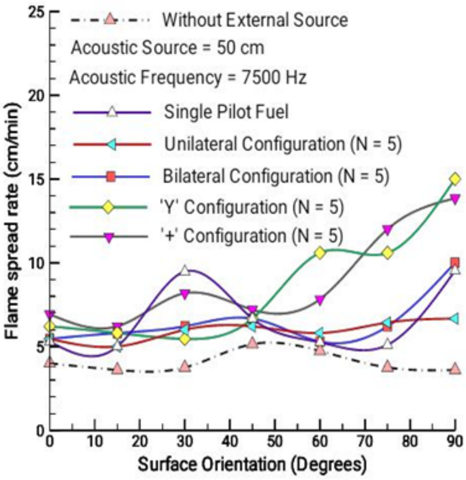

Figure 14. Different Configurations at 7500 Hz when N=1

For figure 15 the number of external sources is fixed at 5. The highest regression rate was obtained for Y configuration at 90 degrees. The massive rise of around 316.66% (FS>1) was seen. The coefficients of the equation for this case are 0.0017, - 0.0509 and 6.0734. The maximum drop was seen for bilateral configuration of around 11.48% (FS<1) at 60 degree. A few cases of blow off was seen for unilateral, Y and + at 60, 30 and 15 degrees respectively. The neutralizing effect was seen unilateral, Y and + configuration at 15,60 and 45 degrees respectively. Here the acoustic and thermal energy both have equal effect on the flame. unilateral, bilateral and + configurations. Neutralizing effect was seen for 0 and 15 degree unilateral and + configurations respectively. For most of cases heat sink effect was seen because of thermal effect dominance with respect to acoustic energy.

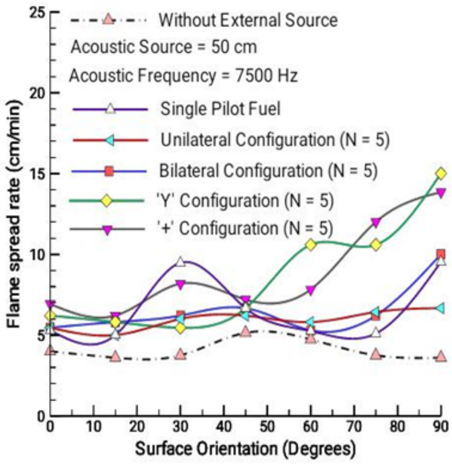

Figure 15. Different Configurations at 7500 Hz when N=5

Figure 17 represents the thermoacoustic energy interaction for unilateral configuration at 4500Hz. The external sources were varied from 1 to 5. The massive increase of around 269.96% (FS>1) was seen for regression rate at 90 degrees when external source was fixed at 3 were as maximum drop of 100% (FS<1) at 0-degree orientation when two external sources were attached from single side. The coefficients of equation for maximum performance is 0.0012, -0.009 and 4.669 were as for no flame case is -0.0002, 0.1326 and 1.4667 respectively. Here the fire extinguished completely before reaching the first 1cm mark. Few cases of blow off was seen for when external sources are fixed at 2, 5 and 3 at 0 and 30 degrees respectively. For the cases of Heat source effect (refer table 2) cumulative heat transfer is dominating in this region because of buoyancy that carries the heat from burnt to the unburnt fuel due to external influence of acoustic

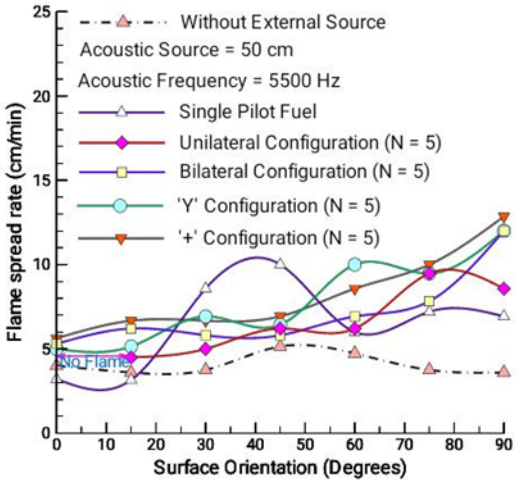

Figure 16. Different Configurations at 5500 Hz when N=5

Figure 16 represents variation of thermoacoustic energy interaction for different configurations for 5500 Hz when external sourced is fixed at 5. For + configuration at 90 degrees it can be seen that the massive increase in regression rate of rise of about 257.13% (FS<1) was seen. The coefficients of a, b and c for this case are 0.001, -0.0183 and 6.0749. The maximum drop was seen for unilateral configuration of around -100% (FS<1) at 0-degree orientation where the fire extinguished completely before reaching the first 1cm mark. The coefficients of a, b and c for this case are 0.0008, 0.162 and 0.8304. The blow off condition was seen only for zero-degree orientation for

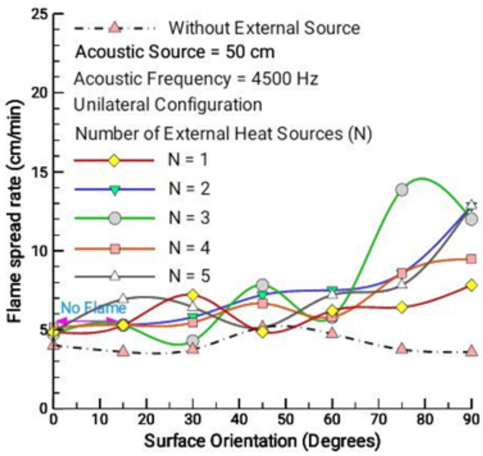

Figure 17. Different Configurations at 4500 Hz by varying External Sources

Table 2. FS Number Variation for Unilateral Configuration when N=2

Orientation (in degree)	3500	4500	5500	6500	7500
0	0.822	0	0.863	1.38	1.016
15	1.0588	1.087	1.232	1.026	1.055
30	1.04	1.118	1.081	0.824	1.018
45	0.8	0.96	0.685	1.142	0.5
60	0.96	1.293	1.07	1.293	1.241
75	0.705	1.360	1.360	1.058	1.360
90	0.6315	0.857	0.666	0.705	0.666

The fluctuation in flame intensity and flame spread rate could be caused by the compression and rarefaction of the sound wave. Presence of sound wave can result in creation of localized pressure and velocity fields around the pilot petrol, which are supposed to influence the forward heat transfer. Under the impact of sound, acoustic energy takes precedence over thermal energy, resulting in a decrease in localized temperature and pressure, which results in a decrease in regression intensity and is referred to as the heat sink effect. In some cases when thermal energy is dominant over acoustic energy due to influence of additional external sources, which results the increment of regression rate. It implies the heat source effect. For both above cases the flame flickers due to interaction of thermal energy and sound energy and it shows destabilizing effect. Instructive to observe that in some cases neutralizing effect is seen, it is appeared when both acoustic and thermal energy interaction is predicted to be same in macroscopic scale. Here flame does not flutter, and regression rate values are just the same to that of base case.

4. Conclusion

The merits of acoustic effects on diffusion flames were investigated using incense sticks in an experiment. The acoustic and thermal effects of differing frequencies were studied with monitoring parameters such as fuel surface orientation and sound source size. The study's basic findings state that: -

A. When five external sources are mounted from one side the Bilateral configuration saw a massive increase of about 400%. The orientation was 90degree, and the frequency was set at 4500Hz. This demonstrates that thermal energy outperforms acoustic energy in terms of fire regression rate, implying the importance of forwarding heat transfer and fire propagation.

B. The most notable observation is for unilateral configuration where the external source number is fixed at 1,2 and 5 at 4500, 5500 and 7500 Hz frequency for 15 and 0 degrees orientation respectively. The flame propagation rate decreased by 100%, implying that no flame was detected since the fire was totally extinguished before hitting the 1 cm mark. Sound, as a wave, is often found in the center of compression and. unusual fraction. Based on the findings of the experiments, it can be inferred that sound has an extraneous effect and that in close proximity, acoustic energy exceeds thermal energy.

C. As the orientation was shifted from 0 to 15 degrees, a few cases of blow and reappearance were observed for unilateral, bilateral, and ‘Y' configurations. It shows that acoustics is directly accustomed in the presence of acoustics.

D. The governing physics of this advancement include:
   (i) Reaction zone adjustment
   (ii) the establishment of a region of energy interaction
   (iii) the relationship between heat and acoustic energy

Applications of work: Modern insights within the fire protection standards on the traditional and additional territorial a be framed based on physical instinct. The work encompasses a broad range of engineering applications such as combustion and propulsion, defense system validation, research, and upgradation such as rocket systems, industrial with power generation systems, operational, usable, and scientific applications. Acoustics should be used to reduce casualties in fire incidents

Suggested Applications:

A few ways of using fire extinguisher in real life situations are proposed below. For its execution, research is required.

A. For case of Industrial, defense systems and home usage installation of large network of small automated permanent devices which shall detect and control the fire using sound waves. Which will result in a faster response to fires and a lower rate of propagation. The instrument will be calibrated to a certain frequency and capable of generating sound in several angles.

B. Through use of acoustic energy to extinguish fires in space can be very effective. Using acoustic signals instead of conventional extinguishers eliminates the possibility of adding additional space debris since sound waves contain no unwanted residues.

C. Sound waves could be very effective in fire suppression in environments that are impossible for humans to access. Long-distance sound waves may be aimed towards the origin of the explosion preventing it from spreading.

D. Acoustic waves may be used to suppress fires in wider areas, such as forests, with help of UAVs. Drones may be equipped with sound generators, enabling them to reach a wide area in a short period while remaining safe distance from explosions

5. Acknowledgements

Our investigative work would not have been possible without the substantial contributions of former global researchers and scholars. In addition, we would like to devote our work to the fire-fighters for their dedication and the endless service they have given over the years. Their rapid reaction time has saved thousands of lives in forest fires, house and compartment fires, factory and household fires.

6. Reference

[1]. Semenov NN. “Chemical Kinetics and Chemical Reactions”. Clarendon Press, Oxford; 1935.

[2]. Toong TY (1972) Chemical effects on sound propagation. Combustion and Flame 18

[3]. Chiu HH, Summerfield M. “Theory of Combustion Noise”, Aerospace and Mechanical Sciences Report, Princeton University, Princeton, New Jersey; 1973.

[4]. Kampen JV. “Acoustic pressure oscillations induced by Confined Turbulent Premixed natural gas flames”. PhD thesis, University of Twente, Enschede, Netherlands; 2006.

[5]. Krivokorytov MS, Golub VV, Volodin VV. “The Effect of Acoustic Oscillations on Diffusion Combustion of Methane”. Tech Phys Lett. 2012;38(5):478-80.

[6]. Shafiq, R.Q., Waqar, A., Robert, and P.: Behaviour of a premixed flame subjected to acoustic oscillations [J]. PLoS ONE 8(12), e81659 (2013)

[7]. Dowling, AP, Mahmoudi Y. “Combustion noise”. Proc Combust Inst. 2014; 35:65-100.

[8]. P. Niegodajew, K. Łukasiak, H. Radomiak, D. Musiał, M. Zajemska, A. Poskart, K. Gruszka, Application of acoustic oscillations in quenching of gas burner flame, Combust. Flame 194 (2018) 245–249.

[9]. A.N. Friedman, S.I. Stoliarov, Acoustic extinction of laminar line-flames, Fire Saf. J. 93 (2017) 102–113.

[10]. T. Yamazaki, T. Matsuoka, Y. Nakamura, Dynamic response of non-premixed flames subjected to acoustic wave, in: 12th Asia-Pacific Conf. Combust. 4, 2019. Jul 2019.

[11]. S. Shekhar, B. Thombare, V. Malhotra, Effect of Acoustic Energy on Onset of Fire Propagation Phenomenon, in International Conference on Advances in Thermal Engineering and Applications March 2021.
[12]. Pratik T., Vikaram R., Vinayak M., : An experimental insight to thermoacoustic smoldering[J]. Space exploration Vol 6 Iss 1 1-14 (2017).

Image processing methods for error bounds of Precision Linear Scanning Mechanisms

Battula Venkata Sai Dinesh
Reliability and Quality
Mechanical systems Group
ISRO
Bangalore
dineshbv@ursc.gov.in

Harshit Baranwal
Reliability and Quality
Mechanical systems Group
ISRO
Bangalore
harshit@ursc.gov.in

Patel Saurabhkumar Hasmukhbhai
Reliability and Quality
Mechanical systems Group
ISRO
Bangalore
spatel@ursc.gov.in

Chandra Shekhar Prasad
Reliability and Quality
Mechanical systems Group
ISRO
Bangalore
csp@ursc.gov.in

Shankar Narayan Y S
Reliability and Quality
Mechanical systems Group
ISRO
Bangalore

Narendra S.
Spacecraft Mechanisms Group
ISRO
Bangalore

Harish T. S.
Reliability and Quality
Mechanical systems Group
ISRO
Bangalore

***Abstract* – Testing of micro displacement mechanisms by conventional methods is strenuous. Use of Image processing techniques for experimentation of these micro displacement mechanisms is highly advantageous and accurate. To measure these displacements a detector is placed on the moving part of the mechanism and a LASER beam is made to incident on the detector. As the detector moves along with the mechanism, the LASER beam also shifts. After every small displacement an image of the LASER beam on the detector is captured. These images are used to identify the errors in x because of change in y, z, θ_x and θ_z when compared to the actual movement given by respective excitation. In this paper the error bounds of a linear precision mechanism moving in the range of ± 1 mm are analyzed using the above-mentioned method. The images are captured with an interval of 10 μm from beginning to end. The data set will consist of 400 black & white images with needs to be processed where each image will have pixels with intensity ranging from [0, 255] describing the LASER spot. No of pixels along the length and width are kept constant so that the spot of the LASER moves within bounds. The centroid of the LASER spot needs to be identified to get the change in [x, z] and the change in diameter of the laser spot determined to calculate the change [y]. The tilt in the spot helps in finding the change in θ_x and θ_z.To determine the center of the laser spot algorithm like weighted-centroid and the max-intensity are used. Similarly, to find out the change in diameter of the laser spot in-house built boundary tracking algorithms are used which is subsequently used to fit circle to it. To establish the tilt many different algorithms were used in which, the mostly effective one was to fit a plane to the second highest intensity peaks in the LASER beam. The results from the above methods are used to establish the error bounds to the guiding parameter [x] in the complete operation. It is found that the errors in the mechanisms are high, during reversal of direction due to large change in tilt angle. The correlations between guiding parameter [x] and other parameters are obtained which shows that correlation of x with y and z is minimal when compared with correlation of x with θ_x and θ_y.**

Keywords– Linear precision mechanism; LASER beam; Error bounds

1. Introduction

High precision translation mechanisms have very stringent accuracies in terms microns. In recent years, the importance of highly accurate mechanisms in space industry has increased by many folds. High accuracies are very essential for proper functioning of telescopes, guidance systems and many more. S T Smith et. al. [1] worked on the design and assessment on monolithic high precision mechanisms using compound rectilinear springs and electromagnetic driving transducers. Saša Zelenika et. al. [2] used optimized flexural hinge shapes.Van-Khien Nguyen et. al. [3] worked on design of complaint linear guide for high -precision feed drive mechanisms.

Measuring accuracies of these high precision mechanisms is very demanding. The accuracies of these mechanisms range between microns to nanometers. Laser interferometry and CMM is some such kind of procedure used for testing these mechanisms. B.Shirinzadeh et. al [4] used laser interferometry-bases guidance for high precision positioning of mechanisms and robots. Laser interferometer is widely used in space antenna applications [5]. H.F.F.Castro [6] derived a method for evaluating spindle rotation errors of machine tools using laser interferometer.

The aim of this paper is to establish a method to determine the accuracy for high precision linear translation mechanism [6]. The mechanism accuracy is tested using a LASER interferometry method where a detector is mounted on the moving elements of the mechanism and a convex laser beam spot is made to fall on the detector. This is done to verify the accuracy of an encoder which is in-built in the mechanism design.

2. Methodology

The linear scanning mechanism works on the principle of converting the rotatory motion to linear motion with the help of a preloaded ball screw mechanism. A mounting platform is accommodated on the bow screw mechanism with the help of a slider bracket. The mounting bracket requires movement accuracy in 10 microns steps. In the final configuration a mirror is mounted on the mounting platform which scans the sun coronal mass ejections. Two numbers of optical encoders are used for sensing the linear motion of the mounting platform. The mechanism provides for a motion of ±1mm starting from the index zero position. Hard stop is provided at starting from the index zero position. Hard stop is provided at ± 1.3mm. The detector is mounted on the mirror mounting platform.

While testing these high precision mechanisms one should look for measuring devices with resolutions in range of 0.5 -1 micron. A detector is mounted on the moving element of the mechanism and LASER beam is made toincident on it and a spot is formed. This spot position on the detector changes with mechanism movement. The final output of this provides us with images of the LASER spot movement and change at each location.

The mechanism is made to move in steps of 10 microns in its whole range from [-1mm to +1mm]. The mechanism moves in X-direction and has very limited translation in Y, Z directions and rotations about X, Z because of clearances and other couplings. An encoder which is in closed loop with the stepper motor the bound to have a variation in its accuracy because of these perturbations. All these perturbations are derived from the images using image processing and various mathematical techniques.

The LASER is placed in out of plane direction to the detector which is fixed on the mounting platform as shown in the fig.1. The out of plane is defined as Y-axis and the linear traversing direction of the mechanism is defined as X-axis. The other direction is defined as Z-axis. The rotation about each axis is established as $\theta_x, \theta_y, \theta_z$.

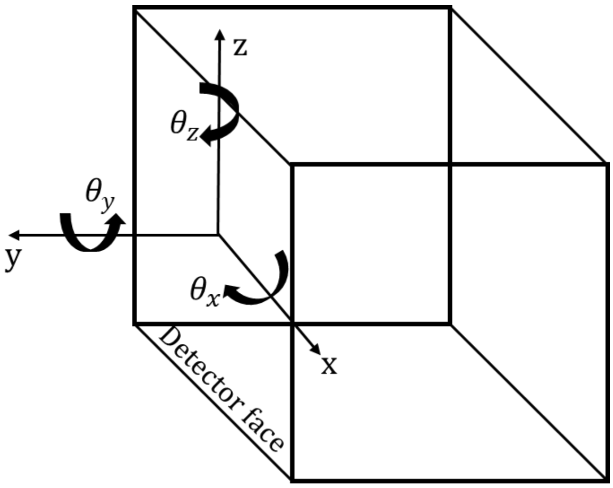

Fig. 1: Axis definition of the test setup

Total of 400 images are obtained as the mechanism is moved 10 microns each time between -1000 to +1000 microns. Each image is a grayscale image with intensities from [0 to 255], with 255 being the highest intensity as shown in fig. 2. All the images have a fixed frame and spot pixels iterates with the movement of the mechanism. The region of spot pixels is identified, and the other outliers are removed. In the fig.3 the 3-dimensional scatter of the spot w.r.t to its intensities is displayed.

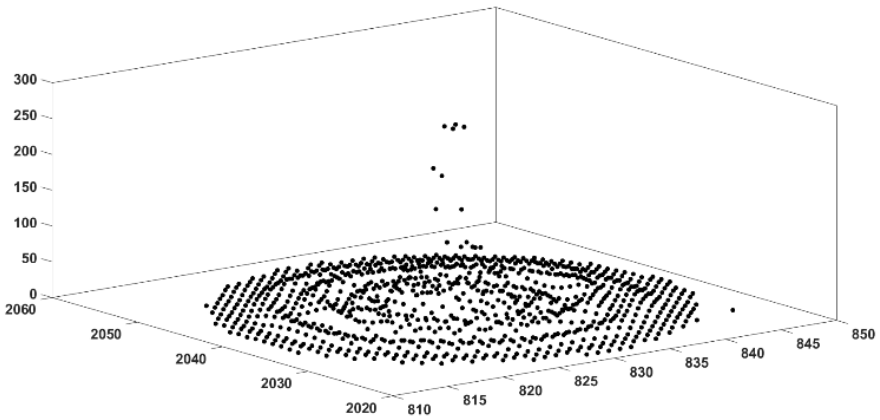

Fig. 2: LASER spot with intensities represented in Z-direction

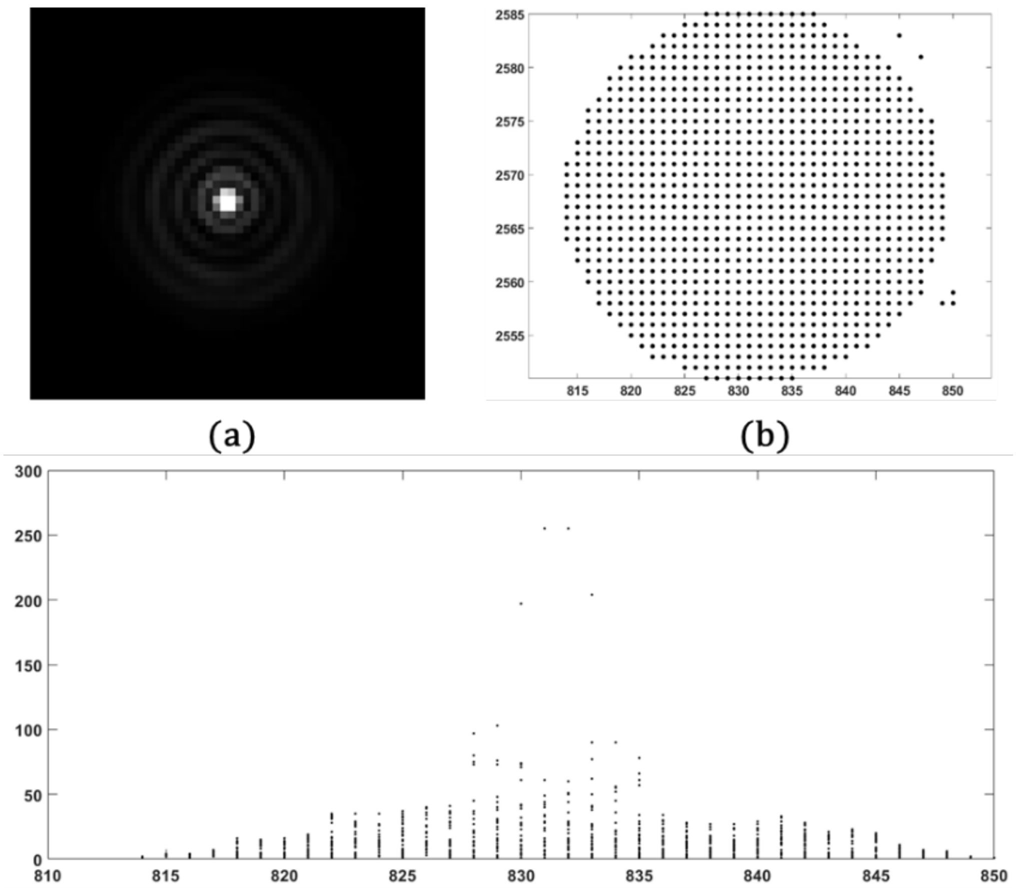

(c)

Fig. 3: (a) Actual LASER spot image representation (b) Laser spot extracted in X-Z plane (c) in X-Y plane

Once the spot is identified the weighted centroid algorithm is used to get the center of the laser spot. In this algorithm each pixel is provided with weights w.r.t its intensity and weighted average is carried out to find out origin of the spot as mentioned in the equation 1 & 2 for each image. This method is a better method for calculating the center as there is high variation in the intensities. Using these techniques, the X, Z coordinates for all the images are obtained. The raw spot center propagation on detector is shown in fig. 4. The Y-axis in fig. 4 is enlarged for better understanding.

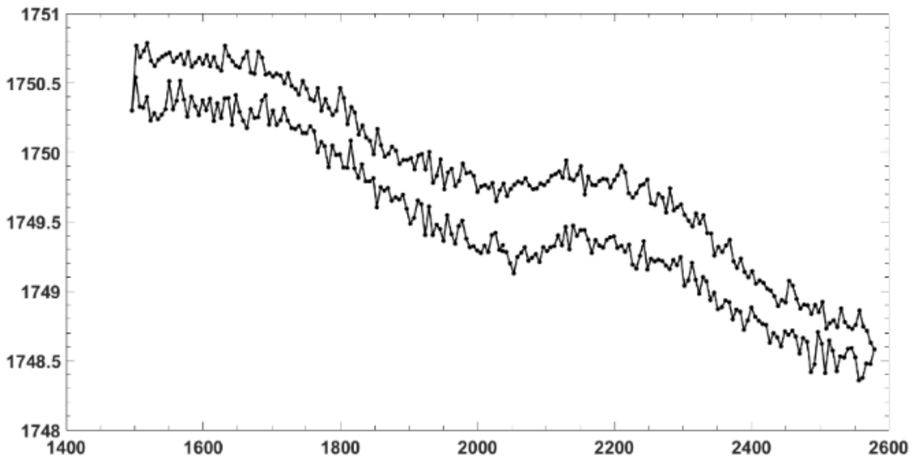

Fig. 4: Raw spot propagation with the movement of mechanism

$\bar{X}_j = \sum w_i x_i$……………………………………………………………………………...………1
$\bar{Z}_j = \sum w_i z_i$……………………………………………………………………………...…2

$where\ w_i = I_i/I_{max}$
$\bar{X}_j, \bar{Z}_j = weigthed\ average\ of\ the\ spot\ in\ x, z\ direction\ for\ j^{th}\ image$
$I_{max} = Maximum\ intensity$ of the spot
I_i = Intensity of the pixel in the spot
$w_i = Weight\ of\ the\ pixel$
$x_i, z_i = pixel\ x, z\ coordinate$

For obtaining the Y-coordinates from the images, the boundaries of the spot are mapped using a unique boundary tracking algorithm. If the intensity point (x_i, z_i) is greater than the intensities of (x_{i-1}, z_i), (x_{i-2}, z_i), (x_{i-3}, z_i), (x_i, z_{i-1}), (x_i, z_{i-2}), $(x_i, z_i - 3)$ then the points gets selected for the particular quadrant as shown in the fig. 5. Similarly, same logic is applied to the other quadrants also. After the points being identified, a best circle fitted for the selected points using least squares method as given in equations 3 & 4 where,$x_o\ and\ y_o$ are the center of the fitted circle and R is the radius of the circle. The term $-R^2 + {x_o}^2 + {y_o}^2$in the equation is negligible when compared to $x_o\ and\ y_o$. The radius of the circle changes with the change in Y-axis plane. The radius is then converted into relative change in distance with linear traversing of the mechanism using basic trigonometry.

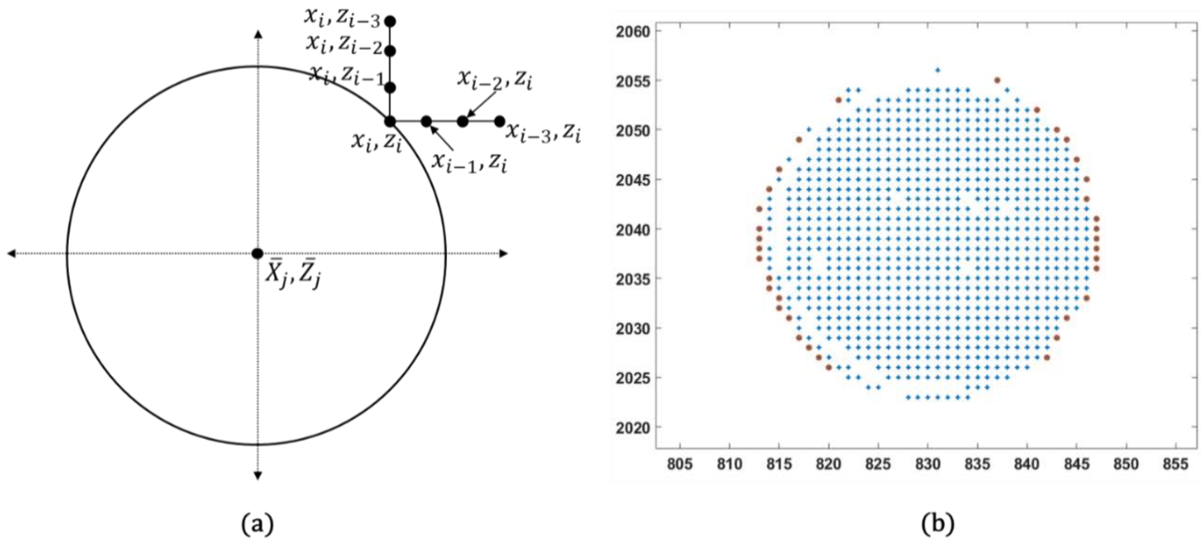

Fig. 5: (a) Boundary tracking algorithm for the LASER spot (b) Point selected by boundary tracking algorithm for fitting least square circle

$(x - x_o)^2 + (y - y_o)^2 = R^2$……………………………………………………………...………3
$[-2x\ \ -2y\ \ 1][x_o y_o\ \ -R^2 + {x_o}^2 + {y_o}^2]' = -(x^2 + y^2)$…………...……………………………4
For calculation of the tilt, many different methods where been used like:

- Method-1: Dissecting the spot with Z-axis and subtracting the left side pixels with right side pixels and fitting a plane for θ_y, and similar things was carried out X-axis for θ_x.
- Method-2: Ellipse fitting of the spot using least square method.
- Method-3: 2nd highest peaks of the spot are selected, and a plane is fitted for those particular points and the directional ratios of the plane are taken to find θ_x, θ_y tilts.

Due to wave nature of the LASER spot the method-1 results were not consistent. The resolution of spot is not sufficient for ellipse fitting thereforeit tends to have higher margin of error. So, the final method was used because the results from this method are more consistent and compatible. 2nd highest peaks are identified by checking the succeeding and preceding pixels intensities, which must be lower than the intensity of the 2nd peak pixel intensity as shown in the fig. 6. The values of tilt obtained are normalized as they are not the absolute values, but they are relative to each other.

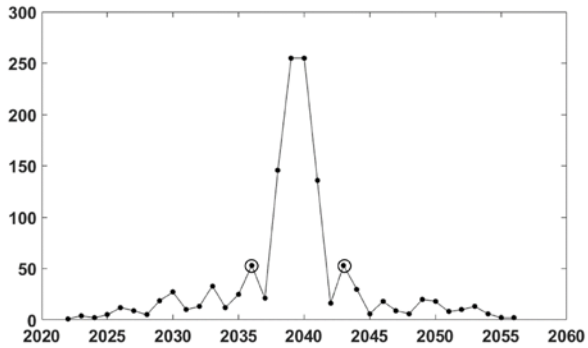

Fig. 6: 2nd highest peaks along the X-Y plane of the LASER spot

3. Results

The images obtained are analyzed and the corresponding coordinates and tilts are calculated for each image. In the fig.7(a) it is seen that the absolute error is within [+5, -5] μm. During reversal the error is going beyond ±5 μm. So, the coordinates and tilts correlations are checked correlations to see which error is inducing the error in the mechanism movement direction i.e., along X-axis. The cumulative error in X-direction is also plotted w.r.t to encoder position and it is found out to be within [+3.1, -28] μm as shown in fig 7(b). It is noticed that during reversal large error was being induced.

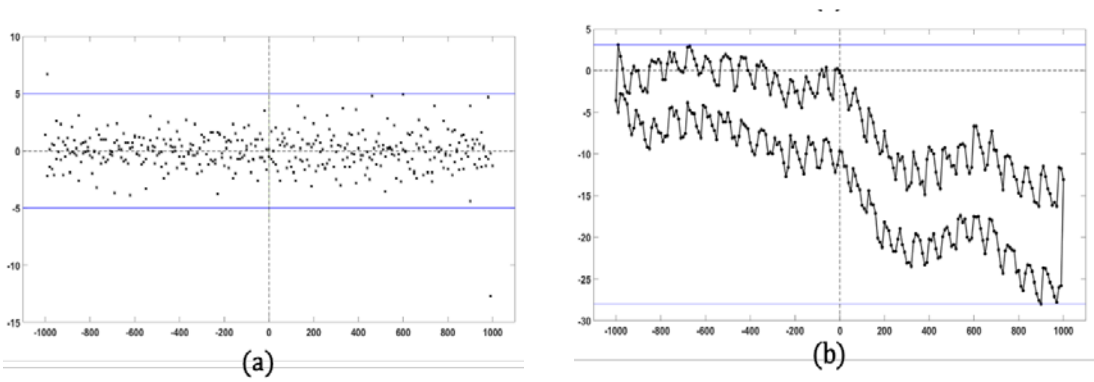

Fig. 7: (a) Absolute error and error bounds in X-direction (b) Cumulative error and error bounds in X-direction

With the error in X-direction identified the error in Z and Y needs to be captured to check the corrections. These errors are calculated as described in the above section. The error plots of y and z directions w.r.t encoder readings are shown in the fig. 8(a). In Z-direction the variations are between +4 to -3 μm and normalized spot radius from which Y-direction is fully corelated to error in Y-direction isplotted in fig.9(a). The correlation of the cumulative error in Y-direction against the error in X-direction is found to be -0.0425 and cumulative error in Y-direction against the error in X-direction is found to be 0.0148. This shows that the error in [Z, Y] directions are not affecting the error in the X-direction as the correlations were minimal.

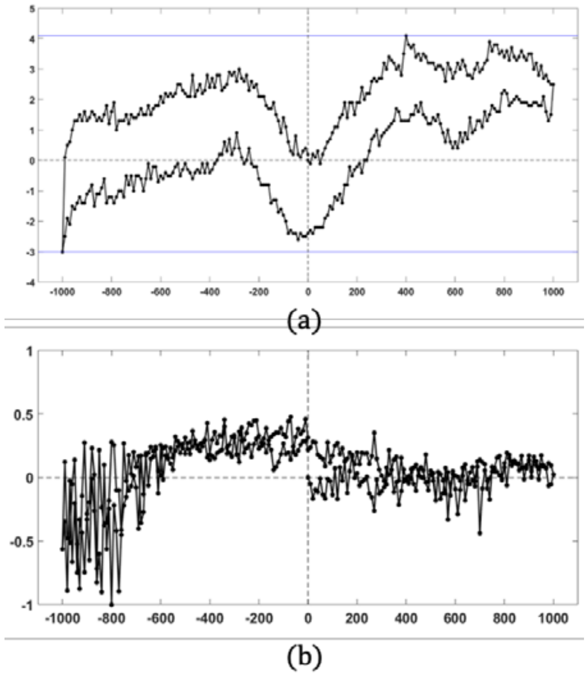

Fig. 8: (a) Error in Z-direction (b) Error in Y-direction

For the tilts, the 2nd highest peaks in all the images were extracted and a plane is fitted for the 2nd highest peaks of each image. And the angle of plane normal with the coordinate axis provides the tilt. The tilts obtained are relative values and these values are sufficient to establish a correlation with X-direction error. The error tilts about X-axis and Z-axis are shown in fig. 9. The correlation of error in tilt about X and error in tilt about Z w.r.t to the error in X-direction are -0.4960 and 0.4843. This gives a clear indication that the error due to tilt have a significant impact on the error in X-direction.

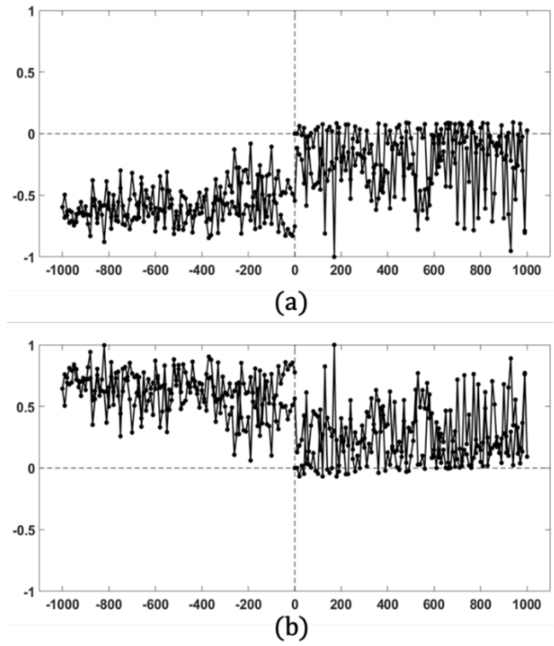

Fig. 9: (a) X-direction tilt error (b) Z-direction tilt error

Taking the above analysis into account the tilts in the mechanism are minimized using additional constrains. After the tilts are reduced the testing is repeated and it is seen that the error in X-direction is significantly reduced from [+3.1, -28] μm to [+2, -3] μm as shown in the fig. 10.

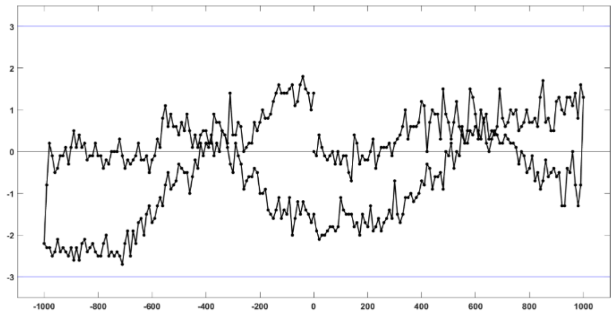

Fig. 10: Cumulative error in X-direction after correction

4. Conclusion

The following conclusions can be drawn from this testing:

- In High precision translation mechanism, the clearances in the mechanism must be very tight or some addition constrains to close the clearances needsto be provided to increase the accuracy.
- Any periodic patterns should be identified, which can be corrected by some modifications in the mechanism.
- From the testing it was found that the angular tilts induce major part of the error than the translational errors.

5. Acknowledgements

We would like to present our sincere gratitude to Spacecraft Mechanism Group, Control dynamics design group and reliability and Quality Assurance mechanical system group for providing with the opportunity to be a part of the testing. We also want to show our sincere acknowledgement for the Indian Institute of astrology to providing us with the test facility and guidance. We would also like to thank for the support, encouragement and guidance given by Group Director, Reliability and Quality Assurance Group, Group Director, Spacecraft Mechanisms Group and U. R. Rao Satellite Centre Bangalore.

6. References

[1] Smith, S. T., D. G. Chetwynd, and D. K. Bowen. "Design and assessment of monolithic high precision translation mechanisms." *Journal of Physics E: Scientific Instruments* 20.8 (1987): 977.

[2] Zelenika, Saša, Mircea Gh Munteanu, and Francesco De Bona. "Optimized flexural hinge shapes for microsystems and high-precision applications." *Mechanism and Machine Theory* 44.10 (2009): 1826-1839.

[3] Nguyen, Van-Khien, et al. "Optimization design of a compliant linear guide for high-precision feed drive mechanisms." *Mechanism and Machine Theory* 165 (2021): 104442.

[4] Shirinzadeh, Bijan, et al. "Laser interferometry-based guidance methodology for high precision positioning of mechanisms and robots." *Robotics and Computer-Integrated Manufacturing* 26.1 (2010): 74-82.

[5] Amaro-Seoane, Pau, et al. "Laser interferometer space antenna." *arXiv preprint arXiv:1702.00786* (2017).

[6] Comprehensive design review of linear scanning mechanism.

Paper Withdrawn

Paper Withdrawn

Paper Withdrawn

Paper Withdrawn

Paper Withdrawn

Paper Withdrawn

Paper Withdrawn

Paper Withdrawn

Modelling of Impulse on Closure Shell of Blast Valve

Praveen Kumar
Defence Institute of Advanced Technology
Pune
praveenkr.ind@gmail.com

Pankaj Kumar Sharma
Defence Institute of Advanced Technology
Pune
pankaj_sharma@diat.ac.in

***Abstract*—Blast valve is a necessary equipment of hardened structures to protect the personal and critical equipment from shock waves originating from various explosions. It provides proper ventilation in the meantime and prevents the shock front leaking inside the hardened structure. As shock front imparts high impulse, the blast valve parts should be designed accordingly to withstand that impulse. The critical and vital part of the blast valve is the closure shell. Different shapes of closure shells with different configuration has been modelled, and each has its own advantages and disadvantages. In this paper, the hemispherical closure shell has been taken into consideration for modelling the impulse. In order to reduce the leakage of shock wave, the response time should be as minimum as possible, which depends upon the impulsive force applied by the shock wave. The impacting impulse due to shock wave is utilized for closing the passage. More the impulse, less the response time and less the leakage of shock wave, means more, safer design. Due to hemispherical shape of closure shell more amount of shock wave is collected and due to reflection, shock waves are multiplied many times and gives more impact**

Keywords: Hardened Structure, Shock wave, Explosion, Blast Valve, Shock front, Closure shell

1. Introduction

A blast valve is a device used for closing air ventilation ducts in case of high-pressure waves that occurs due to an atomic blast or an explosion. The enhancement in modern weapon technology has made the requirement to develop hardened structures which should be capable of withstanding the effect of these new technological warfares[1]. As critical ammunition is stored, and people are staying in these hardened structures, they need fresh air for the purpose of ventilation, maintaining temperature and combustion equipment[2]. To fulfil these requirements, ventilation ducts should be equipped with more than one blast valve to identify and close the duct when the high-pressure shock wave is detected. Also, it should keep the duct open in the meantime to fulfil the requirement of ventilation. When the blast wave impinges on the closure shell, during the positive phase of the blast wave, the closure shell closes the duct by moving in the downstream direction and prevents blast waves from leaking to the inside of the hardened structure. While in the case of the negative phase of blast wave, it moves in a front face direction and prevents the washing out of fresh air from hardened structures. The development of the blast valve mostly took after the nuclear bombing at japan in 1945 for saving the lives of people[3]. The key points to be considered during the design of the blast valves are shock wave leakage, response time, pressure losses, maintenance and cost of manufacturing. These all should be below the permissible limits. The blast valve and its components should be capable of withstanding the effects of shock wave and effects from its operation. When the blast wave impinges on the closure plate of.the blast valve, the closure plate experiences an impact of high magnitude. The blast valve parts should be chemically stable as it may be subjected to NBC (Nuclear, Biological, Chemical) warfare. The schematic of the working of the blast valve is shown in fig. no. 01

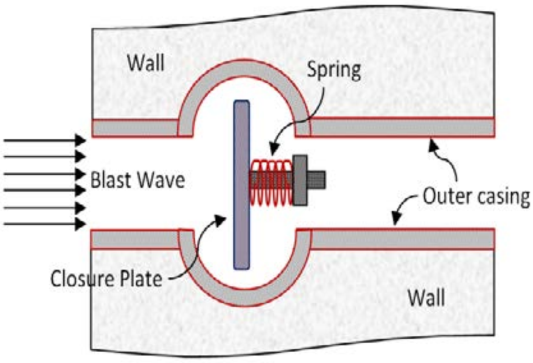

Figure 1. Blast Valve Schematic[10]

2. Formation of Shock Wave and its Important Parameters

The blast wave formation is the result of an explosion. When a large amount of energy is released in a very short span of time, a loud bang sound can be heard called 'Explosion'. Due to explosion, there is sudden change in pressure is observed, which lead to severe destruction. This pressure change forms a shock front which is the key factor of disaster.

In case of Sound waves, the compression and rarefaction profile have a minor change, but if there is a high-pressure wave generated by an intense source, the sound generated by it results in high amplitude along with increment in speed of compression and decrement in the speed of rarefaction, as sound's velocity is directly proportional to the square root of the temperature of the medium.

When there is high pressure, then by ideal gas law (temperature is directly proportional to pressure), the temperature is also high, and this high temperature increases the propagation in compression, but in the rarefaction phase, it gets decreased due to a decrease in temperature

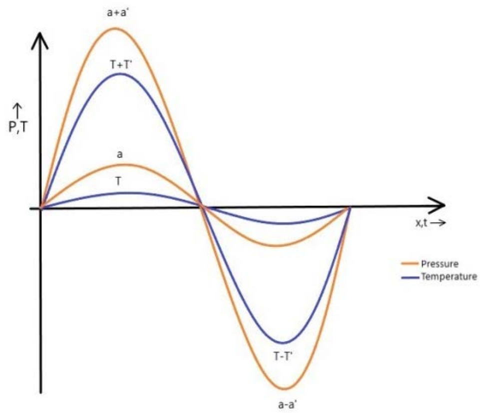

Figure 2.Acoustic Wave and High-Pressure Wave

In fig. 02, the difference between acoustic wave and high-pressure wave propagation can be seen, the acoustic wave is having propagation velocity 'a', ambient temperature 'T' and high-pressure wave whose temperature increases to T+T' and propagation velocity a+a'. In the compression phase, the temperature and propagation velocity drop to T-T'and a-a', respectively. It continues in each propagation, and the wave gets steeper and forms shock front refer to fig. 03

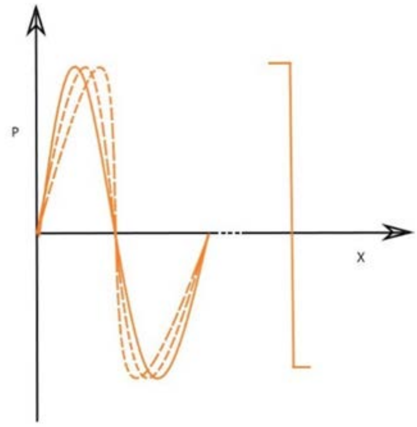

Figure 3. High-Pressure wave to Shock wave

Shock wave decays as it moves further. Otherwise, it needs a continuous supply of energy to maintain its peak. The reason for the decay of shock wave is the dissipation of heat, pressure and velocity to the surrounding due to more considerable temperature gradient and viscous shear. It tends the system to be irreversible. This decaying shock wave is called "Blast wave". There is an abrupt change in pressure along the shock front. Due to the shock front, an impulse of high magnitude is experienced, causing danger to lives and structures. Blast wave starts to decay immediately after the peak is reached. It travels with supersonic speed, and so there is no time to warn someone about it[4].

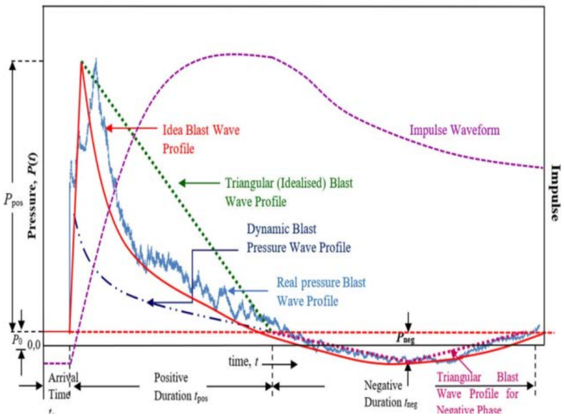

Figure 04. Ideal blast wave due to explosion of air[9]

3. Methodology and Analytical Approach

In analysis, the important parameters like peak positive overpressure, negative pressure, dynamic pressure, positive phase duration, negative phase duration, impulse, wave decay plays an important role in designing blast loaded components. These parameters are equated using empirical formulas for describing the behaviour of blast wave. There are a lot of experimental based empirical relations for evaluating pressure, impulse and other important parameter based on pressure range and type of explosion. Based on equivalent TNT and Scaled parameter all the relation has been standardized.

A. Blast Pressure

As explosion takes place, the pressure rises drastically within few microseconds or few milliseconds and decays exponentially, and this maximum pressure is called peak positive overpressure (P_{so}). After gaining peak, it decays and falls below the atmospheric pressure called negative pressure (P_{neg}). If the positive phase is standing a little long, the peak positive overpressure can cause sufficient damage to surrounding8. Fig. 04 shows the graph of pressure vs time, and impulse vs time, for the blast in air.

The blast profile described by Friedlander's eq. (1) is independent of atmospheric pressure while modified Friedlander's equation which is given in eq. (2) takes atmospheric pressure into account. Also, it is simpler and more accurate than others[5].

$$P(t) = P_{pos}\left(1 - \frac{t}{t_{pos}}\right)e^{-b\left(\frac{t}{t_{pos}}\right)} \quad (1)$$

$$P(t) = P_0 + P_{pos}\left(1 - \frac{t}{t_{pos}}\right)e^{-b\left(\frac{t}{t_{pos}}\right)} \quad (2)$$

Where P(t) is the pressure at time t, t_{pos} is positive phase duration, P0 is atmospheric pressure, P_{pos} is peak positive overpressure and b is the wave decay parameter.

Another widely used empirical relation for determining blast pressure is given in eq. (3), proposed by Kingery and Bulmash. The equation holds valid for the scaled distance Z less than 40 m/kg $^{(1/3)}$[11]

$$P_t = P_r \cos^2\theta + P_i(1 - cos\theta)^2 \quad (3)$$

where, P_i is incident pressure and P_r is reflected pressure.

The equation proposed by Borde[12] after deep analysis of different gas equation for overpressure in the near field, medium, far-field are as follow for different pressure range

$$P_{pos} = \frac{6.7}{Z^3} + 1\ bar\ (P_{pos} > 10bar) \quad (4)$$

$$P_{pos} = \frac{0.975}{Z} + \frac{1.455}{Z^2} + \frac{5.85}{Z^3} - 0.019bar$$
$$(0.1 < P_{pos} < 10\ bar) \quad (5)$$

Eq. (6) is given by Kinney and Grahm based on experimental data from chemical explosion, which is widely used for computer-based calculation. The equation is evaluated by using scaled distance and atmospheric pressure[15].

$$P_{pos} = \frac{P_0 808\left[1+(Z/4.5)^2\right]}{\sqrt{\{[1+(Z/0.048)^2][1+(Z/0.32)^2][1+(Z/1.35)^2]\}}} \quad (6)$$

The negative phase of blast wave has a lesser effect on structures, but still, it has significant effects, primarily on flexible structures. The eq. (7) and eq. (8) is used for evaluating negative pressure and negative phase duration and has been proposed by Krauthammer and Altenberg[13] is given below,

$$P_{neg} = \frac{0.35}{Z}10^5\ Pa \text{ for Z > 3.5 m/Kg}^{1/3} \quad (7)$$
$$P_{neg} = 10^4\ Pa \text{for Z < 3.5 m/Kg}^{1/3} \quad (8)$$

B. Blast Duration

The time required to reach the blast wave to structure after detonation is known as arrival time (t_a). Eq. (9) is used to determine the arrival time[9].

$$t_a = \frac{1}{a_0}\int_{r_c}^{R}\left[\frac{1}{1+\frac{6P_s}{7P_0}}\right]^{1/2} dR\ (ms) \tag{9}$$

The time for which the pressure of the blast wave is above the atmospheric pressure is known as positive phase duration (t_{pos}). Using eq. (10, 11, 12) the positive phase duration is calculated[9]

$$t_{pos} = e^{(-2.75+0.27\log_{10} Z+)+\log_{10} W^{1/3}} \tag{10}$$

The eq. (11) given by Kinney and Grahm[15] for finding positive phase duration using scaled distance (Z) and the mass of charge (W) is given as,

$$t_{pos} = w^{\frac{1}{3}}\left[\frac{980\left[1+(Z/0.54)^{10}\right]}{[1+(z/0.02)^3][1+(z/0.74)^6]\sqrt{[1+(z/6.9)^2]}}\right] \tag{11}$$

And using charge mass (W) and charge radius (R), the eq. (12) is used to find the positive phase duration

$$t_{pos} = 1.2w^{1/6}\sqrt{R}\ (ms) \tag{12}$$

While the time for which the pressure drops below the atmospheric pressure is called negative phase duration (t_{neg}). For evaluating negative phase duration, refer to the equation (13, 14, 15) given by Krauthammer[13] based on scaled distance (Z)

$$t_{neg} = 0.0104W^{1/3} \text{ for Z <0.3} \tag{13}$$
$$t_{neg} = 0.003125\log(Z) + 0.01201W^{1/3} \text{ for } 0.3\leq Z \leq 1.9 \tag{14}$$
$$t_{neg} = 0.0139W^{\frac{1}{3}} \text{for } Z \geq 1.9 \tag{15}$$

C. Impulse due to Blast Wave on Structure

Due to the high-pressure wave impact on the structure, a destructive impulse of considerable magnitude is observed. It plays a significant role in designing structures[14]. The area under the pressure-time graph gives the impulse or integral of pressure over time gives impulse. It is a measure of the energy of incident pressure from an explosion[9]

$$I_s = \int_{t_0}^{t_0+t_a}(P_s)dt \tag{16}$$

Where t_0 is positive phase duration, t_a is the arrival time of blast wave.

According to Kinney[15], positive phase impulse due to blast wave is given by eq. (17)

$$I_{pos} = \frac{0.67\sqrt{1+(z/0.23)^4}}{Z^2 * \sqrt[3]{1+(Z/1.55)^4}}\ \text{(Pa-s)} \tag{17}$$

Negative phase impulse should be considered while designing and analysis of flexible structure. It is the area for the negative phase of the pressure-time curve. Teich and Gebbeken[16] suggested eq. (18) for evaluating negative phase impulse.

$$i_s^- = \frac{P_S t_d}{b^2}e^{-b} \tag{18}$$

D. Blast Wave Decay Parameter

When the peak positive overpressure is gained, the pressure decays very fast. This decay can be estimated by wave decay parameter and is a dimensionless parameter. The profile of the blast wave depends on the decay parameter. For calculation of wave decay parameter, the eq. (19) is used, given by Kinney and Graham[15].

$$\frac{i_s}{A} = \int_0^{t_d} p\,dt = P_s t_d\left[\frac{1}{b} - \frac{1}{b^2}\left(1 - e^{-b}\right)\right] \qquad (19)$$

4. Result and Discussion

A. Pressure and Impulse on Closure Shell of Blast Valve:

The following assumptions are made for modelling the pressure and impulse on the closure shell of the blast valve:

A source of explosion [22kg (~48.5lb) of TNT (Trinitrotoluene)] is exploded on the ground surface at a distance of 5.3m from the building. Assuming, hemispherical closure shell is being loaded as front wall loading type, and it remains stationary, the projected area of the shell is considered for the impulse load imparted by the explosion.

For given source of the explosion, the scaled distance ($Z = \frac{R}{W^{(1/3)}}$) is 4.768 ft/lb$^{1/3}$ (~1.89 m/kg$^{1/3}$). From the graph of UFC 3-340-02 manual[7] as shown in fig. 05, the required parameters are evaluated, which are as follows; for scaled distance 4.768ft/lb$^{1/3}$, the peak side-on pressure (P_{so}) is 2.64 Bar), shock front velocity (U_s) is about 579 m/s, scaled positive phase duration is 1.3 ms, for 48.5lb of TNT the positive phase duration is 4.7 ms, reflected pressure is 9.0 Bar, positive phase wavelength (L_w) becomes 1.3 m. From the graph of UFC 3-340-02 manual[7] as shown in fig. 07, the peak dynamic wind pressure (q_0) is 1.5 Bar, and the reflected pressure $[P_r = \{2 + 0.05(P_{so})\} \times P_{so}]$ is 10.43 Bar,the stagnation pressure ($P_s = P_{so} + C_d q_0$) is 4.14 Bar considering $C_d = 1$.

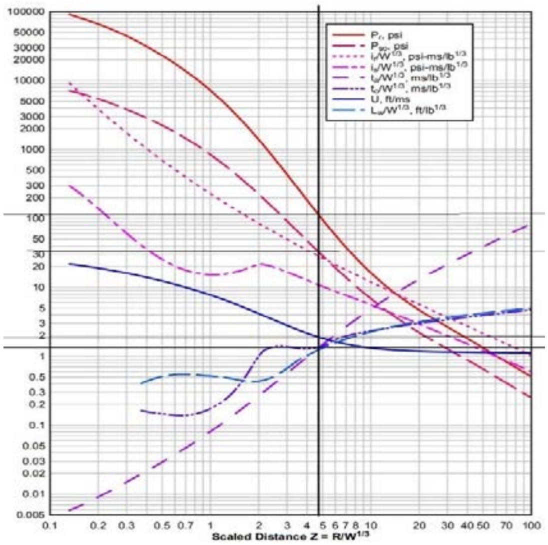

Figure 5. Positive Phase Shock Wave Parameters for Hemispherical TNT Explosion[7]

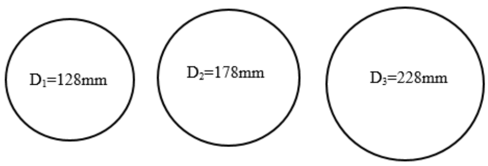

Figure 6. Three models of closure shell having different diameter

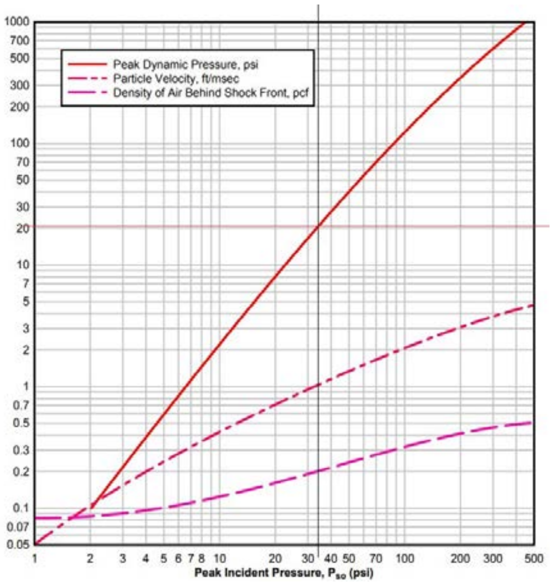

Figure 7. Graph of Peak Pressure Vs Dynamic Pressure, Particle Velocity, Density of Air Behind the Shock Front[7]

B. Clearing Time

The time required for passing the blast wave from the face of the structure is called clearing time. Equation-20 is used to calculate the clearing time for front-loading type structure given by bowling[7]. Based on the geometry, the clearing time (t_c) will be calculated using eq. (20).

$$t_c = \frac{4S}{(1+(S/G))C_r} = \frac{8A_c}{(Perimeter\ )C_r} \tag{20}$$

Where C_r is velocity of sound in that medium which is equal to 347.18 m/s, S is minimum of width or height of building, G is maximum of width or height of building, A_c is cross-section area of the front face of the structure being loaded.

For a circular flat plate having diameter D, the clearing time becomes $t_c = (2D/C_r)$. The clearing time for closure shell having diameter 128 mm, 178 mm, and 228 mm is 0.7378 ms, 1.026 ms, 1.3143 ms.

C. Impulse Evaluation on Closure Shell:

The empirical formula suggested by bowling[7] for positive phase impulse (I_s) having unit psi-ms acting on the structures, assuming front wall loading type is given by eq. (21),

$$I_s = 0.5(P_r - P_s)t_c + 0.5P_s t_0 \tag{21}$$

So, the impulse acting on the closure shell having diameter 128mm, 178mm, and 228 mm are 15.5 Ns, 32.22 Ns, and 56.6 Ns, respectively.

5. Conclusion

The blast valve is being used vastly for strategic purposes. The parts of valve should be designed considering all the effects. Various empirical relation exits for evaluating design parameters, as per surrounding condition one can use these relations and can fulfil the design requirements. In this paper, the modelling of impulse on the closure shell of blast valve has been carried using the empirical relation by bowling (UFC 3-340-02) as it takes the geometrical parameters into consideration for evaluating various parameter. Also, it takes loading type into consideration while calculating the impulse. The impacting impulse is utilised for closing the duct by moving the closure shell. Lower response time is obtained if high amount of force is impinged on the closure shell. Also, the shell should have sufficient strength to withstand the impact.

6. Contributors

Mr. Praveen Kumar received his B.E. degree in Mechanical Engineering in 2018 from Savitribai Phule Pune University Pune, and Currently pursuing MTech in Armament and Combat Vehicles (ACV) in Mechanical Engineering at DIAT (DU) Pune. His area of interest includes: Explosion, CFD, HMT, and FEM. In current study, he has carried out impulse modelling on the closure shell of Blast Valve.

Dr. Pankaj Kumar Sharma received his B.Tech.(Mechanical Engg.) in 2001 from CSJM University Kanpur, MTech. (Thermal & Fluids) in 2008 from IIT Bombay and PhD from IIT Delhi in 2020 and currently working as a faculty at Department of Mechanical Engineering DIAT (DU) Pune. His areas of interest include: Heat transfer, CFD, Fluid-Structure Interaction, Blast and Shock. In present study he has contributed in analysis of impulse load on closure shell of blast valve.

7. Reference

[1] Charles, D. P.; Dayton & Ohio, Blast Closure.US patent 3,015,342 Jan. 2, 1962.
[2] Cohen, E. & Weissman, S. Blast closure systems. In Proceedings of the symposium on Protective Structures for Civilian Populations, Washington DC, 1965.
[3] Sharma, P.K.; Patel, B.P. & Lal, H. Blast Valve Design Related Studies: A Review. May 2016. doi: https://doi.org/10.14429/dsj.66.9618
[4] Ramamurthy, K. Explosions and explosion safety. Tata McGraw Hill, India, 2011.
[5] Goel, M.E.; Vasant A. M.; Anil K. G.; & Steffen M. An Abridged Review of Blast Wave Parameters. Sept 2012. doi: https://doi.org/10.14429/dsj.62.1149
[6] Dusenberry, D.O. Handbook for Blast-Resistant Design of Buildings, John Wiley & Sons, Inc. 2010, 183-192.
[7] Bowling, C. Structures to resist the effects of accidental explosion. Department of Defence USA, User Report No. UFC 3-340-02, December 2008.
[8] Held, M. Blast Waves in Free Air, 1983.
[9] Shirbhate, P.A. & Goel, M.D. A Critical Review of Blast Wave Parameters and Approaches for Blast Load Mitigation. April 2020.
[10] Sharma, P.K. Design and Analysis of Blast Valve.Oct 2020 .
[11] Kingery, C.N. & Bulmash G. Air blast parameters from TNT spherical air burst and hemispherical burst. Technical report ARBRL-TR-02555. CRC Press, Taylor & Francis 1984.
[12] Brode, H.L. Numerical solutions of spherical blast waves. J. App. Phys., 26(6), 766-75, 1955. doi: http://dx.doi.org/10.1063/1.1722085
[13] Krauthammer, T. & Altenberg, A. Negative phase effects on glass panels. Int. J. Imp. Eng., 2000, 24(1), 1-17.
[14] Larcher, M. Pressure-Time functions for the description of air blast waves. Jan 2008.
[15] Kinney, G. F. & Graham, K. J.: Explosive Shocks in Air. Springer, Berlin, 1985.
[16] Teich, M. & Gebbeken, N. The Influence of the under-pressure phase on the dynamic response of structures subjected to blast loads. Mar. 17, 2010, 219-233. doi: https://doi.org/10.1260/2041-4196.1.2.219.

Design and Computational Fluid Dynamics Analysis of 30 mm Gun Muzzle Brake using CATIA and ANSYS

Prateek Shrivastava
CNA(DP)
Hyderabad

Cdr Sandeep Sharma
CINA
NAI
Balasore

Abstract - **Muzzle brake in any gun is used to improve the efficiency and accuracy of hitting the target. It also helps in reducing the recoil force on the gun. This work is the modeling of 30 mm gun muzzle brake using CATIA and computational fluid dynamics (CFD) analysis using ANSYS. This work also proposed a new design of 30 mm gun muzzle brake and compares the standard design and proposed design of muzzle brake on the basis of CFD analysis the parameters mass flow rate of flash , velocity of flash in the direction of barrel axis. The objective of this analysis is to minimize flash coming out after the shell and to maximize the sideway evacuation of the same.**

Keywords - muzzle , muzzle brake, 30 mm gun, CATIA, ANSYS, CFD,

1. Introduction

Muzzle brake is placed at the extreme end of the gun barrel, just after the muzzle. It is used to scavenge the flash or the flue gases generated after the combustion of propellant. This scavenging of flash from the path of shell reduces the recoil force on the gun as well improves the accuracy of the gun. It also positively reduces muzzle climb. From the beginning various designs of muzzle brake are being used depending upon the type of gun, its application, range etc.

The Close Range Naval-91 is a naval version of the Medak 30mm automatic gun installed on the Sarath Infantry fighting vehicle, a variant of the Russian (originally Soviet) BMP-2 manufactured in India under license by the Ordnance Factory Medak. The Medak gun itself is based on the Russian Shipunov 2A42 30 mm automatic cannon.

Standard design of muzzle brake has two flash separators in series in the direction of axis of barrel. Flash separates out through sideway passages. Two flash separators build a two stage side scavenging process. This exerts large pressure on the parting wall of the flash chambers, also high temperature additionally produce thermal stresses. Turbulent nature actually helps in removing flash through sideways.

Modified design which is proposed helps in channelizing flash through side passages in a better way and to utilize the upside and down side wall for scavenging. With improved trajectory of the flash , stresses developed would be less since head on collision of the gases and parting wall will be avoided.

CATIA V5R20 stands for computer aided three dimensional interactive application version 5 revision 20 and ANSYS 18.0 stands for analysis systems revision18. Using CATIA modeling, simulation and analysis can be done but it is basically used for modeling and simulation. ANSYS also has modeling space but it is widely used for analysis. various toolbars inside ANSYS facilitates application based analysis. it works on the principle of finite element method in which a body is divided into number of finite elements, and boundary of each element is called node, specific application conditions are applied on nodes and software processes it collectively.

Computational fluid dynamics under the tool fluid fluent in ANSYS helps in anticipating the fluid flow behaviour against the model. Models are scaled to prototype and created using designing software. Environmental conditions and operation conditions are kept same as per the real life scenario. Applications of CFD include aerospace industry, automobile industry, biomedical applications, fusion of fluid streams, boilers, turbine, marine like ships, submarines etc, CFD saves experiment time and resources but results are approximated not exact.

2. Literature Review

Since the invention of gun, evolution of muzzle brake design has been the topic of researchers. P Abhilash et. al [1] analyzed the heat transfer coefficient inside gun barrel. K Jiang et. al [2] investigated the muzzle brake efficiency. They carried out numerical simulation of muzzle brake and compared it with the experimental results. E Chaturvedi et al. [3] gives review article and proposes a new design for the small arms in which small ports were introduced for more flash evacuation. Liu F-f, et al.[4] described the influence of influenced by projectile mass, mass eccentricity, dynamic unbalance, load deviation, and clearance between projectile and bore on muzzle. Technical specification is provided on wikivisually page about CRN-91 gun[5]. For this study practical data has been used from the navy testing centers at jabalpur and balasore.

3. Proposed Design

Standard design of muzzle brake made using CATIA with approximate dimensions, due to the unavailability of the exact dimension specification.

On the above stated standard design, rear flash separator was modified. The wedge shaped element was made on parting wall on both side of the shell hole along with the wedge elements, holes were made upside and down side of each wedge elements.

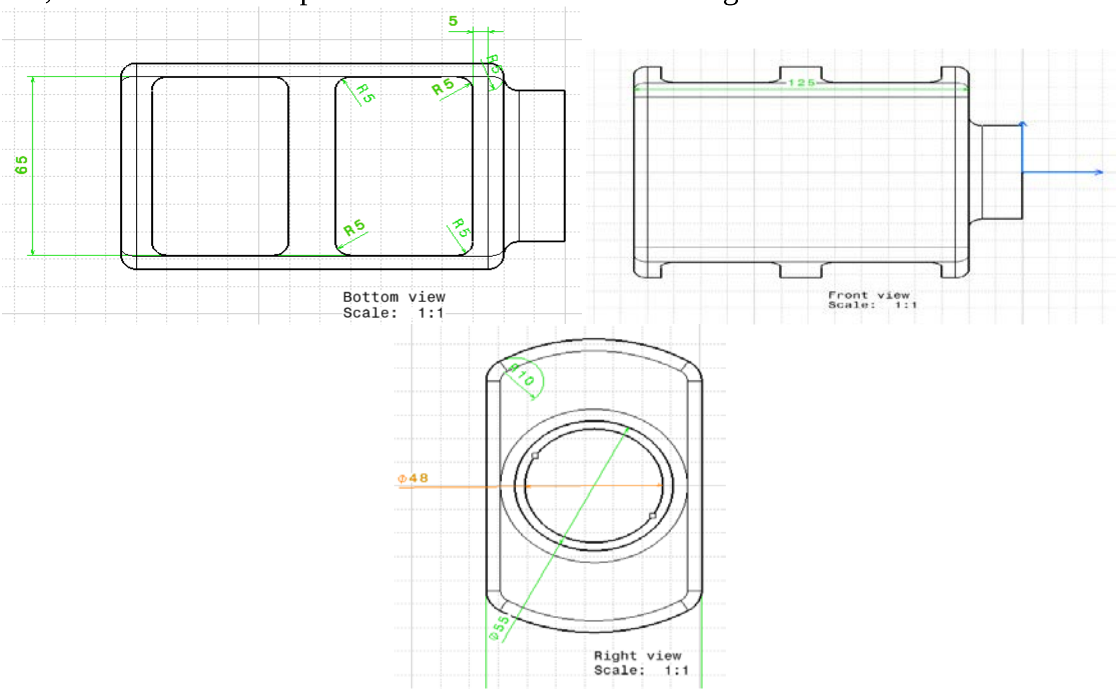

Fig 1. Standard design of 30 mm muzzle brake.

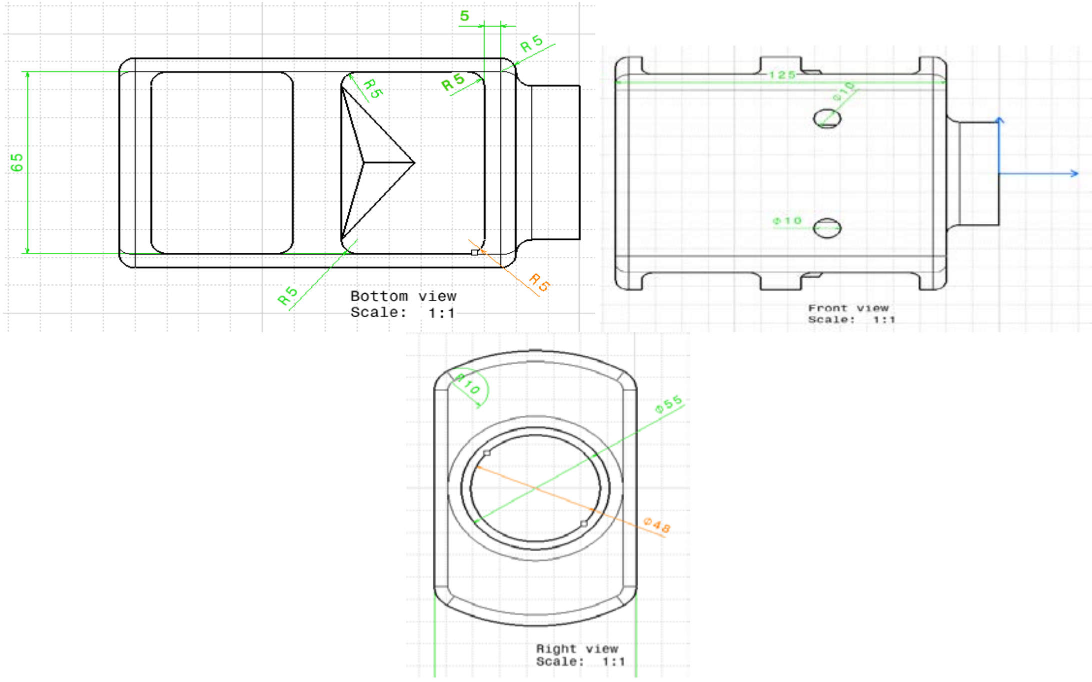

Fig 2: Modified design of 30 mm gun muzzle brake

4. Experimental Methodology

Standard and modified model of muzzle brake after being prepared in CATIA were saved in .stp format and them imported in fluid fluent tool in ANSYS. Hollow portions of the model were filled in design modular space. All the faces were named according to the fluid flow trajectory like inlet, side outlets upside and downside hole outlets, front outlets, fluid domain and muzzle wall. Meshing was done (default) and internal interfaces walls were repaired .

Considering fully developed turbulent flow, Under setup, k-epsilon model were selected, - models: Choose K and Epsilon in the Turbulence Specification Method drop-down list and select the appropriate profile names in the drop-down lists next to Turb. Kinetic Energy and Turb. Dissipation Rate. With air as a working fluid. Boundary conditions were specified with mass flow rate model at inlet with turbulent intensity and hydraulic diameter specifications. Other boundary conditions for outlets and fluid domain were specified.

After that setup was initialized and run for calculation with 1000 iterations. Under graphic space selecting contours, velocity, pressure and turbulence distribution was analyzed.

5. Theory and Equations Involved

The physical aspects of any fluid flow are govern by three fundamental principles. These fundamental physical principles can be expressed in terms of basic mathematical equations, which in their most general form are either integral equations or partial differential equations. Computational Fluid Dynamics is the art of replacing the integral or the partial derivatives in these equations by their discretized algebraic forms, which in turn are solved to obtain numbers for the flow field values at discrete points in time and / or space. The end products of CFD is indeed a collection of numbers which gives quantitative description of the problem i.e. numbers in contrast to a closed-form analytical solutions. The fundamental governing equations which describe the behavior of any type of fluid flow are as follows:-

- Mass Conservation
- Momentum Conservation
- Energy Conservation

6. Navier-Stokes Equation

For real viscous fluids, the resultant system of equations is called as Navier-Stokes (NS) equations. The formulation method of these equations can be referred in the textbook by Anderson Jr. The final conservative form is only presented here.

- $\frac{\partial p}{\partial t} + \nabla.\left(\rho\vec{V}\right) = 0.$ 1
- $\frac{\partial \rho u_i}{\partial t} + \nabla.\left(\rho u_i\vec{V}\right) = -\frac{\partial p}{\partial i} + \sum(\frac{\partial \tau_{ji}}{\partial j}) + \rho f_i$ 2
- $\frac{\partial}{\partial t}\left[\rho\left(e + \frac{V^2}{2}\right)\right] + \nabla.\left[\rho\left(e + \frac{V^2}{2}\right)\vec{V}\right] = \rho\dot{q} + \frac{\partial}{\partial t}\left(k\frac{\partial T}{\partial x}\right) + \frac{\partial}{\partial y}\left(k\frac{\partial T}{\partial y}\right) + \frac{\partial}{\partial z}\left(k\frac{\partial T}{\partial z}\right) - \frac{\partial up}{\partial x} - \frac{\partial vp}{\partial y} - \frac{\partial wp}{\partial z} + \frac{\partial u\tau_{xx}}{\partial x} + \frac{\partial u\tau_{yx}}{\partial y} + \frac{\partial u\tau_{zx}}{\partial z} + \frac{\partial v\tau_{yx}}{\partial x} + \frac{\partial v\tau_{yy}}{\partial y} + \frac{\partial v\tau_{zy}}{\partial z} + \frac{\partial w\tau_{xz}}{\partial x} + \frac{\partial w\tau_{yz}}{\partial y} + \frac{\partial w\tau_{zz}}{\partial z} + \rho\dot{f}.\vec{V}.$ 3

  where,
- The Eqns. 1 to 3 are the equations of conservation of the mass, momentum and energy, respectively.
- The density, pressure and temperature are scalar functions of space and time and are denoted by ρ , p and T, respectively and External forces is denoted by f_i.
- In Eqn. 3, $\dot{q}$ is the rate of volumetric heat addition per unit mass, e is the internal energy per unit mass, and k is the thermal conductivity
- In Eqn. 2, τ_{ji} is the stress tensor. The τ_{ji} is the stress in the j direction exerted on a plane perpendicular to the i axis. For every x, y and z taken by i, j takes variables x, y and z.

7. ANSYS Fluent

For complex geometry,

L = duct length is the parameter for hydraulic diameter

Therefore $D_{h.}$ = 0.007L.

When setting boundary conditions for a CFD simulation it is often necessary to estimate the turbulence intensity on the inlets. To do this accurately it is good to have some form of measurements or previous experience to base the estimate on. Here are a few examples of common estimations of the incoming Turbulence Intensity:

(i) High-turbulence case: High-speed flow inside complex geometries like heat-exchangers and flow inside rotating machinery (turbines and compressors). Typically the turbulence intensity is between 5% and 20%

(ii) Medium-turbulence case: Flow in not-so-complex devices like large pipes, ventilation flows etc. or low speed flows (low Reynolds number). Typically the turbulence intensity is between 1% and 5%

(iii) Low-turbulence case: Flow originating from a fluid that stands still, like external flow across cars, submarines and aircrafts. Very high-quality wind tunnels can also reach really low turbulence levels. Typically the turbulence intensity is very low, well below 1%.

For fully developed pipe flow the turbulence intensity at the core can be estimated as

$$I = 0.16{Re_{dh}}^{-1/8}$$

where Re_{dh} is the Reynolds number based on the pipe hydraulic diameter .

Flash properties:
Density = 70 kg/m^3 [1]
Dynamic viscosity (μ) = 0.00011 kg-m/sec [1]
Velocity at inlet: 960 m/s [Practical data]
Pressure at inlet : 12MPa[2]
Turbulence intensity : 19.63%
Hydraulic diameter at inlet : 0.00074 m

$$\dot{m} = \rho Q$$
$$\dot{m} = \rho A V$$
$$\dot{m} \propto V. \qquad 4$$

Where ṁ is the mass flow rate, Q is the volume flow rate, A is the area of cross section. If A and Q are constant then mass flow rate is directly proportional to the velocity in the direction of flow.

8. ANSYS Analysis

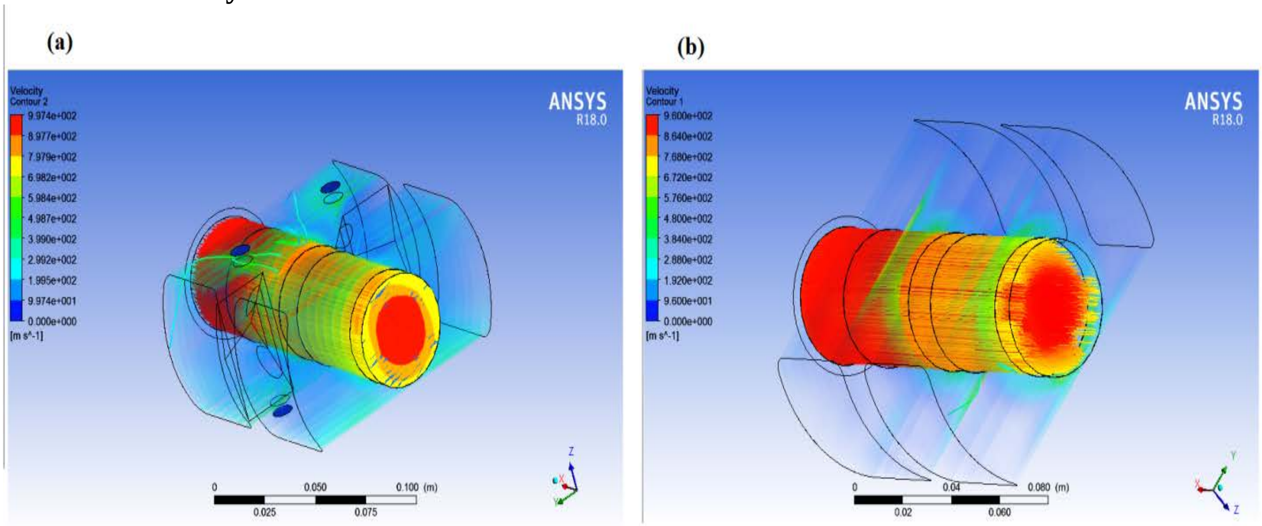

Fig 3. (a) Absolute velocity contour in 30 mm modified design muzzle brake (b) Absolute velocity contour in 30 mm standard design muzzle brake

In the above figure absolute velocity intensity variation is shown, red color stands for maximum value and blue color depicts minimum value. For the contour shown, 1000 velocity lines were featured starting from the back end where were equally spaced.

In part (a) which shows velocity contours of modified design few lines can be exclusively seen having white yellow color . These are the velocity lines deflected due to wedge shaped element . Due to this deflector and vent holes in the rear flash separator excessive mixing of velocity lines took place whose effect can be seen on upside and downside walls and also large portion of the flash exited through this rear flash separator. This is validated by the blue shades on the central outlet. on this outlet central part is red and it gradually fades radially outwards. Blue shades lowers the overall velocity intensity through this outlet.

In part (b) i.e in the standard design, there is no deflector and hence at central outlet red zone is large as compared to modified design and no blue shades. So intensity is high and no exclusive sign of mixing velocity lines as well.

(a)

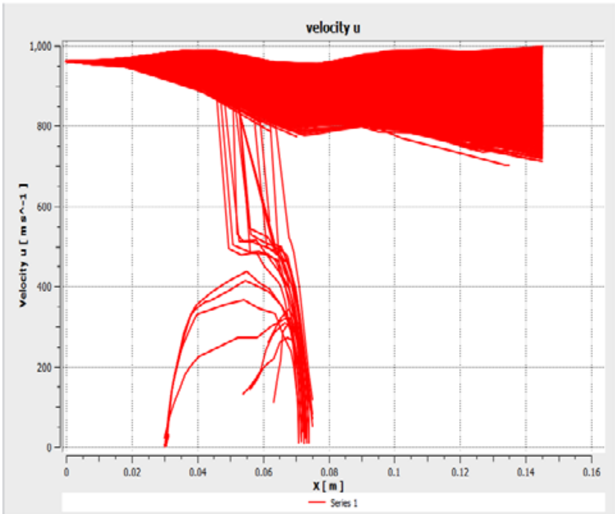

(b)

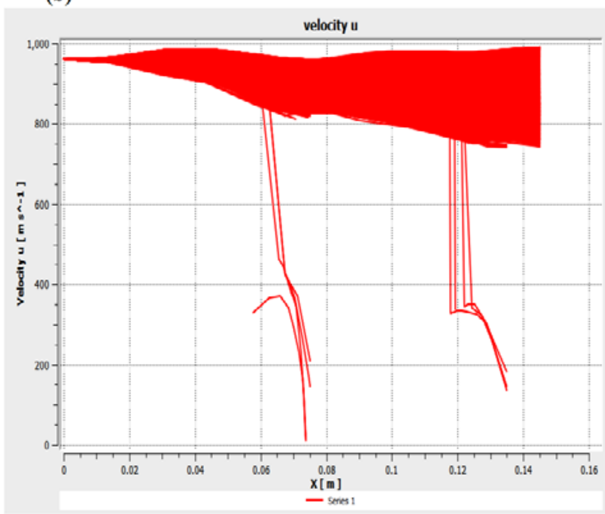

Fig 4. (a) Velocity lines trajectory in X direction in 30 mm modified design muzzle brake. (b) Velocity lines trajectory in X direction in 30 mm standard design muzzle brake.

From the above figure it was observed that with the introduction of wedge elements on the parting wall and holes on top and bottom surfaces, the average velocity in X direction decreases. It is noticeable that even at the beginning of flow the velocity is less, due to better ventilation and overall decrease in the momentum of air particles. In part (a) , trajectory of velocity lines in X direction in modified muzzle brake design are shown. In the rear flash separator due to wedge shaped deflector many velocity lines escaped out , this reduces the intensity of velocity in X direction and it is validated from the figure that velocity lines values fall below 800 m/s around x = 0.06 m in part (a). whereas in part (b) standard design, velocity lines values goes down to 800 m/s around x = 0.08 m. This shows that final intensity as well as average value of velocity coming out normally from central outlet is reduced in part (a) than part (b)

In standard design only few velocity lines deflected from X direction from flash separator's parting wall and outlet end wall. In modified design rear flash separator largely reduced velocity intensity and escaped from rear separator and velocity lines of low intensity did not deflected from end wall in front separator.

(a)

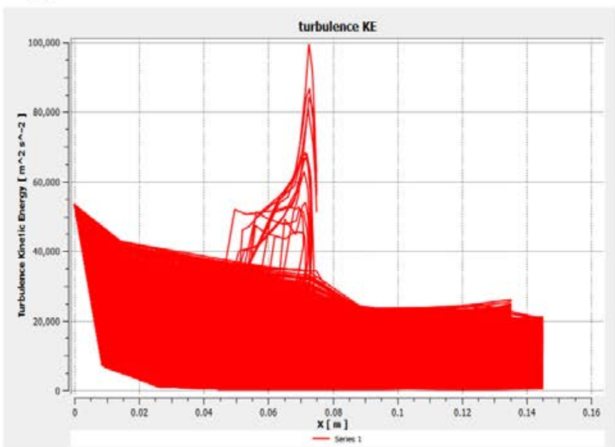

(b)

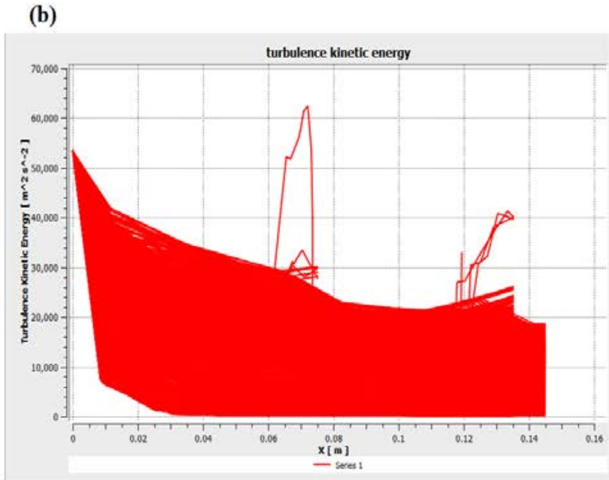

Fig 5. (a) Turbulence kinetic energy chart in 30 mm modified design muzzle brake. (b) Turbulence kinetic energy chart in 30 mm standard design muzzle brake.

As per figure 5 part (a) turbulence kinetic energy in rear flash separator is large because deflector reduces the space and pushes velocity lines to mix up. This largely increases the turbulence kinetic energy around the separator wall and hence embrace the formation of eddies.. Turbulence kinetic energy is due to movement of eddies that formed in the turbulent flow. Due to escaping of flash from rear separator and lowering of intensity, turbulence kinetic energy reduces or the rest of the trajectory.

In part (b) standard design due to striking of flash to the separating wall and end outlet wall turbulence kinetic energy increases around the walls but for overall trajectory, turbulence kinetic energy in muzzle brake is high which is adverse to the muzzle brake efficiency and accuracy of striking the target.

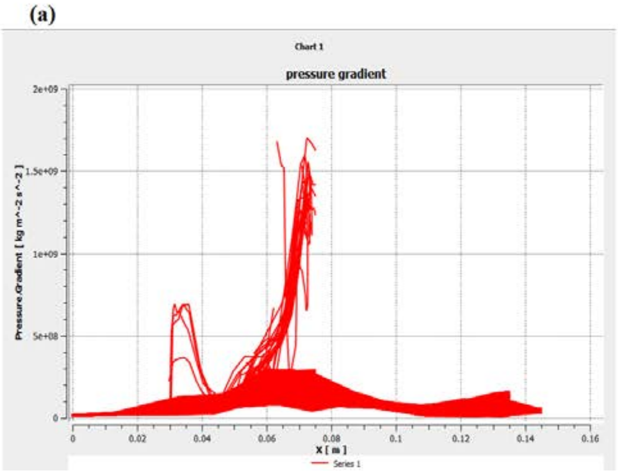

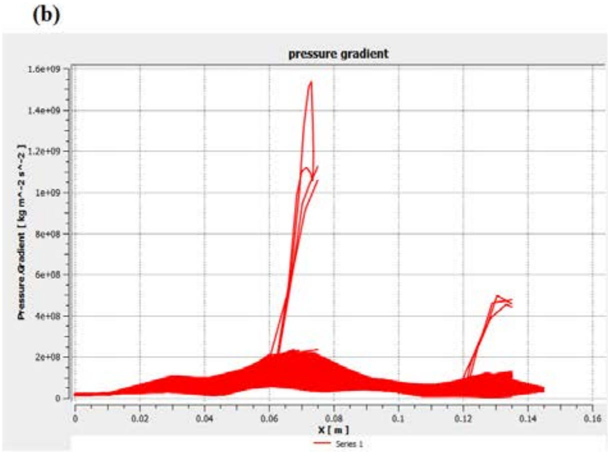

Fig 6. (a) Pressure gradient chart in 30 mm modified design muzzle brake. (b) Pressure gradient chart in 30 mm standard design muzzle brake.

As shown in figure 6 part (a) , in modified design due to the wedge element the pressure gradient increases in rear flash separator but it is lower for the rest of the trajectory as turbulence kinetic energy. This pressure gradient pushes gases to escape from side passages hence large amount of flash separates out from rear flash separator. Because of lower pressure gradient in the front flash chamber small amount of flash escaped from sides.

In part (b) standard design straight separating walls although produced maximum value of pressure gradient but it did not push flash to escape out from the separators

9. Results and Discussion

In modified design many velocity lines have value below 800 m/s from point 0.08 m and this continues till the end whereas in standard design only at the front flash separator , velocity lines values comes around 800 m/s. Thick bank of contour indicates more variation in values of velocity lines and this shift the average of velocity to the lower side as it can be seen in figure 4.

Since large number of velocity lines exited from rear flash separator hence velocity intensity is lowered by 12 to 18 percent from point x = 0.08 m.

Considering 12 percent reduction in velocity lines after passing through the rear flash separator in modified design as compared to the standard design of muzzle brake. Therefore velocity value must be multiplied by factor 0.88 for modified design from point x = 0.08 m.

Table 1 shows average velocity in X direction (u) in m/s

S No	Type of design / Distance from the beginning in X direction in m	Velocity u in Standard Design	Velocity u in Modified Design	Difference in percent with respect to standard design
1	0	960	960	0
2	0.04	940	920	-2.12766
3	0.06	910	880	-3.296703
4	0.08	890	748	-15.95506
5	0.12	850	721	-15.17647
6	0.14	820	712	-13.17073

From equation, velocity in the given direction is directly proportional to the mass flow rate in that direction. hence it was concluded that mass flow rate of flash coming out from central outlet in modified muzzle brake design is 13.17 percent less than that of standard muzzle brake design.

10. Conclusion

- With the modified design, the absolute velocity, directional velocity and turbulence kinetic energy decreases in the muzzle brake and this increases the muzzle brake efficiency and accuracy of the gun.
- The pressure gradient after the rear flash separator is less in modified design of muzzle brake which reduces the muzzle recoil.
- The exit velocity in the X direction in the modified design decreases by 13.17 percent which proportionally decreases the mass flow rate by the same percent.
- With the modified design, the recoil force on the gun also decreases because of the reduced mass flow rate and because of less turbulence kinetic energy and pressure gradient.

11. Scope and Future Work

This analysis introduces the new design for the 30 mm gun muzzle brake, similarly modifications can be done in the design of muzzle brake of other guns. Also different materials can be tested for reduced thermal stresses and better strength.

12. References

[1] Putti Abhilash and M. R. Chopade Analysis of heat transfer coefficient inside gun barrel http://inpressco.com/category/ijcet INPRESSCO IJCET Special Issue- 5(June 2016)

a. Kun Jiang, Hao Wang. Numerical simulation and experimental test on muzzle brake efficiency 978-0-7695-4522-6/11 $26.00 © 2011 IEEE DOI 10.1109/ICM.2011.334

b. E Chaturvedi et al. Materials Today: Proceedings 5 (2018) 18681–18688

c. Liu F-f, et al., Study on the influence of projectile on muzzle disturbance, Defence Technology (2018), https://doi.org/10.1016/j.dt.2018.07.016

d. https://wikivisually.com/wiki/CRN_91_Naval_Gun.

Analytical Ballistic Code – An Integrated Approach of Designing Pyro Mechanisms

Vikas
Space Ordnance Analysis and Devices Group
Vikram Sarabhai Space Centre
ISRO
Thiruvananthapuram
v.sheokand440@gmail.com

Nitish Dhawan
Space Ordnance Analysis and Devices Group
Vikram Sarabhai Space Centre
ISRO
Thiruvananthapuram

Kamal Saroha
Space Ordnance Analysis and Devices Group
Vikram Sarabhai Space Centre
ISRO
Thiruvananthapuram

Bishwajyoti Dutta Majumdar
Space Ordnance Analysis and Devices Group
Vikram Sarabhai Space Centre
ISRO
Thiruvananthapuram

Sheeju Chandran nodkumar
Space Ordnance Analysis and Devices Group
Vikram Sarabhai Space Centre
ISRO
Thiruvananthapuram

Abstract – **Towards design and analysis of Cartridge Actuate Devices (CAD), there is no available general purpose commercial software in the market. Conventional approach based on static closed volume assumption does not accurately predict the performance parameters of CAD required for design iterations. Therefore, programmed burn rate based approach is devised to fill the gap of design and analysis of CAD. The approach is based on fundamental equations like mass, momentum and energy conservation, proven empirical equations of burn rate law and Nobel-Abel equation of state implemented in an Analytical Ballistic Code for CAD (ABC-CAD). Close bomb test is conducted to validate the accuracy of ABC-CAD in static condition. Functional tests of pyro valve and pyro thruster are conducted to validate the performance prediction of the approach in dynamic condition. Comparison of performance prediction of ABC-CAD with experimental results of closed bomb test and functional tests of pyro valve and pyro thruster validate the accuracy of the code for predicting the performance parameters like pressure, velocity, reaction load etc. which can be used for design iterations reliably.**

Keywords*– *Pyro Mechanism, Cartridge Actuated Device (CAD), Analytical Ballistic Code – CAD (ABC-CAD), Nobel-Abel Equation of State, Burn Rate Law, NCB 12, Pyro Valve, Pyro Thruster

1. Introduction

Pyro devices are basically explosive actuated mechanical systems which use chemical energy of explosives to perform an intended work like separation and jettisoning, severance and jamming at specific location etc. within a very short period of time. Pyro mechanisms are widely used in launch vehicles, missiles and satellites due to their simplicity, reliability, high power to weight ratio, fast operation, and lower operating electric current requirement. Modeling and simulation of pyro mechanisms plays a very important role in understanding the physics of the system, design optimization and addressing all possible failure modes with adequate safeguard at the very initial stage of development of any pyro mechanism. Pyro-mechanisms can be broadly categorized into two types; high explosive actuated device (HEAD) and cartridge actuated device (CAD). In CAD pressure generated due to conductive and convective burning of pyrotechnic charge interacts with mechanism of the device in the form of piston cylinder arrangement and does the intended work like severance of notch, retraction of piston of pin puller, pushing the piston of pyro thrusters etc. There is a need to simulate various types of burning of explosive charge which strongly depends upon the instantaneous chamber pressure and the temperature which in turn is governed by the expansion of the chamber due to movement of piston. Towards this a novel approach to design a cartridge actuated pyro mechanism is devised to handle the complex interdependency among pressure, volume, resistance, burn rate of explosive charge, heat loss etc. in an integrated way. Analytical Ballistic Code – for Cartridge Actuated Devices (ABC-CAD) is developed in house using lumped parameter approach in Matlab programming platform. Pressure vs. time history, function time, threshold charge quantity, reaction load, piston velocity history etc. can be predicted using ABC-CAD. Thus the full physics of the pyro mechanism can be better understood which enables design optimization and improved reliability of the system by providing adequate margin against all possible failure modes.

2. Problem Description

Modeling of Cartridge Actuated Device, a typical sketch is shown in Figure 1, involves the challenge of handling interdependent parameters such as burn rate of explosive charge, resistance force due to external work, heat loss through walls, co-volume consideration and equation of state for product gases and condensed matter etc. Simulation of combustion of explosive itself is a challenge, as the algorithm involves equations for burning of charge, interaction of combustion products containing condensed and gaseous phase, solving the 3-dimensional spatial variation of state parameters, chemical kinetics of reaction, inter-dependency of state parameters, real behavior of product gases etc. Researchers have been using simple empirical relationship like burn rate law, equation of state (EOS) which simplify the modelling of combustion of pyrotechnic charges[1]-[7]. With the help of these equations, a ballistic code has been developed to simulate the performance of the pyro mechanisms. In this paper, two approaches of ballistic analysis of CAD are discussed; 1) Conventional approach 2) Programmed burn rate based approach using ABC-CAD. Mathematical model of both the approaches, with the assumptions considered will be discussed in detail in subsequent sections.

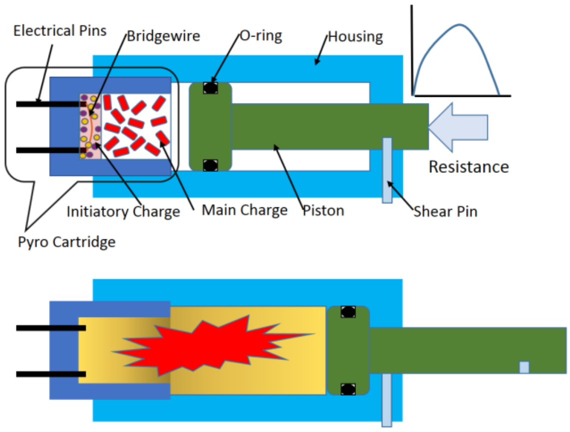

Figure 1 : Typical Schematic of Pyro Mechanism

3. Mathematical Modelling

A. Conventional Approach

In conventional approach, pressure of product gases is calculated using Nobel-Abel equation of state [1] assuming all the explosive charges burns in the initial free volume followed by movement of piston along adiabatic expansion process. Therefore, chemical kinetics of combustion process is ignored in this approach. Pressure due to burning of pyrotechnic charge at t = 0 is calculated using Nobel-Abel Equation of State as shown in equation (1).

$$P_1 = \frac{F}{\frac{1}{\rho} - \eta} \tag{1}$$

Where P_1 is the pressure developed in the initial volume due to complete burning of explosive charge at t = 0, F is the impetus of explosive product gases which is equal to product of specific gas constant of product gases and adiabatic flame temperature, ρ is the initial loading density of the explosive charge, and η is the co-volume of the product gases. It is assumed that there is no significant heat loss during the operation of a pyro mechanism. Therefore, pressure variation as volume of gas chamber changes is computed using adiabatic expansion equation and the work done is equated with the total energy requirement of the mechanism for estimation of initial pressure and explosive charge quantity. Although this method is very simple to implement, it fails to predict the time of occurrence of various mechanical events like shearing, jamming, severance etc. It also fails to predict the accurate velocity of moving piston or severed member and pressure of pyro mechanism in the dynamic condition.

B. Programmed Burn Rate Based Approach

Programmed burn rate based approach incorporates burn rate model, mass conservation, energy conservation, equation of state for product gases, and momentum conservation. Vieille's or St. Robert's burn rate model [2]-[7] is used to simulate the kinetics of combustion process which is given in equation (2). The burn rate model defines the relationship between pressure of product gases and regression of explosive granules along the normal of surface

$$\frac{dr}{dt} = -a \times \left(P_g\right)^n \tag{2}$$

Where r is the characteristic length along the normal of explosive granule surface, P_g is pressure of gas inside the chamber, and a and n are the burn rate constant and burn rate exponent respectively. Due to the regression of surface of explosive granule, volume occupied by the explosives charge decreases and the effective free volume is updated after each iteration. The overall all lay-out of ABC-CAD approach is depicted in Figure 2.

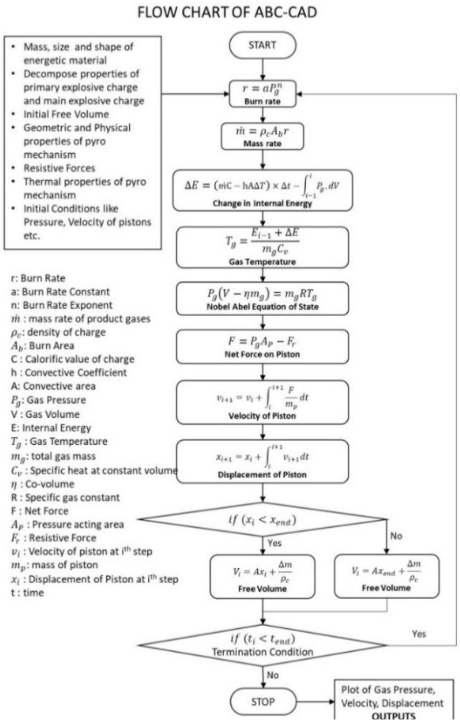

Figure 2 : Flow Chart of ABC-CAD based on Programmed Burn Rate Based Approach

The burn rate parameters for the explosive charges are estimated from closed bomb tests with the input of geometrical dimensions of the charges. All thermo chemical properties of explosive charges are obtained from chemical equilibrium codes like REAL, EXPLO5 etc. Resistance force F_r acting on to the piston is obtained from analytical equations as well as finite element analysis or experiments. The entire scheme of the code is implemented to solve using forward difference scheme

4. Case Studies

Towards finding out the adequacy of both the approaches described before and demonstrating relative advantages of the proposed programmed burn rate based approach implemented in ABC-CAD over the conventional approach two case studies are conducted as detailed in section 4.A and 4.B in a static and dynamic system respectively.

A. Closed Bomb studies

To compare and verify the prediction of both programmed burn rate based approach and conventional approach in static condition, a closed bomb test is conducted. Generally, pressure is taken as the performance parameter for closed bomb test. Therefore, a 10 cc closed bomb is designed with interface for pressure sensor and the schematic of 10 cc closed bomb is shown in Figure 3.

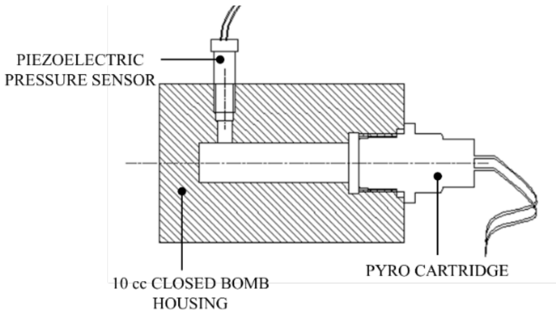

Figure 3 : Schematic of Closed Bomb Test Fixture

Pyro-cartridge contains 180 mg of Zirconium based charge as initiatory explosive and 1000 mg of Nitrocellulose (NC) as main pressure producing charge. Pressure data of the test is plotted in Figure 4 along with pressure prediction of both conventional and programmed burn rate based approach in ABC-CAD. Oscillation are observed o in the tested data which is due to bursting of ZPP disc. The bursting of ZPP disc generate shock pulse which is reflected as oscillation in the measured pressure.

Conventional approach only predicts peak pressure which is assumed to be same throughout the functioning time and predicted pressure from the approach is 62.5 MPa. This approach has an error of 3.1% as compare to experiment. One possible reason for the error may be due to independent consideration of co-volume for computation of pressure generated by initiatory explosive charge and main explosive charge. On the other hand, ABC-CAD predicts full time history of pressure. The predicted pressure from the approach has a fairly good match up to peak pressure point of experimental data as shown in Figure 4. Falling of pressure measured in test after peak, is due to the characteristic of piezo-electric pressure sensor which cannot sense steady state pressure [2]. Maximum pressure measured in test is 64.5MPa whereas maximum pressure predicted using the approach is 65.08 MPa. Therefore, error in prediction of maximum pressure using this approach is 0.7%. Comparison of pressure predictions in static condition with experiment data implies that programmed burn rate based approach is more accurate than conventional approach.

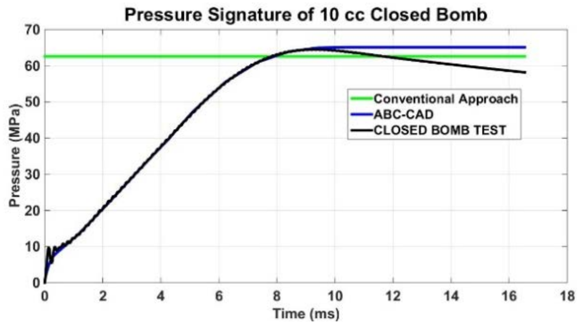

Figure 4 : Comparison of Pressure Predicted through Conventional Approach and ABC-CAD with Experimental Pressure Data of Closed Bomb

B. Simplified Pyro Mechanism

To compare the prediction of both conventional approach and programmed burn rate based approach in the dynamic condition, a simplified configuration of pyro thruster mechanism is studied as shown in Figure 5.

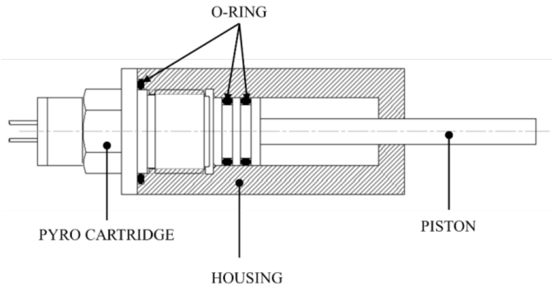

Figure 5 : Schematic of Simplified Configuration of Pyro Mechanism

Pressure, developed due to combustion of pyrotechnic charge, drives the piston to move forward. The piston stops when it reaches the maximum stroke. For simplicity, shear screw is not considered in this case study and only inertial resistance due to piston mass is considered Pressure, velocity and displacement prediction are obtained using both approaches. Pyro cartridge is filled with 40 mg initiatory explosive charge with Boron Potassium Nitrate composition and 120mg NC as main explosive charge. Linear burning of initiatory charge is considered for 0.2 ms. Inputs of conventional approach and programmed burn rate based approach of the pyro mechanism are given in **Table 1**

Table 1: Input Design Parameters of Simplified Pyro Mechanism for ABC-CAD

Input Parameter	**Value**
Volume occupied by Initiatory Charge	16.63 mm^3
Volume occupied by NC	211.64 mm^3
Initial Free Volume	247 mm^3
Diameter of Piston	13 mm
Mass of Piston	127.43 gram

Pressure, velocity and displacement prediction obtained from both conventional approach as well as ABC-CAD are shown in Figure 6, Figure 7 and Figure 8 respectively. Maximum pressure computed from conventional approach and ABC-CAD are 231.8 MPa and 21.56 MPa respectively as shown in Figure 6. Terminal velocity predicted from both the approaches are 53.83 m/s and 15.18 m/s respectively as shown in Figure 7. Similarly function time of pyro mechanism computed from both the approaches is 0.605 ms and 2.812 ms respectively as shown in Figure 8.

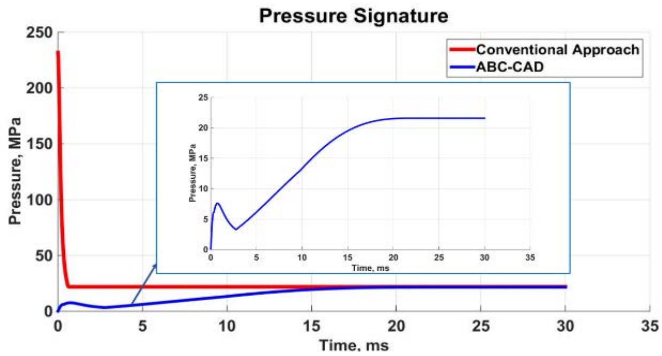

Figure 6 : Chamber Pressure Prediction from Conventional Approach and ABC-CAD for Simplified Pyro Mechanism

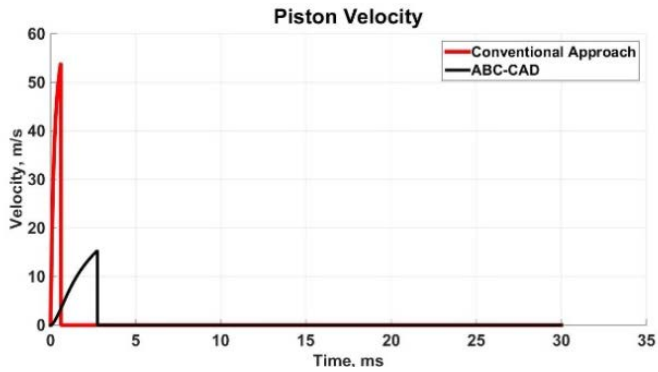

Figure 7 : Piston Velocity Prediction from Conventional Approach and ABC-CAD for Simplified Pyro Mechanism

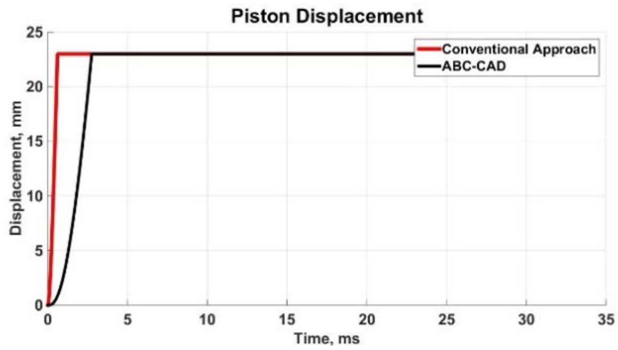

Figure 8 : Piston Displacement Prediction from Conventional Approach and ABC-CAD for Simplified Pyro Mechanism

All the critical design parameters, discussed yet, have large variation in predictions carried out using conventional approach and ABC-CAD. The primary reason for this deviation is attributed to the fact that the entire charge is assumed to be burned instantaneously in to the initial free volume itself attributing to constant volume heat addition leading to higher thermal efficiency in case of conventional approach. This makes the prediction of the piston velocity almost 3.7 times higher the velocity predicted by ABC-CAD and the corresponding maximum pressure almost 10.8 times higher. The higher velocity prediction naturally makes the action time shorter in conventional approach. Because of this fact the higher pressure predicted in conventional approach makes the design bulkier at the same time charge estimation becomes unreliably small ultimately makes it purely dependent upon experimental evaluation through trial and error to arrive at the threshold charge quantity. Whereas in ABC-CAD the end to end performance prediction makes the design cycle shorter and robust

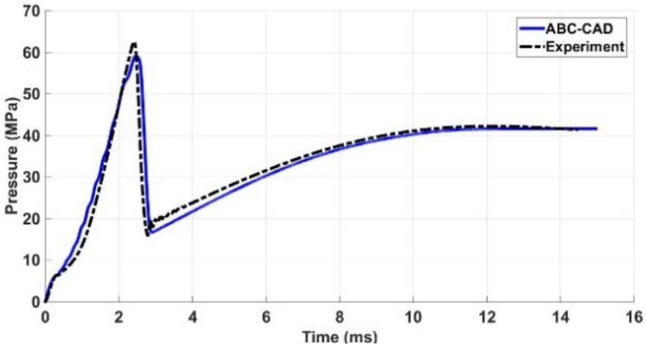

Figure 9 : Comparison of pressure prediction using ABC-CAD with experiment data for Pyro Valve

In order to validate the ABC-CAD predictions under actual dynamic conditions, a series of tests are conducted. Special efforts are made to measure pressure history inside a pyro valve and the same is compared with the prediction and excellent match was found as shown in Error! Reference source not found.. Similarly, towards validation of reaction load and Piston Velocity computed through ABC-CAD for a typical pyro thruster experiments are conducted with reaction load measurement through load cell and velocity measurement through High Speed Camera. For these cases also excellent match is found between the prediction and the experiments as shown in Figure 10 and Figure 11

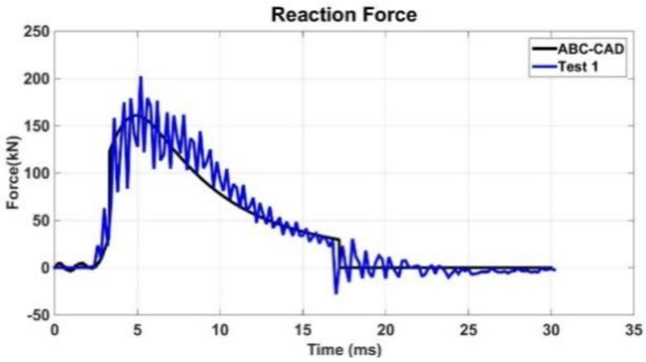

Figure 10 : Comparison of Reaction Load Prediction of ABC-CAD with Experiment Data of Test 1 for Pyro Thruster

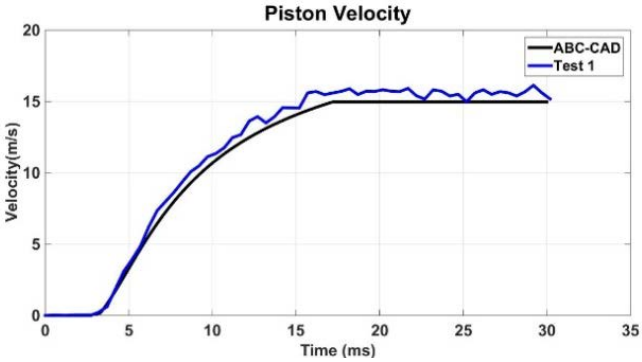

Figure 11 : Comparison of Velocity Prediction of ABC-CAD with Experiment Data of Test 1 for Pyro Thruster

5. Conclusion

Conventional approach for designing CAD is explained in the paper. This approach predicts pressure accurately for a closed bomb scenario. However, it does not predict accurately pressure, velocity and other performance parameters in dynamic condition. Therefore, this approach has to be used only as a starting point and the design can be finalized only after large number of functional tests. Towards design and performance prediction of Cartridge Actuated Devices, an Analytical Ballistic Code, referred as ABC-CAD, is developed using programmed burn rate based approach which is based on fundamental and empirical equations. The code can reliably be used for predicting the performance parameters, like pressure, velocity, reaction load etc. of pyro mechanism which are actuated with deflagrating explosive charges. The accuracy of the code is validated in both static and dynamic conditions. Therefore, ABC-CAD is found to be an efficient tool for ballistic design and analysis of pyro mechanisms. Results of the code can give full insight of the mechanism towards design optimization without the need of carrying out numerous costly experiments thereby reducing overall design cycle time considerably.

6. Acknowledgement

The authors express their sincere gratitude our colleagues Shri Anees, Shri Aneesh Kumar CM, Shri Mathew KK , Shri N Balbantray, Shri Christopher M, and Shri Purushothaman P for their support and guidance towards instrumentation in measuring the pressure, reaction load and piston velocity data in experiments as well as analysis of the test data

7. Reference

[1] Ian A. Johnston, “The Nobel-Abel Equation of State: Thermodynamic Derivations for Ballistic Modelling” Defence Science and Technology Organization, Nov., 2005

[2] Dae-Hyun Hwang, Doo-Hee Han, Hong-Gye Sung andByung-Tae Ryu,” Separation Behavior of Pyrotechnically Actuated Device Considering Small-Volume Effect of Combustion Chamber”,Journal of Spacecraft and Rocket, Volume 57, Number 4, Apr., 2020

[3] Seung-gyo Jang, Hyo-nam Lee and Jong-yun Oh, “Performance Modeling of a Pyrotechnically Actuated Pin Puller” Int’l J. of Aeronautical & Space Sci. 15(1), 102-111 (2014)

[4] Dae-Hyun Hwang, Juho Lee, Jae-Hung Han, YeungJo Lee and Dongjin Kim, “Mathematical Model for the Separation Behavior of Low Shock Separation System”, Journal of Spacecraft and Rocket, Vol. 55, No. 5, Sept-Oct., 2018, pp. 1208-1221

[5] Dae-Hyun Hwang, Jae-Hung Han, Juho Lee, YeungJo Lee and Dongjin Kim, “A mathematical model for the separation behavior of a split type low-shock separation bolt”, ActaAstronautica 164 (2019) 393-406

[6] Powers, J. M. and Gonthier, K. A., “Sensitivity Analysisfor a Pyrotechnically Actuated Pin Puller Model”, 19th International Pyrotechnics Seminar, NewZealand, Feb. 1994.

[7] K. A. Gonthier, and J. M. Powers, “Formulation, Prediction, and Sensitivity Analysis of a PyrotechnicallyActuated Pin Puller Model”, Journal of Propulsion and Power,Vol. 10, No. 4, 1994, pp. 501-507.

CFD Simulation of Gas Operated Control Surface Deployment Mechanism for a Gun Launched Missile

Rahul Chopde
Armament Research and Development Establishment,
Defence Research and Development Organization,
Pune-4110021, India
rahulchopde@arde.drdo.in

M V Ramesh Kumar
Armament Research and Development Establishment,
Defence Research and Development Organization,
Pune-4110021, India
mvrk@arde.drdo.in

***Abstract*— In the current study, ejection of control surface deployment cylinder using exhaust gases from the onboard propulsion system is simulated using CFD. Gun launch of a missile entails control surfaces to be folded in order to avoid spin during the launch. The spring-loaded control surfaces are deployed due to movement of the deployment cylinder in the axial direction. The motion of the deployment cylinder is caused due to high pressure generated by onboard propulsion gases. This complex phenomenon has been modelled using a multiple zone sliding mesh approach with layering algorithm. Motion of the nozzle closure after ignition of the propulsion system is also modelled using CFD.**

Mass generation due to burning of propellant has been modelled using a user defined function. Noble-Abel equation of state has been utilized for accurate simulation of the interior ballistics. Motion of the control surface deployment cylinder was coupled with CFD using a 1 DOF model. Estimated control surface deployment time is utilized for scheduling the other mission critical events.

1. Introduction

Gun launch of a missile entails control surfaces to be folded in order to avoid spin imparted to the missile. A typical configuration of a gun launched missile is shown in Fig.1.The control surfaces are folded towards the nose and they get deployed once the missile exits the barrel. As seen in Fig.2, the control surfaces are held in folded position using a control surface deployment cylinder which is mounted from rear end of the missile. Once the missile exits the barrel, the on-board propulsion system is initiated.

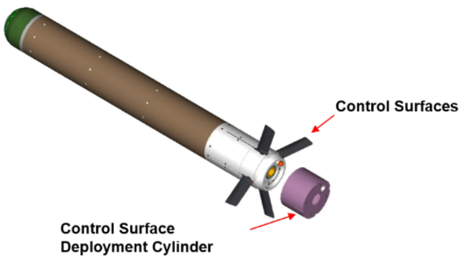

Fig. 1: A typical gun launched missile configuration

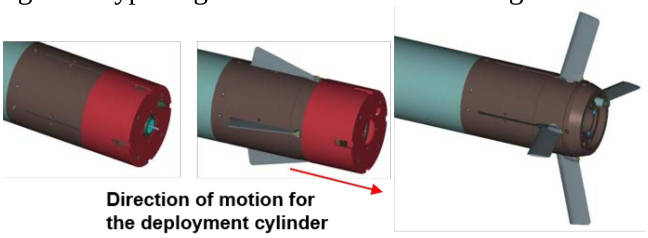

Fig. 2: Sequence of control surface deployment

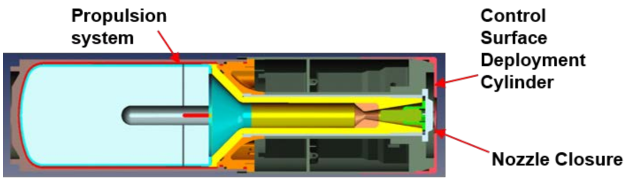

Fig. 3: Control surface deployment mechanism along with the propulsion system

The gas generated by the on-board propulsion system causes this cylinder to slide in axial direction. Once the control surface deployment cylinder has been completely removed, the spring-loaded control surfaces get deployed. The estimation of time required for the removal of control surface deployment cylinder plays an important role in scheduling the other mission critical events.

In the current study, the complex phenomenon of control surface deployment using on-board propulsion system is simulated using ANSYS FLUENT software [1]. The details of the mechanisms are shown in Fig3. A nozzle closure is mounted at the exit plane of nozzle to build the initial pressure for the propulsion system. Motion of the nozzle closure as well as control surface deployment cylinder is simulated using multiple sliding zones along with the layering algorithm [2]. Mass generation due to burning of propellant grain is modelled using user defined function (a macro written in C language.) [3]

2. Computational Domain and Boundary Conditions

Axi-symmetric computational domain and various boundary conditions used during this simulation are shown in Fig.4 and Fig.5. Inlet to the computational domain is modelled as a mass flow inlet. Sliding interfaces are employed to simulated axial motion of the nozzle closure and control surface deployment cylinder. Sliding and stationary zones required for the simulation are shown in Fig. 6

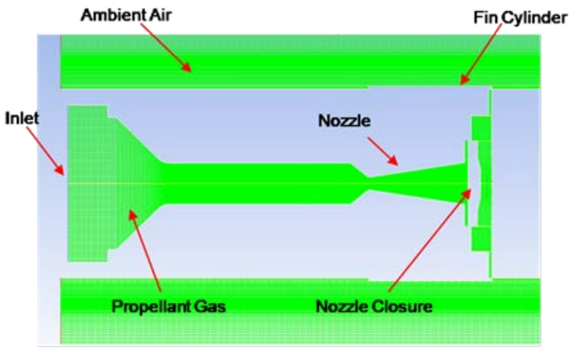

Fig. 4: Computational Domain

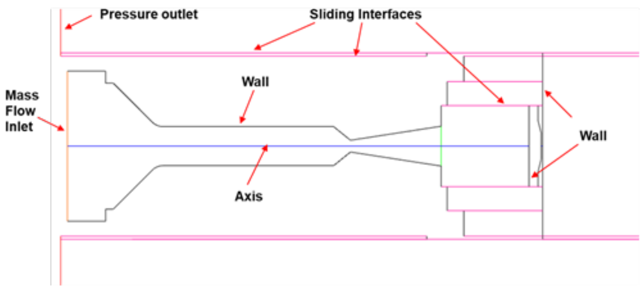

Fig. 5: Boundary Conditions

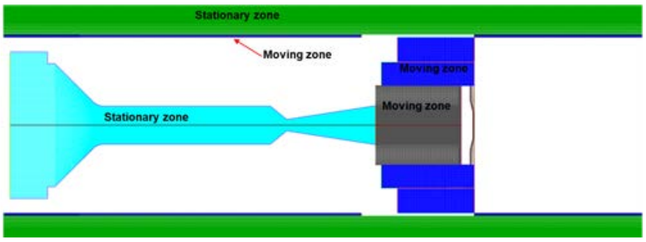

Fig. 6: Grid Zones

3. Numerical Setup

Density based solver of ANSYS FLUENT software was used for the unsteady simulation. Abel-Noble equation of state [4] and 1DOF model was implemented using a User Defined Function (UDF). The UDF was also used to initiate sliding of the nozzle closure and control surface deployment cylinder based on the pressure force exerted by the propellant gas. Variation of mass flow rate was coupled with the propulsion chamber pressure [5] using a separate UDF (See Fig.7).

```
#include "udf.h"
#include "stdio.h"
#include "ctype.h"
#include "stdarg.h"

int it=0;
double rdot,mdot,source,area,p_breach,tm;
double rho=1640;

DEFINE_PROFILE(unsteady_flux, t, pos)
{

it=N_ITER;
tm = RP_Get_Real("flow-time");

area=0.018821;
face_t f;

begin_f_loop(f, t)
{
p_breach=F_P(f,t);
p_breach=p_breach/1000000;
rdot=0.0015047*pow(p_breach,3)+0.073607*pow(p_breach,2)-0.57989*pow(p_breach,1)+11.653;
rdot=rdot/1000;
mdot=area*rdot*rho;
source=mdot/0.00785;


F_PROFILE(f, t, pos) = source;
}
end_f_loop(f, loop)

        if (mdot > 0 && it%200 == 0)
        {
        FILE *fd;
        fd = fopen ("mass_output.txt","a");
        if (tm == 0.000000)
        {
        fprintf (fd, "T \t \t pressure \t\t mdot\n");
        }
        fprintf (fd, "%.12lf\t", tm);
        fprintf (fd, "%.12lf\t%.12lf\t%.12lf\t\n",p_breach,mdot);
        fclose(fd);


        }

}
```

Fig. 7: UDF for unsteady mass flow inlet

4. Results

Variation of chamber pressure with respect to time is shown in Fig.8. At t=4.7 ms, there is sudden change in the slope due to opening of the nozzle closure. Pressure inside the cavity between the control surface deployment cylinder and base of the missile was monitored and is plotted in Fig. 9. Sudden rise of pressure at t=4.7 ms, due to opening of nozzle closure can be observed followed by drop in pressure as the control surface deployment cylinder starts moving under the pressure forces generated by the propellant gas

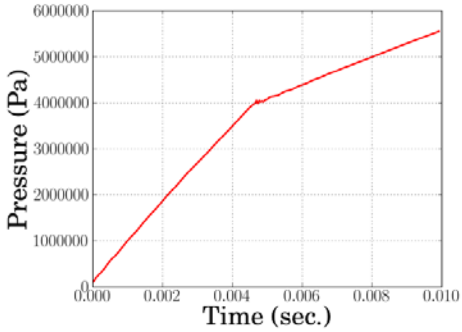

Fig. 8: Chamber pressure vs time

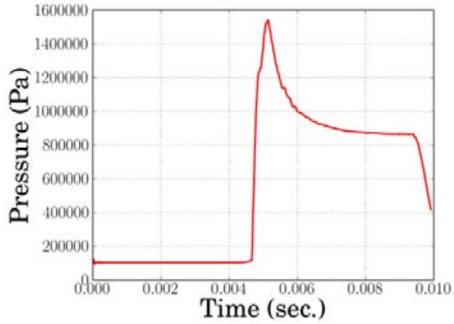

Fig. 9: Pressure at control surface deployment cylinder vs time

Pressure contour at various time instances are shown in Fig.10 through Fig.13. As seen in Fig.7, at t=4.7 ms the pressure force acting on the nozzle closure exceeds the threshold value and causes movement of the nozzle closure. This results in gases entering into the cavity formed between the control surface deployment cylinder and the base of the missile. As seen in Fig.8, a shock wave is formed inside the divergent section due to back pressure generated inside the control surface deployment cylinder cavity. The nozzle closure keeps sliding till it hits the control surface deployment cylinder. As the control surface deployment cylinder starts moving, the shock wave moves towards the nozzle exit. At t=10ms (see Fig.13), the control surface deployment cylinder is completely removed and the propellant gases start exiting into the ambient air.

The time required for ejection of control surface deployment cylinder measured during the static test of the mechanism was 14 ms. The difference between ejection time estimated using CFD simulation and static test can be attributed to various openings present in the actual hardware of the control surface deployment cylinder. These opening were not modeled in the CFD simulation due to the complexity involved in the meshing. The leakage of propellant gas from these openings resulted in higher time required for the ejection of control surface deployment cylinder during the static test

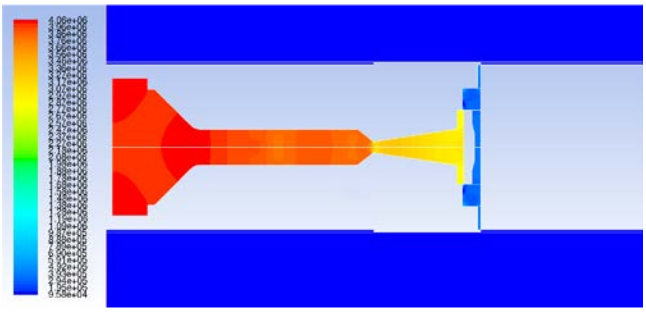

Fig. 10: Pressure contours at t=4.7ms

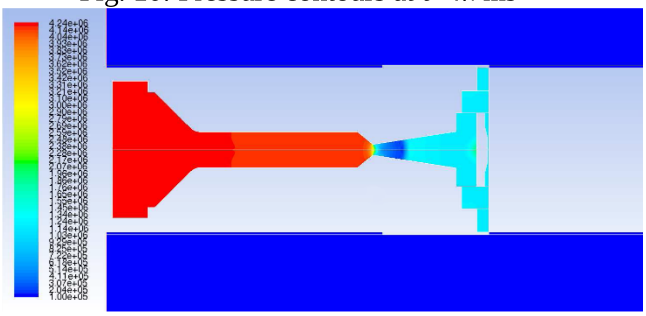

Fig 11: Pressure contours at t=5.5 ms

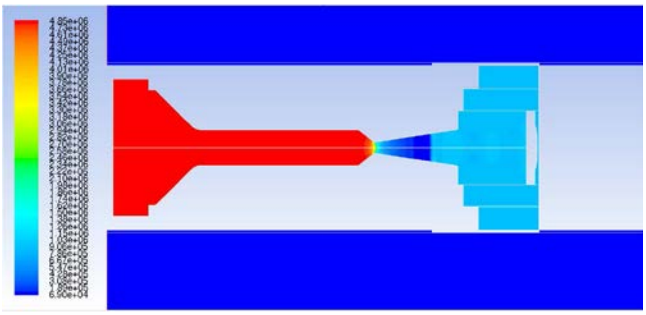

Fig 12: Pressure contours at t=7.5 ms

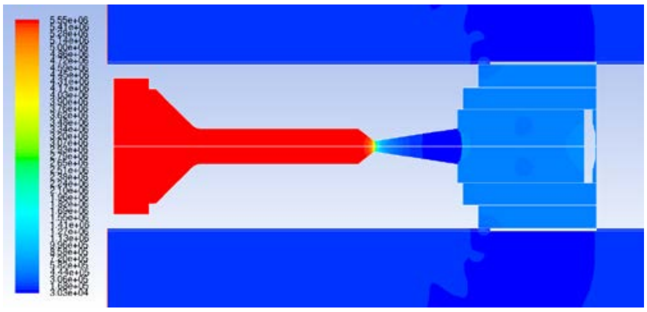

Fig 13: Pressure contours at t=10 ms

5. Conclusion

The numerical simulation of control surface deployment mechanism operated using onboard propulsion system was carried out. Multiple sliding zones were employed to simulate this phenomenon. The difference between the estimated and measured time for ejection of control surface deployment cylinder is attributed to the various openings present in the actual hardware. These openings are not modelled in CFD and therefore the leakage of propellant gas from these openings resulted in higher time required for ejection of control surface deployment cylinder.

Future studies can be carried out with these opening presents in the CFD model for accurate estimation of ejection time.

6. Acknowledgment

Authors are thankful to Dr VV Rao, Director ARDE for providing opportunity and resources for completion of present work.

7. Reference

[1] "ANSYS FLUENT MANUAL 2017" ANSYS Ltd, USA
[2] "THEORY GUIDE SLIDING MESH", 2017 ANSYS Ltd, USA
[3] "ANSYS FLUENT UDF MANUAL" 2017 ANSYS Ltd, USA
[4] Ian A. Johnston "The Noble-Abel Equation of state: Thermodynamic Derivatives for Ballistic Modeling" , DSTO-TN-0670, Nov. 2005
[5] George P. Sutton, Oscar Biblarz, Rocket Propulsion Elements

Aerospace Hardware Clearance using Surrogate Models

Partha Ajit Surve
Vikram Sarabhai Space Centre
Thiruvananthapuram
parthasurve1@gmail.com

Manash Kumar Bhadra
Vikram Sarabhai Space Centre
Thiruvananthapuram

G Vinod,KKRaveendra Babu
Vikram Sarabhai Space Centre
Thiruvananthapuram

Dr. T Sundararajan
Vikram Sarabhai Space Centre
Thiruvananthapuram

L Sowmianarayanan
Vikram Sarabhai Space Centre
Thiruvananthapuram

Dr. Geetha S
Vikram Sarabhai Space Centre
Thiruvananthapuram

***Abstract*— Aerospace hardware are known for their complicated geometries, high reliability and robust design. In order to meet the increasing demand for satellite launches the aerospace industry has to design, manufacture and clear the hardware for flight in a fast track manner. During this process deviations though rare are prone to occur. Such deviations need to be analyzed with extensive structural analysis. The requiredhigh-fidelity analyses are time constraining and act as bottle necks in large scale productionization. The current paper proposes a computational inexpensive replacement of the FE simulations using regression techniques. The focus of the study is on the pinhole deviation problem which is recurrent in solid motor boosters.The Finite Element model used for clearing such deviations was parameterized and used to generate 298 data points using Latin Hypercube Sampling technique. The data was then used to train various regression models such as Polynomial Regression, Artificial Neural Network, Kriging and Radial Basis Function. The 4 pinhole dimensions in the vicinity of the slit act as the input variables while the load augmentation is generated as output. The performance of the models was compared with various error metrics and it was found that Artificial Neural Network provided the best prediction accuracy with Root Mean Square Error (RMSE) of 424.7 N, R2 of 0.88 and validation Mean Absolute Percentage Error(MAPE) of 0.4%.The sensitivity of the 4parameters w.r.t the load augmentation on the pin near the slit hole was studied and it was found that the deviation in the pinhole dimension closest the pinhole under investigation has the maximum effect on load augmentation.**

Keywords*— *Aerospace Hardware, FE simulations, Surrogate modelling, Machine Learning, Artificial Neural Network

1. Introduction

Solid rocket motors are used worldwide in both upper and booster stages, since they provide high thrust at relatively low cost. Such motors are designed in segment configuration with metal end rings, which are assembled prior to casting or launch. The segmented motor case can be assembled either by bolted joint clamping two flanges or by shear pins interlocking the tongue and groove joint. Segment joint with tongue and groove configuration as shown in Fig 1 ensures load transfer as well as performance reliability in effective pressure sealing. The radial expansion enhances the sealing effect of the metal seal between the tongue and the groove and shear pins for the final assembly provide the sealing. For assembly requirement, the tongue ring is designed as discontinuous at discrete locations in the circumferential direction. For this, slit or discontinuity is introduced at a few segment pin hole locations in the tongue ring as shown in Fig 2 which takes care of the circumferential misalignment during the assembly. As a result, the pin load near the vicinity of the slit is enhanced during the motor operation. Very high load augmentation may either shear off the pins or tear off the tongue ring near to the slit location leading to a catastrophic failure of the motor. Hence, the structural assessment of the pin loads near the vicinity of the slit become more important for the adequacy of the motors.

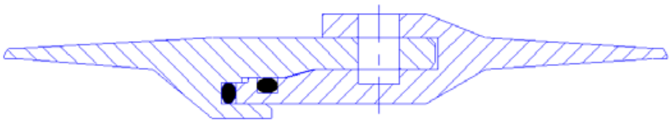

Fig. 1: Typical Tongue & Groove Segment Joint

Pin clearance beyond the specification due to oversizing of the hole during machining at the vicinity of the slit hole results in non-uniform load transfer. The load augmentation in the shearpin adjacent to the discontinuity is evaluated based on a load augmentation factor derived through Finite Element (FE) analysis. Such FE simulations are computationally expensive and become a bottle neck in productionization of aerospace hardware.

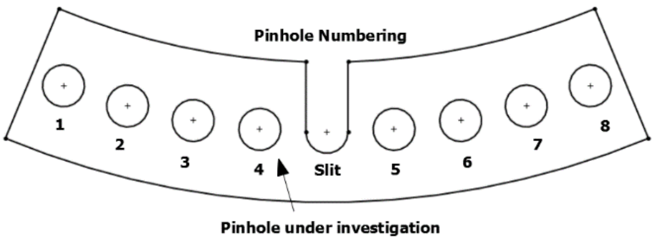

Figure 2: 9-pitch Tongue and Groove Segment Joint schematic

The literature review shows that numerous studies have attempted to resolve such bottle necks with the usage of surrogate models. Such regression-based techniques can be implemented to predict structural loads and deformations. A study by Lei Gu [1] employed finite element simulation data from vehicle crash simulations to train polynomial regression models. Zhang et.al [2] have utilized deep learning models that replace numerical simulations during 4d printing of smart composites. In some scenarios, when the Artificial Neural Network (ANN) model is trained with experimental data it's shown to outperform the FE model. As demonstrated by Tayfur et.al [3], where an ANN and FE model were trained and validated using the measured data from the piezometers used in a dam so as to predict seepage through the body of an earth fill dam. Though both models showed comparable performance, in some scenarios ANN outperformed the FE simulation.

The previous studies have all addressed varied applications of regression models but to our knowledge, no prior studies have examined manufacturing deviations in aerospace hardware like motors cases. The objective of the current study is to develop a surrogate model to predict the load augmentation on the pin which has the highest load augmentation. The hardware margin of safety (MS) is estimated against the minimum strength specification for the clearance of the hardware at the shortest possible time in this route.Thetraining data for the surrogate models is generated from new FE simulations using Design of Experiments. Since, the accuracy of the prediction is of paramount importance, given the criticality of the interface, appropriate regression model has to be selected for training. A performance comparison was carried out with various regression techniques for theprediction of load augmentation. Total of 298 supplementary design points generated by FE simulations were usedfor training the regression models. The performance of Polynomial Regression, Artificial Neural Network (ANN),Kriging and Radial Basis Function (RBF) models were compared for the same training data. The Root Mean Square Error(RMSE) and Maximum Absolute Percentage Error (MAPE) were used as the error metrics. A sensitivity analysisalso has been carried out to understand the correlation between the various parameters and their contribution to theload augmentation at the pin under investigation. Finally, the model was validated and compared with the past High-Fidelity clearance data.

The subsequent sections dwell upon the Finite Element modeling of the pinhole deviation problem and the various surrogate modeling techniques. The analysis methodology is explained in section4. Finally, section 5 and 6elaborate on the results and conclusion drawn from the study.

2. Finite Element Analysis

The geometric configuration of the pin hole deviation study for segmented motor cases along with the details of structural analysis carried out using ANSYS workbench [4] are outlined in the current section. An elaborate description of the Finite Element methodology can be found in a previous study by Vinod et.al [5].

A. Geometric configuration of segment joint with discontinuous end ring

High strength steel is considered for the design of metallic tongue and groove rings. Load transfer between the segments is ensured through steel shear pins. For the easiness in the assembly, slits are introduced at a few locations sacrificing holes in one pitch at those locations (Fig 2). Load transfer in one hole-pin location becomes ineffective and the neighbouring locations on either side of this hole get augmented. This augmentation due to the presence of slit reduced down to the nominal values within a few pitches. A photo elastic model study to investigate the combined effect of the adjacent pins not sharing the load equally with the effect of varying relative tolerance between the pin- hole combination reported similar observations [6]. The load in the pin will be further augmented due to hole and pin clearances, internal pressure and the friction between the metal end rings, out of which the pin clearances due to oversizing of the hole during machining is studied with Finite Element approach.

B. Modeling and Analysis

A FE idealization of the hardware is made considering all the minute details as present in the hardware including the geometric tolerances. A 3D 9-pitch parametric model of the Tongue and Groove Joint for analysis is shown in Fig 3. The model was parametrized such that all the holes in both end rings and pin dimensions can be individually controlled by adjusting the parameters in the model. Symmetry boundary condition on both the circumferential free edges was provided for simulating hoop continuity. Axial boundary condition and meridional stress were simulated at cylinder ends. Analysis has been carried out with internal pressure condition. Slit is simulated at the 5th hole position. All the holes and pins except the fourth were modelled with minimum material condition. The fourth hole and pin were modelled with maximum material condition so as to estimate the maximum possible load on that pin. Structural analysis is performed with a detailed solid model for the segment joint. To validate the model, loads and boundary conditions, meridional & hoop stress and radial dilation noted in cylindrical shell region were compared with the corresponding theoretically expected value [7]

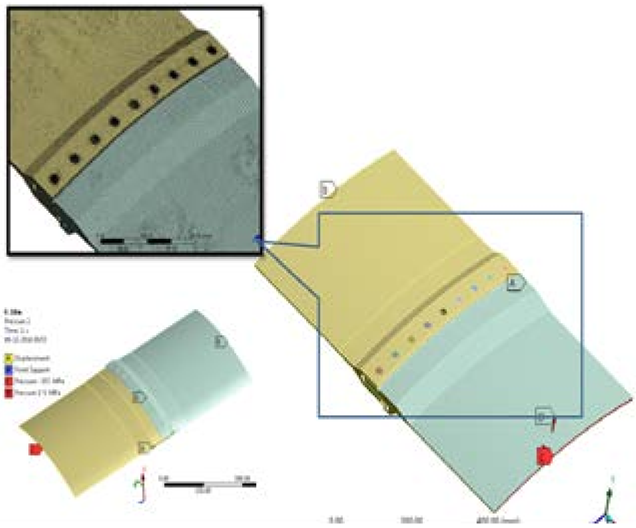

Figure 3: FE idealization Tongue & Groove Joint

A generic non-slit model has been made parallel to the above said model with slit and the average reaction loads arrived at all the nine pin locations. Augmentation Factor (λ) on reaction loads on the pins defined to normalize the results is as follows,

$$\boldsymbol{\lambda} = \frac{\mathbf{PinLoadfromSlitModel}}{\boldsymbol{Avg.PinLoadfromGenericModel}}$$

Load augmentation factor (λ) in the fourth shear pin with maximum material condition (ref Fig 2.) adjacent to the slit hole is the output of the FE analysis which is contributed by the presence of the slit and the relative clearance between the holes and the shear pins.

Hardware margin of safety (MS) based on the highest load augmentation is estimated against the minimum strength specification. Since, each FE simulation corresponding to the deviation from generic tolerance level is time consuming, computationally inexpensive surrogate modeling techniques are attempted for hardware clearance at the shortest possible time.

3. Surrogate Modeling

High Fidelity analyses like Computational Fluid Dynamics and Finite Element can become computationally cumbersome with increasing complexity. Repetitive executions of such simulations tools for optimization, sensitivity analysis or routine work can become a bottleneck in many design cycles. One of the ways to overcome this issue is by using surrogate modeling techniques. The idea is to develop a mapping function($\hat{\boldsymbol{y}}(\boldsymbol{X})$) with the help of the response values($\boldsymbol{y}$)for the corresponding design variables ($\boldsymbol{X}$). This mapped function is an approximation of the original function. In the current study, the design variables or attributes are the dimensions of the pins ($\boldsymbol{d_{pin}}$) while the response value or label is Load augmentation ($\boldsymbol{L}$).

$$\boldsymbol{y}(\boldsymbol{X}) = \hat{\boldsymbol{y}}(\boldsymbol{X}) + \boldsymbol{\epsilon}$$

Where, $\boldsymbol{\epsilon}$ represents the errors in the approximated function. The approximate function can be generated using various techniques such as Polynomial Regression, Artificial Neural Network, Kriging or Radial Basis Functions. While selecting the surrogate modeling technique some factors need to be considered, so as to reduce the error term and to reduce the cost of surrogate building. The model needs to be able to handle large number of design variables without a drastic increase in the design points. It should be able to capture non-linear variations. It's highly likely that the simulation data being used for constructing the surrogate is noisy. The method should be robust enough to handle such noisy behaviour.

The accuracy of the surrogate model is evaluated using various metrics like - Root Mean Square Error (RMSE), correlationcoefficient R2 or Mean Absolute Percentage Error (MAPE) [8]. These error metrics utilize the difference (Δ) between the actual and predicted response value ($\mathbf{y_{actual}}$ - $\mathbf{y_{predicted}}$) for all the test points.

$$\boldsymbol{RMSE} = \sqrt{\frac{\sum_{i=1}^{n}(\Delta)^2}{n}},$$

$$\overline{\boldsymbol{y}}_{\boldsymbol{actual}} = \frac{\sum_{i=1}^{n} \boldsymbol{y}_{\boldsymbol{actual}_i}}{\boldsymbol{n}}, \boldsymbol{SS}_{\boldsymbol{tot}} = \sum_{i=1}^{n}(\boldsymbol{y}_{\boldsymbol{actual}_i} - \overline{\boldsymbol{y}}_{\boldsymbol{actual}})^2$$

$$\boldsymbol{SS}_{\boldsymbol{res}} = \sum_{i=1}^{n}(\boldsymbol{y}_{\boldsymbol{actual}_i} - \boldsymbol{y}_{\boldsymbol{predicted}})^2, \quad \boldsymbol{R}^2 = \mathbf{1} - \frac{\boldsymbol{SS}_{\boldsymbol{res}}}{\boldsymbol{SS}_{\boldsymbol{tot}}}$$

$$\boldsymbol{MAPE} = \frac{\mathbf{1}}{\boldsymbol{n}}\sum_{i=1}^{n}\left|\frac{\boldsymbol{\Delta}_i}{\boldsymbol{y}_{\boldsymbol{actual}_i}}\right| * \mathbf{100\%}$$

A. Polynomial Regression

Polynomial Regression models are one of the basic and popular metamodeling techniques since it provides an explicit function representation. Thelower order polynomial models can be generated easily since they involve fewercoefficients which can be evaluated easily. A first order and second order Polynomial Regression can be written as follows

$$\hat{y} = \beta_0 + \sum_{i=1}^{k} \beta_i \, x_i$$

$$\hat{y} = \beta_0 + \sum_{i=1}^{k} \beta_i \, x_i + \sum_{i=1}^{k} \beta_{ii} \, {x_i}^2 + \sum_{i}\sum_{j<i} \beta_{ij} \, x_i x_j$$

The parameters of the polynomial β_i are evaluated using least square regressionfit of the design data. Using appropriate order of polynomial model ensures thatvarious regions are captured. Polynomial regression has the capability to smoothout the noisy values. Thus, optimization process over such models provides fasterconvergence.One more drawback of the polynomial regressiontechnique is that it fails to capture non-linear behaviours which is a predominant behaviour observed in aerodynamic and structural response quantities. Toaddress this problem higher degree polynomials can be employed but this leads to instability issues. A large number of design points are required to estimateall the coefficients for a high dimensional problem, in such cases ANN, RBF or kriging method is more advantageous.

B. Artificial Neural Network

Artificial Neural Network (ANN) is a machine learning algorithm which aides in building anefficient predictive model by mimicking the human biology. It is comprised of neurons, each of which can makesimple mathematical decisions. Together, the neurons can analyze complexproblems, emulate almost any function including very complex ones, and provideaccurate answers. A shallow neural network has three layers of neurons: aninput layer, a hidden layer, and an output layer. A Deep Neural Network(DNN) has multiple hidden layers, which increases the complexity of themodel thus significantly improving the prediction power [9]. A single node in the neural network is shown in Fig 4

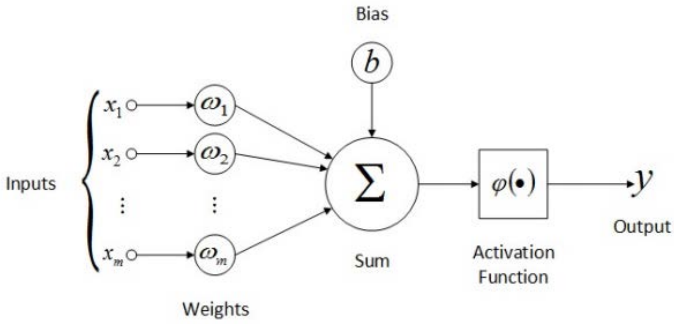

Figure 4: A single node in the neural network [10]

The figure can be represented in an equation form as follows,

$$y(x) = \alpha(b + \omega_1 x_1 + \omega_2 x_2 \dots \omega_m x_m)$$

Where, $x_1, x_1, \ldots x_m$ are the design variables $\omega_1, \omega_2 \dots \omega_m$ are the weights, b is the bias and α is the activation function. During training, a set of input parameters and the corresponding output parameters are provided to the Network. The weights are initialized randomlyfor each node. A feed forward analysis is carried out with the training data toget the predicted value. The error (E) between the predicted output parameter andthe actual parameter value is back propagated. This back propagation allowsthe update of individual weights of each neuron as follows

$$\omega_{m+1} = \omega_m - \eta \frac{\delta E}{\delta \omega_m}$$

Where, η is the learning rate. This process continues till apre-determined number of epochs. At the end of the process we have a convergedset of weights which can then be used for predicting the output parameters. Theaccuracy of prediction depends on numerous factors like - quality of the trainingdata, No. of nodes, No. of hidden layers and No. of epochs for training.

Errormetrics like RMSE and MAPE can be used to evaluate the performance of theANN model. Multiple options for activation functions are available, like sigmoid, tan hyperbolic, RELU or Leaky RELU. They serve the purpose of capturing the nonlinearity in the design space. ANN has demonstrated numerous applications in a variety of domains. A study by Yilmaz and Kaynar [11]utilize RBF and Multi Layered Perceptron (MLP) based ANN in order to predict the swell potential of clayey soils. Their study demonstrated better performance of ANN compared to traditional statistical models.

C. Kriging

Kriging is a method of statistical interpolation of random spatial processes developed for geostatistical applications [12]. The idea of Kriging is to predict the value at a given point by computing the weighted average of the function values at the neighbouring points. The weights are chosen such that the error associated with the predictor is lesser than anyother linear sum. The weights also depend on the location of the sampled point sand upon their covariation.

To construct the model, kriging utilizes basis or correlation functions, the Gaussian function which is one of the popular basis is as follows,

$$cor[y(x^i), y(x^j)] = \psi^i = \exp(-\sum_{j=1}^{k} \theta_j |x_j^i - x_j|^{p_j})$$

Where, $X = [x^1, x^2, \ldots, x^n]^T$ is a set of sample design data along with their observed response values $Y = [y^1, y^2, \ldots, y^n]^T$, θ_j and p_j are the hyper-parameters having dimension equal to that ofthe design variables. The hyper-parameters need to be fine-tuned to acquire accurate predictions. The response values for the design data are correlated using the basis function. Thus, we have a n x $n$correlation matrix for the observed data. The response value is predicted using the kriging model atx^{n+1}, which maximizes the likelihood given the observed data and Maximum Likelihood Estimate (MLE) of the hyper-parameters.

$$\hat{y}(x^{n+1}) = \hat{\mu} + \sum_{i=1}^{n} b^i \psi^i (x^{n+1}, x^i)$$

Where, ψ^i is the correlation matrix and the constants b are given byb = $\psi^{-1}(y - \hat{\mu})$. The value of$\hat{\mu}$ is acquired from the optimization of the likelihoodfunction.

D. Radial Basis Functions

Radial basis functions (RBF) are designed for scattered multivariate data interpolation. RBF surrogates are generated using linear combinations of radially symmetric function. These functions employ distance metrics between the design points, such as Euclidean distance to approximate the response functions. A radial basis function surrogate model canbe expressed as

$$\hat{y} = \sum_{i=1}^{n} a_i || x - x_i ||$$

Where, $a_i$are the coefficients of RBF while $x_i$is a design point and ||.|| represents the Euclidean norm. It is seen in literature that the radial basis functionmetamodels outperform the Polynomial regression models in all the test cases.

In the ANN section, multiple layers were used with different activationfunction, but in the case of Radial Basis Function Networks, a single layerwith gaussian RBF as the activation function. The network uses a linear combination ofGaussians to approximate any function. The training of the network is similarto a conventional Neural Network.

4. Methodology

The current section deals with the methodology followed to train the regression models in order to predict the load augmentation with the pinhole dimension acting as the inputs.

Firstly, Design of Experiment (DOE) was carried out using Latin Hypercube sampling (LHS). A total of298 samples were generated for 4 design variables (Dimensions of the 4 pinholes in the vicinity of pinunder investigation) within bounds based on maximum and minimum historical deviation data. 238design points were used for training while the rest the rest 60 were used to evaluate the accuracy of the prediction. The statistical details of the training data in the form of mean, standard deviation, minimum and maximum values is provided in the Table 1.

Table 1: Statistical details of the training data

	Pin 1	Pin 2	Pin 3	Pin 4	Load
Mean	14.07	14.068	14.069	14.069	80601
SD	0.035	0.035	0.0355	0.0355	3159
Min	14	14	14	14	7326
Max	14.138	14.137	14.138	14.138	91908

The Finite Element analysis as described in section 2 was carried out for all the 298 design points, with the corresponding load on the pin under investigation as the output. The analysis for all the design point was executed using the batch mode in ANSYS workbench. The data set was normalized using a Min-Max scaler.

Subsequently, the data set was used to train the 4 regression models detailed in section 3. The polynomial regression model was trained for various orders using the sk learn library in python [13]. The ANN model was trained using the TensorFlow library in python [14]. Three fully connected layers were used in the ANN model. The tanh activation functionwas used for all the layers. The 16-8-4 combination of neurons were used inthe ANN layers. The training was carried out for 100000 epochs with the Adam optimizer and Mean Absolute Error (MAE) as the error metric.

The DACE toolbox in MATLAB [15] was used to train the kriging model.The toolbox provides regression models with polynomials of orders 0, 1 and 2. Italso contains 7 correlation functions viz. Gaussian, Exponential, Linear, Cubic,Spherical, EXPG and Spline. A comparative study was carried out with the various correlation function.

Finally, the RBF function in MATLAB[16]was used for the RBFmodel. The performance of all regression models was assessed with the error metrics outlined in the previous section.The comparison and discussion of the results from the various models is described in the upcoming section

5. Results and Discussion

The test data generated from the FE simulation of the pin-hole deviation model was used to generate 4 different surrogate models - Polynomial Regression, Artificial Neural Network, Kriging and Radial Basis functions.

The polynomial regression model was trained with varying orders from 1 to 10. The variation of the RMSE, R2 and MAPE coefficient with varying polynomial order is shown in Fig 5.

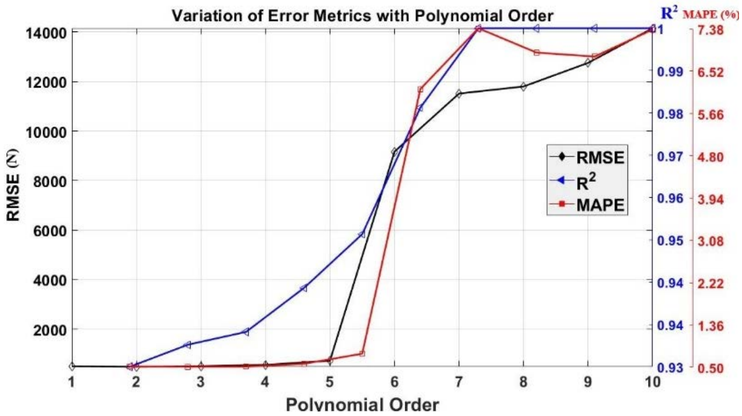

Figure 5: Variation of RMSE, R2 and MAPE withpolynomial order of the regression model

It can be observed that the for the lower order polynomial fit up to 5th order the error values are lower compared to the higher orders. It can be seen that for the higher orders the R^2value is nearly 1, which means that the model has over fitted on the training data. The RMSE and MAPE values for the corresponding order are also very high. The compilation of the error metrics only upto 4th order polynomial regression has been provided in Table 2

Table 2: Compilation of Error metrics for Polynomial

Order	RMSE (N)	R^2	MAPE(%)
1	498.89	0.93	0.51
2	480.32	0.94	0.51
3	501.33	0.94	0.51
4	555.43	0.95	0.57

It was found that the second order polynomial regression provides the best prediction results with the minimum Root Mean Square Error (RMSE) of 447.2N, R2 of 0.94 and validation Mean Absolute Percentage Error (MAPE) of 0.41%.

The training was carried out for 100000 epochs with the Adam optimizer and MAE as the error metric. The variation of MAE with training epochs can be seen in the Fig 6. It can be noted that as the number of training epochs exceed, the model starts to overfit, causing the training and testing losses to diverge. Thus, the training was terminated after 10000 epochs. The actual load augmentation value and the ANN predicted values are compared in Fig 7. It can be noted that the ANN model was able to predict the augmentation with considerable accuracy since the scattered points lie in the close vicinity of the ideal line.

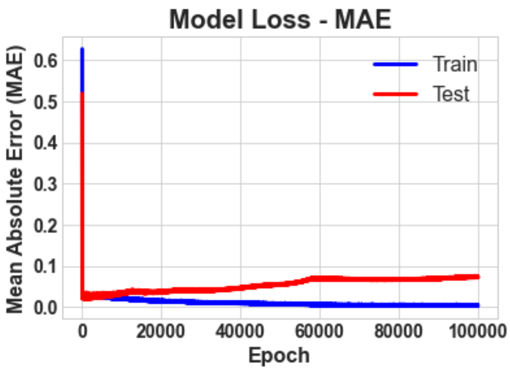

Figure 6: Variation of MAE with epochs for ANN

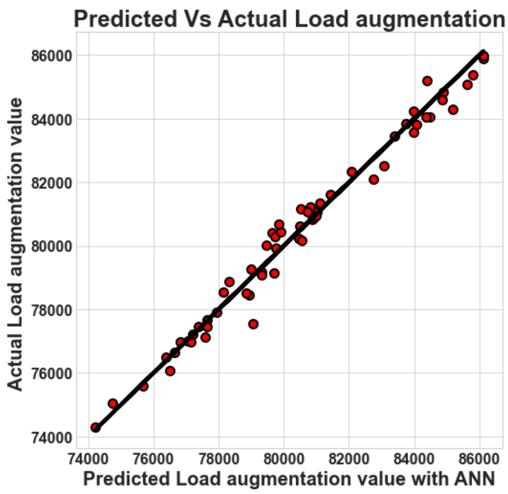

Figure 7: Comparison of the prediction of load augmentation and the actual value for ANN

The ANN model had a RMSE of 424.7 N, R2 of 0.88 and validation Mean Absolute Percentage Error (MAPE) of 0.4%.

The Kriging model was trained with 7 correlation functions and the errors metrics are compared in Table 3. As it can be observed that the results are identical with all the correlation functions, but the best results are provided by the Gaussian function.

Table 3: Compilation of Error metrics for various Kriging Correlation functions

Correlation function	**RMSE (N)**	**MAPE (%)**
Gaussian	479.71	0.49
Exponential	481.13	0.49
Cubic	480.62	0.49
Linear	481.92	0.49
Spherical	480.55	0.49
Spline	479.3	0.49

Spherical	480.55	0.49
Spline	479.3	0.49

Finally, in the case of Radial Basis Functions the RMSE evaluated was 442 N, R2 of 0.937 and validation Mean Absolute Percentage Error (MAPE) of 0.447%.

In order to study the correlation between the various parameters of the regression models a sensitivity study was carried out with the ANN model as the reference. The compilation of the contour plots is shown in Fig 8. It shows the sensitivity plot for the various design variables w.r.tthe load augmentation computed from the ANN model. It can be noted thatthe relation between the output and input variables is nearly non-linear. As thedeviation in pin dimension increases, so does the load augmentation on the pin under investigation.

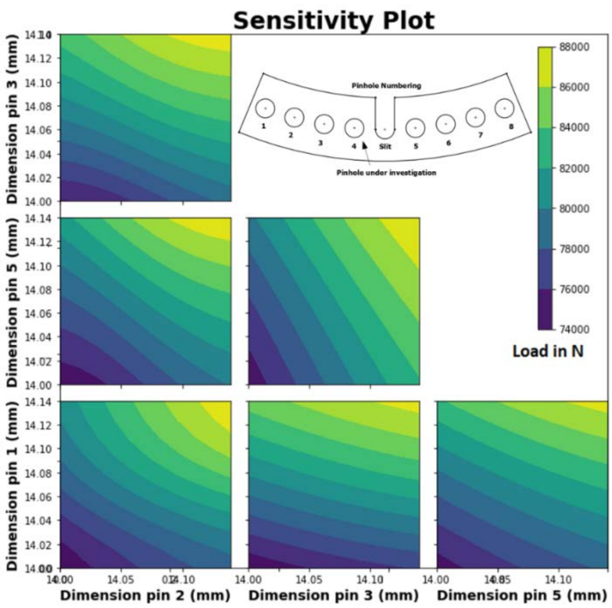

Figure 8: Sensitivity of the dimension of the pinholesw.r.t the load augmentation

6. Conclusions

Segment pinhole deviation is a recurring deviation in segmented motor cases with slits in the tongue rings. Load augmentation on pins is observed due to deviation in the pinhole dimensions adjacent to the slit. In the existingmethodology Finite Element simulations have to be carried out for clearing thehardware for flight. In the current study, an attempt has been made to developa model that can predict the load augmentation with very low computationalcost and incorporating past deviation data. Different regression techniques wereassessed to select the model which can aid in completing the activities in a fasttrack manner, allowing the streamlining of the launch vehicle activities.

The compilation of the best error metrics is provided in Table4. Out of the four models explored in the study, the best prediction accuracy was provided by ANN with a Square Error (RMSE) reported was 424.7 N, R^2 of 0.88 and validation Mean Absolute Percentage Error (MAPE) of 0.4%.

Table 4: Compilation of Error metrics

Model	RMSE (N)	R^2	MAPE (%)
2nd order Polynomial Regression	480.3	0.94	0.51
ANN	424.7	0.88	0.4
Kriging	479.7	1	0.49
RBF	442	0.94	0.45

The findings in the current study demonstrate the accurate predictability of Artificial Neural Networks compared to the classical regression techniques. A sensitivity study was also performed in order to understand the correlation between the various parameters. It was found that the dimension of the pinhole adjacent to the pin under investigation has the most significant effect on the load augmentation. The ANN model can also be trained for other Aerospace hardware, thus aiding in streamlining of the manufacturing processes of a launch vehicle

7. Reference

[1] Gu, L. "A Comparison of Polynomial Based Regression Models in Vehicle Safety Analysis." Proceedings of the ASME 2001 International Design Engineering Technical Conferences and Computers and Information in Engineering Conference. Volume 2A: 27th Design Automation Conference. Pittsburgh, Pennsylvania, USA. September 9–12, 2001

[2] Zhang, Zhizhou, and Grace X. Gu. "Finite-Element-Based Deep-Learning Model for Deformation Behavior of Digital Materials." Advanced Theory and Simulations 3, no. 7 (2020): 2000031.

[3] Tayfur, Gokmen, Dorota Swiatek, Andrew Wita, and Vijay P. Singh. "Case study: Finite element method and artificial neural network models for flow through Jeziorskoearth fill dam in Poland." Journal of Hydraulic Engineering 131, no. 6 (2005): 431-440.

[4] ANSYS User Manual

[5] Vinod, G., ManashKumar Bhadra, K. S. Narayanan, and V. Thaddeus Basker. "Margin of Safety Estimation of Tongue and Groove Joint of Rocket Motors with Discontinuous End Ring." In Applied Mechanics and Materials, vol. 877, pp. 354-359. Trans Tech Publications Ltd, 2018.

[6] Jeby Philip, S A Pillai et al., “Photo elastic studies on the effect of varying relative hole-pin tolerance in a rocket motor tongue and groove joint”.

[7] Shigley’s Mechanical Engg. Design, McGraw−Hill Primis

[8] Alexander I. J. Forrester, András Sóbester, Andy J. Keane, "Engineering Design Via Surrogate Modelling: A Practical Guide”, 2008.

[9] Subana Shanmuganathan, Sandhya Samarasinghe (2016) Artificial Neural Network Modelling. DOI: 10.1007/978-3-319-28495-8

[10] Jadidi, Aydin; Menezes, Raimundo; De Souza, Nilmar; De Castro Lima, Antonio C. 2018. "A Hybrid GA–MLPNN Model for One-Hour-Ahead Forecasting of the Global Horizontal Irradiance in Elizabeth City, North Carolina" Energies11, no. 10: 2641.

[11] Işık Yilmaz, Oguz Kaynar, "Multiple regression, ANN (RBF, MLP) and ANFIS models for prediction of swell potential of clayey soils", Expert Systems with Applications, Volume 38, Issue 5,2011.

[12] Krige, D. G., 1951, "A Statistical Approach to Some Basic Mine Valuation Problems on the Witwatersrand," Journal of the Chemical, Metallurgical and Mining Society of South Africa, Vol. 52, pp. 119-139.

[13] Scikit-learn: Machine Learning in Python, Pedregosa et al., JMLR 12, pp. 2825-2830, 2011.

[14] Abadi et.al., "TensorFlow: Large-scale machine learning on heterogeneous systems", tensorflow.org.

[15] Nielsen HB, Lophaven SN, Søndergaard J. DACE - A MATLAB Kriging Toolbox Informatics and Mathematical Modelling, Technical University of Denmark, DTU. 2002. MATLAB. (2010). version 7.11 (R2010b). Natick, Massachusetts: The Math Works Inc

Novel Transfer Alignment Technique for Autonomous Space Vehicles for Moving Platforms

N Sivasubramaniam
RCI
DRDO
Hyderabad
pgtsivan@gmail.com

Dr. Ramesh Kumar
Guru Kashi University
Bathinda
rkgupta1701@gmail.com

Abstract - **The weapons are launched from either fixed (land) or a moving platform (sea/air) and the inertial measurement unit is aligned through gyro-compassing using the stored data for heading or with master unit (in the moving platform) & slave unit (in the vehicle). The master inertial navigation system (INS) is highly accurate and calibrated with respect to the slave unit. The difference in alignment between the master and the slave has been formulated with the three misalignment angles, three velocity errors, and three positional errors. For fixed platform, the alignment is straight forward and for moving the manoeuvre of the moving base excites the sensors of both the master and the slave INS and the data will be used in aligning the slave IMU of the INS. There are many methods available for this alignment problem and the rate matching technique is mainly focussed here in order to achieve the best result in minimum time & manoeuvre efforts.**

Keywords - inertial navigation system, strapped-down navigation algorithm, launch platforms, misalignment, body rates, transfer alignment scheme, rate matching technique.

1 Introduction

The inertial navigation is a self-contained navigation technique where the measurements provided by gyroscopes and accelerometers were used to track the position and orientation of an object relative to a known starting point, orientation and velocity. Inertial measurement units (IMUs) contain three orthogonal accelerometers, measuring angular velocity, three orthogonal rate-gyroscopes and linear acceleration respectively [4,5]. It is possible to track the orientation and position of a device by processing signals from these devices.

The frame of reference in which the rate-gyroscopes and accelerometers operate is the difference between the Global frame (frame of reference in which we are navigating) and Body frame (navigation system's frame of reference). In stable platform systems, the global frame is held in alignment with the platform by mounting with frames (gimbals) which allows platform rotation in all three axes. In other words, the platform i.e., isolated from any external rotational motion is mounted by the inertial sensors in these types of systems.

The platform rotations can be detected by the mounted gyroscopes. To cancel out such rotations, this signal passes to torque motors where the gimbals rotate in order.

By using angle pick-offs, device orientation can be tracked by measuring the angles between adjacent gimbals. The signals produced by the platform mounted accelerometers were double integrated to calculate the device position. Before performing the integration, it is mandatory to subtract acceleration due to gravity from the vertical channel. The stable platform inertial navigation algorithm is shown in the following figure 1.

In SDINS, the inertial sensors are mounted rigidly onto the device, and therefore instead of global frame, output quantities were measured in the body frame in these systems. The signals from the rate gyroscopes were integrated to keep the track of orientation. Using the known orientation i.e., determined by the integration of the gyro signals to track the position; the global coordinates were resolved from the three accelerometer signals [14,15]. As per the stable platform algorithm, the global acceleration signals are then integrated as shown in Figure 2.

Even though both stable platform and strap down both stable platform and Strapdown inertial navigation systems [SDINS] are based on the same underlying principles, SDINS are tend to be physically smaller than stable platform systems and have reduced mechanical complexity [2]. So, SDINS became the dominant type of INS due to the reduction in cost of computation.

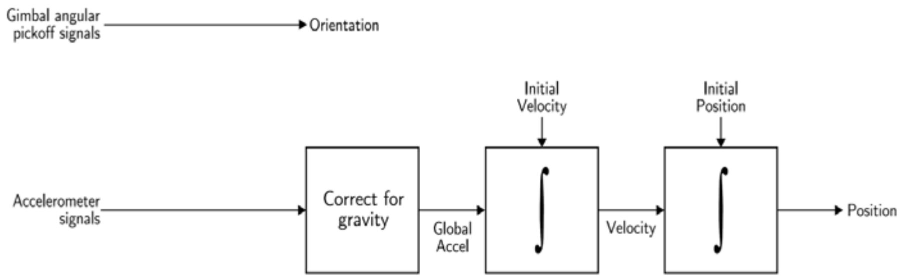

Figure 1: Stable platform inertial navigation algorithm

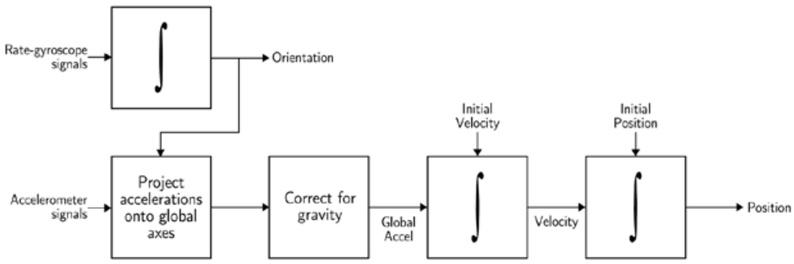

Figure 2: Strap down inertial navigation algorithm

2 Literature Survey

In his monumental paper, Prof. Bar Itzhack elucidated the fundamental estimatability of SDINS by giving the error perturbation model with small angle dynamics [3]. This paper remains the corner stone for all research on attitude estimatability of SDINS. Bar-Itzhack & Porat [1, 21] discussed the enhancement of azimuth Observability in their paper. Azimuth was shown to be weakest observable channel by Prof. Bar Itzhack in this first paper. This fact of least Observability in the Azimuth channel is also described by author in [3]. The improvement of piecewise Observability of azimuth channel is discussed by Prof. Bar Itzhack in [9].

Thus, it is amply clear from foregone studies that the estimatability of attitude is the most involving in the initialization of SDINS and hence this paper is a result to improve upon the aforementioned results by considering angular velocities as observation vector in the Kalman filter formulations [7,8].

Thus, excitation of the platform in the form of some deliberate manoeuvre is important in order to discriminate the signal from noise in the available measurement so that the misalignment can be effectively estimated. With advancement of technology, the prerequisites of accurate alignment have changed and with it the algorithms have also undergone continuous transformations. Extensive work has been done on this topic over the years.

Paper [26] describes the basic principles of navigation. Emphasis is exposed as to why attitude information is critical to start of inertial navigation. Paper [27] explores robust strategies for in-motion inertial navigation explaining various statistically robust methods. The directorate of navigation is also experimenting hemispherical resonating gyro for long range space navigation. A suitable star sensor is also being developed at RCI to aid HrG based navigation for interplanetary sojourns [28]. DARPA, US is relying on MEMS technology for positing of small vehicles, for which attitude information shall become necessary [29]. The need for ubiquitous inertial navigation is given in stovall [30].[26] describes the basic principles of navigation. Emphasis is exposed as to why attitude information is critical to start of inertial navigation.

3 Transfer Alignment Scheme

The Transfer alignment is the process of initializing and calibrating a weapon inertial navigation system using data from the host carrier's navigation master system [3,6]. The inertial navigation systems on weapons are restricted by volume, weight and cost. [12,18,22] Initialization of these systems must be speedy and precise.

Velocity and position matching methods are intended to improve the speed and accuracy of the alignment [19]. Factors like information delay, mounting error, sensor measurement error, lever-arm effect and flexure of the carrier body will affect the accuracy of the transfer alignment.

Acceleration / Rotation Rate Matching Method, Master and slave systems IMU outputs are compared to form an observation [9,10]. In a Kalman filter structure, the evaluation results were used as measurement to discover misalignment between the two systems [13].

The misalignment angles between two systems will change dynamically due to the random vibration and flexure. Hence, it is essential to originate differential equation that governs the transformation in the misalignment angle [23, 24, 25].

4 Rotation Matching Technique

Consider the master to slave transformation will be represented by the following Euler angles that is defined in slave body frame of reference with the rotation order of z, y, x:

$$E = \begin{vmatrix} \alpha \\ \beta \\ \gamma \end{vmatrix} \tag{I}$$

The relation between the derivative of these Euler angles and rotation rate of master with respect to slave can be found as follows (Titterton, (1997)) [16]:

$$\begin{aligned} \dot{\boldsymbol{\alpha}} &= (\cos\alpha\omega x + \sin\gamma\omega y)\sec\beta \\ \dot{\boldsymbol{\beta}} &= \omega y cos\alpha - sin\gamma\omega x \\ \dot{\boldsymbol{\gamma}} &= \omega z + \tan\beta(\cos\gamma\omega x + \sin\gamma\omega y) \end{aligned} \tag{II}$$

where

$$\boldsymbol{\omega}_{\mathbf{SM}}^{\mathbf{S}} = \mathbf{C}_{\mathbf{M}}^{\mathbf{S}}(\mathrm{E})\boldsymbol{\omega}_{\mathbf{IM}}^{\mathbf{S}} - \boldsymbol{\omega}_{\mathbf{IS}}^{\mathbf{S}} = [\omega x \omega y \omega z]\mathrm{T} \tag{III}$$

If it is assumed that Euler angles are small such that "sin E ≈ E" and "cosE ≈ 1", then by neglecting higher order terms, Equation (II) can be written as:

$$\begin{aligned}\dot{\boldsymbol{\alpha}} &= \omega x - \gamma\omega y \\ \dot{\boldsymbol{\beta}} &= \omega y - \gamma\omega x \\ \dot{\boldsymbol{\gamma}} &= \omega z - \beta\omega x\end{aligned} \tag{IV}$$

Using small angle assumption, master to slave transformation matrix can be written as follows:

$$C_M^S(E) = I + S(E) = I + \begin{vmatrix} 0 & -\gamma & \beta \\ \gamma & 0 & -\alpha \\ -\beta & \alpha & 0 \end{vmatrix} \tag{V}$$

Insert Equation (V) into (III) and combine (III) with (IV) then after rearranging the terms following equation can be obtained:

$$\dot{E} = \begin{vmatrix} 0 & \omega_{iM}^M(z) & -\omega_{iS}^S(y) \\ \omega_{iM}^M(z) & 0 & \omega_{iS}^S(x) \\ \omega_{iS}^S(y) & -\omega_{iS}^S(x) & 0 \end{vmatrix} E + (\omega_{iM}^M - \omega_{iS}^S) \tag{VI}$$

where ω(•) represents the corresponding vector element.

The differential equation that governs change in the Euler angles between master and slave systems is defined in Equation (VI). The last phrase in the right hand side of equation represents the deterministic input function. The above equation can also be used by first transferring master rotation rate to a nominal frame of reference, when the Euler angles between two systems are not small.

Equation (VI) should be continuously solved by using the observed master and slave rotation rate in a Kalman filter structure. Therefore, Equation (VI) has to be written as:

$$\dot{E} = M\left(\omega_{iM}^M, \tilde{\omega}_{iS}^S\right)E + \left(\omega_{iM}^M - \tilde{\omega}_{iS}^S\right) + \delta\omega_{iS}^S \tag{VII}$$

Where "$\tilde{\omega}_{iS}^S = \omega_{iS}^S + \delta\omega_{iS}^S$" represents evaluated slave rotation rate, "$\delta\omega_{iS}^S$" represents errors of slave gyroscope whereas it is assumed that master IMU is errorless and an operator which converts its arguments to the matrix is represented by M as shown in Equation (VI).

The propagation model for the misalignment angle "E" is defined in Equation (VII). The aim is to execute a Kalman filter to estimate "E". By using acceleration and/or rotation rate outputs of master and slave IMUs, the measurement for that type of filter can be premeditated. The difference between master and slave systems can be represented by employing small angle assumption, as follows:

$$\tilde{a}_S^S - a_{M_{Comp}}^M = -S\left(a_{M_{Comp}}^M\right)E + \delta a_s + \delta a_{Comp} \tag{VIII}$$

Where "δa_s" denotes slave accelerometer error and "$\tilde{a}_S^S = a_S^S + \delta a_S^S$" denotes observed slave acceleration. "$a_{M_{Comp}}^M$" Corresponds to lever arm compensated master acceleration output that is equal to:

$$a_{M_{Comp}}^M = a_M^M + \omega_{iM}^M \times \omega_{iM}^M \times r^M + \dot{\omega}_{iM}^M \times r^M \tag{IX}$$

"δa_{Comp}" represents lever arm compensation error i.e.,

$$\delta a_{Comp} = C_M^S\,[\ddot{r} + 2(\omega_{iM}^M \times \dot{r}^M)] \tag{X}$$

Equation (VIII) represents the relationship between E and acceleration differences between master and slave systems. On the other hand, measurement for Kalman filter based on rotation rate differences can be formed as follows:

$$\omega_{iS}^S - \omega_{iM}^M = -S(\omega_{iM}^M)E + C_M^S\,\omega_{MS}^M \tag{XI}$$

Using the observed variables, the above equation can be written as:

$$\widetilde{\omega}_{iS}^S - \omega_{iM}^M = -S(\omega_{iM}^M)E + \delta\omega_{iS}^S + \omega_{MS}^S \tag{XII}$$

Where "$\widetilde{\omega}_{iS}^S$" represents observed slave rotation rate and " $\delta\omega_{iS}^S$ " represents corresponding gyroscope error, and "ω_{MS}^S" represents rotation rate of slave with respect to master. The relationship between master and slave rotation rate difference and misalignment angle is defined in Equation (XII).

A Kalman filter with the system equation given in Equation (VII) and measurement equations shown in (VIII) and (XII) is formed to evaluate performance of acceleration/rotation rate matching method. Although the vibration related terms "ω_{MS}^S " and" $a_{M_{Comp}}^M$ " in Equations (VIII) and (XII) represents correlated noises, they are not amplified to the Kalman filter system model and considered as a part of measurement noise.

Moreover, other than random walk none of the gyroscope and accelerometer errors is excited in simulation environment. Therefore, δa_s and $\delta\omega_{iS}^S$ contains only white noises and considered as a part of measurement noise.

At last, it is assumed that known lever arm vector "r" is approximately errorless. Both update and broadcast routines of the Kalman filter will run at 100Hz.

5 Kalman Filter Mechanization

Three different measurement structures are assessed with the intended Kalman filter. In the first structure, only accelerometer outputs are used as measurement (Equation (VIII)), whereas in the second case, only rotation rates are used (Equation (XII)) and in the third case, both accelerations and rotation rates are used at the same time [29].

Figure 3, Figure 4 and Figure 5 represents the covariance estimates of the Kalman filter for each case. The average of standard deviations obtained in the last 10 seconds of each structure is summarized in Table 1.

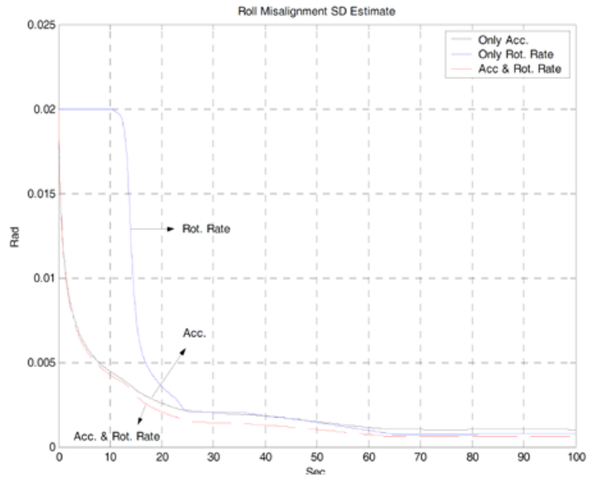

Figure 3: Roll misalignment angle standard deviation estimate

Table1: Misalignment error standard deviation estimate comparison for accelerometer / rotation rate matching method

	Roll Error SD (mrad)	Pitch Error SD (mrad)	Yaw Error SD (mrad)
Acceleration	10	0.9	0.784
Rotation Rate	0.774	0.481	0.484
Acc. & Rot. Rate	0.62604	0.42644	0.42110

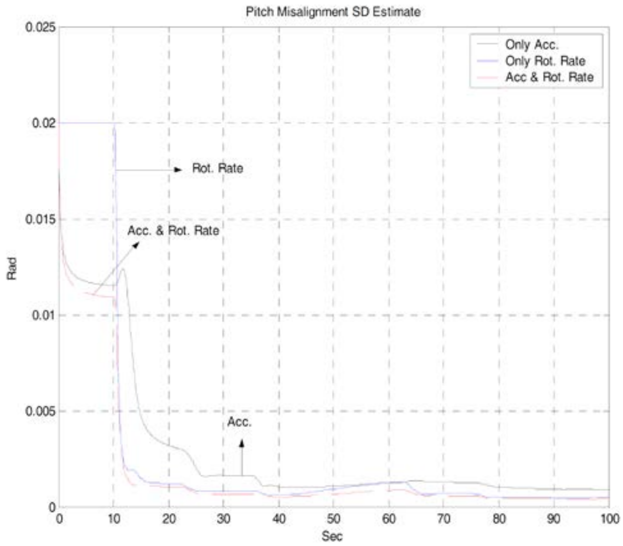

Figure 4: Pitch misalignment angle standard deviation Estimate

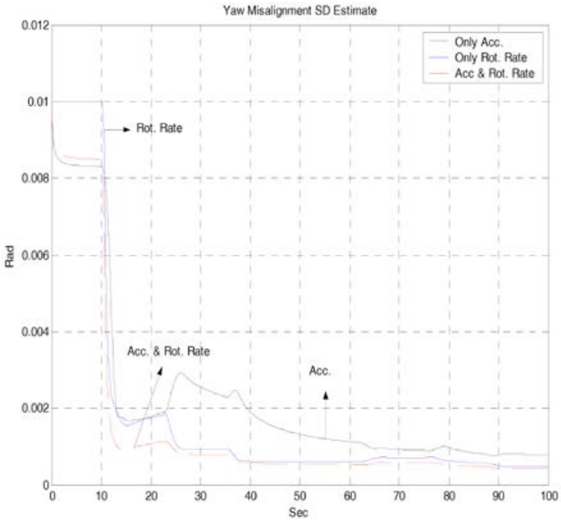

Figure 5: Yaw misalignment angle standard deviation estimate

6 Results

As seen from above figures, the accelerometer/rotation rate matching technique is not adequate to estimate misalignment angles with a preferred precision even in the optimal situation. Best results can be obtained with the utilization of acceleration and rotation rates at the same time; on the other hand, its roll error estimation performance also falls behind requirements which is estimated to be less than 0.4 mrad.

The most important drawback of this technique is the requirement for very high speed propagation of state equations, in addition to the deficient estimation performance. Equation (VII) has to be solved accurately in discrete time to work Kalman filter properly. Master rotation rate must be obtained at least 100Hz to discrete Equation (VII) with sufficient accuracy.

However, it is not possible to acquire data from aircraft avionics at that frequency for a standard mux-bus structure of most aircraft. Hence, the applicability of this method is restricted to few special data bus setups.

On the other hand, the essentiality to solve Equation (VII) comes from the necessity of estimating dynamical change in misalignment angle. The estimation problem can be reduced to estimate a constant parameter when it is assumed that the amount of dynamical change can be neglected. In this case, the problem can be handled by solving the measurement equations given in Equation (VIII) and (XII) in a least square sense to acquire constant misalignment angle “E”.

By using deterministic least square algorithms (Boch (1989), Setterlend (1972)), many studies were conducted previously to solve Equation (VIII) and (XII). But, the problem in this approach is that, until the first contrive of the aircraft, observation equations comprise an underdetermined system which increases the complexity of recursive least square algorithms.

In addition, if only acceleration measurements are used, despite of whether aircraft performs a coordinated turn or not, observation equation for acceleration measurement stays constantly underdetermined that prevents the estimation of azimuth misalignment error which shown as below:

Assume that a misalignment estimate is twisted by using an observation i.e., obtained at initial time (t0), and the other estimate is obtained later. A simple estimation can be formed by using pseudo inverse during this case as follows:

$$\mathrm{E} = (\mathrm{YTY}) - 1\mathrm{YTz} \tag{XIII}$$

Where for acceleration match Y and z correspond to

$$\mathrm{Y} = \left[S\left(a_{M_{Comp}}^{M}(t_0)\right) : S\left(a_{M_{Comp}}^{M}(t_1)\right)\right]^T \tag{XIV}$$

$$\mathrm{z} = \left[\tilde{\mathrm{a}}_{\mathrm{S}}^{\mathrm{S}}(t_0) - a_{M_{Comp}}^{M}(t_0) : \tilde{\mathrm{a}}_{\mathrm{S}}^{\mathrm{S}}(t_1) - a_{M_{Comp}}^{M}(t_1)\right]^T$$

and for both acceleration and rotation rate match Y and z correspond to

$$\mathrm{Y} = \left[S\left(a_{M_{Comp}}^{M}(t_0)\right) : S\left(a_{M_{Comp}}^{M}(t_1)\right) : S\left(\omega_{\mathrm{iM}}^{\mathrm{M}}(t_0)\right) : S\left(\omega_{\mathrm{iM}}^{\mathrm{M}}(t_1)\right)\right]^T \tag{XV}$$

$$\mathrm{z} = \left[\tilde{\mathrm{a}}_{\mathrm{S}}^{\mathrm{S}}(t_0) - a_{M_{Comp}}^{M}(t_0) : \tilde{\mathrm{a}}_{\mathrm{S}}^{\mathrm{S}}(t_1) - a_{M_{Comp}}^{M}(t_1) : \omega_{\mathrm{IS}}^{\mathrm{S}}(t_0) - \omega_{\mathrm{IM}}^{\mathrm{M}}(t_0) \right.$$
$$\left. : \omega_{\mathrm{IS}}^{\mathrm{S}}(t_1) - \omega_{\mathrm{IM}}^{\mathrm{M}}(t_1)\right]^T$$

In the above equations “t_0” corresponds to initial time. In the following figure, the change in smallest Eigen value of “(YTY)” with respect to “t_1” is presented for acceleration and for both rotation rate and acceleration measurements.

The estimation of roll, pitch, yaw misalignments have been conducted by a suitable Kalman filter mechanised with the afore mentioned dynamics. The convergence of the roll channel, pitch channel, yaw channel misalignments have been shown in figures 3, 4 and 5 respectively.

In detailed, the figure 3, shows roll convergence when only accelerometer data and gyro data are both considered separately and together. The accuracy of roll convergence is on par when either gyro data only measurements are considered or both gyro and accelerometer combined data is considered.

However, accelerometer data can be utilized in the presence of negligible lever arm. Hence, this paper considers and recommends use of only gyro data for the purpose of estimation of roll misalignment angle. Also, from figure 4, the convergence of pitch misalignment angle is effectively shown with gyro only measurement data. From figure 5, the yaw misalignment estimation convergence is shown with gyro only measurement data.

7 Conclusion

The heart of strapped-down inertial navigation systems lies in its dead reckoning. Hence, for a successful mission by initialization of angles prior to the start of navigation is in the least overrated.

Herein theory is developed for comparison of angular rates, accelerations or both of two rigidly mounted strapped-down inertial navigation systems and the misalignments in angles of role, pitch and yaw are estimated using a suitable Kalman filter.

The estimation accuracy of misalignments in roll, pitch, and yaw have been found to be within 0.02 deg (3-sigma). Sufficiently several Monte Carlo runs have been used to prove the efficacy of misalignment angle estimation in navigation runs, making it suitable for mission applications.

8 Reference

[1] Bar-Itzhack I. Y., Porat B., Azimuth Observability Enhancement during Inertial Navigation System In-Flight Alignment, Journal of Guidance and Control, Vol. 3, No. 4, 1980

[2] Bar-Itzhack I. Y., Vitek Y., The Enigma of False Bias Detection in a Strapdown System during Transfer Alignment, Journal of Guidance and Control, Vol.8, No. 2, 1985

[3] Bar-Itzhack, Berman N., Control Theoretic Approach to Inertial Navigation Systems, Journal of Guidance and Control, Vol.11, No. 3, 1988

[4] Baziw J., Leondes C. T., In Flight Alignment and Calibration of Inertial Measurement Units – Part I General Formulations, IEEE Transactions on Aerospace and Electronic Systems, Vol AES-8, No:4, 1972

[5] Baziw J., Leondes C. T., In Flight Alignment and Calibration of Inertial Measurement Units – Part II Experimental Results, IEEE Transactions on Aerospace and Electronic Systems, Vol AES-8, No:4, 1972

[6] Boch W., Krogmann U., Fast Transfer Alignment for Air-Launched Missile INS, CP 411

[7] Bortz J. E., A New Mathematical Formulation for Strap down Inertial Navigation, IEEE Transactions on Aerospace and Electronic Systems, Vol: AES-7, No:1, 1977

[8] Brown G. B., Hwang P. Y. C., Introduction to Random Signals and Applied Kalman Filtering, John Willey & Sons, 1997

[9] Goshen-Meskin D., Bar-Itzhack I. Y., Observability Analysis of Piecewise Constant Systems – Part I: Theory, IEEE Transactions on Aerospace and Electronic Systems, Vol 28, No:4, 1992

[10] Goshen-Meskin D., Bar-Itzhack I. Y., Observability Analysis of Piecewise Constant Systems – Part II: Application to Inertial Navigation In-Flight Alignment, IEEE Transactions on Aerospace and Electronic Systems, Vol 28, No:4, 1992

[11] Groves P. D., Wilson G. G., Mather C. J., Robust Rapid Transfer Alignment with an INS/GPS Reference, Institute of Navigation National Technical Meeting, 2002

[12] [12] Groves P. D., Optimizing the Transfer Alignment of Weapon INS, The journal of Navigation, 2003

[13] Hallingstad O., Design of a Kalman Filter For Transfer Alignment, AGARD Lecture Series No. 166 - Kalman Filter Integration of Modern Guidance and Navigation Systems, 1989

[14] Harris R. A., Wakefield C. D., Coordinate Alignment for Elastic Bodies, NEACON 77 Record, pp665-670

[15] Haykin S., Adaptive Signal Processing, Prentice Hall, 2002

[16] Titterton D.H. and Weston J.L., “Strap down Inertial Navigation Technology”, Peter Pergrinus Ltd., London, 1997

[17] Junkins J. L., Schaub H., Analytical Mechanics of Space Systems, AIAA Education Series, 2003.

[18] Kain J. E., Cloutier J. R., Rapid Transfer Alignment for Tactical Weapon Applications, Proceedings of AIAA Guidance, Navigation and Control Conference, pp1290-1300, 1989

[19] Klotz H. A., Derbak C. B., GPS-Aided Navigation and Unaided Navigation on the Joint Direct Attack Munition, IEEE 1998 Position Location and Navigation Symposium, pp412-419, 1998

[20] Oshman Y., Rubanenko A., State Estimation Using Measurements with Uncertain Time-Tag, AIAA Guidance Navigation & Control Conference, 2001

[21] Porat B., Bar-Itzhack I. Y., Effect of Acceleration Switching During INS In-Flight Alignment, Journal of Guidance and Control, Vol.4, No. 4, 1981

[22] Rogers R. M., Weapon IMU Transfer Alignment Using Aircraft Position from Actual Flight Tests, IEEE PLANS, pp328-335, 1996

[23] Ross C. C., Elbert T. F., A Transfer Alignment Algorithm Study Based on Actual Flight Test Data from a Tactical Air-to-Ground Weapon Launch, IEEE PLANS, pp431-438, 1994

[24] Shortelle K. J., Graham W. R., F-16 Flight Tests of a Rapid Transfer Alignment Procedure, IEEE PLANS 1998, pp379-386, 1998

[25] Spalding K., An Efficient Rapid Transfer Alignment Filter, Proceedings of AIAA Guidance, Navigation and Control Conference, pp1276-1286, 1992

[26] Basic principles of Inertial Navigation. Seminar on Inertial Navigation Systems” Tampere university of Technology Page5 April 2018.

[27] Wan Mohd Yakoob Wan Bejuri, Mohd Murtadha Mohamad, Farhana Syed Omar and Nurfarah Ain Limin, “Robust special strategies resampling for Mobile Inertial navigation Systems”. Internation Journal of innovative Technology and exploring engineering. Vol 9(2) PP3196 – 3024.

[28] “The hemispherical resonator gyro: from wineglass to the planets” David Rozelle. Northropgrumman.com.

[29] “Micro Technology for positioning, navigation and Timing darpa.mil. 9 July 2017.

[30] Stovall Sherryl.H. “Basic Inertial Navigation” global security. Org, 1997.

High accuracy Transfer Alignment for Attitude in Strap down Inertial Navigation Systems at sea

N Sivasubramaniam
RCI
DRDO
Hyderabad
pgtsivan@gmail.com

Dr. Ramesh Kumar
Guru Kashi University
Bathinda
rkgupta1701@gmail.com

***Abstract* - Transfer alignment is a key ingredient of Strapdown navigation systems mechanization at sea. Without satisfactory transfer alignment, the mechanization of Strapdown inertial navigation systems would fail to take off and the mission shall be compromised for want of accuracy. In this paper, we describe a novel batch processing technique using the angular velocity observations from both master and slave to conduct transfer alignment of attitude to the weapon systems on-board the ship using the SVD based batch processing technique. The technique would be shown to far outweigh the disadvantages of the traditional Kalman filter based transfer alignment schemes shown to far outweigh the disadvantages of the traditional Kalman filter based transfer alignment schemes.**

Keywords - Attitude Estimation, Singular Value Decomposition, Transfer Alignment, Moving Launch Platform, Critical Error Probability.

1 Introduction

Strapdown inertial navigation systems are dead reckoning in nature. They need initial attitude estimates to start the navigation process. As such at sea, the initialization of attitude is a tedious and time necessitating procedure which can be circumvented by employing an a priori aligned Strapdown inertial navigation system and transfer the alignment angles to a slave system with the weapon system. Such a procedure comes to be known as transfer alignment. In this paper, we conduct satisfactory transfer of alignment at sea using a priori aligned master system to the slave system using a batch of observations of angular velocity from both master and slave. The assumption being that both master and slave are rigid with respect to each other. We do so, with the highly numerically robust Singular Value Decomposition (SVD) technique for batch processing of data.

2 Literature Survey

The attitude interpretations are certainly epitomized as unit vectors in various spacecraft attitude systems. The unit vector in the course of the Earth’s magnetic field and the unit vectors providing the course to the star or a sun are the various instances.

In 1965, Grace Wahba1 [1] proposed a loss function for estimating spacecraft attitude from vector measurements, which are followed by all algorithms:

Resulting the orthogonal matrix, A with determinant +1 that reduces the loss function is the Wahba’s problem [1]

$$\mathrm{L(X)} = \frac{1}{2}\sum_i x_i |\, y_i - Xf_i|^2 \quad (1)$$

where

{xi} indicates non-negative weights

{yi} indicates a set of unit vectors measured in a spacecraft’s body frame and{fi} indicates the corresponding unit vectors in a reference frame.

For comparison of Wahba's problem to Maximum Likelihood Estimation, we indicate the weights to be transposed discrepancies, $x_i = \sigma_i^{-2}$.

For whom anticipated the weights regulated to unity, this choice contrasts from that of Wahba's and various authors.

Providing an outline of the most prevalent algorithms in a cohesive notation, and to provide precision and speed evaluations is the theme of this paper. The efficacy of the proposed algorithms will be evaluated in actual launch scenario with rigid master and slave configuration on ship launched weapon systems.

Paper [17] describes the basic principles of navigation. Emphasis is exposed as to why attitude information is critical to start of inertial navigation. Paper [18] explores robust strategies for in-motion inertial navigation explaining various statistically robust methods. The directorate of navigation is also experimenting hemispherical resonating gyro for long range space navigation. A suitable star sensor is also being developed at RCI to aid HrG based navigation for interplanetary sojourns [19]. DARPA, US is relying on MEMS technology for positing of small vehicles, for which attitude information shall become necessary [20]. The need for ubiquitous inertial navigation is given in stovall [21].

3 Orthogonal Procrustes Problem

The Wahba's loss function can also be written as

$$\mathrm{L(X)} = \sum_i x_i - tr\,(XY^T) \qquad (2)$$

With

$$\mathrm{Y} = \sum_i x_i y_i {f_i}^T \qquad (3)$$

Hence, L(X) is reduced while the trace, tr(XYT), is exploited.

To discover the orthogonal matrix X that is flanking to Y in the sense of the Frobenius norm, i.e., similar to Orthogonal Procrustes problem.

$$|M|_F^2 = \sum_{ij} M_{ij}^2 = tr(MM^T) \qquad (4)$$

Now

$$||X - Y||_F^2 = ||X||_F^2 + ||Y||_F^2 - 2tr(XY^T) = 3 + ||Y||_F^2 - 2tr(XY^T) \qquad (5)$$

Hence, with the prerequisite that the determinant of A must be +1, both the Wahba's problem [1] and the orthogonal Procrustes problem are similar.

4 First Solutions

The first solution of Wahba's problem, according to J. L. Farrell and J. C. Stuelpnagel [2] is, any real matrix including Y, has the polar decomposition

$$\mathrm{Y = OS}, \qquad (6)$$

where O indicates orthogonal, S indicates symmetric and positive semi definite.

Then S can be diagnolized by

$$\mathrm{S = VDVT}, \qquad (7)$$

where

V indicates orthogonal matrix,

D indicates transverse with components organized in reducing order.

Then the optimal attitude estimate can be specified as

$$X_{\text{opt}} = \text{OV diag}[1\ 1\ \text{detO}]V^T \quad (8)$$

Mostly but not assured always, X_{opt} = O whereas det O is positive.

The alternate solution proposed by R. H. Wessner is given:

$$X_{\text{opt}} = (Y^T)^{-1}(Y^TY)^{1/2}, \quad (9)$$

i.e., similar to

$$X_{\text{opt}} = \text{Y}(Y^TY)^{-1/2}. \quad (10)$$

Necessitating Y to be non-singular is the detriment having with Equations (9) and (10) i.e., even though two vector interpretations are adequate to conclude the attitude, still minimum three vector interpretations are required to visualize the pseudo inverse solution.

The various solutions to Wahba's problem are also provided by R. Desjardins, J. E. Brock [5], J. R. Velman and Wahba [1].

5 Unconstrained Least-Squares

Without necessitating the orthogonality constraint, there is a chance of reducing Wahba's loss function i.e., by

$$X_{\text{unconstrained}} = \text{Y}(\textstyle\sum_i x_i f_i {f_i}^T)^{-1}. \quad (11)$$

This signifies

$$Y = X_{\text{unconstrained}} = (\textstyle\sum_i x_i f_i {f_i}^T), \quad (12)$$

Here $X_{\text{unconstrained}}$ is merely approximately orthogonal, hence it's not similar to polar decomposition even though it seems equivalent. Brock [5] proposed a solution which is analysed by Bar-Itzhack and Markley [8].

6 Davenport's q Method

A genuine innovation came when Wahba's problem to spacecraft attitude determination has been modelled by Paul Davenport in search of a quaternion based solution for the attitude estimation [10,11].

X can be parameterized by a unit quaternion [8,9]

$$\text{q} = \begin{bmatrix} q \\ q_4 \end{bmatrix}, \text{ where } |\text{q}|2 = 1, \quad (13)$$

as

$$\text{X} = (q_4^2 - |q|^2)I + 2qq^T - 2q_4[qX]. \quad (14)$$

We can write the homogenous quadratic function of q as,

$$tr(XY^T) = q^TKq \quad (15)$$

where K denotes symmetric traceless matrix

$$\text{K} \equiv \begin{bmatrix} S - I\,trY & z \\ z^T & trY \end{bmatrix} \quad (16)$$

With

$$S = B + B^T \quad (17)$$

And

$$z \equiv \begin{bmatrix} Y_{23} - Y_{32} \\ Y_{31} - Y_{13} \\ Y_{12} - Y_{21} \end{bmatrix} = \textstyle\sum_i x_i y_i\, X\, f_i \quad (18)$$

Hence, we can prove that the normalized eigenvector of K with the largest eigenvalue i.e., the solution of Equation (19) is optimal unit quaternion.

$$K_{q_{opt}} \equiv \lambda_{max\ q_{opt}} \tag{19}$$

For solving the symmetric eigenvalue problem, many robust algorithms exist. They are easy to implement in MATLAB. If the two prevalent eigenvalues of K are identical then there is no solution. The data aren't abundant to conclude the attitude distinctively, which determines that this is not a catastrophe of the q method. It is the absence of sufficient data to conclude the estimation process.

7 Quaternion Estimator (QUEST)

Equation (19) is similar to the following Equation (20) and Equation (21) [14,12]

$$(\lambda_{max} + trY)\mathrm{I} - \mathrm{S}]\mathrm{q} = q_4 Z \tag{20}$$

and

$$(\lambda_{max} - trY)q_4 = q^T Z \tag{21}$$

Equation (20) provides

$$\begin{aligned} \mathrm{q} &= q_4\ [(\lambda_{max} + trY)I - S]^{-1} z \\ &= \mathrm{q}_4 \{adj[\lambda_{max} + trY)I - S]z \,/\, \det[(\lambda_{max} + trY)I - S]\} \end{aligned} \tag{22}$$

For a general 3x3 matrix, the Cayley-Hamilton theorem G states that

$$\begin{aligned} \mathrm{q} &= q_4\ [(\lambda_{max} + trY)I - S]^{-1} z \\ &= \mathrm{q}_4 \{adj[\lambda_{max} + trY)I - S]z \,/\, \det[(\lambda_{max} + trY)I - S]\} \end{aligned}$$

$$G^3 - (tr\ G)G^2 + [\ tr(adjG)]G - (detG)I = 0 \tag{23}$$

where adjG is the typical adjoint (adjugate) of G. Hence the adjoint can be conveyed as

$$adjG = G^2 - (trG)G + [tr(adjG)]I \tag{24}$$

In precise

$$adj[\lambda_{max} + trY)I - S] = \alpha\mathrm{I} + \beta\mathrm{S} + S^2 \tag{25}$$

where

$$\alpha \equiv \lambda_{max}^2 - (trY)^2 + \mathrm{tr(adjS)} \tag{26}$$

and

$$\beta \equiv \lambda_{max} - trY \tag{27}$$

We also enunciate

$$\gamma \equiv \det[(\lambda_{max} + trY)\mathrm{I} - \mathrm{S}] = \alpha[(\lambda_{max} + trY) - detS \tag{28}$$

The optimal quaternion can be specified as

$$q_{opt} = \frac{1}{\sqrt{\gamma^2 + |x|^2}} \begin{bmatrix} x \\ \gamma \end{bmatrix}, \tag{29}$$

Where

$$\mathrm{x} \equiv (\alpha\mathrm{I} + \beta\mathrm{S} + \mathrm{S}^2)\mathrm{z} \tag{30}$$

Maximum eigen value λmax plays vital for all these computations whereas it can be attained by switching Equation (22) into Equation (21), which produces the equation:

$$0 = \Psi(\lambda_{max}) \equiv \gamma(\lambda_{max} - trY) - z^T(\alpha\mathrm{I} + \beta\mathrm{S} + \mathrm{S}^2)\mathrm{z} \tag{31}$$

A fourth-order equation for λmax can be attained by switching Equations (26–28). This can be solved rationally by using the distinctive equation det(K-λmax I) = 0. Conversely, that λmax is very close to

$$\lambda_0 \equiv \sum_i x_i \tag{32}$$

If the enhanced loss function

$$\mathrm{L(\ Aopt\ )} \cong \lambda_0 - \lambda_{max} \tag{33}$$

is solved by Newton-Raphson iteration method, λmax can be effortlessly attained, beginning from λ=0 as the primary estimate. Statistically, a distinct rehearsal is mostly ample. Nevertheless, one of the ways to find eigenvalues is elucidating the specific equation, commonly, Davenport's original q method is more robust than QUEST in principle i.e., distinguished statistically.

Equation (29) doesn't describes the optimal quaternion, if

$$\gamma^2 + |x|^2 = 0, \tag{34}$$

Therefore, the technique of consecutive cycles to lever this circumstance is contrived by Shuster [10,11]. These are slightly lavish computationally as for regulating the number of consecutive cycles accomplished accurate norm is preferred. Switching Equation (30) into Equation (34) and changing the Cayley-Hamilton theorem twice to exclude S4 and S3 contributes, and after tedious algebra,

$$\gamma^2 + |x|^2 = \gamma\,(\mathrm{d}\Psi / \mathrm{d}\lambda\,), \tag{35}$$

Where Equation (31) implicitly defines Ψ(λ), the quartic function. For the Newton-Raphson iteration for λ_{max} to be efficacious, dΨ/dλ is to be invariant underneath cycles, and this capacity must be nonzero. Therefore $(q_{opt})4 = 0$ and the optimal attitude epitomizes a 180˚ cycle which means that the singular condition of Equation (34) is perceived to be correspondent to ɣ = 0.

To find a ɣ, we can always run consecutive cycles of iteration such that

$$(q_{opt})_4 > q_{min} \tag{36}$$

For any qmin in (0, 1/2), by asserting that

$$\gamma > {q_{min}}^2(\mathrm{d}\Psi / \mathrm{d}\lambda\,) \tag{37}$$

To elude loss of numerical precision in the computation, qmin = 0.1 is ample in preparation.

An appraisal of the covariance of the rotation slant error vector in the body frame is also provided by Shuster [3],

$$\mathrm{P} = [\textstyle\sum_i x_i(I - y_i {y_i}^T)]^{-1} \tag{38}$$

And supposing Gaussian measurement errors, disclosed that the optimized loss function $L(X_{opt})$ observes a chi-square probability distribution to a worthy calculation. QUEST, first applied in the MAGSAT mission in 1979, is the most widely used algorithm for Wahba's problem.

8 Singular Value Decomposition (SVD) Method

The matrix Y has the Singular Value Decomposition. [13]

$$Y = U\sum V^T = U\,diag[\,\sum_{11}\,\sum_{22}\,\sum_{33}\,]V^T \quad (39)$$

where U and V are orthogonal, and the particular tenets follow the discriminations ∑11 ≥ ∑22 ≥ ∑33 ≥ 0.

Then

$$tr(AB^T) = tr(A\,V\,diag[\,\sum_{11}\,\sum_{22}\,\sum_{33}\,]U^T = tr(U^T A\,V\,diag[\sum_{11}\,\sum_{22}\,\sum_{33}\,]) \quad (40)$$

For A to be a orthogonal rotation matrix, det A = 1, and the optimal direction cosine matrix is given by

$$U^T A_{opt} V = diag\;[1\;1\;(detU)(detV)] \quad (41)$$

which contributes the ideal attitude matrix:

$$A_{opt} = U\;diag\;[1\;1\;(detU)(detV)]\;V^T \quad (42)$$

Equation (42) is indistinguishable to Equation (8) with U = WV, Subsequently the original solution by Farrell and Stuelpnagel [2] absolutely corresponds to the SVD solution. The variance is that SVD algorithms be existent now.

It is expedient to delineate

$$S_1 \equiv \sum_{11}, S_2 \equiv \sum_{22}\; and$$
$$S_3 \equiv (detU)(detV)\sum_{33} \quad (43)$$

so that s1 s2 |s3|. The error covariance of attitude is given by

$$P = U\;diag[\,(S_2 + S_3)^{-1}(S_3 + S_1)^{-1}(S_1 + S_2)^{-1}]\;U^T \quad (44)$$

The singular values are allied to the eigenvalues of Davenport's K matrix,

$\lambda_{max} \equiv \lambda_1 \geq \lambda_2 \geq \lambda_3 \geq \lambda_4$ by

$$\lambda_1 = S_1 + S_2 + S_3$$
$$\lambda_2 = S_1 - S_2 - S_3$$
$$\lambda_3 = -S_1 + S_2 - S_3$$
$$\lambda_4 = -S_1 - S_2 + S_3 \quad (45)$$

The eigenvalues sum to zero as K is traceless. The condition of vast covariance i.e., the peculiarity condition, is

$$S_2 + S_3 = 0 \quad (46)$$

This is comparable to the previously-stated unnoticeable condition for Davenport's q method i.e.,

$$\lambda_1 = \lambda_2$$

9 Requirement of Time Synchronization

- As the body rates are compared there is a tight synchronization requirement between Master and Slave INS (OBC).
- This has been achieved using a specified protocol formation for command and response including data transmission among FCS (where Filter is executed), Master INS and Slave INS (OBC).

We have done alignment of Strapdown inertial navigation systems at sea for the estimation of master to slave misalignment angles using the batch mode SVD technique in ship.

10 Advantages of SVD Over KF based Methods

The present SVD based transfer alignment procedure has several advantages over the traditional KF based alignment schemes in that

(i) Removal of necessity to conduct specific maneuvers prior to transfer alignment of weapon system INS.
(ii) Direct estimation of parameters of interest without resorting to a linearization of error model as done in usual EKF procedures.
(iii) Batch processing to alleviate quicker timing cycles giving ample time for computations and initialization.
(iv) Error variances are to be known a priori for the initialization of EKF which is done away with SVD based technique. SVD method alleviates the need for knowledge of error covariances of both master and slave.

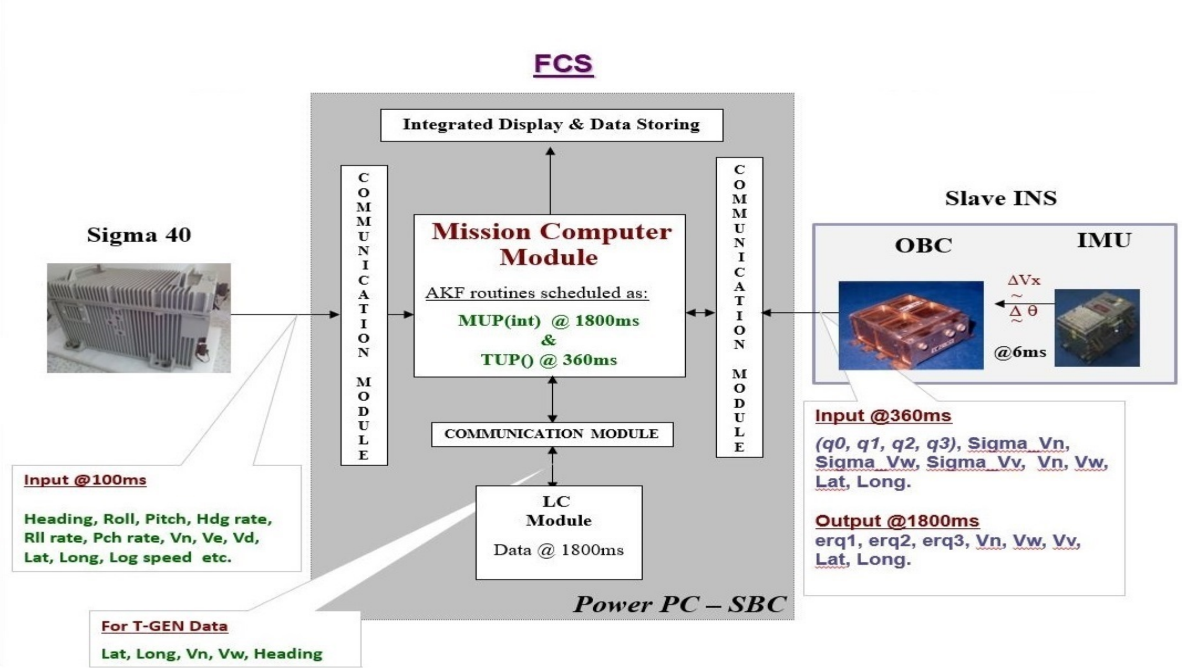

Figure 1. Existing TA Software on FCS

11 Instrument Test Setup At Sea

As shown in figure (1), in the old transfer alignment scheme, the velocity information from the master and the slave are brought to the FCS computer, wherein the velocities are compared with the help of a suitable Kalman filter and the error estimates in attitude are computed. However, the major problem with such a scheme is the necessity of manoeuvres for active convergence of azimuth solution. This can be alleviated if we resort to comparison of angular velocities under suitable excitation of roll and yaw manoeuvres imposed on the launcher platform prior to the lift-off.

In Figure (2), the block diagram shows the setup of new transfer alignment scheme. The Sigma 40 is the master INS and the IMU supplies the incremental angles data, captured via the OBC at the FCS.

The SVD based algorithm operates on the data available both from master and slave to arrive at the optimal solution of attitude of the IMU with respect to the master. The master also supplies the attitude information with respect to the ground. The interalia estimated misalignment is coupled with the master to ground attitude information to arrive at the IMU to ground attitude estimate

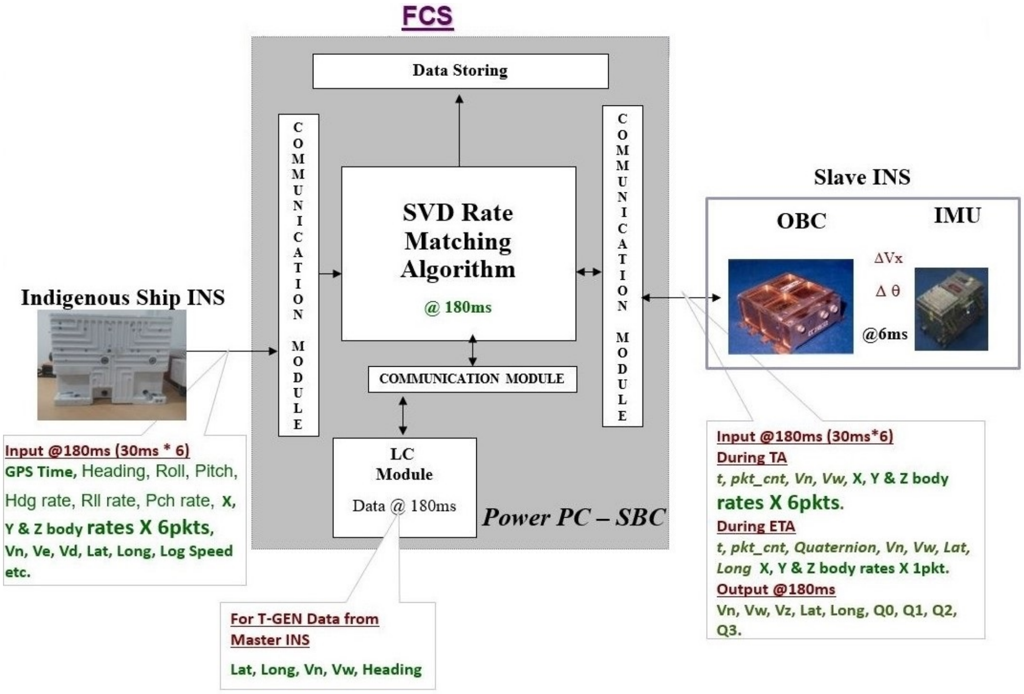

Figure 2. Proposed TA Software on FCS

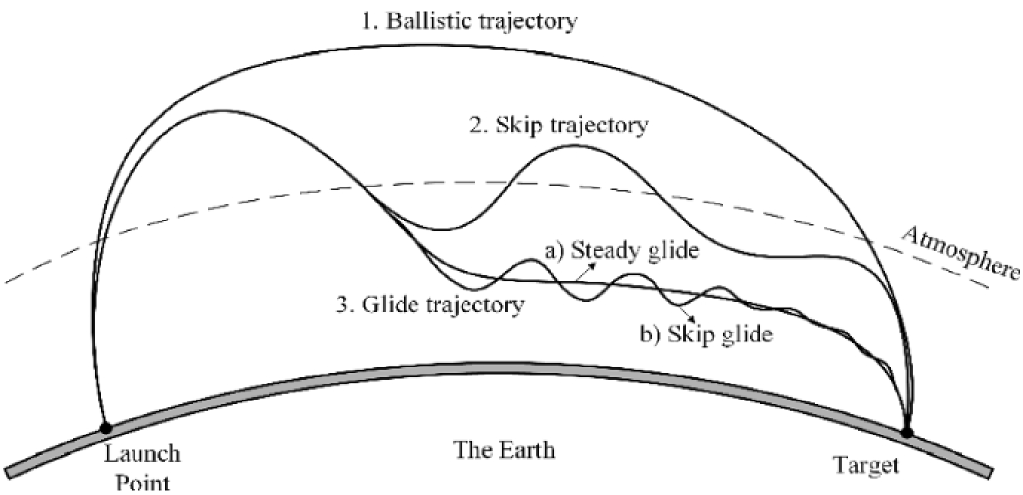

Figure 3. Implicit Missile Trajectory

Figure (3) shows the proposed trajectory modelling of the flight over a downrange of the weapon system. The flight path is modelled to increase the range by conversion of KE-PE energy profile during the flight.

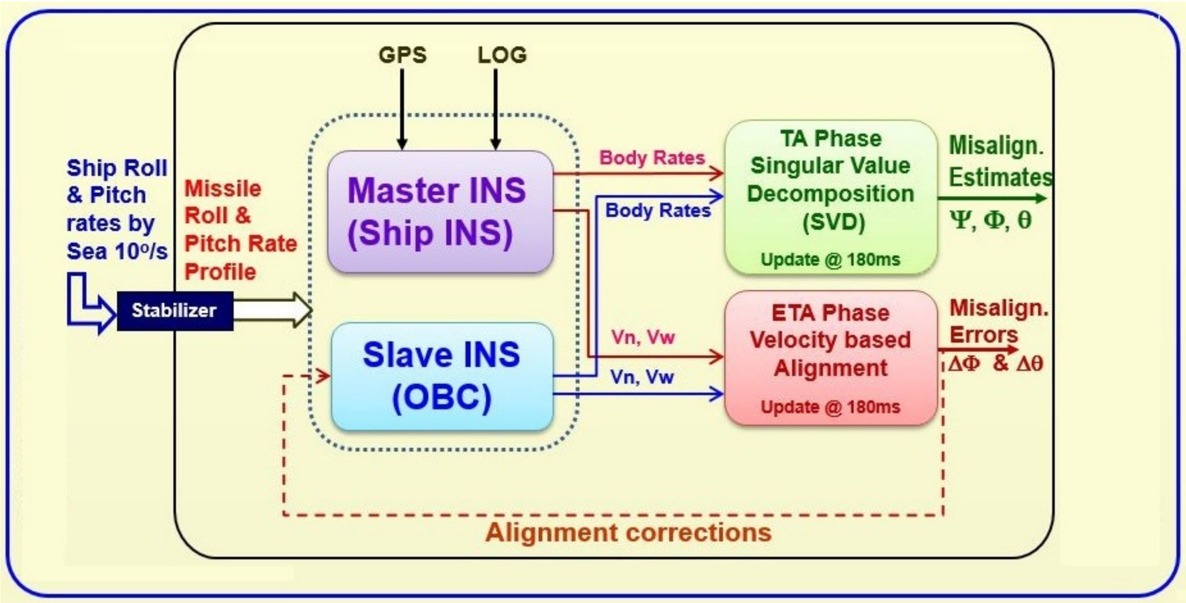

Figure 4. Rate matching based TA Scheme

Figure (4) shows the integration of both SVD and ETA schemes for the estimation of yaw, roll and pitch respectively and the integration is conducted in the FCS computer.

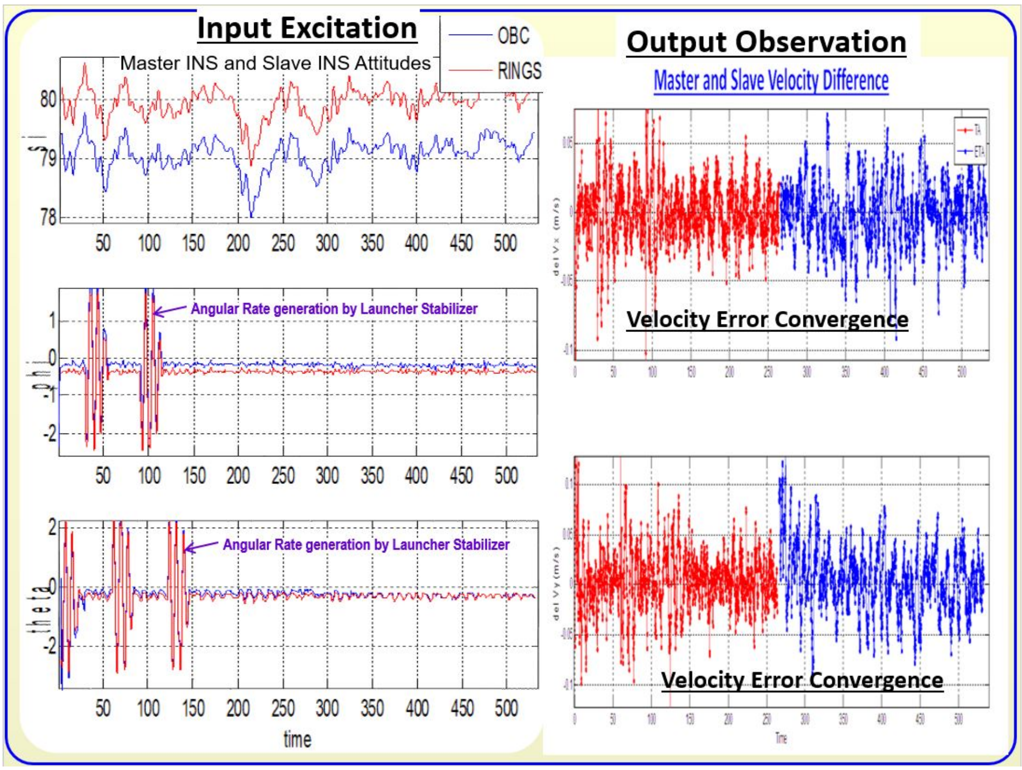

Figure 5. Misalignment estimates and observations

12 Results

Figures (5) and (6) show the convergence of roll, pitch yaw angles under excitation of the roll and yaw channels. The velocities are converged to within 0.01m/sec in both North and East channels. Figure (6) shows the estimation of constant misalignment angle between the master and the slave in rigid mounting condition.

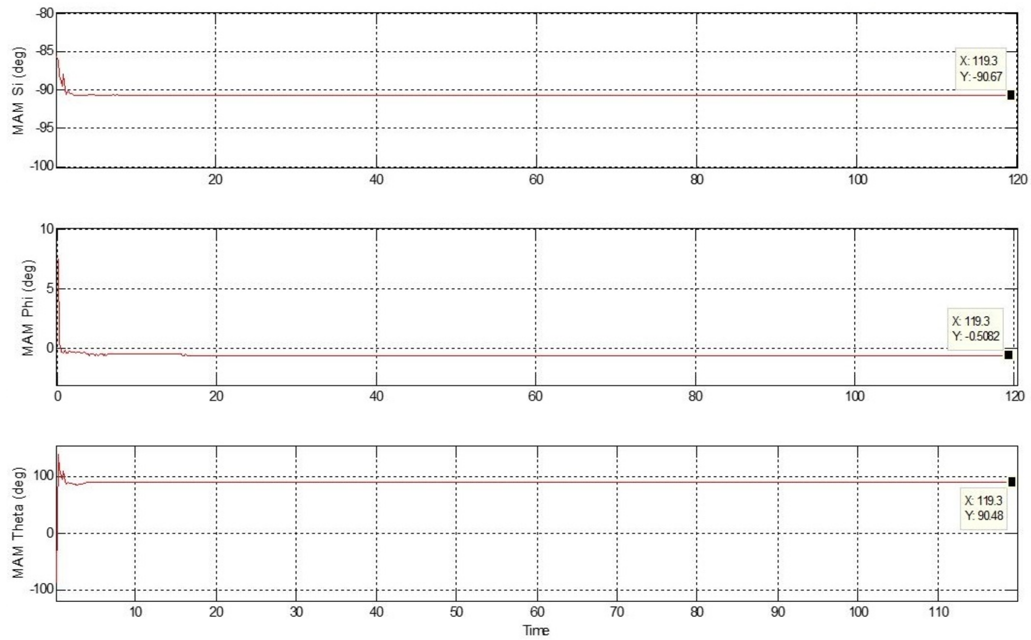

Figure 6. SI, PHI, THETA Misalignment Estimation

Run No	Ψ_{MAM}	Φ_{MAM}	θ_{MAM}	Attitude Rates Rll & Pch (°/s)	Profile time (min)	X_{err} (m)	Y_{err} (m)	Z_{err} (m)
1	-90.67	-0.50	90.48	±2, ±1.8	2	1480	-8	51
2	-90.72	-0.47	90.44	±2, ±1.8	2	453	612	32
4	-90.72	-0.51	90.33	±2, ±1.8	2	859	866	34
5	-90.72	-0.48	90.32	±2, ±1.8	2	-71	-1112	-14
6	-90.73	-0.46	90.37	±2, ±1.8	2	924	-1082	-32
7	-90.71	-0.38	90.40	±2, ±1.8	2	-622	-521	-51
8	-90.75	-0.51	90.34	±2, ±1.8	2	4	800	10
9	-90.77	-0.50	90.36	±2, ±1.8	2	1125	261	-25
10	-90.76	-0.47	90.33	±2, ±1.8	2	17	-512	-60
11	-90.78	-0.51	90.36	±2, ±1.8	2	-240	529	-87
12	-90.78	-0.46	90.35	±1.2, ±0.8	3	-275	203	-112

Figure 7. Ship Trial Results with New TA

Figure 7 shows the repeatability of several runs of the SVD based attitude estimation technique at sea. The estimation of azimuth has a standard deviation of within $0.1^0(3\sigma)$ while roll and pitch have far less variance as compared to azimuth channel as shown in the table.

The position errors at the end of time-of- flight runs are about 1km CEP (3σ). In actual flight trials the cross range error was found to be well with the 500m CEP(1σ) over 350km downrange.

13 Conclusion

SVD based attitude algorithm has developed and also been tested on ship. Very good accuracy have been obtained in roll, pitch and yaw channels. The plots show the convergence of roll, pitch and yaw channels upto an accuracy of 0.02 degree. The accuracy is sufficient to bring the crossrange accuracy of within 500m over a downrange of 350km while the GPS aided error will be well within 30 mts crossrange. SVD aided rate matching technique is most suitable for ship launched weapon systems as the sea undulations aid in the convergence of the attitude misalignment angles without need for additional manoeuvres.

The SVD based technique becomes mainstay due to the several advantages depicted over the traditional KF based techniques in future missions.

14 Future Work

The algorithm assumes rigidity between master and slave for the SVD batch processing to work. However, minute movements between master and slave could never be alleviated in true mechanical launch scenarios. The present strategy may be improvised to include the play inter-alia between the master and the slave, therewith rendering the algorithm to work in all deployable scenarios. The other challenge not considered in the present paper is the coupling of inferior grade gyros with the high grade master gyros employed in the present scenario. The performance of transfer alignment with degraded gyros, if when improved would be useful in employing the SVD technique for short range missile systems. Such an attempt is currently underway in the upcoming ship-to-air launch missions from on-board ships.

15 References

[1] Wahba, Grace, “A Least Squares Estimate of Spacecraft Attitude,” SIAM Review, Vol. 7, No. 3, July 1965, p. 409.

[2] Farrell, J. L. and J. C. Stuelpnagel, “A Least Squares Estimate of Spacecraft Attitude,” SIAM Review, Vol. 8, No. 3, July 1966, pp. 384-386.

[3] Shuster, Malcolm D., “Maximum Likelihood Estimate of Spacecraft Attitude,” Journal of the Astronautical Sciences, Vol. 37, No. 1, January-March 1989, pp. 79–88. Ų

[4] Horn, Roger A. and Charles R. Johnson, Matrix Analysis, Cambridge, UK, Cambridge University Press, 1985.

[5] Brock, John E., “Optimal Matrices Describing Linear Systems,” AIAA Journal, Vol. 6, No. 7, July 1968, pp. 1292-1296.

[6] Markley, F. Landis and Itzhack Y. Bar-Itzhack, “Unconstrained Optimal Transformation Matrix,” IEEE Transactions on Aerospace and Electronic Systems Vol. 34, No. 1, January 1998, pp. 338-340.

[7] Lerner, Gerald M., “Three-Axis Attitude Determination,” in Spacecraft Attitude Determination and Control, ed. by James R. Wertz, Dordrecht, Holland, D. Reidel, 1978.

[8] Markley, F. Landis, “Parameterizations of the Attitude,” in Spacecraft Attitude Determination and Control, ed. by James R. Wertz, Dordrecht, Holland, D. Reidel, 1978.

[9] Shuster, Malcolm D., “A Survey of Attitude Representations,” Journal of the Astronautical Sciences, Vol. 41, No. 4, October-December 1993, pp. 439-517.

[10] Shuster, M. D. “Approximate Algorithms for Fast Optimal Attitude Computation,” AIAA Paper 78-1249, AIAA Guidance and Control Conference, Palo Alto, CA, August 7–9, 1978.

[11] Shuster, M. D. and S. D. Oh, "Three-Axis Attitude Determination from Vector Observations,” Journal of Guidance and Control, Vol. 4, No. 1, January-February 1981, pp. 70-77.

[12] Bar-Itzhack, Itzhack Y., “REQUEST: A Recursive QUEST Algorithm for Sequential Attitude Determination,” Journal of Guidance, Control, and Dynamics, Vol. 19, No. 5, September-October 1996, pp. 1034–1038.

[13] Markley, F. Landis, "Attitude Determination Using Vector Observations and the Singular Value Decomposition," AAS Paper 87-490, AAS/AIAA Astrodynamics Specialist Conference, Kalispell, MT, August 1987.
[14] Markley, F. L., "New Quaternion Attitude Estimation Method," Journal of Guidance, Control, and Dynamics, Vol. 17, No. 2, March-April 1994, pp. 407-409.
[15] Basic principles of Inertial Navigation. Seminar on Inertial Navigation Systems" Tampere university of Technology Page5 April 2018.
[16] Wan Mohd Yakoob Wan Bejuri, Mohd Murtadha Mohamad, Farhana Syed Omar and Nurfarah Ain Limin, "Robust special strategies resampling for Mobile Inertial navigation Systems". Internation Journal of innovative Technology and exploring engineering. Vol 9(2) PP3196 – 3024.
[17] Basic principles of Inertial Navigation. Seminar on Inertial Navigation Systems" Tampere university of Technology Page5 April 2018.
[18] Wan Mohd Yakoob Wan Bejuri, Mohd Murtadha Mohamad, Farhana Syed Omar and Nurfarah Ain Limin, "Robust special strategies resampling for Mobile Inertial navigation Systems". Internation Journal of innovative Technology and exploring engineering. Vol 9(2) PP3196 – 3024.
[19] "The hemispherical resonator gyro: from wineglass to the planets" David Rozelle. Northropgrumman.com.
[20] "Micro Technology for positioning, navigation and Timing darpa.mil. 9 July 2017.
[21] Stovall Sherryl.H. "Basic Inertial Navigation" global security. Org, 1997.

Parachute Mechanisms

Dynamics of Crew Module Under Slung Helicopter

Abdul Salam P M
Aerospace Mechanisms Group
Vikram Sarabhai Space Centre
ISRO
Thiruvananthapuram
salam_abdul@vssc.gov.in

Mathew Tom
Aerospace Mechanisms Group
Vikram Sarabhai Space Centre
ISRO
Thiruvananthapuram

Johns Paul
Aerospace Mechanisms Group
Vikram Sarabhai Space Centre
ISRO
Thiruvananthapuram

Santhosh J Nalluveettil
Aerospace Mechanisms Group
Vikram Sarabhai Space Centre
ISRO
Thiruvananthapuram

U A Subramanian
Aerospace Mechanisms Group
Vikram Sarabhai Space Centre
ISRO
Thiruvananthapuram

***Abstract* – As part of qualification of parachute deceleration system for human in space flight programs, a series of Integrated Air Drop Tests (IADT) with Crew Module (CM), from Chinook helicopter are proposed. These tests will provide necessary data on system performance. Helicopter drops the module from an altitude of nearly 4km by activating a separation system. This paper discusses the dynamics of CM underslung helicopter, loads coming on the separation system and attachment slings using analytical method. The parameters estimated through analytical method validated through MSC ADAMS software**.

Keywords– Crew Module (CM); Integrated Air Drop Test (IADT); Angle of Attack (AoA); Free Body Diagram (FBD); Bending Moment (BM); Clamp band separation system; Mean Sea Level (MSL)

1. Introduction

A parachute-based deceleration system is employed for human in space flight programs during the terminal phase of the re-entry mission to reduce the descent velocity of Crew Module (CM) to less than 12 m/s, for safe landing in water.

As part of qualification of parachute deceleration system, a series of Integrated Air Drop Tests (IADT) with Crew Module (CM), from helicopter are proposed. These tests will evaluate system performance. CM is attached to helicopter through four slings into a single point. The release system planned for these tests is a clamp band separation system that interfaces with CM and shield plate through two interface rings (Ref: Fig. 1). Helicopter drops the module from an altitude of nearly 4km by activating the separation system. The integrated air drop test can be divided into the following three successive phases.

(i) Lifting of CM from ground to an altitude of nearly 4km using Helicopter
(ii) Release of CM from Helicopter and stabilization of module using a stabilizer parachute
(iii) Deployment of parachute deceleration system and splashdown in sea

The CM is released from the helicopter at an altitude nearly 4.0 km from the MSL. The Angle of Attack (AoA) of CM is nearly 90° during the release of CM from helicopter as the helicopter is flying normal to CM axis. The normal force acts on the CM due to this 90° AoA induces large oscillations on CM after separation from helicopter. The stabilizer parachute is deployed immediately after release from helicopter; it stabilizes the module and provides a favourable condition for the initiation of parachute system deployment sequence. The following parameters affect stability of the module after separation

(i) Attitude of module at the instant of separation due to pendulum motion.
(ii) The rate of pendulum motion at which module separates.
(iii) AoA of CM at the instant of separation.

The rate and the attitude of CM during the release of CM is a critical parameter affecting the dynamics of CM after release from the helicopter. The simulation using ADAMS software shows that underslung mass undergoes pendulum motion during the forward acceleration of helicopter. The pendulum motion of CM creates additional moments on clamp band separation system. This paper discusses the under slung dynamics of CM with helicopter, various loads acts on to the separation system and attachment slings using analytical method. The parameters estimated through analytical method were validated through MSC ADAMS software

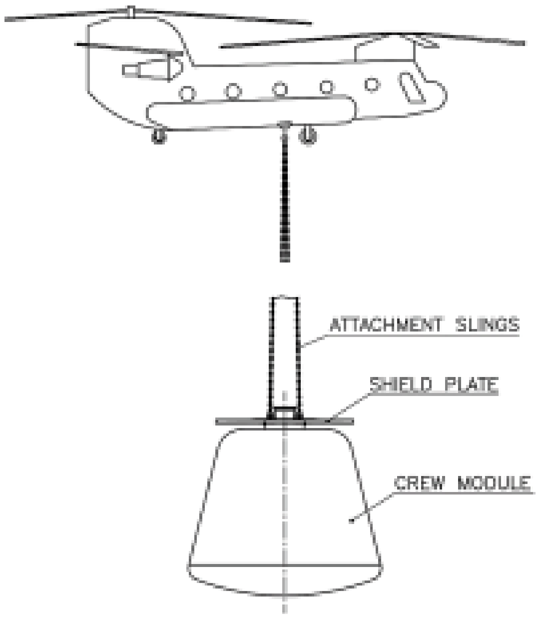

Figure 1: IADT configuration

2. Analytical Methodology

The CM is assumed as a simple pendulum in an accelerating frame (Two Dimensional plane of paper), neglecting the aerodynamic loads. The CM behavior will be similar to a simple pendulum in an accelerating frame (Ref: Fig. 2).

By using the newton's equation of motion, the following parameters are estimated.

(i) Mean angle during pendulum motion.
(ii) Time period of oscillation.
(iii) CM maximum angular acceleration.
(iv) Maximum BM on separation plane.

The parameters used for the study are given below;
Crew Module (CM) mass, m;
CM moment of inertia about C.G, ICG;
Helicopter forward acceleration, a;
Angle b/w sling and shield plate, Φ;
Vertical distance b/w C.G to the attachment point, y;

Horizontal distance b/w attachment point and CM center, x;
Distance b/w C.G of CM to the helicopter attachment point, r (or L);
Perpendicular distance from separation point to the sling tension, d.

A. Estimation of Mean angle during pendulum motion,

CM will undergo a pendulum oscillation during horizontal acceleration of helicopter. Mean angle of oscillation depends upon the acceleration of the helicopter.

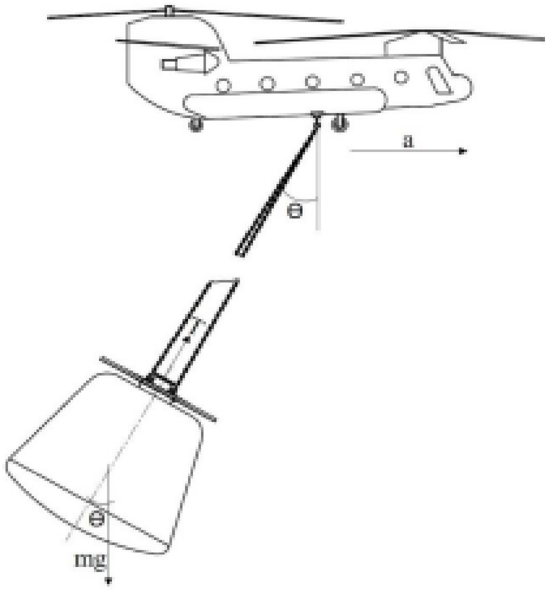

Figure 2: CM-FBS at mean position

Following equations can be made at mean position from the CM FBD. Suppose T is resultant sling tension. Applying equilibrium equations

$$\sum F_X=0,\ T\sin\theta = ma \qquad (1)$$

$$\sum F_Y=0,\ T\cos\theta = mg \qquad (2)$$

(1)/(2) gives,

$$\theta = \tan^{-1}\frac{a}{g} = 14°$$

B. Estimation of Time period of oscillation

A simple pendulum motion under gravity will oscillate with a time period of oscillation is given by,

$$t=2\pi\sqrt{\frac{L}{g}}$$

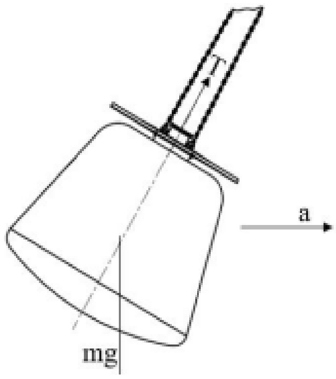

Figure 3: CM-FBC at mean position

For a simple pendulum placed in an accelerating body, time period of oscillation is given by,

$$t=2\pi\sqrt{\frac{L}{\sqrt{a^2+g^2}}} = 7.3s$$

(Since, resultant acceleration $\sqrt{a^2+g^2}$)
is

C. Estimation of maximum angular acceleration of the module

Since CM undergoes a pendulum motion it will have an angular acceleration which will vary harmonically. Maximum angular acceleration of the CM will be at extreme positions. It will be zero at mean positions.

Applying free body equilibrium equations to the system at the extreme position (Ref: Fig.4 and Fig.5)

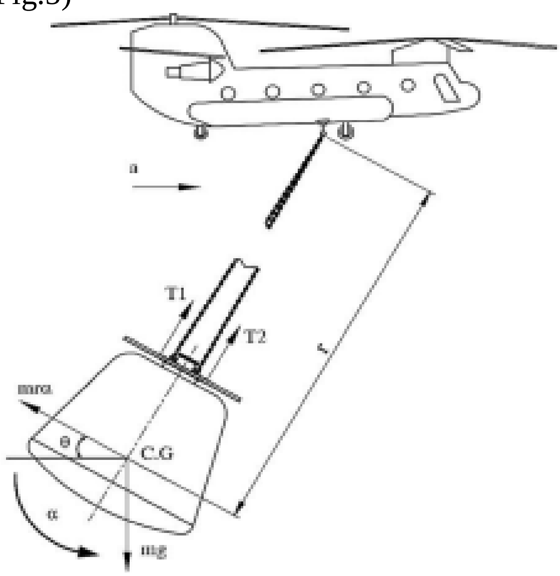

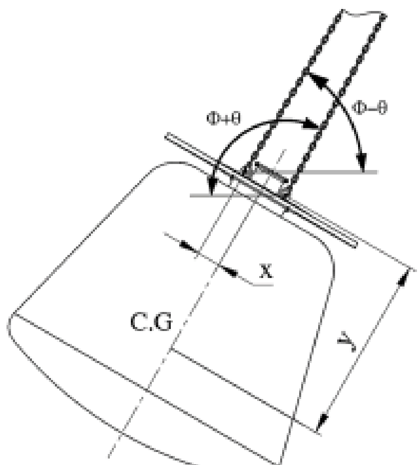

Figure 4: FBD at the extreme position Figure 5: CM-FBD at the extreme position

$$\sum M_{CG}=0,$$

$$-T_1\cos\emptyset * y + T_2\cos\emptyset * y - T_1\sin\emptyset * x + T_2\sin\emptyset * x = I_{CG} * \alpha$$

Rewriting the above equation

$$\alpha = \frac{(T_2-T_1)(y*\cos\emptyset+x*\sin\emptyset)}{I_{CG}} \quad (3)$$

$$\sum F_X=0,$$

$$T_1 \cos(\emptyset - \theta) - T_2 \cos(\emptyset + \theta) = ma + mr\alpha * \cos\theta \quad (4)$$

$\sum FY=0$,

$$T_1 \sin(\emptyset - \theta) + T_2 \cos(\emptyset + \theta) = mg - mr\alpha * \sin\theta \quad (5)$$

Solving equations (3), (4) and (5)

$\alpha = 10.2$ degree/sec^2, $T_1 = 25369$N and $T_2 = 27887$ N.

D. Estimation of maximum bending moment on the separation plane

Bending moment on the separation plane depends upon sling tension and its difference. Large difference in the sling tensions causes large bending moment and needs a high capacity separation system. Bending moment, M can be calculated as;

$$M = (T1-T2) * d$$
$$= (25369-27887) \times 0.254$$
$$= 640\text{Nm}$$

3. MSC ADAMS Analysis

The entire geometrical configuration is modelled and mass/inertia properties are assigned. Suitable connections are made between different bodies. Simulated for acceleration as mentioned (Ref: Fig. 4). Results parameters which are calculated above are plotted.

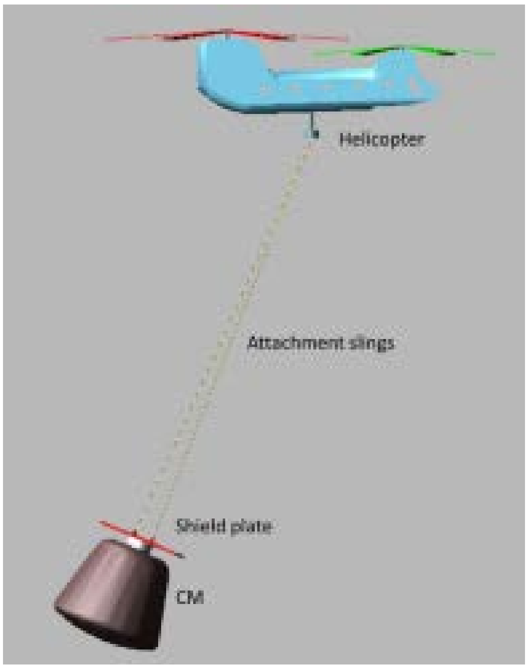

Figure 6: MSC ADAMS Model at extreme position

A. Mean angle during pendulum motion

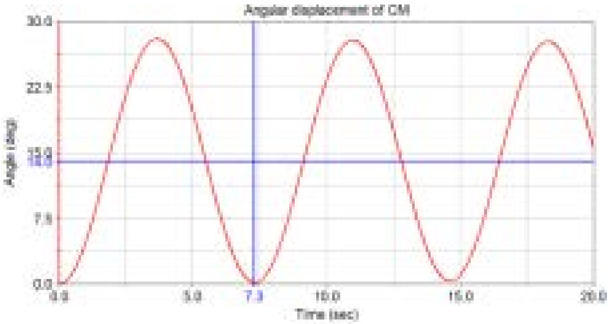

Figure 7: MSC ADAMS plot for angular displacement of model with time

From the Fig. 7,
Mean angle of oscillation = 14°

B. Time period of oscillation
From the Fig. 7,
Time period of oscillation = 7.3s.

C. Maximum angular acceleration of the module

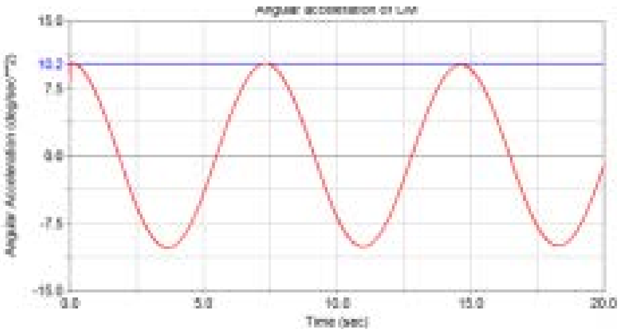

Figure 8: MSC ADAMS plot for angular acceleration of module with time

Maximum Angular acceleration happens at extreme position.
From Fig.8, maximum angular acceleration = 10.2 degree/sec^2

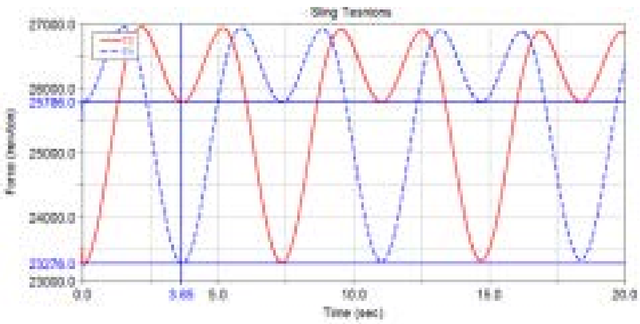

Figure 9: MSC ADAMS plot for sling tensions with time

From Fig. 9, at extreme positions sling tensions are,
T1 = 23276N and T2 = 25786N.

D. Maximum bending moment on the separation plane
From Fig.10 maximum bending moment on the separation plane is M= 642Nm

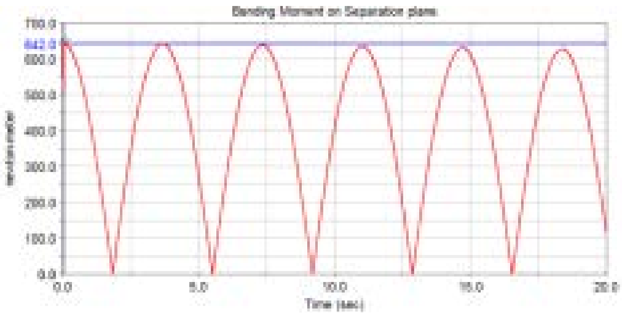

Figure 10: MSC ADAMS plot for BM on separation plane with time

4. Results

Parameter	Analytical	ADAMS
CM Angular displacement	14°	14°
CM Time period of oscillation	7.3s	7.3s
CM angular Acceleration n.	0.28 rad/sec^2	0.285rad/sec^2
Sling tensions at extreme point	T1=23576N T2=29554N	T1 = 23194 N T2 = 29956 N
BM on Separation plane	M=1.72kNm	M=1.76kNm

The measured parameters from MSC ADAMS are closely matching with calculated data using analytical method.

5. Conclusions

IADT is a major milestone in the development of parachute deceleration system for human rated missions. The predictions of dynamics of module underslung helicopter and the loads are extremely important for achieving this goal. Hence the effort is put to evaluate the same analytical method and the procedure is validated using MSC Adams software.

6. Acknowledgement

The accomplishment of IADT for Gaganyaan parachute system is a collective effort by Vikram Sarabhai Space Center, Human Spaceflight Center, Satish Dhawan Space Center, Aerial Delivery Research and Development Establishment, Indian Air Force and Indian Cost Guard. The authors wish to acknowledge the immense contributions made by IADT team members from the above centers

Development of Four Points Swivel for Aerostat

K K Katiyar
Aerial delivery Research and development
Establishment
DRDO
Agra
krishan_katiyar@adrde.drdo.in

Rajeev Jain
Aerial delivery Research and development
Establishment
DRDO
Agra

***Abstract* – Aerostat is basically tethered inflatable balloon fly at certain height and carries necessary payload for collecting the ground information and transmitting the same to a Defence unit. The aerostat has many potential advantages for intelligence, surveillance and reconnaissance (ISR) applications, such as threat identification and documentation, antiterrorism, border security, harbour & port security and loss prevention. Aerostat mainly consists of inflatable balloon, winch and mooring system, power management system, ground control station, tether and ground support systems. Tether is a flexible link between ground winch system and airborne balloon and connected to the balloon with the help of the swivel.**

The purpose of swivel is to de-couple the rotary motion of the aerostat balloon from tether. When the balloon of aerostat is raised to a desired height then heading of aerodynamic balloon is continuously changes due to wind direction. This causes the balloon to rotate continuously along the wind direction which is required to be decoupled from tether to avoid its strength loss and loss of payload data.

This paper presents the configuration of the swivel which can connect the four rigging lines of the balloon and curing cup arrangement for the end termination of the tether. This paper also covers design of various components of the swivel and its testing to simulate the actual condition. This swivel was also successfully tested during the deployment trials of aerostat.

1. Introduction

Swivel is the mechanical link between rigging lines of Aerostat and tether. The basic purpose of swivel is to decouple the rotary motion of balloon from tether. Swivel mainly consists of housing, thrust bearing, load cell and cup. Housing is used to house the all components of swivel. Cup is used for end termination of tether by curing the strength members with the help of suitable epoxy and hardener mixture. Thrust bearing is used for isolating the rotary motion of the balloon from tether and load cell is used to measure the actual load/lift of the balloon during the flight trials. The configuration of the swivel is given at Figure 1

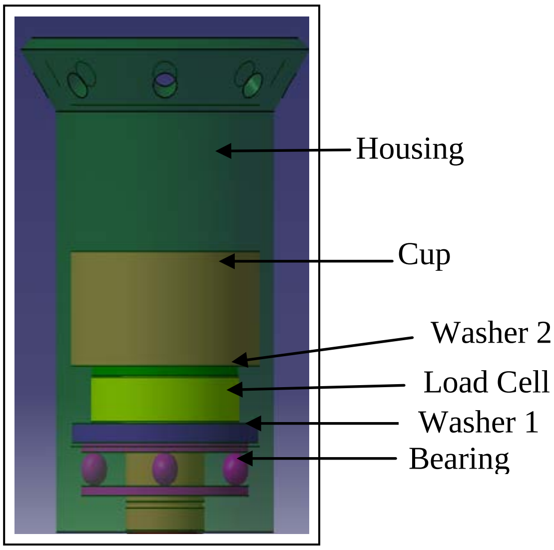

Figure 1: Configuration of swiwel

This swivel is used to connect the balloon with 04 confluence lines/rigging lines to tether. The Rigging lines of balloon are connected to the housing upper portion with the help of the shackles. Attachment of swivel with balloon is shown at Figure 2.

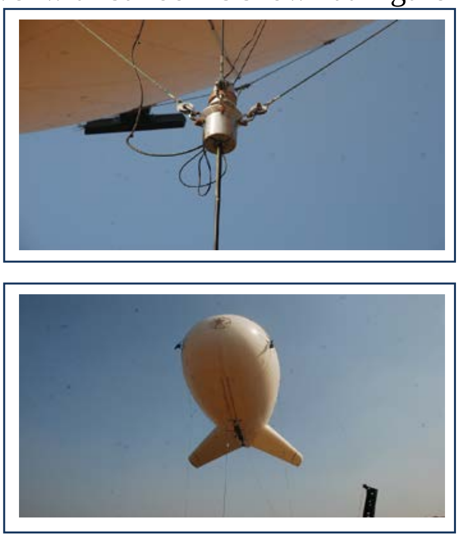

Figure 2: Attachment of Swivel with Balloon

2. Requirements

Important requirements of swivel in Aerostat are given;

(i) Provide a mechanical link between tether and rigging lines of balloon.
(ii) Decouple rotary motion of balloon from tether to avoid twisting in tether.
(iii) Provide mounting for connectors of electrical joint (power wire), fibre optical joint (fibre optical cable) and lightening down conductor.
(iv) To sustain load on tether

3. Design

The swivel is experiencing the lift generated by the balloon during flight trials. Swivel (housing) is designed on the basis of Max load of tether in worst wind condition.

Design load for swivel = Load factor * Max load on tether

A suitable load factor based on literature survey is considered for calculating the design load. Since the confluence lines of balloon are converging at confluence point with an angle from vertical, so, effect of angle has also been considered for calculation the design load.

A. Housing

Housing is the main body of the swivel and contains all components of the swivel. Housing of the swivel has been designed against tensile failure, shearing failure and tearing failure.

Area under failure section is calculated as follows:

Tensile Failure: The collar of the housing can be fail under tensile load of swivel. For tensile failure, minimum cross-sectional area of collar is calculated by subtracting area of collar under holes on collar which is used for connecting the four rigging lines of the balloon with the help of shackles.

Shearing Failure: The collar of the housing can also be fail under shearing load. The hole of the collar may double shear under the load of rigging lines. So, the shear area from the center of the hole to the edge of the collar has been considered in this paper.

Tearing Failure: The collar of the hole can also be fail under tearing load. For tearing failure cross-section area of the collar from edge of the hole to edge of the collar has been considered.

The stress in all modes was calculated by using the following formula

Stress = Load/Area under failure section

B. Cup

Cup is housed inside the housing of swivel and used for the end termination of the tether. One end of tether is terminated in cone shape space of cup by using Epoxy resin with suitable hardener.

Cup of the swivel will fail in shear mode. Minimum shearing area was calculated during the design of cup and shear stress is calculated by following formula:

Shear Stress = Load/Min shearing Area

C. Washer 1 & 2

Washer 1 & 2 is used on both side of load cell and made of hardened material so that lift load of the balloon can be properly transferred to load cell to measure the actual lift load. The thin collars of the load cell are in contact with both washers. washer will fail under crushing load and area of load cell collar has been considered for the design of the washer1 & 2.

D. Thrust Bearing

The thrust bearing is fitted at lower part of the housing which is used to decouple the rotary motion of balloon from tether. A suitable SKF make thrust bearing has been selected with 18000 kg static capacity and 6200 kg dynamic capacity for swivel.

E. Load cell

The load cell is placed over the thrust bearing along with washer 1 & 2 placed on the both side of the load cell. A Suitable hollow disc type load cell with measuring capacity of 11 Ton has selected for this swivel.

F. Summary of Design

S. No.	Part	Load Factor	Stress (Calculation) N/mm^2	Stress (FEM Analysis)
1.	Housing	2.25	325.15	406.5
2.	Cup	2.25	21.3	27.5

4. Testing of Swivel

Functional and load testing of the swivel have been carried to before its usage in deployment/flight trial of aerostat. Functional testing was carried out after integration of all components to check the free rotation of the swivel and proper functioning of thrust bearing. For load testing, a test fixture was developed to maintain the proper load angle to simulate the actual loading direction. Tensile load was applied on swivel using horizontal load testing machine. All required instruments were also attached to load cell of swivel during the testing to calibrate the load cell as well as to measure the load applied. Load testing of the swivel is given at Figure 3.

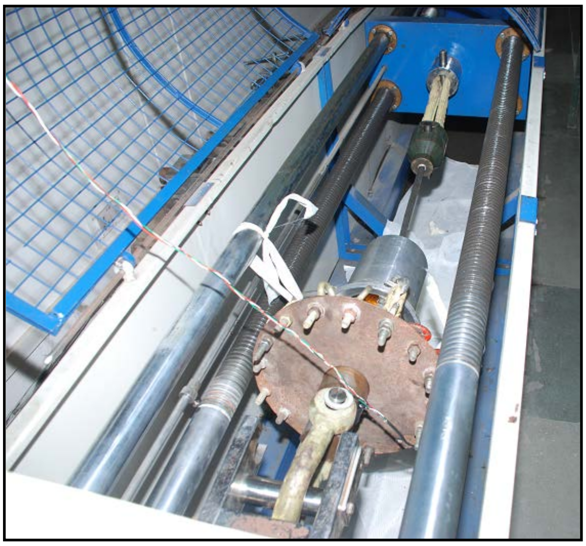

Figure 3: Load Testing of Swivel

5. Conclusions

04 Points swivel has been successfully developed for aerostat balloon with 04 confluence lines. This swivel was successfully tested in actual environment during aerostat flight trials. The real time monitoring of the lift generated by the balloon was done with this swivel during all flight trials.

6. Acknowledgement

The authors are grateful to Director ADRDE, Agra for giving this opportunity to publish this paper. Authors also would like to appreciate aerostat trial team for their valuable inputs provided for betterment of system.

7. Reference

[1] Sequeira, G., Bhandari, K., Wanjari, N., Kadam, S., “Design, Fabrication and Field testing of Winch for Aerostat”, Proceedings of National Seminar on Strategic Applications of Lighter-Than-Air (LTA) vehicles at High Altitudes (SALTA-07), 12th-13th October 2007, SASE, Manali.

[2] Airstar Aerostat System Final Site Support Equipment Maintenance Technical Manual As-F-9m 71 Meter Aerostat System January 2004 Tcom, L.P 7115 Thomas Edison Drive Columbia, Md 21046.

[3] Raina, A. A., Gawale A. C., and Pant, R. S., “Design, Fabrication and Field Testing of Aerostat

system", National Seminar on Strategic Applications of Lighter-Than- Air (L-T-A) Vehicles at Higher Altitudes, Snow and Avalanche Study Establishment, Manali, India, 12-13 October 2007.

Design & Development of Velocity Reduction Mechanism for Supersonic Release Article

Vipin Kr Verma
Aerial Delivery and Development Establishment
DRDO
Agra
Vipin_verma@adrde.drdo.in

Gunjan Kumari
Aerial Delivery and Development Establishment
DRDO
Agra

K D Diwakar
Aerial Delivery and Development Establishment
DRDO
Agra
kumar_dharmendra@adrde.drdo.in

Vivek Agrawal
Aerial Delivery and Development Establishment
DRDO
Agra

A K Saxena
Aerial Delivery and Development Establishment
DRDO
Agra

***Abstract* – Velocity Reduction Mechanism has been design & devolvement and qualified for supersonic release article which is required to slow down the safe splash speed of article. The velocity reduction mechanism system also successfully worked in flight test. This paper presents the application of Velocity Reduction Mechanism and its import article. The analytical estimate has also been compared with the experimental results. The experimental results are found to be in close agreement with the estimated value.**

Keywords–Velocity Reduction Mechanism, parachute

1. Introduction

Velocity Reduction Mechanism (VRM) i.e. Parachute system owing to its inherent advantage of lightweight, flexibility, compact storage and low cost finds wide application in a diverse field of paratroopers' parachute, store delivery, aircraft brake, UAV & space capsule recovery and as a stabilizer or decelerator for projectiles (Ref [1]-[4]). The maximum aerodynamic load during the opening of a parachute is a critical design parameter whenever there is a requirement of high-speed deployment. This criterion often limits the use of parachute at higher deployment speed and any effort to reduce opening load provide significant operational advantage. However, not much literatures have been published for deployment of VRM for supersonic release article. This paper describes the development of VRM. The physics of deployment of parachute has been studied in details and the deployment process has been divided into two main phases, viz., reefed phase in high speed and dis-reefed phase. The detailed mathematical model has been developed analytically for each phase. The opening load profile estimated analytically has been compared with the experimental data of the parachute system. The VRM consists of following sub-system and details are shown in Fig.1.

- Auxiliary parachute &Riser
- Pyro delay cutter
- Main parachute
- Pack cover & Para container

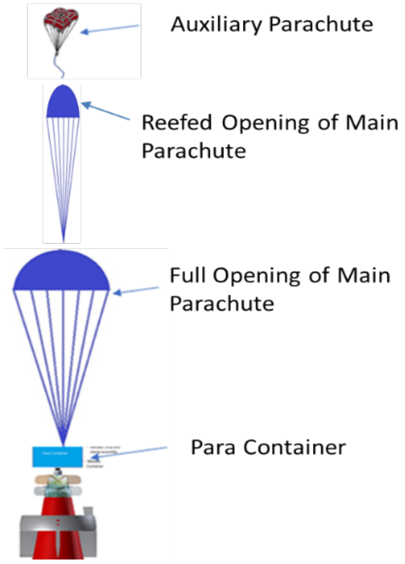

Fig 1: Details of VRM

2. Details Design of Velocity Reduction Mechanism

Two stage VRM having auxiliary parachute (spring loaded,) to extract the main reefed parachute. VRM has been design and development for required supersonic release of article. The interface between VRM & article is Release Mechanism. The vane type auxiliary Parachute with spring and Ring slot as a main Parachute with reefing system has been designed. The Reefing is a method of controlling the parachute drag area and opening loads during inflation. In a reefed parachute the skirt's inflated diameter is restricted by a reefing line threaded through a series of rings sewn along the skirt as shown in Fig.2. To allow the parachute to reach full inflation the reefing line is severed by a reefing line cutter.

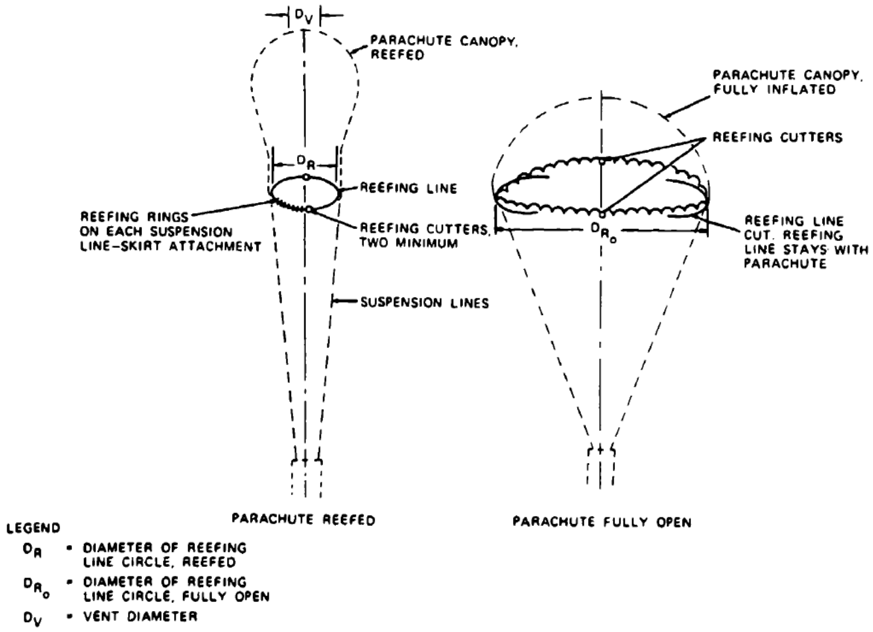

Fig 2:Details of Skirt Reefing System (ref.2)

A. Experimental Investigation of Aerodynamics Characteristics of VRM

Wind tunnel testing of VRM with & without article has been carried out to generate the aerodynamics Characteristics. The Schematic setup of VRM with article is shown in Fig. 3. The measured aerodynamics coefficients of Main Parachute of VRM with & with article are presented in Fig. 4, Fig.5 & Fig. 6 respectively.

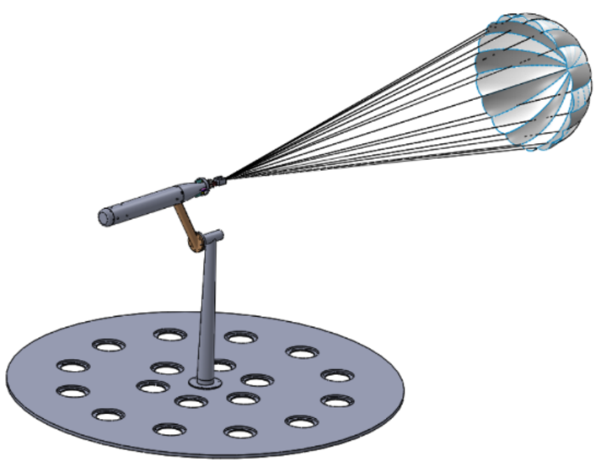

Fig 3:Schematic setup of VRM with article

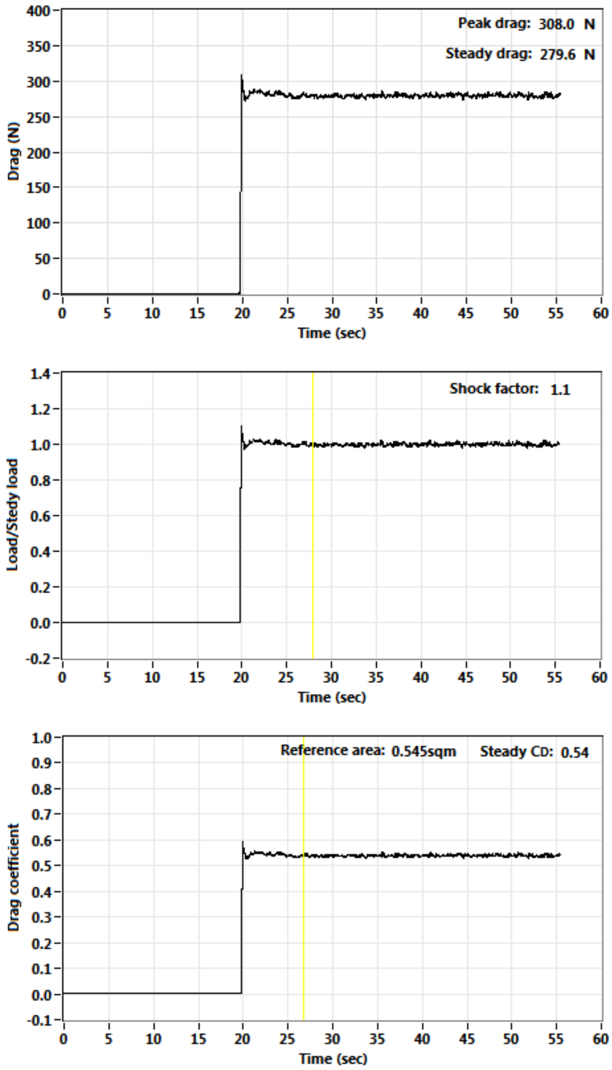

Fig 4: Wind Tunnel Results of VRM without article

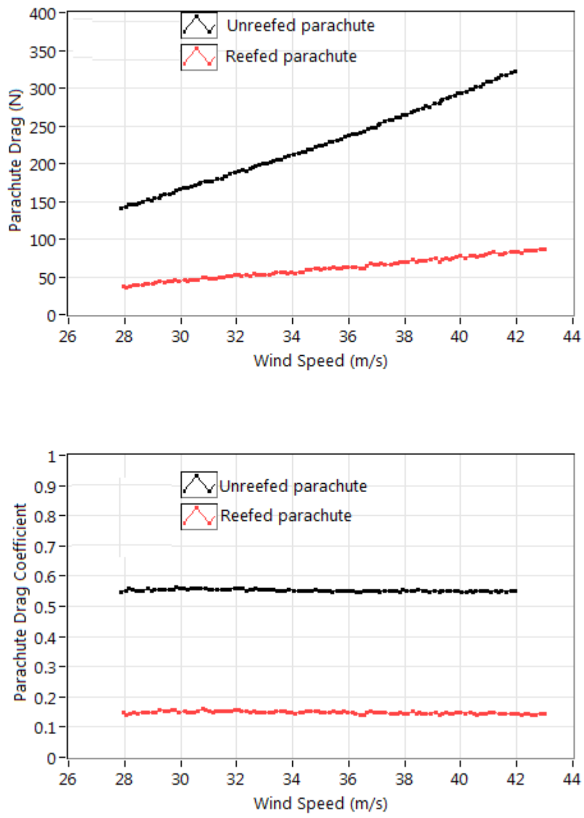

Fig 5: Aerodynamic characteristics comparison of reefed and unreefed VRM with article

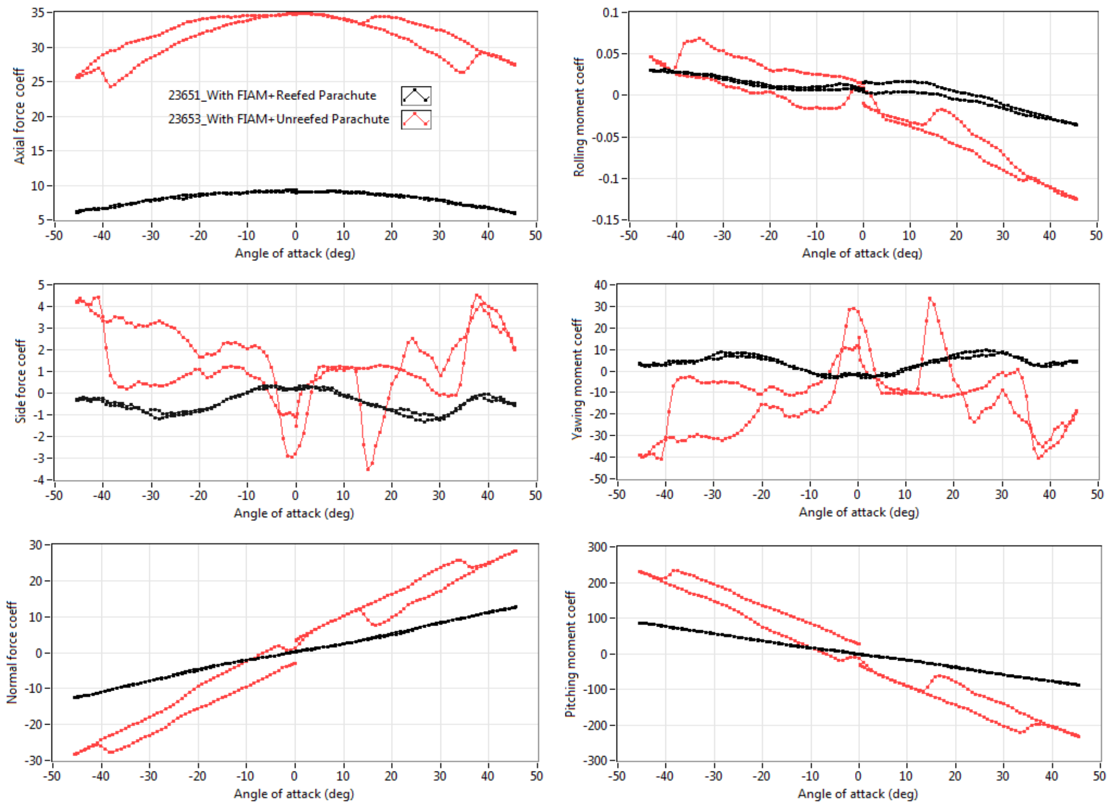

Fig 6: Aerodynamic characteristics Article with VRM

3. Results, validations and discussions

After designing of parachute system several qualification tests were carried out to prove the system. The VRM system has been qualified in flight air drop for proving the deployment sequence and high speed trial in Rail Track Rocket Sled for proving of Extraction of Main Parachute by Auxiliary Para, Integrity & Efficacy of Reefing System, Measurement of Reefed & Dis-reefed Opening Shock of Parachute and structural integrity of the VRM. Effect of transonic region presented in Fig 7 elucidates that the reduction of Cd of parachute in transonic region were also validated during qualification of VRM. The results of qualification are presented in Fig. 8 & Fig.9. The opening load of a parachute is dependent upon total kinetic energy of the system during the deployment phase which a function of payload mass and deployment speed. After qualification the VRM system was successfully performed in flight test as presented in Fig.10.

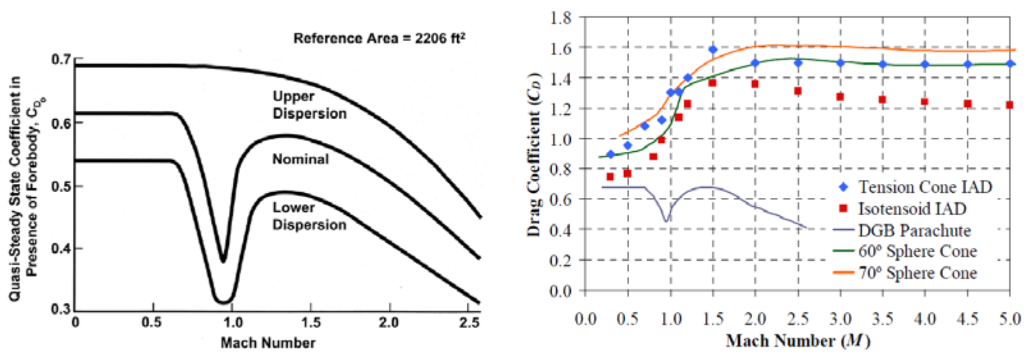

Fig 7: Variation of Aerodynamic characteristics during Transonic region [5]

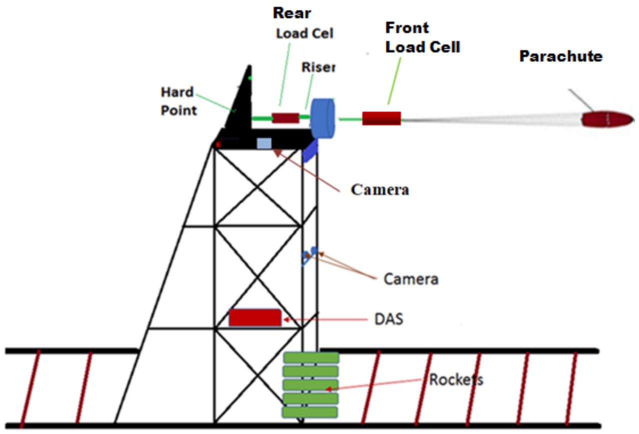

Fig 8: Test Configuration for RTRS test

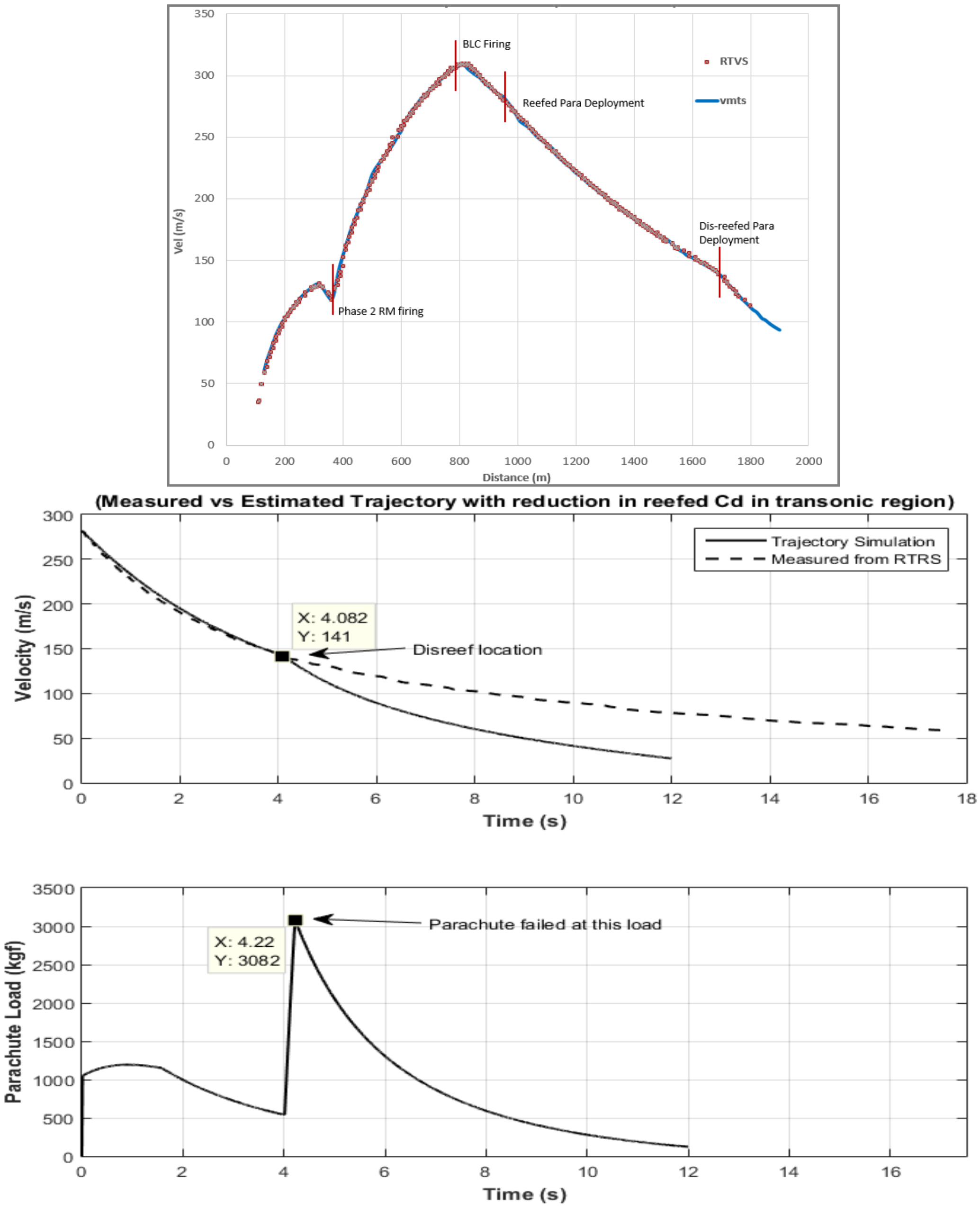

Fig 9: Measured Velocity Profile with Distance

Fig 10: Flight test of VRM System [6]

4. Conclusion:

The estimated results are validated with the experimental results during qualification tests of VRM. The measured opening load is found to be in close agreement with the estimated opening load. The design features of VRM system for Supersonic Release Article are validated during various test. The system has gone regress qualification testing followed by flight test.

5. References:

[1] E. G. Ewing, H. W. Bixby, T. W. Knacke, ‘Recovery System Design Guide’, Technical Report AFFDL-TR-78-151 (Dec 1978)
[2] T. W. Knacke, ‘Parachute Recovery System Design Manual’, 1992
[3] S. F. Hoerner, ‘Fluid-Dynamic Drag’, Bricktown New Jersey, 1965.
[4] ‘Performance and Design Criteria for Deployable Aerodynamics Decelerators’ TR – ASD TR - 61-576. 1963.
[5] Juan R Cruz and J s Lingard, ‘Aerodynamic Decelerators for Planetary Exploration: Past, Present, and Future’, American Institute of Aeronautics and Astronautics.
[6] Ian G. Clark, Allison L. Hutchings, Christopher L. Tanner, Robert D. Braun, ‘Supersonic Inflatable Aerodynamic Decelerators for Use On Future Robotic Missions to Mars’, IEEE.
[7] https://indianexpress.com/article/explained/explained-what-is-smart-test-and-why-it-matters-6705811/

Biaxial Testing of Textile Fabrics

Imtiaj Khan
Aerial delivery Research and development Establishment
DRDO
Agra
imtiaj_khan@adrde.drdo.in

Kamlesh Kumar
Aerial delivery Research and development Establishment
DRDO
Agra

***Abstract* – Aerostat and airship systems are based on lighter than air technology. These provides elevated platform for mounting payloads. Inflatables radome is inflated cover for the protection of ground-based sensors. Parachutes are used for safe recovery of airborne systems. During operation they are exposed to harsh variable environmental conditions. Continuous degradation of textile parameters occurs due to continuous environmental exposure. Comprehensive testing with accurate methodology (prior to manufacture) is very important from design point of view. Results obtained by Uniaxial Textile testing machine are conservative as they do not simulate the actual loading conditions. Material properties obtained from the analysis are input to the Finite element analysis, hence accuracy of estimation is very important from design point of view.**

Present concepts will simulate the actual loading conditions. Solid modelling of concepts was carried out using CATIA V5 software. This paper discusses the advantage/disadvantages of each concept. Best concept can be selected based on the design criteria.

Keywords– biaxial testing, Digital image correlation, cruciform specimen

1. Introduction

Parachutes and Inflatable's i.e. Aerostat, Airship, Radome (Figure 1) are made up of textile fabrics. They are loaded in bi-axial direction. Material used for fabrication is highly anisotropic in nature. Parachutes are fabricated by stitching and sealing techniques. Testing of joints and seams poses serious challenge to the designers. These structures experiences internal pressure, aerodynamic loads, inertia loads, buoyancy loads etc.

In the past Abu-Farha et al. [1] developed gear-controlled fixture for obtaining biaxial deformation at different preselected ratios. The different ratios are provided by utilizing different gear sets in testing machine. Sadegh et al. [2] developed a testing apparatus having four linkages and a hydraulic system. Variable load ratios can be applied. C Mahender et al. conceptualized a apparatus for stretching of dielectric elastomer. The apparatus comprises of four sliding bars connected to power screw through umbrella rod. Concept presented here comprises of a data acquisition system based on DIC. Concept proposed is simple from manufacturing aspect and parts are less in numbers. This fixture can be used directly on existing uniaxial textile testing machines.

Uniaxial textile testing machine used for testing is shown in Figure 2. Test sample is mounted on the machine twice to evaluate the material properties in warp and weft direction respectively. Simultaneous loading of warp and weft directions of textiles is essential for accurate structural analysis. To overcome this difficulty present concept was conceptualized

Figure 1: Aerostat and Parachute System

Figure 2: Textile Testing Machine

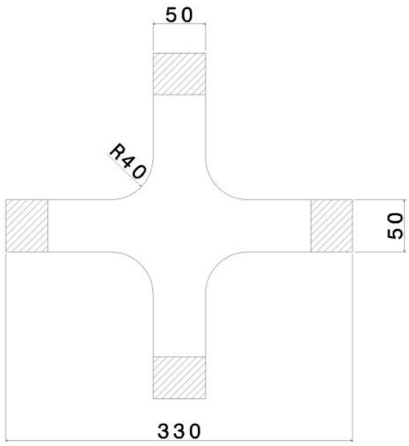

Figure 3: Cruciform test specification

2. Development of Specimen

Bi-axial test Specimen design parameters are as follows:

(i) Least stress concentration
(ii) Low manufacturing cost
(iii) Ease of mounting sample on machine
(iv) Accuracy of test data with other methods
(v) Wide range of achievable stress states

Cruciform specimen represents direct approach for obtaining true biaxial stress states, and consequently this method has gained wide acceptance. Basic dimensions (in mm) were selected from a specimen reported in literature [3] and shown in Figure 3.

3. Data Measurement and Acquisition Techniques

Digital image co-location (DIC) is a strain measurement technique that works on the principle of capturing a series of images and analyzing them. A typical setup includes a camera and data acquisition system to capture the image and conduct post test analysis. Present method provides the full characterisation of 2D deformation i.e. length and width under load [4].

To capture the deformation pattern, speckle with suitable surface colour paint [5] is done on the surface of test specimen. The processed data is viewed for strain and displacement in 2D axis. Sometimes the surface pattern of fabric is sufficient to apply any additional marking. The number of images captured during a test depends on time, speed, and the sample itself, but 50 to 100 images are usually adequate. The image is then split into small subsets and the patterns within each subset of subsequent images are compared to the reference image, and displacements are calculated. DIC strain maps of a material approaching failure are shown in Figure 4.

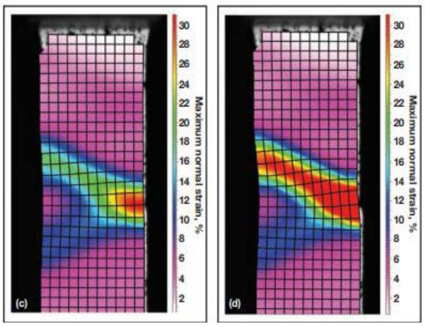

Figure 4: DIC strain maps of a material approaching failure

Following output variable are obtained by DIC analysis:

u - horizontal displacement of this point
v - vertical displacement of this point
εxx - strain in horizontal direction
εyy - strain in vertical direction
$\varepsilon 1$ - major principal strain
$\varepsilon 2$ - minor principal strain

4. Proposed Machine Concepts

A. Concept 1:

This comprises of a base plate and a top plate, with four arms to allow the transformation of vertical displacement of the top plate via loading, into horizontal displacement in the plane of the specimen, the plates have also been provided with a hole in the centre for camera.

The cruciform specimen is first properly fitted into the gripping mechanism (Figure 5) at the four joints on the arms. The load is applied on the top plate, which in turn makes the arms move outwards in the plane of the specimen, pulling the arms and providing a strain in the specimen, which will be noticed in the gauge region of the specimen. The DIC camera records the required data until failure. Data collected is image processed used to obtain the full field strain of the material specimen under biaxial stress.

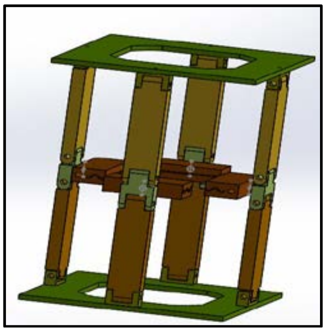
Figure 5: Concept 1

B. Concept 2

This design is conceptualized as an extension to the first Concept, keeping in view the other design parameters i.e. ease of manufacture, material cost, quantity of material required, etc.

Mechanism comprises of a top and a bottom plate, attached to each other via four arms having two metal bars, which are connected by a metal rod. The gripping mechanism (Figure

6) is placed on this rod. This helps us save costs of production of the holder joint discussed in the previous Concept, also enabling us to use slimmer rods.

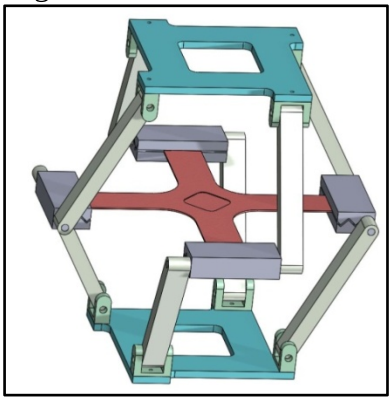

Figure 6: Concept 2

C. Concept 3

Mechanism consists of four arms being operated using hydraulic actuators (Figure 7). The frame has been designed as a rectangular hollow build to support the arms in place.

Each arm consists of a gripping mechanism, where one of the arms of the cruciform material specimen is fixed. These gripping mechanisms are, in turn, connected to the moveable pistons of the hydraulic actuator. All four of the actuators are connected to a control mechanism, which facilitates proper distribution of the load on each arm, and at the same time enables us to vary and apply different loading ratios in the perpendicular directions, which is one of its biggest advantages.

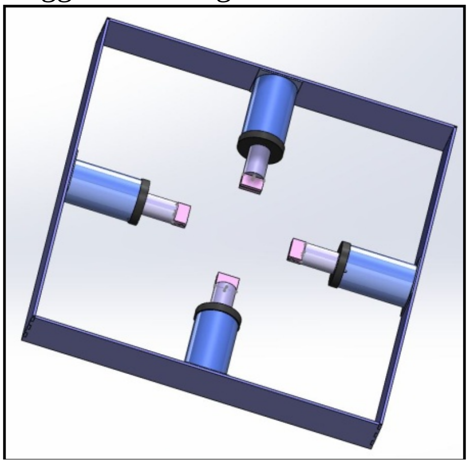

Figure 7: Concept 4

D. Concept 4:

Keeping the advantages and short-comings of the previous Concepts in mind, the final Concept (Figure 8) was developed. It comprises of a cross shaped base, on which four blocks are arranged (one on each arm), to slide. All four of these arms are supported by walls, to ensure a fixed linear path for the movement of the block. These four blocks serve as holders for the gripping mechanisms, into which an arm of the cruciform shaped specimen was fixed. Holders were also placed on the top of these blocks, to connect an arm bar which rotates on these holders, and is connected to the top plate on the other end. This results in a slider-crank-slider mechanism, with the top plate serving as the first slider, the arms as the cranks, and the holder blocks as the second sliders. Holes large enough to ensure a clear view for the camera of the DIC setup were cut in both the top plate, as well as the base plate, which also helps save up on material used, and lowers the weight of the setup.

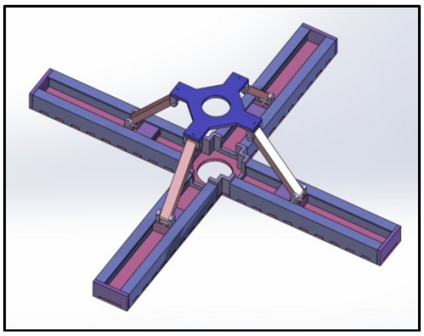

Figure 8: Concept 4

5. Advantages and disadvantages

A. Concept 1

Advantages

(i) The volume required for the mechanism is less compared to others.
(ii) Equal load distribution due to symmetry
(iii) Parts are easy to manufacture and assemble.
(iv) Less material is required, low cost
(v) A purely mechanical system has been developed

Disadvantages

(i) Friction between parts might result in inaccuracies and errors.
(ii) High loads aren't possible.

B. Concept 2

Advantages

(i) Less space required
(ii) Amount of material required is less than the Concept 1
(iii) Low cost. Ease of manufacturing
(iv) A purely mechanical system
(v) Symmetric loading on system

Disadvantages

(i) Structure's strength is less compromised than before, but in controllable levels
(ii) A biaxial load ratio other than 1:1 is not possible.
(iii) Errors have to rectified keeping friction and other mechanical restraints
(iv) A biaxial load ratio other than 1:1 is not possible

C. Concept 3

Advantages

(i) Biaxial loading with different load ratios is possible
(ii) The system is easy to control
(iii) Heavy loads in the range of 500 kN are possible

Disadvantages

(i) cost increases, hydraulic system along with control system is required
(ii) simultaneous control of all arms makes operation difficult
(iii) Larger space is required for the setup

D. Concept 4

Advantages
- (i) Can take heavy loads without failing or compromising rigidity
- (ii) Space required might be more than the first two setups
- (iii) Symmetric load distribution. Centre of the specimen have minimum shift
- (iv) A purely mechanical system has been developed

Disadvantages
- (i) Amount of metal required is more, since the number and size of parts has increased
- (ii) High cost as compared to Concept 1 & 2.
- (iii) Space required is more
- (iv) Frictional errors need to rectified
- (v) Load ratio variation is not possible

6. Comparison based on Design Drivers

The above presented four concepts are compared based on the major consideration parameters

S. No.	Design Drivers	Concepts			
		1	2	3	4
i	Fit	4	4	2	3
ii	Slip	2	2	2	3
iii	Cost	3	4	2	3
iv	Material	3	4	2	3
v	Rigidity	2	2	4	4
vi	Load Allowance	3	2	4	4
vii	Total	17	18	16	20

The table helps us in finalizing the most feasible concept for the application.

7. Conclusions

Concept to estimate Bi-axial material properties of textile fabrics evolved. Present method eliminates use of costly Textile testing machines. Also, this technique can be used for any material i.e Plastics, metals, composites, rubber, foam, textiles etc. Concepts were compared based on design parameters i.e. fit, slip tendencies, costs, material required, and load allowance.

Although the presented models establish a viable and cost-effective method for the biaxial testing of materials, there still exists scope for improvement. This work can be further be extended to include the life estimation studies of the fabrics, which in turn will play an important role in the determination of the life cycle of the Inflatable's and parachutes.

8. Reference

[1] Abu-Farha et al. Uniaxially– driven controlled biaxial testing fixture Patent no. US, 712, 379 B2 dated May 11, 2010.

[2] Sadegh et al. Biaxial and Shear testing apparatus with force controls Patent no. US 7,204,160 B1 dated Apr. 17, 2007.

[3] Cruciform Specimen Design for Biaxial Tensile Testing of SMC by Juliane Lang, Anton Helfrich, Thomas Seelig, Thomas Böhlke J. Compos. Sci. 2018, 2(1).

[4] D.W. Lloyd, D.G. Neilly and D.B. Brook, Strain measurement in fabrics prt I: general considerations and the development of an extensible strain sensor, RJTA vol. 5 No.1

[5] Allison L. Hutchings, Experimental determination of material properties for Inflatable Aeroshell structures, Georgia Institute of Technology, USA

Development of Slider Reefing Mechanism for Reduction of Opening Load of Round Parachute

Ravi Krishna
Aerial Delivery and Development Establishment
DRDO
Agra
ravi_krishna@adrde.drdo.in

Kamal S Nikhurpa
Aerial Delivery and Development Establishment
DRDO
Agra
kamalnikhurpa@adrde.drdo.in

K D Diwakar
Aerial Delivery and Development Establishment
DRDO
Agra
kumar_dharmendra@adrde.drdo.in

A K Saxena
Aerial Delivery and Development Establishment
DRDO
Agra

Abstract **– Slider reefing system is effective in significantly reducing opening load of a ram air parachute. Though slider reefing has been in use for ram air parachute system, it is rarely used in the case of a round parachute. This paper presents the application of slider reefing and its impact on the opening load of an extended skirt round parachute. A mathematical model has been developed and opening load has been estimated analytically for both with and without slider configuration. The analytical estimate has also been compared with the experimental results. The experimental results are found to be in close agreement with the estimated value.**

Keywords: Slider reefing, round parachute, trajectory, opening load

1. Introduction

Parachute system owing to its inherent advantage of lightweight, flexibility, compact storage and low cost finds wide application in a diverse field of paratroopers' parachute, store delivery, aircraft brake, UAV & space capsule recovery and as a stabilizer or decelerator for projectiles (Ref [1]-[4]). The maximum aerodynamic load during the opening of a parachute is a critical design parameter especially in the case of paratroopers' application whenever there is a requirement of high-speed deployment during an emergency. The opening load for the paratrooper's parachute should be well below the human tolerance limit to avoid any injury. As per widely accepted norms, the maximum g-load due to parachute should be below 5g for regular para jump and below 16g for a limited duration during emergency condition (Ref [6] – [9]). This criterion often limits the use of parachute at higher deployment speed and any effort to reduce opening load provide significant operational advantage. Slider reefing mechanism has been widely used in gliding parachute as method of controlled inflation and reducing opening load (Ref [9]). The added advantage of slider reefing system is that it works completely on aerodynamic forces and there is no additional requirement of electro-mechanical triggering mechanism. However, not much literatures have been published for slider reefing applied to non-gliding round parachute system as a mechanism to reduce opening load. This paper describes the slider reefing mechanism applied to non-gliding round parachute system as an effective means of reducing opening load. The physics of inflation of parachute has been studied in details and the inflation process has been divided into three main phases, viz., Slider up phase, Canopy expansion phase and Slider down phase. The detailed mathematical model has been developed analytically for each phase to arrive at time dependent drag area model. The mathematical model has been incorporated into force-time two-dimensional trajectory simulation model to obtain time dependent load profile of inflating parachute. As a parallel approach, parachute prototypes have been fabricated and airdrop tested. The opening load profile estimated analytically has been compared with the instrumented load cell data fixed between the riser and payload of the parachute system. The flight tests have been conducted for a range of payload mass and drop speed and compared with analytical estimates. The analysis shows significant reduction of up to 40% in the opening load of the parachute with slider reefing mechanism as compared to no slider configuration. The database hence generated provide significant information about the behavior of non-gliding parachute under slider reefed condition and can be effectively used in wide range of applications.

2. Numerical formulations for estimation of Trajectory

The numerical formulation trajectory calculation is based on point mass model as presented below:

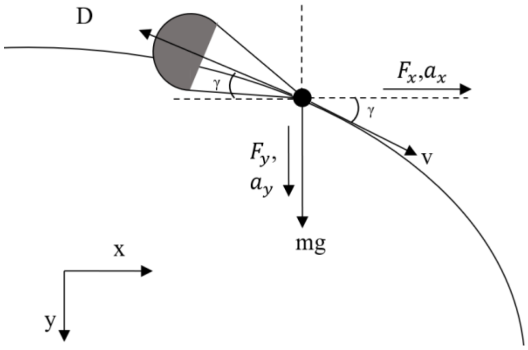

Fig 1: Free body diagram for point mass trajectory calculation

A. Governing Equations:

Resolving Forces along x direction:

$$F_x = -D\cos\gamma = \mathrm{ma}_x = m\frac{dv_x}{dt} \quad \text{.......(1)}$$

$$\therefore \quad \frac{dv_x}{dt} = -\frac{C_D \rho v^2 S\cos\gamma}{2m} \quad \text{.......(2)}$$

Resolving Forces along y direction:

$$F_y = mg - D\sin\gamma = \mathrm{ma}_y = m\frac{dv_y}{dt} \quad \text{.......(3)}$$

$$\therefore \quad \frac{dv_y}{dt} = g - \frac{C_D \rho v^2 S\sin\gamma}{2m} \quad \text{.......(4)}$$

Here, $v^2 = {v_x}^2 + {v_y}^2$

And $\gamma = \tan^{-1}\left(\frac{v_y}{v_x}\right)$

B. Numerical Solution using Runge-Kutta Method

Initial condition at t = t_o, $v_x = v_{xo}$ and v = v_{yo}.

Let time step, $\Delta t = h$, change in velocity $\Delta v_x = p,\ \Delta v_y = q$.

Let $$f_x(v_x, v_y) = -\frac{C_D \rho ({v_x}^2 + {v_y}^2) S\cos\gamma}{2m} \quad \text{.......(5)}$$

And $$f_y(v_x, v_y) = g - \frac{C_D \rho (v_x{}^2 + v_y{}^2) S \sin\gamma}{2m} \quad \text{.......(6)}$$

Applying Runge-Kutta method to evaluate change in velocity after time step of ‘h’ we have:

$$p_1 = hf_x(v_{xo}, v_{yo})$$

$$q_1 = hf_y(v_{xo}, v_{yo})$$

$$p_2 = hf_x(v_{xo} + \frac{1}{2}p_1, v_{yo} + \frac{1}{2}q_1)$$

$$q_2 = hf_g(v_{xo} + \frac{1}{2}p_1, v_{yo} + \frac{1}{2}q_1)$$

$$p_3 = hf_x(v_{xo} + \frac{1}{2}p_2, v_{yo} + \frac{1}{2}q_2)$$

$$q_3 = hf_y(v_{xo} + \frac{1}{2}p_2, v_{yo} + \frac{1}{2}q_2)$$

$$p_4 = hf_x(v_{xo} + p_3, v_{yo} + q_3)$$

$$q_4 = hf_y(v_{xo} + p_3, v_{yo} + q_3)$$

Hence,

$$v_{x1} = v_{xo} + \frac{1}{6}(p_1 + 2p_2 + 2p_3 + p_4) \quad \text{.......(7)}$$

$$v_{y1} = v_{yo} + \frac{1}{6}(q_1 + 2q_2 + 2q_3 + q_4) \quad \text{.......(8)}$$

Equation (7) and equation (8) gives updated value after time step ‘h’. This becomes the initial condition for next iteration.

C. Drag area variation

The drag area varies with time due to changing shape of the parachute during inflation. The estimation of drag area vs time contribute significantly to the calculation of opening load during inflation of the parachute. In order to estimate the drag area vs time, it is important to understand the behaviour of canopy during inflation. The inflation process is mainly categorized into three phases as described below:

<table>
<tr>
<td>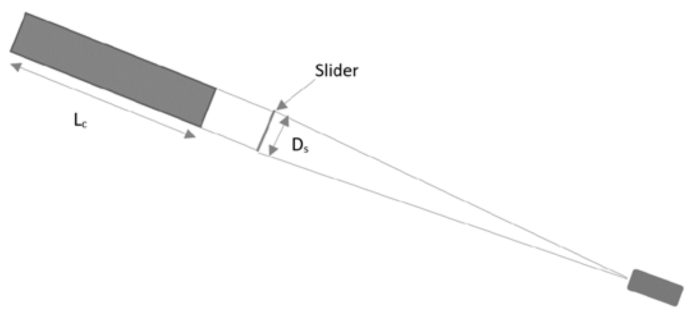
</td>
<td>Stage I: Slider up
• Parachute line stretch and inflation starts
• Slider is at topmost location
• Airflow into the canopy through netted slider. Volumetric flow of air is given by:
$$Q = \frac{kA_s}{\mu L}\Delta p$$
(k: fabric permeability, A_s: Slider area, μ: dynamic viscosity, L: Slider thickness, Δp: differential pressure)
• Stage I ends till canopy takes cylindrical shape</td>
</tr>
</table>

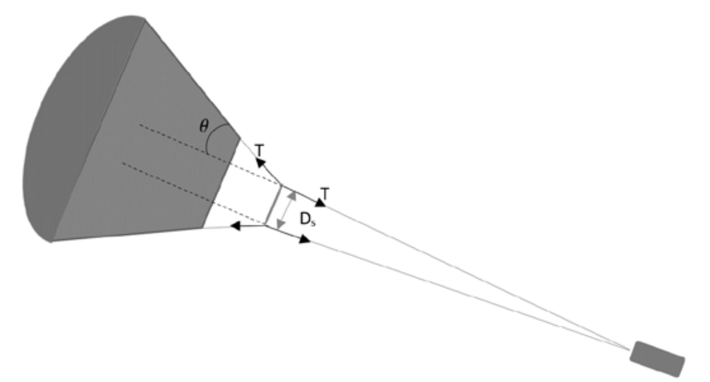	**Stage II: Canopy expansion** • The canopy further expands sideways and takes truncated cone shape • Slider remains at topmost point due to excess drag force $Drag_{slider} > T(1 - cos\theta)$
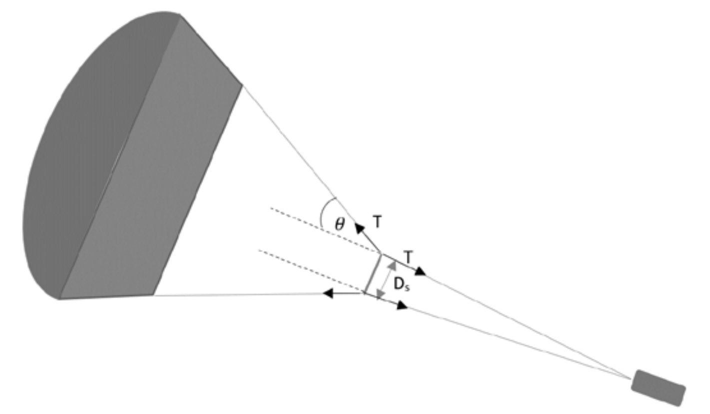	**Stage III: Slider down phase** • The canopy further expands sideways and takes truncated cone shape. • The resultant downward force due to line tension is greater than drag force on slider $Drag_{slider} < T(1 - cos\theta)$ • This results in sliding down of canopy followed with full inflation.

Ref. [1] & [2] provides C_DS vs time for different canopy types as shown in Fig 2.

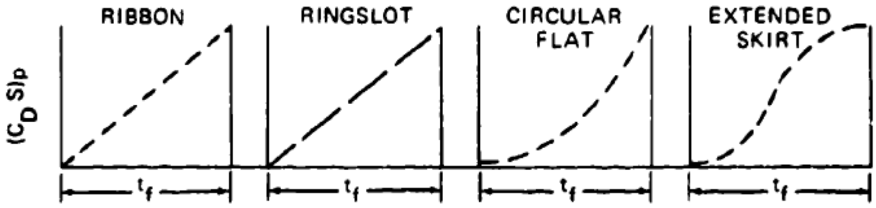

Fig 2: Drag area vs inflation time for different types of parachutes

The statistical data for the C_DS vs time variation for slider reefed Extended Skirt canopy is not available. Hence, the drag area variation has been obtained from mathematical modelling of stages of inflation as well as correlation with airdrop trial video of slider reefed extended skirt parachute (Fig 3).

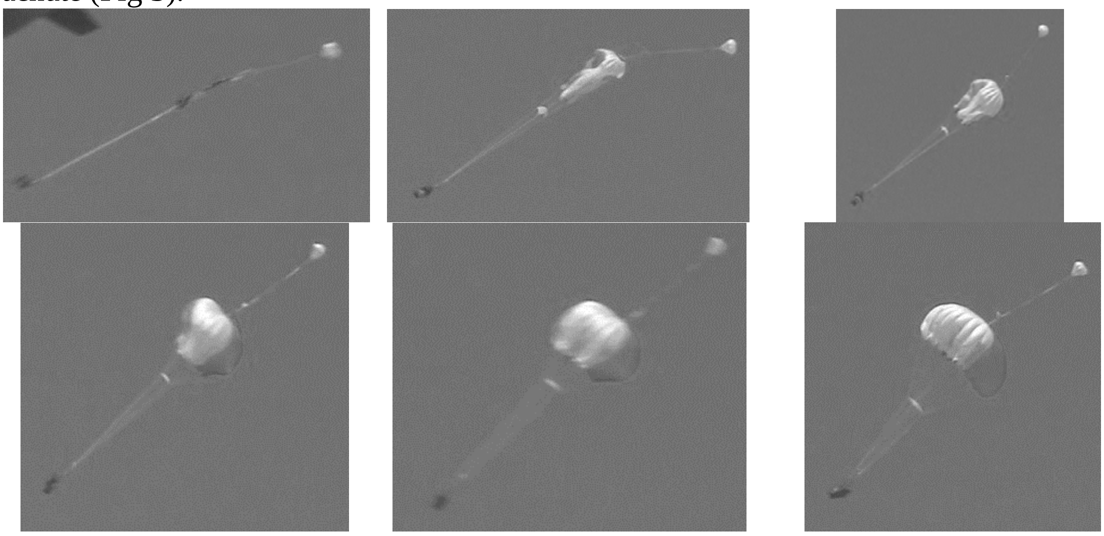

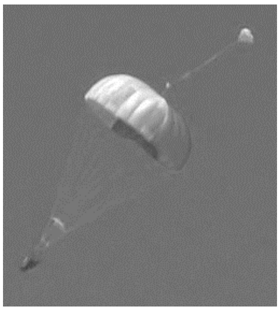

Fig 3: Stages of reefed extended skirt parachute during airdrop trial

The derived drag area variation for 'reefed' extended skirt parachute has been compared with 'un-reefed' extended skirt parachute based on modelling described in Ref [1] & [2]. The drag area variation with time is further made non-dimensional using curve fitting algorithm as formulated below and presented in Fig 4:

$$C_D S = a1 * \sin(b1 * t_f + c1) + a2 * \sin(b2 * t_f + c2)$$

Where, a1 = 1.134; b1 = 2.846; c1 = -0.4058; a2 = 0.6807; b2 = 4.251; c2 = 2.438;

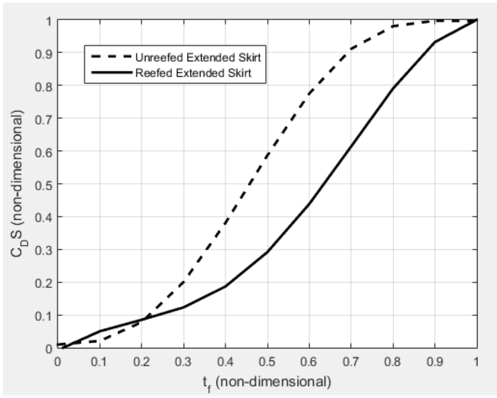

Fig 4: Drag area vs time comparison of reefed and un-reefed extended skirt parachute

The variation in drag area vs t_f is modelled in trajectory simulation after suitable scaling to match the current system.

3. Results, validations and discussions

The opening load of a parachute is dependent upon total kinetic energy of the system during the deployment phase which a function of payload mass and deployment speed. A comparison of opening load estimation for with-slider and without slider configuration as a function of kinetic energy is presented in Table 1:

Table 1. Comparison of opening load for with and without slider configuration and measured load

Trials	**Kinetic Energy = $\frac{1}{2}mv^2$ (KJ)**	**Calculated Opening Load (N)**		**Measured Opening load (N)**
		No Slider	**Slider**	
Test – I	267	7915	4900	5064
Test – II	300	8957	5234	5175
Test – III	380	12134	7093	6597

It can be observed from Table 1 that the opening load due to slider reefing configuration is reduced by around 40%. A typical comparison of measured load profile vs estimated load profile is presented in Fig 5.

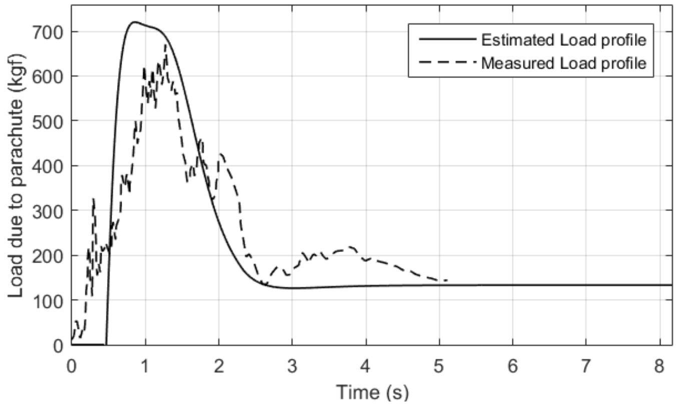

Fig 5: Comparison analytical data with the measured data

Large number of airdrop trials have been conducted for different mass and deployment speed conditions (Ref [10] – [13]). Opening load vs kinetic energy is presented in Fig 6 for measured vs estimated opening load.

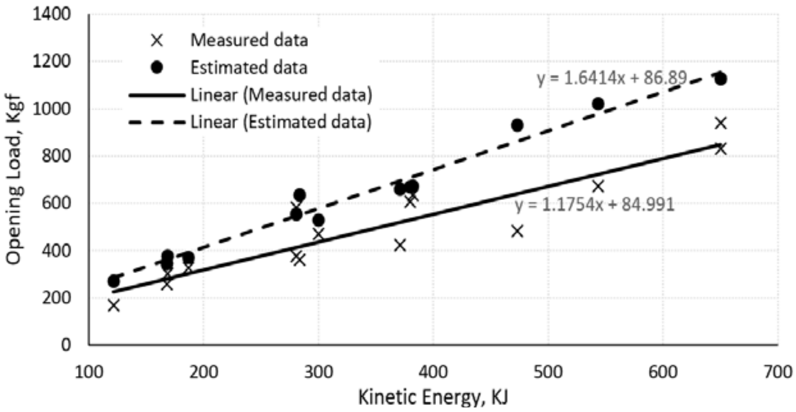

Fig 6: Plot of experimental and calculated opening load vs kinetic energy

The mathematical model predicts marginally higher opening load as compared to measured value.

4. Conclusion

A mathematical model for slider reefed extended skirt round parachute has been developed. The model has been validated with the experimental results using instrumental airdrop tests. The measured opening load is found to be in close agreement with the calculated opening load. The analytical estimates for with and without slider configuration shows significant reduction in the opening load which allows for use of slider reefing system in round parachute for higher deployment speed applications.

5. References:

[1] E. G. Ewing, H. W. Bixby, T. W. Knacke, 'Recovery System Design Guide', Technical Report AFFDL-TR-78-151 (Dec 1978)

[2] T. W. Knacke, 'Parachute Recovery System Design Manual', 1992

[3] S. F. Hoerner, 'Fluid-Dynamic Drag', Bricktown New Jersey, 1965.

[4] 'Performance and Design Criteria for Deployable Aerodynamics Decelerators' TR – ASD TR -61-576. 1963.

[5] Maj. Gen Harry G. Armstrong, USAF (Ret.), Aerospace Medicine, The Williams & Wilkins Co., 1961. Page 423-425.

[6] Alice M. Stoll, Human Tolerance to Positive G as Determined by the Physiological End Points.

[7] F. Latham, “A Study in Body Ballistics: Seat Ejection” Proc. Roy. Sec. 197:121-139, 1957.
[8] William R. McKenney, “Human Tolerance to abrupt accelerations: A summary of the literature”, Dynamic Science Report 70-13, May 1970.
[9] J. Stephen Lingard, ‘Precision Aerial Delivery Seminar Ram-Air Parachute Design’, 13th AIAA Aerodynamic Decelerator Systems Technology conference, May 1995.
[10] “Trial # 1 & 2” Report no. DRDO-ADRDE-P8I-EEPSA-TR-20-2020 dated 24th Jan 2020.
[11] “Trial # 3 & 4” Report no. DRDO-ADRDE-P8I-EEPSA-TR3&4-33-2020 dated 17th Jul 2020.
[12] “Trial # 5, 6, 7 & 8” Report no. DRDO-ADRDE-P8I-EEPSA-TR-57-2020 dated 3rd Dec 2020.
[13] “Trial # 9, 10 & 12” Report no. DRDO-ADRDE-P8I-EEPSA-TR-64-2020 dated 15th Dec 2020.

Attitude Stabilization of Quadrotor using Event-Trigger Sliding Mode Control

Vibhu Kumar Tripathi
Department of Electrical Engineering
Indian Institute of Technology Kanpur
vibhukt@iitk.ac.in

Anuj Nandanwar
Department of Electrical Engineering
Indian Institute of Technology Kanpur

Laxmidhar Behera
Department of Electrical Engineering
Indian Institute of Technology Kanpur

Nishchal K. Verma
Department of Electrical Engineering
Indian Institute of Technology Kanpur

Abstract – **This paper aims to develop event-triggered sliding mode control strategy for the attitude control of the Quadrotor in the presence of external disturbances. A nonlinear sliding manifold and a constant rate proportional reaching law have been employed to guarantee the convergence of the tracking error in the finite time. An event triggering condition for control updates while maintaining the closed-loop finite-time stability has been derived using Lyapunov stability theory. Besides, a lower bound of the inter execution time is also computed to avoid zeno execution of the triggering instants. The performance of the proposed methodology is tested using extensive numerical simulations. Results have been compared with recent work to show the superiority of the proposed scheme in terms of communications and computational cost reduction without sacrificing the nominal closed-loop tracking performance.**

Keywords– Quadrotors, Sliding-Mode Control, Event-trigger, Tracking Control

1. Introduction

Rotor craft unmanned aerial vehicles have the capability to take-off and landing vertically along with aggressive maneuvering. Quadrotors have been evolved as a popular rotor-craft unmanned aerial vehicles due to its simple mechanical structure nowadays. Over the last decades, quadrotor is being used in several industrial applications such as surveillance, crop decease monitoring, aerial cinematography etc. In order to accomplish aforementioned autonomous task, a robust flight controller is mandatory that can give desired performance in spite of external disturbances and modeling uncertainty. However, designing a robust control system for Quadrotor motion control is tedious and very challenging, as Quadrotor kinematics and dynamics are very sensitive towards the unpredictable flying environment variations. There are several control schemes have been successfully developed and implemented for controlling the motion of the quadrotor in the past. PID based flight controllers are generally used for autonomous operations, as gain parameters tuning does not require the model information. However, PID controllers are very sensitive and not robust against the large class of the disturbances. Apart from PID control schemes, LQR, backstepping control and sliding mode control (SMC) [1]–[3]. have also successfully deployed in the real time applications. The SMC has several features like insensitivity and robustness against the system uncertainty as compared to other control schemes. Attitude control plays a vital role in the autonomous operation of the quadrotor despite the external disturbances. SMC [4] based attitude controllers have been developed stabilizing the angular motion of the quadrotor. In SMC, control law forces the system states towards the predefined sliding manifold in finite time and maintain the states on the manifold thereafter [5]. There are basically two phase namely reaching phase and sliding phase in the SMC design. In reaching phase, states are driven towards the sliding manifold whereas states are sliding towards the equilibrium point along the sliding manifold in the sliding phase. In [6], a SMC for the quadrotor attitude stabilization and a backstepping control for position tracking is developed. Generally, these schemes are time triggered approach in which control laws update at regular interval. Therefore, these approaches become uneconomical as they do not provide the optimal computational cost for achieving the better tracking performance. Event-triggered control [7], [8] is a resource-aware sampling strategy in which control updation is possible only when a certain condition is violated. This technique permits reduction in the control computational and communications cost. In the event-triggered control, the system stability is governed by event-triggering rules. In [9], [10], an event-triggered nonlinear state feedback controller was developed for the quadrotor attitude stabilization. A unit quaternion representation is used to derive the event triggering condition. Guerreroet. al. [11] proposed an event triggered attitude controller for quadrotor attitude stabilization. In [12], an event-based attitude controller with fixed and relative thresh-old strategy is developed. An event triggered-based robust control schemes using neural network is developed in [13]. Apart from the aforementioned work, there is some work in which event-triggered control is applied on mobile robots, robotic manipulators. Moreover, an event-triggered control strategy is also used to design the controller for multi-agent systems and consensus schemes. Furthermore, the flight controller must have the ability to provide the desired tracking performance rapidly and in a finite time. Motivated from the above discussion, the main objective of this paper is to develop a finite-time event-triggered sliding mode controller for the attitude stabilization of the quadrotor in the presence of the external disturbances. Following contributions have been done while designing attitude controller for the quadrotor.

(i) Event trigger condition is derived for reducing the total control effort.
(ii) A nonlinear terminal sliding mode manifold for the quadrotor has been proposed to ensure finite-time stabilization.
(iii) A constant rate proportional reaching law is proposed for improving the convergence speed of the sliding variables.
(iv) The inter execution time has been derived to avoid zeno phenomenon.
(v) Extensive simulations have been performed for attitude stabilization in order to check the efficacy of the proposed methodology.

The paper outline is summarized as follows. The Quadrotor dynamical model is presented in section 2. The control problem is formulated in section 3. The proposed attitude controller design with stability analysis is presented in section 4. The simulation results and conclusion are presented in sections 5 and 6 respectively

2. Quadrotor Model

The Newton Euler approach is used to obtain the dynamical model [14] [15] of the quadrotor. By taking some assumptions, the simplified model is obtained as:

$$\ddot{\phi} = \dot{\theta}\dot{\psi}(\frac{J_y - J_z}{J_x}) + \frac{u_2}{J_x}$$
$$\ddot{\theta} = \dot{\phi}\dot{\psi}(\frac{J_z - J_x}{J_y}) + \frac{u_3}{J_y}$$
$$\ddot{\psi} = \dot{\phi}\dot{\theta}(\frac{J_x - J_y}{J_z}) + \frac{u_4}{J_z} \quad (1)$$
$$\ddot{z} = \frac{u_1}{m}(\cos\phi\cos\theta) - g$$
$$\ddot{x} = \frac{u_1}{m}(\cos\phi\sin\theta\cos\psi + \sin\phi\sin\psi)$$
$$\ddot{y} = \frac{u_1}{m}(\cos\phi\sin\theta\sin\psi - \sin\phi\cos\psi)$$

Where (x, y, z) are three positions; (ϕ, θ, ψ) are three Euler angles, denoting roll, pitch and yaw respectively that satisfies the conditions $-\frac{\pi}{2} < \phi < \frac{\pi}{2}$ for roll angle, $-\frac{\pi}{2} < \theta < \frac{\pi}{2}$ for pitch angle and $-\pi < \psi < \pi$ for yaw angle. J_x, J_y and J_z are the moments of inertia in x, y and z axis respectively and $u_{i(i=1,2,3,4)}$ are the control inputs defined as:

$$u_1 = b(\omega_1^2 + \omega_2^2 + \omega_3^2 + \omega_4^2)$$
$$u_2 = bl(\omega_4^2 - \omega_2^2) \quad (2)$$
$$u_3 = bl(\omega_1^2 - \omega_3^2)$$
$$u_4 = d(\omega_4^2 + \omega_2^2 - \omega_1^2 - \omega_3^2)$$

where, ω_i denotes the angular velocity of the i^{th} rotor; l denotes the distance from a rotor to quadrotor center of mass; thrust and drag coefficients are represented by b and d respectively. we can divide dynamic model (1) in to six second order subsystems [14] $\ddot{\phi}, \ddot{\theta}, \ddot{\psi}$ represents the roll, pitch and yaw subsystems respectively and $\ddot{x}, \ddot{y}, \ddot{z}$ represents the x, y and z motion dynamical subsystems. In this paper, our main focus on the attitude stabilization problem and since attitude dynamics is independent to the translational motion, hence one can neglect the $\ddot{x}, \ddot{y}, \ddot{z}$ dynamics from (1).

3. Problem Formulation

Consider $x_1 = [\phi, \theta, \psi]^T$, $x_2 = [\dot{\phi}, \dot{\theta}, \dot{\psi}]^T$ and $x = [x_1^T, x_2^T]^T$ are considered as state vectors and $u = [u_2, u_3, u_4]^T$ is considered as the system control input vector. Now, the quadrotor model (1) subjected to modeling uncertainty and external disturbances can be represented as:

$$\dot{x}_1 = x_2$$
$$\dot{x}_2 = f(x) + G(u + d) \quad (3)$$

where $f(x) \in \Re^3$, $G \in \Re^{3\times3}$ and $d \in \Re^3$ denote the system matrix, input matrix and external disturbance respectively, given as:

$$f(x) = \begin{bmatrix} (\frac{J_y - J_z}{J_x})\dot{\theta}\dot{\psi} \\ (\frac{J_z - J_x}{J_y})\dot{\phi}\dot{\psi} \\ (\frac{J_x - J_y}{J_z})\dot{\phi}\dot{\theta} \end{bmatrix} d = \begin{bmatrix} d_\phi \\ d_\theta \\ d_\psi \end{bmatrix} \qquad (4)$$

And

$$G = \begin{bmatrix} 1/J_x & 0 & 0 \\ 0 & 1/J_y & 0 \\ 0 & 0 & 1/J_z \end{bmatrix} \qquad (5)$$

For the nonlinear model represented in (3), design a control law u that updates according to the derived event-triggering conditions which forces the Euler angles ϕ, θ, ψ to follow a desired trajectory ϕ_d, θ_d, ψ_d in a finite time t_f in the presence of bounded external disturbances. Mathematically, one can write:

$$\lim_{t \to t_f}(\phi, \theta, \psi) = (\phi_d, \theta_d, \psi_d).$$

4. Proposed Methodology

A. Finite-time Sliding-Mode Controller Design:

This section deals with the design of u for quadrotor attitude stabilization using nonlinear terminal sliding manifolds. It is to be noted that the bounded matched perturbation is acting on the system (3) such that $\| d \| \leq d_s$. Let us define tracking error as follows:

$$\begin{aligned} \xi_1 &= x_1 - x_1^d \\ \xi_2 &= x_2 - \dot{x}_1^d \end{aligned} \qquad (6)$$

Hence the system error dynamics will be

$$\begin{aligned} \dot{\xi}_1 &= \xi_2 \\ \dot{\xi}_2 &= f(\xi) + G(u + d) \end{aligned} \qquad (7)$$

To obtain SMC law, the nonlinear terminal sliding variable is selected as

$$S = \xi_2 + \beta |\xi_1|^\gamma \operatorname{sign}(\xi_1) \qquad (8)$$

The first-time derivative of S will therefore be

$$\begin{aligned} \dot{S} &= \dot{\xi}_2 + \beta\gamma |\xi_1|^{\gamma-1} \\ \dot{\xi}_1 &= f(\xi) + Gu + Gd + \beta\gamma |\xi_1|^{\gamma-1} \\ \xi_2 &= Gu + Gd + f(\xi_1, \xi_2) \end{aligned} \qquad (9)$$

Now u can be chosen as

$$u = -(G)^{-1}[f(\xi_1, \xi_2) + K\operatorname{sign}(S) + \Gamma S] \qquad (10)$$

Where $f(\xi_1, \xi_2) = f(\xi) + \beta\gamma |\xi_1|^{\gamma-1} \xi_2$.

B. Event-Triggered based Controller

In this subsection, preliminaries of event-trigger control, design of an event-based control law and triggering conditions are discussed.

(i) Preliminaries: Generally classical discrete implementation also known as time triggered implementation, requires control updation periodically at the plant. Sometimes this classical approach not economical and not uses resources optimally.

Therefore, it is most of the time desired to compute and update the control less frequently. Event trigger control is a new way of discrete implementation and deals with the aperiodic updation of the control laws whenever some event occurs. In the event-triggering technique, the idea of the Lebesgue sampling is used for the control update. Now consider a dynamical system $\dot{\zeta} = \varphi(\zeta, v)$ where v is the control input. Let us design control v as $v = \mu(\zeta)$ such that the closed-loop system $\dot{\zeta} = \varphi(\zeta, \mu(\zeta))$ is asymptotic stable. Let the control $\mu(\zeta)$ be implemented through computer with zero-order hold technique, i.e., for all $t \in [t_i, t_{i+1})$, the control $\mu(\zeta(t)) = \mu(\zeta(t_i))$. Define $e(t) = \zeta(t_i) - \zeta(t)$ as the error induced in the system due to discrete implementation of control law $v = \mu(\zeta)$. Then there exists a Lyapunov function $V(\zeta)$, such that

$$\alpha_1(\|\zeta\|) \le V(\zeta) \le \alpha_2(\|\zeta\|) \text{ and } \frac{\partial V}{\partial \zeta}\varphi(\zeta, \mu(\zeta + e)) \le -\alpha_3(\|\zeta\|) + \delta(\|e\|) \quad (11)$$

The following assumptions are used for designing a design an event-based controller of quadrotor applied to the system (3)

Assumption 1:

The function $f(\xi_1)$ and $f(\xi_2)$ are system dynamics and known quantity.

Assumption 2:

The function $f(\xi_1)$ and $f(\xi_2)$ are assumed to be Lipchitz [16] on compact sets such that $\| f(\xi_1(t_i)) - f(\xi_1(t) \| \le L \| \xi_1(t_i) - \xi_1(t) \|$.

(ii) Event-triggered sliding mode control: The power rate proportional reaching law-based event-trigger Control input u at time t_i will be

$$u(t) = -(G)^{-1}[f(\xi_1(t_i), \xi_2(t_i)) + K\text{sign}(S(t_i)) + \Gamma S(t_i)] \quad (12)$$

where $t \in [t_i, t_{i+1})$,and t_i is the triggering time. The event-trigger error is defined as

$$\begin{aligned} e_1 &= \xi_1(t_i) - \xi_1(t) \\ e_2 &= \xi_2(t_i) - \xi_2(t) \end{aligned} \quad (13)$$

The triggering scheme is designed such that the control will be triggered for each agent at its own event time only. The control input remains piecewise constant during the inter execution time.

Theorem 1: Consider the system (3). If the sliding variable is chosen as (8) and the event-trigger control law (12), make the system stable in the presence of disturbance if the triggering function is chosen as

$$L(\|e_1(t)\| + \|e_2(t)\|) < \eta\alpha \quad (14)$$

where α is predefined threshold value The parameter $\eta \in [0,1]$ is a constant quantity.

Proof: Let us consider a candidate Lyapunov function as

$$V = \frac{1}{2}S^T S \quad (15)$$

Taking time derivative of V, one can get

$$\dot{V} = S^T \dot{S} = S^T[Gu + Gd + f(\xi_1(t), \xi_2(t))]$$

$$= S^T[-f(\xi_1(t_i), \xi_2(t_i)) - K\text{sign}(S(t_i)) - \Gamma S(t_i) + Gd + f(\xi_1(t), \xi_2(t))]$$

$$\leq \ \|S\|\|\|f(\xi_1(t_i),\xi_2(t_i)) - f(\xi_1(t),\xi_2(t))\| + \|S\|\|\|G\|d_s - S^T\lambda_{\min}(K)\text{sign}(S(t_i))$$
$$-\lambda_{\min}(\Gamma)S^T S(t_i)$$
$$\leq \ \|S\|L\|\xi_1(t_i)-\xi_1(t)\| + \|S\|L\|\xi_2(t_i)-\xi_2(t)\|$$
$$+\|S\|\|\|G\|d_s - S^T\lambda_{\min}(K)\text{sign}(S(t_i)) - \lambda_{\min}(\Gamma)S^T S(t_i) \tag{16}$$

If the system trajectories start from a region where $\text{sign}(S(t_i)) = \text{sign}(S(t))$, then the afore-mentioned relation can be further reduced in the following form

$$\dot V \leq \ \|S\|L\|e_1(t)\| + \|S\|L\|e_2(t)\| + \|S\|\|\|G\|d_s - \lambda_{\min}(K)\|S\| - \lambda_{\min}(\Gamma)\|S\|^2$$
$$\leq \ \|S\|(L\|e_1(t)\| + L\|e_2(t)\|) + \|S\|\|\|G\|d_s - \lambda_{\min}(K)\|S\| - \lambda_{\min}(\Gamma)\|S\|^2 \tag{17}$$

if $L(\|e_1(t)\| + \|e_2(t)\|) < \alpha$ then

$$\dot V \leq \ \|S\|\alpha + \|S\|\|\|G\|d_s - \lambda_{\min}(K)\|S\| - \lambda_{\min}(\Gamma)\|S\|^2$$
$$\leq \ -\|S\|(-\alpha - \|G\|d_s + \lambda_{\min}(K)) - \lambda_{\min}(\Gamma)\|S\|^2$$
$$\leq \ -\frac{\eta_1}{\sqrt{2}}\|S\| - \frac{\eta_2}{2}\|S\|^2 = -\eta_1 V^{1/2} - \eta_2 V \tag{18}$$

For closed-loop stability, controller must satisfy the following conditions

$$\lambda_{\min}(K) \geq \alpha + \|G\|d_s + \frac{\eta_1}{\sqrt{2}}$$

$$\lambda_{\min}(\Gamma) \geq \frac{\eta_2}{2}$$

and the reaching time denoted by t_r can be easily computed from (18) by using variable separation method. The expression of t_r is given by

$$t_r = \frac{2}{\eta_2} ln\Big(\frac{\eta_1 + \eta_2\sqrt{V(0)}}{\eta_1}\Big) \tag{19}$$

Where $V(0)$ is the value of Lyapunov candidate function at the beginning of reaching phase.

(iii) Inter Execution Time: Admissibility in event triggered system is defined as the inter-execution time for update of control law which is always lower bounded by a finite value.

Theorem 2: For system (3), event-driven control is updated on violation of condition (14). For admissibility of system the inter-event time defined by $T_i = t_{i+1} - t_i$ should always be lower bounded by a positive constant given by

$$T_i \geq \ln\left(1 + \eta \frac{\alpha}{(\text{ù}\ (\|\xi(t_i)\|) + \kappa)}\right) \tag{20}$$

Proof: The time required for event-trigger error $\|e\|$ to rise from zeros at last triggering instant to threshold value should be lower bounded. phenomenon can be avoided ensuring a stable system. The event driven system is represented as

$$\frac{d}{dt}\|e(t)\| \leq \|\frac{d}{dt}e(t)\| = \|f(\xi) + G(u+d)\|$$
$$= \|f(\xi) + Gd - f(\xi_1(t_i),\xi_2(t_i)) - K\text{sign}(S(t_i)) - \Gamma S(t_i)\|$$
$$\leq \ L\|\xi\| + \|G\|d_s + L\|\xi(t_i)\| + K + \Gamma$$

$$\le L(\|\xi(t_i)\| + \|e(t)\|) + \|G\| d_s + L\|\xi(t_i)\| + K + \Gamma$$
$$\le \grave{u}(\|\xi(t_i)\|) + L\|e(t)\| + \kappa \tag{20}$$

where $\kappa = \|G\| d_s + K + \Gamma$ and $\grave{u}(\|\xi(t_i)\|) = 2L\|\xi(t_i)\|$. The solution of above differential equation is solved by comparison lemma [16] with initial condition $\|\xi(t_i)\| = 0$ as

$$\|e(t)\| \le \frac{\grave{u}(\|\xi(t_i)\|) + \kappa}{L}\left(e^{L(t-t_i)} - 1\right) \tag{21}$$

The triggering instant t_{i+1} is triggered as soon as (14) is satisfied. So, we can get

$$\frac{\eta\alpha}{L} = \|e(t_{i+1})\| \le \frac{\grave{u}(\|\xi(t_i)\|) + \kappa}{L}\left(e^{LT_i} - 1\right) \tag{22}$$

Now, rearranging the above system

$$T_i \ge \ln\left(1 + \eta \frac{\alpha}{(\grave{u}(\|\xi(t_i)\|) + \kappa)}\right) \tag{23}$$

Hence, it is seen that the inter event time $T_i = t - t_i$ is always bounded below a positive finite quantity.

5. Simulation Results

This section deals with investigating the tracking performance of the developed controller using extensive numerical simulations. The numerical simulations have been carried out using MATLAB/Simulink. The quadrotor and controller parameters are selected as $J_x = 10.8*10^{-3} kg.m^2$; $J_y = 10.8*10^{-3} kg.m^2$; $J_z = 21.6*10^{-2} kg.m^2$; $g = 9.81 m/s^2$; $m = 1.8\ kg$; $\gamma = 0.5$; $\beta = 0.5$; $\alpha = 0.02$; $L = 0.5$; $\Gamma = diag\{0.5, 0.5, 0.5\}$; $K = diag\{2,2,2\}$. The initial conditions are chosen as $\mathbf{x} = [0; \pi/3; 0; \pi/8; 0; \pi/2]^T$. The controller goal is to follow the desired Euler angles namely roll, pitch and yaw angles. The desired angular positions are considered as $\phi_d = \cos(t), \theta_d = 0.5\cos(t), \psi_d = 0.6$ for the numerical simulations. The sampling time is kept at 0.01 second. To check the robustness of the proposed methodology in the presence of various internal and external disturbances, the lumped disturbances are assumed to be bounded and selected as $0.2\sin(t)$.

The tracking response and control inputs are shown in Figs. 1 and 2 respectively. From the response, it is clear that the desired trajectory is accurately tracked by the quadrotor in the finite time. The high frequency oscillations in the control input response is caused by the use of proportional constant reaching law. By using boundary layer approximation method, the control signal can be made smooth. The tracking response clearly demonstrate the effectiveness and efficacy of the proposed methodology

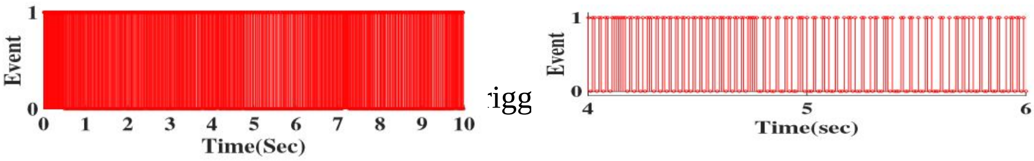

Figure 3: Triggering instants profile.

The triggering instants profile is shown in Fig. 3. In contrast to time triggered approach, the control laws are updating 648 times for the simulated duration of (i.e., 1000 sampling instants) in case of proposed event triggered approach. In the proposed event triggered approach, the control updates are reduced to that clearly ensures the control efforts reduction as well. These results ensure resource optimization along with stability of system. Therefore, flight controller developed based on proposed methodology can be easily deployed in the real-time application where large flight time required.

6. Conclusions

A robust attitude stabilisation of a quadrotor system is obtained by using event-triggered finite-time sliding mode control strategy. The event-triggering rules for sliding mode control updates are developed using Lyapunov stability theory. The proposed strategy has been shown finite-time stable that ensures the orientation angles remains within a band which depends on the event parameters. Numerical simulations clearly demonstrate the effectiveness of the proposed finite-time event-triggering sliding mode control scheme. Results clearly shows the reduction in control update count as compared to time triggered approach that ensures the actuators load reduction to guarantee resource optimization.

7. Reference

[1] J. Ghommam and M. Saad, "Autonomous Landing of a Quadrotor on a Moving Platform," IEEE Transactions on Aerospace and Electronic Systems, vol. 53, no. 3, pp. 1504–1519, 2017.

[2] A. T. Hafez, A. J. Marasco, S. N. Givigi, M. Iskandarani, S. Yousefi, and C. A. Rabbath, "Solving Multi-UAV Dynamic Encirclement via Model Predictive Control," IEEE Transactions on Control Systems Technology, vol. 23, no. 6, pp. 2251–2265, 2015.

[3] Y. Yu, S. Yang, M. Wang, C. Li, and Z. Li, "High Performance Full Attitude Control of a Quadrotor on SO (3)," in 2015 IEEE International Conference on Robotics and Automation (ICRA). IEEE, 2015, pp.1698–1703.

[4] V. I. Utkin, Sliding modes in control and optimization. Springer Science & Business Media, 2013.

[5] Y.-J. Huang, T.-C. Kuo, and S.-H. Chang, "Adaptive Sliding-mode control for nonlinear systems with uncertain parameters," IEEE Transactions on Systems, Man, and Cybernetics, Part B (Cybernetics), vol. 38, no. 2, pp. 534–539, 2008.

[6] F. Chen, R. Jiang, K. Zhang, B. Jiang, and G. Tao, "Robust Backstepping Sliding-Mode Control and Observer-Based Fault Estimation for a Quadrotor UAV," IEEE Transactions on Industrial Electronics, vol. 63, no. 8, pp. 5044–5056, 2016.

[7] A. K. Behera and B. Bandyopadhyay, "Event-Triggered Sliding Mode Control for a Class of Nonlinear Systems," International Journal of Control, vol. 89, no. 9, pp. 1916–1931, 2016.

[8] A. Nandanwar, N. K. Dhar, D. Malyshev, L. Rybak, and L. Behera, "Finite-Time Robust Admissible Consensus Control of Multi-Robot System Under Dynamic Events," IEEE Systems Journal, vol. 15, no. 1, pp.780–790, March 2021.

[9] J.-F. Guerrero-Castellanos, J. J. T́ellez-Guzḿan, S. Durand, N. Marc-hand, Alvarez-Munoz, "Event-Triggered Nonlinear Control for Attitude Stabilization of a Quadrotor," in 2013 International Conference on Unmanned Aircraft Systems (ICUAS). IEEE, 2013, pp. 584–591.

[10] D. Almeida, "Event-Triggered Attitude Stabilization of a Quadcopter," 2014.

[11] J. Guerrero-Castellanos, J. T́ellez-Guzḿan, S. Durand, N. Marchand, and J . Alvarez-Mũnoz, and V. R. Gonzalez-Diaz, "Attitude Stabilization of a Quadrotor by Means of Event-Triggered Nonlinear Control," Journal of Intelligent & Robotic Systems, vol. 73, no. 1, pp. 123-135, 2014.

[12] W. Zeng, H. Fan, and W. Wang, "Event-triggered adaptive attitude tracking control of a Quadrotor UAV," in 2019 Chinese Control and Decision Conference (CCDC). IEEE, 2019, pp. 2855–2860.

[13] S. Shao, M. Chen, J. Hou, and Q. Zhao, "Event-Triggered-Based Discrete-Time Neural Control for a Quadrotor UAV using Disturbance Observer," IEEE/ASME Transactions on Mechatronics, vol. 26, no. 2, pp. 689–699, 2021.
[14] V. K. Tripathi, A. K. Kamath, N. K. Verma, and L. Behera, "Fast Terminal Sliding Mode Super Twisting Controller for Position and Altitude Tracking of the Quadrotor," in 2019 International Conference on Robotics and Automation (ICRA), IEEE, 2019, pp. 6468–6474.
[15] K. Kamath, V. K. Tripathi, and L. Behera, "Vision-based Autonomous Control Schemes for Quadrotor Unmanned Aerial Vehicle," Unmanned Robotic Systems and Applications, 2019.
[16] H. K. Khalil, "Nonlinear systems third edition," Patience Hall, 2002

Estimation of Dynamic Characteristics of Parachutes using Image Processing Techniques

K L N Sai Nitish
Reusable Launch Vehicle Project
Vikram Sarabhai Space Centre
ISRO
Thiruvananthapuram
nitish k@vssc.gov.in

Karthik B
Reusable Launch Vehicle Project
Vikram Sarabhai Space Centre
ISRO
Thiruvananthapuram

Jayakumar M
Reusable Launch Vehicle Project
Vikram Sarabhai Space Centre
ISRO
Thiruvananthapuram

Basker VT
Reusable Launch Vehicle Project
Vikram Sarabhai Space Centre
ISRO
Thiruvananthapuram

***Abstract* - Military aircrafts and winged re-entry vehicles land on runways at high velocities when compared to commercial aircrafts. Aerodynamic decelerators such as parachutes act as effective means of reducing velocities of these vehicles while catering to mission requirements. Dynamic characterisation of the parachutes is required to understand the behaviour of these aircrafts in the ground roll phase post landing. Incorporating parachute dynamics into 6 Degree of Freedom (DoF) autonomous simulation platforms increases the fidelity of the simulations thus enhancing the overall mission reliability. Numerical simulations of Fluid Structure Interaction (FSI) or wind tunnel testing techniques to capture parachute dynamics have limitations as elucidated in this paper. Therefore, a methodology is devised using image processing techniques to estimate the dynamic characteristics of a full scale ringslot parachute, based on data obtained from high speed traction tests. Pitch and Yaw plane parachute oscillations are derived from the test videos and the results obtained are found to be in coherence with the literature.**

Keywords: Parachute; Dynamic Characteristics; Stability; Image Processing

1. Introduction

Stability is the tendency of a body to return to its equilibrium position (if any) when acted upon by external disturbances. Different parachute canopies exhibit different stability characteristics based on material porosity, geometric porosity and stiffness of the fabric. It is imperative to understand the parachute dynamics as it directly impacts the stability of its forebody. Dynamic characteristics of parachute canopies are largely governed by their wake [1]. In many ways, flow past circular parachute canopies is similar to flow past circular cylinders. For an imporous solid circular canopy as shown in Fig.1 [2], the flow separates alternatively on the leading edge of the hemisphere, giving rise to the von-Karman vortex street. The alternate shedding of vortices causes change in the pressure distribution over the canopy, resulting in oscillations which can be detrimental to the stability of the forebody. On the other hand, for a slotted porous canopy such as a ringslot or a ribbon parachute, part of the flow through the slots directly enters the wake, thereby suppressing the strength of vortex shedding and producing a uniform wake with smaller vortices. Hence slotted parachutes, albeit generating lesser drag force, are more stable compared to their solid imporous counterparts. Dynamic characteristics of several canopies obtained through theoretical relations and experimental data are put forward by [2] and [3]. Importance of increasing porosity in parachute canopies is further corroborated by excerpts from Space Shuttle missions. For early Orbiter flights [4], low porosity parachutes were used which saw the parachute oscillating at an elevated angle of 7 degrees, resulting in extra pilot workload due to parachute instability. The chute was made more stable by incrementally cutting ribbons out of the canopy at key locations, thus increasing its geometric porosity. By removing 5 of the 97 concentric ribbons in the canopy, total porosity was augmented, causing a loss of drag, although within an acceptable limit. This change was incorporated and all subsequent Orbiter landings have been free of the instability issue.

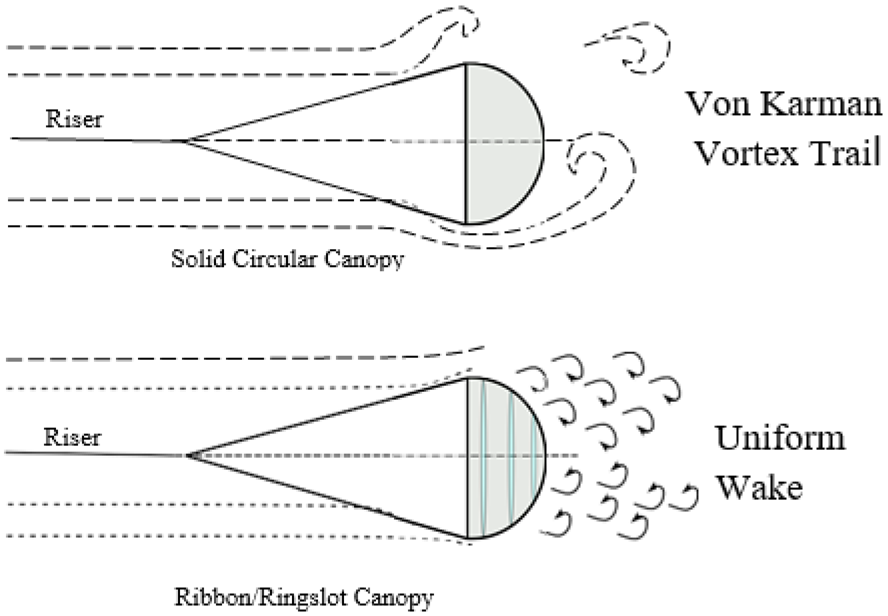

Fig. 1: Fluid Flow around Parachute Canopies

Numerical simulations of parachute dynamics require modelling the FSI of the parachute canopy and the surrounding fluid flow. Fully coupled three-dimensional FSI simulations of parachute canopies have been presented by [1] and [5]. This process has limitations of its own; it is computationally intensive and requires modelling of the parachute fabric, incorporating structural characteristics such as stiffness and material porosity. Another technique to study the parachute dynamics is through extensive wind tunnel testing. According to [6], parachute models for wind tunnel testing should be as similar in geometry (number of gores, geo- metric porosity) and flexibility to full-scale parachutes. Scaling of the model parachutes based on Froude's number, i.e. the ratio of inertial to gravitational forces is essential as emphasized by [7]. However, full scale parachute dynamics may not be accurately simulated as the fabrication process of the scaled down parachutes may result in higher dimensional tolerances which can significantly affect its geometrical porosity. Further, testing of full-scale parachutes in wind tunnel is a challenging task considering the tunnel size, blockage and boundary layer effects. In addition, it is challenging to capture the dynamic characteristics of the parachutes in a wind tunnel with the available instrumentation. This paper discusses an alternative technique to arrive at the dynamic characteristics of the parachute, using image processing algorithms. The algorithm was implemented on video footage obtained from high speed traction tests using rocket sleds.

2. Test Setup and Instrumentation

High speed traction tests are used to test the structural integrity and investigate the inflation characteristics of parachutes by simulating velocities experienced in flight. The rocket sled is accelerated to the required velocity before the parachute is deployed. Two cameras recording at 30 frames per second are mounted on the sled to capture the pitch and yaw plane motion of the parachute riser. The ringslot parachute was deployed at different forward velocities, details of which are summarised in Table I

Table 1: High Speed Traction Test Summary

Parameter	**Test 1**	**Test 2**
Max. Sled Velocity, m/s	138	162
Velocity at fire command, m/s	128	146
Velocity at snatch, m/s	125	143
Velocity after inflation, m/s	113	125

3. Computational Methodology

Dynamic characteristics of a parachute i.e. the amplitude and frequency of canopy oscillations are computed by tracking the parachute riser's trajectory with respect to the reference rods using image processing techniques involving cropping, filtering, segmentation and estimation. The test footage, available at 30 frames per second, is used to extract discrete images.

After extraction, the region of interest encompassing the riser is cropped out from the rest of the image. Once the image is cropped, the high frequency noise in the image, arising due to the motion of the sled on the rail track is removed. This is done by sweeping a discrete rectangular Gaussian kernel across the image. A standard continuous Gaussian in two dimensions is given by

$$g(x,y)=1/(2\pi\sigma^2)\, e^{(-(x^2+y^2)/(2\sigma^2))}$$

Blue (RGB) color space. A suitable range of intensities in RGB color space is selected to detect the edges of the riser. Using this threshold, the edges of the riser are tracked at every time instant. Mean of the two edges of the riser is used to obtain the center line of the riser. Slope of this line was obtained by using a linear curve fit on the points detected. This slope with respect to the reference rod gives the instantaneous angle of the riser and hence the parachute. This methodology is summarised in Fig. 2.

4. Results and Discussion

The ringslot parachute is deployed from the rocket sled at forward velocities as tabulated in Table I. Cameras mounted on the sled captured the pitch and yaw plane oscillations of the parachute riser, assuming that the high frequency oscillations of the camera and the reference rod are in phase.

A. Pitch Plane

Time series of parachute oscillations in the pitch plane and the Fast Fourier Transform (FFT) of the data is as shown in Fig. 3. Entire time series data is used to obtain the n-point FFT without any overlap between the segments. In test 1, outliers in the time series data around t = 6s is due to loss of video footage for a brief period of time. In the pitch plane, the parachute is lifted above the attachment point and the amplitude of oscillations of the parachute is approximately 2-3 degrees about the mean for both the tests. Further, the dominant frequency modes are less than 2.5 Hz which is in accordance with the findings of [8]. The peaks occurring in the frequency spectrum corresponds to different forward velocities of the sled.

The velocity of the sled changes constantly causing the flow velocity (and hence the Reynolds number) which the parachute encounters to change continuously. Also, the instantaneous angle of the riser and the parachute are assumed to be same as the double pendulum effects are negligible

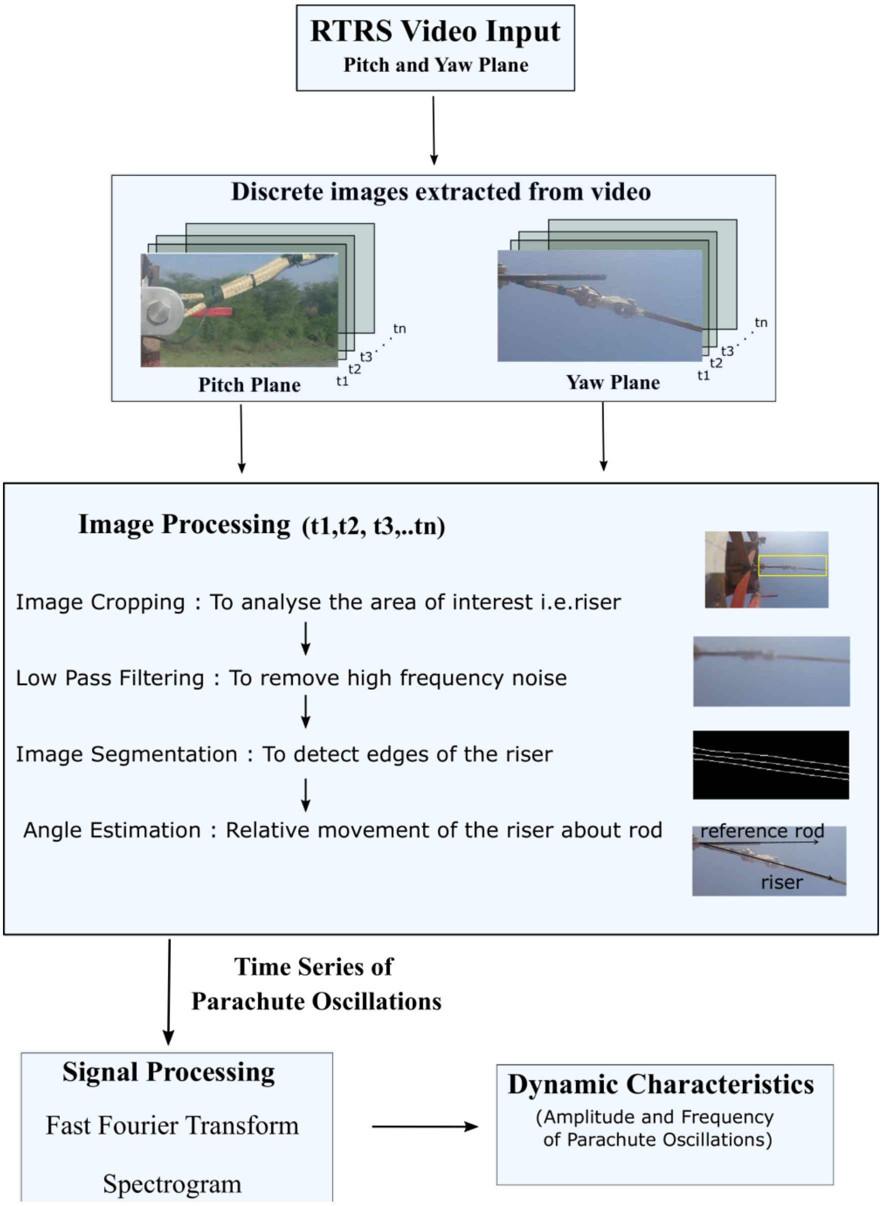

Fig 2: Flow chart of the image processing algorithm

B. Yaw Plane

In contrast to the pitch plane, the yaw plane parachute dynamics is governed predominantly by the crosswinds. The angle of the parachute in the yaw plane directly depends on the forward velocity and the crosswind at that instant (angle of sideslip faced by the canopy). Assuming a crosswind of 6 m/s, angle of sideslip (β) is computed using the sled velocity as the freestream velocity. This is compared with the estimated yaw plane angle from the image processing algorithm for Test 1. Fig.4 shows the difference in the estimated yaw plane angle and the computed sideslip angle. This underscores the importance of measuring crosswinds during the test to understand the yaw plane parachute dynamics.

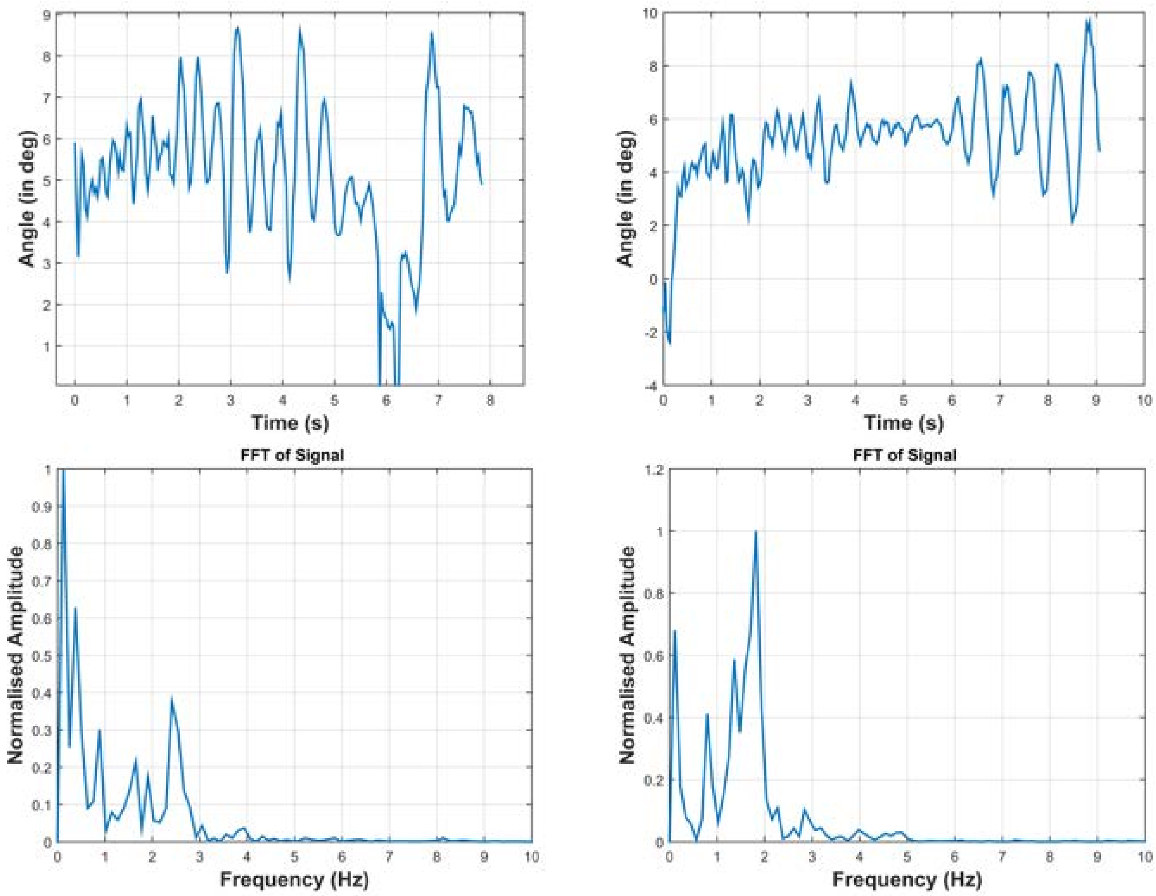

Fig. 3: Time Series data and FFT of pitch plane parachute oscillations

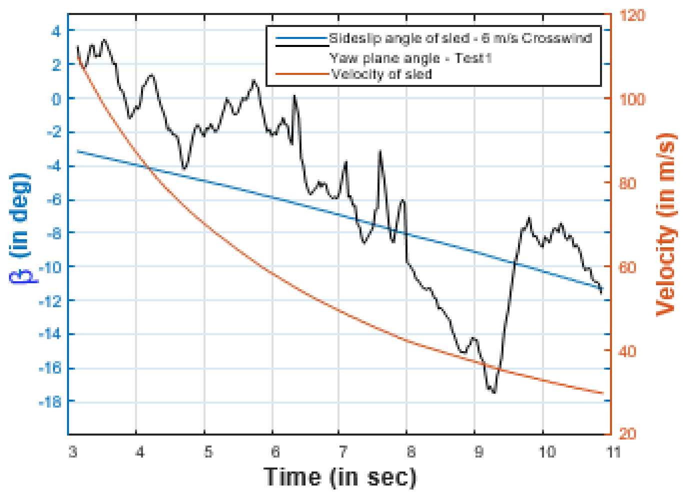

Fig. 4: Variation of yaw plane angle, sled forward velocity and computed side slip angle for Test 1

C. Polar Plot

Trace of the parachute canopy with respect to the attachment point elucidates its stability characteristics. Time series data of pitch and yaw plane angles are used to obtain the trace of the canopy on a polar plot with the attachment point at the center as shown in Fig. 5. In the polar plot, the radius signifies the radial distance of the parachute center point with respect to the attachment point (in metres) and the angle signifies the quadrant in which it lies as seen from the reference rod location on the sled. An important inference from the polar plot is that the parachute is always lifted above the parachute attachment point, as expected from literature. In addition, the drift in the lateral direction is lesser for Test 2 compared to Test 1. One possible reason for this could be the difference in the magnitude of crosswinds during both the tests. A parachute canopy is more stable if its trace is confined to a particular region (less spatially distributed) in the polar plot. Further, when the points are closer to the center, the drag component of the parachute along the direction of motion of the forebody is higher which results in higher deceleration, as seen in Test 2

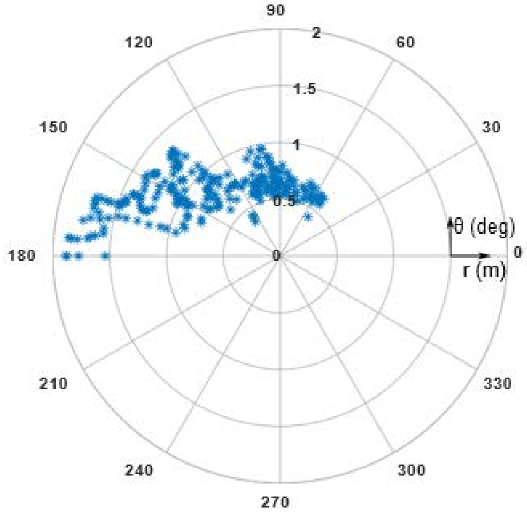

(a) Test 1

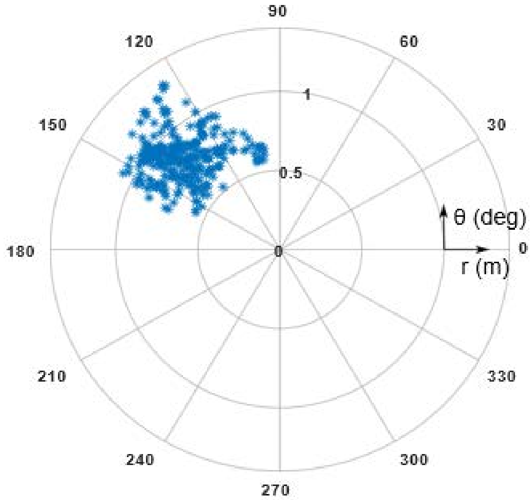

(b) Test 2

Fig. 5: Polar plot showing the trace of the parachute

5. Conclusion

High speed traction test facility is used to deploy a ringslot parachute from a moving sled at two different forward velocities. The pitch and yaw plane oscillations of the parachute are captured using the cameras mounted on the sled. A procedure using image processing techniques is employed to estimate the dynamic characteristics of the parachute canopy from the recorded video footage. The estimated pitch plane oscillations conformed with the findings from the literature. On the other hand, the yaw plane parachute characteristics require precise in- formation of the crosswinds during the test.

Dynamic characteristics of the parachute are estimated to understand the behaviour of the re-entry vehicle during the ground roll phase.

This methodology can also be extended to understand the dynamic characteristics of other aerodynamic decelerators employed in ballistic re-entry vehicles such as crew modules, thus achieving high fidelity in trajectory simulations.

6. Acknowledgements

The authors would like to express their gratitude to the AVID team, VSSC for their guidance through the entirety of work. In addition, the authors sincerely thank the engineers from Aerospace Mechanisms Group, VSSC, RLV project team, VSSC and the parachute fabrication & testing agencies for their relentless support.

7. Reference

[1] J C. Peterson, J. Strickland, and H. Higuchi, “The fluid dynamics of parachute inflation,” Annual Review of Fluid Mechanics, vol. 28, no. 1, pp. 361–387, 1996.
[2] T. Knacke, Parachute Recovery Systems: Design Manual. Para Pub., 1992

[3] E. Ewing, H. Bixby, and T. Knacke, 1978, Recovery system design guide, vol. 46, Department of Defense, Department of the Air Force, Systems Command,
[4] C. H. Lowry, “Space shuttle orbiter drag chute summary,” in AIAA Aerodynamic Decelerator Systems (ADS) Conference, p. 1364, 2013.
[5] K. Stein, R. Benny, V. Kalro, T.E. Tezduyar, J. Leonard, and M. Accorsi, “Parachute fluid-structure interactions: 3-d computation”, Computer Methods in Applied Mechanics and Engineering, vol 190, no. 3-4, pp. 373-386, 2000
[6] J. Macha, “Introduction to testing parachutes in wind tunnels”, in 11th Aerodynamic Decelerator Systems Technology Conference, p. 858, 1991.
[7] R. Meyerson, “Space Shuttle orbiter drag parachute design”, in 16th AIAA Aerodynamic Decelerator Systems Technology Conference and Seminar, p. 2051, 2001
[8] J. Tyagi, P. Khandelwal, and R. Kale, “Performance data acquisition from flexible aerodynamic decelerators,” in 11th Aerodynamic Decelerator Systems Technology Conference, p.861,1991

Pyro Mechanisms

Thermodynamic Aspects of Solid Propellant Gas Generator for Aircraft Application

Bhupesh A Parate
Armament Research and Development Establishment
DRDO
Pune
baparate@gmail.com

KD Deodhar
Armament Research and Development Establishment
Pune
DRDO

VK Dixit
Armament Research and Development Establishment
DRDO
Pune

Dr V Venkateswara Rao
Armament Research and Development Establishment
DRDO
Pune

Abstract **-This research work present mainly on various thermodynamic aspects of solid propellant gas generator for aircraft application. A gas generating device is hot gas generator that creates high temperature and pressure combustion gas on burning of the propellant inside the cartridge case. Thermodynamics is the branch of science which deals with energy transformation into work and vice versa. These devices are filled with energetic materials (EMs) and used to perform a critical operation in an emergency under adverse conditions. It releases the energy very quickly. Gas generator has a large number of applications and its demand is continuously increasing in the areas of aerospace and aeronautical technologies. A data acquisition system is used to record time to maximum pressure (TP_{max}) and maximum pressure (P_{max}) generated in closed vessel (CV) for solid propellant gas generator. A double base (DB) propellant is used as medium for gas generation. The purpose of this research paper is to establish the various relationships and to determine various thermodynamic properties for solid propellant gas generator used in aircraft application. Specific heat of propellant varies from 0.25 to 0.35 cal/g/^{0}C, calorimetric value 925 cal/g, force constant 1052 J/g, co-volume 0.989, flame temperature 2944 K and etc. were experimentally determined.**

Keywords: booster; closed vessel; data acquisition; gas generator and propellant

1. Introduction

Solid propellant gas generators are basically used in special applications such as short term power supply or jet engine starting, launch tubes etc. They are designed to produce hot gases. Therefore their burn rates are much slower (a factor of 5 to 6 times less) and combustion temperatures are much lower at 800 to 1600K. This then allows these propellants to be used with un-insulated metals in applications such as launch tubes. However, work and heat are path functions and they depend on the processes adopted. Their cumulative sum gives a non-zero number. The operational systems based on thermodynamic cycle are used in solid propellant gas generator by propellant burning. Operation of solid propellant gas generator is based on propellant combustions, its gas generation and heat energy that are converted into useful work.

As far as, solid propellant gas generator is concerned, fuel, in the form of solid propellant, is already stored in the system. There is no for gas generator as in an internal combustion (IC) engine. Pictorial representation for gas generator of pressure *vs.* volume and temperature *vs.* entropy are illustrated in figures 1 and 2 respectively [1]. However, if solid propellant gas generator is considered as internal combustion (IC) engine, the process does not have any intake step. This is shown by dotted line 1-2. When the propellant is ignited, heat addition starts and equilibrium pressure is attained. The heat addition process is assumed to be occurring at constant pressure. This is shown by dotted line 2-3. In many cases, the heat addition process may be at varying pressure. This combustion process, increases pressure in the beginning and this transient phase may be treated as a compression stroke. The process is not an isentropic one and cannot be represented one thermodynamic plane correctly. This is shown by dotted line 3-4 as expansion stroke. However, pressure and temperature rise in gas generator occurs in miliseconds. Simultaneously, produced combustion gases are expelled out giving a combination of both expansion and heat rejected step. So, solid propellant gas generator has only two valid processes on thermodynamic plane. Another significant variation is that once solid propellant is initiated, there is no cycle. After completion of propellant only the system is resorted to original state. This indicates that solid propellant gas generator operates as a single stroke thermodynamic cycle. There is no periodicity of operation. There is continuous generation of work till complete propellant (fuel) is consumed.

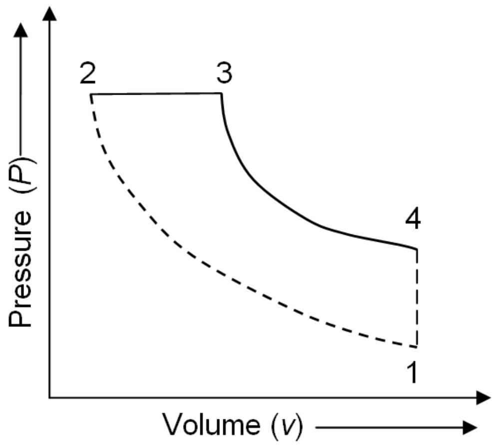

Fig 1: Pressure vs. volume

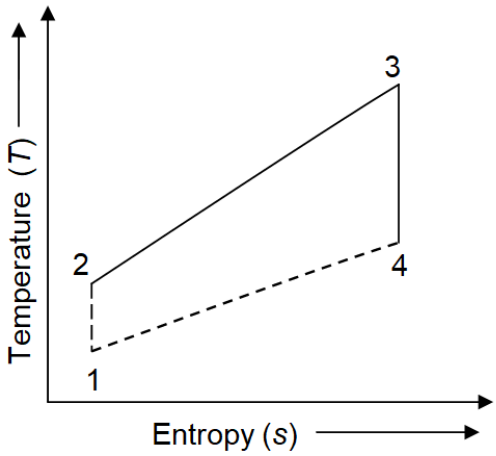

Fig 2: Temperature vs. entropy

Solid propellant gas generator device consists of pyrotechnic composition and the propellant [2]. On suitable initiation, huge amount of gases are developed due to the rapid chemical reaction. Gas generator comprises of various components and other chemicals in the form of reducing and oxidizing agents. Gas generator key performance factors consist of propellant force, combustion heat and its temperature, specific volume, burn rate etc. This article will outline closed vessel (CV) firing gas generator and determination of various thermodynamic properties of solid propellant gas generator [3]. Design and performance of nano gas generator was carried out by Karen et al [4].

2 Thermodynamic Properties

A. Ratio of Specific heat (*γ)*

Specific heat of gaseous product of combustion is basically a measure of temperature rise for a given heat input per unit mass of a given material. For a constant heat input, given mass of material with a high specific heat, result in low temperature rise. Reverse is true for a material with low specific heat. Alternatively, for a given rise in temperature, constant mass of a material with a high specific heat need more heat input. The difference in specific heat is equal to gas constant of the gas and their ratio is expressed by Greek letter Gamma **(γ)** for ideal gases. It is also called as heat capacity ratio and adiabatic index. It is basically isentropic expansion factor. Thermodynamically it is also equal to enthalpy (*h*) and internal energy of ideal gas (*u*). The value of **γ** is related to degree of freedom available in the molecule (*f*) and is defined as [1+(2/*f*)]. However, the combustion gases, containing traces of fuel, the value of γ is reduced. The reduction is dependent on molecular weight of combustion gases and their relative compressibility. The value of γ is taken as 1.2 for DB propellant. The value of γ is reduces with rise in temperature and pressure.

B. Mass generation rate (m_g)

It represents rate at which solid propellant is getting converted into gaseous form by combustion. It is given by density of propellant multiplied by rate of volume consumption of propellant. The rate of volume consumption is given by product of burning area (A) of the propellant and its burn rate (r). It is consumption rate of the propellant grain or of a whole propellant mass per unit time at a constant pressure P. volume of grain which is consumed in unit time is the product of the burning surface area (A) and rate of regression (r). Rate of mass discharge is a function of pressure. Higher the value of pressure, higher will be rate of discharged. This is the mass of explosive consumed in unit time. The expression for the mass generation rate due to propellant consumption is given below:

$$m_g = dm/dt = \rho \times A \times r \text{ ------ } (1)$$

Using Vieille's equation to the mass burning rate

$$\frac{dm}{dt} = P^{\alpha} \times k \times \rho \text{ -------- } (2)$$

where k = constant which consider the values of ρ, A and β.

The burning rate (r) plays an important role in formulation of the propellant as it indicates the propellant functional performance. The burn rate of the propellant is calculated from the small slabs. Generally, the burn rate is expressed either in mm/s or cm/s. It is dependent on surface area and the pressure (P). This is expressed by the relation $r = \beta P^{\alpha}$ where α = pressure index and β = burning rate coefficient. Further, it also depends on propellant composition (fuel and oxidiser content of the propellant) and conditions prevailing inside the combustion chamber. The burn rate affects the gas pressure and gas velocity. This affects heat transfer rate from hot gas into propellant. If the initial propellant temperature is high, the burn rate also enhances. The propellant which has already gain the heat, tend to burn faster due to temperature gradient which drives burning rate, and not the bulk temperature. The smaller the grains size of particular propellant, the total surface area per unit weight for burning increases. As the propellant density is constant, then the total surface area per unit volume will increase as grain size decreased. The surface area per unit volume is known as specific surface of the propellant and measured in cm^{-1} units.

C. Combustion heat

It is determined as

$$Q_v = Q_p + RT \times \Delta n \text{ -------- } (3)$$

Where, Q_p = heat of combustion at constant pressure (kJ/mol); Q_v = the heat at produced at constant volume (kJ/mol); R = gas constant (8.314 J/mol K); T is temperature (K); Δn = moles difference between reactant and products of one kg gas.

D. 2.4 Specific volume (v)

It is determined as

$$Specific\ \ volume = 22.4 \sum n_i(g) \text{ -------- } (4)$$

This is measured in (L/kg) and $n_i(g)$ is amount of substance for i^{th} gas products of one kg of combustion gas.

E. Maximum Pressure (P_{max})

Using first-order approximation, the peak pressure generated inside the cartridge is obtained by assuming instantaneous propellant burning.

$$P_{\max} = \frac{m_p R\ T_f}{(V-b)} = \sum \frac{m_{p_i} R_i\ T_{f_i}}{(V-b_i)} \text{ -------- (5)}$$

where m_p =mass of combustion product gases, P_{max}=Maximum pressure, R universal gas constant, R_i Gas constant of i^{th} propellant product gases, T_{fi} =Adiabatic flame temperature of i^{th} propellant, b = co-volume of i^{th} propellant product gases, V = Volume

The values of R in various units are as follows.

R = 82.054 ml-atm/mole/K
= 8.31343 J/mole/K
= 1.9872 Cal/mole/K

At any given instance, m_p generated by the propellant burning is related to grain geometry of propellant and can be expressed in a polynomial of powers of λ and is dimensionless length which characterise the geometry of the propellant defined as web.

$$\mathrm{m}_p = \mathrm{m}_{p_o} \sum_j k_j \lambda^j$$ where m_{po} = Initial mass of unburned propellant-------- (6)

The above relation is also known as form function. The coefficients k_j are determined in accordance using propellant grain geometry. At each time frame, the combustion gases inside chamber are assumed in thermodynamic equilibrium and the pressure is related using equation of state for non ideal gases.

F. Force constant (F)

This is a one of the essential parameter of the propellant related to maximum work carried out by the propellant unit mass. The portion of an energy which can be utilised in doing the measurable work is the sum of force × distance travelled, is called as force constant. It gives a much lower energy per unit mass than heat of explosion. Usually there is important relation between the propellant mass and maximum pressure called as impetus or force constant. It is denoted by F

$$F = \frac{P_{\max}\ (\mathrm{V-\ b})}{\mathrm{m_p}} \text{ -------- (7)}$$

or $F= T_f$

The term n, being the number of moles of a gas per unit mass, is directly proportional to V, the gas volume at standard temperature and pressure (STP). Substitute V for n, Q for T_f because the two are mutually proportional.

F = Power = $T_{f\,\times}$α× Q×V

The expression $Q.V$ is called as characteristic product of the propellant.

The CV technique is generally used to determine the various parameters such as co-volume and F by burning the propellant with a 0.2 g/cc loading density. Maximum pressure and burning rate can be also determined. The propellant testing in a CV is economical as compared to actual dynamic firing that requires about 200 – 300 g of the propellant against the several kilogram quantity of propellant. Using F, the maximum energy (E) available from a solid propellant is estimated as

$$E = \frac{\mathrm{F\,C}}{(\gamma - 1)} \text{ -------- (8)}$$

G. Thermodynamic relations

As per the first law of thermodynamics, state of gas in the system can be determined [5].

$$Q = \Delta U + W \text{ -------- (9)}$$

Here Q= the energy supplied to the system, W= work done by the system, ΔU = change in internal energy.

Work by the system is expressed as

$$W = \int F.\ dx \text{ -------- (10)}$$

The right hand side is the dot product of the two vectors and gives scalar quantity.

Equation 7 can be written as

$$W = \int F\ dx \text{ -------- (11)}$$

Using material mechanic

$$F = P \times A \text{ -------- (12)}$$

where, F= resultant force is that expressed as product of average pressure P acting on cross sectional area A of the body.

Substituting this in equation 11, gives

$$W = \int P \times A \times dx \text{ -------- (13)}$$

Here dx is the displacement of length, then volume is expressed as i.e. $dv = A \times dx$. Putting this in equation 13, gives

$$W = \int P \times dv \text{ -------- (14)}$$

Here it is assumed that, the gas compression is adiabatic frictionless compression and no leakage. Gun chambers possess a very small room for oxygen as it is filled with the propellant. Free volume in the chamber is always available. A chamber has volume V_c where combustion of propellant takes place is given by

$$V_c = \frac{\pi \times d^2}{4} \times l \text{ -------- (15)}$$

According to ideal gas law, pressure P can be expressed as

$$P = \frac{m_g \times R \times T}{\mathrm{V}} \text{ -------- (16)}$$

Here, m_g= mass of gas, V= specific volume of the gas, P= gas pressure, T= absolute gas temperature and R= gas constant. Putting equation 13 in equation 11

$$W = \int m_g \times R \times T \frac{dV}{\mathrm{V}} \text{ -------- (17)}$$

The above equation shows that work done on the projectile is a function of temperature and volume of gas. For a closed system, the absolute temperature T and initial temperature T_i is related as

$$T = T_i \left(\frac{V_c}{V} \right)^{(\gamma-1)} \text{ -------- (18),}$$

Here γ= specific heat ratio. Putting equation 15 in equation 14 gives

$$W = m_g \times R \times Ti \times V_c^{(\gamma-1)} \int_{V_C}^{V} V^{-\gamma} dV \text{ -------- (19)}$$

The concept of entropy is defined by second law of thermodynamics

Tds=du+ Pdv-------- (20)

From enthalpy relation, *Tds=dh - vdP*-------- (21)

$$s_2 - s_1 = C_p \ln \left[\frac{T_2}{T_1} \right] - R \ln \left[\frac{p_2}{p_1} \right] \text{ -------- (22)}$$

$$s_2 - s_1 = C_v \ln \left[\frac{T_2}{T_1} \right] + R \ln \left[\frac{v_2}{v_1} \right] \text{ -------- (23)}$$

Here subscript '1' and '2' represent the initial and final states of the substances. An isentropic process is reversible wherein it remains constant. In real practise, an entropy increases or constant. The isentropic processes is written as

$$\frac{p_2}{p_1} = \left[\frac{\rho_2}{\rho_1} \right]^{\gamma} = \left[\frac{v_2}{v_1} \right]^{-\gamma} = \left[\frac{T_2}{T_1} \right]^{\frac{\gamma}{\gamma-1}} \text{-------- (24)}$$

3. Solid Propellant Gas Generator Description

The main explosive filling of gas generator must not be prone to accidental initiation. To achieve this, explosive compositions are chosen which are relatively insensitive but have large energy outputs to give the required performance. Materials are known which are readily initiated by relatively small energy inputs but, in general, they have fairly low energy outputs. Also, due to their sensitiveness, it would be inadvisable to have a large quantity for safety reasons. To utilize these two types of explosive, a booster is used with a properties intermediate between two extremes. Together they make up an explosive train. Great safety and reliability is achieved in this way. The safety arises from the ability to break the chain either between initiator and booster or between booster and propellant. The gas generator is one cartridges used in seat ejection seat of trainer aircraft. The cartridge consists of a Case and Foil Assembly and End Cap. The cartridge case is designed to accommodate the propellant and booster. It is made up of case material *i.e.* brass, the base of which is closed with cap assembly for initiation and the other end is closed by a copper foil. Case and End Cap are made up of Brass. Base of the End Cap is having a centrally located cap chamber at one end where percussion cap is fitted. Two flash holes are provided in the cap chamber. The cartridge is filled with DB propellant and booster. The End Cap is threaded to the filled cartridge case with applying thread sealant for hermetic sealing. The design aspect for brass cartridge case for using bilinear kinematic hardening model is explained [6]. The schematic construction detail of the propellant gas generator, its image and seats of fighter aircraft illustrating the location of gas generator is shown in Fig. 3. The firing pin strikes the cap and generates the flash. This initiates the booster. Booster further ignites the propellant. The propellant gases so generated acts on harness mechanism which produces the force. This is responsible for functioning of harness system of seat ejection.

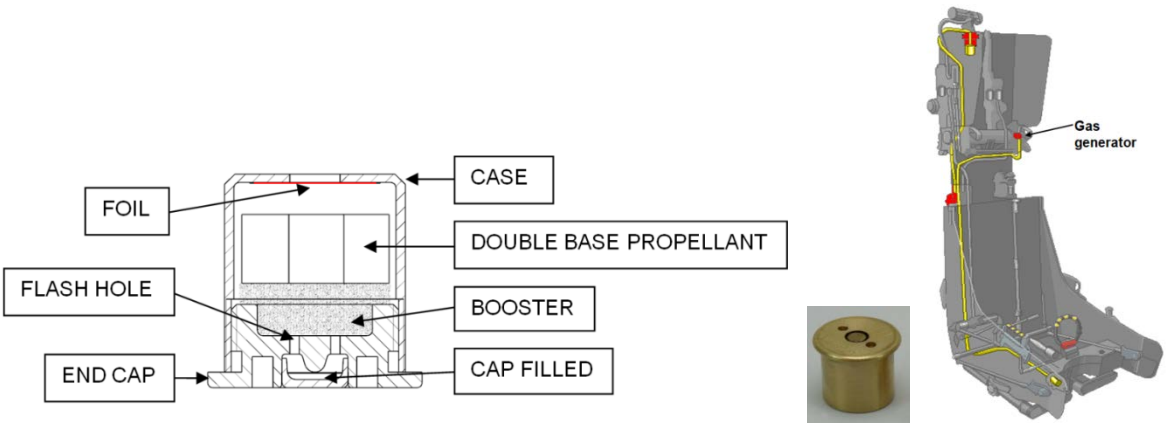

Fig. 3. The schematic construction detail of solid propellant gas generator its photo and seats of fighter aircraft illustrating the location of gas generator

4. Ingredients and Materials

A. Double Base (DB) Propellant for gas generator

In this study propellant with tubular in single axial perforation without inhabitation with neutral type burning is selected so as to achieve build up of pressure. The propellant so selected should be compatible with case material and non hygroscopic in nature. Based on above requirements, DB propellant type is selected which consist of nitro-cellulose (NC), nitro-glycerine (NG) and other additives. The basic chemical composition and physical properties of DB propellant that is used for aircraft application indicated in Table 1. The photo of DB propellant used in CV is shown in Fig. 4.

Fig. 4. DB propellant

Table 1 Basic chemical composition and physical properties of DB Propellant [7]

Chemical Composition		
NC (12 % N content)	:	59 ± 1.5 %
NG	:	32 ± 0.5 %
DEP	:	6 ± 0.5 %
Carbamite	:	2 ± 0.2 %
Candela wax	:	1 %

Dimensions of propellant grains		
OD	:	14.1±0.2 mm (Nominal)
Web	:	5.10 ± 0.15 mm
Length	:	6.5 mm (Nominal)
Density	:	1.57 g/cc
Shape	:	Tubular in single axial perforation

The chemical content in the propellant dictate the total amount of thermal energy released by burning it. Solid propellant for gas generator application invariably contains polymeric macro-molecules. Pure substances, in which fuel and oxidiser are present in the same molecule is called base for propellants. DB propellant is homogenous propellant type contains NC and NG. Homogenous propellant is also called colloidal propellants as it forms colloidal mixture of components or smokeless propellants because their combustion products contain water vapour, oxides of nitrogen and carbon and are free solids, soot, coloured gas, liquids or condensable gases. Although both bases of DB propellant are explosive in nature with a velocity of detonation of order of 6-7 km/s, but with combination and proper compounding, they undergo slow deflagration. This gives a burning rate of order of few mm/s at standard operating conditions. This propellant is thermoplastic in nature and can be softened on application of high temperature. NG is main plasticizer in DB propellant.

5. Experimental Set Up of Closed Vessel (CV)

A. Pressure~Time (*P~t*) profile of solid propellant gas generator

A CV is cylindrical in shape where the cartridge is loaded. It is a laboratory apparatus. Experimental firing procedure consists of CV body, gauge adapter, cartridge, firing mechanism, copper washer and closing plug. The firing mechanism is placed at one end and closing plug at opposite end. Copper washer is placed on closing plug to avoid the leakage of combustion products after propellant burning. Yokogawa scope corder and charge amplifier are used to record pressure. A gauge adapter with pressure sensor is fitted to the vessel body. The pressure sensor is selected to have a fast response, small size, durability, hermetically sealed construction, measurement range 15000 psi, sensitivity 0.39 *pC/psi* and a rise time of $\leq 1\ \mu s$. The vessel has been designed and fabricated for realisation of performance parameters [8]. The sketch of CV is shown in Fig 5. The striker of mechanism strikes the cap and indents it. This action crushes the sensitive composition between the cap and anvil in the base of the cartridge case. The flash passes through the two flash holes to ignite booster and propellant. Typical Pressure-time (*P-t)* profile produced after firing of the cartridge in CV is shown in Fig. 6. The methodology is similar to the performance parameters of cartridge in CV [9].

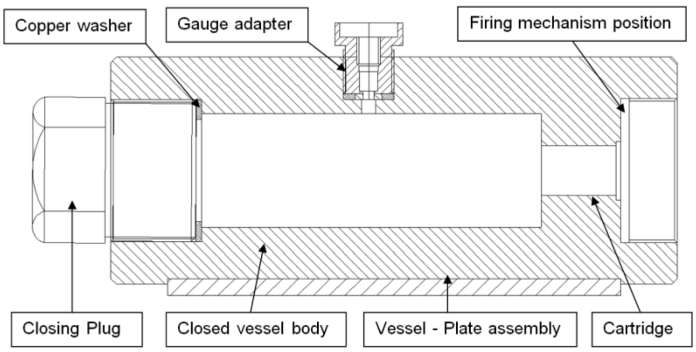

Fig. 5. An engineering sketch of CV

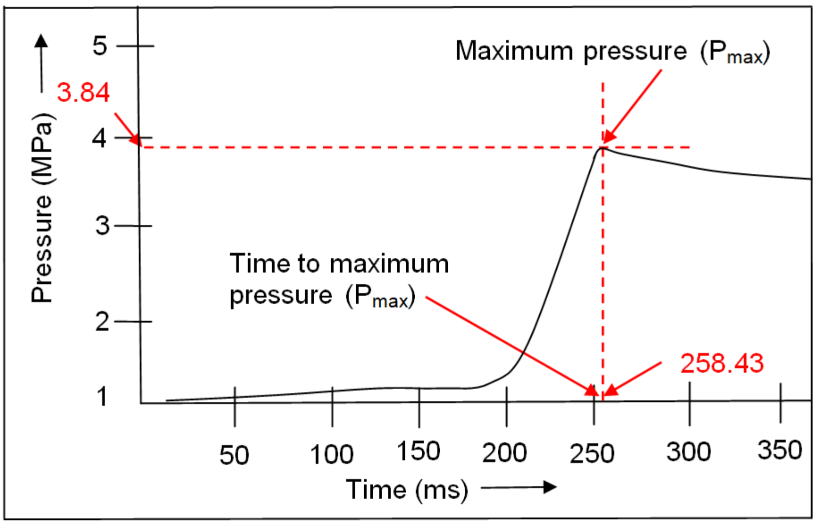

Fig. 6. P~t profile in a CV

B. Energy Balance equation

As propellant ignites inside the CV, the chemical energy is converted into gas energy resulting into high pressure and high temperature of combustion products. In this burning, two assumptions are to be used [10]-

- The system is adiabatic (no heat transfer, due to rapid burning process) where propellant ignition takes place and
- Exothermic reaction within CV due to decomposition

According to first assumption, Solid $\longrightarrow$ Gas + Energy

Using the first law of thermodynamics

$dQ = dW + dU$-------- (24)

where, dQ, dU, and dW are heat supplied to the system, an internal energy and work performed. As the vessel experiences no heat transfer and no deformation, dU=0.

6. Result & Discussion

The performance evaluation of the gas generator is carried out in a specially designed test vessel i.e. CV. A gas generator generates the pressure in the range of 2.7 to 5.3 MPa, TP_{max} : 216 to and 332 ms in CV at hot (45^{0}C) and cold (-26^{0}C) conditions having 150 cc volume. The cartridges are conditioned for minimum of six hours before firing. The cartridges are filled with propellant and booster masses 1.5 g and 0.4 g respectively during CV firings. Performance characters such as *Pmax* and *TPmax* of solid propellant gas generator are experimentally evaluated in a suitable test vessel designed and fabricated for that application [11,12]. The various thermodynamic parameters of solid propellant gas generator such as co-volume, flame temperature, force constant, calorific value, maximum pressure etc. are obtained experimentally with the facilities in the laboratory are enumerated at Table 2.

Table 2 : Thermodynamic properties of solid propellant gas generator

Thermodynamic properties		**Values**
Mean molecular weight	:	23.27 g /mole
No. of moles of gas	:	0.04542 mole/g
Combustion heat of propellant	:	531.32 cal/g
Gamma	:	1.2448
Flame temperature	:	2944 K
Internal energy of product gases	:	830 cal/g
Specific heat	:	0.3488 cal/g/^{0}C
Ratio of Specific heat	:	1.2
Gas volume	:	962.75 cc
Co-volume	:	0.989
Force constant	:	1052 J/g
Calorimetric value	:	925 cal/g
Maximum Pressure at 0.2 loading density	:	260 MPa

The burn rate and calorimetric value of the propellant is determined using strand burner and bomb calorimeter instruments. The other parameters flame temperature and force constant are obtained by the propellant burning in a CV at loading density of 0.2 g/cc. Differential scanning calorimeter (DSC) is used to determine the specific heat. Specific heat of propellant is determined and varies from 0.25 to 0.35 cal/g/^{0}C depending on the propellant composition. This paper addresses all goals and an objective that meets in a full scale test demonstration for the solid propellant gas generator for aircraft application.

7. Conclusions

In this paper, the present work is summarised to the different thermodynamic aspects to evaluate the various properties of solid propellant gas generator for aircraft application. The major parameters of solid propellant gas generator are dependent on volumetric loading, pressure time profile, propellant grain configuration and chemical contents. Performance characterisation of solid propellant gas generator in CV is also explained in this paper. This data helps for ballistic study, serviceability, safety and propellant life before induction into actual use. All calculations are generally made with an applicability of ideal gas law and temperature and pressure. While predicting and assessing the results, it is necessary to keep in mind the various assumptions. Such type of solid propellant gas generator has to qualify various design tests during development phase till gets inducted into service.

8. References

[1] Rocketry with solid propellants - Himanshu Shekhar, 2018, Studium Press (I) Pvt. Ltd, New Delhi. ISBN :978-93-85046-15-5

[2] Adam S. Cumming, New trends in advanced high energy materials, *Journal of Aerospace Technology and Management*, 1(2), **2009**, pp 161-166

[3] Z. Y. Han, Y. P. Zhang, Z. M. Du, Z.Y. Li, Q. Yao, and Y. Z. Yang, The Formula Design and Performance Study of Gas Generators based on 5-Aminotetrazole, *Journal of Energetic Materials*, **2017**, pp 1-8, DOI:10.1080/07370652.2017.1311969

[4] Karen S. Martirosyan, Leizheng Wang, Arol Vicent, Dan Luss, Nano energetic Gas-Generators: Design and Performance, *Propellants Explos. Pyrotech.* **2009,** vol. 34, pp 532–538, DOI: 10.1002/prep.200800059

[5] Engineering Thermodynamics, P K Nag, Sixth Edition, McGraw Hill Education (India) Pvt. Ltd, Chennai, 2018

[6] Parate B A; Chandel Sunil and Shekhar Himanshu. Cartridge Case Design and its Analysis by Bilinear, Kinematic Hardening Model, *Advances in Military Technology*, **2019**, Vol 14 (2), pp 231-244, ISSN 1802-2308, eISSN 2533-4123, DOI 10.3849/aimt.01283

[7] Double Base Propellant Specification No. HEMRL SPECN No. HEMRL/GP/PS/410

[8] Parate B A; Chandel Sunil and Shekhar Himanshu. Design Analysis of Closed Vessel for Power Cartridge Testing, *Problems of Mechatronics Armament, Aviation, Safety Engineering*, **2019**, Vol. 10 1 (35), pp 25-48, ISSN 2081-5891, DOI :10.5604/01.3001.0013.0794

[9] Parate B A; Chandel Sunil and Shekhar Himanshu. Performance Evaluation of Power Cartridge in Closed Vessel for Water-Jet Application, *International Journal of Energetic Material*, **2021**

[10] Parate B A; Chandel Sunil and Shekhar Himanshu. An experimental and numerical approach - Characterisation of Power Cartridge for Water-jet Application, *Defence Technology,* **2018**, Vol. 14(6), pp 683-690, DOI :10.1016/j.dt.2018.04.003

[11] Oliveira J L S P de, Filho A A M F , Platt G M, Peixoto FC. Estimation of ballistic parameters of gun propellants through closed vessel experiment modelling, Thermal Engineering, **2005**, Vol. 4, pp 50-55

[12] Parate B A; Deodhar K D and Dixit V K. Qualification Testing, Evaluation and Test Methods of Gas Generator for IEDs Applications, *Defence Science Journal*, 2**021,** Vol. 71, No. 4, pp. 462-469, DOI : 10.14429/dsj.71.16601.

Experimental Modelling and Analysis of Acoustic Impingement on Propagating Fires

K. Sunil Kumar
Advanced Systems Laboratory
DRDO
Hyderabad
ksunildrdo@gmail.com

Amitabh Chakraborty
Advanced Systems Laboratory
DRDO
Hyderabad

Dr R.Srinivasan
Advanced Systems Laboratory
DRDO
Hyderabad

Dr I Srikanth
Advanced Systems Laboratory
DRDO
Hyderabad

Dr S Srinath
Dept of Chemical Engg
NIT Warangal
Warangal

Abstract - **Explosives are substances which produce high temperature gases instantaneously within a few micro seconds. Detonation occurs in explosives where combustion rates are extremely higher than velocity of sound in explosive medium. In long range missiles and satellite launch vehicles, high explosives in small quantities were used for stage separation application for separating spent stage from the ongoing stage and in large quantities for destruction of vehicles.**

In the present study, efforts are made to convert High explosive energy into useful and controlled gas generating compositions to perform useful work. PETN based linear Mild Detonating Cord (MDC) with core load density of 5 g/m was chosen for present study. MDC of 500 mm length was tested in 500 cc Closed Vessel (CV). Pressure generated was measured with piezo resistive transducers. Pressure generated was compared with theoretical calculations which were showing good agreement. Upon cord initiation, explosive reaches maximum pressure and it exponentially reduces with time. CV material thickness and its physical properties determine the rate of pressure drop. This novel method of converting high explosive energy for gas generation purpose finds application in mechanisms which require actuation in micro seconds. On the other hand conventional Gas generators from Pyrotechnic compositions have actuation time in the order of few milli-seconds. In gas generator based applications, gas chamber is to be designed with complete leak proof ness. It can be used in stage separation events which may require smoke less separation

Keywords: High Explosives, Pyrotechnic compositions, MDC, Detonation, Gas Generators, Missiles, Launch vehicles, Stage separation, Closed Vessel.

1. Introduction

Explosives are reactive substances which when properly initiated produce a large volume of high temperature gases accompanied by heat, light and sound. Generally, High explosives are mostly used in defence sector for destruction of enemy targets. They are extensively used in missile warheads, mining industry. Based on their sensitivity and rate of reaction, explosives are generally categorized as low explosives and high explosives [1][2]. High explosives are those reactive substances in which the chemical reaction rate front (explosive decomposition reaction) moves faster than the speed of sound in unreacted medium. This supersonic combustion phenomenon is called detonation. Common high explosive materials include RDX, HMX, PETN, TNT et. High Explosives are more stable and their velocity of detonation is above 7500 m/sec [2]. Low explosives are those reactive substances in which chemical reaction rate are less than speed of sound. This subsonic combustion phenomenon is called deflagration [3]. This type of deflagration phenomenon is exhibited by all fuel combustion processes, Pyrotechnic compositions, propellants etc. Explosives are also categorized by their sensitivity to initiate. Primary explosives are the explosive substances which initiates with small amount of heat or impact, for instance mercury fulminate, lead azide, lead styphnate etc. These explosives are extremely dangerous to handle and hence proper care has to be taken while handling primary explosives. These primary explosives are handled in few milli grams by ensuring safety and proper discharging of static charge of body. On the other hand, secondary explosives are less sensitive and can be handled in large quantities like HMX, RDX, PETN, TNT etc., For safe functioning of any explosive or propellant initiation, explosive train is employed in which a few milligrams of primary explosive is initiated followed by required quantity of High Explosive[4].

For the evaluation of the functional testing of these high energy materials, CV tests are exclusively used. During CV tests, a small quantity of pyrotechnic composition or propellant is fired inside a closed volume. These vessels are designed to withstand pressure developed by propellant [5]. Pressure developed in CV is monitored by pressure transducers through high speed data acquisition system. Several studies were made for estimation of heat loss in CV testing [6]. Generally, CV tests are conducted to estimate the shelf life of power cartridges and ammunition [7]. Many pyro actuated mechanisms like fighter aircrafts seat ejection mechanism have been designed based on the available free volume of CV tests [8].

When the propellant sample size is fairly large, semi closed vessel tests are carried out [9]. In semi closed vessel test, exhaust gases are vented out of the vessel and chamber pressure is recorded. Generally composite propellant and double base propellant burn rates are evaluated in CV [10][11]. During propellant burn rate evaluation, CV is initially pressurized with inert gases generally upto 7 MPa pressure. The burn rate is thus evaluated by measuring the time taken for burning of a known length of propellant sample. Gun propellant which are single, double or triple base propellant grains are functionally tested in CV.

Most of the works on CV test shows were carried out on low explosives like power cartridges, pyro cartridges, gas generators, gun propellants or rocket propellants. There is not much of literary work carried out on CV tests with high explosives. The present work focuses on CV tests of PETN based MDC with a core loading density of 5g/m. MDC are widely used in mining industry for blasting of rocks. Advantage of using MDC cord for gas generating compositions is that it produces gas extremely fast due to detonation. In addition, these MDC cords are available in 4 mm diameter wires, which can be used in the development of very quick reaction separation system in satellite launch vehicles which move at higher Mach speed.

Aim of the present work is to study the pressure developed by high explosive when detonated in CV and correlate it with theoretical calculations.

2. Experimental Work

PETN based MDC cord is taken and assembled in a 500 cc CV, which is made up of SS304 material. Schematic test setup is shown in Figure 1. MDC cord is attached to detonator. Detonator assembly is placed inside the vessel with a leak proof joint. Vessel is equipped with 2 types of pressure transducers. In addition, the test has been carried out with high speed video which can capture any black smoke coming out of the CV in event of any leakage through the joints. Pressure is recorded by piezo-resistive type transducer. The electrical resistance of the detonator has been checked and found to be varying between 0.8 to 1.2 ohms. Recommended firing current for Detonator is 2 to 5 Amps. During test, recommended fire current is passed to detonator through DC power supply. Detonator produces shock wave which further initiates the MDC cord and the vessel is filled with hot gases. Pressure generated in CV is measured through data acquisition system at 10,000 samples per sec. MDC cords of 500 mm length was used for CV measurement.

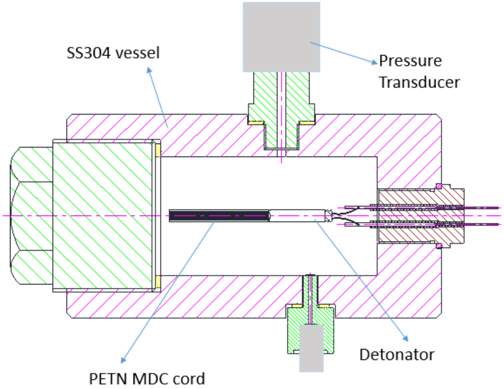

Fig 1: CV test set-up.

3. Result and Discussion

Fig 2 shows the pressure versus time data of MDC cord which is plotted along with start signal and current drawn by detonator. The recording of the data acquisition was started nearly 5 seconds before detonator initiation. In Fig 2, zero time is taken based on the start signal input. It can be seen that instantly pressure rises to 59.2 ksc (5.8MPa) in the CV due to detonation of cord with consumption of cord. As the CV material SS304 conducts heat, gas temperature drops exponentially to 4 ksc (0.4MPa)[6]. This final gas pressure was retained until vent holes were opened

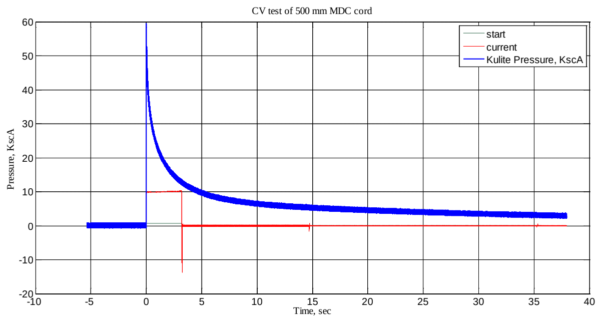

Fig 2: Test results of 500 mm MDC cord in CV

Ignition delay is found to be 5 milli seconds (ms) and time to reach maximum pressure Pmax is 5.6 ms. In case of gas generators air bottles are generally used where delay is in seconds duration. Pyrotechnic gas generator compositions produce gas with ignition delay of 30-100 ms [7]. In contrast, by using this novel method of using MDC cord as gas generator gases can be produced within a few milliseconds (<10 ms). Hence, explosive cord based gas generators are the fastest source for pressurization. Explosive based gas generators can be used in events which need to be operated from microseconds to less than 10 ms duration. These events find their application in case of payload fairing separation where the delay between the vertical and horizontal separation are designed to be within few microseconds duration. In addition, it can be used in various other stage separation or panel separation mechanism.

4. Theoretical calculations:-

Amount of explosive present in 500mm PETN cord of 5 g/m core load density cord is 2.5 g. Amount of explosive (PETN) in Detonator is 150 mg i.e., 0.15 g. Hence, the net explosive quantity is 2.65 g. For theoretical calculation, the hot gases produced by MDC cord initiation were assumed to be ideal gases. As per NASA SP273 chemical equilibrium program which minimizes Gibbs free energy, molecular weight of exhaust gases is 25.63 g/gmole. Exhaust gas temperature is 3100 K [2].

Net PETN explosive quantity = W = 2.65 g = mass of produced gases
Temperature of gas = 3100K
Molecular weight of exhaust gases = M = 25.63 g/gmole
Universal gas constant R = 8.314 J/gmole/K
Using ideal gas equation, PV = nRT = WRT/M,

$$P = \frac{WRT}{VM} = \frac{2.65 * 8.314 * 3100 * 1000}{0.5 * 25.63} = 53.3\ bar = 54.35\ \mathrm{ksc}$$

Pressure calculated is 5.33 MPa against experimental value of 5.9 MPa, which is in close agreement. The difference in the experimental to theoretical value is mainly attributed to the ideal gas assumption.

5. Conclusion

For the first time, the pressure developed by high explosive is measured in CV. 500 mm MDC cords was tested in 500 cc CV. On initiation of Detonator within 4.8 milli seconds Pmax is reached and exponentially pressure dropped to 4 ksc as the vessel dissipates heat by conduction. Theoretical calculations were carried out by assuming ideal gas equation and the results are closely matching with experimental Pmax. Lower ignition delay and lower Pmax time obtained with high explosive system finds very promising application for high altitude stage separation systems in launch vehicles and long range missiles where separation needs to be completed in micro seconds to less than 10 milliseconds duration.

6. Acknowledgements:-

The authors express sincere gratitude to The Director, Advanced Systems Laboratory for extending support during the course of this work.

[1] Reference
[2] High Energy Materials: Propellants, Explosives and Pyrotechnics", JP Agrawal, Wiley-VCH, Verlag GmbH & Co. KGaA Weinheim
[3] "Propellants and Explosives: Theoretical aspects of Combustion", Naminosuke Kubota, Wiley-VCH Verlag GmbH.
[4] "The Chemistry of Explosives", Jacqueline Akhavan, 3rd edition, RSC publishers
[5] "Introduction to Technology of Explosives", Paul W Cooper, Wiley "An experimental and numerical approach - characterisation of power cartridge for water-jet application", Parate et al, Defence Technology, Volume 14, Issue 6, December 2018, Pages 683-690
[6] "Estimation of Heat Loss in a Closed Vessel", Parate et al., Defence Science Journal, Vol. 57, No. 2, March 2007
[7] "Prediction of operational life and shelf life of power cartridge based on ballistic performance in closed vessel after accelerated ageing", Sahu et al, 2014, Int. Conf. on High Energy Materials Conference and Exhibit
[8] "Design, Development, Testing and Performance Evaluation of Main Ejection Seat Cartridges for fighter Aircraft", Parate et al, 2009 Int. Conf. on High Energy Materials Conference and Exhibit
[9] "Combustion Study of Power Cartridge in Closed and Semi-Closed Vessel for Water Disruptor Application", Parate et al, Journal of Physics: Conference Series 1507 (2020) 022023, 2020 Spring International Conference on Defence Technology.
[10] "Use of closed vessel as a constant pressure apparatus for the measurement of the rate of burning propellants", Vittal D et al., Defence Science Journal, 1980, 30(2), 69-74
[11] "Pressure development in closed and vented vessel", John et al,1982, Plant/Operations Progress, Vol. 1, No. 2, pp 75-85

Double - Action Initiating Mechanism for a Detonation Circuit

SS Khandagale
Armament Research and Development Establishment
Pune
sskhandagale@arde.drdo.in

Prabhakar Kumar
Armament Research and Development Establishment
Pune
E-mailpkumar@arde.drdo.in

KD Deodhar
Armament Research and Development Establishment
Pune

VK Dixit
Armament Research and Development Establishment
Pune

S. Shrivastava
Aeronautical Development Agency
Bengaluru

Abstract – **The Ground Egress System (GES) is a life-saving system mounted inside the cockpit of a modern fighter aircraft. It is a mechanical-cum-explosive system used for clearance of escape path for the aircrew in case of ground emergencies. The system requires mechanical initiation by hand that involves two deliberate actions. The paper presents various design schemes which can introduce two deliberate actions instead of single pulling action. A novel mechanism incorporating a dual action initiating system, "Rotate-and-pull" type, was selected and developed in discussion with the user and other stakeholders. The paper also brings out the operating constraints like minimal design envelope and minimum functioning time and they were overcome during the design of the mechanism**

***Keywords*– Severance System, Ground Egress System, Initiating mechanism, Detonation, Detonating cord, Explosive Transfer Line, Torsion Spring, Ergonomics.**

1. Introduction

All modern fighter aircraft are equipped with emergency escape systems for aircrew. These systems become operational only when the aircrew is required to abandon the aircraft or they are not able to use normal means of coming out of the aircraft. In case of inflight emergencies, seat ejection system and escape path clearance system both are integrated for safe and rapid rescue of the aircrew. Whereas in case of ground emergencies, there is separate Ground Egress System (GES) that is used for rescue of aircrew. The escape path clearance is generally achieved by cutting or pre weakening the canopy bubble [1]. The bubble then can be further cleared during ejection with minimum or no injuries to the aircrew. In case of ground operation, the bubble is cut peripherally and can be manually dislodged by the aircrew inside or by rescue party from outside. The system discussed here consists of mechanical initiators, junction boxes, pyrotechnic or specifically, explosive lines and MDC i.e. Flexible Linear Shaped Charge (FLSC). The principle of controlled propagation of detonation wave is utilized in the operation of the system. The FLSC detonates and cuts the canopy bubble to achieve escape path clearance. Thus, the GES is a mechanical-cum-explosive system used for clearance of escape path for the aircrew in case of ground emergencies. The detonation wave starts from initiator and travels through explosive lines, junction boxes, connector and finally to FLSC, hence the system can be rightly thought of as a detonation circuit. A circuit-like representation of the system is shown in line diagram - Fig 1 below.

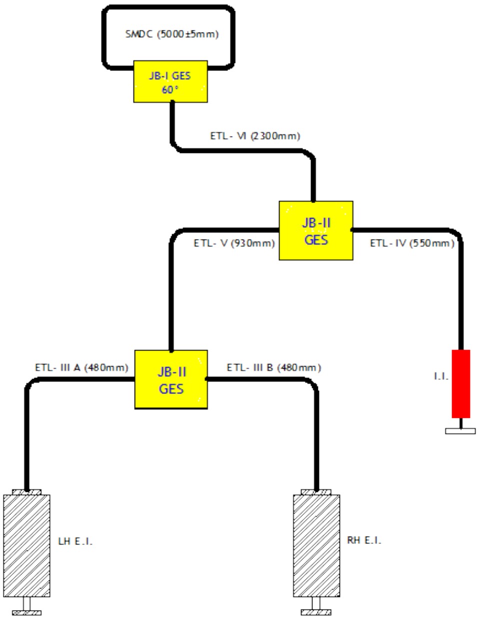

Fig. 1: Layout of Ground Egress System (GES)

2. Operating Principle

There is a mechanically operated initiator that uses a stab type detonator, which when struck by a firing pin, initiates the system. The mechanical operation involves pulling the handle by a minimum force of about 8 kg. This causes the sear release mechanism to move backward and compress the spring. After some movement the sear and firing pin disengage and the pin accelerates forward under the influence of spring force. The firing pin hits a stab detonator containing initiatory explosive composition. This creates burning to detonation transition inside the detonator. The detonation is further reinforced by a booster at the end of detonator, after which it travels through explosive lines.

The initiator has a safety pin to avoid pulling the initiating handle by mistake while the aircraft is on ground. However, the pin is removed before take-off. This situation may give rise to inadvertent operation of the initiator just by pulling the handle by aircrew or maintenance crew. As a matter of fact, this type of inadvertent pulling has caused the system to function unintentionally and resulted in minor accidents [2]. Various measures to rule out such kind of accidents were thought of and it emerged that introducing two deliberate and specific mechanical actions for functioning of the initiator would be the most satisfactory solution. That's why the initiator will be referred to as Double - Action Initiator.

3. Requirements of Mechanism

The necessary and preferred requirements of the system were worked out prior to design, these are as following:

A. The initiating mechanism shall incorporate two deliberate hand operated actions for initiation of detonation instead of present single pulling action so as to avoid inadvertent operation.
B. Preferably, the two actions should be orthogonal to each other and should be of different nature.
C. The main pulling handle shall not be accessible initially to the operator. This automatically avoids inadvertent functioning.
D. The design constraints like minimum mass and envelope dimensions have to be complied.

E. The mechanism shall not be in a pre-cocked condition. This entails that the firing pin should be in free or unarmed condition always and be armed only when operation of the initiator is desired.
F. The mechanism shall be hand operated following ergonomic norms.
G. The assembly shall meet all the military qualification and acceptance criteria as brought out in technical specifications from users and certification agencies [3].

4. Conceptual Design & Selection

In view of the above requirements, various hand operated mechanical actions can be thought of for inclusion in the design e.g. pressing a switch, pulling or pushing a handle, rotating a lever etc. Some similar systems in other aircraft also employ this kind of dual action initiation. For example, in one aircraft, the handle is initially flush with the cockpit frame. After pushing the same, it pops out, which is then grabbed and pulled so that a cable comes out leading to operation of sear release mechanism [4]. In a similar system of very modern aircraft, a switch is pressed to turn a lever about 400 from its rest position. This makes a flat surface on the lever accessible to the crew. The flat portion is then further pressed down to operate the mechanism.

However, requirement of unarmed firing pin as in present design requires that the sear release mechanism to be kept as it is, which means the final or second action always will be of pulling the handle causing the main spring to compress. The first action can be turning, pressing, pushing etc. Accordingly various schemes incorporating each of these actions have been worked out and shown in Fig. 2 – 4 and are described below:

A. Press Pull Type Scheme

In this scheme, first action is the pressing a switch so that a ring type handle pops out. The ring is then pulled to fire the detonator, refer Fig. 2.

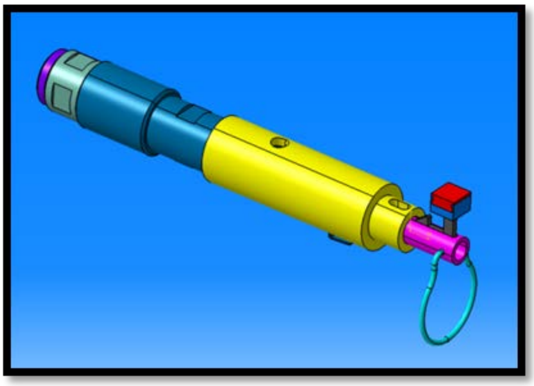

Fig.2: Press Pull Type Scheme

B. Push Pull Type Scheme

There is a single handle in this scheme which is first pushed inside to engage a dog mechanism and later pulled to operate the initiator, see Fig. 3

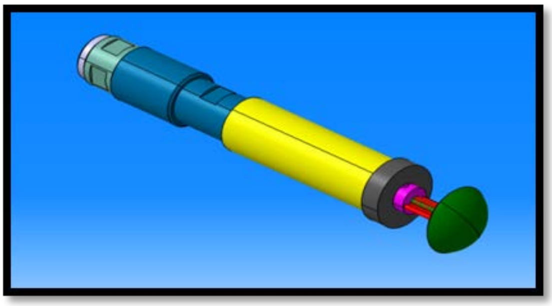

Fig.3: Push Pull Scheme

C. Rotate – Pull Type Scheme

Here, first a lever is rotated by about 90 degrees so that a handle comes out. The handle is then pulled to compress the firing pin spring and after certain movement, sear is released to set the firing pin free to hit the detonator with high velocity, refer Fig. 4

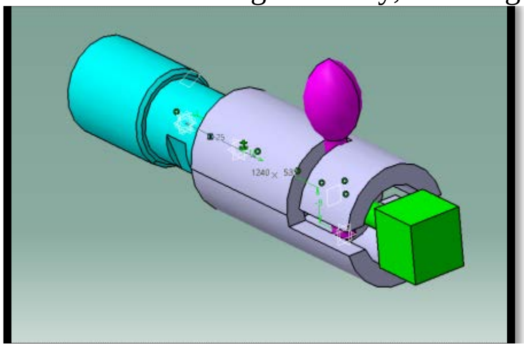

Fig.4: Rotate Pull Lever Scheme

Out of these schemes, the third one i.e. Rotate and Pull type was chosen as most satisfactory by users due to following reasons:

A. Distinctly identifiable two separate actions in orthogonal direction
B. Ease of operation
C. Little chance of malfunctioning or damage due to mechanical abuse e.g. transit drop, vibration, shock etc. The switch type devices may operate during drop or shock type of environment. Hence this scheme can pass the MIL grade qualification testing.

5. Details of Mechanism

The mechanism has been developed in three sections viz. detonator and firing pin section, sear and auxiliary spring section and third, the lever and handle section.

A. Detonator and firing pin section:

Since the detonator has to be mechanically initiated, stab type of detonators are suitable. The diameter of explosive lines and cup-type boosters assembled on their tips is kept much small compared to other HE charges i.e. about 5 mm. Therefore small detonators are required. The 350 mg detonator has a diameter of about 10 mm and has more peripheral effect on the explosive lines. Hence a detonator of approx matching diameter and less than half charge mass is chosen. But a booster is placed immediately after the detonator so that the wave is sufficiently strong before entering the explosive lines. This avoids the run-up distance effects in the lines and thus possibility of failure [5]. Reduction in overall diameter is also possible with this arrangement.

As brought out earlier, the firing pin should not be in a pre-cocked condition, hence, the pin and sear release mechanism is kept as it is. It is shown in Fig. 5. The firing pin should have a minimum velocity of 1 m/s to positively initiate the detonator [5]. This is achieved by spring loading the pin. However, hand pulling is governed by ergonomics and military standards requirements. Accordingly, a force of 8 - 12 kg can be applied by hand while performing pulling action with normal effort [6]. These two criteria govern the design of this section. Considering 8 kg force to fully compress the spring by about 7 mm, the stiffness is calculated as follows:

Given Parameters:

i. Actual Deflection (δ) = 7mm
ii. Force = 8 kg = 78.48 N
iii. Mean coil Dia (D) = 8 mm
iv. Mass of Firing Pin (m) = 7.5×10^{-3} kg
v. Modulus of Rigidity (G) = 79.5×10^{3} MPa

Stiffness of spring:

$$K = \frac{F}{\delta}$$

$$K = \frac{78.48}{7}$$

$$K = 11.21\ \mathrm{N/mm}$$

And the spring parameters can be easily found out by equation [7]:

For Stiffness of spring,

$$K = \frac{G \times d^4}{8 \times D^3 \times N}$$

Let us assume that Number of effective coils are, N = 6 Nos.

$$\therefore 11.21 = \frac{79.5 \times 10^3 \times d^4}{8 \times 8^3 \times 6}$$

$$d^4 = 3.46\ \mathrm{mm}$$

$d = 1.36mm$, say 1.4 mm.

The firing pin velocity can be found out by equating the PE of the spring to the KE of the pin. So,

Potential Energy in spring (P.E)

$$P.E = \frac{1}{2} \times K \times \delta^2$$

$$P.E = \frac{1}{2} \times 11.21 \times 7^2$$

$$P.E = 0.274\ \mathrm{Nm}$$

Potential Energy of Spring (P.E) = Kinetic Energy of firing pin after release.

Therefore,

$$\frac{1}{2} \times K \times \delta^2 = \frac{1}{2} \times m \times v^2$$

$$0.274 = \frac{1}{2} \times 7.5 \times 10^{-3} \times v^2$$

$$v = 8.54\ \mathrm{m/s}$$

Therefore, velocity of firing pin is 8.54 m/s which is much higher than the minimum required, hence fulfils the criteria. The firing pin and main spring are shown in Fig.5.

B. Sear and auxiliary spring section:

This is also shown in Fig. 5. The lug is engaged with the sear but is free to move inside the slot made on the sear and thus caters for lost motion arrangement

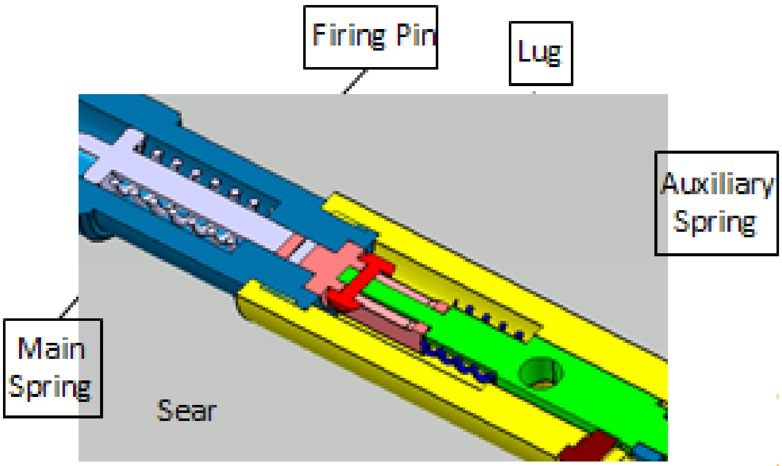

Fig.5: Firing pin and sear mechanism

The auxiliary spring parameters are found out below. This has to be of about half strength than the main spring so that the main spring should not get compressed and release the firing pin. At the same time the handle should come out quickly. Considering this and space constraints, possible movement of handle etc., following are spring parameters in hand:

(i) Force (F) = 6 kg = 58.86 N
(ii) Maximum allowed deflection (δ) = 10 mm
(iii) Mean Dia (D) = 9 mm and free length of Coil = 20 mm
(iv) Assuming a spring of 6 to 7 coils, pitch (P) is about 3.5 mm.
(v) For spring steel, G = 79.5* 103 N/mm^2

So, wire diameter is found out as below:

Stiffness (K):

$$K = \frac{F}{\delta}$$

$$K = \frac{58.86}{10}$$
$$K = 5.886\ \mathrm{N/mm}$$

Pitch of the coil (P):

$$P = \frac{Freelengthofcoil}{n-1}$$
$$3 = \frac{20}{n-1}$$

$$\therefore n = 7.66 \approx 8$$
$$\therefore No.ofactivecoil,$$
$$N = n - 2 = 6$$

The spring wire diameter is found out by stiffness formula for helical spring from Sec. 5.1 as 1.25 mm [7, 8].

C. The lever and handle section:

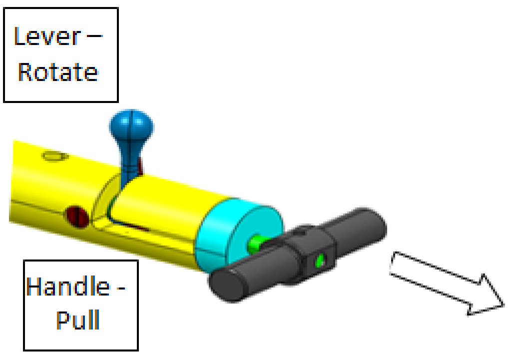

Fig.6: Lever and handle

This is additional development meeting all the stipulated requirements and is shown in Fig.6. Here the rotating lever and pulling handle are configured such that the handle comes out only when lever is rotated to align with the slot made on casing. This means it has to be preloaded and at the same time shall not compress the main spring. Hence arrangement of auxiliary spring and some kind of lost motion has to be made. The same is done in the Sear and auxiliary spring section. The lever is held in position by a mild torsion spring (Fig. 8).

The axis of torsion spring aligns with axis of the mechanism. The torsion spring parameters are found as follows [7]:

Available parameters:
(i) Force (F) = 3.5 kg = 34.33 N (mild force to turn the spring)
(ii) Length of arm (l) = 2 5mm
(iii) Mean Diameter (D) = 10 mm
(iv) Number of active coils (N) = 4
(v) Angular deflection (Ø) = 70º

$$Moment(M) = F \times I$$

$$M = 34.33 \times 25 = 858.25 \text{ Nmm}$$

$$Stiffness(K) = \frac{M}{\emptyset} = 12.26$$

$$K = \frac{Ed^4}{10.8 \times D \times N_a}$$

$$12.26 = \frac{210 \times 10^3 \times d^4}{10.8 \times 10 \times 4}$$

$$d = 0.3985 \text{ mm} \approx 0.4 \text{ mm}$$

6. Operation of the Mechanism

The whole system is enclosed in cover module (not shown) and fixed to Cockpit airframe besides the seat of the Pilot. In normal flight, the main pull handle is in retracted position and is unavailable to pilot for initiation of GES system as shown in Fig. 7. In case of any emergency, the pilot will rotate the lever by about 900 to bring the mechanism from safe to ready-to-initiate condition. This causes the lever to align with the slot on the casing. This forces the lever to move backwards as it is already preloaded due to compression of the auxiliary spring. So, the main pull handle or plunger pops out of GES module as shown in Fig. 8. However, this motion is not felt by the sear and firing pin due to lost motion arrangement made. But at the end of stroke by auxiliary spring, the handle is directly engaged with sear and firing pin, and then finally can be pulled by the Pilot to initiate the explosive system of GES and create escape path.

Consequently, the mechanism eliminates the possibility of any inadvertent operation by configuring the two enabling motions in orthogonal direction as well as of different nature i.e. rotation (lever) and translation (pull).

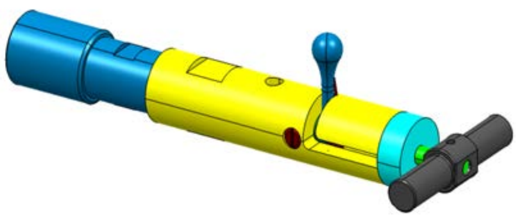

Fig.7: Mechanism in fail-safe configuration

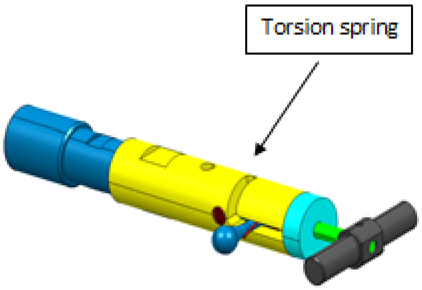

Fig.8: Mechanism in loaded configuration

7. Result and Conclusion

A double action initiating mechanism has been developed for emergency escape of the aircrew in case of ground emergencies. Overall reduction in weight and size is achieved. The mechanism also ensures firing of the detonator positively by double action and eliminates any inadvertent operation.

8. Reference

[1] HAL technical appreciation Note No. ARM/07 of June 2003
[2] Users feedback on accidents of GES by pulling handle - July 2017
[3] Type Test Schedule (TTS) for Egress System, May 1999
[4] Technical Manual for aircraft 10/2014
[5] Bailey A; Murray S G, “Explosives, propellants and pyrotechnics” Brasseys 1989
[6] MIL-C-83124, “Propellant Actuated Devices – General design specification for”, AMCP 1969
[7] Shigley, “Mechanical Engineering Design”, 10/e, 2015
[8] IS 4454:2001, “Steel wire for Mechanical Springs”, BIS, New Delhi.

Shelf life Extension study of Dual Igniter Air Pyro assembly based on ballistic evaluation for Operating Gas releasing Mechanism for Missile Application

A K Sahu
Armament Research and Development Establishment
Pune
aksahu@arde.drdo.in

PG Karande
Armament Research and Development Establishment
Pune

RM Kumar
Armament Research and Development Establishment
Pune

BA Parate
Armament Research and Development Establishment
Pune

KD Deodhar
Armament Research and Development Establishment
Pune

Abstract – **Electrically initiated pyro devices are employed for operating compressed gas releasing mechanism to initiate Turbo Generator of Missile system. The energy required for operating the mechanism derived from the energetic pyrotechnic composition of the pyro device. Shelf life extension study was carried out for the Air Pyro assembly. In the pyro assembly two pyro cartridges are connected in parallel mode with a single connecter assembly. Shelf life of the device is crucial because of its operational requirements within the service life of the system where it is istalled. Shelf life extension of electrically initiated Pyro Device were studied. The experimental methods are accelerated environmental testing followed by ballistic parameters evaluation in constant volume closed chamber in laboratory. The test set up was fabricated to measure the generated pressure on firing the Pyro device. For operating the severe mechanism instantaneous pressure is required, which is measured by using pressure sensor. It fulfils the technical requirements for the system. The trials conducted in three phases. The performance of environmentally simulated cartridges are comparable with the standard test data confirms the serviceability. This paper explain about the experimental method adopted during shelf life extension study. The life extension helps to keep the operational readiness of the User Agency**

Keywords– Air Pyro device, Dual Igniter, Energetic composition, Bridge wire, Shelf Life.

1. Introduction

Pyro device also called Pyro cartridges are used in a number application for operating system & sub system in critical military application. The use of Pyro device has importance due to it's better power to weight ratio. The energy generated in the form of gaseous pressure operate the sub system where it is installed. The application should be reliable & suit the initiation energy source available in the system.

The subject cartridge initiates on receipt of electrical pulses from the on board battery of the system, it fires & generate gaseous pressure, that activate the balancing mechanism. These cartridges are assigned certain shelf life based on the qualitative requirement of the system & experimental results of the pyro device.

The shelf life of Pyro Cartridge was determined by carrying out life extension trials. Based on the performance of the device shelf life could be reassigned. The performance of the cartridge depends upon the chemical stability of the energetic material contained inside it.

On firing the cartridge, the energetic material burns& generate pressure rapidly that cause the sub system operate. This will operate the turbo generator. The shelf life extension of the Pyro assembly needed due to insufficient life cartridge for service requirement. The cartridges consist of an initiation device, Booster & propellant charge. These explosive materials are enclosed inside a metallic case. The propellant charges are responsible for the energy generation of the store.

It is hermetically sealed by applying ammunition protective coatings & sealant. These type of devices are employed for a number of application e.g. Fire Extinguisher system, Operating Escape aid Device, Release compressed gas to operate the turbo generator of missile, Cable Cutter mechanism and many more.

Ageing of the energetic components are spontaneous and can't be prevented but it can be slow downed. The components shelf life can be maintained by storing them in required Magazine condition. The degradation of the energetic materials could be reduced by controlling the environmental conditions like humidity and temperature of the storage magazine.

The energetic material utilised in the pyro cartridge has a limited shelf life because of its characyterstics of auto catalytic degradation during service due to environmental effect. The energetic ingredients in contact with the moisture & humidity degrades. However the ballistic shelf life can be confirmed by environmental simulation in laboratory followed by performance evaluation in test vessel. [1]

The accelerated ageing method adopted is based on the assumption that all materials contained in the pyro cartridge react either with the environment or with themselves. These reactions are continuous at all temperature and all material undergo degradation with ageing. [2] Assuming that the reaction is continuously occurring during the simulation period, the test sample were withdrawn and tested for performance analysis. The stores subjected to requisite environmental simulation followed by performance evaluation in test vessel.

The test schedule for the trials are as per the storage life extension required. The energetic composition has its inherent properties of degradation of chemical shelf life. The autocatalytic properties of the energetic material responsible for the total life of the cartridge. The cartridge is hermetically sealed, so there is less possibility of moisture to ingress inside the cartridge and affect the composition

2. Material & Method

The methods for life extension study, viz the simulation process, the data acquisition & the comparison were studied.

A. Air Pyro cartridge

This **Air pyro Cartridge** is a Single Shot Devices. There are two individual pyro assembly connected in parallel mode. The pyro cartridge case is made up of Aluminum metal houses the Igniter assembly. The heating element along with the primary explosive & pyrotechnic composition enclosed inside the casing [3,4]. The cable fitted at the bottom along with the pyrotechnic composition. The pyrotechnic filling (gas generating material) in the main body [5,6]. The mouth of the case is closed with Celluloid Disc. Electrical Squib are Simple & reliable means of initiation. The pyro cartridge is shown in Fig 1.

Fig. 1. Cartridge Air Pyro Assembly

Nichrome wire is soldered between the two electrodes of the Cap. It acts as heating element. The minimum amount of heat energy required to initiate the explosive train is generated from the heating element.

B. Function & Use

Air Pyro Cartridge initiated upon receipt of electrical energy from the onboard missile. The Electrical initiator squib along with pyrotechnic composition is placed /located centrally at the base of Case.

The Squib is having heat sensitive initiatory explosive composition and heating element. When the electric current pass through the heating element, it heats up & becomes red hot and initiate the initiatory composition in its vicinity, generating flash that caught by the immediate pyrotechnic composition which generate gaseous pressure with high temperature flame. This pressure operates the shearing mechanism to release the compressed air to initiate the turbo generator.

The cartridge undergoing life extension study contains of two major components Hardware & explosive. The hardware is a metallic case accommodating the explosive material. The electrical initiator assembly consist of a bridge assembly as heating element and housing for explosive material. In bridge assembly resistance wire is soldered between the two electrodes. The overall resistance of the electrical Cap is between 0.2 to 0.3 Ω. Over the bridge wire initiatory explosive is filled. Hot particle generated from the pyrotechnic composition sustain the explosive train required for the cartridge. It is the major energy source for the device. The functional life is the period of time during which the pyro cartridge perform safely meeting adequate performance as required.

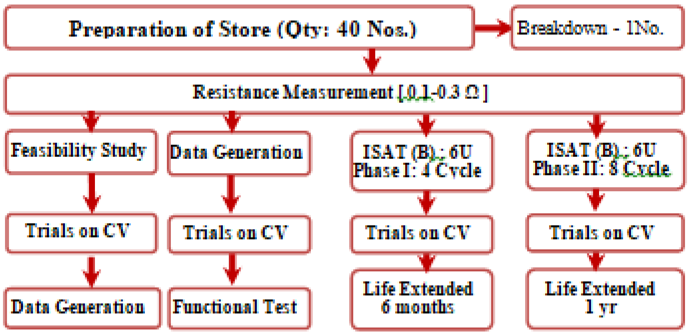

Fig. 2. Test Schedule

The subject cartridge undergone the natural as well as operation life cycle during its services. Additional life extension required for One year shelf life. The trials were carried out considering the functional aspect & service condition it further encounter. For confirming the Electrical properties Resistance measurement were carried out with safety ohm meter. The test schedule is given below

3. Test Schedule

The life extension study carried out considering the life extension required. To achieve it of One year shelf life the test scheduled is finalized, it shown in Fig 2. The performance of the cartridge is evaluated in four stages.

A. Environmental Simulation

Simulation with required environmental conditions is carried out considering the shelf life extension projected. India being a tropical country is having diverse atmospheric conditions. Considering the environmental conditions the pyro device will encounter, the simulation methodology (Unpackaged trials schedule) i.e Temperature, Relative Humidity (RH) and duration were scheduled. The trial schedule consists of environmental test cycle like 6U followed by firing in constant closed volume, described as follows in the Test Schedule, Fig 1. To achieve One year storage life the test scheduled is finalized.

The performance of the cartridges was evaluated in four stages. In each trial the cartridges were tested for electrical continuity and constant volume closed vessel firing. The environmental simulation for shelf life is Intensified Standard Alternating Trials (B) [7] ISAT (B) designated as 6U. For explosive stores, which are likely to experience temperature up to 750C this test is applicable. The store exposed to the following Time & Temperature schedule

Table 1.

(i)	2 days: 46 ± 2 °C,	**95 ± 2% RH**
(ii)	1 day: 60 ± 2 °C,	**60 ± 2% RH**
(iii)	1 day cooling	
(iv)	8 hrs: 75 + 0.4 °C	**dry**
(v)	16 hrs cooling	
(vi)	1 day: 46 ± 2 °C	**95 ± 2% RH**
(vii)	1 day cooling	

This 7-day cycle in simulation condition is equivalent to six weeks in magazine storage conditions. [6]

B. Closed Vessel (CV) trials

The cartridges are test fired in constant volume closed vessel. The test vessel designed & fabricated considering the charge mass of the energetic material, the parameter to be measured & the physical construction of the pyro cartridge. The test vessel and Data acquisition system shown in Fig 3. & Fig 4. respectively.

Fig. 3. Constant Volume Closed Vessel

Fig. 4. Data acquisition arrangement

The performance of the cartridge evaluated in Phase wise. The details of the results obtained in the experimentation as per the test plan are discussed as follows. A typical Pressure –time curve is presented in Fig 5.

Fig 5.: P- t curve

The trial results are compared with that of test data of various stages.

C. Feasibility Study & Data generation

Qty 10 Nos. of Air pyro assembly test fired in CV. The test results are generated to compare for further trials. The electrical power supply is 24V DC. The trials carried out in ambient condition. The test results obtained were analysed. It is found that it is consistent. These air pyro cartridges were within their shelf life. So the data generated were considered as ideal.

Table 2. Data generation

	$P1_{max}$ (Kg/cm^2)	$T1P_{max}$ (µs)	$P2_{max}$ (Kg/cm^2)	$T2P_{max}$ (µs)	R (Ω)
1	89.31	278	91.77	352	0.204
2	88.60	370	88.25	310	0.212
3	105.13	318	96.69	338	0.216
4	86.85	208	90.36	396	0.209
5	101.69	208	85.79	330	0.214
6	87.20	276	93.88	246	0.209
7	101.97	356	101.32	288	0.204
8	89.66	253	97.75	237	0.153
9	114.6	458	103.38	305	0.209
10	114.28	314	92.8	420	0.120

D. Functional Trial

Qty 06 Nos. of Air pyro assembly test fired in CV. The results generated are recorded with the data acquisition system. The electrical power supply is 24V DC. The performance parameter are mentioned in Table 3.

Table 3. Functional Trial

	$P1_{max}$ (kg/cm^2)	$T1P_{max}$ (μs)	$P2_{max}$ (kg/cm^2)	$T2P_{max}$ (μs)	R (Ω)
1	98.57	289	95.28	328	0.203
2	109.72	350	104.78	304.8	0.219
3	95.12	186	76.36	316	0.206
4	119.31	268.2	88.02	221.4	0.206
5	80.28	282.6	70.44	265.6	0.204
6	78.88	317.8	71.26	269.6	0.211

The trial results obtained are comparable and consistent as the results obtained earlier. The cartridge after four cycle of environmental simulation are test fired in closed vessel the results obtained are given in Table 4.

Table 4 Phase I: Life Extension Trial

c	$P1_{max}$ (kg/cm^2)	$T1P_{max}$ (μs)	$P2_{max}$ (kg/cm^2)	$T2P_{max}$ (μs)	R (Ω)
1	105.72	331	90.24	257.2	0.201
2	116.62	294.8	95.17	331.4	0.214
3	109.35	361.6	95.64	345.4	0.223
4	101.38	251	94.35	347.4	0.221
5	105.25	251.8	83.92	372.4	0.228
6	78.06	269.4	82.79	273.6	0.221
7	84.62	302.6	87.31	390	0.211
8	95.01	278.4	98.21	381	0.213
9	78.06	381	92.67	811	0.204
10	72.43	246	81.57	272.4	0.210
11	92.47	338.4	77.05	279	0.201
12	92.82	298	87.9	113.2	0.232

The cartridges are simulated for life extension upto were One year for that cartridge were subjected for 8 Cycle of intensified tropical simulation and test fired in closed vessel the results obtained are given in Table 5.

Table 5 Phase I: Life Extension Trial

	$P1_{max}$ (kg/cm^2)	$T1P_{max}$ (μs)	$P2_{max}$ (kg/cm^2)	$T2P_{max}$ (μs)	R (Ω)
1	162.1	94.0	109.3	358.8	0.201
2	98.8	312.6	102.67	460.2	0.211
3	100.9	312.6	108.6	377.8	0.203
4	102.3	199.0	117.79	406.4	0.203
5	NR	--	--	--	0.216
6	80.87	284.6	91.42	376.6	0.210
7	88.25	242.6	110.76	322.6	0.208
8	96.34	194.6	124.12	205.4	0.211
9	105.13	260.6	112.87	284.6	0.223
10	89.31	314.6	112.17	238.6	0.213
11	78.76	332.6	84.03	342.6	0.200
12	84.74	428.6	73.86	386.6	0.213

E. First Phase result

Phase wise the cartridges were subjected to experimental evaluation. The resistance measured before & after the environmental trials, were found within specified range. After that the cartridges test fired in closed vessel in ambient condition. 24 Volt DC Power Source is used supplying the Firing current. The summary of the trial results of the trials result of first Phase were given in Table 4.

As mentioned in the test schedule, trials results during Data generation and First Phase were consistent, the storage life of the pyro cartridge extended for Six months.

F. Second Phase result

Cartridge prepared for second phase trials. The resistance were measured, were found within specified limit. The trial results of the cartridges of Second Phase were given in Table 4.

The trials results of during Data generation, the upper limit & lower limit were finalised. First Phase and Second Phase trial results were comparable. Fig 6. shows the graphical comparison of TPmax & Fig 7. comparison of Pmax.

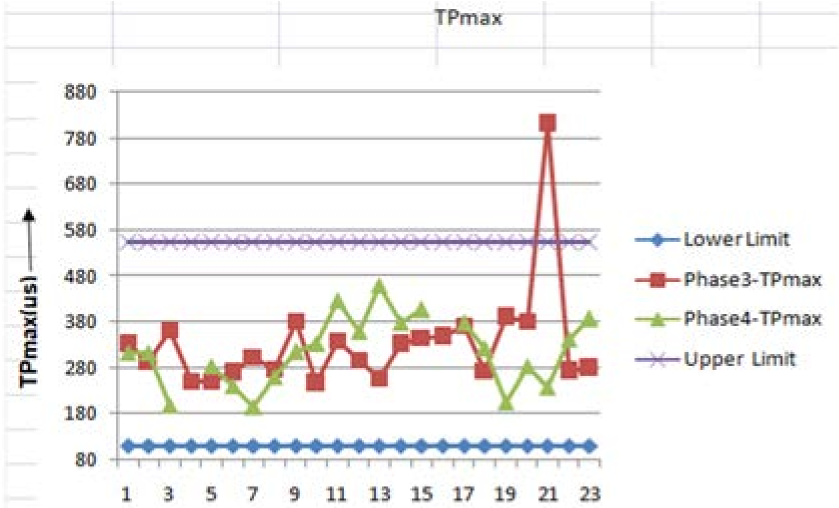

Fig 6. Comparison of TPmax

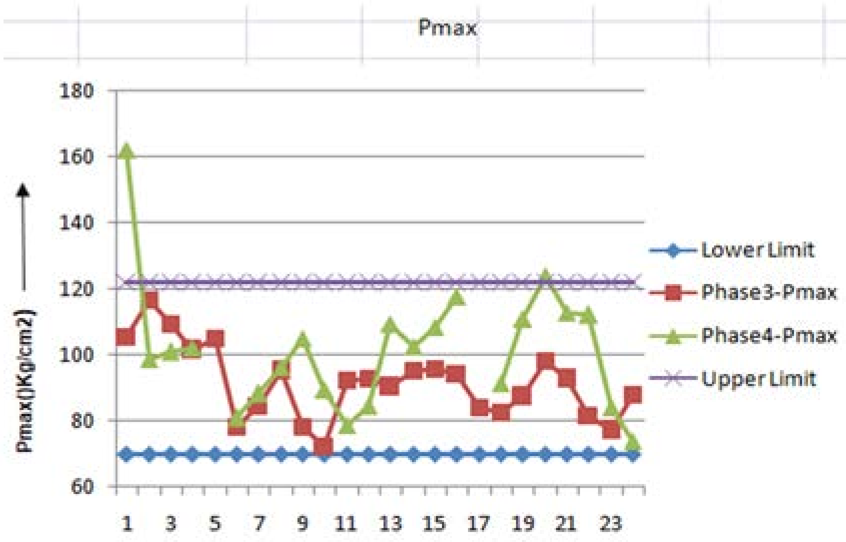

Fig 6. Comparison of Pmax

G. Validation with Berthelot Equation

An acceptable relationship between accelerated ageing and Natural ageing for having single molecule explosive as well as explosive composition or device is determined by using Berthlot Equation, [8] It can be expressed as follows-

$P_1 / P_2 = A^{[(T2- T1) /10]}$

The value of constant A = 2 to 3 is conventionally used for single/ double base propellant. Considering the ageing temperature at 25ºC, 70ºC as described in para 3.2.1, value of A as 2.7. The ratio of accelerated ageing to natural ageing is 1:9 [9]. It is based on the satisfactory ballistic performance of the cartridge after accelerated ageing.

4. Conclusion

The shelf life extension of the pyro cartridge studied. During this study the cartridges were subjected to environmental simulation and CV trial. The performance parameter of the pyro device generated by carrying out by firing trials in test vessel. The climatic simulation of the store carried out in the laboratory conditions. It has undergone intensified standard alternating trial (b) tropical environmental cycle in two phases. After each withdrawal the electrical continuity checked & found satisfactory. Then the cartridges were test fired for confirming the functional aspect. On completion of the trials the storage life of the cartridge extended by 6 months & One year in phase wise. The purpose of all these trials were to ensure that the store should function satisfactorily under worst environmental conditions within it’s service life. The test successfully carried out. It will help for utilizing the installed life Expired cartridges of same lot for maintaining operational readiness.

5. Acknowledgement

Authors are grateful to Dr VV Rao, DS & Dirrector ARDE, Pune - 21 for providing necessary support & kind permission to present this work. The authors also extend their sincere thanks to Shri VK Dixit, Sc ‘H’ Associate Dirrector for guidance during preparation of this paper.

6. Reference

[1] Ringer AG, “Environmental Testing of Explosive Ordnance to Determine Safety and Suitability for Service” Australian Defence Force1994

[2] Yoshinori Kin*/Yasuko Sasaki* “What is Environmental Testing?” ESPEC Technology Report No.1

[3] Neyer Barry T. “Bridgewire Heating” Proceedings of the Sixteenth Sym. on Explosives & Pyrotechnics, Essington, PA, April 1997.

[4] Weinman L et al " A Brief Description of the Construction and Function of Common Electric Matches" Journal of Pyrotechnics, No. 19, 2004.

[5] Lead Styphanete Robert Matyáš, Jiří Pachman “Primary Explosives "Springer-Verlag Heidel Berg 2013, pp147

[6] Fathollahi, M et al "A comparative study of thermal behaviors and kinetics analysis of the pyrotechnic compositions containing Mg and Al." Journal of Thermal Analysis and Calorimetry 120.2 (2015): 1483-1492.

[7] Joint Service Guide (JSG) 0102: Environmental Testing of Armament stores1984

[8] Raha KC et al., “Thermal stability & Shelf life of High Energy Fuel for Torpedo.” DSJ Vol 52, No.2 Apr 2002, pp 165-171

[9] JK Jain et al Type certification of Power Cartridge E-24-28.

Challenges in Development of Ø50 mm IR Flare for Protection of Su-30 MKI Aircraft against IR Guided Missiles

S Debnath
High Energy Materials Research Laboratory
Pune
soujoy.debnath@gmail.com

Abhishek Raj
High Energy Materials Research Laboratory
Pune

PK Rej
High Energy Materials Research Laboratory
Pune

SV Pedgaonkar
High Energy Materials Research Laboratory
Pune

Abstract – **Airborne Infrared (IR) Decoy flare is a key element in aircraft survivability against an increasingly sophisticated and widely proliferated arsenal of infrared-guided Man-Portable Air Defense Systems (MANPADS) and other surface-to air and air-to-air missile threats. IR flare is used to divert an IR seeker away from the target by having a stronger signature than that of the target itself. Imported flare currently being used by IAF in SU-30 MKI aircraft does not have Safety and Functioning Unit (SFU) and the flare pellet neither has a priming coating nor is wrapped.**

The design of imported flare was modified incorporating safety and better performance parameters. SFU was designed, realised and successfully test fired during Design Qualification testing (DQT). The priming composition was applied over the flare pellet which helps in turn giving out a very high IR intensity in the desired waveband in a very short time. The desired IR output in Band I (mid IR waveband) is achieved within 0.2s while in the case of imported flares desired IR output in Band I is achieved within <0.6s. Also the primed flare pellet is wrapped by an Aluminium tape to avoid the contact between explosive and metallic container. Prototype design was finalised based on various in-house testing such as static, dynamic, ejection velocity testing. Thereafter, Design Qualification testing was carried out as per test schedule approved by Airworthiness certification agency. The flight testing was carried out by IAF team after successful completion of DQT. The performance of the flare was found to be satisfactory for protection of SU-30MKI aircraft against various IR guided missiles.

The paper brings out various challenges encountered during flare design, finalisation of composition/pelleting technique, DQT and steps undertaken to overcome the same.

***Keywords**– Infrared, Flare, Aircraft, Decoy, Missile, Seeker*

1. Introduction

Aerial vehicles, both military and civilian, such as aircrafts and helicopters are targeted by missile systems. Increase in terrorist activities in most part of the world has increased the threat to these aerial vehicles. The most easy and effective way to bring down these vehicles is to target them with hand held IR guided missiles which are effective even for low flying targets. Infrared guided Surface-to-Air (SAM) as well as Air-to-Air missiles (AAM) are used to 'lock' on to aerial vehicles such as fast moving jets, transport aircrafts, helicopters etc. Most of the missiles are 'fire and forget' type missiles and they guide themselves towards the target actively by locking on to their infrared radiations. The aerial vehicles are mostly targeted by Infrared (IR) homing missiles since the aerial vehicle has a very prominent IR signature in various wavebands. The IR signature is obtained from various parts, which [1] include the skin (λmax@8-10µm), plume (λmax@3-5µm) and the tail pipes (λmax@2-3µm). The IR radiations are most prominent from the plume and the tail pipes and hence most missile detectors work in either 2-3µm and/or 3-5µm waveband. Based on the type of detectors used and the methodology adopted for missile guidance, classification has been carried out into various generations of IR guided missiles [2]. The first generation IR guided missiles had seekers with detectors operating in a single waveband i.e. 2-3 µm waveband and, the first Generation missiles had a narrow Field of View (FOV) (30 degrees). The FOV increased to 45 degrees in the second Generation of missiles. The missiles of the third generation have detectors (Indium Antimonide) operating in single waveband i.e. 3-5µm waveband. These missiles had a much larger FOV and such missiles could be decoyed by generating more IR intensity than the target [3]. The fourth generation missiles incorporated advanced seeker technologies like Focal Plane Array (FPA) and an effective Electronic Counter-Counter Measures (ECCM). The fifth generation missiles have IR imaging seekers. The missile head has an active array of elements through which the IR image of the scene is captured and tracked.

Today pyrotechnics decoy flares are still the most commonly used active countermeasures to lure away incoming heat seeking missiles. Their wide applications can be attributed to ease of handling, very high probability of target rejection and cheap constituents such as metallic fuels and oxidisers. There was a requirement for development of Ø50mm IR Flare for protection of Su-30 MKI aircraft. Due to a very large IR signature of SU-30 MKI aircraft, the IR intensity requirement was also large as compared to IR decoy flares developed for smaller aircrafts such as Mirage 2000, MiG 21 Bison etc. Ejection of the flare is triggered either manually by the pilot or automatically by the Counter Measure Dispensing System (CMDS).

The flare was required to have a high performance and reliability as the flare is considered to be the last line of defence when an aircraft is being ‘lock down’ by an IR guided missile. Imported flare currently being used by IAF does not have Safety and Functioning Unit (SFU) and the flare pellet neither has a priming coating nor is wrapped. Development of the individual components was a challenge as the performance of one component depends on the performance and reliability of all other components. The task of development was sub divided into design and development of hardware and chemical composition. The challenges encountered during the development process are brought out under the subsequent sub headings in this paper and discussed in detail.

2. Components of IR Flare for CMDS

The flare has five major components:

A. Flare Container:

The flare container is made of Draw quality steel. The container has a circular cross section Its length is 200 mm and outer diameter is 50 mm. One end is open for introduction of the flare pellet with Safety & Functioning Unit (SFU) & the other end is closed having a hole for assembly of impulse cartridge.

B. Flare Pellet:

The flare pellet is a cylindrical solid block made out of pyrotechnic composition which on ignition emits an IR radiation to decoy the incoming IR guided missile. The flare pellet is coated with a priming composition and then wrapped with an aluminium tape.

C. SFU:

Its main function is to ignite the IR flare pellet after the pellet has ejected out from the dispenser/container. This ensures safety of the aircraft by preventing ignition of IR flare pellet in the container/dispenser. Igniter composition is filled inside the SFU body and gets ignited by the hot gases/flash from impulse cartridge which in turn ignites the priming composition of flare pellet.

D. End disc:

The end disc is a circular piece made up of Aluminium Alloy and has an ‘O’ ring for purpose of sealing. The sealing is maintained with the help of a rubber gasket (Nitrile rubber).

E. Impulse Cartridge:

It is an electro explosive device. On functioning by electrical pulse, it produces sufficient gas pressure in confined space and ejects the flare pellet with SFU out of container with designed velocity and simultaneously ignites the igniter composition of SFU.

The Ø50mm IR Flare is shown in Fig. 1.Test Schedule

Fig. 1 Ø50mm IR Flare for CMDS

3. Challenges during development

The development of the flare started with the design of components such as Safety & Functioning Unit (SFU), Flare container, End cap etc. The design of the various components was carried out with a view to provide the IAF, a decoy flare with the highest reliability and simple design, capable of decoying the incoming IR guided missiles. The challenges encountered during design and manufacturing/processing is brought out in the subsequent paragraphs.

A. Flare container

The Flare container is a cylindrical hollow tube with wall thickness of 0.8mm. The flare container is manufactured by machining route. During the firing of Impulse cartridge(IC), the gases would expand behind the SFU and pressure would build up near the collar of the container. Imported flare container was analysed for tensile strength and hardness. Hardness values of more than 210 VPN was finalised for the indigenous container. This would ensure that the container has enough strength to withstand stresses inside the flare container generated by expansion of gases from the Impulse cartridge. Draw quality steel was finalised for use in manufacturing of the flare material.

The photograph of the flare container is shown in Fig. 2 and the flares fitted into the aircraft dispenser is shown in Fig. 3.

Fig. 2 Flare Container


Fig. 3 Flares fitted into aircraft dispenser

B. Flare Pellet

The flare pellet is the heart of the Ø50mm IR Flare and there are many challenges associated during its development. The flare composition was to be developed in such a way that it should provide a very high IR intensity in the required waveband with sufficient burn time so that the flare stays in the missile FOV and has a higher IR intensity than the target aircraft. Another requirement was that the flare pellet should not disintegrate while it is released from the aircraft at supersonic speed as the flare pellet shall experience very high compressive stresses. The challenge in the flare pellet development was thus to develop a composition by choosing the proper chemical ingredients, optimise the processing parameters for mixing of the ingredients and finalise pelleting technique to obtain a high strength for the flare pellet. Apart from maintaining a high IR intensity, a low rise time i.e. the time required to attain the peak IR intensity should be within 0.6s. To obtain a very low rise time, a fast burn rate priming composition was to be finalised along with a proper coating technique. Finally, to ensure that the priming coating is intact inside the flare container, wrapping of a tape is required over the primed flare pellet.

In the present development, achieving the desired rise time of <0.6s and an IR output of >80 kW/sr in Band I (near IR waveband) and >1.6 kW/sr in Band II (far IR waveband), simultaneously was a challenge. The enormous amount of energy requirement in the near IR waveband requires a very high temperature of the flare so that the wavelength of maximum IR radiation shifts to the shorter waveband (as per Wein's displacement law). Such high flare temperature could be achieved by Magnesium/Teflon/Viton (MTV) based compositions which are widely used in IR decoy flares formulation because of their large energy output compared to other pyrotechnic mixtures, low hygroscopicity, low dependence of burning rate on pressure and temperature, and relatively high degree of safety in preparation [1]. Viton (a binder) is commonly added to Mg-Teflon mixtures to ease processing by improving homogeneity of the mixture, and also to protect the magnesium against oxidation by moisture during storage. Also, Viton is a fluorinated compound which adds to the exothermic energy of the system during combustion reaction.

Missile detectors working in these wavebands can easily be decoyed by such flares. The flare upon combustion delivers highly intense radiation due to the heat of formation of MgF2 that heat up the carbon black body to temperatures upto 2200K. The pelleting of the composition was carried out in a split mould designed in such a way that after the completion of the pelleting operation, the pellets are taken out of the mould by splitting open into two halves. This ensures that the flare pellet does not experience the frictional loads during the extraction operation.

The pelleting was initially carried out in a single increment but the required density could not be achieved. Hence incremental pressing was proposed. The challenge in incremental pressing is to maintain the pellet integrity as the pellet often break near the incremental joints due to the smooth surface created by pressing of the single increment. To avoid the breaking, an epoxy based MTV composition in between the two increments was used. The compressive strength was measured for the flare pellet using a Universal Testing Machine the strength as high as 6 MPa was achieved which is sufficient for deployment of flare at supersonic speeds [3]. The stress-stain plot is shown in Fig. 4.

Airborne IR decoy flares are designed to meet various stringent technical parameters, such as IR efficiency, IR intensity, IR output vs time profile, rise time and total burn time. There are number of factors that affect the performance of IR flares. Although IR output achieved was as per the requirement, the burn time was less as per the project requirement. To achieve the required burn time along with IR intensity, MTV composition along with Barium Stearate as a burn rate modifier was used. It was found out that higher Magnesium along with suitable amounts of Teflon and Viton with a suitable burn rate modifier [4] (MTVB composition) gave a higher IR intensity with higher burn time in Band I. The composition was compacted in the required size and upon conduct of static trial, gave a burn time which was as per the requirement. The composition was finalised for use in the decoy flares.

Studies were undertaken to develop suitable priming formulation to achieve the desired rise time of <0.6s. A suitable prime coating [5] given over the flare pellet ensures that the peak IR intensity in the required waveband is obtained in the shortest possible time while the flare is still within the FOV of the missile ‘locked on’ to the aircraft. A fuel rich MTV composition with a very low particle sized Teflon was thus proposed to be used as a priming composition. Priming composition was optimized and finalised and the required rise time was achieved. The desired IR output in Band I (mid IR waveband) is achieved within 0.2s while in the case of imported flares desired IR output in Band I is achieved within <0.6s. The prime coated flare pellet is shown in Fig. 5

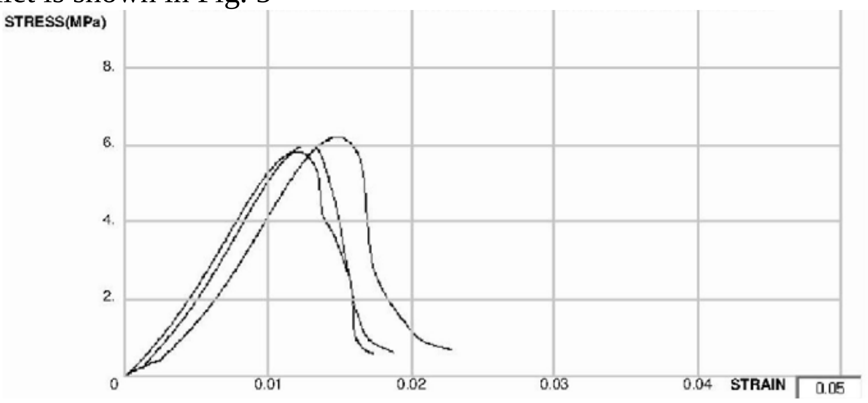

Fig. 4: Stress-strain plot for flare pellet using UTM

Fig. 5: Prime coated flare pellet

The wrapper required for the prime coated flare pellet should have a good tensile strength so that the wrapper does not tear off while it is being pushed in during assembly and while it is being ejected out during dispensation. Also, it should have a low surface roughness so that it smoothly travels inside the flare container. Based on the successful dynamic trials, wrapper was selected for use in the flare assembly. The wrapping of the flare pellet with an Aluminium adhesive tape with cross linked glass fibre ensures that the explosive is not in direct contact to the metallic container which would otherwise pose safety hazard while the flare encounters mechanical vibration, shock, impact etc. The wrapped flare pellet is shown in Fig. 6.

Fig. 6: Wrapped flare pellet

C. Safety and Functioning Unit (SFU)

The challenge was to obtain a simple SFU design with a very high reliability of functioning. Initially, SFU design was carried out with the SFU having a slot into the SFU body for holding the Igniter composition which takes the flash from the Impulse Cartridge and provides it to the flare pellet. The SFU has a top cover, which fixed to the SFU body with the help of two screws. Slider is held within the body with the help of springs and is held in position by a dowel pin. SS disc is placed over the top cover with screws to provide additional strength to withstand the sudden pressure imparted by the Impulse cartridge. The top cover is held over the SFU body with a metallic top strip and four screws. The SFU was designed to be operated by a spring loaded slider which would be in compressed position while it was within the flare container and would be released upon exit from the flare container thereby providing flash to the flare pellet only outside the container. Initially problems encountered were the breaking of the top cover during dynamic trials after conditioning at cold temperatures. The top cover material was then changed from Nylon 6 to Nylon 6 with Glass fibre which prevented breaking of the top cover even after cold conditioning. The reliability of functioning was established by conducting dynamic trials in large numbers. SFU was designed, realised and successfully test fired during Design Qualification testing (DQT). The SFU is shown in Fig. 7.

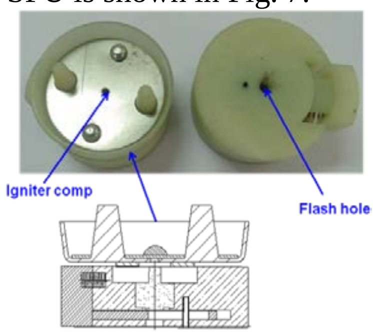

Fig. 7: Components of SFU

D. End Disc

During the development of Ø50mm MTV flare, End cap made of Nylon 6 was used for securing the components of the flare. The End cap was used with a resin/hardener mix. However, during the Users trial, in few cases, the end cap was seen flying off during the aircraft sortie, which poses a safety hazard. Hence, the design was changed and metallic end disc was used thereafter, which is held on to the flare container by turnover of the container ends over the disc. The end disc is a circular closing disc which is fitted to the ejection end of the flare container. The sealing is maintained with the help of a rubber gasket (Nitrile rubber). The challenge was to secure the end disc which should be strong enough to hold the end disc even during supersonic speeds attained by the aircraft. The strength required to open up the end disc was found out to be >1MPa with the help of Universal Testing Machine, which is enough to hold the end disc during supersonic speeds of the aircraft, as observed for 2”x1”x8” MTV IR flare which has successfully undergone flight testing. This strength is obtained by turnover of the end of the flare container by placing the container into the mould and placing the disc over the container by 7o angle. For this purpose, the flare container end was softened for ease of turnover without cracking of the container body. The strength and sealing achieved by the end disc was validated during Qualification testing and flight trials. The end disc is shown in Fig. 8.

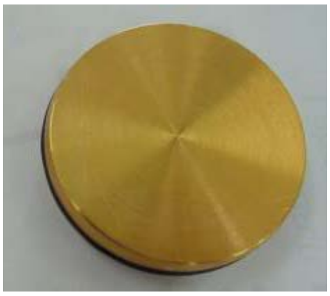

Fig. 8: End disc with ‘O’ Ring

E. Impulse cartridge (IC)

IC is the first fire unit of the flare and it was necessary to design the hardware and chemical composition so that No-Fire Current (NFC) of minimum 1 A is obtained. Such high NFC ensures that the IC does not get initiated by the EMI/EMC induced by various electronic components installed in the aircraft and thus ensures safety. The challenge was to design a bridgewire and a suitable chemical composition which ensures a high NFC. Based on the NFC requirement, bridgewire of nichrome material with required thickness was finalised. Boron based composition was pressed over the bridgewire. This composition has a high ignition temperature which ensures that the ignition of the composition occurs only when a current of more than 1A passes over the bridgewire for the required time. The gases generated by the IC are due to the propellant composition that is loosely filled over the booster composition ME-436(a). The IC is evaluated by firing in 45cc closed vessel and various parameters such as peak pressure, ignition delay, time to peak pressure etc. The filling schedule and the photograph of the IC are shown in Fig. 9.

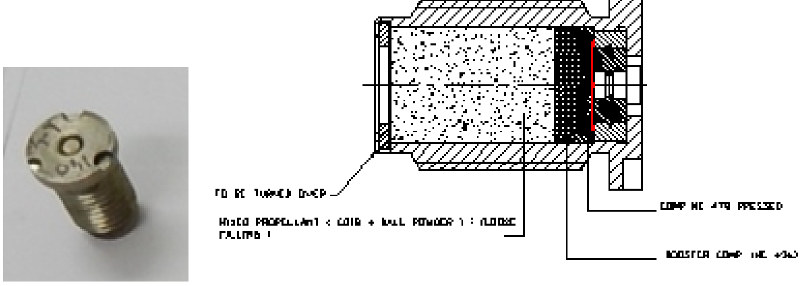

Fig. 9: Impulse cartridge

4. Performance evaluation

After completion of Design Qualification testing, flares were subjected to various performance evaluation testing.

A. Static testing

The static performance such as burn time, rise time and IR intensity in the required waveband was carried out by firing of pellet in a wind tunnel and recording the IR radiations with the help of SR-5000 IR radiometer [Fig. 10].

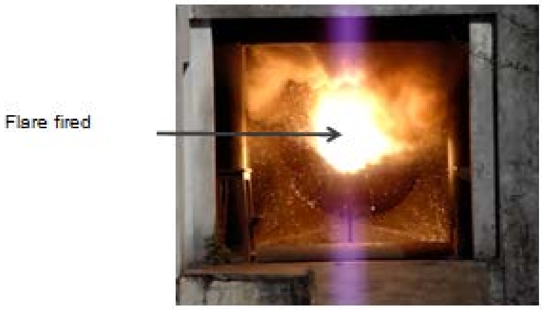

Fig. 10: Static trial in IR tunnel for IR intensity measurement

B. Ejection velocity testing

The Ejection velocity trials are conducted by using a board of known dimensions and by assembly of a dummy Aluminium pellet (weight same as that of IR Flare pellet) into the Flare casing and firing the Flare from a locally fabricated Launcher. The time taken for the Flare pellet to travel a known length of the board was recorded by a high speed camera and the ejection velocity was calculated. Ejection velocity measurement setup is shown in Fig. 11.

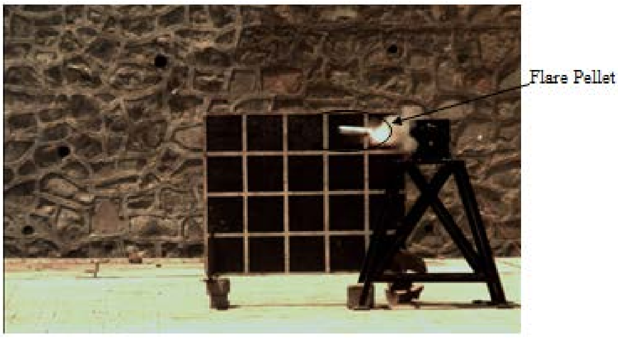

Fig. 11: Measurement of Ejection velocity

C. Dynamic testing

Dynamic evaluation of IR Flares was carried out by using a locally fabricated dispenser. The functional trials of IR Flare are conducted to assess the proper functioning of all the Flare components during actual firing. The Flare was launched from a locally fabricated dispenser and the performance was assessed. Thereafter the flare trials were carried out using BDL CMDS. The firing of flares from BDL CMDS is shown in Fig. 12

Fig. 12: Dynamic testing of IR Flare

D. Reaction force measurement

The reaction force was measured by using an MS vessel which had internal dimensions similar to that of the flare container. The components of flare were loaded inside the measurement vessel and secured with an end disc. Provision was made for placing a pressure gauge perpendicular to the surface of the vessel to measure pressure imparted to the top cover of the SFU. Load cell was held as shown and the setup was mounted over a rail. The setup is shown in Fig 13.

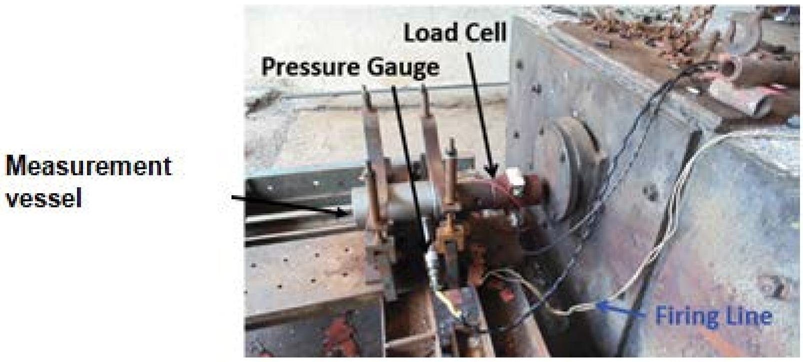

Fig. 13: Reaction force measurement

5. Conclusions

Infrared decoy flares have proven to be the most effective, reliable and inexpensive countermeasures for self-protection of various aerial vehicles. The requirement for development of Ø50mm IR Flare for use in SU-30 MKI for protection against incoming IR guided missiles was well understood and accordingly the development was undertaken. Initially the various challenges were overcome component wise and then the integrated trials were undertaken to rule out the various problems encountered. The design of various flare components have been carried out successfully. MTV based IR flare has been successfully developed. Various new evaluation techniques have also been developed in-house which has provided useful data for proceeding with the flight trials. The flare has successfully under gone Users trial in various phases for proving the flare with respect to safe dispensation and efficacy against Surface to Air and Air to Air IR guided missiles and is likely to be inducted shortly and integrated with the EW systems of fighter aircraft of IAF.

6. Acknowledgement

Authors thank Shri KPS Murthy, Outstanding Scientist and Director HEMRL for the support during the entire course of the work.

7. Reference

[1] E.-C. Koch, ‘Review on Pyrotechnic Aerial Infrared Decoys’, Prop.,Explos.,Pyrotech. 26 2001, 3-11.
[2] Gp Capt NK Nair, ‘A New test technique for flight evaluation of Infrared flares’, Aero India Seminar, Bangalore, Feb 2013.
[3] David H. Pollock, “Countermeasure Systems – The Infrared and Electro-optical Systems Handbook’, Vol.7, 289-329, 1993.
[4] S. Debnath, P.S Chowdhury, P.P Singh, Abhishek Raj, S.M. Danali, “Effect of Barium Stearate on MTV based Infra Red (IR) Flare Performance”, 8th International High Energy Materials Conference and Exhibit (HEMCE) 2011.
[5] P.S. Chowdhury, S. Debnath, V.P. Ambekar, S.M. Danali, A. Singh, “Effect of Priming Composition on Rise Time of Airborne IR Decoy Flare”, 8th International High Energy Materials Conference and Exhibit (HEMCE) 2011.

Pyrotechnic Reefing Cutter for Airborne Descent Devices of Sahayak Mk I Aircraft

P Saha Chowdhury
High Energy Materials Research Laboratory
Pune
paramita.sahachowdhury@gmail.com

N D Mhaske
High Energy Materials Research Laboratory
Pune

M A Siddiqui
High Energy Materials Research Laboratory
Pune

S V Pedgaonkar
High Energy Materials Research Laboratory
Pune

1. Introduction

Extensive work has been going on in the field of Pyrotechnic Reefing cutters for last 60 years (1-3). The pyrotechnic cutter played a key role for the success and acceptance of Advanced Airborne Devices. These devices are particularly useful in the field of airborne descent control devices, such as for staged deployment of parachutes or capsules used for return of individuals/equipment from space travel or aero dropping systems. Such devices need to be reefed in order to restrict the sudden, uncontrolled inflation of the canopy during parachute deployment. Reefing cutters ensure a gradual movement of the canopy from the fully closed position to full deployment of parachutes. A parachute system is used to decelerate the carrier to the desired impact speed, so that impact load does not exceed designated limit (4-5).

Air droppable containers (ADC) are required by Indian Navy to provide logistic support to ships and submarines at sea during war as well as peace time. 1sec Delay pyro reefing cutter is required in the parachute system for Sahayak MK I/ IL 38 aircraft with payload capacity of 50 kg. Reefing cutters are placed during final closing of parachute deployment flap. ADC 150 along with packed parachute system is installed in the bomb bay of IL 38 aircraft with a static line. The cutter is initiated by static line on release of container from bomb bay. After 1±0.2 sec, pyro cutter is fired and results in deployment of auxiliary parachute. Each assembly is about the size of a fountain pen and consists of a slow burning delay composition, blade and hole through which the reefing cutter passes. Burning composition initiates a charge, which drives the blade into the reefing line, severing it. If a reefing cutter fails, it leads to the non-uniformity of balancing forces during canopy inflation, damaging the whole system. Thus it is very important for the reefing cutter device to be extremely reliable (>99%). In this study, a pyrotechnic delay element has been used for reefing action with suitable delay time of 1sec.

The present paper describes the system in brief along with all the activities involved in the execution and development of this system, i.e. design, testing/inspection.

2. Concept of pyro cutter and function

A typical Pyro cutter (Fig. 1) has three parts: Cutter, Pyrotechnic charge and Safety Pin

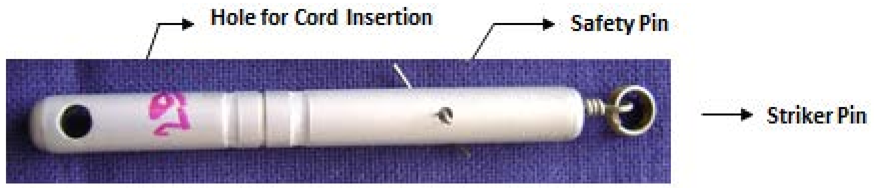

Fig.1: Reefing Cutter Photo

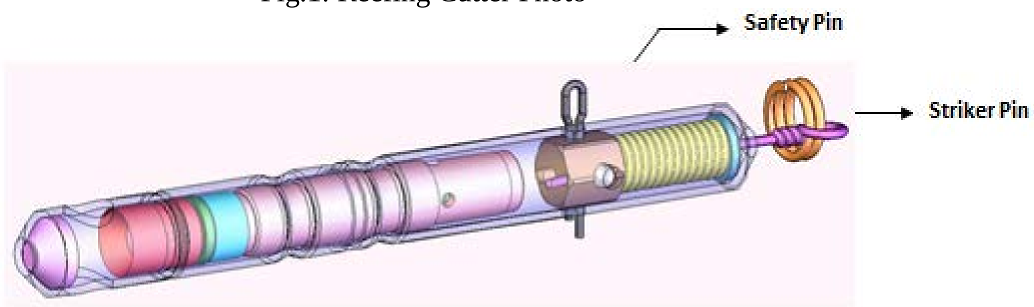

Fig 2: 3D view of Pyro delay reefing Cutter

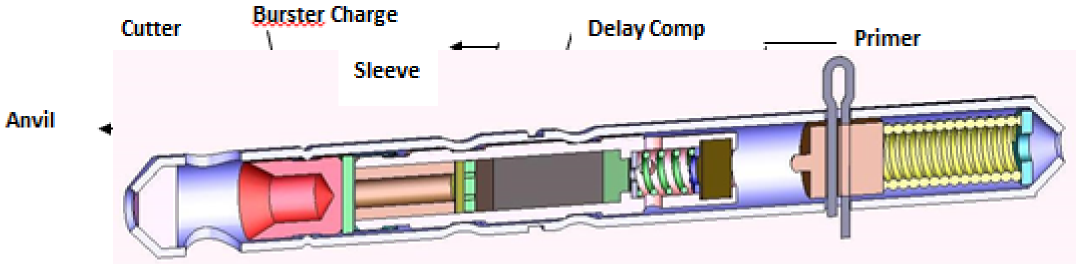

Fig 3: Cross Sectional View of Filled Reefing Cutter

Cutter assembly (Fig.3) consists of an anvil and a cutter. Considering the fact that the pyrocutter is used for cutting a cord made of a relatively soft and ductile material, the anvil is made of soft material, lead (Pb), and the cutter from stainless steel with sharp edges. There is a distance between the cutter and the anvil (Fig.4). A nylon 6/6 cord of tensile strength of 12400 psi and 17000 psi flexural strength is inserted into this place. Under the pressure of combustion gasses from the pyrotechnic delay composition, the cutter moves and blade cuts off the cord, by successfully inserting itself in the anvil and successfully breaking every thread of the rope.

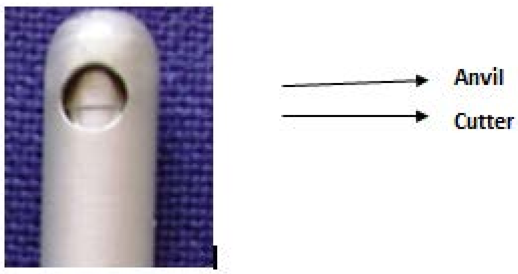

Fig 4: Cutter Functioned

Delay composition of pyrocutter guarantees the movement of cutter with the specified delay time from the moment of removing the safety pin. Pyrotechnical charge consists of a cap, priming, delay, booster and relay composition. All these elements are pressed in the body of the pyrotechnical system (Fig.5).

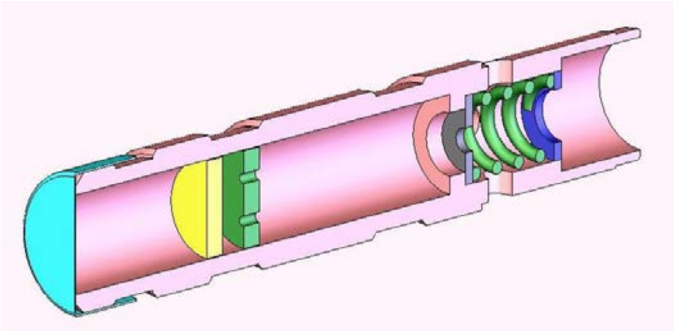

Fig 5: Delay Assembly

Once the safety pin is removed, the striker pin is ready for movement. Once the striker pin is pulled, the cap activates the priming composition, which in turn activates the delay composition. Rate of combustion and burning characteristics of delay composition guarantees the required delay time. After activating the burster mixture, products of combustion generate pressure that presses the cutter and enables the function of the pyrocutter.

Safety Pin and striker Pin (Fig.2) attached to the reefing cutter are safety mechanism for single use. Safety pin is in a secured position; a stainless steel ball is placed between the safety pin and spring striker. A sulphur based composition has been used as delay composition in this study, as it burns in very reliable fashion. The priming composition based on ferrosilicon and Red Lead was chosen as the suitable candidate as it burns fast with very small amount of gas and gives slag facilitating the cutter action in a reliable manner. Lead Ferrocyanide/Potassium Perchlorate is selected as burster composition which after burning produces pressure of 4-5 MPa per gram in 100 cc volume. Therefore, very small quantity of this composition (50-60 mg) pressed at the end of the delay column produces sufficient pressure that exerts on cutter due to which it moves and cuts the cord placed in between anvil and cutter. A flowchart of the functioning of the cutter has been given in Fig 6.

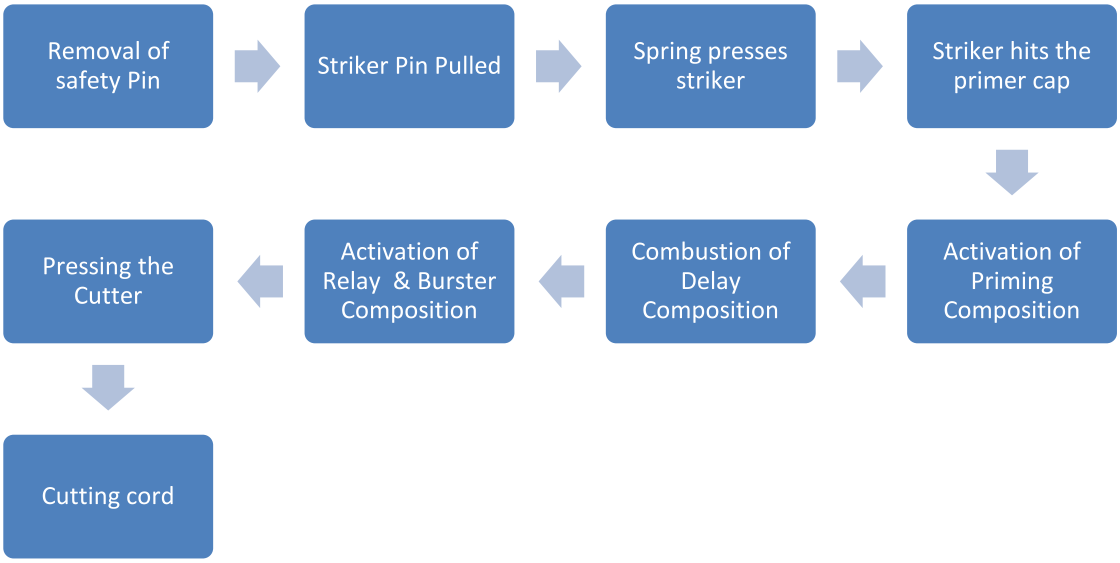

Fig 6: Block Diagram of Cutter Function

3. Technical Parameters of the cutter

Sl no.	Parameter	Specification
1	Delay	1 ± 0.2s
2	Type	Percussion type
3	Initiation	Mechanical
4	Casing shape	Cylindrical
5	Cutting capacity	Cord Nylon BS 250 – 300 kgf
6	Cutter dia	5 mm
7	Safety pin	Yes
8	Overall size and weight	Ø 8.9 x 93 mm, 19 g
9	Operating temperature	- 40 ^{0}C to 60 ^{0}C

4. Experiments

The details of pyrotechnic composition used in this development are given below:

Composition Details	Role
$FeSi/Pb_3O_4$	Priming Composition
$FeSi/Pb_3O_4/B/BaCrO_4/$ NC	Booster Composition
$B/BaCrO_4/$ NC	Delay Composition
$Zr/Pb_3O_4/NC$	Relay Composition
$LFCN/KClO_4$	Burster Composition

5. Methods

A. Preparation of Compositions:

For preparing the delay composition, accurately weighed quantities of Boron, Barium Chromate were intimately mixed by sieving through 25 BSS sieve using a soft brush for 6 times. The purpose of the sieve-brush-mixing operation was to break up same-particle agglomerates and to facilitate intimate mixing of the formulation components. Then the mixture was granulated with nitrocellulose lacquer added to the mixture. The composition was air dried for 6 hrs and kept in air oven for 6 hrs at 60ºC.

The priming, booster, relay and burster compositions were prepared in the same way.

6. Results and discussion

Composition	Cal Val Cal/g	Gas Output g/cc	F of I	Friction Insensitive upto (kg)	Spark Insensitive upto (J)
$B/BaCrO_4$ /NC	353	2.3	0% at 170 cm	36	5
$FeSi/Pb_3O_4$	222	17.5	95	16	5
$Zr/Pb_3O_4/NC$	340	42	22.3	25.2	5

From the results it is clear that the delay composition is a gaseous composition with moderate sensitivity to impact and friction. The figure of insensitiveness of these mixes shows that the relay composition is quite sensitive to friction and should be handled with care.

A. IBR Determination:

Instead of burning rate, inverse burning rate (IBR) is calculated for easy determination of column length of the delay element. IBR results from Lead fuze rolling machine are given in table 4:

Composition	IBR s/cm
$FeSi/Pb_3O_4$	0.8
$B/BaCrO_4$ /NC	1.0
Zr/Pb_3O_4/NC	0.8

B. Results of Pyro cutter tests:

Series of functional tests were performed before testing the reefing cutters. They were checked for visual and dimensional control as well as transport safety by undergoing the drop test. Finally, they were tested for cutting action with the desired delay time. In this study, reefing cutter is used to provide the delay for 1s. The compositions are pressed with 410 kg load with 10s dwell time. Function test was performed in a test set up (Fig.7) with the temperature conditioned samples at temperature of +25°C, +60°C and -40°C (10 no. Of each) and the rope was successfully cut in all tests.

Fig 7: Pyro cutter in testing apparatus

Delay time was measured using a stopwatch and the test results are given below

Table for 1s Delay:

Sl No.	Delay time (s)		
	Ambient	Hot(60°C)	Cold (-40°C)
1	1.10	1.01	1.15
2	1.15	1.11	1.18
3	1.15	1.12	1.17
4	1.15	1.10	1.19
5	1.16	1.13	1.18
6	1.04	1.11	1.19
7	1.10	1.12	1.19
8	1.11	1.07	1.14
9	1.15	1.10	1.18
10	1.10	1.06	1.16
Min	**1.04**	**1.01**	**1.14**
Max	**1.16**	**1.13**	**1.19**
Average	**1.121**	**1.093**	**1.173**
Spread	**0.037**	**0.036**	**0.017**

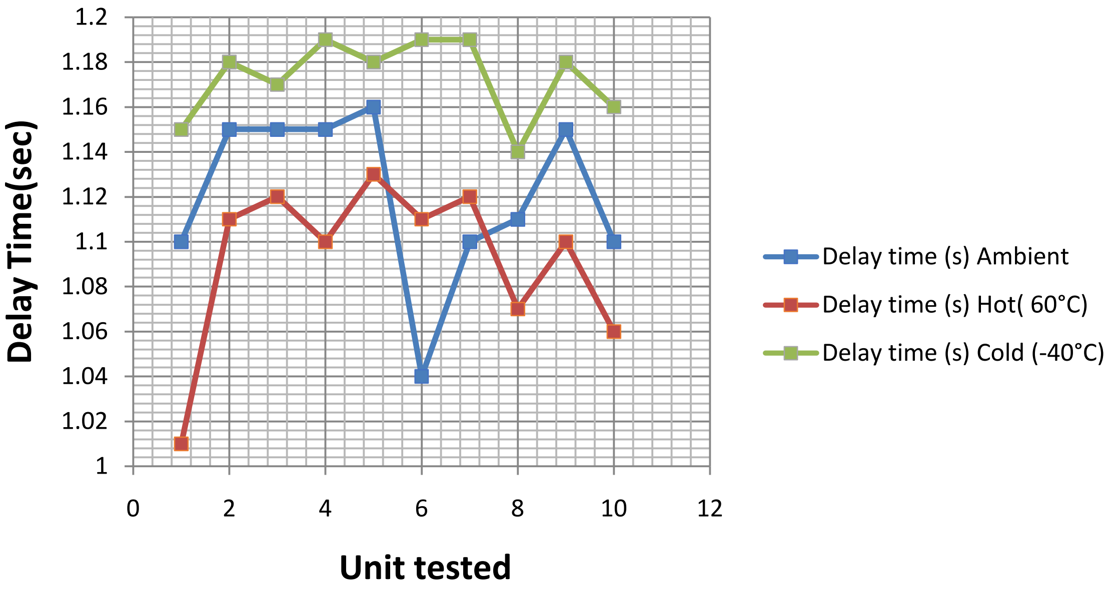

Fig 8: Performance Graph of 1s Delay Reefing Cutter

It is inferred from the graphs, that the behaviour of the cutters are similar in all temperature conditions. After analysing the results of delay time, it was observed that all the delays were observed to be in the range of 1 ± 0.2 sec as required by QR. The delay units were tested at different intermediate temperatures to see the proper functioning of the delay. These delays were found to be very accurate and reliable.

7. Conclusions

From the above trial results, it is inferred that the pyro reefing cutter fulfils all its prerequisites as time delay element to be fitted in a parachute system. This application can be further used in civil applications, such as in process industry i.e. Gas generator, Cutters etc. The reefing cutters gave excellent results when tested at extreme cold and hot operating temperatures. Further work is in progress to develop a pyrotechnic reefing cutter with variable time delay elements with very high reliability.

8. Reference

[1] M S Kriesel, US patent No. 3408026,1968.
[2] Frieder et al, US patent No. 2581645, 1952.
[3] Grandy et al, US patent No. 2996989, 1961
[4] McElroy et al, US patent No. 3362664, 1968.
[5] Mark Hewish, Bringing safety down to earth, Janes international defence review, 1999, No.5, pp.48-53.

Redundant Detonator Initiator Scheme for Canopy Severance System

DM Munemanik
Armament Research and Development Establishment
Pune

DY Gaikwad
Armament Research and Development Establishment
Pune

RB Lawate
Armament Research and Development Establishment
Pune

SS Khandagale
Armament Research and Development Establishment
Pune
sskhandagale@arde.drdo.in

KD Deodhar
Armament Research and Development Establishment
Pune
kashinathdeodhar@arde.drdo.in

Abstract – **CSS is a lifesaving system installed inside the cockpit of all modern aircraft. It provides safe escape path for aircrew in case of in-flight and ground emergencies. The principle of "Controlled Propagation of Detonation wave" is used in the functioning of CSS. It consists of Mechanical initiators, Junction Boxes, Explosive Transfer Line, Miniature Detonating Cord etc. In case of in-flight emergency, initiator will be functioned by tapping gas from seat ejection cartridges and striker hit the stab type detonator. If detonator fails to function then whole CSS will fail. Out of all explosive components in the system, detonator is the least reliable component. To improve reliability of the system and add redundancy, the concept of "Redundant Detonator Initiator" has been developed. This paper discusses about various design schemes that can make the dual detonator initiator arrangement possible. Effort is also made to calculate reliability of the improved arrangement**

Keywords*– *Mechanical Initiators, Junction Box, Explosive transfer line, Detonator, In-flight Egress System, Redundant Detonator Initiator, Reliability

1. Introduction

Canopy Severance System (CSS) consists of two subsystem i.e. In-flight Egress System (IES) and Ground Egress System (GES) [1]. Both the systems operate in the different emergency situations. Initiator is main device to operate any system. Various types of initiators are used in Canopy severance system i.e. Pressure Actuated Initiator (PAI), Internal Initiator (I.I) & External Initiator (E.I) [2]. In case of In-flight emergency PAI is used to initiate the IES system and in case of ground emergency External or internal Initiator is used to operate the GES.

In both emergency conditions functioning of systems depends on initiators. Initiators used in CSS has single stab type detonator [2]. Detonator is an important explosive component as it is used to initiate the explosive train. When the striker hits the detonator, detonation wave will generate. Detonation wave travels through Explosive Transfer Lines, (ETL), Junction Boxes and initiates the Shaped Miniature Detonating Cord (SMDC) pasted on Canopy. Canopy is severe by functioning of the SMDC. In whole process of canopy severing detonator is least reliable component since it contains sensitive primary explosives. If detonator fails to function then whole CSS system will fail. So reliability of detonator has to be ensured. Therefore development of redundant Detonator initiator is presented because it improves the reliability by adding redundancy in the system operation.

2. Literature Review

In the past initiator has been developed for Canopy Severance System. These initiators are mechanically operated. All Initiators have single detonator for initiation of explosive train. So to improve the reliability of In-flight Egress System, two initiators are used. It leads to increase the number of components in the system. Ultimately increase the overall weight of the system.

In a similar system of other aircrafts mechanically operated initiator is used. Initiator has two detonators in single body frame. It has two output ends for propagation of detonation wave. So it adds the extra component for propagation.

3. Design Description

A. Scheme-1

In case of In-flight Egress System initiator (Pressure Actuated Initiator) is mounted behind the pilot seat. It has gas connection for operation [1]. In case of In-flight emergency, when pilot pull the seat ejection handle, cartridges will initiate & generates gas pressure. This high pressure gas tapped by initiator through pipe connected to it. The gas input end of initiator is shown in Fig 1 below.

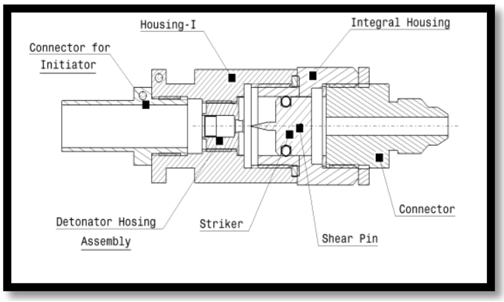

Fig. 1: Regular Initiator

Regularly used initiator has only one detonator as shown in fig.1 below.

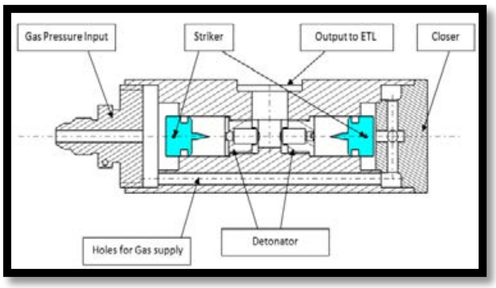

Fig.2 Improved Initiator

In this scheme "Two Detonator" is used instead of single detonator. Fig.2 shows the arrangement of two detonators inside initiator. Detonators are arranged in parallel and opposite in direction to each other. Two strikers are used in initiator for hitting purpose. Strikers are arranged in parallel facing pin point towards each other. There is a common booster is placed between the detonators for positive contact. There is one output end provided on periphery of initiator to screw connector for initiator. Tip booster of connector for initiator is in positive contact with common booster. Three holes provided inside the body at an angle of 1200 as shown in fig. Tapped gas will flow to other end of initiator through these holes. Due to gas pressure both strikers will hit the detonators by duly shearing the shear pin. Detonation wave will be generated and propagate further to ETL through connector for initiator by initiating common booster. In case if any one of the detonators fails to initiate other detonator will initiate the explosive train. Therefore this scheme reduce chances of failure of initiation of explosive train, ultimately reduces the chances of failure of In-flight Egress System. It also reduces number of initiator in the system.

B. Scheme-2:
In this scheme, there is only one striker used inside initiator as shown in Fig 3 below.

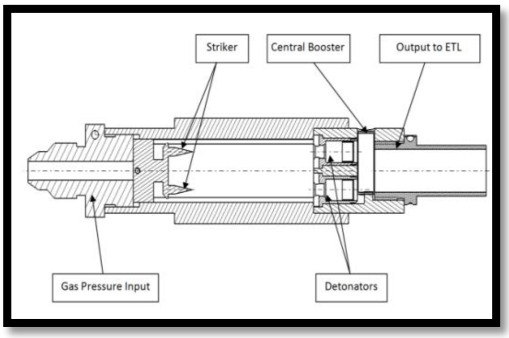

Fig. 3: Scheme 2

Striker has two sharp extended portions just like pin. Two detonators are placed in single initiator. Detonators are arranged parallel to each other inside the detonator holder. Initiator has one gas input end at left side of initiator and one output end at right side as shown in Fig 3. Connector for Initiator is screwed to the right end of initiator. There is a common central booster is placed below the detonators for positive contact between the tip booster of connector for initiator and detonators. In case of in-flight emergency, seat ejection handle pulled by pilot, cartridges will initiate & generates gas pressure. Portion of gas is tapped by initiator through pipe connected to it. Due to gas pressure striker hit both detonators simultaneously by duly shearing shear pin. Detonation wave propagates to ETL through connector for initiator by initiating the central booster.

Similar arrangement of scheme 2 is also used in GES initiator. In GES external initiator or internal initiator used for initiation of explosive train. Sear mechanism is used for release of striker instead of gas pressure. Currently used striker & detonator of external & internal initiator can be modified like scheme 2. Striker has two sharp extended portions like pin. Two detonators are used instead of single one. After pulling the handle of External Initiator or Internal Initiator striker will be disengaged from sear and hits the both detonators with high velocity. Detonation wave will be generated and propagate through ETL to SMDC and cut canopy bubble of aircraft.

4. Reliability Calculation

Reliability of striker hit the detonator calculated from the previous data [3, 4]. Striker hit the detonator duly shearing the shear pin. Shear pin load test was carried out on UTM machine and their breaking load data recorded as mention in table 1 below

Table.1 Breaking load

Sr. No	Breaking Load (N)	Sr. No	Breaking Load (N)
1	861	26	861
2	857	27	864
3	884	28	853
4	861	29	843
5	857	30	859
6	863	31	857

Table.1 Breaking load (contd..)

Sr. No	Breaking Load (N)	Sr. No	Breaking Load (N)
7	861	32	843
8	849	33	851
9	872	34	855
10	864	35	835
11	849	36	837
12	866	37	861
13	864	38	849
14	847	39	851
15	863	40	870
16	855	41	841
17	866	42	859
18	866	43	849
19	870	44	847
20	843	45	857
21	870	46	845
22	866	47	835
23	857	48	835
24	847	49	864
25	854	50	873

A. Breaking Strength Analysis

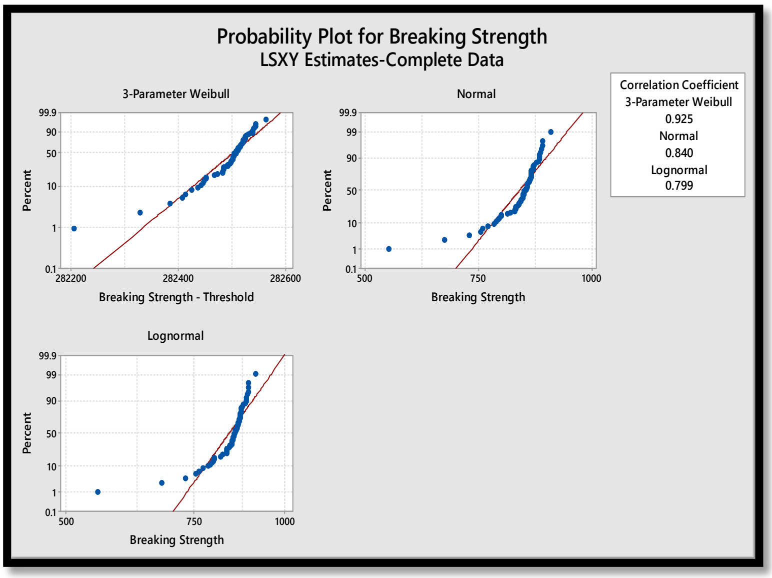

Fig. 4 Probability plot for breaking Strength

Analysis of breaking load required to shear the Shear pin is done and got values of correlation coefficients. These values are 0.925, 0.840 & 0.799 for 3-Parameter Weibull, Normal and lognormal respectively as mention in graph- Fig.4. 3-Parameter weibull distribution model is most suitable as their correlation coefficient is higher i.e 0.925 as compare to others.

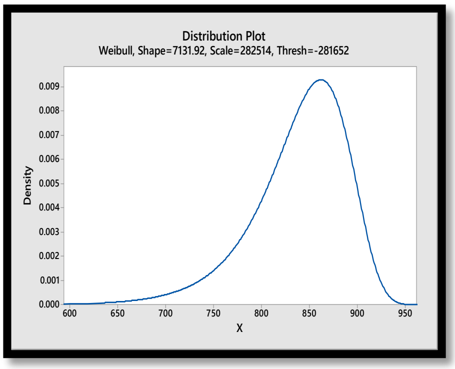

Fig.5 Weibull Distribution Plot

3-Parameter weibull distribution model [4] is used to plot the breaking load distribution. In this model shape factor, scale factor and threshold factor have values 7131.92, 282514 and -281652 respectively as mentioned in above graph fig.5. The maximum density of breaking load distributed between ranges of 750 N to 950 N.

B. Applied Load Analysis:

Gas pressure acts on the striker is generated by cartridges. So force developed due to gas pressure is calculated. Gas pressure data is collected from previous CSS trials report.

Gas pressure (P) = 113.69 kg/cm2 considering the dimension of striker applied force developed due to gas pressure is

$$F = 1706.9645 \text{ N}$$

Subsequently forces acting on striker at different gas pressure are calculated which is mentioned below:

Table 2: Applied load

Sr No	Pressure (kg/cm^2)	Load (N)
1	113.69	1706.9645
2	111.11	1668.2283
3	117.09	1758.0132
4	167.19	1640.1517
5	107.24	1610.1234
6	118.73	1782.6365
7	111.23	1670.0300
8	113.92	1710.4182
9	116.50	1749.1548
10	117.56	1765.0699

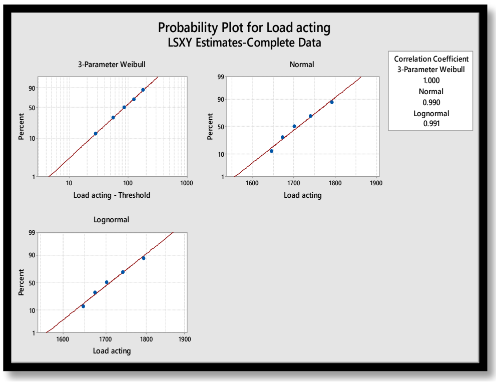

Fig.6 Probability plot for Applied Load

Analysis of load applied on striker is done by using table 2 data. Correlation coefficient has values 1, 0.990 & 0.991 for 3-Parameter Weibull, Normal & lognormal respectively as mention in graph fig 6 above. Out of all distribution 3-Parameter Weibull is most suitable as it has 1 correlation coefficient.

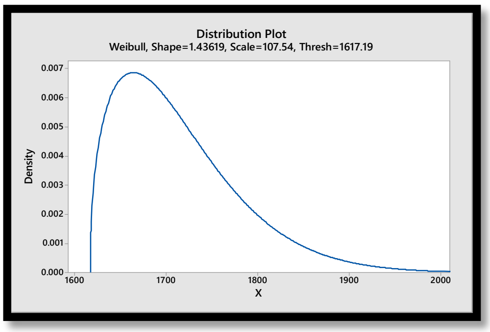

Fig. 7 Applied load distribution

Distribution of the applied load on striker to shear the shear pin is shown in graph- Fig.7 above. In this distribution plot shape factor, scale factor & threshold factor have values 1.43619, 107.54 & 1617.19 respectively. It shows the maximum density of applied load distributed between the 1650N to 1900N.

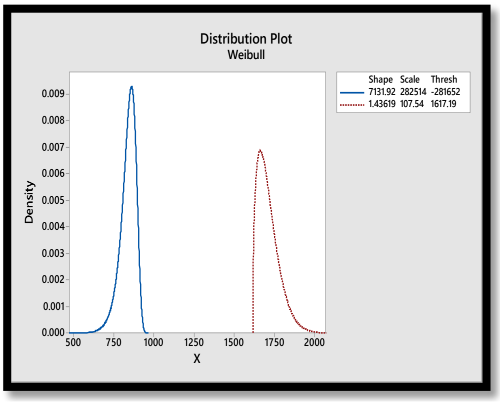

Fig.8: Breaking load Vs Applied load

Above graph Fig.8 shows the comparison between breaking load Vs Applied load. Left side curve represent the breaking load & right side curve represents the applied load. There is no interference between these two graphs because applied load is greater than breaking load. Therefore striker hit the detonator duly shearing the shear pin. Therefore reliability of striker hitting the detonator can be assumed as 1.

C. Reliability of Detonator

Reliability of Detonator is calculated from previous firing data of CSS. The lower bound R_L for reliability at given confidence level when r failures are observed in n trials is given by [4]

$$R_L = [1 + F\{\frac{r+1}{n-r}\}$$

Where

R_L = Lower bound for reliability

n = Number of trials

r = Number of failures

$(1 - \alpha) \times 100$ = Confidence level

In this case n = 504, r = 5, α = 0.1

F = $(\alpha, 2(r+1), 2(n-r)$

F = $(0.1, 12{,}998)$

From F-table for α = 0.1

F=1.6263

Therefore, Reliability is

$$R_L = [1 + F\{\frac{r+1}{n-r}\}$$

In the regular initiator striker and detonator are arranged in series.

Therefore reliability of regular initiator is

$$R = R_1 * R_2$$
$$R = 1 * 0.9816$$
$$R = 0.9816$$

In case of new scheme for initiator, both detonators are arranged in parallel. Therefore Reliability of parallel system

$$R = 1 - (1 - R_2)(1 - R_2)$$
$$R = 1 - (1 - 0.9816)(1 - 0.9816)$$
$$R = 0.9996$$

5. Results & Discussion

A. Reliability calculation showed that regular initiator has reliability 0.9816 and modified initiators have 0.9996

B. Reliability of modified initiator is more than regular initiator.

C. In both schemes, initiator has single input and output end. Therefore, it required single explosive transfer line for propagation of detonation of wave compared to using two initiators in the system

6. Conclusion

Redundant detonator improves the reliability of initiator and adds the redundancy. Thus it will lead to improve the reliability of CSS. It also reduces the number of components in the system as compared to two separate initiators.

7. Reference

[1] Technical manual on CSS

[2] Bailey A; Murray S G, "Explosives, propellants and pyrotechnics" Brasseys 1989

[3] Trial reports of CSS

[4] W. Grant Ireson, Clyde F. Coombs Jr "Handbook of Reliability Engineering and Management"

[5] Charles Ebling "An Introduction to reliability and maintainability engineering" Mc Graw-Hill 1997and Exhibit (HEMCE) 2011.

Design Optimisation and Evaluation of a Thermal Barrier for an Ignition Safety Device – Solid Rocket Motor Interface

Shete Mayuresh Kailas
Aerospace Ordnance Entity
Vikram Sarabhai Space Center
ISRO
Thiruvananthapuram
mayuresh_shete@vssc.gov.in

Sijimon. T. P
Aerospace Ordnance Entity
Vikram Sarabhai Space Center
ISRO
Thiruvananthapuram

Ani Daniel Kurien
Aerospace Ordnance Entity
Vikram Sarabhai Space Center
ISRO
Thiruvananthapuram

N. Vinod Kumar
Aerospace Ordnance Entity
Vikram Sarabhai Space Center
ISRO
Thiruvananthapuram

Baby Abraham
Aerospace Ordnance Entity
Vikram Sarabhai Space Center
ISRO
Thiruvananthapuram

Abstract – **Head end Mounted Safe Arm (HMSA) is an electromechanical device used to safely initiate a Solid rocket motor. It provides intrinsic safety against inadvertent initiation of the explosive train when in the SAFE position by mechanically separating the output ordnance from the internal electrical initiators. HMSA is directly mounted on the igniter at the dome region of the solid motor and the interface is sealed using redundant elastomeric o-rings (shaft seal and face seal). As a primary defence to protect these o-rings from the hot combustion products generated during igniter and motor operation, the interface originally incorporated a butadiene-acrylonitrile rubber ('ROCASIN') gasket ahead of the o-rings, which also served as a thermal insulation barrier. However, after a few developmental tests, as part of an overall reliability improvement effort, the interface was analysed and redesigned to make certain that no direct hot gas jet impingement on the elastomeric o-rings occur in the event of a local breakdown of the barrier. Such a scenario can lead to failure of the motor as reported in the case of operational solid motors [1,2].**

A detailed literature survey was conducted to study various thermal defense mechanisms, materials, configuration viz. cross section, type of groove provided in the hardware as well as assembly parameters such as compression, porosity and volume fill. A braided Carbon Fibre Rope (CFR) based thermal barrier was chosen as the optimal candidate for the application considering its abilities to act as a thermal sink and also to resist erosion and oxidation under high temperature. Further, being a porous medium, adequate diffusion and pressure gradient at the o-ring seal is ensured. In addition, Carbon filaments have excellent burn resistance and are also ideal for reducing environments apart from their comparatively high thermal conductivity and thermal stability, low coefficient of thermal expansion, good mechanical properties and low density.

The chosen configuration consisted of a center core with a specified number of carbon filaments over which a few outer layers are braided resulting in an overall rope diameter of about 4 mm. The rope was confined in a triangular groove formed in the hardware by assembly due to space constraints and also to provide pressure-assisted squeeze. Design iterations were carried out on the CFR seal parameters related to compression, porosity and volume fill ratio. This was followed by rigorous testing which included simulation of several worst-case scenarios. Based on a minor blow-by of particles observed across the rope seal during initial tests under the solid motor environment, the seal parameters were modified. In addition, to restrict the amount of combustion products reaching the rope, an elastomeric spacer ring was accommodated upstream of CFR, on the annulus region at the HMSA-igniter interface, with a positive clearance of about 0.2 mm. A subscale (20 seconds duration) motor simulating three

different interface configurations confirmed adequacy of this modification. Finally, a full-scale motor static test of a solid motor, with a 90-ton propellant of ammonium perchlorate-hydroxy terminated polybutadiene- aluminium formulation, firmly established the efficacy of the design modifications. Post-test examination of the interface, after dismantling the hardware, confirmed efficient particle screening by CFR with no signature of blow-by past the barrier and no erosion or charring of the o-rings.

This paper presents an overview of the design philosophy of a solid motor interface using a carbon fibre rope thermal barrier, addresses the development challenges and reports the results of an investigative test campaign which provided useful insight into the failure modes and avoidance techniques.

Keywords– Head end Mounted Safe Arm (HMSA), Igniter, Carbon Fibre Rope (CFR), Solid Motor, Ignition systems

1. Introduction

Head end Mounted Safe Arm (HMSA) is a safety mechanism used with ignition systems for solid motors of launch vehicles (Fig 1). In the safe position, it helps to mechanically misalign or block the explosive train to prevent propagation in case of an inadvertent initiation of the first fire elements. In the arm position, the explosive channel gets aligned and is made ready for initiation on receipt of the firing command. HMSA is assembled with the igniter head end at the motor head end dome region using high strength fasteners. The leak tightness at the HMSA- Igniter interface, essential to withstand the operating pressure of the solid motor as well as the igniter, is provided by a pair of elastomeric (‘Viton’) o-rings. As the maximum temperature to which o-rings can sustain is limited to about 200oC, the interface incorporated a butadiene-acrylonitrile rubber (‘ROCASIN’) gasket ahead of the o-rings as a primary defense as shown in Fig. 2. This also served as a thermal insulation barrier. However, after a few developmental tests, as part of an overall reliability improvement effort, the interface was analysed to make certain that no direct hot gas jet impingement on the elastomeric o-rings occurs even in the event of a breakdown of the barrier locally. Such a possibility exists at the gasket interface in case of non-uniform compression or existence of gaps at the sealing surface. This scenario can even lead to failure of the motor as has been reported in the case of operational solid motors1,2. Hence, a redesign of the interface was attempted by incorporating a modified thermal barrier.

Fig. 1 HMSA with Igniter head end

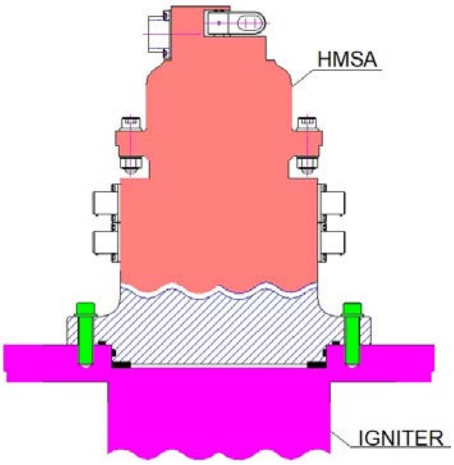

Fig. 2(a) HMSA-Igniter assembly (pre-revised version)

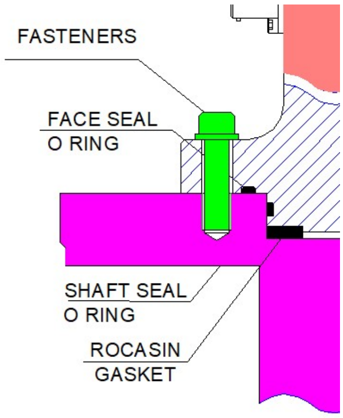

Fig. 2b HMSA-Igniter interface (pre-revised version-zoomed view of interface)

2. Design of thermal barrier:

The major design drivers for the thermal barrier are as follows [3]:

(i) Survive as well as maintain integrity under high temperature igniter-solid motor combustion gases (gas temperatures reaching 3300oK, max, in the motor propulsion chamber, with durations exceeding 100 seconds) and cool the gases to prevent deterioration of o-rings.

(ii) Filter the hot molten alumina slag carried by the gases, so that joint integrity is not affected.

(iii) Diffuse the concentrated gas jet, in case of minor breach in a sector, to allow uniform energising of o-ring seal and facilitate pressure equalization across the barrier to restrict gas flow.

(iv) Maintain flexibility and effectiveness during functioning even in the case of a minor joint opening under chamber pressure.

A detailed literature survey was conducted to study thermal defense mechanisms, various materials used, cross section, hardware groove configuration and assembly parameters such as compression, porosity and volume fill.

A. Selection of thermal barrier material

The first question was related to the selection of an optimal material for thermal barrier. The oxy- acetylene torch experiments conducted by Steinetz et al3 on various candidates namely stainless steels, Viton, ceramics, hybrid materials and carbon confirmed that only carbon could withstand such high temperatures for long durations. Though density is much higher for metals such as Tungsten, Rhenium, Nickel, SS304, Copper as compared to Carbon, the specific heat is lower. Nickel, AISI304 & Copper with melting temperatures less than 3000oC are not suitable considering the higher temperature of solid motor combustion products. Tungsten & Rhenium poses manufacturing difficulties due to their brittleness. Even though carbon oxidize and lose mass at temperatures even from 600oK, it is reported that, as a braided rope, they have very high temperature withstanding capability for long periods4. Considering all these aspects, a braided carbon rope (CFR) based thermal barrier was chosen as the most suitable candidate for the application considering its ability to act as a thermal sink, to resist erosion and oxidation under high temperature. Further, being a porous medium, adequate diffusion and pressure gradient at the o-ring seal is ensured.

In addition, carbon filaments are advantageous due to the following

(i) excellent burn resistance and also ideal for reducing environments.
(ii) comparatively high thermal conductivity and thermal stability,
(iii) low coefficient of thermal expansion,
(iv) low density.
(v) good mechanical properties

B. Selection of rope geometry

Among the various cross section geometries such as square, triangle, rectangle, ellipse or circle, a circular cross-section was selected based on simplicity and easy availability. It is made up of an inner core surrounded by several braided layers. The inner core helps in holding the rope in place whereas the braided layers provide filtering capability to the rope. The selected configuration consists of an inner core with about 6 x 3k filaments. This is followed by 3 numbers of 45o braided layers consisting of 8 x 3k filaments in first and second layers and 4 x 3k filaments in third layer rendering an overall cross section of about 4mm. This rope, manufactured by industry, is formed into a closed ring by a lap joint bonded using silicone RTV at the end interface. In addition, carbon filaments are wound over the lap joint in hoop direction for improving the joint strength to facilitate field assembly. Rope configuration is given in fig. 3 (a), (b) & (c).

Fig. 3(a) CFR

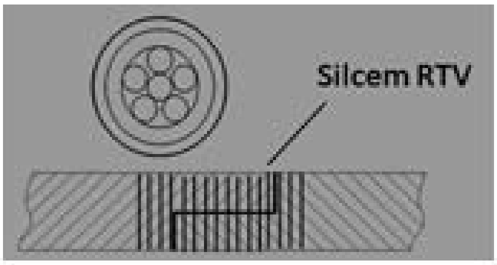

Fig. 3b CFR ring joint details

Fig. 3c CFR ring

C. Selection of groove parameters

Various types of groove configurations were considered. These included (1) triangular (on the hardware face, (2) trapezoidal, (3) rectangular and (4) triangular groove (on the edge of hardware) as illustrated in Fig. 4. Among these, the triangular groove (place in the edge) permits easy positioning of CFR within the limited space available at the HMSA- Igniter interface. Also, this arrangement aids the CFR to be forced deeper towards the apex of the triangle under pressure, which produces effective sealing. Considering these aspects, the triangular groove configuration depicted in fig 4 (d) was selected. A photograph of the CFR ring placed on the igniter face is given in fig. 5

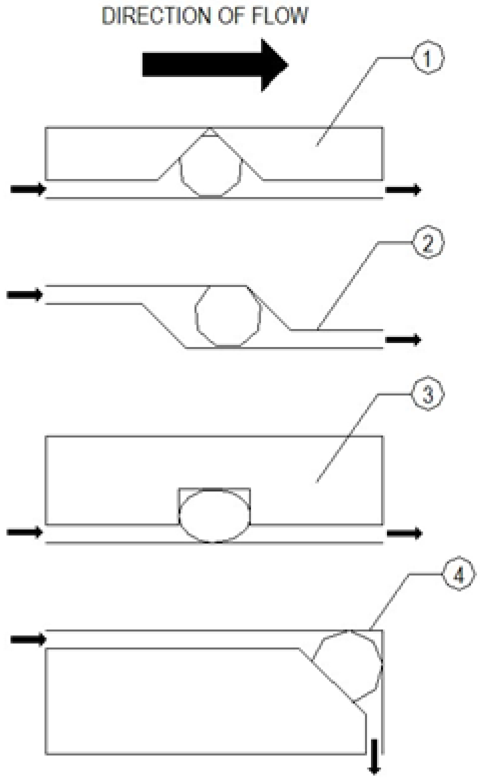

Fig. 4 Groove configurations

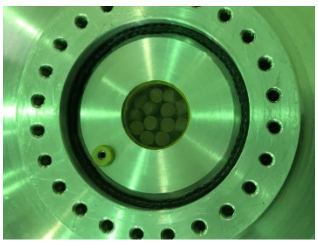

Fig. 5 CFR ring placed on igniter interface

D. Selection of primary and secondary thermal defense mechanisms

Detailed literature survey was conducted to study the thermal defense mechanisms used in various solid motors for launch vehicles worldwide [5,6,7]. Table 1 gives the gist of the findings.

Sl. No	Details of surveyed motor & interface	Mode of defense and remarks
1	Titan SRM segment joint	• Single CFR • Deviated flow path is provided upstream of CFR
2	RSRM Nozzle-to-case joint	• Single CFR • J-seal with pressure sensitive adhesive (PSA) upstream of CFR
3	RSRM Nozzle joint -2	• Dual CFR • Each thermal barrier has the capability to cool and filter propellant gases. • Two barriers provide additional factor of safety
4	RSRM Nozzle joint -3	• RTV backfill upstream of CFR (Ø3.1 mm) • Assy gap 0.076 mm
5	RSRM Nozzle joint-5	• Single CFR separating the boot cavity from the primary O ring. • Since the boot cavity temperatures are already quite low, a single CFR barrier is

Table 1: Thermal barrier mechanisms

Sl. No.	Parameter	Preliminary specification	Typical specification for surveyed motors
1	Material	Carbon fibre (T300 type)	Carbon fibre (T300/Grafil/ Amoco, Kynol)
2	Geometry	3k x 6 Nos. core followed by 3 sheaths	12k x 1 core followed by 5-10 sheaths
2	Rope cross sectional dia., mm	4	3-6
3	Compression %	20-25	20-25
4	Porosity, %	25-30	28-50
5	Joining method for ends	Lap joint with Silcem and hoop knitting	Lap joint with RTV

Table 2: Thermal barrier parameters

It can be seen that CFR is generally used in dual redundant mode for critical areas except in areas where the temperatures are low. In the present case, being a stagnant region, thermal analysis at HMSA- Igniter interface has predicted a relatively lower temperature when compared to other motors. Hence it was decided to use only a single CFR ring upstream of the o-ring seals.

E. Assembly parameters

The effectiveness of the thermal barrier and its particle screening ability depends upon the compression, porosity & spring back. Unlike other seals such as o-rings or gaskets, “cook-book” solutions for fixing these parameters are not available for this type of interface. Since the compression and porosity are inversely related, an optimum trade-off has to be evolved through tests such that the rope effectively screens the particles while allowing gas passage and, at the same time, does not allow blow-by across the interface. Similarly, tests were conducted to evaluate the spring back and ensure that sealing is effective even under operational conditions. Considering all these factors, preliminary specifications for assembly parameters were fixed as listed in Table 2

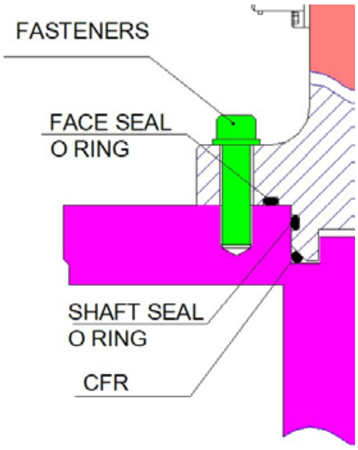

Fig.6 Interface incorporating CFR

The modified interface incorporating CFR, as shown in fig.6, was evaluated in an 8-ton class ammonium perchlorate-hydroxy terminated polybutadiene- aluminium formulation based solid motor. Even though the overall performance was normal for the motor, post-test inspection, after dismantling the elements, revealed heavy blow-by of alumina particles beyond CFR up to the shaft seal interface (fig.7). However, both O-rings were intact and showed no signature of erosion. Based on further analysis, it was concluded that even though CFR design was adequate, an uncontrolled flow of combustion products would have clogged the thermal barrier reducing its effectiveness, thereby leading to the observed anomaly. It may be recalled that the survey carried out on motors with similar interfaces (Table 2) had also indicated that CFR, when used in singular mode is generally supported by mechanisms for restricting the exposure of the rope to the combustion products. These are in the form of a J seal, a deviated path (S-curve) or RTV putty applied upstream of CFR. In comparison, it was observed that an axial gap of about 2 mm existed ahead of CFR for the tested configuration which would have allowed profuse flow of alumina resulting in clogging and blow-by.

Fig.7 Post-test observation on interface

To circumvent the issue, design iterations were carried out with modifications in the interface. The approach was to reduce the alumina reaching CFR. The final solution involved incorporating an elastomeric (ROCASIN) ring in the location where gap existed so as to bring down the clearance (to about 0.2 mm). This small clearance was maintained to ensure that the motor pressure is felt by CFR and thereafter the shaft seal o-ring, which is a requirement for its efficient functioning. The final configuration is shown in Fig. 8.

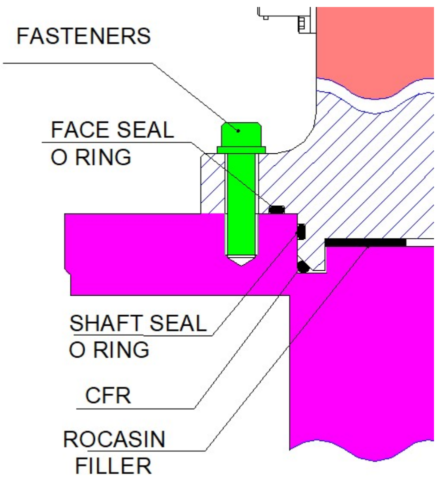

Fig.8 Finalised interface configuration

The effect of modifications was initially studied in a sub-scale test motor which used a similar propellant composition as for the proposed application. The nozzle was tuned to obtain the same peak operating pressure, even though for a reduced duration, as for the flight motor (due to hardware constraints). The test also simulated the interface with and without ROCASIN filler to enable a direct comparison between the two. During the test, gas temperature and pressure were monitored close to CFR at a downstream location. Fig. 9 gives the test configuration and interface details. The sub-scale motor test proved the efficacy of CFR since excellent cooling was observed across the barrier (maximum temperature of gases reaching the o-ring was just 3oK above ambient measurement). Pressure-time data also confirmed the fact that o-ring interfaces in both the cases (with and without ROCASIN filler), experienced motor pressure as shown in fig.10. However, in the modified interface, a time delay of 2seconds was observed for the motor gases to reach the instrumented location, confirming slow entry of combustion products, as desired, at the o-ring interface. Post-test inspection further confirmed that the improvements were effective, with no breach of alumina slag observed across CFR.

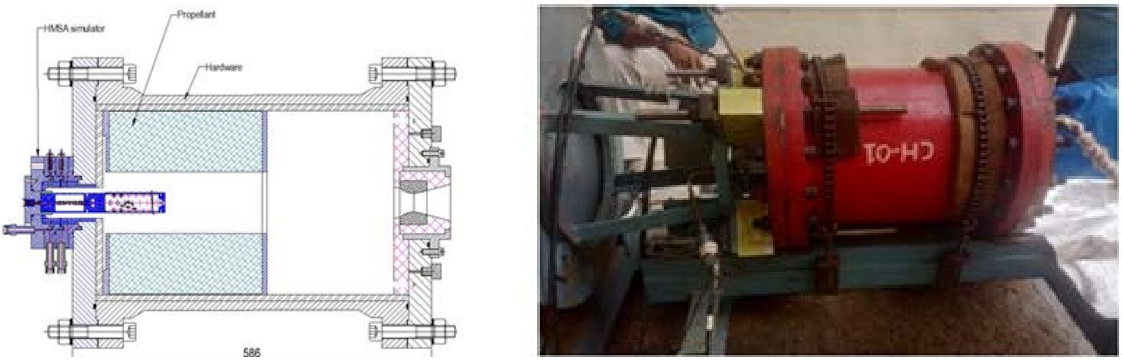

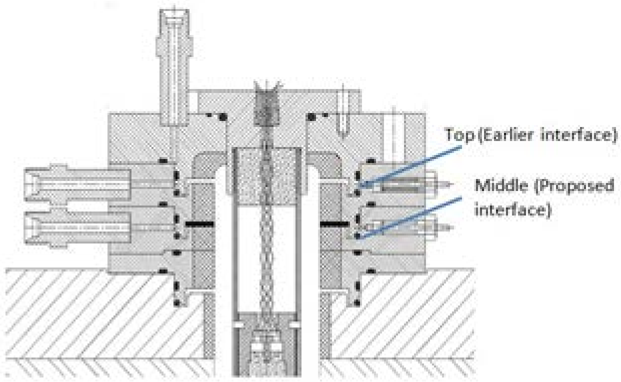

Fig.9 Sub-scale test configuration

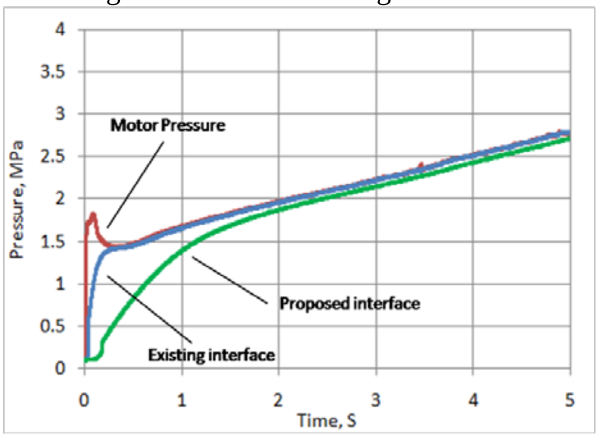

Fig 10: Pressure-time data at o-ring location (only 5 sec. plot out of 20 sec. is shown)

After successful evaluation in the test motor, a second test of the 90-ton motor was conducted with all the modifications incorporated in the interface. Excellent test performance as well as the post- test observations confirmed adequacy of the modifications. Fig. 11 shows the HMSA-Igniter interface after dismantling of the hardware components. CFR was found to be effective in filtering the solid combustion products with the downstream zone clean and free of combustion products.

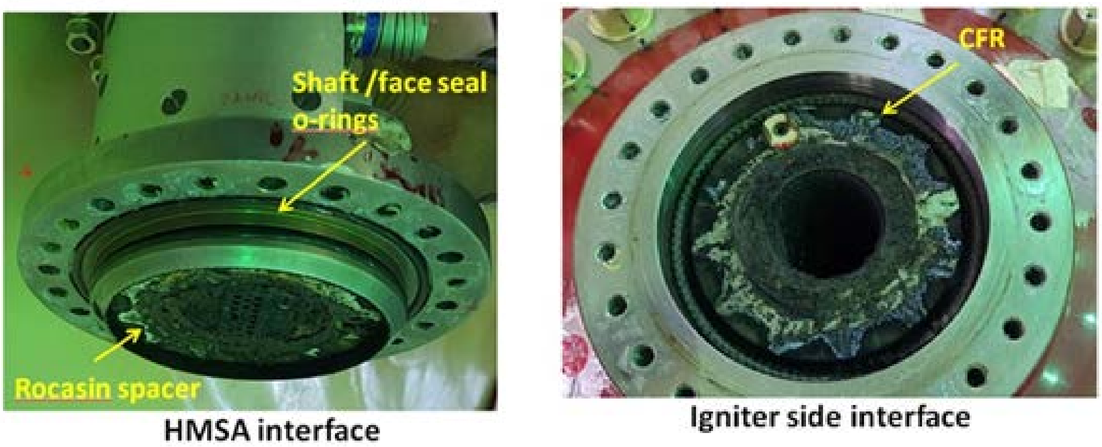

Fig. 11 HMSA-Igniter post-test observations (90-ton solid motor static test)

3. Conclusion

Design philosophy of an interface between an ignition safety device and a solid motor utilizing a carbon rope thermal barrier is discussed in this paper. The rationale behind the selection of rope material and choice of optimal geometry and groove configuration to meet the critical assembly parameters such as compression, porosity and spring back are addressed.

Further, challenges faced during development followed by details of an investigative test campaign are described. At the end of the development programme, a more robust design of the interface has been demonstrated. This study also advanced the understanding of the system and provided useful insight into the failure modes and avoidance techniques.

4. Acknowledgement

The authors wish to thank Sri. S. Somanath, Director, VSSC, along with Chairman and members of Design Review Team for their valuable advice and guidance. Support of colleagues of IDPD, RSTD & TDD divisions, SSLV project of VSSC for carrying out the investigative tests are also gratefully acknowledged.

5. Reference

[1] Feasibility Assessment of Thermal Barrier Seals for Extreme Transient Temperature", Bruce M. Steinetz & Patrick H. Dunlap Jr., NASA/TM-1998-208484

[2] https://ntrs.nasa.gov/archive/nasa/casi.ntrs.nasa.gov/20040000630.pdf

[3] "Rocket motor joint construction including thermal barrier", Steinetz et al., US Patent 6,446,979 B1 dated Sep. 10, 2002.

[4] Steinetz et al. United States Patent No.: US6,446,979 B1 Date of Patent: Sep. 10, 2002.

[5] "Performance enhancement of the space shuttle RSRM nozzle to case joint using carbon rope barrier", M E Ewing et al., AIAA A99-31547, 1999

[6] "Development of an enhanced thermal barrier for RSRM nozzle joint", Paul Bauer, AIAA A00-36749

[7] Development of thermal barriers for solid motor nozzle joints", Bruce M Steinetz et al., Journal of Propulsion & Power, Vol 17, No. 5

Studies on A Pyrovalve Diaphragm for Low Temperature Applications

Anil Kumar Tiwari
AeroSpace Ordnance Entity
VSSC, ISRO
Thiruvananthapuram
anil_kumar_tiwari@vssc.gov.in

Priyanka Chaudhary
AeroSpace Ordnance Entity
VSSC, ISRO
Thiruvananthapuram

Vikas
AeroSpace Ordnance Entity
VSSC, ISRO
Thiruvananthapuram

Md. Moinuddin Hassan
AeroSpace Ordnance Entity
VSSC, ISRO
Thiruvananthapuram

Sheeju Chandran
AeroSpace Ordnance Entity
VSSC, ISRO
Thiruvananthapuram

Ani Daniel Kurien
AeroSpace Ordnance Entity
VSSC, ISRO
Thiruvananthapuram

Vinod Kumar N
AeroSpace Ordnance Entity
VSSC, ISRO
Thiruvananthapuram

Baby Abraham
AeroSpace Ordnance Entity
VSSC, ISRO
Thiruvananthapuram

Abstract – **Pyrovalves are pyrotechnically actuated devices with piston-cylinder configuration that are extensively used in aerospace systems to perform mission critical fluid flow control functions. These valves basically fall into the Normally Closed (NC) type or Normally Open (NO) type depending on the nature of the application. In NC pyrovalves, the flow line is initially closed using a leak tight integral/ welded metallic diaphragm. During the actuation of the pyrovalve, high pressure combustion products from the pyrocharge drives a suitably configured piston to sever the diaphragm and open the flow path enabling smooth fluid flow. The configuration of the valve diaphragm is made in such a way that it is capable of withstanding the initial fluid pressure and also shears and uniformly separates during valve function. Various configurations of pyrovalves are used for low temperature applications for cyrogenic stages in launch vehicles. For these valves, the valve diaphragm configurations are made differently to meet specific requirements. In one such application, there was a random occurrence of non-severance of diaphragm during valve actuation. As this anomaly occurred after several successful tests under low temperature conditions, a detailed study of the anomaly was done to identify the probable cause. A number of evaluation tests were also conducted to isolate the problem. Based on these, a modified diaphragm configuration was proposed addressing the issues concerned and with a focus to incorporate minimum changes so that the existing design pedigree is retained. The modified diaphragm was also studied with respect to the earlier configuration using FEA and the improvements were verified. For more realistic simulation, low temperature properties for the diaphragm material was evaluated by specimen testing in a Cryostat UTM. Further, to facilitate repeated testing during the design finalization phase, a test device was configured wherein the diaphragm is only consumable element in each test. In addition, break-down studies were carried on earlier successfully tested valves followed by critical inspection on earlier diaphragms to find the cause of the anomaly. This paper brings out the details of the anomaly and the studies undertaken to understand the cause of anomaly and it also address the proposed modifications of valve diaphragm.**

Keywords– pyrotechnic, elastomeric, diaphragm, membrane

1. Introduction

Pyrotechnically actuated valves, both Normally Closed (NC) and Normally Open (NO) are extensively used in liquid stages of launch vehicles. In NC pyrovalves, the flow line is initially closed using a leak tight metallic diaphragm, either integral or welded. During the actuation of the pyrovalve, high pressure combustion products from the pyrocharge drives a suitably configured piston to sever the diaphragm and open the flow path enabling smooth fluid flow. In the case of valves for cryogenic stages, the construction is more complex since the use of elastomeric components is not permitted, especially those for critical sealing functions. Hence, in these valves, towards meeting the intended mechanical function, thin membranes are predominantly used to seal the actuators, or pistons moving inside a cylindrical housing.

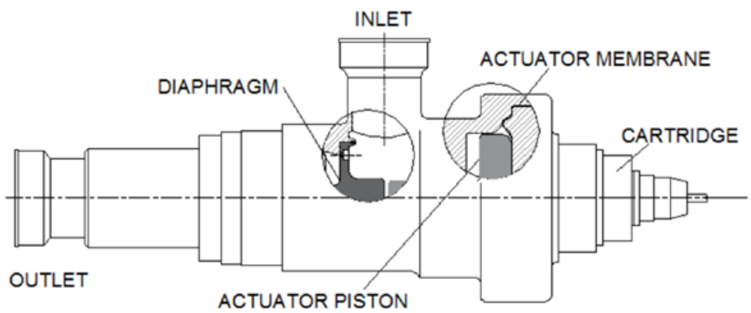

Figure 1: Valve configuration (pre-actuated)

However, the use of membranes for dynamic sealing poses several challenges. The major configuration related issue is the need that it should be fully supported in the final expanded position to avoid rupturing due to residual pyro-gas pressure and the piston movement has to be limited. Thus, in such pyrovalves, the useful piston stroke is less. Because of this limitation, the diaphragm shearing has to be efficient within a minimum shear displacement. In addition, the diaphragm should meet its basic requirement of withstanding the working fluid operating pressure with adequate structural margins.

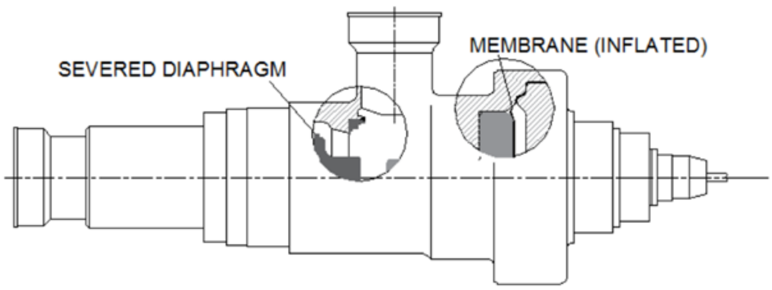

Figure 2: Post actuated valve configuration

The study presented here is with respect to a NC pyrovalve used for a cryogenic application operating at 20K. Towards shelf-life evaluation of the pyrovalve, aged units from an earlier batch were being tested and one of the valves failed to function at 20K environment. The NC pyrovalve has a diaphragm separating the inlet and outlet of the valve. This acts as the hermetical isolating element between the inlet and outlet. The energy source of the device is a pyro cartridge which consists of an electrical initiator and a gas generating pyrotechnic charge composition. The valve configuration is such that the pyro-gas generated on actuation pressurizes the free volume of the device and inflates the actuator membrane. In this process, the piston aligned with the membrane moves forward and severs the diaphragm.

Further, towards achieving a controlled shearing, a weak location is defined on the diaphragm in the form of a notch. The severed diaphragm is retained in its final position by a compression spring to facilitate undisturbed fluid flow.

2. Observations on the failed pyrovalve

The subject pyrovalve was from a 12-year-aged batch of valves and was being tested for shelf-life evaluation along with other devices of similar life. All the other units from the same batch of pyrovalve were successfully tested without any abnormal observations. To simulate the engine operating conditions, the functional test was done in a Cryostat at 20K thermal environment. The observations during the functional test and the subsequent breakdown analysis are listed as follows:

A. All the electrical parameters recorded during the test including bridge wire resistance, firing current and bridge wire fuse time were within specification.
B. First, an X-ray of the unit was taken to record the internal features.
C. Thereafter a systematic break-down analysis was conducted after dissection of the fired device.
D. The actuator part was seen to have functioned normally. There was no signature of rupture of the actuator membrane. Its integrity was later confirmed by a leak check by Helium (< 1x10-10 mbar lit/sec).
E. The diaphragm was not severed. Instead, it was found to be deformed and the thin section was elongated. The integrity of the diaphragm was confirmed by Helium leak check. Sliding interfaces of the diaphragm shank was inspected and found to be free from any damage. Smooth movement of diaphragm was confirmed.
F. A critical inspection of the retrieved diaphragm revealed the following
   (i) thickness of intended shear region (U groove) at support diameter was lesser by about 50 microns
   (ii) groove width was measured to be increased by about 120 microns
   (iii) flange portion of the diaphragm was deformed and elongated permanently.

3. Investigative studies

Based on the observations on the anomalous unit, a systematic study addressing each aspect of the valve functioning was carried out to investigate the root cause of the anomaly. Further, towards capturing the batch-tobatch variations, details of two batches of pyro valves were studied for analysis. The details are given below:

A. Energy from the pyro cartridge

The energy source of the pyrovalve is pyro cartridge and inadequate energy from the source can cause such an anomaly. However, these valves using the same batch of cartridge had functioned normally and as per the processing logs there is no reason to single out the cartridge used in the anomalous unit. Further, for an additional confidence, a closed bomb test of a cartridge from the same batch was conducted and the pressure vs time and other parameter like time to peak pressure were found normal. Hence, batch wise there is no issue with the energy source and also no age-related deterioration of the charge is observed.

B. Dimensional analysis

The failed diaphragm and other components were inspected for critical dimensions. This includes sliding interface inspection, actuator piston stroke and groove geometry verification. Sliding interface dimensions of actuator diaphragm and support were within specification with clearance 10-30 microns without any visual mark. The actuator piston stroke was also confirmed again meeting the spec ~ 5mm and verified with log. But for the post-actuation deformation of the diaphragm, there were no abnormal observations in the dimensional inspection.

C. Dimensional analysis - batch to batch variations

Data of tested units including tested valves and unused components were available from two batches – earlier and recent batch realized by two different fabricators. Critical dimensions of diaphragm were re-inspected critically. These inspected features were diaphragm groove thin section OD & ID, diaphragm flange fillet radius and root radius at groove OD & ID. A comparison on these parameters of the two batches was made which is summarized as it follows.

(i) Dimensions of all features were within specification.
(ii) Thin section OD values for both batches were precise and comparable.
(iii) Thin section ID values for old batch were close to extreme limits while for recent batch, it was more precise and falling middle of limits.
(iv) Fillet radius values for old batch diaphragm were close to lower limit while for recent batch, it was vice versa.
(v) Both inner and outer groove root radius values for old batch diaphragms were higher than that of same feature in recent batch by almost 2 to 3 times.

D. Diaphragm severance pattern – batch to batch variations

NDT was done on the diaphragm units (post-actuated) from old and recent batches to see the severance pattern. From the available tested units from two batches, it was observed that the diaphragms in old batch severed at the OD of the thin notch section and has a small fin like lip on the severed central portion of the diaphragm. However, in recent batch units, the diaphragm was severed at the ID of the thin notch section with no fin like feature. From the metallographic study of both the type of severances, it was seen that failure at the OD of the thin notch section due a combination of both tension and shear, where the failure at the ID of the thin notch section is by predominantly shear. These aspects are clearly discernable in the material failure pattern.

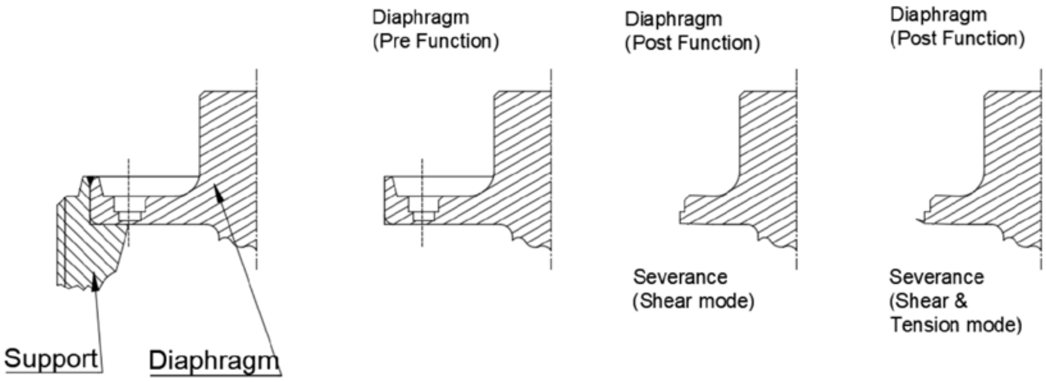

Figure 3: Diaphragm severance pattern

E. Material composition and metallographic analysis

Failed diaphragm material compositions were checked for verification of material with help of both X ray Fluorescence (XRF) and Chemical analysis method. The % elemental constituents of diaphragm material were found matching with design material AISI 3XX series, ruling out the possibility of change in material. Further, metallographic studies of the failed diaphragm indicated higher hardness in region close to the notch due to strain hardening. This was confirmed with Ferrite number also, which was found to be higher for notch region compared to the other portion.

F. Diaphragm shear load evaluation

Though weak section is provided on the diaphragm to achieve a consistent severance, the variation in the resistance offered by the diaphragm against severance can cause such a failure. In addition to the force required for severance, the stroke required for complete severance is also critical as the useful stroke in the actuator is also limited. Towards understanding this, shear load evaluation of diaphragm was done in the actual configuration with a setup for testing in UTM at room temperature and at 77K. It was observed that force required for diaphragm severance at 77K is more than twice of what recorded at room temperature. Similarly stroke for severance at 77K is almost double as at room temperature.

In order to investigate the reasons for failure, FEA simulations were carried out for the valve with various deviations, which could not be verified by means of experiments. The finite element model consisted only of diaphragm and support anvil of the housing. The material strength models for ICSS07XX 3XX (housing material) and AISI 3XX (diaphragm material) are shown in Fig. 4.

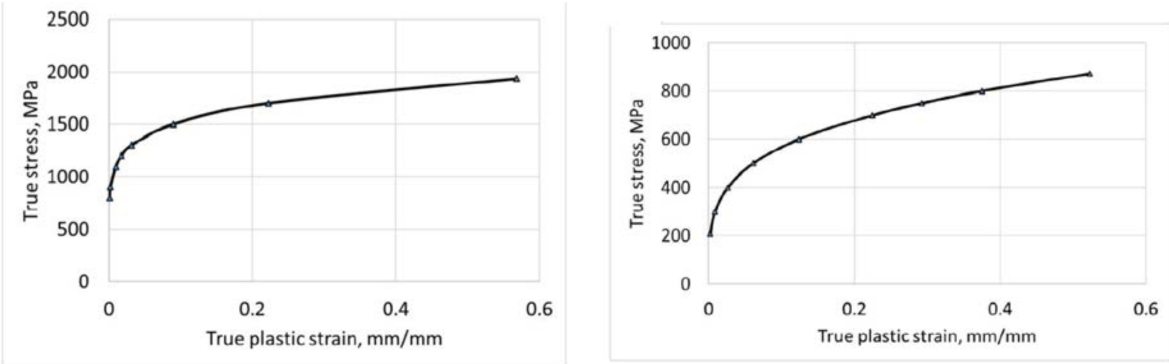

Figure 4: Stress Strain curve for ICSS07XX-3XX (support) and AISI 3XX (diaphragm)

As a validation case, the load curve for severance of diaphragm at RT was estimated first, based on explicit dynamic analysis. The results from finite element analysis and actual tests in the same configuration in UTM yielded same results.

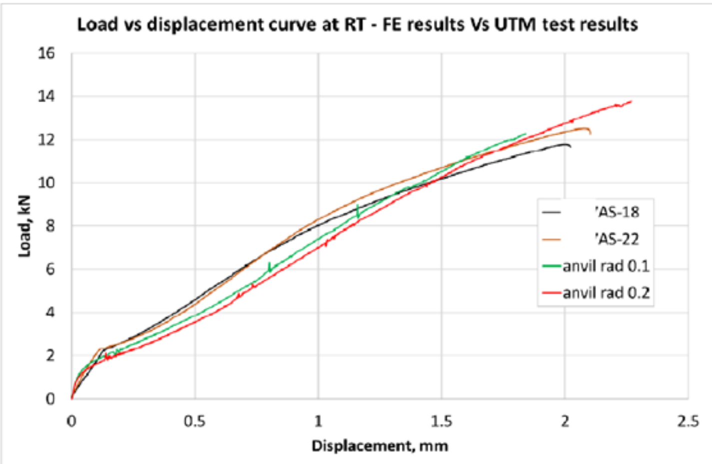

Figure 5: Load curve for severance of diaphragm at RT

Having validated the model with properties at RT (Fig. 5), the same model was subsequently used to simulate diaphragm severance pattern at 20K. For estimating material strength model at 20K, a specimen of diaphragm material AISI 3XX was tested in cryostat and the true stresstrue plastic strain curve was derived (Fig. 6).

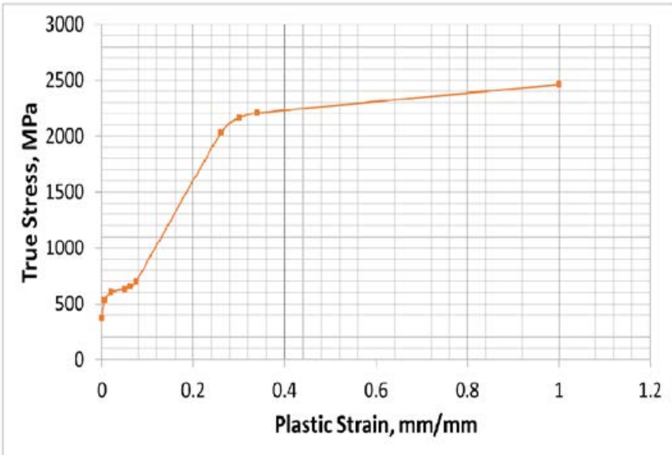

Figure 6: True stress-true plastic strain curve (AISI 3XX) at 20K

This strength model was then used for diaphragm material and the severance pattern of diaphragm at 20K was simulated. It was found that the profile of deformed diaphragm obtained from the failed valve matched closely with the profile of deformed diaphragm as obtained from finite element analysis as shown in Fig. 7.

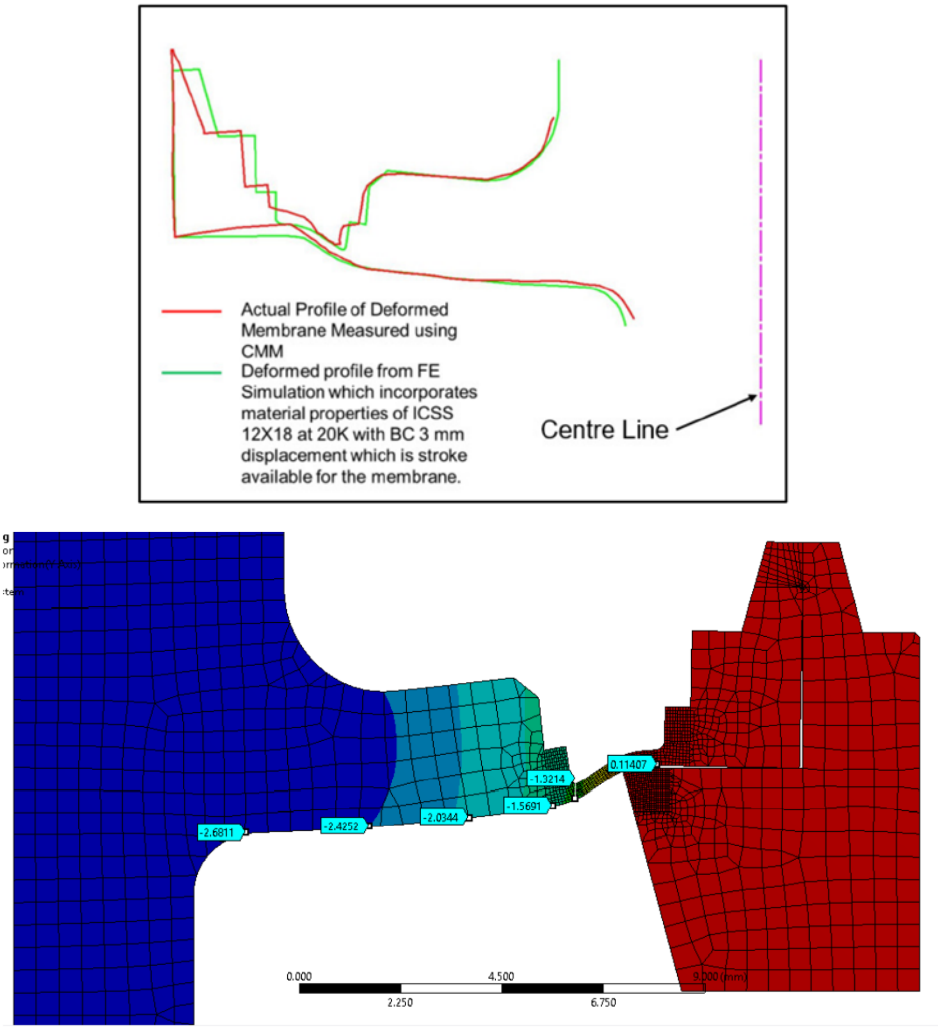

Figure 7: Profile of deformed diaphragm

Hence, numerical analysis brings out the effect of material properties of AISI 3XX on notch severance characteristics and agrees well with the experimental results. It can be observed that diaphragm material undergoes typical single hardening when tested at room temperature; however, at low temperature, the material exhibits double hardening behavior and shows increased toughness. Due to this double hardening behavior at low temperature, a large amount of the energy supplied by piston stroke is absorbed by thicker region of diaphragm as it deforms to a great extent due to strengthening of the notch due to higher plastic strain. Since the stroke of piston is limited, the double strain hardening behavior lead to requirement of higher piston stroke for successful severance of notch at desired location. Hence, as the temperature decreases, toughness of AISI 3XX increases and the stroke and force required for successful severance of diaphragm notch also increases. This inference is also well supported by the experimental & simulation results, summarized in Table 2 and Fig. 8.

Table 2: Experimental & simulation results

Temp.	RT	77K	20K
Stroke for severance, mm	2.2	3.6	4.5
Max force at severance, kN	12	26	35.3
Remarks	Test Simulation	Test	Test /Simulation

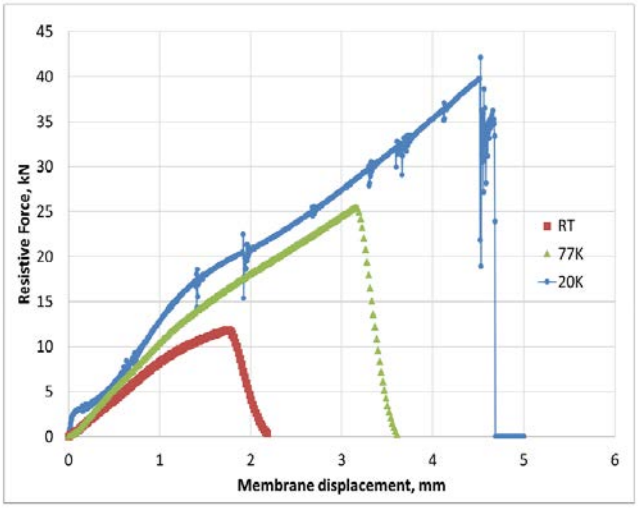

Figure 8: Comparison of resistive force variation with membrane displacement curve for various temperatures

4. Inference from the investigative studies

Based on breakdown analysis & investigative studies on the failed unit and from data analysis of two batches of valves the following observations are made.

A. Actuator side of the valve performed normally. With no observation of leak and age effect on cartridge as investigative test result suggests, it confirms the availability of sufficient energy.

B. The anomalous unit was comparable with all other units with respect to the specified dimensions. In spite of being within specification, there is a clear batch to batch variation with respect to critical dimensions. This affects the severance pattern of the diaphragm. This explains why units from old batch exhibited a combined tensile & shear mode of failure at the OD of the thin notch section of the diaphragm whereas units from recent batch had a shear mode of diaphragm severance at the ID of the notch. Further, geometrically also, the force requirement of ID severance is less compared to OD severance.

C. The need for higher force for severance at 77K is explainable, but the requirement of a higher stroke along with it indicates marginality when compared to the limited stroke in the device. The material property evaluation at 20K done in the Cryostat UTM also indicates higher elongation at failure. FE analysis of the diaphragm incorporating the actual tested properties brings out the marginality of stroke in the device leading to the failure scenario.

D. The configuration of the diaphragm was such that during actuation, the energy provided by the actuator was also used for deforming the diaphragm in addition to severance. In due process, the limited stroke of the actuator was consumed.

Thus, the combination of above factors such as geometry of the diaphragm, material characteristics at 20K, the root radius of the notch and the limited actuator stroke led to the non-severance of the diaphragm leading to the pyrovalve failure.

5. Modifications

Considering the fact that the pyrovalve configuration has a long history of successful performance, to make the design more fault tolerant, modifications were proposed to improve the diaphragm configuration to achieve efficient severance retaining the pedigree of the device. The highlights of proposed modifications are:

A. For efficient diaphragm severance, the rectangular ‘U’ notch is changed to ‘V’ notch with the thin section width reduced. The shear thickness is retained same without any change.

B. The diaphragm flange thickness and fillet radius were also increased to strengthen it against bending during valve actuation.

C. To optimize the utilization of stroke of actuator piston, gap between the diaphragm and actuator piston is reduced. d. To strengthen weld joint between diaphragm and valve and to avoid strain during actuation, weld depth is increased.

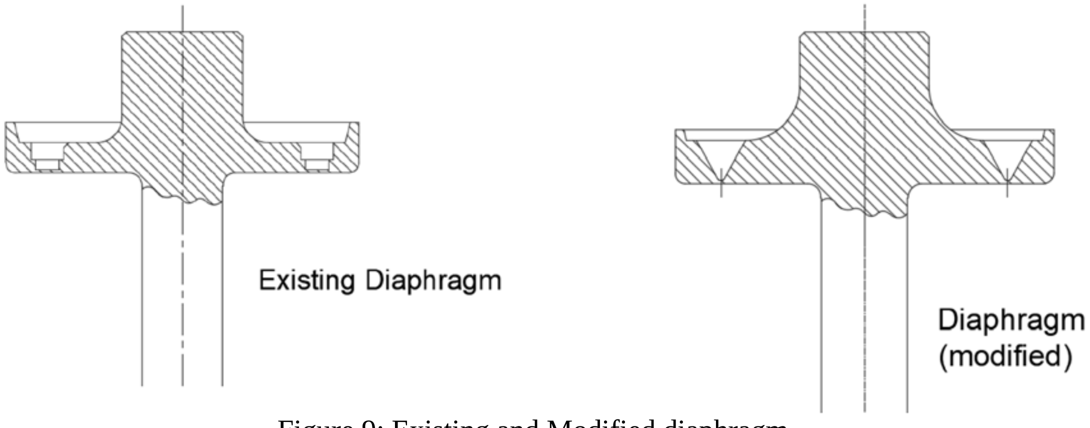

Figure 9: Existing and Modified diaphragm

The diaphragm is supposed to withstand inlet pressure and vibration load in the pre-actuated condition. The modified diaphragm was also analyzed for margins under operating conditions.

Finite element analysis was carried out to study diaphragm severance characteristics at 20K, and it was found that the new V-notch configuration can be severed at almost one-third the stroke required for severance in old U-notch configuration. The force required for severance is slightly higher than required in old configuration. It can be seen that the new configuration is better than the old one in terms of piston stroke requirement.

In order to study the effect of deviations in notch dimensions on diaphragm severance characteristics, various configurations of notch geometry were simulated by varying relative position of housing anvil to notch centerline, and by varying the fillet radii of V-notch. The sensitivity study revealed that diaphragm stroke required for fracture can vary from 1.2 to 2.32mm, while the maximum force varies from 40 to 50 kN. The total energy required to be delivered by piston to diaphragm ranges from 30 to 70J. This energy requirement is very benign as compared to the energy imparted to piston by pyrocartridge.

6. Functional demonstration

A. Simulated hardware test

Towards initial functional demonstration with modified configuration, a simulated hardware test setup with provision of flanged/fastened interfaces was realized. With this setup, the lead time required to prepare the final configuration was minimized as repeated testing on the same hardware was possible with minimum consumables like cartridge, Gasket, actuator membrane and diaphragm only need to be replaced. The setup configuration is shown in Fig. 10.

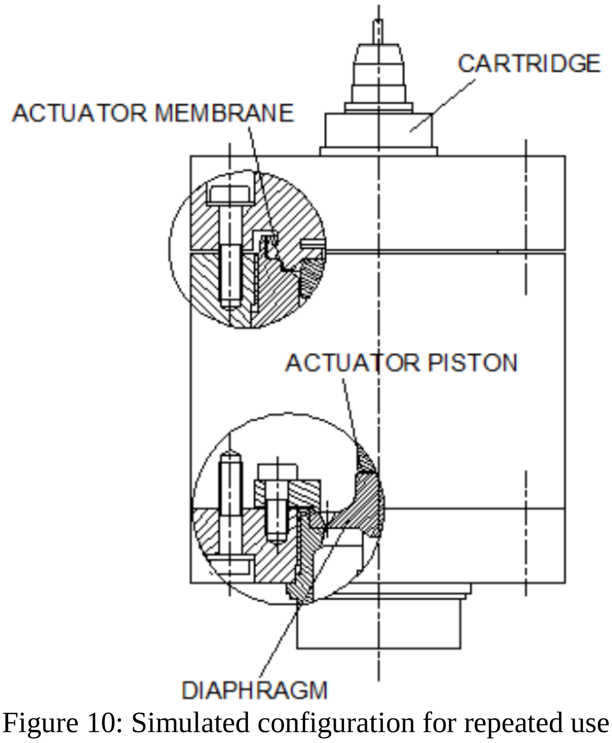

Figure 10: Simulated configuration for repeated use

All initial developmental trials were conducted at ambient as well as 77K. Functional tests to demonstrate energy margin with lower charge and cutoff charge qty were conducted successfully. Based on these trials, modified diaphragm configuration was cleared for qualification and acceptance.

B. Qualification tests

As per process document, processing of valve batch was carried out starting with critical dimensional inspection. After processing, in the final assembled condition NDT was taken to verify the assembly correction. Energy margin tests as well as hardware margin test were done on final units as per standard. The qualification units were then exposed to specified environmental conditions. After environmental exposure, the qualification units were functionally tested at low temperature with line pressure. Towards verifying the post test integrity of the actuator diaphragm, pneumatic pressure test in aquarium mode under water was also done.

7. Conclusion

Detailed analysis and studies of the pyrovalve enabled to narrow down on the probable reason for the failure of the pyrovalve. The effect of the diaphragm configuration and the material characteristics at low temperature is understood. The case also highlights the need to have efficient diaphragm severance and effective use of stroke in configurations with limited actuator stroke. The modifications made for improving the pyrovalve is minimum and is only limited to the diaphragm thereby retaining the pedigree of the original valve. The design adequacy is verified by analysis, margin tests and the qualification tests. This failure has prompted the designers to re-visit relevant aspects of similar valves. Further, this case will serve as a guideline for future pyrovalve designs.

Towards a Design Approach for a Pyrotechnic Pressure Generator used in Deployment Mechanisms

S Kumanan
Aero Space Ordnance Entity
Vikram Sarabhai Space Centre
Trivandrum
kumanan.srinivasan@gmail.com

G M Vineeth
Aero Space Ordnance Entity
Vikram Sarabhai Space Centre
Trivandrum
vineeth.gm@gmail.com

S Nimesh
Aero Space Ordnance Entity
Vikram Sarabhai Space Centre
Trivandrum

B Hari Hara Nath
Aero Space Ordnance Entity
Vikram Sarabhai Space Centre
Trivandrum

N Vinodkumar
Aero Space Ordnance Entity
Vikram Sarabhai Space Centre
Trivandrum

Baby Abraham
Aero Space Ordnance Entity
Vikram Sarabhai Space Centre
Trivandrum

***Abstract* – Pyrotechnic pressure generators (PPGs) use chemical reactions to produce a specific amount of gas. The pressure of the generated gas can be used to perform mechanical work. A case study is presented for designing a PPG for a high velocity deployment system wherein a specified mass is propelled using a high-pressure working fluid (gas). The pressure generating system consists of an electrical initiator, a pyrotechnic booster and a nitrogen rich gas generating pelleted composition as main charge. The combustion products are vented to a gas generator chamber having a set of fixed orifices through which the gas flows into the chamber containing the projectile. This pressurizes the chamber which propels the projectile and leads to its ejection.**

The design methodology consisted of defining the requirements, selection of materials, theoretical analysis and modeling. Apart from conventional approaches for ballistic and structural design, an in-house developed mathematical code was developed and successfully employed. Prototyping and functional testing were carried out in a closed vessel and the design was validated. Subsequently, all performance parameters were experimentally evaluated in a full-scale test with the deployment device and found to be within acceptable limits. In this paper, we present details of a successful design process which has resulted in the functional demonstration of a Pyrotechnic Pressure Generator for the specified application

Keywords– Pyrotechnic; Gas Generator; Ballistics; Deployment; Combustion process

1. Introduction

Pyrotechnic Pressure Generator (PPG) is a device used to produce a specified volume of gas by a precisely controlled chemical reaction. The resulting gas pressure is used to perform mechanical work for deployment or for inflatable systems. PPG is a critical component in several enabling technologies in the field of defense and aerospace engineering including parachute deployment mortars, emergency escape systems in aircrafts, missile launching systems and airbag inflation systems [1 2 3]. Limited literature is available on the modelling and simulation of such systems. Pawlikowski4 discusses the development of a simulation for a drogue mortar system.

The current work deals with the use of PPGs in deployment systems. The elements of a typical deployment system are (1) pyrotechnic pressure generator, (2) tube or housing (3) sabot or piston (4) projectile to be ejected such as a parachute and (5) lid or cover1 assembled to the tube using shear screws. The tube and the sabot constitute a typical piston-cylinder arrangement. The tube houses the projectile to be ejected and also guides the movement of the projectile. This projectile is retained within the device using a lid. Schematic of a deployment system is given in Figure 1.

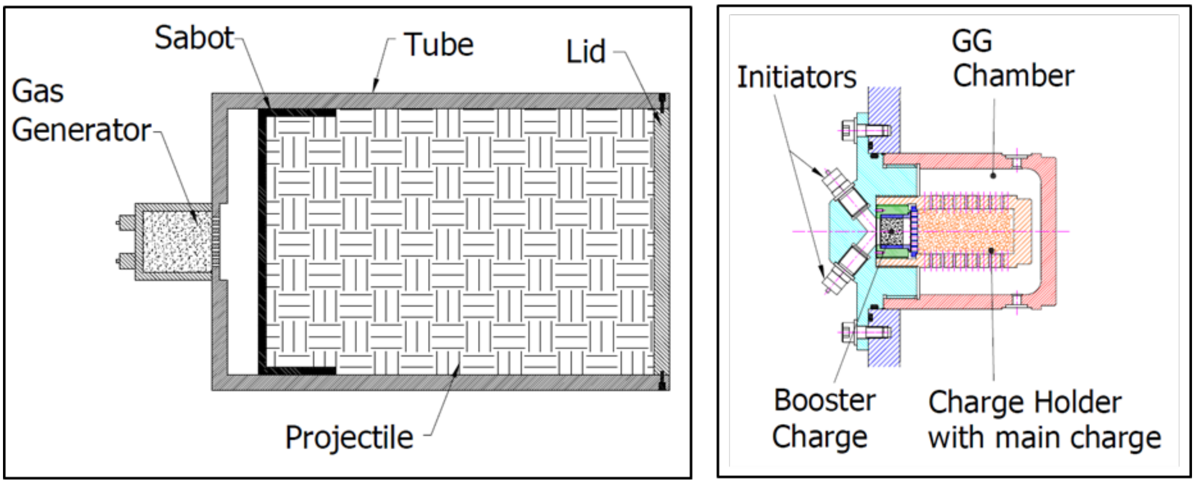

Figure 1. (Left) Schematic of a deployment device using a pyrotechnic pressure generator. (Right) Schematic of a pyrotechnic pressure generator

The pyrotechnic pressure generator (PPG), shown in Figure 1, consists of a dual redundant electrical initiator - booster ignition train which triggers the main pyrotechnic charge, held in a charge holder in the form of pellets. The charge holder is a vented structure. The hot gas produced by combustion of the pelleted charge fills a gas generator (GG) chamber. This chamber has control orifices through which the gas flows to the closed volume behind the sabot and forces the sabot out of the tube, causing ejection of the projectile by shearing the pins and separating the lid.

2. Requirement

The key functional requirements specified for the ejection system were ejection velocity in the range of 40 -50 m/s, ejected mass of about 20 – 30 kg, stroke length of 400-500 mm and the reaction load, limited to 100-150 kN. Further, the system mass had to be maintained as low as possible. It should be noted that the objective is to design a pyrotechnic pressure generator which is capable of imparting the above velocity for the specified mass at the time of ejection. Further, the reaction load generated should be minimized so that the supporting structure can withstand the load with minimum mass.

3. Design Methodology

A. Type of pressure generator

The pressure generator can be of different types depending on the design of the GG chamber. In the simplest form, the combustion gases are directly vented to the tube, doing away with the GG chamber. In a few designs, the GG chamber has a very large vent area. Both these configurations lead to a large initial pressure spike as illustrated in Figure 2, resulting in high reaction loads. In a more common design, the GG chamber has fixed orifices with low vent area and hence functions under high pressure5. The release of gases from the GG chamber is controlled through choked orifices so that the pressure rise is more gradual and the pressure peak is reduced, albeit still present. In a few cases, 'erodible' orifices are made use of, which provide a continuously increasing vent area and correspondingly, the mass flow rate. With proper design of the eroding orifice, the volume increase in the mortar tube can be compensated with the increasing mass addition due to the eroding orifice, thereby producing a nearly constant and minimum reaction load[6]. However, the design of such a system is complicated and hence a pressure generator configuration consisting of a GG chamber with fixed controlling orifices was perused.

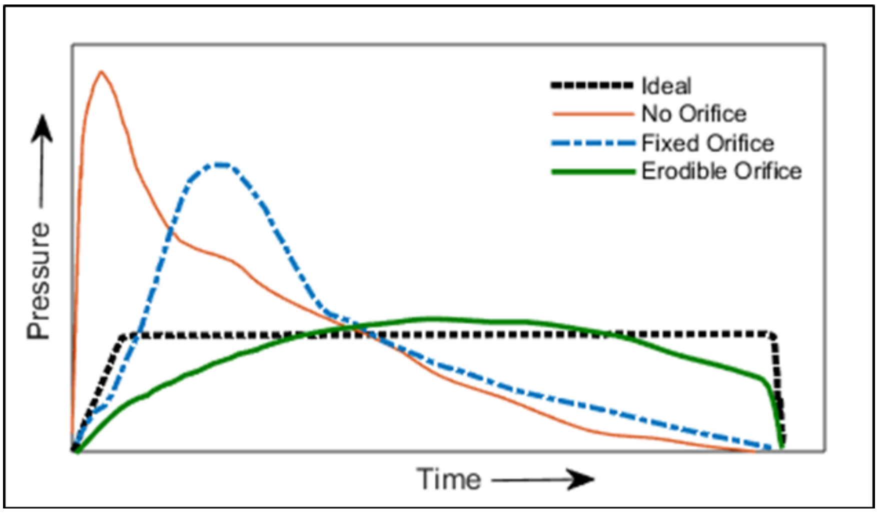

Figure 2. Performance of different type of pressure generators2

B. Ballistic Model

In order to model the performance of the PPG, a control volume based approach can be used wherein the pressure generator internal volume (GG chamber and charge holder free volume) and the tube internal volume are taken as two control volumes with gas flow between them. Assuming uniform properties for the gas inside each control volume, predicting the Pressure-time history during the functioning of the device will enable us to predict its performance. The charge holder and GG chamber internal volumes can be assumed to have same pressure because the charge holder is typically well vented.

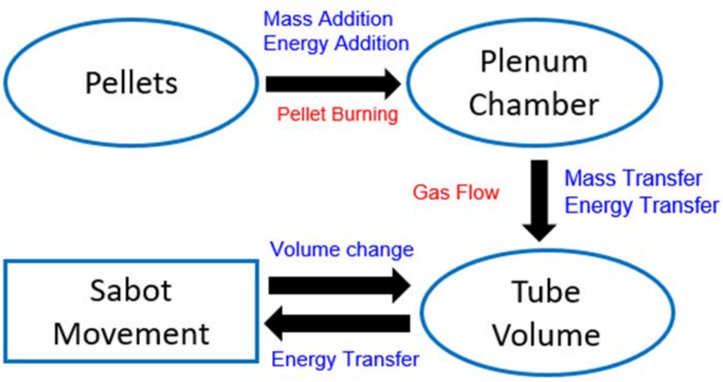

Figure 3. Major processes in a deployment mechanism using a PPG

Consider the equation of state for the gas, the ideal gas equation of state,

$$P\ V = n_g R_u T \ \#(1)$$

This can be re-written as,

$$P\ V = m_g R_g T \ \#(2)$$

where, m_g is the mass of the gas and

R_g is the specific gas constant

Differentiating this w.r.t time,

$$\frac{dP}{dt} = P\left(\frac{1}{m_g}\frac{dm_g}{dt} + \frac{1}{T}\frac{dT}{dt} - \frac{1}{V}\frac{dV}{dt}\right) \#(3)$$

Considering the plenum chamber volume as the control volume, the law of conservation of mass can be expressed as,

$$\left.\frac{dm_g}{dt}\right|_c = \dot{m}_{in,p} - \dot{m}_{out,c} \#(4)$$

where, the subscript p refers to the pyrotechnic and c refers to the plenum chamber respectively. The mass addition into the plenum chamber is due to the burning of the pelleted pyrotechnic charge. Hence, the mass addition can be written as

$$\dot{m}_{in,p} = S_b\ r\ \rho_p \#(5)$$

where, S_b is the burning surface area

ρ_p is the density of the pellets

r is the burn rate

The burn rate of the pyrotechnic pellet can be modelled using Vieille's Law

$$r = a\ P^n \#(6)$$

The mass leaving the plenum chamber is due to the gas flow through the orifices. This can be written as,

$$\dot{m}_{out} = (\rho\ A\ v\ )_t \#(7)$$

where, the subscript t denotes the properties at the throat. As will be mentioned previously the vent holes/orifice are usually choked. Thus,

$$\dot{m}_{out} = \frac{P_c\ A_t}{C^*} \#(8)$$

Similarly, applying the law of mass conservation for the tube volume,

$$\left.\frac{dm_g}{dt}\right|_{tube} = \dot{m}_{in,tube} = \dot{m}_{out,c} \#(9)$$

The conservation of energy equation for the gas in the plenum chamber can be written as,

$$\left.\frac{dE}{dt}\right|_c = \dot{E}_{in,p} - \dot{E}_{out,c} - \dot{Q}_{loss} \#(10)$$

where,

$$\left.\frac{dE}{dt}\right|_c = \frac{d\left(m_{g,c}\ C_v T_c\right)}{dt} \#(11)$$

The energy added to the control volume is due to the burning of the pyrotechnic. Thus

$$\dot{E}_{in,p} = \dot{m}_{in,p}\ C_v\ T_f \#(12)$$

where, T_f is the adiabatic flame temperature of the pyrotechnic.

The energy associated with the gas flow out of the control volume is

$$\dot{E}_{out,c} = \dot{m}_{out,c}\ h_t + \dot{m}_{out,c}\frac{v_t^2}{2} \#(13)$$

where, h_t is the enthalpy of the gas flowing at the throat and v_t is the velocity of the gas at the throat.

From the definition of stagnation enthalpy,

$$h_0 = h_t + \frac{v_t^2}{2} \#(14)$$

where,

$$h_0 = C_p\ T_c \#(15)$$

Hence,

$$\dot{E}_{out,c} = \dot{m}_{out,c}\ C_p T_c \#(16)$$

Thus,

$$\frac{d\left(m_{g,c}\, C_v T_c\right)}{dt} = \dot{m}_{in,p}\, C_v\, T_f - \dot{m}_{out\,,c}\, C_p T_c \#(17)$$

which can be solved to obtain $\frac{dT_c}{dt}$.

In the tube volume, energy is added due to mass flowing into the tube and lost due to work done in moving the projectile. Neglecting heat loss, the conservation of energy equation can be written as

$$\left.\frac{dE}{dt}\right|_{tube} = \dot{E}_{in,tube} - \dot{W} \#(18)$$

where,

$$\left.\frac{dE}{dt}\right|_{tube} = \frac{d\left(m_{g,tube}\, C_v T_{tube}\right)}{dt} \#(19)$$

The work done is the boundary work done due to the pressure force on the projectile. This can be written as

$$\dot{W} = P_{tube}\ A_{tube}\ v \#(20)$$

where, A_{tube} is the projected area of the tube and v is instantaneous velocity of the projectile. Also, recognising that

$$\dot{E}_{in,tube} = \dot{E}_{out\,,c} \#(21)$$

Equation (18) can be re-written as,

$$\frac{d\left(m_{g,tube}\, C_v T_{tube}\right)}{dt} = \dot{m}_{out\,,c}\, C_p T_c - P_{tube}\ A\, v \#(22)$$

which can be solved to obtain $\frac{dT_{tube}}{dt}$.

There is a volume increase in the plenum chamber due to burning of the pyrotechnic pellets i.e.

$$\left.\frac{dV}{dt}\right|_{c} = S_b\, r = \frac{\dot{m}_{out\,,c}}{\rho_p} \#(23)$$

And the volume of the gas inside the tube increases due to the movement of the projectile i.e.

$$\left.\frac{dV}{dt}\right|_{tube} = A_{tube}\ v \#(24)$$

The velocity of the projectile at every instant can be obtained by integrating its acceleration. Assuming that the projectile is rigid and there is negligible friction between the projectile and the tube, the only external force acting on the projectile is the force due to the tube pressure.

$$m_{projectile}\ \ a_{projectile} = F = P_{tube}\, A_{tube}$$

It should be noted that a force, equal and opposite to the force F, acts on the device as a reaction load.

The acceleration of the projectile is,

$$a_{projectile} = \frac{P_{tube}\, A_{tube}}{m_{projectile}} \#(25)$$

$$v(t) = \int_0^t a_{projectile} = \int_0^t \frac{P_{tube}\ A_{tube}}{m_{projectile}} \#(26)$$

Substituting the above in equations in Equation (3) viz.

$$\frac{dP}{dt} = P\left(\frac{1}{m_g}\frac{dm_g}{dt} + \frac{1}{T}\frac{dT}{dt} - \frac{1}{V}\frac{dV}{dt}\right) \#(3)$$

and integrating, we get the pressure as a function of time. This equation however, does not have an analytical solution and hence, numerical integration techniques need to be used to integrate it. Thus, employing this model enables us to predict the pressure-time history in the two chambers (and thus the reaction load) and also to predict the ejection velocity of the projectile. Based on this model, a mathematical program was developed in-house to design and predict the performance of the PPG.

C. Selection of pyrotechnic charge

The acceleration of the projectile to the specified ejection velocity takes place over a very short distance and hence the device has to function within a short time period (15-20 milliseconds). This requirement precludes the use of conventional composite or double base propellant compositions used in rocketry. Hence a nitrogen rich gas generating composition (designated as 'GAN'), having a high impetus and a high burn rate, developed for similar gas generating applications, was selected. This composition produces approximately 95% gaseous combustion products. Further, the products are not fuel rich in nature and hence eliminates the formation of a secondary fireball when the combustion gas comes in contact with atmospheric air. This composition is used in the pelleted form (processed using suitable binders) to control the pressure rise with respect to time.

The electrical initiators are intrinsically safe as they comply with the 1A/1W no-fire ratings. The pyrotechnic booster is Boron-Potassium nitrate (BKNO3) in granular form. It is a standard igniter composition with desirable properties viz. high energy density, high burn temperature, thermally and vacuum stable along with a burn rate nearly independent of pressure and temperature

D. Design of pressure generator

The major parameters affecting the performance of the PPG are

(i) Charge quantity.
(ii) Plenum chamber volume.
(iii) Plenum chamber vent area.

These parameters have to be selected such that the required ejection velocity is achieved and the reaction load is minimized.

In order to design an optimum gas generator, a chart (Figure 4) is created by running the program for various plenum chamber vent areas (x-axis) and plenum chamber volumes (y-axis) and iteratively calculating the charge quantity required to achieve the required ejection velocity. The dotted isolines denote the charge quantity required for and the contours show the Peak Reaction Load generated during the device function.

An optimized design is chosen from this chart considering the structural design of the plenum chamber (due to high plenum chamber pressure) while at the same time minimizing reaction load. The performance of this design is shown in Figure 4. It may be noted that the plenum chamber pressure is much higher (500-700 bar) than the tube pressure (10-20 bar peak pressure) and the orifices remain choked almost throughout the device functioning as is typical of a fixed orifice pressure generator.

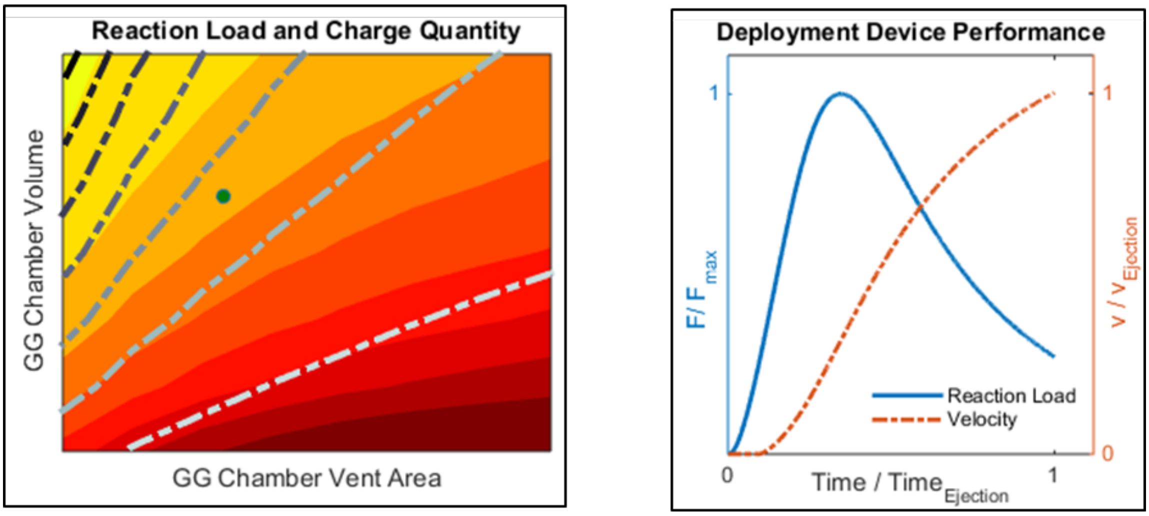

Figure 4. (Left) Chart of design parameters to obtain the required ejection velocity. The coloured contours denote the reaction load (increasing from yellow to red) and the dotted lines denote charge quantity (increasing from white to black). The green dot denotes the selected design point. (Right) Reaction load and velocity versus time for the optimized design.

E. Structural design

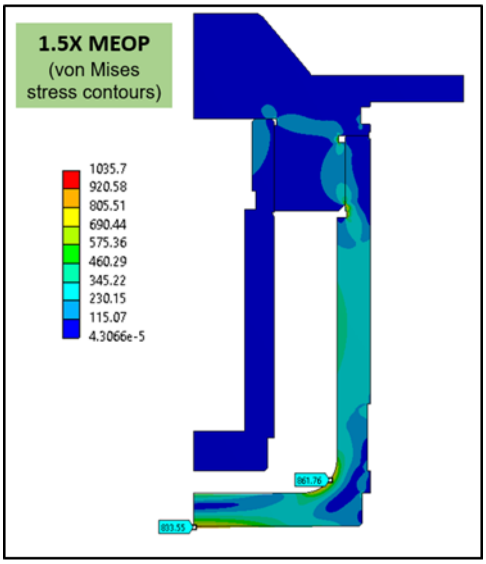

Figure 5. von Mises stress contours from FE analysis of the PPG

Due to the very high pressures in the plenum chamber (500-700 bar) the stresses in the GG chamber are high. Hence, a high strength stainless steel with suitable heat treatment is selected as the material chosen for the chamber. The von Mises stress contours of the gas generator components are shown in Figure 5. It can be seen that the charge holder and head end have very high margins. The stress in the GG chamber is high but localized and can be optimized further. Sufficient margins are available in all cases

4. Test Results

A. Tests in closed vessel

The performance of the pyrotechnic pressure generator is critical to the functioning of the entire device. In order to simplify and expedite the development activities, preliminary evaluation of the PPG was decoupled from the tests of the deployment system. Towards this, the pressure generator was fired in a closed vessel and the pressure-time performance monitored. As stated previously, the pressure generator works in a choked condition throughout the functioning of the mortar. Thus, care should be taken so that the volume chosen is large enough to keep the pressure generator in a choked condition throughout the desired duration. The tests were completed successfully. It can be seen that (Figure 6) the performance matches well with the prediction

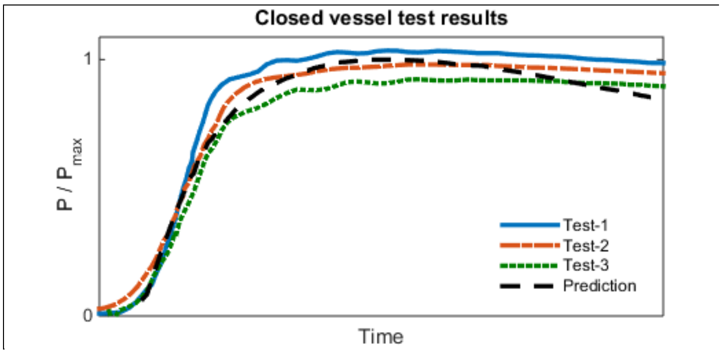

Figure 6. Comparison of closed vessel test results of PPG with prediction.

B. Tests at device level

With the confidence gained from closed vessel test, complete device level tests were carried out to evaluate the performance of the PPG. The velocity, reaction load and pressure were measured in these tests; the pressure in the mortar tube was measured with Kistler piezo-resistive pressure transducer, the reaction load using a Honeywell 50000 lbf load cell and the ejection velocity using high speed videography. The projectile was successfully ejected from the device (Figure 7) with the required velocity. Also, due to the selection of the charge there is no secondary fireball. Additionally, from the reaction load vs time plot, we can see that the test results match very well with the prediction from the ballistic model

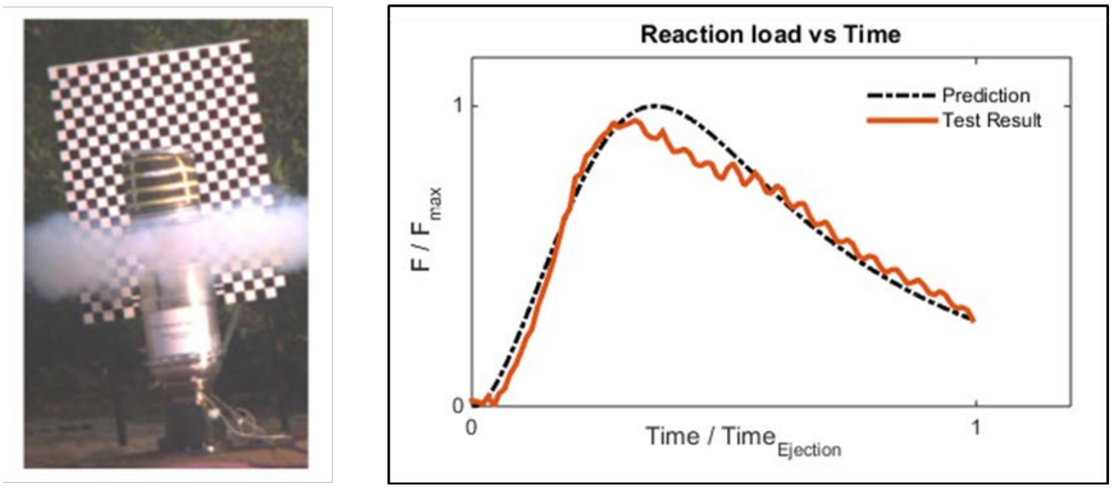

Figure 7. (Left) Successful deployment of projectile in test. (Right) Reaction load vs time for the deployment test.

5. Conclusion

This paper has presented the details of a successful design process which culminated in the functional demonstration of a pyrotechnic pressure generator (PPG) for a deployment mechanism. The methodology for selection of charge composition, structural and ballistic design including the mathematical model developed for the design and performance prediction is explained. The device successfully passed the functional verification tests and all the performance parameters benchmarked were met.

6. Acknowledgements

The authors wish to thank Chairman and members of Design Review Team for their valuable advice and guidance. Support of colleagues of SODG, HTDG, ASMG, STED & RSTD of VSSC for carrying out the investigative tests are also gratefully acknowledged

7. Reference

[1] Pleasants, J. E. Parachute Mortar Design. AIAA Journal Spacecraft and Rockets, Vol. 11, No. 4, 1974.

[2] I. Whalley. Parachute Mortars; An Engineering Review. 44th AIAA /ASME/SAE/ASEE Joint Propulsion Conference, 2008.

[3] Sutton, George P., and Oscar Biblarz. Rocket Propulsion Elements. New York: John Wiley & Sons, 2001.

[4] T. Pawlikowski, “Drogue mortar system simulation development and performance evaluations,” 9th Aerodynamic Decelerator and Balloon Technology Conference, Albuquerque, U.S.A., Oct. 1986.

[5] Vasas.R and J.Styner. Mars Exploration Rover Parachute Mortar Deployer Development. AIAA paper no. 2003-2137, 2003

[6] J. Brecht, J. Pleasants, and R. Mehring. The Viking mortar - Design, development, and flight qualification. 4th Aerodynamic Deceleration Systems Conference, Palm Springs, CA, U.S.A., May 1973.

A Novel Approach to Ballistic Design of Isolation Pyrovalve for Cryogenic Applications

Kamal Saroha
Space Ordnance Analysis and Devices Group
Vikram Sarabhai Space Centre, ISRO
Thiruvananthapuram
kamalsrh@gmail.com

Priyanka Chaudhary
Space Ordnance Analysis and Devices Group
Vikram Sarabhai Space Centre, ISRO
Thiruvananthapuram

Anil Kumar Tiwari
Space Ordnance Analysis and Devices Group
Vikram Sarabhai Space Centre, ISRO
Thiruvananthapuram

Bishwajyoti Dutta Majumdar
Space Ordnance Analysis and Devices Group
Vikram Sarabhai Space Centre, ISRO
Thiruvananthapuram

Sheeju Chandran
Space Ordnance Analysis and Devices Group
Vikram Sarabhai Space Centre, ISRO
Thiruvananthapuram

Kumar H
Space Ordnance Analysis and Devices Group
Vikram Sarabhai Space Centre, ISRO
Thiruvananthapuram

Abstract – **A numerical algorithm is developed to characterize the flow of gaseous products from pyrotechnic charge, through multiple layers of orifices in a typical Pyrovalve. The valve has two perforated walls, named grid and lattice, in the flow path of gas. The effects of these perforations on gas flow are mathematically modelled including various other effects such as sudden choking of the orifices etc. An internal ballistic analysis code is developed and augmented with quasi 1-D isentropic flow assumptions. The augmented algorithm is discussed in detail with all the parameters tuned to capture various characteristics of gas flow. The parameters are calibrated and the algorithm is also validated against experimental data. The paper discusses various design and functional parameters of the Pyrovalve as well. The algorithm is found to have good agreement with experimental results.**

Keywords– Pyro Valve, Cartridge Actuated Device (CAD), Analytical Ballistic Code – CAD (ABC-CAD), Nobel-Abel Equation of State, Burn Rate Law, Nitro Cellulose (NC)

1. Introduction

Pyrovalves are widely used in propellant feedlines of launch vehicles owing to their reliable performance and high power to mass ratio. Some pyrovalves are “normally open” which upon actuation, block the line to stop fluid flow; while some others are “normally closed” pyrovalves that actuate to open the line allowing unrestricted flow of fluid. Such valves that enable initial isolation of working fluid from rest of the flow circuit are called isolation pyrovalves. The basic mechanism of any isolation pyrovalve involves generation of large amount of gas from pyrotechnic charge that push a piston leading to severance of a closure, which in turn, opens the flow. The design of isolation pyrovalves used in cryogenic propellant lines has special features for pyrogas sealing and for ensuring proper shearing of closure under cryogenic conditions. In general, dynamic gas sealing is provided in such valves by welding metallic bellow to the valve component. The pyro-cartridge used in cryo valves use Zirconium based initiatory charge (hereafter referred as IC) and NC as the main charge. The combustion of initiatory charge produces high temperature particles of zirconium oxide (zirconia) which can affect the integrity of the thin metallic bellows, used in the immediate vicinity, for hermetic sealing of the pyro gas. In order to avoid this, the flow of zirconia particles need to be restricted by perforated walls in the flow path. For a typical valve considered in this work, two such walls (namely grid and lattice) are employed. These members have small orifices arranged in a particular configuration so that no solid particles can reach the metallic bellow. The design of this pyro valve aims at estimating the quantity of pyro-charge needed to carry out the intended function of severing the diaphragm. This is achieved by simulating of ballistic performance of the valve using an in-house developed mathematical code named as ABC-CAD (Analytical Ballistic Code for Cartridge Actuated Devices). The model simulates expansion of pyro gas across three volumes separated by the two perforated members – lattice and grid. The mass flow rate of gas through the volumes is computed using isentropic relations and continuity equation. This is followed by estimation of pressure, temperature and density in each volume using Nobel-Abel EOS [1] and energy conservation principle. Equation of motion along with conservation of momentum is used simultaneously to model the expansion of bellow, shearing action of shear screws, movement of knife and severance of closure etc. Generally, the overall pressure time profile is only estimated as it dictates the functional characteristics of pyro devices. However, in this case, multiple pressure chambers are involved and the flow has to take a circuitous path to reach the actuator, the pressure at all station points to be computed for full understanding of the problem. In addition, to know the physical state of combustion products, the temperature distribution also to be studied, as the local temperature decides phase change of certain combustion products, which can have damage potential on the metallic diaphragm. For the detailed characterization of the valve, it was required to map the pressure, temperature and velocity profile of the pyrogases in the valve both in temporal and spatial domain. To capture complex ballistic behaviour and performance prediction of the valve, simulating all the hardware elements, a novel approach has been adopted.

2. Problem Definition:

The configuration of isolation pyro valve discussed in this paper is shown in Figure 1. The valve is of normally closed type, where a thin diaphragm isolates line fluid from rest of the circuit before actuation. This diaphragm is severed by an axially moving knife upon actuation. Prior to actuation, the knife is locked in its place by means of two shear screws. As the pyro-cartridge is fired, the gases push a thin metallic bellow which in turn moves the adjacent knife shearing the shear screws and severing the diaphragm. The bellow seals pyro gas hermetically and prevents contamination of working fluid. Figure 1 shows the flow path of gases produced by pyro cartridge with the two perforated members called grid and lattice. These perforations are provided to protect the thin metallic bellow from impingement of solid hot particles generated upon combustion of initiator charge. The post- actuation configuration of this isolation valve is depicted in Figure 2. In subsequent sections, simulation methodology and approach are provided in detail.

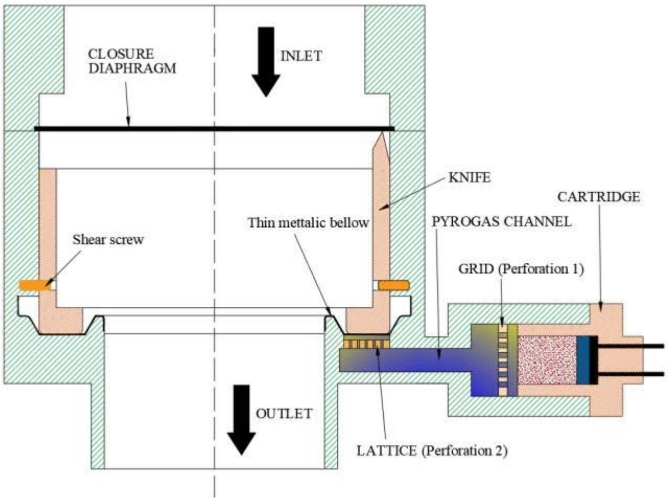

Figure 1: Isolation pyrovalve before actuation

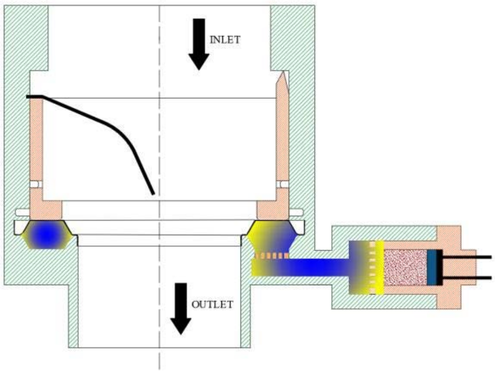

Figure 2: Isolation pyrovalve after actuation

3. Solution Methodology

The end products of combustion of initiatory charge (IC) contain particles of hot zirconia (ZrO_2). Burn time of this charge is estimated experimentally from closed bomb test data. The main charge (Nitrocellulose) consists of several small solid cylindrical grains, loosely packed. The burn rate of these grains is extensively studied using closed bomb tests and the burn rate law parameters are evaluated. In ideal condition, only the hot gases produced by pyro cartridge should flow through the grid and lattice and inflate the thin metallic bellow towards moving the knife for shearing the closure diaphragm. However, as NC grains are loosely packed inside the cartridge and the burn rate of IC is very high compared to NC, there is a possibility of ejection of NC charge through the grid and lattice in the initial phase as well as during its surface regression. The possibility of fragmentation of NC grain due to impact of solid particles of Zirconia also makes the problem more complex. This fragmentation of NC grains can cause sudden increase in their surface area exposed to deflagration, thereby increasing gas generation rate. This, in turn, can easily cause the smaller grains fragments to pass through the grid and lattice along with hot gases. For mathematical modelling of solid particles passing through the orifices of grid and lattice, the effective co-efficient of discharge (Cd) of orifices needs to be varied accordingly and studied. To address all these issues following strategies are adopted–

A. To model the effect of NC charge ejection through orifices of grid and lattice, the charge grains are divided into various proportions across the chambers as shown in Table 1.
B. The fragmentation of NC grains can cause significant increase in gas generation rate Hence, an appropriate augmentation is applied to burn rate by calibrating the analysis results with the experiment. This factor is applied to the proportion of ejected charge mass as shown in Table 1.
C. To include the effect of blockage of orifice due to ejection of NC grains, the Cd in this analysis is reduced to a constant value over certain time intervals as shown in Table 1, by studying the experimental data.

Table 1: Properties of flow across the orifice

Coefficient of Discharge (C_d) for grid and lattice	0.2 (0≤t≤1.4ms) 0.6 (t≥1.4ms)
Gas mass generation augmentation in Chamber 2 and 3	3.9 (0≤t≤2ms) 1.0 (t >2ms)
Proportion of Charge thrown to Chamber 2 and 3	10% to Chamber2 20% to Chamber 3

With the adoption of above strategies, the present problem can be solved as a problem with three chambers connected by orifices as shown in Figure 3. The in-house developed ABC-CAD code is modified as quasi 1D code to model the isentropic flow through orifices. The gas state properties like pressure, temperature, density etc. are assumed to be uniform in each chamber

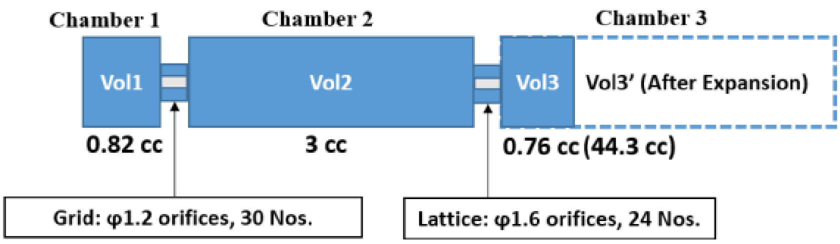

Figure 3: Different chambers across pyro gas channel

ABC-CAD incorporates burn rate model, mass conservation, energy conservation, equation of state for product gases, and momentum conservation. Vielle's burn rate model [2]-[7], as defined by equation (1), is used to simulate the kinetics of combustion process. The burn rate model defines relationship between pressure of product gases and burn rate of explosive as it regresses normal to the exposed surface

$$\frac{dr}{dt} = -a \times (P_g)^n \qquad (1)$$

Where r is the burn depth normal to exposed surface, P_g is pressure of gas inside the chamber, and *a* and *n* are the burn rate constant and burn rate exponent respectively.

The overall ABC-CAD approach is depicted in Figure 4.

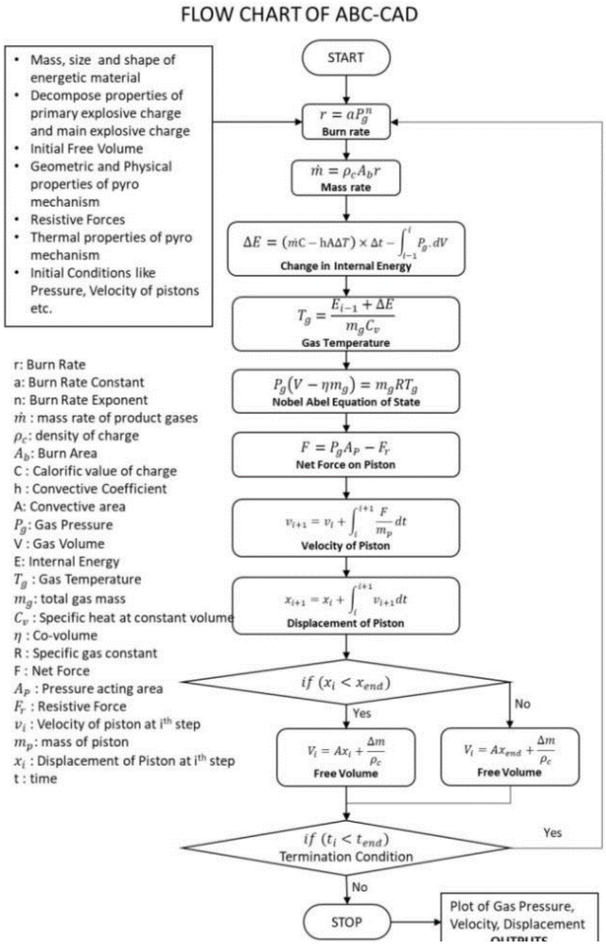

Figure 4: Flow Chart of ABC-CAD algorithm with Programmed Burn Rate Based Approach

The burn rate parameters for explosive charges are estimated from closed bomb tests. Resistance force F_r acting on to the piston is obtained from analytical equations as well as finite element analysis or experiments. The entire algorithm is implemented to solve using forward difference scheme

All the resistive forces are generated due to bellow inversion, shear screw shearing and closure diaphragm shearing are found out using an explicit dynamic solver of ANSYS in which knife is simulated to move after filtering out the effect of inertia which is accounted in the equation of motion in ABC- CAD. Thus, the total resistive force vs the knife displacement from the explicit dynamic analysis is shown in Figure 5

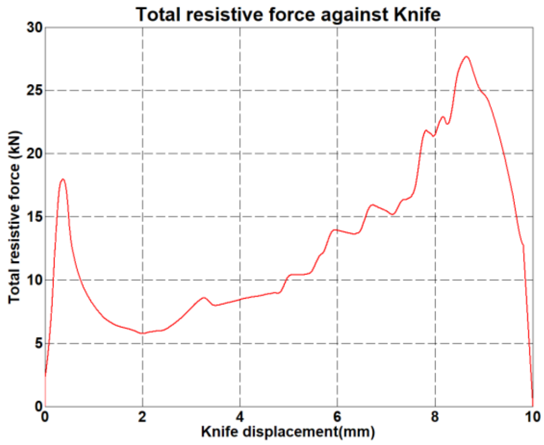

Figure 5: Plot of total resistive force vs knife displacement

As discussed before, the fragments of main charge can flow into chamber 2 and 3. Therefore, the burn rate equation is also applied in these chambers. The proportion of solid charge present in chamber 2 and 3 is tuned by calibrating the estimated bellow pressure from analysis with the experiments.

Moreover, the ejected charge in chambers 2 and 3 can also have high gas generation rate. The estimated value of burn rate augmentation parameter for ejected charge and the mass fraction of ejected charge in chamber 2 and 3 are obtained from the calibration studies is shown in Table 1. The choked and un-choked mass flow rate across all the orifices is calculated using isentropic flow relations as given in Equation (2) and (3). The critical pressure ratio Pr is defined in Equation 5. If pressure ratio falls below this value, the orifices are choked, otherwise they are not.

$$\dot{m}_i = NA\left(\frac{c_1 c_2 P_{upstream}}{T_{upstream}^{0.5}}\right) \quad \text{if } P_r \geq c_3 \tag{2}$$

$$\dot{m}_i = NA\left(\frac{c_4 P_{upstream}}{T_{upstream}^{0.5}}\right) \quad \text{if } P_r < c_3 \tag{3}$$

$$c_3 = \left(\frac{2}{\gamma+1}\right)^{\frac{\gamma}{\gamma-1}} \tag{4}$$

where,

$$P_r = \frac{P_{downstream}}{P_{upstream}};$$

$$c_1 = \sqrt{\frac{2\gamma}{R(\gamma-1)}};$$

$$c_2 = \left(\sqrt{1 - P_r^{\gamma-1}}\right) \times P_r^{\frac{1}{\gamma}} \sqrt{\frac{\gamma}{R}\left(\frac{2}{\gamma+1}\right)^{\frac{\gamma+1}{\gamma-1}}}$$

$$c_4 = \sqrt{\frac{\gamma}{R}\left(\frac{2}{\gamma+1}\right)^{\frac{\gamma+1}{\gamma-1}}}$$

where, γ is the adiabatic exponent, R is equivalent gas constant of the gas mixture, N is the number of orifices and A is cross sectional area of each orifice. The upstream and downstream pressures are chamber pressures on either side of the orifices. The total mass of gas in chamber is calculated using, continuity equation as given in Equation (5)

$$m_i^k = {m_{NCB12}}_i^k + {m_{ZPP}}^k + \Delta t(\dot{m}_{in}^k - \dot{m}_{out}^k) \tag{5}$$

In chamber 1 there will be only outward mass flow through grid. In the chamber 3, there will be only inward mass flow rate through the lattice. Using the energy conservation equation (6), The internal energy of gas in each volume can be estimated by using energy generated by NC and IC, the net flow rate of internal energy across orifices, the work done by system and the heat loss to surroundings. The energy delivered by charge is estimated using calorific value of NC and IC as given in equation (7). Equation (8) is used to estimate the net flow rate of energy using flow rate across the orifices. The work done is described in equation (9) as product of pressure and volume change. It is to be noted that non-zero work is done only in third chamber as the metallic bellow expands and pushes the knife further. The temperature of gas in each volume can be calculated using total mass and energy in the system as given by equation (10). Subsequently, the pressure of gas can be calculated using the Noble Able equation of state in eq. (11), where b is co volume correction

$$E_i^k = E_i^{k-1} + E_{charge}^k + E_{flow}^k - W_i^k - H_{loss}^k \qquad (6)$$

$$E_{charge}^k = Q_{cal}^{NCB12} {m_{NC_i}}^k + Q_{cal}^{ZPP} {m_{IC}}^k \qquad (7)$$

$$E_{flow}^k = C_p \Delta t (T_{in}^k \dot{m}_{in}^k - T_{out}^k \dot{m}_{out}^k) \qquad (8)$$

$$W_i^k = P_i^k dV_i^k \qquad (9)$$

$$T_i^k = \frac{E_i^k}{m_i^k C_v} \qquad (10)$$

$$P_i^k = \frac{m_i^k}{(V_i^k - b)} R T_i^k \qquad (11)$$

4. Results and Discussions

The algorithm is validated with experimentally evaluated bellow pressure inside the valve under room temperature. However, the algorithm holds good for any environmental temperature including cryogenic conditions.

Figure 6 shows pressure history in all the three chambers (magenta, blue and red curves for chamber 3, 2 and 1 respectively) compared with experimentally determined bellow pressure (black solid line). The estimated pressure history inside the bellow closely follows the experimental results except for the deviation in the initial pressure rise observed in estimated bellow pressure profile.

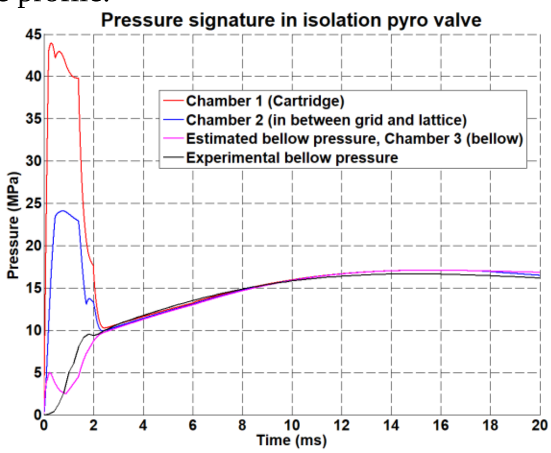

Figure 6: Pressure history plot of all chambers

From the estimated profile of bellow pressure, it can be seen that initially the bellow pressure rises to 4.98 MPa @ 0.23 Ms and then falls to 2.48 MPa @ 0.89 ms. This the initial rise is a result of charge burning in the constant volume until the knife moves. As the knife completes its full stroke of 10 mm, the pressure falls. Hence, the fall of pressure from a peak point must exist in the experimental pressure signature since knife takes some time to complete its full stroke. However, this signature is not captured in experimental results, may be due to the low sampling rat e or higher-pressure sensor response time. After the fall in pressure at 0.89 ms, the pressure starts rising again as the gases from chamber1 and 2 enter chamber 3 with a fully expanded bellow. The maximum bellow pressure reached is 17 MPa @ 16.16 ms, closely matching with the experimental peak bellow pressure of 16.6 MPa @ 16 ms.

This peak pressure denotes the point where charges are completely burned and gas pressure is at equilibrium. After this point, the drop-in bellow pressure is due to heat loss that takes away the energy of pyrogas. The blue curve that denotes pressure in chamber 2, has peak pressure of 24.08 MPa @ 0.81ms. The pressure remains close to peak value until it starts falling rapidly after 1.4 ms. This is due to abrupt change in coefficient of discharge (Cd) of orifices in grid and lattice. As discussed earlier, this change is applied to capture the effects of varying blockage factor in the orifices. The same rapid fall can be seen in cartridge pressure (red curve) in chamber 1, where the pressure reaches a peak of 44 MPa @ 0.3 ms. In the pressure plot, there is a kink near the region of peak pressure point. This kink is due to the movement of piston with sudden expansion of bellow volume. All the pressure curves roughly merge at 2.48 ms, at which the whole system is roughly under equilibrium pressure. After this point, the flow rate across the orifices is negligible

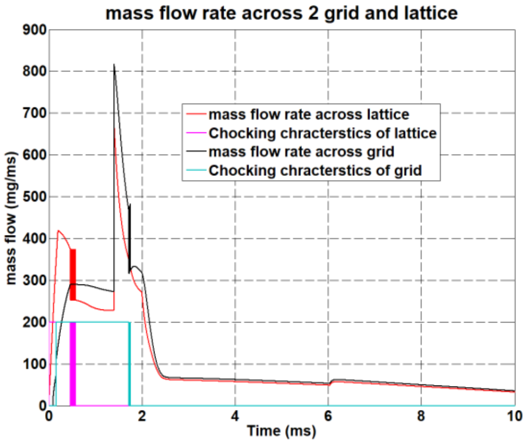

Figure 7: Orifice mass flow history plot of all chambers

Figure 7 shows the mass flow rate history across the lattice and grid. From the plot, it can be observed that the peak mass flow rate across grid reaches 417 mg/ms @ 0.23 ms while across lattice, it reaches 818 mg/ms @ 1.4 ms. The step signature curves (cyan and magenta), from 0 to 200, denote choking of the orifices. Here, the peak step 200 is to denote the choked orifices i.e. the pressure ratio is below the critical value. The step 0 in the unchecked orifices means pressure is above critical value. From the figure it can be seen the grid remains choked for larger time than the lattice. This is due to higher pressure ratio in upstream region of grid as compared to lattice. There is also a transition region from choking to un-choking in the plot. However, the transition region lasts for a small time and should not affect the overall ballistic analysis.

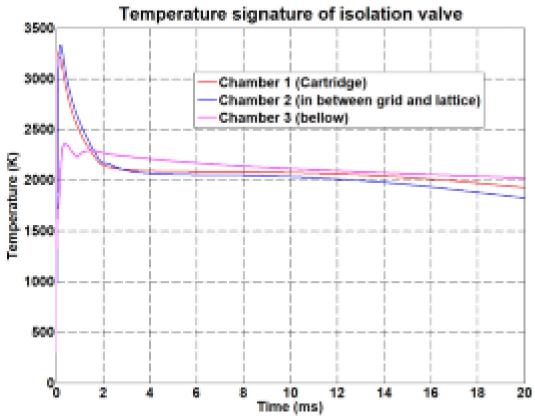

Figure 8: Temperature history plot of all chambers

Figure 8 shows the gas temperature signature in chamber 1, 2 and 3. Similar to pressure plot, the temperature of pyro gas is roughly under equilibrium after 2.48 ms. It can be seen from the plot that the gas temperature in cartridge (chamber 1) reaches maximum of 3235 K. The bellow (chamber 3) gas temperature reaches to maximum of 2354 K and then falls suddenly due to the expansion of bellow. The gas temperature in this chamber consistently falls after 1.5 ms. It can also be seen from the figure, that gas temperature falls consistently in all chambers after equilibrium due to heat loss. However, gas temperature in bellow volume falls at a higher rate. since it is exposed to larger surface area causing more heat loss than in other chambers.

5. Summary

In this study, a quasi1-D ballistic code is developed to predict the flow of pyrogas inside an isolation pyrovalve. This valve contains two layers of flow restrictors. The work discusses different characteristics of charge and orifices that can affect the performance of valve. These effects such as ejection of charge into subsequent chambers and associated blockage of the orifices in grid and lattice, fragmentation of charge grains due to interaction with solid combustion products of IC etc., are modelled in the analysis. The complete algorithm is described with different parameters, which are validated with experimental data. The pressure, temperature and mass flow rates in various chambers on the pyrovalve, as estimated from the mathematical model are plotted and pressure history is compared with experimental data. Following are the major inferences from these plots:

A. The pressure history inside bellow closely matches with the experimental result except the initial rise observed in the estimated value. It is inferred that the bellow pressure recorded in experiment might be missing the initial rise due to higher response time and lower sampling rate of pressure sensor data.
B. In the mass flow rate plot, it can be seen that the grid orifices are choked for longer time than lattice.
C. The temperature history profile shows that the bellow gas temperature falls quickly than in the other chambers due to its larger exposed surface area to heat loss. Inferring from all the estimated history plots, the algorithm seems to be in good agreement with experimental data. The initial slope mismatch in bellow pressure data needs to be explored further through additional experiments with improved instrumentation scheme. The temperature profile shows that during the functioning time of the device, the pyro gas temperature never falls below 2000K

6. Reference

[1] Ian A Johnston, "The Nobel Abel Equation of State: Thermodynamic Derivations for Ballistic Modelling" Defence Science and Technology Organization, Nov., 2005

[2] Dae-Hyun Hwang, Doo-Hee Han, Hong- Gye Sung and Byung-Tae Ryu," Separation Behaviour of Pyrotechnically Actuated Device Considering Small- Volume Effect of Combustion Chamber", Journal of Spacecraft and Rocket, Volume 57, Number 4, Apr.,2020

[3] Seung-gyo Jang, Hyo-nam Lee and Jong- yun Oh, "Performance Modeling of a Pyrotechnically Actuated Pin Puller" Int'l J. of Aeronautical & Space Sci.15(1), 102-111 (2014)

[4] Dae-Hyun Hwang, Juho Lee, Jae-Hung Han, YeungJo Lee and Dongjin Kim, "Mathematical Model for the Separation Behaviour of Low Shock Separation System", Journal of Spacecraft and Rocket, Vol. 55, No. 5, Sept-Oct., 2018, pp. 1208-1221

[5] Dae-Hyun Hwang, Jae-Hung Han, Juho Lee, YeungJo Lee and Dongjin Kim, "A mathematical model for the separation behaviour of a split type low-shock separation bolt", Act a Astronautica 164 (2019) 393-406

[6] Powers, J. M. and Gonthier, K. A., "Sensitivity Analysis for a Pyrotechnically Actuated Pin Puller Model", 19th International Pyrotechnics Seminar, New Zealand, Feb. 1994.

[7] K. A. Gonthier, and J. M. Powers, "Formulation, Prediction, and Sensitivity Analysis of a Pyrotechnically Actuated Pin Puller Model", Journal of Propulsion and Power, Vol. 10, No. 4, 1994, pp. 501-507.

Role of High Strain Rate Material Properties in Design and Analysis of Pyro Mechanisms

Bishwajyoti Dutta Majumdar
Vikram Sarabhai Space Centre
ISRO
Thiruvananthapuram
bdmmech@hotmail.com

Vikas
Vikram Sarabhai Space Centre
ISRO
Thiruvananthapuram
v.sheokand440@gmail.com

Aditya Narayan Malla
Vikram Sarabhai Space Centre
ISRO
Thiruvananthapuram

Nitish Dhawan
Vikram Sarabhai Space Centre
ISRO
Thiruvananthapuram

Sheeju Chandran
Vikram Sarabhai Space Centre
ISRO
Thiruvananthapuram

Kumar H
Vikram Sarabhai Space Centre
ISRO
Thiruvananthapuram

***Abstract*— Pyro mechanisms design involves quantification of energy requirements for achieving various mechanical functions such as thrusting, shearing, cutting, jamming, etc. to accomplish many critical operations in launch vehicles and satellites. As these functions take place within a very short period of time, materials used in pyro mechanisms undergo high strain rate deformation. Among various material models to capture this, Johnson-Cook (JC) material model is the most commonly used due to its simplicity. The conventional approach for pyro system design involves finding out energy requirement considering static properties of the material, followed by extensive testing to fine-tune the design. Having an accurate material model for the actual strain rate experienced by the material greatly improves the accuracy of energy estimate and thereby shortens the development cycle time. The procedure used for the extraction of JC Parameters for the materials used in pyro systems is explained in this paper. In addition, a few case studies with the conventional material model as well as with JC Model are explained in detail. From these results, it is evident that for accurate prediction of the performance of the pyro mechanism, and quantification of stroke requirement and total energy towards the design of pyro mechanisms, a numerical model incorporating high strain rate material properties is highly desirable.**

Keywords*— *High Strain Rate, SHPB, Johnson-Cook Model, Explicit Dynamic Analysis, Pyro Bolt, AISI 304, 17-4-PH (H1025), Resistance Force

1. Introduction

All pyro mechanisms are essentially explosive actuated systems having very high power to weight ratio and action time ranging from few microseconds to milliseconds. Hence, they invariably work at a very high rate of pressurization due to the explosively release of energy from the explosive charge employed. In addition, due to various end functions of pyro devices such as cutting of bolts, shearing of pins and metallic membranes, locking, taper sealing, etc., they encounter a very high rate of deformation. All these phenomena lead to high strain rate deformation response of materials, which largely governs the design of these mechanisms. Unlike in conventional structural designs, where the designer can conservatively choose the minimum guaranteed properties of the material for a design safe under service conditions; the main challenge for the pyro mechanism designer is to handle the contradictory requirements of ensuring pre and post functional structural integrity of the mechanism under quasi-static loading as well as adequate severance margin based on the maximum material properties at high strain rate. The strain rate hardening of materials and thermal softening effects is an essential factor to be coupled with quasi-static elasto-plastic strain hardening of materials. The above non-linear behavior of material response under high strain rate is a very critical aspect of pyro mechanisms design which can only be handled with numerical codes. The high strain rate material constitutive and failure model are generally evaluated through experimental techniques using equipments such as Split Hopkinson Pressure Bar (SHPB) and treated in a phenomenological manner through various material models in numerical codes. Thus, numerical simulation is a vital element in the pyro mechanism design and development with the relevant material models as input.

2. Johnson-Cook Constitutive Relations for High Strain Rate Loading

Several phenomenological constitutive relationships are developed to model the high strain rate deformation response in ductile material during high strain rate loading. These include Johnson-Cook Model, Zerilli-Armstrong Model, Cowper-Symonds Model, etc. Johnson-Cook Model [1],[2]captures the change in mechanical properties at high strain rate loading with three independent terms; viz, strain hardening, strain rate hardening, and thermal softening as given in equation (2.1).

$$\sigma = [A + B\varepsilon^n][1 + C\ln(\dot{\varepsilon}^*)][1 - (T^*)^m] \qquad (2.1)$$

Where σ is the flow stress, A is yield stress at reference strain conditions, B is strain hardening coefficient, n is strain hardening exponent, ε is effective plastic strain, C is strain rate hardening coefficient, $\dot{\varepsilon}^*$ is dimensionless plastic strain rate (defined as the ratio of plastic strain rate and reference plastic strain rate), T^* is dimensionless homologous temperature defined as $(T - T_{ref})/(T_{melt} - T_{ref})$ and m is the thermal softening exponent.T_{melt} and T_{ref} are the melting point and reference temperature of the material. Johnson-Cook model is commonly used as constitutive relation for ductile materials to model their behavior at high strain rate loading due to its simplicity. The J-C model parameters can be evaluated with the limited number of experiments and the same is explained in the section 3.

3. High Strain-Rate Tests with SHPB

Split Hopkinson Pressure Bar (SHPB) is the most widely used instrument for testing materials under a high strain rate by creating uniaxial stress condition. The typical construction of the SHPB test setup and typical strain history signals recorded is shown in Figure 3.1.The elementary wave equation, which is given in equation 3.1, is used to derive the relation between stress and strain using the strain data of incident bar and transmitted bar [5]-[7]. The recording of the strain data is carried out through high-speed data acquisition system.

$$\frac{\partial^2 u}{\partial x^2} = \frac{1}{c_b^2}\frac{\partial^2 u}{\partial t^2} \qquad (3.2)$$

Where u can be written as for the incident bar:

$$u = f(x - c_b t) + g(x + c_b t) = u_i + u_r$$

where f and g are functions describing the incident and reflected wave shapes and cb is the longitudinal wave speed in the pressure bars. Using equation (3.1), the relation between stress and strain of the specimen is derived. Stress, strain rate, and strain of specimen are computed using equations(3.2), (3.3), and (3.4)respectively.

$$\sigma = \frac{AE\varepsilon_t}{A_s} \qquad (3.3)$$

$$\dot{\varepsilon} = \frac{2c_b}{l_s}(\varepsilon_r) \qquad (3.4)$$

$$\varepsilon = \int \dot{\varepsilon}dt \qquad (3.5)$$

In equations (3.2)-(3.4), σ is axial (tensile/compressive) stress in the specimen, ε is strain in the specimen, $\dot{\varepsilon}$is strain rate of the specimen, Ais cross section of the pressure bar (both incident and transmitted bar have same cross-section area), E is Young's modulus of the pressure bar, ε_t is transmitted bar strain recorded by stain gauge on the transmitted bar, ε_r is strain in incident bar due to reflected wave, l_s is length of the specimen, and A_s is the cross-section area of the specimen.

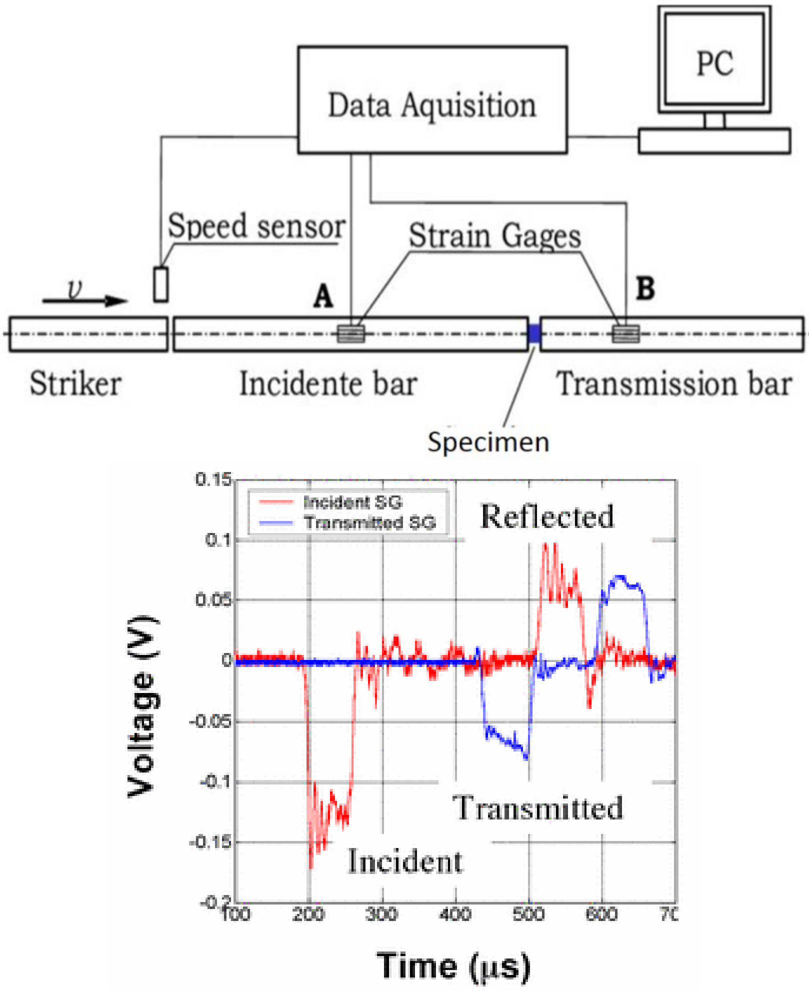

Figure 3.1: SHPB Test Setup with Typical Strain Gauge Signals

4. Evaluation of Johnson-Cook Model Parameters

At reference strain rate and reference temperature, the Johnson-Cook equation can be reduced to equation (4.1).

$$\sigma = [A + B\varepsilon^n] \qquad (4.6)$$

Where, A is the yield strength at reference plastic strain condition. It can also be written as equation (4.2).

$$\ln(\sigma - A) = \ln B + n\ln(\varepsilon) \qquad (4.7)$$

If the equation (4.2) is plotted with $\ln(\sigma - A)$as ordinate and $\ln(\varepsilon)$ as abscissa then it becomes straight with lnB as y-intercept and n as the slope of the line. Hence, the values of B and n can be determined.

To compute material constant, C, several tests need to be conducted under various strain rates at reference temperature conditions. In this condition, equation (2.1) can be reduced to equation (4.3).

$$\sigma = [A + B\varepsilon^n][1 + C\ln(\dot{\varepsilon}^*)] \qquad (4.8)$$

Equation (4.3) can be rearranged in the following manner as given in equation (4.4).

$$\frac{\sigma}{(A + B\varepsilon^n)} = 1 + C\ln(\dot{\varepsilon}^*) \qquad (4.9)$$

If equation (4.4) is plotted with $\frac{\sigma}{(A+B\varepsilon^n)}$ as ordinate and $\ln(\dot{\varepsilon}^*)$ as abscissa, then equation (4.4) represents a straight line with 1 and C as the y-intercept and slope of the line respectively. To compute C, plastic strain shall be taken as small as possible to avoid the thermal softening effect during the test. In a very similar way thermal softening exponent m also can be obtained from a series of tests at reference strain rate at various temperatures [8].

5. Case Studies

Since pyro mechanisms works under high strain rate loading, their design based on quasi-static properties lead to under-estimation of ballistic parameters like explosive charge quantity, reaction loads, pyro pressure etc. To accurately compute the above mentioned ballistic parameters as well as structural margin, the resistance of the pyro mechanism as a function of strain rate must be accounted in the design. One way to ensure the same is coupled ballistic-structural analysis with a high strain rate constitutive relation. As part of case study, severance of a notched pyrobolt is considered. Most widely used materials 17-4-PH (H1025) and AISI 304 are selected as part of the study. The 17-4-PH (H1025) material represents the category of ductile materials which are having ultimate strength close to yield strength and AISI 304 represents the material category where ultimate strength is much higher than yield strength. The high strain rate behavior of these materials is modeled with Johnson-Cook Strength Model. The schematic of the pyro bolt is shown in Figure 5.1. The function of the pyro bolt commences with the initiation of explosive followed by pressurization of housing and movement of the piston. When pressure force on piston exceeds the bolt housing maximum resistance, it severs the bolt housing at a specified notched location. The J-C Model parameters and plastic strain at fracture of 17-4-PH (H1025) and AISI 304 used for the simulation are depicted in Table 5.1.

Table 5.1: J-C Model Parameters and Equivalent Plastic Failure Strain

Sl. No.	Material	A, (MPa)	B, (MPa)	n	C	m	ε_{fpl}
1	17-4 PH (H1025)	1050	258	0.27	0.02	1	1.12
2	AISI 304 [8]	310	1000	0.65	0.07	1	1.6

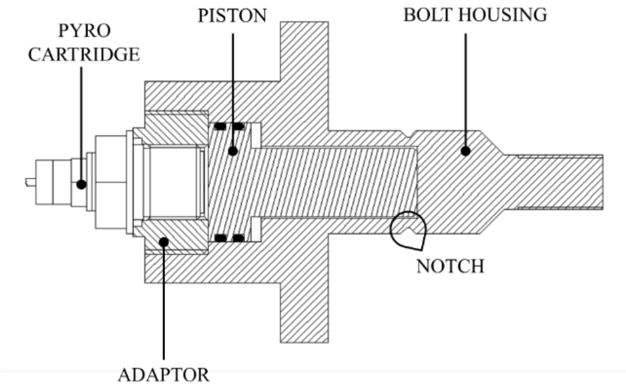

Figure 5.2: Schematic of Pyro Bolt

A. Pyro Bolt with 17-4-PH Material

The speed of the piston in a typical pyro bolt is estimated to be between 0.5 m/s to 10 m/s. Therefore, to study the effect of strain rate hardening of 17-4-PH (H1025)on the pyro bolt design, 5 cases as given in Table 5.2 are analyzed using the Explicit Dynamic Analysis Module of ANSYS commercial software.

Table 5.2: Details of Case Studies for 17-4-PH (H1025) and AISI 304

Analysis ID	Piston Velocity (Vp)
1	Quasi Static
2	0.5 m/s
3	1 m/s
4	5 m/s
5	10 m/s

The first case is performed to compute the bolt housing resistance in quasi-static condition and the remaining cases are for high strain rate condition governed by piston velocity as given in Table 5.2.

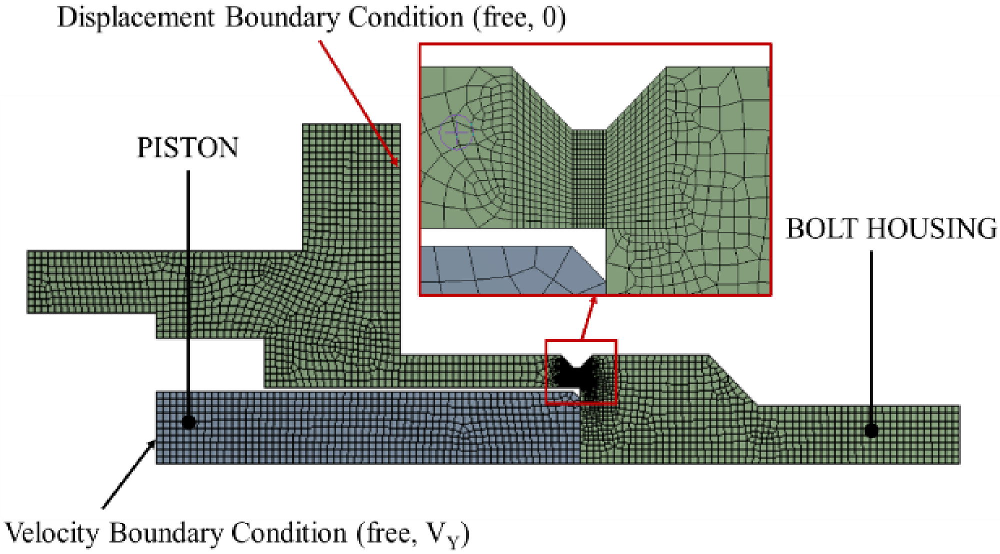

Figure 5.3: Discretized Model of Bolt Housing and Piston for the Analysis

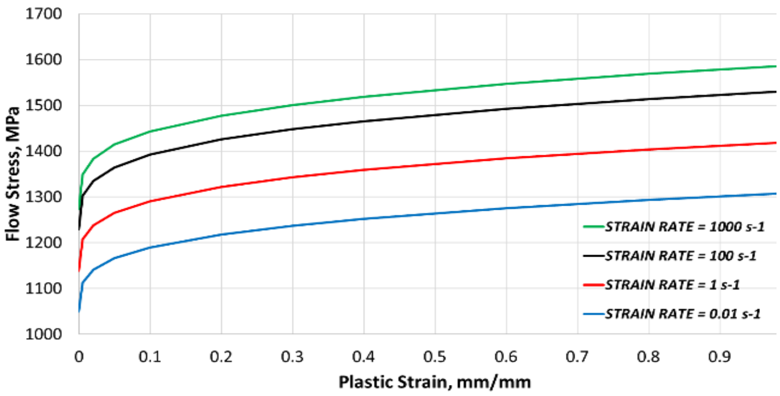

Figure 5.4: Flow Stress-Plastic Strain Curve for 17-4-PH at 0.01 s-1 (Quasi Static Condition), 1s-1, 100 s^{-1} and 1000 s^{-1}

The FE Mesh for the pyro bolt and its boundary condition is shown in Figure 5.2. Flow stress vs plastic strain curve computed using JC Model are given in Figure 5.3. The maximum plastic strain rate and maximum temperature computed in the analyses are summarized in Table 5.3. There is a significant change in maximum strain rate just before fracture (2503 s^{-1} to 39993 s^{-1}) from case 2 to case 5. Whereas, the maximum temperature just before fracture does not change much. Therefore, the change in resistance force of bolt housing may be attributed to strain rate hardening only.

Table 5.3: Strain Rate and Temperature Results of the Analyses of Pyro Bolt with 17-4-PH (H1025) as Bolt Housing Material

Analysis ID	Maximum Strain Rate Just Before Fracture (s^{-1})	Maximum Temperature Just Before Fracture (^0C)
2	2503	378.75
3	5129	386.31
4	26025	389.31
5	39993	394.72

The distribution of strain rate and temperature just before fracture of bolt housing for highest strain rate case (i.e. case 5) is depicted in Figure 5.4 and Figure 5.5 respectively.

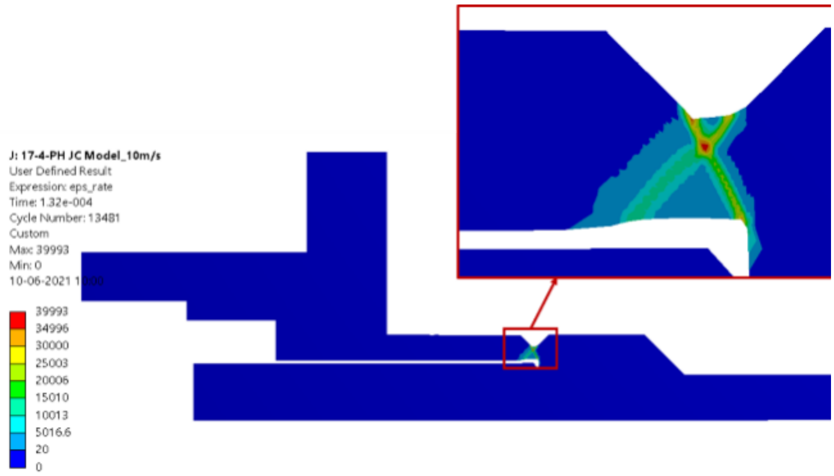

Figure 5.5: Contour Plot of Strain Rate Just Before Fracture for Case 5(Piston velocity = 10 m/s)

For this case, variation of strain rate is localized to notch region which implies the locally strengthening of notch region of bolt housing due to strain rate hardening. Similarly, temperature distribution is also localized near the notch region due to localization of plastic strain in this region as shown in Figure 5.5. This indicates strain hardening as well as the thermal softening of the notch region.

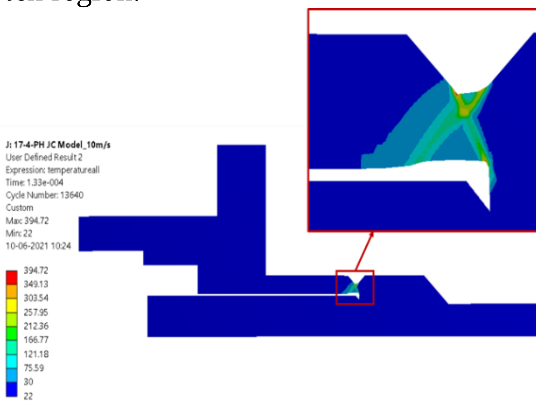

Figure 5.6: Contour Plot of Temperature Just Before Fracture for Case 5 (Piston Velocity = 10 m/s)

i. *__Effect of Strain Rate Hardening__*

To compute the increase in resistance of the bolt housing due to strain rate variation, reaction load results are over plotted in Figure 5.6.

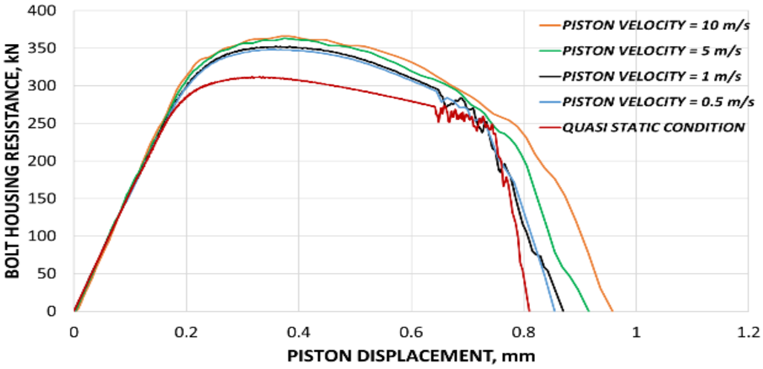

Figure 5.7: Resistance Force of Bolt Housing Under Quasi-Static and High Strain Rate Conditions

It is depicted in Figure 5.6 that the maximum resistance of bolt housing in case 1 and in case 5 are 311.69 kN and 366 kN respectively. There is a 17.4% increase in peak resistance of bolt housing at the strain rate corresponding to piston velocity of 10 m/s as compared to quasi-static condition. The peak resistance for all other cases is lying in between. Similarly, piston stroke at fracture of the notch is 0.81 mm and 0.958 mm respectively. As mentioned earlier, the strain rate is localized to the notch region. Therefore, the increase of piston displacement at fracture is due to the strengthening of the notch in high strain rate condition which increases the elongation of the thick wall of the bolt housing. The same phenomenon is illustrated in Figure 5.7 where the deformation of point 1 is plotted against piston displacement. Furthermore, in this case, deformation of point 1 starts decreasing after reaching peak value which is due to the elastic spring back of bolt housing after notch severance. This can be substantiated with Figure5.8 where equivalent plastic strain is plotted along the thick wall of bolt housing. There is insignificant equivalent plastic strain up to 15mm of length from point 1 of line path defined in Figure 5.8 and then equivalent plastic strain exponentially increases to 0.86% and 1.38% for case 1 and case 5 respectively. It can be inferred that bolt housing except the notch region remains in the elastic zone of material in all cases. An increase of equivalent plastic strain near to notch region can lead to an increase in the total piston stroke at fracture at high strain rate condition.

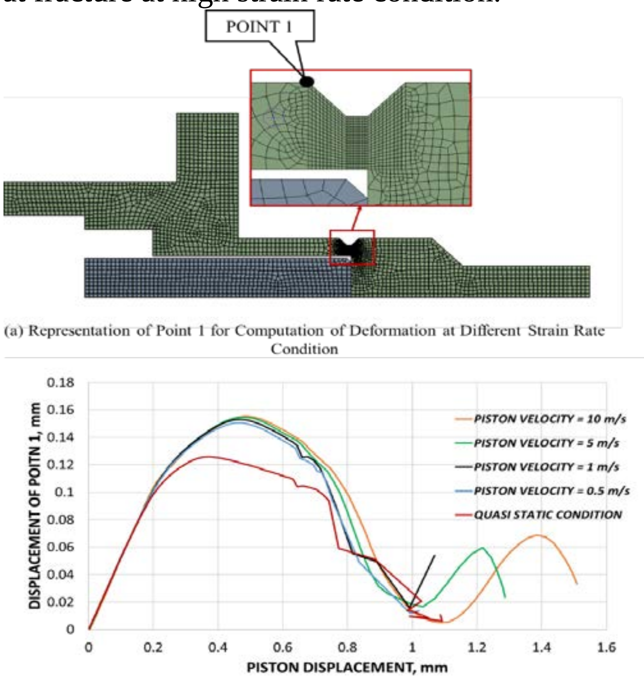

Figure 5.8 : Deformation of Point 1 With Respect to Piston Displacement at quasi static condition, 0.5 m/s, 1 m/s, 5 m/s and 10 m/s

The energy required to break the notch is also an important parameter for the ballistic design of the pyro mechanism which is the area under the curve of the resistance-displacement curve. The energy required for the severance of bolt housing is 197 J and 248 J in case 1 and case 5respectively. There is a 25.8% increase in energy required to severe the bolt housing at strain rate condition corresponding to piston velocity of 10m/s as compared to quasi-static condition. It is inferred from the results of these analyses that maximum resistance, as well as energy required to break the notch, is substantially higher in high strain rate conditions.

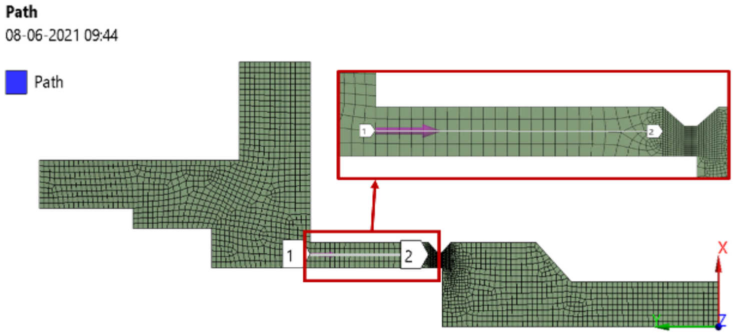

(a) Construction of Line Path on Bolt Housing

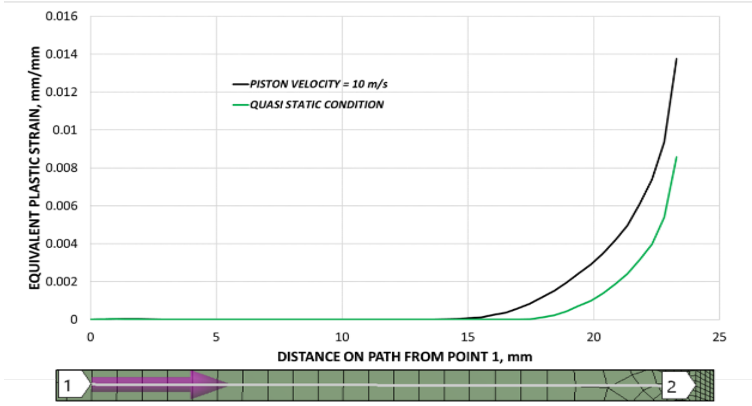

(b) Distribution of Strain Rate On the Line Path

Figure 5.9: Variation of Equivalent Plastic Strain Along the Thick Wall of Bore of Bolt Housing

ii. Effect of Thermal Softening

To distinguish the effect of thermal softening behavior of the material, an analysis without considering specific heat capacity at constant pressure is carried out and the resistance plot of the analysis is plotted with the result of case 5 as illustrated in Figure 5.9.

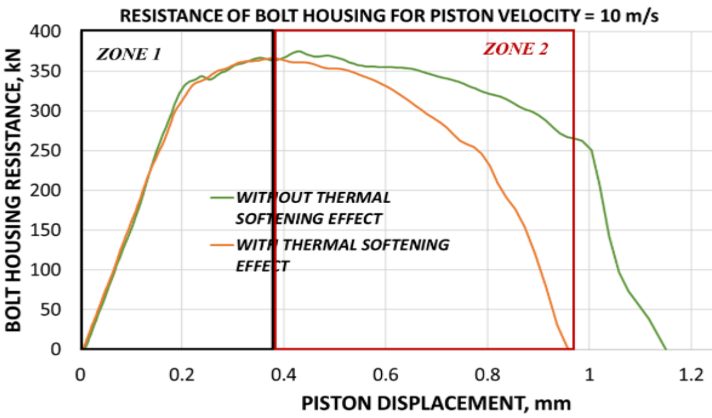

ZONE 1: STRAIN RATE HARDENING DOMINATING ZONE

ZONE 2: THERMAL SOFTENING DOMINATING ZONE

Figure 5.10 : Resistance of Bolt Housing With and Without Thermal Softening Effect

There are 2 zones in Figure 5.9. Zone 1 is dominated by strain rate hardening as both the analysis results coincide which implicates the thermal softening effect is insignificant in the zone 1. Whereas, zone 2 is dominated by thermal softening where the resistance as well as piston stroke at fracture is considerably less than that of the case without thermal softening consideration. This can be attributed due to local temperature rise which leads to softening of elements at a particular location. This contributes towards the weakening of structure locally which fails with less piston stroke as compared to analysis without thermal softening.

B. Pyro Bolt with AISI 304 Material

To study the effect of strain rate hardening and thermal softening of AISI 304 on the performance of the pyro mechanism, same numerical model, mentioned in section 5.1,is used except bolt housing is assigned with AISI 304 material properties with Johnson-Cook Strength Model. Similar to section5.1, material constant, C, of JC Model is kept as 0and specific heat at constant pressure is not included in material model towards computation of resistance of bolt housing in quasi static condition. Similar to secion5.1, 5 cases are studied to quantify the effect of strain rate hardening on resistance offered by the bolt housing. The details of these case studies are given in Table 5.2. Maximum strain rate and maximum temperature developed just before the fracture of housing in the cases are given in Table 5.4.Maximum strain rate just before fracture of bolt housing varies from 366.9 s-1 to 7731.6 s-1 from case 2 to case 5. The contour plot of strain rate for case 5 is depicted in Figure 5.10.

Table 5.4: Strain Rate and Temperature Results of the Analyses of Pyro Bolt With AISI 304 as Bolt Housing Material

Analysis ID	Maximum strain rate (s^{-1})	Maximum temperature (℃)
2	366.9	520.42
3	776.22	538.59
4	4275.3	575.59
5	7731.6	584.62

Strain rate more than 20 s-1 is present through the thick section of bore of bolt housing. In contrast to this, bolt housing made of 17-4-PH (H1025) material, the strain rate more than 20 s-1 is only limited to notch region as shown in figure Figure 5.4.Similarly, temperature rise more than 30^0C is present throughout the bore of bolt housing whereas, in case of 17-4-PH (H1025) it is only limited to notch region.

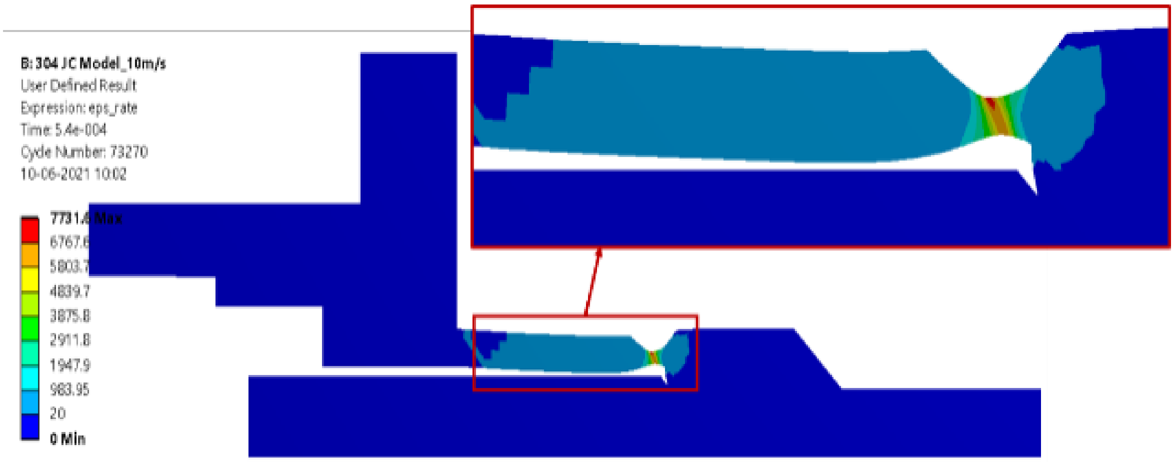

Figure 5.11: Contour Plot of Strain Rate for Case 5(Piston Velocity = 10 m/s)

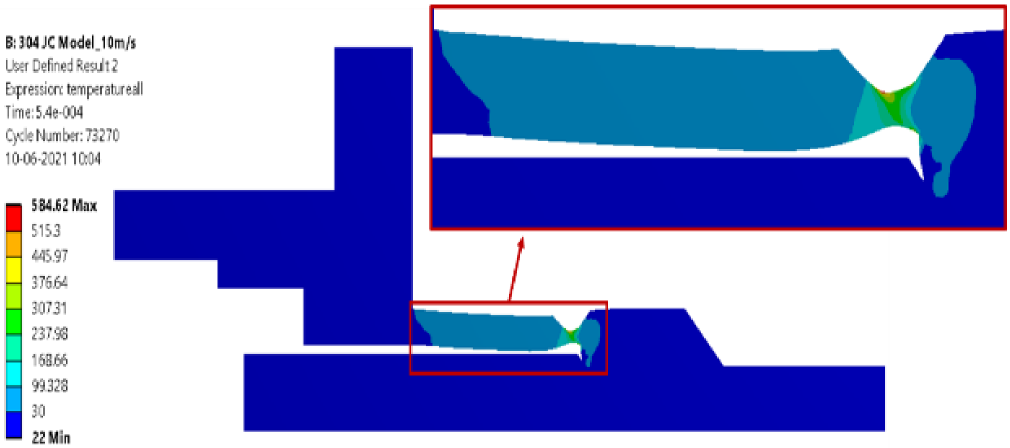

Figure 5.12: Contour Plot of Temperature for Case 5(Piston Velocity = 10 m/s)

i. Effect of Strain Hardening

Resistance of the bolt housing is computed at different strain rate conditions as shown in Figure 5.12. Maximum resistance in case 1 and case 5 are 108.6 kN and 229.31 kN respectively. There is a significant (111.15%) increase in resistance of bolt housing for case 5 with respect to case 1. The increase in resistance is attributed due to strain rate hardening of material. Piston stroke at fracture of bolt housing in case 1 and case 5 are 4.11 mm and 5.14 mm respectively. There is a 25% increase in piston stroke at fracture for case 5 as compared to case 1. Strengthening of notch due to strain rate hardening along with through section yielding of bolt housing bore thicker region contributes towards increase in pistion stroke at fracture.

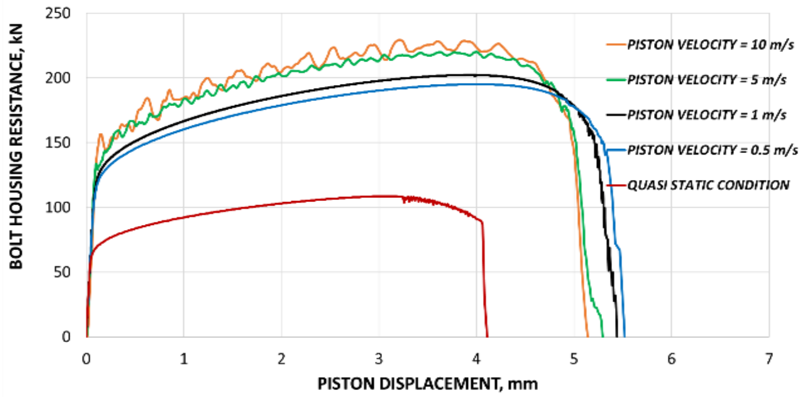

Figure 5.13: Resistance Force of Bolt Housing at Quasi Static Condition and Strain Conditions Corresponding to Piston Velocity of 0.5 m/s, 1 m/s, 5 m/s and 10 m/s

To illustrate the deformation of bolt housing, equivalent plastic strain onto the bolt housing is analysed with contour plot and distribution of equivalent plastis strain along the path defined in Figure 5.13. It is clear from the figure that there is yielding of thick wall of bore of housing in both case 1 and case 5.

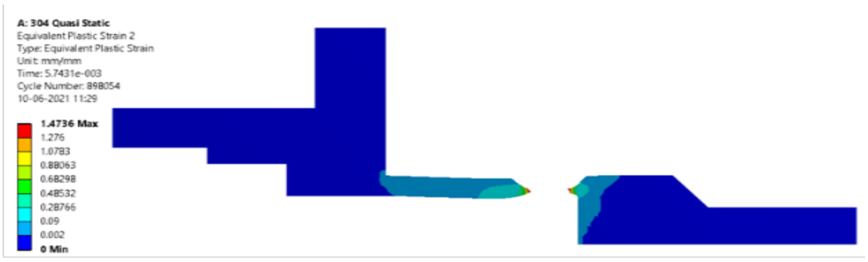

(a) Contour Plot of Equivalent Plastic Strain for Case 1

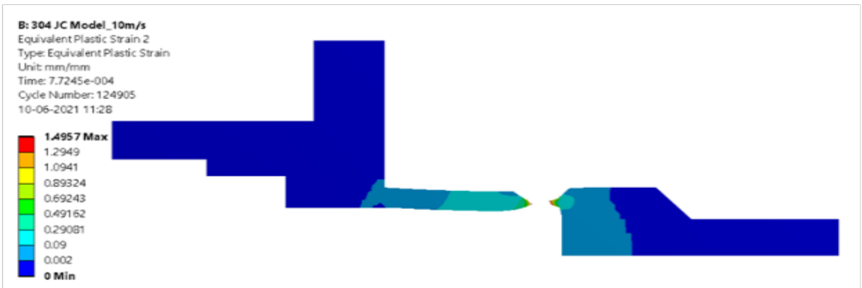

(b) Contour Plot of Equivalent Plastic Strain for Case 5

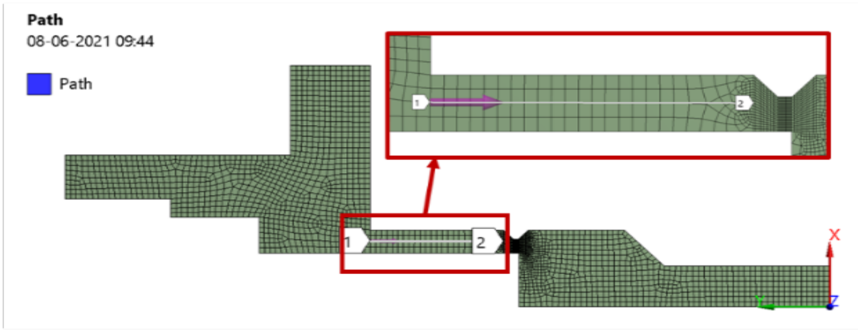

(c) Construction of Line Path on Bolt Housing

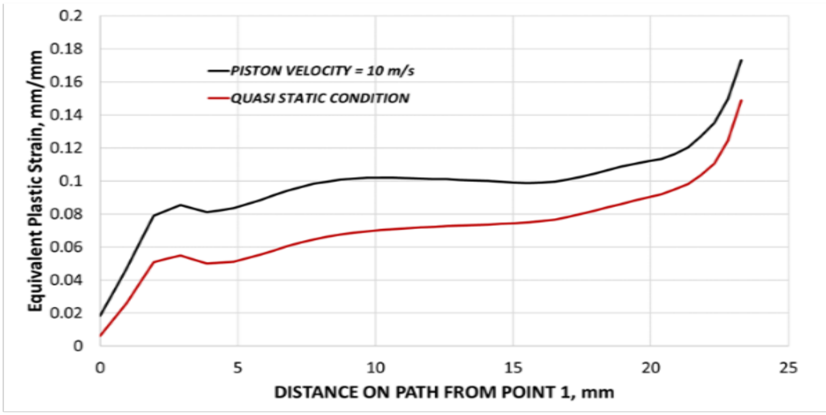

(d) Comparison of Equivalent Plastic Strain On the Line Path for Case 1 and Case 5

Figure 5.14: Equivalent Plastic Strain of Bolt Housing for case 1 (Quasi Static Condition) and Case 5(Piston Velocity = 10 m/s)

In addition to increase in resistance when strain rate hardening is considered, there is a decrease in piston stroke at fracture when piston speed is increased beyond 0.5 m/s. As the piston velocity increases, the strain rate in the thick wall of bore of the bolt housing increases as depicted in Figure 5.14. This attributes to increase in the resistance of thick wall of bore of the bolt housing which results in decrease in piston stroke at fracture when piston speed increases.

(a) Construction of Line Path on Bolt Housing

(b) Distribution of Strain Rate On the Line Path

Figure 5.15: Variation of Strain Rate Along the Path Line for Case 3 and Case 5

ii. Effect of Thermal Softening

To explore the effect of temperature, analysis with and without heat capacity at constant pressure are carried out similar to the case with 17-4PH material. The results of the analyses are shown in Figure 5.15 which depicts that thermal softening effect dominates over strain rate hardening after significant deformation of bolt housing. Fracture of bolt housing with lesser piston stroke can be attributed due to local rise of temperature and associated softening at the location and leads to failure in less piston stroke as compared to piston stroke where thermal effects are not considered.

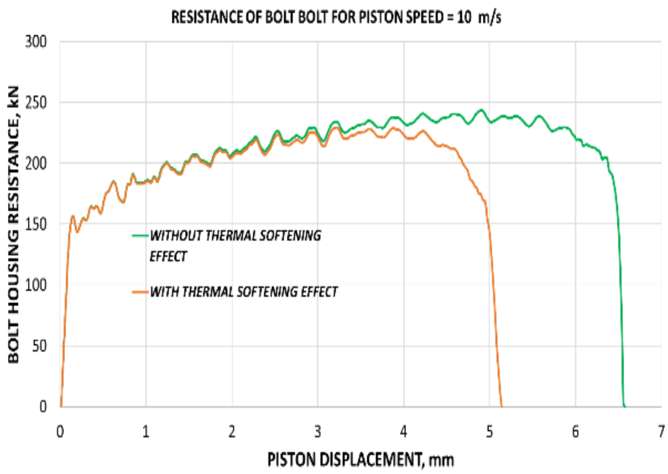

Figure 5.16: Resistance of Bolt Housing for Case 5 With and Without Thermal Softening Effect

C. Discussions

As mentioned earlier, 17-4-PH (H1025) and AISI 304 represents two classes of ductile materials. Comparison of the results of both material under high strain rate condition provides insight towards selection of suitable material of the pyro mechanism. Deformation of point 1 w.r.t. piston displacement of notch of the bolt housing is illustrated in Figure 5.16. In 17-4-PH (H1025) case, the point deforms up to certain value and then comes back near to zero. This implies that the bolt housing is plastically deformed only in the vicinity of notch. However, in case of AISI 304, the point deforms and remains there which implies that there is through section yielding of bolt housing along its length.

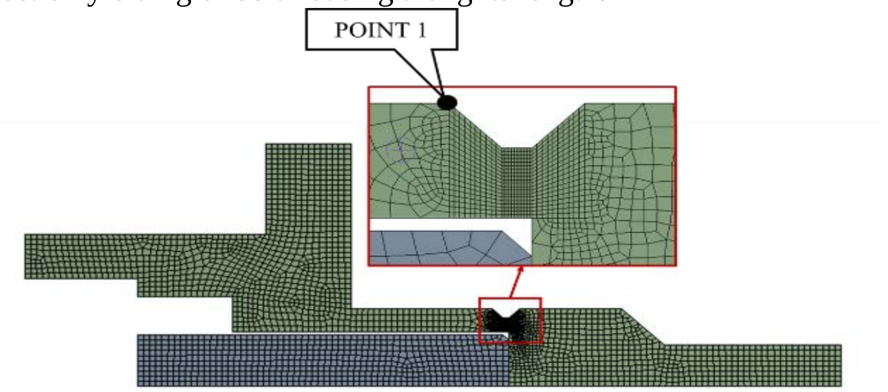

(a) Representation of Point 1 for Deformation Plot

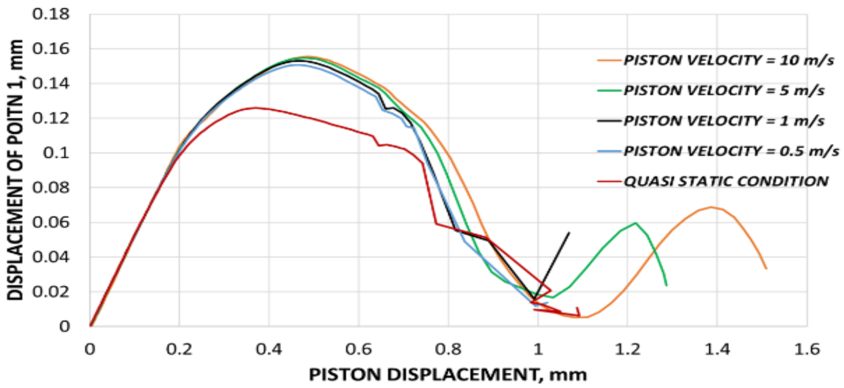

(b) Deformation of Point 1 of Pyro Bolt With Bolt Housing Made of 17-4-PH (H1025)

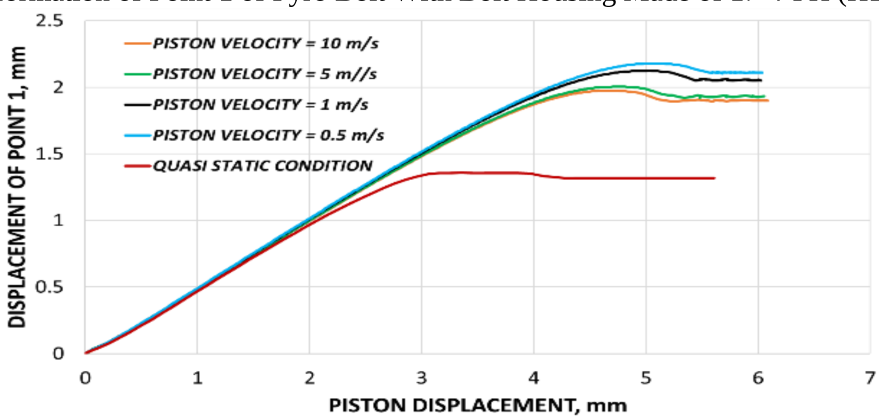

(c) Deformation of Point 1 of Pyro Bolt With Bolt Housing Made of AISI304

Figure 5.17: Deformation of Onset Point Notch of Bolt Housing for (b) 17-4-PH (H1025) and (c) AISI 304

This is happened because of significant difference between ultimate strength and yield strength of AISI304 as compared to 17-4-PH (H1025).

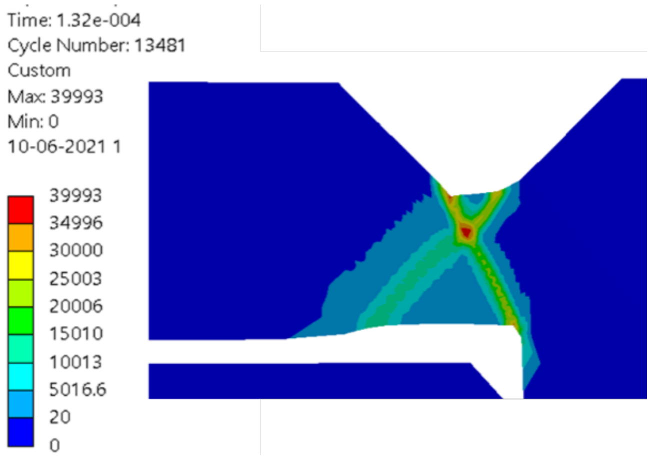

(a) Contour Plot of Bolt Housing of Case 5 of Pyro Bolt with Bolt Housing Made of 17-4-PH (H1025)

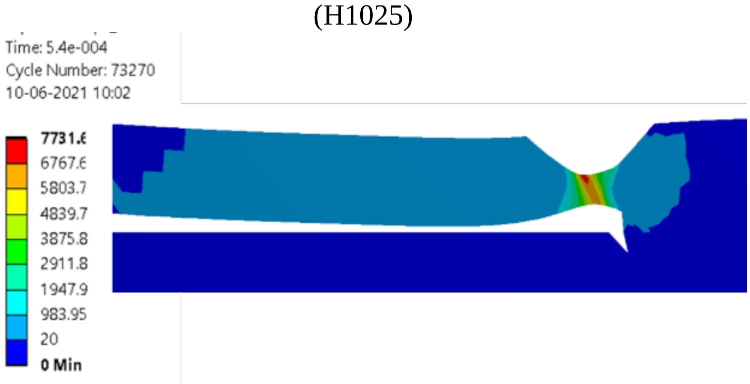

(b) Contour Plot of Bolt Housing of Case 5 of Pyro Bolt with Bolt Housing Made of AISI 304

Figure 5.18: Exaggerated View of Contour Plot of Strain Rate of Bolt Housing (a) 17-4-PH (H1025) (b) AISI 304

Due the significant difference between yield strength and ultimate strength of AISI 304, the thick wall of bore of bolt housing experiences strain rate more than 20 s-1 in case 5 which makes the wall stronger than low strain rate cases and bolt housing fractures in less piston stroke as compared to other cases. In contrast to this, the bolt housing experience more 20 s-1 only to notch region in case of 17-4-PH (H1025). Therefore, stiffness of thick wall of bore of the bolt housing does not change with piston speed and piston stroke at fracture increases with strain rate as shown in Figure 5.6. Similar to strain rate, temperature rise more than 300C is observed throughout the bolt housing in case of AISI 304.

6. Comparison of Ballistic Parameters

As discussed in section 5, resistance of bolt housing as well as energy required to sever it increases with strain rate. The increase in resistance and energy requirement affect the ballistic parameters like maximum expected operating pressure (MEOP), threshold charge quantity, etc. To quantify the change in the ballistic parameters, ballistic analysis of the case mention in section 5 is carried using in-house developed Analytical Ballistic Code for Cartridge Actuated Device (ABC-CAD). The results of the ballistic analysis are summarized in Table 6.1. Maximum pressure of product gases of combustion of explosive is 326.1 MPa and 383.2MPa for case 1(q-s) and case 5 (piston velocity of 10 m/s) respectively of pyro bolt with bolt housing made of 17-4-PH (H1025) material. Threshold charge quantity of pyro bolt are 660 mg and 755 mg for case 1 and case 5 respectively. There is a 17.5% and 14.4% increase in pressure and threshold charge quantity respectively in case 5 as compared to case1.

Table 6.5: Comparison of Ballistic Analysis Results of Pyro Bolt for 17-4-PH (H1025) and AISI 304for various strain rates

Piston velocity (m/s)	17-4-PH (H1025)		AISI 304	
	Pressure (MPa)	Threshold Charge Qty. (mg)	Pressure (MPa)	Threshold Charge Qty. (mg)
Quasi-Static	326.1	660	116	715
0.5	364.6	715	207.5	1700
1	368.9	720	214.6	1735
5	379.8	740	232.4	1810
10	383.2	755	240.4	1845

Similarly, maximum pressure of product gases of combustion of explosive is 116 MPa and 240.4 MPa for case 1 and case 5 respectively for pyro bolt with bolt housing made of AISI 304 material. Threshold charge quantiy of the pyro bolt change is 715 mg to 1845 mg for case 1 to case 5 respectively. There is a 107.2% and 158% increase in pressure of product gases and threshold charge quantity respectively in case 5 as compared to case 1. The increase in pressure due to strain rate hardening of material affects the structural margin of the pyro mechanism. Therefore, effect of high rate in material properties should be considered to accurate prediction structural margin of safety

7. Conclusion

From the case studies it is quite evident that high strain rate material constitutive models plays a vital role in pyro mechanism design. The sensitivity of high strain rate deformation and associated change in flow stress varies considerably with different types of materials. Neglecting the contribution of high strain rate properties results in under-estimation of threshold charge quantity and thereby pyro gas pressure. Hence, selection of material model plays a significant role in accurately assessing total energy requirement for fracture as well in ballistic performance of pyro mechanisms.

8. References

[1] Gordon R. Johnson, William H. Cook, “A Constitutive Model and Data for Metals Subjected to Large Strains, High Strain Rates and High Temperatures”, Proceedings 7th International Symposium on Ballistics, The Hague, 19-21 April 1983, 541-547.

[2] Johnson, G.R.; Cook, W.H. “Fracture characteristics of three metals subjected to various strains, strain rates, temperatures and pressures”. Eng. Fract. Mech. 1985, 21, 31–48.

[3] Frank J. Zerilli and Ronald W. Armstrong, “Dislocation Mechanics Based Constitutive Relations for Material Dynamics Calculations”, J. Appl. Phys. 61, 1816(1987); doi: 10.1063/1.338024

[4] G. Cowper, P. Symonds, Strain hardening and strain-rate effects in the impact loading of cantilever beams, Tech. Rep., Brown University Division of Applied Mathematics, 1957

[5] U.S. Lindholm, High Strain Rate Testing, Part 1: Measurement of Mechanical Properties, Techniques of Metals Research, Vol 5, R.F. Bunshah, Ed., Wiley Interscience, New York, 1971, p 199–271

[6] P.S. Follansbee, The Hopkinson Bar, Mechanical Testing, Vol 8, ASM Handbook, American Society for Metals, 1985, p 198–203

[7] V.P. Muzychenko, S.I. Kashchenko, and V.A. Guskov, Use of the Split Hopkinson Pressure Bar Method for Examining the Dynamic Properties of Materials: Review, Ind. Lab. (USSR), Vol 52, 1986, p 72–83

[8] Murugesan, Mohanraj& Jung, Dong Won. (2019). Johnson Cook Material and Failure Model Parameters Estimation of AISI-1045 Medium Carbon Steel for Metal Forming Applications. Materials. 12. 609. 10.3390/ma12040609.

Shelf Life Prediction of Imported Life Expired Ignition tube TV-10 Cartridge for Fighter Aircraft Application

Bhupesh A Parate
Armament Research & Development Establishment
Pune
v.baparate@gmail.com

Sgt S K Sahoo
Armament Research & Development Establishment
Pune

Y B Salkar
Armament Research & Development Establishment
Pune

Abstract – **The objective of this research article is to carry out the internal ballistic measurement of life expired imported ignition tube TV-10 cartridge for fighter aircraft application. The purpose of this cartridge is to facilitate ejection of the pilot in an emergency and used in ejection seat of Su-30 Mk I aircraft. It is intended for activating the explosive bar deployment system, parachute deployment mechanism and Ignitor in catapult seat engine. The cartridge itself is initiated at a pre-set height by an automatic firing mechanism known as JVB which is controlled by a barostatic unit. The deterioration of various chemical compositions takes place over a period of time and their properties takes place for the propellants or pyrotechnics inside the ejection cartridges, even at ambient storage conditions. Life extension is a methodology/technique to assess the impact of environment and induced stresses as per selected methods. Internal ballistics parameters like maximum pressure and corresponding time to maximum pressure are generated by firing this cartridge in a Closed Vessel (CV). A CV is designed and fabricated for evaluating and recording these parameters. These parameters are measured using the Data Acquisition System (DAS). Experiments are performed to assess the remaining useful life in terms of internal ballistic performance parameters and accordingly extended the shelf life of cartridge. The analysis of these performance parameters are evaluated after subjecting to Highly Accelerated Life Trials (HALT). The trial results show that performance parameters are within specified limits, both in cold and hot conditions. This research article describes about the life extension methodology of imported life expired ignition tube TV-10 cartridges to enhance the installed life for aircraft application by six (6) months, twelve (12) months and eighteen (18) months in three different phases. This kind of study is essential and helps to keep the entire aircraft fleet in operational readiness. Considering the overall performance of ignition tube TV-10 cartridge in hot and cold conditions, the maximum pressure (P_{max}) varies from 45.92 to 62.51MPa, and time to Pmax varies from 105 to 220 ms. It is observed that after environmental trials Pmax decreases as compared to phase I and time to P_{max} increases.**

Keywords*– *internal ballistics, life extension, Ignition tube TV-10 cartridge, shelf life and closed vessel

1. Introduction

The life of any defence store containing chemical substances such as the propellants, an explosives and pyrotechnics material undergoes degradation over a period of time. However, it is interesting to note that these chemical substances required the attention by the services. The life of Energetic Materials (EMs) used for seat ejection cartridges in service has assigned conservative life considering the safety aspects of the pilot and its reliability of functioning in a stated condition and period. The performance of these cartridges is crucial being one shot devices in all adverse conditions. The general policies are to replace the life expired store with fresh one “irrespective of their state of deterioration or use them for training rather than operational use” [1]. Initial service lives of EMs are extended based on satisfactory trials after subjecting them to accelerated ageing tests such as diurnal temperature, humidity, mechanical stress and vibrations. Due to constant degradation, deterioration of EMs enhances with an increase in temperature and pressure which speeding up of chemical reactions. The service life or useful life of these materials is limited and therefore these cartridges are generally replaced after the expiry of their service life. The cartridges fitted on the aircraft are due for replacement. However, there are indications that there would be a delay in the supply of fresh cartridges from Original Equipment Manufacturer (OEM). In order to keep the entire aircraft fleet in operational readiness, it became essential to enhance the life of cartridges installed on the aircraft till the availability of fresh cartridges. The user submitted life expired cartridges to conduct life extension study.

All modern fighter and trainer aircraft are fitted with state-of-art of ejection seat to abandon the aeronaut from disable aircraft in crisis. Different power cartridges are installed in the seat ejection to execute various operations in an emergency. Ignition tube TV-10 cartridges give precise parameters which are highly essential to operate the actual system. In the fighter aircraft, the seat is propelled out of the cockpit by the propellant or under-seat rocket motor, carrying the seat-pilot with it. Cartridges are extensively used to abandon the pilot from the disabled aircraft. For safe ejection, therefore, a fully automatic and reliable seat ejection escape system is provided in all modern military aircraft.

2. Description of Imported Ignition tube TV-10 Cartridge

This cartridge is made of steel body. It is filled with the pyrotechnic composition. It has a percussion cap that is initiated by actual aircraft firing mechanism. The images of imported Ignition tube TV-10 cartridge are shown in Figure 1(a). This cartridge has diameter, flange diameter and length 7mm, 10.2mm and 23mm respectively. The explosive train is ignited inside the cartridge, thus generating hot combustion gas. The actual aircraft firing mechanism of ejection seat which forms the part of the Cartridge Seat Ejection (CSE) system is depicted in Figure 1(b). The firing pin of firing mechanism has protrusion of 4.2 ± 0.2 mm that penetrates the percussion cap. This firing mechanism is used one time operation in actual firing.

Figure 1(a): Images of the imported Ignition tube

Figure 1(b): Images of aircraft firing mechanism for firing TV-10 Cartridge

The shelf life of imported ignition tube TV-10 cartridges is assessed by carrying out life extension trials in the laboratory. Ageing of the explosive content are taking place over a period of time and the reaction rate is accelerated with an increase in pressure and temperature. The ignition tube TV-10 cartridge has a limited shelf life because; the degradation of the explosives occurs due to storage and induced forces during its flight, handling and transportation. The ageing of any store limits its useful life and the extension method is utilised to predict the safe storage life. The life extension approach validates the performance as ageing increases. There are following certain reasons why the need is arise to assess the life extension of defence store.

(i) Non- availability of imported defence store (arms, ammunitions and rockets etc.) from OEM
(ii) Production holds up in the ordnance factories of defence store
(iii) OEM stops the production and supply of imported defence store
(iv) Inordinate delay in getting the store
(v) Life study helps in the identification and analysis of similar trends for further use
(vi) Identifies the deficiencies because of the environmental effect
(vii) This kind of methodology is used for serviceability, reliability and quality associated with all components
(viii) In case, guaranteed period expires, it is great significance to find out periodic checks

3. Laboratory environmental simulation

The effect of the environment to access the performance of ammunition is reported by Ferrira et al. [2]. The shelf life of defence store due to oxidation, ageing of chemical degradation and mechanical loads are to be predicted under induced stresses and various environmental factors such as humidity, pressure and temperature which encounter their service span. The induced stresses are due to handling, transportation and environmental factors such as pressure, temperature and humidity. The accelerated ageing of the propellant samples used in combustible cartridge case at elevated temperature is carried out by monitoring stabilizer content by Peshave and Singh [3]. The shelf life prediction of the propellant using a novel method utilizes Arrhenius equation was given by Zhao et al. [4]. Accelerated ageing of power cartridge in Closed Vessel (CV) was discussed by Sahu et al. [5]. The authors carried out a chemical analysis of single base propellant and compared at each phase. A major variation in the percentage of stabilizer i.e. [Di-phenyl Amine (DPA)] was found. It gradually decreases from phase I to phase III. This is due to the formation oxides of nitrogen and subsequently neutralized by the stabilizer. In Phase I, the initial stabilizer content was 0.95% and decreases to 0.06% in Phase III after completion of highly accelerated life trials followed by air exposure and vibration. In Phase II the stabilizer content was 0.26 %. The stabilizer content of the propellant is estimated by HPLC. It is found that there is a considerable decrease in the percentage of stabilizer. To prevent autocatalytic decomposition of NC based propellant DPA was added as a stabilizer. This amine reacts with nitrogen oxides forming different substituted products of DPA called daughter products, like 2NDPA, 4NDPA and many others. The chemical degradation over a period of time changes the mechanical properties of the propellant. The life extension of any defence ammunition after its expiry could be serviceable (i.e. functional and safe) has been a concern to the producer and user for many decades. The shelf life extension is provided to store for a limited period of extension. There are many studies available related to the propellant ageing at an elevated temperature. Nevertheless, much fewer studies are available in the life extension of imported seat ejection cartridges. The numerical and design analysis of brass cartridge was discussed by Parate et al. [6, 7]. Jiang et al. [8] studied the combustion characteristics of the propellant at a high temperature. This study is related to shelf life extension under high and cold conditions. The main aim of this study was to fulfil the requirements of shelf life extension of imported ignition tube TV-10 cartridges by evaluating the ballistic parameters in a CV.

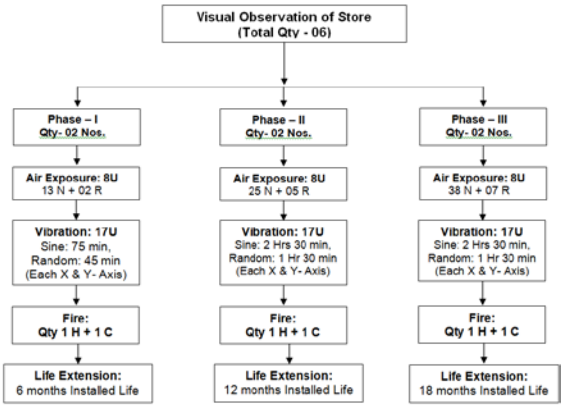

C: Cold (- 26^0C), H: Hot (+ 45^0C), N: Normal cycle, R: Rapid cycles, U: Unpackaged

Figure 2: Flowchart for life extension trial schedule

The details of Air exposure (8 U) are given below [9] -

All types of armament stores to be carried by or installed in aircraft shall undergo these trials.

This particular store was undergone for 25 two days cycle as below -

(i) 17 hours at 65 0C ± 2 0C
(ii) 1 hour at 25 0C ± 20C and 75 % ± 5 % Relative Humidity (RH)
(iii) 3 hours at - 65 0C ± 20C
(iv) 3 hour at 25 0C ± 20C and 75 % ± 5 % RH
(v) 17 hour at 70 0C ± 20C and 50 % ± 5 % RH
(vi) 7 hour at 25 0C ± 20C and 75 % ± 5 % RH

Further 5 two-day cycles should then be run under the following conditions to cover the rapid transitions form hot to cold and cold to hot which aircraft flight can experiences.

(i) 3 hours at - 65 0C ± 20C
(ii) 4 hour at 70 0C ± 20C and 50 % ± 5 % RH
(iii) 17 hour at 25 0C ± 20C and 75 % ± 5 % RH
(iv) 4 hour at 70 0C ± 20C and 50 % ± 5 % RH
(v) 3 hours at - 65 0C ± 20C
(vi) 17 hour at 25 0C ± 20C and 75 % ± 5 % RH

The low-pressure period should be continued for each cold phase of these 5 cycles.

The phase I trials are carried out with an objective to extend the total life by a period of six (6) months, exposing the cartridges for air exposure trials, vibration trials and functional trials in a CV. Phase II trials are carried out to enhance the total life by a period of twelve (12) months. Phase III trials are carried out to enhance the total life by a period of eighteen (18) months. The details for vibration tests are explained in paragraph 4.1. The experimental test set-up was explained at paragraph 5.

4. Test apparatus and materials

The following materials and methods are used for data generation and life extension trials.

(i) Ignition tube TV-10 cartridges

(ii) Closed Vessel (CV)
(iii) Firing mechanism
(iv) Gauge adaptor with a pressure sensor
(v) Data Acquisition System (DAS)
(vi) Vibration fixture
(vii) Conditioning chamber for subjecting them cyclic temperature, humidity and pressure.

Vibration test and pressure measurement are described in the following paragraphs 4(A) and 5.

A. Vibration Test

To simulate the induced stresses such as transportation loads, these stores are subjected to vibration trials. The imported ignition tube TV-10 cartridges are subjected to vibration tests (17U) using suitably fabricated vibration fixture. The images of ignition tube TV-10 cartridges mounted on vibration bed are shown in Figures 3(a). The maximum displacement is 12 mm and frequency range is 5 to 70 Hz with sinusoidal vibration is applied [10]. In due course, random vibration with uniform spectral density of 0.03 g2/Hz in the frequency range from 70 to 2000 Hz in each phase on both the axes are applied. After completion of air exposure and vibration, cartridges are fired in a CV as per above schedule. The graphs for Sinusoidal and Random Vibration Cartridge TV-10 are illustrated in Figures 3(b).

Figure 3(a): Ignition Tube TV-10 cartridges mounted on vibration bed

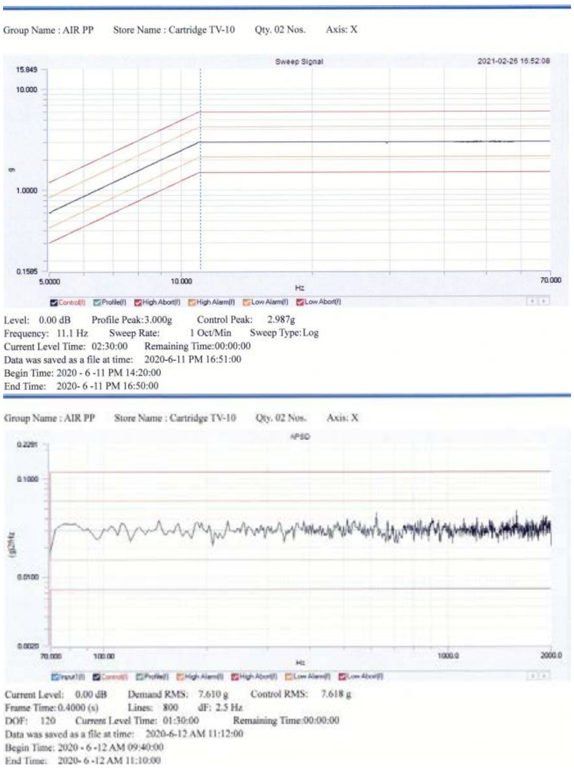

Figure 3(b): Graphs for Sinusoidal (Top) and Random Vibration (Bottom).

5. Experimental test set-up

An experimental test set-up comprises firing mechanism, a Closed Vessel (CV) as test equipment, DAS [monitor, printer, pressure sensor and amplifier] and an imported life expired cartridges are used for evaluating the internal ballistic parameters. The functional trials of imported ignition tube TV-10 cartridges are carried out in a specially designed /fabricated CV to ascertain the service condition. The cartridges were subjected to firing trials in a CV after subjecting them to air exposure trials followed by vibration as explained at paragraph 4. The complete experimental test set-up is shown in Figure 4.

The imported life expired ignition tube TV-10 cartridges were used for the data generated in a CV i.e. specially fabricated. The vessel volume is 5 cc. The volume of the vessel is confirmed with a measuring beaker. For evaluating the internal ballistic parameters, the gauge adaptor is located in the Y direction. One ignition tube TV-10 cartridge is assembled in a CV. This cartridge is initiated by the percussion firing mechanism. As the actual aircraft mechanism is used one time, a new firing mechanism with a protrusion of 4.1 mm is designed and fabricated in-house. Internal ballistic parameters i.e. maximum pressure and time to maximum pressure were recorded by DAS.

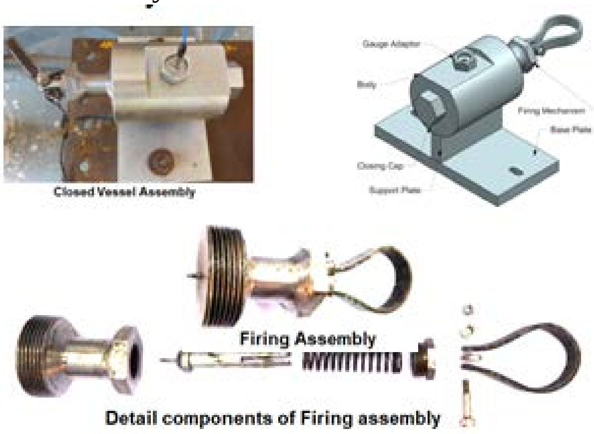

Figure 4: Test set up of ignition tube TV-10 cartridge

6. Performance Evaluation of the Cartridges in a Closed Vessel (CV)

A CV is a test method, utilised to simulate the ballistic parameters of ignition tube TV-10 cartridge. It is one of the techniques through which an energy developed by cartridges (here propellant and pyrotechnic composition) are evaluated in terms of internal ballistic parameters. The ignition tube TV-10 cartridges are assembled with a CV as shown in figure 4. Finally, a spring loaded firing mechanism is screwed to a CV in front of igniter TV-10 cartridge. The other end of a CV is closed with the end plug. Performance parameter evaluation of power cartridge in CV determines two important ballistic parameters i.e. the time to maximum pressure and maximum pressure [11]. The main objective was to measure the internal pressure. Pressure sensor is used to measure the ballistics parameters. The engineering drawing of CV is depicted in Figures 5. The dimensions where expansion of gases after firing of cartridges takes place are diameter 15 mm and length 25 mm.

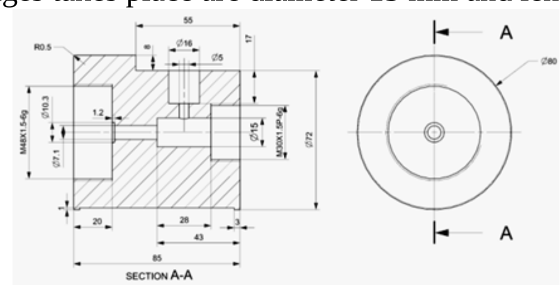

Figure 5: Engineering drawing of CV

The pressure - time (P-t) graphs in a CV at hot (+450C) and cold (-260C) conditions are generated. Internal ballistic parameters for ignition tube TV-10 cartridges in hot and in cold conditions are represented by red and blue colours. The pressure is plotted on Y-axis and time is plotted on X-axis. All the inputs parameters for plotting pressure versus time are taken from Tables 1, 2 and 3 for phases I, II and III respectively. P-t profiles generated after firing of the cartridges on DAS are shown in Figures 6.

7. Results and Discussion

This section explains about the results and analysis of various internal ballistic performance parameters to assess the shelf life extension of imported ignition tube TV-10 cartridges. The ballistic performance parameters of ignition tube TV-10 cartridges are evaluated using DAS in three phases at hot and cold conditions.

A. Phase I:

The cartridges are subjected to experimental evaluation as per phase I. The cartridges were exposed to 13 normal (N) cycles and 2 rapid (R) cycles of 8U (Unpackaged) as per Figure 2. The performance parameters were evaluated at hot and cold conditions in a CV after the completion of environmental trials followed by vibration trials. The results are found to be within the specified limits for various parameters. Before firing, the cartridges are subjected to hot and cold temperature conditions for minimum period of six hours. On the basis of the satisfactory results, the shelf life of the cartridges (installed and storage) life was extended by six (6) months. The summary of the functional trial results of the cartridges withdrawn after phase I are illustrated in Table 1

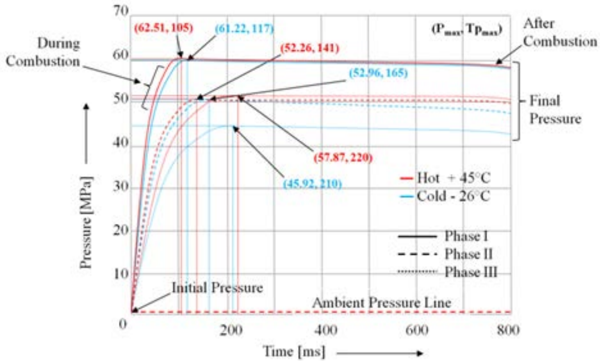

Figure 6: Pressure vs. time (P-t) profile for Phase-I, II and III

Table 1: Functional Trials Result - Phase I.

Sl. No.	*Pmax* [MPa]	*TP max* [μs]	Condition
1	62.51	105	Hot 45^{0}C
2	61.22	117	Cold -26 ^{0}C

B. Phase II :

After successful completion of phase I trial, the cartridges were subjected to full cycle of air exposure (8U) followed by vibration (17U) i.e. 25 normal (N) cycle and 5 rapid (R) cycles of 8U. The performance parameters were evaluated at hot and cold conditions after the completion of environmental trials followed by vibration trials. Before the firing, the cartridges were subjected at hot and cold temperature conditions for a minimum six (6) hours. The results are found satisfactory. On the basis of the satisfactory results, the shelf life of the cartridges (installed and storage) life is extended by a period of twelve (12) months. The summary of the functional trial results of the cartridges withdrawn after phase II were illustrated in Table 2.

Table 2 Functional Trials Result - Phase II.

Sl. No.	*Pmax* [MPa]	*TP max* [μs]	Condition
1	52.26	141	Hot 45^0C
2	52.96	165	Cold -26 ^{0}C

C. Phase III:

After successful completion of phase I and II trials, the cartridges were subjected to 38 normal cycle and 07 rapid cycles of air exposure 8U followed by 17 U vibrations. On the basis of the satisfactory results, the shelf life of the cartridges (installed and storage) life is extended by eighteen (18) months. The summary of the functional trial results of the cartridges withdrawn after phase III were illustrated in Table 3.

Table 3 Functional Trials Result - Phase III.

Sl. No.	*Pmax* [MPa]	*TP max* [μs]	Condition
1	57.87	220	Hot 450C
2	45.92	210	Cold -26 0C

The two ballistic parameters i.e. maximum pressure and time to maximum pressure were generated by firing the cartridges in a CV at hot and cold temperature. The ballistic evaluation techniques for the measurement of various parameters were explained in Section 6. The internal ballistic parameters for ignition tube TV-10 cartridges were given in Tables 1, 2 and 3 respectively.

Considering the performance parameters of ignition tube TV-10 cartridges in cold and hot conditions, it has been observed that pressure decreases and time to Pmax increases. All the performance parameters were observed within limits of cold and hot condition. One of image of fired cartridge after the firing is illustrated at Figure 7.

Figure 7: Image of fired cartridge

8. Conclusions

From the foregoing deliberations, it is concluded that the shelf life extension of ignition tube TV-10 cartridges was undertaken with a request from user to avoid the grounding of a large aircraft fleet. This helps to keep the entire aircraft fleet in operational readiness. These cartridges have a shelf life of six years. The experiment was conducted in three phases and shelf life of ignition tube TV-10 cartridges was extended by six months in the first phase, twelve months in the second phase and eighteen months in third phase. After static ground tests in a CV, the internal ballistic performances of cartridges follow the same pattern in hot and cold conditioning. These cartridges are responsible for generation of pressure during seat ejection. This kind of internal ballistic assessment may be applied to any defence ammunition for extending the shelf life. The overall ageing effect leads to changes in chemical, physical, ballistic, thermal and mechanical properties of the propellant with storage time, i.e. the reduction of the propellants performances and safe service life.

An attempt has been made to describe life extension methodology and approach followed for the ignition tube TV-10 cartridges of trainer aircraft of various performance parameters as a part of internal ballistics generated so as meet the requirements of the services on priority. This life extension study was useful in keeping the entire fleet of fighter aircraft in operational readiness.

Systematic life extension of ignition tube TV-10 cartridges was performed in hot and cold conditions in the laboratory using in-house test facilities. Based on satisfactory performances in all phases, it concluded that the shelf life extension of imported ignition tube TV-10 cartridge can be safely extended for eighteen months without compromising safety, reliability and function.

9. Acknowledgements

The authors are obliged to Dr. V Venkanteswara Rao, Outstanding Scientist and Director ARDE, Pashan, Pune - 411 021 for his kind consent to bring out this life extension work. The authors also extend their genuine thanks to Shri. V K Dixit, Sc. 'H', Outstanding Scientist and Associate Director for his priceless assistance. The authors would like to show appreciation to Mrs. Devyani Jadhav, Sc 'F' Division Head (Range Group) for providing the required support for the data acquisition facility to execute all experimental trials smoothly. The authors express their gratitude to the test team for diligently carrying out the firing trials during the life extension assessment process of imported ignition tube TV-10 cartridges.

10. Reference

[1] G. Manton, Accelerated aging of pyrotechnics: Evaluation of pyrotechnic degradation. International Conference on Ageing Studies and Lifetime Extension of Materials, 619-626, (2001) ISBN 0306464772.

[2] C. Ferreira, J. Ribeiro, S. Almada and F. Freire: Environmental Assessment of Ammunition: The importance of a Life –Cycle Approach, Propellants Explosives and Pyrotechnics, 42(1), 44-53 (2016).

[3] J. R. Peshave and H. Singh, J. Energ. Material, 20, 345-356 (2002).

[4] Xin Zhao, Xiaoting Rui, Yan Wang, and Ruihua Zhang, Propellants Explosives and Pyrotechnics, 43, 1-8 (2018).

[5] A. K. Sahu, B. A. Parate, S. B. Borkar, Y. S. Dhoke, International High Energy Materials Conference & Exhibit (2014).

[6] B. A. Parate, S. S Khandagale, S. Chandel, H. Shekhar, 7th International and 28th All India Manufacturing Technology, Proceedings of AIMTDR, Chapter 63, 759-772 (2018).

[7] B. A. Parate, S. Chandel, H. Shekhar, Defence Technology, 14, 683-690 (2018).

[8] Jiang Li, Kai Ma, Xiang Lv, Peijin Liu, Guoqiang He, Yang Liu, Jian Chen, Combustion & Flame, 204, 49-57 (2019).

[9] Joint Service Guide (JSG) 0102: Environmental Testing of Armament stores (1984)

[10] Ordnance Board Proceeding (OBP) 41254: Environmental testing of Armament stores.

[11] B. A. Parate, and C. M. Kulkarni, Def. Sci. J, 57, 223-228 (2007).

[12] B. A. Parate, A. K. Sahu and V. Kumar: International High Energy Materials Conference & Exhibit (2009).

[13] B. A. Parate, S. Chandel, H. Shekhar, Sci. Techol. Energ. Mater., 81, 432, 47-52 (2020).

Quality and Reliability in Mechanisms

Reliability Assessment of Radial Rib Antenna Mechanism

Mohnish Chaurasiya
U R Rao Satellite centre,
Bangalore 560017
mohnish@ursc.gov.in

Shankar Narayan Y S
U R Rao Satellite centre,
Bangalore 560017
yssn@ursc.gov.in

Milind Undale
U R Rao Satellite centre,
Bangalore 560017
milindu@ursc.gov.in

Abstract- **Reliability is the ability of a product or system to perform as intended (i.e., without failure and within specified performance limits) for a specified time, in its life cycle conditions. An ideal system is the one that remains operational and attains objective without failure during specified life. Since the variables and factors involved in design are multivalued, so the prediction of failures is inherently probabilistic in nature. Reliability assessment will help us to predict failure probability and to address it probabilistically. Radial Rib Antenna (RRA) is a 3.6-meter spacecraft based antenna. Its reflector consists of a deployable parabolic ribs and a reflector mesh that is folded during launch and deployed in orbit. As RRA is mission critical appendage, successful deployment of RRA is must for spacecraft to achieve is mission goal. Hence reliability assessment of RRA is essential part of product assurance. Failure Modes Effects and Criticality Analysis (FMECA) and Detailed Design Review are completed for RRA development. Reliability assessment of RRA is carried out by separating it into subassemblies, calculating reliability of subassemblies and combining it together with the help of reliability block diagram to find overall reliability. Functionally critical components for these subassemblies have been identified from FMECA. For the components with known mode of failure, reliability calculation tools like stress-strength method, one shot failure and time to failure have been chosen. Proper testing is also done to eliminate unknown modes of failure.**

Keywords- Antenna, Reliability analysis, Mechanism

1. Introduction

Radial Rib antenna is 3.6 m spacecraft based antenna. Radial rib antenna mechanism is designed to meet the constraints to launch antenna along with spacecraft and to deploy it successfully in orbit. Reliability assessment has been carried out to ensure its deployment in orbit and proper working for the defined life.

With consideration of requirements and constraints, the design was evaluated to meet expectation and fulfil mission objective. The design consists of four subassemblies i.e. deployable hinge, metallic mesh, hold down and release mechanism and drive module.

The design parameters, their specifications and tolerances are calculated taking consideration of required function in different stages of design. All the processes are qualified through proper testing and analysis.

2. System and Formulation

Radial rib antenna consists of hold down and release mechanism, deployment hinge mechanism, and parabolic ribs with metallic mesh and drive module.

Hold down and release mechanism is used to stow antenna to meet launch vehicle constraints and to release it by firing the pyrocutter after reaching the orbit. After release, drive cable passing through hinge pulley controls the movement of ribs attached to the hinge.

Both ends of the cable are connected to motor present in drive module. The cable length along the pulley is controlled with the help of lead nut moving over lead screw, pulleys and brushed DC motor present in Drive Module. After the deployment, latching mechanism is incorporated to fix the ribs to get designed stiffness. The metallic mesh fixed to the curved ribs is used as reflective surface for antenna.

The deployment takes place in two stages. Hold down will be released by firing pyrocutter and ribs will be free to rotate around hinge. Motor is then operated to shorten the cable, subsequently causing ribs to move outward. At the end of deployment, latching occurs causing final configuration of ribs along with metallic mesh in between to be rigid (Figure 1). Metallic mesh forms parabolic surface for reflection.

Fig. 1: Radial Rib Antenna in deployed configuration

Failure modes for the critical components are taken into consideration from FMECA. Reliability evaluation techniques used for critical components are as follows:

A. Stress-strength analysis

For critical elements whose failure mode is based on static failure types like bending, shearing, tensile failure etc. stress-strength analysis has been carried out considering the probabilistic design approach. Both stress and strength are function of design variables each of which are random variables [1]. The probability that strength will exceed stress must equal or exceed a specified performance measure (R) called Reliability. P {S-s}>0 = R.

Here the strength (S) and stress density (s) functions are considered normally distributed with mean μS, μs and standard deviation σS, σs respectively. Since the distributions for both the stress and the strength both follow a Normal distribution, then the reliability (R) of a component can be determined by the following equation: R=1-P(Z), where

$$Z = -\frac{(\mu S - \mu s)}{\sqrt{(\sigma S2 + \sigma s2)}}$$

P(Z) can be determined from a Z table or a statistical software package.

As the components involved in assembly are manufactured with high quality standards, 3σ variation is assumed to be 10% of mean strength. The mean and variance of stress function has been found with data available for load and with geometric tolerances on design.

B. Time to failure

To calculate the reliability for the elements like motor and bearing, time to failure approach has been considered. For motor, failure rate has been taken from Probability Application in Mechanical Design by Franklin E. Fisher, Joy R. Fisher [2] and failure is considered to undergo exponential distribution.

$$\text{Reliability (R)} = e{-}\lambda t$$

$$\lambda = \text{Failure rate}$$

For bearings percentiles of life approach has been considered.

L90= Rated life, 90% of identical bearings can serve or exceed speed without any failure
R = Reliability for a corresponding service life
(L/L90) = (ln(1/R)/ln(1/R90))^ 1/1.17
L90 = (c/pe) ^ k in Million Rev
K = 3 for ball bearing
K = 10/3 for roller contact bearing
C/Pe = Max load/Design load= loading ratio,

C. One shot failure:

For element like pyro- cutter Reliability is calculated by taking lower bounds of reliability for 60% confidence since there is no failure observed till now. Formula for reliability with zero failures is given by R= (1-α) 1/n where n is the number of components tested and α is the confidence (3).

3. Reliability Evaluation

Reliability of RRA is evaluated by calculating reliability of subassemblies and combining it together with the help of reliability block diagram to find overall reliability (4) (5) (6). Choice of method for calculating reliability numbers depends on the failure modes and empirical data available. Only critical components are considered for reliability evaluation. Selections of critical components is based on FMECA (7) conducted earlier. Only critical failure modes are addressed in the study.

RRA has four subassemblies and failure of any of the subassembly will be catastrophic. So, these sub-assemblies are considered as a series system.

Reliability of RRA

$R_{rra} = R_{dm} \times R_{mg} \times R_{hdrm} \times R_{hinge}$, Where R_{dm}: Reliability of drive module

R_{mg}: Reliability of mesh gore.

R_{hdrm}: Reliability of hold down and release mechanism.

R_{hinge}: Reliability of deployment hinge mechanism.

4. Reliability of Subassemblies

A. Reliability of drive module

In RRA, there are two drive module at 180° phase on the bottom side of the base plate. Both the drive module will operate during the nominal operation (one of the two drive module is sufficient to carry entire operation). Each drive module has a dc brush motor connected to the lead screw, where the lead screw is supported using bearings in support brackets. Each lead screw has a lead nut that has pulleys on the either side. Kevlar rope of diameter 2mm passes over pulleys which shortens the length of rope around deployable hinge. As the Kevlar rope is pulled inside radial rib antenna start getting deployed.

The critical elements from FMECA has been taken along with the mode of failure and reliability of each component has been calculated in Table 1.

Table 1

Drive module				
Support bracket sub assembly				
S. No.	Component	Failure mode	MOS	Reliability
1	Ball bearing type-1	Bearing ball deformation	>1	1
Plummer block sub assembly				
2	Plummer block	Bending	>8	1
3	Angular Contact Bearing	Bearing ball deformation	2.40	1
4	Ball bearing type -1	Bearing ball deformation	1.08	1
5	Pin	Bending	>8	1
Lead screw sub assembly				
6	Lead screw nut	Bending	>8	1
7	Ball bearing type-1	Bearing ball deformation	1.08	1
8	Ball bearing type -2	Bearing ball deformation	6.09	1
Alignment plate sub-Assembly –Terminating / Non-Terminating				
9	Kevlar rope	Breaking	7.45	1

By taking failure mode as life, Reliability has been calculated for Ball bearing type -1 (Support bracket), Angular contact bearing (Plummer block) and DC motor which is shown in the Table 2.

Table 2

S. No.	Component	Failure	Reliability
1	Ball bearing type -1 (R_{bb})	Life	0.99998
2	Angular contact ball bearing(R_{ab})	Life	0.99999
3	DC motor (R_{dc})	Life	0.99617

All the drive module components are in series and both the drive modules are in parallel. Calculation for reliability is shown below. Overall reliability for Drive module is 0.99998.

$R_{dm1} = R_{dm2}$ = Reliability of each of the drive module.

$R_{dm1} = R_{dm2} = R_{bb} * R_{ab} * R_{dc} = 0.99614$, $R_{dm} = 1-(1-R_{dm1}) *(1-R_{dm2}) =0.99998$

B. Reliability of hold down and release mechanism (R_{hrdm})

All the ribs are terminated with a hook which provides guiding interface for hold down loop wire and a mating interface with the top. A clamp band type, tensioned loop passes over the hooks and holds the deployable ribs against the top plate in stowed orientation. Pyro cutter is used to cut the loop and release tension. A GFRP rod is attached to the loop to guide its shape once the tension is released. Its critical components consist of hook and restraining hook, top plate, turn buckle, turn buckle terminal LH and RH, GFRP rod and Pyro cutter. The critical elements from FMECA has been taken along with the mode of failure and reliability of each component has been calculated in Table 3.

Table 3

S. No.	Component	Failure mode	MOS	Reliability
1	Hook	Bending	>10	1
2	Turnbuckle	Thread failure	6	1
3	Hold down loop	Tensile failure	3.8	1

Proof loading has been done for turn buckle with swaged terminals with 1.2 times the load to be given, for hook bonding is supported with fastening, for top plate alignment checks has been done. Repeatability test of hold-release is done to ensure the stiffness of the GFRP. Reliability of pyro-cutter devices are calculated by One-shot failure method. Testing of 1100 pyro-cutters with no failure observed and for α equal to 60%, reliability is found to be 0.9991. All the components are considered connected in series. Overall reliability of the system is 0.9991.

C. Reliability of deployment hinge mechanism. (R_{hinge})

Deployable Hinge mechanism is designed to give mesh the parabolic profile on deployment in orbit. It includes bearing, Eye-end, Fork-end bracket, hinge shaft, hinge pulley and hinge pulley shaft as its major parts. The critical elements from FMECA has been taken along with the mode of failure and reliability of each component has been calculated in Table 4.

Table 4

S.	Component	Failure mode	MOS	Reliability
1	Deep groove ball bearing	Bearing ball	4.39	1
2	Eye end Bracket	Bending	>10	1
3	Fork end bracket	Bending	6	1
4	Fork end bracket drive	Bending	6	1
5	Hinge shaft	Bending	5.1	1
6	Hinge pulley shaft	Bending	>8	1

As quoted from above table least margin of safety available for critical components is 4. For Deep groove ball bearings in this assembly, in each deployment less than single rotation is occurring, therefore failure cause as bearing life is not considered, so only radial loading as a failure mode is considered. All the components are connected in series, therefore, reliability of deployment hinge mechanism can be stated as 1.

D. Reliability of Mesh Gore (R_{mg})

A gold plated metallic mesh is used as the RF reflecting surface. The parabolic shape of the mesh surface is provided by curved ribs. To meet the surface RMS requirement for X-band, the RRA is configured with 45 deployable ribs. Between these deployable ribs, RF reflective mesh segment is attached which are called as Mesh gores. It consists of Gold molybdenum mesh, CFRP layup and mesh fasteners and nuts as its major components.

Coupon test has been done to qualify bonding strength of mesh. Electrical characterisation (Return Loss, Bandwidth, Gain, Beam width measurement) of the mesh was done at subsystem level covering all 9 feeds (eight for X-Band SAR Payload & one for X-

Band Data Transmitter) and performance was satisfactory. Tensile (destructive) testing, Humidity, thermal cycling and shock test has been done for qualification of CFRP lay-up. Proper torqueing and Hysol putting has been mentioned in the procedure. Therefore, reliability of mesh gore can be stated as 1.

5. Performance Testing of RRA

During spacecraft level CATF test, spacecraft was biased to align RRA bore sight for X-Band Data Transmitter feed with CATF feed and EIRP (Effective isotropic radiated power) & cross polar isolation measurement was carried out. RRA bore sight for SAR payload feeds also aligned with CATF Feed and SAR Payload measurements were carried out. The performance of X-band SAR and X-Band Data Transmission chain was satisfactory. RRA has gone through thermovac test and dynamic test as well. Tests have been carried out as per test matrix with levels specified in ETLS document. Deployment have been carried out with two configurations, with ribs only and with mesh, repeatability was found satisfactory. Alignment after each deployment has been carried out, initial phase's alignment was done taking 181 RMS points after that 201 RMS points were taken. The results for RMS values were within specification. To find the variability, the measurement of RMS values was plotted on Q-Q plots of normal distribution (Figure 2). The data fits well with normal distribution except for 3 values, two of which on the lower side were caused by changing RMS points from 181 to 201 while one on the higher side is an off value as the RMS value succeeding after that were along the distribution fit. Reliability for alignment is 0.999

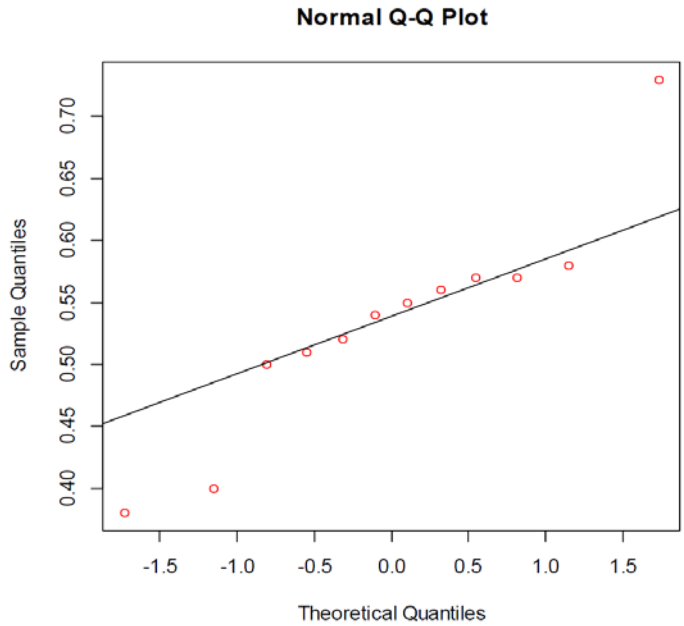

Figure 2: Q-Q plot for normal distribution

6. Reliability of RRA

Reliability block diagram for Radial Rib Antenna is given below. All the subassemblies are in series, two drive modules are in parallel and Overall reliability of RRA is 0.99908.

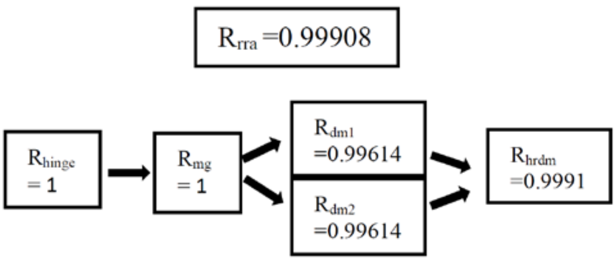

7. Conclusion

As part of the reliability assessment of Radial Rib Antenna Mechanism, Reliability was evaluated using block diagrams, by separating RRA into four subassemblies. The critical components of subassemblies were identified from FMECA. With the tools like stress-strength analysis, time to failure, one-shot failure, reliability of components was found out and sufficient margins of safety was ensured. Estimated reliability for RRA Mechanism is 0.99908.

RRA has undergone various test like CATF, Thermovac and dynamic test which will eliminate unknown modes of failure. After tests, deployment has been carried out to verify proper functioning. RRA has also undergone extensive reviews including detailed design review, critical design review, non-conformance review, pre shipment review etc. to ensure quality throughout realization phase.

8. Acknowledgement

We would like to present our sincere gratitude to Spacecraft Mechanism Group for providing us the data.

We would also like to thank for the support, encouragement and guidance given by Group Director, Reliability and Quality Assurance Group and Deputy Director, Reliability and Quality Area, U. R. Rao Satellite Centre Bangalore.

9. References

[1] Edward B Haugen, Probabilistic Mechanical Design.
[2] Franklin E Fisher, Joy R Fisher, Probability Applications in Mechanical Design (Mechanical Failure Rates for Non-Electronic Reliability- Defense technical Information Centre, USA).
[3] Ministry of defense standard 00-42 Part1, Defense procurement agency UK. Reliability and maintainability (R&M) Assurance activity- Part1: One short devices and systems.
[4] Sujithkumar N, Chandra Shekhar Prasad, Shankar Narayan Y S, Kamesh D. Reliability Assessment of Unfurlable Antenna.
[5] K.C. Kapur, L.R. Lamberson,. Reliability in Engineering.
[6] Kamesh D, S S Patil, Paramjeet Singh, R Arunachalam, H S Ramarao, T S Nanjundaswamy. Reliability assessment of solar sail deployment mechanism.
[7] Dinesh, B V S. FMECA OF RISAT-2B Deployment Mechanisms.

Risk Assessment of Orbital Debris Impact on Spacecraft Mechanism Element

Sachin Barthwal
Reliability & Quality Area
U. R. Rao Satellite Centre
Bangalore

M. P. Singh
Reliability & Quality Area
U. R. Rao Satellite Centre
Bangalore

Shankar Narayan Y S
Reliability & Quality Area
U. R. Rao Satellite Centre
Bangalore

Shanmuga Sundaram N
Reliability & Quality Area
U. R. Rao Satellite Centre
Bangalore

***Abstract* – The man made orbital debris and its continuous growth has become serious concern to satellite mechanism elements and its appendages, manned and unmanned missions. The safety of spacecraft elements against orbital debris can be done either by protecting spacecraft elements or manoeuvring against orbital debris. The action chosen to ensure safety of spacecraft elements depends upon the type of debris, size of debris, time and cost involved in manoeuvring. In this paper, analysis of impact of debris will be discussed on different configuration of mechanism elements. Orbital debris will be analyzed through Orbital Debris Engineering Model (ORDEM-3.0), NASA and same will be used as input to analyze the impact on spacecraft model at different location and orientation.**

Keywords– Orbital debris, Risk Assessment, Ballistic limit equations (BLE)

1. Introduction

Orbital debris is the term for any object in Earth orbit that no longer serves a useful function. These objects include non- operational spacecraft, derelict launch vehicle stages, mission-related debris, and fragmentation debris. In low-Earth orbit, unmanned spacecraft is believed to be impacted by submillimetre-sized debris several times during its operational lifetime. These debris were formed from previous spacecraft missions as well as from naturally occurring meteoroids and pose a serious threat to spacecraft as it can strike the spacecraft with a very high velocity.

In NASA study, the researchers used a second methodology to correlate impacts with orbital debris of various sizes to reported motions of satellites in LEOs. The relative velocity distribution of orbital debris particles, in 800 km nearly polar orbits, varies from approximately 1 km/s to 15 km/s for debris impacting the “side” and “front” of a spacecraft (perpendicular and normal to the velocity vector). Over 50% of impacts between 14 and 15 km/s occur nearly parallel and opposite to the spacecraft velocity vector [1].

This can consequently damage mission critical mechanism elements. Any of these objects can cause harm to an operational spacecraft.

2. Type of orbital debris

Orbital debris objects are categorized into two categories: larger, trackable pieces or smaller, non-trackable particles in orbit about Earth. Debris objects larger than about 10 cm in LEO and larger than about 1 m in GEO are typically tracked by ground-based radar and optical sensor systems.[2] Chances of future collision with another spacecraft or object can be assessed for these trackable orbiting objects. This provides the opportunity for some spacecraft operators to implement orbit-change manoeuvres to avoid a potential collision if assessed risks are deemed to be too high.

Table-I: Type of orbital debris as per size

Size of debris (cm)	Status	Quantity	Risk	Protection method
< 1	non-trackable	Millions	mission degradation or loss	Debris shield
1 to 10	non-trackable	Thousands	Disable or Disrupt a mission	Not available
>10	trackable	Hundreds to thousands	Catastrophic collision	Conjunction assessments and collision avoidance

3. Sources of orbital debris

The sources of orbital debris are given below:

Table -II: Source of orbital debris

Name	Origin
Fragmentation	It consists of pieces of destroyed vehicles (antisatellite (ASAT) tests, upper stage explosions) and fragments dislodged from satellites (paint flakes, pieces of thermal blankets, etc.). about 40 percent of the total.
Nonfunctional spacecraft	These are intact structures that have completed their mission or have had shortened mission life due to a nondestructive malfunction.
Rocket bodies	These are spent upper stages
Mission related items	These include explosive bolts, vehicle shrouds, etc., released during staging and spacecraft separation.

4. Growth in orbital debris

The number of objects being tracked by the Space Surveillance Network (SSN), at any given year during the Space Era. Numbers of satellites and rocket bodies show steady increases. This is increasing with the advent of multiple small satellites being placed into orbit by a single launch vehicle.

While the number of debris pieces also shows a steady increase, several events have occurred that produced sharp increases. Specifically, large increases were observed from the Pegasus and Ariane rocket body explosive events. The largest increases were observed from the Fengyun-1C [3] and Iridium/Cosmos [4] collision events.

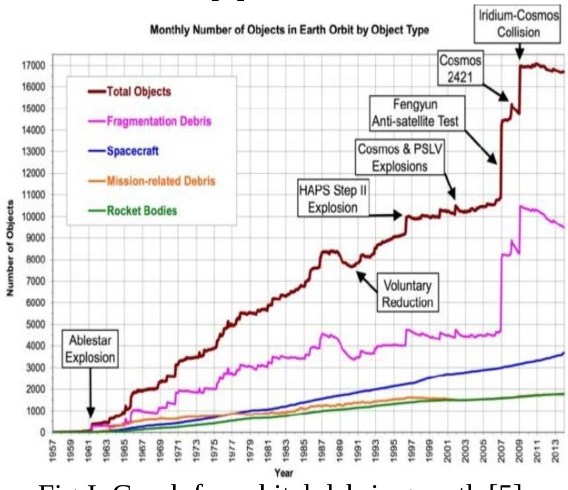

Fig-I: Graph for orbital debris growth [5]

5. Risk assessment methodology

Risk assessment methodology consists of following major parts:

- Debris environment modeling
- Failure/ Damage equations
- Determination of probability of survival

A. Debris Environment Modelling

The limitation of the available database, mainly the non-availability of the characteristics of the small debris objects other than the bigger catalogued ones compels people working in the area of orbital debris to model the on-orbit breakups and the time evolution of the debris environment.

Space debris models are expected to provide a mathematical description of the distribution of objects in space, their orbital characteristics, the flux of objects and the useful physical characteristics of objects such as their size, mass, density, reflection properties. These models can be deterministic in nature wherein each object is described individually by its orbital parameters and physical characteristics, or statistical in nature based on a probabilistic characterization or perhaps even the combination of the above two types.

Two major debris environment models used for debris environment modelling are:

- Orbital Debris Engineering Model-3.0 (ORDEM-3.0), NASA [6]
- Meteoroid and Space Debris Terrestrial Environment Reference Model (MASTER)-2009, ESA [7]

B. Failure/ Damage equations

Ballistic limit equations (BLE) are analytical equations that define the particle size on the threshold of “failure” of the spacecraft system/component and the respective dia. of particle is known as ‘**critical diameter’ (d_c)**. A combination of hypervelocity impact test results and analyses are used to determine the BLEs. Many ballistic limit equations are semi- empirical, combining data from impact tests as well as the results of analytical models or numerical simulations.

C. Determination of probability of survival

Most impacts from meteoroids and space debris will occur on forward-, side-, and space-facing surfaces with the forward-surface defined as the leading surface in the direction of motion of the spacecraft; i.e., the velocity direction or “ram” direction.

The number of impacts (N), from particles larger than a given diameter, increases linearly with exposed area (A), flux (F), and exposure time (T):

$$\mathbf{N = F\,A\,T}$$

where F is the cumulative number of impacts (of a given diameter and larger) per unit area and time.

Once N has been determined, the probability of number impacts occurring in the corresponding time interval is given by Poisson statistics [8]:

$$P_n = \frac{N^n * e^{-N}}{n!}$$

The probability for no impacts, P_0 is thus given by:

$$P_0 = e^{-N}$$

Q, for at least one impact ($Q = 1 - P_0$) is approximately equal to N:

$$Q = 1 - e^{-N} \sim 1 - (1 - N) = N$$

and the probability for no impacts P_0 is:

$$\boldsymbol{P_o} = e^{-N} \sim 1 - N$$

Flowchart for steps to analyses the risk of orbital debris impact on spacecraft is given below

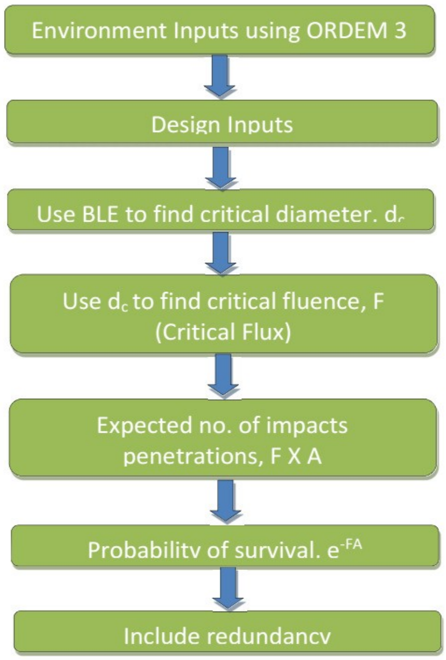

Fig-II: Flow chart to analyses the risk of orbital debris impact on elements of spacecraft

6. Case Study: Computation of Probability of survival for Low Earth orbit satellite

A. Debris environment model:

Inputs: Orbit inputs parameters, Perigee: 760km, Apogee: 760 km, Inclination: 98°, Year of observation: 2021

Outputs: Flux distribution with respect to diameter, azimuth and velocity is obtained.

- Variation of average flux with respect to debris size: It represents the particle flux at specific sizes and larger (i.e., cumulative flux) on a satellite over an orbit
- Variation of Flux with respect to velocity Maximum flux at the altitude of 760km (LEO orbit) exit with velocity ranging from 14km/s to 15km/s.

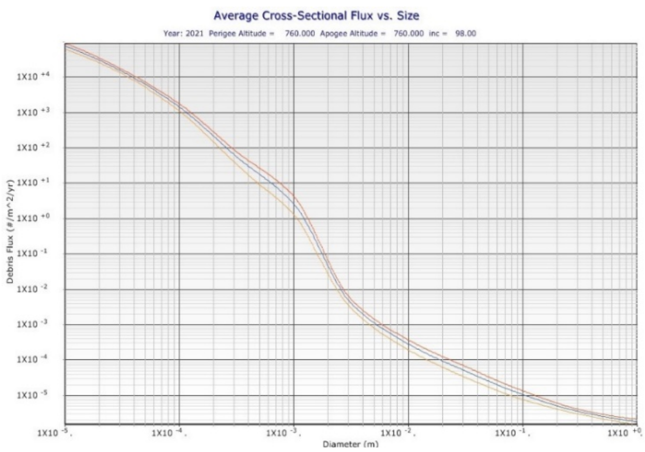

Fig-III: Graph of average flux for LEO with respect to debris diameter for observation year 2021 [6]

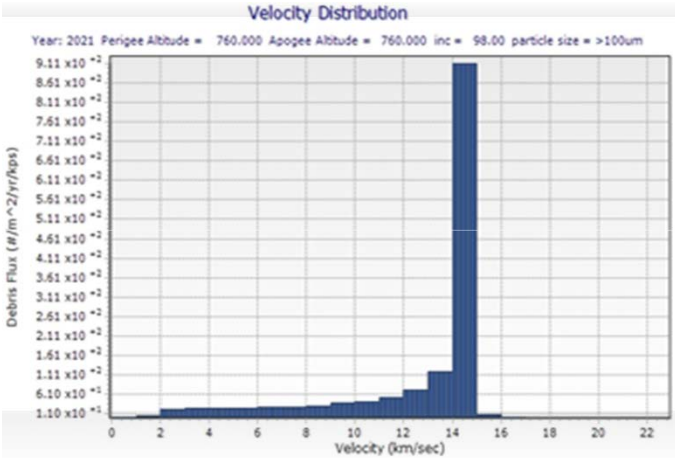

Fig-IV: Graph of average flux with respect to velocity [6]

B. Case Studies for different mechanism element configuration

- **Case-I:** Single wall (Mechanism element with no protection)
  To study the effect of impact of debris on packages outside the panel single wall BLE is considered because the only protection against debris is housing wall.
  Design inputs:
  $\mathbf{K_f}$ = factor allows specifying what type of damage = 1.8 for perforation
  $\mathbf{d_P}$ = Particle (impactor) diameter
  $\mathbf{t_T}$, $\mathbf{t_S}$= Thickness of Target, Back-up wall, Shield = 2.5mm = 0.25 cm
  ρ_t, ρ_p, ρ_s = Density of Target, Particle, Shield = 2.7 g/cm^3
  v= Impact velocity
  α= Impact Angle = 0°
  Area = 10 x 10 cm =100cm^2
  Standard factors [9]
  λ = 1.056, β = 0.519, γ = 0.667, ξ = 0.667, κ = 0.0
  Failure / damage equation [9]

$$d_C = \left[\frac{t}{K} \frac{BHN^{0.25} \left(\frac{\rho_t}{\rho_P}\right)^{0.5}}{5.24 \left(\frac{V\,Cos(\theta)}{C_t}\right)^{\frac{2}{3}}} \right]^{\frac{18}{19}}$$

Critical diameter: Critical diameters (d_c) from velocity of 1km/s to 15km/s are given below

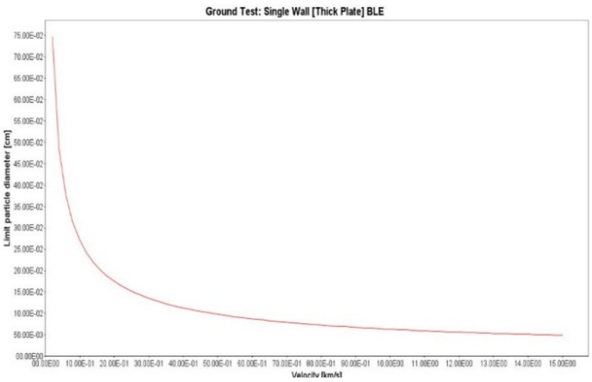

Fig-V: Graph of variation of critical dia with velocity

Probability of survival: Risk assessment for the aluminum of thickness 2.5mm and area 10 * 10 cm

For failure flux of 6.808 /m^2/year and time period of 3 years **[6]**

Critical fluence (F_c) = Flux (F) * Time (T) = 0.2043E+02 / m^2

Expected No. Of Impact = Critical fluence (F_c) X Area (A) = 20.43*0.1*0.1*2 = 0.4086

Probability of survival (P) =

$e^{-\text{expected no. of impact}}$

Probability of survival (P) = $e^{-0.4086}$

Probability of survival (P) = 0.66

- **Case-II Mechanism element made of Honeycomb panel**

  To study the effect of impact of debris on the Mechanism element made of Honeycomb panel & for same double wall BLE is considered

  Standard factors

  λ = 1.056 (v < 3 km/s) & 1.50 (v > 7 km/s)

  β = 0.500

  γ = 0.667 (v < 3 km/s) & 1.00 (v > 7 km/s)

  ξ = 0.667 (v < 3 km/s) & 1.00(v > 7 km/s)

  κ = 0.0

  μ = 1.0 (v < 3 km/s) & 0.0(v > 7 km/s)

  ν = 0.0 (v < 3 km/s) & 0.167(v > 7 km/s)

  δ = 0.0 (v < 3 km/s) & -0.50(v >7 km/s)

  Failure/Damage equation [9]

$$d_{P,lim} = \left[\frac{t_B + K_2 t_s^{\mu} \rho_s^{\nu_2}}{K * \rho_P^{\beta} * \nu^{\gamma} * (Cos\alpha)^{\xi} * \rho_B^{\kappa} * S^{\gamma} * \rho_s^{\nu_1}}\right]^{\frac{1}{\lambda}}$$

Critical diameter: Critical diameters (dc) from velocity of 1km/s to 15km/s are given below

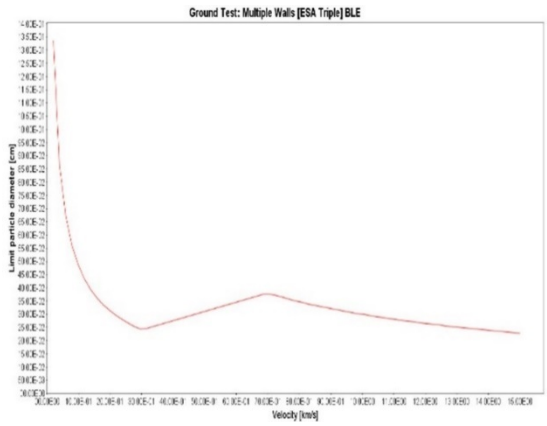

Fig-VI: Graph of variation of critical dia. with velocity

Probability of survival

Risk assessment for the aluminium sheet of thickness 2.5mm and area 10 * 10 cm

For failure flux of 5.615 /m^2/year and time period of 3 years **[6]**

Critical fluence(Fc) = Flux (F) * Time (T) = 16.845/ m^2

Expected No. Of Impact = Critical fluence (Fc) X Area (A) = 16.845 *0.1*0.1*2 = 0.3369

Probability of survival (P) = $e^{-0.3369}$

Probability of survival (P) = 0.71

- **Case-III: Honeycomb panel mounted on mechanism element wall**
  To study the effect of debris on mechanism element mounted with honeycomb panel on outside & for same double wall BLE is considered. The rear wall thickness is considered as sum of spacecraft deck rear sheet thickness plus package wall thickness.

  Design inputs equation Standard factors

  λ = 1.056 & 1.50

  β = 0.500

  γ = 0.667 & 1.00

  ξ = 0.667 & 1.00

  κ = 0.0

  μ = 1.0 & 0.0

  ν = 0.0 & 0.167

  δ = 0.0 & - 0.50

  Failure / damage [9]

$$d_{P,lim} = \left[\frac{t_B + K_2 t_s^{\mu} \rho_s^{\upsilon_2}}{K * \rho_P^{\beta} * v^{\gamma} * (Cos\alpha)^{\xi} * \rho_B^{\kappa} * S^{\gamma} * \rho_s^{\upsilon_1}}\right]^{\frac{1}{\lambda}}$$

Critical diameter: Critical diameters (dc) from velocity of 1km/s to 15km/s are given below

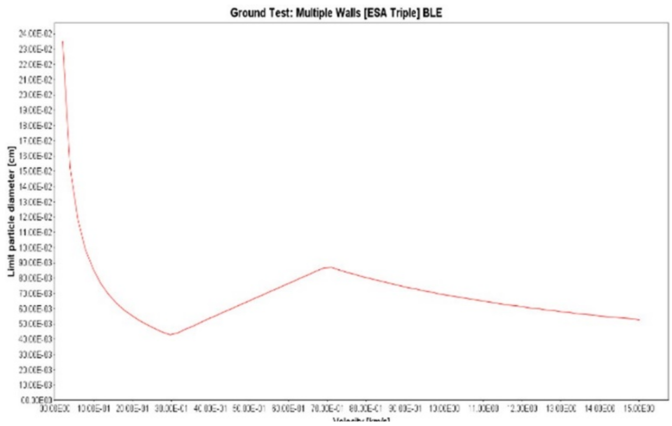

Fig-VII: Ballistic limit curve for aluminium honeycomb

Probability of survival:

Risk assessment for the aluminium sheet of thickness 2.5mm and area 10*10 cm for failure flux of 0.005864 /m^2/year and time period of 3 years.

Table-III: Comparison Probability of survival for different configuration of element with protection

Sl No	Configuration	Failure Flux (/year/ m^2)	Expected No. of impacts (N)	Probability of survival (P)
1	Single wall **Aluminium** mechanism element (2.5mm wall thickness)	13.616	0.4085	0.66
2	Single wall **Magnesium** mechanism element (2.5mm wall thickness)	64.74	1.94	0.143
3	**Aluminium** honeycomb mechanism element (face sheet thickness 0.25mm, core thickness 40mm)	11.23	0.3369	0.71

Sl No	Configuration	Failure Flux (/year/ m^2)	Expected No. of impacts (N)	Probability of survival (P)
4	**Aluminium** Honeycomb mechanism element (face sheet thickness 0.25mm, core thickness 40mm+ 2 mm package base)	0.01172	0.0003518	0.9996
5	**Magnesium** mechanism element mounted inside with Honeycomb (face sheet thickness 0.25mm, core thickness 40mm + 2 mm package base)	0.14	0.0042	0.9957

Critical fluence(Fc)=Flux (F) *Time (T) = 0.01759/ m^2

Expected No. Of Impact=Critical fluence (Fc)*Area (A) = 0.01759*0.1*0.1*2 = 0.00035184

Probability of survival (P) = $e^{-\text{ expected no. of impacts}}$

Probability of survival (P) = $e^{-0.00035184}$

Probability of survival (P)= 0.99

7. Conclusions

Risk analysis methodology for orbital debris impact on mechanism elements in spacecraft is presented. Risk analysis for different configurations (element without any protection and with honeycomb protection) is carried out. Risk analysis for LEO satellite mechanism element is carried out. The following conclusions can be deduced from above study

- The impact flux and failure flux are maximum for the forward-facing element in the velocity direction.
- Element with honeycomb protection have high probability of survival.
- Effectiveness of shielding via Multiple shielding changes with distance between shielding walls. Maximum for a specific range of velocity (e.g. 40mm distance between shielding walls for 0.25mm thick walls for velocity of 15km/s)

8. References

[1] Joel Williamsen, Daniel Pechkis, Asha Balakrishnan, Stephen Ouellette *Characterizing the Orbital Debris Environment Using Satellite Perturbation Anomaly*, First Int'l. Orbital Debris Conf. (2019)

[2] National Research Council. 1995. Orbital Debris: A Technical Assessment. Washington, DC: The National Academies Press. https://doi.org/10.17226/4765.

[3] Carmen Pardini, Luciano Anselmo, *evolution of the debris cloud generated by the fengyun-1c fragmentation event*

[4] Jakhu R.S. (2010) Iridium-Cosmos collision and its implications for space operations. In: Schrogl KU., Rathgeber W., Baranes B., Venet C. (eds) Yearbook on Space Policy 2008/2009. Yearbook on Space Policy. Springer, Vienna. https://doi.org/10.1007/978-3-7091-0318-0_10

[5] Mohammed Chessab Mahdi, Study the Space *Debris Impact in the Early Stages of the Nano-Satellite Design,* Artificial satellites, Vol. 51, No. 4 – 2016 DOI: 10.1515/arsa-2016-0014

[6] NASA Orbital Debris Engineering Model, ORDEM 3.0, https://www.orbitaldebris.jsc.nasa.gov/modeling/engrmodeling.html

[7] Meteoroid and Space Debris Terrestrial Environment Reference Model (MASTER)-2009, ESA, https://sdup.esoc.esa.int/

[8] Klinkrad H., Wegener P., Wiedemann C., Bendisch J., Krag H. (2006) Modeling of the Current Space Debris Environment. In: Space Debris. Springer Praxis Books. Springer, Berlin, Heidelberg . https://doi.org/10.1007/3-540-37674-7_3

[9] Handbook for Designing MMOD Protection, Astromaterials Research and Exploration Science Directorate (KA) Human Exploration Science Office (KX) NASA Johnson Space Center (JSC) January 28, 2009

Qualification and Acceptance of Heavy Drop Platform Assemblies – A Simulated Testing Approach

B K Singh
ADRDE, DRDO
Agra Cantt
bk_singh@adrde.drdo.in

A K Saxena
ADRDE, DRDO
Agra Cantt

***Abstract*—Heavy Drop Systems (HDS) are required by Indian Armed Forces for quick delivery of heavy combat payloads for their combat operations at target areas such as battlefields, training fields, border areas etc. These locations can be inaccessible or accessible with a great difficulty by available means of transport. HDS facilitates the paradrop of such heavy combat payloads using transport aircraft. At present, Indian Air Force operates transport aircrafts of Russian and US origins for Heavy Drop operations. AN-32 & IL-76 transport aircraft are of Russian origin and C130J & C17 transport aircraft are of US make. ADRDE is a pioneer DRDO laboratory, involved in the design, development, production and life extension of HDS. Different versions of HDS for paradrop of 3000-16000 kg weight class military stores have been designed and developed by ADRDE and are under production. AN-32 HDS is used for paradrop of 3000 kg weight class payloads and is under productionization against Users' requirements. P-7 HDS and HDS-16T are used to paradrop 7000 kg and 16000 kg weight class military stores respectively, using IL-76 aircraft and are also under productionization. Naval versions of AN-32 HDS &P-7 HDS, termed as Duck Drop Systems have also been designed and developed and are being used by Indian Navy. Indigenous realization of these heavy drop systems has not only boosted the "Make in India" program of Nation but also has assisted the Users in achieving self-reliance in the area of HDS. HDS comprises of Platform and Parachute Sub-systems. Platform is required for arranging and lashing of paradrop combat payload and for the purpose of mounting of Parachutes in packed condition. Configuration requirements for these Heavy Drop Platforms include a Pallet along with associated mechanical Devices and Accessories, required, for palletization and lashing of payload, guidance of loaded platforms inside aircraft and their locking on aircraft monorail, actuation of parachute sub-system, separation of parachutes from Platform and attenuation of ground impact at ground touchdown, etc. These assemblies of heavy drop platforms, being of unconventional nature in size, shape and functioning, their qualification and acceptance prior to usage, is a challenging task. In several cases, use of existing test facilities and methodologies is not possible for testing of such specific stores. Testing of such customized assemblies and components require customized test fixtures and procedures involving simulation of actual performance parameters. Actual behaviour of these assemblies is simulated by means of evolving assembly-specific test fixtures and procedures and using them on existing test facilities. Few such critical assemblies are Platform Fastening & Release Lock (PFRL), Automatic Disengaging Unit (ADU), Air Shock Absorber Bags, PFRL Lock Engagement Mechanism, Wedge Lock etc. The present paper describes simulated testing approach evolved and used in qualification and acceptance of these assemblies of Heavy Drop Platforms for IL-76 transport aircraft. Qualified and accepted systems are under production and being used by Indian Armed Forces.**

Keywords— Platform; HDS; Load; PFRL; ADU; Fixture

1. Introduction

Indian Armed Forces use different types of heavy combat payloads at various locations throughout the country for their combat operations. These locations can be target areas such as battlefields, training fields, border areas etc. [1]. Many of them are far flung areas, inaccessible or accessible with a great difficulty by available means of transport. The situation becomes critical, when, these combat payloads are required in quick time. Execution of this quick delivery at these locations is facilitated by use of Heavy Drop Systems (HDS), which are used for paradrop of such heavy combat payloads using transport aircraft. Indian Air Force operates transport aircrafts AN-32, IL-76, C130J & C17 of Russian and US origins for Heavy Drop operations.

ADRDE is a pioneer DRDO laboratory, involved in the design, development, productionization and life extension of various types of HDS. In fact, ADRDE is the only institution in the country, which deals with the entire technological gamut of activities related to HDS. Different versions of HDS for paradrop of 3000-16000 kg weight class military stores have been designed and developed by ADRDE and are under production against Users' requirements.

The details are as follows:

- AN-32 HDS
- AN-32 Duck Drop System (Naval Version of AN-32 HDS)
- P-7 HDS for IL-76 Aircraft
- P-7 Duck Drop System (Naval Version of P-7 HDS)
- HDS-16T for IL-76 Aircraft

AN-32 HDS is used for paradrop of 3000 kg weight class payloads using AN-32 Aircraft. P-7 HDS and HDS-16T are used to paradrop 7000 kg and 16000 kg weight class military stores respectively, using IL-76 aircraft. Naval versions of AN-32 HDS & P-7 HDS, termed as Duck Drop Systems have also been designed and developed and are being used by Indian Navy [2]. These HDS are used to paradrop miscellaneous heavy combat payloads/equipment of Indian Armed Forces such as Jeep, Gypsy, LFG Gun, Truck 1 Ton, BMP, Rubberized Boats, Arms & Ammunition etc. Indigenous realization of these HDS has not only boosted the "Make in India" program of Nation but also has assisted the Users in achieving self-reliance in this domain. Heavy Drop Platforms are one such Force Multipliers, which are responsible for enhancing mobility of Armed Forces. The ability of Armed Forces to move towards a military objective quickly has been upgraded by incorporation of these systems. Indigenous HDS have established their **All-Terrain Drop & Drive capability** after conduct of a series of paradrop trials and demonstrations in different terrains.

HDS comprises of two sub-systems : Platform and Parachutes. The present paper throws light upon qualification and acceptance of few Heavy Drop Platform Assemblies of HDS for IL-76 transport aircraft using simulated testing approach.

2. Configuration Of Heavy Drop Platforms

As mentioned earlier, HDS comprises of Platform & Parachutes. In Heavy Drop terminology, Platform and Parachute Sub-systems along with the combat payload to be paradropped are termed as "Load". Fig. 1 depicts one such heavy drop load prepared on HDS-16T Platform for IL-76 Aircraft. [3]

Fig. 1: Heavy Drop Load

Platform Sub-system is meant for arranging and lashing of the combat payload to be paradropped and also for mounting of Parachutes in packed condition. Parachute Sub-system comprises of a number of multistage parachutes with related metallic/textile accessories.

Configuration requirements for these Heavy Drop Platforms include a Pallet along with associated mechanical Devices and Accessories, required, for palletization and lashing of payload, mounting of parachutes, transportation of Load from load preparation site to Airfield, guidance and loading of loaded platforms inside aircraft, locking on aircraft monorail, actuation of parachute sub-system, separation of parachutes from Platform & attenuation of ground impact at ground touchdown etc.

3. Qualification and Acceptance of Heavy Drop Platform Assemblies

The assemblies of heavy drop platforms have been designed and developed based upon configuration requirements mentioned earlier, as design drivers. Since, these assemblies are of unconventional nature in size, shape and functioning, their qualification and acceptance prior to actual usage, is a challenging task. In several cases, use of existing standard test facilities and methodologies is not possible for testing of such specific stores. Testing of such customized assemblies and components require customized test fixtures and procedures involving simulation of actual performance parameters. Furthermore, for qualification and acceptance of many assemblies, actual test conditions involving use of transport aircraft are not possible every time. Considering all these requirements, a simulated testing approach has been evolved for qualification and testing of such specific assemblies, in which, actual behaviour of these assemblies is simulated by means of evolving assembly-specific test fixtures and procedures and using them on existing test facilities. Since, these HDS being airborne stores, their airworthiness certification is obtained through the designated certification agency. Simulated testing of such assemblies is also required for fulfilling certification requirements. Few such significant simulated testings in this regard are as follows:

(i) Load Testing of Pallet Structure Assembly
(ii) Load & Functional Testing of Platform Fastening & Release Lock (PFRL)
(iii) Drop Test of Air Shock Absorber Bags
(iv) Performance Test of Folding Panels & Folding Guide Rollers
(v) Performance Test of PFRL Lock Engagement Mechanism/Tripler Assembly
(vi) Functional Testing of Automatic Disengaging Unit (ADU)
(vii) Aircraft Ground Fixture Test
(viii) Load Testing of Accessories

4. Load Testing of Pallet Structure Assembly

Pallet Structure Assembly is the main load bearing assembly of Platform. It is a welded/riveted metallic structure, made of a number of longitudinal and transverse beams along with top palletization surface (Floor). A number of brackets are mounted on this assembly to fix other assemblies, devices and accessories. This assembly is designed on the basis of opening shock of main parachutes, transferred to this. It is not possible to test this assembly each time with actual dynamic test load conditions. Hence, qualification test procedure for load testing of Pallet Structure Assembly has been evolved, in which, customized hydraulic load test fixtures have been realized for different Pallets to apply the static load, equivalent to dynamic conditions. Earlier dummy weights were used, but this crude procedure was replaced by evolvement of simulated hydraulic load test fixtures, which are unique of their kind. This test fixture comprises of Frame structure to which, Pallet Structure Assembly is connected. The load is applied through Hydraulic Jacks of suitable capacity. Instrumented recording of strains and deformations can also be done using strain gages and LVDTs, placed at suitable locations of Pallet Structure Assembly[4]. Post load test, absence of any type of structural damage in Pallet Structure Assembly is also ensured. Fig. 2 depicts one such test fixture for Load Testing of Pallet Structure Assembly.

Fig 2: Load Testing of Pallet Structure Assembly

5. Load & Functional Testing of PFRL

Platform Fastening & Release Lock (PFRL) Assembly serves to secure the Heavy Loads to the aircraft cargo floor and release it when extractor parachute becomes operative. It also helps in deployment of other parachutes. It is a very critical mechanical device of any HDS.

Hence, 100% of the PFRL are subjected to load & functional testing. Since, these are customized and specific mechanisms, their integration with the UTM was a challenge. To suit the UTM requirements and to simulate the load functioning of PFRL, a customized fixture was realized. This fixture facilitates the proper integration of PFRL with UTM for load testing and functionality of PFRL is also simulated during Load Test. This customized and simulated test procedure simulates the loading condition akin to the Aircraft. Load & Functional Testing of PFRL is shown in Fig. 3.

Fig 3: Load & Functional Testing of PFRL

6. Drop Test of Air Shock Absorber Bags

Air Shock Absorber Bags are used in P-7 HDS and serve to protect the cargo load from any damage at the time of touchdown. When a platform with the payload is dropped from an aircraft, it attains a certain terminal velocity in air. At the time of touchdown, the payload experiences severe ground impact. To reduce the damage resulting due to this impact, air bags are mounted beneath the platform, which act as shock absorbers. Air bags are made of textile, wood and metallic components.

For qualification and acceptance of these bags, it is mandatory to conduct their drop test with proper test load from a height equivalent to the specified terminal speed at ground touchdown. It is not feasible to conduct this test with actual platform and transport aircraft. Hence, to simulate the same, a special fixture for conducting the drop test was evolved. An aluminium module was customized for simulating the performance of a pair of bags. The fixture loaded with the dummy load is lifted up using a crane to the height equivalent to the specified terminal speed. Now, the module is released from this height using a release device. After the drop test, proper condition/integrity of dummy load is to be ensured. The simulated drop test fixture is shown in Fig. 4.

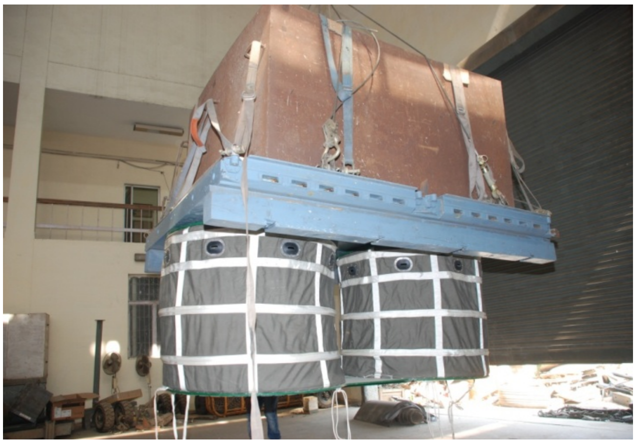

Fig. 4: Drop Test of Air Shock Absorber Bags

7. Performance Test of Folding Panel Assembly & Folding Guide Roller Assembly

Folding Panel Assemblies (one pair) provide movement of P-7 platform on aircraft roller tracks, holding of air shock absorbers in folded positions and prevention of pallet from tilting during its descent phase and landing. Folding Guide Roller Assemblies are fixed in pairs on the front and rear sides of pallet of P-7 platform and serve as a means for fixing pallet to monorail of aircraft and for ensuring its guided movement along the roller tracks during aircraft loading and extraction phases.

These two assemblies are initially in folded condition by release cables, which are connected to Pallet Suspension Frames. As soon as, main parachutes are deployed, these cables are taut and unfold the Folding Panel and Guide Rollers Assemblies. Air bags deploy mid-air out of these Folding Panels and Guide Rollers unfold so as to avoid their damage at ground touchdown. Hence, for ensuring proper deployment of these panels and guide rollers, it is mandatory to conduct the performance test for the same. Scarce availability of IL-76 Aircraft for such test led to evolvement of a simulated performance test procedure, in which, the actual deployment sequence was simulated using an overhead crane. In this simulation, Pallet with all the integrated assemblies is placed on four wooden supports of sufficient height required for unrestricted unfolding of both the Folding panels. Release cables are integrated with Folding panels, Guide Rollers and Suspension Frame assemblies. Pallet is lifted gradually using suitable textile rings/straps with overhead crane. Smooth deployment (unfolding) of all the Folding Panel & Folding Guide Roller Assemblies is ensured. Refer Fig. 5.

Fig. 5: Performance Test of Folding Panel & Folding Guide Roller Assemblies

8. Performance Test of PFRL Lock Engagement Mechanism/ Tripler Assembly

PFRL Lock Engagement Mechanism Assembly used on P-7 HDS serves to disconnect extractor parachute from the pallet when it leaves tilting roller of aircraft. It is installed at front side of pallet. Tripler Assembly performs the same task in HDS-16T.

Since both these assemblies actuate the PFRL for further deployment of other parachutes, their performance test to ensure simultaneous functioning with PFRL is must. The same was simulated at ground using actual Platforms after establishing the required test procedure. For this, Test Assembly is integrated with Pallet Structure Assembly & PFRL Engagement Wire Rope. Other free end of PFRL Engagement Wire Rope is connected to PFRL. The lever of Test Assembly and Lug & Shackle of PFRL are pulled simultaneously to simulate the performance of Test Assembly. Refer Fig. 6.

Fig. 6: Performance Test of PFRL Lock Engagement Mechanism/Tripler Assembly

9. Functional Testing of ADU

Automatic Disengaging Unit (ADU) serves the purpose of detaching the Parachute Sub-system from the Platform Sub-system at the time of touchdown at ground, so as to avoid toppling of the later due to high surface winds at ground. This device is mechanical (HDS-

16T) or pyro-mechanical (P-7 HDS) in nature. This device is actuated by the deployment of main parachutes. The provision of built-in delay for the activation of separation has also been catered. The test challenge in this technology was to measure the delay time period and to ensure positive separation after landing on the ground. The same was simulated using overhead crane for mechanical version and for pyro-mechanical type, firing of used cartridge for providing the delay was simulated at ground. Functional Testing of ADU for P-7 Platform is depicted in Fig. 7.

Fig. 7: Functional Testing of ADU

10. Aircraft Ground Fixture Test

There are specified clearances between different assemblies of Platform and Aircraft Cargo Floor Monorail, as prescribed by the Operators. These clearances are to be ensured during Aircraft fitment prior to conduct of paradrop. During the development of P-7 HDS, a problem was faced to check the fitment of all the platforms inside the aircraft, since; actual A/C was not available each time. To address this issue and to cater the future production requirements, a simulated Cargo Floor Roller Fixture similar to IL-76 A/C Cargo Floor was designed and developed for this test. The fixture is used to ensure smooth rolling movement of loaded platform over the aircraft cargo floor and proper engagement and clearances of mating assemblies w.r.t. Aircraft monorail. Fig. 8 shows one such Aircraft Ground Fixture.

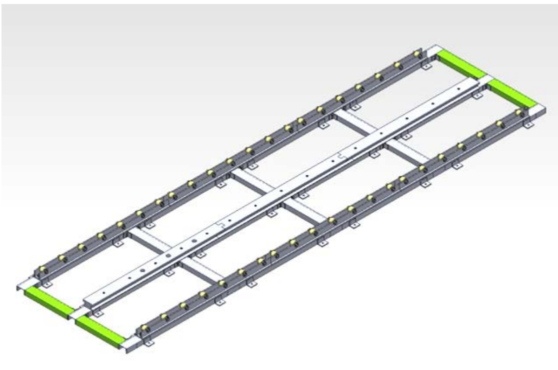

Fig. 8: Aircraft Ground Fixture Test

11. Load Testing of Accessories

Different types of accessories are used to lash the military equipment and cargo on the platform. These accessories include Shackles, Adaptors, Quick Release Fasteners, Wedge Locks, Textile Nets/Straps etc. Wedge Lock is used to connect the tie down cables to shackle. Proof load test of these wedge locks was not possible due to their customized and specific shape. An innovative test procedure was evolved for their load testing, in which, Qty 2 Nos.

Wedge Locks are interconnected using a tie-down cable piece and then this integrated assembly was tested at UTM, facilitating easy fitment of Qty 2 Nos. wedge Locks at UTM along with testing both of them in one go, thereby, reducing the testing effort also. Refer Fig. 9.

Fig. 9: Load Testing of Wedge Lock

12. Conclusion

The present paper describes simulated testing approach evolved and used in qualification and acceptance of assemblies of Heavy Drop Platforms of P-7 HDS & HDS-16T for IL-76 transport aircraft. Qualified and accepted systems are under production and being used by Indian Armed Forces.

This paper provides a glimpse of the efforts made by ADRDE in testing of such customized and specific stores during Project phase. The test procedures and test fixtures innovated during Project execution are being used by the inspection agencies for the qualification and acceptance of production lots of these different types of Heavy Drop Platforms. Surely, this simulated testing approach evolved by ADRDE has simplified the testing/inspection of these assemblies by reducing efforts and in many cases, dispensing with the requirements of aircraft.

13. References

[1] Singh, B K, Development of Heavy Drop Platform (P-7) System for IL-76 Aircraft, DRDO Science Spectrum 2009.

[2] Singh, B K, Development of Platform Sub-system for Heavy Drop System-16T for IL-76 Aircraft, DRDO Technology Spectrum 2016.

[3] Saxena A K & Singh B K, Reconfiguration of Duck Drop Systems/Supply Drop Equipments for Civil Applications, National Conference on Aerial Delivery & Airborne Surveillance Systems (ADASS) 2017, ADRDE, Agra.

[4] Jagat, Manohar Singh; Sharma R K; Saxena A K & Singh B K, Finite Element Analysis of Pallet Structure of Heavy Drop System-16T, Indian Conference on Applied Mechanics (INCAM) 2017, MNNIT, Allahabad.

ARAVIT: Augmented Reality based Aircraft Visual Inspection Trainer

CRS Kumar
Dept of Computer Science and Engineering
Defence Institute of Advanced Technology (DIAT)
Pune
suthikshnkumar@diat.ac.in

***Abstract*—Visual inspection of Aircraft plays a vital role in ensuring the flight safety. It is mandatory to visually inspect every aircraft before takeoff. The well trained staff who can detect the minutest of the faults are crucial to the success of Visual Inspection. In this regard, many new methods of effective training are being developed. Augmented Reality (AR) is one such technology which enhances the training quality through interactive experiences. AR based Aircraft visual inspection Trainer (ARAVIT) is being designed and developed for modern aircrafts. AR with data/ text/ graphics/ animation/ speech/multimedia overlay in real time with the real aircraft images, can enhance the learning experience. The AR devices such as Halolens, Tablet PCs, Smart phones etc can be programmed with training modules. The trainee carries these devices around a real aircraft while learning the techniques of Visual inspection. The trigger images are various aircraft parts, which are recognized by the AR applications. The checklists, animations, graphics, speech etc are incorporated into the AR application to deliver real time learning. The Visual inspection tasks are gamified based on treasure hunt games to make the experience more interesting and engaging.**

Keywords—Augmented Reality; Mixed Reality; Computer Graphics; Visual Inspection; Aircraft Maintenance; Trainer; Checklists

1. Introduction

Visual Inspection of Aircrafts is carried out to ensure the aircraft is in flying condition and free from visible defects. The visual inspectors play a crucial role in ensuring the safety and reliability of the flight of the aircraft [1]. The training of visual inspectors significantly enhances their capabilities to effectively carry out visual inspection tasks.

Importance of Visual Inspection of Aircraft: Detailed and careful Visual Inspection of aircrafts can prevent many catastrophic accidents. There are many instances of errors in inspection which have resulted in air crash [8]. The visual inspection plays a significant role in spotting faults and visual signs of fatigue, cracks, damages etc. Also, the visual inspection can significantly enhance the confidence level of the aircrew and pilot. The good quality visual inspection can provide assurance regarding the flight safety. It can contribute to improved safety and reliability of the flights. For a wide bodied aircraft such as Boeing 747 having a large fuselage, wing span and height, it is almost impossible to inspect the top surfaces of wings or horizontal stabilizer through naked eye. Similarly, AR based system will be helpful in checking the leaks or cracks in the compartments which are difficult to access like the Undercarriage bay. The system will not only be useful for the technicians but also for the pilots as they have to mandatorily carry out visual inspection before taking up any aircraft for flying. This system will help in saving the turn-around time as the externals (visual inspection) can be done much faster.

Training the Maintenance Engineers for Visual Inspection: The training of the Aircraft Technicians and Engineers in carrying out visual inspection is essential to ensure good quality of work [4]. There are many types and makes of aircrafts and they also serve different purpose such as transport, cargo, defence, etc. Also, the aircraft industry is rapidly advancing in adapting new technologies. In this myriad of situations, the effective training of staff to carry out visual inspection can be challenging task. The training can be consisting of theory and practice sessions. The tools and techniques of visual inspection need to be mastered by the staff who are entrusted with these responsibilities.

Current scenario: The visual inspection of aircrafts is manual with engineers trained by experienced professionals. There is also Virtual Reality based training for visual inspectors[1]. Big MNCs such as Airbus have also demonstrated the use of drones for visual inspection of big jet planes. The visual inspection training is customized for specific aircrafts. There may be significant differences in visual inspection procedures for different aircrafts. The visual inspection is a time consuming task which needs to completed with utmost precision. For bigger commercial aircrafts, the time taken for visual inspection may be few hours.

Augmented Reality is a technology that is finding many new applications. With powerful AR devices such as Halolens, SmartEyeglass etc, the users can perceive the real world with augmented information, and multimedia. The AR applications have advanced to the level of recognizing images and patterns in real time and can overlay the multimedia. There are now many tools and SDKs for Augmented Reality application development. Also, Augmented Reality is finding many new applications in Industry, transportation, medical domain, training, construction, maintenance [12] etc.

Augmented Reality enhances the effectiveness of Visual Inspection Training [2]. While the classroom training and practical training can be interactive with the fully qualified trainer, it can further be made effective with AR devices and applications. The AR applications can guide the candidates while training on a real aircraft through providing appropriate multimedia information such as graphics, animation, checklists, remainders, text, audio etc. The AR application ARAVIT, which is designed for the Aircraft Visual inspection training, is presented in this paper. The design and development details, testing methodology etc are discussed in detail. ARAVIT application helps improve the effectiveness of the training while being cost effective, reducing training time, providing interactive training and enhancing the knowledge and skill levels of the trainees.

This paper is structured as follows: In the next section, details about visual inspection of aircrafts are presented. In section 3, the Augmented Reality technology is discussed with details about AR devices, applications, etc. The ARAVIT design and implementation details are presented in Section 4. Results and discussions are articulated in section 5. In section 6, summary and conclusions are presented.

2. Visual Inspection of Aircrafts

Visual Inspection is a regular feature for Aircrafts before they are allowed to take off. The aircraft engineer or trained maintenance staff, closely inspect the aircraft and ensure that there are no visible faults which can be problematic for the flight of the aircraft. The visual inspection may vary for different types of aircrafts and may also be dependent on the age or flying conditions of it. The Visual inspection can be General Visual Inspection (GVI) or detailed visual inspection (DVI), depending upon the need. The human visual inspector is trained to carry out the activity with all his/her senses such as vision, sound, touch and smell. Sometimes, rudimentary instruments may be utilized during the inspection activities. Visual inspection is time bound activity which is to be quick and efficient. The type of defects found during Visual Inspection are : cracks, corrosion, disbanding, burning, leakages, missing components, damages etc. Sometimes the proper closing of doors, inlets and sensors are also checked during visual inspection to ensure that they are in proper condition.

Mistakes during the visual inspection can be minimized with checklists. Checklists are extensively used while carrying out visual inspections. The inspector is expected to closely examine various parts of aircraft and identify missing/damaged parts or components. The checklists are handy and ensure that not even a single check is missed due to human errors. The checklist may vary from aircraft to aircraft and mostly are text based. The checklist may also be modified based on the maintenance record of the specific aircraft.

Regulatory Compliance: The aircraft visual inspection procedures are expected to be compliant with various regulatory authorities such as DGCA, FAA etc. These are mandatory requirements and need to be fulfilled before a flight is permitted to take off.

Visual Inspection reports: The Visual Inspectors are to record their findings and submit the reports. These reports are useful in tracing any problems. They are also useful for Maintenance staff in handling the aircraft repairs. Pilots can also be made aware of condition of the aircraft by the visual inspectors.

Human error: The biggest impediment to success of the visual inspection is the human error[8]. There are many instances of human error which can lead to catastrophic incidents. The errors can be reduced by better prepared and trained staff. The effectiveness of the training plays a critical role in enhancing the accuracy of the visual inspection.

3. Augmented Reality

Augmented Reality (AR) enhances or overlays multimedia such as text/speech/audio/video/animation/graphics on the real time video through AR devices such as Smart Phones, Tablet PCs, Head Mounted Displays (HMDs), Halolens, etc. [5]. The AR devices are able to capture real time images/video/audio through High resolution cameras, sense position and orientation in 3D through MEMs sensors and GPS. The AR Devices also have high performance graphics processing capabilities and in real time recognize the trigger images and overlay programmed graphics and animation. The AR is different from Virtual Reality (VR) where the immersive interactive virtual environments are simulated through VR devices. In the Augmented Reality, the user is perceiving the real images and environment unlike VR where the user is completely blacked out from the real environment into the virtual world.

Halolens 2 by Microsoft is the most exciting AR device development in Augmented Reality [9]. It is a head mounted display with many interesting features. It has various sensors, Display, Camera, processing etc. The following are the detailed specifications of the Halolens 2:

- Display: Uses see through holographic lenses which use eye based rendering
- Sensors: It uses variety of sensors such as head tracking, Eye tracking, Depth, Accelerometer, gyroscope, magnetometer and high resolution camera (8MP).
- Audio and Speech: Uses the microphone array and speakers capable of spatial sound.
- Human and Environment Understanding: It uses hand tracking, Eye tracking, voice for commands, Iris recognition, Spatial mapping, World scale position tracking and mixed reality capture.

- Computer: It has an onboard computer with operating system and high end memory, rechargeable lithium ion battery backup, and WiFi and Bluetooth connectivity.

Sony has also introduced the SmartEyeGlass which is somewhat similar to Halolens. Google has also developed a prototype called google Glass for augmented reality.

A. Augmented Reality Applications

AR has many applications for Medical Surgery, Education, Training, Driving, Navigation, Defence, Games, etc. [3,13]. There are many AR based games such as PokemonGo which have become popular. AR based Medical Surgery and Anatomy are becoming common place. AR aids for pilots and drivers are built into HMDs. Augmented Reality applications have been attributed with many benefits such as:

- Time savings: AR speeds up the data access and provides helpful hints, directions, checklists, remainders etc.
- Error Reduction: AR can aide the personnel in their tasks and ensures the errors are reduced through remainders, cross checks etc.
- Mental workload reduction: As the user need not have to memorize many details and volumes of data are made available through AR application.
- Collaboration: Several AR users can communicate and collaborate through networked application and server.
- Reduction in the cost: AR devices are cost effective and application development is also standardized. The AR applications can enable a well trained professional match the expert while performing their tasks.

B. AR in Training

AR applications have been extensively used in many training programs. Specifically, medical AR applications useful for surgery training, AR applications for Maintenance training are finding popularity. Due to portability of AR devices, the technician or Engineer or Surgeon can easily carry these devices and get assistance in various steps of the work being performed. AR applications have been evaluated for effectiveness in training the personnel and found to be favoured[2, 11]. Better trained personnel are in high demand in aircraft industry due the industry's stringent requirements.

C. AR for Visual Inspection Training

While various technologies such as 3D animation, Virtual Reality [1] have already been tried with success for Aircraft Visual Inspection Training, the AR can be beneficial in many ways. AR devices are nowadays easily available and are inexpensive such as Tabs and Smart phones. Also, powerful programming platforms and SDKs, both commercial and open source for development are now ubiquitous. The AR based training can be carried out on real aircrafts or in the lab. Hence, the practical training imparted is of high value. Also, the log file with recording of the training session can be stored for analysis. The AR application can be utilized for testing the knowledge and skills of the trainee inspector through onsite quizzes and tests. AR applications can also provide instant access to aircraft manuals, reference materials, drawings etc.

As AR technologies are percolating many aspects related to Aircraft maintenance and inspection, the AR based training also provides an opportunity for staff involved in appreciating and understanding the AR better. This step may go a long way in adapting the AR applications to various tasks. The exposure to staff to the AR technology is essential in successful use of these technologies in many different aspects of Aircraft maintenance.

D. Gamification

The Visual Inspection Training can be made more interesting for the participants by gamification. The themes of games such as treasure hunt or capture the flag are utilized. The participants in the game need to discover a particular item/fault while inspecting the aircraft which is purposely hidden from normal view. The winners are the one who discover most of the flags. Also, point based system can be utilized. The ARAVIT can facilitate in scoring and also giving hints for the participants while playing the game.

4. ARAVIT: Implementation

ARAVIT: AR based Aircraft Visual Inspection Trainer (ARAVIT) is developed using Unity3d software. The application is installed on AR devices such as Smart Phones or Tablet PCs. The staff carries this device near the aircraft for inspection. The modules get triggered and function as follows:

- Introductory Module: Brief introduction to aircraft and methodology of inspection. The animation will describe the steps of visual inspection with image of aircraft. It will also highlight important aspects of visual inspection.
- Trigger images: The trigger images are selected for the aircraft, where the staff have to do close inspection. The AR application is trained to recognize the aircraft parts through training module.
- Auras: The auras consist of 3d Animations which demonstrate the various aspects of visual inspection given a particular trigger image. The animations will be superimposed on the real aircraft parts and match the inspection tasks and procedures.
- Checklists: At each stage of the Visual inspection, the appropriate checklists are presented which the trainee keeps filling as and when completing the step. The checklists ensure that the visual inspection is exhaustive and minute details are taken care. The checklists also serve as remainders for the inspector trainees in carrying out their tasks diligently.

Unity3D: Unity3D is a cross platform Game engine supporting development of Animations and AR applications [6]. The C# programming language is utilized in Unity3D for programming. Unity3D supports Google ARCore, Apple ARKit, PTC Vuforia, Microsoft Halolens, Sony Smartglass etc. Unity3D provides a Integrated Development Environment (IDE) for developing the AR application and testing it. Unity3D is highly professional development environment with extensive resources and support.

ARAVIT user interface Design: A set of menus in the user interface enables the user to choose an aircraft among many choices available. The user can navigate to different parts of aircraft. The display also provides text based checklists, typical faults which need to be checked for and online help through expert or documentation. The users get reminders and alarms in case they miss the points in checklists. The user can record their responses; take snapshots for logging, record videos, write notes etc. The zooming facility, contrast and brightness adjustments help the user clearly examine the aircraft. The tasks of inspection which are yet to be completed, percentage of inspection, time spent, list of defects or suspicious instances found can be checked any time during the inspection. The interaction with the application is through gestures, gaze, speech and touch screen.

ARAVIT Server communication: The real time data base update and server logging is enabled by WiFi connectivity of AR device with server. The ARAVIT application updates also can be downloaded to AR devices whenever necessary. The expert communication, AI based assistance, Deep learning modules, Aircraft manuals and images can be located on the server. This offloads the storage requirement for the AR device as it is battery powered, light weight and portable. Also the compute intensive tasks can be carried out at the server and results can be updated at the AR device.

ARAVIT Collaboration: The several trainee inspectors can learn in a co-ordinated fashion. The expert trainer can be located at the server and track the progress of the trainees. Also, communication through messages and commands, speech can be enabled to guide the trainees by the expert. The WiFi enabled AR devices ensure that the trainees can be much far apart from the coach and also from other trainees.

ARAVIT for testing: The testing of the candidates during and after the training is facilitated by the ARAVIT. In these instances, the user's awareness of various procedures, their knowledge and skills can be tested with quiz format inbuilt into the application. The final outcome in terms of grades can be uploaded to the server and grade statements can be generated.

5. Results

The ARAVIT is an application useful for the Aircraft Visual Inspection Training. The ARAVIT is developed on a Windows platform using Unity3D and deployed on an Android Smartphone. The work is in progress to test the application and analyze its impact on training the engineers and technicians.

The Confusion matrix is an important visualization technique that is useful in quantifying the outcome of the training of visual inspectors.

- Confusion Matrix: Following table (Table 1) shows an example confusion matrix for a particular fault which is identified by visual inspection:

Table 1

	Actual Condition		
Visual Inspection Report		***Fault***	***No Fault***
	Fault	**n(TP)**	p (FP)
	No Fault	q(FN)	**m(TN)**

The values n and m are true positives (TP) and true negatives (TN), while p and q are false positives (FP) and false negatives (FN). The improvements due to effective training will contribute to better TP while reducing the FN and FP. The accuracy of the fault detection is improved. The Accuracy (ACC) is defined as follows:

$$ACC = (TP + TN) / (TP + TN + FP + FN)$$

The reported results are presented in Table 2 as follows:

Table 2

	Accuracy	**False Negative**	**False Positive**
Normal Training	ACC1	FN1	FP1
Augmented Reality based Training (ARAVIT)	ACC2	FN2	FP2

The ARAVIT is found to be effective if ACC2 > ACC1, FN2 < FN1 and FP2< FP1. The goal for the ARAVIT application is to enhance accuracy, reduce the false positive rate.

Feedback Analysis: Another approach to evaluate the effectiveness of ARAVIT over the conventional training is feedback. After the training is imparted, the feedback is collected from the participants. The feedback contains questions which help analyze the participants opinion of the benefits or drawbacks of ARAVIT. Also, feedback analysis will help in improving the ARAVIT functions and features.

6. Summary and Conclusion

Aircraft Visual inspection is a critical process which needs highly skilled and experienced staff. The training the inspectors to be highly competent in their visual inspection tasks plays a vital role in flight safety. The latest technologies such as Virtual Reality, Augmented Reality, Artificial Intelligence, Machine learning etc are being incorporated into training modules.

ARAVIT, the AR based Aircraft Visual Inspection Trainer has been presented in this paper. The AR technologies enhance the training effectiveness through their inter-activeness and intuitiveness. ARAVIT is cost effective, reduces training times, improves training effectiveness, and enhances the learning experience. The ARAVIT also makes the process of learning visual inspection tasks an enjoyable and memorable experience through gamification.

7. Acknowledgements

Author thanks Shree Ravi Prasad, Sc G, ADA and Wg Cdr Akshay Saxena, IAF for reviewing the draft of the paper and providing review comments and suggestions for improvements.

8. References

[1] J.Vora et al., Using Virtual Reality for Aircraft Inspection Training: Presence and Comparison Training, Applied Ergonomics (Elsevier), 2002, 33, 559-570. DOI: 10.1016/s0003-6870(02)00039-x

[2] F.De Crescenzio et al., Augmented Reality for Aircraft Maintenance Training and Operations Support, IEEE Computer Graphics and Applications, 2011, 31(1), 96-101. DOI: 10.1109/MCG.2011.4

[3] Schmalstieg, Hollerer, Augmented Reality: Principles & Practice, Pearson Education India, 2016.

[4] H Timothee, Fundamentals of Aircraft Maintenance Management, Notion Press, 2016.

[5] E Pangilinan, S Lukas, V Mohan, Creating Augmented and Virtual Realities: Theory and Practice for Next-Generation Spatial Computing, O'Reily Publishers, 2019.

[6] Jesse Glover, Linowes, Complete Virtual Reality and Augmented Reality Development with Unity: Leverage the power of Unity and become a pro at creating mixed reality applications, Packt Publishing, 2019.

[7] Kroes, Watkins and Delp, Aircraft Maintenance and Repair, Sixth Edition, McGraw Hill International, 1993.

[8] K Latorella, P Prabhu, A Review of Human Error in Aviation Maintenance and Inspection, International Journal of Industrial Ergonomics (Elsevier), 2000, 26, 133-161. DOI: 10.1016/S0169-8141(99)00063-3

[9] Hoover, Melynda, An evaluation of the Microsoft HoloLens for a manufacturing-guided assembly task., Graduate Theses and Dissertations. MS Thesis, Iowa State University, 2018.

[10] Sei Wei Yong, Aun Naa Sung, A Mobile Application of Augmented Reality for Aircraft Maintenance of Fan Cowl Door Opening, International Journal of Computer Network and Information Security (IJCNIS), 2019, 11(6), 38-44. DOI: 10.5815/ijcnis.2019.06.05

[11] M. Sirakaya and E.K. Cakmak, Effects of Augmented Reality on Student Achievement and Self Efficacy in Vocational Education and Training, International Journal for Research in Vocational Education and Training (IJRVET) 2018, 5(1), 1-18, DOI: 10.13152/IJRVET.5.1.1
[12] T. R. Herbert, Impact of Using Augmented Reality for Aircraft Maintenance, MS Thesis, Air Force Institute of Technology, 2019. DOI: AFIT-ENY-MS-19-M-121.
[13] S. Lavelle, Virtual Reality, Cambridge University Press, 2019.
[14] Prathapa A.P., Automated Visual Inspection of Military Aircraft Fuselage with Machine Learning Techniques, MTech Dissertation (supervision by Prof CRS Kumar), Dept of Computer Science and Engineering, DIAT, 2020.

Reliability Estimation of a Power Cartridge

Rishikesh C Badgujar
Armament Research and Development Establishment
Pune
rishikesh.badgujar19@gmail.com

R S Deodhar
Armament Research and Development Establishment
Pune
rsdeodhar@arde.drdo.in

A K Sahu
Armament Research and Development Establishment
Pune

P K Bakshi
Armament Research and Development Establishment
Pune

B A Parate
Armament Research and Development Establishment
Pune

***Abstract* – Power cartridges are used in different mechanisms in a fighter aircraft, such as, seat ejection mechanism for ejecting pilot at the time of emergency, bomb release mechanism, cutting of cable etc. These are one shot explosive devices. Hence, these cartridges are designed for highest reliability standards so as to perform their intended function at a particular time without any failure. Field failure such as leakage of seal, improper burning of propellant, low current may result into improper working of power cartridges. Due to its critical operation in different environment conditions failure of power cartridges may compromise the safety of the pilot as well as aircraft. In view of this reliability of power cartridges become highly essential. In this paper, reliability assessment of specific power cartridge is estimated with the help of test data. Appropriate statistical distributions are identified to fit the collected data. The parameters of the distributions are estimated and used to predict failure probability. The reliability of power cartridges is estimated using the fitted distribution for cold as well as hot conditions. The functional reliability is also calculated using the firings data at 95% confidence level.**

Keywords– Power cartridge, Reliability

Notation:

P_{max}	Maximum Pressure
T_{pmax}	Time to Maximum pressure
β	Shape parameter
θ	Scale parameter
γ	Location parameter

1. Introduction

Power cartridges are used to perform different critical operations in aircraft such as seat ejection of pilot at the time of emergency, release of bomb, cutting of cables etc. These are one shot explosive devices. The cartridge studied in this paper is used in the release mechanism of externally carried store i.e., bombs from parent aircraft. Hence, these cartridges need to be highly reliable.

Reliability is the probability that the system will perform its intended function, at a stated environmental condition without any failure for a given period of time [1]. The study of reliability helps us to understand that how the product or the system will perform at the time of actual working condition. Reliability estimation is the study of reliability which is carried out based on the field data or the testing data. The failure data recorded at the time of testing helps us to identify that how well the system or the product is functioning within the given specification limits. Before the product is released for the customer, the product has to pass through different qualification test fixed by the producer, based on actual field requirement.

Qualification tests such as environmental test, vibration test, thermal shock, ramp test are carried out. The information gathered in the form of data helps to estimate the reliability of the product. Data generated from testing are likely to be more precise than the field data. The statistical analysis of the collected data can lead to the reliability of the product in the specific operating environment. At the time of testing specific number of samples are selected from the entire population. Testing of entire population is not so economical and time consuming.

In this paper we have estimated the reliability of power cartridge based on the testing data. By applying electrical pulse from the power supply of aircraft cartridge gets initiated & generate pressure, that push the piston of the ejector release unit & unlock the externally carried store. For reliable functioning of power cartridges, the critical performance parameters such as maximum pressure $\boldsymbol{P_{max}}$ and time to maximum pressure $\boldsymbol{T_{pmax}}$ are taken into consideration. For this study the data collected during the testing of cartridge in both hot and cold condition is used. The testing data includes $\boldsymbol{P_{max}}$ and $\boldsymbol{T_{pmax}}$ values observed during the testing of 392 cartridges. The acceptable limits for peak pressure are 90 kg/cm^2 to 130 kg/cm^2 and acceptable limit for time to reach maximum pressure are 76 ms to 130 ms. If the value observed for any parameter is outside the acceptable range, it will be considered as a failure. Appropriate statistical distributions are identified to fit the collected data. The parameters of the distributions are estimated and are used to predict failure probability. The reliability of cartridge under consideration, at a given condition is given by equation (1).

$$\boldsymbol{R} = \boldsymbol{P_r}\ (\mathbf{90} < \boldsymbol{P_{max}} < \mathbf{130}) \times \boldsymbol{P_r}\ (\mathbf{76} < \boldsymbol{T_{pmax}} < \mathbf{130}) \tag{1}$$

This paper includes method of estimating the reliability of the power cartridge through testing data.

2. Preliminaries

The analysis of the collected data involves three important steps. These steps are identifying family of the distribution, estimating parameters of the distribution and using the fitted 3 distribution for probability estimation. Different statistical distributions such as Weibull, lognormal, exponential, normal are used in the reliability study. Generally exponential distribution is used for modeling constant failure rate. This is used in reliability analysis of electronic components. It is also used in reliability prediction. Weibull and lognormal distribution is used in reliability analysis of mechanical systems. In this paper we have used Weibull and Lognormal distribution for study of reliability of power cartridges.

A. Weibull distribution

It is one of the most important and useful probability distributions in reliability. The Weibull failure distribution may be used to model both increasing decreasing and constant failure rate. Generally, 3-parameter Weibull distribution is preferred to observe the failure distributions of mechanical components [2].

The probability density function for Weibull distribution is given by equation (2).

$$f(t) = \frac{\beta}{\theta}\left(\frac{T-\gamma}{\theta}\right)^{\beta-1} e^{\left(\frac{\gamma-T}{\theta}\right)^{\beta}} \tag{2}$$

$T \geq 0, \beta > 0, \theta > 0 - \infty < \gamma < \infty$

B. Lognormal Distribution

For the data that are highly skewed or that contain outliers, the normal distribution is generally not appropriate. The lognormal distribution which is related to the normal distribution is often a good choice for these data. Random variable following lognormal distribution always assumes nonnegative values. This distribution is used for modeling stress related failure modes.

If the random variable T, the time to failure has a lognormal distribution, the logarithm of T has normal distribution equation (3).

The probability density function for lognormal distribution is given by equation (3).

$$f(x) = \frac{1}{\sigma x \sqrt{2\pi}} e^{-\left[\frac{1}{2\sigma^2}(\ln x - \mu)^2\right]} \quad \text{if } x > 0 \tag{3}$$

The lognormal distribution has been is one of the good mathematical models for times to failure for electronics and mechanical products, such as bearing. This distribution is also used for modeling stress related failure modes [2].

C. Probability Plot

Probability plot tells us that how well the particular data fits the given distribution. It is important to determine probability distributions that approximately describe that population, Probability plot guides in selecting the distribution which can be used to model the data under consideration [3]. The parameter that should be taken into consideration in probability plots are location parameter, scale parameter and the shape parameter. After plotting the probability plots, the straightness is observed. The correlation coefficients help in selecting appropriate distribution from various probability plots.

D. Estimation of Parameters

After selecting the family of distribution, the parameters are estimated from the observed data. There are various methods of estimating the parameters of the distribution. In this paper maximum likelihood method is utilized. In this method those parameter values are selected which assign maximum probability to the observed data. E) Functional Reliability In case of one shot devices, like the cartridge under consideration, binomial distribution is used during the reliability study. As number of successes change from sample to sample, in general, lower bound of reliability is specified at given confidence level. When r failures are observed during the testing of n one shot devices, the lower bound for reliability at specified confidence level is given by equation (4).

$$R_L = \begin{cases} \dfrac{(n-r)}{(n-r)+(r+1)F_{\alpha,2(r+1),2(n-r)}} & if\ r > 0 \\ \alpha^{1/n} & if\ r = 0 \end{cases} \tag{4}$$

where 100 $(1-\alpha)$% is the confidence level and F is the F-distribution [4]

3. Approach for Reliability Analysis

The test data of 392 power cartridges was available for the analysis. This data is taken from the lot acceptance test of the power cartridge initiator during the last five years. The tests were carried out in two different conditions Hot and Cold. At hot condition 195 number and at cold condition 197 number of cartridges were tested. For hot condition testing the cartridge was kept at 60°C for 06 hrs, while for cold condition the cartridge was kept at −40°C for 06 hrs. The parameters observed were maximum pressure $\boldsymbol{P_{max}}$ and time to reach maximum pressure $\boldsymbol{T_{pmax}}$.

The acceptable limit for peak pressures is within 90 kg/cm^2 to 130 kg/cm^2. The acceptable limits for time to reach maximum pressure are 76 ms to 130 ms. If the value observed for any parameter is outside the acceptable range for that parameter, it would be considered as the failure.

Steps to estimate Reliability of cartridge

(i) Collection of data.
(ii) Identifying a probability distribution for the observed data.
(iii) Estimating the parameters for the selected distribution.
(iv) Calculating reliability i.e., probability that the parameter under consideration will be within acceptable limit.

The reliability of cartridge under consideration, at given condition, is given by equation (1).

4. Analysis and Results

A. Reliability Estimation for Hot Condition

The data obtained during the testing of 195 power cartridges at hot conditions were fitted to various probability distributions. The parameter observed at the time of testing were maximum pressure $\boldsymbol{P_{max}}$ and time to reach maximum pressure $\boldsymbol{T_{pmax}}$.

(i) Analysis of Maximum pressure

The collected data of $pmax$ were used to plot the Histogram. Based on the histogram, it was decided to fit Weibull, 3- parameter Weibull, Normal, and 3- parameter lognormal distribution to this data. Fig 1. shows Histogram of collected data of $\boldsymbol{P_{max}}$.

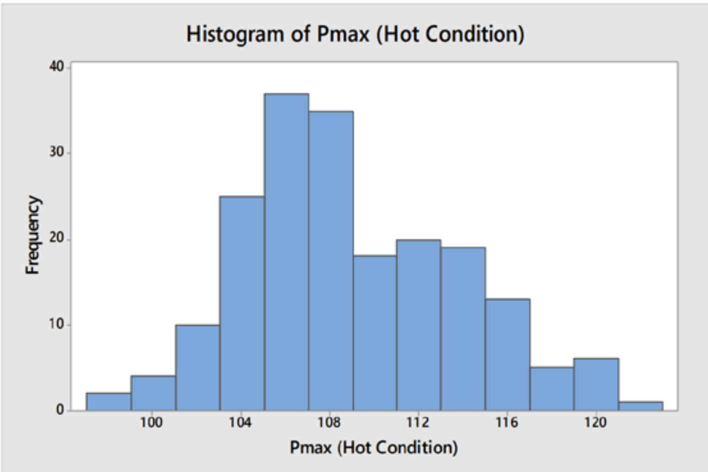

Fig 1. Histogram of $\boldsymbol{P_{max}}$ in case of hot conditioning

The probability plots obtained are shown in Fig 2. Based on the correlation value it was decided to fit 3 – parameter lognormal distribution to this data. The parameters of the distribution are estimated and they are location parameter 3.23796, Scale parameter 0.188192 and shape parameter 82.9805. The 95% confidence bounds for this parameter are shown in Fig 3.

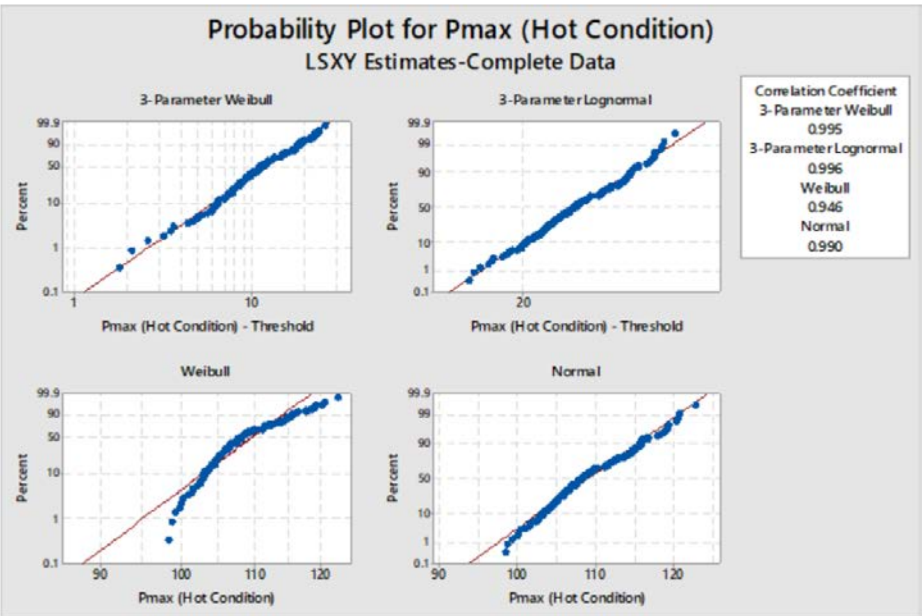

Fig 2. Probability Plots for various distributions fitted to $\boldsymbol{P_{max}}$ data obtained during testing at hot conditions

The probability that for a randomly chosen cartridge initiator $\boldsymbol{P_{max}}$ will be within acceptable limits is area under the probability density function between the limit 90 kg/cm^2 to 130 kg/cm^2 as shown in Fig 4. In this case, this area is 0.9994.

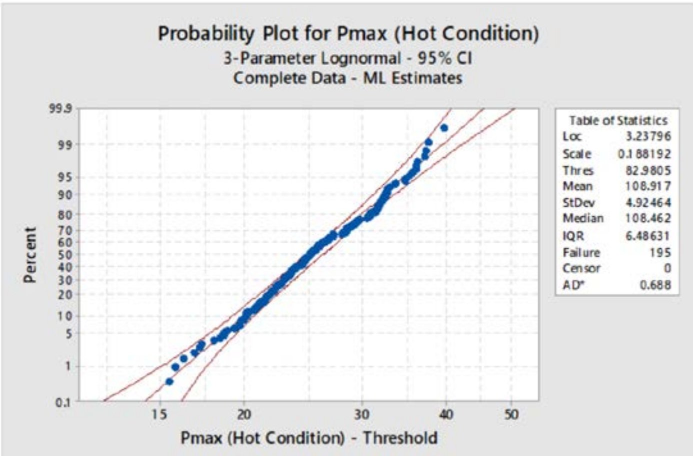

Fig 3. Estimation of parameters for 3-parameter lognormal distribution

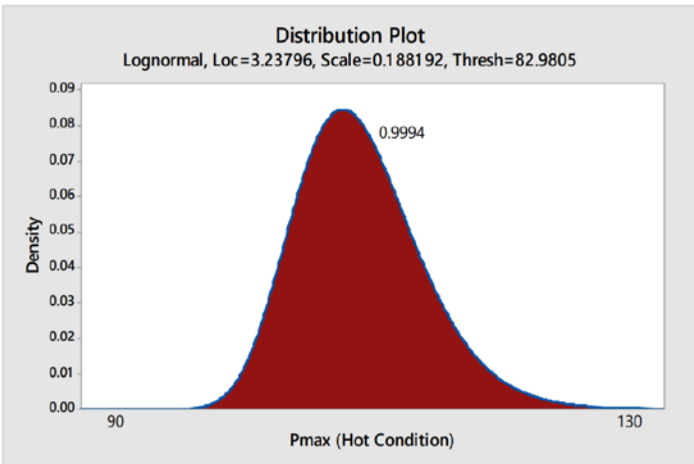

Fig 4. Area under the probability density function between the acceptable limits

(ii) Analysis of time to reach the maximum pressure

As in the case of pressure value, histogram of the time to reach maximum pressure value is obtained and presented in Fig 5. Based on the histogram it was decided to fit normal, Lognormal, 3-parameter lognormal, 3- parameter Weibull distribution to this data. The probability plots obtained are shown in Fig 6.

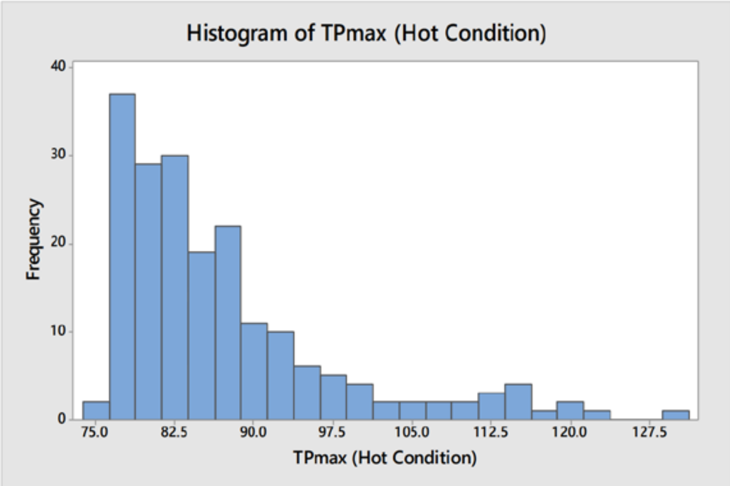

Fig 5. Histogram of T_{pmax} in case of hot conditioning

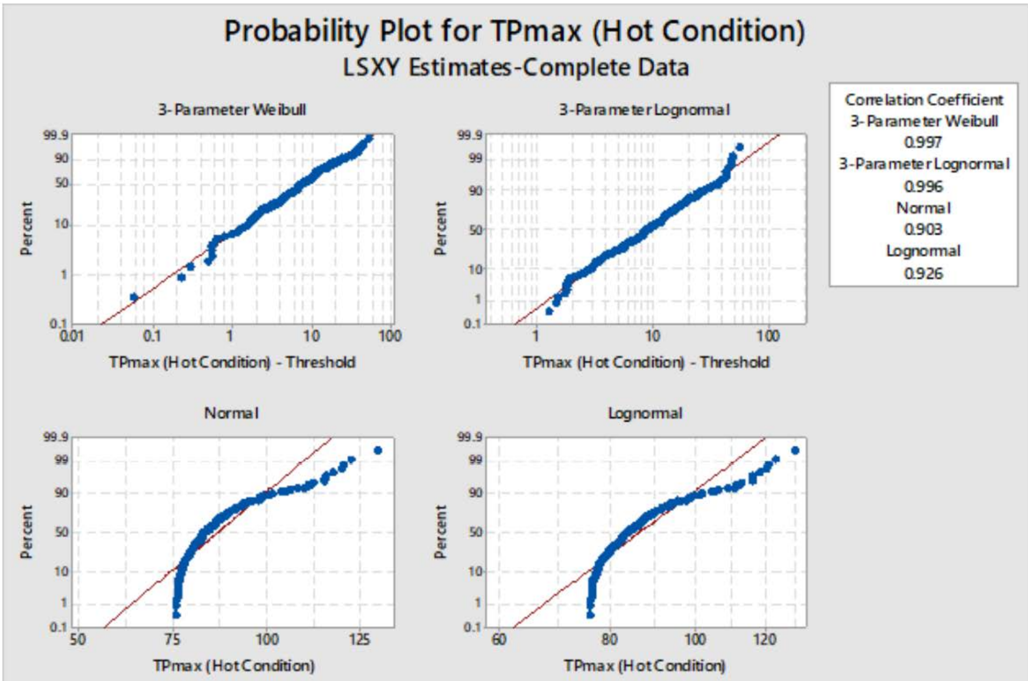

Fig 6. Probability Plots for various distributions fitted to T_{pmax} data obtained during testing at hot conditions

Based on correlation values obtained it was decided to use 3-parameter, Weibull distribution to model the time to reach maximum pressure in hot condition. The estimated parameters of this distribution are shape parameter, scale parameter, and location parameter. The 95% confidence intervals for this distribution is shown in Fig 7.

The area under the curve between 76 ms to 130 ms gives the probability of Time to maximum pressure T_{pmax} value lying in the acceptable limits and is shown in Fig 8. This probability is 0.9943.

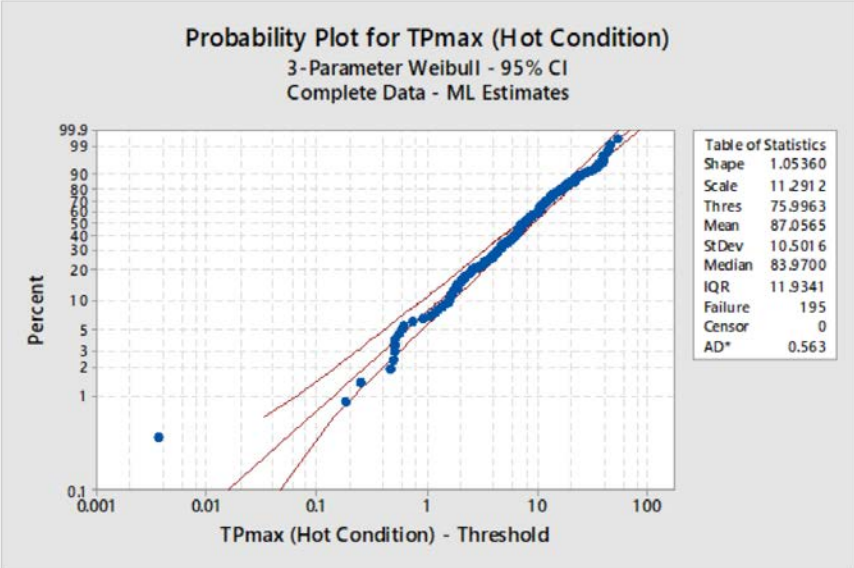

Fig 7. Estimation of parameters for 3-parameter Weibull Distribution

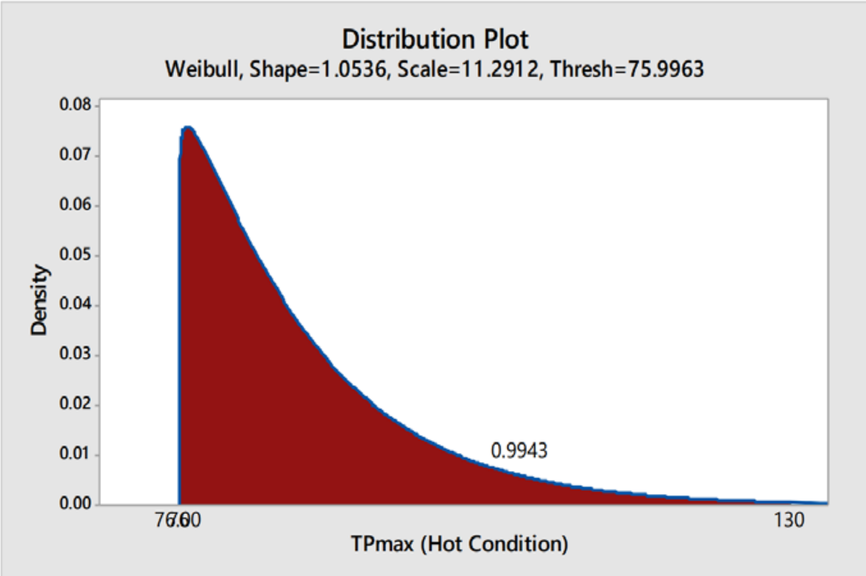

Fig 8. Area under the selected probability density function between the acceptable limits, for $\boldsymbol{T_{pmax}}$ at Hot conditions

From Equation (1) it follows that the reliability of the cartridge under consideration at hot condition is R = 0.9994 × 0.9943 = $\mathbf{0.99370342}$

B. Reliability estimation for cold condition

The data obtained during the testing of the cartridges at cold condition was analyzed in a similar way to obtain the reliability at cold condition. A 3-parameter lognormal distribution was found suitable for the $pmax$ data and 3-parameter Weibull was a good fit for $Tpmax$ data. The parameters were estimated using maximum likelihood method. The probability that for a random cartridge when tested in cold condition, the parameter values will be in the acceptable range is estimated from the fitted distributions. These are shown in Fig 9 and Fig 10. Thus, from Equation (1) it follows that the reliability of the cartridge under consideration at hot condition is R = 0.9999 × 0.9833 = $\mathbf{0.\ 98320}$

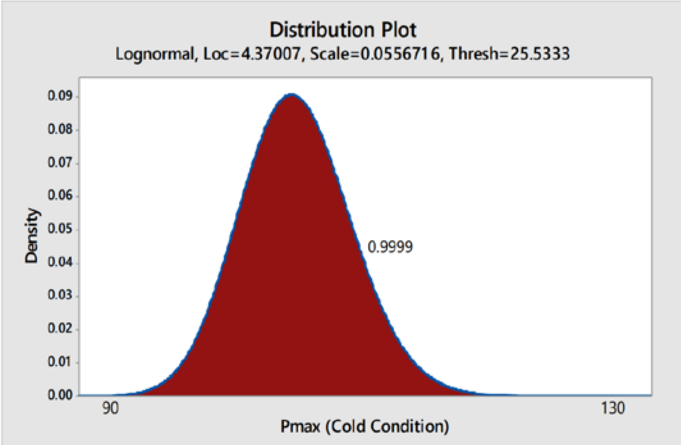

Fig 9. Area under the selected probability density function between the acceptable limits, for maximum pressure at cold condition

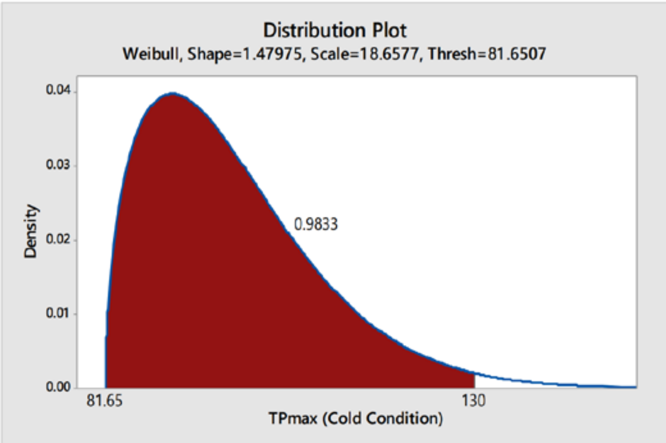

Fig 10. Area under the selected probability density function between the acceptable limits, for $\boldsymbol{T_{pmax}}$ at cold conditions

5. Functional Reliability of Cartridges

In case of one-shot devices, the functional reliability is estimated by conducting n trials and observing number of successes. The lower bound for reliability at 95% confidence level is given by equation (4) by taking α = 0.05. In this case total 392 trials were performed and no failures were observed. Hence from equation (4)

6. Conclusion

The paper presents reliability study of power cartridges. The reliability of power cartridge at hot conditions is 0.9937 while the same at cold condition is 0.98320. In both the cases the observed parameters were maximum pressure and time to reach maximum pressure. If the value of any of these parameters was outside the acceptable range it was considered to be a failure. The functional reliability is also calculated and 95% lower bound was found to 0.992387. This indicates that the power cartridge under study is reliable.

7. References

[1] Charles E Ebeling, An Introduction to Reliability and Maintainability Engineering, 12th Ed, McGraw Hill Education, 2017.

[2] Joel A Nachlas, Reliability Engineering Probabilistic Methods and Maintenance Methods, 2nd Ed., CRC Press, 2016.

[3] William Navidi, Statistics for Engineers and Scientists, 3rd Ed., McGraw Hill, 2011.

[4] Donald W Benbow and Hugh W Broome, The certified Reliability Engineer Handbook, 2 nd Ed., ASQ Quality Press, Milwaukee, 2013

Predictive Maintenance of Engines Using State-of-the-Art Tools and Techniques

Lt Cdr Vijay Raghavendra
Defence Institute of Advanced Technology
Pune

Vinothkumar S
Defence Institute of Advanced Technology
Pune
vinothsudalaimani@gmail.com

CRS Kumar
Defence Institute of Advanced Technology
Pune

***Abstract*—Most of the maintenance is of Planned Preventive Maintenance (PPM) / running hour-based routines. The breakdown or the failure of the system is diverse. For that reason, the condition-based predictive maintenance (CBPM) is considered more appropriate where the system condition can be monitored from the real-time parameters (vibration, temperature, lubricating oil, contaminants, and noise levels), and maintenance is performed based on the need. The system is designed in a way that certain critical parameters are monitored during the operation of the equipment and there is a predefined range in which the parameters should fail. Any deviation from this range is an indication of abnormal behavior which will lead to a failure. Based on this factor, the real-time parameters can be used to predict the health of the equipment. This paper is oriented towards the maintenance of diesel engines, by studying its present maintenance schedule, past defects history, so on and creating a model for predictive maintenance by applying the various Machine Learning tools and techniques. The important aim is to reduce the present turnaround time required for the time-based maintenance of the engines by incorporating the Condition Based Predictive Maintenance technique.**

Keywords—classification, regression, predictive experiment, RUL

1. Introduction

A mathematical model (multiple logistic functions of risk variables to be monitored) for CBPM can be considered to be more appropriate than traditional, time-based preventive maintenance and the system failures always exhibit an exponential nature [1]. The condition maintenance is based on information from real-time data of equipment health monitoring. The developments in health monitoring of mechanical systems are achieved by implementing CBM with an emphasis on various models, algorithms, and technologies for data processing and maintenance decision-making [4]. Remaining Useful Life (RUL) must be estimated from the available sources such as maintenance logs and parameters log book. RUL could be estimated with the help of the recent modeling developments [5]. The reliability of the engine can be enhanced if identification and forecast of the wear-out materials are carried out in the time domain. Proposed SVM model to identify and predict the wear-out fault from the given sample size. Particle swarm analysis PSO and reclusive feature elimination RFE are used to enhance the identification and prediction accuracy. PSO-SVM model could predict more accurately than grid search optimization SVM [2]. Emphasizing the methodology for selecting an optimal Machinery Health Monitoring (MHM) strategy. Features of detectability and prognostic ability are incorporated in a multi-objective maintenance optimization model based on the Markov process and genetic algorithm [3].

2. Model Methodology

The dataset required for supervised learning for various models is created based on actual lubricating oil reports obtained from both basic and advanced analysis. The attributes obtained are listed below.

Sl. No.	Attribute	Limits
01	Viscosity at 40c	(75-114 c)
02	Viscosity at 100c	(12.5-18 c)
03	Viscosity index	> 150
04	Water content	< 0.2
05	Flash point	< 190
06	Base number	>7.5
07	Pour point	____
08	Carbon content	< 3
09	Aluminium, Al	(10-30) ppm
10	Lead, Pb	(40-100) ppm
11	Copper, Cu	(10-50) ppm
12	Chromium, Cr	(10-30) ppm
13	Ferrous, Fe	(100-200) ppm
14	Silicon, Si	(10-30) ppm

From the metal traces, the engine problem can be assessed and correct defect rectification can be carried out.

Sl. No.	Metal Particle	Limits	Engine Problem
01	Aluminium, Al	(10-30) ppm	Piston & Piston thrust Bearing
02	Lead, Pb	(40-100) ppm	Bearing corrosion
03	Copper, Cu	(10-50) ppm	Bearing wear Radiator corrosion
04	Chromium, Cr	(10-30) ppm	Piston ring wear
05	Ferrous, Fe	(100-200) ppm	Wear of cylinder liner Valve and fear train Oil pump Rust in the system
06	Silicon, Si	(10-30) ppm	Dirt Ingression

A. Model Framing

To do predictive maintenance, data that has a time frame is required with the set of readings. The important goal is to ensure the system's limit beyond which the condition fails. Here the two ways of formulating the predictive maintenance are as follows:

(i) Classification approach: this classifies the present condition of the engine whether it is a Healthy state, Observable state, or Failure/faulty state.

(ii)

(iii)Regression approach: this approach predicts cycles and enables us to know the operating cycles before failure. Also called as Remaining Useful Life (RUL)

Root Mean Squared Error (RMSE) = $\sqrt{\frac{1}{n}\sum_{i=i}^{n}(y_i - \hat{y}_i)^2}$

y_i = predicted value
$\hat{y}_i$ = actual value

B. Constraints of Proposed Model

The proposed model has certain constraints as follows:

- The model will not cater for failure prediction during the installation, running in and wear out the face of the system as the failure rates are not constant. Failure is similar to the bath tub curve in these conditions.
- There can be some catastrophic failure due to certain operating conditions in which the predictions can't be made.
- The model will not cater if the working fluid i.e., Lube oil is changed, lube oil 10W40 is used in the engine under consideration.

3. Machine Learning Approach

Using Classifier Learner Application for implementation of Classification algorithms. This application can also be instead of writing classification algorithms. The dataset is trained with the Gaussian Naïve Bayes, Kernel Naïve Bayes and SVM algorithms. After the dataset is assessed, the Principle Compound Analysis is also carried out on the above-mentioned algorithms for further assessment. PCA technique is used to bring strong variation in data and to emphasize any slight variation by reducing dimensionality and increasing the interpretability.

A. Model framing with Azure ML Studio

Creation of Machine Learning Model: The dataset is used for training various classification models that have predefined classes hence supervised learning will be undertaken on the various models

Filter Based Feature Selection: This determines the features of the dataset that are most relevant to the results that we want to predict.

Training a model: one segment of the data will be used to train the model while the other will be used for scoring. “Multiclass Neural Network” algorithm is used. The output of the ‘Train Model’ module is one of the input parameters of the ‘Score model’ module. The scoring model adds a new column to our dataset.

Classification of New Data: The first step is to develop a predictive experiment for the trained models and then deploy a web service for predicting new instances. New data can be entered into the web services and the condition can be predicted.

4. Regression Approach

Using Classifier Learner Application for implementation of Regression algorithms. The dataset is trained with Linear Regression, Robust Linear, and Step Wise Linear and is assessed. Then Principal Compound Analysis is carried out on the above-mentioned algorithms for further assessment.

Assessment of the Linear regression model is done. Out of all the linear regression models RMSE value of Interaction Linear Regression was found to be the least.

Prediction of new dataset: The function should be generated by selecting the regression algorithm that has the least RMSE.

Code for prediction of the new dataset and evaluation.

Model Framing with Azure ML Studio

The dataset required for RUL prediction should be in a time-series format and can be visualized. Choosing and applying the algorithm. As the dataset didn't have any missing values there was no requirement of pre-processing the data and was used to construct various training models for the prediction of RUL.

Analysis of Regression models

Creating RUL predictive Experiment: From the trained model which has a maximum coefficient of determination i.e., Booted decision tree a predictive experiment is created. 'Web service input' and 'web service output' are the segments that are to be added. Input values are all the attributes and output is the predicted value of the pump condition under the "scored labels" column of the 'score model' output.

Web service for the created predictive experiment is deployed and is used for predicting the RUL for new data.

A. Prediction of Remaining Useful Life (RUL)

Parameter 1

When the engine has just finished repair and the lubricating oil is changed. The parameters are in the normal limits and the RUL of the pump should be high. This can be seen from the predictions model which has used Linear Regression for training the data. RUL for the pump is 312 hours.

Parameter 2

The second set of parameters was taken in the mid-time period of the lube oil change as the viscosity of lube oil is decreased and water content is increased. RUL predicted is 185 hours.

Parameter 3

The third set of parameters was taken in the period close to the lube oil change as the viscosity of the lube oil is very less and water content is high. RUL predicted is 14.65 hours.

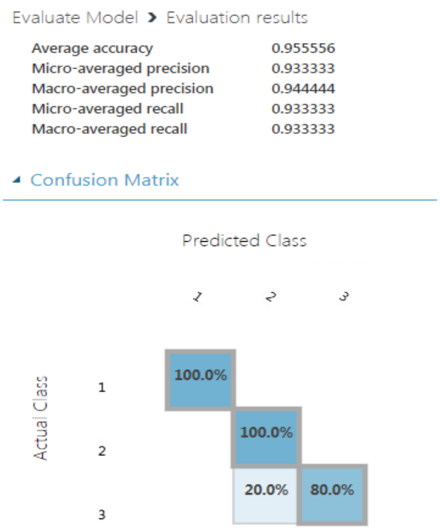

Fig 1: Multi class Neural Network

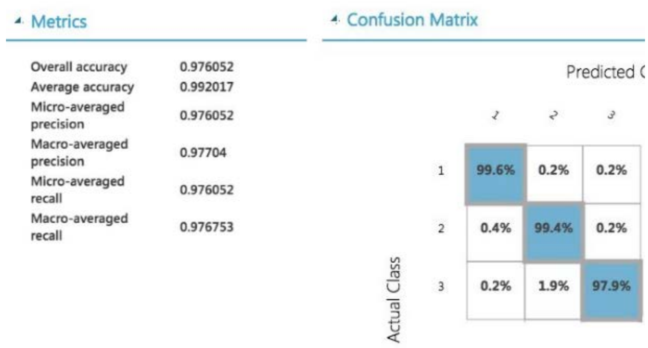

Fig 2: Multi class Decision Jungle

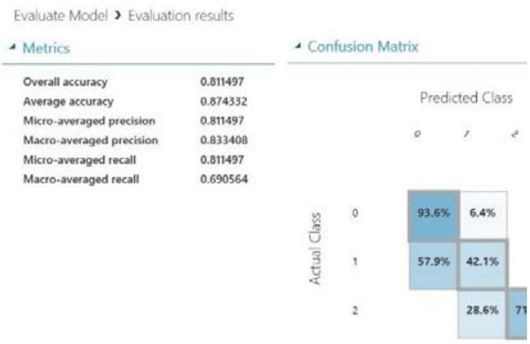

Fig 3: Multi Class Logistic Regression

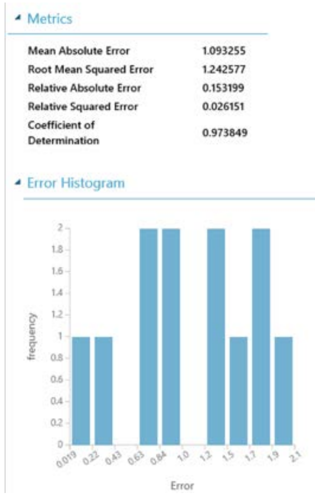

Fig 4: Neutral Regression

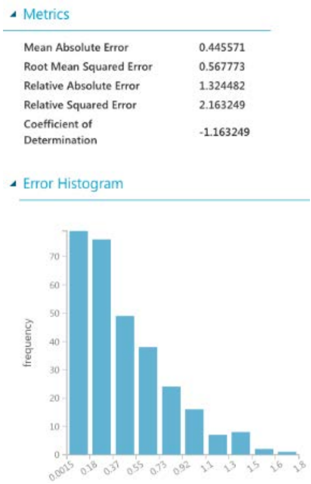

Fig 5: Booted decision tree

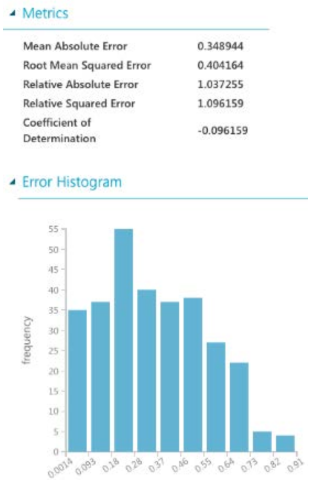

Fig 6: Logistic Regression

5. Comparison of Model's Accuracy

Classification task: Precision and recall can be used to specify the accuracy of the model. Precision means how many percentages of our results are relevant. The recall is the percentage of the results classified by our algorithm which are correct.

PRECISION = TRUE POSITIVE / TRUE POSITIVE + FALSE POSITIVE
RECALL = TRUE POSITIVE / TRUE POSITIVE + FALSE NEGATIVE
ACCURACY = TRUE POSITIVE + TRUE NEGATIVE / TOTAL

In case we recall everything, we would lower or maximize the precision by generating results that are not accurate. The metric which is the harmonic mean of precision and recall is the F1 score.

F1 SCORE = 2 * (PRECISION * RECALL / PRECISION + RECALL)

It can be observed that the classification task using the SVM algorithm in MATLAB has given the highest F1 score of 1.0 and the Multiclass Jungle training model has the highest F1 Score of 0.991 in Azure ML Studio.

Regression task (Predicting RUL): The highest coefficient of determination among the various regression models in Azure ML Studio for the dataset was obtained for Booted Decision Tree with a coefficient of determination of 99.9%.

6. References

[1] Park, Kyung. (1994). Condition-Based Predictive Maintenance by Multiple Logistic Function. Reliability, IEEE Transactions on. 42. 556 - 560. 10.1109/24.273579.

[2] Li, Lei & Chang, Wenbing & Zhou, Shenghan & Xiao, Yiyong. (2017). An identification and prediction model of wear-out fault based on oil monitoring data using the PSO-SVM method. 1-6. 10.1109/RAM.2017.7889670.

[3] Verma, A. & Srividya, A. & Goyal, Alok & Ramesh, P.. (2012). Application of fuzzy logic for selection of Machinery Health Monitoring strategies. 2012 Annual Meeting of the North American Fuzzy Information Processing Society, NAFIPS 2012. 1-6. 10.1109/NAFIPS.2012.6290983.

[4] Zhang, Cheng & Xu, Liqing & Li, Xingwang & Wang, Huiyun. (2018). A Method of Fault Diagnosis for Rotary Equipment Based on Deep Learning. 958-962. 10.1109/PHM-Chongqing.2018.00171.

[5] Jardine, Andrew & Lin, Daming & Banjevic, Dragan. (2006). A review on machinery diagnostics and prognostics implementing condition-based maintenance. Mechanical Systems and Signal Processing. 20. 1483-1510. 10.1016/j.ymssp.2005.09.012.

[6] Si, Xiao-sheng & Wang, Wenbin & hu, Changhua & Zhou, Dong-Hua. (2011). Remaining Useful Life Estimation—A Review on the Statistical Data-Driven Approaches. European Journal of Operational Research. 213. 1-14. 10.1016/j.ejor.2010.11.018.

[7] “Microsoft Azure, Azure ML Studio” https://docs.microsoft.com/en-gb/azure/machine-learning/classic/ create-experiment

Test and Evaluation of Mechanisms

Design and Testing of Dummy Hinge & Hold down Mechanism for the Dynamic Testing of Dual Gridded Reflector

Deepak Kumar Singh
Human Spaceflight Technology Group
Space Application Centre
Ahmedabad
deepak_singh@sac.isro.gov.in

Nitin Kumar
Human Spaceflight Technology Group
Space Application Centre
Ahmedabad

Samir Sakhare
Human Spaceflight Technology Group
Space Application Centre
Ahmedabad

Shashank Saxena
Human Spaceflight Technology Group
Space Application Centre
Ahmedabad

***Abstract*— Communication satellite reflectors usually span larger than the space available inside the payload fairing and are flown in the stowed configuration & they can be deployed in orbit by tele command using appropriate drives on reflector assembly once they reach the orbit. On the reflector antenna assembly, when the drive is actuated, reflector is deployed & pointed into its intended position. The release/deployment of reflector from the stowed condition and positioning the reflector to the required orientation are performed by using hold-down & release and hinge mechanism elements. This paper brings out the similar case of one of the upcoming satellite of Indian Space research organization (ISRO) consisting the Dual Gridded Reflector (DGR) antenna, where an alternate method of the testing of the DGR is proposed without using the actual flight model mechanism elements like Hinges, hold down, yet completely qualifying the DGR. The paper presents the details of design [1,2] philosophy, mechanical design challenges involved in mechanism elements keeping in view the spacecraft requirements meeting all the functional specification laid out. The hardware required for the mechanism elements are realized and tested. A novel concept of using pseudo elements representing the mass, stiffness and Moment of inertia of the actual flight FM elements has been conceptualized and implemented. This Paper also presents the FEM simulation used in realizing the hardware and to validate the simulated and tested results by Environmental test level specification (ETLS) [3] specified dynamic vibration test.**

Keywords—DGR, Hinge, Hold-down.

1. Introduction

2.4 x 2.2 m Dual gridded antenna reflector consist of two reflector shells. The front reflector shell, which is RF transparent, made out of Kevlar fiber reinforced plastic (KFRP) sandwich having Copper gridded Kapton in strip form co cured on the front dish) and rear reflector shell is made of Carbon Fiber reinforced plastic (CFRP). The Front reflector shell connected to the rear shell by a sandwich intercostal (IC) ring and ribs. The bonded regions are further strengthened by Kevlar L-clips. Front Reflector shell is also supported by KFRP Intercostal struts at discrete locations.

In the launch phase, the reflector is stowed against the spacecraft through a pair of hinge and hold down mechanisms as shown in Fig. 1(a). In orbit pyro, devices release the hold-downs and the reflector deployed, and locked in position by suitable mechanisms. Reflector interface definition shown in Fig. 1(b).

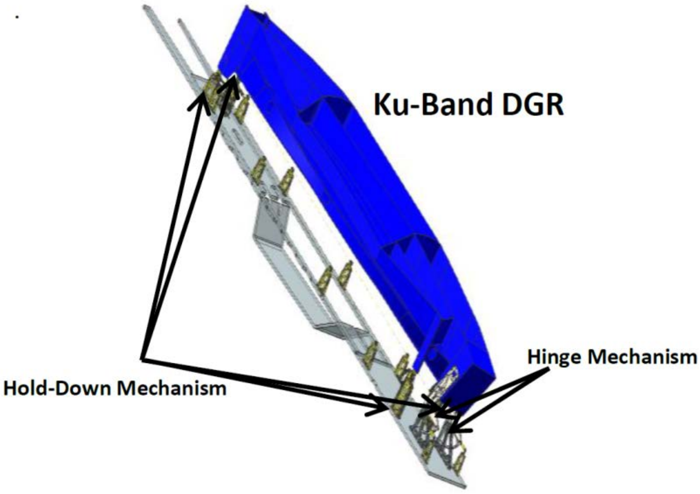

Figure 1(a) Reflector in Stowed Condition with spacecraft panel

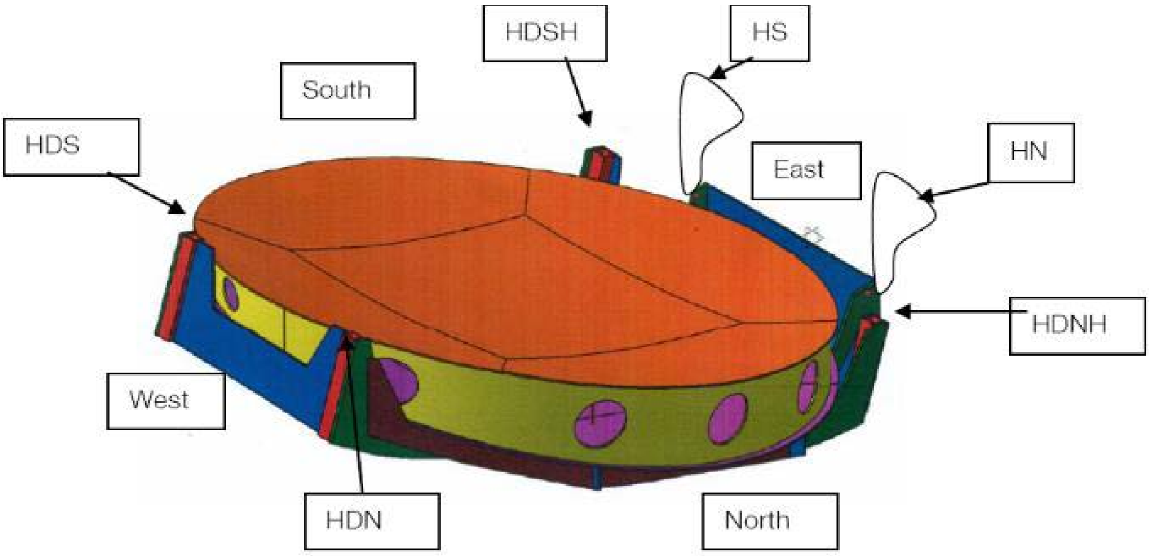

Figure 1(b) Reflector interface definition with spacecraft panel

Abbreviation:

HDN : HOLD DOWN NORTH
HDS : HOLD DOWN SOUTH
HDNH : HOLD DOWN NORTH HINGE
HDSH : HOLD DOWN SOUTH HINGE
HN : HINGE NORTH
HS : HINGE SOUTH

2. Mechnism Configuration and its Stiffness

The reflector has to undergo qualification & acceptance tests on ground using the actual flight mechanism elements hardware. During the development of satellite sub-systems, particularly when the hardware development takes place in many geographically isolated places it becomes necessary to go ahead with the qualification of various individual subsystems by developing flight equivalent hardware to meet the targets. To cater such needs alternate design, substituting the flight models versions, which are robust, simpler, easily realizable at low cost and time is the need of the hour. This will enable meeting the stringent time schedule & eliminate repetitive testing of flight worthy space system.

A. Definition of Boundary Conditions of the mechanism elements is given in Fig. 2.
   - Hold-Down Interface: All DOF's constrained at Separation Plane and at Spacecraft interface locations.
   - Hinge Interface: All DOF's constrained at Inboard Bracket-Spacecraft interface.
   - Tx, Ty and Tz constrained & Rx, Ry, Rz released at North Hinge Bearing Centre.
   - Tx and Ty constrained & Tz, Rx, Ry, Rz released at South Hinge Bearing Centre.

FE model as shown in Fig. 3(a & b) is prepared for FE analysis to carry out to estimate the equivalent stiffness of actual mechanism element. Simplified simulated mathematical model prepared, with hold down & hinge assemblies represented by equivalent stiffness value. These stiffness values as shown in table. 1 is introduced as bush elements at separation plane for hold-downs and at bearing center for hinges. Mass of mechanism elements are lumped at these locations.

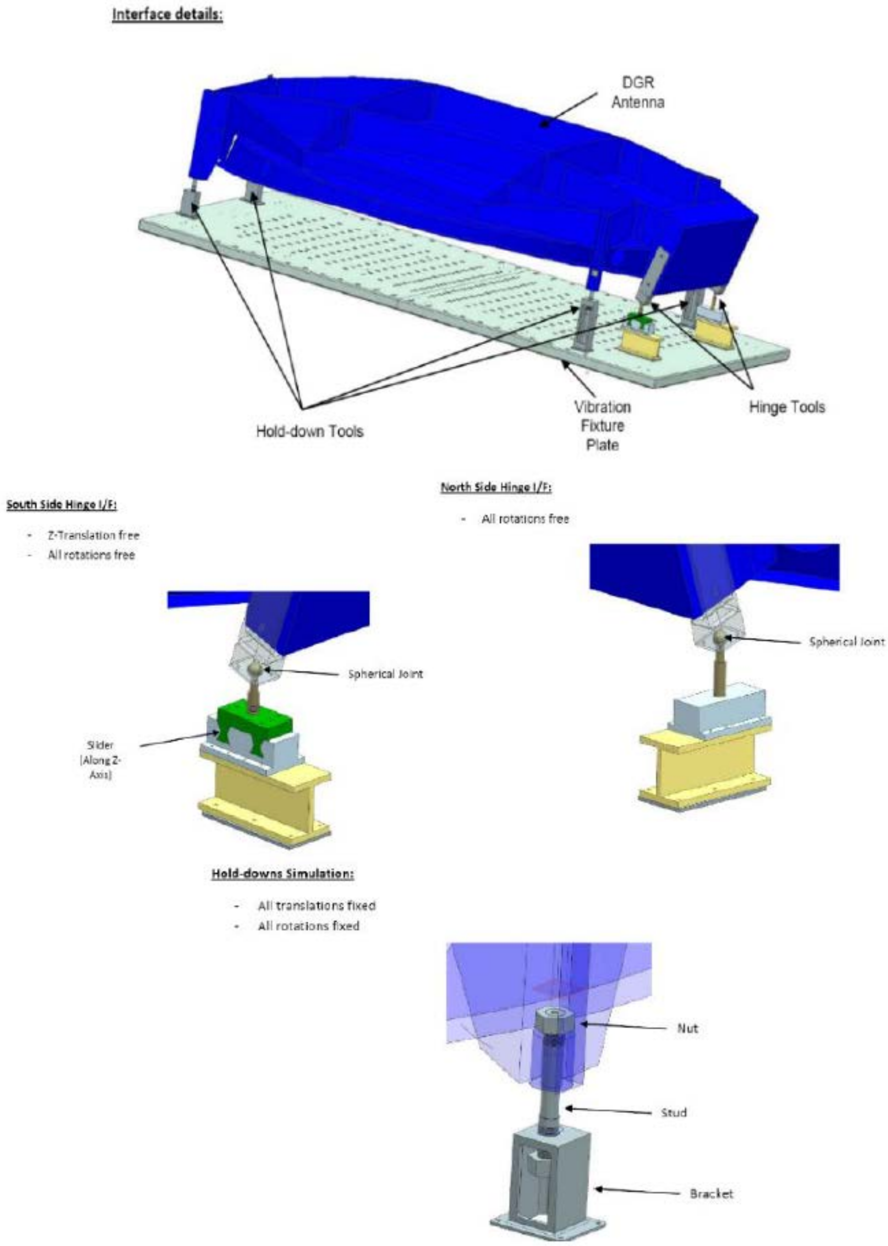

Figure 2, Interface Details& DOF constraint shown for Reflector in Stowed Condition

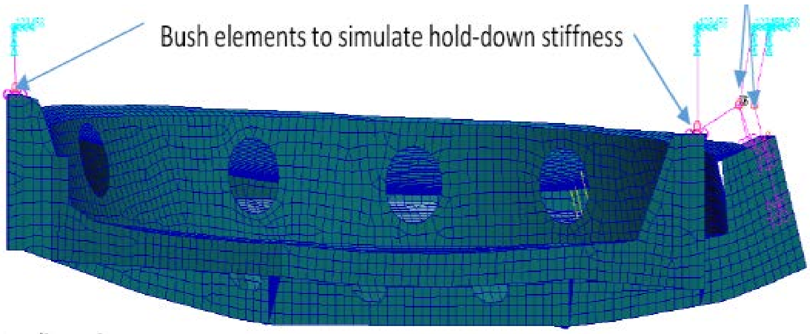

Figure 3(a), Simplified reflector Assembly

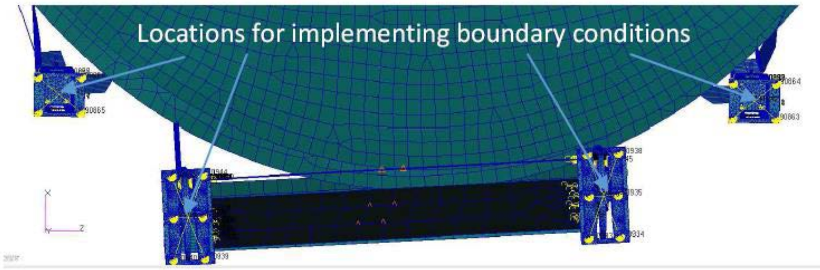

Figure 3(b), Location for Boundary Condition

Table 1: Simulated Stiffness Value of Hinges & Hold-Downs

	Translational stiffness (N/m)			Rotational stiffness (Nm/rad)		
	kx	ky	kz	$k_{\Theta x}$	$k_{\Theta y}$	$k_{\Theta z}$
All 4 Holddowns	2.44e6	1.04e8	2.69e6	7.19e3	6.41e3	7.19e3
North Hinge	5.32e7	4.15e6	1.50e6	0	0	0
South Hinge	5.32e7	4.15e6	0	0	0	0

3. Dummy Mechnism Design

Dummy mechanism designed, simulated and fabricated as per load and boundary condition of actual flight mechanism elements and tested for validation. Table 2 shows mass & stiffness properties of simulated dummy mechanism. The interface details of dummy mechanism are given in Fig. 2. All DOF has constrained at separation plane and at Spacecraft interface been locations for hold down interface. Tx, Ty and Tz constrained & Rx, Ry, Rz released at North Hinge Bearing Centre. Tx and Ty constrained & Tz, Rx, Ry, Rz released at South Hinge Bearing Centre.

Analysis & testing of the dummy mechanism is done as per actual Flight Model and dummy hold down & hinge validated for mechanism equivalent stiffness and load bearing capacity. The static analysis done for 1g load and results shown in Fig. 4.

Table 2: Mass and stiffness properties of Dummy Mechanism

Sl. No.	Component	Mass (Kg)	Stress (MPa) (Von-Mises)	Translation Stiffness (N/m)		
				Kx	Ky	Kz
1	HDN &HDS	0.50	1.02E-2	3.35E7	2.57E8	2.81E8
2	HDNH & HDSH	0.50	1.02E-2	3.35E7	2.57E8	2.81E8
3	North Hinge (Outboard Bracket)	1.04	2.14E-1	6.0E6	3.89E6	6.26E6
4	South Hinge (Outboard Bracket)	1.04	2.14E-1	6.0E6	3.89E6	0.0

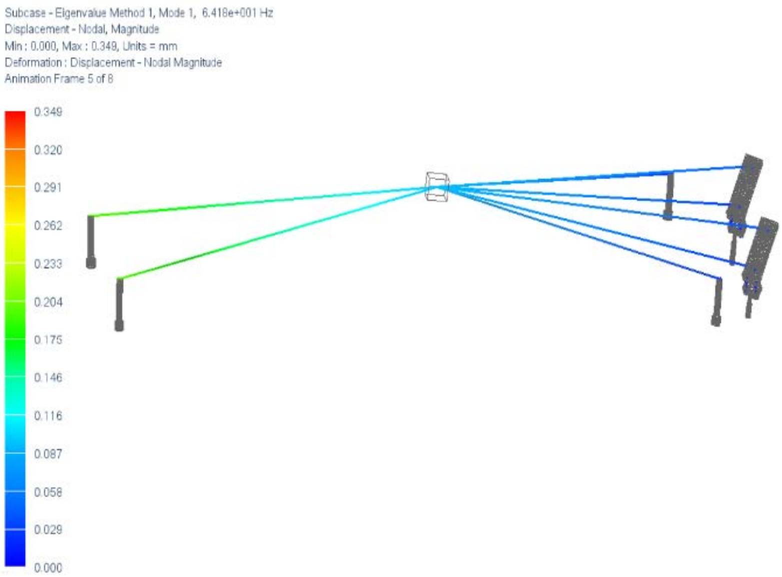

Figure 4: 1'st Mode of Reflector with Dummy Mechanism and Point Mass of 30kg at C.G.

4. Alignement of Dummy Mechncism with Reflector

The alignment of the dummy mechanism done with the Dual Gridded Reflector in slip table with vibration fixture as shown in Fig. 5.

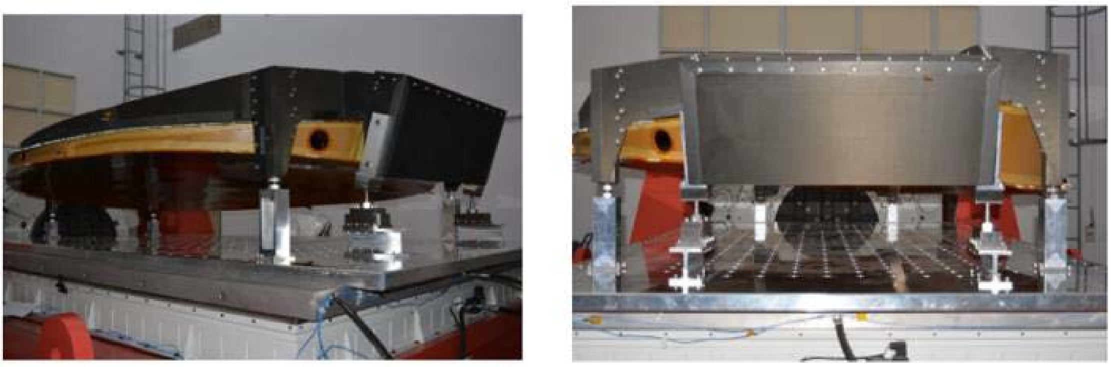

Figure 5: Alignment of Dummy Mechanism with Ku-DGR-I on Fixture Table

5. Testing of Dummy Mechncism and Flight H/W Reflector

Dummy mechanism was vibrated as per proposed plane shown in Fig. 6. Dummy mechanism was qualified for most critical axis, i.e., Z & Y-axis w.r.t. spacecraft coordinate system as shown in fig. 7. First mode of dummy mechanism while simulating Hinge & Hold-down comes 210Hz.

Actual flight H/W testing in vibration fixture is shown in fig. 8. Table 3 presents, simulated and actual frequency comparison of DGR.

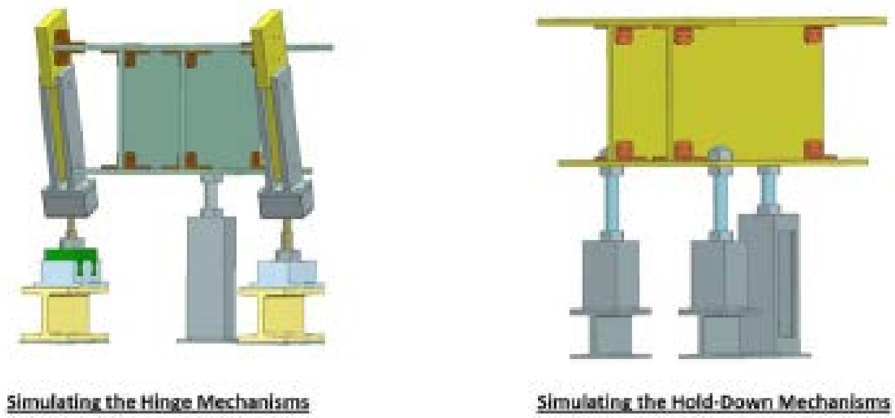

Figure 6: Proposal of Qualifying the Dummy Mechanism

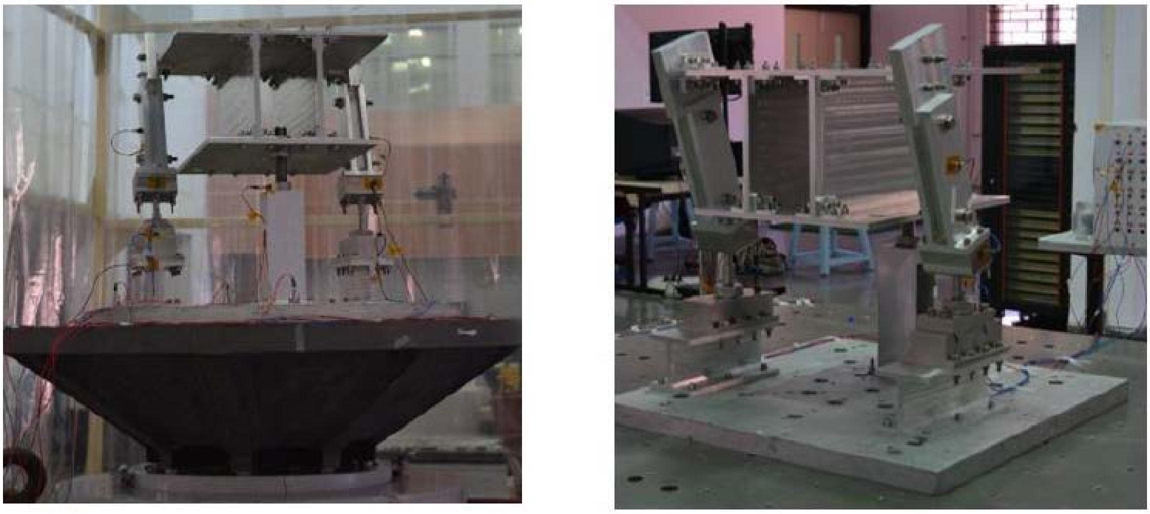

Figure 7: Qualification of Dummy Mechanism in Z- & Y- Axis w.r.t. SCS

6. Results

To meet project schedule on time without compromising capability of actual flight models, an alternate design substituting flight version can be used for validation and testing of FM H/W. Table 3 shows simulated and testing results of DGR. The results thus obtained are presented below.

Table 3: Results Summary of the Vibration Test

Sl. No.	Axis	I/P Level	Min. 'g' level	First Mode Frequency		Quasistatic Load (@ 0db, Full Level)
				FEM Analysis	Vibration Testing	
1.	X-Axis	-3dB	1.95g @58.2 Hz	62.6 Hz	59.92 Hz	25.5g
		0dB	2.16g @57.6 Hz			
2.	Y-axis	-3dB	4.08g @ 49.81Hz	52.7 Hz	54.2 Hz	25.1g
		0dB	3.78g @52.2Hz & 1.74g @90Hz			
3.	Z-axis	-3dB	3.28g @57 Hz	50.8 Hz	49.74 Hz	20.2g
		0dB	4.17g @59Hz			

7. Conclusion

It is validated that dummy mechanism was well equipped for replacing actual Flight model mechanism. 1st mode of dummy mechanism comes 210Hz and simulated 1st mode of reflector comes to 60Hz. The actual flight model mechanism element could be made available before starting structural test. Therefore, DGR was tested with actual FM mechanism elements. After testing it was found that the results were closely matching with FE simulation which was done for dummy mechanism. It can be concluded that dummy mechanism would have served purpose in absence of actual mechanism hardware. The realized dummy mechanism is preserved so that it can be utilized for qualification of similar DGR in future.

8. References

[1] The Shock Absorber Handbook, John C. Dixon, John Wiley & Sons.
[2] Engineering Dynamics, Meriam and Craige, John Wiley & Sons.
[3] Textbook of Machine Design by Shigley
[4] Environmental Test Level Specifications, ETLC Doc No: ISRO-ISACST-0124

Simulated Wind Survivability Test for a Launch Vehicle Payload Cooling Umbilical

Vikas Kumar Agrawal
Aerospace Mechanisms Group
ISRO
Thiruvananthapuram
agrawal_vk@vssc.gov.in

M.Gopakumar
Aerospace Mechanisms Group
ISRO
Thiruvananthapuram

Damodaran P
Aerospace Mechanisms Group
ISRO
Thiruvananthapuram

***Abstract*— Launch pads are mostly situated at the sea shore side, where higher wind velocities are observed. Payload cooling umbilical system is used for maintaining cool and clean environment for spacecraft in launch vehicles. Design of the system should be robust under such extreme conditions. Payload cooling umbilicals are connected to launch vehicle using a separable mechanism to enable the disconnection during lift-off. Higher wind velocity at launch pad develops an end tension on the mechanism which tries to pull out the mechanism from launch vehicle. Therefore, mechanism design should have sufficient pull out load capability to avoid inadvertent disconnection. This paper describes the experimental method used for simulating the launch pad conditions on ground for a maximum wind velocity and pull out load test. Wind load was simulated by applying uniformly distributed normal load (corresponding to maximum wind velocity with gust factor, load factor and a minimum margin) on the pressurized cooling hose to generate the end axial tension. Axial tension on the mechanism due to wind load was estimated both by analytically and experimentally. Mechanism pull out load capability is also verified throught separate tests.The results shows that the system is having sufficient structural margin and design is robust. With the above mentioned tests, the system was structurally qualified for flight applications.**

Keywords—PCU, Wind velocity, Full scale test, Gust factor, Load factor

Nomenclature:

PCU	Payload cooling umbilical
PLF	Payload fairing
UT	Umbilical tower

1. Introduction

Payload fairing (PLF) protects the spacecraft during the aerodynamic ascent phase from aerodynamic loads and heating. During the ground operation till liftoff, Payload cooling umbilical (PCU) system maintain the temperature inside the PLF within acceptable levels. PCU system provides a flexible link between the payload fairing (PLF) and umbilical mast for the passage of cool and clean air to the spacecraft and avionics packages inside PLF (Figure 1). This cool air takes away the heat generated by the spacecraft packages and escapes through the vent holes provided in the payload fairing. The system mainly consists of a vehicle half assembly, ground half assembly, release mechanism assembly, a flexible hose and a compensator.

Ground half assembly, release mechanism assembly and vehicle half assembly together make the mechanism which is assembled on the payload fairing. Compensator is assembled on the umbilical tower and allows expansion and contraction of hose by bellow action and thus prevent unwanted load acting on mechanism due to hose movement. Flexible hose connect the mechanism to the compensator and supplies cool and clean air to PLF compartment (Figure 1).The umbilical system gets disconnected from the vehicle during lift off by pull force exerted by a traction lanyard. The opening in the payload fairing gets closed by vehicle half which has a shutter that closes by action of two spring-loaded clamps.

Figure 1: Payload cooling umbilical system with cooling hose

Launch pads are situated at the sea shore side, where very high wind velocity are observed. Therefore, structural requirement for the payload cooling umbilical system is that it should be capable of withstanding the load corresponding to maximum wind velocity.

This paper describes the experimental analysis which explains wind load calculation, test setup, and available margin on the system.

2. Working principle of payload cooling umbilical

Ground half is mated with the vehicle half at two locations through clamp and pin arrangement, on the top by means of a wedge and at bottom by removable cam, against jettisoning spring load. In the assembled condition of the vehicle and ground halves a spring loaded clamp of the release mechanism presses the cam against the release pin arresting the movement of the cam. On releasing the pin, cam is free to move and there by the ground half gets unlocked. In case the pin does not get released first, as the cable attains required tension, the clamp gets released, this also unlocks both the halves and separation takes place.

The axial load due to wind load acting on the cooling hose is resisted by the wedge and cam clamp. Spacer plates are provided between housing and ring to increase the reaction force between Cam clamp and cam. This will increase the frictional force which act as a resistance against sliding of the cam clamp.

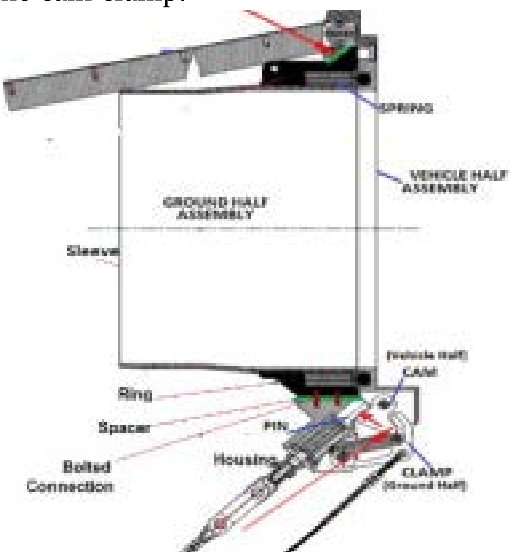

Figure 2: Payload cooling umbilical assembly Configuration

From the fig 2 it is clear that during wind load due to rotation of cam clamp, direction of reaction force changes and opening moment overcomes the closing moment provided by friction force; resulting in separation of ground half from the vehicle half.

3. Background of qualification test

During development and qualification test for a cooling duct system for a launch pad in which distance between vehicle and umbilical tower is ≈10m, simulated wind survivability test was carried out by using blowers. But higher wind velocities could not be achieved. To study the behaviour under oscillating condition, an oscillation test was conducted for 2hours by connecting the hose to an oscillating mechanism. The behaviour of hose under simulated wind condition was studied from the observations. It was seen that the hose deflected from the mean position and the compensator extended from the zero position. The sag was measured at the centre of the hose with respect to the end connections. The end connections and all joints were intact after the test. After the wind survivability test, a functional release test was successfully conducted on the mechanism with the blowers on and with retention cable load, hose & thermal insulation.

The survivability of the entire system has to be tested under high wind conditions. The interface for vehicle half and compensator assembly were made on a steel structure at 3m height. The test was conducted for 280hrs continuously .The hose was seen bending in the direction of wind and the ompensator also extended from the zero position. The hose was pressurized from a gas cylinder and the leak rate was compensated. The system withstood the wind conditions successfully.

It was decided that a minimum margin of 0.2 shall be demonstrated on on Payload cooling umbilical system considering the wind velocity of 30m/s with gust factor of 1.4 and load factor of 1.25.

4. Estimation of wind load

Aerodynamic force on the hose of payload cooling umbilical system is calculated below.

Length of the hose facing wind, L=10.4 m
Max wind velocity, V =30 m/s
Density of air, þ =1.169 kg/m^3
Dynamic pressure, q = þV^2/2=526 Pa
Aero force coefficient, dCo/dx =5.01 per m (Upper bound for smooth surface, Re<1 million)
Reference area, S =0.0491 m^2
Aero force, F=q*S*dCo/dx*L =1345 N

Considering load augmentation due to vortex shedding (Gust factor=1.4)
The total limit force on hose=1345 x 1.4=1884 N≈2000 N

When load factor of 1.25 and 0.2 margin is taking into consideration [2], the total normal load acting on hose=2000x1.25x0.2=3000 N This load can be applied as uniformly distributed load (UDL) on the hose. The length of the cooling hose is 11 m.

From catenary equation, we get tension at end (T) = $\frac{W\,L^2}{8\;y}$

Where, w =weight per unit length = (3000/11) N/m
L =Length of hose = 11 m
y =Sag at centre =1.05 m

Substituting these values in the above equation, Tensile/pull load on the mechanism based on catenary equation is 4000N (Figure 3).

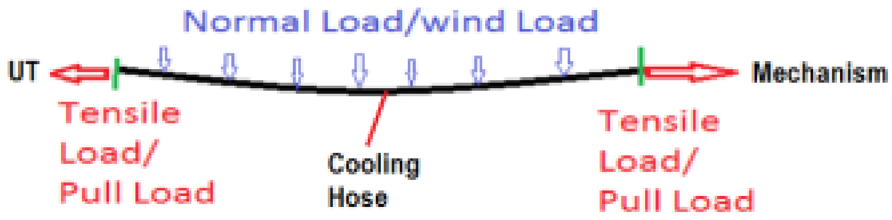

Figure 3: Tension at End due to wind load

Two independent tests were carried out to assess the system capability & to demonstrate margin.

(i) Mechanism level pull test with tensile load of 4000 N applied on hose to check the adequacy of mechanism clamping force of 4000 N to have adequate margin against the estimated wind load.

(ii) Full scale load test on the payload cooling umbilical system simulating the launch pad conditions.

5. Mechanism level pull load test

The effect of wind load will act on the cooling hose as UDL and it will generate an axial load on the mechanism. So, the system has to withstand this axial load due to wind load by clamping force. Corresponding to a normal load of 3000N acting on the cooling hose the tensile/pull load on the mechanism based on catenary equation is 4000N. Ideally the mechanism should be structurally integral for an axial load of 4000N. The clamping force of the mechanism can be increased by increasing the thickness of the spacer used for adjusting the release load of the system Mechanism level pull test was conducted with varying the spacer thickens for obtaining the required clamping force and to get the pull-out load of mechanism for various spacer thickness.

A. Test set up for pull load test

- The mechanism was assembled to a fixture mounted on the floor.
- Cooling hose was assembled to the ground half as in-flight condition
- Vertical/pull load was applied on the UT side of the cooling hose under pressurized condition by a crane through a crane balance (Figure 4)

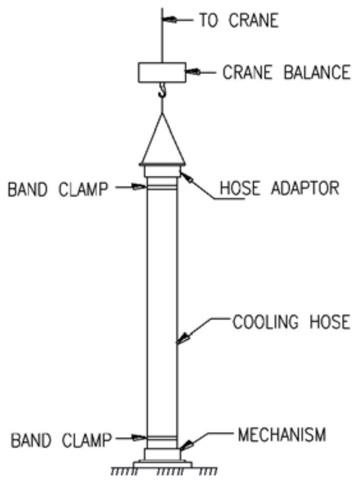

Figure 4: Pull load test setup

B. Test results of pull load test

The load at which the ground half releases from the vehicle half was noted for varying thickness of spacer plate and the test results are shown in Table 1.

Table 1

Spacer thickness, mm	Trial	Pull load value, N
X1	1	3450
	2	3680
X2	1	3900
	2	4200
X3	1	4320
	2	4530

For each thickness of the spacer two trials were carried out. Test results shows that increasing the spacer thickness will increase the pull load. By increasing spacer thickness, the pull load values achieved were more than 4000N.

6. Full scale wind load simulation test

To assess the system capability & to demonstrate margin on the system a wind load simulation test was conducted. Wind load and self-weight of the cooling hose are acting as UDL. Wind load on the hose has to be applied in horizontal plane as UDL. As a worst-case loading, wind load was applied in the vertical plane. Axial load acting on the mechanism was measured using two tensile load cells.

A. Test set up

Test setup identical to the flight configuration was made. Interface for vehicle half and compensator assembly are made and mounted on a steel structure at 3m height. The test configuration is as given below (Figure 5). The 11m length hose with thermal insulation and rubberized cotton fabric hose is supported at intermediate locations with nylon belts through sliding rings. The retention cable is loaded and is passing over a pulley at the compensator side. Hose was pressurized using air. Wind load was simulated by applying uniformly distributed normal load of 3000N on the pressurized cooling hose by loading the plastic bags wound around the cooling hose with plastic cylinder weight of 4.5kg each. Tension on the hose was measured using two load cells (diametrically opposite) mounted in between the flanges of compensator.

B. Test results

Test were carried out with following load steps and kept under loaded condition for 15 minutes. Sag corresponding to each step was noted down. The two load cell values were added to get the axial tension at the end. A graph is plotted from the test data, wind load vs axial tension at the end as shown in figure 6. The linear variation of the axial tension is obtained from the wind load. Test were carried out up to load of 3150 N and kept under loaded condition for 15 minutes and the tension at the end was measured as 3920N using load cell. The system was intact in the above load cases.

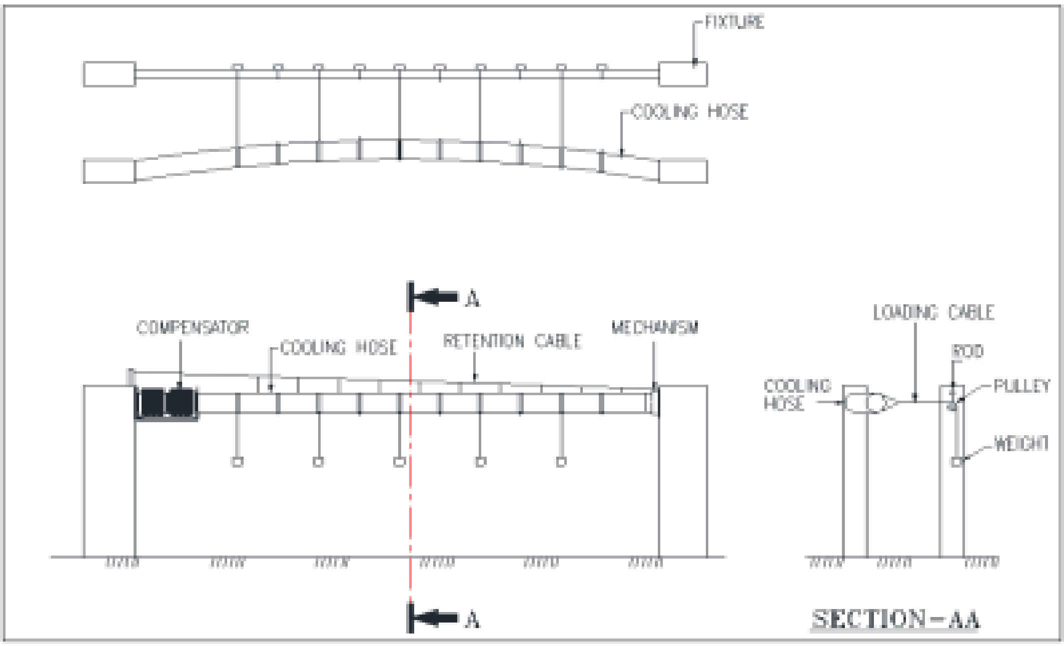

Figure 5: Full scale wind load simulation test setup

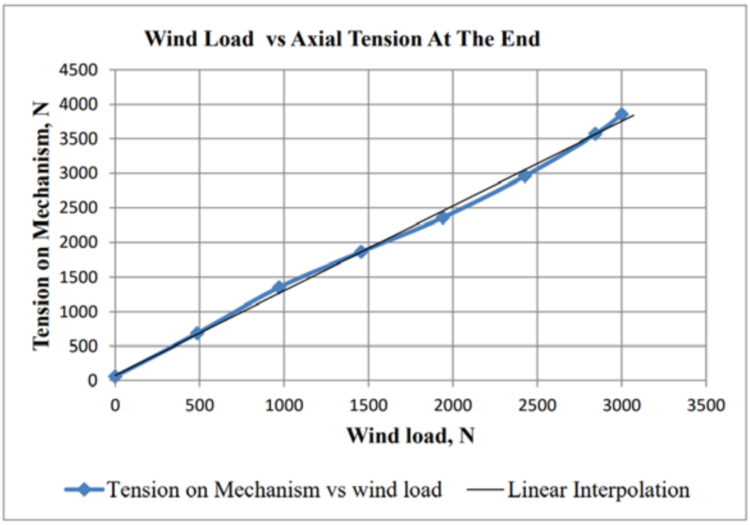

Figure 6: Simulated wind load vs Axial Tension at Cooling Hose End

Table 2

Sl no	Total weight, N	Total tension at the end, N
1	0.0	56.9
2	485.6	681.8
3	971.2	1348.9
4	1456.8	1861.0
5	1942.4	2360.4
6	2428.0	2961.6
7	2844.9	3567.9
8	3001.9	3854.9

Table 3

Wind load, N	**Tension at the end, N**
2000 (with 1.4 Gust factor)	2400
2500 (with 1.25 load factor)	3000
3000 (with 0.2 Margin)	3800

C. Test summary & margin demonstration

The result shows the tension at the end i.e. on the mechanism at different wind load. Wind load of 3000 N, which is corresponding to wind velocity of 30m/s when gust factor, load factor and margin of 0.2 is taken into account, applies a tension of 3800N on the mechanism (ref Table-3).

This tension tries to pull out the mechanism. But with the results of pull out test we have observed that with use of optimal spacer plate thickness, a minimum pull out load of 4320N is required to separate the mechanism from vehicle. Therefor system has a structural margin of 0.44.

7. Conclusion

Launch pad environmental condition w.r.t. wind velocity of 30 m/s was simulated for payload cooling umbilical system. Aerodynamic force on the hose of payload cooling umbilical system was 2500N corresponding to wind velocity of 30m/s with 1.4 gust factor and 1.25 load factor taken into account. To show system robustness, a minimum margin of 0.2 was taken and therefore a load of 3000 N was finalized to simulate wind velocity of 30m/s. Axial tension on the mechanism due to this load was found both analytically and experimentally. Catenary equation is used to get the axial tension analytically Axial tension at the end i.e. on the mechanism was found 4000 N with analytical method, therefore a pull out test was done with 4000 N load. System was found intact during the test and a minimum pull out load of 4320 N was observed. Full scale wind simulation test was done with 3000 N of load applied as uniformly distributed load on the cooling hose. During the test system performed satisfactorily and tension at the end was found 3800 N. On the basis of above results it was concluded that payload cooling umbilical system has a structural margin of 0.44 and design is robust.

8. Acknowledgement

The authors wish to acknowledge Deputy Director, MVIT & Director, VSSC who permitted us to pursue this study and publish the findings.

9. References

[1] B.N Suresh, K. Sivan, chapter 7.9 (thermal environments) and chapter 11.11 (environmental testing for space structures), Integrated design for Space Transportation (Springer, New York,2015), pp. 258–259, 489– 491

[2] Dynamic Environmental criteria, NASA-HDBK-7005, in NASA Technical Handbook, (National Aeronautics and Space Administration,2001), pp. 194–195

Comparission of the Thrust of Electrohydrodynamic Thruster under Magnetic Fields with Paramagnetic and Diamagnetic Electrodes

L Yethinder Ragav
Jain University
Bengaluru
yethinder@gmail.com

Manu Jain N
Jain University
Bengaluru

Raghu NG
Jain University
Bengaluru

Kadripathi KN
Jain University
Bengaluru

Shusheel KC
Jain University
Bengaluru

***Abstract*– Studies of the thrust force variation of an Electrohydrodynamic (EHD) thruster under the influence of magnetic fields with different combinations of magnet positions and collector shapes were performed in our previous experiments. The best result was observed with a rhombus-shaped grid and a particular arrangement of alternating magnetic poles. In this paper, the performance of copper (diamagnetic metal) as an electrode is compared to a paramagnetic non-metal – carbon-carbon composite. It is known that carbon is a diamagnetic material, but this particular composite was made by mixing carbon, graphite and binder, which resulted in its paramagnetism nature. The electrodes have an inter-electrode gap of 50 mm. The tests were done for the copper and carbon electrodes with the rhombus-shaped grid and a specific combination of magnets. The magnetic field's influence on the emitter electrode and the thrust produced is studied in this paper. The maximum thrust given by the copper electrode, without any magnets, was 0.871 mN, which is lower than that of the carbon electrode of 1.288 mN. The addition of magnets has improved the thrust output in both cases, the highest being 1.427 mN of the carbon electrode.**

Keywords*– *Electrohydrodynamic (EHD) thruster, magnetic field, rhombus-shaped grid collector, carbon, copper, diamagnetic, paramagnetic.

1. Introduction

Space research has undoubtedly become a hot topic among curious minds and unconventional investors. Outer space exploration is an essential step to broaden our perspective and understanding, and it is an integral part of human life. We look further into space to discover more potential habitats where life might exist or where we will most likely live in the future. On the other hand, near-space observatories and satellites play an essential role in tracking geological phenomena for human well-being. Near-space is described as the region between 20 kilometres above the earth's surface and the Karman line. Remote sensing, geological exploration, meteorological analysis, telecommunication, geographical positioning, weather forecasting, and other applications are possible in this field. The scientific payload must be delivered to near space in a cost-effective manner, and long-term operation must be ensured by compensating for orbital decay, which nanosatellites do not do. It is our moral obligation to keep our space environment clear of debris by eliminating non-operational junk satellites from orbit. Numerous academic and industrial researches aim to design near-space mission-friendly thrusters to realize the need, as mentioned earlier in the aerospace industry [1].

An electrohydrodynamic (EHD) thruster, which is operated by a high voltage source, is another choice for near-space thrust generation. These devices can be used for a variety of purposes, including producing thrust, implementing near-space station-keeping manoeuvres, and repositioning [2].

Electrohydrodynamic flow studies and applications are a rapidly growing field of study. Electroaerodynamic (EAD) vehicles, lifters, and ionocrafts are some of the names given to aircraft models based on the same concept [3,4,5]. The absence of moving parts (no propellers or high-lift devices are required), direct conversion of electrical energy into thrust; it is almost noiseless, has high efficiency of up to 100 mN/W in the earth's atmosphere (at near-normal conditions), and is of a simple design are the key advantages of EHD principle-based aircraft [6,7].

2. Electrohydrodynamic propulsion

Electrohydrodynamics, also known as electro-fluid-dynamics, is the study of the motion of electrically charged fluids. It's the study of ionized particles or molecule motion, as well as their interactions with electric fields and the fluid around them.

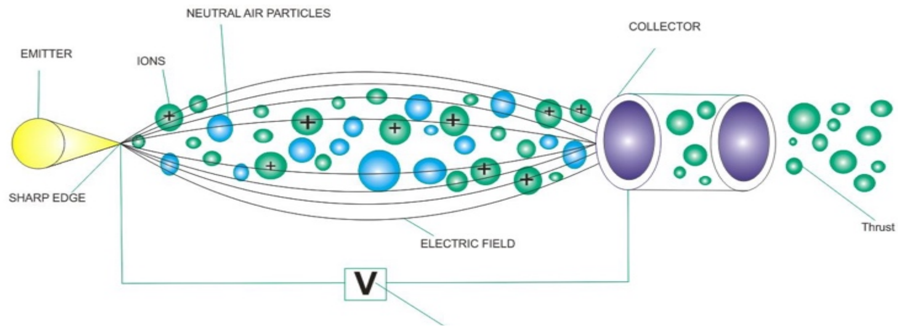

Figure. 1. Electrohydrodynamics phenomenon

The substance is made up of atoms, each of which has the same number of protons and electrons. Atoms are neutral as the proton balances with the electrons. Consider connecting sharp objects to the high voltage power supply's positive terminal and smooth objects to the negative terminal. The polarities can be interchanged, but regardless of the polarity, the emitter should always be sharp. As the sharp object is bound to the positive terminal, electrons from nearby atoms are pulled away, leaving the atom with more positive protons than negative electrons, making it positively charged [8,9,10].

Smooth or blunt electrodes are similarly attached to the negative side of the terminal, and the extra electron that was stripped from the atom near the emitter is sent to the smooth object. As a result, the atoms closest to the emitter become positively charged. When a sharp object is used at the positive terminal, the atoms on the sharp object are more tightly packed than on the smooth object. As shown in Figure 1, an electric field is produced between the positive and negative terminals. However, due to the close packing of atoms at the sharp edge of the sharp object, the electric field is more concentrated there [11].

The electric field strength at the sharp emitter exceeds the air breakdown voltage, causing surrounding electrons to gain enough energy to ionize air molecules. This electric breakdown of air is called corona discharge [11]. The generated ions in the region between the emitter and the collector are greatly accelerated by the electric field.

The ions collide with neutral air molecules as they drift towards the collecting area. The neutral wind, also known as EHD thrust, is caused by momentum transfers from charged to neutral particles and this momentum is transferred during the collision.

The thrust produced depends on a number of factors, such as the distance between the emitter and the collector, the potential difference and current, electric field strength (V/m), shape and size of the emitter electrode with respect to the collector, the medium of operation, surrounding pressure and a few other minor aspects. The highest thrust can be achieved when the electrodes are close to each other, without arcing over, and the emitter is as sharp as possible. This equation is known to the scientific world and hence will not be stressed upon in this paper; instead, new factors – magnetism and the electrode material – are at the centre stage.

3. Experimental setup

The experimental setup consists of an EHD thruster, controlled test chamber, High voltage (flyback) transformer, Direct Current (DC) power supply, Zero Voltage Switching (ZVS) Driver, and a deflection meter.

The power supply outputs a maximum of 24 volts 40 amps direct current and is connected to the ZVS driver, where the input voltage is converted to a high-frequency output. It is then stepped up to a higher voltage (33000V DC) using a High voltage step-up transformer (flyback transfer). The transformer's high voltage positive terminal is connected to the thruster's emitter electrode using a thick high voltage wire, and the negative is connected to the collector. The thruster is placed inside a test chamber, as shown in Fig. 2, which functions as a controlled environment, oriented in a horizontal direction, and the thrust is measured using a deflection meter.

EHD thruster is fabricated using an additive manufacturing technique (3D printing), made of Polylactic Acid (PLA) plastic. The outer diameter of the thruster is 73 mm, the inner diameter is 58 mm, and the length is 70 mm. The thruster is built with 36 slots, 12 in each row, on the outer circumference, to incorporate neodymium magnets. The diameter of a neodymium magnet is 10 mm, thickness is 5mm, and it weighs 2.89 grams. The thruster has six inlets of 5 mm diameter around a central hole of 25 mm diameter. The emitter electrode is aligned with the central axis of the thruster. A total of 3 emitters were used (including the previous research mentioned in Section 5), a spiral copper electrode, a straight copper electrode and a straight carbon electrode. The spiral and straight copper electrodes are made using a copper wire of 17 gauge. The spiral emitter is wound from a total wire length of 175mm, the outer diameter is 32mm, and the total height of the emitter is 36mm, which is 34mm from the collector. The straight electrodes are both 20 mm long, 50 mm behind the collector.

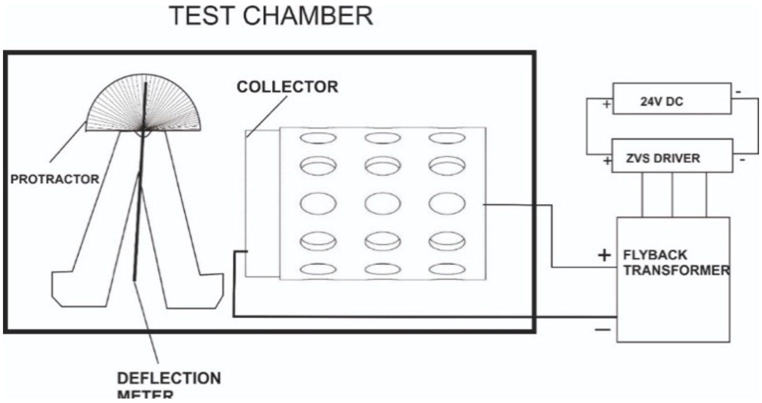

Figure. 2. Thruster in a controlled test chamber

For the experiments discussed in section 5, two types of collectors were used, as shown in Fig. 3. The first is a rhombus-shaped grid mesh of 189 rhombi-shaped holes with a thickness of 0.5mm and a diameter of 70mm. The other was made with aluminium foil, rolled into a hollow cylinder of 70 mm diameter and a height of 25 mm. The weight of the hollow cylindrical collector is 1.5 grams, and the rhombi-shaped grid collector is 2 grams. Four different magnetic fields were produced using the magnets placed at different locations around the thruster; each placement combination is considered a configuration. For the current research, results of which are discussed in Section 9, only the rhombus-shaped grid was used with the copper and carbon electrodes, at an inter-electrode gap of 50 mm, and with one magnetic configuration.

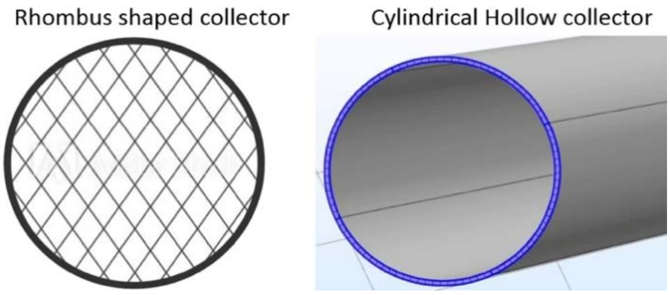

Figure. 3. Shapes of collectors

4. Thrust measurement

With the development of space technology, the demand for precise satellite positioning and orbital manoeuvring is growing. As a result, precise thrust measurement techniques for micro-scale thrusters are necessary. Traditional methods, such as load cell-based thrust calculation, are ineffective because low thrust values are generated are significantly affected by the amplifier's background noise, and the thruster's small impulse goes unnoticed [12]. Furthermore, the strong electric and magnetic fields used to study the thruster's characteristics appears to be interfering with the load cell's operation. Because of the strong electromagnetic interference between the cell and the applied external magnetic field, the results obtained from the milligram load cell were uncertain. Hence a simple pendulum-based thrust measurement setup is designed, as shown in figure 9 and discussed further in the later section. The thrust force is determined indirectly by mathematical modelling by resolving the resultant forces acting on the pendulum to create the deflection. This approach is indeed not ideal for calculating absolute thrust, but it's good for comparing thrust between different setups while keeping other parameters constant.

A. Design specification and mathematical modelling

A freely oscillating pendulum with only two degrees of freedom is fixed to rigid support at the point. Since the area of the pendulum base equals the area of the thruster exit, it is presumed that all of the thrust force acts directly on the pendulum base, with zero energy loss to the surrounding. The thruster is positioned horizontally with its collector 70 millimetres away from the pendulum's mean point. Since the total mass of a freely moveable component of a pendulum is 1.07 grams, the earth's acceleration due to gravity exerts a force of 10.48 x 10^{-3} Newtons on it (g). The thruster, which is horizontally facing the pendulum, attempts to push it, allowing the pendulum to produce the deflection θ due to the interaction of these two perpendicular forces. As a consequence, the thrust value can be calculated by resolving the resultant power.

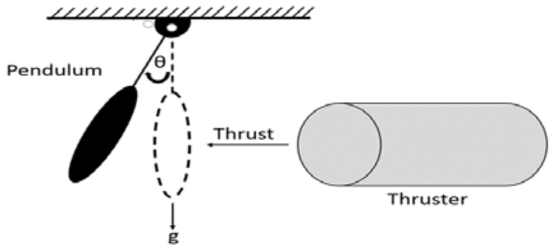

Figure. 4. Illustration of the thrust measurement setup

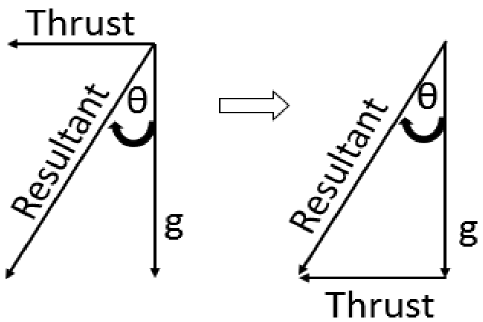

Figure. 5. Force resolution and Force triangle

From the figure 5.

$\tan\theta = \frac{Thrust}{g}$

Therefore, Thrust = g x tan θ …. Equation 1.

Where g = 9.8 x 10^{-3} Newtons and θ in degrees.

The thrust bench's accuracy and sensitivity are determined by the sensor used and the thrust measurement mode. In the space industry, both direct and indirect measurements are used, but direct measurements are often preferred because they are more precise in the case of microsatellites [13]. It is a direct calculation of thrust force if the micro-thruster is installed on the test bench, but it is an indirect method if the thruster's exhaust is used to achieve deflection, as in the pendulum setup. The dissipation of energy as unknown elasticity during the momentum exchange between the exhaust plume particles and the target (pendulum) causes problems in indirect thrust measurements [14,15]. This method, on the other hand, can be used to estimate the change in thrust during various testing configurations while keeping all other variables constant. For a constant distance between the thruster and the pendulum's mean distance, the energy loss in the indirect calculation is the same [16,17,18].

5. Previous Works

In the previous research, the influence of different magnetic fields on the thruster was studied [19]. The tests were conducted with the spiral copper emitter electrode, two types of collectors and five configurations of the thruster.

In configuration 1, no magnets were used, as shown in Fig. 6, and is considered a baseline. Configuration 2 has eight magnets in total, separated into two sets of 4 in each, placed in row 1. One set has the North Pole facing towards the centre and the other South Pole. In configuration 3, the intensity of the magnetic field in configuration 2 was increased by increasing the number of magnets to 24, with two magnets stacked on top of the base magnets. Configuration four’s magnetic placement differs from that of the previous; a total of 6 magnets are divided into two sets of three, with alternating poles facing towards the inside, as shown in Fig. 7. In configuration 5 all the 36 slots are packed with magnets, with the North Pole facing the centre.

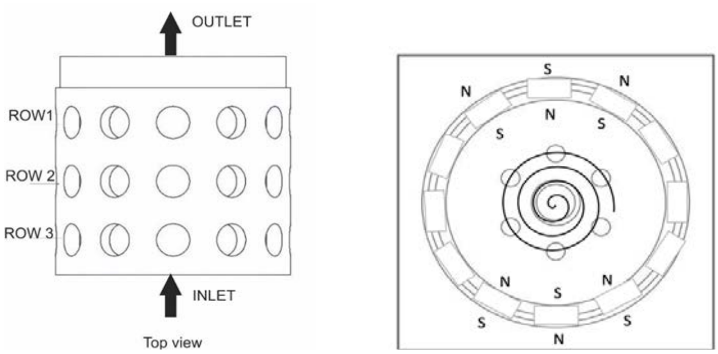

Front view

Figure. 6. Thruster Design – Configuration 1

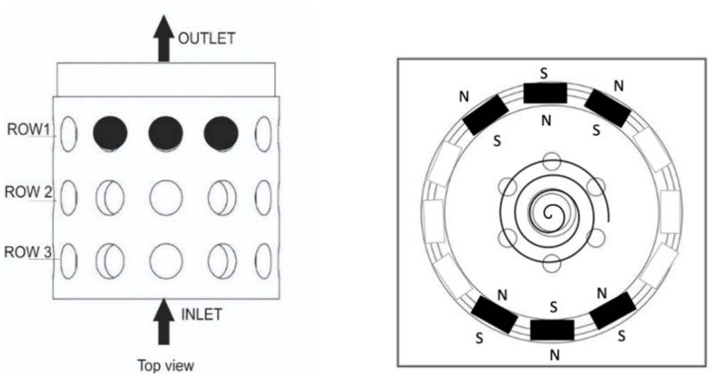

Front view

Figure. 7. Thruster Design – Configuration 4

Each configuration was tested with the hollow cylindrical collector and rhombus-shaped grid collector separately, five tests for every collector-configuration combination while maintaining all other parameters the same for all the tests with the controlled environment system's help. The average thrust was calculated from the deflection meter and compared.

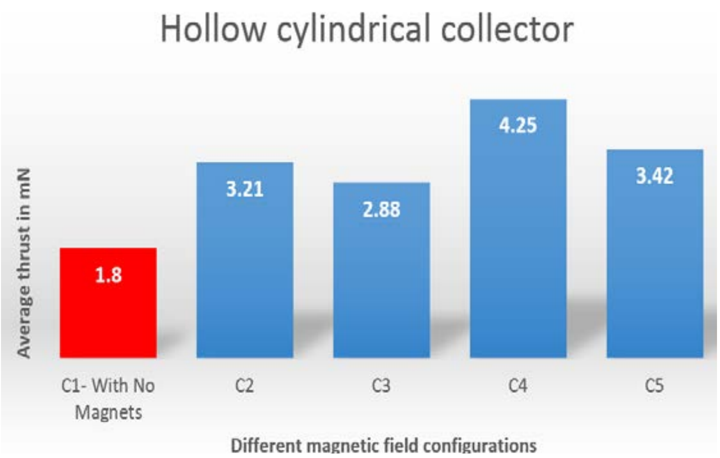

Figure. 8. Graph of thrust produced by the hollow cylindrical collector with different configurations of the magnetic field

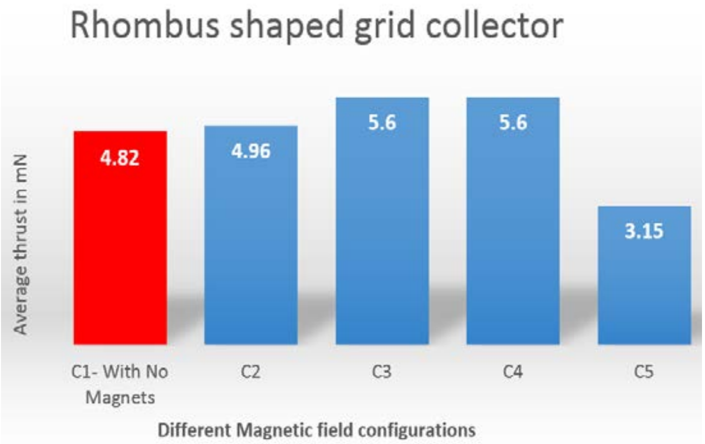

Figure. 9. Graph of thrust produced by the rhombus-shaped grid collector with different configurations of the magnetic field

The highest thrust, 5.6 mN, was recorded with the rhombus-shaped grid and configuration 4. This configuration also produced the highest thrust with the hollow cylindrical collector. The reason for the improved performance is a circumferential magnetic field and magnetic cusps produced by the alternating poles, which was discussed in detail in our previous paper [19]. The rhombus-shaped grid collector worked better than the hollow cylindrical collector because it provides maximum electric field exposure and maximum contact area along the path of the ions, while the field of the hollow collector is only near the walls. Hence, for the next experiments, the rhombus-shaped grid and a modified version of configuration 4 were chosen. Although the thrust-to-weight ratio is lower for configuration 4 than configuration 1 (no magnets) with this electrode, further tests were conducted to study the magnetic fields' influence on carbon electrode and the difference in thrust it can generate.

6. Emitter Material Properties

A. Copper Electrode

Amongst all non-precious metals, copper has the highest electrical conductivity, with an electrical resistivity of 16.78 nΩ•m at 20 °C. The theory of metals can explain this unusually high electrical conductivity in their solid state. In the atom of copper, the outermost energy zone or conduction band (4s) is only half-filled; hence, to carry electric current, many electrons are available. "Mean free path" of copper is too long, which means the average distance travelled between each collision is large compared to other metals; (i.e. when a current is applied to copper, the electrons encounter resistance to their passage due to collision with vacancies, lattice ions, impurity atoms and imperfections.) which indicates that the electrical resistivity is low. The mean free path can be increased rapidly by cooling the copper.

Most of the electrically conductive metals require larger cross-sections to carry the same amount of current but are less dense than copper. Hence, copper is preferred for most electrical uses and can also be used in low space application. Copper in metal form as the odd electron is sent into the pool of electrons making the metallic bond; thus, the metal is diamagnetic, it remains for Cu^{+} salts, whereas Cu^{++} salts are paramagnetic.

B. Carbon Electrode

The carbon electrode used in this study was produced by mixing a powder of coal coke or petroleum coke with graphite powder and a binder (impurities), extruding to form the rod, and heating to form a carbon/carbon composite. It was sourced from a zinc-carbon battery. The electrical and magnetic properties are primarily a result of graphite. But, the impurities added in the form of binders to provide strength has a significant effect on the electrode's magnetic property. Graphite is a form of carbon where covalent bonds are formed by one carbon atom with three other carbon atoms. Usually, carbon forms four covalent bonds. Because of the heterolytic fission nature of graphite, a covalent bond between two neighboring atoms is broken unequally, resulting in the bond pair of electrons being retained by one of the atoms, while the other atom does not retain any of the electrons from the bond pair. Hence an electron is set free to the conduction band. This free electron contributes to the conductivity of the graphite. This conductivity makes graphite useful as electrodes for electrolysis. It is known that pure graphite cannot exhibit ferromagnetism. Each carbon atom has six electrons, of which three exhibits a spin pointing up and the rest pointing down; consequently, the magnetic moment of a carbon atom is zero making it a "diamagnet", repelled by an external magnetic field. However, there have been doubts that carbon can be made magnetic by doping it with nonmagnetic materials, changing its order slightly. A research was conducted in which different grades of graphite pencil leads were mixed with $CoFe_2O_4$ (CF) nanoparticles to analyse magnetic properties. It was found that they exhibit soft ferromagnetism at room temperature, and this property largely depended on the impurities (mainly SiO_2 and a minor amount of metal oxides) added to the graphite to provide hardness [20]. The soft ferromagnetism is mostly due to a ferromagnetic impurity like Fe. In the present case, the electrode was sourced from a dry cell; hence the composition of the impurity is different, due to which it is paramagnetic. This property was also confirmed by a test where the electrode aligned itself in a strong magnetic field but did not retain its magnetism.

The conductivity of copper is higher than that of graphite, but the melting point of graphite is more than three times greater than that of copper; thus, it can sustain high current density.

C. Geometry of electrodes

The copper emitter electrode used for the next tests is 20 mm long, 1.4 mm diameter, and straight, unlike the spiral-shaped electrode in the previous tests. This emitter configuration was chosen to compare the performance: because a spiral-shaped carbon electrode could not be sourced. The carbon electrode is also 20 mm long and straight, with a diameter of 4 mm. The inter-electrode gap is maintained at 50 mm. The carbon electrode was sanded and shaped manually to form a sharp conical shape at the emitting end, whereas the copper electrode acquired a two-dimensional wedge shape while it was cut.

7. Thruster Design

A. Configuration 6

In this configuration, three magnets are arranged consecutively with alternating poles – South, north, and south poles facing inwards on one side on row 1, and the same pattern is followed on row 2, just behind the row 1 magnets. Similarly, the north, south, and north poles face inwards on the opposite side of row 1 and row 2, as shown in Fig. 10.

This configuration is an extension of the fourth configuration, mentioned in Section 5, where only 6 magnets are used in total instead of 12 in this case. This addition was made because of the increase in the distance between the emitter end and the collector. Previously, the distance or the inter-electrode gap was just 34 mm, which is almost half of the thruster's length; in this case, the electrode stretches beyond row 2, and only row 1 had the most influence on the discharged ions. So, the magnets were only placed in row 1. However, with the inter-electrode gap of 50 mm, the emitter electrode is shorter and ends before row 2. By only having the magnets in row 1, the thrust cannot be optimized to the maximum level. Hence, by placing the magnets in both rows, the magnetic field can have the highest effect on the discharged charged particles.

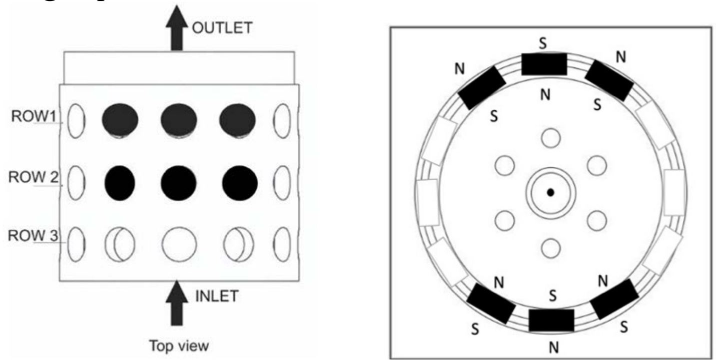

Front view

Figure. 10. Thruster design – Configuration 6

8. Theory

Paramagnetic and diamagnetic materials behave differently from each other while carrying current in a magnetic field. If the current flow is perpendicular to the external magnetic field, Hall Effect and Anomalous Hall Effect can be observed in non-magnetic materials and ferromagnetic materials, respectively. When current flows through a conductor with a direction perpendicular to the external magnetic field, a transverse electrical current may be produced in the third perpendicular direction, known as the Hall Effect, due to the Lorentz force on the charge carriers [21]. A similar effect can also be observed in ferromagnetic and strongly paramagnetic materials; here, Spin Hall Effect also contributes to the result and is known as the Anomalous Hall Effect (AHE) [22]. Similar effects can be observed in paramagnetic systems also [23,24]. These outcomes may be observed only if certain conditions are matched.

Electrons exhibit two types of motion in an atom – orbital and spin. Orbital motion is the motion of an electron around the nucleus of the atom. As the electron (charged particle) moves, it creates a magnetic field, generally referred to as the magnetic field generated due to the flow of current. But electrons also spin around their centres, creating yet another magnetic field. In a diamagnetic material, the spins of electrons cancel each other, making it prone to a magnetic attraction. However, in paramagnetic materials, unpaired electrons are present, due to which there is a resultant net spin and when an external magnetic field is applied, the electrons' spin aligns parallel to the field, causing an attraction. While in the field, the side closest to an external magnetic pole becomes the opposite pole. In such cases, the magnetic field due to the orbital motion and the magnetic field due to the spin could cancel or add depending on the direction of the fields at that point. Although the strength of these fields is low, it can still affect the current flow and the charged particles' behaviour. Furthermore, the electrodes also experience a force in a perpendicular direction determined by Fleming's Left-Hand Rule due to the circular magnetic field produced by the flow of current.

9. Results

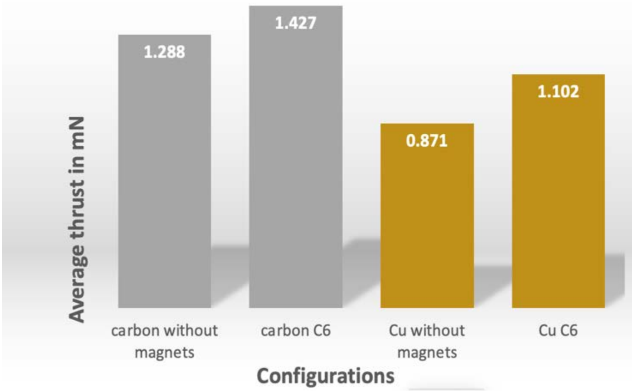

Figure. 11. Graph of thrust produced by copper and carbon electrodes with rhombus-shaped grid collector, with and without magnets

The tests were performed in a controlled environment, five times each for each electrode, with and without magnets, and the average thrust is considered for the final result.

With the carbon electrode as the emitter, the average thrust produced without magnets was 1.288 mN, which is higher than that of the copper electrode – 0.871 mN. Under the influence of configuration six's magnetic field, carbon emitter produced a thrust of 1.427 mN, which is approximately 11% more than that with no magnets. The copper emitter output 1.102 mN, which is 26% higher than its non-magnetic version. The potential difference between the emitter and the collector was approximately 33000 volts, and the average power consumed by the setup was 23 Watts.

10. Conclusion

The results show that the thrust produced by the carbon electrode is considerably higher than the copper electrode, both with and without magnets. Magnets placed in configuration 6 improved the thruster's performance effectively for both the electrodes.

The difference in the thrust between the two electrodes, without magnets, is mainly due to the variation in shape. The sharper the emitter is, the higher the electric field strength (V/m) will be. The carbon electrode with the three-dimensional cone, sharpened manually, has a larger ionization area and a higher V/m value than the two-dimensional wedge of the copper electrode, which is not as sharp. Since this paper's primary focus is on the influence of magnetic fields, the parameter of the shape and sharpness isn't given much importance. Although, a detailed study on the material compositions' effect on the thrust must be carried out.

The magnets arranged in the sixth configuration produce a magnetic field similar to that of configuration 4 in the previous experiment (Section 5). The field is produced along the inner circular wall, reducing the charged particles' collision with the wall and improving the thrust. Although this configuration is slightly different from that of the fourth – the area of the field is widened by replicating the configuration four's field lengthwise – the increase in thrust performance is comparable. The increase in thrust with the copper electrode in the magnetic field is very high compared to that of the carbon electrode, mainly because of the magnetic nature of the materials. Copper, being diamagnetic, experienced negligible interaction with the field. Although a force perpendicular to the magnetic field, due to the current flow, was being acted on it, since the electrode was secured in its place, there was no drastic effect. The thrust improvement observed was mainly due to the magnetic field's effect on the discharged beams, reducing the collisions with walls and containing the momentum transfer process. In the case of the carbon electrode, it experienced the interaction of forces in a complex manner due to it being paramagnetic. Since all other main parameters were the same compared to the copper electrode, except the magnetic nature and the shape, one of these must have affected the result. Considering the shape, the main parameter it influences is the V/m. The magnetic field does affect the charged particles after they are formed, which is a result of ionization, but they do not have a distinct effect on V/m. Even if the magnetism affects the ionization, it must have the same influence in both cases as the process of ionization is the same. At least in this particular configuration, the magnetic field's effect on the ionization is believed to be the same with copper and carbon electrodes or negligible for the sake of the comparison between them. Next, taking the magnetic property into account, the lower performance of the carbon electrode must be due to its interaction with the magnetic field. Possibly losses due to the Anomalous Hall Effect might have played a role. A slight increase in temperature of the carbon electrode was noticed after its operation in the magnetic field, which did not happen when operated without the magnetic field. The increase in temperature less but noticeable and was confirmed with tests performed with magnets placed close to the electrode.

The magnetic field around the electrode due to the current flow and the alignment of electrons' spin due to the external magnetic field can also affect the performance. While the thrust was higher than that of without magnets, it is because of the magnetic field's effect on the charged particles. However, it did not have the same effect as it did in the case of the copper electrode due to the resultant magnetic field in the emitter region and the losses associated with it. A particular explanation cannot be picked owing to a lack of observable evidence. Nevertheless, it can be concluded that magnetism has an effect on the electrode material and the thrust produced.

11. Suggestions for Future Research

The current research mainly focused on the magnetic properties of the materials and their effect on the thrust produced, neglecting the materials' electrical and chemical properties. Research needs to be performed with various materials, studying the thrust performance and effects of oxidation/corrosion in the long run at various pressure levels. In this study, the dimensions and shape of electrodes were different. Future experiments should be conducted with electrodes of similar dimensions and shapes to make a better comparison. Thrust equipment used in these tests is not ideal, a better thrust measuring equipment will provide more accurate data**.**

12. Acknowledgment

We would like to express our deep gratitude to Professor Raju Garudachar, ISRO Ex-Project Director, and Professor S Charutatha, our project guides, for their patient guidance, enthusiastic encouragement, and useful critiques of this research work.

13. References

[1] I.V. Ostoslavsky, Aircraft Aerodynamics (Russian Edition Aerodinamika Samoleta), Book on Demand Ltd., Moscow, 2019.

[2] E. van Wynsberghe, A. Turak, Station-keeping of a high-altitude balloon with electric propulsion and wireless power transmission: a concept study, Act Astronaut. 128 (2016) 616–627.

[3] K. Masuyama, Performance Characterization of Electrohydrodynamic Propulsion Devices, Massachusetts Institute of Technology, 2012.

[4] K. Masuyama, S.R.H. Barrett, On the performance of electrohydrodynamic propulsion, Proc. Math. Phys. Eng. Sci. 469 (2154) (2013), 20120623–20120623.

[5] N.A. Gatsonis, Y. Lu, J.J. Blandino, M.A. Demetriou, N. Paschalidis, Micropulsed plasma thrusters for attitude control of a low earth orbiting cubesat, in: 54th AIAA Aerospace Sciences Meeting, 2016, 0692.

[6] B. Goksel, ¨ I.C. Mashek, First breakthrough for future air-breathing magneto-plasma propulsion systems, J. Phys.: Conf. Ser. 825 (1) (2017), 012005.

[7] D.S. Drew, K.S.J. Pister, First takeoff of a flying microrobot with no moving parts, in: 2017 International Conference on Manipulation, Automation and Robotics at Small Scales (MARSS), 2017, pp. 1–5.

[8] C.K. Gilmore, S.R.H. Barrett, Electrohydrodynamic thrust density using positive corona-induced ionic winds for in-atmosphere propulsion, Proc. Math. Phys. Eng. Sci. 471 (2175) (2015), 20140912–20140912.

[9] L. Pekker, M. Young, Model of ideal electrohydrodynamic thruster, J. Propul. Power 27 (4) (2011) 786–792.

[10] E. Moreau, N. Benard, J.-D. Lan-Sun-Luk, J.-P. Chabriat, Electrohydrodynamic force produced by a wire-to-cylinder dc corona discharge in air at atmospheric pressure, J. Phys. Appl. Phys. 46 (47) (2013) 475204.

[11] L. Pekker, M. Young (2010). A Model of an Ideal Electrohydrodynamic Thruster. From researchgate.net

[12] Mueller, J., Hofer, R., & Ziemer, J. (2010). Survey of propulsion technologies applicable to cubesats. Retrieved August 11, 2017, from https://ntrs.nasa.gov/search.jsp?R=20100032899.

[13] Bijster, R. J. F. (2014). Design, Verification and Validation of a Micropropulsion Thrust Stand (Doctoral dissertation), Delft University of Technology, Delft, Netherlands.

[14] Jean-Yves (2006). Test bench for pop-pop engines. [Web log post]. Retrieved August 11, 2017, from http://www.eclecticspace.net/poppop/jy/Test_bench_for_pop-pop_engines_V3.1.pdf

[15] Marhold K, Tajmar M. Direct thrust measurement of in-FEEP clusters. IEPC2005-235. Princeton University; 2005.

[16] Phipps CR, Luke JR, Helgeson WD. A 25 nN low-noise thrust stand for microthrusters. IEPC-2005-318. Princeton University; 2005.

[17] S. Chakraborty, "An electrostatic ion-guide and a high-resolution thruststand for characterization of micro-propulsion devices," Ph.D. dissertation (EPFL, Switzerland, 2015).

[18] S. Chakraborty, C. Ataman, S. Dandavino, and H. Shea, in Proceedings of PowerMEMS, Atlanta, USA, 2-5 December 2012, pp. 528–53

[19] L Yethinder Ragav, Kadripathi KN, Raghu NG, Shusheel KC, Manu Jain N, Dr. S. Charulatha, Dr. Raju Garudachar. Performance study of electrohydrodynamic thruster under the influence of external magnetic fields.[In-Press]

[20] Bhowmik, Rabindra, Ferromagnetism in lead graphite-pencils and magnetic composite with CoFe 2O 4 particles, Composites Part B-engineering, V43, I2.

[21] Karplus, R., & Luttinger, J. M. (1954). *Hall Effect in Ferromagnetics. Physical Review, 95(5), 1154–1160.*

[22] Bergmann, G. (1979). *The anomalous Hall effect. Physics Today, 32(8), 25–30.*

[23] Cumings, J., Moore, L., Chou, H., Ku, K., Xiang, G., Crooker, S., Goldhaber-Gordon, D. (2006). *Tunable Anomalous Hall Effect in a Nonferromagnetic System. Physical Review Letters, 96(19).* doi:10.1103/physrevlett.96.196404

[24] Sheng, L., Sheng, D. N., & Ting, C. S. (2006). *Theory of the Phonon Hall Effect in Paramagnetic Dielectrics. Physical Review Letters, 96(15).*

An Instrumented Experimentally Measured Dynamic Parameters of a Recoil System of 155mm Gun

DU Bagde
Armament Research and Development Establishment
Defence Research and Development Organisation
Pune
bagde.d@gmail.com

Devyani K Jadhav
Armament Research and Development Establishment
Defence Research and Development Organisation
Pune
devyani70@gmail.com

AA Babar
Armament Research and Development Establishment
Defence Research and Development Organisation
Pune
ajitbabar.arde@gmail.com

***Abstract*—This paper discusses the experimentally measured characteristics of a recoil system of 155mm X 52 cal. artillery gun during dynamic firing of ERFB projectiles from 155mm X 52 cal. artillery gun equipped with double baffle muzzle brake. Instrumentation is essential to record all the important recoil system parameters during dynamic firing. Some of the recorded results of recoil oil pressure in recoil cylinder, breech acceleration, and recoil displacement are presented in this paper. The data from pressure sensor, breech accelerometer and draw wire displacement sensor are recorded in multichannel data acquisition system and after trials it is copied to a PC for further analysis which is done using Matlab. The data generated helped the designer in evaluating the recoil system design and carry out necessary modification. The combined use of a pressure sensor in recoil cylinder, recoil displacement sensor and accelerometer on breech block found to be essential to achieve a complete characterization of the firing shock force due to the recoil. The extent of instrumentation used to measure recoil parameters is explained in this paper. This paper will show some of the results found during dynamic firing of 155mm X 52 cal. artillery gun at PXE Balasore with different propellant charge mass. This experiment was carried out to test and evaluate newly developed recoil system. Analysis of the recorded data was useful in finalizing the design of recoil system by validation of the performance parameters.**

Keywords—Recoil motion, counter-recoil motion, pressure sensor, draw wire sensor, accelerometer, velocity, recoil force, data acquisition, instrumentation.

1. Introduction

Recoil mechanism is one of the most critical subsystem of artillery gun, and gun performance depends largely on it. Recoil is the rearward movement of the barrel and connecting parts after the weapon has been fired. It is caused by the reaction of the forward motion of the projectile as the projectile is driven through the barrel due to expanding propellant gases. A recoil mechanism is designed to absorb the energy of recoil gradually, the recoil movement of the weapon is controlled by the flow of the recoil oil through certain throttling devices of the recoil system. Recoil follows Newton's law of motion, which states, that for every action there is an equal and opposite reaction. The gun has a recoil and counter-recoil mechanism, which serves two important functions. Firstly, such a system absorbs extremely high recoil energy generated during gun firing. Secondly, the system also ensures that the barrel gets back to its original position post firing of the projectile is shown in fig 1. The cradle houses the recoil system.

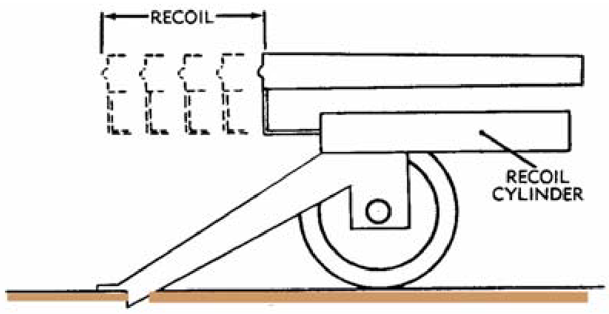

Figure 1: Gun recoil mechanism

Recoil/Counter-recoil Systems: Hydro-pneumatic type of recoil mechanism are widely used for high caliber artillery weapon system The recoil and counter-recoil mechanism is made up of a recoil brake assembly, and a recuperator assembly. While the former element absorbs recoil energy so that only a small fraction of it is transmitted to the chassis, the latter element ensures that the gun barrel returns back to its original position after the recoil period.

The recoil brake is hydraulic and consists of four elements: a cylinder; a piston; a liquid, such as glycerin and water; and some form of orifice in the piston that allows the liquid to flow from one side of the piston to the other. The recoil brake system is essentially a damper and has a hydraulic piston–cylinder arrangement. Its cylinder is bolted to the cradle while its piston is connected to barrel assembly through yoke. The cylinder is filled with viscous oil, which is forced through a large number of orifices by compressive forces generated because of recoil motion of the piston. A piston attached to the recoiling parts by a recoil rod causes the flow of fluid through the orifice. The motion of the piston within the cylinder forces the liquid through the orifices, absorbing the energy of recoil and controlling the return of the gun to battery during counter recoil. The principle method is throttling a fluid through an orifice that varies in area during the recoil stroke.

2. Recoil cylinder oil pressure measurement

Pressure sensors were mounted on the left side as well as right side cylinder of recoil system for oil pressure measurements as shown in Figure 2.

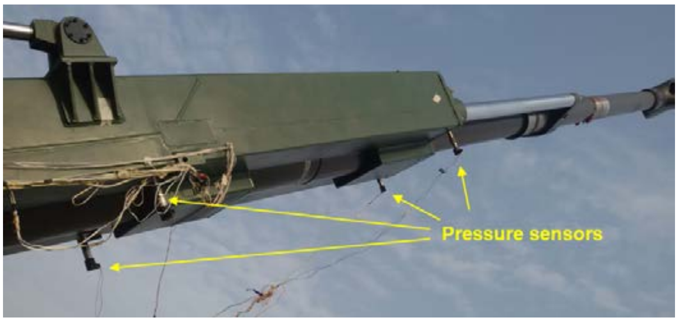

Figure 2: Installation of four pressure sensors in recoil cylinder of oil pressure measurement

The S-11 is specifically designed for the measurement of viscous fluids. 4-20 mA 2-wire output signal. The compact, rugged design makes these instruments suitable for applications including hydraulics and pneumatics

Figure 3: Pressure Sensor Wika make Model S-11

An electronic circuit module consisting of four 250 Ω resistors was made as an interface between four pressure sensors as shown an Figure 3, and Yokogawa data acquisition system DL750 as shown in Figure 4 for recording hydraulic oil pressure in both recoil cylinder.

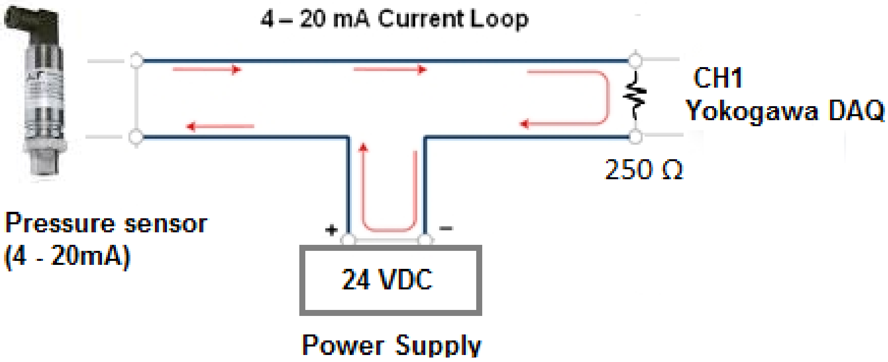

Figure 4: Pressure Sensor interface to data acquisition system

The pressure transducer uses two wire 4-20mA current loop for both power and signal. The 4-20mA current loop is economical to install, using the same two wire for power and signal. It is also ideal for sending a signal over long distances with high resistance to noise. Most data acquisition system, however are configured to accept voltage signal. So how to interface two-wire 4-20mA current loop to the data acquisition system is described in the Figure 4. A resistor is placed in the loop and the voltage drop across the resistor is connected to the data acquisition system. The voltage drop across the resistor is 1VDC when the signal is 4mA and 5VDC when the signal is 20mA being proportional in between. Instrumentation setup in shown in Figure 5

Figure 5: Instrumentation setup

Data recorded during gun recoil and counter recoil motion from of four pressure sensors are shown below shown in Figure 6

Expected fluid pressure before, during and after firing, were recorded and were compared with design parameters.

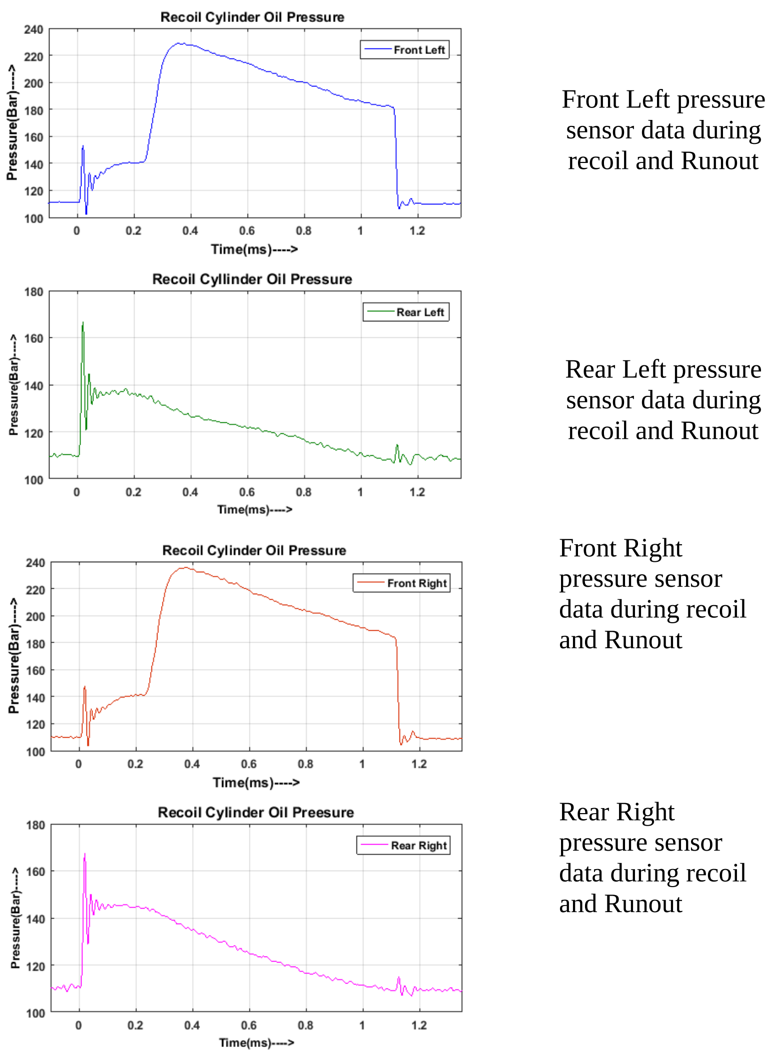

Figure 6: Pressure-time plots of recoil-and runout mechanism

3. Recoil Displacement Measurement

Figure 7 shows the draw wire displacement sensor mounted on gun's recoil system. The Draw wire sensor mounting adaptors/brackets were carefully designed to resist shock during gun firing. The output signal of the transducer is connected to a data acquisition system, Yokogawa DL750 Scopecorder. It has built-in signal conditioner with a sampling rate of 10 M samples and 12-bit ADC. The data is recorded during firing trials in DL750 and after trials it is copied to a PC for further analysis which is done using MatLab.

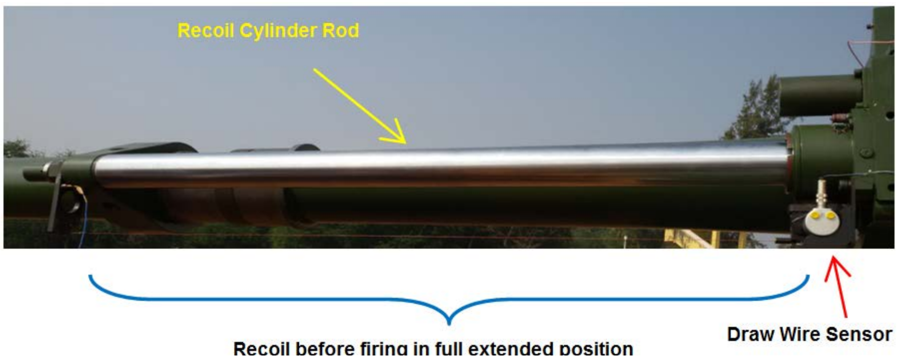

Figure 7: Mounting of displacement sensor on recoil system

Micro-epsilon make WDS-p96-2000 cable extension draw wire as shown Figure 8 was used for recoil displacement measurement The output of sensor is a voltage proportional to the displacement of the motion of the recoil mechanism.

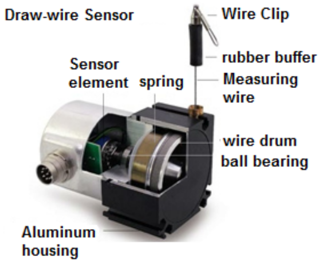

WDS-p96-2000:
Measuring range: 2m
high flexible steel wire on drum, voltage output with integrated electronics
Robust, durable for linear movement

Figure 8: Cut-view of Draw wire sensor

Figure.9 shows the recoil displacement v/s time for few rounds fired with different charge mass. Data recorded for various Charge mass: (CH7, CH9, CH9+3.95kg, CH9+5.15kg)

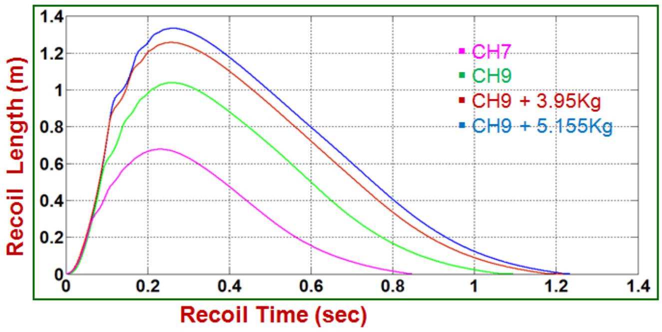

Figure 9: Recoil displacement-time plot

Data was processed using Matlab. The displacement data is smoothed to eliminate the noises occurring on acquisition of signal, the recoil time, counter recoil time and recoil & counter recoil time are computed from the recoil motion curve, finally the velocity is obtained by differentiating the displacement. This measurement system was used to evaluate the performance of recoil system design. Fig10 shows the recoil velocity displacement v/s recoil length for few rounds fired with different charge mass.

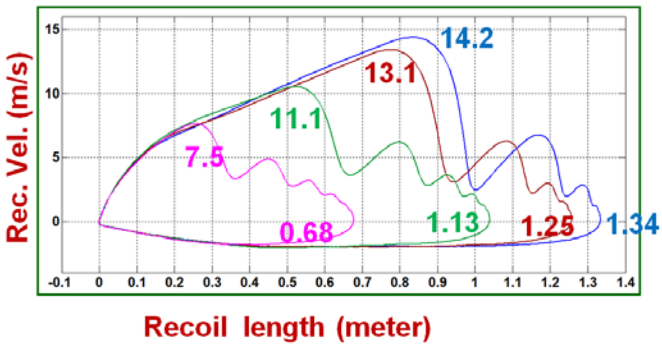

Figure 10: Recoil velocity vs recoil length plot

Figure 11 shows recoil velocity vs time plot. The recoil velocity in negative direction shows the counter recoil motion. After studying the recoil and counter recoil motion curve it was understood that recoil system was behaving closer to the desired behavior (design values - recoil time close to 250 ms, total time should not be more than 2 s)

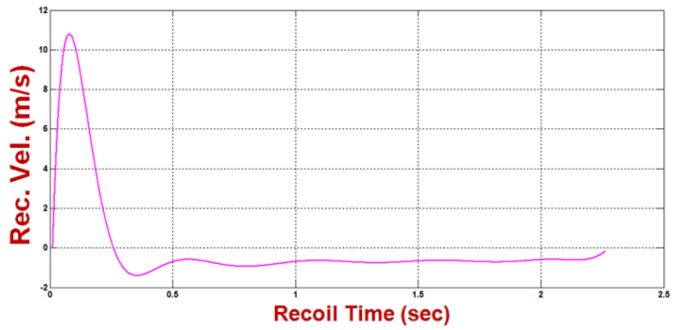

Fig 11. Recoil velocity vs time plot

Table 1: Recoil parameters for various charge mass

Sr. No.	Propellant Charge Mass	Max recoil velocity (m/s)	Max displacement (m)	Total Recoil time (s)	End vel. (m/s)
1.	CH7	7.5	0.68	0.84	0.17
2.	CH9	11.1	1.13	1.1	0.19
3.	CH9+3.9kg	13.1	1.25	1.2	0.22
4.	CH9+5.1kg	14.2	1.34	1.25	0.24

Counter-recoil end velocity, the velocity at a distance of 5 mm before impact was recorded for every trial. All runout operation was smooth and no jerky motion was observed. It was observed that the impact velocity was less than 0.3 m/s as per recoil design. It is found to be within acceptable values after evaluating (around 0.24 m/s at 5mm displacement).

4. Recoil Acceleration Measurement

Real time data on recoiling part acceleration is key in the development of artillery gun. Recoiling forces during the firing are a result of the propellant gases to propel the ERFB projectile. Kistler 8792A, 500g triaxial accelerometer (sensitivity: 200mv/g), was used to record recoil acceleration. as shown in Figure 12.

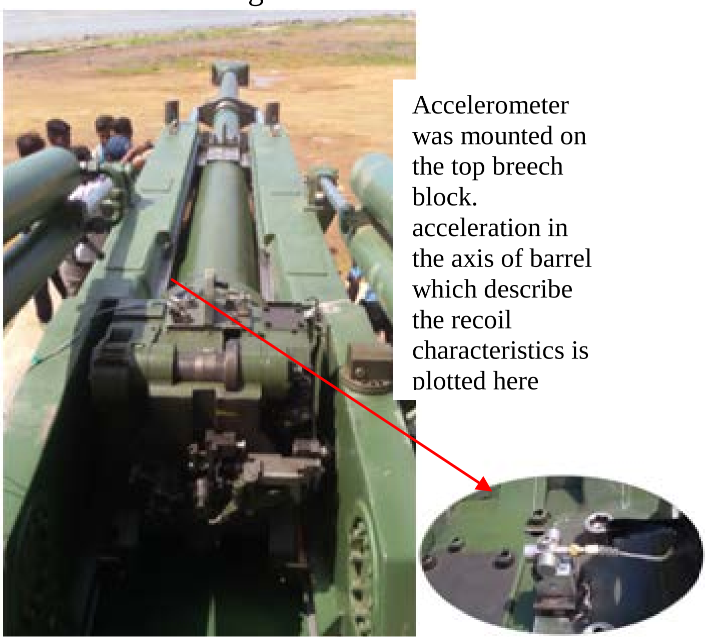

Figure 12: Ordnance recoiling part with accelerometer mounted

Following is the typical plot of recoil force/acceleration-time plot with and without muzzle brake shown in Figure 13.

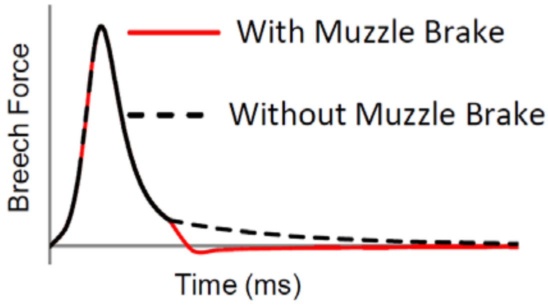

Figure 13: Typical plot of recoil force/acceleration-time

An accelerometer is a device that measures acceleration (G-force). Accelerometers are typically purposed for vibration (periodic) measurement or shock (transient) measurement. Data is provided that shows the acceleration in all three axes. As you would expect, the main recoil has the highest acceleration, followed by a vertical acceleration, then a lateral (sideways) acceleration. Designer uses this real-world data of gun accelerations is useful for development of products. The most important element in a measurement system is the sensor. Typically, a sensor cannot be directly connected to the instruments that record, monitor, or process its signal, because the signal may be incompatible or may be too weak and/or noisy.

Figure 14 shows recorded acceleration-time plot recorded on the Yokogawa DL750P data acquisition system

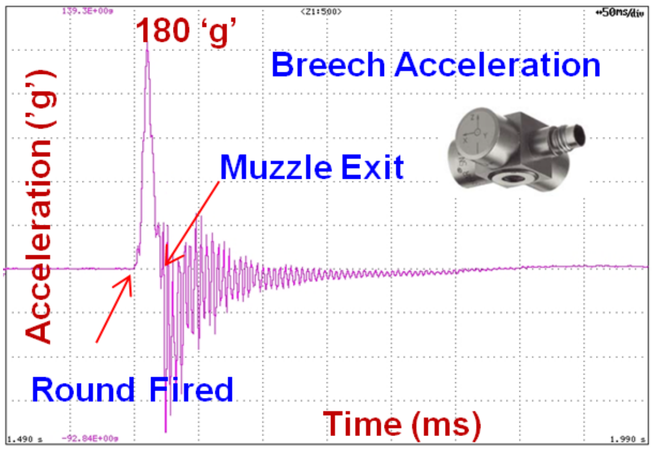

Figure 14: Recorded acceleration-time plot

Above plot shows round firing and projectile muzzle time with max acceleration as 180 g. the complete recoil and runout complete acceleration profile. Acceleration data was filtered and presented in Figure 15 the profile shows how recoil part (ordnance) mass acceleration can be used to calculated recoil force F=ma. muzzle brake efficiency can be calculated from this force. The negative spike in the graph is effect of muzzle brake gas existing sideway, from this plot it is clear that muzzle bake reduces the recoil force.

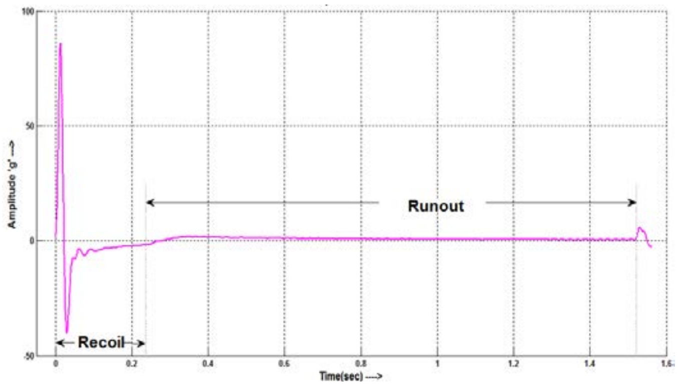

Figure 15: Filtered accelerometer data

Real time Accelerometer data acquisition measurement chain used for this experiment is shown in Fig.16. The signal must be conditioned i.e., cleaned up, amplified, and put into a compatible format. Data was recorded in DL750 scope coder it then taken into PC for processing into mat lab.

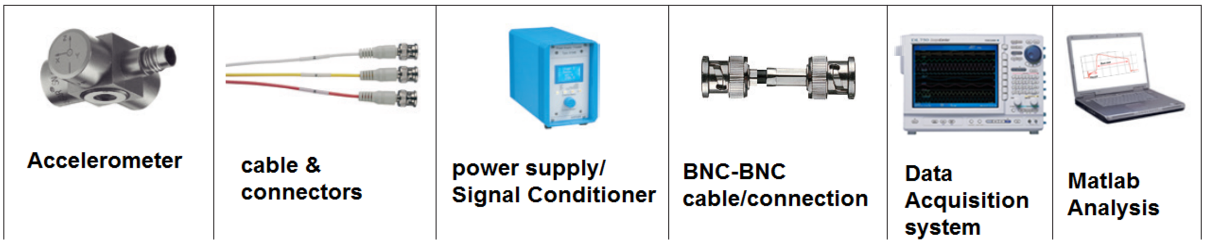

Figure 16: Accelerometer data measuring chain

It is very good foundation for future study and design in recoil system and muzzle brake design. Complete operation can be understood from theses plots. Trials were well planned and extensive care was taken during data acquisition and cable handling.

5. Obsevatuions

All the expected parameters such as recoil displacement, recoil time, recoil velocity, counter recoil time, counter-recoil velocity, counter-recoil end-velocity, oil pressure at four location, and breech acceleration/force measurement were well in limit and in agreement with designers expected values. End velocity well under 0.3m/s. recoil cycle time for maximum charge mass was under 2 sec. maximum recoil length was less than 1500mm for maximum charge mass, breech acceleration was under 200g in agreement with expected value of recoil force considering large recoil mass. and maximum recoil velocity was 15m/s. Before firing and after firing recoil oil pressure was maintained and stable, i.e., 110 bar as per design requirement and maximum oil pressure was 340 bar which was as per design. value. Recoil length and recoil velocity was varied linearly as per increasing charge mass and recoil and counter recoil operation was smooth.

6. Conclusion

The aim of this project is to provide the experimental data of recoil system performance to designer. This data was used to compare expected performance parameters and finalize the design. The paper brings out the importance of data acquisition to improve the design of the armament system. An experimental technique of evaluation of recoil system is presented. The technique and facility developed in this experiment will be helpful to the recoil designer to study and evaluate the performance of new development of recoil system. This methodology can also be used to various different caliber artillery gun in real time dynamic firing. These results provide useful insights in our understanding of the functioning of the overall system.

All the expected parameters such as recoil displacement, recoil time, recoil velocity, counter recoil time counter recoil velocity, counter recoil end velocity, oil pressure at four location, and breech acceleration / force measured. Recorded and analyzed data from these experiments helped the designer to finalize design first time right with minimum changes in configurations.

7. Acknowledgement

Authors are very thankful to Director ARDE for granting permission to publish this work

8. References

[1] Peter, H., 2004, "Principles of Armament design", Trafford publishing, Bloomington, USA.

[2] A Development of Recoil & Counter Recoil Motion Measurement System Using LVDT Ju-Ho Choi, Sung-Soo Hong, and Joon Lyou Science, ICASE: The Institute of Control, Automation and Systems Engineers, KOREA

[3] Gun Recoil System Performance and Prediction, M A Hajihosseinloo, BSc, PhD, C J Hooke, BSc, PhD, D Walton, BTech, PhD, MI Mech E, March 1, 1989, Proceedings of the Institutions of Mechanical Engineers

[4] Armament Research, Development, and Engineering Centre (US Army Armament Munitions, and Chemical Command, 1988, "Military Hand book on Recoil Systems"

[5] U.S. DEPARTMENT OF COMMERCE National Technical Information ServiceAD-A029 073-Recoil Motion Measurement. Part C, Journal of Mechanical Engineering Vol. 2, No. 3, September, 2000

Range Safety Assessment for Air delivered Guided Weapon

Balkrishna Prasad
Armament Research Development Establishment
Defence Research & Development Organisation
Pune
bkpnit1942k2.gmail.co.in

Shweta Dadarya
Armament Research Development Establishment
Defence Research & Development Organisation
Pune

KB Jadhav
Armament Research Development Establishment
Defence Research & Development Organisation
Pune

***Abstract*– Before conducting mission trial of medium range guided bomb, the assessment of range safety and corresponding danger area predictions required in case of weapon failure. This is required so as to as to ascertain safety of population, equipment and infrastructures build around it. The present work describes the range safety assessment of guided bomb using combined model of 6-Dof and point mass. Here the point mass model is included in the 6-Dof model to simulate the vehicle dynamics or its position post weapon failure. Numerous close loop Non-Real-time simulations are carried out to evaluate the danger zone considering all probable failure cases of different subsystems occurring at different intervals of flight. Finally, for the assessment of Danger zone the impact of aerodynamic perturbation, wind and launch aircraft separation disturbances acting on the vehicle is also considered.**

1. Introduction

Guided bomb operates in a close loop autonomous feedback system as shown in the Figure 1. The INS-GPS sensor measures the body dynamics and computes the navigation solution for the guidance and control algorithms embedded in OBC hardware. OBC (On board computer) generates the required fin commands for the actuators to achieve the desired lateral accelerations during flight and engage the target with a minimum miss distance. The above goal will not be fulfilled in case there is a failure either in actuator system or the INS-GPS/OBC Hardware (systems marked in red). Once the failure is initiated in any of the avionics systems in loop, the vehicle will become uncontrollable and the control and guidance computations will diverge and become unstable.

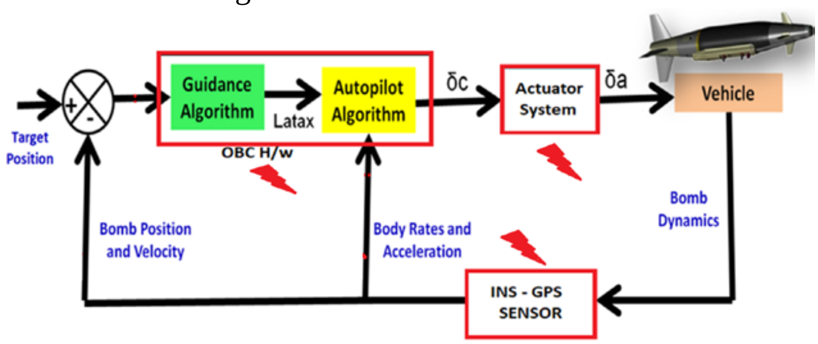

Figure 1: Close Loop Weapon Control

Due to vehicle instability a wide dispersion area is expected on ground post impact. The maximum impact point dispersion over the ground is termed as the danger zone for the launch of the guided bomb during trial and evaluation. This danger zone area is required to be cleared off before any launch.

Outline of this article is as follows. Vehicle failure model is presented in section-2. Flight avionics system failure modes are presented in section-3. Fin actuation system failure modes are covered in section-4. Failure test cases for range safety assessment in covered in section-5. Aerodynamic perturbations and disturbances test matrix are presented in section-6. Simulation results for the non-failure and the failure cases are presented in section-7 & section-8. Impact of wind on range safety corridor are presented in section-9. Conclusion is drawn in section-10.

2. Vehicle Failure Model

There can be two reasons for the failure of the bomb during flight. Structure failure & aerodynamic failure. As the bomb is highly rigid (say Length/Diameter ≤ 9) and can take up to higher inertial loads, chances of airframe structure failure (disintegration into pieces) are rare. Thus, here only aerodynamic failure of the bomb is considered for the impact point prediction and danger zone assessment.

Aerodynamic Failure: Bomb is an aerodynamic body hence it has a limitation up to which its total angle of attack can go. Hence, we are assuming that whenever the missile Total angle of attack goes beyond certain angle (say ~30°), a severe stall condition prevails, which causes the bomb to tumble from that point onwards. Stall angle of attack limit is derived from aerodynamic prediction of the airframe in consideration. During flight high angle of attack is achieved due to actuator failure or wrong fin commands to the fin actuation system. The tumbling part of trajectory is being simulated through point mass model of the bomb, i.e. equation of motion with tumbling drag coefficient.

The trajectory parameters before the tumbling starts is simulated using 6-Dof model whereas the point mass simulation is continued from (t =t_Tumble) to the point at which bomb impacts on the ground (t = t_Impact). During tumbling the following assumptions are considered

(i) Drag Coefficient in the point mass model is assumed to be k∗CD at t =t_Tumble. Here CD is the nominal drag coefficients & the scale factor k is derived considering the vehicle drag coefficient as a blunt body post tumbling.
(ii) Vehicle is assumed to fly without breaking into pieces (any structural disintegration).
(iii) Bomb will follow a ballistic trajectory from the point at which it starts tumbling till the point of impact. If the vehicle starts tumbling then only a point mass model with tumbling drag coefficient is utilized for the impact point prediction.

3. Flight avionics system failure modes

Flight avionics system failure modes and their effect on vehicle dynamics are listed below.

(i) Actuation system failure - Vehicle is uncontrolled and may starts tumbling
(ii) Navigation sensor failure
(iii) Hardware & Software failure – Incorrect actuator fin and command saturation. Vehicle is uncontrolled and may starts tumbling
(iv) On Board Computer (OBC) failure Hardware & Software failure - Incorrect actuator fin and command saturation. Vehicle is uncontrolled and may starts tumbling
(v) Power Failure – Complete avionics system failure. Incorrect actuator fin and command saturation. Vehicle is uncontrolled and may starts tumbling

It may be noted that all the avionics system failures modes affect the vehicle trajectory through control fins deflections.

4. Fin Actuation system failure modes

There are two major ways by which the actuators fins can be non-functional leading to mission failure.

(i) Failure of Actuator Hardware - Local level failure
(ii) Failure of Actuator Power Supply – Global failure

By considering the above two types of failures, chance of single actuator fin failure or together the four-actuator failure is much higher comparable to other combinations of multiple actuator failure cases. Hence the more emphasis has been given on these types of failures. Individual fin actuator has been failed in following four ways

(i) Actuator fin goes to maximum deflection: +ve Side and gets stuck there after
(ii) Actuator fin goes to maximum deflection: -ve Side and gets stuck there after
(iii) Actuator fin remains at NULL Position:0 deg and does not respond to any incoming commands
(iv) Actuator Stops Responding to incoming commands after t = t_{Tumble} and remains stuck at that particular deflection (lock in place failures)

5. Failure test cases for range safety assessment

Different combinations of actuator fin failure modes are considered and in total 261 cases are analysed. The following failure test matrix describes all these cases.

Table 1: Actuator Fin failure test matrix

Case No.	Act_01	Act_02	Act_03	Act_04	Description
1-256	2,10,0,-10	2,10,0,-10	2,10,0,-10	2,10,0,-10	Hard Over & Float Failure
257	1(Stuck)	2	2	2	Actuator fin 1 is stuck at time t & rest are working fine
258	2	1(Stuck)	2	2	Actuator fin 2 is stuck at time t & rest are working fine
259	2	2	1(Stuck)	2	Actuator fin 3 is stuck at time t & rest are working fine
260	2	2	2	1(Stuck)	Actuator fin 4 is stuck at time t & rest are working fine
261	1(Stuck)	1(Stuck)	1(Stuck)	1(Stuck)	All the fins are stuck at time t

Cases 1-256 are for simulating Max., Min & Zero fin position failures. Cases 257-261 are for Lock in Place Failure. These cases are meant for simulating fin stuck failures at time t.

In above test matrix, fins are assigned either of flags (2, 10, 0, -10). The meanings of each of these flags are:

(i) Flag (2): Actuator fin is working fine
(ii) Flag (-10): Actuator fin is Stuck at -10 deg deflection
(iii) Flag (0): Actuator fin is Stuck at 0 deg
(iv) Flag (10): Actuator fin is Stuck at +10 deg deflection
(v) Flag (1): Actuator fin is Stuck at time t (failure injection time)

These 261 cases are run for different failure occurrence time during flight (say 0s, 1s, 3s, 5s, 10s, 15s, and 20s…… and so on till time of impact on ground).

6. Aerodynamic Perturbation & Disturbance test matrix

The weapon should be able to engage the target with all possible combinations of aerodynamic perturbations, wind and launch aircraft separation disturbances. Here the perturbation parameters and disturbances are considered so as to capture the effect of these parameter uncertainties and disturbance combinations on the vehicle impact point dispersion.

A. Separation Disturbances during launch

During release of the weapon, airflow over the vehicle is strongly influenced in the vicinity of the launch aircraft. This acts as a disturbance for the released weapon and is termed as separation disturbances. For simulation of different failure cases separation disturbances from station No. 07 of launch aircraft from maximum altitude and 0.875 Mach release is considered. A worst-case separation forces and moments including the launch aircraft ejection force is considered in the simulation model which acts on the weapon only during T0 to T0+dt sec (for dt duration weapon is in the vicinity of the launch aircraft). During this period no control is applied to the weapon due to the launch aircraft safety.

B. Aerodynamic perturbation

The major aerodynamic parameters uncertainty which are considered for the simulation are as follows

(i) $\varepsilon_{C_D} = \pm x\ \% \ [C_D\ nominal]$
(ii) $\varepsilon_{C_Z} = \pm x\% \ [C_Z\ nominal]$
(iii) $\varepsilon_{C_{z\delta}} = \pm y\% \ [C_{z\delta}\ nominal]$
(iv) $\varepsilon_{C_{m\delta}} = \pm y\% \ [C_{m\delta}\ nominal]$
(v) $\varepsilon_{C_{l\delta}} = \pm y\% \ [C_{l\delta}\ nominal]$
(vi) $\varepsilon_{X_{CP}} = \pm mDia\ [\, X_{CP}(m)\ nominal]$
(vii) $\varepsilon_{X_{CG}} = \pm n\ [\, X_{CG}(m)\ nominal]$

With the combinations of above uncertainty parameters, a total of 2187 perturbations combinations are possible. Out of these combinations 05 extreme perturbations combination are considered for the simulation. These combinations are 1) Nominal, 2) Low Drag More Unstable, 3) Low Drag More Stable, 4) High Drag More Unstable and 5) High Drag More stable. Apart from this, mass up and down cases (02 cases) are also possible. With the inclusion of these two cases 10 worst cases are identified as mentioned in Table 2.

So now a total of 261x10 = 2610 cases has been identified for the simulation of the failure cases. These 2610 cases are run for the different failure occurrence time during flight (0s, 1s, 3s, 5s, 10s, 15s, and 20s…… and so on till time of impact on ground).

Table 2: Aerodynamic Perturbation Matrix

Case No.	Mass(kg)	C_D	C_Z	X_{CP}	X_{CG}	$C_{Z\delta}$	$C_{m\delta}$	$C_{l\delta}$	Perturbation Description
1a & 1b	M ± dm	Nom	Nom	Nom	Nom	Nom	Nom	Nom	Nominal
2a & 2b	M ± dm	-	+	-	+	-	-	-	Low Drag More Unstable
3a & 3b	M ± dm	-	-	+	-	+	+	+	Low Drag More stable
4a & 4b	M ± dm	+	+	-	+	-	-	-	High Drag More Unstable
5a & 5b	M ± dm	+	-	+	-	+	+	+	High Drag More stable

C. Wind Disturbances Perturbation

The following wind profile is used as an input disturbance for the close loop simulation. Here the maximum wind magnitude considered is 50 m/sec at 7-10 km altitude. The wind magnitude and direction are injected in simulation model as a function of altitude.

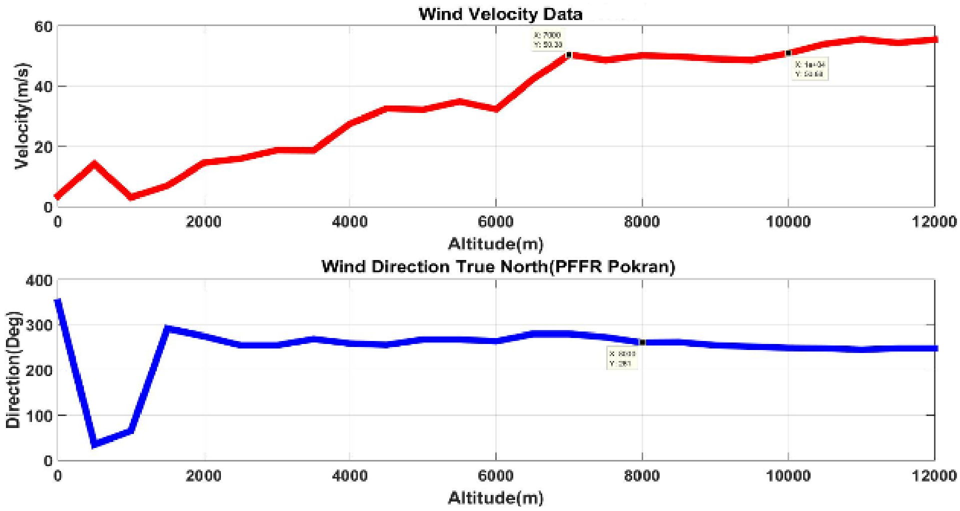

Figure 2: Wind Profile

7. Simulation: Non-failure Cases

Here the trajectory parameter for the normalized maximum altitude and 0.875 mach release from the launch aircraft is presented. The down & cross range is normalized wrt the maximum target range and flight time is normalized wrt to the maximum flight time observed with the perturbation test matrix (Figure 4). The total angle of attack is normalized wrt the maximum stall angle of attack as indicated in section-2. The non-failure trajectory profile is mentioned below.

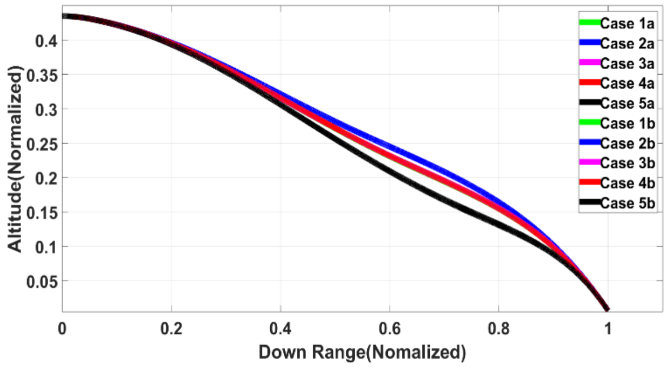

Figure 3: Normalized Altitude vs Down range

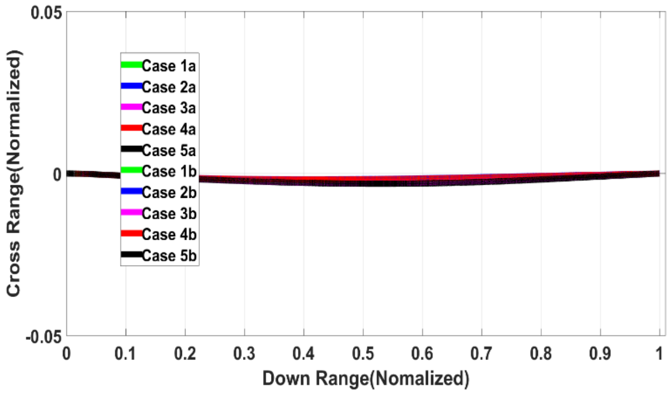

Figure 4: Normalized Cross vs Down range

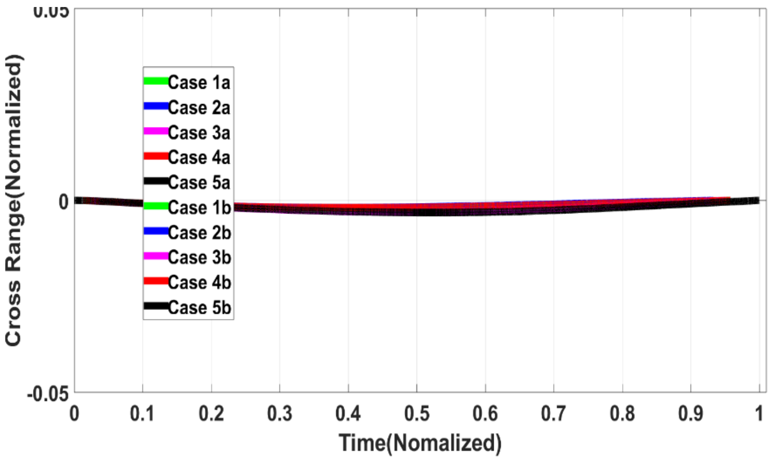

Figure 5: Normalized Cross Range vs Time

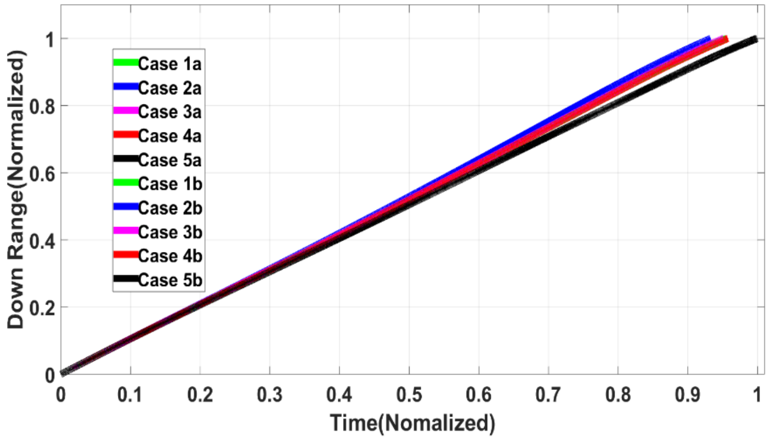

Figure 6: Normalized Down Range vs Time

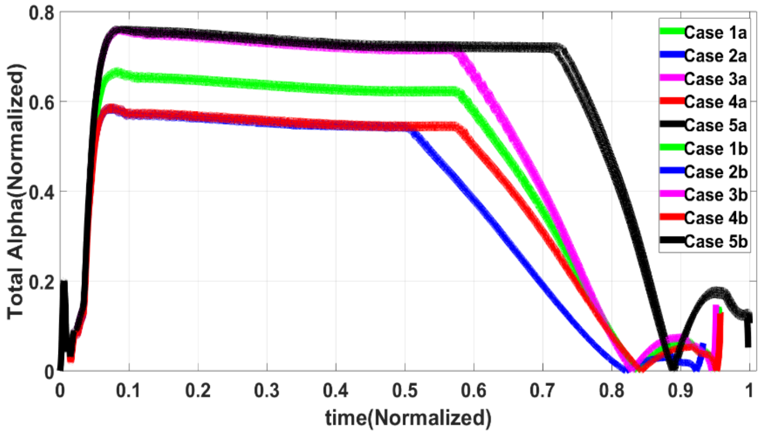

Figure 7: Normalized Total AoA vs Time

8. Simulation: Failure cases

Range safety study has been carried out for all the test cases mentioned in section-6 and the corresponding safety corridor has been identified.

Range safety code for all the perturbation cases without wind are shown in Figure 8. Identification of danger zone for the normalized target range is done by plotting the Impact points in NED local frame.

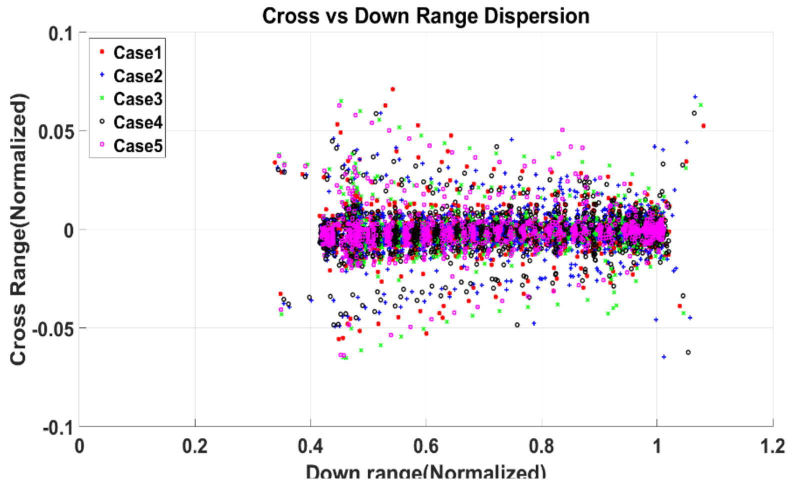

Figure 8: Normalized Impact Points for all the failures cases with no wind condition

9. Impact of wind on range safety corridor

Wind can have impact on the range safety corridor. The wind profile to be used for simulation is mentioned in section 6. Here the wind perturbations combinations (12 nos.) as shown in Table 3 is injected in simulations, only for the extreme ground impact points which are outside the ABCD corridor as marked in Figure 9.

Table 3: Wind perturbations for extreme Impact Points

Max. Wind Velocity	Wind Directions	Wind Perturbations	Failure cases for the Wind Perturbations
50 m/s@10km altitude	Wind direction + (0° to 360° at an interval of 30°)	12 nos. of wind profile combinations for each extreme impact points outside ABCD corridor	77 impact points x 12 = 924 cases

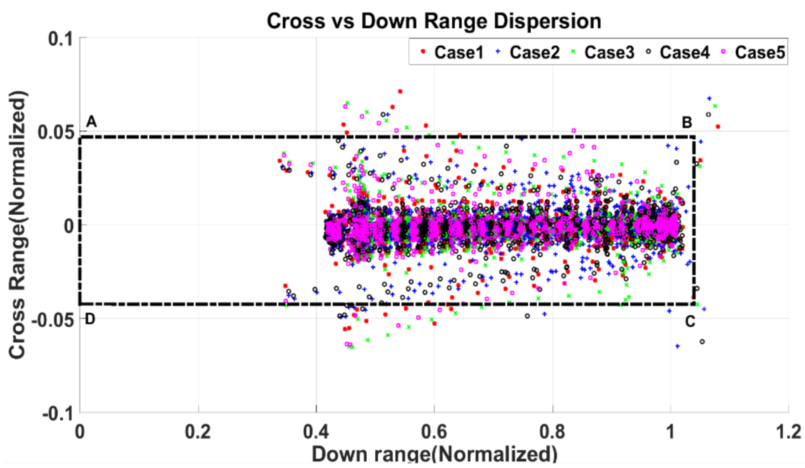

(a)

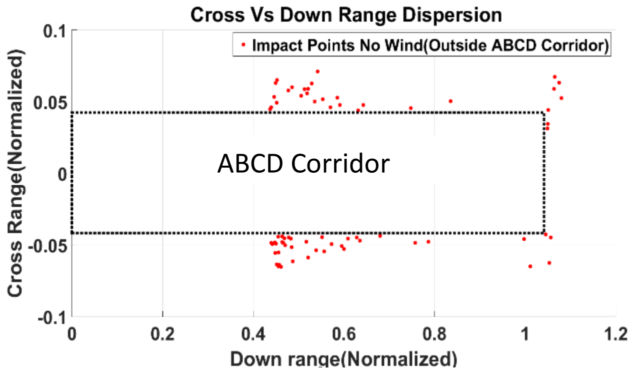

(b)

Figure 9: Impact Points Cases for the wind Perturbations outside ABCD Corridor

In Figure 9 there are about 77 impact points which are outside the ABCD corridor (± 4.3% in cross range and 8% in down range). Now only these extreme impact point cases are considered further for the 12 nos. wind combinations to estimate any expansion of the danger zone area.

From Figure 10 it can be observed that with wind perturbations maximum expansion of the danger zone in cross range is about ±9.1% from 4.3% (without wind) where as in the down range is about +10% from +8% (without wind).

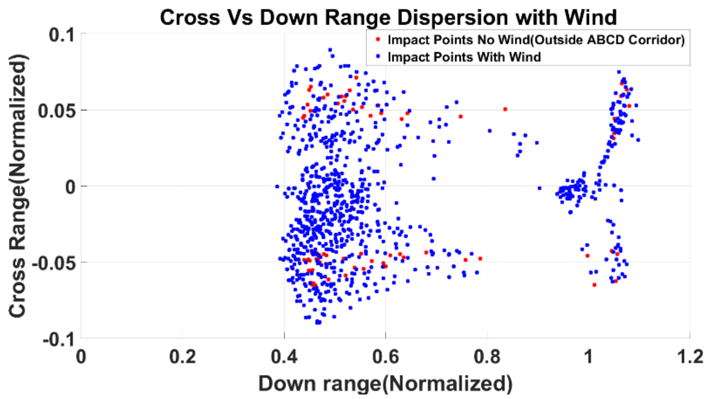

Figure 10: Impact Point Dispersion with wind Perturbations

Finally, the range safety assessment considering all the failure cases including with wind and no wind conditions are generated and mentioned in the following Figure 11.

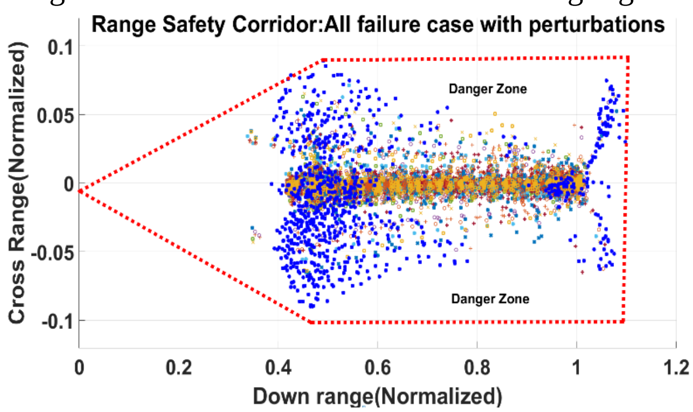

Figure 11: Range Safety Corridor for all impact points

The corridor marked in red is considered as the Danger zone which is about 10% in down & cross range for the given target range, release altitude and Mach number. Thus 10% of the maximum down & cross range clearance is required for the release trial of the guided bomb in the current scenario.

10. Conclusion

A systematic step wise vehicle failure model and avionics subsystem failure cases during flight has been identified in this article which can be responsible for the mission failure. Further this failure cases are combined with aerodynamic and wind perturbations cases to check any expansion in the impact point dispersion on ground to identify the danger zone for the range safety clearance for the release trials. The above model & simulation methodology has been used to predict the danger zone and range clearance for the release trials of medium range tactical guided bomb. The above danger zone has been validated in one of the dynamic trials.

11. Acknowledgments

Authors are thankful to Dr. V Venkateswara Rao, OS and Director, ARDE and MV Ramesh Kumar Group Head, PGM Projects for their continuous encouragement and support.

12. References

[1] Guided Pinaka Range Safety Document Dated Aug 2016
[2] Aircraft trajectory simulator using a three degree of freedom aircraft point mass model by Javier García-Heras Carretero, Francisco Javier Sáez Nieto, Ricardo Roman Cordon.

Development of Automated Test Equipment for Controller Based Actuation Control Unit

Papiya Das
PGM Group
Armament Research & Development Establishment
DRDO
Pune
papiyadas29@gmail.com

C.C. Dharmani
PGM Group
Armament Research & Development Establishment
DRDO
Pune

K.B. Jadhav
PGM Group
Armament Research & Development Establishment
DRDO
Pune

***Abstract*– This research work presents the design and development of Modular Automated Test Equipment for Functional testing and troubleshooting of an Electro-Mechanical Actuation Control Unit. This unit has a complex, densely populated Printed Circuit Board (PCB) with two different controllers, Power electronics devices, high-speed switching circuits, Sensors, and motors. Manual testing of this unit involves simulation of multiple input-output signals/pulses, providing power supplies, monitoring health signals, Documentation, Report generation, etc. Execution of this task in an efficient, economical, and timely manner imposes some severe challenges. The designed ATE executes these tasks in an automated fashion and provides full functional coverage during a test.**

Keywords– Automated Test Equipment, ATE, Test Methodology, Testing of controller based Actuation Control Unit

1. Introduction

Complex Electronics have become an integral part of every Smart and advanced weapon system like Missiles, Guided Munitions, etc. Design verification, troubleshooting, and in-depth testing of these electronics are often time-consuming, laborious, and repetitive. The actuation Control Unit (ACU) of a guided munition rotates its control surfaces which in turn provide motion to the vehicle body in the desired direction. ACU employs four Brushless DC (BLDC) motors to provide precise movements to the control surfaces. Two different Controllers execute the motion control algorithm, process feedback data from sensors, operate relays, and manage serial communication for inter-module communication. Functional testing of this feedback control system involves activities like stimulating and checking system response using different test signals, etc. This is a repetitive process and needs highly skilled manpower to perform the test. In case of some fault in ACU, problem identification becomes hectic and time-consuming. These problems are intrigued not only during the developmental phase but also at the post-production phase. A modular Automatic Test Equipment (ATE) is developed using plug-and-play, Commercial-Off-the-shelf (COTS) equipment to perform these tasks more efficiently, in a time-bound manner with a moderately skilled workforce.

2. Design of ATE

ATE design process was started by preparing a Requirement Specification Document with Market and Literature survey. Soly et al., 2017 developed an ATE for ESP controller using an ARM processor to eliminate manual testing involving mechanical pushbuttons and switches [1]. H. Alper TOKU et al., 2013 developed an ATE using systematic design approaches to tackle the problem of obsolescence [3]. José Moreira1 et al., 2013 utilized an active test fixture approach to perform high-speed testing using a standard ATE [4].

In this line, authors of this paper designed a modular ATE using High performance, low-cost deployment platform PXI. This ATE is modular and generic hence the same ATE can be used to test Electronic units other than ACU, simply by writing new test programs. In case of modifications or design changes in Unit under Test (UUT), the same ATE could be used for testing the modified electronics with minor modification in Test software [6]. Keeping in view the obsolescence problem, standard PXI chassis is used with spare slots to cater to future needs [3]. All the peripheral modules and accessories of ATE like Power supplies, Electronic loads, etc. could be replaced on one to one basis.

An Interface Test Adaptor (ITA) is designed for each UUT to provide electrical interconnections of all six edge connectors of ACU and also access to its test points with ATE. ATE communicates with ACU controllers at the rate of 1Mbps but it can be re-programmed on a requirement basis. ATE and its Test software simulate different signals and instructions received by these interfaces, including sourcing and sinking currents with the help of power supplies and Electronic loads. The control and communication with all these test equipment are performed by ATE Controller, using Ethernet, and RS-232 communication Protocols. Fig. 1 shows the simplified block diagram of ATE.

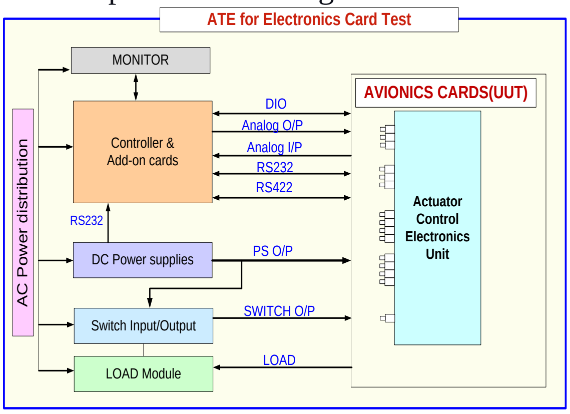

Figure 1: Hardware Architecture of Modular ATE

It also has administrative and operator login modes so that a semi-skilled or unexperienced operator can use them for routine testing. The realized ATE is shown in Fig. 2.

Figure 2: ATE with Display unit & other peripherals

Since the UUTs have both DSP and FPGA-based controllers, testing of embedded software is equally important. ATE uses the communication protocol of ACU controllers to exchange information between them. Chongwu JIANG et al., 2009 published a Study on Real-Time Test Script in Automated Test Equipment using script-based Python [2]. In contrast, the present development work used the Graphical programming language G in the Lab-view environment to write ATE Test programs [7].

3. Test Methodology

The complete functionality of UUT is divided into small independent tasks. The test methodology adopted for testing ACU using ATE is shown in Fig3.

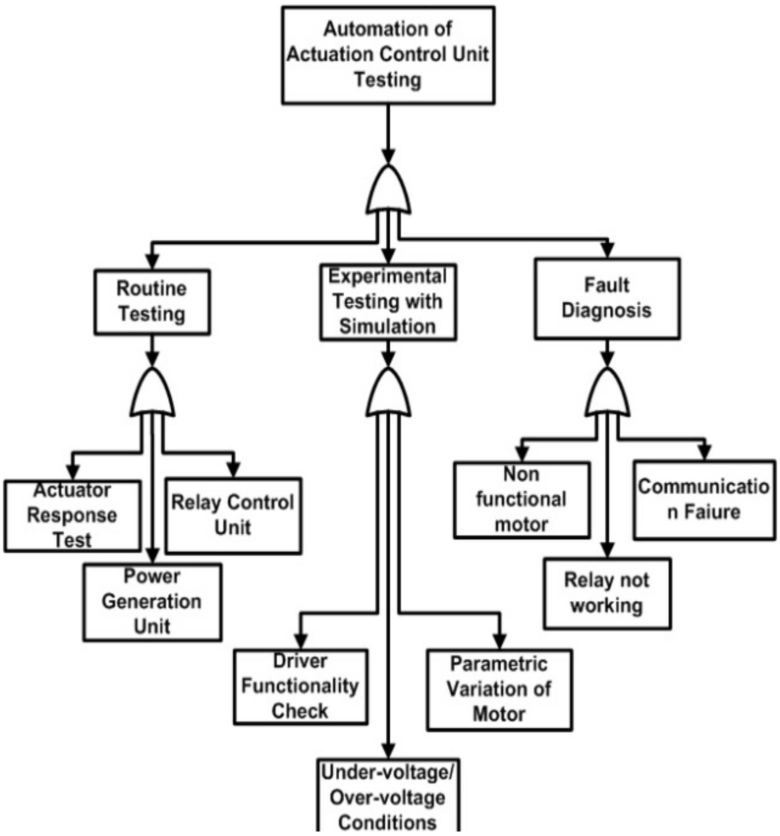

Figure 3: Test Methodology of ACU Test

As per Test methodology, ACU testing shall be conducted under three categories. This test tree was helpful to identify the different types of tests required to provide the full test coverage to the ACU. Each test is then further divided into small individual tasks to include the whole gamut of the functions performed by it. An umbrella software was written for each type of test which further provides options of multiple test cases to the operator.

A. Routine Testing

Routine Testing is the First test method in which characterisation and performance evaluation of Actuator mechanism was performed. These tests are repetitive and also performed on actuators as periodic maintenance. The actuator response test is one such routine test during which the actuator response is measured with Sinusoidal and Step type input signals. Fig. 3 shows the interconnection of ATE and UUT with ITA as interface and Fig. 5 shows the flow chart of this test.

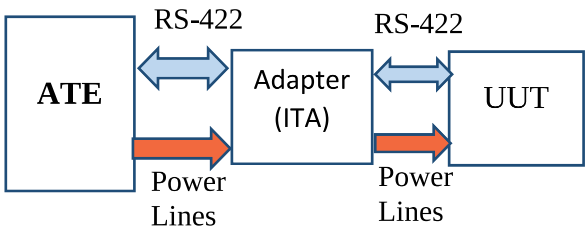

Figure 4: Interconnection of ATE. ITA & UUT

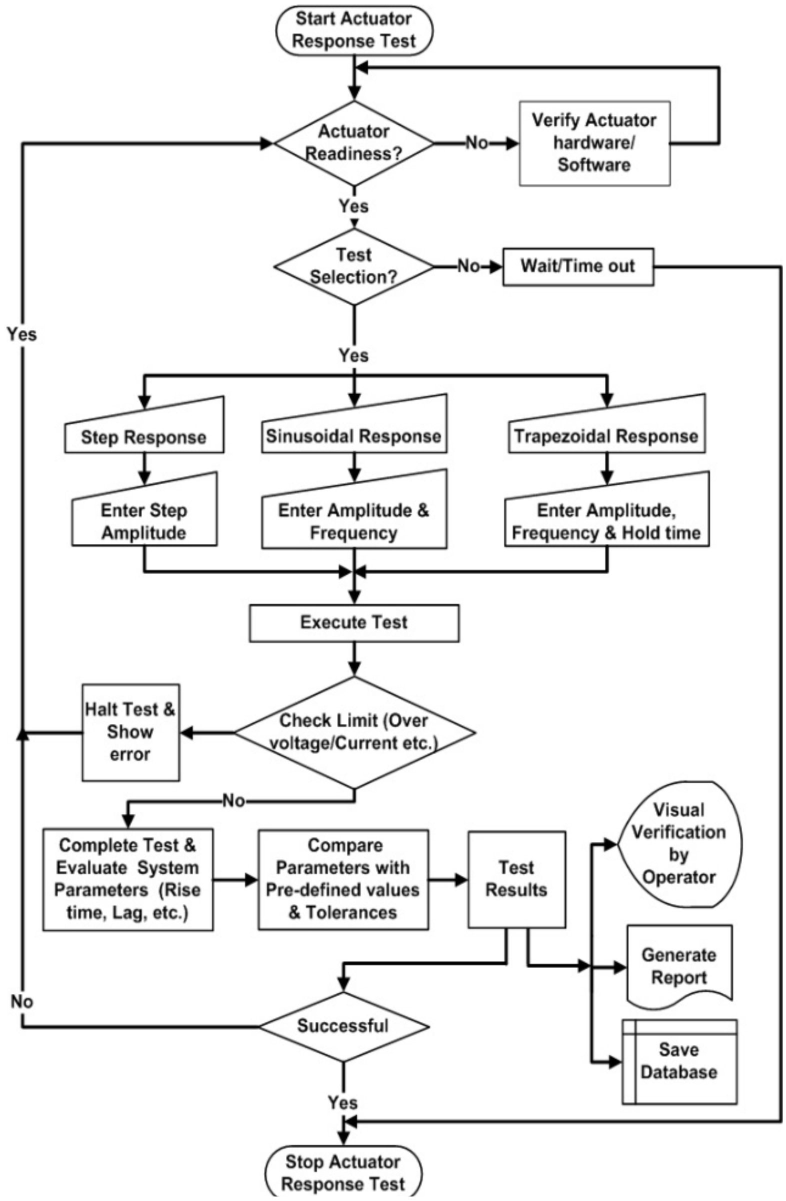

Figure 5: Flow Chart of Actuator Response Test

When the actuator is commanded by a step stimulus of predefined amplitude, the rise time, settling time, and overshoot of response are measured. The test is considered successful if the values of the above-mentioned parameters remain within the tolerance limit. If any of these parameters fall beyond their tolerance limit, the test is considered to fail. All four actuator are tested simultaneously and this test repeated for 20 types of different input test signals. When performed by a highly skilled person, completion of this task in manual mode takes one working day. In contrast, ATE performed this task automatically within 1 to 2 hours including the time required to establish the test set-up. Also, it summarises the test results in one-page summary with the display of graphs and derived parameters.

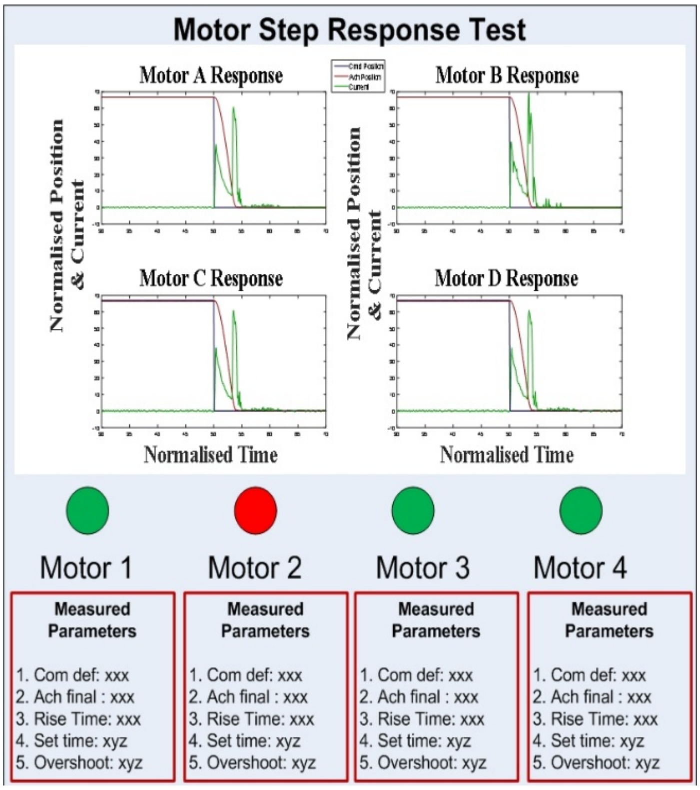

Figure 6: ATE Motor Response Test

Fig. 6 shows the display window of motor responses when the step input signal is fed to them simultaneously by ATE. Here the current demanded by motor 2 is outside the set maximum limit hence it is indicated red. Also, parameters derived from the measured response mentioned in a separate table for quick reference of the operator. The whole sequence i.e. Motor test, parameter measurement, calculation of derived parameters, and display could be completed in few seconds. This is a noteworthy improvement when compared with manual testing. ATE stores these test results into its database in both data as well as the graphical form for future references. It also prepares test reports in a predefined format including plots, important test parameters, and their measured values in multiple runs for quality assurance purposes. ATE also displays the test results instantaneously after every test on its screen for quick analysis and performance checks.

B. Experimental Check with Simulation

One major task of ACU is to drive four BLDC motors. This is a Feedback Control System, which receives commands to move the motor shaft to a specified angle. A Magnetic encoder produced and transmits position feedback to the controller, and motor commutation occurs using Hall sensor pulses. The functional checks of this task need multiple test cases, like Motor driver IC checks, Feedback line checks from Hall and Encoder sensors, etc. Fig. 7 represents the major function of the BLDC motor driver and Fig. 8 shows the flow chart for the in-circuit automated testing of this driver IC.

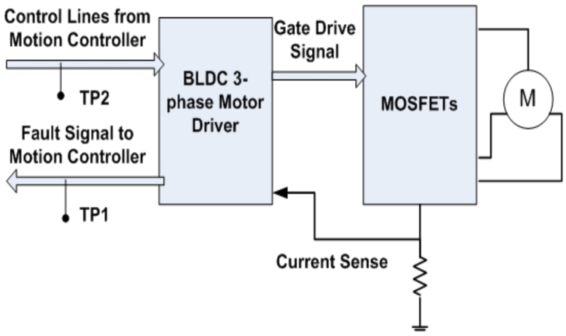

Figure 7: Primary Function of Driver IC

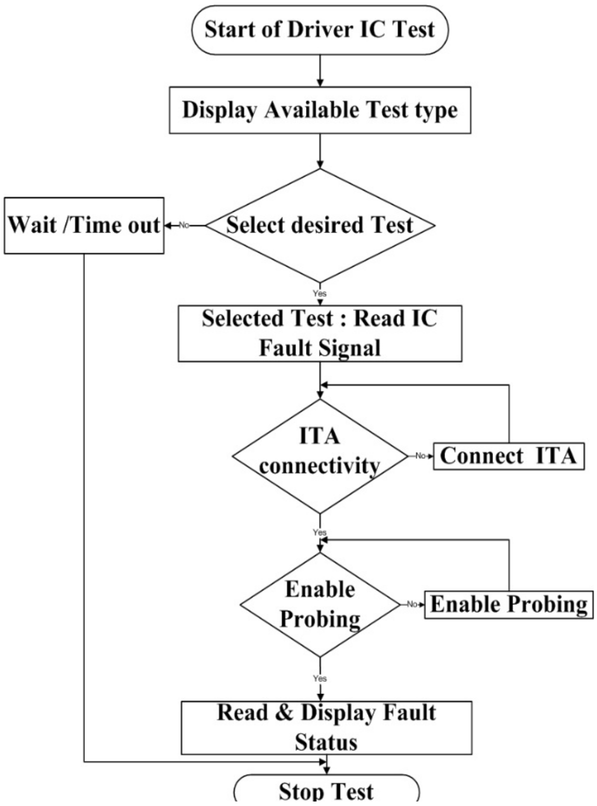

Figure 8: Flow Chart of Driver IC Fault Read

This IC generates a fault signal whenever driver IC functions reach beyond their designed limits. For example, if the current demanded by the BLDC motor is more than its predefined maximum value, one fault signal generated. This fault signal is not routed to UUT edge connector and hence during normal testing, it cannot be observed. In contrast, while performing this test using ATE a fault message will be displayed if this condition arises during the test. It uses specially fabricated mechanical spring-mounted probes which access these fault signals from test points of ACU Printed Circuit Board. This helps the designers to identify the root causes of the faults and subsequently controller parameters or IC settings could be modified to more optimised set of parameters. This specific feature is very useful when some modifications are implemented in either hardware or software of UUT.

C. Fault Diagnosis

Another significant feature of this ATE is to detect faults which may occur in UUT due to component failure, dry solder, etc. For example, let suppose 3.3V power failure occurred while PCB health checks were in progress. In such conditions, operator can invoke the diagnostic mode of ATE where it can specify the area of PCB which might be responsible for the fault using ITA. This way, single ATE can facilitate testing of UUT in multiple test conditions.

4. Safety features of ATE

During the design of ATE, a special safety feature was embedded in every test program to ensure the safe operation of UUT. In case of overvoltage or overcurrent during the test, ATE instantaneously disconnects the power supply to UUT ensuring damage-free automatic operation, without manual intervention.

5. Results & Conclusion

A modular ATE is designed, realized, and tested to examine and troubleshoot a complex Actuator Control unit with 80-90% test coverage. The ATE can test and troubleshoot a UUT in three different methods.i.e. Routine Testing, Experimental Testing with simulation, and test in Diagnostic mode. A fault tree has been created and different test cases have been written to test different functions of UUT. This ATE not only performs tests automatically but can also prepare Test reports in predefined formats. Equipped with these features, this development has drastically reduced the testing time from few days to few hours.

6. References

[1] Soly Elsa Thomas, Nishanth P R, Development of Automated Test Equipment for ESP Controllers, 2nd IEEE International Conference On Recent Trends in Electronics Information & Communication Technology (RTEICT), May 19-20, India, 2017

[2] Chongwu JIANG, Bin LIU, Yongfeng YIN, Chang LIU, Study on Real-Time Test Script in Automated Test Equipment, 978-1-4244-4905-7/09/$25.00©2009 IEEE, 2009

[3] H. Alper TOKU, Developing New Automatic Test Equipments (ATE) using Systematic Design Approaches, 978-1-4673-5683-1/13/$31.00 ©2013 IEEE, 2013

[4] José Moreira1, Bernhard Roth1, Hubert Werkmann1, Lars Klapproth2, Michael Howieson3, Mark Broman3, Wend Ouedraogo3 and Mitchell Lin4, An Active Test Fixture Approach for 40 Gbps and Above At-Speed Testing Using a Standard ATE System, 1081-7735/13 $31.00 © 2013 IEEE, 2013

[5] Automatic Test Equipment, Keith Brindley, Newnes, July 1991

[6] Eric Bean, Virtual Machines and Automated Test Equipment, 978-1-5090-0790-5/16/$31.00 ©2016 IEEE, 2016.

[7] Stephen S. Yoon & Ricardo Soza, Aaron M. Dalton, AI-BASED Automatic Test Equipment with Component Interchangeability, 0-7803-5432-X/99/$10.00 0 1999 IEEE, 1999

Uncertainty Assessment of Force Measurement Data of Wind Tunnel Test

Shreyas Misra
Dept. of Mechanical and Manufacturing Engg.
Manipal Institute of Technology
Udupi
shreyasmisra13@gmail.com

Rakesh Kumar
Aeronautical Development Establishment
DRDO
Bangalore

Abstract*– Experimental data contains uncertainty that arises from random errors in the measurement. The uncertainty gives rise to spurious results which do not represent the true dynamics of the system accurately. The force measurement obtained from wind tunnel tests for the aerodynamic investigation of an aircraft configuration is one such example of an experiment that requires a tremendous amount of data, thereby, increasing the chance of errors. The techniques for estimating the uncertainties in measurements, and in the experimental results calculated from them, must be structured to combine statistical and engineering concepts in a way that can be methodically applied to each step in the data uncertainty assessment process. This paper gives an overview of the uncertainty assessment methodology and its adoption to an experimental measurement. The procedure reported in this paper for the uncertainty assessment is a combination of methodologies adapted from various literature sources, including AGARD. This assessment is applied to estimate the uncertainty in the aerodynamic coefficients measured at a Low-Speed Wind Tunnel Test facility, OCWT-IISc on a UAV configuration. The expanded uncertainty and percentage uncertainty are also presented. It was concluded from the uncertainty assessment that the per cent uncertainty obtained is within the required 5% range for the Lift, Drag and Pitching Moment coefficients over the operating range of the aircraft.

***Keywords*– Unmanned Aerial Vehicle, Sampling, Uncertainty, Confidence Level, Aerodynamic Coefficients, Probability Distribution.**

Nomenclature:

α/AoA = Angle of attack
ρ = Density
C_L = Coefficient of Lift
C_D = Coefficient of Drag
C_Z = Coefficient of Normal Force
C_X = Coefficient of Axial Force
C_Y = Coefficient of Side Force
C_m = Coefficient of Pitching Moment
C_r = Coefficient of Rolling Moment
C_n = Coefficient of Yawing Moment
F_Z = Normal Force
F_X = Axial Force
F_Y = Side Force
M_Y = Pitching Moment
M_X = Rolling Moment
M_Z = Yawing Moment
S_{ref} = Reference area
C_{ref} = Mean Aerodynamic Chord
B_{ref} = Reference Wing Span
M = Mach Number
WT = Wind Tunnel
CFD = Computational Fluid Dynamics
MCM = Monte Carlo Method
TSM = Taylor Series Method
GUA = General Uncertainty Analysis
DUA = Detailed Uncertainty Analysis
DRE = Data Reduction Equation
ε = Sampled Random Uncertainty
β = Sampled Systematic Uncertainty
S_x = Random Standard Uncertainty
b = Systematic Standard Uncertainty
$\bar{X}$ = Sample Mean
$S_{\bar{X}}$ = Standard Error of Mean
N = Number of Samples
A = Limits of the uniform distribution

1. Introduction

Modern experiments are performed based on assumptions and generalizations which help simplify real-world systems. Data obtained from such experiments are bound to contain errors and uncertainties that skew the measurements toward false values. In situations like commercial or military flight, the errors present in the data obtained from either a WT or a CFD simulation can have devastating effects if not quantified in the design stage.

An UAV is a flight system that is either remotely piloted or completely autonomous. In either case, the control laws design requires a true representation of the air vehicle configuration in terms of various aerodynamic force/moment coefficients. Hence, to achieve the better representations of the air vehicle throughout the flight range, an uncertainty estimation process is conducted during the design phase to define the errors in the aerodynamic coefficients the effect of that can be ascertained in pre-flight studies on flight mechanics model, saving a lot of time and money.

Uncertainty estimation is a part of statistical theory in which statistical concepts are applied to real-world datasets to quantify the errors and confidence in the data obtained from experiments. Uncertainty is defined as a 'possible value' of the error and represents the interval within which the error lies. The term uncertainty analysis refers to the procedure of computing uncertainties in independent parameters and the results obtained from them. Uncertainty consists of two components namely a systematic part and a random part as given by *AGARD* [1]. Systematic errors are also called bias errors and random errors are also called precision errors. The methodology defined by *AGARD* [1] uses an analytical method based on Taylor Series to compute the uncertainty in the result obtained from a data reduction equation. The procedure is similar to the one provided in *Coleman and Steele* [2] where the uncertainty estimation process in a result is defined as a combination of a General Uncertainty Analysis and a Detailed Uncertainty Analysis. *Coleman and Steele* [2] also provide a sampling method based on the Monte Carlo algorithm to simulate the experiment for several iterations.

Many prior studies on uncertainty estimation and statistics have been conducted on aerodynamic data. *Belter* [3], in his paper used the uncertainty estimation procedure defined by *AGARD* [1] to compute uncertainty limits and confidence intervals for Balance measurements in the Boeing Aerodynamics Lab. *Subagyo* [4] used a statistical analysis method called Analysis of Variance to compare experimental data obtained from 3 WT tests. *Dijana* [5] computed measurement uncertainties using TSM and also tested the dataset for repeatability using thresholds obtained from *Steinle* [6]. *Springer* [7] showed that the aerodynamic coefficients obtained from two different sizes WTs can be compared using the balance accuracies. A detailed uncertainty quantification for the Ares 1 WT that considered errors arising from various sources was provided by *Houlden* [8]. The paper by *Moffat* [9] described the uncertainty analysis procedure similar to *AGARD* [1] and also provided a detailed review of the various sources of uncertainty. Although some of these papers have provided a detailed review of the uncertainty analysis procedure, no paper applies the MCM, which is considered to be a better method than the TSM for a DUA (*Coleman and Steele*[2]), to an aerodynamic dataset to compute the uncertainties.

This paper uses MCM to propagate the uncertainties in independent variables by simulating the experiment many times. MCM is used due to its robustness in measuring the various sources of errors. To perform the computations, a complete analysis of the error sources in wind tunnels is carried out. The calibration data obtained from the measurement sources (pressure sensors, velocity sensors, balance etc.) is used to define a bias limit and the measured data is used to compute random uncertainty, which together represents the combined uncertainty in the data. The calculations in this paper use a 95% confidence level to compute the expanded uncertainty which is aligned with recommendations from literature. The per cent uncertainty is also computed to highlight the significance of the uncertainty relative to the true value.

2. Data Reduction Equations

The measured variables such as velocity, density, force and moment on body axis system have to be converted to appropriate aerodynamic coefficients. The equations to perform the conversion are

$$C_Z = \frac{F_Z}{\frac{1}{2}\rho V^2 S_{ref}}$$

$$C_X = \frac{F_X}{\frac{1}{2}\rho V^2 S_{ref}}$$

$$C_Y = \frac{F_Y}{\frac{1}{2}\rho V^2 S_{ref}}$$

$$C_m = \frac{M_m}{\frac{1}{2}\rho V^2 S_{ref}\, c_{ref}}$$

$$C_r = \frac{M_r}{\frac{1}{2}\rho V^2 S_{ref}\, b_{ref}}$$

$$C_n = \frac{M_n}{\frac{1}{2}\rho V^2 S_{ref}\, b_{ref}}$$

Moreover, we define the Lift and Drag coefficient in the wind axis to better understand the aerodynamics of the flight. These are computed using the following equation

$$\begin{bmatrix} CL \\ CD \end{bmatrix} = \begin{bmatrix} cos(\alpha) & -sin(\alpha) \\ sin(\alpha) & cos(\alpha) \end{bmatrix} \begin{bmatrix} C_Z \\ C_X \end{bmatrix}$$

These DREs will be utilized to compute the aerodynamic coefficients at each iteration of the Monte Carlo algorithm. Hence, these sets of equations are used to propagate the uncertainty in each measured variable to the result.

3. Instrumentation and Data Acquisition Systems

All data presented in this section is obtained from the *Wind Tunnel Test* Report [10]. Few repeat runs are conducted at zero side-slip angles without any control surface deflections. The tests were performed at relatively low speeds and corresponding to M=0.3. The data acquisition system consists of a PXie 16 channel ADC board with a 250 ks/sec sampling rate and a universal signal conditioner-amplifier system configured for custom voltage with excitation mode for strain gauge signal conditioning. The individual balance measurements were connected to the universal amplifier using a special interfacing connector SCXI-1314. A standard sampling rate of 1ks/sec was used for force data acquisition. The WT had a 2-axis semi-automatic turntable that can load up to 360 kgf. For testing the alpha-sweep condition, the Pitch and Pause method of data acquisition was used.

All of the balance components were calibrated in a two-step process consisting of a positive loading step and a negative loading step. The negative loading step starts by rotating the balance by 180 degrees and performing the loading. The bridge elements response is normalized by a bridge excitation voltage of 5 V. The applied forces and moments (F_L) are obtained by multiplying the balance response (F_R) by the balance response matrix or calibration matrix $\left([K_{ij}]^{-1}\right)$.

$$[F_L] = [K_{ij}]^{-1}[F_R]$$

Balance accuracies are shown in Table 1. They are 0.1% of the rated load of the component. The standard density is taken from the Indian Reference Atmosphere at 1000 meters. A 1:4 model designed with aluminum alloy AL 6061-T6 is used. The maximum blockage observed was 2.3% at AoA equal to 24 degrees. The model tolerances are shown in Table 2.

Table 1: Balance Accuracies

Balance Component	**Accuracy**
Normal Force	$\pm$0.150 kgf
Axial Force	$\pm$0.0675 kgf
Side Force	$\pm$0.0675 kgf
Pitching Moment	$\pm$0.020 kg-m
Rolling Moment	$\pm$0.012 kg-m
Yawing Moment	$\pm$0.015 kg-m

Table 2: Geometric tolerances

Parameter	**Tolerance**
S_{ref}	$\pm 0.1\%\ m^2$
C_{ref}	$\pm 0.0002\ m$
B_{ref}	$\pm 0.001\ m$

4. STATISTICAL BACKGROUND

In the uncertainty assessment procedure, some of the key terms used in this paper are defined in the following section for better clarity.

A. Mean

The mean is defined as the average of all the observations in a sample dataset. The mean is an estimator of the true mean of the parent distribution.

$$\bar{X} = \frac{1}{N}\sum_{i=1}^{N} X_i$$

B. Standard Deviation

It is defined as the scattering of data around the mean. The standard deviation is the best estimator of the standard deviation of the parent distribution.

$$S_X = \sqrt{\frac{1}{N-1}\sum_{i=1}^{N}(X_i - \bar{X})^2}$$

C. Standard of the Mean

This term represents the standard deviation of the true mean.

$$S_{\bar{x}} = S_X/\sqrt{n}$$

D. Least Squares Method for Parameter Estimation

The Least Squares method is an optimization technique that minimizes the sum of squared errors in a given set of measured values to find the best estimate of the parameter. If the errors are normally distributed, this method gives the Maximum Likelihood Estimate of the parameter. H is the Jacobian matrix, found by partially differentiating the DRE. The best estimate of the parameter is then given by $\hat{x}$.

$$argmin\ L_s(e^T e), e \in R^{N\times 1}$$
$$\hat{x} = (H^T H)^{-1} H^T Y$$

E. Confidence Intervals

Confidence intervals estimate the range within which the true value of the parameter could lie with a specified percentage of confidence. The upper and lower confidence intervals are usually found using symmetric distribution called the *t-distribution* by specifying the parameters p and n. The 100(1-p) confidence interval for the true mean of a sample is given by

$$\bar{X} \pm t_{n-1;p/2} S_{\bar{x}}$$

Confidence intervals, however, require the distribution of the variable to be known. Estimating a distribution can be challenging, however, as the MCM is applied, the distribution of the result is readily available. Hence, to specify a confidence associated with the uncertainty obtained, an interval called the coverage interval is computed. The coverage interval is defined as the interval which contains a specified % of values as given by *Coleman and Steele*[2]. A 95% coverage interval is used for this study.

F. Chauvenet's Criterion for Outlier Rejection

This criterion checks the difference between the sample mean $\bar{X}$ and a sample point in the distribution. A point is considered to be an outlier if the difference is greater than or equal to τS_X. τ is obtained from Table 3 corresponding to the number of readings or measurements in a dataset.

Table 3: Values of the parameter τ [AGARD[1]].

Number of Readings (N)	τ
3	1.38
4	1.54
5	1.65
6	1.73
7	1.80
8	1.87
9	1.91
10	1.96
15	2.13
20	2.24
25	2.33
50	2.57
100	2.81
300	3.14
500	3.29
1,000	3.48

5. Methodology

First, an outlier rejection procedure is performed on the data obtained from the measurements. The random standard uncertainties are computed using the standard deviation of these measurements, as given by *Coleman and Steele* [2]. Bias values for the variables are obtained from their respective instrument information. The random uncertainties can be modelled using a Gaussian distribution due to the Central Limit Theorem (*Peters* [11]). The bias errors on the other hand do not change from one measurement to another and are hence, invariant. A uniform distribution within the limits $\pm A$ is used to model the bias errors in a sample. The parameter A depends on the instrument, for example, the least count of the instrument.

A total of 216 observations are present for Velocity and Dynamic Pressure which are used in the calculation of the random uncertainty after outlier rejection. The bias error in velocity is taken as zero due to careful calibration and testing of the instrument. Density is taken as a constant throughout the test series because of the incompressible flow condition at low Mach numbers. The best estimate of Density is calculated using the Least Squares method on the Dynamic Pressure equation given by

$$\rho = \frac{Qg}{\frac{1}{2}V^2}$$

Nine Balance measurements are available per force component per AoA. Each of these force components has a different bias error which is obtained from the accuracy of the instrument used for that component as shown in Table 4.1. Moreover, all of the force and moment components will have different random uncertainties for each value of AoA. The best estimates of the balance components at each AoA are obtained by using Least Squares estimation. To model the errors in the geometry parameters, only systematic uncertainties are considered as the geometry is invariant throughout the test series. The bias errors are modelled using uniform distributions with limits defined in Table 2.

A General Uncertainty Analysis is then performed using the TSM on each of the DREs. The GUA is an important part of the uncertainty estimation procedure as it provides information about the sensitivity of the result with respect to each independent parameter. A more important quantity computed from the GUA is the *Uncertainty Magnification Factor (UMF)*. The UMF of a result *r* with respect to an independent variable *x* is given as

$$UMF_x = \frac{x}{r}\frac{\partial r}{\partial x}$$

The uncertainties in the independent variables propagate through the DRE and are either magnified or diminished. The UMF highlights the magnification or reduction of the uncertainty in each independent variable when it propagates through the DRE. The parameter whose uncertainty is magnified (> 1) is treated with greater caution during the experiments.

A Detailed Uncertainty Analysis is a more exhaustive procedure and is conducted after the experiments have been completed and the entire data is available. The DUA is performed using the MCM as shown in Figure 6.1. The DUA is performed for each independent variable and then performed for the result using the DREs.

The uncertainty in the result u_r is then calculated as the standard deviation of the distribution obtained from the MCM. Per cent uncertainties are calculated using the best estimate of the result obtained from the Least Squares method.

$$\%\, Uncertainty = u_r / r$$

Lastly, an expanded uncertainty is calculated for Lift and Drag coefficients. The expanded uncertainty associates a confidence level with the uncertainty computed. It is calculated via a 95% coverage interval. The expanded uncertainty represents the range between which 95% of the *M* values lie, hence estimating the range for the true value of the coefficient at each AoA.

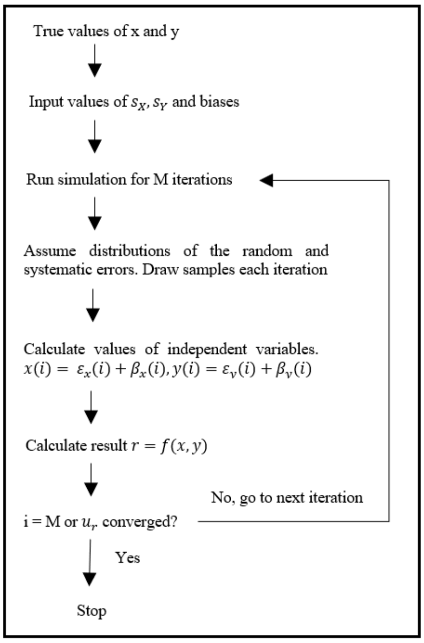

Figure 1: Detailed Uncertainty Analysis for a result obtained from a DRE using the MCM.

6. Results and Discussion

A. General Uncertainty Analysis

The GUA is performed using TSM and the Uncertainty Magnification Factors are shown in Table 4. It is clear from the results that the uncertainty in velocity is magnified as it propagates through the DRE. This is because of the order of velocity in the DREs which becomes a multiplication factor when the partial derivative for velocity is computed. The order of the rest of the variables is 1. Hence, during the experiment series, velocity is carefully controlled and it is ensured that no systematic errors propagate through the data reduction equation.

Table 4: Uncertainty magnification factors obtained during the General Uncertainty Analysis

	Measured variables						
	Velocity	ρ	Force	Moment	S_{ref}	C_{ref}	B_{ref}
C_Z	2	1	1	-	1	-	-
C_X	2	1	1	-	1	-	-
C_Y	2	1	1	-	1	-	-
C_m	2	1	-	1	1	1	-
C_r	2	1	-	1	1	-	1
C_n	2	1	-	1	1	-	1

B. Detailed Uncertainty Analysis

(i) Velocity

The random uncertainty is the only error component present in velocity and is taken as the standard deviation of all measurements after outlier rejection. The true value of velocity used in the MCM is estimated using Least Squares and is equal to 46.124 m/s. MCM is conducted for 10,000 iterations and an early stopping condition is applied to stop the algorithm when the uncertainty is converged to 0.5%. The distribution of velocity and convergence of the uncertainty is shown in Figure 2 and Figure 3, respectively. The uncertainty in velocity converged after around 7000 iterations as seen in the figures and is equal to 0.3523 m/s or 0.763 %.

(ii) Balance Measurements

The systematic error being just 0.1% of the rated load does not have a significant impact on the combined uncertainty. Random errors account for a majority of the combined uncertainty in the balance measurements. This can be due to high scatter in measuring the forces and moments. The combined uncertainty in the balance components obtained from MCM simulation and its variations with AoA are presented in Figure 4. The best-estimated value of each balance measurement is computed using the Least Squares method and is shown in Figure 5 for a typical normal force at a given AoA.

From Figure 4, it is observed that the Normal force component has the highest uncertainty at all values of AoA. This is due to the relatively large Normal forces generated by the aircraft. Furthermore, Figure 4 also shows high uncertainties at larger AoAs for all balance components. The flow separation phenomena which occur when the boundary layer separates from the wing at high AoAs causes a high scatter in the data recorded thereby, increasing the random uncertainty and combined uncertainty thereafter. The maximum uncertainties obtained are shown in Table 5.

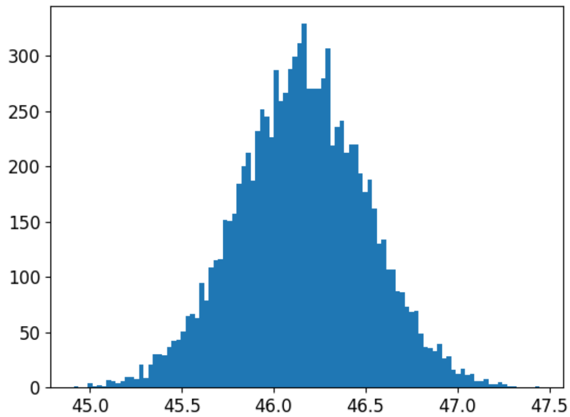

Figure 2: Distribution of Velocity (m/s).

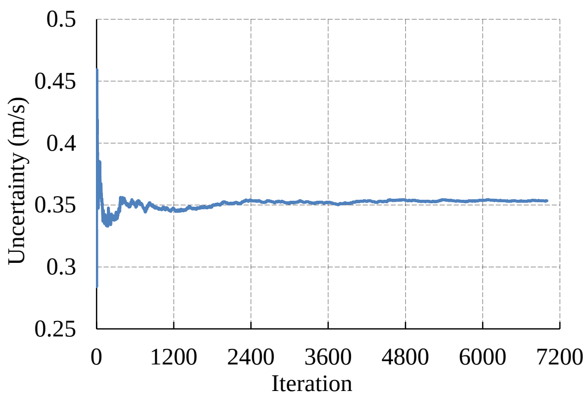

Figure 3: MCM Convergence history: Velocity.

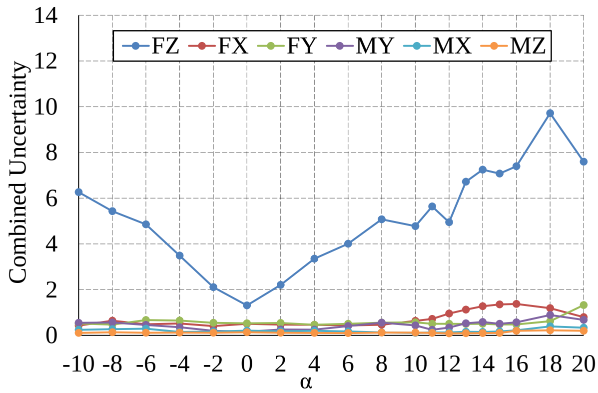

Figure 4: Combined Uncertainty: Balance Measurements.

(iii) Uncertainty in Force and Moment Coefficients

The MCM shown in Figure 1 is applied to compute the uncertainty in the force and moment coefficients. The early stopping criteria is similar to that used for velocity. 9000 iterations are executed and the computing time is around 52 secs including the data reading and processing procedures. The combined uncertainties in the coefficients are shown in Figure 6.

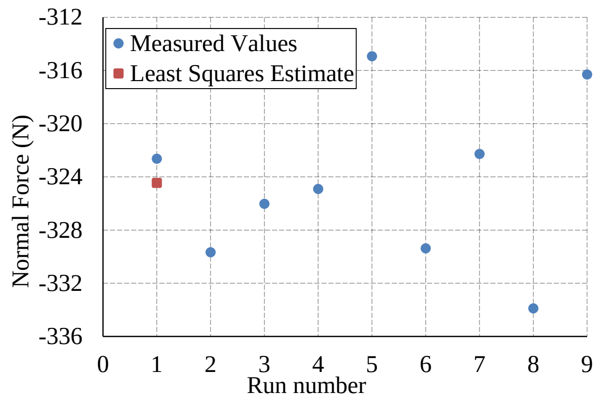

Figure 5: Least Squares Estimate: FZ (α = -100).

Table 5: Max. Uncertainty: Balance Components

Balance Component	Max Uncertainty
Normal Force	±1.2329 kgf
Axial Force	±0.3786 kgf
Side Force	±0.3193 kgf
Pitching Moment	±0.0933 kg-m
Rolling Moment	±0.2357 kg-m
Yawing Moment	±0.0655 kg-m

The uncertainties follow the same trend as seen in the force measurements because the uncertainty in velocity and S_{ref} affect all the coefficients equally and the uncertainty in C_{ref} and B_{ref} is not significant enough to make a large difference. The reason for the trend is similar to that of balance measurements. Maximum uncertainties present in each component are shown in Table 6

Due to the similarities in the uncertainty value for all coefficients, per cent uncertainties are calculated using their respective best estimates to analyze the significance of the uncertainty. The per cent uncertainties for force coefficients with AoA are shown in Figure 7 and the per cent uncertainties for moment coefficients with AoA are illustrated in Figure 8.

The per cent uncertainties of CZ, CX and Cm are all within $\pm5\%$ over most of the operating range of the aircraft. The reason for the relatively large uncertainty obtained at a few angles is due to the actual value of these coefficients being close to zero at those angles. Although the uncertainties are very small, these coefficients reduce to almost 0 at those AoAs and give rise to high per cent uncertainties.

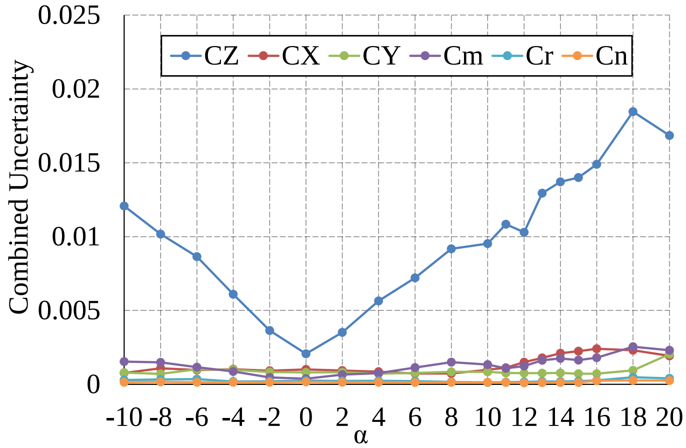

Figure 6: Combined Uncertainty: Force/Moment Coeff.

Table 6: Max. Uncertainty: Force/Moments Coeff.

Coefficient	**Max Uncertainty**
C_Z	±0.0238
C_X	±0.0055
C_Y	±0.0048
C_m	±0.0026
C_r	±0.0028
C_n	±0.0008

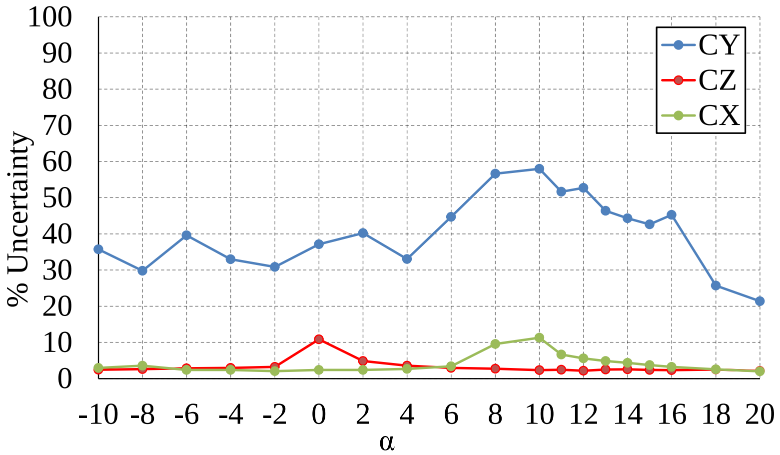

Figure 7: Per cent Uncertainty: Force Coeff.

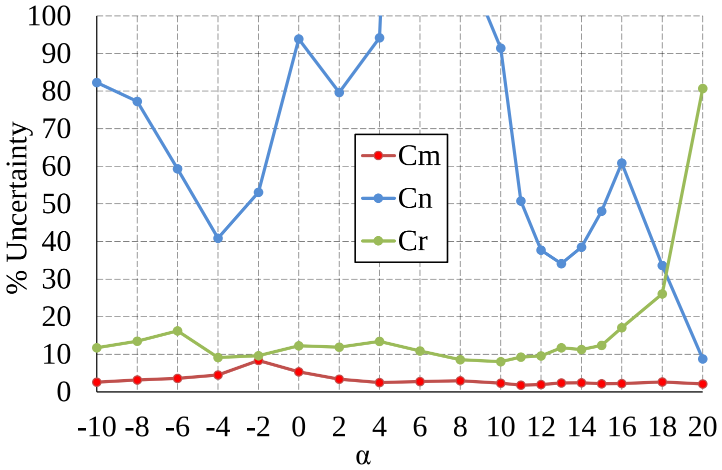

Figure 8: Per cent Uncertainties: Moment Coeff.

High relative uncertainty is obtained in Cr at a 20-degree AoA. Large per cent uncertainties are observed at almost all values of AoA for C_Y and C_n. The values of C_Y, C_r and C_n for α-sweep configuration are very small at all angles. The high scatter of the Side force, Rolling moment and Yawing moment along with very small actual values result in high uncertainties. To obtain better estimates of uncertainties in these coefficients, a configuration with Vertical Tail or control deflection must be used.

(iv) Uncertainty in Lift and Drag coefficients

The uncertainties in C_L and C_D are calculated from the uncertainties in C_Z and C_X. The data reduction equation is given in section 3. The uncertainties in the Lift and Drag coefficient also depend on AoA, which is taken as a constant. The per cent uncertainty present in C_L has a similar trend as C_Z and is within 5% for all angles, except at $\alpha = 0$ (11% uncertainty) as the actual value is almost zero, as shown in Figure 9. The per cent uncertainty for CD is also displayed in Figure 9. From the figure, it is clear that the uncertainty in the Drag coefficient is very small at all angles with a maximum value of 4%.

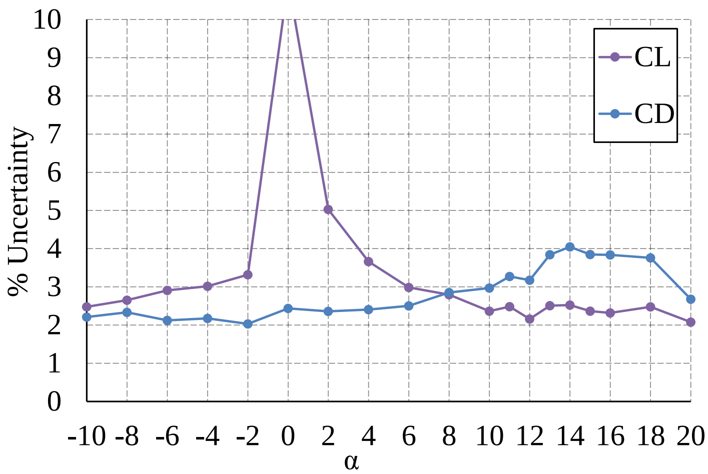

Figure 9: Per cent Uncertainty: Lift/Drag Coeff

(v) Expanded Uncertainty in Lift and Drag Coefficients

The Expanded Uncertainty in C_L and C_D are calculated as elaborated in Section 5. The maximum expanded uncertainty is 0.0692 and 0.0207, obtained at 18-degrees AoA, in Lift and Drag, respectively. This means that the largest interval between which the true value of the coefficient lies is obtained at 18-degrees AoA with 95% confidence. The expanded uncertainties of Lift and Drag are shown in Figure 10 and Figure 11 respectively.

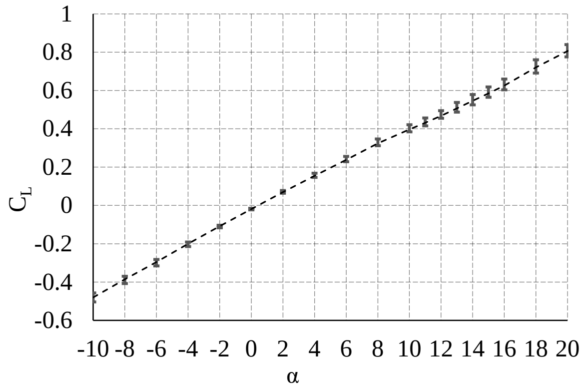

Figure 10: CL with the Expanded Uncertainty

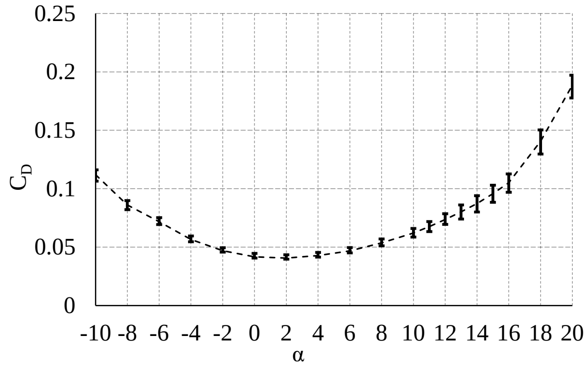

Figure 11: CD with the Expanded Uncertainty

7. Conclusion

Uncertainty estimation is a crucial part of the experimental design and planning stage and has to be followed meticulously. The uncertainties in force and moment coefficients were estimated using the Monte Carlo Method and a General Uncertainty Analysis is conducted using Taylor Series Method. The summary of the results obtained is as follows

- The GUA procedure showed the importance of controlling velocity during the experiment to reduce the uncertainty in the result.
- The maximum uncertainty in the F_Z, F_X, and F_Y are $\pm$1.2329, $\pm$0.3786 and $\pm$0.3193 kgf, respectively. Whereas, the maximum uncertainty in M_Y, M_X and M_Z are $\pm$0.0933, $\pm$0.2357 and $\pm$0.0655 kg-m, respectively.
- High uncertainties are obtained at large AoAs because of the separated flows.
- Maximum uncertainty in C_Z, C_X, C_Y, C_m, C_r and C_n are $\pm$0.0238, $\pm$0.0055, $\pm$0.0048, $\pm$0.026, $\pm$0.0028 and $\pm$0.0008, respectively.
- As C_Y, C_r and C_n do not have a major contribution during α-sweep test, the values are really small and the scatter in forces and moments measured is relatively large resulting in very high uncertainties.

Per cent uncertainties obtained for C_L, C_D, C_Z, C_X and C_m are within the required 5% threshold throughout the operating range. The coefficient expanded uncertainties presented in this paper show that the true values of C_L and C_D lie in a small interval with 95% confidence, therefore, the noise level in the experimental data is very little. Hence, the Low-Speed WT facility used for this test campaign has a high degree of trustworthiness and can be used for future experiments, if the same instrument and flow qualities are maintained.

9. References

[1] *Quality Assessment for Wind Tunnel Testing =: L'appréciation de La Qualité Pour Les Essais En Souflerie*; NATO, Ed.; AGARD advisory report; 1993.

[2] Coleman, H. W.; Steele, W. G. *Experimentation, Validation, and Uncertainty Analysis for Engineers*, Fourth Edition. Wiley: Hoboken, NJ, USA, 2018.

[3] Belter, D. Comparison of Wind-Tunnel Data Repeatability with Uncertainty Analysis Estimates. In 20th AIAA Adv. Measurement & Ground Testing Technology Conf.; 1998, https://doi.org/10.2514/6.1998-2714.

[4] Subagyo. Statistical Analysis of Aerodynamic Forces and Moments Measurements in Indonesian Low-Speed Wind Tunnel. International Journal of Engineering and Advanced Technology 2019, 8 (4).

[5] Damljanović, D.; Isaković, J.; Rašuo, B. T-38 Wind-Tunnel Data Quality Assurance Based on Testing of a Standard Model. *Journal of Aircraft* 2013, *50* (4), 1141–1149. https://doi.org/10.2514/1.C032081.

[6] Steinle, F.; Stanewsky, E.; Dietz, R. O. *Wind Tunnel Flow Quality and Data Accuracy Requirements*; AGARD advisory report; AGARD: Neuilly-sur-Seine, 1982.

[7] Springer, A. Comparison of the Aerodynamic Characteristics of Similar Models in Two Different Size Wind Tunnels at Transonic Speeds. In *20th AIAA Adv. Measurement & Ground Testing Tech. Conf.*; 1998. https://doi.org/10.2514/6.1998-2875.

[8] Houlden et al. - 2010 - Quantification of the Uncertainties for the Ares I.

[9] Moffat, R. J. Describing the Uncertainties in Experimental Results. *Experimental Thermal and Fluid Science* 1988, https://doi.org/10.1016/0894-1777(88)90043-X.

[10] Rakesh Kr et al. 2020- Wind Tunnel Data Analysis & Report for UAV Configuration: Internal. Report.

[11] Peters, C. A., 2001. Statistics for Analysis of Experimental Data. In: *Environmental Engineering Processes Laboratory Manual.* Champaign, Illinois: S. E. Powers, Ed.

Real Time Hardware in Loop Simulation for Precision Guided Munition Using LabVIEW

Shalini Gupta
Armament Research
Development Establishment
DRDO
Pune
shalinigupta@arde.drdo.in

R Jaitly
Armament Research
Development Establishment
DRDO
Pune

BK Prasad
Armament Research
Development Establishment
DRDO
Pune

S Dadarya
Armament Research Development Establishment
DRDO
Pune

KB Jadhav
Armament Research Development Establishment
DRDO
Pune

***Abstract*– The present work describes a real time-based hardware in loop simulation set up for verification of the on-board avionics hardware and software in hardware in loop environment to certify that right system is build and prepared for the flight environment. Apart from sensor (INS) motion on rate table all other high-fidelity guided munition dynamics, controller, actuator models/interface-hardware logics and communication interfaces are established as per flight trial. This paper presents the details of HILS setup, system configuration and HILS simulation results for OBC in loop, OBC-ACU-Sensor in loop in full simulation configuration. This simulation setup has a feature of flexibility and expansibility. By use of the proposed setup the flight control algorithm for guided munitions can be effectively tested and validated in this platform. To validate the PGM system adequacy for harsh environment different disturbance signals are injected and performance is analysed for each perturbed case. A HILS test setup like the one is described here can help to solve the problems of future flight control system and to recognise the problems in early development process.**

1. Introduction

Hardware- in-loop simulation testing has played an important role in the successful development of many modern military weapons and commercial systems. HIL simulation contributes to shorten the new weapon development cycle time and reduce the development cost effectively.

Precision guided munitions like guided bombs are one of the effective and potent arsenal for military weapons. Guided bombs are air-to-surface aerial guided munitions, which are used to achieve air raid and precision strike. In order to meet the demands of modem warfare, some conventional bombs are converted into smart bombs using INS based sensor and fin control actuation system, which will greatly improve the sustained combat capability of the military.

On Board Computer (OBC) which is known as flight control computer, is a major part of the guided avionics of smart bombs, and is also the key subsystem to achieve combat capability. OBC executes the guidance and control algorithms in real time and act as a central processing unit for whole weapon system. In the design process of flight control avionics, some problems brought by hardware and software deficiency cannot be found through mathematical simulation, so it is necessary to do hardware in loop flight simulation to test the real-time performance of weapon's guidance and control system [1], [2]. To verify and validate the flight control algorithms a virtual but real time 6 DOF flight simulator is required to mimic the weapon dynamics. This flight simulator act as a semi-physical simulated test interface between the flight control avionics of smart bomb.

A HILS setup should include all possible real parts of the system in order to verify the correct implementation of the Flight Control system design, check its performance for harsh environment by injecting the different disturbance signals and performance should be analysed for each perturbed case [4].

Outline of this paper is as follow. In section 2, a brief of HILS architecture is presented. Real Time 6 DOF simulator and serial interface implementation is presented in section 3. In section 4, Methodology for two HILS configurations viz. OBC in loop and OBC-ACEU-Sensor (full simulation) in loop is described. In section 5 results for different perturbation cases are illustrated, Finally, conclusion of this work is drawn in section 6.

2. HILS architecture

In HILS setup, the subsystems of guided avionics are gradually introduced into the closed-loop system until a complete HIL simulation platform is formed. The hardware structure of the HILS setup is shown in Fig. 1. As shown in Fig. 1, the HIL simulation system is composed of an On-Board computer, an INS unit, an actuator model/ Actuator unit, a data acquisition computer and a 6 DOF simulation computer with its control panel. The simulation process is shown as follows:

(i) When the power is on, the flight control computer receives the target parameters and INS initialisation data by the aircraft simulator.

(ii) The 6-DOF simulation computer starts computing the weapon's dynamic and sends acceleration and rates data to INS sensor after acquiring the simulated release/start command from a hardware switch.

(iii) The INS sensor has two mode of operation viz flight mode and HILS mode. In HILS full simulation mode it acquires the acceleration and rates data from 6-DOF computer and provides the navigation solution with respect to ECEF frame to the flight control computer.

(iv) The flight control computer executes guidance and control algorithm, and transmits fin deflection command to the actuation control unit.

(v) The 6 DOF simulation computer acquires fin deflection commands and compute the virtual autopilot angles (aileron, elevator and rudder). These angles are used to determine the proper value of aero coefficients which in turn required to compute the bomb's dynamics in inertial space.

(vi) The data acquisition computer records the trajectory data of the bomb sent by the flight control computer and six DOF simulator.

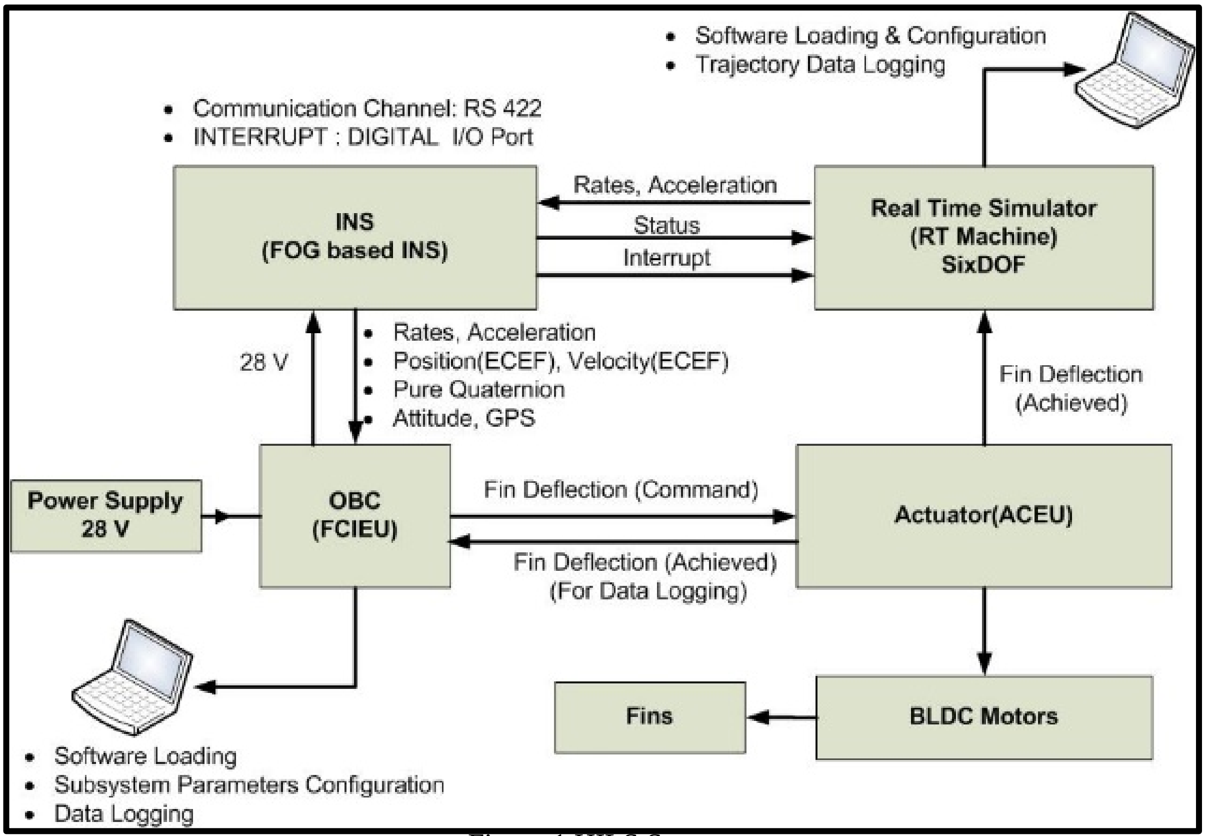

Figure 1 HILS Set-up

3. Real Time 6 DOF Simulator and Serial Interfaces Implementation

The NI PXIe-8135 PXI Express embedded computer has Real Time Operating System (RTOS) and it is chosen as real-time trajectory simulator for HILS setup. RTOS computer is a high bandwidth(8GB/sec) PXI Express compatible system controller is used to simulate the guided bomb dynamics. The real time flight dynamics simulator contains 12 ordinary differential equations (ODE) solved with RK-4th order method with fixed step size of 1 msec. Control Design Simulation tool of LabVIEW is used to simulate the 6 DOF trajectory of vehicle and it was ensured by timestamping each iteration that the flight simulation is deterministic for step size of 1ms. The determinism of control design loop is achieved by avoiding shared resources (eg. Global variables), contiguous memory conflicts (build arrays function), and sub VI overhead. Because the LabVIEW memory manager is a shared resource, therefor memory reduction techniques is used to improve the determinism of an application. As 6 DOF loop is a time critical loop thus special care is taken to avoid allocating memory within a loop. Pre-allocating arrays are used instead of using the Build Array function. This will prevent the access of LabVIEW memory manager at every iteration [3]. Memory technique has reduced the loop iteration time from 20 msec to 1 msec.

The NI PXI-8433 Serial Instrument Control Module is used for RS422 interface which support flexible baud rates for data transmissions. Serial Data transmission /acquisition VIs are developed in LabVIEW and used to transfer the simulated INS data to the INS sensor and simulated flight dynamics data to the data acquisition computer. In addition to this one more serial interface is developed to acquire the achieved fin deflection data from Actuation Control Electronics Unit (ACEU). These, Multiple serial interfaces are implemented using NI-VISA (Virtual Instrument Software Architecture) instrument driver of LabVIEW. VISA is a standard for configuring and programming the systems comprising serial (RS232/RS485/RS422) and USB interfaces. Above mentioned serial data acquisition or transmission is ensured using a Timed Loop which can executes an iteration of the loop at the specified period of time. Overall HILS implementation is done using three parallel Timed Loop and One Control Design Loop. As RTOS system is quad core processor thus each loop is assigned with different processor and configured with suitable priority number to perform the deterministic task and have idle time during every iteration to allow lower priority loops to execute.

A host computer is used to develop the six DOF and serial data acquisition & transmission VIs for the real-time system. After developing the real-time system VIs, it's deployed and run on the RTOS system. Development of all VIs is done under real time environment with Labview2015 software. The host computer can run VIs that communicate with VIs running on RT targets and also provide a user control interface as shown in Fig 2.

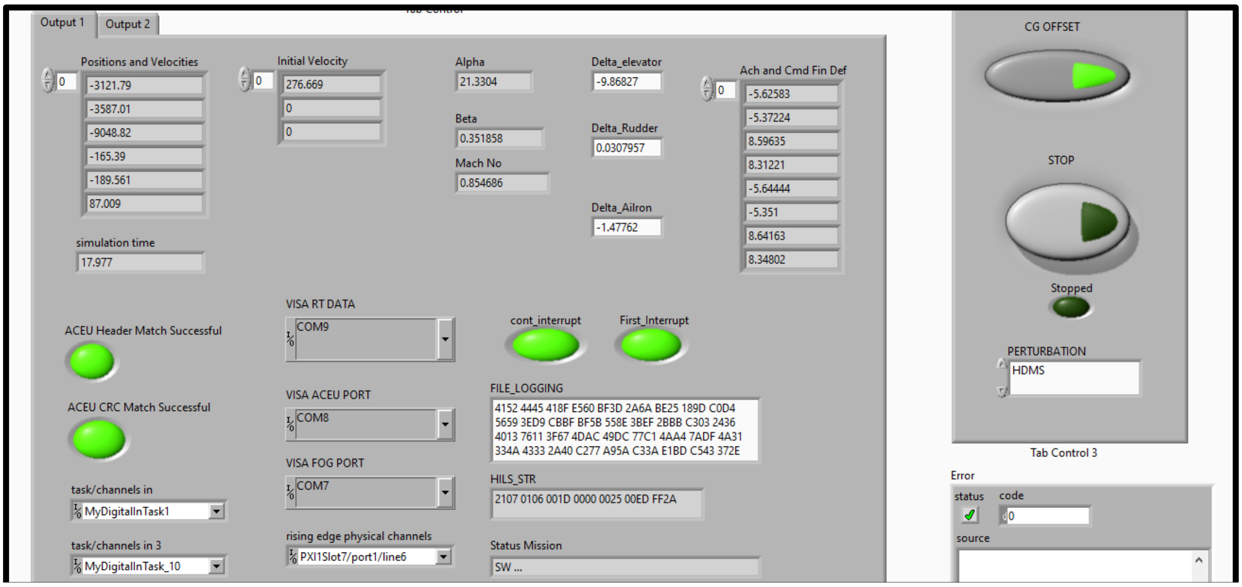

Figure 2 : RT Control Panel

4. OBC in Loop & OBC-ACEU-Sensor in loop (Full-simulation)

Guided avionics of bomb is validated in HILS in following two configurations:

(i) OBC in loop:

(ii) OBC-ACEU-Sensor in loop(Full-simulation)

Each configuration is explained as below:

A. OBC in loop

For OBC in loop architecture, an actuator is mathematically modelled as second order transfer function and unit transfer function is used for Inertial Navigation System. Remaining Interfaces and structure are same as OBC-ACEU-Sensor in loop configuration which is described in the following section.

B. OBC-ACEU-Sensor in loop (Full-simulation)

In this configuration, actuator model is replaced by the actual ACU hardware and integrated with OBC and the acceleration and rates are fed through RT to OBC via INS, thus establishing communication between the two and also incorporating hardware delay. This method is identified as Full simulation method because both the sensor's data viz. rates and acceleration is derived from the six DOF simulator.

In both the mode INS unit acquires acceleration and rates data from 6-DOF computer and provides the navigation solution to the OBC with respect to ECEF frame. Thus, flight dynamics in both the configurations is simulated in RTOS and serially communicated to the on-board computer via INS.RTOS machine executes the six DOF iterations of guided vehicle @ 1msec on the reception of achieved actuator deflections and transfer the vehicle dynamics data to the INS @ 2.5 msec. OBC executes the flight control algorithm on reception of vehicle dynamics data and send control surface deflection commands to the actuator control unit @ 5msec. Actuator unit is interfaced with four BLDC motors and send the feedback response of motors/control surfaces to OBC. Same feedback is utilised by the RTOS system using RS4222 parallel dropping technique and it acquires the feedback @ 5msec for further trajectory generation of bomb. Different serial interfaces of HILS setup are shown in below Fig 3. The RTOS system sends the full trajectory data of the bomb to the data acquisition computer @ 20msec, till bomb hit the ground.

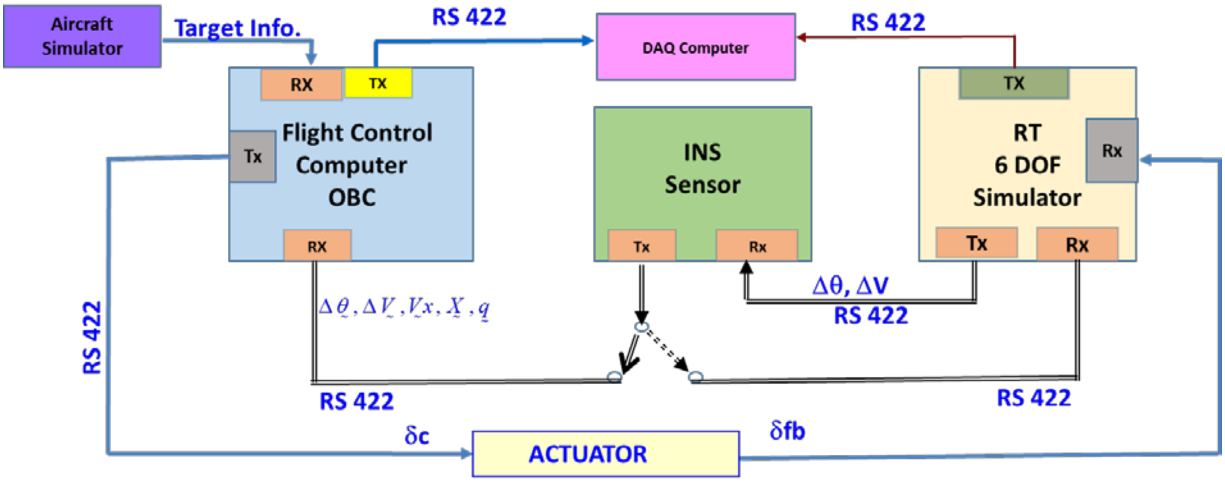

Figure 3: HILSSerial Interfaces

5. Result and Analysis

In the above mentioned configurations, the HILS tests have been carried out. The design simulation results are shown for the configuration of OBC-ACEU-Sensor in loop in Fig. 4 to Fig. 7. Results shows the close resemblance among them and proves the acceptability of the testing methodology. Test results are analysed for different perturbation cases [5] which are mentioned below:

- Nominal: All nominal values of aero coefficients are used.
- Low Drag More Unstable (LDMU): Drag Coefficient and Value of Static Margin was reduced
- Low Drag More Stable (LDMS):
  Drag Coefficient was reduced and value of Static Margin was increased
- High Drag More Unstable (HDMU)
  Drag Coefficient was increased and value of Static Margin was reduced
- High Drag More Stable (HDMS)
  Drag Coefficient was increased and value of Static Margin was increased

After conducting and analysing the test results for different perturbation cases the guided avionics of aircraft bomb was cleared for the flight trial. Some of the results with all perturbed cases are shown in below figures.

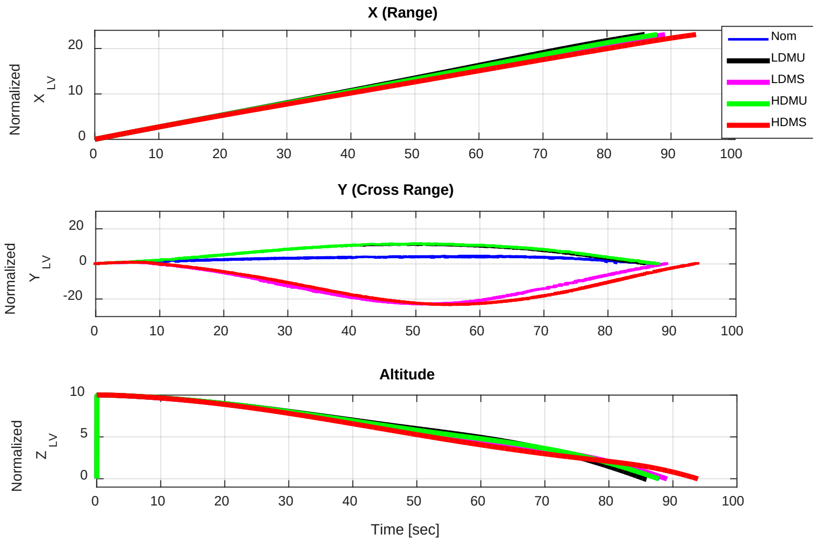

Figure 4: Trajectory

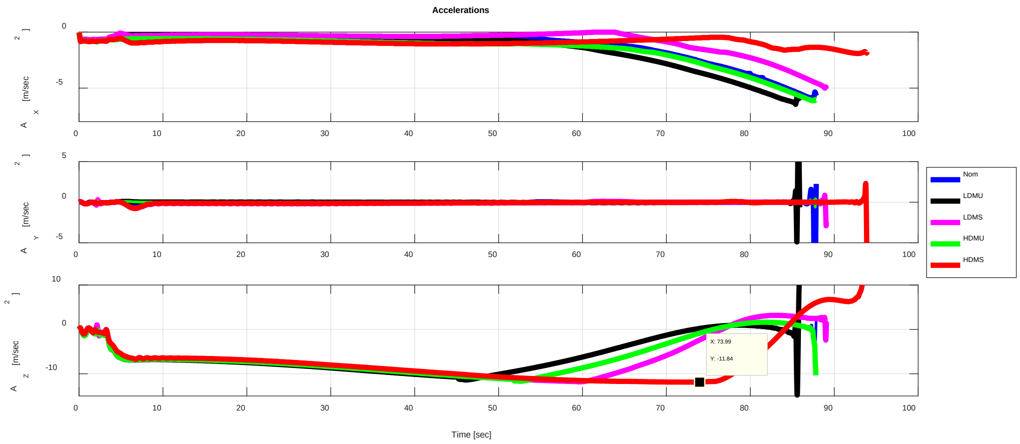

Figure 5: Body Accelerations

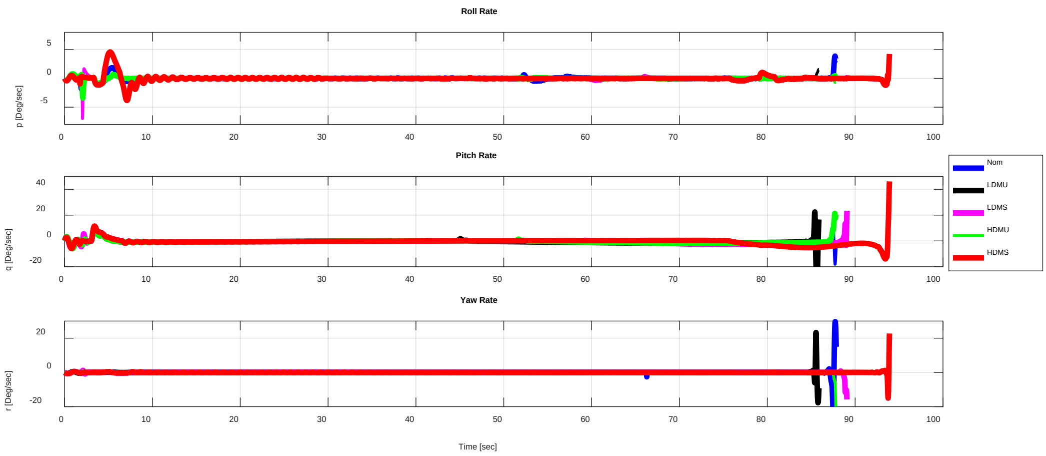

Figure 6: Body Rates

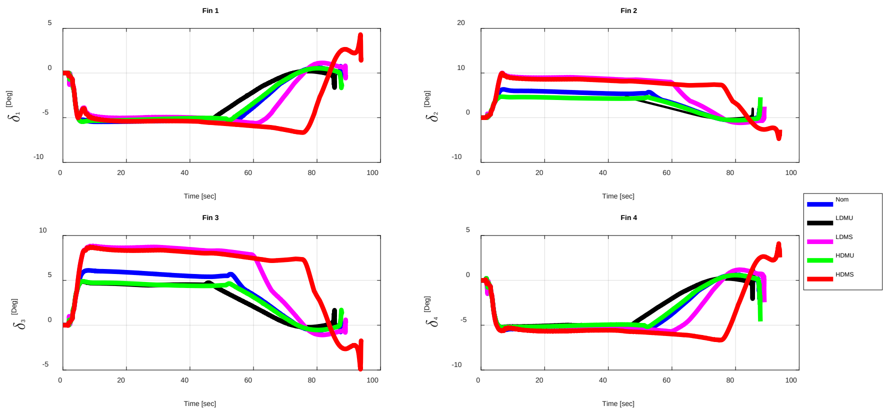

Figure 7: Fin Deflections

6. Conclusion

This paper has illustrated the design architecture and implementation scheme of the HIL simulation system for the guided avionics of aircraft dropped bomb. Special attention has been drawn to the real time Six DOF computations and serial data acquisition/transfer to the on-board computer and other subsystems. Various configurations under different perturbed conditions are used to validate GNC algorithms and to analyse the close loop system performance. The simulation results show that the guidance and control system have strong robustness and disturbance rejection capability. A HILS test setup like the one is described here can help to solve the problems of future flight control system and to recognise the problems in early development process.

This paper does not include the HILS test details of Sensor in Loop configuration. In this configuration, gyros are excited by rate table by mounting the INS unit on Rate table and accelerometers are still stimulated so it is also known as half simulation test. In ARDE separate team is working for this configuration of HILS.

Moreover, the proposed HILS setup in this paper does not include the GPS receiver in the closed-loop test which will also exhibit an impact on the simulation results. Therefore, further research should focus on the development of GPS simulator with high performance for improving the simulation worthiness of the close loop HILS test.

7. Acknowledgment

Authors are thankful to Dr. V Venkateswara Rao, OS and Director, ARDE for his continuous encouragement and support, also M V Ramesh Kumar Group head, PGM Technology Centre, for the support during HILS testing.

8. References

[1] Rajesh S Karvande and B. Ramesh Kumar “Development of Hardware-In-Loop Simulation Testbed for testing of Navigation System-INS” International Conference on Machine Intelligence and Research Advancement 2013.

[2] Xin Li, Daobo Wang and Qi Wang “Design and Realization of a Hardware-in-the-Loop Simulation System for Aerial Guided Bombs” 2008 IEEE conference

[3] LabVIEW™ Real Time-1 Course Module, Course Software Version 2010, Part Number 373246A-01

[4] S.K. Choudhari, G.Venkatachalam and M. Prabhakar “Hardware in Loop Simulation for Missile Guidance & Control Systems” 1997 Defence Science Journal, DESIDOC.

[5] BK Prasad, R Chopade, D Maurya and S Hiwale, Technical Report “GNC Review Document for Guided Bomb”.

Pipeline Inspection Robot using NDT Techniques

Mani Sankar Kadali
Defence Institute of Advanced Technology
Pune
manishankarkadali@gmail.com

D G Thakur
Defence Institute of Advanced Technology
Pune
thakur@diat.ac.in

Soumya S
Defence Institute of Advanced Technology
Pune
soumya_s@diat.ac.in

***Abstract* – This paper details on the design and development of pipe inspection robot using mobile screw jack mechanism using teleoperation. Pipelines are the main core elements in the transportation in oil industries because transportation through vehicles is dangerous and costly. Hence pipelines are designed in manner were there will not be any leaks and damages. But due to external weather conditions or aging of pipes leads to leakage therefore frequent inspection is must. There is a difficulty or constrain in inspection normally due to the diameter of the pipe where human cannot enter. Here comes the use of NDT techniques were inspection can be done without breaking the pipe. Thus, our aim of the project is to make a prototype of a pipeline inspection robot with new mechanism having some advantages comparing with existing methods. Using the proposed method, the robot can be position to move easily within the pipeline wirelessly and provides a visible view while moving inside the pipe. Therefore, this paper detail on the work flow of design and development of robot or automation that can do pipeline inspection successfully.**

1. Introduction

Robotics is one of the fastest growing sectors. Automation started in the industries to increase the accuracy, skill of the employers and to carry out the dangerous work. Automation is upgraded in to the fields of manufacturing where difficult works were done by robotics some of the examples are welding, shaping and lathe works which are cause injuries to even a skilled labour. [5]

To transport the oil and natural gases industries are using pipeline transportation considering the safety and cost. As per the protocol such kind of pipeline has to be inspected in a frequent interval of time. If inspection is not performed at right time, there would be cause of serious accident which will even cause loss of human lives. MIC leakage from Bhopal based industry which causes the death of many is a best example for this. [3]

Pipe line inspections are not carried out by humans because of the high temperature, pressure or presence of poisons gas. In literature various pipe line inspection robot's details are available to find the corrosion level, sludge's, breakages Pipeline ageing, cracks, and mechanical injury and so on. This leads to the demand of a mobile robotic platform which can inspect inside the pipeline and identify the state of pipelines. [13]

Fig 1: IPIR[2]

2. Need of pipe line inspection

The inspection robots have their constraints while inspecting the pipe mainly in nuclear and petro-chemical industries there is a need of high level inspection. Since the pipes carry dangerous substances where a small damage can cause destruction. Regular inspection should be done before any fateful incident can be occurred. By having NDT (Non-destructive testing) techniques we can visual inspection. So that defect and default will be detected and it can be solved. [13]

Some defects in pipes square measure listed below:

(i) Corrosion within the pipe
(ii) Internal defects like cracks, holes
(iii) Material Loss and Dent Marks
(iv) Defects caused by welding
(v) Internal blockages

Fig 2: Corrosion [11]

Fig 3: Crack [11]

The robot which is using for the inspection should follow the following procedure to identify the fault present inside the pipeline. At first a visual inspection should be carried out. In continuation to that if the robot identifies any damage it should give clear visibility of the damage. And finally, it should not self-damage the pipe while inspecting.

3. Structural requirement

Robots require flexible structures which can easily adaptable to the surrounding environment, mainly with respective to the pipe diameter. It should have the ability to manoeuvre easily inside the dangerous environment. Therefore, wheeled robots have very high capabilities in other ways like efficiency, energy, simplicity and ability to move long range traction. Here the wheels will be joined with chain so, that it also has benefits like easy moving of robots in the uneven surfaces and able to remain in steady position without any slipping or sliding. They are in additionally miniature in size. [7]

A wheeled type robot which has excellent manoeuvring ability has given great advantage in inspection of the gas pipelines. Therefore, we are using wheeled type robots with modifications in its mechanism. [10]

As we know that the reference for our concept is taken from car model and crane wheel concept. So, this modification on wheels makes easy manoeuvre inside the pipe. They are classified below with their advantaged, disadvantages and principle of motion. [14]

Generally, gas and oil pipes having a diameter ranging from 4inch(101.6mm) to 16inch (406.4mm) so the size of the robots are also compact in their size and structure.

Table 1: classification of IPIR [1, 6, 12]

Type	structure	Principle of motion	advantage	disadvantage
Caterpillar	Wall press type	Moving by pressing and walking on walls	Adaptable to changes of inner pipe diameter	Due friction force chance wear on the inner surface of the pipe
Mobile robot	Car-like robot	Moving on the ground	Does not damage the inner surface of the pipe due to the small contact area	Unable to move in a vertical path
Wheeled type	Wall press type	Moving by pressing and walking on walls	Moves fast as wheels provide highly efficient propulsion	The wheel can be stuck in holes on the inner pipe

During the initial phase, drawing is one of the important element should be taken care. Drawing gives the required assumptions that any modifications tobe done while doing fabrication. Additionally, it also adds the interested components which can easily noticed by everyone. Therefore, for this project, CATIA-V5 software is used in getting final look of the required design of the prototype. CATIA-V5 may be a solid modeling software package and computer-aided engineering platform.

A. Conceptual Design of Robot

In this work, wheel type is selected for the IPIR's. Wheels are used as prime movers in the pipe for inspection. It consists of mechanism which can be adjustable to the required diameter of the pipe. Four DC motors which is attached to the wheels enable the robot to move.

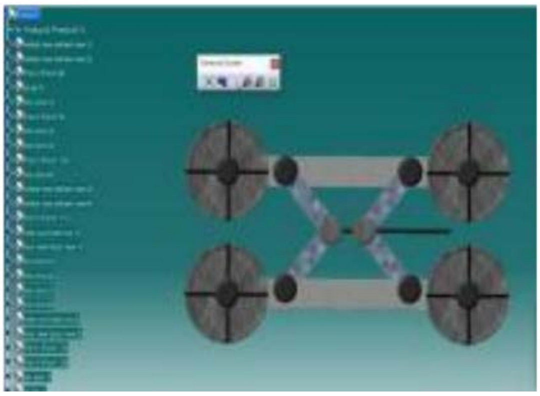

Fig 4: conceptual design of the robot

Figure 3 gives a basic idea of the prototype. In the preliminary stage of the work a basic structure is designed in the computer using CATIA-V5 software. Since it is a conceptual design it does not show entire concept of the work apart from the basic chassis it consists of some internal mechanism and control system too. Apart from the chassis a screw jack mechanism is added to the design which is driven by servo motor.

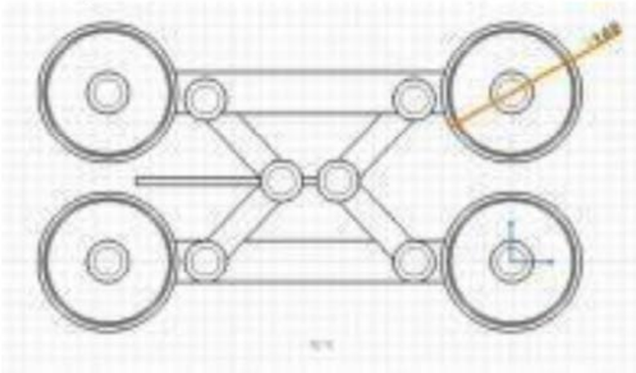

Fig 5: structural design of robot

B. Calculations

P = load applied at the circumference of the screw to lift the load,

α = Helix angle,

d = Mean diameter of the screw,

p = Pitch of the screw

W = Load to be lifted, and

μ = tan φ (Coefficient of friction, between the nut and screw) where φ is the friction angle.

Weight on Screw jack =832 g =0.832 kg

Tension=T_1, T_2

$2\ T_2 \sin(25) = (0.832*g)/2$

$g = 9.8\ m/s^2$

$T_1 = T_2$

$T_1 = 4.85$ N

$d_1 = 0.6$ mm

$T_2 = 4.85$ N

$d_2 = 0.4$ mm

$\alpha = \tan^{-1}(p / d)$

$= \tan^{-1}(1/ 0.5)$, p = 1 mm, d=0.5 mm

$= 3.64$

$\varphi = \mathrm{Tan}^{-1}(0.4)$

$= 21.8$

$W = (T_1 \cos\alpha + T_2 \cos\alpha)$

$= (4.85 \cos(3.64) + 4.85 \cos(3.64))$

$= 9.68$

T = Torque = $9.68 \times 5 \times 10^{-3} \tan(\alpha + \varphi)$

$= 9.68 \times 5 \times 10^{-3} \tan(3.64 + 21.8)$

$= 0.0153$ N-m

Motor torque = 0.5 kg-cm

$= 0.005$ kg-m $9.81\ m/s^2$

$= 0.04905$ N-m

As per calculations the predicted required toque is 0.0153 N-m. During market survey, it was found that 0.04905 N-m motor is available off the shelf and thus itis chosen.

4. Development of Inspection Robot

From free hand sketch to it is transformed to part design and then to design of model using modeling software CATI-V5. By obtaining the technical sketches a prototype design can be developed.

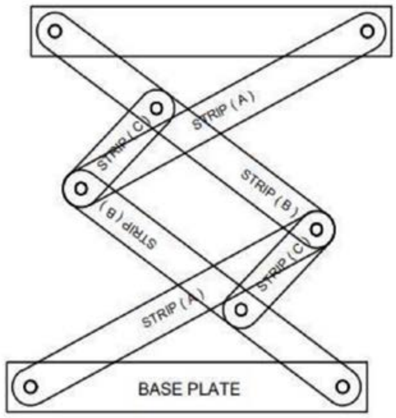

Fig 6: Final structural design of robot

As in Fig 5 the final structure of the prototype after going through different phases of design therefore required prototype is completed. Design software’s like AUTOCAD and CATIA were used for creating the model.

A. Structure of the Robot

Designing the robot frames is one of the primary elements in the construction and development of a robot. Design makes the robot to move seamlessly inside the pipe without any obstruction.

Particularly, the main idea of this robot moves like a scissors. When the servo motor turns the screw of bracket it starts moving upwards till the upper surface of the pipe comes into contact. As we know that the pipes are having cylindrical structure, our design will accommodate required extra gripping to the wheel so that it can roll on the above surface of the pipe, and can easily manoeuvre within the pipe. The gap between the upper part and the bottom part gives space for mounting the control part and 9V battery.

Continuously, DC motors had a gear box and wheels are attached to the body or frame of the robot. Total four DC motors are placed at the bottom section of the robot frame. Whereas front section of the wheels is used for the forward movement of the robot and back section used for backward movement. Second half speaks about the additional parts that are attached to the Arduino board like Bluetooth module, LED display and so on. Besides, the screw jack mechanism is fastened between the upper part and the lower part of the robot. This screwjack mechanism makes sure that the robot wheels are in the prime position and wheels should touch the inner wall of the pipe so that it can move forward and backward.

Finally, for the visual inspection camera mounting must be taken care, therefore there is need for arranging extra casing to fix the camera at the prime position such that it can give required positions or views for inspection.

B. Control system of the robot

In this subchapter we discuss about IPIR (In-Pipe Inspection Robot) control system that describes the method for the design and development of control part to control the robot. Aurdino, the heart of the control system, it is the micro controller which controls the robot movements and action. Bluetooth is attached to the control system to operate the robot wirelessly and manoeuvres with in the pipe. To control the speed of the DC motor a driver module board is used. LED'S, battery, different resistors and bread board were also used in designing of control part. Online software can be used in creating the representational diagram for control part. Online simulation software is used for the electronic circuits. As we know that it is an open source which is available for all.

So, it is useful in creating a project where a Aurdino controller is used. Since the software is user friendly which is easy to understand weather the connections are in correct position or not. This package additionally contains a board of all the electronic devices and instruments that helps in creating the control system economical. Therefore, parts used in system are listed below.

Parts	Quantity
WIFI Camera	1
Aurdino Board	1
Wifi/Bluetooth module	1
I2C Module	1
Motor drive channel	2
LED Display	1
Servo motor (MG 90)	1
DC Cooling Fan	1
Sonar Sensor	1
IR Sensor	1
30 RPM MOTOR	2
150RPM MOTOR	2
BATTERY 12V 4A rechargeable	1
Buzzer	1
Resistance Box	1
Circuit Board	1

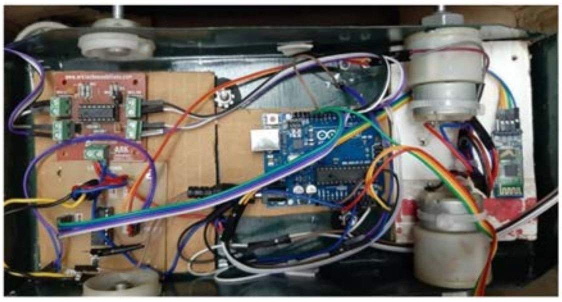

Fig 7: Control system of the robot

C. The Assembly method

As soon as the completion of the designing of control system the assembly process starts. Every part that is needed for the assembly was created with resources available at nearest hardware market. For the time being the robot frame is made using aluminum. Each

aluminum frame is subjected to drilling. Cutting, filing and finishing which will give finished robot structure. Since the parts are at the movement when it is locked with the upper part of the pipe.
To test the robot prototype, a few steps are to be compiled before conducting the test run. Since the prototype is working through wireless connection necessary tuning is to be happened between prototype and the mobile or any wireless communication device. Additionally, a 9V battery supply was given to the robot motor and the Aurdino. Primary test is done by means of backward, forward and turning motion by getting the commands wirelessly and behavior of motion is observed. The prototype is developed by following all the required proportions and measures which are used in drawings are carefully followed.

Fig 8: final assembly of the robot

5. Motion Analysis of Developed Robot

Our biggest concern of the project is successful travelling of the robot through pipeline having required frictional forces on the robot and easy moving or traction of the robot on the interior walls of the pipeline. If there are insufficient frictional forces there may be occurrence of slip to the robot since it is Manmade there will be some inaccuracy which will concern the precision of the robot.

A. Testing of the Developed Robot

During the developing stage several problems occurred like the mechanism is not that much stable. So slight changes were done in the mechanism such that stability is acquired.

Next, we are using aluminum alloy as a material for developing the prototype so sufficient rigidity and stability should be attained for the robot if not it will fail to travel inside the pipeline. This will make the robot to defeat its own purpose. Therefore, from testing the developed model it has successfully able to exert required frictional forces so that easy and smooth movement of the robot is obtained.

The next objective of the project is after completing the design of the prototype. Interfacing of the control system to the prototype for operating the robot. This will be the main section in developing the prototype of the IPIR. In designing of control system, the robot functions will be identified first. In this paper the prototype is able to move in required directions like forward, backward, turn, start, stop, and turn on/off the LED'S. Since the control system consisting Aurdino and Bluetooth control module which allows the prototype to be operated wirelessly. Programming to the control system is done using c language in the integrated development environment offered by the Aurdino. After the completion of programming of the control system testing is done which our task is accomplished by operating the robot control system wirelessly.

For testing of the model some steps are to be followed. Steps are given below:

(i) To get power supply to the Aurdino and Bluetooth 9v battery should be attached
(ii) Start scanning for HC-05 Bluetooth and pair with the mobile or computer.
(iii) Now open the software Aurdino Bluetooth software in your mobile and 6 change controls according to your programme. Check with the robot weather controls are in correct order or not
(iv) Ensure that the robot is ready for inspection, after establishing the connection between the robot and tele operational blue tooth module.
(v) Now click required control in software so that robot will receive the command and it will move according to the command.

B. Observations

From conducting the required tests some of the observations are made regarding to the aim of our project. The primary test was made on maneuvering of the prototype/model. The test has given no errors in movement of forward, backward and stoppage and thestraight motion is also attained without any deviation. The secondary test was done on the wireless connection that how far it can receive command. The test was successful approximately it can receive signal up to 10m in open area without any obstructions between the system and the prototype. In the closed area or pipe line our objective can attained.

Fig 9: Prime position of screw jack mechanism

Robot height ranging from 10 cms to 20 cms where actual oil and gas pipe diameter ranges between 10 cms to 40 cms so that our prototype is designed with in the standard pipes that are used in the industries.

6. Conclusions

Our aim of the project is to design and develop a working model of inspection robot which is useful in oil and gas industries. It should have the ability to maneuver in the pipe line without any slip. Secondary objective of the project is to integrate the control system to the prototype. So that it can be operated easily and wirelessly.

Primary objective is accomplished by maneuvering of the robot inside the pipe and getting the visual inspection done. Therefore, according to the result, the wheel type of IPIR was chosen. Required arrangements are done to the wheeled type robot using screw jack mechanism.

7. References

[1] F. Mascarich, S. Khattak, C. Papachristos and K. Alexis, "A multi-modal mapping unit for autonomous exploration and mapping of underground tunnels," 2018 IEEE Aerospace Conference, Big Sky, MT, 2018, pp. 1-7.

[2] A. Kakogawa and S. Ma, "Mobility of an in-pipe robot with screw drive mechanism inside curved pipes," 2010 IEEE International Conference on Robotics and

[3] Hajjaj, Sami & Khalid, Ilyas. (2018).“Design and Development of an Inspection Robot for Oil and Gas Applications,” International Journal of Engineering and Technology(UAE). 7. 5-10. 10.14419/ijet.v7i4.35.22310.

[4] M. F. Yusoff , B.S.K.K. Ibrahim, H. Hamzah and H.A. Kadir, Development of Air Conditional Route Wireless Inspection Robot, International Symposium on Robotics and Intelligent Sensors 2012 (IRIS 2012), pp 874-880.

[5] H. Pi et al., "Transmission optimization design of mini-multimodule crawler robot," 2018 13th IEEE Conference on Industrial Electronics and Applications (ICIEA), Wuhan, 2018, pp. 858-862.

[6] M. Muramatsu, N. Namiki, R. Koyama, and Y. Suga, “Autonomous mobile robot in pipefor piping operations,” in Proc. IEEE/RSJ Int. Conf. Intell. Robots Syst., Oct. 31–Nov.5, 2000, pp. 2166–2171.

[7] S. Roh and H. R. Choi, “Differential-drive in-pipe robot for moving inside urban gas pipelines,” IEEE Trans. Robot., vol. 21, no.1, pp. 1–17, Feb. 2005.

[8] Min J, Setiawan Y, Pratama P, Kim S, & Kim H, “Development and Controller Design of Wheeled-Type Pipe Inspection Robot”, 2014 International Conference on Advances in Computing, Communications and Informatics (ICACCI), (2014).

[9] H.Fujii, A. Yamashita and H. Asama, "Improvement of environmental adaptivity of defect detector for hammering test using boosting 7 algorithm," 2015 IEEE/RSJ International Conference on Intelligent Robots and Systems (IROS), Hamburg, 2015, pp. 6507-6514.

[10] Gargade, Atul & Ohol, Shantipal. (2016). Development of In-pipe Inspection Robot. IOSR Journal of Mechanical and Civil Engineering. 13. 64-72. 10.9790/1684-1304076472.

[11] E. Prada et al., "New approach of fixation possibilities investigation for snake robot in the pipe," 2015 IEEE International Conference on Mechatronics and Automation (ICMA), Beijing, 2015, pp. 1204-1210,doi: 10.1109/ICMA.2015.7237657

[12] Schoonahd J, Gould J, & Miller L, “Studies of Visual Inspection”, Ergonomics, Vol.16, No.4, (1973), pp:365-379.

[13] K. Loupos et al., "Robotic intelligent vision and control for tunnel inspection and evaluation - The ROBINSPECT EC project," 2014 IEEE International Symposium on Robotic and Sensors Environments (ROSE) Proceedings, Timisoara, 2014, pp. 72-77.

[14] C. Ou et al., "Design of an adjustable pipeline inspection robot with three belt driven mechanical modules," 2017 IEEE International Conference on Mechatronics and Automation (ICMA), Takamatsu, 2017, pp. 1989-1994.

Warhead Mechanisms

Methodology to Evolve Network of Channels for Hydra-Based Plane Wave Initiation

P N Verma
Armament Research and Development Establishment
Pune
pnverma@arde.drdo.in

M V Suryawanshi
Armament Research and Development Establishment
Pune

K D Dhote
Armament Research and Development Establishment
Pune

S Harikrishnan
Armament Research and Development Establishment
Pune

V K Dixit
Armament Research and Development Establishment
Pune

***Abstract*– Plane wave initiation of high explosives finds various applications such as detonics for launching flyer plates to study shock loading behavior of materials, weaponization of directional warheads required for futuristic weapon systems, etc. Hydra based plane wave initiation system is one of the many systems which offers a compact and reliable solution. It employs a network of thin explosive filled channels which transmit detonation from a single input point to multiple output points. Planarity of the emerging detonation wave front is the key characteristics of a plane wave initiation. Simultaneity of initiation of the output points is one of the major factors to ensure planarity of the hydra based plane wave initiation which demands equality of length of channels connecting the output points from a single input. Further, to increase reliability, redundancy of the channels feeding the output points is desired. Determining a layout for the network of channels, to achieve equality of length & redundancy in feeds, becomes very challenging and cumbersome especially when number of the output points is maximized within a given area. A methodology has been developed to evolve the network of channels. The paper presents details of the methodology developed and designs of the channel network for plane wave initiation system having 42 output points in 160 mm diameter hydra plate.**

Keywords*– *Plane wave initiation system, Hydra plate, explosive filled channel, planarity, simultaneity

1. Introduction

Typically, high explosive charges are initiated at a single point. The emerging detonation wave front grows spherically and detonates the complete charge. The explosive energy released by such an initiation acts uniformly in all the direction. With advances in fuzing sensor technology, it has become possible to obtain real-time target information such as size, location and orientation etc. precisely during terminal phase of weapon and target interaction. This offers an opportunity or rather demands for weapon kill effects to be focused[1] towards the target in order to improve the weapon effectiveness. Such focusing of the kill effects can be achieved by ways such as making suitable geometrical configuration of charge, introducing inert barriers in the path, employing novel initiation systems etc., which help in shaping emergent detonation wave front such that the action of the energy released by the detonation of the explosive charge is focused in desired direction. Plane wave initiation system generates flat detonation wave front. One of the applications of flat detonation wave front generated by plane wave initiation is to produce a directional fragmentation effect wherein a dense fragment cloud moves in one direction without considerable drop in cloud density over distance unlike the conventional fragmentation where the fragment spatial density decreases as square of the distance from the point of detonation. The plane wave initiation is also used to launch flyer plates which are made to obtain planar impact onto a flat target in shock physics experiments. Explosive lensing[2] and multi-point initiation[3] are the two main techniques to generate plane detonation wave. The explosive lens relies on a combination of two explosive charges having remarkably different velocities of detonation (VOD), i.e. one having high VOD and the other low VOD, to focus a diverging spherical detonation wave front generated by single point initiation into a planar wave front. In multi-point initiation, the explosive charge is simultaneously initiated at multiple points arranged uniformly in a plane. Spherical detonation wave fronts originating from each point interact with each other as they grow eventually evolve into a single emergent planar detonation wave front. Hydra based multi-point initiation system offers a compact and reliable solution to generate plane detonation wave front. It employs a network of thin explosive filled channels which transmit detonation from a single input point to multiple output points. In this paper, authors present key design aspect of hydra based plane wave initiation system namely methodology to evolve the network of the channels. A prototype incorporating the presented design of the channel network has been successfully test evaluated.

2. Hydra Based Plane Wave Initiation

It consists of a circular disc called hydra plate on which a network of channels is created such that they branch out from a single point in centre called junction to all the output points maintaining equal path length. Junction is practically not a point but typically a circular area. The channels emanate from the periphery of the junction. The planarity of the emerging detonation wave front is dependent on number of output points & their spatial array within the given area as well as on simultaneity of initiation of the output points. Equality of the path length is very essential to simultaneous detonation of output points. Increasing number of output points and ensuring uniformity of their spatial array help in improving the planarity of the wave front. Further, to increase reliability, redundancy of the channels feeding the output points is desired. To determine a layout for the network of channels becomes very challenging and cumbersome especially when the number of output points is maximized within a given area. A methodology has been developed to evolve the network of channels.

3. Layout of Channel Network

The methodology to evolve the network of the channels is based on a background uniform triangular grid wherein the circular plane of the hydra plate is discretized into a grid of equilateral triangles such that the output points distributed uniformly lie on vertices of the triangular elements and the input point is located at the centroid of a central triangular element. Connecting the output points with equal path lengths following the edges of the triangular elements from the input point leads to formation of a network of the channel. The network is evolved on the basis of premises: 1) that there must exist a uniform grid of equilateral triangles which allows finding out the desired network of the channels; 2) the network can be determined by following the sides of the triangular elements of the grid. A channel path consists of: a primary branch which originates from the input point; secondary branches, which emanate from a primary branch, feeding to the output points. In addition to the basic premises, there are a few conditions which needs to be satisfied while working out the layout of the network: i) number of sides used to connect an output point from the input must be same for all the output points to guarantee equality of channel path length; ii) No two paths intersect each other; iii) Branching of paths from a point on a path should be minimized; iv) Turning angle of a path should be minimum, i.e. the minimum angle possible for equilateral triangular grid is 60°; v) Redundancy of feeds from the primary branches should be maximized, i.e. the number of redundant paths emanating from two different primary branches to be maximized. Using this methodology, channel network for a hydra plate having 160 mm diameter with 42 equi-spaced output points has been worked out as shown in figure 2 & 3. Step-by-step procedure is explained in the following paragraphs.

Figure 1: Seed element

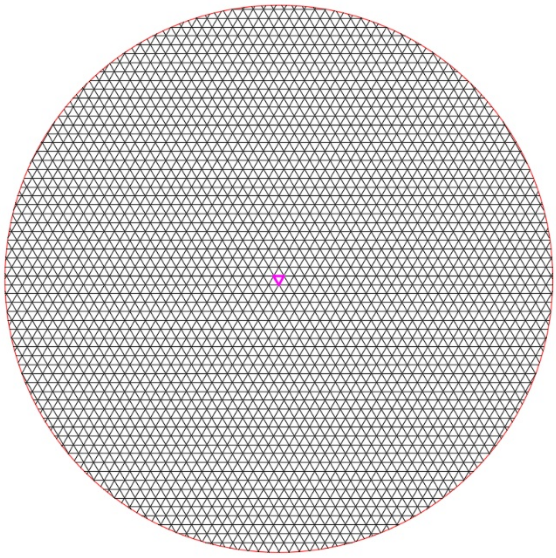

Figure 2: Triangular grid

A. Generation of grid

First of all, grid line spacing 's' is chosen. The choice of grid spacing is governed by the critical minimum separation distance between the two explosive filled channels such that detonation transmission through one channel does not affect the transmission through the other. The main factors affecting the minimum separation distance are hydra plate material, channel cross section size and the explosive filling. The single element as equilateral triangle whose height is equal to 's' is seeded at the centre such that its centroid lies at the centre of the circular area as shown in Figure 1. The orientation of this triangle with respect to the circular area is arbitrary as the circle is infinitely symmetric in rotation. Then the sides of this seed element are translated normal to itself with an interval equal to 's' resulting in a triangular grid over entire circular area as shown in Figure 2. The seed element is highlighted in the figure.

B. 3.2 Array of output points

Array of output points is determined by the output point spacing 'd' which in turn is dependent on the number of output points in a given area. The output points lie on the vertices of the triangular elements such that the 'd' is the integral multiple of side of the element to maintain uniformity of array. After choosing 'd', an equilateral triangle with side equals to 'd' is drawn such that its centroid is at the centre of the circular area and its orientation is flipped by 180° with respect to the seed element. First three output points are located on the vertices of this triangle as shown in Figure 3. By translating these seed output points along the grid lines with an interval of 'd' the complete array of the output points is determined as shown in Figure 4.

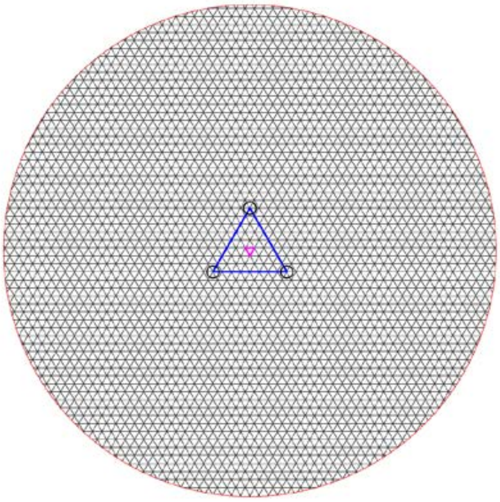
Figure 3: Output point seeding

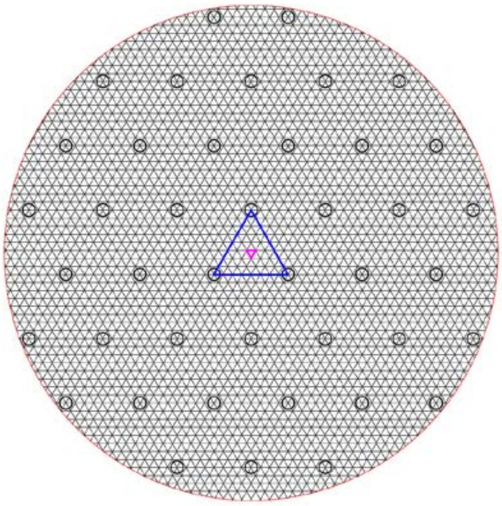
Figure 4: Array of output points

C. Channel network

To evolve the channel network, first of all size of input point (actually a circle) called junction diameter is chosen. The choice of 'D' is constrained as this circle has to pass through the vertices of an equilateral triangle having its orientation and centroid identical to the seed element. Additionally, the vertices of the triangle must lie on the nodes of the grid as shown in Figure 5. The vertices of this triangle form nodes from which the primary channels emanate as shown in Figure 6.

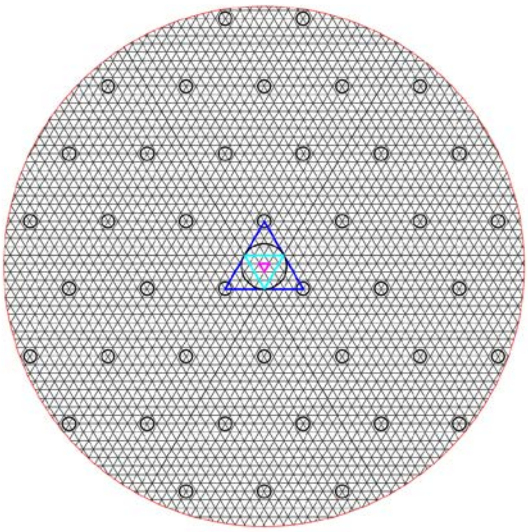
Figure 5: Input Circle (Junction)

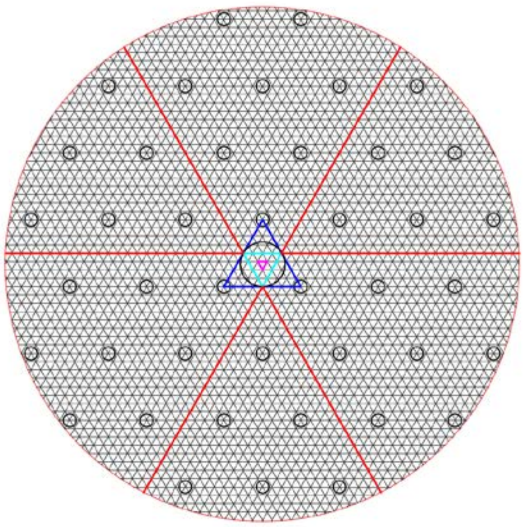
Figure 6: Primary Channels

Branching of the primary channels provides secondary channels and subsequent branching as required satisfying the conditions as discussed allows tracing of channel path from input to various output points. This process is analogous to solving a puzzle and hence often needs many attempts to find the desired network of the channels. The channel network worked out for 42 output points uniformly arranged in a circular area of diameter 160 mm is shown in Figure 7 and Figure 8.

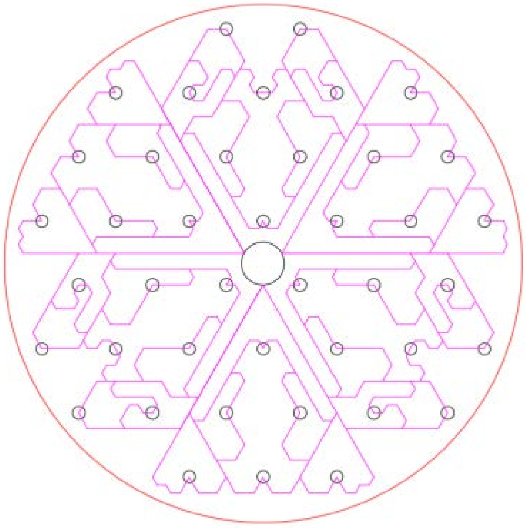

Figure 7: Channel path tracing over grid

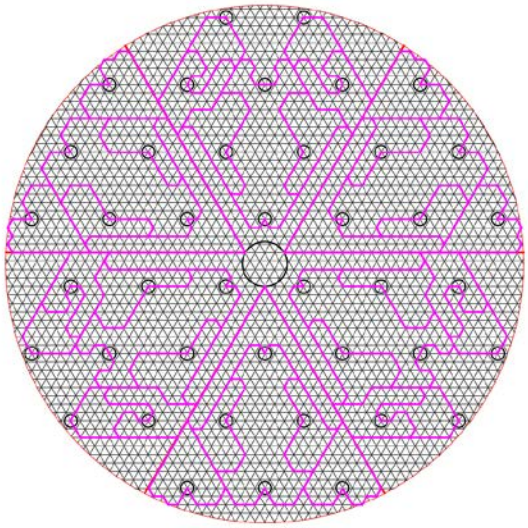

Figure 8: Network of channels - 42 OP

4. Hydra Plate Prototype

Prototype hardware as shown in Figure 9 incorporating the proposed channel layout has been realized. Thin channels of 0.5 mm size are made in a 12 mm thick aluminum plate called hydra plate by CNC milling. The input point is actually a circular cavity at the centre of the plate. From the input cavity, there are six primary branches originated which further branch out creating secondary branches feeding to various output points. There are other engineering aspects which are incorporated in prototype design, eg. air pockets between two channels passing very closely to avoid shock disturbance from one to the other; holes for integration; and holes drilled at all the output point locations to take output to the other side of the plate such that the detonation breakout timing can be measured.

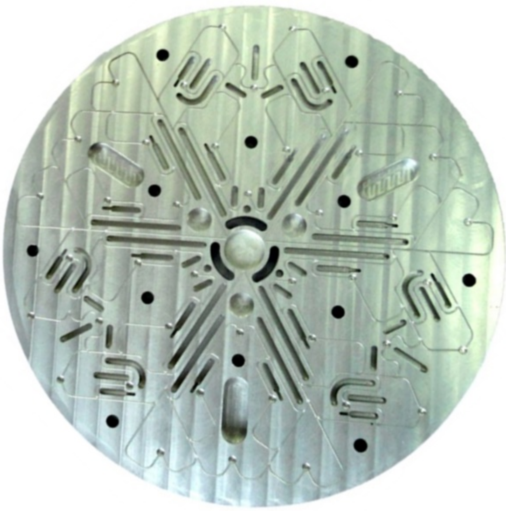

Figure 9: Hydra plate prototype - 42 OP

The performance of the prototype has been successfully demonstrated in static firing.

5. Conclusions

Hydra based plane wave initiation system is a very compact system. It has smaller number of components. The key aspect in design of such system is to find out the network of channels which connect multiple output points to the single input points. The methodology presented in this paper is very useful in evolving the network of channels for a given array of output points. The process is iterative and the number of iterations may be required for finding a network which fulfills the desired conditions in respect of equality of path lengths, minimum branching and redundancy. Prototype test result of static firing has shown the effectiveness of the design.

6. Acknowledgment

The authors are thankful to the Director ARDE for his support and motivation for conducting this study and permitting to publish the work. The contribution ARDE Range & Instrumentation team and Warhead Technology team is thankfully acknowledged.

7. References

[1] Lloyd, R.M. Conventional Warhead Systems Physics and Engineering Design, Progress in Astronautics and Aeronautics, Vol. 179, 1998.
[2] Svingala, F.R.; Giannuzzi, P.M. & Sandusky, H.W. Simple explosive plane wave booster designs for 1-D shock experiments. AIP Conference Proceedings 1979, 160027, 2018.
[3] Resnyansky, A; Wildegger-Gaissmaier, A.E. & Katselis, G. Directional Fragmentation Warheads: A theoretical and experimental investigation. Proceedings of 18th International Symposium on Ballistics, San Antonio, TX, 1999. 543-550.

Innovative Design of Cylindrical Detonation Wave Initiation System for Multilayered KE Rod Warhead

M V Suryawanshi
Armament Research and Development Establishment
Pune
mrajsurya@yahoo.co.in

B Raghu Varna
Armament Research and Development Establishment
Pune

P N Verma
Armament Research and Development Establishment
Pune

K D Dhote
Armament Research and Development Establishment
Pune

Satwinder Singh
Armament Research and Development Establishment
Pune

***Abstract*– Kinetic Energy (KE) Rod Warhead technology is generally employed to defeat the TBMs carrying sub-munition payloads. KE rod has ability to penetrate multi-layered spaced target structure in hypervelocity impact conditions with high obliquity. However, this ability is utilized well only when the KE Rod warhead delivers the rods on the target with least yaw. Tumbling of rods during deployment is one of the major causes for generation of impact yaw. Minimizing the tumbling rate helps in controlling the impact yaw. This poses a great challenge to the KE Rod warhead designers. An innovative design of cylindrical detonation wave initiation system using miniaturized detonating cords is proposed which produces more uniform loading along the length of the rods to reduce the rate of tumbling. The design is very compact and involves a smaller number of components making it suitable for light weight KE Rod warheads requiring high level of functional reliability. The prototype KE Rod warhead has been tested successfully using proposed design of the cylindrical wave initiation system. The paper presents the concept, salient features of the proposed cylindrical wave initiation system design and assembly and testing aspects.**

Keywords*– *KE Rod Warhead, Initiation system, Miniaturized detonating cords, Tumbling.

1. Introduction

Tactical ballistic missiles (TBM) generally carry sub-munition payloads. The structure of the payload is typically simulated by multilayer spaced structure wherein the relatively thinner outermost layer is separated by some air gap from the inner layers. The terminal velocity of the TBMs is high usually of the order of 1 km/s or more. Interceptor missiles targeting these TBMs are also fast typically having interception velocities in the range of 1 km/s to 2 km/s. Considering simplest anti-parallel engagement, the relative interception velocity can be more than 2 km/s. Conventionally, the fragmentation warheads containing compact preformed fragments like balls, and cubes are employed in interceptors for defeating aerial targets. However, the compact fragments start shattering on impacting thin targets at high velocity and the large portion of the shattered mass ricochets when high impact velocity is coupled with large impact obliquities. Thus, the effectiveness of compact fragments against multilayered spaced target structure drastically reduces as the impact velocities and obliquities increase. Rods as fragments offer an advantage against multilayered spaced targets since it typically erodes while penetrating and thus longer rods can be used to perforate multiple layers. However, unlike the compact fragments, the rods penetration capability is significantly affected by impact yaw. Longer the rod, greater is the reduction in penetration capability with increase in yaw. It is reported that in a typical hypervelocity impact conditions, the rods start performing poorer than a compact fragment above a critical value of impact yaw [1] (critical value of impact yaw for rods having length to diameter ratio (L/D) of 3is about 30°). Hence to take advantage of rods ability to perforate multilayered targets at hypervelocity impact conditions, it is necessary to minimize impact yaw below the critical value which depend on the impact conditions and the rod parameters. Impact yaw of rods is dictated by terminal encounter conditions. Nevertheless, the low tumbling rates during launch of rods have been found to reduce impact yaw in a statistical sense. The authors propose an innovative design of cylindrical detonation wave initiation system using miniaturized detonating cords which produces more uniform loading along the length of the rods resulting in reduced rate of tumbling. The design is very compact and involves minimum number of components making it suitable for light weight KE Rod warheads requiring high level of functional reliability. The prototype KE Rod warhead has been tested successfully using proposed design of the cylindrical wave initiation system. The paper presents the concept, salient features of the proposed cylindrical wave initiation system design and assembly and testing aspects.

2. KE Rod Warhead

A typical KE Rod warhead comprises of rods arranged in multi-layers around the casing filled with high explosive as shown in Fig. 1. Traditionally, single point initiation system at the end is used to detonate the warhead which induces high rates of tumbling. Ideally, a cylindrical detonation wave front is required which provides uniform loading over the length of rods and thus prevents rotation of the rods.

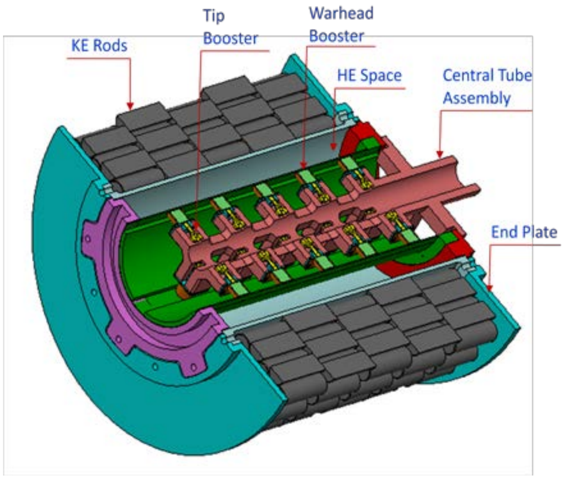

Fig. 1: KE Rod Warhead

The design of the cylindrical wave initiation system has been worked out for 5 layered conventional KE Rod warhead consisting of 750 nos. of KE Rods weighing 50 g each. KE Rod Laying pattern is shown in Fig. 2.

Fig. 2: Laying Pattern of KE Rods

The initiation system is based on miniaturized detonating cords. It provides four lines of detonation equi-spaced on the inner surface of the annular explosive charge. Each line consists of five points of initiation corresponding to the five rods in a layer (i.e. each point placed at the centre of the corresponding rod). Simultaneous initiation of the all the twenty initiation points leads to evolution of nearly cylindrical detonation wave front interacting with KE Rods arranged on outer surface of the casing. To ensure the simultaneous initiation, length of each miniaturized detonating cord running from a common junction to all the points is kept identical. The design is very compact and involves a smaller number of components making it suitable for light weight KE Rod warheads requiring high level of functional reliability. The prototype KE Rod warhead has been tested successfully using proposed design of the cylindrical wave initiation system.

To assess the advantage of the proposed initiation system over the conventional end initiation, hydro-code simulation using AUTODYN software[2] has been carried. The hydro-code model for both end initiation and the proposed multi-point initiation are shown in Fig. 3 and Fig. 4 respectively. The KE rods are modeled using Lagrange solver and all the remaining components are created using Euler Multi-material solver. Explosive detonation is modeled by program burn technique. For simulating end initiation, a detonation plane is created at one end of the warhead as shown in Fig. 3. The multipoint initiation has been modeled by providing five detonation points along each line of detonation as shown in Fig. 4. The material model and the properties are taken from AUTODYN material library. Materials for KE Rods, explosive, and casing have been selected as STEEL 1006, PBX-9010, and ALUMINUM respectively. The rotation of KE Rod for same time instant for both the model is given in Fig. 5. A rod as shown in case of end initiation has rotated by about 40 degrees in 067 milliseconds whereas the same rod in case of multi-point initiation has rotated only by 12 degrees in the same time. From simulation results it has been worked out that the tumbling rate for end initiation and the proposed multi-point initiation are in the order of 165 revolution per second and 50 revolution per second respectively. The KE Rod velocity has been found from simulation data in the range of 315 m/s to 350 m/s for end initiation and 375 m/s to 395 m/s for multi-point initiation case.

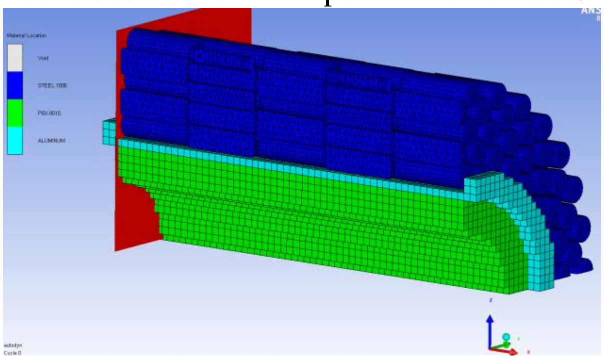

Fig. 3: End initiation model

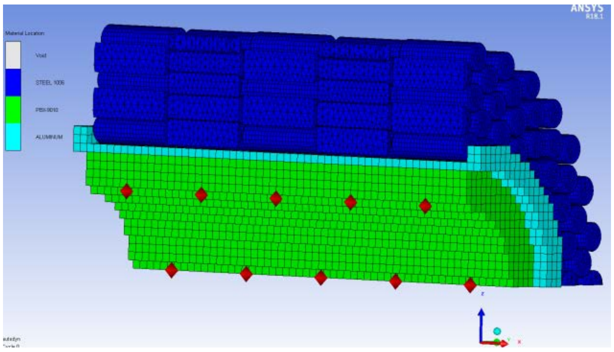

Fig. 4: Multi-point initiation model

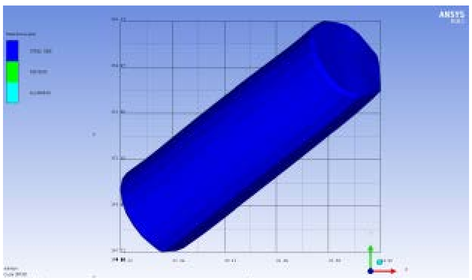

(a) End initiation

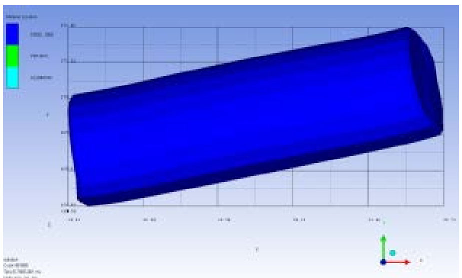

(b)Multi-point initiation

Fig. 5: Rotation of KE Rod at 0.67 ms

3. Initiation System

The initiation system is based on miniaturized detonating cords as shown in Fig. 6. Detonating cord contains RDX powder filling with loading density of 0.6 g/m and each tip booster has PETN powder of 80 mg.

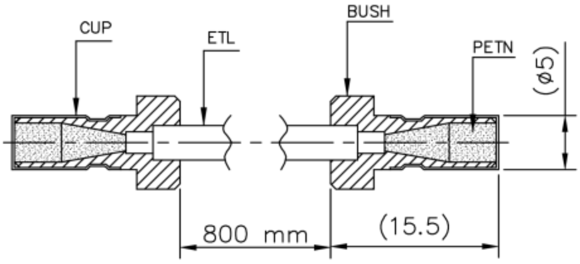

Fig. 6: Detonating Cord with Tip Boosters

There are 20 Nos. of Warhead Boosters initiated simultaneously using miniaturized detonating chord with Tip Boosters formation at the ends of the cords which are fitted in Central Tube.

A. Central Tube Assy. Procedure

Fig. 7: Central Tube (Empty)

(i) One end of cord to be positioned in the first row of Central Tube (Empty as shown in Fig. 7) in such a way that the other end will go through the slot of the tube on the opposite outside of the tube. Insert the Sleeve - Connecting Tip on the Tip Booster so that Tip Booster center position is maintained.

(ii) Take a Cap-B & put Booster Pellet 10x10 mm in the cavity of Cap-B. Place the Cap-B over the Sleeve Connecting Tip & fix it with the help of 04 screws of M3. The screws are to be tightened very delicately in such a way that Booster Pellet just touches with the Tip Booster & then half thread to be loosened. A sketch of the Central Tube Assembly (Filled) is shown in Fig. 8.

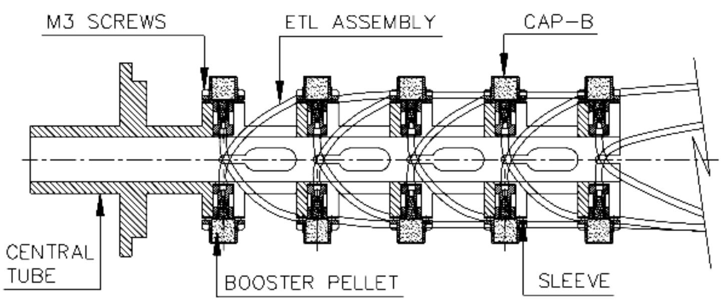

Fig. 8: Sketch of Central Tube (Filled)

(iii) Likewise, 03 Nos. of cord assemblies of Row-I to be completed.

(iv) Repeat the procedure mentioned at Sr. 1,2 & 3 for remaining 16 Nos. (Row - 2,3,4 & 5 - 04 Nos. each) of cord assemblies as shown Fig. 9.

(v) Wind the tape circumferentially on the Central Tube between the gap of Booster Collar in order to hold loose cords.

(vi) Ensure that all the M3 screws - 80 Nos. are half thread loosened.

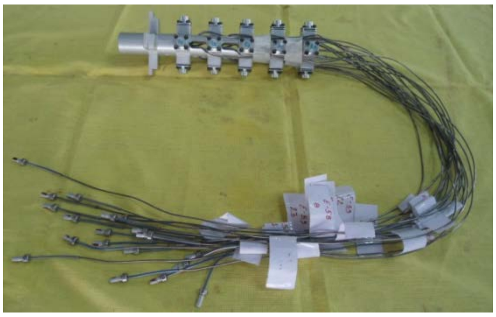

Fig. 9: Central Tube Assembly

(vii) Insert the other end of the cord Assemblies through the Inner Tube slots of LVKERWH assembly & rest the Central Tube Assembly on LVKER WH Assembly as shown in Fig. 10. Take out the other ends of cord assemblies out of the Firing Stand. Hold the Central Tube with the End Plates of HE Filled Assy. using adhesive tape. Ensure that there is no dangling of Central Tube & Central Tube will not be coming out of the Inner Tube.

Fig. 10: Insertion of Central Tube Assembly in LVKER WH

(viii) Take the Base-Junction Box. Position all the Tip Boosters - 20 Nos. of cord assemblies in the cavity of the Base-Junction Box. Position Booster Pellet in the cavity of the Junction Box. Place Cap-Junction Box on the Base-Junction Box. Assemble M2 screws which will push the Bush (Tip Booster) & ensure positive touching of the Tip Booster with the Booster Pellet. Hold the assembly of Base & Cap with the help of 04 Nos. of M3 Screws & Nuts.

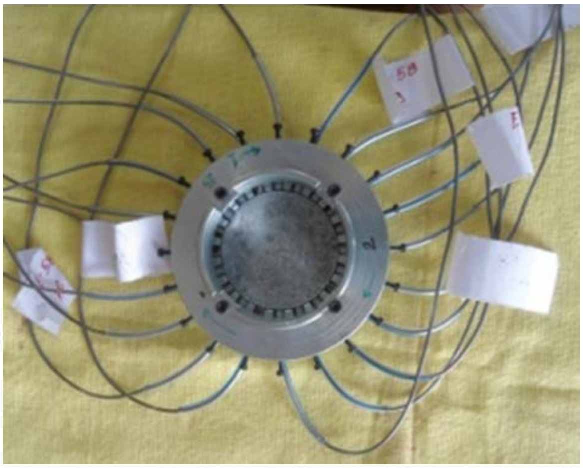

Fig. 11: Junction Box Assembly

Junction Box Assembly is shown in Fig. 11. Booster fitted in the Junction Box will simultaneously initiate all the 20 cords. The explosive train followed for initiation of KE Rod Warhead during static trial is as mentioned below.

(a) Electrical Detonator (No. 33)
(b) Booster Pellet Φ 10 x 10 mm - 1 No.
(c) Booster Pellet Φ 50 x 10 mm - 1 No.
(d) Tip Booster - 20 Nos.
(e) Detonating Cord - 20 Nos.
(f) Tip Booster - 20 Nos.
(g) Booster Pellet Φ 10 x 10 mm - 20 Nos.
(h) High Explosive

4. KE Rod Warhead Testing

Static trial configurations of Multi-Layer LVKERWH Assy. (HE Filled), is shown in Fig. 12. Straw board soft recovery blocks are arranged in 3 sets at a distance of 7 m for recovery of KE Rods. All the soft recovery blocks are grid marked to evaluate velocity using High Speed Camera. Two High Speed Video Camera are deployed for evaluation of KE Rod Velocity & tumbling of KE Rods. From test results, the tumbling rate is found in the range of 30 revolution per second to 80 revolution per second. The KE Rod velocity has been observed in the range of 325 m/s to 400 m/s.

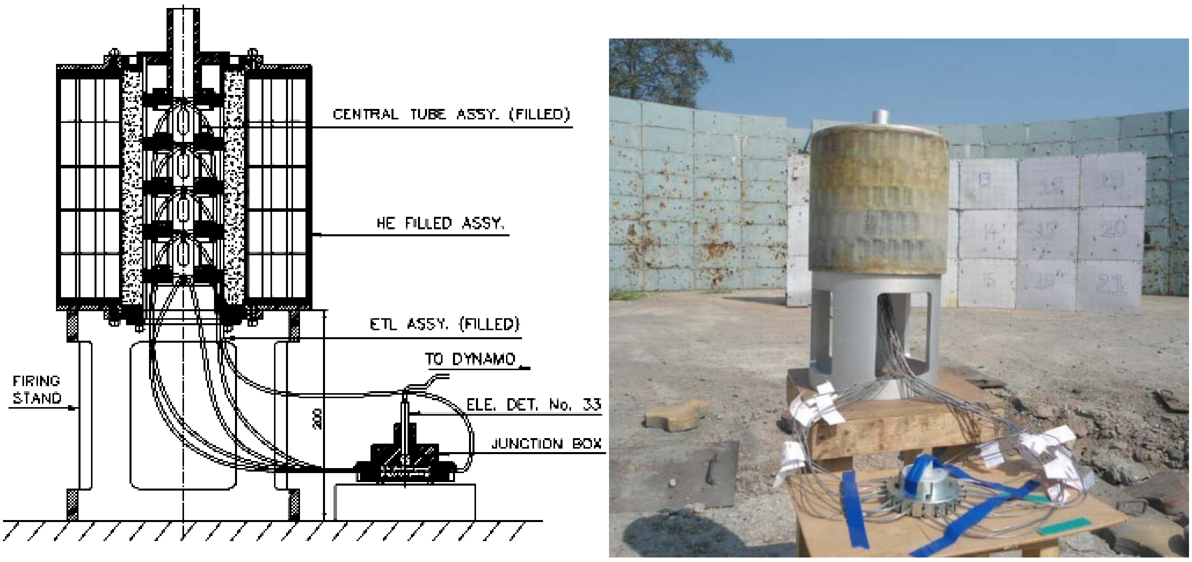

Fig. 12: Test Configuration of KE Rod Warhead

5. Discussions

The trial data of High Speed Video Camera i.e. position of KE rod during flight, the Impact points & position of KE rod during impact on the Straw Board Recovery Blocks has been critically analyzed. It is observed that the KE rod tumbling rates are in good agreement with the hydro-code results. The KE Rod velocity data also is matching with the simulation data. From the simulation results and the experimental data, it can be concluded that the rod tumbling rate after ejecting out from KE Rod Warhead using cylindrically detonated wave front generated by the proposed Multi Point initiation system has drastically reduced the tumbling of KE Rods.

6. Acknowledgment

The authors are thankful to the Director ARDE for his support and motivation for conducting this study and permitting to publish the work. The authors are grateful to the Director HEMRL for valuable suggestions and support in explosive filling.

7. References

[1] Lloyd, R.M. Conventional Warhead Systems Physics and Engineering Design, Progress in Astronautics and Aeronautics, Vol. 179, 1998.
[2] ANSYS Autodyn User Manual. Release 18.0, ANSYS Inc.

Performance Evaluation of a Hybrid Warhead for Enhanced Blast Applications

M S Katore
High Energy Materials Research Laboratory
DRDO
Pune
katore.mahesh@hemrl.drdo.in

A K Vishwakarma
High Energy Materials Research Laboratory
DRDO
Pune

A W Gaikwad
High Energy Materials Research Laboratory
DRDO
Pune

M Balaji
High Energy Materials Research Laboratory
DRDO
Pune

J Saji
High Energy Materials Research Laboratory
DRDO
Pune

***Abstract*– Fuel rich explosive charges are being pursued for development of warheads with enhanced lethality in terms of high impulse blast and thermal output. The enhanced effects are achieved due to the post detonation combustion of excess fuel – liquid or solid type- with detonation products as well as with oxygen in air. In the present study, a hybrid warhead concept based on combining fuel rich thermobaric and fuel air explosive charges were designed and tested for performance assessment in field trials. The performance was found to be higher than conventional equivalent charges in terms of high blast impulse and longer duration thermal pulse.**

Keywords*– *Fuel air explosive, thermobaric, warhead, evaluation, enhanced blast

1. Introduction

Current explosive research is focused on application in advanced warheads which produce tailored effects in terms of enhanced blast and temperature effects [1]. Earlier, Fuel Air explosives (FAE) were developed with larger lethal radii for soft targets by creating high impulse blast utilising atmospheric oxygen to take part in detonation reactions. More recently, thermobaric explosives (TBE) have been developed using refined FAE techniques with capability to produce enhanced blast and thermal output. One approach for improving the warhead performance will be to develop hybrid warheads with multiple effects, i.e., combination of two or more of blast, thermobaric, fuel aerosol explosion, or fragmentation effects. Both FAE and TBE belong to wider class of volumetric weapons which make use of external oxygen to enhance the blast or thermal output. In the case of TBE, an excess quantity of metal powder (Al/Mg) is used which react in post detonation phase to sustain the pressure pulse along with a high temperature output (>1500^{o}C) that lasts for hundreds of milliseconds. These fuel rich compositions are optimized to partition the energy release in multiple stages resulting in moderate overpressures which sustain for a longer period along with high temperature output making them highly effective for defeating soft targets with reduced collateral damage [2].

FAEs were developed using liquid fuel which is dispersed in air to form a detonable aerosol which is then initiated to obtain a blast output. FAE weapons have proved the potential for increased performance with high impulse blast and larger lethal radii for soft targets as compared to conventional high explosive warheads [3]. Similarly, thermobaric (TB) explosives are developed using advanced and refined fuel air explosive techniques, to create sustained temperature and overpressure on detonation to defeat soft targets in enclosed spaces [4]. The enhanced blast and thermal effects are achieved by the use of excess metal fuel in the base composition. In the case of TBEs, the compositions may be of liquid or solid type. Solid TBEs consists of high explosive (HE), metal powder and binder whereas liquid TBE are made of exothermically decomposable fuel along with HE and metal powder.

This paper presents the study carried out to assess the feasibility for development of a hybrid warhead consisting of Fuel Air Explosive (FAE) and Thermobaric Explosive (TBE) modules. The primary objective of the work was to test the feasibility of the concept along with assessment of the enhancement in performance in comparison with conventional type of HE (TNT) / FAE / TBE compositions. The FAE and TBE modules were designed, prepared, integrated and static evaluated to assess the performance in terms of blast parameters and thermal output. TNT charge of equivalent charge weight were also prepared and evaluated for comparative performance assessment.

2. Materials and Methods

Solid TBE composition was prepared using RDX and Al powder with hydroxyl terminated poly-butadiene (HTPB) based binder system. The ingredients in required proportions were mixed in a 15 litre capacity vertical planetary mixer and the sequence of additions was selected to maintain process ability. After addition and mixing of curing agent, the composition is cast under vacuum into steel containers and left for complete curing. Propylene oxide was used as fuel for FAE module. FAE charge was prepared by filling the fuel in a serrated cylindrical container (Φ180 x 225 x 1.6 mm) provided with a central burster charge (Φ65 x 235 x 0.5 mm) used for fuel dispersion. The aerosol thus formed, is initiated using TBE charge after a pre-determined delay. An integrated warhead was conceptualized which consist of independent FAE and TBE modules, mechanically and electrically integrated to function in tandem mode. The modules were designed to accommodate 4.2 kg fuel (propylene oxide) and 3.5 kg TBE charge (RDX/Al/HTPB) respectively. The warhead was designed to function in two events with a pre-determined time delay. The integrated FAE-TBE hybrid warhead attached to the stand (stand-off- 1.2m) is shown in Figure 1.

Figure 1: Integrated FAE-TBE warhead module

The schematic arrangement of the integrated FAE- TBE Hybrid warhead is as shown in Figure 2.

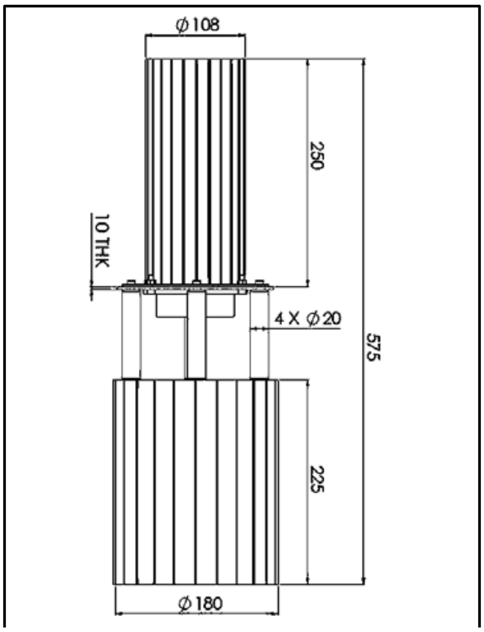

Figure 2: Schematic of Integrated FAE- TBE Hybrid warhead

The performance of warhead has been evaluated by blast pressure and temperature measurements. Blast peak over pressures (POP) was recorded using ICP free field pressure transducers placed at different distances from charge at a height of 2.0 m from ground. The temperature of the event and the duration is measured using two colour pyrometer by non-contact method from a safe distance of about 100 m.

3. Results and discussion

A. Fuel dispersion and aerosol formation

The radius of aerosol and the velocity of fuel dispersion are dependent on the fuel to burster explosive charge weight ratio (F/B) and canister design for a given type of explosive. For FAE-TBE hybrid warhead, (fuel – 4.2 kg propylene oxide, F/B – 105) the fuel dispersion resulted in an aerosol dimensions of Φ 10m x ht. 2.0m at 100ms after bursting. The velocity of fuel dispersion decreased from 178 m/s to 50 m/s during the time period from 1 ms to 100ms. In the case of FAE warhead (fuel - 7.7 kg, F/B - 77), the aerosol dimensions were Φ 11m x ht. 2.1m at 100ms and the velocity decreased from 172 m/s to 55 m/s. Results indicate there is no significant effect on rate of dispersion and area coverage due to the reduced F/B ratio used in FAE-TBE warhead. The use of lower burster charge quantity in this case has resulted in relatively fuel rich aerosol, which was detonated using a higher booster charge ensuring optimal performance. Use of lower F/B ratio in hybrid warhead will help in reducing the shock loads experienced in TBE module during warhead operation. This will result in use of thinner shock barriers and hence will lead to higher explosive loading. Further, the results also indicate possibility for optimisation of time delay subject to detonability of aerosol since there is no significant change in radius or velocity of dispersion after 80ms.

B. Blast performance of warheads

The comparative plots of blast peak overpressure (POP) and blast impulse against scaled distance for FAE, TBE, FAE-TBE (Hybrid) and TNT charges is shown in Figure 3&Figure 4.

The results revealed that FAE-TBE hybrid warhead has performance characteristics of both FAE and TBE compositions.

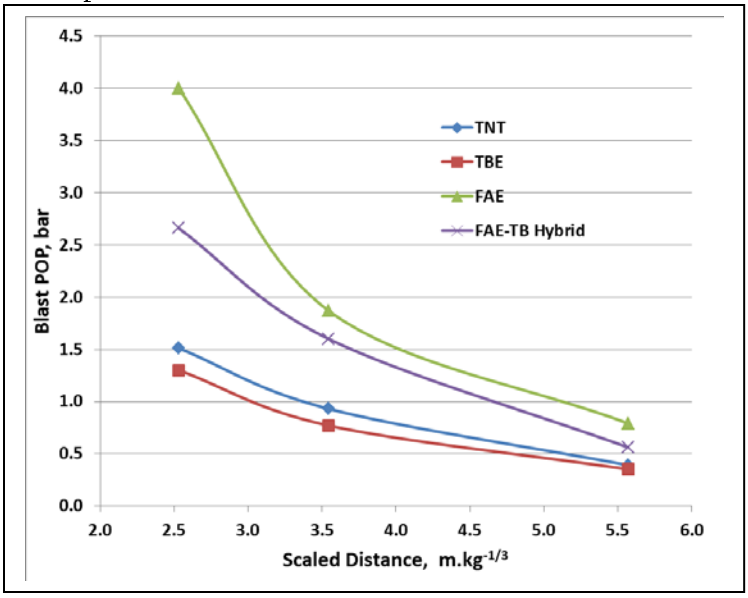

Figure 3: Blast peak overpressure vs scaled distance for FAE, TBE, TNT and FAE-TBE warheads (7.7 kg)

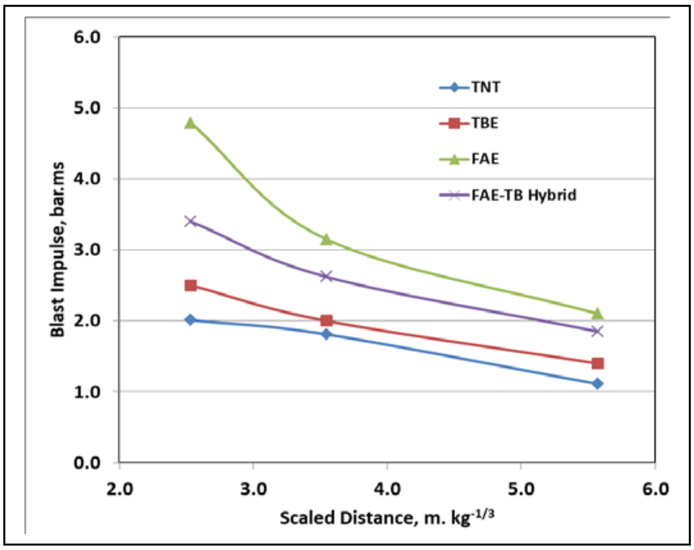

Figure 4 Blast impulse vs scaled distance for FAE, TBE, TNT and FAE-TBE warheads (7.7 kg)

The blast performance for FAE-TBE hybrid warhead in terms of over pressure and impulse was higher than TBE charge but lower than FAE warhead of equivalent weight. The TNT blast data was in agreement with the reported literature for surface burst [6]. The blast profiles measured at distance of 5m from warhead was noisy and provided inconsistent or incomplete profiles. This is due to the proximity of sensors to the detonation zone (FAE aerosol radius - 5.5 m, TBE fireball radius ~ 10m). Further, the blast profiles showed multiple peaks due to incident and ground reflected shock at distance of 7 m which was found to merge at a larger distance of 11m. Considering the repeatability in measurements and effectiveness in operational situations, the blast performance at 11m was considered appropriate for comparative estimations. Hence, TNT data for surface burst were chosen for comparative assessment which agreed quite well with the present experimental data of TNT.

The variation in blast peak over pressure and blast impulse for TNT w.r.t. scaled distance estimated by various scaling laws reported in literature [5-7] is shown in Figure 5 & Figure 6.

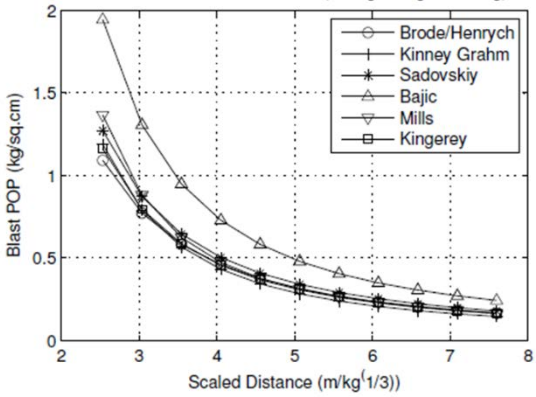

Figure 5: Blast overpressure for 7.7 kg TNT based on scaling laws reported in literature [5-7]

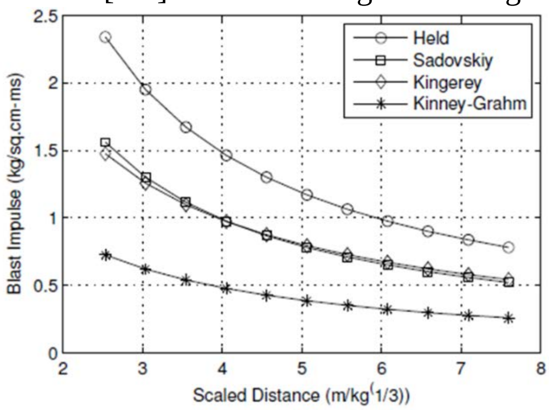

Figure 6: Blast Impulse for 7.7 kg TNT based on scaling laws reported in literature [6-8]

The TNT performance data estimated using equation suggested by Kingery and Bulmash for surface blast has been chosen for further comparison because of wide acceptability, representative values and moderate output [8].

The TNT equivalence for FAE, TBE and FAE-TBE hybrid warheads in terms of blast peak overpressure and impulse at 7m and 11m were estimated by following the standard method.

The weight of TNT required, W_{TNT} to generate same blast POP or impulse as that of equal weight of test warhead at each scaled distance was computed and the corresponding TNT equivalences were calculated by the ratio, W_{TNT}/W where, W is 7.7 kg. The calculated TNT equivalence for hybrid warhead was found to be 1.78 and 2.24 in terms of blast pressure and impulse respectively at a distance of 11m from point of burst as shown in Table 1.

Table 1: TNT equivalence of FAE, TBE and FAE-TBE hybrid warheads.

Explosive	TNT equivalence 11m	
	POP	Impulse
TBE	0.78	1.38
FAE	3.28	2.74
FAE-TB	1.78	2.24

The estimated values can be considered to be conservative since the casing effect of TBE charge is not accounted in the calculations. The enhanced blast performance indicates the improved damage potential of FAE-TBE hybrid warhead compared to conventional TNT or TBE warheads.

C. Fireball characteristics

The analysis of results given in Table 2 of shows that average temperature (1990^{o}C), duration (170ms) and thermal impulse (330^{o}C.s) of TBE are highest which is in agreement with available data [7]. The thermal output from FAE could not be measured in the given experiments. Earlier studies have shown that FAE produced an avg. temp of 1300^{0} C for 5 kg propylene oxide as fuel. In the case of higher weight class warheads (Fuel > 200 kg of Propylene oxide), the avg. temp. obtained was 1352^0 C (Duration 251.5ms) which shows that the thermal output is the characteristic of type of Fuel used. Hence there was not increase in temperature with increase in fuel loading.

Table 2: Thermal output of TNT, FAE, TBE and FAE-TBE hybrid warheads

Explosive charge	Max. Temp., °C	Avg. Temp., °C	Duration, ms	Thermal impulse, °C.s
TNT	2681	1339	57	76
TBE	2739	1994	170	339
FAE	NR	1300	125	162
FAE-TB	1960	1464	96.5	141

FAE-TBE warhead produced a moderate thermal output in terms of average temperature (1460^{o}C) and thermal impulse (141^{o}C.s) which lies in between performance levels of FAE and TBE. The duration of TNT fireball is the lowest wherein post detonation combustion reactions are absent. High speed video records indicated that fireball produced by TBE and FAE-TBE warheads sustained for long duration (>200ms) and has dimension of Φ11m diameter and 6.0m height. The difference in thermal output can be correlated to the net oxygen balance of the compositions wherein the relatively oxygen deficient FAE (OB: -220%) and TNT (-74%) showed inferior performance as compared to TBE (-45%) warhead. The excess fuel component in TBE helped for a better thermal effect by FAE-TBE hybrid warhead (OB: -140%) when compared to FAE or TNT charges. Thus, for FAE-TBE hybrid warhead, the enhanced blast effects (POP and impulse) are supported with a moderate thermal output which is not normally available from an equal sized FAE or conventional HE warhead. Previous studies have shown that thermal output is a strong function of charge weight and will be higher for a scaled up warhead consisting of a higher TBE filling.

4. Conclusions

The following conclusions are drawn from this study:

(i) The results of the static experimentations indicate the feasibility of FAE-TBE hybrid warhead incorporating advantages of both FAE and TBE with improved performance parameters as compared to conventional HE warhead.

(ii) The hybrid FAE-TBE warhead produced superior blast performance (TNT equivalence) in terms of pressure and impulse as compared to TBE and TNT charge of equivalent weight.

5. Acknowledgments

The authors are grateful to The Director, HEMRL, Pune for permission to present the paper in the conference. The authors are also thankful to members of Fuel Air Explosives division, High explosives division and Instrumentation division for the support and help extended during the course of the work.

6. References

[1] Xing, X.L.; et al., Discussions on Thermobaric Explosives, PEP, 39 (2014)14.

[2] Schaefer, R.A.; Nicolich, S.M.; Development & evaluation of new high blast explosives. 36th Int. Ann. Conf. ICT (2005) 9/1.

[3] Murray, S.B., Thibault, P.A., Spray Detonation, in: Shock Wave Science and Technology Reference Library,Vol. 4, Heterogeneous detonation, Zhang, F. (Ed), Springer publishing company, New York (2009).

[4] Gaissmaier, A.E.W.; Aspects of Thermobaric weaponry, ADF Health, 4 (2003) 3.
[5] Goel, M.D.; Matsagar, V.A.; Gupta, A.K. & Marburg, S. An Abridged Review of blast wave parameters. Def. Sci. J., 2012, 62(5), 300-306. doi: 10.14429/dsj.62.1149.
[6] Bajic, Z.; Bogdamov, J.; Jeremic, R. Blast effects evaluation using TNT equivalent. Sci. Tech. Rev., 2009, 59(3-4), 50-53.
[7] Tan, C.M.M.; Masters thesis, Rapid estimation of building damage by conventional weapons, Naval Postgraduate school, Monterey, California.
[8] Spread sheet program based on Kingery, C.N. and Bulmash, G., Airblast parameters from TNT spherical air burst and hemispherical surface burst, Report ARDRL-TR-02555, US Army Ballistic Research Laboratory, 1984 by Williams, M.R., DA-CMT, Cranfield University, Shrivenham, UK.

Insensitive Munition (IM) Compliance Tests for Pre-Fragmented (PF) warhead

(Ms) D N Joshi
Armament Research and Development Establishment
Pune
deepajoshi1911@gmail.com

KK Kulhare
Armament Research and Development Establishment
Pune

Satwinder Singh
Armament Research and Development Establishment
Pune

V K Dixit
Armament Research and Development Establishment
Pune

***Abstract*– Munition implies weapons filled with high explosive which are sensitive to their boosters or igniters, while "Insensitive" implies that the weapon aren't. Insensitive Munitions are munitions that are designed to withstand stimuli representative of severe but credible accidents. The current range of stimuli are shock and impact (from bullets, fragments and Shaped charge jet), heat (from fires or adjacent thermal events and adjacent detonating munitions). The purpose of Insensitive Munitions (IM) testing is to establish the response of a munition to unplanned stimuli when tested under specified conditions and to assess the safety of a munition. Insensitive Munition (IM) Compliance tests applied to all non-nuclear munitions (i.e. all missiles, rockets, pyrotechnics) and munition subsystems (warheads, fuzes, propulsion units, safe & arm devices, pyrotechnic devices, chemical payloads) and other explosive devices. Six unique tests have been required to be conducted to establish insensitivity of munitions as per STANAG as per mission role of weapon subsystem. These tests are summarized as Fast Cook off test (STANAG 4240), Slow Cook off test (STANAG 4382), Bullet Impact test (STANAG 4241), Fragment Impact test (STANAG 4496), Sympathetic Detonation test (STANAG 4396) and Shaped charge jet impact test (STANAG 4526). IM compliance tests for warheads subjected to Air related applications are Fast cook off, Slow cook off, Fragment impact, Bullet impact and Sympathetic detonation. The above mentioned IM tests for Pre Fragmented (PF) warhead are carried out and details for the same are presented in this paper.**

Keywords– Insensitive munitions, safety tests, STANAG specification, Fragmentation warhead, AOP-39

1. Introduction

As far as the name concerned, **Insensitive munitions (IM)** are the weapons filled with high explosive composition i.e. energetic material which are not sensitive to their igniters, boosters or initiation means. Unpredicted behavior of energetic material may lead to major accidents which results in loss of personnel/machineries and equipments. Hence, there is need to carry out IM Compliance tests for Munitions/weapon subsystems filled with high explosive composition i. e. energetic material which may be initiated by means other than intended mode. It minimizes the probability of initiation of high explosive and the severity of subsequent damage to weapon platforms and human life, when munitions are subjected to un anticipated stimuli during manufacture, storage, handling, transportation and disposal or due to accidents. These dangers may exist in both friendly and hostile environment. Due to accidents and subsequent loss of human life, cost of repairing, replacing material and using alternate process IM improvements are mandatory.

Therefore, **Insensitive Munitions (IM) testing** is required to be carried out to establish the response of a munition to unplanned stimuli when tested under specified conditions and to assess the safety of munitions. Introduction of IM into services is intended to enhance the survivability of logistic and tactical combat systems, to minimise injury to personnel, to protect weapons & weapon system platforms and to ensure improved weapon safety & decreased risk for the occurrence of unplanned hazardous events. It provides more cost effective, efficient and safe transport, storage and handling of munitions. Some important features of IM tests are given below.

(i) IM testing differs from all other ordnance and munitions safety testing in that the passing criteria for each test involves a violent response (explosive response).
(ii) In IM testing, the reaction of the munition under test may range from full detonation to no reaction which includes responses with varying degrees of severity between these extremes.
(iii) Munition designers need to incorporate IM features into the design early in design/development phase.
(iv) Use of insensitive explosive materials is one of the most important factors to consider in designing IM.
(v) Insensitive munitions determination based on tests of munition items in the service configurations.
(vi) It will not react violently in an accidental situation.
(vii) Mitigation features can be incorporated into the component/ system design, particularly combination of filling plus casing provides inadequate IM responses.
(viii) Evaluating the effectiveness of external mitigation concepts such as packaging & barriers and establishing the IM characteristics of specific design/system during development stage.
(ix) The results of IM testing define the IM signature for a munition.

2. History of IM testing

US became the foundation of our present IM test standards. In 1964 a system safety directive was established by the US Navy to record warhead vulnerability characteristics and certain safety related characteristics. These included fast and slow cook off tests and bullet impact response. No pass/fail criteria were identified but resulting response to the thermal / impact stimuli was recorded as well as reaction time for the thermal events. IM acceptance was achieved throughout the international community and the test requirements followed with the help of NATO. In 1995 NATO established IM policy and technical requirements. In 2003 US incorporated NATO technical requirements in MIL-STD-210C.

NATO Standardization Agreements (STANAGs) are used for assessment of munition safety and Insensitive Munitions (IM) characteristics of non-nuclear munitions. This standard provides reference tests and test procedures for assessment of safety, hazard classification of munitions/ weapon system. There are two documents that provide guidance for IM testing. STANAG 4439 policy for introduction and assessment of IM tests all of the STANAGs that provide guidance for the individual IM tests. Additional information is provided in AOP-39, guidance on the development, assessment and testing of IM. This document includes the test requirements & assessment methodology for IM signature.

3. Type of reactions from external stimuli

Following types of reactions that could be reported and used to assess IM compliance.

Type	Reaction	Details
I	Detonation	A supersonic decomposition reaction propagates through the energetic material to produce an intense shock in the surrounding medium.
II	Partial Detonation	A supersonic decomposition reaction propagates through partial energetic material. A shock wave is formed & some of the case is fragmented as in detonation.
III	Explosion	Ignition and rapid burning of confined energetic material leading blast. Large or small pieces of the case are often thrown long distances. Unreacted & burning energetic material is also thrown about. Air shocks are produced that cause damage to nearby structures.
IV	Deflagration	Ignition and rapid burning of confined energetic material. No blast or fragmentation damage to the surrounding. Only heat & smoke damage from burning energetic material.
V	Burning	Ignition and burning of energetic material non propulsively. The case may melt or weaken sufficiently to allow mild release of the combustion gases. Debris stays in the area of fire.

4. Configuration of warhead subjected to IM Compliance Tests

Conventional fragmentation warhead consists of a casing filled with high explosive and pre-formed fragments are laid over casing surface. Configuration of pre-fragmented (PF) warhead which is subjected to IM compliance tests is shown in Fig. 1. Overall Weight of warhead is 15 kg. HMX based high explosive composition weighing 4.8 kg was filled in the warhead configuration.

Warhead casing was made of aluminum alloy having thickness 3.5 mm. The outer surface of casing was laid with Tungsten Alloy (TA) cuboid fragments of mass 2.9 gm using resin mix.

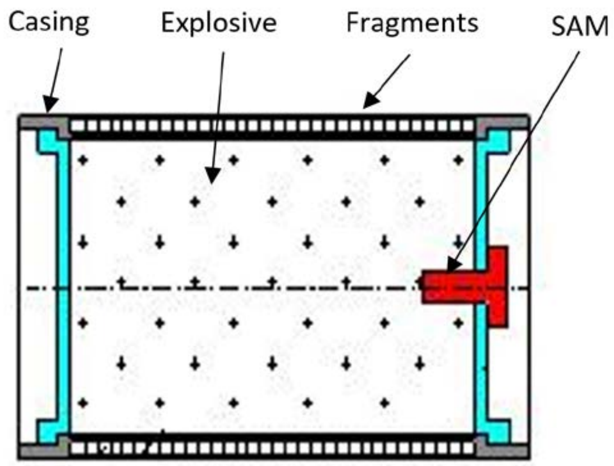

Fig. 1: Configuration of Warhead

5. Tests for Insensitive Munitions (IM) for PF warhead

Fast cook off, Slow cook off, Fragment impact & Bullet impact are carried out in operation mode with bare warhead and Sympathetic detonation with packaging box.

A. Fast cook-off test

Ref: STANAG 4240 & STANAG 4439. This test is required to be performed in accordance with STANAG 4240.

Scope: This test consists of engulfing the test item in the flame envelope of a liquid fuel fire and recording its reaction as a function of time.

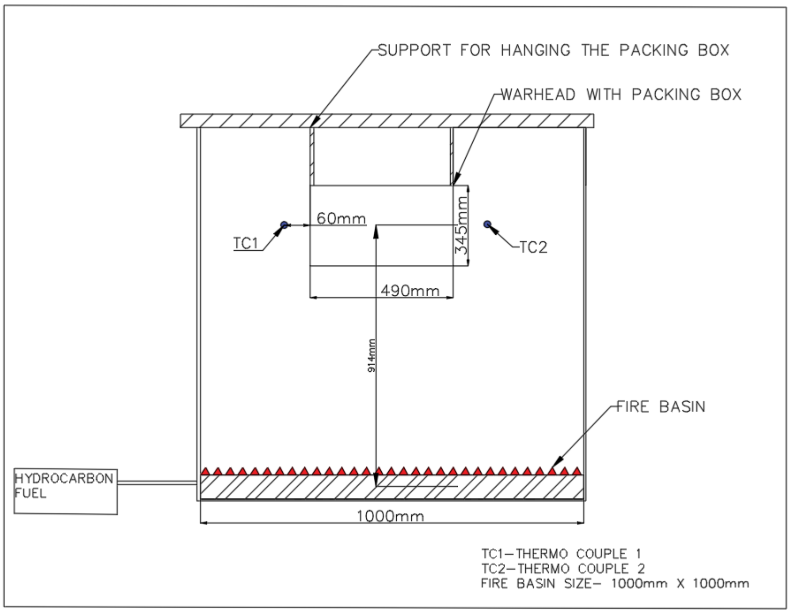

Fig. 2: Fast cook off test

Store required: Explosive filled warhead with dummy SAM

Test procedure: It consists of engulfing the test item in the flame envelope of fire and recording its reaction as a function of time. For air launched weapons, centre line of the item will be 914 mm above the surface of fire basin. The minimum height of the bottom surface of the store above the fuel surface must not be less than 0.2 m as mentioned in STANAG 4240. Any medium such as wood, Hydrocarbon, JP-4, JP-5, Jet A-1, propane and the Natural gas can be used for heating. The article shall be kept in fire till the temperature, as measured by the two thermocouples reaches 540°C±10°C (time zero for measuring reaction time). The thermocouples shall be mounted 40-60 mm from the surface of test article at positions fore, aft, starboard and port along a horizontal plane through the centerline of the test item. The average flame temperature should be at least 870°C at the test item without contribution of burning item. The temperature is determined by averaging the temperature from the time flame reaches 540°C until all ordnance reaction is completed. Details of test are shown in Fig. 2. This test will give an indication of the minimum time in which thermally induced events will occur.

Note: For Storage & Transport conduct this test with packaging. For Operation conduct this test without packaging.

Passing criteria: No reaction more severe than Type V. All safety devices shall remain in safe condition.

Application: Storage/Operation

B. Slow cook-off test

Ref: STANAG 4382 & STANAG 4439. This test is required to be performed in accordance with STANAG 4382.

Scope: This test consists of exposing the test item to slowly increasing temperatures and recording any reaction of the test item as a function of time.

Store required: Explosive filled warhead with dummy SAM

Test procedure: As no analysis has been done earlier, a rate of 25^0C per hour should be used as a default rate for testing. The test facility shall be capable of providing the required thermal environment. Temperature and the elapsed time shall continuously be monitored. A minimum separation of 203 mm between all outer surfaces of test item and inner walls of the oven is required. Details of test are shown in Fig. 3. Stores subjected to the slow heating test shall be deemed to be acceptable if a reaction no greater than a type IV (Deflagration) reaction occurs.

Note: For Storage & Transport conduct this test with packaging. For Operation conduct this test without packaging

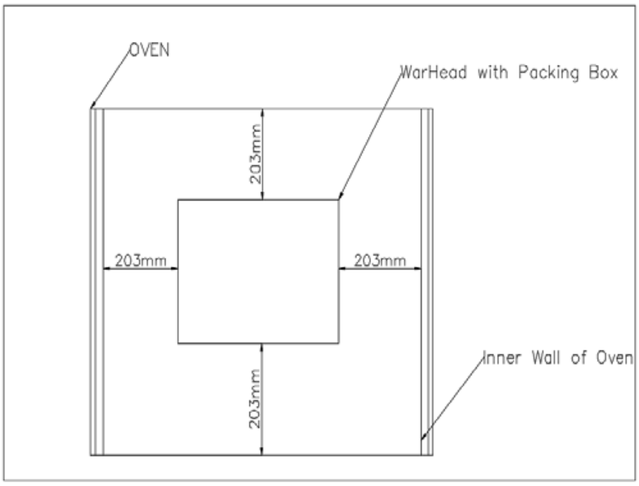

Fig. 3: Slow cook off test

Passing criteria: No reaction more severe than Type V (Burning).

Application: Storage/Operation

C. Bullet impact test

Ref: STANAG 4241 & STANAG 4439. This test is required to be performed in accordance with STANAG 4241.

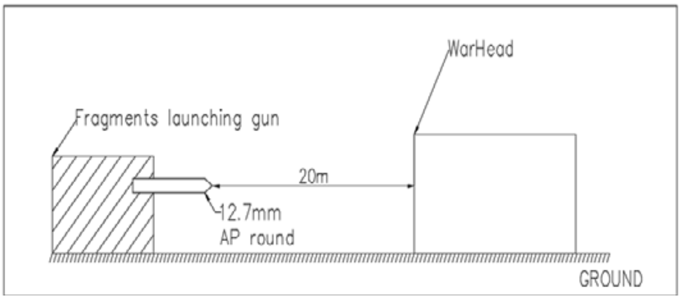

Fig. 4: Bullet Impact test

Scope: This test consists of exposing the test item in the service environments (including storage, transport and processing) in the packaged configuration.

Store required: Explosive filled warhead with dummy SAM

Test procedure: The test item shall normally be positioned with its longest axis horizontal, on a suitable stand at a height to facilitate ease of attack. Test item is impacted by 12.7 mm armor piercing (AP) round fired from a rigidly mounted gun with a velocity of 850 ± 60 m/sec. For bullet attacks a range of approx. 20 m to the target is accepted.

The first point of aim selected is to be one likely to simulate the worst reaction i.e. booster in case of warhead, igniter in case of rocket motor. If no reaction occurs, the point of aim may be changed by agreement with trial authority and a further shot fired. Layout of test is shown in Fig. 4.

Note: For storage and Transport conduct this test with packaging. For Operation conduct this test without packaging

Passing criteria: No reaction more severe than Type V. All safety devices shall remain in safe condition.

Application: Storage/Operation

D. Fragment impact test

Ref: STANAG 4496 & STANAG 4439. This test is required to be performed in accordance with STANAG 4496.

Scope: This test provides procedure for assessing the reaction, if any of a munition to the high velocity impact of a calibrated fragment representative of a bomb or artillery fragment.

Store required: - Explosive filled warhead with dummy SAM

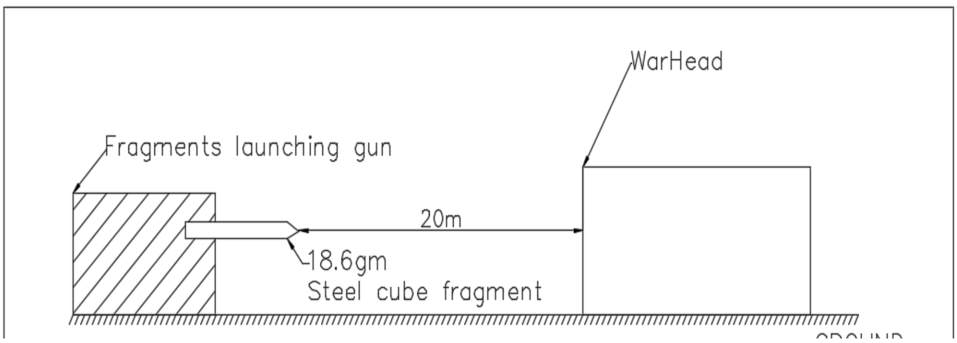

Fig. 5: Fragment Impact test

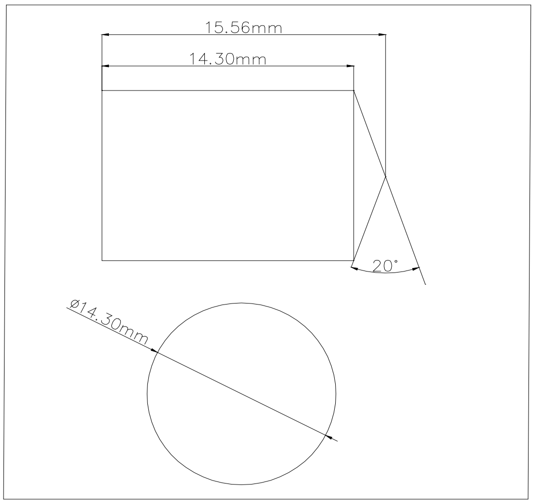

Fig. 6: Std fragment for Fragment Impact test

Test procedure: Fragment impact corresponds to fragment munitions attack. Test item is impacted with high velocity fragments. The fragment has a right circular cylindrical body with a conical nose as shown in Fig. 6. The fragments having weight 18.6 gm travelling with a velocity of 2530 ± 90 m/sec, with an impact of at least 2 but not more than 5 upon the test item. The point of impact of the fragment will be chosen in order to generate the worst reaction. One test is conducted with impact in the centre of the largest presented area of energetic material or component and a second in the most shock sensitive region. The orientation of impact will be normal to the surface of the munition. Details of test are shown in Fig. 5.

Passing criteria: No reaction more severe than Type V. All safety devices shall remain in safe condition.

Application: Operation

Additional Remarks: If test item does not withstand velocity of 2530 m/s, then test shall be carried out with impact velocity of alternate procedure 1830 ± 60 m/s as specified in STANAG 4496.

E. Sympathetic detonation test

Ref: STANAG 4396 & STANAG 4439. Perform this test in accordance with STANAG 4396.

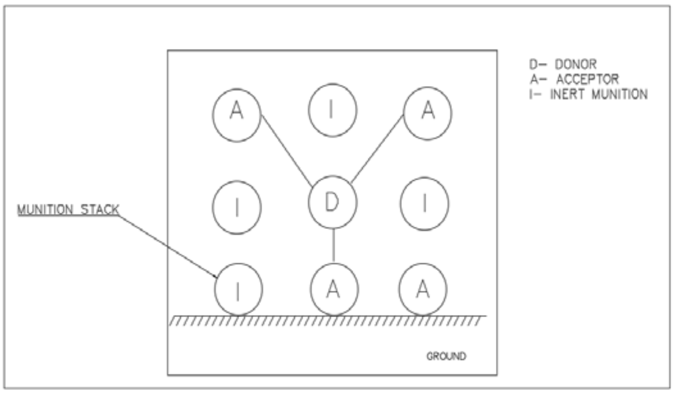

Fig. 7: Sympathetic Detonation test

Scope: This test provides procedure to assess the potential for a munition to sympathetically react to the initiation of an adjacent munition.

Store required: Explosive filled warhead with dummy SAM packed in designated package box. Minimum of one donor and two acceptor packages are required per test.

Test procedure: Munitions are positioned in adjacent locations in a magazine/ storage only. A reacting munition (donor) may transmit blast, shock, fragments to other munitions (acceptor) stored in the vicinity. When stack of munitions, unpackaged or packaged are to be used, explosively inert munitions other than donor and acceptor munitions, may also be used to obtain a reasonable simulation of confinement. The structure, mass and shape of these inert munitions should be similar to those of donor and acceptor munitions. Donor should be initiated using an external stimulus. Detonate one munition (donor) adjacent to one or more like munitions (acceptors). Evaluates likelihood that a detonation reaction may be propagated from one unit to another within a group/stack of munitions. Layout of munition arrangements is shown in Fig. 7.

Passing criteria: No more than Type III (Explosion) is the passing criteria.

Application: Storage

6. Conclusion

The paper presents the requirement of Insensitive Munitions (IM) testing for Pre-Fragmented warhead and various IM compliance tests to be carried out to determine insensitive characteristics of store. To study this effect, configuration of pre-fragmented (PF) warhead with overall mass of 15 kg was subjected to IM compliance tests. HMX based high explosive composition weighing 4.8 kg was filled in the warhead configuration. Warhead casing was made of aluminum alloy having thickness 3.5 mm. The outer surface of casing was laid with Tungsten Alloy (TA) cuboid fragments of mass 2.9 gm using resin mix. The IM compliance tests are carried out are Fast Cook off test, Slow Cook off test, Bullet Impact test, Fragment Impact test and Sympathetic Detonation test. Warhead is qualified three tests which are Fast cook off test (STANAG 4240), Bullet impact (STANAG 4241) and Sympathetic reaction (STANAG 4396). The presented work is useful for IM assessment of warheads during design and development phase and evaluating the effectiveness of external mitigation concepts such as packaging barriers.

7. Acknowledgement

The authors are thankful to the Director ARDE for his guidance and motivation during the conduct of trials and giving permission for the publication.

8. References

[1] Mr. Thomas Swierk "IM testing and Assessments ", NATO OTAN, S & T organization, STO-EN-AVT-214
[2] Kenneth J Graham, President and Chief Technical Officer, Judson Consulting Service, Warrenton, USA, " Insensitive Munitions- Industry Problems and Solutions" ", NATO OTAN, S & T organisation , STO-EN-AVT-214.
[3] AOP-39, Edition-1, "Guidance on the Development, Assessment and Testing of Insensitive Munitions (MURAT), October 1998.
[4] STANAG 4439, Edition-3, "Policy for Introduction and Assessment of Insensitive Munitions (IM), March 2010
[5] STANAG 4240, Edition-2, "Liquid Fuel / External Fire Munitions Test Procedures" April 2003

[6] STANAG 4382, Edition-2, "Slow Heating, Munitions Test Procedures" April 2003
[7] STANAG 4241, Edition-2, " Bullet Impact, Munition Test Procedures" April 2003
[8] STANAG 4496, Edition-1, "Fragment Impact, Munition Test Procedures" Dec 2006
[9] STANAG 4396, Edition-2, "Sympathetic Reaction, Munitions Test Procedures" April 2003
[10] MIL-STD-210C, "Hazard Assessment Tests for Non Nuclear Munitions", July 2003.


ISRO
INDIA
DRDO
HSTDV
RUSTOM-II